GSI

GSI Report 2009-1
May 2009

SCIENTIFIC REPORT 2008

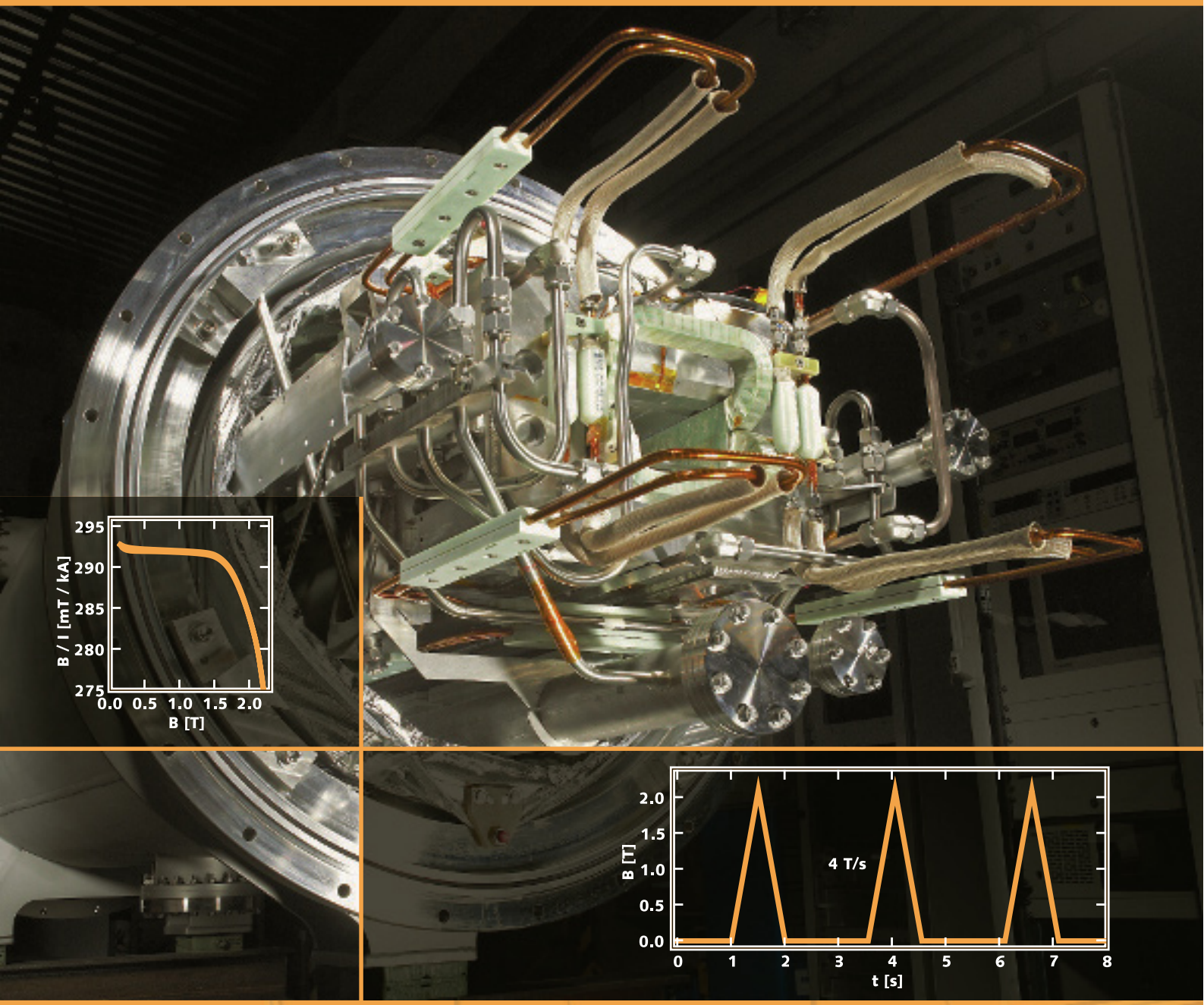

GSI Helmholtzzentrum für Schwerionenforschung GmbH

HELMHOLTZ GEMEINSCHAFT

GSI Scientific Report 2008

GSI Report 2009-1
<http://www.gsi.de/library/GSI-Report-2009-1/>

ISSN: 0174-0814
and GSI Report 2009-1

Publisher: GSI Helmholtzzentrum für Schwerionenforschung GmbH,
Planckstr. 1, 64291 Darmstadt, Germany, <http://www.gsi.de>
GSI is a member of the Helmholtz association of national research centres <http://www.helmholtz.de>.
E-only-edition: <http://www.gsi.de/library/GSI-Report-2009-1/>

Editor: Katrin Große,
Contact: gsilibrary@gsi.de, phone: +496159 712610, fax: +496159 713049.
Cover: Design Bauer & Guse GmbH, Mühltal, Germany and Photograph Babcock Noell GmbH, Würzburg, Germany
Publication Date: May 2005
Technical Team at GSI: T. Badura, I. Giese, K. Große, U. Meyer, V. Schaa and K. Schiebel.

For the production of this report templates and scripts of the JACoW collaboration (Joint Accelerator Conferences on Web <http://www.jacow.org>) were used.

Contents

Status of the FAIR Project

FAIR Joint Core Team*

In 2008 Slovakia joined the FAIR project thus increasing the number of member states to sixteen. The Kingdom of Saudi Arabia has been granted observer status.

The Convention and Articles of Association, which are the prerequisites for the creation of the FAIR company, have been finalized. Further progress is now in the hands of the Foreign Ministries of the partner countries and the German Department of Foreign Affairs, all involved in cross-checking the Convention text in its seven languages (Chinese, German, English, French, Italian, Spanish, Russian).

The key positions of the Scientific and Administrative Directors of FAIR have been advertised. For civil construction planning companies (architect, structural engineer, landscaping and site engineers, technical trades) as well as further experts (health and safety coordinator, surveyor) have been assigned. After an intensive collection of requirements their plans will be finalized in early spring 2009. The progress report on FAIR accelerators can be found in its own chapter.

The FAIR community could celebrate the opening of the first building dedicated to FAIR. It is called FAIR Russia Research Center (FRRC) and is located at the ITEP in Moscow. This joint venture of ROSATOM and the Helmholtz Association will serve the Russian FAIR community as gathering point but can also be used by experiment collaborations for workshops and meetings.

Figure 1: FAIR Russia Research Center

In Germany several similar initiatives were started. The Helmholtz International Center for FAIR , a joint research center of the Universities Frankfurt, Darmstadt and Giessen, the Frankfurt Institute for Advanced Studies (FIAS), GSI and the Helmholtz Association and more than 30 nationally and internationally renowned academic partners, is currently established in the framework of the Hessian initiative for scientific and economic excellence (LOEWE). It will constitute a think tank for forefront interdisciplinary theoretical and experimental research at FAIR.

The ExtreMe Matter Institute (EMMI) will be created on GSI grounds. With EMMI Europe will get a unique infrastructure for interdisciplinary investigations of matter under extreme conditions (from extremely hot matter of the big bang to ultra-cold quantum gases). Although not explicitly dedicated for FAIR, EMMI will have a strong impact on the research at FAIR.

The Helmholtz Graduate School for Hadron and Ion Research ”HGS-HIRe for FAIR” was installed as joint endeavor of the GSI the universities at Darmstadt, Frankfurt, Giessen, Heidelberg and Mainz together with FIAS to promote and support structured PhD education for research associated with GSI and FAIR experimental collaborations.

The first Technical Design Reports (TDR) have been submitted by experiments to the FAIR working group on Science and Technical Issues (STI). The evaluation of the LYCCA calorimeter of HISPEC/DESPEC and the PWO electro-magnetic calorimeter of PANDA have been evaluated positively. In case of PANDA this lead to the purchase of almost one half of the needed crystals already in 2008.

CBM successfully tested micro-strip and gas-electron multiplier detectors together with a self triggering readout chain with proton beams at GSI. This novel type of data acquisition is needed to cope with the high interaction rates at the SIS-300. This was a joint effort of institutes in Kolkata, Krakow, Heidelberg and GSI.

Beam tests with prototype detectors were also performed by other collaborations. R3B for example tested their NeuLAND prototypes in Dresden-Rossendorf and GSI.

Additionally the experiments met in dozens of collaboration meetings of which many were held in the various partner states.

* i.augustin@gsi.de

Mass Production of PWO-II Crystals for the EMC of PANDA*

R. W. Novotny[1], W. Döring[1], V. Dormenev[2], P. Drexler[1], T. Eissner[1], M. Moritz[1], R. Schubert[1], and for the PANDA collaboration

[1]2nd Physics Institute, JLU, Giessen, Germany; [2]RINP, Belarus State University, Minsk, Belarus

The electromagnetic calorimeter (EMC) of the target spectrometer of PANDA is one of the major components to provide high-resolution photon and meson spectroscopy. The calorimeter is based on high resolution lead tungstate crystals (PWO-II) and has to cope with photons in the energy range starting at a few tens of MeV up to several GeVs.

The design concept has been approved based on the R&D of the different components and the expectable overall performance as documented in several test experiments [1]. As a consequence, the mass production of high quality PWO-II crystals has been started in fall 2008 at the manufacturer BTCP (Tula region, Russia) producing the approx. 4000 crystals of the forward endcap.

The tapered crystals are of identical geometry with a total length of 200mm. Based on the ambitious performance of the calorimeter very strict specification limits have been required with respect to optical transmittance, homogeneity, scintillation yield and kinetics. The operation at low temperatures of T=-25°C requires extremely high radiation resistivity. Detailed investigations have confirmed [2] that recovery processes of radiation induced colour centres become extremely slow. The overall loss of the effective light yield depends strongly on the radiation hardness, which can be quantified even at room temperature by the radiation induced change of the absorption constant at the relevant wavelength of 420nm.

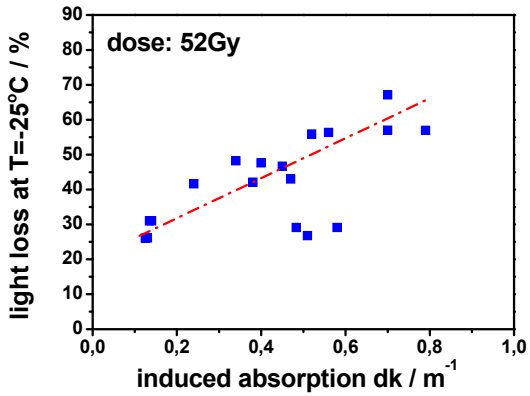

Figure 1: Correlation of the light loss with the induced absorption coefficient dk measured at room temperature. The assembled PWO-II detectors have been irradiated with an integral dose of 52Gy when operated at a temperature of T=-25°C.

According to the correlation shown in Fig. 1 crystals for the most forward region of the endcap can be selected to restrict light losses to a tolerable level. The integral dose of 52Gy imposed by γ-rays corresponds to the expected dose within an experimental period of 6-8 months.

The quality control of the crystals is performed in close collaboration with the CMS-ECAL group at CERN. One of the semiautomatic ACCOS machines was adapted to the PANDA geometry and requirements. Geometrical tolerances as well as optical and scintillation properties are measured for each crystal. The system has been calibrated using metal replica of high accuracy and absolute measurements with reference crystals. Figs. 2 and 3 illustrate the quality parameters of the first lot of 600 samples.

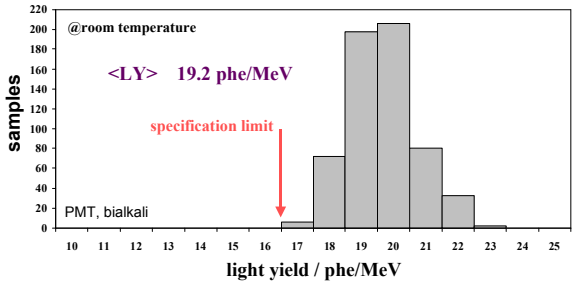

Figure 2: Distribution of the luminescence yield given as photoelectrons measured with a bialkali phototube at room temperature.

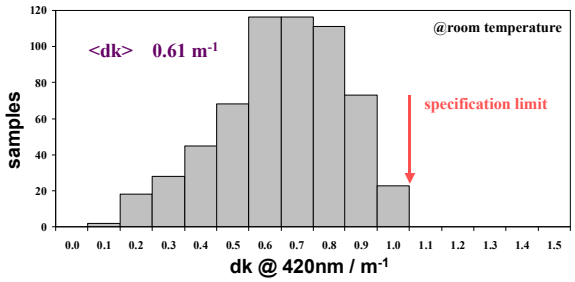

Figure 3: Distribution of the change of the induced absorption coefficient dk at the wavelength of 420nm due to an integral dose of 50Gy measured at room temperature.

Fig. 3 indicates a significant fraction of extremely radiation hard crystals, which is guaranteed by an additional quality requirement that the mean value of dk for each delivery (800-1000 crystals) has to stay below the value of 0.75m^{-1}. The radiation hardness is confirmed at the irradiation facility at the Justus Liebig University at Giessen exploiting an assembly of strong ^{60}Co-sources.

References

[1] "Technical Design Report for: PANDA Electromagnetic Calorimeter (EMC)", arXiv:0810.1216v1, October 2008.

[2] R. W. Novotny et al., IEEE Transactions on Nuclear Science 55(3) June 2008, 1283-1288.

Prototyping a Disc DIRC Detector for PANDA*

M. Düren† [1], I. Brodski[1], A. Hayrapetyan[1], P. Koch[1], K. Kreutzfeldt[1], B. Kröck[1], O. Merle[1], P. Schönmeier [1], M. Sporleder [1], H. Stenzel[1], and M. Zühlsdorf[1]

[1]II. Phys. Inst., Justus-Liebig Universität, Heinrich-Buff-Ring 16, 35392 Giessen, Germany

The endcap disc DIRC for PANDA

One main focus of the PANDA experiment at FAIR is hadron spectroscopy, especially the study and identification of candidates for exotic states such as glueballs and hybrids. To accomplish this challenging task the PANDA detector has to have an excellent capability to identify particles in the whole acceptance region, especially in the forward endcap region. A very compact design of the PANDA detector is possible by having a forward particle identification (PID) detector that is based on the DIRC principle [1], i.e. based on the *detection of internally reflected Cherenkov light* that propagates to the rim of a radiator disc. The Giessen group currently studies a design where the time of propagation (TOP) of the Cherenkov photons inside the radiator disc is used to extract the Cherenkov angle [2]. In this report we present a first prototype of a TOP disc DIRC.

A first TOP disc DIRC prototype

The design of the TOP disc DIRC has been studied in detail using Monte Carlo simulations based on Geant and PandaRoot. As a next step we have built a first simplified prototype to be tested in a real particle beam. The prototype (see Fig. 1) consists of the upper half of the original design and is scaled down by a factor of 2 in size for practical reasons. The prototype radiator is made from Borofloat-33 glass. As seen in Fig. 1, it is made from 3 pieces that are glued together using Epotek 301-2 radiation hard and transparent glue. Nine multi-channel-plate PMTs (MCP-PMTs) from BINP Novosibirsk Institute were installed at the rim of the radiator to detect the internally reflected Cherenkov photons. The dichroic mirrors that are foreseen in the final design to select certain wavelength ranges and to make the light paths of the internally reflected photons longer, were replaced in this simplified prototype by simple mirrors that were placed at the rim of the glass radiator at the positions between the MCP-PMTs.

The prototype has been installed at the test beam facility at DESY using 4 GeV electrons. The analysis of this test run is still ongoing. Fig. 2 shows a preliminary result. Plotted is the difference of the arrival time of the Cherenkov photons in MCP#5 and #6 in picoseconds. The histogram shows two peaks about 2 ns apart, the first one from internally reflected light that propagates to MCP#6 directly, a second one that is first reflected at one of the mirrors at the rim before it continues to propagate to MCP#6. The MCP#5 is used as time reference. A fit of the first peak yields $\sim$ 188 ps time resolution for each of the two MCP channels, which is much larger than the specifications of the MCPs and has its reason mainly in an insufficient electronic set-up during the test experiment. That is currently being improved. In 2009, we plan to continue the test experiment with proton and pion beams at GSI.

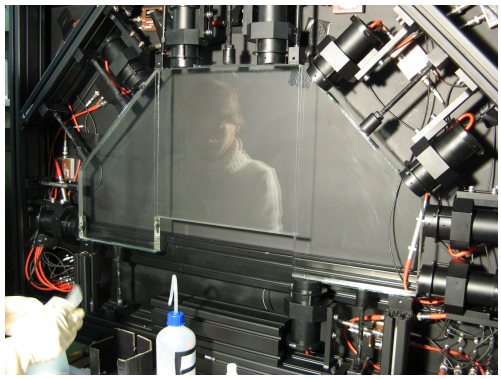

Figure 1: Photo of the DIRC Prototype, before closing the light tight box to go for the test beam measurement.

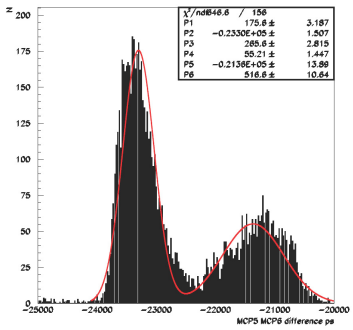

Figure 2: The time difference spectrum of two MCP detectors shows peaks of direct and reflected Cherenkov photons.

References

[1] R. Aleksan et al., Nucl. Inst. Meth. A397 (1997) 261; B. Ratcliff, Nucl. Inst. Meth. A502 (2003) 211.

[2] P. Schönmeier et al., Disc DIRC endcap detector for PANDA@FAIR, Nucl. Inst. Meth. A595 (2008) 108.

* Work supported by GSI and BMBF

† Michael.Dueren@uni-giessen.de

Beam test of a DIRC-barrel-segment for the PANDA Experiment*

R. Hohler[1,2], D. Lehmann[1], K. Peters[1,2], G. Schepers[1], C. Schwarz[1], and C. Sfienti[1,3]

[1]GSI, Darmstadt, Germany; [2]Goethe Universität Frankfurt, Germany; [3]Università degli Studi di Catania, Italy

For the PANDA detector a DIRC-barrel (Detection of Internally Reflected Cherenkov photons) for particle identification is planned around the interaction point [1]. The R&D process proceeds mainly at GSI. A prototype of a segment of this Cherenkov counter was tested in a beam time in September 2008 at GSI. The proton beam had an energy of 2.3 GeV.

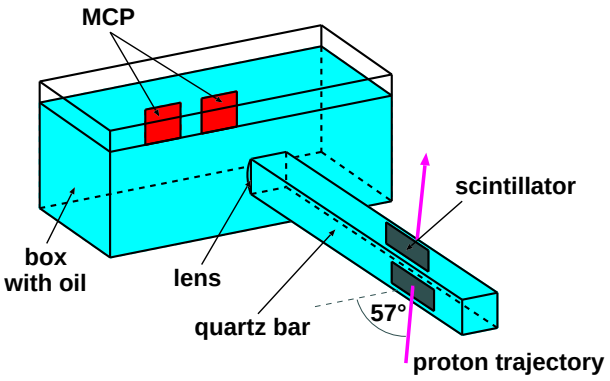

Figure 1: Schematic setup of the beam test.

The setup for the beam time, shown in Figure 1, was installed in a light-tight box. The proton beam hits the quartz bar with an angle of 57° at which two scintillator paddles act as a coincidence trigger. The focussing readout is realized by a lens attached at the bar end followed by a box filled with oil to avoid optical image distortions. Two 8 × 8 pixel MCP-PMTs (Burle 85011-501) at the rear side of the box, which corresponds to a distance bar–detector of 23 cm, measure the incoming Cherenkov photons. The discriminators of each MCP-channel were set to 20 mV. A single photon signal is about 50 mV after all amplification stages. Finally, for the data acquisition the HADES trigger and readout board (TRBv2) was used [2].

Figure 2 shows the expected Cherenkov ring fragments on the rear side of the box and the position of the MCPs on that drawn as rectangulars. For the simulation, a realistic beam spot with a 1-σ-radius of 2 cm was assumed. The color of the markers corresponds with the wavelength of the photons whereas for the ultraviolet range grey is used.

A part of the recorded dataset after multiplicity- and time-cuts is shown in Figure 3. Both MCPs show roughly an accumulation in the region where it is expected. Due to the count statistic we can identify these accumulations of hits as Cherenkov photons. So the simulation and the data are in agreement considering that the position of the two MCPs had an uncertainty of about 1 cm. Furthermore for some pixel, especially for the left MCP, the electronics was not fully working during the beam time (two dead columns). Next, a calibration for the whole setup with LEDs will be performed. Particularly, the signal-to-noise ratio will be investigated first in laboratory and then realistic experimental conditions.

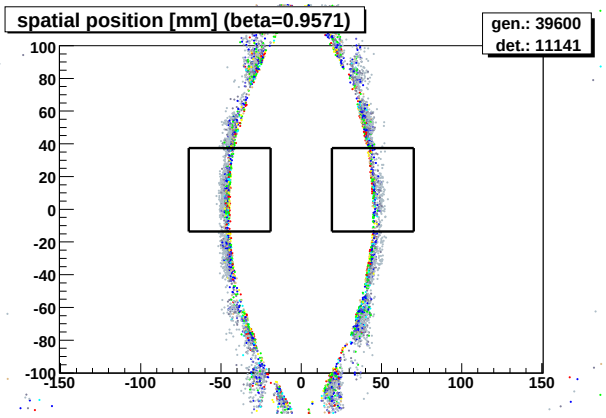

Figure 2: Simulation of the expected Cherenkov ring fragments and the position of the two MCPs.

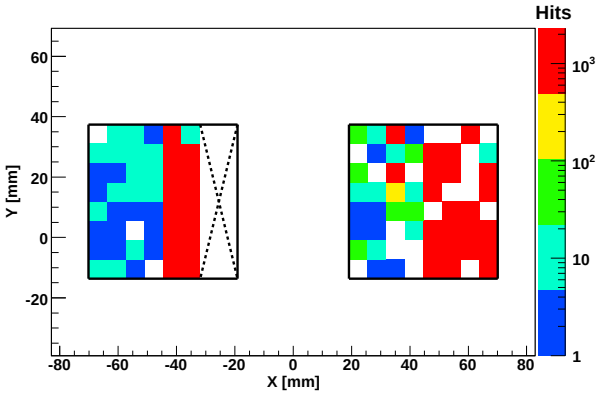

Figure 3: Hits on the two MCPs. Color code is in a logarithmic scale.

References

[1] C. Schwarz et al., NIM A 595 (2008) 112, "The barrel DIRC of the PANDA experiment"

[2] M. Traxler et al., Scientific Report 2006, "A general purpose Trigger and Readout board (TRB) for HADES and FAIR-Experiments"

* Work supported by the European Community RESEARCH INFRASTRUCTURES ACTION under the FP6 program: Structuring the European Research Area - Specific Support Action - DESIGN STUDY (contract 515873 - DIRACsecondary-Beams)

Response of Multi-Anode Microchannel Plate PMTs*

A. Lehmann†[1], A. Britting[1], W. Eyrich[1], A. Teufel[1], F. Uhlig[1], and PANDA Cherenkov group

[1]Physikalisches Institut IV, Universität Erlangen-Nürnberg, Erwin-Rommel-Str. 1, D-91058 Erlangen

Introduction

The identification of charged particles in the PANDA detector will be accomplished with Cherenkov detectors using the DIRC principle. The photon sensors of both subdetectors, the barrel DIRC and the endcap disc DIRC, will be placed inside the PANDA solenoid. This requires devices capable of detecting single photons inside the magnetic field of up to 2 Tesla, leaving currrently as the only candidates microchannel plate (MCP) PMTs or Geiger-mode photo diodes. The readout planes will be rather compact in area; therefore the photon sensors must have pixel sizes of around 5x5 mm^2 to allow a precise reconstruction of the Cherenkov angles.

General Performance Parameters

The performances of three different types of multi-anode MCP-PMTs will be discussed in this report: two 8x8 pixel PMTs of Photonis-Burle (the Planacon 85011 with 25 μm and a prototype with 10 μm pore diameter) and a 1x4 pixel PMT from Hamamatsu (R10754-00-L4 with 10 μm pores). The pixel size of these sensors is 6x6 mm^2 and 5x20 mm^2, respectively. The MCP-PMTs were illuminated with fast light pulses of $\sigma = 14$ ps width at a wavelength of 372 nm.

The maximum gains of these PMTs without a magnetic field are in the range of $(1-2)*10^6$. Inside the high magnetic field of the PANDA solenoid a pore size of 10 μm or less is necessary to ensure a gain high enough for an efficient single photon detection [1]. The time resolutions are better than $\sigma = 50$ ps. The dark count rates per cm^2 of all three types of MCP-PMTs were measured to be in the several kHz-range. These performance parameters would be suitable for the application in the PANDA DIRCs.

More problematic is the rate stability. We expect single photon densities of up to 10 MHz/cm^2, while the gain of the Burle-Photonis MCP-PMT with 25 μm pores starts to drop already at 2*10^5 MHz/cm^2. The 10 μm Burle PMT is better and stays stable up to 1 MHz/cm^2. Only the Hamamatsu PMT shows a constant gain of up to about 10 MHz/cm^2.

Response as a Function of the Surface

An important aspect of a multi-anode PMT is the uniformity of response over its active surface as well as its cross-talk between the individual pixels. To measure the response of the PMTs (count rate homogeneity and cross-talk) as a function of the photon position on the photo cathode we set up an automatic tool to scan the surface of the PMTs.

The results of such scans are shown in Fig. 1. It is evident from the spikes, located at the border lines between the pixels, that some of the photons have been registered by both adjacent channels. The behaviour indicates significant charge sharing among the anode pads for both Burle devices. This effect is not seen for the Hamamatsu PMT.

There are other differences between the three types of MCP-PMTs. Clearly, the 10 μm Burle PMT behaves worst in both count rate homogeneity and cross-talk. The 25 μm device shows a good homogeneity but quite a significant cross-talk, while the Hamamatsu PMT shows a fair count rate homogeneity. Most of the measured cross-talk in the latter device has an electronic nature.

Concerning the requirements for the PANDA DIRCs the 1x4 pixel Hamamatsu MCP-PMT shows the best overall performance among the investigated sensors. It will be a serious candidate for us if its life time is appropriate.

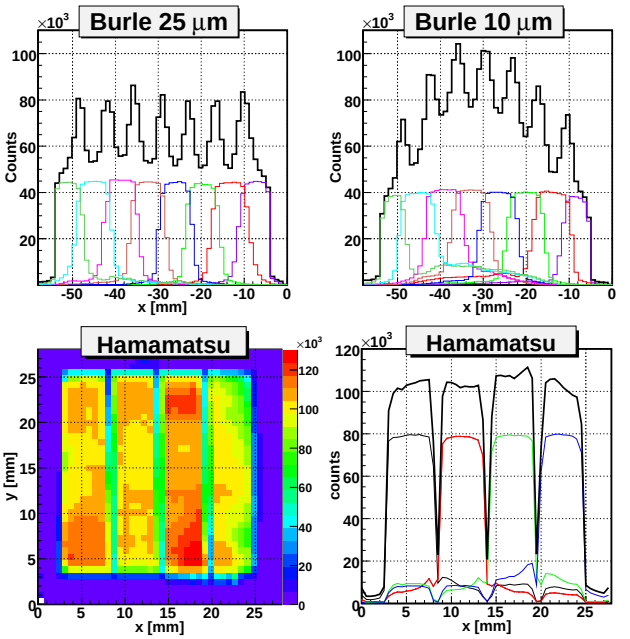

Figure 1: Count rate homogeneity of the Burle-Photonis MCP-PMTs with 25 μm (upper left) and 10 μm pores (upper right) and of the Hamamatsu MCP-PMT (bottom row). The 1D-plots show a sliced distribution along the y-center of the MCP-PMT. The thick black line is the sum, the thin coloured lines are the measured count rates of the individual pixels when the sensor was illuminated at position x.

References

[1] A. Lehmann et al., Nucl. Instr. and Meth. A 595 (2008) 173.

* Work supported by BMBF and GSI

† lehmann@physik.uni-erlangen.de

Spectroscopic studies of $\Lambda\Lambda$–Hypernuclei at PANDA *

A. Sanchez Lorente[†1] and J. Pochodzalla[1]
[1]U Mainz, Germany

Double hypernuclei will be produced at PANDA via a two–steps mechanism[1, 2]. Therefore, spectroscopic information on double hypernuclei will only be obtained via their decay products. Except for the case of very light hypernuclei also neutral particles are emitted unfortunately. Therefore, a unique identification of the double hypernuclei can only be reached via the emitted γ-rays from excited, particle stable states[4].

In order to check the feasibility of performing γ-spectroscopy of double hypernuclei at PANDA, a full devoted simulation of the above mentioned two-steps mechanism has been performed in the standard PANDA framework PANDAroot[3].

In the present work, we introduce a strategy to uniquely assign observable transition to the corresponding hypernuclei. We have assumed that excited double hypernuclei will decay electromagnetically to the ground state, and inmediately a sequential pionic decay will take place. Our strategy is based in measuring the total energy spectra of the corresponding deexcitations of the produced double and single hypernuclei. Since the momenta of the two pions emitted sequentialy are strongly correlated their coincident measurement provides an effective method to tag the production of a double hypernuclei. Fig. 1 shows the momentum correlation of all negative pion candidates emitted from the sequential mesonic decay. The various bumps correspond to the differents double hypernuclei in a secondary ^{12}C target. Those which are mostly produced are marked with empty boxes. The region enclosed by each box will be used to gate the energy spectra of the corresponding double hypernuclei as it is shown in Fig. 2. The arrows mark the expected γ–transitions energies from single and double hypernuclei. In the plots (a) and (d) the 1.684 MeV $\frac{1}{2}^+$ and the 2.86 MeV 2^+ states of $^{11}_{\Lambda\Lambda}$Be and $^{10}_{\Lambda\Lambda}$Be, respectively, can clearly be identified. Because of the limited statistics in the present simulations the states in $^{9}_{\Lambda\Lambda}$Li at 4.55 and 5.96 MeV cannot be identified in (b). The two dominant peaks seen in part (c) result from the decays of excited single hyperfragments produced in the $\Xi^- + C \rightarrow ^4_\Lambda H + ^9_\Lambda Be$ reaction, with an excitation energy of 1.08 MeV and $^9_\Lambda Be$ at an excitation energy of 3.029 and 3.060 MeV respectively. With additional factors[4], the spectra shown in Fig. 2 correspond to a runnig time at PANDA of about two weeks. It is important to realize that gating on double non mesonic weak decays or on mixed weak decays may significantly improve the final rate by up to a factor 10.

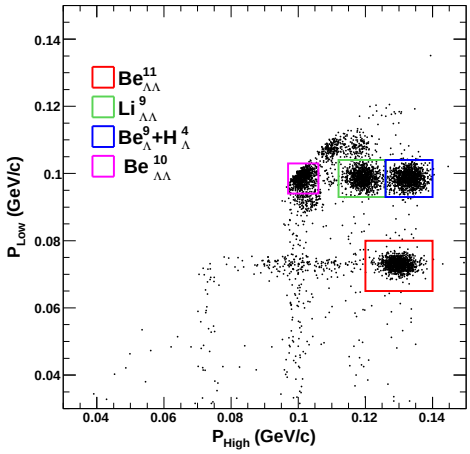

Figure 1: Momentum correlation of all negative pion candidates resulting from the decay of double hypernuclei in a secondary ^{12}C target.

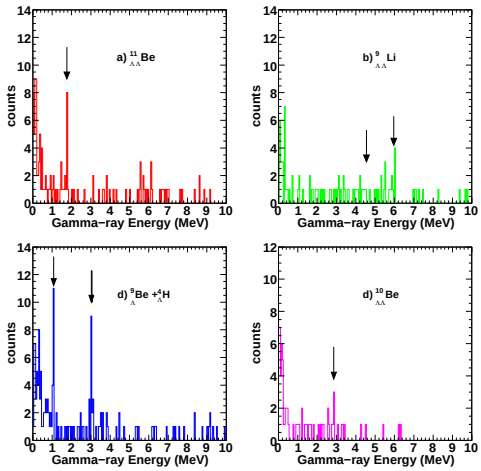

Figure 2: γ–spectra detected in the HPGe–Array by cutting on the two pion momenta. The expected γ–transitions are marked by arrows

References

[1] A. Sanchez Lorente et al., Particle Background simulation for a triple Germanium Cluster detectors at PANDA, in GSI Sci. Rep. 2007

[2] Technical Progress Report for PANDA

[3] A. Sanchez Lorente. PhD thesis, U Mainz.

[4] Physics Book Report for PANDA

*This research is part of the EU integrated infrastructure initiative Hadronphysics project under contract number RII3-CT-2004-506078 and by the BMBF under contract number 06MZ225I.

† lorente@kph.uni-mainz.de

Progress with layout studies of the CBM Silicon Tracking System *

R. Karabowicz[1], A. Kotynia[2], and J. M. Heuser[1]
[1]GSI, Darmstadt, Germany; [2]Warsaw University, Poland

Efficient charged particle tracking and high momentum resolution is one of the central performance requirements for the CBM Silicon Tracking System (STS). The aim of ongoing layout studies is to design a highly granular and low mass detector system that can track the 1000 charged particles that are typically generated in Au+Au collisions at 25 GeV/u projectile energy. A low mass detector is required to achieve a momentum resolution down to 1%. Progress has been made with implementing realistic detector response functions. The performance of the next prototype detectors to be manufactured have been studied.

Detector Layout

The current STS layout comprises eight detector stations fully based on micro-strip detectors. The stations have a ladder structure and are build of 300μm thick double-sided silicon micro-strip sensors with horizontal size of 6 cm and a strip pitch of 60 μm. The strip length was matched to a maximum occupancy of less than 5% and results in a vertical size of one sensor from 2 to 6 cm. Groups of sensors (sectors) are individually read out with the read-out electronics at the perimeter of the STS. Signals from the sectors are sent through thin capton micro-cables to the front-end boards. One of the changes in the current STS layout compared to the version presented in [1] is the orientation of the sensor strips. Previously, one side of the detector had its strips under a 15° stereo angle. The new layout describes strips rotated by a stereo angle of $\pm$7.5° on the front and back planes. This is illustrated in Fig. 1.

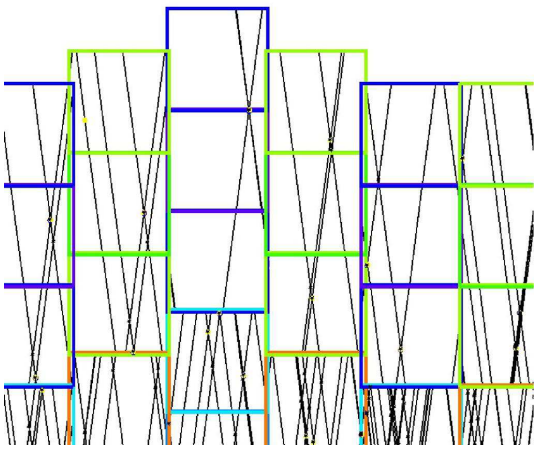

Figure 1: Event display showing active strips in a STS station. The angle between front and back strips is 15°.

Performance Studies

The performance of STS detector was evaluated. Realistic detector response functions were implemented that include signal sharing between strips and the formation of hit clusters. The cluster finding method is based on charge smearing due to particle diffusion in the electric field. The algorithm defines a cluster by finding nearby strips with a signal above a certain threshold. The left part of Fig. 2 shows a graphical illustration of the cluster finding method. The cluster position is calculated by means of a center-of-gravity algorithm. The right part of Fig. 2 shows the distribution of cluster sizes when reconstructing tracks from central collision at 25 GeV/u.

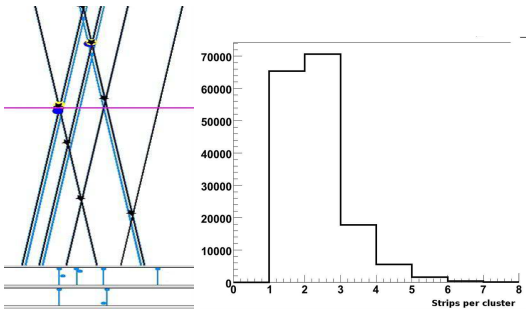

Figure 2: Left: Illustration of the cluster finding method. The bottom part of the figure shows the charge division sampled at the horizontal line in the middle of the picture. Right: Distribution of the number of fired strips per cluster.

When we apply the Cellular Automaton for track finding and the Kalman Filter for track fitting [2] as tuned for previous studies of ideal detector response, the tracking efficiency drops from 97% down to about 90%, for tracks with momenta exceeding 1 GeV/c.

Next steps

To recover the tracking efficiency, we will include the cluster finding method and further aspects of a realistic response model, e.g. channel dead time, into the reconstruction code. The correct determination of the errors of the hit positions is another topic being studied at the moment.

References

[1] R. Karabowicz and J. M. Heuser, "Layout studies of the Silicon Tracking System for the CBM experiment", CBM Progress Report 2007 33

[2] I. Kisel et al., "Fast SIMDized Kalman filter based track fit", CBM Progress Report 2007

* Supported by EU/FP6 HADRONPHYSICS (see anex) and INTAS

Status of the CBM experiment at FAIR*

P. Senger, GSI Darmstadt, and the CBM Collaboration

Observables and experimental challenges

The Compressed Baryonic Matter (CBM) experiment at FAIR is designed to explore the QCD phase diagram in the region of high baryon densities. With CBM we will enter a new era of nuclear matter research by measuring rare diagnostic probes never observed before at FAIR energies, and thus CBM has a unique discovery potential. In order to obtain a complete picture, a comprehensive set of observables will be measured in proton-proton, proton-nucleus, and nucleus-nucleus collisions over the full FAIR energy range. The observables include particles containing charm quarks (D-mesons and charmonia), low-mass vector mesons decaying into lepton pairs (ρ, ω and ϕ mesons), and Ω hyperons (consisting of 3 strange quarks). The measurement of event-by-event fluctuations, correlations, and of the collective flow of hadrons (including rare probes) will provide important information on the dynamics of the fireball.

The experimental challenge is to identify hadrons and leptons in collisions with up to 1000 charged particles at event rates of up to 10 MHz. These measurements require fast and radiation hard detectors, free-streaming read-out electronics, online event-selection based on future CPU/GPU architectures, and a high-speed data acquisition (DAQ) system. Particularly demanding is the measurement of particles with open charm which is based on the real-time selection of displaced vertices with an accuracy of 50 μm.

The CBM experimental facility

The CBM detector system comprises various components. Inside a large aperture dipole magnet there is a Silicon Tracking and Vertexing System which consists of two parts: a Micro-Vertex Detector (MVD, 2 silicon pixel layers) and the Silicon Tracking System (STS, up to 8 layers of silicon micro-strip detectors). The Silicon detector array has to provide the capabilities for track reconstruction, determination of primary and secondary vertices, and momentum determination. A large area detector array consisting of Resistive Plate Chambers (RPC) serves for hadron identification by measuring the particle time-of-flight with high precision. An electromagnetic calorimeter (ECAL) will be used for the identification of photons. Projectile spectator fragments will be detected with a hadron calorimeter (PSD). Both calorimeters are based on lead/scintillator "Shashlik" technology. Electron-positron pairs from the decay of low mass vector mesons will be identified by a Ring Imaging Cherenkov (RICH) detector and a Transition Radiation Detector (TRD). The upper part of figure 1 depicts the CBM experimental setup with RICH and TRD. The RICH will be constructed such that it can be removed and replaced by a muon detection system consisting of hadron absorber layers (made of iron) sandwiched by large area tracking detector layers (see lower part of figure 1. In the following we briefly review the status of the feasibility studies and the detector R&D for CBM.

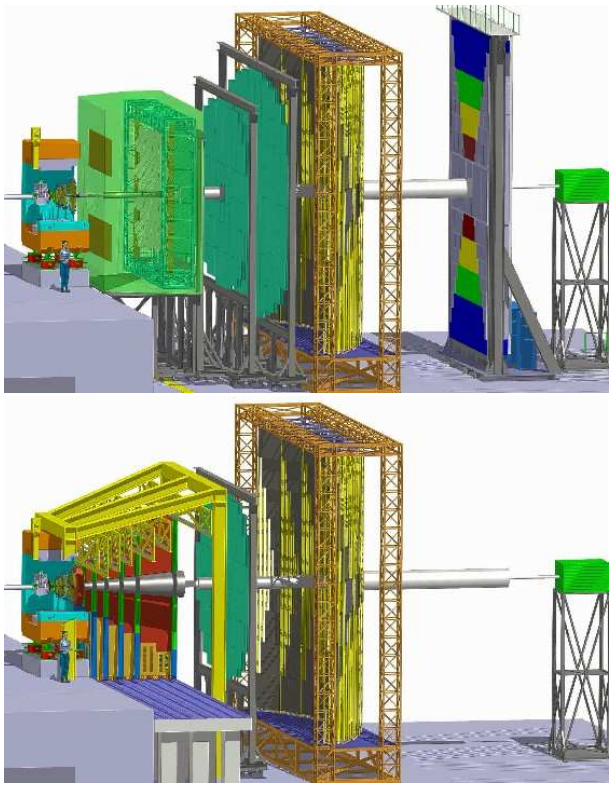

Figure 1: The Compressed Baryonic Matter (CBM) experiment at FAIR with RICH and TRD (upper part), and with the muon detection system replacing the RICH (lower part).

The Silicon Tracking System

Progress with the development of the Silicon Tracking System was achieved in several fields. The prototype micro-strip detectors CBM01, designed and produced in 2007, were assembled into a first small STS demonstrator system. Equipped with prototypes of self-triggering front-end electronics, the system was successfully tested with a 2.5 GeV proton beam at GSI. Another demonstrator system consisting of micro-strip detectors read out through first prototypes of ultra-thin micro-cables was successfully

* Work supported by EU/FP6 HADRONPHYSICS (see Annex) and by INTAS

tested with a 20 GeV proton beam at IHEP Protvino. The CBM demonstrator was integrated into the beam tracker of the SVD-2 experiment and contributed to data taking. The simulation studies of the STS system were improved by implementing realistic detector response functions and cluster finding at the input of the track reconstruction code. The next generation full-size CBM micro-strip prototype detector has been simulated and its performance has been assessed. The development of radiation hard detectors has been addressed with the prototype wafer CBM02, designed and produced in 2008 in cooperation with CIS, Erfurt. It provides various test detectors to explore several radiation tolerant designs. Simulation tools are being set up at GSI to carry out detailed calculations of the radiation tolerance of forthcoming CBM silicon detectors.

D meson identification and vertex detector

The Micro-Vertex Detector (MVD) is needed for open charm measurements which require high-precision vertexing. The MVD consists of two layers of Silicon pixel detectors composed of Monolithic Active Pixel Sensors (MAPS) which can be made very thin in order to reduce multiple scattering. The R&D on the MVD concentrates on the development of radiation hard and fast sensors. A large MAPS with massive parallel read-out has been built and successfully tested. The construction of a demonstrator is in progress. Feasibility studies have been performed for the measurement of particles with open charm ($D^0, D^{\pm}, D_s$, and Λ_c) using a detector setup consisting of the MVD and 8 double-sided micro-strip Silicon detector stations. The MVD was implemented with a realistic material budget which includes sensors, cooling and support structure.

Hadron Identification by Time-of-Flight

Hadron identification in CBM is performed by combining the tracks in STS and TRD with hits in the timing RPC. The total reconstruction efficiency is on the level of 86%. With 80 ps time resolution kaons and pions are separated by 2σ in the squared mass distribution for $p < 3.5$ GeV/c. In order to achieve a certain purity of selected kaons for event-by-event K/π fluctuations momentum cutoffs have to be applied. Simulations demonstrate that this procedure results in a systematic increase of dynamical fluctuations on the order of (1-2)% compared to an analysis in the full momentum range. The R&D on prototype timing RPCs concentrates on high rate capability, low resistivity material, long term stability and the realization of large arrays with overall excellent timing performance.

Electron identification with RICH and TRD

The gaseous RICH detector was redesigned in order to reduce its size and costs without loss of performance. This was achieved by changing the radiator from N_2 to CO_2, and by improving the ring recognition algorithm for high ring densities. Detailed simulations have shown that 6 mm thick glass mirrors and an aluminum support structure do not deteriorate the global tracking performance. First glass mirror prototypes purchased from a standard production process from FLABEG, Germany, have been tested and showed good reflectivity, however still have a deficiency in surface homogeneity. The use of wavelength-shifter films for an enhanced number of measured Cherenkov photons is reinvestigated and shows promising results. The TRD concept has been optimized such that it is possible to reduce the number of stations. Real size prototype detectors with a double gas layer and central pad readout are under construction. This technology is well suited for high rate operation, and will be used in inner part of the TRD stations. For the detectors placed in the outer parts of the stations the rate requirements are less harsh, and the gas gap could be larger. Simulations for low-mass dileptons and charmonium clearly show the feasibility of these measurements. The development of a J/ψ trigger algorithm is in progress.

Muon measurements with hadron absorbers

The CBM muon detector consists of an alternating absorber detector system located just behind the Silicon Tracking System (STS). Optimized tracking routines provide a tracking efficiency of more than 95% for muons passing the absorber. The largest source of background tracks are muons from weak decays of hadrons in the muon absorber system. The track reconstruction efficiency is robust against additional background from uncorrelated and correlated noise hits. The muon detector system has been optimized with respect to the number and thickness of absorbers, and the number of detector layers. A flexible detector segmentation algorithm has been developed in order to find a compromise between track reconstruction efficiency and number of readout channels. Feasibility studies on muon pair reconstruction have been performed for several beam energies and collision systems. Finally, a dimuon trigger concept has been developed. The muon detector development concentrates on the construction and test of prototype gaseous detectors based on GEM technology. A successful test of prototype GEM detectors coupled to a free-streaming data read-out and acquisition system has been performed at GSI with a proton beam.

Online event selection

A stand alone package for on-line event selection has been developed in order to investigate its performance on different modern and future CPU/GPU architectures. A Kalman filter based track fitting procedure has been ported to NVIDIA graphics cards. As a result, the speed of track reconstruction could be improved to 46 ns/track. The scalability of the SIMD Kalman filter based track fit has been investigated on different multi-core CPU systems.

Development of microstrip detectors for the CBM Silicon Tracking System*

J.M. Heuser[1], C.J. Schmidt[1], A. Lymanets[2], R. Röder[3], and L. Long[3]
[1]GSI, Darmstadt, Germany; [2]FIAS, University of Frankfurt, Germany; [3]CIS, Erfurt, Germany

The first prototypes of double-sided microstrip detectors for the CBM Silicon Tracking System, designed and produced in 2007 in cooperation of GSI and CIS [1], have meanwhile been applied to in-beam experiments of CBM prototype detector systems. These *CBM01* [2] sensors were primarily designed for investigations of a detector topology compatible with the proposed construction of particularly low-mass tracking stations.

New detector developments in 2008 addressed the exploration of radiation tolerant design features. With support from BMWI [3], a new wafer *CBM02* has been designed at CIS carrying 2 pixel detectors, 18 strip detectors and various test structures including *pin* diodes. The layout of the 4" wafer is shown in Fig. 1. The largest structures are double-sided orthogonal microstrip detectors with 256 AC-coupled strips of 50 and 80 μm pitch per side. Every detector is different and includes either structures for punch-through biasing, poly-silicon biasing, or a combination of both. On the n-side, the strip insulation was realized in p-stop, p-spray and field plate technology. Various guard ring structures have been implemented. A batch of 18 wafers was produced on 285 μm thick n-type float-zone material, every wafer with a different p doping concentration. The detectors, shown in Fig. 2 after wafer dicing, are being characterized in the laboratory. A bias voltage scan for a 50 μm pitch strip detector is shown in Fig 3. A reference tracking telescope under construction for the CBM beam test runs at GSI will utilize these detectors. First irradiation experiments with *pin* diodes as shown in the photo have been performed very recently in neutron beams. Their evaluation is ongoing and are supposed to yield information on the effectiveness of the different designs towards radiation tolerance.

We plan to design a next full-size double-sided CBM detector prototype with poly-silicon biasing and a $\pm$7.5 degree stereo angle of the strips w.r.t. the detector edge. The new layout has several advantages for the engineering of module components. The detector, to be produced in several sizes, i.e. strip lengths, will feature a double-metal interconnection layer on both stereo sides.

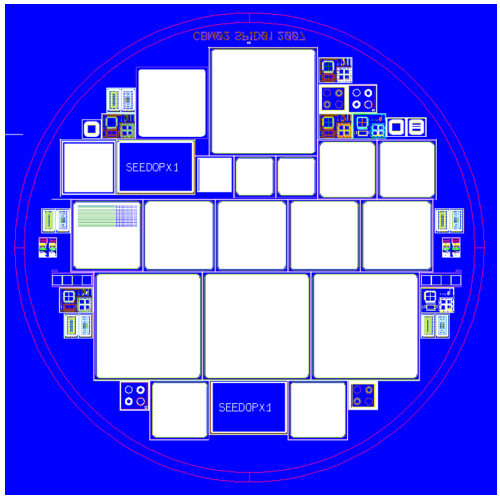

Figure 1: Layout of the CBM02 wafer with various double-sided microstrip test detectors and other test structures.

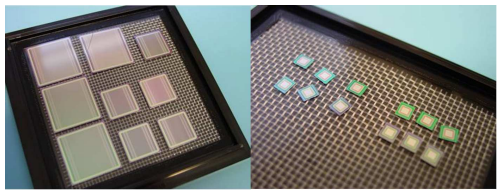

Figure 2: CBM02 test detectors and pin diodes.

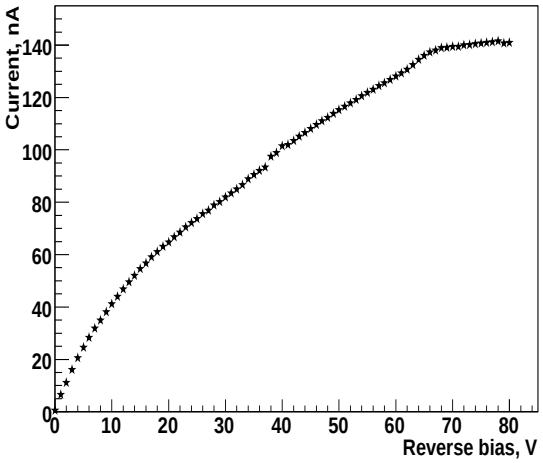

Figure 3: Operation of a CBM02 test detector with poly-silicon biasing structure. Full depletion is reached at about 70 V reverse bias.

References

[1] CIS Research Institute for Micro Sensors and Photovoltaics GmbH, Erfurt, Germany, http://www.cismst.de

[2] J.M. Heuser et al., GSI Report 2008-1 9

[3] German Federal Ministry of Economics and Technology (BMWI), project INNOWAT SPID

* Supported by EU/FP6 HADRONPHYSICS (see annex) and INTAS

First test of a prototype CBM silicon detector system in a proton beam at GSI*

J.M. Heuser[1], W. Niebur[1], R. Karabowicz[1], W. Müller[1], V. Friese[1], C.J. Schmidt[1], R. Lalik[2], A. Lymanets[3], Y. Murin[4], P. Nomokonov[4], and the CBM Collaboration

[1]GSI Darmstadt; [2]AGH Krakow; [3]FIAS University of Frankfurt; [4]JINR Dubna

In September 2008, the CBM collaboration performed the first essential test of two prototype detector systems in a 2.5 GeV proton beam at GSI. The experiment at the HTD beam line in Cave C comprised prototype micro-strip detectors of the Silicon Tracking System, and gas-electron-multiplier (GEM) detectors. The detectors were coupled to a self-triggering front-end electronics and data acquisition system. This novel data read-out and acquisition concept is being developed for nuclear interaction rates of up to 10 millions per second. It aims at enabeling the online reconstruction of collision events with up to 1000 produced particles. In a further measurement the radiation tolerance of Field Programmable Gate Arrays (FPGAs) was investigated.

The silicon detector setup is shown in Fig. 1. It comprised two detector boards equipped with prototype microstrip sensors *CBM01* developed by the GSI-CBM group and CIS Erfurt [1], and two readout boards developed at GSI around the *n-XYTER* [2] chip, developed in a different project. The readout chain included further *Syscore* controller boards [3] for communicating with the *n-XYTER* electronics, and the GSI data acquisition system *DABC* [4].

The commissioning of the silicon detector system was performed with a radioactive source. The ADC spectra of several readout channels are shown in Fig. 2. Response to the proton beam is shown in Fig. 3. The correlation of fired horizontal and vertical strips from the up-stream and the down-stream detector is clearly visible, only linked through the time measurement done by the front-end electronics.

The test demonstrated the validity of the CBM data acquisition concept based on detector systems read out with self-triggering front-end electronics. Three different detector partitions were commonly read out. The full data chain was successfully realized, from the detectors' front end to data in the acquisition system's raw format and FairRoot format, allowing for on-line monitoring during the experiment and subsequent detailed off-line analysis. For the characterization of forthcoming prototype components of the CBM Silicon Tracking System, a reference tracking telescope is under preparation.

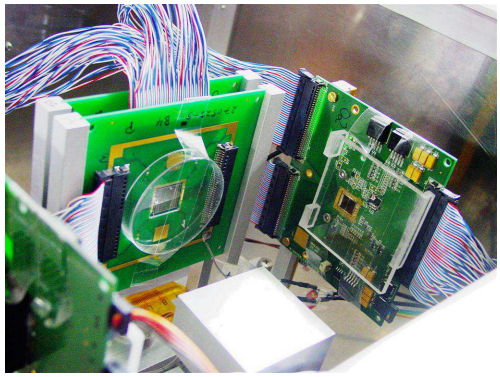

Figure 1: Test system with two CBM01 silicon microstrip detectors and n-XYTER readout boards.

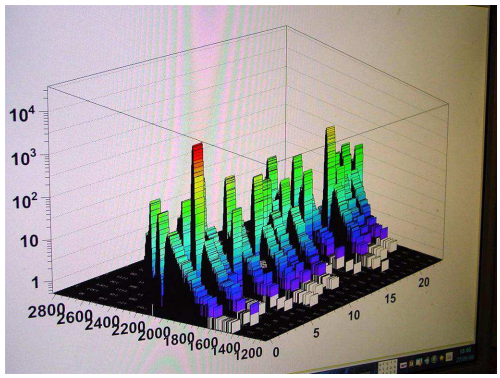

Figure 2: Commissioning of the test system: ADC spectra from a ^{90}Sr β^- source in several readout channels.

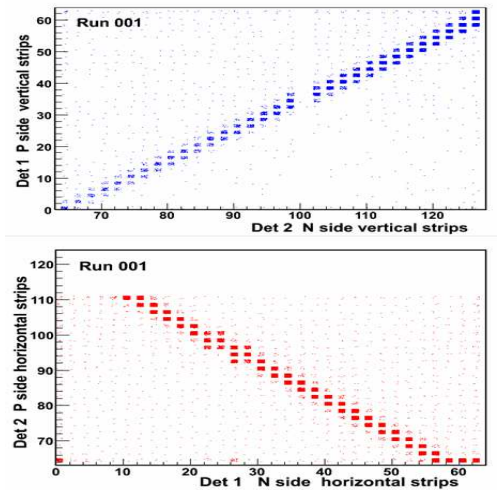

Figure 3: Correlation of fired strips in two silicon microstrip detectors.

References

[1] J.M. Heuser et al., GSI Report 2008-1 9

[2] A.S. Brogna et al., Nucl. Instr. Meth. Phys. Res. A568 (2006) 301-308

[3] W.F.J. Müller, GSI DOC-2007-Apr-100

[4] http://dabc.gsi.de

* Supported by EU/FP6 HADRONPHYSICS (see annex) and INTAS

First test of a CBM silicon detector prototype in a physics experiment*

J.M. Heuser[1] and the CBM-MPD Silicon Tracking System Consortium[2]

[1]GSI Darmstadt; [2]GSI Darmstadt, JINR Dubna, SINP-MSU Moscow, KRI St.Petersburg, SU St.Petersburg, BITP Kiev, SE SRTIIE Kharkov, IHEP Protvino

From November 19 to December 1, 2008, the first prototype of a silicon microstrip tracking module for the FAIR experiment CBM, shown in Fig. 1, was tested in the SVD-2 detector at the Institute for High Energy Physics (IHEP) Protvino, Russia, and contributed to the physics data taking of the experiment.

The *Spectrometer with Vertex Detector* (SVD) experiment at the U70 accelerator of IHEP was designed to explore charm production in proton-proton and proton-nucleus collisions. In the current setup, the SVD-2 experiment [1] investigates the physics of "thermalization" in collisions of a proton beam of up to 70 GeV energy with a liquid hydrogen target. The experiment comprises a 3-station beam tracker upstream and a 5-station vertex detector downstream of the target, all built from high-resolution silicon microstrip detectors. For the recent test, one of the SVD-2 beam tracker stations was exchanged with the CBM demonstrator (see Fig. 2), allowing characterizing its performance during the start-up period of the experiment with a parasitic beam. The results include measurements of the detector response acquired with the SVD-2's Gassiplex front-end boards, the spatial resolution (see Fig. 3) and particle detection efficiency. The CBM station performed well and remained fully integrated in the experiment for the subsequent physics data taking.

The CBM detector prototype has been built by the CBM-MPD Silicon Tracking System Consortium [2], a cooperation of teams from several institutes, including GSI Darmstadt, JINR Dubna, SINP-MSU Moscow, SE SRTIIE Kharkov and IHEP Protvino. The consortium, established by GSI and JINR, focuses on the technical realization of an ultra-light silicon tracking detector system for the CBM experiment at FAIR and the MPD experiment at NICA. The utilized double-sided silicon microstrip detector with orthogonal strips of 50.7 μm pitch, *CBM01* [3], originates from a development of the CBM group at GSI in cooperation with the CIS Research Institute for Micro Sensors and Photovoltaics in Erfurt, Germany. The integration of the silicon sensor, very thin readout cables and front-end electronics into an operational detector station, followed by its successful characterization with beam in the SVD-2 experiment and application to the physics data taking, was achieved in an efficient cooperation of the teams from Germany, Russia and Ukraine.

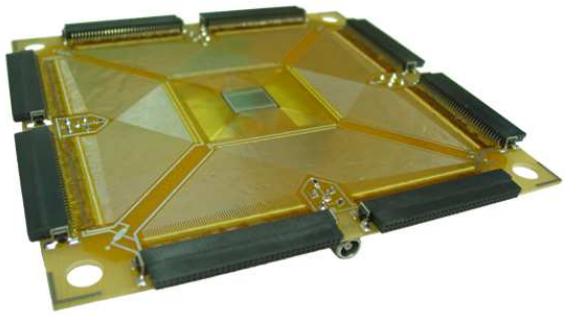

Figure 1: Demonstrator tracking module comprising a CBM01 microstrip detector and microcables.

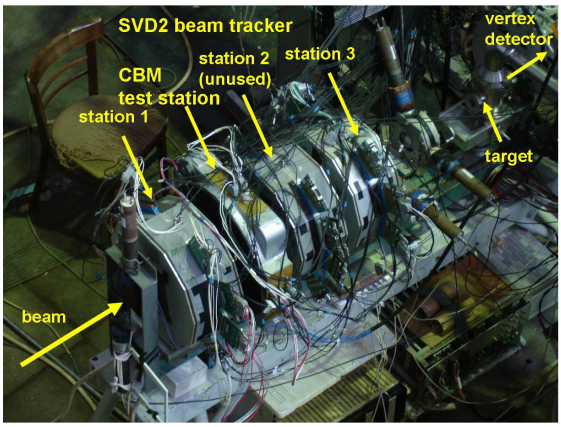

Figure 2: CBM01 test tracking station integrated in the beam tracker of the SVD-2 experiment.

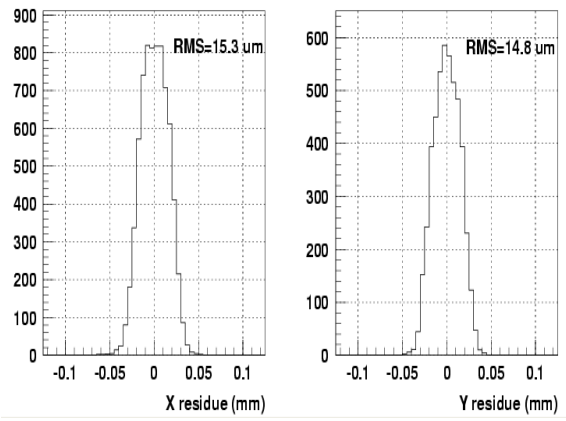

Figure 3: Spatial resolution of the CBM01 sensor including the full chain of front-end electronics, alignment and tracking with the SVD-2 beam tracker and vertex detector.

References

[1] http://www-svd.sinp.msu.ru
[2] http://sunse.jinr.ru/projects/sts/abstract_sts.html
[3] J.M. Heuser et al., GSI Report 2008-1 9

* Supported by EU/FP6 HADRONPHYSICS (see annex) and INTAS

Cellular automaton track finder in realistic STS detector geometry

D. Golubkov[1], R. Karabowicz[2], I. Kisel[*2,3], I. Rostovtseva[1], and Yu. Zaitsev[1]

[1]ITEP, Institute for Theoretical and Experimental Physics, Russia; [2]GSI, Darmstadt, Germany; [3]KIP, University of Heidelberg, Germany

The cellular automaton (CA) based track finder of the CBM experiment [1, 2] is a flexible algorithm operating on space-points which makes it maximally independent of the actual geometry of the STS detector. Nevertheless, the requirements on the speed and accuracy of the algorithm due to its application at the trigger level force one to optimize and continually adjust the algorithm to the changing geometry of the STS detector and sometimes even influence the choice of the detector configuration.

Following the recent developments of the STS detector several important modifications have been implemented in the CA track finder:

1. change of the detector geometry from a single-layer one to the geometry with overlapping sensors;
2. adaptation to various updates of the STS digitization which include realistic detector response and clusterization;
3. making the algorithm work independent of the number of stations;
4. support for different stereo-angles of the strips located on the front and back-planes of the STS sensors.

The largest amount of modifications to the algorithm and the most detailed studies were dedicated to the introduction of the geometry with overlapping sensors since the required changes were related to the procedure of the extrapolation through an inhomogeneous magnetic field which is the most computationally expensive part of the algorithm.

In the original geometry all hits in a station had the same position Z_{station} and the track candidates were extrapolated between the centers of the stations. The more realistic geometry with overlapping sensors has 8 sensors located at different Z positions in each station (with a typical distance in Z between the sensor and the center of the station $\Delta Z \leq 0.25$ cm). The unmodified algorithm used with such geometry lost $\sim 20\%$ in the efficiency. On the other hand a straightforward solution involving extrapolation through an inhomogeneous magnetic field to each sensor would be too computationally expensive, therefore the task was split in two separate steps:

- extrapolation of the track candidate to the center of the station Z_{station};
- linear extrapolation of the track candidate to Z_{hit} inside the station, $\Delta Z \leq 0.25$ cm.

The described modifications were implemented throughout the algorithm in both the tracklet construction and in the Kalman Filter track fit. After the modification the CA track finder recovered the high efficiency and speed for the STS geometry with overlapping sensors.

The validity of the linear extrapolation step has been further investigated in detail. Neglecting the energy loss, multiple scattering and the magnetic field variation inside a station, an estimate of the accuracy of the linear extrapolation depending on the field strength and track momentum was obtained. Fig. 1 shows the track finding efficiency as a function of the distance of the linear step of the extrapolation inside a station. The results were obtained using an

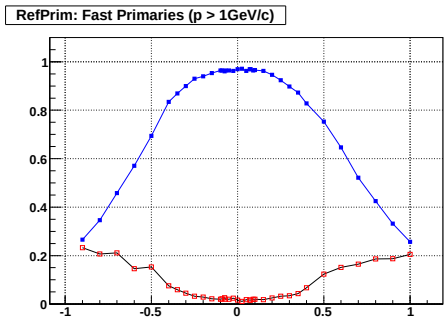

Figure 1: Track finding efficiency (filled squares) and kill fraction (open squares) versus ΔZ distance of the linear extrapolation

MC sample of central Au+Au collisions at 25 AGeV and demonstrate [3] that the linear extrapolation is valid without losses of efficiency up to the distances $\Delta Z \sim 0.2$ cm.

All mentioned modifications have been included in the cbmroot framework of the CBM experiment. Both the STS detector geometry and the digitization scheme are still under development which will require further adaptation of the CA track finder.

Currently we also investigate parallelization of the CA algorithm and its behavior depending on the smoothness of the magnetic field.

References

[1] Compressed Baryonic Matter Experiment, Technical Status Report, GSI, Darmstadt, 2005.

[2] I. Kisel, Event reconstruction in the CBM experiment. Nucl. Instr. and Meth. A566 (2006) 85–88.

[3] I. Kisel, I. Rostovtseva, Study of L1 CA track finder with new STS geometry and possibilities of parallel computing, 12th CBM collaboration meeting, Dubna, 14 October 2008.

* I.Kisel@gsi.de

Development of radiation hard silicon detectors for the CBM Silicon Tracking System using Simulation approach*

Sudeep Chatterji and Johann M. Heuser
GSI Darmstadt

The very intense radiation environment of the planned Compressed Baryonic Matter (CBM) experiment at the international research center FAIR makes radiation hardness a very important issue for the Silicon Tracking System (STS). The STS will consist of eight stations of double sided strip detectors at a distance between 25 cm to 100 cm downstream of the target. It is expected that the total integrated fluence will reach 1×10^{15} cm^{-2} 1 MeV neutrons equivalent which is more than expected at LHC at CERN. The major macroscopic effect of radiation damage in determining the viability of long-term operation of silicon sensors is the change in the effective charge carrier concentration (N_{eff}), leading to type inversion. For the safe operation over full CBM life time, detectors are required to sustain very high voltage operation, well exceeding the bias voltage needed to fully deplete the heavily irradiated sensors. Thus, the main effort in the development of silicon sensors is concentrated on a design that avoids p-n junction breakdown at operational biases.

Simulations are carried out to study the effect of change in N_{eff} on the breakdown performance of the device using device simulation package PISCES [1]. The simulation grid is shown in Fig. 1. Detailed calculations with the Hamburg Model [2] have allowed the parameterization of these effects to simulate the operation scenario of silicon detectors over full CBM life time. Also, the impact of various crucial geometrical parameters like device depth (W_N), width of back N^+ layer (W_{N^+}), strip width (W) and strip pitch (P) on the guard ring equipped structure after type-inversion has been studied in detail. It is clear from Fig. 2 that the peak electric field occurs at the junction curvature which is responsible for the premature breakdown of the device. Also process simulations have been performed using SUPREM-4 [3] for studying the annealing behaviour of Boron implanted in silicon. Fig. 3 shows the impact of annealing parameters on the electrical characteristics of the device.

We plan to procure 3-dimensional simulation packages from Synopsis [4] through EuroPractice Software Service of which GSI is a member so that we can accurately simulate double sided strip detectors.

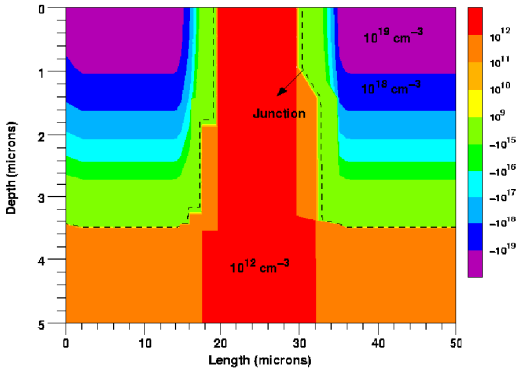

Figure 1: Cut through two neighbouring strips of a microstrip detector. Doping concentration profile in the PISCES simulation grid.

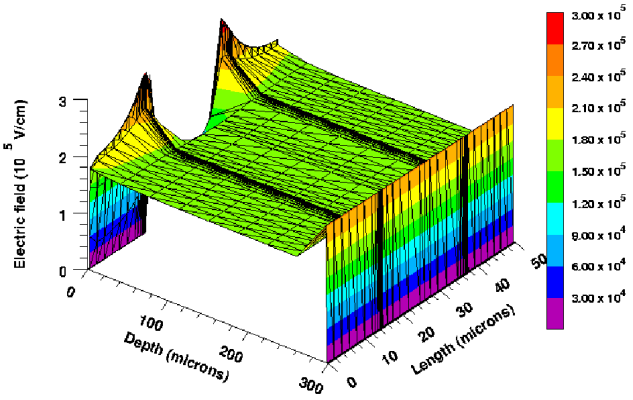

Figure 2: 3-D Electric field profile within the detector at breakdown.

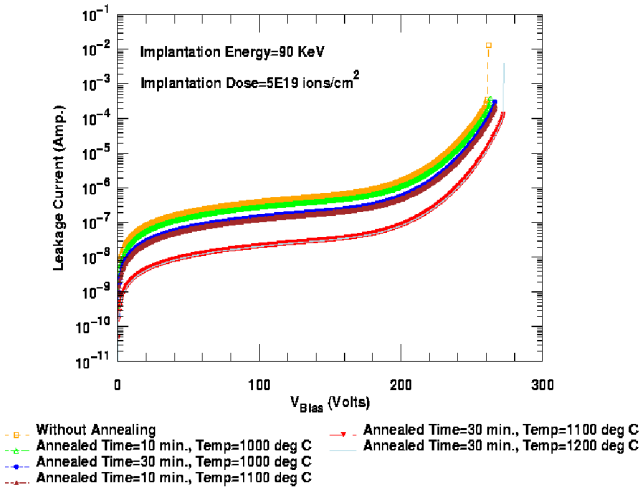

Figure 3: Impact of annealing time and temperature on the electrical characteristics of the device.

References

[1] http://home.comcast.net/ john.faricelli/tcad.htm
[2] M. Moll et al., Nucl. Instr. Meth. A439 (2000) 282
[3] http://mems.mirc.gatech.edu/ece4752/suprem.html
[4] http://www.te.rl.ac.uk/europractice/software/synopsys.html

* Supported by EU/FP6 HADRONPHYSICS (see annex) and INTAS

Layout study of the RICH detector in the CBM experiment*

S. Lebedev† [1,2], E. Belolaptikova[3], C. Höhne[1], and the CBM collaboration
[1]GSI, Darmstadt, Germany; [2]JINR LIT, Dubna, Russia; [3]MIREA, Moscow, Russia

Progress of the CBM RICH layout has been achieved in two important points: in simulation studies it could be shown that standard glass mirrors do not deteriorate the global tracking efficiency. Second, a largely improved layout of a RICH strongly reduced in size was prepared. This layout will now be subject of further feasibility studies.

The influence of the RICH material budget to the STS, TRD and global (STS+TRD) track reconstruction performances was studied. Detailed simulations have been performed in order to obtain limitations for the material budget of the RICH mirrors. Three RICH geometries with different thicknesses of the mirrors - 3 mm, 6 mm and 10 mm were simulated. The mirror support structure was implemented in form of a grid of aluminum tubes with a radius of 1.5 cm, wall thickness of 2 mm, and 40 cm distance between two tubes. Such a relation between radius and thickness of the tube wall is a standard for industry and can support the foreseen glass mirrors of appr. (40x40) cm^2 size.

Central UrQMD Au+Au collisions at 25 $AGeV$ beam energy were used for the simulation. 25 primary e^+ and 25 primary e^- were embedded in each event in order to enhance statistics. The L1 STS track reconstruction algorithm was applied [2]. Two different methods were used for TRD track reconstruction: L1 [2] and LIT[1].

We observed only changes on a few percent level in the tracking efficiency (see eg. Figure 1) and also no big changes concerning ghosts and mismatches with STS tracks. This reassures for planning a "standard" RICH mirror of 6 mm glass thickness and aluminum support. This will save money and efforts.

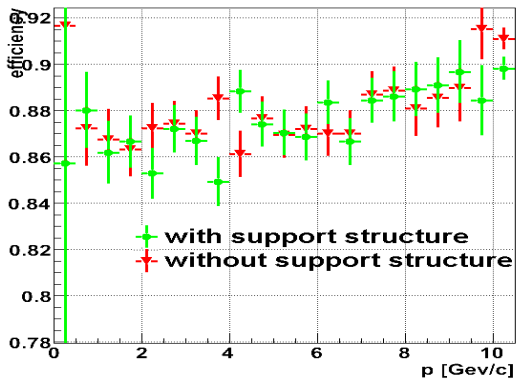

Figure 1: Efficiency of TRD track reconstruction for electrons embedded in central Au+Au collisions at 25 AGeV beam energy for a RICH with 6 mm thick glass mirror.

A first step in the RICH geometry optimization with respect to minimizing its dimensions was already made in the previous year [3]. This year progress has been achieved in the optimization of the new "Compact" RICH layout. In Table 1 one can see a comparison of the now established Compact and Standard RICH geometry. This layout was optimized in particular with respect to the photodetector and mirror positions as this influences the ring parameters. Several parameters were chosen to be optimized among them the RICH detector acceptance, which is here defined as the number of accepted electrons (more than 5 hits in RICH) devided by the number of generated electrons with parameters $\theta = (2.5°, 25°)$, $\phi = (0°, 360°)$ and $p_t = (0.1, 3) GeV/c$. Also the distribution of minor (B) and major halfaxis (A) of the ellipse, the B/A ratio, the number of hits per electron ring and the hit and ring density were investigated.

Table 1: Comparison of layout parameters for the large and compact RICH detector.

	large	compact
radiator gas	N_2	CO_2
p^{π}_{th} [GeV/c]	5.6	4.65
λ_{th} [nm]	<160	~ 175
radiator length [m]	2.5	1.5
full length [m]	2.9	1.8
mirror radius [m]	4.5	3
mirror size [m^2]	~ 22.8	~ 11.8
photodetector size [m^2]	~ 9	~ 2.4
No. of channels	$\sim 200k$	$\sim 55k$

Different geometries were simulated and investigated in order to find the best one. As a reference point the standard RICH layout was taken. For this we have a mean acceptance of 89%, $< A >$ =6.1 cm, A_{RMS}=0.28 cm, $< B >$ =5.6 cm, B_{RMS}=0.22 cm, $< B/A >$=0.9. Analyses of different compact geometries were done by the parameters mentioned above. The most appropriate geometry was chosen with the best correlation of the selected parameters. Thus, for the optimized compact RICH the geometrical acceptance is 84%, $< A >$ =5.08 cm, A_{RMS}=0.33 cm, $< B >$ =4.61 cm, B_{RMS}=0.24 cm, $< B/A >$=0.91.

With the chosen compact RICH geometry a comparable performance to the standard RICH setup [4] is achieved.

References

[1] A. Lebedev et al., *CBM Prog. Rep. 2007*, p. 15.
[2] I. Kisel et al., *CBM Prog. Rep. 2007*, p. 10.
[3] C. Höhne, *CBM Prog. Rep. 2007*, p. 17.
[4] S. Lebedev et al., "Electron Identification in CBM".

* Supported by EU/FP6 HADRONPHYSICS
† s.lebedev@gsi.de

Development of a CBM-RICH mirror prototype – first measurements

M. Dürr[1], A. Braem[2], and C. Höhne[3]
[1]University of Applied Sciences, Esslingen, Germany; [2]CERN, Switzerland; [3]GSI, Darmstadt,Germany

Electron identification in a ring imaging Cherenkov detector (RICH) requires efficient reflection of UV-photons by the spherical mirrors which act as imaging elements. For the CBM-RICH detector, test mirrors based on a standard float glass process were produced by FLABEG GmbH, Furth im Wald, Germany; an example of the 40×40 cm^2 large mirrors is shown in Fig. 1. The reflecting coating consisted of an Al-layer, for protection of the Al-surface, especially to avoid formation of aluminium oxides which are strongly absorbing in the UV-region, a protection layer of MgF_2 was applied. Scanning electron microscopy (SEM) measurements yielded $d_{\mathrm{Al}} = 55$ nm and $d_{\mathrm{MgF_2}} = 120$ nm for the Al- and MgF_2-layer, respectively.

Figure 1: Photograph of test mirror, the concave profile is easily observed in the reflection on the mirror surface.

The reflectivity of the mirrors as a function of wavelength down to $\lambda = 160$ nm was tested at CERN. The result for one of the mirrors is shown in Fig. 2. One observes high reflectivity down to approx. 300 nm with a first drop in reflectivity at 280 nm and a second, steeper drop around 180 nm. The latter is assumed to be due to the formation of aluminium oxides already during the film growth. The former can be understood in terms of interference between light reflected at the MgF_2/vacuum interface and light reflected at the Al/MgF_2 interface. The solid line in Fig. 2 is a simulation taking into account both effects. For the absorbing part, the absorbance of Al_2O_3 was used; with respect to interference, the measured reflectivity curve is reproduced the best if a thickness of the MgF_2-layer of $d_{\mathrm{MgF_2}} = 110$ nm was applied in the simulations, in very good agreement to the SEM measurements.

Further discrepancies between the measured and simulated curve might be due to microroughness of the mirror surface. As a measure for the surface and interface roughness, atomic force microscopy (AFM) images were taken of the mirror surface (Fig. 3). The surface was found to show a roughness below 10 nm, a similar value was obtained both for the MgF_2-surface and the Al/MgF_2 interface when investigated by means of SEM. Further tests included D_0-measurements. However, due to an uneven surface plane on the cm-scale, only a small fraction of incoming light was found to be reflected into a defined spot.

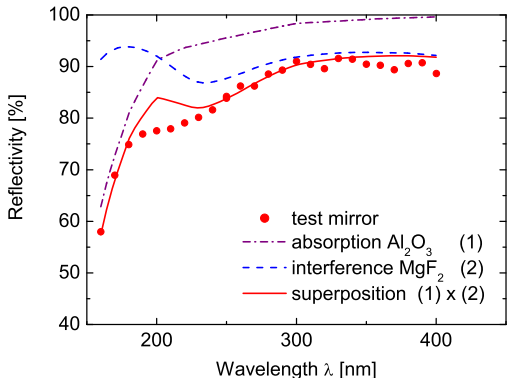

Figure 2: Measured reflectivity as a function of wavelength for one of the test mirrors (dots). The dashed line indicates the effect of interference at a 110-nm-MgF_2-protection-layer (simulation), the dot dashed line illustrates possible contributions by the absorption of Al_2O_3. The solid line represents the superposition of the two latter effects.

In summary, overall good reflectivity was measured and optimized growth process parameters might lead to a further improvement of the reflectivity in the short wavelength region avoiding the formation of aluminium oxides. Improvements with respect to surface homogeneity on the cm-scale are mandatory.

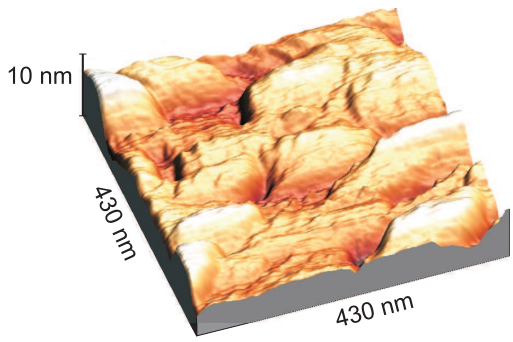

Figure 3: Pseudo-3D-plot of the surface topography as obtained by means of AFM measurements (contact mode). The measured roughness was approx. 6 nm (peak-to-peak).

Investigation of wavelength shifter properties of p-terphenyl and TPB

P. Koczoń[1], C. Höhne[1], M. van Stenis[2], A. Braem[2], and C. Joram[2]
[1]GSI, Darmstadt, Germany; [2]CERN, Geneva, Switzerland

Abstract: Wavelength shifter materials like p-Terphenyl and Tetra Phenyl Butadiene (TPB) of thicknesses between 65 and 250 μg/cm^2 have been studied in order to improve the quantum efficiency (QE) of a photomultiplier in the UV range. The best result has been obtained for p-Terphenyl of 100 μg/cm^2 thickness. In this case the quantum efficiency integrated over a broad range of photon energies up to 6.2 eV shows a gain of a factor 1.6 compared to an uncovered photomultiplier.

Introduction

The rate of photons from Cherenkov radiation per energy bin is constant (dN/dE = const) therefore the bulk of the photons is produced in the UV and far UV region. The quantum efficiency of standard photomultipliers with glass windows reaches only 25% around 400 nm and drops down essentially to 0% below 250 nm. The aim of this work

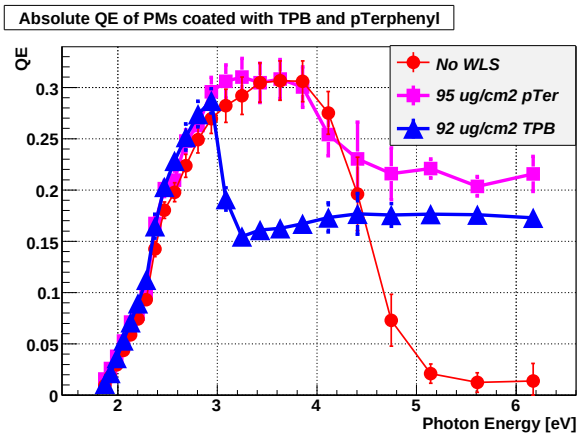

Figure 1: Quantum efficiency versus photon energy for the uncoated PMT (Photonis XP3102) and with TPB and p-Terphenyl coating.

was to reinvestigate the potential of the quantum efficiency improvement in the UV region using wavelength shifting substances on top of the glass window.

Technical details

Two of such wavelength shifter substances have been evaporated in vacuum with well controlled thickness on the entrance windows of several Photonis XP3102 photomultipliers. The quantum efficiency of those photomultipliers was measured in a wavelength range from 200 to 650 nm in a monochromator by comparison to an absolutely calibrated photodiode [1].

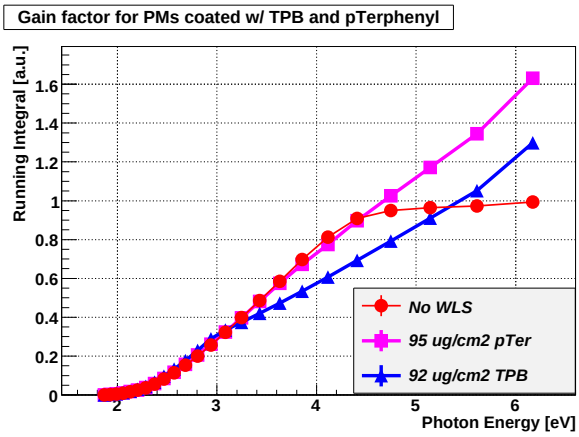

Figure 2: Gain of quantum efficiency obtained by integration of the QE curves from Fig. 1.

Results

Fig. 1 shows the improvement of the quantum efficiency as a function of photon energy for 95 μg/cm^2 p-Terphenyl and 100 μg/cm^2 TPB evaporated on the entrance window of the PMT compared to the quantum efficiency of an untreated PMT. TPB improves the efficiency for highest energies (around 5 eV=246 nm) moderately but deteriorates it in the visible region by a factor of 2. For p-Terphenyl we observe a clear improvement of QE in the UV and no change in the visible range. In order to quantify the overall QE improvement all curves have been integrated over the whole energy range. Running integrals are presented in Fig.2 and compared to the integral of the pure PMT (which is normalised to 1 at 6 eV). The value of the running integral for TPB lies below the reference PMT between 3.2 and 5.3 eV and finally reaches a gain of 30% only. The result for p-Terphenyl clearly shows a gain of 60 % above the uncovered PMT. Extrapolating to the far UV one can expect still higher gain values.

In order to investigate possible ageing processes of the wavelength shifter film in the radiator gas of the future RICH detector of CBM at FAIR the photomultipliers with an evaporated p-Terphenyl layer have been stored in CO_2 atmosphere and will be remeasured to monitor their performance every 6 - 12 months.

References

[1] A. Braem et al., NIM A 504 (2003) Pages 19-23

Electron Identification in the CBM experiment*

S. Lebedev† [1,2], C. Höhne[1], G. Ososkov[2], and the CBM collaboration
[1]GSI, Darmstadt, Germany; [2]JINR LIT, Dubna, Russia

In this contribution we present systematic studies and improvements for electron identification in the CBM experiment.

A RICH ring recognition algorithm based on the Hough Transform (HT) [1] was improved especially for a high ring density environment. This is necessary because an optimization of the RICH detector for CBM with respect to minimization of its dimensions was done [2]. This results in increased ring density in the photodetector plane of this "Compact RICH".

In systematic studies of the ring recognition algorithm different parameters were varied. At maximum 120 $e+$ and 120 $e-$ were simulated for each event, the number of rings in such events is roughly 250, therefore, in the inner and central part of the RICH PMT plane the majority of rings overlaps. The ring finding efficiency varies from 91% for rings with more than 5 hits to 95% for rings with more than 15 hits. So far, for the H8500 photodetector only the quantum efficiency was implemented, however an additional reduction of the photodetector collection efficiency (CE) by 30% might be realistic. In this case the ring finding efficiency drops down by 2% in comparison to 100% CE. The ring finding efficiency was investigated in dependence on the number of hits per ring and the ratio of the minor half axes (B) and major half axes (A) of the ellipse as typically the rings are slightly distorted. It was found that the efficiency drops to less than 80% once the number of hits per ring reaches a low probability value, i.e. the mean value minus 2·RMS. The efficiency in dependence on the A/B ratio stays constant in the range between 0.8-1 and rapidly drops down for smaller ratios. The A/B ratio thus is an important parameter for the Compact RICH design [2].

An algorithm for electron identification in the RICH detector based on an ANN was implemented. After studying distributions of different parameters related to the RICH rings, 9 of them were choosen : major and minor half axes, rotation angle etc. These parameters are used as input to a trained ANN. It has shown somewhat better results in comparison to standard cuts (see Table 1).

A systematic study of electron and pion identification in the TRD was also done. The ANN method [3] has been used for this task. The dependence of energy loss on momentum has been investigated. Three approaches of ANN training have been proposed and investigated. The momentum information is needed for two of these approaches.

The electron Identification algorithm in TRD was adopted to identify electrons which have 6 to 12 hits in the TRD. This is necessary because 1) different geometries with different number of layers have to be investigated; 2) detector inefficiency; 3) tracks which do not pass through all layers should also be identified; 4) track finding algorithm might find only a part of track. Also it was optimized for an alternative geometry (Münster-Bucharest), which uses a double gas layer.

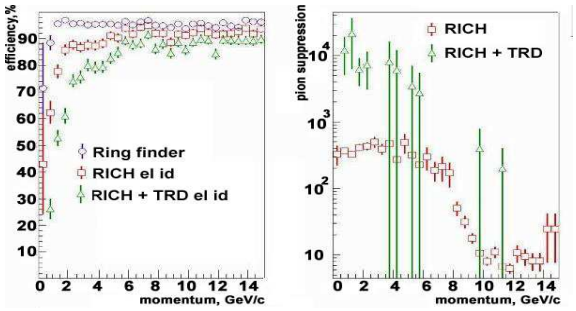

Figure 1: Efficiency of electron identification (left) and pion suppression factor (right) as function of momentum for electrons embedded in central Au+Au collisions at 25 AGeV beam energy and the standard RICH layout.

	Standard RICH		Compact RICH	
	St. cuts	ANN	St. cuts	ANN
RICH, eff. %	87.1	90.3	81.9	83.8
RICH, π supr.	240	250	110	250
RICH+TRD, efficiency %	81.0	83.3	73.4	74.6
RICH+TRD, π suppression	9800	10500	6800	13000

Table 1: Electron identification efficiency and pion suppression averaged over all momenta.

These improved methods allow for a high purity and efficiency of reconstructed electron rings (see Table 1). For momenta above 2 GeV/c the ring reconstruction efficiency for electrons embedded in central Au+Au collisions at 25 AGeV beam energy is 95% resulting in an electron identification efficiency of 90% at a pion suppression factor of 500. Including information from the TRD a pion suppression of 10^4 is reached at 80% efficiency.

References

[1] S. Lebedev et al., CBM-RICH-note-2008-001, GSI, 2008.

[2] C. Höhne, *CBM Prog. Rep. 2007*, CBM-RICH layout optimization.

[3] E. Akishina et al., JINR Comm. E10-2007-17, Dubna, 2007.

* Supported by EU/FP6 HADRONPHYSICS
† s.lebedev@gsi.de

R&D for the demonstrator of the CBM-Micro-Vertex Detector (MVD) *

S. Amar-Youcef[1,2], N. Bialas[1], M. Deveaux[1], D. Doering[1], J. Heuser[3], I. Fröhlich[1], J. Michel[1], C. Müntz[1], S. Seddiki[1,4], C. Schrader[1], J. Stroth[1], T. Tischler[1], and B. Wiedemann[1]

[1]IKF, University Frankfurt; [2]Helmholtz Research School, Frankfurt; [3]GSI, Darmstadt; [4]IPHC, Strasbourg

In CBM open charm mesons will be identified by reconstructing their secondary decay vertices. This requires a vertex detector with very good secondary vertex resolution ($\sigma_{SV} \sim 50\ \mu m$ along the beam axis). To match this requirement, a highly granular pixel detector with excellent spatial resolution ($\sim 5\ \mu m$) and minimum material budget (few $0.1\ \%X_0$) will be installed in the vacuum close to the target. A short readout time ($\sim 10\ \mu s/frame$) and good radiation hardness (few tens MRad, $> 10^{13}\ n_{eq}/cm^2$) are needed to handle the high collision rate ($10^5 - 10^6$ Au+Au collisions / s) required for studying open charm.

To define a starting point for the future CBM Microvertex-Detector, the so-called Demonstrator is set up in the IKF Technology Lab (see Fig.1). 2 Mimosa20-sensors are used (each sensor: 204800 pixels, covering $10 \times 20mm^2$, read out via 2 channels with 50 MHz per pixel). Their resulting data rate up to 2.4 Gbit/s makes high demands on the readout electronics. The demonstrator will

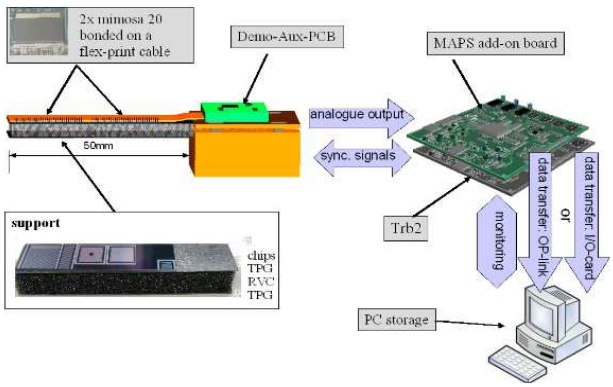

Figure 1: Sketch of MAPS Demonstrator

by far not match the ultimatives goals for the CBM Vertex Detector, but focusses on the integration of available technologies.

Mechanics

Constrained by the thermal and mechanical requirements a support structure was elaborated in terms of thermal management and low material budget. In this process the thermal performance was evaluated by means of FEM simulations. The support structure consists of 2 layers of TPG (Thermal Pyrolitic Graphite), a material optimized for high heat conductivity, and with RVC foam (Reticulated Vitreous Carbon) as spacer. First structures have been built and are being evaluated for their thermal as well as mechanical properties. For optimum heat transport the sensor is directly glued on the TPG, with the FPC on top.

Figure 2: Add-on board and TRBv2 on back side.

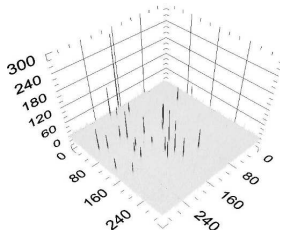

Figure 3: CDS-corrected frame of a Mimosa20 matrix with several hits.

Flexprint Cable

In order to drive signals from the chip to the r/o electronics a Flexprint Cable (FPC) has been designed by the electronic departement of the IKF. This cable integrates all electronical needs focussing on little material budget. The FPC will be connected to the chip via bonding wires and to the readout electronics via a fine pitch connector.

Readout

A fast readout add-on board for the TRBv2 standard (link to HADES-DAQ for beam tests) [1] was developed with on-board functionality for data reduction (see Fig.2). To process the MAPS data on-line the system has to work with pipelined algorithms for correlated double sampling (CDS) and hit discrimination like zero suppression and cluster - finding. Therefore the board comprises 4 analog input channels to readout 2 Mimosa20-chips, digital signals for chip controlling and an FPGA with internal FIFO and external memory banks (3 GB) [2] to process the data in real-time. The identified clusters reduce the data rate to few bits/s and are transmitted externally via the optical link (2 Gbit/s) of the TRBv2. A considerable part of the r/o analysis software for the demonstrator is ready. Data can be written to a hard drive, can be read in by ROOT-based offline analysis software (see Fig.3) and will be used for developing data sparsification algorithms.

References

[1] I. Froehlich et al.,A General Purpose Trigger and Readout Board (TRB), IEEE Trans. Nucl. Sci., 2007.

[2] C. Schrader et al., A Readout System for the CBM-MVD Demonstrator, GSI Report 2007.

* In co-operation with IPHC. Work supported by BMBF (06FY173I), GSI Darmstadt (F&E) and Helmholtz Research School Frankfurt

Radiation hardness studies on Monolithic Active Pixel Sensors*

M. Deveaux[1], S. Amar-Youcef[1], J. Baudot[2], A. Büdenbender[1], D. Doering[1], W. Dulinski[2], M. Koziel[2], C. Müntz[1], J. Stroth[1], F. M. Wagner[3], and M. Winter[2]

[1]Goethe University Frankfurt, Frankfurt/Main, Germany; [2]IPHC Strasbourg, France; [3]Forschungsneutronenquelle Heinz Maier-Leibnitz (FRM II), Technische Universität München, Garching, Germany

CMOS Monolithic Active Pixel Sensors (MAPS) form a promising sensor technology for the micro vertex detector (MVD) of the Compressed Baryonic Matter (CBM) experiment. The technology allows for building very thin ($\sim 50\ \mu\mathrm{m}$) detectors with a spatial resolution of few μm and a satisfactory time resolution of $10\ \mu$s. It is expected that within one run of CBM, the MVD will be exposed to a radiation dose of ~ 3 Mrad and $10^{13}\ \mathrm{n_{eq}/cm^2}$. A joined research program of GSI, the Goethe University Frankfurt and the IPHC Strasbourg aims to expand the radiation tolerance of MAPS beyond this level.

Our activities in 2008 followed three research lines which were the study of the Random Telegraph Signal observed in irradiated sensors[1], the search for improved sensor designs based on conventional CMOS processes and the identification and evaluation of dedicated CMOS processes allowing for building depleted sensors.

RTS is a non-Gaussian noise of CMOS components. As illustrated in figure 1, it manifests itself as a rectangular modulation of the dark signal of neutron irradiated MAPS, which is sufficient to exceed the discrimination threshold of the sensor and to generate false hit indications. We studied RTS as function of temperature and radiation dose with MIMOSA-18[1] and MIMOSA-19[2] prototypes, which were irradiated with fission neutrons [2] at the MEDAPP facility of the FRM II reactor. We observed that up to few 10% of all pixels show occasionally RTS signatures. However, at a temperature of $-20°\mathrm{C}$, the SB-pixels of MIMOSA-18 showed a reasonably low fake hit rate of $\ll 10^{-4}$ after a dose of $10^{13}\ \mathrm{n_{eq}/cm^2}$. This low rate (one order of magnitude lower than observed with the conventional 3T-pixels of MIMOSA-19) is due to the intrinsic leakage current compensation of the SB-pixels.

Our studies on MIMOSA-18 and -19 aimed also to test strategies to improve the signal over noise ratio (S/N) of MAPS being irradiated with non-ionizing doses. This S/N is mostly degraded by a drop of the charge collection efficiency (CCE) of the sensor, which is due to the shrinking lifetime of the signal electrons in silicon suffering from radiation induced bulk damage. The CCE is partially recovered if an accelerated charge collection process collects the electrons before they recombine. As already demonstrated [3], this acceleration may be reached by reducing the pixel pitch, which however substantially increases the number of channels in the MVD. An alternative strategy, the use of big sensing diodes, was tested with MIMOSA-19.

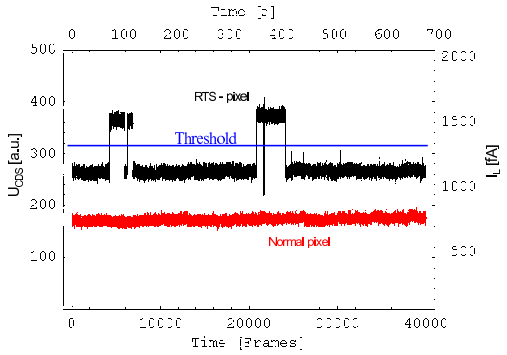

Figure 1: Dark signal of a 3T-pixel showing RTS (black) and of a normal pixel (red/gray).

The CCE and radiation hardness of this chip was studied with a ^{55}Fe source and compared with the performances of the conventional pixels of MIMOSA-18. As expected, the pixels of MIMOSA-19 reach a significantly higher CCE than the pixels of MIMOSA-18 but show also a substantially higher capacitive noise ($\sim 20\mathrm{e}$ ENC instead of $\sim 12\mathrm{e}$ ENC). The S/N of MIMOSA-19 is therefore smaller than the one of MIMOSA-18. However, according to our preliminary results, MIMOSA-19 is expected to show a fairly good detection efficiency ($> 95\%$ for MIPs) up to the highest neutron dose applied ($2 \cdot 10^{13}\ \mathrm{n_{eq}/cm^2}$).

An even higher radiation tolerance might be reached by depleting the sensors, which is however not compatible with the highly (some $10^{15}\mathrm{at/cm^2}$) doped silicon of standard CMOS processes. This attracted our attention to the XFAB 0.6 μm process, which includes a substantially lower doped epitaxial layer. A prototype (MIMOSA-25) featuring partially depleted sensors was designed in order to evaluate this process. First promising test results from neutron irradiated MIMOSA-25 were obtained.

References

[1] J. Bogaerts, B. Dierickx, R. Mertens, "Random Telegraph Signals in a Radiation-Hardened CMOS Active Pixel Sensor", IEEE Trans. Nucl. Sci. **49**, 249 (2002).

[2] H. Breitkreutz, F. M. Wagner, A. Rhrmoser, W. Petry, "Spectral fluence rates of the fast reactor neutron beam MedApp at FRM II", Nucl. Instrum. Meth. A **593**, 466 (2008).

[3] A.Besson et al., "Achievements of CMOS Pixel Sensors for the CBM Micro-Vertex Detector", GSI Scientific Report 2007.

*Supported by BMBF (06FY173I), GSI Darmstadt (F&E) and Helmholtz Research School Frankfurt

[1]262k pixels with 10 μm pitch, $15\mu\mathrm{m}^2$ collection diodes.

[2]73k pixels with 12 μm pitch, 40 and 57 $\mu\mathrm{m}^2$ collection diodes.

Occupancy study of the Micro-Vertex Detector for the Compressed Baryonic Matter experiment*

S. Seddiki[1,2], M. Deveaux[1], I. Fröhlich[1], C. Müntz[1], J. Stroth[1,3], and C. Trageser[1]
[1]IKF, Frankfurt, Germany; [2]IPHC, Strasbourg, France; [3]GSI, Darmstadt, Germany

The Micro-Vertex Detector (MVD) [1] of CBM is intended to detect the hadronic decays of open charmed particles by means of the identification of their displaced decay vertex. Therefore the MVD is located close to the collision point and will be exposed to the very high track densities from the high heavy ion collision rates foreseen in CBM. The design of the MVD requires a detailed knowledge of the detector occupancies and the corresponding data rates, which were simulated in this work.

We focused on the study of δ-electrons, which are produced by the Au-beam passing the Au target. They were generated with GEANT3+GCALOR by shooting Au ions with 25 AGeV through the target of CBM. The yield and spectrum of the simulated δ-electrons were checked with [2] and were found to exceed this prediction by few 10% in the electron momentum region of interest ($p = 10\ \mathrm{MeV/c}$ to $p = 100\ \mathrm{MeV/c}$). Accounting for the 1% interaction target, 100 of those ions were combined with the particles produced by one nuclear collision with random impact parameter. The latter were generated with UrQMD. This normalization assumes that a time resolution of the MVD of $\sim 10^{-5}$ s is sufficient to separate the individual nuclear collisions.

After some centimeters of trajectory, the 1 Tm dipole field of CBM deflects most of the δ-electrons out of the detector acceptance. The occupancy of the MVD stations varies thus strongly with the distance (dz) between the stations and the target. Moreover, as illustrated in figure 1 (right panel) for a station at $dz = 10\ \mathrm{cm}$, the occupancy of the individual stations is very inhomogeneous.

The contribution of the δ-electrons increases the mean occupancy caused by a nuclear collision (see figure 1, left panel) by up to a factor 13.5 (at $dz = 5\ \mathrm{cm}$). The maximal occupancy in the hot spots reaches 3.5 and 1 hit / mm^2 / collision at $dz = 5\ \mathrm{cm}$ and $dz = 10\ \mathrm{cm}$.

In order to reduce those high occupancies, the examination of the deposition time of the hits permitted us to elaborate several strategies. We observed that raising the magnetic field by 1 T within a small volume around the target improves the deflection of δ-electrons and decreases the number of first hits. This modified field configuration increases the amount of late coming hits from spiraling electrons, absorbed however by the mechanical support ring of the MVD stations. This strategy reduces the total occupancy by a factor of 2.5 at $dz = 5\ \mathrm{cm}$ and 2 at $dz = 10\ \mathrm{cm}$

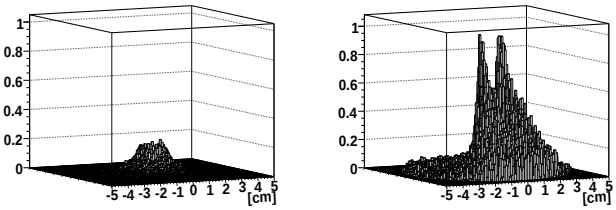

Figure 1: Number of hits per cell (1 mm^2) per collision for a MVD station at 10 cm : originating from nuclear collisions only (left panel), and including δ-electrons (right panel)

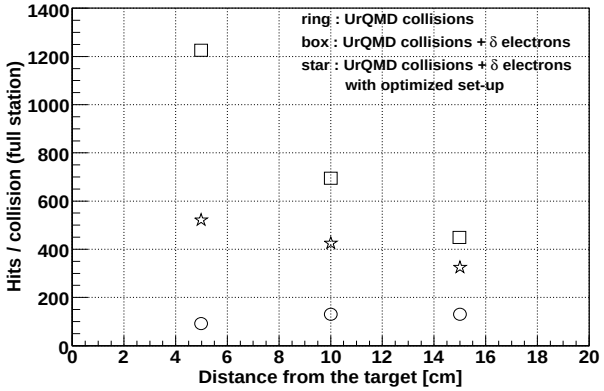

Figure 2: Occupancy per event for different distances of the MVD station

(see figure 2). Nevertheless the peak of occupancy is only decreased by 30% as it is caused by very stiff electrons.

Our studies were completed by estimating the data flow of the MVD. We assumed a collision rate of 10^5/s and an on-chip zero suppression as tested with SUZE-01[3]. The resulting data flow of several $\mathrm{GBits/s}$ per station may be increased by one order of magnitude, if the MVD is operated with a moderate pile-up of nuclear collisions. Moreover, a security margin for fake hits has to be foreseen.

References

[1] A. Besson et al., 'Achievement of CMOS Pixel Sensors for the CBM Micro-Vertex Detector', CBM progress report, 2007

[2] R.M. Barnett et al., 'Review of particle physics' PhysRev D V.54 Iss.1, pp. 1-708 (p.134)

[3] M. Winter et al., 'A Swift High Resolution Pixel Sensor for the CBM MVD', this report.

* In collaboration with IPHC. Work supported by BMBF (06FY173I), GSI Darmstadt (F&E)

Detector response simulation of the CBM Micro Vertex Detector

C. Dritsa[1,2], J. Baudot[2], R. De Masi[2], M. Deveaux[3], V. Friese[1], F. Rami[2], and M. Winter[2]

[1]GSI, Darmstadt, Germany; [2]IPHC, Université de Strasbourg, Strasbourg, France; [3]IKF, Johann Wolfgang Goethe-Universität, Frankfurt, Germany

One of the major physics topics of the CBM experiment is the study of the production of open charm in nucleus-nucleus collisions at FAIR energies. For this purpose, the CBM Collaboration is planning to use a high-performance Micro-Vertex Detector (MVD) based on Monolithic Active Pixel Sensors (MAPS) [1]. CBM running conditions call for a MVD with high granularity, radiation tolerance, and readout speed. The efficient optimisation of the detector design requires detailed simulations of the detector response.

So far, the MVD detector response in the CBM simulation software (CBMRoot) [2] has been described by applying a Gaussian smearing of the hit position provided by GEANT. This simple approach ignores effects like generation of clusters of pixels from impinging particles and is therefore not suited for reproducing the high track-density environment of the MVD. In the present work, we implemented a more realistic MVD detector response simulation program based on a software package which was developed recently within the framework of the ILC in order to describe the response of MAPS sensors to the passage of charged particles [3]. This package employs a MAPS response model which takes into account the sensitive volume of the sensor, its pixel structure, and its intrinsic noise. The path of a charged particle traversing the thin sensitive layer of the detector is subdivided into n segments. The energy deposited by the particle in the silicon is translated into a signal charge using a conversion factor of 3.62 eV per electron/hole pair. The diffusion of the signal electrons in the sensitive layer of the sensor is modeled by a Gaussian distribution with width tuned to measured data. This allows to convert the hit associated to the particle trajectory into a charge distributed over several pixels. It is possible to simulate the readout with a discrimination threshold and a digitisation with up to 12 bit ADC.

A cluster finder algorithm was also implemented in the CBM simulation framework in order to reconstruct the hit position on the readout plane. This is done by determining the center-of-gravity of the charge stored in the fired pixels.

The model was validated with real data collected with a MAPS prototype, called MIMOSA-17 (30 μm pixel pitch, 14 μm thick epitaxial layer), exposed to a 120 GeV/c pion beam at the CERN-SPS. On the left of Fig. 1, the probability is shown that the charge collected by neighbours of an already identified seed pixel (index 0) exceeds the discrimination threshold of 75 electrons (5 times the noise of MIMOSA-17) for simulated and for real data. If restricted to this comparison, an excellent agreement is observed between experiment and simulation for particles with incident angles of 40^o-90^o with respect to the detector's plane; nevertheless, disagreements observed for very small incident angles (10^o-30^o), e.g. reproducing the cluster shape, remain to be investigated.

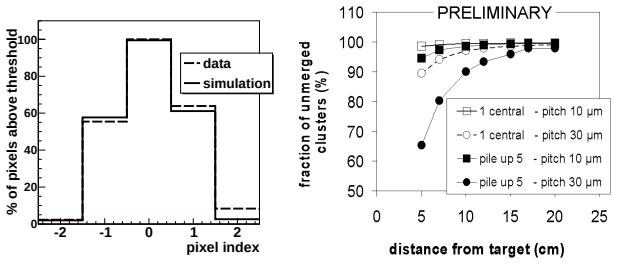

Figure 1: (Left) Percentage of pixels above threshold for the row of the cluster to which the seed pixel belongs. The impinging particle's trajectory is vertical to the detector plane (90^o). (Right) Percentage of unmerged clusters as a function of distance between the station and the target, for different combinations of pile-up and pixel pitch. A pile-up of 5 collisions is defined as 1 central and 4 minimum bias collisions.

A typical objective of the digitiser is illustrated in Fig. 1 (right), where the evolution of cluster merging with respect to the distance of each station from the target is studied for different assumptions. Cluster merging occurs if several individual clusters get combined in a single one after cluster reconstruction. Because of the high collision rate, several collisions may pile up in a single MVD readout cycle. One of the consequences of this pile-up is an increased probability that clusters merge. The merging probability is governed by pixel size and track density and, hence, by the distance to the target.

The software is now mature for the detailed studies needed to optimise the MVD conceptual geometry, accounting for the most influential parameters such as radiation hardness, occupancy, pixel pitch, and readout speed. These studies will incorporate software improvements mitigating the residual discrepancies between real and simulated data.

References

[1] `http://iphc.cnrs.fr/-CMOS-ILC-.html`

[2] M. Al-Turany and F. Uhlig, *FairRoot Framework*, submitted to Proceedings of Science (ACAT08)

[3] M. Battaglia, Nucl. Instr. Meth. Phys. Res. A572 (2007) 274

PADI2-3, the second iteration of FEE for CBM Time-of-Flight Measurements

M. Ciobanu[1,2], I. Deppner[2], D. Gonzalez-Diaz[1], N. Herrmann[2], K.D. Hildenbrand [1], M. Kiš[2,3], and A. Schüttauf[1]

[1]GSI,Darmstadt, Germany; [2]Physikalisches Institut, Heidelberg, Germany; [3]RBI, Zagreb, Croatia

From the in-beam tests of the PADI1 prototype [1] we have recognized that the minimization of the crosstalk between channels has a priority for further developments. In the upcoming design we have changed the biasing type from voltage biasing to current biasing. The bias block used in PADI2-3 ASIC is a constant-transconductance bias circuit having a wide swing cascode current mirrors similar to the one described in [2]. It gives two currents for each channel and at the channel level all needed biasing voltages are created locally. For the bias block we have used a special layout routing technique in order to realize a good matching of the eight output currents. The layout was designed in a few successive optimization steps involving the simulation with parasitic elements extracted. Finally the eight currents are in a few percent close to the medium value. According to simulations, the increase of CTRR at chip level relative to PADI1 will be of minimum 20 dB. We

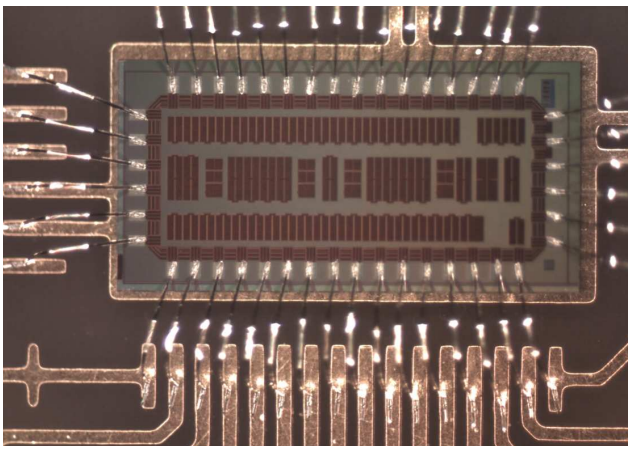

Figure 1: PADI2 (1.5 mm x 3.2 mm) bonded on test PCB.

have increased the number of channels to four and we have added the OR feature which allows to daisy-chain chips for trigger purposes. The PADI2-3 chip will be connected to the TDC chip which is currently being developed at GSI [3]. The inputs of this chip accept LVDS signals. We have designed two variants PADI2 and PADI3 which differs in the time output signal levels: +/-100 mV (fixed value, with the common mode dc voltage fixed at the optimum point of the LVDS receiver, e.g., 2/3*VDD) and +/-350 mV (programmable value by an external resistor) on 100 Ω differential load.

In the new design, all the resistors involved in the main amplification path in preamplifier and in discriminator are implemented by the dynamic impedance of MOS transistors in diode configuration. All differential amplifiers use the same type the wide swing cascode current mirrors (used already in bias block) and scaled for the needed current. Together with the new biasing, which stabilizes the g_m, the new design has less dispersion of parameters in technological corners related to PADI1. The preamplifier should have a gain G_{PA} ∼86 at an increased bandwidth f_H ∼300 MHz. The external threshold voltage range is extended to ±300 mV. In the tests of PADI1 we have not used the hysteresis facility and hence it is removed in the new design. Furthermore, in tests with the diamond detectors for counting applications, we have shown that in the ideal case, the discriminator should work with a threshold level within 3-6 times of the noise level. Hence, the discriminator designed for PADI2-3 has an increased gain enabling operation at very low threshold.

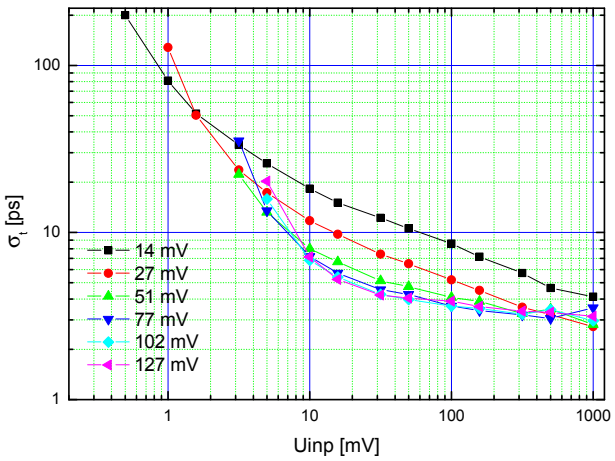

Figure 2: The PADI2 time resolution dependence to input signal amplitude for different threshold voltages.

We have designed test PCB, for direct bonding of the ASIC (Fig. 1) and the first tests shows that the PADI2 prototypes are fully operational. In the Fig. 2 we present first mesured result, an intrinsic time resolution as a function of input signal amplitude for different threshold voltages (preliminary result).

References

[1] M. Ciobanu et al., IEEE NSS Conf. Rec., N30-18 (2008) 2018 - 2024

[2] D. Johns and K. Martin, "Analog integrated circuit design", John Wiley & Sons, Inc., p.259, 1997.

[3] H. Flemming and H. Deppe, IEEE NSS Conf. Rec., N15-25 (2007) 322 - 325

Cross-talk studies oriented to stripped tRPCs at high multiplicities

A. Berezutskiy[1], M. Ciobanu[2], D. Gonzalez-Diaz[2], I. Deppner[3], and A. Gil[4]

[1]SPbSTU, St Petersburg, Russia; [2]GSI, Darmstadt, Germany; [3]PI, Heidelberg, Germany; [4]IFIC-CSIC, Valencia, Spain

The presence of large cross-talk in meter-long stripped timing RPCs was recognized experimentally time ago [1]. Understanding its practical importance is, however, far from easy. To start with the origin of cross-talk is capacitive, so no net charge is transported when integrating over a time span sufficiently long. Because of that, in low-multiplicity environments even in the case where cross-talk would travel throughout the whole detector making several strips firing at once, such events could be discarded off-line on the basis of having null charge [2]. A different effect, to be distinguished, will be called 'charge sharing' in the following and arises from the induction onto several strips during the avalanche formation ([3], for instance). However, as long as the transverse dimension of the strip is much bigger than the avalanche size, and the inter-strip gap is large, this process will have generally less impact than cross-talk, and will be omitted here for shortness.

On the other hand, cross-talk is 'a priori' a concern for any stripped tRPC aimed at operating at high multiplicities. The practical influence on the detector performances will depend on the time distribution of the impinging particles, the inter-strip capacitance C_i, the impedance of the line Z_o (that rules the time duration of the cross-talk and the signal itself) and very critically on the detector length L, signal rise-time t_{rise} and FEE threshold v_{th}. A simplified picture can be drawn under some assumptions [4] where the contribution to the resolution due to baseline oscillations originated from cross-talk (rms_{ct}) can be sketched as:

$$\mathrm{rms}_{ct} \simeq \frac{\bar{v}}{v_{th}} \left(\frac{\mathrm{rms}_v}{\bar{v}}\right) \frac{t_{rise}}{\ln 9} F(L, C_i, t_{rise}) \qquad (1)$$

being $\bar{v}$ the average signal amplitude and F the fraction of cross-talk that depends on L, C_i and t_{rise}. Taking usual values ($\frac{\bar{v}}{v_{th}} \simeq$ 5-10, $\frac{rms_v}{\bar{v}} \simeq 1$, $t_{rise} \simeq 200$ps), the jitter arising from 10% cross-talk from an adjacent cell would be $\sim$ 100ps, that would add quadratically to the resolution of the interesting event (of the same order, in tRPCs).

The detector design task is much simplified if analytical or numerical tools are available, so that the very broad phase-space can be explored without need to build an exhaustive amount of prototypes. The main difficulty in HF simulation arises from non-perfect grounds, impedance steps at connectors and non-perfect soldering points. So, we built an 'electrically equivalent' of an RPC (without glass, for simplicity) and with an impedance close to $Z_o = 50\Omega$ trying to minimize those effects. The 'RPC' consisted of 3 equal electrode planes with air in between and segmented into 2.2cm strips (with 0.3cm separation) placed inside a metallic box (see [4] for details). The outer electrodes were joined and all ports terminated by 50Ω resistors, emulating a pseudo-differential read-out. For the electrical simulation we used the APLAC software. Simulation was checked for signals with t_{rise} 10ns, 1ns and 0.36ns of which here the 1 ns are shown (Fig. 1), illustrating the good agreement. The induction after injection in (i) the central electrode (left-up) is shown for (ii) the outer one (right-up), (iii) the central one of the adjacent strip (left-down) and (iv) the corresponding outer one (right-down).

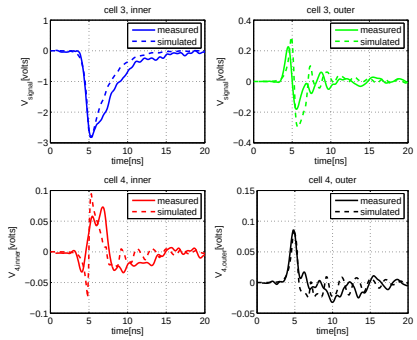

Figure 1: Induction in different strips when signal is injected in the central electrode (up-left).

The general propagation behaviour is presented in Fig. 2 when 200ps rise-time differential signals were simulated in a typical 8-gap glass-tRPC with 2.2cm strip width and 0.3cm gap. Clearly, if a cross-talk above 10% is to be avoided, the detector length must be considered critically. A comprehensive description of all the available data is in progress and will be subject of an internal CBM gap-note.

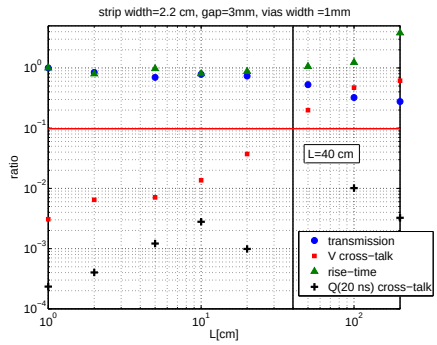

Figure 2: Transmission coefficient, cross-talk fraction, t_{rise} deterioration and cross-talk charge in 20ns as a function of the detector length L for signals with t_{rise}=200 ps.

References

[1] A. Blanco et al., NIM A 485(2002)328.

[2] D. Belver et al., doi:10.1016/j.nima.2008.12.090.

[3] N. Majumdar et al., NIM A 595(2008)346.

[4] D. Gonzalez-Diaz, talk at XII CBM coll. meeting (2008).

Feasibility evaluation of the straw tube detector option for the CBM muon system*

A. Zinchenko[1], D. Peshekhonov[1], V. Peshekhonov[1], and L. Naumann[2]
[1]JINR, Dubna, Russia; [2]FZ Dresden-Rossendorf, Germany

The emission of lepton pairs out of the hot and dense collision zone of heavy ion reactions is a promising probe to study the electromagnetic structure of hadrons under extreme conditions. The reconstruction of vector mesons ($\rho, \omega, \phi, J/\psi, \psi'$) is one of the prime tasks of the CBM experiment. To perform such a study using a dimuon decay mode, a muon system consisting of a set of absorbers and detector stations will be built.

Since the muon absorber should efficiently suppress the particle flux, the downstream detector stations can be made using detector technologies different from those in the first stations. The straw tube option looks quite promising due to a good coordinate resolution of such detectors ($\sim$200 μm in the drift direction) and the fact that they have been widely used for more than a decade and this detector technology has shown to be rather simple and reliable[1].

A possible muon system configuration is shown in Fig. 1, where the last 3 detector stations (behind absorbers 4-6) are built from the straw tubes. Each station consists of 3 double layers (doublets) with different doublets rotated around the beam axis to create stereo views. Three doublets of the same station, separated in Z by some distance, can be used to make track vectors necessary for efficient suppression of the background.

In order to check the ability of the straw detectors to work in the CBM experimental conditions, the simulation and reconstruction software has been modified to properly handle the new detector type. The Monte Carlo simulation has shown that the detector occupancy (the most limiting factor of the tubes) can stay within acceptable limit even with the maximum tube lengths covering the entire absorber diameter (Fig. 2). In addition, it is possible to further reduce the occupancy by making the anode wires segmented[2, 3].

It is planned to further proceed in the direction of evaluating the muon system performance with straw tube stations and optimizing the detector geometry (in particular, tube diameter and stereo angle).

The foreseen software changes aim at the possibility to use the same Monte Carlo event samples for different detector options by simulating detector specific features at the hit production level.

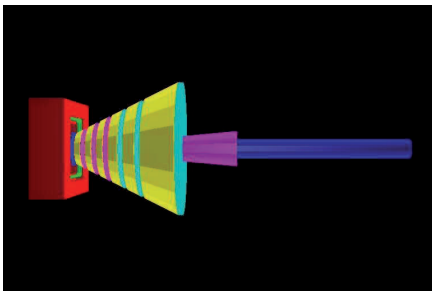

Figure 1: CBM muon system configuration with straw tubes: 3 last detector stations (behind absorbers 4-6) are built from straw tubes.

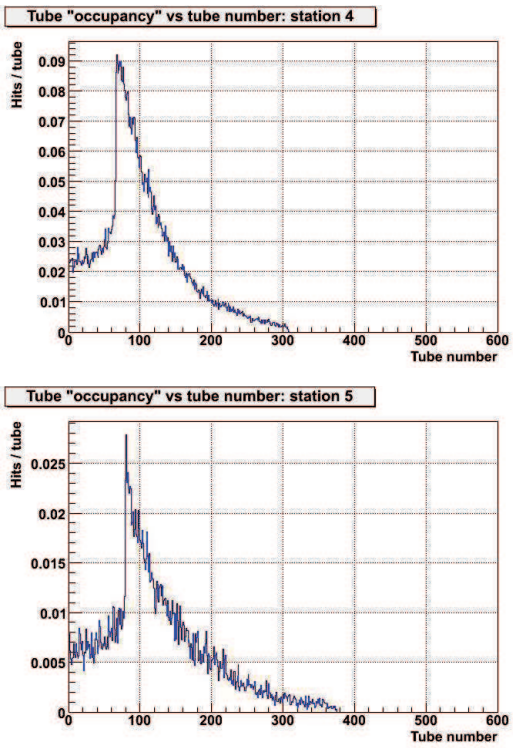

Figure 2: Occupancy (average number of hits per event per tube) vs tube number in muon stations 4 and 5 for Au+Au collisions at 25 AGeV. The straw tube diameter is 4 mm.

References

[1] G. D. Kekelidze and V. D. Peshekhonov, Phys. Part. Nucl. **33** (2002) 343 [Fiz. Elem. Chast. Atom. Yadra **33** (2002) 669].

[2] 12th CBM collaboration meeting, October 2008, Dubna, http://cbm2008-oct.jinr.ru/files/15_MUCH_15-00_Peshekhonov.pdf.

[3] K. Davkov *et al.*, Nucl. Instrum. Meth. A **584** (2008) 285.

* Work supported by GSI-INTAS grant No. 8729.

Segmentation study of the CBM Muon Detector *

D. Dutta †, A. Kiseleva, and C. Höhne for the CBM collaboration
GSI, Darmstadt, Germany

This contribution persuits first step towards a full detector design study for the CBM Muon Chamber(MUCH) detector. For a realistic detector design and optimization of the detector layout with respect to the physics signals, a simple description of the segmentation of the detector is required allowing for more flexibility. The present study demonstrates a new "Flexible Segmentation Scheme" (FSS) with multidimensional flexibility which needed to develop a detailed detector layout.

The aim of the present segmentation study is to get a realistic description of the MUCH detector. In order to take into account the variation of the hit density with the distance from the beam axis, the MUCH stations are segmented in different annular regions with appropriate pad size (rectangular in this case) required to achieve the desired hit occupancy. Nine different regions are defined sequentially doubling the pad area. A segmentation scheme was achieved already earlier[1] based on 5% hit occupancy, where the radius of each ring-like region was chosen such that the mean hit density got reduced by a factor of 2 in adjacent regions and correspondingly the pad area was doubled. However, for a realistic detector design, the pad sizes and detector layout should be developed in close connection to the detector R&D. It is essential to have a maximum coverage within the detector acceptance. The present study implements a "Flexible Segmentation Scheme"(FSS) which is essential for the optimization of the detector layout. The following flexibility is achieved in the present scheme:

- Flexible number of regions with different pad sizes in each detector.
- Flexible radial size of each ring region.
- Flexible number of channels.
- Flexible pad size.

The first step of the optimization of the detector layout is to study the hit reconstruction efficiency. In the present study, a CBM Muon Chamber (MUCH) geometry is used which consists of 15 tracking stations made up of GEM detectors, sandwiched between 5 iron absorber layers of variable thickness (125cm in total) with an additional shielding near the beam pipe. Events are generated using the UrQMD event generator for central Au+Au collisions at 25AGeV and transported through the detector setup using a transport code based on GEANT3 in the CBMROOT simulation framework. Hits are generated from the pad centre of the GEANT Monte Carlo(MC) points.

Figure 1 shows the hit efficiency in $\%$ (No. of Hits/No. of MC Points) from the "Flexible Segmentation Scheme" for different stations. The segmentation of detector stations is optimized with respect to the hit efficiency in the FSS. The regions and pad dimensions used in FSS for different stations are described in Table 1. The minimum pad dimension is $2.77\text{mm}\times5.54\text{mm}$ which is well suited for GEM detectors. Figure 1 shows average hit efficiency $\approx 98\%$ which reflects a good match of the reconstructed hits with the MC points in the present FSS scheme throughout all the stations. Hit efficiency loss by 3% in the first station of each triplet is due to multiple hits in the presence of secondary electrons from the absorber.

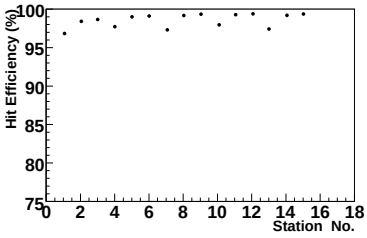

Figure 1: Hit efficiency in $\%$ from the "Flexible Segmentation Scheme" for different stations of MUCH.

Table 1: Ring regions and pad dimensions in different stations used for estimating the hit efficiency with FSS

Stations	Region No.	Radius (cm)	Pad size (cm × cm)
1,2,3	3	13.7 -25.0	0.277×0.554
	4	25.0 -45.0	0.554×0.554
	5	45.0 -62.3	0.554×1.108
4,5,6	4	17.4 -32.0	0.554×0.554
	5	32.0 -48.0	0.554×1.108
	6	48.0 -81.4	1.108×1.108
7,8,9	5	21.4 -40.0	0.554×1.108
	6	40.0 -56.0	1.108×1.108
	7	56.0 -100.5	1.108×2.217
10,11,12	5	26.2 -40.0	0.554×1.108
	8	40.0 -124.5	2.217×2.217
13,14,15	6	31.5 -50.0	1.108×1.108
	9	50.0 -151.0	2.217×4.434

The present segmentation scheme shows a good coverage of the detector acceptance with pads and a good hit efficiency with negligible loss due to multiple hits for a simple detector layout. The final layout of the detector will be optimized by studying the physics signals. Next step is a realistic description of detector signals using routines for producing real charge distributions.

References

[1] E. Kryshen et al. *Digitization and hit finding in the CBM muon detector*, CBM Progress Report 2007.

* Work supported by EU/RP7, JCT-WP6 No. 50706.
† D.Dutta@gsi.de

Optimization of the CBM muon detection system*

A. Kiseleva[1], C. Höhne[1], E. Kryshen[2], A. Lebedev[1], and M. Ryzhinskiy[3]
[1]GSI, Darmstadt, Germany; [2]PNPI, Gatchina, Russia; [3]SPbSPU, St.Petersburg, Russia

The experimental challenge for muon measurements in heavy-ion collisions at FAIR energies is to identify low-momentum muons in an environment of high particle densities. The CBM concept is to track the particles through a hadron absorber system, and to perform a momentum-dependent muon identification. This concept is realized by segmenting the hadron absorber in several layers, and placing triplets of tracking detector planes in the gaps between the absorber layers. The iron absorbers are located downstream from the Silicon tracking system which provides the momentum measurement. In order to reduce meson decays into muons the absorber/detector system has to be as compact as possible.

The absorber layout has been optimized in simulations performed for central Au+Au collisions at 25 AGeV. The primary particles are produced with the UrQMD event generator, and the GEANT3 transport code is used to propagate the particles through the material, and to create secondary particles. The hit density in the first detector layer behind an iron absorber of 10 cm thickness is about 1 hit $(\mathrm{cm}^2\ \mathrm{event})^{-1}$. This hit density would result in a detector pad size of $1.4\times2.8\ \mathrm{mm}^2$ if the occupancy should be kept below 5%. The particle multiplicity behind the first absorber can be reduced by increasing the thickness of the iron plate. In this case, however, small angle scattering in the absorber material is increased, and the matching efficiency between the ingoing and outgoing tracks decreases. In order to find a compromise between detector granularity and matching efficiency we have conducted a study in which the thickness of the first iron absorber has been optimized with respect to the detector granularity, and the number of reconstructed background tracks.

In a first step we studied the particle multiplicity behind the first iron absorber layer as function of the absorber thickness. The result is shown in figure 1 for (primary and secondary) particle multiplicities per event detected behind an iron absorber of variable thickness. The multiplicity at thickness zero corresponds to the number of particles in front of the absorber. The particle multiplicity is dominated by the yield of secondary electrons which rises steeply up to an absorber thickness of about 5 cm, and then drops with increasing material thickness. The particle multiplicity varies also strongly with the radial distance from the beam. The decrease of multiplicity with increasing radial distance is shown in the left panel of figure 2 for different absorber thicknesses. This effect is important for the segmentation of the tracking chambers into pads which may vary in size by more than one order of magnitude from the inner to the outer area of the detector.

* Work supported by EU/FP6 HADRONPHYSICS and by INTAS.

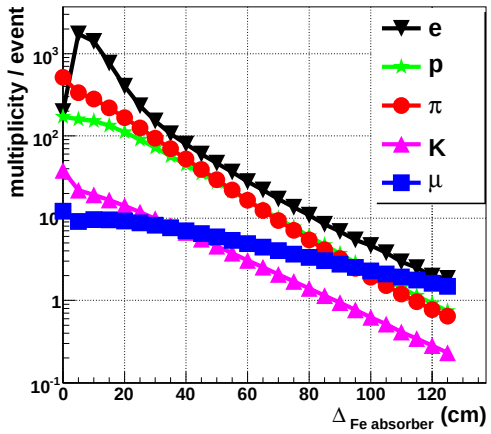

Figure 1: Particle multiplicity per event as a function of Fe absorber thickness.

In a second step we investigated the influence of the thickness of the first iron absorber on the track reconstruction performance. For this study, we used a complete muon detection system consisting of 5 absorber layers and 15 tracking chamber planes, grouped in triplets behind each absorber slab. The total absorber thickness is kept constant to 125 cm, whereas the thickness of the first layer is varied between 10 and 40 cm. After track reconstruction, we calculated the invariant mass spectrum which represents the background for the dimuon measurements. The resulting spectra are shown in the right panel of figure 2 for different thicknesses of the first absorber layer. It turns out that the background increases by almost one order of magnitude when increasing the thickness of the first absorber layer from 10 cm to 40 cm. In summary, a first iron absorber of 20 - 30 cm thickness seems to be the best compromise between hit density and background tracks.

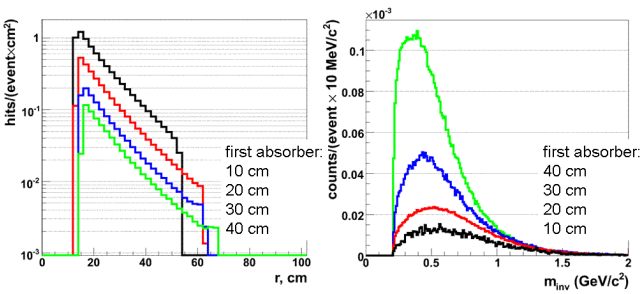

Figure 2: Number of hits per event (left) and invariant mass spectra of reconstructed background tracks (right) for different thicknesses of the first absorber.

Muon reconstruction at high particle multiplicities in CBM*

A. Kiseleva[1], C. Höhne[1], E. Kryshen[2], A. Lebedev[1], and M. Ryzhinskiy[3]
[1]GSI, Darmstadt, Germany; [2]PNPI, Gatchina, Russia; [3]SPbSPU, St.Petersburg, Russia

The major technical challenge of muon measurements in CBM is the large hit density of up to 1 hit/cm^2 per event in the muon tracking chambers after the first iron absorber with 20 cm thickness. According to simulations using the TGEANT3 transport code about 50% of all hits in these chambers are caused by secondary electrons knocked out of the absorber by the primary particles. The electron hits per event calculated for central Au+Au collisions at 25 AGeV are shown in figure 1 for the different muon tracking chambers which are grouped in triplets. When using the transport codes TGEANT4 and TFLUKA the multiplicity of secondary electrons is increased by 60% and 80%, respectively, with respect to TGEANT3. Due to the lack of experimental data it unclear which of the results is closer to reality. Therefore, we have performed simulations where we artificially increase the number of secondary electrons in order to test the robustness of our track reconstruction algorithms.

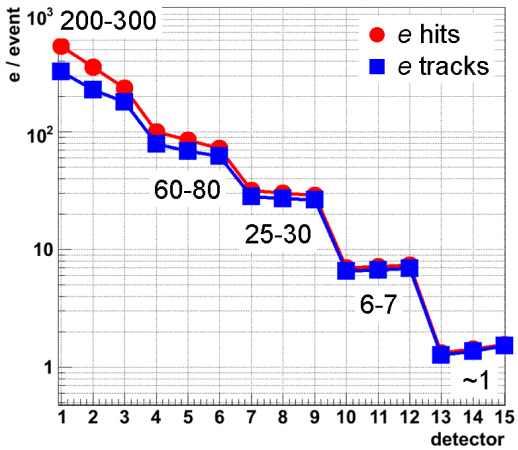

Figure 1: The number of electron hits and tracks in muon system for Au+Au central collisions at 25 AGeV.

Our first approach was to add uncorrelated hits in the tracking chambers. In order to generate a realistic noise pattern we produce additional hits according to the distribution of secondary electrons as calculated with TGEANT3. The results of the track reconstruction with additional noise hits are shown in table 1 for ω mesons from central Au+Au collisions at 25 AGeV. The signal-to-background (S/B) ratio decreases by about 30% when injecting 10 noise hits per secondary electron as calculated with TGEANT3. The increase of secondary electrons by a factor of 10 corresponds to an increase in total multiplicity by a factor of 5.3. I this case the ω reconstruction efficiency decreases by almost a factor of 2.

noise	no noise	+1 hit	+5 hits	+10 hits
$N_{hits+noise}/N_{hits}$	1	1.4	3.2	5.3
S/B ratio	0.1	0.09	0.07	0.07
efficiency (%)	1.9	1.6	1.4	1

Table 1: Signal-to-background ratio and efficiency for ω meson from Au+Au central collisions at 25 AGeV without and with additional electron hits up to 10.

Our second approach is based on additional electron tracks. According to the simulations with TGEANT3 about 98% of the secondary electrons produced in the absorber have a total momentum of less than 0.5 GeV/c and a transverse momentum of less than 0.2 GeV/c. Using these data as an input for the BOX'generator in the CBMroot framework we calculated single particle tracks. The results of the simulation with additional electron tracks are presented in table 2.

additional tracks	no tracks	+1 track	+5 tracks	+10 tracks
$N_{hits+e_{Box}}/N_{hits}$	1	1.5	3	5.4
S/B ratio	0.1	0.09	0.09	0.06
efficiency (%)	1.9	2	2	1.4

Table 2: Signal-to-background ratio and efficiency for ω meson from Au+Au central collisions at 25 AGeV without and with up to 10 additional electron tracks.

* Work supported by EU/FP6 HADRONPHYSICS and by INTAS.

The di-muon trigger for CBM*

A. Kiseleva[1], D. Gonzalez Diaz[1], C. Höhne[1], E. Kryshen[2], and M. Ryzhinskiy[3]
[1]GSI, Darmstadt, Germany; [2]PNPI, Gatchina, Russia; [3]SPbSPU, St.Petersburg, Russia

High statistics measurements of lepton pairs from the decay of vector mesons ($\rho, \omega, \phi, J/\psi$) produced in heavy-ion collisions require high reaction rates, and, hence, a selective trigger. The low particle multiplicities behind the hadron absorber of the CBM muon detection system enable the implementation of a fast trigger on muon pairs. The concept is to develop a flexible trigger scheme according to the muon momentum which depends on the mass of the vector meson and on the beam energy. For beam energies above 15 AGeV we will use only the last 3 muon chambers (MuCH) located behind the full absorber of 225 cm iron for the generation of a charmonium trigger, whereas the trigger on low-mass vector mesons will be derived from hits in the 3 muon tracking chambers in front of the last absorber, i.e. after 125 cm of iron. The trigger generation proceeds via the following steps: (i) selection of events with at least 6 hits in the last (or second last) detector triplet, (ii) calculation of a tracklet by a linear fit of the hit positions, (iii) extrapolation of the tracklet to the vertex, and selection of tracks according to the fit parameters (χ^2 and vertex constraint), and (iv) selection of the proper time-of-flight using the RPC-TOF wall (for charmonia). The event selection will be performed online by the CBM computer farm based on many-core processors.

The quality of the track extrapolation depends on the position resolution of the muon trigger chambers. Therefore, the trigger performance has been investigated for different granularities (version 1: pad size 2.23×8.96 cm^2, version 2: pad size 2.23×4.48 cm^2). For the simulations we assume a detector efficiency of 100%. The track selection criteria, i.e. the χ^2 of the fit, the X- and Y-distributions at $Z = 0$ cm vary with the pad size. If these selection criteria ("MuCH cut") are fulfilled, the time-of-flight information is used for final track selection ("ToF cut"). For the ToF detector we assume a position resolution of 300 μ and a time resolution of 80 ps. The momentum of the particle is calculated from the time-of-flight (assuming a muon mass), and the invariant mass of the muon pair is derived from the momenta and the opening angle of two tracks. The invariant mass is shown in figure 1 as a function of the opening angle for the J/ψ signal (left panel) and for the background (right panel). The different shapes of the distributions permit to reduce the background further by a "ToF cut". The trigger performance is quantified by the background suppression factor (which is the fraction of minimum bias events which survive the trigger cuts) and by the efficiency for J/ψ mesons which pass the trigger conditions. The background suppression factor and the J/ψ trigger efficiency for minimum bias Au+Au collisions at 25 AGeV are listed in table 1 for the detector segmentation version 2. The background suppression factor decreases by about a factor of 2 if the pad size of the muon detectors is increased by a factor of 2 (segmentation version 1).

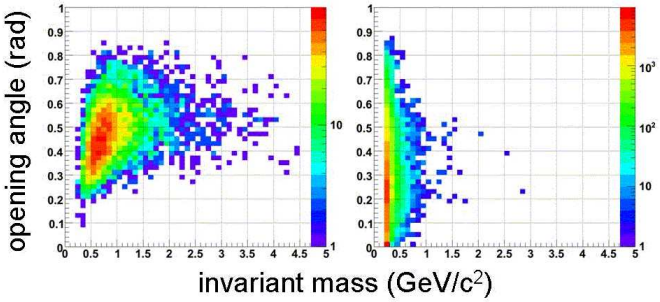

Figure 1: Invariant mass versus opening angle for J/ψ (left panel) and for the background (right panel) calculated for minimum bias Au+Au collisions at 25 AGeV.

trigger cuts	no cuts	MuCh	MuCh+ToF
suppression factor	1	606	2222
J/ψ efficiency (%)	20.3	15.2	13.7

Table 1: Background suppression factor for minimum bias Au+Au collisions at 25 AGeV and detection efficiency for J/ψ mesons after different trigger cuts.

The CBM data acquisition system is able to process minimum bias Au+Au collisions up to a reaction rate of 25 kHz without trigger reduction. Hence, the CBM experiment can be operated at the full design luminosity of 10 MHz if the event rate is reduced by a factor of 400. This factor is easily achieved by the dimuon trigger even without time-of-flight selection (see table 1).

In order to test the robustness of the trigger concept with respect to additional detector noise we added 10 hits in each muon chamber of the trigger triplet. Using the "MuCh+ToF" trigger conditions background is suppressed by a factor 1923, i.e. the background suppression factor is reduced by only 15 % as compared to the calculations without additional noise.

For low-mass vector mesons only the selection criteria based on the track quality can be applied ("MuCh cuts"). Due to the high hit density in the detector triplet in front of the last absorber layer a background suppression factor of about 20 can be achieved without appreciable loss of signals. This factor would permit to run the CBM experiment with about 500 kHz. Studies are in progress to improve the trigger concept for low-mass vector-mesons.

* Work supported by EU/FP6 HADRONPHYSICS and by INTAS.

Muon measurements at different beam energies in CBM*

A. Kiseleva[1], C. Höhne[1], E. Kryshen[2], A. Lebedev[1], and M. Ryzhinskiy[3]
[1]GSI, Darmstadt, Germany; [2]PNPI, Gatchina, Russia; [3]SPbSPU, St.Petersburg, Russia

The CBM muon detection system is designed to measure muon pairs from the decay of vector mesons ($\rho, \omega, \phi, J/\psi$) produced in heavy-ion collisions. At FAIR energies the muon momenta can be rather low, and, therefore, we developed a muon detection concept which a dynamical definition of absorber thickness according to the muon momentum. The actual design of the muon detector system consists of 6 hadron absorber layers (iron plates of thickness 20, 20, 20, 30, 35, 100 cm) and 15-18 gaseous tracking chambers located in triplets behind each iron slab. The absorber/detector system is placed downstream of the Silicon Tracking System (STS) which determines the particle momentum. The definition of a muon depends on its momentum which varies with the mass of the vector mesons and with beam energy. For example, for beam energies above 15 AGeV muons from the decay of J/ψ mesons have to pass all 6 absorber layers with a total iron thickness of 225 cm corresponding to 13.4 interaction length λ_I. The muons from the decay of low-mass vector mesons (ρ, ω, ϕ) only have to penetrate through 5 iron absorber layers with a total thickness of 125 cm (corresponding to 7.5 λ_I).

The multiplicity of vector mesons is calculated with the HSD event generator, whereas the dimuon decay kinematics is computed with the PLUTO code. The signals are embedded in a heavy-ion collision which is simulated with the UrQMD event generator. Both signal and background tracks are transported through the detector setup using the TGEANT3 code within the cbmroot simulation framework. The L1 tracking procedure [1] is used for the track finding and for momentum reconstruction in the STS. LIT tracking [2] is used for track finding in MuCh. Tracks reconstructed in the STS are extrapolated through the full hadron absorber system, and then are accepted as muons. For the track reconstruction we assume that the detector layers are segmented into pads according to an occupancy of 5%. The efficiency for vector meson detection and the signal-to-background ratio, calculated in a $\pm 2\sigma$ window around the signal peaks for Au+Au collisions at 15, 25 and 35 AGeV are presented in table 1.

The signal-to-background (S/B) ratio for low-mass vector mesons does not vary significantly with the beam energy, whereas for J/ψ mesons it increases strongly with beam energy due to the steeply rising charm production excitation function close to threshold. The signal efficiency decreases with decreasing beam energy due to muon absorption: muons with momenta below 1.6 GeV/c are stopped in 125 cm of iron. The efficiency for muons from low-mass vector mesons can be improved by accepting tracks as muons which pass only 4 iron absorber layers with a total thickness 90 cm ("soft muons"). By reconstructing pairs from "soft" muons and "hard" muons (which pass 125 cm of iron) one can increase the efficiency of about a factor of 2 without decreasing the S/B ratio.

	ρ	ω	ϕ	J/ψ	ψ‘
beam energy	S/B ratio				
15 AGeV	0.002	0.08	0.01	3	-
25 AGeV	0.002	0.1	0.03	7	0.09
35 AGeV	0.001	0.09	0.03	11	0.2
	efficiency (%)				
15 AGeV	1.4	1.3	2.2	11.8	-
25 AGeV	1.9	1.9	4.3	16	19
35 AGeV	1.8	3.3	5.4	16	19

Table 1: Signal-to-background (S/B) ratio and efficiency for vector mesons from central Au+Au collisions at 15, 25 and 35 AGeV.

We have also investigated the possibility to perform muon measurements at beam energies below 10 AGeV. For such low beam energies we study two different definitions of muons: tracks which pass at least 3 iron layers (60 cm), or tracks which pass at least 4 iron layers (90 cm). Simulations have been performed for ω mesons produced in central Au+Au collisions at 8 AGeV. The resulting signal-to-background ratios and signal efficiencies are S/B = 0.05 and ϵ = 1.65 for 60 cm iron, and S/B = 0.1 and ϵ = 0.95 for 60 cm iron. At low beam energies the detector acceptance can be improved by reducing the magnetic field. The simulations show that a reduction of the magnetic field by 50% enhances the signal efficiency up to 22%.

Finally, we have performed a simulation of J/ψ production in proton-carbon collisions at the maximum SIS100 energy of 30 GeV. The resulting S/B ratio and efficiency for ω mesons are listed in table 2 both for the PLUTO and the HSD event generator.

	PLUTO		HSD
	ω	J/ψ	J/ψ
S/B ratio	11	147	115
efficiency (%)	4.3	22.7	13.3

Table 2: Signal-to-background ratio and efficiency for ω and J/ψ mesons from p+C collisions at 30 GeV simulated with HSD and PLUTO.

References

[1] S. Gorbunov, I. Kisel and Iou. Vassiliev, CBM-PHYS-note-2005-001.

[2] A. Lebedev et al, see this report

* Work supported by EU/FP6 HADRONPHYSICS and by INTAS.

Progress in the development of the fast-TRD chip for the CBM experiment at FAIR

H.K. Soltveit[1], J. Stachel[1], and M. De Gaspari[1]
[1]Physikalisches Institut Universität Heidelberg (Germany)

In 2006 the first prototype of the fast-TRD PASA [1, 2, 3] for the Compressed Baryonic Matter (CBM) experiment at FAIR was produced and successfully operated in a test beam at GSI Darmstadt [4, 5]. The purpose of this first prototype production was to show that the chip fulfills the physics needs given the high rate expected for the fast-TRD with a known and reliable technology, AMS 0.35 micron. The next step was then to migrate from AMS 0.35 to IBM 0.13 micron technology. The motivation for going to 130 nm CMOS technology was to achieve a lower material budget, increased speed and less power, and better radiation hardness performance. Moreover, this technology is presently the standard in the industry.

The mixed-mode circuit shown in Figure 1 is under development in IBM 0.13 micron technology. The first version contains 128 channels, each of them consists of a programmable charge sensitive amplifier with dual polarity performance, a detector leakage compensation, a power calibration and an adaptive gain setting. Since the anticipated capacitive load operation region is in the range from 10-40 pF, an internal bias generators controlled by DACs is implemented in order to be able to use the chip for detectors of various capacitance and to optimize the front-end noise performance for a given input capacitive load. This also has the possibility of compensating the bias drifts due to possible radiation effects. To be able to cope with both charge polarities a polarity circuit is implemented, that in addition is used as an amplifier. The circuit has an adjustable power setting depending on the pulse rate and on the peaking time for power optimization.

A calibration circuit to perform system calibration and test with the final assembly is under development, as well as a programmable shaper peaking time CR-$(RC)^2$. The time constants are changed by changing the capacitors, since the resistors suffer from large distortion due to the variation of the switch resistance with the applied voltage. To ensure a good energy resolution and peak position stability at high count rate a baseline restorer is under development to eliminate the baseline shift. A peak detector is used to sample the maximum event voltage, and therefore the energy of the detected signal.

In addition, a programmable (8-12) bit pipeline Analog-to-Digital Converter (ADC) with an adaptable sampling rate from 5-80 MHz is under development. The 12-bit ADC version is progressing well and the following blocks are already in the final design phase: The Multiplying Digital to Analog Converter (MDAC), which is the most critical, since it performs the sample and hold, the D/A conversion, and the subtraction and multiplication. A bootstrapped circuit was designed and implemented to reduce charge injection by keeping the gate-source voltage constant. A Beta-multiplier biasing circuit and an amplifier was already designed and layed out. These components have been implemented and submitted together with a 10-bit ADC developed at CERN [6].

To allow remote set-up and to control the individual channels and their different blocks, a set of registers that control the mask bits and DAC values is under development. The extensive range of peaking times and conversion gains will allow the circuit to be used for a broader spectrum of detectors.

The chip can be masked in groups of 16 channels (16-32-64 and 128), depending on the segmentation needed. Further signal processing at the shaper output of this chip depends strongly on the specific requirements of the foreseen applications.

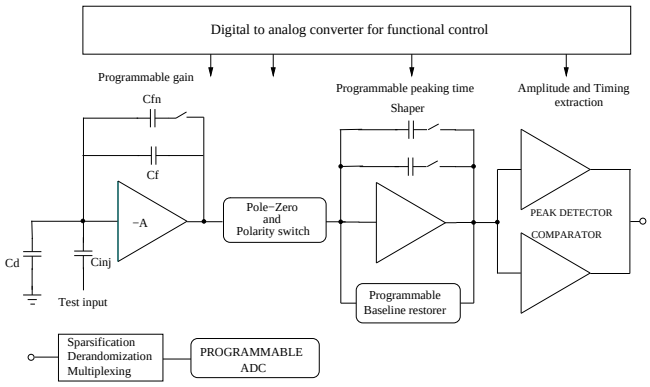

Figure 1: A simplified schematic of the fast-TRD chip

References

[1] H.K. Soltveit et al., GSI Annual Report 2004, p 364

[2] H.K.Soltveit et al., GSI Annual Report 2005, p 72

[3] http://documents.cern.ch/cgi-bin/setlink?base=yellowarticle&categ=2007-001&id=p520

[4] Klein-Boesing, et al., Nucl. Instr. Meth. Phys. Res. A 585 (2008) 83-87

[5] A. Andronic et al., GSI Annual Report 2006, p 233

[6] H. Franca and L. Musa, Privat communication.

The rate challenges of the CBM-TRD

D. Gonzalez-Diaz[1], A. Andronic[1], A. Battiato[1], C. Garabatos[1], A. Kalweit[1], and F. Uhlig[1]
[1]GSI, Darmstadt, Germany

J/Ψ and Ψ' trigger and detection in the di-electron decay channel with the CBM experiment requires a π suppression of 100 and a position resolution better than 300 μm at particle fluxes of 100 kHz/cm^2. A TR detector based on MWPCs with Xe/CO_2 gas appears to be suited for the task, as it was proved in a series of works [1], [2], [3]. Through a complementary effort consisting of an analytical study substantiated by a series of systematic measurements, we have looked into the practical limits of the MWPC technology for TR detection, regarding both the maximum operating gain and particle flux (details in [4], [5], [6]).

A maximum working gain of $m_o = 3 \times 10^5$ was determined for Xe/CO_2 mixtures both in chambers with $s = 3$ and 4 mm anode wire pitch, being independent from the fraction of quencher. This behaviour is suggestive of a major role of electron feed-back from ion collisions with the cathodes. At the above-mentioned gain, operation was halted due to a form of self-sustained discharge, being the chamber performances recovered after a power cycle. Since gains $m_o = 5\times10^3$-10^4 have been proved to be sufficient for high efficiency and energy resolution [3], a safety factor of 30-60 in the initial charge (for dealing with nuclear fragments or highly ionizing secondaries) is assured.

Another aspect that was scrutinized in detail due to the existence of analytical methods was the rate capability of the device under different conditions, of which we focus on the Xenon mixtures. To start with, the Mathieson model [7] together with the Blanc's law for ion mobilities was used. A correction due to finite beam effects is important (up to a factor 10 in the estimated rate capability) when the beam and the chamber typical dimensions are comparable. So, this effect was studied in detail and indeed a remarkable agreement with the analytical behaviour of the correction factor d_m [8] was found for a series of measurements at different beam sizes. In order to extrapolate the measurements to the behaviour under minimum ionizing particles (mips) irradiation we took as reference the measured values for the energy loss in Xe/CO_2 mixtures [9]. By defining the rate capability at 10% gain drop and $m_o = 10^4$ as the figure of merit of a MWPC, we found a convenient representation by plotting it as a function of the fraction of quencher and chamber pitch, shown in Fig. 1. The lines correspond to the Mathieson model when the existing values for the mobility of CO_2^+ in the primary gas components are used (no free parameter). The absorption probability for characteristic TR photons is also depicted on the right y-axis. In particular, previous measurements from [3] can be accurately described by the same model [6].

Under reasonable assumptions (see [6]) the most critical dependence of the rate capability with the chamber gap ($\propto 1/h^3$) can be shown in a single picture, where the shadowed

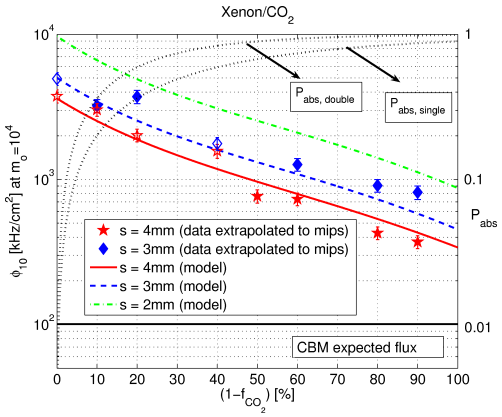

Figure 1: Rate capability (data and model) for mips at 10% gain drop (ϕ_{10}) and $m_o = 10^4$.

area indicates the region of gap sizes where a MWPC could fulfill the CBM requirements in terms of rate capability and X-ray absorption probability. This study confirms that the value chosen for the prototypes ($h = 3$ mm) is indeed a very good choice.

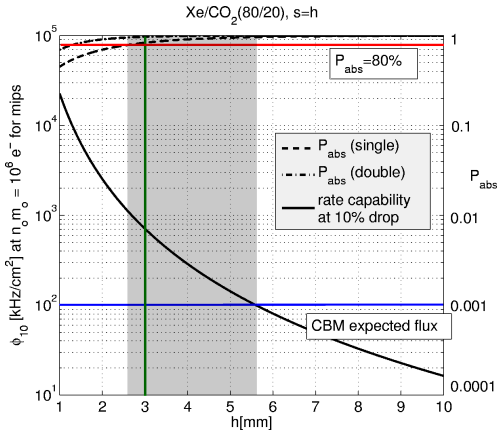

Figure 2: Rate capability and TR absorption probability vs the chamber gap h. The shadowed area is the region where a chamber would be well suited for the TRD of CBM.

References

[1] A. Andronic NIM A, 563(2006)349.
[2] M. Klein-Bosing et al., NIM A, 585(2008)83.
[3] M. Petris et al., NIM A, 581(2007)406.
[4] C. Garabatos et al., GSI report(2006), INSTR-METH-41
[5] D. Gonzalez-Diaz, GSI report(2007), FAIR-EXP-21.
[6] D. Gonzalez-Diaz et al., to be submitted to NIM A.
[7] E. Mathieson, NIM A, 249(1986)413.
[8] G.C.Smith, E. Mathieson, IEEE, TNS 34-1(1987)411.
[9] A. Andronic et al., NIMA A, 525(2004)447.

Track reconstruction in the MUCH and TRD detectors of CBM

A.Lebedev[1,2], C.Höhne[1], I.Kisel[1,3], G.Ososkov[2], and the CBM collaboration*
[1]GSI, Darmstadt, Germany; [2]LIT JINR, Dubna, Russia; [3]KIP, University of Heidelberg

In this contribution we present new developments and results for the LIT track reconstruction package for CBM in the CbmRoot framework.

The reconstruction package is organized to be flexible with respect to feasibility studies of different physics channels and to optimization of the detector geometries. The tracking software has been redesigned to make it more general and to simplify the support. The main components of the reconstruction package include track finding, fitting, propagation and selection.

The track propagation algorithm has been improved considerably. The algorithm consists of track extrapolation, calculation of material effects and the geometry navigator, managed by the track propagator, which performs the transport of the track. The extrapolation part relates to the geometrical extrapolation, governed by the equations of motion. In case of the absence of a magnetic field a straight line model is used for the tracks. In the presence of a magnetic field the equation of motion for a charged particle is solved with the 4th order Runge-Kutta method with a parallel integration of the derivatives. Material effects are taken into account by updating the track parameters and covariance matrix due to energy loss (ionization, bremsstrahlung and direct pair production) and multiple Coulomb scattering (Highland formula). The implementation of the geometry navigator is based on the ROOT geometry package which allows track propagation independent on the geometry. The track propagation algorithm is done in steps to allow for more precise calculation for material effects. The GEANE algorithm is also included in the track reconstruction as an alternative to the LIT propagation algorithm. A detailed description of the developed track propagation algorithm and its comparison with GEANE is given in Ref. [1].

The track finding algorithm was divided in two parts, track recognition and track selection. The track recognition is based on the track following method with branches and Kalman Filter. Reconstructed tracks are selected for their quality afterwards. The track selection is based on track quality criteria and checks for shared hits between tracks.

The detailed layout of the detectors is still under discussion. For the TRD and the MUCH stations in the high track density region pad layout is forseen based on MWPC or GEM chamber technology. For the later detector stations in MUCH where track densities are low, straw tube chambers are under discussion.As this detectors provide not pad size but long strip like hits, the tracking algorithm was modified in order to support all these structures.

The track reconstruction algorithm has been tested for the standard TRD setup and three different MUCH geometries. A total absorber length of 125 cm iron ("compact") separated into 5 slices with 2 detectors in between each and 2 afterwards; and 2 versions with 225 cm iron absorber ("standard") in 6 slices with 3 detector stations in between each once using pad layout for all, once straw tubes for the last 9 stations ("straw").

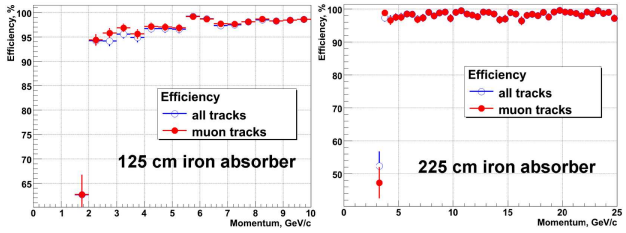

Figure 1: Track finding efficiency in dependence on momentum for 125 cm of iron (left) and 225 cm of iron (right).

The following simulation events have been used for testing. Central Au+Au collisond at 25 AGeV beam energy from UrQMD were used as background. 25 primary e+ and 25 primary e- with momenta 1 GeV/c $\leq$ p $\leq$ 10 GeV/c were embedded in each event for TRD tests. 5 primary μ^+ and 5 primary μ^- with momentum 1.5 GeV/c $\leq$ p $\leq$ 10 GeV/c for compact MUCH, 2.5 GeV/c $\leq$ p $\leq$ 25 GeV/c for standard and straw MUCH were embedded in each event.

The mean TRD track finding efficiency for reference tracks is 96%, for electron tracks 91%, the ghost rate is 3%.

The MUCH track finding efficiency for the three discussed geometries is presented in Table 1, the momentum dependence is shown in Figure 1.

Geometry	Compact	Standard	Straw
All	96.2	97.5	95.4
Reference	97.1	97.6	95.4
Muon	96.8	97.5	95.4
Ghost	1.5	0.2	0.2

Table 1: Track finding efficiency for compact, standard and straw MUCH geometries

References

[1] A.Lebedev, G.Ososkov, *LIT Track Propagation for CBM, CBM note* (2008) http://www.gsi.de/documents/DOC-2008-Dec-182-1.pdf

* supported by EU/FP6 HADRONPHYSICS

Front End Electronics for CBM

T. Armbruster[1], P. Fischer*[1], and C. Kreidl[1]
[1]University of Heidelberg, Germany

Abstract

Several sub-detectors of the CBM experiment will require front end amplifier chips optimized for their particular requirements. The FEE group is collecting the various needs and will provide one or more suited chips. During the ongoing preparatory phase, prototypes of important building blocks are studied by the various groups. One main activity in Heidelberg was the design of a preamplifier / shaper / discriminator test chip with varying front end characteristics, scaled on-chip load capacitors for detector emulation and a versatile injection circuit.

CBM FEE Goals

The CBM FEE group is developing self-triggered multi channel charge amplifiers with integrated time stamping, which is required due to the asynchronous operation of the experiment. The requirements of the various interested CBM sub-detectors (STS, TRD, MUCH, RICH) as well as from PANDA (MVD, GEM, TPC) may require more than one design because key parameters like the number of channels, the allowable power, input capacitance, input signal amplitude and distribution and the required amplitude resolution differ significantly. Two architectures are presently pursued: A low power, multi channel system with a moderate amplitude resolution and a chip with less channels, integrated ADC and more sophisticated amplitude processing. Both designs will required a charge amplifier so that a prototype test chip has been developed.

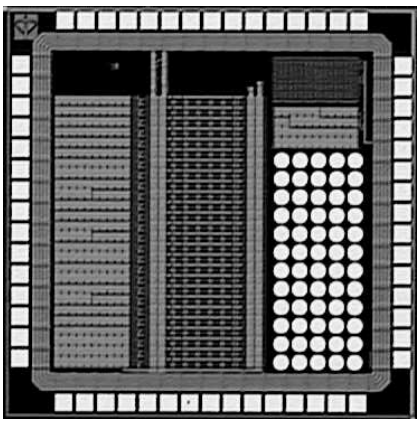

Figure 1: Photograph of the charge amplifier test chip.

Charge Amplifier Test Chip

After an initial design in 2007, a second test chip with 11 channels has been designed, submitted and tested. Each channel contains a charge amplifier with dc feedback, a second order shaper with $80\,\mathrm{ns}$ shaping time, a versatile injection circuitry and a discriminator with local threshold trim. All bias currents are generated with on-chip DACs. As it is visible on the chip micro-photograph in fig. 1, the channels (in the middle) are connected to a large amount of capacitors (on the left) to emulate varying detector capacitances. An array of bump bond (on the right) will be used for bumping tests. The chip also contains capacitance measurement circuits (upper right) to determine the exact values of the injection and the load capacitors.

Testing of the chip has started end of the year. All blocks operate as expected. As an example result, fig. 2 shows the noise for $\approx 10\,\mathrm{pF}$ input load for varying input bias current. The variation of the current maintaining constant bias conditions is achieved by connecting several instances of the amplifier in parallel. The behavior is as expected in simulation, albeit at a slightly higher level. The origin of this extra noise (bad calibration, noise injection through ground line) still needs to be determined.

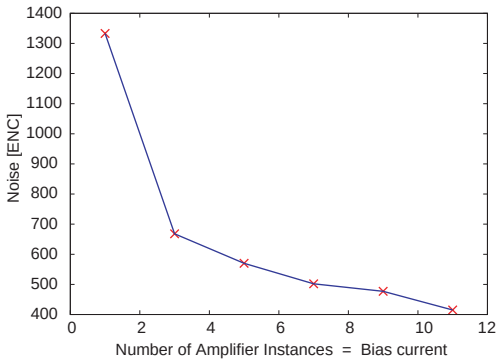

Figure 2: Preliminary ENC for varying input bias currents.

Further Work

In the same framework, bump bonding tests have been carried out, chips in the UMC $0.18\,\mu\mathrm{m}$ technology have been irradiated and work on a radiation hard library has been continued. Work on other building blocks, in particular a low power ADC, has been started.

* peter.fischer@ziti.uni-heidelberg.de

Improved Active Buffer Board of CBM*

W. Gao† [1], A. Kugel[1], A. Wurz[1], R. Männer[1], G. Marcus[1], and N. Abel[2]

[1]Chair for Computer Science V, ZITI, University of Heidelberg, Mannheim, Germany; [2]KIP, University of Heidelberg, Heidelberg, Germany

Abstract: The current PCIe interface of the Active Buffer Board of CBM was enhanced to enable run-time modifications of the functionality using dynamic paritial reconfiguration of the FPGA. The DMA logic was ported to the newest FPGA technology which provides a 64 bit PCIe module in contrast to the previous 32 bit version. The DMA engine works well without changing the software environment. A dual-ported event buffer mechanism was developed, using external SDRAM instead of the FPGA internal memory.

Introduction

The Active Buffer Board (ABB) receives CBM events, performs local buffering and formatting and forwards them to the host PC. The present ABB prototype is based on a 4-lane PCI Express (PCIe) card with one XILINX Virtex-4FX60 FPGA, a 2.5Gbit/s optical interface, 32MB of DDR memory and expansion connectors.

The basic PCIe interface uses a commercial IP core with a user-logic interface operating at the transaction layer. To achieve acceptable bandwidth (several 100MB/s) a custom data-flow controler – the DMA engine – is required which links the transaction layer interface with the memory subsystem.

32 bit PCIe DMA design ported to 64 bit

So far the DMA engine uses a PCIe interface module with a soft core in the Virtex4 FX20 FPGA [1]. The design took over 95% of the FPGA resources already for a 32 bit version. Since the new Virtex5 LX110T development board offers better performance and more logic resources, we ported the existing test environment to it. To keep the software including driver and test program unchanged, the 32 bit DMA logic and the simulation environment were ported to 64 bit because the PCIe core in Virtex5 is a 64 bit version only. This required to modify state machines and other logic in the DMA engine.

PIO and DMA tests are no problem on the Virtex5 development board with the block RAM as the target memory. The Virtex5 test in the existing Virtex4 software environment was successful. The DMA performance is about the same as that of the Virtex4 board.

* Work supported by EU, EURONS # RII3-CT-2004-506078, BMBF Hadr.- & Kernphys. # 06MN2291, GSI Hochschulpr. # MAMAEN

† wenxue.gao@ziti.uni-heidelberg.de

Dynamic Partial Reconfiguration on Virtex4

Operating systems require that certain peripheral devices must be permanently operational from boot time. This conflicts with the need to modify functionality, which is typical for re-configurable peripherals like the ABB, as a reconfiguration disconnects the PCIe interface until a subsequent reboot. One solution is dynamic partial reconfiguration (DPR) which allows to modify part of the FPGA, while another part remains unchanged and operational. In our design the PCIe interface is static and keeps running, while the DMA engines are dynamic and reconfigured, without computer reboot. Such an approach is very efficient, but it requires careful partitioning of the FPGA logic. The boundary between the static and the dynamic part requires the use of special interconnect elements that introduce one extra cycle of delay so that the original design has to be modified accordingly.

The DPR mechanism was implemented and tested on the ABB [1], by using 2 DMA engines as dynamic modules. To meet the timing constraint of 250 MHz for the global clock, synchronous busmacros are essential and hence, logic rewrite and reverify were done to preserve the original logic behaviour. The DMA performance tests show less than 1% penalty due to the busmacros, because the DMA channels are well pipelined [2].

Event buffer using paired SDRAM modules

The present memory interface of the DMA engine uses dual-ported memories available within the FPGA of a few 10 kB size only [1]. To allow larger dual-port buffers, a mezzanine for the Virtex-5 board has been designed. By interleaving the address areas of two SDRAM modules and providing both address and control buses independently to the FPGA, an almost perfect dual-port emulation can be obtained for the dominant access pattern of short bursts. In this way the memory size can be enlarged to several 10 MB or even GB. This fulfills the concurrent requirement of the Event Buffer, delivers the expected performance, and can be generalized for similar high performance concurrent memory design. Logic design and verification for this buffer are done, and tests are in preparation.

References

[1] J. Adamczewski, et al. Data Communication Tests on Active Buffer Board. GSI Scientific Report 2007. July 2008.

[2] W. Gao, et al. DPR in CBM: an Application for High Energy Physics. DATE'09 (accepted).

A Generic Link Protocol for the CBM DAQ-System*

F. Lemke, U. Bruening[1]
[1]University of Heidelberg, Mannheim, Germany

Introduction

The availability, reliability and the cost-effectiveness of high speed serial optical links increase the demand for using such links to connect the front end electronics (FEE) of a detector to the back end processing farm. This requires developing efficient protocols for such links, which fulfills the requirements of a detector control and data transport system. The developed generic link protocol (GLP) combines all functions for a detector control and data transport system including the time synchronization into one transmission link by using virtual channels in order to provide quality of service for the various tasks. The GLP can be used to interconnect modules providing high speed serializer/deserializer (SERDES) functions. It is a point-to point interconnect function using one SERDES lane and an internal 16+2 bit interface. The various features of this protocol will be described.

The GLP features and message types

The goal of the GLP [1] is to fusion all required functions of the detector network into one link protocol, as there are the time synchronization, the data read out and the detector control. Different traffic classes are provided in order to fit the requirements of the specific message types. Every traffic class is supported by a virtual channel to make these classes independent of each other. Moreover the classes have different priorities to access the physical link. The following traffic classes are supported:

- Deterministic Latency Messages (DLM)
- Data Transport Messages (DTM)
- Detector Control Messages (DCM)

The link layer has a speciality build in for the time synchronization of large networks, the Deterministic Latency Messages (DLM). This type of message is of fixed length with a packet size of only (16+2) bit. They are more a special control character than a message because they carry no real payload. The 16 special coded variants can be inserted at any time into the message stream and are received in the DLM channel. This allows synchronizing the time with a deterministic latency. The resolution of the time synchronization is related to the bit clock of the link, e.g. below 400ps for a 2.5Gbit/s link speed. If there are intermediate switch level required the DLM is forwarded by a special switch layer with deterministic latency. Data Transport Messages (DTM) are used to read out data from the FEE with high data rate. A variable payload of 8 Bytes to 64 Bytes is supported. The link allows bidirectional data transfers although the data stream is mainly unidirectional. Each data packet carries a CRC for link error detection.

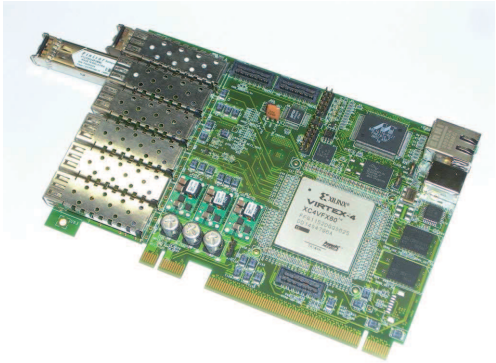

Figure 1: Data Combiner Board

Detector Control Messages (DCM) use its own virtual channel with CRC check and automatic hardware retransmission and an acknowledge message to provide a secure transport channel. The payload is defined by the user and can be used to access external register files in the FEE by using PUT GET semantics.

When the system is started an automatic sophisticated link initialization is performed. After the initialization is done the network can be used be the GLP to send messages. In case of a synchronization loss, the network links automatically reinitialize. The initialization, the packaging, the CRC checking and the handling of special network functions is done in the Link Port Module, which is provided as a synthesizable HDL module with an easy to use interface [2].

The GLP uses bidirectional point-to-point connections, therefore it works without routing on this level. Routing information can be easily added later in the next layer, if it is needed to forward the messages into larger networks.

The GLP eases the task of constructing DAQ systems and will be verified with a verification environment and with the existing Xilinx V4 Data Combiner Board (DCB) shown in figure 1.

References

[1] F. Lemke, GLP Design Document, CAG, University of Heidelberg, (2008).

[2] F. Lemke, CBM Network Interface, CAG, University of Heidelberg, (2008).

* Work supported by GSI, BMBF FAIR-CBM 06MN229I

A standalone package for on-line event selection in the CBM experiment

I. Kisel*[1,2], I. Kulakov[3], and I. Vassiliev[1,2]

[1]GSI, Darmstadt, Germany; [2]KIP, University of Heidelberg, Germany; [3]University of Kyiv, Ukraine

One of the most challenging tasks of the CBM experiment [1] is the on-line identification of D-mesons [2] at input rates up to 10 MHz. In order to investigate feasibility of the on-line selection of D-mesons a package of reconstruction and selection procedures (Fig. 1) has been implemented. It includes a cellular automaton based track finder [3], a Kalman filter based track fitter [4] (both are SIMDized), a primary vertex finder and a procedure for finding short lived decayed particles (both are implemented within the KF Particle package [5]) and a procedure for selecting charm track candidates. These routines exist already in the cbmroot framework, but in order to develop and test the full selection chain on different modern and future CPU/GPU architectures they have been substantially modified and reorganized into a standalone package. Input data consist of detector geometry, simulated data in form of registered hits and Monte Carlo tracks for performance evaluation. Each part of data is stored in a separate text file produced with a special routine.

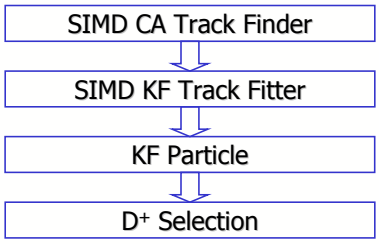

Figure 1: D^+ selection chain

The total reconstruction efficiency (see Fig. 2) for all tracks is about 92%. The reconstruction efficiency clearly depends on the particle momentum. High energetic particles have efficiency of about 97%. Secondary tracks from D^+ decay have momentum larger than 1 GeV/c and, in addition, come from the target region, which can be used during the reconstruction, and, therefore, they have even higher efficiency of 99%. Let us note that only simple Gaussian smearing was used in these investigation, and no double hit effects in the sensor considered. Most of other secondary tracks are low energetic tracks which suffer significant multiple scattering in the detector material. The efficiency of low energetic tracks is about 82%. Particles with momentum lower than 100 MeV/c are mostly out of geometrical acceptance of the STS detector. Splitting of reconstructed tracks into short parts is negligible. The level of wrongly reconstructed tracks (ghost tracks) is about 3% and these tracks are similar to tracks of short low energetic particles.

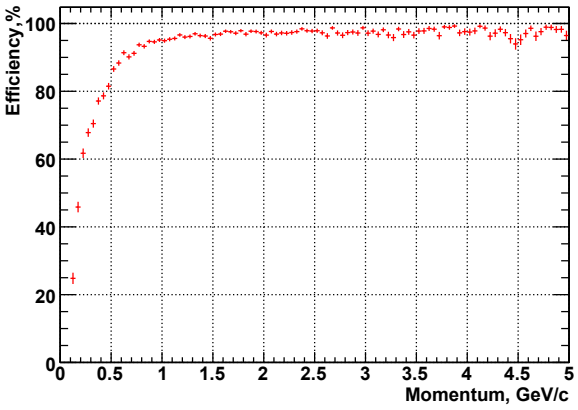

Figure 2: Track reconstruction efficiency of the standalone package as a function of momentum

Test of the SIMD KF track fit part of package was done by comparing results with the SIMD KF track fitter of the cbmroot framework. Results of both implementations of the fitting routine show similar results.

Test of the KF Particle part of the package has been performed using simulated data with D^+ signal events only. The efficiency of D^+ selection was found to be 48.9%, which is similar to the result obtained in the cbmroot framework.

Concluding, a standalone package for feasibility studies of the on-line event selection is created by extracting the corresponding routines from the cmbroot framework. Comprehensive tests of the package have shown good agreement between the results obtained by the package and the results of the corresponding routines of the cmbroot framework.

References

[1] Compressed Baryonic Matter Experiment, Technical Status Report, GSI, Darmstadt, 2005.

[2] S. Gorbunov, I. Kisel and I. Vassiliev, Analysis of D^0 meson detection in Au+Au collisions at 25 AGeV. CBM-PHYS-note-2005-001, 23 June 2005.

[3] I. Kisel, Event reconstruction in the CBM experiment. Nucl. Instr. and Meth. A566 (2006) 85–88.

[4] S. Gorbunov, U. Kebschull, I. Kisel, V. Lindenstruth and W.F.J. Müller, Fast SIMDized Kalman filter based track fit. Comp. Phys. Comm. 178 (2008) 374–383.

[5] S. Gorbunov and I. Kisel, Reconstruction of decayed particles based on the Kalman filter. CBM-SOFT-note-2007-003, 7 May 2007.

* I.Kisel@gsi.de

Implementation of a Hough Tracker for CBM*

C. Steinle[1], A. Kugel[1], and R. Männer[1]
[1]University of Heidelberg, Department of Computer Engineering V, 68131 Mannheim, Germany

The Hough transform multi-chip concept is introduced in [1]. Even if a CELL BE is not a multi-chip system, it can be easily used to develop the neccessary distributed Hough tracking algorithm, because it is a system with a main processing element (PPU) and many coproccessing elements (SPUs) which are connected by a bus system (EIB). By using a Sony Playstation III, as cheap and flexible rapid prototyping system, we have investigated such an algorithm with regard to the special features of a CELL BE.

For this purpose we use the PPU to divide the input data in so-called jobs, which can then be processed by the SPUs. So the whole Hough transform algorithm except the LUT transformation and the 3D peak finding is done by the SPUs in parallel. During the whole process the PPU is at any time the master which controls all slave SPUs. For this purpose the CELL BE mailbox system is used for transporting the 32 bit wide commands from the PPU to the SPU and handshakes from each SPU to the PPU.

So the whole algorithm is now quite easy. At first the PPU takes each hit of the input data and evaluates the corresponding transformed Hough value which is 64 bits wide. This value is composed of 8 bits for the station index, 8 bits for the start and stop layer index each, 8 bits for the histogram starting position and 32 bits for the histogram command. Afterwards the PPU creates the job packages for the SPUs. The neccessary amount of memory is determined by the sum of the coding table, the histogram itself and the input data. It must be not bigger than the available memory size, given by the 256kB local storage minus the program code size and reservations for the stack and the heap. Due to this restriction, the job packaging has to take care of the second level of parallelism which is given by the vector processing ALU of the SPUs. Because of this 128 bit wide vector capable ALU, it is possible to work on 128 / 8 = 16 histogram cells in parallel. As the systolic processing of the histogram layer restricts the parallel cell access, it is not possible use this parallelism. But a closer look to the Hough value shows that each hit has a start and stop layer index. So by arranging the histogram memory in a special way, it is possible to access the same histogram cell in up to 16 layers in parallel. Of course it is not a perfect parallelism but it is guaranteed that each hit in a job package is just used once. And if a single hit has to be inserted in more than 16 layers, it would be spreaded across consecutive packages. The next step for the PPU is then given by sending the jobs to the SPUs and waiting for successful processing. This sending is done by telling each SPU the memory address in the XDR RAM which contains the corresponding data for the job. Each SPU establishes then itself a DMA transaction to load the 16kB data blocks in its own local storage. When all data is processed by the SPUs the PPU fetches the results from the SPUs and does the 3D peak finding. Important is that the fetching of the results is done in the same way than the delivering of the input data. That means that the SPU has to tell the PPU the amout of memory which is neccessary to store the results. With this information the PPU allocates memory in the XDR RAM and gives the address to the SPU which establishes then again a DMA transaction with a maximum block size of 16kB.

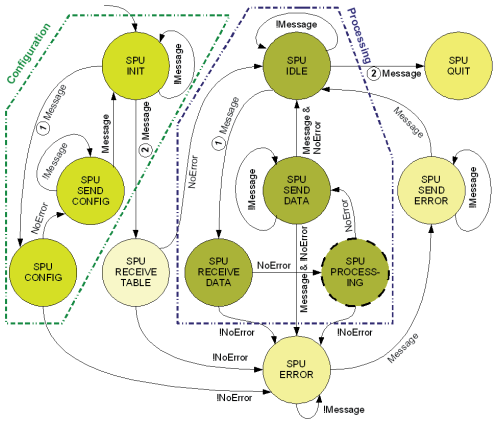

Figure 1: SPU state diagram

A taking a closer look to the SPU state diagram (Figure 1), shows that in addition to the processing states, there are also a few configuration states. These states help to determine the earlier mentioned amount of memory, available for the data, because the local storage of a SPU contains the program code in combination with the data. So the PPU can request the available amount of memory for each SPU before the generation of the jobs. The distributed Hough tracking algorithm for the CELL BE is ready. The next step is the implementation of the SPU processing stage.

References

[1] C. Steinle, A. Kugel, R. Männer, "Implementation of a Hough Tracker for CBM", CBM Progress Report 2007, May 2008, http://www.gsi.de/documents/DOC-2008-May-3.html.

* Supp. by EU/FP6 HADRONPHYSICS # RII3-CT-2004-506078, BMBF Hadr.- & Kernphys. # 06MN2291, GSI Hochschulpr. # MAMAEN

Porting a Kalman filter based track fit to NVIDIA CUDA

M. Bach[1], S. Gorbunov[1], I. Kisel[*1,2], V. Lindenstruth[1], and U. Kebschull[1]
[1]KIP, University of Heidelberg, Germany; [2]GSI, Darmstadt, Germany

Finding particle trajectories is usually the most time consuming part of modern experiments in high energy physics. In many present experiments with high track densities and complicated event topologies a Kalman filter based track fit is used already at this combinatorial part of the event reconstruction. Therefore speed of the track fitting algorithm becomes very important for the total processing time.

In 2007 a Kalman filter based track fitting algorithm of the CBM experiment [1] had been ported to SSE and the Cell SPE [2]. On the CPU a speedup of 10000 compared to the initial version was achieved. To gain this speedup two major changes to the existing Kalman filter implementation were done. The magnetic field map was replaced by a functional approximation based on fourth order polynomials. In addition the algorithm was tuned to work with single precision calculations only, without the need for compensating computations or numerical instabilities.

Today CPUs are no longer able to increase their peak performance by increasing clock speeds. Modern GPUs however continue to increase their peak performance utilising manycore architectures, with NVIDIA GT200 based GPUs nearly reaching 1 TFlop/s in single precision [3]. Thus they are a promising candidate for further acceleration of the algorithm.

This performance comes at a cost. Different than on CPUs access to the main memory is not cached, all threads running on one multiprocessor, which is similar to a core of a GPU, share a small 16 kB processor local storage called shared memory which needs to be explicitly programmed. To compensate for that each multiprocessor has a large register file of 16384 registers and can have 1024 threads concurrently active. On eight ALUs it processes warps of 32 threads in 4 cycles, switching between warps without costs, allowing to hide memory accesses by calculations. A GT200 chip contains 30 of these multiprocessors.

In contrast to the single instruction multiple data (SIMD) based architectures of the NVIDIA GPUs are based on a single instruction multiple threads (SIMT) model, which means each ALU is connected with an own instruction counter. Therefore the algorithm needs to be parallized on a thread level instead of the below as in the SIMD case. While in the SIMD case we have one thread that works on a vector of numbers, in SIMT we have multiple threads working on scalars. However in both cases a number of arithmetic units is fed by the same instruction decoder, making it important for the code not to rely on different code branches depending on the data of each thread.

The original port relied on operator overloading to have only one implementation of the algorithm for multiple platforms, as does this port to CUDA. To accommodate for the SIMT nature of the GPU instead of a vector type the scalar type `float` is now the basis of the algorithm.

The implementation of the algorithm requires 91 registers reducing the maximum amount of threads that fit into one multiprocessor to 160. This makes it difficult to hide memory access by calculations. Therefore access to the memory was minimized by storing the parameters for the magnetic field in the small cached constant memory of the GPU. The track and hit data is explicitly transferred to shared memory and back using cooperation between threads executing in one warp for optimum memory transfer speed.

NVIDIA Unit	Clock, GHz	Throughput, 10^6 tr./s
8800 GTS 512	1.6	13.0
GTX 280	1.3	21.7

Table 1: Real time performance of the SIMDized version of the Kalman filter based fitting routine for a single track

In Tab. 1 the performance for computations located solely in the local caches and storages is shown [4]. Keeping in mind the slow clock, the GPU can show how well it can profit from the high parallelism of the track fitting problem. While its latency for a single track is at a comfortable $44\ \mu$s it profits from calculating 960 instead of four tracks in parallel. This way performance peaks at a rate of 21.7×10^6 tracks/s. Fitting larger datasets located in the GPU's main memory the NVIDIA GTX 280 is still able to process tracks at a rate of 9.6×10^6 tracks/s.

References

[1] Compressed Baryonic Matter Experiment, Technical Status Report, GSI, Darmstadt, 2005.

[2] S. Gorbunov, U. Kebschull, I. Kisel, V. Lindenstruth and W.F.J. Müller, Fast SIMDized Kalman filter based track fit. Comp. Phys. Comm. 178 (2008) 374–383.

[3] NVIDIA, NVIDIA CUDA programming guide, version 2.1, 2008.

[4] M. Bach, Utilization of Graphics Processing Units in Applications for High Energy Physics, Diploma Thesis, University of Heidelberg, 2009.

* I.Kisel@gsi.de

Scalability of a Kalman filter based track fit on Intel many-core CPUs

H. Bjerke[1], S. Gorbunov[2], I. Kisel*[2,3], V. Lindenstruth[2], P. Post[4], and R. Ratering[4]

[1]CERN, Geneva, Switzerland; [2]KIP, University of Heidelberg, Germany; [3]GSI, Darmstadt, Germany; [4]Intel, Cologne, Germany

As a result of increasing density of transistors and heat and power constraints, computers increasingly implement parallelism in hardware in order to speedup computation. This has manifested itself in multi-core processors and wider vector instructions. Future computer architectures are expected to increase parallelism in both dimensions.

There are many strategies for extracting parallelism from a workload or a set of workloads. Popular taxonomies for parallel computing are, Multiple Instructions Multiple Data (MIMD), Multiple Instructions Single Data (MISD), Single Instruction Multiple Data (SIMD) and Single Instruction Single Data (SISD).

The feasibility of a strategy depends on the characteristics of the parallelism exhibited by the algorithm and its data-structures. Also, the forward-scalability of a strategy depends on the level of parallelism given by it and its constraints. Programs that exhibit data level parallelism can often be characterized as forward-scalable, although, in this case, the degree of parallelism in the data can put a constraint on the scalability. Parallelizing with an SIMD model alleviates the constraint of shared resources, but adds the constraint of synchronization. Finally, parallelizing any program usually also adds a new set of constraints intrinsic to the problem, which also has to be taken into account.

A Kalman filter based track fit of the CBM experiment [1] has shown to be a well suitable benchmark [2] for parallelizing the algorithms of data reconstruction in high energy physics. Therefore it is important to investigate its scalability and usage of Intel many-core architectures for the Kalman filter based algorithms.

Type	Time/track, μs	Speedup
Scalar double	2.6	–
Vector double	1.6	1.6
Vector single	0.7	2.3

Table 1: Speedup of the Kalman filter based fit on the Xeon 5140 (Woodcrest) at 2.4 GHz using icc 9.1

Table 1 shows that the total speedup of 3.7 is reached when changing the data representation from the scalar double precision to the vector (SIMD) single precision.

Figure 1 shows that on the Xeon 5345 (Clovertown) maximum speedup of 30 is reached when running 16 threads of the SIMD version of the Kalman filter tracking routine in parallel.

Table 2 gives the real time performance of the multi-threaded SIMD Kalman filter benchmark on different Intel CPU platforms.

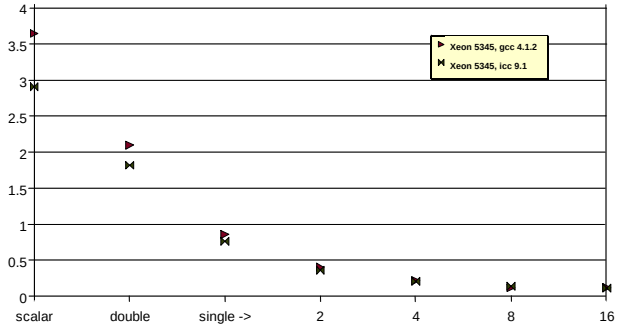

Figure 1: Real time performance of the Kalman filter based fitting routine per track fitted on the Xeon 5345 (Clovertown) at 2.4 GHz

Type	Cores	Clock, GHz	Time/track, μs
Core 2	2	2.66	0.26
Core i7	4	3.2	0.1

Table 2: Real time performance of the multi-threaded SIMD Kalman filter based fitting routine per track fitted on different Intel CPU platforms

In addition to multi-core CPU architectures a many-core architecture code named Larrabee [3] can be considered as an interesting platform to further scale the Kalman filter based tracking code in the threading and vectorization dimensions. Larrabee uses multiple in-order x86 CPU cores that are augmented by a wide vector processor unit, as well as some fixed function logic blocks. This provides dramatically higher performance per watt and per unit of area than out-of-order CPUs on highly parallel workloads. It also greatly increases the flexibility and programmability of the architecture as compared to standard GPUs.

Less architecture dependent programming frameworks, such as OpenCL and Intel Ct, may also better support future changes in architecture.

References

[1] Compressed Baryonic Matter Experiment, Technical Status Report, GSI, Darmstadt, 2005.

[2] S. Gorbunov, U. Kebschull, I. Kisel, V. Lindenstruth and W.F.J. Müller, Fast SIMDized Kalman filter based track fit. Comp. Phys. Comm. 178 (2008) 374–383.

[3] L. Seiler et al., Larrabee: a many-core x86 architecture for visual computing, ACM Transactions on Graphics, Vol. 27, No. 3, 18, August 2008.

* I.Kisel@gsi.de

Systematic investigations on di-electron reconstruction in CBM

T. Galatyuk[1,2], C. Höhne[1], and J. Stroth[1,2]
[1]GSI, Darmstadt, Germany; [2]IKF, Frankfurt am Main, Germany

The CBM experiment at the future accelerator facility FAIR will make use of proton beams with energies of $10 - 89$ GeV, and of nuclear beams with energies of $10 - 44$ GeV/u. The experimental strategy how to assess best the low-mass vector mesons by means of their electromagnetic decay at different collision energies and system sizes is under careful investigation. The systematic behaviour of the signal-to-background (S/B) ratio as function of collision energy will be presented in this report.

The general challenge of di-electron measurements in heavy-ion collisions is to cope with the large background of electrons originating from other than the desired sources. Several topological cuts have been developed to reduce the background. The analysis strategy described in Ref. [1] was applied for electron pair reconstruction in central $Au+Au$ collisions at 15 and 35 GeV/u beam energy. The S/B ratio for the three beam energies (15, 25 and 35 GeV/u), assuming no excess over the known decay sources, is depicted in Fig. 1. It is naturally higher at lower energies, as particle multiplicities at lower energies decrease (see Ref. [2]). This of cause reduces the signal and combinatorial background at the same time. However, the signal decreases linearly while the background goes down quadratically. The larger increase of the S/B ratio from 15 to 25 GeV/u beam energy compared to the one from 25 to 35 GeV/u is due to the fact that the pion multiplicity increases by 27% in the first and only by 13% in the second step.

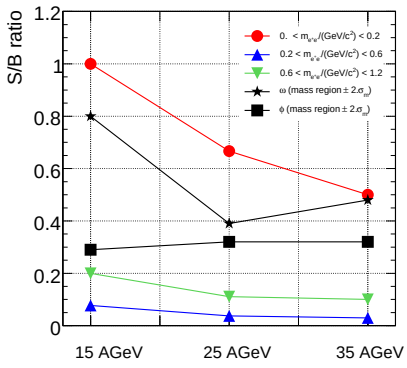

Figure 1: Signal-to-background ratio for central $Au + Au$ collisions at different beam energies after all cuts have been applied

Clear signs of an excess of dileptons above the known decay sources were obtained by the HELIOS/CERES and NA60 Collaborations at SPS energies and by the PHENIX Collaboration at RHIC energies. A clear correlation between the S/B ratio and $dN_{ch}/d\eta$ can be seen. Interestingly, all experiments so far seem to follow this dependence (see Fig. 2), although the sources of the combinatorial background are very different. The $dN_{ch}/d\eta$ for CBM were taken from Ref. [3]. Thus for central $Au + Au$ collisions at 15 GeV/u beam energy, we expect 250 charged particles per rapidity unit at midrapidity, 300 for $Au + Au$ collisions at 25 GeV/u beam energy, and 350 for $Au + Au$ collisions at 35 GeV/u beam energy. From a parametrization of the published enhancement factors as function of center of mass energy, for CBM we might expect an enhancement factor not smaller than 6. We therefore deduce a S/B ratio of $6 \times 1/9$ for central $Au + Au$ collisions at 15 GeV/u, $6 \times 1/16$ for central $Au + Au$ collisions at 25 GeV/u and $6 \times 1/18$ for central $Au + Au$ collisions at 35 GeV/u ($M_{inv} > 0.2$ GeV/c^2). As Fig. 2 demonstrates, this performance is well competitive with previous experiments measuring dileptons in heavy-ion collisions at similar charged track densities.

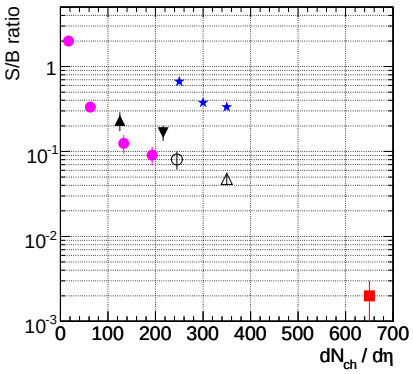

Figure 2: Integrated S/B ratios for M_{inv} larger than 0.2 GeV/c^2 measured by existing dilepton experiments as a function of the number of charged particles at midrapidity in one rapidity unit. Circles: NA60 data for four centrality bins; triangles, open circle: CERES data, square: PHENIX data, star: CBM simulations assuming an enhancement factor of 6.

References

[1] T. Galatyuk *et al.*, *Strategies for electron pair reconstruction in CBM*, GSI Scientific Report 2005/FAIR-QCD-CBM-06

[2] CBM Collaboration, *Compressed Baryonic Matter experiment, Technical Status Report*, QCD_CBM-report-2005-001

[3] A. Andronic, P. Braun-Munziger, and J. Stachel, *Hadron production in central nucleus-nucleus collisions at chemical freeze-out*, Nucl. Phys. A 772 (2006) 167

Measurement of direct photons via conversions into e^+e^- pairs in CBM

M. Klein-Bösing[1], C. Höhne[2], F. Uhlig[2], and J.P. Wessels[1]
[1]IKP, Münster, Germany; [2]GSI, Darmstadt, Germany

In CBM, the ECAL is foreseen to provide photon identification. In addition, a measurement of di-electrons from γ conversions can be used to increase the precision: this method is very auspicious especially at low momenta because of the good momentum resolution of the electron tracking. Moreover, it does not suffer much from misidentified charged and neutral hadron background.

The e^+e^- pairs from γ conversions can be measured with the charged particle tracking (STS and TRD) and electron identification detectors (RICH, TRD, and TOF). They can subsequently be used for photon reconstruction, which is based on a Kalman filter method. Most of the γ conversions (86%) occur in the target and here, the main contamination is caused by e^+e^- pairs from π^0 Dalitz decays. In Fig. 1a), the p_{T}-distribution of the reconstructed e^+e^-

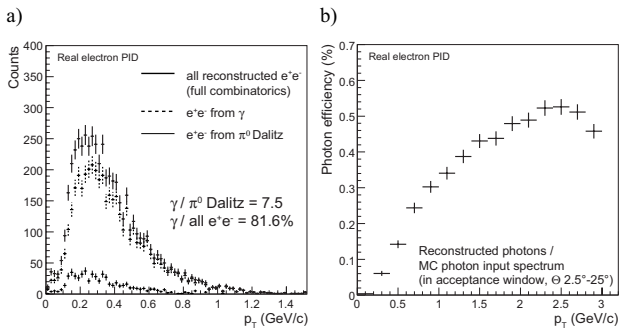

Figure 1: a) p_{T}-distribution of all reconstructed e^+e^- pairs (thick), contribution from γ conversions (dashed), and π^0 Dalitz decays (thin) from 20000 central Au+Au events at 25 AGeV; b) reconstruction efficiency for γ by conversions into e^+e^- pairs as function of p_{T}.

pairs can be seen after applying cuts to the opening angle ϑ and the invariant mass. With these cuts, the γ/π^0-Dalitz ratio increases from 4.2 to 7.5, and the fraction of γ mothers to all (true and fake) reconstructed e^+e^- pairs increases from 3.2% to 81.6%. This is the purity of the reconstructed photon signal. In Fig. 1b), the corresponding γ reconstruction efficiency is shown for the condition that two out of three PID detectors have given a positive electron decision. The reconstruction efficiency is determined by the ratio of the number of reconstructed photons to the number of photons in the MC input spectrum. The efficiency decreases towards low p_{T} because of the smaller PID efficiency and electron acceptance. The difference to the theoretical conversion probability of photons in the gold target (250 μm) of 2.9% is reflected in the losses due to electron/positron acceptance and efficiency. The momentum resolution of the reconstructed photons as a function of momentum is flat and below 2.5% for $p < 8\,\mathrm{GeV}/c$, considerably better than the expected momentum resolution in the ECAL.

The measurement of direct photons requires precise knowledge of the contribution from decays (mainly $\pi^0 \rightarrow \gamma\gamma$) to the inclusive photon spectrum. An enhancement of photons compared to the expectation from hadron decays is attributed to a direct photon signal. The π^0-signal is determined by an invariant mass analysis of the reconstructed photon pairs. Considering all possible $\gamma\gamma$-combinations in addition to the π^0-signal leads to a large combinatorial background. This background can be determined through *event mixing*: the result obtained by combining particles within one event is compared to the result for particle combinations from different events, which are per definition not correlated. After subtraction of the normalized back-

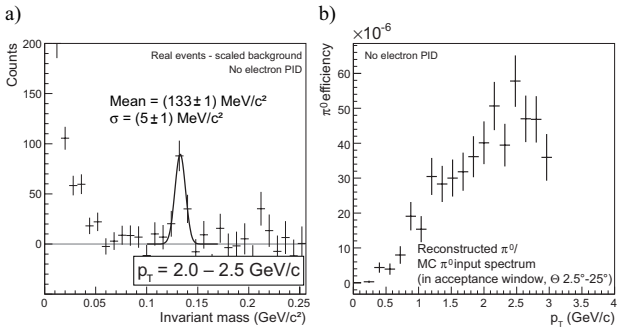

Figure 2: a) Invariant mass distribution of $\gamma\gamma$-pairs after background subtraction; b) p_{T}-distribution of the π^0 reconstruction efficiency.

ground, a π^0-peak can be extracted (see Fig. 2a)). Here, no PID conditions are applied in order to increase the statistical accuracy. The RMS of a Gaussian fit to the π^0-peak is of the order of $5\,\mathrm{MeV}/c^2$. The efficiency of π^0 reconstruction with photons via conversions is shown in Fig. 2b). The low overall reconstruction efficiency is a consequence of the photon reconstruction efficiency entering squared. In addition, the efficiency decreases towards low p_{T} because of the larger opening angle for photon pairs, which reduces the geometrical acceptance. Multiplying this efficiency with the π^0-signal of an UrQMD spectrum (central Au+Au collisions at 25 AGeV), one can deduce that $5 \cdot 10^8$ UrQMD events lead to 100 π^0s at $p_{\mathrm{T}} = 2\,\mathrm{GeV}/c$. With an expected data storage rate of 20 kHz in CBM, this would require 7 hours of data taking in order to obtain a π^0-signal with a statistical error of 7.3%, with decreasing yield towards large p_{T}.

This work was supported by BMBF and the JRA4-I3HP project (RII3-CT-2004-506078) financed by EU-FP6.

H-dibaryon $\rightarrow \Lambda\Lambda$ detectability study in the CBM experiment

I. Vassiliev[1,2], I. Kisel[1,2], and the CBM Collaboration
[1]GSI, Darmstadt, Germany; [2]KIP, Ruprecht-Karls University, Heidelberg, Germany

Recent measurements found evidence for the existence of a H-dibaryon ($uuddss, I = J = 0$) decaying into a pair of Λ hyperons [1]. In the following we discuss the possibility to detect H-dibaryons via the $\Lambda\Lambda$ channel with the CBM setup. Our simulations are based on a H-dibaryon decay length of $c\tau \approx$ 1-5 cm as predicted by [2]. The Silicon Tracking System (STS) of CBM is well suited to reconstruct Λ hyperons (decay length 7.89 cm), and to distinguish the signals from the background.

The feasibility study of H-dibaryon detection is based on 10^4 central Au+Au UrQMD events at 25 AGeV . In each event a decay of a $(\Xi^0\Lambda)_b$ ($c\tau$ = 3 cm) into $\Lambda\Lambda$ has been added in order to simulate the signal in the environment of background hadrons.

The background is dominated by about 32 primary Λ hyperons which are produced per central UrQMD event. Within the STS detector acceptance 11 Λ particles are reconstructed on average. The STS comprises 2 Silicon pixel detectors (MAPS) at 10 cm and 20 cm (thickness 500 μm), and 8 detector layers consisting of double-sided Silicon micro-strip sensors. Particle identification via time-of-flight has been performed for protons only (not for kaons or pions), in order to reconstruct $\Lambda \rightarrow p\pi^-$ decay. A typical signal event $H \rightarrow \Lambda\Lambda \rightarrow p\pi^- p\pi^-$ is shown in Fig. 1.

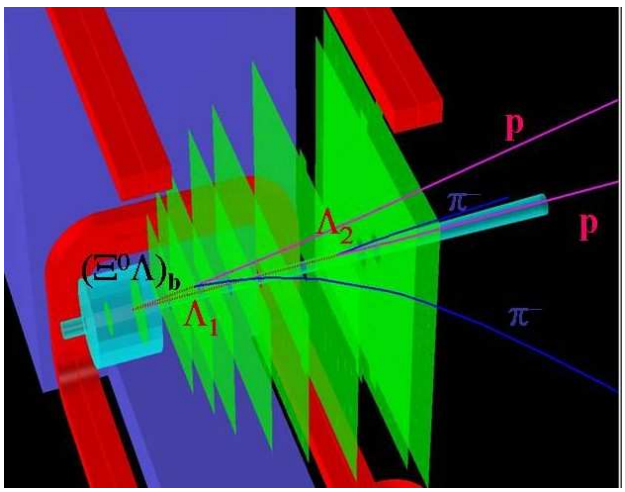

Figure 1: The event display with the H-dibaryon decay to $\Lambda\Lambda$

The H-dibaryon decay vertex typically is located between the MAPS stations about 5-15 cm downstream from the target. Λ particles mostly decay in between the STS detector stations. The reconstruction of the event topology comprises several steps: (i) track reconstruction, where all tracks are found but only tracks with $\chi^2_{primary} > 3\sigma$ are selected; (ii) Λ search, where protons identified by the TOF detector are combined with the π^- tracks, and the invariant mass of the reconstructed particle is compared with the PDG's Λ mass value; (iii) rejection of primary Λs where only Λs with $\chi^2_{primary} > 3\sigma$ have been chosen; and (iv) finally, the reconstruction of detached H-dibaryons (vertex located more then 5 cm downstream from the target). In the last step, good geometrical $\chi^2_{geo} < 3\sigma$ and topological $\chi^2_{topo} < 3\sigma$ vertices are required for the reconstructed H-dibaryons. The shape of the background invariant mass spectrum has been obtained using the event mixing technique.

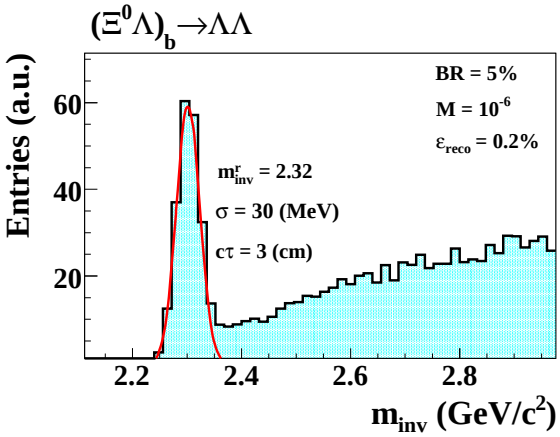

Figure 2: Reconstructed invariant mass distribution of $\Lambda\Lambda$ candidates

The signal and background invariant mass spectrum is shown in Fig. 2. The signal reconstruction efficiency is about 0.2%. For the simulations we assume a multiplicity of 10^{-6}, and a branching ratio of 5%, which means in 20 million events there is only one H-dibaryon decay. The reconstructed mass value of $2.32 \pm 0.03 GeV/c^2$ is in a good agreement with the simulated one (2.318 GeV/c^2). The invariant mass resolution (σ = 30 MeV/c^2) is limited by the fact that the tracks of the Λ daughter particles produce hit in 4 or 5 detector stations only.

References

[1] C.J. Yoon et al., Search for the H-dibaryon resonance in $C(K^-, K^+\Lambda\Lambda\, X)$. Phys. Rev C 75, 022201(R) (2007).

[2] J. Schaffner-Bielich, R. Mattielo and H. Sorge, Dibaryons with strangeness: their weak nonleptonic decay using SU(3) symmetry and how to find them in relativistic heavy-ion collisions. arXiv:nucl-th/9908043v2, March 2000.

Event-by-event fluctuations of the K/π yield ratio in the CBM experiment

D. Kresan[1] and C. Höhne[1]
[1]GSI, Darmstadt, Germany

Non-statistical event-by-event fluctuations are considered an important signal for the critical endpoint of the QCD phase diagram. In future, the CBM experiment at FAIR will investigate the intermediate region of this phase diagram in great detail, searching for the first-order phase transition line and the expected critical endpoint. It is therefore important to closely investigate its sensitivity towards particle ratio fluctuations in Au + Au collisions at 10-45A GeV beam energy.

A detailed description of the track reconstruction and hadron identification in the STS, TRD, and TOF systems of CBM is given in [1]. In this report, we employ a more advanced TOF detector response simulation, including features like segmentation and double hits, as well as improved TRD track reconstruction algorithms [2], which yield a global track reconstruction efficiency of 86.4 %. Figure 1 shows the reconstructed squared mass of the particles as function of momentum. The m^2 distribution is nearly Gaussian, with small tails caused by track mismatches between TRD and TOF, and by double hits in the TOF detectors. For this fluctuation study, particles are identified on a track-by-track basis using a momentum-dependent window in m^2 around the expectation value. As the width of the m^2 distribution is a quadratic function of p, the required purity of kaon selection sets an upper momentum limit; clean kaon identification is possible up to $p = 3.5$ GeV. The momentum range can be extended to $p = 5$ GeV when a contamination of maximal 50 % is allowed.

Figure 2 (left) shows the eventwise distribution of the ratio $(K^+ + K^-)/(\pi^+ + \pi^-)$ derived for central Au+Au collisions at 25A GeV generated with UrQMD, after full detector simulation, reconstruction, and particle identification. It is dominated by statistical fluctuations arising from finite number statistics and detector resolution. This background is reproduced using the event mixing technique which destroys all correlations inside one event. Dynamical fluctuations are then extracted by geometrically subtracting the relative width of the mixed-event distribution from that obtained for same events.

The dependence of the fluctuation result on the required purity of the kaon sample is shown in Fig. 2 (right). The restricted momentum range for a higher purity of the selected kaons introduces a shift of the dynamical fluctuations on the (1 - 2) % level compared to an analysis in the full acceptance or in 4π. This acceptance effect is also seen when using the MC truth for the kaon identification, but applying the same upper limit on momentum. From this agreement we conclude that the kaon identification procedure does not introduce a significant bias in the non-statistical K/π fluctuation results. The acceptance changes the measured fluctuation by less than 1 %, which expresses the sensitivity of the CBM experiment to the physical fluctuation signal.

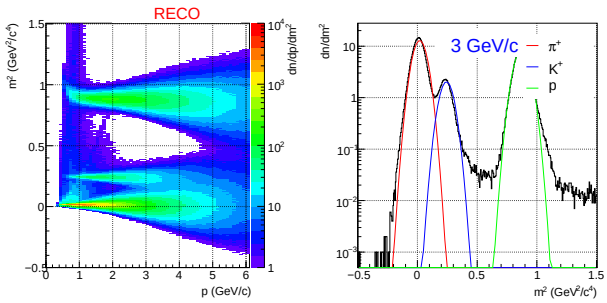

Figure 1: (Left) Squared mass vs. momentum of reconstructed hadrons; (right) m^2 distribution for p = 3 GeV.

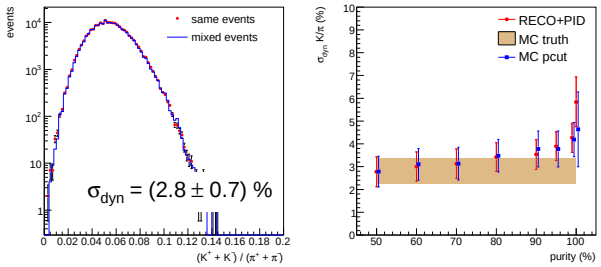

Figure 2: (Left) Distributions of the event-wise kaon-to-pion ratio for data and mixed events, obtained for central Au+Au collisions at 25A GeV from UrQMD. A minimal kaon purity of 50 % was required. (Right) Dynamical fluctuations of the kaon-to-pion ratio as a function of purity of the kaon identification.

References

[1] D. Kresan and V. Friese, *Global tracking and hadron identification in the CBM experiment*, CBM Progress Report 2006, Darmstadt 2007, p. 7
http://www.gsi.de/documents/DOC-2007-Mar-137.html

[2] A. Lebedev et al., *Track reconstruction in the TRD and MUCH detectors of CBM*, this report

D^0 decay feasibility study in the CBM experiment

I. Vassiliev[1,2], I. Kisel[1,2], and the CBM Collaboration
[1]GSI, Darmstadt, Germany; [2]KIP, Ruprecht-Karls University, Heidelberg, Germany

One of the major experimental challenges of the CBM experiment is to trigger on the displaced vertex of the D-meson via hadronic decay modes $D^0 \rightarrow K^-\pi^+$ in the environment of a heavy-ion collision. This task requires fast and efficient track reconstruction algorithms and high resolution secondary vertex determination. Particular difficulties in recognizing the displaced vertex of the rare D meson decays are caused by weak K^0_S, Λ- and Σ-barion and hyperon decays which produce displaced vertices 1 cm downstream the target, very low multiplicity of the D meson production, low branching ratios and multiple scattering in the beam pipe and detectors.

To study the feasibility of D^0 and $\bar{D}^0$ mesons measurement in the CBM experiment a set of 10^4 central Au+Au UrQMD events at 25 AGeV have been simulated. D^0 (or $\bar{D}^0$) decay to $K^{\mp}\pi^{\pm}$ has been forced and added to each event in order to simulate a signal in the environment of background hadrons. The most realistic STS geometry with 2 MAPS at 5 cm (thickness 300 μm) and 10 cm (thickness 500 μm) and 8 double-sided segmented strip detectors has been tested. The 5.5 mm inner radius of the first MVD detector has been choosen in order to reduce radiation damage. The primary vertex was reconstructed with high accuracy (5.7 μm in z direction, 1.0 μm in x and y) from about 400 tracks fitted in the STS with a non-homogeneous magnetic field by the SIMDized Kalman filter procedure described in [1].

An ultra fast track finder has been developed to reconstruct the D^0's. The algorithm first finds the primary vertex using all reconstructed tracks, and then the D^0 meson is reconstructed from its two daughter particles using the primary vertex as the production point. Since geometrical acceptance of the MVD detectors and STS strip detectors are not the same, the sample of the reconstructed D^0 mesons consist of 3 subsets shown in Figure 1 with different z-vertex resolutions: 36 μm, 56 μm and 66 μm corespodently. Because of originating from a displaced decay vertex, the D^0 meson daughter tracks have a non-vanishing impact parameter at the target plane. Since the majority of the primary tracks have very small impact parameter, a significant part (99%) of the background tracks was rejected using a cut on their χ^2 distance to the primary vertex. The combinatorial background is suppressed mainly by the vertex χ^2_{geo} and χ^2_{topo} cut for good quality detached vertices. Numbers for multiplicity, cut efficiencies, acceptance, z-vertex resolution, mass resolution, signal to background ratios and yields per 10^{12} central interactions are presented in Table 1.

After applying all cuts the $D^0 \rightarrow K^-\pi^+$ reconstruction efficiency is 2.4% . The shape of the background in the signal IM region has been estimated using the event mixing technique. The resulting background plus D^0 and $\bar{D}^0$ signal spectra are shown. The signal to background ratio is about 2.1 for $D^0 \rightarrow K^-\pi^+$ and about 6.4 for $\bar{D}^0 \rightarrow K^+\pi^-$.

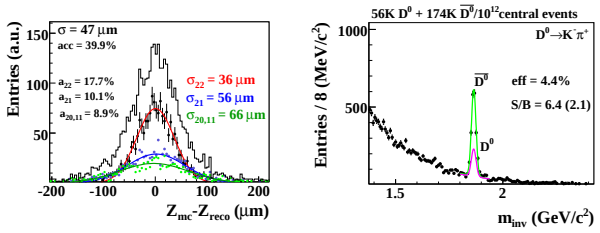

Figure 1: Left: z-vertex resolution of the reconstructed D^0 mesons. Black dots corespond the case where each of two daughter particles has 2 MAPS hits, blue dots - one of the daughter particles has no hit in the first MVD station, green dots - one of the daughter particles has no hit in the MVD stations or both daughter particles have no hits in the first MVD station. Right: D^0+$\bar{D}^0$ signal and combinatorial background invariant mass spectra. The estimated signal and combinatorial background corresponds to 10^{12} central events.

	$D^0 + D^0$
decay channel	$K^-\pi^+$ and $K^+\pi^-$
multiplicities	$0.37 \cdot 10^{-4}$ and $1.15 \cdot 10^{-4}$
branching ratio	3.8%
geometrical acceptance	39.9%
reconstruction efficiency	99%
z-resolution	47 μm
total efficiency	4.4%
$\sigma_m[MeV/c^2]$	10.0
$S/B_{2\sigma}$ ratio	2.1 (6.4)
yields	56KD^0 + 174K$\bar{D}^0$

Table 1: Acceptance and efficiencies, mass resolution, and signal-to-background ratio (S/B) in a $2\sigma_m$ region around the peak for open charm reconstruction in central Au+Au collisions at 25 AGeV beam energy. The total efficiency is calculated from the product of geometrical acceptance, reconstruction and cut efficiencies.

References

[1] S. Gorbunov, U. Kebschull, I. Kisel, V. Lindenstruth and W.F.J. Müller, Fast SIMDized Kalman filter based track fit. Comp. Phys. Comm. 178 (2008) 374-383.

D^+ decay feasibility study in the CBM experiment

I. Vassiliev[1,2], I. Kisel[1,2], and the CBM Collaboration
[1]GSI, Darmstadt, Germany; [2]KIP, Ruprecht-Karls University, Heidelberg, Germany

A measurement of the different charmed mesons, and the Λ_c is important for getting a solid estimate on the total charm production cross section at the threshold. $D^{\pm}$-mesons have lifetime of 312 μm, therefore, the most important step in their identification is a precise detection of the secondary decay point. For this purpose the high resolution realistic MVD detector (two MAPS detectors of 300 μm at 5cm and of 500 μm at 10 cm downstream the target) is used in order to suppress the background from kaons and pions emitted at the primary vertex. No kaon or pion identification with TOF is applied, however, it is important to use the time-of-flight measurements in order to reject proton tracks from the sample. A novel ultra fast (10 times faster than the standard one) track finder has been developed for $D^{\pm}$-meson daughter particles selection. Only tracks with momentum above 1 GeV/c from the target region have been selected. In order to reconstruct the $D^{\pm}$-

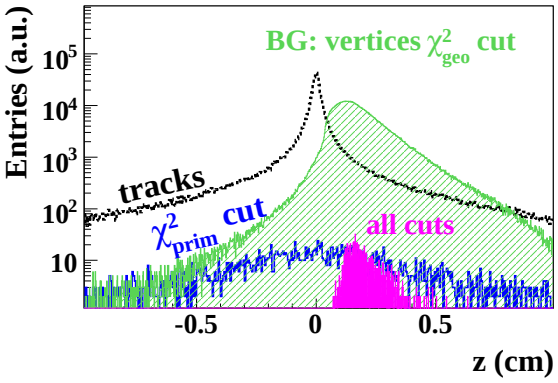

Figure 1: Distribution of single tracks and secondary vertices along the beam line for $D^+ \to K^-\pi^+\pi^+$ reconstruction. All primary tracks (black line) and those selected by χ^2_{prim} cuts as single track candidates for D^+ daughters (blue), 3-particle secondary vertices after first geometrical cuts (light green), and finally selected D^+ candidates including more stringent topological cuts (magenta).

mesons with a reasonable signal-to-background ratio, a set of mainly topological cuts applied to single tracks as well as to reconstructed vertices. As example, Figure 1 presents the resulting background suppression of such cuts for the 3-particle decay of the D^+ meson. Single track χ^2_{prim} cuts mainly rely on the back-extrapolation of the tracks to the primary vertex requiring them to miss it. For the reconstructed charmed mesons, the back-extrapolation is required to stem from the primary vertex which allows to reduce strongly the geometrically reconstructed 3-particle vertices.

The reconstructed invariant mass spectra of the $D^{\pm}$-mesons in central Au+Au collisions at 25 AGeV beam energy are shown in Figure 2. Numbers for efficiency and acceptance are presented in Table 1. Multiplicities have been taken from the HSD model.

	D^+ and D^-
decay channel	$K^-\pi^+\pi^+$ ($K^+\pi^-\pi^-$)
multiplicity HSD	$4.2 \cdot 10^{-5}$ and $8.9 \cdot 10^{-5}$
multiplicity SM	$8.4 \cdot 10^{-5}$ and $2.9 \cdot 10^{-4}$
branching ratio	9.5%
geometrical acceptance	39.6%
reconstruction efficiency	97.5%
z-resolution	47 μm
total efficiency	2.6%
$\sigma_m[MeV/c^2]$	10.0
$S/B_{2\sigma}$ ratio	1.1 (2.4)
yield (10^{12}central)	103K D^+ and 195K D^-

Table 1: Acceptance and efficiencies, mass resolution, and signal to background ratio (S/B) in a $2\sigma_m$ region around the peak for open charm reconstruction in central Au+Au collisions at 25 AGeV beam energy. The total efficiency is calculated from the product of geometrical acceptance, reconstruction and cut efficiencies.

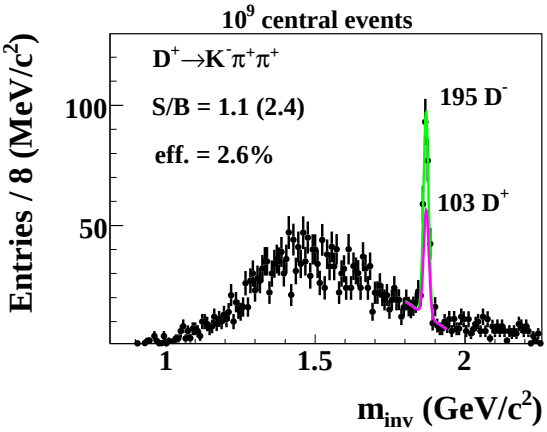

Figure 2: Reconstructed $D^{\pm}$-mesons in 10^9 central Au+Au collision at 25 AGeV. Magenta - D^+ signal, green line is D^-.

Grid setup for CBM

M. Al-Turany[1], K. Schwarz[1], and F. Uhlig[1]
[1]GSI, Darmstadt, Germany

Abstract

Since the computational requirements (5 PB Raw data per year and according storage capacities) of the **C**ompressed **B**aryonic **M**atter Experiment [1,2] will be enormous it will be impossible to reconstruct, analyze and store the data only at one dedicated computer center. The computing facilities for CBM will be therefore implemented as a global computational Grid. This means computing and storage capacities will be installed in a virtual net of worldwide geographically distributed computer centers. This article describes the setup of the CBM Grid and the results from the first production run.

AliEn

The Grid software AliEn [3] developed by the ALICE experiment was choosen as flexible middleware for the secure and coordinated access to the worldwide distributed computing resources. AliEn is a lightweight and simple Grid environment build on top of existing open source software. This includes the latest Internet standards for information exchange and authentication. To choose AliEn as one of many available Grid flavours has some pragmatic reasons. First of all the GSI IT department gained already a lot of experience with AliEn due to operating an ALICE tier2 center at GSI. The second reason for the decision was that the PANDA experiment [4], which uses the same software framework, FairRoot, as CBM does, already tested ALiEn with big success. This preparatory work enabled us to setup the CBM Grid within 3 month with only limited manpower.

Central Services

The heart of the Grid implementation of CBM is the central installation of the CBM Virtual Organization at GSI. These central services consist of the LDAP-Database which holds the necessary data, e.g.. information about hard- and software of the participating sites, people and their roles and many more. The information about the virtual file space used to organize the data inside of AliEn is stored in a MySQL-Database. This database includes information about e.g. running jobs and the file catalogue. The file catalogue provides mapping between the Physical File Name (PFN) on some storage element to the Logical File Name (LFN) used inside AliEn Beside these two main parts there are several other services dedicated e.g. for optimizing the file catalogue, optimizing the job submission or user authentification. For the complete grid monitoring we use MonaLisa [5], with the server also running at GSI.

Since the AliEn software is only provided for Scientific Linux, one of the main tasks during the installation procedure was to port the complete software to Debian.

Site Services

On each site (computing center) there are several services for the communication with the central services on one hand and the real computing environment on the other hand. These are for example the Computing Element (CE) which is the interface to the local batch system (LSF,PBS,BQS, DQS, Globus, Condor) or the SE (Storage Element) which is the interface to the local storage. The first and at present only site is at GSI. Here the CE is the front-end to the local LSF batch system and the SE stores the data via xrootd [6] on the lustre [7] file system.

First results

To study the behavior of the AliEn environment and the interplay between the site services and the central services as a first step after the installation of the central services a stand-alone virtual site on a single computer has been installed. This computer executed the jobs locally and also used only the local hard-disk as storage. Only after the successful test of this test-bed the GSI Grid site has been setup. End of December the complete system was in a state that the first real test of the CBM Grid environment could start. Since there was urgent need for a large scale (100.000 Events) simulation and reconstruction with the complete experimental detector setup including the electromagnetic calorimeter, which is very slow, we choose this configuration as our first real production run. To make use of the batch farm system the dataset was subdivided in 100 jobs with 1000 Events each. The total runtime for one job was around 48 hours. After 4 days all jobs finished successfully and 0.5 TB was stored on the lustre file system. This data are now available for further analysis.

Conclusion

The Grid software AliEn was successfully ported to Debian. The central and the site services were installed at GSI and successfully tested in a production run. The next steps will be on one side to use the running installation at GSI for further productions. On the other side we will include new sites into the CBM Virtual Organization. The first site already worked on is the computing center in Dubna, Russia.

References

[1] CBM experiment, http://www-cbm.gsi.de

[2] C. Höhne, *The CBM experiment at FAIR – exploring the QCD phase diagram at high net baryon densities*, International Journal of Modern Physics E 16 (2007) 2419

[3] http://alien.cern.ch

[4] http://www.gsi.de/panda

[5] http://monalisa.cern.ch/monalisa.html

[6] http://project-arda-dev.web.cern.ch/project-arda-dev/xrootd/site/index.html

[7] http://www.lustre.org

Double electron transfer with an ultracold atom target as a preparation for experiments at HITRAP

S. Götz[1], I. Blank[2], G. Hasan[2], R. Hoekstra[2], T. Mullins[1], W. Quint[4], A. Sokolov[4], R. Wester[3], and M. Weidemüller[1]

[1]Universität Heidelberg, Germany, [2]KVI Groningen, The Netherlands, [3]Universität Freiburg, Germany, [4]GSI Darmstadt, Germany

We are setting up an ultracold target of rubidium atoms combined with a recoil ion momentum spectrometer for kinematically complete scattering experiments at the GSI-HITRAP facility. First experiments will focus on multiple electron-transfer reactions in collisions of many electron atoms with highly charged ions such as Rb + U^{92+}. In particular, we want to investigate correlation effects in multi-electron transfer which will serve as a model for dynamics in quantum mechanical many-particle systems.

Multiple electron transfer has so far been investigated in supersonic jet targets, where the initial momenta of the atoms limit the resolution on the recoil ion momentum. Laser-cooled targets, where temperatures down to a few hundreds of microkelvin can be reached, provide a stationary target which allows to measure the differential cross-sections in multiple charge transfer with very high accuracy [1]. Furthermore, full control over the internal state of the target can be obtained easily with optical pumping.

The ultracold target that we developed for the HITRAP experiments consists of an ultracold gas of Rubidium atoms which are stored in a MOT in dark-SPOT configuration, reaching densities of $10^{11}cm^{-3}$ in a volume of 0.8mm diameter. The temperature of the captured gas is around 100μK which corresponds to momentum uncertainties of the individual target atoms of 0.01a.u. The trap captures atoms of the isotope ^{85}Rb with nearly 100% isotope selectivity, and can, if desired, be changed to store ^{87}Rb. Furthermore, the dark-SPOT configuration allows storing the target atoms in a single hyperfine state of the electronic ground state with an efficiency of 99%. The trap has been combined with a recoil ion momentum spectrometer. Classical over-the-barrier models [2] show that in collisions of U^{90+} and Rb(5s) at 9keV/amu transfer up to four electrons can be measured (see figure 1) [3]. The whole setup is fully transportable and can be implemented into various setups at the GSI [4].

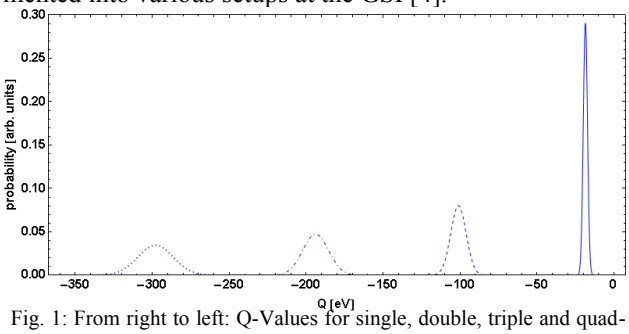

Fig. 1: From right to left: Q-Values for single, double, triple and quadruple electron transfer in collisions of U90+ and Rb(5s) at 9keV/amu calculated with the classical over-the-barrier model.

In preparation for the planned experiments at HITRAP we performed energy dependent experiments on double electron transfer in the system Na + O^{6+} in collaboration with the KVI Groningen. The results show two distinct channels, where the dominant channel corresponds to sequential double capture (SDS) of two electrons into asymmetric final channels with different principal quantum numbers (3lnl', n>4) [5]. A second channel populating the symmetric final states 3l3l' via correlated double electron capture (CDC) has also been observed. As shown in figure 2 the measured partial cross sections show the remarkable result that, despite the large difference in binding energies between the valence electron and the inner electron, about 15% of the double electron transfer takes place via correlated capture. In the energy range investigated, we observe a constant branching ratio for the two channels indicating no dependence on the interaction time. In further experiments we plan to increase the range of the collision energy.

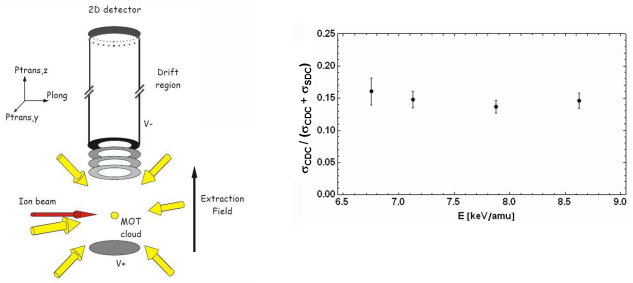

Fig 2: left: The Groningen MOTRIMS setup where experiments on the energy dependence of double electron transfer have been performed [6]. right: Partial cross-section ratio of the population of the symmetric 3l3l' final states via CDC at different collision energies.

References

[1] B. DePaola *et al*, Ad. in Atomic, Molecular and Optical Physics **55**, 139 (2008)
[2] A. Niehaus, J. Phys. B **19**, 2925 (1986)
[3] I. Blank, Diplomarbeit, Universität Freiburg (2008)
[4] W. Salzmann, Dissertation, Universität Freiburg (2007)
[5] S.Knoop *et al*. Europhys. Lett. **74** (6), pp. 992 -998 (2006)
[6] S. Knoop, Dissertation, Rijksuniversiteit Groningen (2006)

The SPARC Program at FAIR: Structure and Dynamics of Heavy Highly Charged Ions

D.F.A. Winters[1,2], Th. Stöhlker[1,2], R. Schuch[3], and the SPARC Collaboration
[1]GSI Darmstadt, Germany; [2]Heidelberg University, Germany; [3]Stockholm University, Sweden

The Stored Particle Atomic Research Collaboration (SPARC) developed a broad research program for experiments at the future Facility for Antiproton and Ion Research (FAIR) in Darmstadt. These studies will focus on precision spectroscopy of heavy highly charged ions, and will cover a wide range of (collision) energies.

Introduction

Heavy highly-charged ions (HCI) are the simplest few-body systems and the strongest laboratory sources of electromagnetic fields. The new storage rings and synchrotrons that will be built for the future Facility for Antiproton and Ion Research (FAIR) in Darmstadt, will offer unique possibilities to study the structure of such HCI, and the dynamics of their interaction with matter or light [1]. Combining unique ion beams with novel techniques and sophisticated instrumentation, high-precision experiments in a hitherto unexplored area of atomic physics can be performed.

SPARC Science @ FAIR

The SPARC program essentially covers three themes: structure, dynamics, and technology. The medium- and high-energy experiments will take place at the New Experimental Storage Ring (NESR), and at the 'Schwer-Ionen-Synchrotron' (SIS300). The low-energy experiments are planned for the FLAIR building [2], using the Low- and Ultra-low-energy Storage Rings (LSR and USR), and the HITRAP facility [3].

For example, at the NESR, it is planned to determine QED effects in strong fields. For this purpose, radioactive nuclei or even chains of isotopes can be used to disentangle QED and nuclear effects. In addition, by means of optical pumping with lasers, spin-polarized ion beams will be produced for *e.g.* PNC studies. Tests of atomic structure theory in the strong field regime can be done via studies of $2s - 2p$ transitions in high-Z ions, using the x-rays generated by PHELIX [4]. In the SIS300, laser cooling and x-ray spectroscopy of Li-like heavy ions are planned [5]. Here, the large Doppler boost ($\gamma \approx 25$) will be exploited twice: firstly to cool the ions with a laser, and secondly to perform x-ray spectroscopy with a crystal spectrometer or a microcalorimeter.

The SPARC themes

STRUCTURE - In HCI extreme electromagnetic fields prevail, which expose the true quantum nature of physics under unique conditions. Via high-accuracy measurements of the $1s$ Lamb shift [6] and the $1s$ and $2s$ hyperfine splittings in H- and Li-like ions [7], respectively, one can probe QED effects. In He-like systems, for example, one can study the electron-electron correlation in the strong field domain, or even study atomic PNC effects.

DYNAMICS - Exploiting inverse kinematics, measurements of radiative electron capture (REC) [8] and Bremsstrahlung enable us to investigate the photon-matter interaction in strong fields, and to study fundamental processes like photoionization of HCI. Here, via angular differential or polarization measurements, the coupling of the electron's magnetic moment to the fast ion's radiation field can be uniquely identified. These effects can *e.g.* be used to identify spin-polarized ion beams.

TECHNOLOGY - All these experiments rely on state-of-the-art experiment technology: Compton polarimeters (2D/3D x-ray detectors [9]), ion traps, electron/positron spectrometers [10], novel targets (cryogenic cluster jet [11]), as well as laser cooling & spectroscopy.

Please also visit the SPARC website [12] for news and information, for an overview of the working groups, and for meetings or workshops.

References

[1] Th. Stöhlker *et al.*, Nucl. Instr. Meth. Phys. Res. B **261** (2007) 234.

[2] E. Widmann, Phys. Scr. **72** (2005) C51.

[3] Th. Beier *et al.*, Nucl. Instr. Meth. Phys. Res. B **235** (2005) 473.

[4] Th. Kühl *et al.*, Hyp. Int. **162** (2005) 55.

[5] H. Backe, Hyp. Int. **171** (2007) 93.

[6] A. Gumberidze, Th. Stöhlker *et al.*, Phys. Rev. Lett. **94** (2005) 223001.

[7] V.M. Shabaev *et al.*, Phys. Rev. Lett. **86** (2001) 3959.

[8] J. Eichler and Th. Stöhlker, Phys. Rep. **439** (2007) 1.

[9] Th. Stöhlker, U. Spillmann, *et al.*, J. of Phys. **58** (2007) 411.

[10] S. Hagmann *et al.*, Nucl. Instr. Meth. Phys. Res. B **261** (2007) 218.

[11] M. Kühnel, R.E. Grisenti *et al.*, *accepted for* Nucl. Instr. Meth. Phys. Res. A (2009).

[12] http://www.gsi.de/fair/experiments/sparc/

Progress in the HypHI project *

T.R. Saito† [1,2], P. Achenbach[2], S. Ajimura[3], S. Bianchin[1], O. Borodina[1,2], T. Fukuda[4], Y. Hayashi[5], T. Hiraiwa[5], J. Hoffmann[1], M. Kavatsyuk[6], K. Koch[1], T. Koike[7], N. Kurz[1], F. Maas[1,2], S. Minami[1], Y. Mizoi[4], T. Mochizuki[8], M. Moritsu[5], T. Nagae[5], D. Nakajima[1,9,10], A. Okamura[5], W. Ott[1], B. Özel[1], R. Pleskac[1], J. Pochodzalla[2], C. Rappold[1,11], A. Sakaguchi[8], M. Sako[5], M. Sekimoto[9], H. Sugimura[5], T. Takahashi[9], K. Tanida[5], W. Trautmann[1], and S. Voltz[1]

[1]GSI, Darmstadt, Germany; [2]Mainz University, Mainz, Germany; [3]RCNP, Osaka University, Ibaraki, Japan; [4]Osaka Electro-Communication University, Neyagawa, Japan; [5]Kyoto University, Kyoto, Japan; [6]KVI, Groningen, The Netherlands; [7]Tohoku University, Sendai, Japan; [8]Osaka University, Toyonaka, Japan; [9]KEK, Tsukuba, Japan; [10]Tokyo University, Tokyo, Japan; [11]Strasbourg University, Strasbourg, France

The HypHI collaboration prepares currently for the precise hypernuclear spectroscopy with stable heavy ion beams and rare isotope beams at GSI and FAIR in order to enable studies of structures of hypernuclei at extreme isospin and direct measurements of hypernuclear magnetic moments for the first time [1]. The first step of the HypHI project is so called the Phase 0 experiment to demonstrate the feasibility of the precise hypernuclear spectroscopy by studying light hypernuclei such as ${}^{3}_{\Lambda}$H, ${}^{4}_{\Lambda}$H and ${}^{5}_{\Lambda}$He. Invariant mass of these hypernuclei will be reconstructed by by observing charged particle channels of their weak decay as ${}^{3}_{\Lambda}\mathrm{H}\rightarrow{}^{3}\mathrm{He}+\pi^{-}$, ${}^{4}_{\Lambda}\mathrm{H}\rightarrow{}^{4}\mathrm{He}+\pi^{-}$ and ${}^{5}_{\Lambda}\mathrm{He}\rightarrow{}^{4}\mathrm{He}+\pi^{-}+\mathrm{p}$ [2, 3]. In the Phase 0 experiment, the following physics will be studied in addition to prove the method of the experiment; (1) reaction mechanism to produce hypernuclei as projectile fragments, (2) week decay of light hypernuclei, (3) lifetime of hypernuclei, (4) hypernuclear resonance states, and (5) hypernuclear radii.

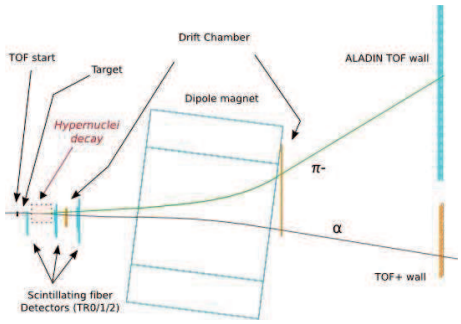

Figure 1: Experimental setup for the Phase 0 experiment

Figure 1 shows a schematic experimental setup of the Phase 0 experiment. It is a charged particle spectrometer with a large dipole magnet, ALADiN. In front of the ALADiN magnet there are a start detector for Time-of-Flight (TOF) measurements (TOF-start) [4], three sets of scintillating fiber detectors (TR0, 1 and 2) [5] and a drift chamber from KEK. Beams of ^{6}Li at 2 A GeV with an intensity of 10^{7} particles per second are impinged on a carbon target with a thickness of 8 g/cm^{2} placed between TOF-start and TR0. Behind the ALADiN magnet, a large drift chamber from KEK and two TOF walls (ALADiN TOF wall and TOF+) which are hodoscopes with plastic scintillator bars [4] are mounted. The ALADiN TOF wall and TOF+ are used to measure respectively π^{-} and positively charged particles. The construction of the fiber detectors has been finished [5], and TOF-start and TOF+ are to be completed [4]. For the data acquisition system, there are three stages of triggers. The secondary vertex trigger for events with decay of hyperons and hypernuclei is produced by signals of the fiber detectors with newly developed universal logic modules VUPROM2 [6]. Triggers associated with π^{-} and positively charged particles are created by signals from the ALADiN TOF wall and TOF+, respectively [6].

The vertical layers of the fiber detectors (TR1 and TR2), the full set of TR0 and prototypes of TOF-start and TOF+ as well as the TOF+ trigger and partial functions of the secondary vertex trigger are tested in Cave A in 2008 with events produced by ^{6}Li beams impinged on a carbon target at 2 A GeV. Details of the results of the test experiment are discussed in these reports [4, 5, 6].

For the data analysis of the Phase 0 experiment, a new analysis method with Hough transformations has been developed, and the performance of the event reconstruction is also discussed in these reports [7].

The Phase 0 experiment is currently scheduled in summer 2009, and a few thousands events for each hypernucleus are estimated to be reconstructed [2].

References

[1] T.R. Saito, *et al.*, Letter Of Intent of "Hypernuclei with Stable Heavy Ion Beam and RI-beam Induced Reactions at GSI (HypHI)". Submitted to GSI EA 30.

[2] T.R. Saito, *et al.*, Proposal of the HypHI Phase 0 experiment submitted to the G-PAC 33 in October 2006.

[3] T.R. Saito, *et al.*, Progress Report on Proposal of the HypHI Phase 0 experiment submitted to the G-PAC 34 in April 2007.

[4] S. Bianchin, O. Borodina *et al.*, in these reports.

[5] D. Nakajima, B. Özel *et al.*, in these reports.

[6] S. Minami, C. Rappold *et al.*, in these reports.

[7] C. Rappold *et al.*, in these reports.

* The HypHI project is supported by the Helmholtz Association as Helmholtz University Young Investigators Group VH-NG-239 and by DFG with the research grant SA 1696/1-1.

† t.saito@gsi.de

Development of the trigger system for the HypHI project *

S. Minami †[1], C. Rappold ‡[1,2], P. Achenbach[3], S. Ajimura[4], S. Bianchin[1], O. Borodina[1,3], T. Fukuda[5], J. Hoffmann[1], M. Kavatsyuk[7], N. Kurz[1], F. Maas[1,3], Y. Mizoi[5], T. Nagae[6], D. Nakajima[1,10], A. Okamura[6], W. Ott[1], B. Özel[1], R. Pleskac[1], J. Pochodzalla[3], T.R. Saito[1,3], A. Sakaguchi[4], M. Sako[5], H. Sugimura[6], K. Tanida[6], W. Trautmann[1], and S. Voltz[1]

[1]GSI, Darmstadt, Germany; [2]Strasbourg University, Strasbourg, France; [3]Mainz University, Mainz, Germany; [4]Osaka University, Ibaraki, Japan; [5]Osaka Electro-Communication University, Neyagawa, Japan; [6]Kyoto University, Kyoto, Japan; [7]KVI, Groningen, The Netherlands; [8]Tohoku University, Sendai, Japan; [10]Tokyo University, Tokyo, Japan

The first experiment of the HypHI project is planned to measure mesonic decays of the lightest hypernuclei, ${}^{3}_{\Lambda}\mathrm{H} \rightarrow {}^{3}\mathrm{He} + \pi^-$, ${}^{4}_{\Lambda}\mathrm{H} \rightarrow {}^{4}\mathrm{He} + \pi^-$ and ${}^{5}_{\Lambda}\mathrm{He} \rightarrow {}^{4}\mathrm{He} + \mathrm{p} + \pi^-$, produced by collisions of a 2 *A* GeV ^{6}Li beam with an intensity of 10^{7}/sec and a ^{12}C target with a thickness of 8 g/cm^2 [1]. The reaction rate at the thick target could reach 4 MHz, yet the trigger signal need to be issued with the rate of less than 3 kHz within 500 nsec decision time to fulfill the requirement by the DAQ system and the electronics [2]. The trigger system has following 3 trigger functions;

1. The vertex trigger selecting events with decay vertices which are approximately 20 cm in average behind the target by examining hit patterns on scintillating fiber (SciFi) detectors, TR0, TR1 and TR2 [3].

2. The He trigger requesting at least one hit with large energy deposit by He at the time-of-flight (TOF) wall for positively charged particles, TOF+[4].

3. The π^- trigger requesting one hit at the TOF wall for negatively charged particles, ALADiN-TOF.

The 40 VUPROM2 modules, a 1-unit-wide VME 6U module with 256 LVDS I/Os and a FPGA, have been produced to implement the whole trigger functions. Logic for the vertex trigger to be implemented on the FPGA has been organized as following 4 stages;

1. The signals from SciFi detectors are or-ed with 2 or 4 neighboring signals and adjusted for proper delay. TDC, scaler and fan-out functions are also implemented.

2. The order of the signals from the first stage are shifted to produce necessary coincidences at next stage, also with adjustment of delay and fan-outs.

3. The signals are clustered together with up to 3 neighboring signals, then straight tracks crossing TR0, TR1 and TR2 are found by matrix coincidences. The signals corresponding to straight tracks are vetoed. The remaining signals are sent to the next stage as candidates produced by the decay vertices.

4. The signals from TR1 and TR2 are or-ed and coincidences of both layer are produced as the vertex trigger.

The signals on x- and y-planes of SciFi detectors are processed separately at first and combined at the 4th stage. The latest experiment for performance test of the detector system took place at August 2008 using a 2 *A* GeV ^{6}Li beam. The logic of the vertex trigger have been implemented for the y-plane with 17 VUPROM2 modules and the TDC information on 1st, 3rd and 4th stages were recorded. The reduction of trigger rate by the vertex trigger roughly agreed with the MC simulation. Detailed analysis to compare the online trigger and the recorded hit patterns is in progress.

The He trigger discriminates electric charge of the particles from time over threshold (TOT) of the signals [5]. TOF+ is made of plastic scintillator bars with a length of 1 m and read by 2 PMTs at the both ends. Each side of the PMT gives different TOT depending on the position, therefore it is necessary to take the average of TOTs. The TOF+ uses discriminators with FPGAs mounted on the same circuit boards[6]. The logic to produce mean width of TOT has been implemented together with the logic to discriminate the pulse width on the discriminator. The efficiency of He by the He trigger had been studied at the latest experiment. The charges of particles were identified by their energy deposit on the TOF+ bar measured by charge sensitive ADCs and the efficiency of the He trigger was obtained by applying a He gate on the TOT spectra. The efficiency was 99% with the He trigger and it issued trigger signals for 0.4% of particles with electric charge one.

References

[1] The HypHI collaboration, A proposal of the HypHI Phase 0 experiment, submitted to GSI PAC EA33 with a realization as S319. ; T.R. Saito, *et al.*, in these reports.

[2] S. Minami *et al.*, GSI Scientific Report (2007) p.223

[3] D. Nakajima, B. Özel, *et al.*, in these reports.

[4] S. Bianchin, O. Borodina, *et al.*, in these reports.

[5] C. Rappold, *et al.*, GSI Scientific Report (2007) p.221

[6] T. Yoshioka, *et al.* IEEE Trans. Nucl. Sci. Vol.51, No.3,(2004) p.334

*The HypHI project is supported by the Helmholtz Association as Helmholtz University Young Investigators Group VH-NG-239 and by DFG with the research grant SA 1696/1-1.

† s.minami@gsi.de

‡ c.rappold@gsi.de

The HypHI project at GSI and FAIR: Hypernuclei event reconstruction analysis

C.Rappold*[1,2], S. Bianchin[1], O. Borodina[1,3], M. Kavatsyuk[4], F. Maas[1,3], S. Minami[1], D. Nakajima[1,5,6], B. Özel[1], J. Pochodzalla[3], T.R. Saito[1,3], and W. Trautmann[1]

[1]GSI, Darmstadt, Germany; [2]Univ. Louis Pasteur, Strasbourg, France; [3]Mainz University, Mainz, Germany; [4]KVI, Groningen, The Netherlands; [5]KEK, Tsukuba, Japan; [6]Tokyo University, Tokyo, Japan

The HypHI project aims to study hypernuclei by means of collisions of stable heavy ion and rare-isotope beams on stable target materials [1, 2]. As the first step (Phase 0), the feasibility of precise hypernuclear spectroscopy with heavy ion beams will be demonstrated with ^{6}Li beam at 2 A GeV impinged on a ^{12}C target by identifying $^{3}_{\Lambda}$H, $^{4}_{\Lambda}$H and $^{5}_{\Lambda}$He hypernuclei [3].

For preparation of the Phase 0 experiment scheduled on August 09, the data analysis method has already been under development with data produced by Monte Carlo (MC) Simulation of the full setup[4] in order to study the performance of the proposed setup and to estimate the physics outcome. After the first study reported in ref.[4], two sets of drift chambers were included in the experimental setup to increase tracking information, as shown in the figure of ref. [5]. Thank to this new tracking information, a new approach of the data analysis could been considered. With sufficient available detectors in the proposed setup, pattern recognition algorithms can be used to build track candidates in the earliest steps of the data analysis. Those methods are commonly used offline and/or online to reduce the data flow and to consider anything but track candidates. This particular step had to be included to the data analysis of the Phase 0 experiment because of time consuming and outdated MC simulation input of the previous analysis code.

Among viable global methods of pattern recognition, a specific Fuzzy Radon method so called Hough Transform [6] is adopted and implemented in the new data analysis. This implementation of the Hough transform algorithm for track recognition was a good opportunity to reorganize the previous analysis code. The current structure of the algorithm is as follow :

- Hit extraction from detectors.
- Hough transform in the parallel plane of the magnetic field for building track candidates.
- Momentum and mass calculation in transverse plane of the magnetic field for all track candidates.
- Particle selection for the hypernuclei invariant mass calculation.
- Secondary vertex cut for best candidate selection.
- Invariant mass reconstructed from selected events.

* c.rappold@gsi.de

Before the complete implementation in the data analysis, the pattern recognition algorithm have been tested independently. After full satisfaction of the pattern recognition process, the analysis for hypernuclei was again checked step by step, by reconstructing single proton, pion, alpha and Λ event, then by reconstructing single hypernucleus event and finally hypernucleus event with associated background. Those events were from the MC simulation with three different set of conditions :

- No multiple scattering & energy lost, ideal detectors.
- Air & With effects by the detector materials but still perfect detector.
- With realistic detector resolutions as in [5].

The impact of each differences have been studied by the new data analysis program. The following two tables summarize the RMS values for each invariant mass peak of studied hypernuclei and the number of reconstructed hypernuclei integrated in the peak against the number of effectively detected particles from their decay.

RMS of inv mass	$^{3}_{\Lambda}$H	$^{4}_{\Lambda}$H	$^{5}_{\Lambda}$He
perfect	0.7 MeV	0.9 MeV	0.8 MeV
semi perfect	1.6 MeV	1.8 MeV	1.7 MeV
realistic	3.0 MeV	3.6 MeV	3.6 MeV

Yield	$^{3}_{\Lambda}$H	$^{4}_{\Lambda}$H	$^{5}_{\Lambda}$He
perfect	49.1%	50.4%	35.7%
semi perfect	44.4%	47.0%	22.5%
realistic	32.3%	35.2%	12.5%

For further steps for the development of the data analysis methods, we are currently implementing Kalman Filter algorithm for track fitting in order to involve more precisely scattering, energy loss and detector resolutions, and it should finally provide full fitted track for hypernuclei reconstructions and the improve results of realistic simulations.

References

[1] T.R. Saito *et. al.*, and the HypHI collaboration, in these Scientific Reports.

[2] T.R. Saito *et. al.*, proceedings of HYP2006, pp171.

[3] A proposal of the HypHI Phase 0 experiment, the HypHI collaboration.

[4] S. Minami *et. al.*, in GSI annual report 2006.

[5] T.R Saito *et. al.*, in these reports.

[6] R. Mankel. Rep. Prog. Phys. 67 (2004) 553-622.

Efficiency measurements of RPC detectors with relativistic heavy ions

E. Casarejos[1], H. Alvarez[1], F.Y. Ayyad[1], J. Benlliure[1], I. Durán[1], N. Montes[1], A.I. Morales[1], J.R. Pereira[1], and D. Perez[1]

[1]USC, Santiago de Compostela, Spain

Resistive Plate Chambers (RPCs) are widely used in recent experiments as time detectors due to their high time resolution and performance in large surfaces. Fast progress made it possible to define canonical construction designs and working parameters to achieve maximum efficiency and resolution for minimum-ionization particles (MIPs) and quasi-MIPs. As part of the R3B experiment in the new FAIR facility, the detection setup includes a time-of-flight (ToF) wall for relativistic ions. The wide experimental program of R3B, including fission and multi-fragmentation studies, requires large detection surfaces and very demanding time resolutions, needed to separate and identify residual nuclei up to the mass 200. In order to fulfill these requirements it has been proposed to build a large area ToF-wall made of RPCs [1] and dedicated to fast ions.

The R&D program on this detector started in 2006 with the construction of small sized prototypes, tested at GSI with relativistic heavy ions to investigate their performances in terms of detection efficiency and time resolution [2]. The RPCs prototypes are designed as a symmetric twin stack with one 0.3 mm gas-gap per stack. We use commercial soda-lime glass (1mm) as resistive plates, and copper tape (2.5 x 15 cm^2) as electrodes. We have designed the front-end electronics, with a gain stage based in two trans-impedance amplifiers, able to deal with the high frequencies typical of fast RPC signals. The gain is adapted to the detection of heavy ions, with a noise low enough to separate ion signals from noise level.

We tested the prototypes placed inside a gas-tight aluminum box used as gas container, with a mixture of R134a (0.8) and SF6 (0.2). Plastic scintillators placed in front and behind the RPCs provided not only the trigger for efficiency measurements, but also information on the charge of the ions. The use of flash-ADC boards in a VME-MBS daq-system, gave us a maximum of information about the RPC signals. Two different beam tests were performed at GSI along 2008, with ^{12}C (700 AMeV) and ^{64}Ni (600 AMeV) beams. Figure 1 summarizes the main results. In the upper panel we represent the dependence of the RPC efficiency with the voltage applied, for ions with different charges. As can be seen, charges 2 and above reach 100% efficiency at about 3.0 kV while ions with charge 6 reach that value already at 2.5 kV. The efficiency for protons is lower; neither MIPs, not shown here, are completely resolved by our front-end. This limitation will be overcome in future designs.

In the lower panel we plot the efficiency as a function of the ion charge, for a fixed value of voltage (3 kV). Efficiency evolves very fast with charge.

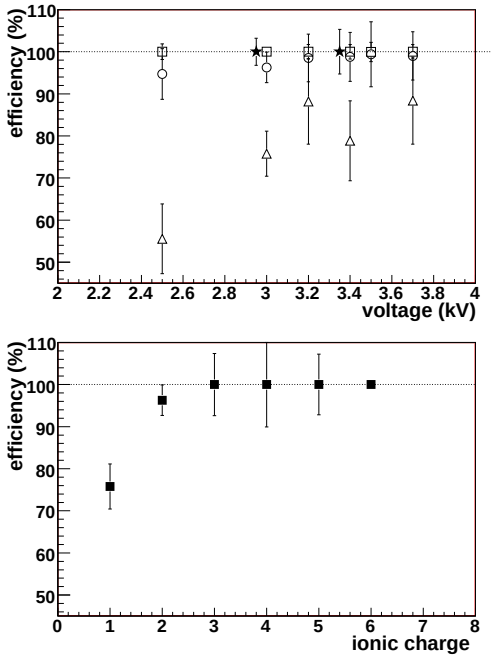

Figure 1: Efficiency for ions. Upper panel: efficiency as a function of the HV applied. Data for ions with charges≈28 (stars), 6 (squares), 2 (circles), and 1 (triangles). Lower panel: efficiency as a function of the ion charge at 3.0 kV. The efficiency of charges≈28, not seen in the plot, is 100%.

Our front-end also allows for a separation between the so called avalanche and streamer signals. Their ratio depends on the gap field. For a field of 100 kV/cm, with high efficiency for charges 2 and above, the ratio of streamers was less than 1% for charges up to 6, but 28% for charges about 28. This value has to be optimized to guaranty the performance of the detector, being the final gain a balance between efficiency, including protons, and the streamers ratio. Tests with single-gap RPC prototypes were also performed: 100% efficiency was observed at 100 kV/cm for ions with charge around 28. Moreover, the ratio of streamers was drastically reduced below 2%.

These results allow us to conclude that RPCs are well suited for the detection of relativistic heavy ions in a wide range of charges with large efficiencies. Single-gap RPCs may improve the working conditions of these detectors, but also the design of multi-layer configurations when the detector matter represents a serious limitation for the detection of heavy ions at energies below 500 AMeV.

[1] Nuclear Physics B (Proc. Suppl.) 158 (2006) 186-189
[2] GSI Scientific Report 2006, pag. 22

Prototyping of DSSD detectors for the EXL/R^{3}B collaboration

B. Streicher[1], P. Egelhof[2], V. Eremin[3], J.V. Kratz[1], X. C. Le[2], M. Mutterer[2,4], N. Pietralla[4], M. von Schmid[4], and the EXL and R^{3}B collaborations*

[1]JGU Mainz, Germany; [2]GSI Darmstadt, Germany; [3]PTI St. Petersburg, Russia; [4]TU Darmstadt, Germany

Motivation

The EXL experiment as a part of future FAIR facility [1] will provide the means for studying many physics phenomena in unstable exotic nuclei. Reactions will be done in inverse kinematics using new storage-ring techniques and a universal detector system providing high resolution and large solid angle coverage for kinematically complete measurements. Our work focuses on prototyping and testing DSSDs as a part of EXL's Silicon Particle Array (ESPA) [2]. DSSD chips were manufactured at PTI St. Petersburg. In the course of technical development potential synergies in particular with the R^{3}B experiment is expected.

Technical Procedure And Results

Within a first stage of prototyping eight detectors were built and tested. Four of these are of 64×64 strips type and the other four of 64×16 type, respectively with the first number referring to the P^+ side and the second to the N^+ side of the detector. Detector chips of active area of 21×21mm^2 are 300μm thick and have a strip pitch of 300μm for the 64 strips side and 1250μm for the 16 strips side, respectively. The same epoxy PCB was designed for

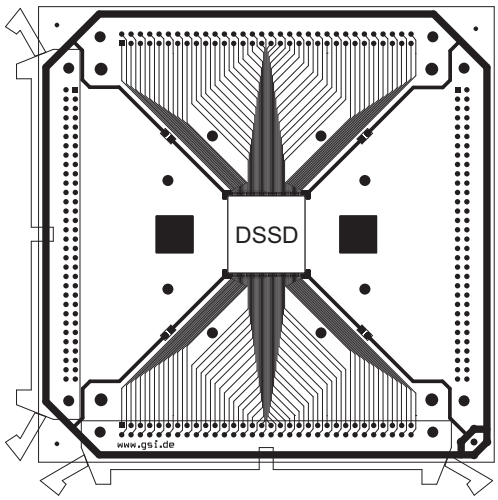

Figure 1: PCB layout for 64x64 and 64x16 DSSDs.

both types of DSSDs (see Fig.1) with standard 64-way IDC connectors enabling to read signals from both sides. The chips were glued with a special low outgasing epoxy to a small step machined on the edge of the inner opening of the PCB and manually bonded. Biasing of the detector was done with the punch-through method using a bias ring surrounding the strips. Total depletion voltage was established at -50V, but overbias of up to -200V was applied to the P^+ side with AC-coupled preamps. The grounding through DC-coupled preamps was used on the N^+ side. The readout used 16 data channels on each side with 4 strips coupled together in the case of the 64 strip sides. Measurements in vacuum of about 3×10^{-7}torr were performed using a ^{241}Am α source.

Out of 752 tested strips 97% showed good spectroscopic properties. Using P^+ (and N^+) injection we achieved an energy resolution down to 15.6 keV (and 35.3 keV) for the P^+ and 17.9 keV (and 44.6 keV) for the N^+ side. Worse resolution for N^+ injection is due to distorted field in between the N^+ strips caused by P^+ implants used to enhance interstrip isolation. Important part of our tests was the study of interstrip events on both sides of the detector whose induced signal is shared between two neighboring strips. Two dimensional correlation analysis of simultaneously occurring signals on both sides of the detector, i.e. P^+ vs. N^+ strips, was performed to evaluate the interstrip contribution. All events fall into four categories of: 1) strip-strip type with energy signal induced in a single strip on both sides of the detector, 2) strip-interstrip and 3) interstrip-strip type with N^+ or P^+ respectively, sharing the energy between two neighboring strips and 4) interstrip-interstrip type with both sides having the induced signal shared between two strips. The results show that for P^+ injection strip-strip events and those events from strip-interstrip category induced on the P^+ side of the detector contribute to about 95% of all events and have average resolution of 18.6 keV. The reconstructed energy E_{strip1}+E_{strip2} from interstrip events has an average resolution of 195 keV and 82 keV and relative contribution of 5% and 20% for P^+ and N^+ side, respectively. Reconstructed interstrip-interstrip events have a resolution of 336 keV and represent 1% of all events. The percentage distribution of events corresponds within the error bars with the geometry of active and interstrip areas of our detectors. Our prototyping reveals good properties of tested DSSD chips and their usability in future EXL experiment. Further detailed tests as well as a proton beam experiment at KVI, Groningen using a telescope arrangement to test the tracking and energy reconstruction properties of our DSSDs together with Si(Li) detectors are scheduled for the first half of 2009.

References

[1] **FAIR homepage:** http://www.gsi.de/fair/index_e.html

[2] **EXL homepage:** http://ns.ph.liv.ac.uk/ mc/EXL/ns-instrum-exl.html

A closed-circuit gas system for an RPC-based neutron detector*

D. Rossi[1], K. Boretzky[2], H. Simon[2] for the R^{3}B collaboration
[1]Institut für Kernchemie, Johannes Gutenberg-Universität Mainz, D-55128 Mainz; [2]GSI, D-64291 Darmstadt

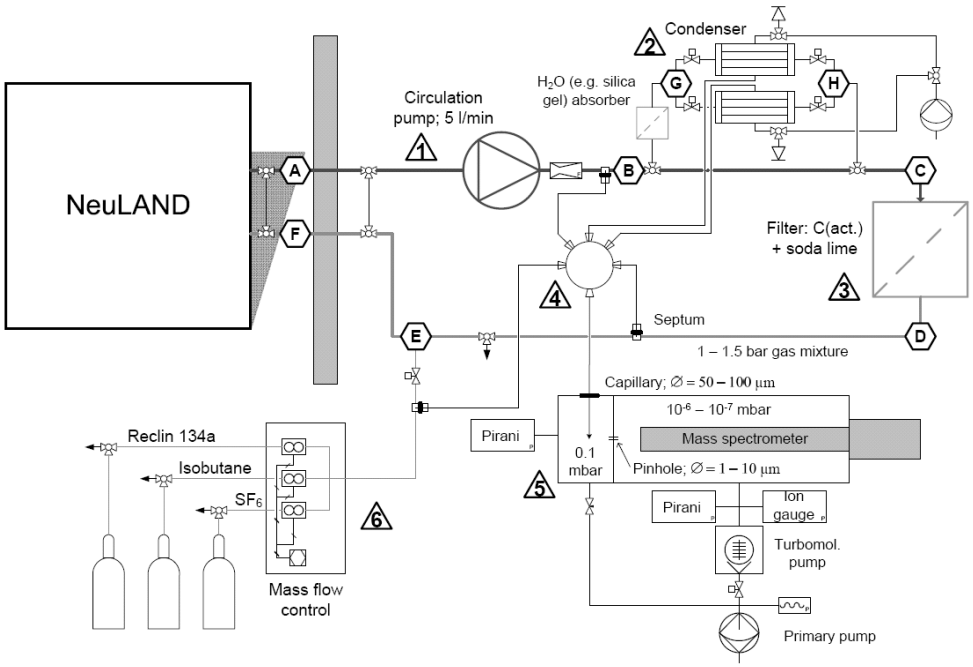

Figure 1: Proposed closed-circuit gas system for the NeuLAND neutron detector. For description, see text.

As a core component of the R^{3}B experimental setup [1] in the future FAIR facility, a new neutron detector – NeuLAND – is currently under development at GSI. It is foreseen that NeuLAND will be based on a resistive plate chamber (RPC) concept. RPCs are gas detectors running on a gas mixture of approximately 85% Reclin 134a (1,1,1,2-tetrafluoroethane), 10% SF_6 and 5% Isobutane. Reclin 134a and SF_6 are both greenhouse gases, whose emission will be subject to emerging legal constraints. Even though a detector system such as NeuLAND is a negligible emitter of such gases, a closed-circuit gas system also improves the long-term stability of the gas mixture inside the detector, and reduces the total running cost of the detector, since only a limited amount of fresh gas needs to be supplied to the system.

The proposed closed-circuit gas system, as shown in fig. 1, would be located outside the experimental area, allowing maintenance even during an ongoing experiment. It consists of a main recirculation circuit (1), a condensation and storage sub-circuit (2), an analysis system (5) and an injection sub-circuit (6). Under normal operation (path: ABCDEF), the gas flow is driven by a circulation pump through a chemical filter (3) filled with activated charcoal and soda lime, removing gas contaminants produced by the RPCs.

One of the central issues in this closed-circuit gas system is the continuous monitoring of the composition of the gas. This is achieved by using a quadrupole mass spectrometer (5) linked to a multi-port valve (4) with capillary tubes running to various locations in the gas circuit. In a scanning mode, the mass spectrometer is able to determine precisely the mixing ratio of the three working gases, as well as to detect various contaminants.

The gas pressure in the RPCs and the recirculation circuit is chosen to be slightly higher than atmospheric pressure, to avoid contamination of the detector gas with air. Due to inevitable leaks, this also means that a small amount of fresh gas must be supplied continuously through the injection branch (6), where the total flow and composition of fresh gas is adjusted to be introduced into the main circuit at point E.

To clean the gas, e.g. during filling of the detector system, the gas can be collected by condensation (in 2). Contaminated gas runs into one of the two condenser units (path: ABG), while the other unit releases the gas into the main circuit again (path: HCDEF). All three gas species used in RPCs condensate before nitrogen and oxygen do, meaning that several cleaning cycles can be used to remove all air from the detector.

With the injection branch (6) existing already, it is foreseen to build a pilot system consisting of a circulation pump and mass spectrometer, and to investigate the gas composition on-line with a working RPC.

References

[1] R^{3}B technical proposal; http://www-land.gsi.de/r3b

* Work supported by BMBF contract No. 06MZ222I.

Prototype developments for a high-resolution neutron detector at R^{3}B

T. Aumann[1], D. Bemmerer[2], K. Boretzky[1], M. Elvers[2,3], J. Endres[3], J. Hehner[1], M. Heil[1], J.V. Kratz[4], W. Prokopowicz[1], R. Reifarth[5,1], D. Rossi[4], G. Schrieder[1], D. Stach[2], A. Wagner[2], D. Yakorev[2], A. Zilges[3] for the R^{3}B collaboration

[1]GSI, Darmstadt, Germany; [2]FZD, Dresden, Germany; [3]IKP, Universität zu Köln, Köln, Germany; [4]Johannes-Gutenberg-Universität, Mainz, Germany; [5]Goethe-Universität Frankfurt, Frankfurt, Germany.

INTRODUCTION

A detector for momentum measurements of high-energy neutrons in the energy range 200 MeV to 1000 MeV is being developed for the R^{3}B experiment at FAIR. The detection principle is based on a combination of converter material and subsequent detection of charged particles from reactions in the converter material. Multi-gap Resistive-Plate Chambers (MRPC) are used for the detection of charged particles. A modular system with about 10'000 electronic channels is considered. The total depth of 1 m, 50% of which are high-Z converter (nuclear interaction length ~17 cm) ensures a detection efficiency close to 100% for neutron energies above 200 MeV. The detector is subdivided into 60 planes with active areas of 2×2 m^2 adding up to a total area of 240 m^2 MRPC modules. A time resolution of the full detector below σ=100 ps and a spatial resolution of less than 1 cm in all three dimensions are desired. In addition, the detector should provide a good efficiency for detecting and reconstructing multi-neutron events.

NeuLAND pre-design based on MRPC

The detection concept for the new neutron detector relies on the combination of converter plus detection material, as also realized in the current detector for fast neutrons LAND (Blaich et al.). A detector composed out of active material only has been considered in the preparatory phase of the R^{3}B Technical Proposal. In principle a dense scintillation material like PbWO4 would be well suited for combining converter and scintillator in one homogeneous layer. However, the high costs as well as the timing properties of the scintillator rule out this option.

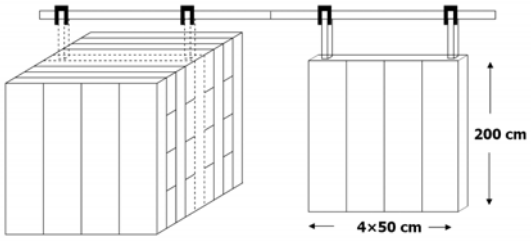

Figure 1: Schematic drawing of the modular structure of the NeuLAND detector.

Resistive Plate Chambers (RPC) are detectors for ionizing particles and presently these types of detectors are used in many different experiments involving cosmic rays and accelerators such as STAR, RICK, CMS and ATLAS at LHC, CERN, AGRO etc. Excellent time resolutions down to σ_t<50 ps were achieved for minimum ionizing particles using multi-gap resistive plate chambers (MRPC). Large detector arrays with high granularity are feasible, thus the MRPC detector systems partly take over the classical application of scintillators for ToF-arrays. A. Blanco et al. showed that a large area MRPC (160 cm ×10 cm, 2 strip readout) can provide good time resolutions of σ_t~50-70 ps and a position resolution of 1.2 cm along the strips using the time difference method. In addition, an efficiency for minimum ionizing particles of more than 95% was achieved.

The present design concept foresees a modular structure of MRPC modules with a size of 200×50 cm^2 each. Four modules build up one detector plane (s. Figure 1).

Prototype development and tests at FZD

The Forschungszentrum Dresden-Rossendorf (FZD) is involved in building and testing MRPC structures capable of sustaining high rates (R. Kotte et al.), as they are expected in the CBM experiment. Now the development of MRPC prototypes with intrinsic neutron converter structure for the NeuLAND detector at FAIR is under investigation. The 40 MeV electron beam from the ELBE facility at FZD with its picosecond time structure is used as a high-intensity defined source of minimum ionizing particles. The timing of the prototypes built at FZD and also at GSI is studied in regular short beamtimes at ELBE.

Based on the R^{3}B-Technical Proposal a first prototype has been developed where design decisions can be verified experimentally. As converter material for producing charged particles from the initial high-energy neutrons, stainless steel has been selected due to its good handling and commercial availability in pre-cut sizes. For the actual MRPC structure, commercial float glass (0.55 mm thick) has been used, with 0.3 mm diameter standard fishing line as spacer. All prototypes tested so far had an active area of 200 x 400 mm. Figure 2 shows the result of a measurment of the time resolution.

* Work supported by BMBF (06MZ222I), (06DR134I), (06DA129I) GSI FuE DR-GROS

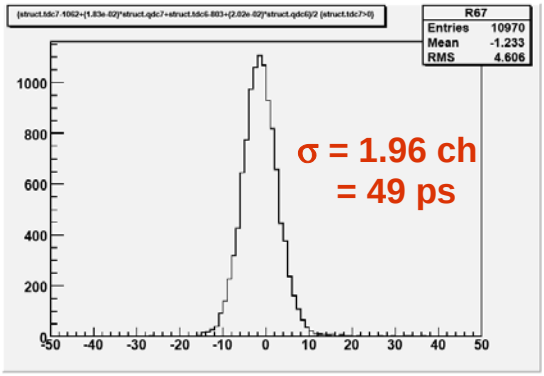

Figure 2: Typical time spectrum of a NeuLAND prototype with single-ended readout after applying a linear walk correction.

Prototype developments and tests at GSI

The prototype constructed at GSI is similar to the FZD type, but addresses some different aspects concerning in particular number of gaps, distances between anodes strips, and impedance matching.

The active area is 400×200 mm^2, subdivided in 8 anode strips, each 400 mm long, 25 mm wide and 4 mm thick Fe-material, acting as the same time as converter for the neutrons. The distance between the anode wires is kept to a minimum value of 0.3 mm, which is essential in terms of converter and detection efficiency. We use 2×4 gaps, built from 0.55 mm glass plates and gap sizes of 0.3 mm using fishing lines as distance holders (Figure 3).

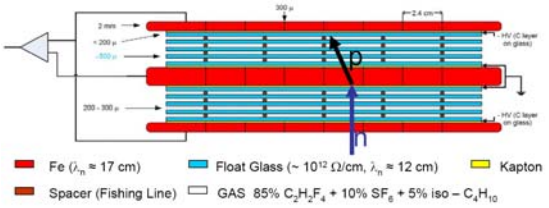

Figure 3: Schematic view of the GSI prototype.

The outer electrodes are 2mm thick Fe-plates, again acting as a converter at the same time. The high voltage is applied through a semiconductive layer which is sprayed on the outer glass plates.

One critical issue addressed is the impedance matching of the anode wires to the frontend electronics. The impedance of the anode wires was determined with a signal analyser to be 9.5 Ω. This valiue has to be compared with the typical input impedance of the electronics is 50 Ω. Measurements of the behaviour of the signal reflection and transmission as a function of the frequency of the signal in case of no impedance matching between anode strips and readout were performed using a network analyser. The transmission was found to be below 10% for most of the frequencies and high frequencies play a dominant role for the excellent timing properties.

In order to improve the signal transmission, the use of transformers or resistor networks for the purpose of adapting the impedances were investigated. For the high bandwidth transformer TC 4-11 a decrease of reflections to values below 10% was found for a wide range of frequencies. Because of this promising result the transformers were coupled to the anode strips using a special type of PCB board. The measurements with the network analyser show that reflection and transmission of the combination of anode strip and transformer board are significantly improved, but not for the full bandwidth (Figure 4).

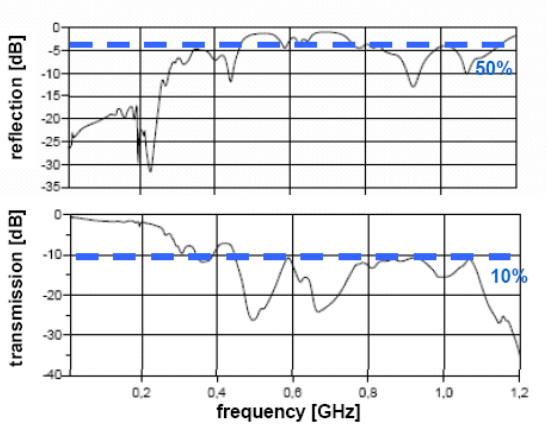

Figure 4: Presented here are the reflection and transmission properties as a function of frequency for the anode strip read out via the transformer board.

Gas recycling concept

The standard gas mixture for timing MRPCs consists of 85% Reclin-134a (1,1,1,2-tetrafluoroethane), 10% SF_6, and 5% isobutane (i-C_4H_{10}). Reclin with its high primary ionization density fulfills the role of the main ionization medium, whereas SF_6 serves as an electron scavenger for low energy electrons and isobutane is used as an UV photon quencher. Although Reclin and SF_6 both are neither flammable nor reactive or toxic, special attention has to be paid when using these gases since they contain a significant global warming potential (factor 103 and 105 versus CO_2 for Reclin, SF_6 respectively). Therefore technical solutions need to be found avoiding the emission of these two gases.

A pre-concept was developed to overcome this difficulty. Two variants of a gas recycling circuit are currently being discussed; both aim for a reuse of the gas mixture for the detector after cleaning and controlling the quality (s. contribution by D. Rossi et al.).

References

A. Blanco et al., IEEE Trans. Nucl. Sci **48** (2001) 1249
T. Blaich et al., NIM **A314** (1992) 136
R. Kotte et al. NIM **A 564** (2006) 155

Calibration of a Position Sensitive Photo Diode Using Digital Readout and Real Time Signal Analysis*

P. Lubberdink[1], H. Simon[2], M. Babai[1], C. Langer[2], S. Paschalis[2,3], P. Schakel[1], V.I. Stoica[1], and H.J. Wörtche[1]

[1]KVI/RU Groningen, The Netherlands; [2]GSI, Darmstadt, Germany; [3]LBNL Berkeley, USA.

Fast beam tracking and identification is one of the corner stones for applications within the reaction setups using secondary beams like e.g. the R³B experiment or the SuperFRS. Position sensitive pin diodes (PSPs) exhibit a small channel count and provide excellent energy loss signals at sufficiently large rate capabilities. However, the use of conventional readout electronics results in substantial pile-up and limits their use to a few kHz incoming beam rate.

In this paper the PSP for the R³B/Cave-C setup has been studied in order to develop digital filter algorithms that allow for an on-line treatment of pile-up signals. The diode has four front contacts and one back contact. The charges from these four contacts were amplified using the routinely being used charge sensitive preamplifiers (CSTA2). The measurement hardware consisted of a Quad ADC board connected to a General Purpose Trigger and Readout Board (Hades TRB). The measurement setup is described in [1,2]. The QuadADC provides 4 channels with a resolution of 14 bits at a speed of 100 MSamples/s. The TRB is equipped with a FPGA that was programmed with the "baseline follower" trigger algorithm described in [3]. For the current application as a beam-tracking system, a high event rate (typically over 100 kHz) is expected, since it is used to identify the incoming mixed secondary beams in front of a reaction target. The trigger and readout system should be able to deal with these high rates. In April 2008, the measurement hardware has been tested at GSI. The setup was placed behind a 1 g/cm^2 Pb target which was irradiated by a 600 MeV/n ^{12}C beam. Beam intensities were varied from 1 kHz up to 50 kHz. Figure 1 shows value of the baseline as a function of the event number. As can be seen from this image, the variations of the baseline are significant and would lead to problems when using a trigger system with a fixed threshold. Therefore a new discriminator scheme has been developed, being capable of dealing with both the fluctuating baseline and the high event rate. The behaviour of the diode has been investigated aiming at being able to reconstruct and calibrate the position information on-line. Unexpected pulse shape variations have been observed, that are likely to vanish when using more appropriate current sensitive preamplifiers that are currently under construction.

Different approaches can be followed relating the charge measured at the four contacts of the diode to the position of irradiation. A simple and common approximation is evaluating the position by assuming a simple charge division in both coordinates. This, however, leads to distortions in the reconstructed position patterns known as the 'pin-cushion effect' [4]. Two general approaches were followed for this study: (i) optimization of the diode characteristics towards this simple charge division approximation or (ii) the implementation of different relations. The PSP under test can be reliably operated using the simple relation with corrections, although large non-linearities were observed with 6.4 % and 10.7 % in y and x direction, respectively. It has also been investigated if it is possible to use the PSP as a ΔE detector by relating the charge measured to the energy loss. It is found that both the sum of the charges measured at the front contacts and the charge measured at the back contact are position dependent. Therefore, further position dependent corrections need to be worked out together with an improved amplitude measurement. Although the calibration procedure cannot be simplified for the described setup, it can be automated. The addition of a mechanical arm which can move a light fibre over the diode is proposed. This way, in addition to the existing coincidence method using a pixel matrix of scintillators, a well defined irradiation of the diode can be performed automatically, on which the gain matching procedure and the determination of optimal bias voltage rely.

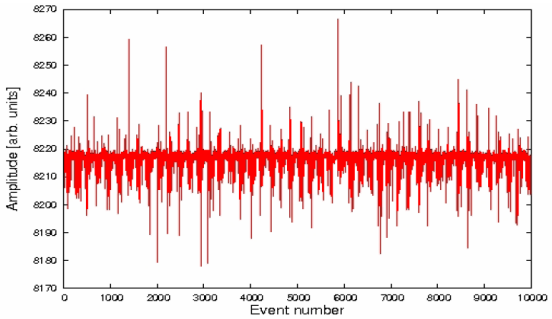

Figure 1: Baseline variation at 20 kHz event rate, using ^{12}C at 600 MeV/u on one anode channel of the PSP.

References

[1] "A Watchdog and Radionuclide Identification Detection System for Gamma-Ray Emitters in Aquatic Environments", J.Jungmann, Masters thesis, University of Groningen / KVI, August 2008.

[2] Calibration of a Position Sensitive Photo Diode Using Digital Readout and Real Time Signal Analysis", Masters thesis P. Lubberdink, University of Groningen / KVI, October 2008.

[3] "Simplified optimal digital trigger with an interface for experimental controls", J.H. Jungmann, M. Vencelj (JSI, Ljubljana, Slovenia), H.J. Wörtche, KVI Annual Report 2008.

[4] W. Morawek, U. Gollerthan, W. Schwab, NIM **A258** (1987)82.

Developments for Isochronous Mass Spectrometry in the CR at FAIR

N. Kuzminchuk[1,2], B. Fabian[1,2], H. Geissel[1,2], R. Knöbel[1,2], C. Kozhuharov[1], S. Litvinov[1], Y. Litvinov[1], Z. Patyk[1], W. R. Plaß[1,2], C. Scheidenberger[1,2], B. Sun[1], H. Weick[1]
[1]GSI, Darmstadt, Germany; [2]II Physikalisches Institut, Justus-Liebig-Universität Gießen, Germany

At the FAIR facility, the projectile fragment separator Super-FRS will provide beams of exotic nuclei with unprecedented intensity. The new Collector Ring (CR) is optimized to accept large-emittance secondary beams provided by the Super-FRS. High-precision mass measurements of exotic nuclei with life-times as short as a few tens of microseconds will be performed with Isochronous Mass Spectrometry (IMS) at the CR.

For these measurements a dual time-of-flight (TOF) detector system is under development (Fig.1). In the detectors, ions passing a thin carbon foil release secondary electrons, which are transported in forward and backward directions to microchannel plates by electric and magnetic fields.

For even better performance of the TOF detector, a prototype was optimized for transmission and detection efficiency, rate capability [1] and timing characteristics. Timing characteristics were tested by measuring the coincidence between the backward and forward detectors with a fast sampling digital oscilloscope (40Gs/s). The measurement shows coincident time-of-flight distribution with a standard deviation of 68 ps (Fig 2). The dispersion in the time-of-flight of the secondary electrons due to their initial velocity spread and their spatial distribution after emission from the foil was investigated.

The software for the TOF data analysis was extended to determine the time-stamps of online experimental data and offline data acquired with different oscilloscopes and different time discrimination methods. The uncertainty of the time-stamp determination is limited by fluctuations, which are caused by jitter, amplitude and rise time walk effects. The precision of the timing methods was tested using the online experimental data and they agree within about 30 ps, while the resolution of the oscilloscope is 25 ps.

The influence of the MCP dead time on the rate capability of the detectors was examined experimentally and compared to a theoretical model [2]. When a large output current is drawn from an MCP, the channel walls near the exit end are charged due to the secondary electron emission.

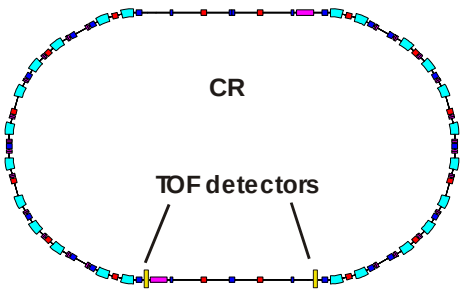

Figure 1: Layout of the CR and position of the TOF detectors for IMS.

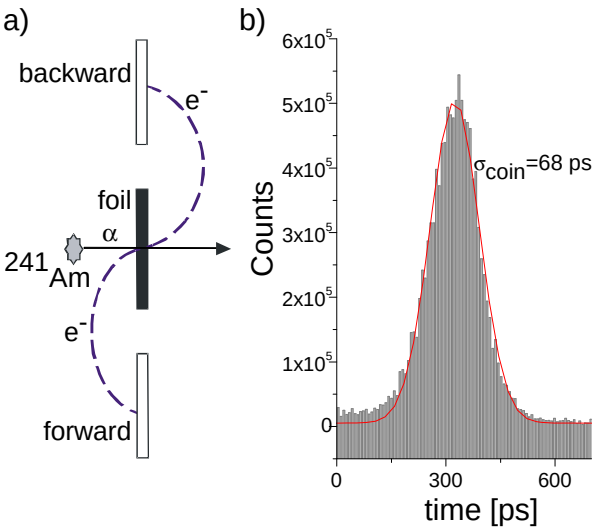

Figure 2: a) Schematic figure of the detector used for the timing measurement. b) Measured coincidence time-of-flight distribution between the forward and backward detectors.

The strip current flowing through the channel walls neutralizes this charging effect. However, the neutralization takes time because the strip current is small due to the high resistance of the channel walls. This time causes dead time effects. The measured rate at which the linearity between the number of incident electrons and the outgoing current starts to deviate is $8 \cdot 10^6$ Hz and breaks at a value of $3.5 \cdot 10^7$ Hz. Microchannel plates with the a size of 5µm instead of 10µm would increases the number of channels and hence improve the rate capability by a factor of four.

Further plans for the detector system include position-sensitive detection using a delay line detector. This would allow for an experimental investigation of the dynamics of the ion motion in the ring and potentially for a correction of time-of-flight variation caused by large beam emittance.

References

[1] B. Fabian, PhD thesis, Justus-Liebig-Universität Gießen 2008: Characterization and Optimization of a Time-of-Flight Detector for Isochronous Mass Measurement at the ESR

[2] G.W. Fraser et al., Nucl. Instrum. Methods A 306 (1991) 247.

The interaction zone of the ELISe experiment at NESR and EAR*

H. Simon[1], T. Adachi[2], G.P. Berg[3,4], M. Fujiwara[2], L.V. Chulkov[1,5], M. Couder[4], M.N. Harakeh[3], N. Kalantar-Nayestanaki[3], I.A. Koop[6], Yu.M. Shatunov[6], P.Yu. Shatunov[6], D.B.Shwartz[6], H.J. Wörtche[3], for the ELISe collaboration

[1]GSI, Darmstadt, Germany; [2]RCNP, Osaka, Japan; [3]KVI, Groningen, The Netherlands; [4]JINA, Notre Dame, U.S.A; [5]RRC "The Kurchatov Institute", Moscow, Russia; [6]BINP, Novosibirsk, Russia

The ELISe experiment at FAIR [1] will address elastic, inelastic, and quasielastic electron scattering studies off secondary beams, provided by the SuperFRS, being stored in the new experimental storage ring (NESR) and intersecting with an electron (antiproton) storage ring (EAR), for the first time. The achievable CM energy will be up to 1.5 GeV in colliding beam kinematics, and a sufficiently good resolution for nuclear structure studies puts rigid constraints on the electron spectrometer to be used : (i) a momentum resolution of $\delta p/p \approx 10^{-4}$, and (ii) an angular resolution of $\delta\Theta \approx 1$mrad, while covering the largest technologically achievable solid angle.

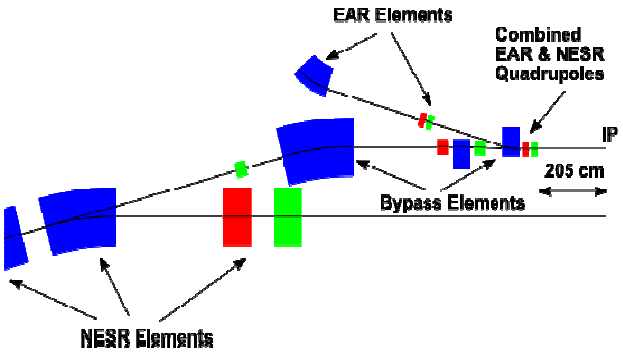

Figure 1: New lattice design near the interaction zone (IP) at the intersection of NESR and EAR with 205 cm of free space to both sides.

Furthermore, this spectrometer has, to be operated as part of the storage ring infrastructure. The currently envisaged interaction zone [2] is depicted in Figure 1 showing one half of the straight section of the NESR where the setup will be located. A so called bypass solution has been chosen in order to accommodate the different boundary conditions given by the operation of the electron ring and scattering experiment.

The physics case of ELISe requires covering a transferred momentum range of about 50 MeV/c up to about 600 MeV/c. This can be achieved by covering scattering angles from 10° to about 60° in the laboratory and by varying the electron energy from 125 MeV to 500 MeV. The best possible resolution in excitation energy (about 150 keV) in the secondary beams can only be achieved by reducing their velocity. This is possible in a range down to about 100 MeV/u, starting form the 740 MeV/u maximum beam energy and requires a flexible magnetic setup around the interaction zone in order to keep the overlap of both circulating beams.

The electron spectrometer consists of two parts (i) a pre-deflector magnet being installed close to the interaction

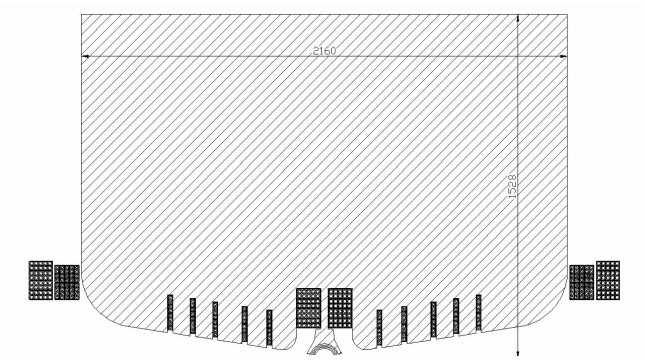

Figure 2: Design for the pre-deflector magnet (top half).

zone that will bend the scattered electrons to a maximum of about 90° and (ii) a standing spectrometer viewing the pre-deflector. A suitable design for such a pre-deflector is shown as cross section in Figure 2, and a schematic overview picture of the full setup the total system is depicted in Figure 3. The length of the pre-deflector is governed by the minimal scattering angle that needs to be covered. On the other hand one would like to keep the free space around the interaction zone as short as possible in order to achieve perfect overlap for the circulating beams. A good compromise has been achieved, keeping the pre-deflector short enough to fit into the straight section after the interaction point, as indicated in Figure 1. To keep the maximum values of beta-functions in EAR reasonably small a first pair of quadrupole magnets had to be placed in the interaction region. The design values for the interaction region of 150µm(h) × 250µm(v) × 5cm could be kept with this new ion optical setup. The combined magnetic systems for electron and heavy ion storage ring put, however, increased demands on the operation of both rings. Of utmost importance is to keep the region occupied by the circulating beams free form magnetic fields. Therefore, 2d field calculation have been performed along the beam axis. As a result, the field strength is smaller than ±0.1 mT in a circle with a radius of 40mm around the beam axis owing to the double-layered shielding shown in the centre of Figure 2. For larger horizontal distance to the beam axis the field magnitude $|B_y|$ increases quickly to its maximum average value of about 1.65 T with an effective field boundary at a distance of 11.8 cm from the axis. It is further constant in a region of about 60 cm. At maximum the field shows ripples of about ± 2% resulting from the correction coils indicated in the drawing by dark areas. At the exit, the magnet field drops off much slower compared to the entrance due to the larger iron gap. The

geometry of the correction coils are designed to minimise the ripple and calculations in a magnetic field range of 0.5 to 1.65 T. They have shown that the currents can be adjusted to minimize the ripple to less than ± 2% for the full range.

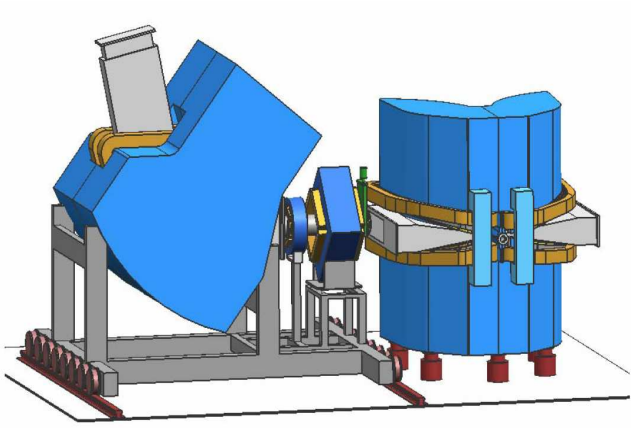

Figure 3: Overview of the complete ELISe spectrometer system [3] consisting of the pre-deflector (right) and the following QHD magnet system with a vertical bending dipole.

The design for the standing spectrometer is not yet as matured as the pre-deflectors. Figure 3 shows a 3D rendering of the recoil separator based on the design parameters. The electron beam enters the pre-deflector (right) and passes, being scattered, through the central beam pipe. The wedge shaped vacuum chambers between the dipole fields accept the scattered electrons on both sides of the beam. The electrons are bent by the dipole fields away from the beam line. After the pre-deflector the magnet system (QHD) shown on the left side consists of quadrupole (Q) hexapole (H), and vertically bending dipole (D) magnets. The centre of the focal plane is located approximately at the exit flange of the vacuum chamber of the vertical bending dipole magnet. The QHD system is mounted on a support system and can be moved along tracks at an angle relative to the beam direction. This angle is defined such, that the entrance of the quadrupole Q is at a distance of 50 cm from the points where two reference rays corresponding to scattering angles of 22.7° and 43.9° cross the exit effective field boundary of the pre-deflector. This movement is accommodated by a sliding seal at the exit of the vacuum chamber of the pre-deflector and is provided to cover the full angular range from about 10° to 60° in about six magnet settings. Since the effective field boundary at the exit is strongly curved, 'safe' distance and higher-order magnetic components change with the angle setting. These effects have to be compensated ion-optically using the indicated quadrupole and hexapole magnets.

Ion optical calculations with the ion-optical code COSY INFINITY have been performed in order to verify the achievable resolution. Since the pre-deflector is a unique design, special arrangements in the COSY setup had to be made for a realistic modelling of the fields. Especially, attention has been drawn to the fringe fields appearing at the exit of the pre-deflector.

As a result of the calculations, it could be verified that the achievable resolution assuming a moderate spatial resolution for the focal plane detectors of 100 µm exceeds, with a comfortable safety margin, the required 10^{-4} in $\delta p/p$, and the angular resolution can be achieved. A next step in our developments will address the full design for the standing spectrometer. Further calculations will have to show e.g. if a hexapole magnet can correct higher order aberrations in combination with the detector system sufficiently well for the design resolution or if a special multipole magnet has to be provided.

In summary, the technically challenging pre-deflector design for ELISes electron spectrometer has been worked out and a full schematic design for the complete system is now on the way. The design parameters are met with moderate assumptions on the associated detector systems. The interaction zone, where electron and ion storage rings intersect could be finally fixed in size, and it could be shown by lattice calculations, that the luminosity requirements are still met. Next steps include a full calculation of the dynamic apertures in both rings, and shall take into account the demands given by the necessity to detect target like recoil ions in coincidence with the scattered electrons in order to be able to tag certain exit channels in inelastic scattering processes leading to particle emission or fission. A full detection scheme for these ions is currently being worked out in detail.

Maximum rigidity Bρ	2.2 Tm
Minimum rigidity Bρ	0.3 Tm
Angular acceptance, azimuthal	±150 mrad
Angular acceptance, polar at 11.4°	±24 mrad
Angular acceptance, polar at 22.7°	±70 mrad
Energy acceptance	± 5 %
Resolving power $\delta p/p$	10^{-4}
Angular resolution	1 mrad
Kinematic compression factor	0.3 - 0.6

Table 1: Design parameters for the ELISe spectrometer. The 'kinematic compression factor' parameterises the effects of the colliding beam kinematics on the achievable resolution and is the proportionality between electron exit energy and transferred energy in the CM system.

*This work was supported by the EC via the Intas programme contract number 05-1000008-8272.

References

[1] Baseline technical report for the FAIR facility, **Vol 4** (2006) 383; http://www.gsi.de/fair/reports/btr.html

[2] I.A. Koop, Yu.M. Shatunov, P.Yu. Shatunov, D.B. Shwartz, *Further Details of EIC Project Design,* Internal Report, July 2008.

[3] G.P.A. Berg et al., Nucl. Inst. Meth. **B**, in preparation.

A Time-of-Flight-Based Isobar Separator and Mass Spectrometer for the LEB*

T. Dickel[1], W. R. Plaß[1,2], A. Becker[1], U. Czok[1], T. Fleckenstein[1], H. Geissel[1,2], C. Jesch[1], M. Petrick[1], T. Schäfer[1], A. Simon[1], C. Scheidenberger[1,2], R. Thöt[1], and M. I. Yavor[3]

[1]Justus-Liebig-Universität, Gießen, Germany; [2]GSI, Darmstadt, Germany; [3]Institute for Analytical Instrumentation of the Russian Academy of Sciences, St. Petersburg, Russia

At the Low-Energy-Branch (LEB) of the Super-FRS at FAIR, precision measurements of very short-lived nuclei will be performed. For these experiments (MATS, LASPEC), the nuclei have to be stopped, cooled, separated and measured as fast and efficiently as possible. To achieve this goal, a multi-purpose, non-scanning mass spectrometer with single-ion sensitivity, a multiple-reflection time-of-flight mass spectrometer (MR-TOF-MS), has been developed [1,2].

Applications. The MR-TOF-MS will be positioned behind the gas-filled stopping cell at the LEB, where it can be used as a broadband mass spectrometer, an isobar separator or a high-precision mass spectrometer: (i) The broadband mode will be used for optimization of the range and range-compression [3] in the Super-FRS and the stopping and extraction from the gas cell. A precise tuning of the range and the range compression is essential for experiments at MATS and LASPEC, because the range of the nuclei produced in the Super-FRS is 1000 times higher than the areal weight of the gas cell. (ii) Isobaric contamination that is produced by secondary reactions in the degraders or by charge-exchange reactions [4] in the gas cell can be orders of magnitude larger than the ions of interest. In particular for fission fragments, the abundance of contaminants transmitted through the Super-FRS can be up to two orders of magnitude higher than that of the nuclei of interest. To remove these ions, the isobar separator mode is required, in which up to 10^7 isobaric ions/s can be handled. (iii) The high-precision mode will enable mass measurements with an accuracy of 10^{-6} to 10^{-7} in about 2 ms. Thus the life-time of the ions to be measured is limited only by the extraction-time from the gas cell. The mass spectrometer is non-scanning and all isobaric ions can be measured simultaneously.

Developments. The start of the time-of-flight measurement in the MR-TOF-MS is given by the injection of ions from an RF trap. The performance of the mass spectrometer is significantly determined by the characteristics of the injected ion population. An injection trap system has been developed to provide cooled ion bunches of low emittance. It consists of three stages for fast ion cooling, while avoiding collisional losses during ion ejection. A fast-switching square wave RF source has been developed. It allows to switch off the RF during ejection in order to avoid a mass-dependens of the ion energies. The trap system has been set up and commissioned. Time-of-flight peak widths of about 5 ns (Fig. 1) have been measured, which would correspond to a mass resolving power of the MR-TOF-MS of 10^5 after a flight time of 1 ms. Cooling times of down to 1 ms and a high transmission efficiency have been achieved.

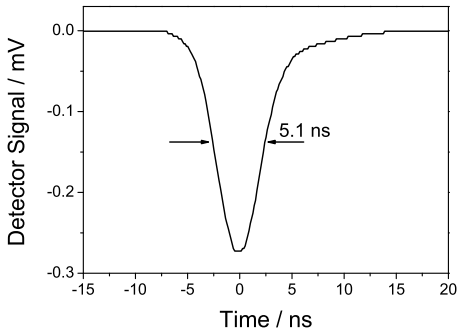

Figure 1: Time-of flight peak of ^{133}Cs-Ions ejected from the injection trap with an extraction field of 125 V/mm.

A prototyp of the MR-TOF-MS (Fig. 2) has been constructed and is being commissioned. An online test is scheduled at the MLL in Garching for March 2009.

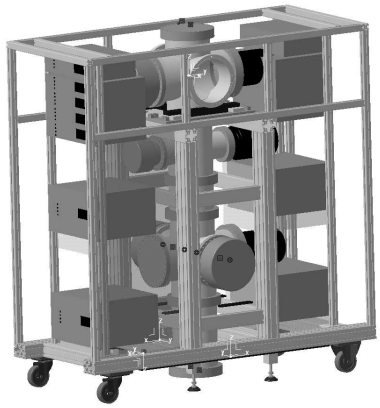

Figure 2: Schematical drawing of the MR-TOF-MS Setup.

References

[1] T. Dickel et al., GSI Scientific Report 2007, p. 211.

[2] W.R. Plaß et al., Nucl. Instrum. Methods B, 266 (2008) 4560.

[3] C. Scheidenberger et al., Nucl. Instrum. Methods B 204 (2003) 119.

[4] M. Petrick et al., Nucl. Instrum. Methods B 266 (2008) 4493.

* Work supported by the BMBF under contract 06GI185I and by GSI under contract GIMET2

TRIGA-LASER: Prototyping the *LASPEC* collinear laser spectroscopy beamline at the TRIGA reactor Mainz*

J. Krämer[1], K. Blaum[3], K. Eberhardt[1], Ch. Geppert[2], A. Krieger[1], and W. Nörtershäuser[1,2]

[1]Universität Mainz, Institut für Kernchemie, Germany; [2]GSI, Darmstadt, Germany; [3]Max-Planck-Institut für Kernphysik, Heidelberg, Germany

Collinear Laser spectroscopy of radioactive nuclei can provide fundamental information on the structure of radioactive nuclei. The dependencies of the hyperfine splitting and isotope shift on the nuclear moments and mean square nuclear charge radii are well known and the theoretical framework for the extraction of nuclear parameters is well established. At the low-energy branch of the *FAIR* facility the *LaSpec* laser spectroscopy experiment will be installed, which will allow the study of nuclei not accessible or not being produced at sufficient rates at other facilities [1].

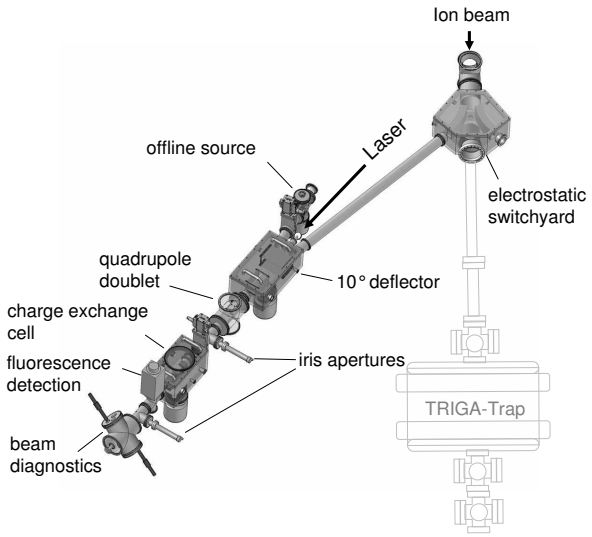

Figure 1: Drawing of the collinear beamline. All components except the switchyard and the detection unit are already installed.

We have started to set up the *TRIGA-LASER* experiment at the University Mainz. It will allow us to perform new measurements on neutron rich isotopes produced at the research reactor [2], but it will also serve as a development platform for the *LaSpec* experiment, especially with respect to detection methods. Also the performance of high precision voltage supplies for acceleration and the online measurement of these voltages with a high precision voltage divider [3] to the 10 ppm level will be tested. Accurate knowledge of the acceleration voltage is critical for high precision measurements of isotope shifts.

*Work supported by HGF under contract VH-NG-148 and 'Stiftung Rheinland-Pfalz für Innovation' under contract 854.

The vacuum system of the laser beamline was assembled after machining of the electrostatic deflection chamber and the chamber for the charge exchange cell according to our custom design. A vacuum pressure of 2×10^{-7} mbar could be reached without baking. In Fig. 1 a drawing of the complete laser beamline is shown. For commissioning purposes, an offline surface ion source based on an electro-thermally heated graphite oven was constructed. The source is operated in a HV cage and can be set to voltages up to 10 kV. For fast loading of the ionizer tube, the source chamber is separated from the laser vacuum system with a valve and can be pumped with a separate turbo pump. First tests showed 70 % ion beam transmission with 3.5 nA current on the Faraday cup after the non-operating charge exchange cell. For beam profile monitoring a fork scanner system 5100 from Danfysik was installed to get a good control of the ion beam diameter, which is essential for a good overlap between the laser and ion beam. In Fig. 2 a plot of the beam profile at the end of the ion beamline in both, horizontal and vertical plane is shown.

First laser spectroscopy test measurements will be performed with Rb atoms after charge exchange. The transition at 780 nm wavelength can be excited with a diode laser which will be frequency locked to a HighFinesse WS7 wavemeter. This allows to install a compact laser system next to the beamline.

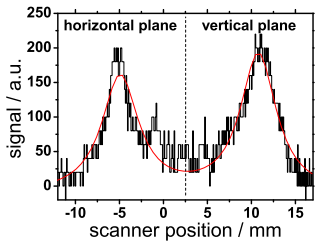

Figure 2: Beam profile of a 300 pA Li^+ beam at 2 keV energy in horizontal and vertical plane. The corresponding beam diameter was estimated to be 5 mm.

References

[1] W. Nörtershäuser, P. Campbell, and the LaSpec collaboration, Hyp. Int. **171** (2006) 149.

[2] J. Ketelaer, J. Krämer, et al., Nucl. Instrum. Methods Phys. Res., Sect. **A 594** (2008) 162-177.

[3] T. Thuemmler, Dissertation, Münster (2007)

Design studies for the PANDA electromagnetic calorimeter

J. Zhong, B. Kopf, M. Pelizäus, M. Steinke, and U. Wiedner
Institut für Experimentalphysik I, Ruhr-Universität Bochum

For detection of neutral particles and for electron identification in the target spectrometer region, PANDA will use an electromagnetic calorimeter consisting of about 16000 lead tungstate crystals. In combination with the shashlyk type calorimeter in the forward spectrometer, which is optimized to detect high energy photons at small polar angles, PANDA can cover nearly the full solid angle, which is important for the exclusive reconstruction of channels with many photons in the final state.

Due to the short radiation length and small Moliere radius of lead tungstate, good spatial resolution can be achieved with a compact detector design. Especially for the forward endcap, good spatial resolution is needed for reconstruction of high energetic π^0 with good mass resolution. Figure 1 shows the expected π^0 mass resolution as a function of the π^0 momentum for several opening angle resolutions σ_α. α is defined as the angle between the photons from π^0 decay. From Monte Carlo simulation studies $\sigma_\alpha = 0.1^\circ$ can be achieved for 5 GeV π^0 reconstructed with the forward endcap, which results in a π^0 mass resolution of about 4 MeV.

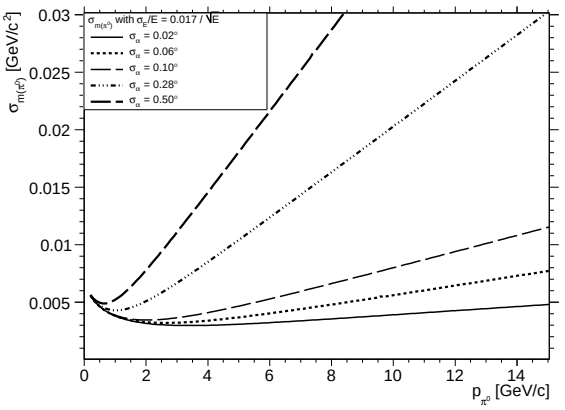

Figure 1: π^0 mass resolution for various opening angle resolution values vs. π^0 momentum. For the EMC forward endcap $\sigma_\alpha = 0.1^\circ$ could be achieved in simulation studies.

For antiproton beam momenta up to 15 GeV/c, the calorimeter has to cover an energy range from 10 MeV and 15 GeV. As one can see from Figure 2, the largest photon energies can be found in forward direction, while photons with polar angles larger than 90° have energies below 1 GeV.

Essential for the feasibility of the PANDA physics program is the background rejection capability of the detector. The main background of the process $\bar{p}p \to \eta_c \to \gamma\gamma$ for example is caused by the process $\bar{p}p \to \pi^0\gamma$ with one low energy photon undetected. As shown in Figure 3, about 1%

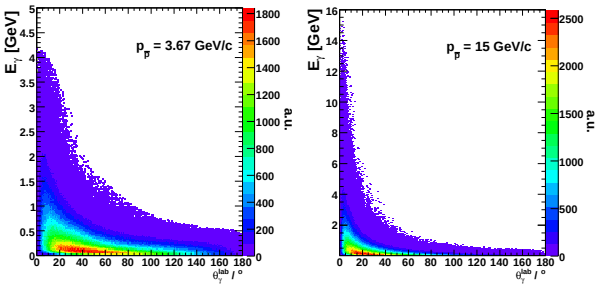

Figure 2: Energy vs. polar angle distribution of photons from $\bar{p}p$ collisions, using the Dual Parton Model based event generator (DPM)

of all 1 GeV π^0 decay into 2 photons with one photon below 10 MeV. Therefore a low photon energy threshold is needed in order to achieve a good separation between isolated photons and π^0. Of course a low material budget in front of the calorimeter is required in order to avoid losses of low energy photons due to γ conversion.

Detailed information about hardware specifications, prototype tests and simulation results are reported in the Technical Design Report for the PANDA Electromagnetic Calorimeter [1].

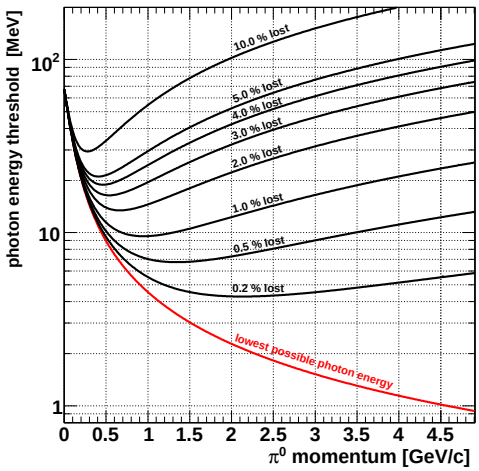

Figure 3: Percentage of π^0 loss as a function of photon energy threshold.

References

[1] Technical Design Report for PANDA Electromagnetic Calorimeter, arXiv:0810.1216v1

Opacity measurements in warm dense matter produced with heavy ion beams

An. Tauschwitz [1], V.G. Novikov[2], A. Tauschwitz[3], F.B. Rosmej[4,5], J. Abdallah[6], E. Onkels[3], J. Jacoby[1], J. Wiechula[1], and J.A. Maruhn[1]

[1]University of Frankfurt am Main, Germany; [2]Keldysh Institute of Applied Mathematics, Moscow, Russia; [3]GSI, Darmstadt, Germany; [4]Université Pierre et Marie Curie, Paris, France; [5]Centre de Recherche LULI, Ecole Polytechnique, PAPD, Palaiseau, France; [6]Los Alamos National Laboratory, USA

Opacity measurements of warm dense matter (WDM) will provide a valuable benchmark for the diverging theoretical models and clarify the influence of non-ideality on the absorption coefficients in this regime. Intense charged particle beams provide a useful tool for creating isolated samples of warm dense matter. In this work we propose measurements of frequency-dependent opacities in WDM created by an ion beam [1]. The target parameters for opacity measurements in ion beam produced WDM are chosen assuming an energy deposition of 10 kJ/g in high-Z materials within a 100 ns pulse, which can be realized using bunches of 10^{10} uranium ions at SIS-18. For the first experiments lead will be chosen as the target material for the opacity measurements because the highest temperatures are obtained by ion beam irradiation in high-Z materials. For a sub-μm foil target the plasma after the ion beam heating will have a density of about $\rho \approx 0.01$ g/cm^3 and a temperature of $T \approx 2$ eV.

Figure 1 shows the calculated transmission for the Pb plasma of 0.02 cm thickness with the above parameters. The calculations were made using two completely different models the Saha model with continuum lowering [2] using atomic data obtained by the code FAC [3] and the quasizone model (QZM) [4], which includes electron-ion interaction in the mean spherical cell approximation. The quasizone model uses an average atom approximation, and its accuracy may be insufficient at the considered low temperatures. The Saha approximation does not include interaction between particles in the plasma and works for dilute plasmas only. The Saha approximation of ideal plasma at such conditions is problematic and models which include the effects of ion-electron interactions give results very different from the ideal-plasma approach and between each other. Measurements can clarify the question how the strong interaction affects the plasma properties.

Hydrodynamic calculations were performed to predict the spatial distribution of the plasma parameters after ion beam heating. The foil thickness was optimized according to the calculated radiation transmission. The calculated temperature and density profiles along the ion beam axis in the initially 0.3 μm thick foil are presented in Fig. 2. The time t = 105 ns was chosen to ensure thermodynamic equilibration of the plasma after ion beam heating. According to the simulation the temperature in the heated target of about $T = 1.9$ eV is nearly constant, which is prerequisite for the interpretation of the measured plasma transmission. The density profile is gaussian and has to be taken into account in the analysis of experimental transmission data.

The calculations show that the plasma conditions achievable in ion beam heated foils are well suited for opacity measurements. At the FAIR facility opacity measurements will be an essential part in the work of the WDM collaboration. At FAIR plasmas of higher temperatures and densities can be created without the present limitation to high-Z materials. The high-power laser will enable backlighter sources with a wide range of temperatures.

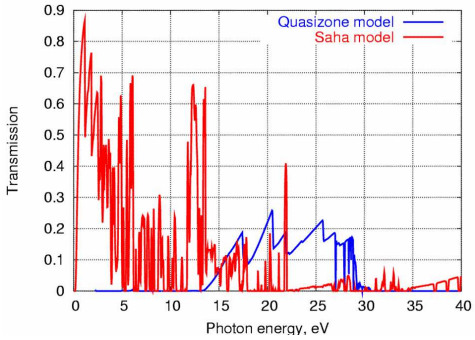

Figure 1: Transmission of a Pb plasma slab with 0.01 g/cm^3 density and 2 eV temperature calculated with two different models; the plasma layer has a thickness of 0.02 cm.

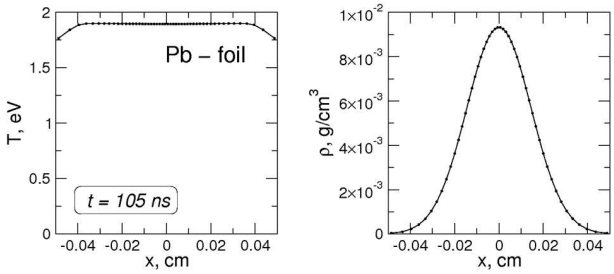

Figure 2: Density and temperature distribution in an ion–beam heated lead foil at t = 105 ns; x is the beam axis.

References

[1] A. Tauschwitz et al., Appl. Phys. B, in print (2009).

[2] D. Salzmann, *Atomic physics in hot plasmas* (New York Oxford, Oxford University Press, 1998)

[3] M.F. Gu, Flexible Atomic Code. Available at http://kipac-tree.stanford.edu/fac/

[4] A.F. Nikiforov, V.G. Novikov, V.B. Uvarov, *Quantum-statistical models of hot dense matter: methods for computation opacity and equation of state* (Birkhauser Verlag, 2005)

The FLAIR Facility

A. Bräuning-Demian[1], W. Quint[1], J. Walz[2], and E. Widmann[3]
[1]GSI, Darmstadt, Germany; [2]Johannes-Gutenberg Universität, Mainz, Germany; [3] Stefan Meyer Institut, Wien, Austria;
for the FLAIR collaboration

The scientific program proposed by the FLAIR and SPARC collaborations is based on the availability of low and ultra-low energy beams of antiprotons, highly charged heavy ions and exotic nuclei at FAIR, and imposes special requirements on the beam energy, intensity, emittance and time structure, beyond the standard range of the FAIR accelerators [1].

The beam preparation scheme at FLAIR presently involves three decelerators (see Fig. 1): one magnetic synchrotron, the LSR, the electrostatic synchrotron USR (up to now a unique design regarding the parameters and functionality [2]), the linac-based HITRAP decelerator currently being commissioned at GSI [3] and diverse schemes of particle stopping and cooling in different traps. Together with more than 10 different planned experimental areas, the facility will be a combination of machines and experiments, requiring an elaborate beam transport system which permits a certain degree of parallel operation for the experiments.

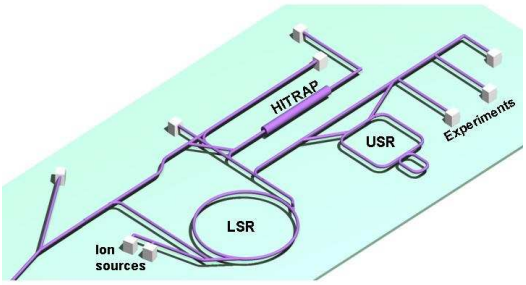

Figure 1: The FLAIR facility layout.

Considering the wide energy range of the FLAIR beams, which stretches over eight orders of magnitude, the beam transport system is divided into three distinct parts: the high energy part for ion beams above 4 MeV/u and antiprotons with energy above 30 MeV, based on magnetic elements, and the two electrostatic, low-energy parts for antiprotons with energies below 300 keV via USR and for the highly-charged ions and antiprotons extracted from HITRAP.

The facility design, including the beam transport and distribution, described in [4], has recently been refined in connection with the civil construction planning. New ion optical simulations followed by mechanical design of the whole magnetic part of the beam line have been performed. In parallel, the development of a concept for the vacuum system for the beam transport system started. More work is needed for its optimization and the integration into the existing ion-optical layout. Also a detailed design of the magnets and beam diagnostics is under way.

Considerable progress was made in the design, prototyping and construction of some experimental setups. For the experiments with low-energy highly charged ions substantial progress in the construction and commissioning of HITRAP was achieved. The deceleration of heavy-ion beams from the ESR storage ring to an energy of 500 keV/u with the IH structure has been demonstrated and studied in detail. The commissioning of the RFQ structure and the cooler trap is ongoing. The HITRAP facility at FLAIR/SPARC can be equally well used for highly charged ions and antiprotons to bring them down to sub-thermal energies as all components have been carefully designed to be operable in an A/q range below 3.

Another important installation will be the magnetic charge analyzer for highly charged ions, with energies higher than 3 MeV/u. Ion optical simulations followed by and mechanical design studies (see Fig. 2) have been performed.

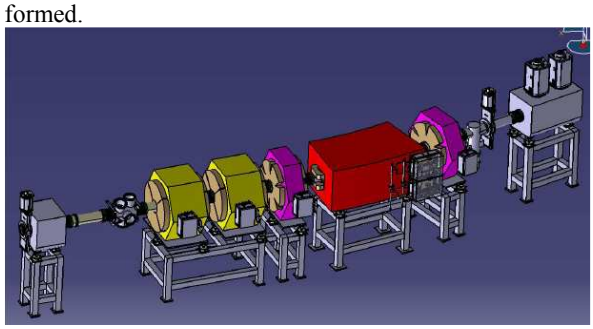
Figure 2: Design of the magnetic spectrometer for highly charged ions at FLAIR.

Experiments with antihydrogen at FLAIR aim at testing the symmetry between matter and antimatter (CPT symmetry) at unprecedented levels of experimental precision, and to measure the gravitational acceleration of antimatter and thus, to test Einstein's Principle of Equivalence in the antimatter domain. For both types of experiment it is essential to cool the antihydrogen as much as possible. Laser-cooling of antihydrogen can be done at 122 nm wavelength (Lyman-alpha). For this, the first production of continuous-wave coherent radiation at Lyman-alpha with solid-state lasers has recently been achieved at Univ. Mainz [5].

References

[1] E. Widmann, *Plans for a next-generation low-energy antiproton facility,* Phys. Scr. A **72**, C51–C56 (2005).
[2] C.P. Welsch, et al., *An ultra-low-energy storage ring at FLAIR*, NIM A 546, 405–417 (2005).
[3] HITRAP, see the contribution in this Annual Report.
[4] A. Bräuning-Demian et al., GSI Report 2008-1, p.45.
[5] M. Scheid et al., *Continuous-Wave Lyman-alpha Generation using Solid-State Laser,* submitted for publication.

FAIR Accelerator and Civil Construction Status Report *

Simone Richter# for the FAIR Technical Division
GSI, Darmstadt, Germany

Status of FAIR Accelerators

After the Start Event for FAIR on November 11th, 2007 the detailing work on the FAIR accelerators was carried on. This led to the finalization of the Technical Design Reports (TDR) for the accelerators of the Start Version [1] in December this year. The International Steering Committee for FAIR approved the formation of a new Machine Advisory Committee (MAC) led by the world renowned expert Lyn Evans (CERN). The 12 new MAC members were carefully chosen to be experts on their respective fields but are not directly involved in FAIR accelerators. It is planned that the TDR for SIS100 will be the first to be reviewed in early 2009.

As the following contributions will cover important developments, this status report will focus on the cross sectional aspects of GSIs superordinated managerial work for the FAIR accelerators and civil construction.

Without loss of generality it should be noticed that the system design for the High Energy Storage Ring HESR is provide by the Forschungszentrum Jülich and the HESR consortia.

Specifications

To cope with the complexity of more than 800 specifications for the FAIR accelerators a structured approach has been chosen. The governing contract – in case of an in-kind contribution a trilateral contract between FAIR GmbH, the funding agency and the delivering institute or in the case of a procured component the contract of purchase – governs the specifications as shown in Figure 1.

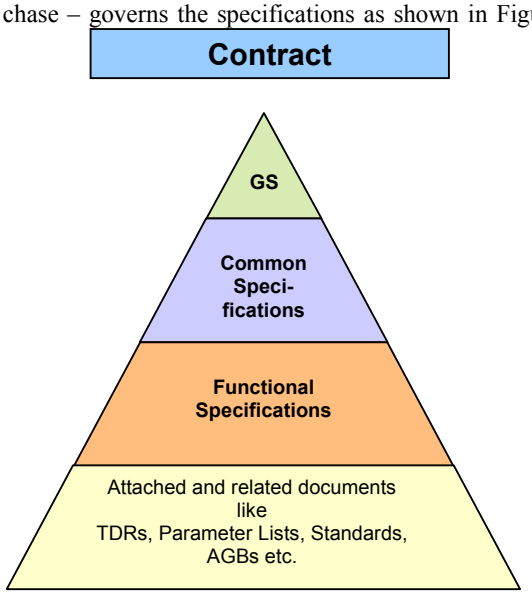

Figure 1: Structure of the FAIR accelerator specifications.

The *General Specifications* (GS) describe the general conditions to supply a component to FAIR which are identical for all equipment. The *Common/Specifications* (Cs) concentrate all specifications universal to a family of equipment such as superconducting magnets, vacuum chambers, rf components, etc. The Functional Specification describes the component itself. The specifications are accompanied by additional information giving the full picture of the facility.

To assure that all specifications and relevant data is accessible for all partners, the management decided on the use of a document and workflow manangement.

EDMS

The FAIR project has successfully introduced the CERN engineering Data Management System (EDMS) for the storage, retrieval, and workflow management of the organisational and technical project documentation [2].

The FAIR EDMS project is mainly structured in the project relevant part with clearly defined release and approval procedures and a storage area, aimed and oriented more as a "working area" for the various technical groups. Thus the FAIR EDMS supports the FAIR project in a very efficient and effective way ensuring that always the latest agreed and approved versions of any relevant project documentation is available for project stakeholders as well as technical groups. Furthermore, the system supports both the technical groups and FAIR partners in exchanging and accessing the technical and administrative information and documentation.

With the status end of January 2009, nearly one hundred accounts have been enabled and more than fifty users have been trained. Since October 2008, more than sixty documents, containing in total more that 100 document files, have been stored. One of the documents showing the possibilities and functionalities of the document management system is the "Hüllkontur" of the planned accelerator complex (see Figure 2 and next subsection). The definition and construction of this document has clearly shown that all the planned and envisaged advantages of a document management system in legal aspects (storing and recording relevant documents), administrative aspects (collecting and combining various technical input information) and usage aspects (storing, exchanging and retrieving documents and information "in work"). The workflow and document management system already proved to reduce the workload of all impacted groups and partners.

Competence Center DMU

To ensure that the compliance of all mechanical engineering data of accelerator, beam transport lines and experimental set-ups with the civil construction a full 3D

* Work supported by EU and BMBF
#s.richter@gsi.de

representation of the facility is aimed for. To support this challenging task the *Competence Center Digital Mock-Up* CC DMU was build up. This competence center is formed as a project team bringing together experts from the mechanical engineering, civil construction, accelerator physics and experiments.

The rules for data exchange are drafted and will also be an integral part of the specifications. It is defined that all construction and engineering data should be represented by 3D models preferably in Catia V5 [3], as neutral format STEP, and 3D pdf as printable version.

Before the mock-up and clash detection procedures can take place, package volumes for the components will be defined. These volumes together with the master coordinate will then be transferred to the FAIR partners. The process for the data exchange is shown in Figure 3.

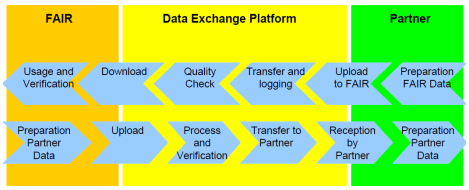

Figure 3: Process visualisation for the Data Exchange.

Civil Construction Progress

In summer 2008 the contracts to the architects and civil engineering companies have been awarded. Since then 15 planning offices work on the detailing of the civil construction for FAIR. The BUNG study proved on a feasibility level that civil construction can accommodate the FAIR accelerators and the experiments. The work carried out now is targeted to the approval planning and a secure cost estimate. In addition to the requirements given by the so called *Z-Bau-Verfahren* the approval for the operation authorization. Thus extensive dose calculations for operational modes and shutdown periods are carried out in close collaboration with the radiation protection group at GSI. As an example for those FLUKA calculations is shown in Figure 4.

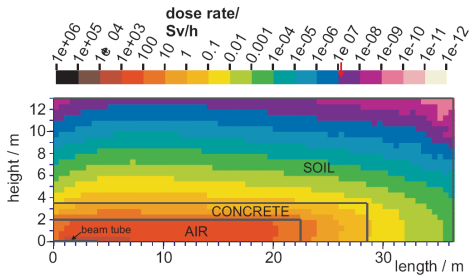

Figure 4: FLUKA calculations for the dose calculation.

Based on the ion-optical layout and the data compiled by the so called *Gebäudeansprechpartner* (GAP) lead to the architect's impression for the FAIR buildings as show in Figure 5.

Figure 5: Bird's eye view for FAIR as seen by the Architects consortium ion4

Conclusion

Next to the system design work on the accelerators many tools have been developed or set up to support the managerial aspects of the FAIR project during 2008. Within 2009 the service work for FAIR will be focused on the establishment of mere administrative tasks such as the set-up of a SQL-based, web-accessible project server that will also be coupled to the financial systems for the project.

References

[1] Technical Design Reports, to be published
[2] https://edms.cern.ch/nav/FAIR-000000002
[3] http://www.3ds.com/products/catia/catia-discovery/

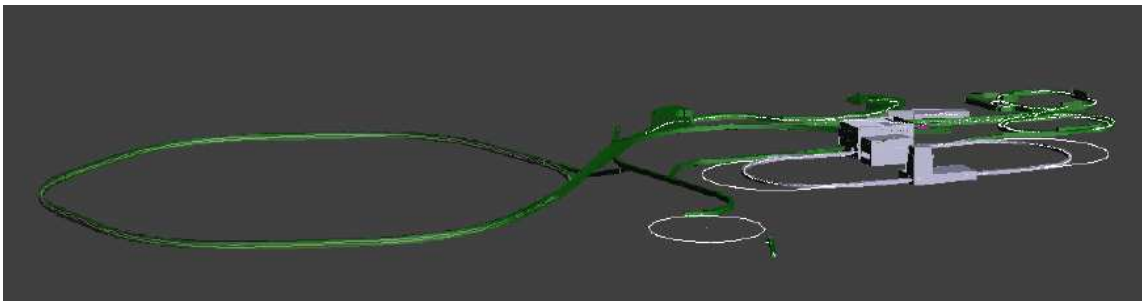

Figure 2: The "Hüllkontur": Based on the ion-optical layout for the FAIR accelerators and beam transport lines, the accelerator and detector envelopes and transport volumes are modelled in 3D. To check with civil construction data these volumes can be displayed within the same file.

STATUS OF THE FAIR SYNCHROTRONS SIS100 AND SIS300

P. J. Spiller, U. Blell, O. Boine-Frankenheim, P. Fabbricatore ([1]), E. Fischer, E. Floch, G. Franchetti, F. Hagenbuck, M. Kirk, A.D. Kovalenko ([2]), A. Krämer, D. Krämer, H. Klingbeil, G. Moritz, C. Mühle, J. P. Meier, H. Müller, N. Pyka, S. Ratschow, H. Ramakers, H. Welker, C. Omet, A. Saa-Hernandez, M. Schwickert, J. Stadlmann

GSI, Darmstadt, Germany, ([1]) INFN, Genua, Italy, ([2]) JINR, Dubna, Russia

System Design and Ionization Beam Loss

The world wide unique operation with high intensity, intermediate charge state heavy ions (e.g. U^{28+}) is one of the most demanding features of the FAIR project [1]. Due to the high cross sections for ionisation in combination with ion induced gas desorption, significant beam loss may result from pressure bumps during the acceleration cycle. As described in [2], the SIS100 lattice has been optimised for the control of ionisation beam loss with the goal to restrict the dynamics of the residual gas pressure. For the simulation of vacuum dynamics and beam loss due to charge changing processes, the program STRAHLSIM has been developed [3]. In 2008, the beam scrubbing effect and the dependence of the pumping speed of NEG-coated and cryogenic surfaces as a function of the number of mono-layers of adsorbed gases have been accounted. Thereby, long term simulations and predictions on the ionization beam loss, the number of extracted ions, the pumping power, the number of monolayer and the mean residual gas pressure have been enabled.

Meanwhile, the STRAHLSIM code comprises the following features:

- Linear beam optics with several in- und export filters
- Static vacuum simulations
- Dynamic vacuum simulations
- Beam loss due to charge changing processes

The linear beam optics module enables the calculation of the beam loss pattern due to charge change and the collimation efficiency for a given synchrotron lattice. The static and dynamic vacuum simulations are based on:

- Static pressure and static residual gas components;
- Vacuum conductance;
- Properties and pumping power of conventional pumps;
- An analytic description of the pumping power of cryogenic and NEG surfaces as a function of the pressure and temperature including saturation
- Cross sections for ionisation for different ionization degrees as a function of energy
- Desorption yield scaled with the square of the specific energy loss
- Beam scrubbing
- Coulomb scattering
- Target ionization
- Intra beam scattering
- Beam loss in a realistic accelerator cycle.

The simulations on the dynamic vacuum and the correlated ionization beam loss in SIS100 confirmed the assumption that for stable operation conditions, a strong distributed pumping system is required. The pumping power needed to achieve an acceptable low amount of ionization loss, is provided by the cryogenic surfaces. Because of the highest cross sections for ionization, the SIS100 scraper system has been optimized for the most heavy ions. Light ions and ions with intermediate mass and heavy ions after multiple ionization miss the catchers to a certain fraction. Since the cross section for lighter ions is significantly lower, the generated pressure bumps do not create a major beam loss increase, but contributes to the grow-up of adsorbed monolayers. In contrary to NEG coated surfaces, the stack of monolayers of adsorbed molecules can be removed from cryogenic surfaces as often as required e.g. in short shut down periods once a year.

Main Magnets

Based on the results achieved in the R&D project phase, manufacturing of a number of SIS100 full length model magnets has been performed [4,5].

- Straight, full length dipole magnets have been manufactured at BNG (Würzburg) (Figure 1) and at JINR (Dubna) (Figure 2);
- A curved dipole magnet has been produced at BINP in Novosibirsk (Figure 3);
- A prototype quadrupole magnet has been produced at JINR (Dubna) (Figure 4) [6].

The production of both full length magnets at JINR is supported by the EU FP6 DIRAC program.

The large hydraulic resistance of the two layer coils built for all prototype dipoles does not provide the cooling power for operation with pure triangular cycles. Triangular cycles are considered as fall-back option in case problems connected with high beam losses occur on the long injection flat-top of the reference cycles. The Nuklotron-type coils are made of a s.c. cable consisting of a too long He-pipe with a too small cross section. Therefore, the next prototype magnet, which is the first pre-series magnet will be equipped with a single layer coil with slightly increased cross section and a new high current cable (13 kA instead of 7 kA).

* Work supported by EU and BMBF

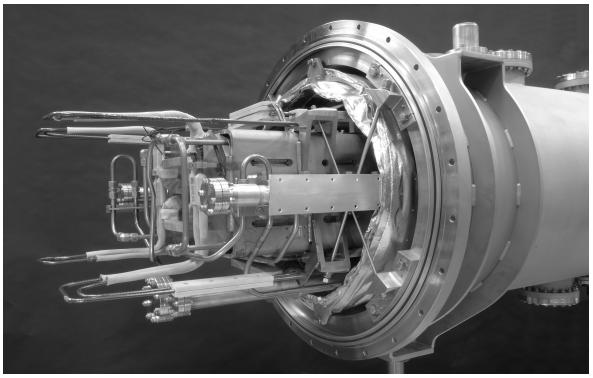

Figure 1: Full length, straight SIS100 model dipole built by BNN, Würzburg, Germany.

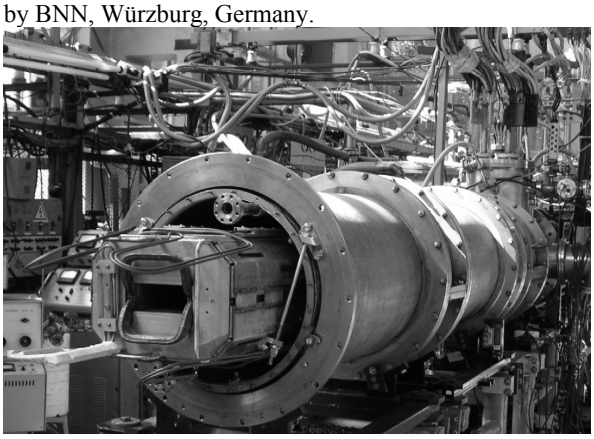

Figure 2: Full length, straight SIS100 model dipole at cold test built by JINR, Dubna

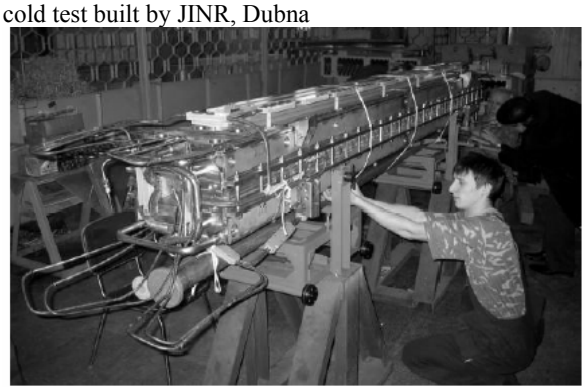

Figure 3: Curved, SIS100 full length dipole model after assembly at BINP

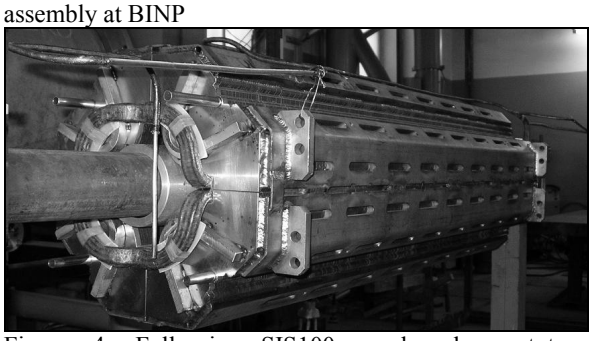

Figure 4: Full size SIS100 quadrupole prototype manufactured at JINR, Dubna

For SIS300, the design and R&D of a fast ramped curved (ρ=66 2/3 m) 4.5 T dipole magnet has been continued at INFN, Italy [7]. This model development is focused on solving the mechanical problems with the production of a curved coil made of a stiff, low loss cable with stainless steel core and its integration into the collar and yoke. Figure 5 shows the results of a winding test of a curved coil with a standard Rutherford cable. In parallel, the production of a straight, two layer s.c. 6 T dipole magnet has been completed at IHEP, Protvino. The manufacturing of the 1 m long, two layer coil magnet and the cold testing has been finished in January 2009. Both magnets are optimised for low AC loss and make use of a cable with the bare cable geometry of the LHC dipole outer layer conductor, but with a stainless steel core inside.

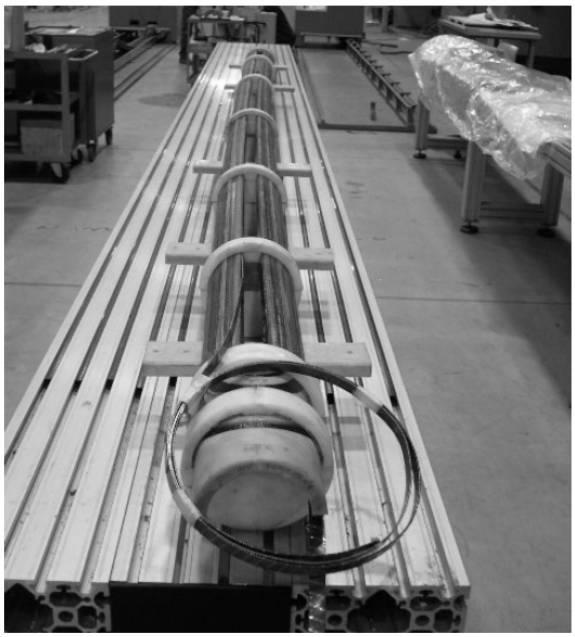

Figure 5: Winding tests of a curved coil for the short SIS300 dipole magnet.

REFERENCES

[1] FAIR Baseline Technical Report (FBTR), GSI, (2006)
[2] P. Spiller et al., "Optimization of the SIS100 lattice and a dedicated collimation system for ionization beam losses" (2004), 33rd ICFA Workshop, AIP Conference Proceedings, Volume 773, pp. 40-44 (2005).
[3] C. Omet et al, New Journal of Physics 8, 284 (2006)
[4] E. Fischer et al, IEEE transactions on applied supercond., Vol. 17. No2, 1078(2007)
[5] E. Fischer et al, this scientific report
[6] A. D. Kovalenko et al, "Full size prototype magnets for heavy ion s.c. synchrotron SIS100 at GSI: Status of manufacturing and test at JINR", Proc. of EPAC08
[7] F. Alessandria et al, "Technical design report of a superconducting model dipole for FAIR SIS300", INFN/code 08/0011, (2008)

Development of FAIR superconducting magnets and cryogenic system*

D. Acker, A. Bleile, E. Fischer, E. Floch, O. Gumenyuk, G. Hess, M. Kauschke, F. Klos, Th. Knapp, H. Leibrock, J. Macavei, F. Marzouki, A. Mierau, J.P. Meier, G. Moritz, C. Muehle#, H. Mueller, P. Schnizer, C. Schroeder, S.Y. Shim, A. Stafiniak, K. Sugita, F. Walter, B. Weckenmann, M. Weipert, Y. Xiang
GSI, Darmstadt, Germany

Introduction

R&D continued during 2008 for FAIR superconducting magnets, for the main dipoles, quadrupoles, the correctors, and the corresponding cryogenic distribution / cryostat system as well. Based on the R&D results of the last years several prototype and full size models were constructed in 2008. R&D was conducted by GSI employees, in collaborations, or by contracts, funded by GSI or the European Union (EU FP6 Design study).

Superconducting Magnets

Rapidly-Cycling Magnets for SIS 100

A good overview of the status of the R&D is given in [1].

Three full length dipole prototype magnets, including cryostats, were manufactured by BNG (Würzburg), JINR (Dubna) - both straight - and by BINP (Novosibirsk) - curved. The experimental investigations on the dipole manufactured by BNG have been started at the GSI cryogenic facility. Already the first power tests have shown an excellent quench training behaviour and gave a good confirmation of AC losses, estimated based on short model results [2] and obtained with help of detailed ANSYS calculations [3,4].

At FZ Karlsruhe mechanical tests on the coil structure were continued using samples from a superconducting coil already powered at low temperatures.

The actual manufactured full size dipoles operate at their physical limit to provide the most intensive triangular cycle. The adopted design of a dipole based on a single layer coil was completed. It can provide the requested triangular cycles as well as a safety cooling margin for additional, not yet identified heat loads.

A first full size quadrupole was manufactured at JINR. The option of a superconducting coil based on the Nuclotron-type cable with insulated strands was adopted for the corrector magnets [5]. According to the results of the electromagnetic computation, the mechanical design is to be finalized. A mock-up of the error compensation multipole corrector as most complex magnet, which has three nested coils to induce quadrupole, sextupole and octupole magnetic field, was built in order to prove the feasability.

* Work supported by EU, DIRAC contract No. 506065, BMBF, and HMWK.
# C.Muehle@GSI.DE

Rapidly-Cycling Magnets for SIS 300

The 6 T dipole at IHEP (Protvino) was built and was successfully tested in liquid helium in December. Besides this, IHEP expressed its interest in building the SIS 300 main quadrupoles and corrector magnets. A design of the quadrupole was finished, an open question is still the use of a cable with core.

The R&D for the curved 4.5 T dipole at the Italian National Institute of Nuclear Physics INFN (DISCORAP-project) has well advanced in the last year. The design work is nearly finished now and a technical design review was held in November with external experts. Two curved test coils have successfully been built at ASG. Details on the progress of the project can be found in the presentation of P. Fabbricatore [6].

Magnets for the Super-FRS

The FAIR China Group, consisting of three collaboration partners Institute of Modern Physics (IMP, Lanzhou), CAS; Institute of Plasma Physics (IPP, Hefei), CAS, and Institute of Electric Engineering (IEE, Beijing), CAS, developed in cooperation with GSI a superconducting dipole magnet for the Super-FRS. IPP tested successfully the superconducting coils within the prototype of the cryostat. Also the iron yoke has been finished and successfully checked at IMP.

A collaboration between CEA (France) and CIEMAT (Spain) is planned to deliver the Super-FRS Multiplets as in-kind contribution [7]. Several meetings of the partners took place to discuss different design studies.

Quench and Electrical Systems

A complete and detailed quench study was carried out on a short SIS 100 dipole model [8]. Experimental results fit very well with quench simulations. In [9] the corresponding quench tests and computations are presented. Radiation sensitive magnet parts (such as insulated cables, wires, etc.) and insulators (polyimide, fibre glass, etc.) were irradiated at GSI with a U beam in conditions close to machine operation [10]. The basic design of superconducting electrical connections for the SIS 100 was defined and presented in [11].

Test Facility for Model and Prototype Magnets

The test bench dedicated for cryostated magnet was launched [12] with the test of the above mentioned 1st full size SIS 100 prototype by BNG.

Cryogenics

The cryogenic system for FAIR is optimized in respect to number of consumers and their request of cooling power and helium quality. The cooperation with the planners of the new building topology was started. The requirements for the cryogenic infrastructure were revised, adapted to the new topology and transferred to the planners. The introduction of this new building topology made a rearrangement of some of the components (i.e. distribution boxes) necessary. The liquefier for the central helium supply for small experiments is now placed in the south part of FAIR. Therefore the way of delivery will be shorter. The liquefier is planned to be installed at the same place than the refrigerator that supplies mainly the Super-FRS. Therefore the same service personal can operate the systems.

Additionally for the local cryogenic system of the Super-FRS the first feed box design is finalized and the magnet groups are now combined in that respect that the resulting scheme will be reliable operated and the demands for the experiments can be fulfilled. These feed box informations are implemented to the design of the Super-FRS tunnel building.

Cryostats

SIS 100 Cryostats

Two full length model dipole cryostats were delivered. The first one designed and built by BNG, the second one designed and built by BINP. The major differences in design are their concepts of flange mounted- and dome mounted cold mass suspensions. A successful site acceptance test was carried out for the BNG cryostat. The BNG cryostat was taken into operation at GSI's magnet test facility. Within the first cold run, a measurement of structural stability of the BNG model cryostat was performed. A test setup for position stability of cold masses in the cryostats was developed. The planning of the conceptual design for missing dipole cryostats and the layout of cryogenic inter-connections was started by Cracow University of Technology (CUT) [13]. The development includes beam vacuum-, helium flow- and thermal shield inter-connections. The development for the bus bar splices of SIS 100 was started as well as the conceptual layout of the quadrupole doublet magnet suspension. An installation space study for the bypass line was performed and the results taken as input for the 3D-CAD-model of the synchrotron ring assembly.

SIS 300 Cryostats

The cryogenic and beam line interconnection and compensation concept was finalised by CUT [13]. The development of the beam line cold warm transition was continued in combination with the relevant development for SIS 100. INFN continued the design for the short curved dipole cryostat [14]. It was decided to take over the concept for the cold mass support from the LHC development. The preliminary design review was completed in November 2008.

References

[1] E. Fischer et. al., "Manufacturing of the first full size model of a SIS100 dipole magnet", WAMSDO at CERN, June 2008.

[2] E. Fischer, H. Khodzhibagiyan, and A. Kovalenko, "Full size model magnets for the FAIR SIS100 synchrotron", The 20th international conference on magnet technology, ser. IEEE Trans. Appl. Supercon.,vol. 18, no. 2. IEEE, June 2008, pp. 260-263.

[3] E. Fischer H. Khodzhibagiyan, A. Kovalenko, and P. Schnizer, "Fast ramped superferric prototypes and conclusions for the final design of the SIS 100 main magnets", Proceedings of ASC08, Chicago, Illinois, USA, August 2008.

[4] E. Fischer P. Schnizer, R. Kurnyshov, B. Schnizer, and P. Shcherbakov, "Numerical analysis of the operation parameters of fast cycling superconducing magnets", Proceedings of ASC08, Chicago, Illinois, USA, August 2008.

[5] K. Sugita et. al., "Design Study of the Multipole Corrector Magnet for SIS 100", Proceedings of ASC08, Chicago, Illinois, USA, August 2008.

[6] P. Fabbricatore et al., "R&D activity in 2008 at INFN for fast cacled magnets with curved shape for FAIR", this annual report.

[7] Minutes of the "Super-FRS: Multiplet Design Meeting", https://indico.gsi.de/conferenceDiplay.py?confId=374

[8] E. Floch et.al., "Quench Measurement on SIS100 Dipole Model", In Proceedings of ASC08, Chicago, Illinois, USA, August 2008.

[9] E. Floch, GSI F-MT internal note MT-INT-ErF-2008-008, GSI, Darmstadt, Germany, 2008

[10] L. Latysheva, ACC_THEORY-report-2009-001, GDS-ID: DOC-2009-Jan-47

[11] E. Floch, GSI F-MT internal note MT-INT-ErF-2008-002, GSI, Darmstadt, Germany, 2008

[12] A.Stafiniak E. Floch, C. Schroeder, F. Walter, and F. Marzouki, "The GSI Cryogenic Prototype Test Facility - First Experience Gained on 2-Phase-Flow Superconducting Prototype Magnets of the FAIR Project", In Proceedings of ASC08, Chicago, Illinois, USA, August 2008.

[13] B. Skoczen, A. Wroblewski, M. Sitko, and D. Marcinek, Final report on the Design of Interconnections and Auxiliary Components of the SIS100/300 Synchrotrons, CUT, Cracow, Poland, December 2008

[14] P. Fabbricatore et al., Technical Design Report of a Superconducting Model Dipole for FAIR SIS300, INFN, Genova, Italy, November 2008

Selected Topics on SIS 100 Magnet R & D *

E. Fischer †[1], P. Schnizer[1], P. Akishin[2], H. Khodzhibagiyan[2], R. Kurnyshov[3], A. Mierau[1], B. Schnizer[4], and P. Shcherbakov[5]

[1]GSI, Darmstadt, Germany; [2]JINR, Dubna, Russia; [3]Elektroplant, Moscow, Russia; [4]TUG, Graz, Austria; [5]IHEP, Protvino, Russia

Design optimization

The SIS 100 synchrotron utilises superconducting magnets providing a field of 2 T (dipole), ramped with a cycle frequency of 1 Hz (4 T/s). The superconducting magnets have to be operated at 4.5 K and use the Nuclotron cable as its ancestor, the Nuclotron at JINR Dubna[1]. In this cable the superconducting wires are wrapped around a tube which is cooled by a two phase forced helium flow. The magnets create heat when they are ramped due to hysteresis and eddy current effects, which were reduced by a factor of two during previous R&D [2]. The maximum ramp rate and repetition frequency is limited by the maximum cooling power which can be applied on the magnet which in turn in limited by the length of the cable in the coil.

Beginning this year the most demanding cycle period was reduced from 1.8s to 1s (triangular cycle). It was predicted that the straight dipole with a two layer coil, as foreseen, can not be operated in a stable thermodynamic regime [3, 4] and thus the design was changed to a curved dipole with a single layer coil. This magnet can be operated in 1 Hz cycle (with a 2T amplitude) and it provides an increased beam aperture and an improved field quality [3, 4, 5].

Numerical Calculations

For the Nuclotron Cable the current carrying element is round which is not supported by the FEM tool TOSCA. An intensive R&D allowed to still model this cable in 3D using standard elements [6, 7]. Numerical studies using ANSYS calculated the heat due to ramp effects [2] as well as the field parameters for static and the transient operation [6, 8, 9].

Field Description for SIS 100

Beam dynamic calculations for synchrotrons normally approximate the magnetic elements as thin lenses using circular multipoles of the type

$$\mathbf{B} = \mathbf{C_m} \sum_{n=0}^{M} \mathbf{c_n}\ (r/R_R)^n\ e^{in\theta} \qquad (1)$$

with $\mathbf{B} := B_y + iB_x$ and $\mathbf{C_m}$ the main multipole of the magnet and $\mathbf{c_n}$ the higher order errors [10]. The expansion coefficients may be computed from field values given along the reference circle $r = R_R$.

Elliptic multipoles were developed for elliptic coordinates of the type $x = e\cosh\eta\cos\psi$, $y = e\sinh\eta\sin\psi$ with x and y the Cartesian coordinates and η and ψ the elliptic coordinates with $0 \le \eta \le \eta_0 < \infty$ and $-\pi \le \psi \le \pi$ [11, 12] . The field $\mathbf{B} := B_y + iB_x$ can be described within the whole ellipse using

$$\mathbf{B}(\eta,\psi) = \sum_{q=0}^{M} \mathbf{E}_q\ \cosh[q(\eta + i\psi)]/\cosh(q\eta_0), \qquad (2)$$

with $\eta_0 = \tanh^{-1}(b/a)$ the reference ellipse and a and b its half axes [11, 12, 13]. These $\mathbf{E}_q$ can be recalculated to circular multipoles

$$\mathbf{B}(\mathbf{z}) = \mathbf{B}_m \sum_{n=1}^{M} \mathbf{c}_n\ (\mathbf{z}/R_R)^{n-1} \qquad (3)$$

using an analytic linear transformation, with $\mathbf{B_m}$ the main field, $\mathbf{z} = x + i\,y$, R_R the reference radius and $\mathbf{c}_n = b_n + i\,a_n$ the relative higher order multipoles. The b_n's and a_n's are dimensionless constants.

An appropriate coordinate system is required to describe the field in a curved magnet. Dimensionless local toroidal coordinates are defined by

$$X + iY = R_C\ h\ e^{i\varphi},\ \ Z = R_R \sin\vartheta,\ \ h = 1 + \epsilon\rho\cos\vartheta$$

with R_R (R_C) the minor (major) radii of the torus, $-\pi \le \vartheta \le \pi$ the poloidal angle , $-\pi \le \varphi \le \pi$ the toroidal angle, $R_R{\cdot}\rho\ 0 \le \rho \le 1$, the quasi-radius and $\epsilon := R_R/R_C$ the inverse aspect ratio, on which the curvature effects depends. $\epsilon << 1$ justifies using a power series approximation in ϵ Only toroidally uniform fields are considered; thus B_ρ, B_θ are confined to the planes φ = const. and are independent of φ. The potential equation independent of φ is solved by an approximate R-separation. Thus the approximate multipole solution for the potential is (m = integer)

$$\begin{aligned}\Phi_m \quad &= \quad \rho^{|m|}\ e^{im\vartheta} \qquad (4)\\ &\quad -\frac{\epsilon}{4}\,\rho^{|m|+1}\big(e^{i(m+1)\vartheta} + e^{i(m-1)\vartheta}\big) + O(\epsilon^2).\end{aligned}$$

The curvature adds just the two adjacent multipoles which are not larger than $\epsilon/2$. Expressions for the corresponding magnetic fields as well as interpretations of measurements with rotating coils are given in [14, 13].

First Prototype Tested

The first magnet prototype was delivered by Babcock Noell Gmbh and tested at GSI. The first quench (i. e.

*Work supported by the EU FP6 Design Study (contract 515873 - DIRAC secondary beams) and the BMBF

† e.fischer@gsi.de

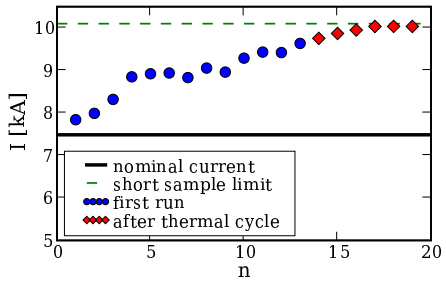

Figure 1: The training curve for the first prototype

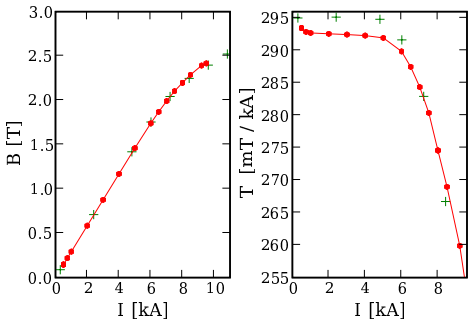

Figure 2: The load line (B vs I) and the transfer function (T = B / I vs I). The line with the dots indicate the measured values while the crosses show the calculated ones.

break down of superconductivity) was reached well above the nominal current (see Fig. 1; the last training quenches occurred on identical currents identical to the limit of the individual cable (short sampling limit) with the quench developing over the whole coil asserting that the magnet mechanics are of sound quality. The field of the magnet was measured (see Fig. 2) and compared to the calculations. The dipole term B_1 agrees well with the calculated values especially given that the iron properties were not available for 4.5 K. B (in T) can be approximated by $B(I) = I(294.0 - 1.44I + 0.249I^2 + 5.34 \cdot 10^{-2} I^3 - 1.25 \cdot 10^{-2} I^4)/1000$ for $I = 0.5 \ldots 8\,kA$ with an error less than $0.1\,\%$.

Vacuum chamber effects

The vacuum chamber of SIS 100 is to be used as a cryogenic adsorption pump this its temperature should be below 15 K. The chamber itself is elliptic made of steel sheet with 0.3 mm thickness, mechanically reinforced by ribs with cooling tubes attached to the ribs. The first design foresaw that these tubes were, beside thermally, also electrically connected to the ribs.

Calculations using ANSYS showed (see Fig. 3) that large eddy currents are then induced into the vacuum chamber during ramping the magnet [8, 9, 7]. When the ramp starts, the created field distortion is so strong that the sextupole increases by more than a factor of 10.

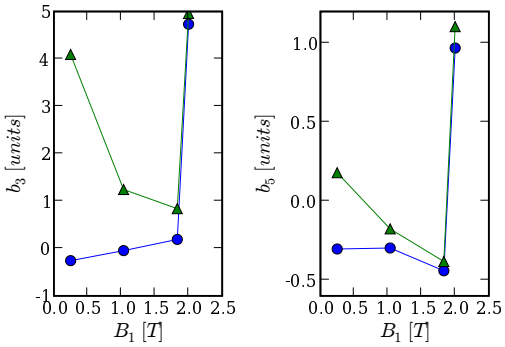

Figure 3: The sextupole and the dekapole versus the main field for the static field without vacuum chamber (circles) and on the ramp with the vacuum chamber inserted (triangles). One can see that at injection all multipoles on the ramp are much larger on the ramp than in the static case.

References

[1] H.G. Khodzhibagiyan and A. Smirnov. “Concept supercon. magnet system for the Nuclotron” ICIC12, 1988, pp 841

[2] E. Fischer et. al. “Manufacturing of the first full size model of a SIS100 dipole magnet” WAMSDO, May 2008, CERN

[3] E. Fischer, H. Khodzhibagiyan, and A. Kovalenko. “Full size model magnets for the FAIR SIS100 synchrotron” *IEEE Trans. Appl. Supercon.* June 2008 18:260-63

[4] E. Fischer, H. Khodzhibagiyan, A. Kovalenko, and P. Schnizer, “Fast Ramped Superferric Prototypes and Conclusions for the Final Design of the SIS 100 Main Magnets”, ASC08, August 2008, Chicago

[5] Technical DesignReport, SIS 100

[6] P. Schnizer et al. “Superferric magnets; optimized field design and measurement” WAMSDO, May 2008, CERN

[7] P. Schnizer et al. “Superferric magnets for SIS 100 Design and optimization” IGTE September 2008. Graz

[8] P. Schnizer et al., “Magnetic field of SIS 100 dipole.” EPAC 08, June 2008, Genova, pp 2452, http://www.JACoW.org.

[9] E. Fischer, P. Schnizer, R. Kurnyshov, B. Schnizer, and P. Shcherbakov. “Numerical analysis of the operation parameters of fast cycling superconducing magnets”, ASC08, August 2008, Chicago

[10] R. A. Beth. Applied Physics, 37:2568–71, 1966.

[11] P. Schnizer et al., *IEEE Trans. Appl. Supercon.* vol. 18, pp. 1648–1651, June 2008.

[12] P. Schnizer, B. Schnizer, P. Akishin, and E. Fischer, “Field representation for elliptic apertures”, GSI, January 2008.

[13] P. Schnizer, B. Schnizer, P. Akishin, and E. Fischer. “Theoretical field analysis for sf. acc. magnets using plane elliptic or toroidal multipoles” EPAC 08, June 2008, Genova, pp 1773 http://www.JACoW.org.

[14] P. Schnizer, B. Schnizer, P. Akishin, and E. Fischer “Plane elliptic or toroidal multipole expansions w. t. gap of straight or curved acc. magnets.” IGTE, September 2008, Graz

3D Field Quality in the SIS100 Dipole Magnet during Fast Ramping*

S. Koch§[1], H. De Gersem[2], and T. Weiland[1]

[1]Technische Universität Darmstadt, Institut für Theorie Elektromagnetischer Felder, Darmstadt, Germany;
[2]Katholieke Universiteit Leuven, Faculty of Science, Kortrijk, Belgium

Transient Finite Element Simulations

In order to calculate the field quality in the aperture of the SIS100 dipole magnet, a finite element discretization based on a tetrahedral mesh is applied. An anisotropic nonlinear material model resulting from a homogenization of the laminated iron yoke is necessary to model the effects of ferromagnetic saturation [1]. The excitation current in the superconducting coils amounts to $48\,\mathrm{kA}$ and varies with time according to cycle 2c corresponding to a ramp rate of $4\,\mathrm{T/s}$ for the magnetic flux density [2]. In the numerical model used for the simulations (Fig.1(a)), yoke modifications such as air slots and negative pole shimming (Fig.1(b)) are considered while the yoke length is shortened from $3.002\,\mathrm{m}$ to $0.5\,\mathrm{m}$. Furthermore, the conductive

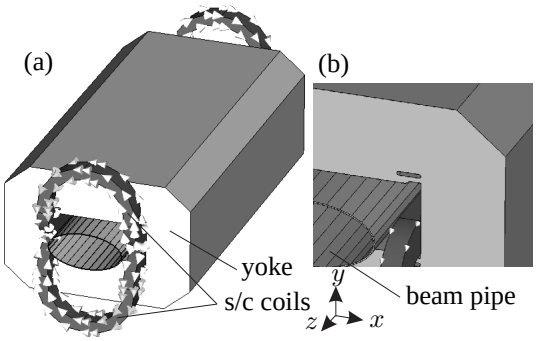

Figure 1: (a) Simplified model of the SIS100 dipole, shortened in length to 0.5 m, (b) detailed view of the yoke cross section and the conductive beam pipe.

beam pipe is included in the simulations by means of a direct representation in the volume mesh. In order to avoid a strong deterioration of the aspect ratio of the mesh cells, the thickness of the pipe is set to $1\,\mathrm{mm}$. Therefore the reported results yield an overestimation of the effect which have to be expected for realistic values around $0.5\,\mathrm{mm}$.

Field Quality

The field qualtity is calculated on the basis of an expansion of the aperture field in terms of circular multipoles. In Fig. 2 the sextupole component normalized to the dipol coefficient is shown. In particular at the beginning of the acceleration phase at $t = 0.1\,\mathrm{s}$ a dynamic increase is observed in presence of the beam pipe due to eddy-current effects. However, at the magnet center the coefficients of the sextupole remain below the limit of $6 \cdot 10^{-4}$ over the complete excitation cycle.

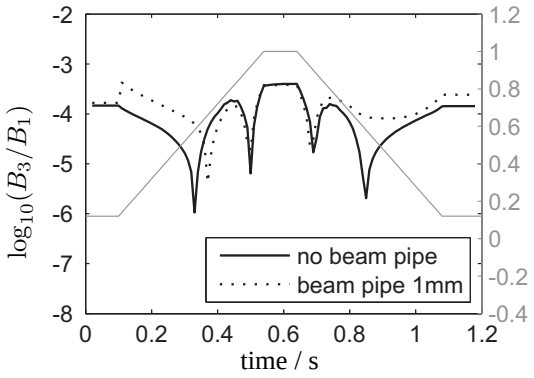

Figure 2: Influence of the presence of the conductive beam pipe on the third circular harmonic component at the magnet center. The excitation cycle, in which the injection phase is shortened to $0.1\,\mathrm{s}$ for the simulation, is shown in the right ordinate.

Table 1: Integrated multipole coefficients. Maximum and average over one excitation cycle are given. Extrapolated values for the full size model are shown in parenthesis.

	sextupole B_3^{int} / 10^{-4}		decapole B_5^{int} / 10^{-4}	
	max.	average	max.	average
short	78	48	-14	-6
(full size)	(16)	(8)	(-6)	(-2)

In order to incorporate the 3D effects arising at the end regions of the magnet due to eddy currents and local saturation, integral multipole coefficients are defined as

$$B_n^{\mathrm{int}} = \frac{\int_0^{z_{\max}} g(z) B_n(z) \mathrm{d}z}{\int_0^{z_{\max}} g(z) \mathrm{d}z} \,. \qquad (1)$$

The coefficients related to the short magnet as well as extrapolated values for full length are shown in Tab. 1.

References

[1] S. Koch, H. De Gersem, T. Weiland, E. Fischer, and G. Moritz, "Transient 3D Finite Element Simulations of the SIS100 Magnet Considering Anisotropic, Nonlinear Material Models for the Ferromagnetic Yoke", IEEE Trans. Appl. Supercond, vol. 18(2), p. 1601-1604, June 2008.

[2] "FAIR Baseline Technical Report", March 2006, http://www.gsi.de.

* Work supported by GSI, Darmstadt under contract F&E, DA-WEI1.
§ koch@temf.tu-darmstadt.de

SLOW EXTRACTION SIMULATIONS FOR SIS300

A. Saa-Hernandez, G. Franchetti, N. Pyka, U. Ratzinger, P. Spiller
GSI, Darmstadt, Germany

Single particle tracking simulations of slow resonant extraction are being performed for the proposed SIS300 design. The study is performed using the Elegant tracking code [1] to determine the appropriate extraction conditions and settings for a stable, low-loss extraction under the influence of the sextupole magnets and sextupole field errors of the main dipole magnets. A scheme for the compensation of the influence of sextupolar errors, transient and steady, of the superconducting (s.c.) magnets shall be derived.

To minimize beam losses during slow extraction a machine setting that fulfills the Hardt condition has been proposed. The Hardt condition aims at removing the momentum dependence of the entrance angle of the particles at the extraction septum. Therefore the electrostatic septum must be placed in a dispersive straight section and it was estimated that the chromaticity should be corrected and set to (ξ_x/ξ_y = -5.19/-9.45) for the studied working point (13.31/9.27). A full correction of the Hardt condition can be achieved by means of the 24 chromatic sextupoles, of 2 different families as presently foreseen in SIS300. The resulting DA is a factor 2 bigger than the physical aperture.

To excite the 3rd order resonance 12 "resonant" sextupoles from 6 different families have been used. This excitation generates 3 unstable fixed points linked by 3 separatrices, the corresponding area within them being now the dynamic aperture thus limiting the stable motion. The direction of the separatrices enables the particles to jump over, within three revolutions, the extraction septum. Though the "resonant" sextupoles are not placed in positions with zero dispersion, their net contribution to chromaticity is zero, and thus the Hardt condition is still fulfilled. As seen in figure 1a, slow extraction is achieved with the separatrices of different momenta δ (≡Δp/p) entering the septum with similar angle. But extraction is shown, figure 1b, only to work for particles in the plane y=0. For particles off-plane, the DA is now too small and particles outside it do not reach the septum.

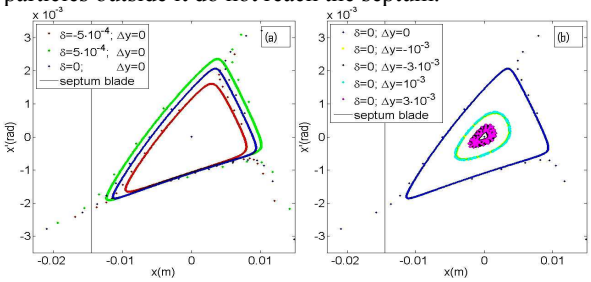

Figure 1: Hardt condition and its consequences on the separatrices: for Δy=0, overlapping of the separatrix heading towards the septum for different δp/p (a), for different Δy and δp/p=0, Hardt condition reduces the size of the separatrix (b).

Two alternative working points were studied for the same lattice design and an optimization of the sextupoles' strength is being done to improve these results.

The field imperfections of the s.c. dipole magnets were implemented into the modelling with the aim of setting tolerances to them at slow extraction. Simulations of magnetic field were done with ROXIE [2,3] including the characteristic field sources for s.c. magnets; persistent currents, inter-filament and inter-strand coupling currents, together with geometrical and saturation effects. Data corresponding to a ramp rate of 1 T/s at the flat top were used. Since the simulations include only the ideal geometry, data from dipole D0 of RHIC [4] were used to evaluate the otherwise zero components which can affect the DA.

The corresponding phase plots for slow extraction including field errors multiplied by a factor *f* are shown in figures 2(a,b,c). The strength of the chromatic sextupoles needs to be reset to match the Hardt condition for each value of *f* studied. It can be seen that for an *f* bigger than 3 the strengths of the chromatic sextupoles perturb the phase space trajectories bending the separatrices and creating stable islands foreclosing slow extraction. As seen in figure 2 the presence of skew components perturbs the phase space trajectories being a1, the skew quadrupolar component, the most dangerous one.

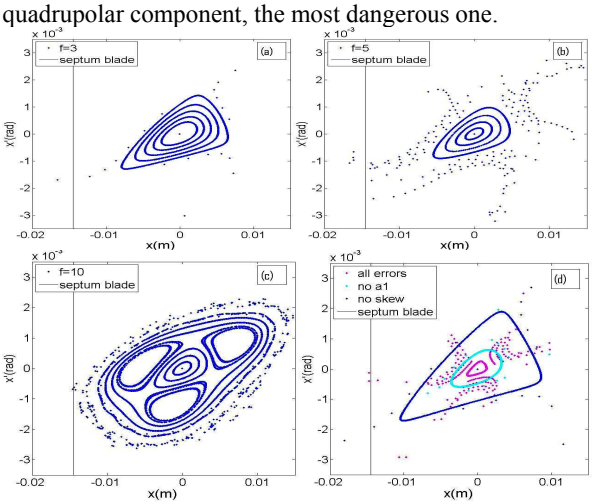

Figure 2: Phase plots at the extraction septum including: simulated field imperfections multiplied by a factor 3 (a), 5 (b) and 10 (c), experimental field imperfections from a similar dipole at RHIC (d).

REFERENCES

[1] M. Borland, "Elegant", APS (2000) (LS-287).
[2] S. Russenschuck, "Roxie", CERN (1999).
[3] H. Mueller, private communication.
[4] M. Anerella et al. *The RHIC magnet system.* NIM-A (2003).

Status of the Design of the FAIR Storage Rings

C. Dimopoulou, A. Dolinskii, O. Gorda, V. Gostishchev, R. Hettrich, U. Jandewerth, T. Katayama, K. Knie, S. Litvinov, F. Nolden, C. Peschke, P. Petri, I. Schurig, M. Steck[1], D. Möhl, L. Thorndahl[2], and D. Obradors-Campos[3]

[1]GSI, Darmstadt, Germany; [2]CERN, Geneva, Switzerland; [3]MCINN, Madrid, Spain

The general design work for the FAIR storage rings was continued and is documented in the Technical Design Reports of the different storage rings, which will be published after evaluation by external committees [1]. Technical details of the rings have been worked out. Design of subsystems focussed on the proposed German in kind contributions, i.e. stochastic cooling systems for CR and RESR, rf systems for the CR and all the subsystems and interfaces which are common to all accelerators of FAIR. The latest status of the ring design was communicated to the civil construction division and to the external companies which are working on all civil construction issues. A new concept for the buildings which will accommodate the storage rings and the technical systems which are needed for the operation of the storage rings is in preparation.

1 Ion Optical Design

Although the basic ion optical design of the storage rings is fixed, still various details are investigated which either simplify the rings or which are needed to achieve the required large acceptance of the storage rings. For the CR the studies were focussed on the the dynamic aperture that can be achieved for this large acceptance storage ring. In particular, interference effects due to the large gap size and the small distance between the main ring magnets were studied in order to determine the appropriate higher order corrections [2].

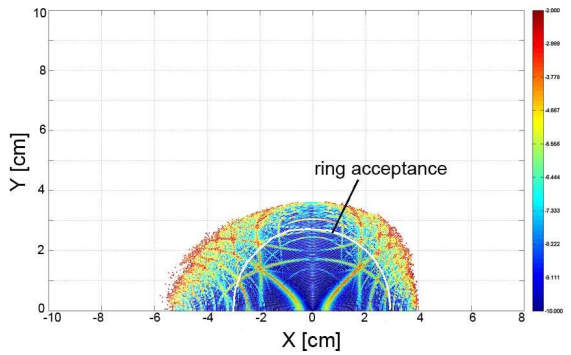

Figure 1: Calculations with the frequency map method to determine the dynamic aperture of the RESR. The stability of beam orbits for a particle circulating with a momentum offset of $\Delta p/p = 1.0$ % in the RESR is represented by a color code. Unstable particle motion occurs in the red colored regions.

For the accumulation of antiprotons in the RESR many details of ion optical parameters, particularly the transition energy of the ring, had to be readjusted in the process of the design of the stochastic cooling system. The performance of this cooling system is strongly linked to the ion optical properties of the RESR and the lattice has to support the accumulation process. The RESR lattice was investigated for a variable transition energy ($\gamma_t = 3.3-6.4$) and a large momentum acceptance ($\Delta p/p = \pm 1$ %) and moderate transverse acceptance ($\epsilon_{x,y} = 25$ mm mrad). For the design tunes $Q_x = 3.12$ and $Q_y = 4.104$ the dynamic aperture was calculated taking the higher order field components of the individual magnets into account (Fig. 1). These simulations are aiming at the reduction of higher order resonances by proper choice of the working point and addition of higher order correction magnets.

2 Stochastic Cooling

2.1 Stochastic Cooling Developments for the CR

The hardware developments for the stochastic cooling system of the CR have reached an advanced stage showing that important system parameters can be achieved. The new slotline pick-ups are integrated into modules which can house 8 slotline electrodes on the front side and signal combination circuits on the rear side, both for the beam signal and for switchable test signals.

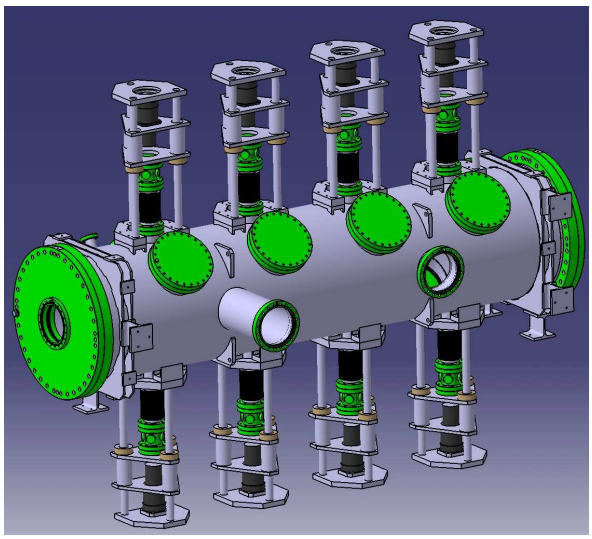

Figure 2: Design drawing of the prototype tank of the stochastic cooling system for the CR. The electrodes can be moved by linear motor drives. Electrodes and amplifiers inside the tank can be cooled by cold heads.

A prototype vacuum tank was manufactured and is being prepared for testing (Fig. 2). It can house two rows of eight modules, giving a total of two times 64 slotline electrodes. The tank can be equipped with 4 times 2 movable drives which are used for keeping the electrodes as close as possible to the beam during the cooling process. This

is beneficial for antiproton beams which are only singly charged, as well as for low-intensity rare isotope beams which require fast cooling due to their short lifetime. The key components of the drives are linear servo motors. The servo drives are freely programmable to get mechanical movement profiles, which follow the beam during the cooling process according to the reduction of emittance. These conditions vary along the length of the tank. When cooling is finished, the electrodes must be moved out in shortest possible time. This requires jerk free movement profiles producing as little mechanical vibration as possible. Eventual vibrations are measured using 3D accelerometers. The electrical control loops for the motor drives are optimized on a customized test bench.

The pick-up electrodes will be operated at cryogenic temperatures around 20 K in order to reduce thermal noise to a minimum. All necessary helium refrigerators have been purchased. The heat is transferred across silver-coated copper-beryllium foils similar to those which were successfully applied at CERN over many years. A gilded copper shield at roughly 80 K will be installed between the inner surface of the tank (at about 300 K) and the cold electrodes. The gold surface minimizes the thermal emissivity. The necessary galvanization procedures were tested successfully.

2.2 *Antiproton Accumulation System in the RESR*

The proposed accumulation system for antiprotons in the RESR comprises various subsystems. Three longitudinal cooling systems will be needed, two for cooling of the tail and the acceleration of the antiprotons towards the stack which operate in the frequency range 1-2 GHz, and a third one for cooling of the core of the intense stack operating in the frequency band 2-4 GHz. Two moderate power transverse cooling systems should preserve the small emittance of the stack. The main activities were devoted to the definition of the longitudinal cooling system. The injected beam from the CR will be accelerated by the rf system from the injection orbit (momentum offset $\Delta p/p = -0.8$ %) to the deposit orbit ($\Delta p/p = 0$ %) were the tail cooling system acts. The tail cooling system continuously drives the particles towards the stack orbit ($\Delta p/p = +0.8$ %). At the stack orbit the core cooling system forms an intense core of up to 1×10^{11} antiprotons with an accumulation rate of 1×10^{7} antiprotons/s. This is consistent with the cooling time of 10 s for a bunch of 1×10^{8} antiprotons in the CR.

The performance and the required parameters of the RESR cooling system have been determined in computer simulations. The simulations take the ion optical parameters of the RESR into account and allow an optimization of the ring lattice with respect to efficient accumulation. The electrode design is optimized for fast accumulation, but also takes into account that rare isotope beams will be decelerated in the RESR, which gives constraints on the geometry of the electrodes. A power of the order 100 W for the tail cooling and of the order 100 mW for the core cooling system will provide the necessary cooling rate. The longitudinal distribution of the antiprotons after accumulation over 1000 stacking cycles according to the simulations is shown in Fig. 3 together with the geometrical arrangement of the various electrodes. For less than 1×10^{11} antiprotons the simulations predict no significant heating by intrabeam scattering. A reduction of the cooling rate due to feedback by high intensity stacks will be minimized by proper electrode design.

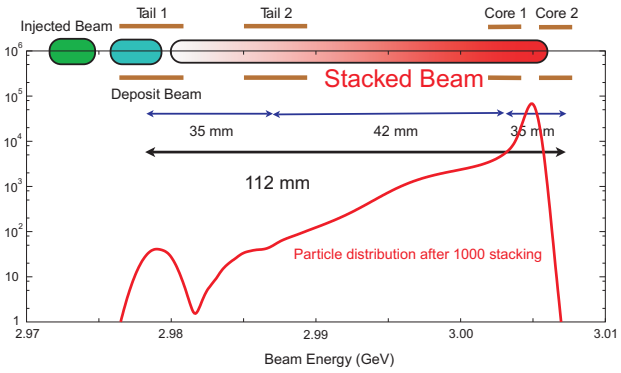

Figure 3: Set of electrodes for the accumulation of antiprotons by stochastic cooling in the RESR. The distribution of the antiprotons after 1000 injections from the CR for optimized system parameters was obtained by computer simulations.

3 NESR Design

The basic concept of the NESR, with four 18 m long straight sections for experimental installations, and the ion optical structure of the NESR remained unchanged. A new concept has been adopted for the collision region with high energy electrons, the so-called bypass section. By switching off the main dipoles adjacent to this straight section the beam is displaced by about 2.2 m horizontally outside of the normal straight section. After the decision to use normal-conducting dipoles the problem to pass the undeflected ion beam straight through the magnet is no longer obstructed by the cryostat for the dipole coil. Although two additional large dipoles are needed in order to deflect the ion beam into the bypass section, the optics for merging and focussing of the two colliding beams is considerably simplified compared to the previous scheme. The bypass offers easier access for the installation of a magnetic spectrometer for high energy electrons and equipment detecting collision products. Special components, like a high harmonic cavity to bunch the rare isotope beam for the collision mode, can also be installed in the bypass. The concept for the ring building and for the installation of technical systems has been modified accordingly.

References

[1] Technical Design Reports, GSI, to be published.
[2] O. Gorda et al., contribution to this report.

FIELD INTERFERENCE OF DIPOLE AND QUADRUPOLE MAGNETS AND ITS INFLUENCE ON BEAM DYNAMICS IN THE CR

O. Gorda, C. Dimopoulou, A. Dolinskii, F. Nolden, M. Steck
GSI, Darmstadt, Germany

The collector ring CR [1] is planned to be used for stochastic cooling of hot antiproton and rare isotope beams. Large aperture magnets [2] are needed to guide and focus such beams. The horizontal and vertical pole gap width of the dipoles is 48 cm and 17 cm respectively. The quadrupole magnets were designed to provide a useable horizontal aperture of 40 cm and a vertical aperture of 18 cm. The distance between the dipole and quadrupole magnets in the CR arcs is about 60 cm. The large apertures as well as the close arrangement lead to the overlap of the fringe field of the magnets. Therefore the interference of the edge fields can change the field quality and result in higher order field errors.

Magnetic field simulations using the OPERA software were performed [3] in order to quantify the effect of the field interference. The field maps were computed and analyzed for the dipole and quadrupole magnet separately and for two magnets combined together into one model. The derived field dependencies were then used to calculate the corresponding sets of multipole components. Table 1 shows the results obtained for the dominant integral field harmonics.

Table 1: Field integral harmonics at a reference radius of R_{ref} =7 cm, in units 10^{-4} $m^{-(n-1)}$. n = 1, 2, 3.. correspond to the dipole, quadrupole, sextupole comp. etc. All values are normalized to the dipole strength 1.6 T.

n	Quadrupole	Dipole	Dip+Quad
3	1.6502	0.4692	2.6805
4	0.7172	0.1151	0.8853
5	0.3764	-0.3078	0.2642
6	0.2451	0.0157	0.2657
7	0.1562	0.1027	0.2492
8	0.1128	-0.0194	0.1458
9	0.0933	-0.0206	0.0244

As one can see, the multipole components calculated for the model with the dipole and quadrupole combined together can not be represented as a superposition of the corresponding multipoles obtained for the separate magnets. As an example the integral sextupole component becomes larger by about 20% due the field interference effect.

The calculated sets of multipole components were used to evaluate the impact of the field interference on the beam dynamics of the ring. Figure 1 illustrates the betatron tunes calculated using the MAD-X code. The dotted curves correspond to the tune spread including only the field errors of the magnets. The field interference leads to a slight change of the tune spread as represented by the solid curves. To check the impact of the field interference effect on the dynamic aperture of the CR a series of calculations were performed using the Polymorphic Tracking Code (PTC) integrated into the MAD-X.

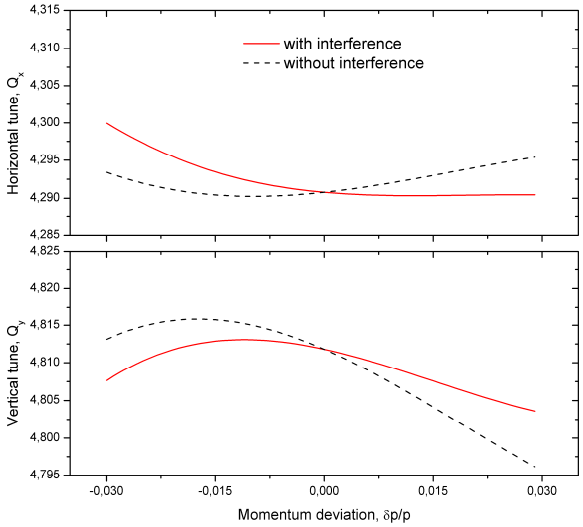

Figure 1: Tune spread for Δp/p=±3% in the antiproton mode.

Figure 2 shows the dynamic aperture of the CR calculated for off-momentum particles. As one can see, taking the field interference into account, does not lead to a decrease of the dynamic aperture. Even a small growth due to a slight compensation of the field errors can be observed.

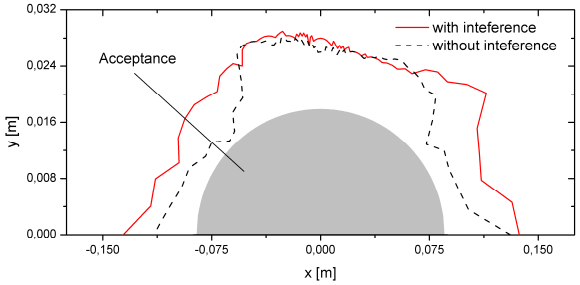

Figure 2: Dynamic aperture for Δp/p=-3% in the antiproton mode.

REFERENCES

[1] A. Dolinskii et al., Proc. of COOL07, TUA2C08, p. 106 (2007).
[2] A. Kalimov, GSI internal notes, 2004-2005.
[3] O. Gorda et al. Proc. of EPAC 2008, THPC067, p. 3113 (2008).

Status of the FAIR Proton Linac*

L. Groening[1#], W. Barth[1], G. Clemente[1], H.-L. Dambowy[1], H. Podlech[2], U. Ratzinger[2], G. Schreiber[1], W. Vinzenz[1]

[1]GSI, Darmstadt, Germany; [2]IAP, University of Frankfurt a.M., Germany.

Introduction

The FAIR proton linac has to provide the primary proton beam for the production of antiprotons [1]. It will deliver a 70 MeV beam to the SIS18 with a repetition rate of 4 Hz. The room temperature linac will be located north of the existing UNILAC complex. Its conceptual layout is shown in Fig. 1 and its main beam parameters are listed in Tab. 1.

Tab. 1: Main parameters of the proton linac for FAIR.

Final energy	70 MeV
Pulse current	35 mA
Protons per pulse	$7 \cdot 10^{12}$
Repetition rate	4 Hz
Trans. beam emittance	2.1 µm (tot. norm.)
Rf-frequency	325.224 MHz

Collaborations

At the time being, planning asumes that a consortium comprising GSI, the Goethe University of Frankfurt (GU), and CEA at Saclay.

Rf-System

In April 2008 the first 3 MW Klystron for the proton linac has been delivered to GSI (Fig. 2). Its design is very close to the one used for the klystrons currently operated at J-PARC. This klystron is the key component for the dedicated rf-test stand to be built at GSI. This test stand is needed for testing of the rf-coupled CH-cavities [2] as well as for demonstration of operation of a klystron power converter without crow-bar. The call for tender for a first power converter has been launched and delivery of the device is expected for the end of 2009. Prototyping of the low-level-rf-system is under progress [3]. It will be based on the system to be installed also for the FAIR synchrotrons employing digital control FPGA/DAC solutions.

Figure 2: First 3 MW-Klystron for the proton linac.

Cavity and Beam Dynamics Development

The design of the high energy end of the DTL section is currently under revision. Initially it was foreseen to use rf-coupled CH-cavities all along the DTL section in order to exploit the high power capabilities of the klystrons. Recent studies on the rf-properties of the cavities revealed that for energies above 35 MeV this potential can be used even by a one single prolonged CH-cavity. The latest DTL design now foresees the use of three pairs of rf-coupled cavities for acceleration to 35 MeV and three singe CH-cavities to final acceleration to 70 MeV. Beam loss studies confirmed that the new simplified design does not cause increased beam losses or any dilution of the beam quality.

References

[1] *FAIR Baseline Technical Report*, Vol. 2, GSI Darmstadt, Germany, p. 335, (2006).

[2] G. Clemente, PhD thesis, Goethe University of Frankfurt, (2007).

[3] W. Vinzenz et al., Proc. of 24th Linac Conf., (2008).

* Work supported by EU, CARE contract No. RII3-CT-2003-506395, BMBF and HMWK.

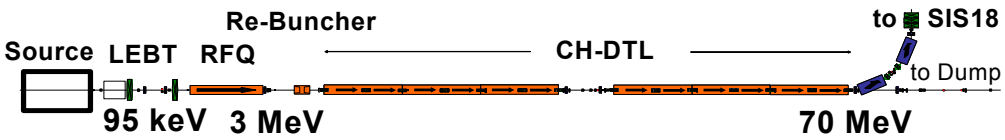

Figure 1: Conceptual layout of the FAIR proton linac.

#la.groening@gsi.de

Development of a coupled CH-Power cavity from 11.7MeV to 23.4MeV

U. Ratzinger[1], R. Brodhage[1], G. Clemente[2], L. Groening[2], H. Podlech[1], and R. Tiede[1]
[1]IAP, University of Frankfurt, Germany; [2]GSI, Darmstadt, Germany

For the 70MeV, 35mA proton injector for FAIR a beam dynamics design based on a CH-DTL was developed successfully during the last years. This paper will discuss the development and the construction of the first CH prototype cavity for FAIR.

Introduction

The proton linac for FAIR is mechanically grouped in two tanks, each having a length of about 10m. Based on the actual design the two tanks will consist of 3 coupled CH-cavities each. In between there will be a diagnostics section with an additional rebuncher inside.

The coupled prototype cavity

The prototype cavity corresponds to the second coupled cavity in the first section of the injector. The low energy part consists of 13 gaps, followed by the coupling cell and by the 14 gap high energy part. The whole cavity has an inner length of about 2.8m and a inner diameter of about 375mm.
The coupling cell has a length of $2\beta\lambda$ and hosts the focusing triplet lens within one drift tube. The intertank sections will also house triplet lenses as well as beam diagnostics. They will mechanically connect neighbored cavities.

Mechanical Design

The concept based on two very long linac sections leads to very tight tolerances with respect to the plane orientation of the flanges as well as with respect to the transverse positioning against the beam axis. To avoid mechanical deformation by gravity the linac will be placed on a rail system with flexible supports - as applied on the GSI Unilac.
Every intertank hosts a drift tube mounted on a metal sealed flange. No bellow connection along the beam line is needed by that concept.

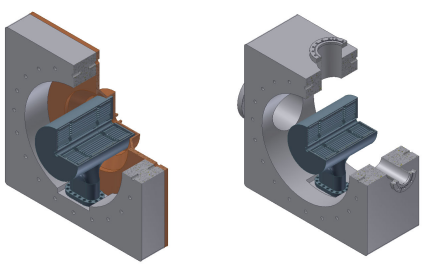

Figure 1: 3D - view of intertank and coupling cell

The coupling cell has four CF-flanges on the sides, which will be needed for:

a) incoupling loop c) plunger
b) vacuum pump d) quadrupole lens

As was demonstrated successfully by the prototype the drift tube stems can be welded into the tank wall at the inner surface. Special techniques were developed to inte-grate long drift tubes with modest transverse stem diame-ters. Additionally care must be taken to limit longitudinal stress along the stem caused by temperature differences between tank wall and drift tube structure.
The cooling concept was investigated and also special welding techniques were found to work satisfying. The outer tanks are already in production.

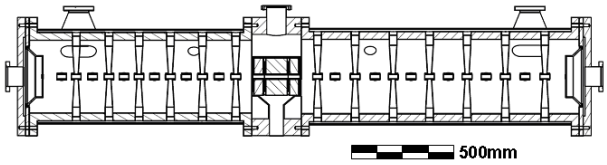

Figure 2: cross sectional view of 2nd coupled cavity

RF Properties

The coupling between an acceleration section and the coupling cell is accomplished by RF-fields around the coupling drift tube as well as by the gap capacity. The coupling factor is around 0.3%. This means, the spacing between the 0-mode and the $\pi/2$-mode is about 1.3MHz, which seems sufficient. Possibilities for an increased mode separation are actually investigated at the rf model.
Concepts for fine tuning of the voltage distribution already during cavity fabrication are studied as well and seem promising.
The acceleration sections of the cavity contains no screwed connections. Therefore a Q-value within 5% of the theoretical value is expected. This was demonstrated successfully by the 8-cell prototype.

References

[1] G. Clemente, H. Podlech, U. Ratzinger, R. Tiede, S. Minaev, "HIPPI-Relevant Activities at IAP-Frankfurt on the Development of the Room Temperature CH-DTL", CARE-Report-2008-014-HIPPI

Estimation of radiation levels around the FAIR antiproton target

K. Knie, V. Gostishchev, T. Radon, and M. Steck

For the region around the antiproton target [1] extensive simulations of the expected radiation levels were performed in order to ensure that a sufficient radiation protection of the neighboring areas can be achieved.

For these simulations the Monte-Carlo particle transport code FLUKA [2,3] was used. A very detailed geometry file is needed as input to obtain reliable results. In addition, magnetic fields in the magnetic horn right after the target, the quadrupole magnets between target and beam-dump and all dipole magnets were considered.

Due to the high energies and the long ranges of the primary and secondary particles a large region of 50 × 20 × 150 m³ ($x \times y \times z$) was used for a first simulation (see figure 1). Between and above the tunnels, concrete is used as shielding material. Inside the tunnels wet air is used to account for the moderation of neutrons. The target and magnetic horn are located in an iron shielding with 1.6 m thickness on the downstream side and 1.0 m thickness on all other sides. An additional iron shielding (0.5 × 1.6 × 22 m³, ~ 140 t) in the wall will enable the access to the Super-FRS tunnel during antiproton production. According to the German Radiation Protection Ordinance areas with dose rates below 0.5 µSv/h (purple and white) are accessible without restrictions.

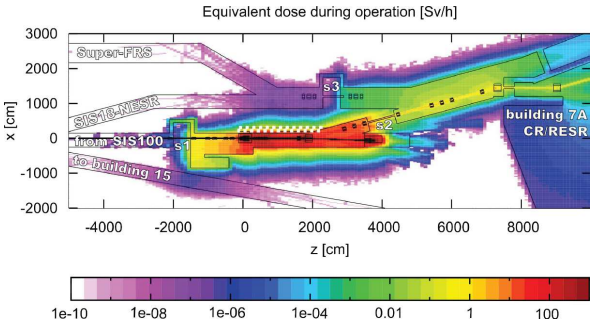

Figure 1: Equivalent dose rates during operation with 2×10^{13} protons per pulse and a repetition rate of 0.1 Hz. The data are averaged over a height interval of ± 1.0 m relative to the beamline. The target is located at (0,0). The iron shielding is indicated by the white dots. The primary beam is dumped at $z \approx 4000$ cm, the antiprotons are transported to the CR/RESR hall.

It turned out that the shielding wall s3 has to be moved behind the last Super-FRS quadrupole triplet because this space is needed for detectors. Moreover, s3 would complicate the supply of that triplet, which is the last in a series of superconducting magnets. To guarantee the accessibility of the Super-FRS tunnel with s3 at the new position, about 400 t of additional iron shielding is needed at $z \approx 3000$ cm (see figure 2).

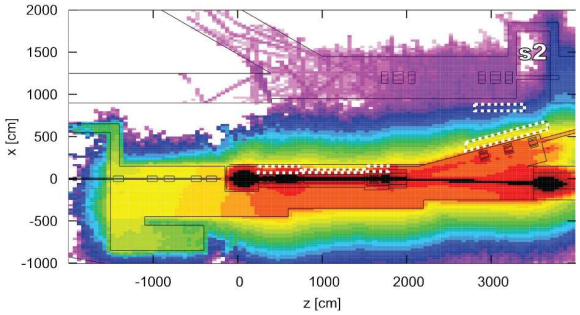

Figure 2: Similar as fig. 1, but (besides some minor changes) with the shielding wall s3 behind the last Super-FRS quadrupole triplet and additional iron shielding in the walls. For the color coding see fig. 1. Note the different scale in x and z.

In contrast to figures 1 and 2, figure 3 shows the dose rates due to induced activity after operation. Although the region will not be freely accessible, the dose rates in the tunnel can be kept well below 3 mSv/h, which is the limit for restricted access. To achieve this, all large iron parts (target shielding, collimators, all magnets between the target and the first dipole at $z \approx 2000$cm) need to be housed with concrete. It will be activated to a much smaller amount than iron and shields the radiation originating from radionuclides like ^{54}Mn ($T_{1/2} = 312$ d).

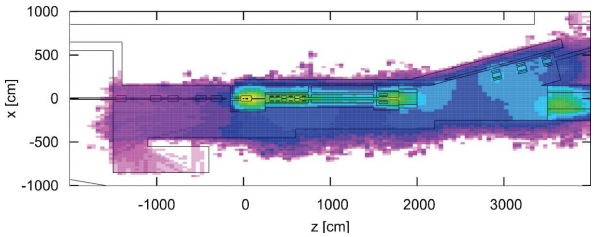

Figure 3: Equivalent dose rates due to induced radioactivity three month after shutdown. Before shutdown one year of continuous operation with 50 % of the nominal activity is assumed. For the color coding see fig. 1.

References

[1] GSI Scientific Report (2007) 59.
[2] A. Fassò, A. Ferrari, J. Ranft, and P.R. Sala, CERN-2005-10 (2005), INFN/TC_05/11, SLAC-R-773.
[3] G. Battistoni, S. Muraro, P.R. Sala, F. Cerutti, A. Ferrari, S. Roesler, A. Fassò, J. Ranft, Proceedings of the Hadronic Shower Simulation Workshop 2006, Fermilab 6-8 September 2006, M. Albrow, R. Raja eds., AIP Conference Proceeding 896, 31-49, (2007)

Design Studies of an Antiproton Production Target

N.A.Tahir[1], K.Knie[1], S.Richter[1], D.Kraemer[1], A.Shutov[2], V.Kim[2], A.Matveichev[2], A.Ostrik[2], V.Sultanov[2], I.V. Lomonosov[2], and A.R. Piriz[3]

[1]GSI, Darmstadt, Germany; [2]IPCP, Chernogolovka, Russia; [3]UCLM, Ciudad Real, Spain

In this contribution we present numerical simulations of thermodynamic and hydrodynamic response of a proposed production target (see Fig. 1) for generation of antiprotons at the Facility for Antiprotons and Ion Research (FAIR), at Darmstadt. As seen in Fig. 1, it consists of a Ni cylinder which has a radius of 0.15 cm and a length of 10 cm and is enclosed in solid graphite casing which is followed by an aluminum layer.The dimensions of the different layers are shown in the figure. One face of the cylinder is irradiated by a beam of 29 GeV protons that are delivered in a single bunch which is 50 ns long. The beam intensity is considered to be 2 $\times$ 10^{13} and two different radial intensity distributions have been considered. In one case we consider a rectangular distribution with a focal spot radius = 1 mm while in the second case we use a Gaussian distribution with σ = 1 mm.

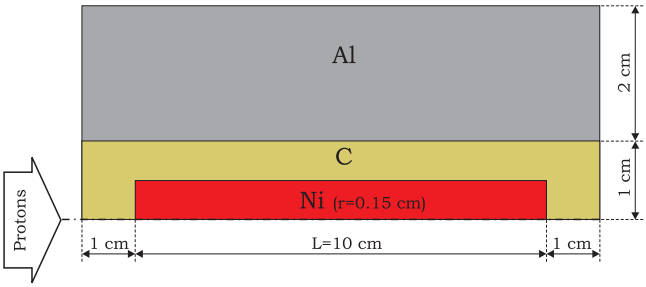

Figure 1: Target configuration

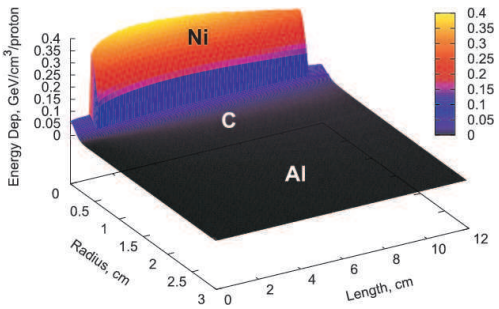

Figure 2: Energy loss by a single proton per unit volume calculated by FLUKA for a Gaussian intensity profile, leads to about 0.14 kJ/g specific energy in Ni.

The protons interact with the target material, thereby generating cascade particles. These processes are treated using the FLUKA code [1] and the energy loss data is shown in Fig. 2. This data is converted into specific energy deposition (kJ/g) which is used as input to a 2D computer code BIG2 [2] to study target beam–target interaction. .

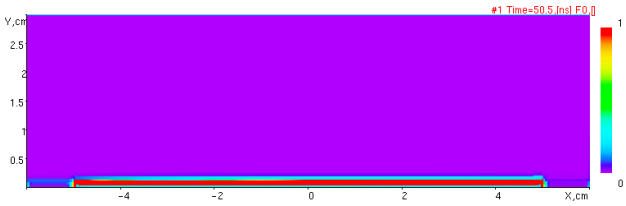

Figure 3: von Mises parameter at t = 50 ns.

In case of a rectangular intensity distribution in the focal spot, a maximum specific energy deposition of 0.27 kJ/g is achieved in the Ni part while the corresponding temperature and pressure are 940 K and 2.6 GPa, respectively. For a Gaussian distribution, the maximum specific energy is 0.14 kJ/g, the temperature is 629 K and the pressure is 2.4 GPa. It is to be noted that the target temperature remains safely below the melting temperature of Ni (1726 K) so the target will remain in the solid state.However the high pressure in the target launches an outgoing radial compression wave which generates stress in the material that could lead to plastification of certain parts of the target. In Fig. 3 we plot the von Mises parameter, M, on a length–radius plane at t = 50 ns which shows that M = 1 in the Ni region which indicates material plastification. Figure 4 presents M at t = 1 μs which shows that the plastification wave has entered into the graphite by this time. Calculations at later points in time show that the aluminum region remains in an elastic regime. These calculations indicate that although plastification occurs in the interior, the target will still survive.

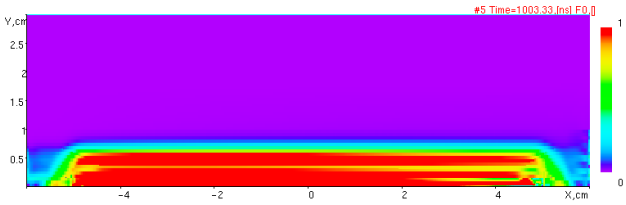

Figure 4: von Mises parameter at t = 1 μs.

References

[1] A. Fasso et al., "FLUKA: A Multi-Particle Transport Code", CERN-2005-10, INFN/TC-05/11, SLAC-R-773 (2005).

[2] V.E Fortov *et al.,* Nucl. Sci. Eng. 123, 169 (1996)

Super-FRS Design Status Report*

M. Winkler[1,#], K.-H. Behr[1], E. Berdermann[1], D. Boutin[1,2], A. Brünle[1], H. Geissel[1,2], S. Gordeev[3], M. Gleim[1], M. Hillenbrand[3], C. Karagiannis[1], A. Kelic[1], B. Kindler[1], E. Kozlova[1], A. Kratz[1], M. Krause[1], H. Leibrock[1], Yu.A. Litvinov[1], B. Lommel[1], J.A. Maruhn[4], G. Moritz[1], C. Mühle[1], G. Münzenberg[1], C. Nociforo[1], W.R. Plaß[2], A. Prochazka[1], C. Scheidenberger[1,2], H. Simon[1], R. Stieglitz[3], L. Soppel[3], K. Sümmerer[1], An. Tauschwitz[4], M. Tomut[1,5], H. Weick[1], J.S. Winfield[1], and M. Yavor[6]
[1]GSI, Darmstadt, Germany; [2]JLU Giessen, Germany; [3]FZ Karlsruhe, Germany; [4]JWGU Frankfurt, Germany; [5]NIMP, Bucharest, Romania; [6]IAI RAS, St. Petersburg, Russia;

Layout of the Super-FRS

The ion-optical design of the Super-FRS has been finalised to a large extent and its layout presented in [1]. Last year we concentrated on the optimization of the focussing system in front of the production target, the highly-activated target area itself, and the Low-Energy Branch including its instrumentation. In particular an ion-optical layout of the low-energy beam transport system from the stopping cell at the exit of the Energy Buncher to the different experimental areas (LASPEC/MATS) has been developed. It is based on electrostatic lenses and magnetic dipoles. It comprises a gas-filled RFQ cooler, a beam line between the cooler and a 60° separator (beam transport through the shielding wall), the 60° magnetic separator (mass-resolving power of about 1000), and a beam line between the exit slit of the separator and the experimental areas including a RFQ buncher and a beam distribution system (see Figure 1).

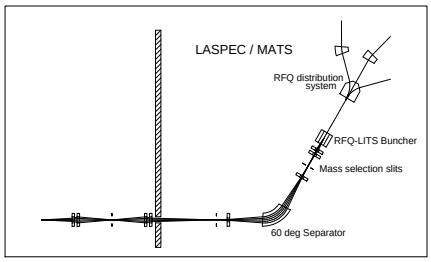

Figure 1: Ion-optical layout of the beam transport system behind the Energy Buncher of the Super-FRS connecting the stopping cell with the various experimental areas.

High-Power Targets

The target development for the Super-FRS has to consider both the slow and fast extraction mode of the synchrotrons SIS100/300. We envisage a rotating graphite wheel as the standard target. In addition, a feasibility study has been undertaken which explores the possibility of a liquid-metal jet target as a production target in case of highest energy deposition.

Rotating graphite wheel target

A rotating graphite-wheel target has been developed, based on a proven design in operation at the Paul-Scherrer-Institute (PSI, Switzerland). A prototype has been constructed (see Figure 2) by an industrial partner and delivered to GSI where it is presently tested off-line. The remote-handling concept of the prototype target has been adapted to the present FRS scheme since it is planned to operate it already in the near future at the FRS target station using SIS18 beams.

An important aspect of the solid-target development is radiation damage [2]. A dedicated research has been undertaken in close collaboration with the Material Science group at GSI. Experimental investigations of graphite samples exposed to high-intensity pulses show some thermal fatigue signs unlikely to affect the integrity of the material [3]. Another important issue is the stability of the target under the influence of large stresses created by the passage of short-extracted heavy-ion beam pulses. An experiment studying the impact of short high-intensity pulses of fast-extracted uranium beams on graphite [4] has been analyzed and compared to finite-element (FE) calculations which have been performed in collaboration with TU Darmstadt [5]. The maximum target stress obtained from this analysis was found to be compatible with the tensile strength of the graphite grade to be used at the Super-FRS.

Figure 2: Prototype of the rotating graphite wheel target.

Liquid-metal target development

The feasibility study of a windowless liquid-metal jet target, funded by the 6th framework program of the European Commission, has been completed by the KALLA group at FZ Karlsruhe. The pertinent results from this study are the following:

* Work supported by the European Community under the FP6 DESIGN STUDY (contract 515873 - DIRACsecondary-Beams).
#m.winkler@gsi.de

- Tests with a water loop have proven that continuous-flow dynamics (CFD) calculations of the water jet are in agreement with the observed jet behaviour if proper turbulence models are used. The numerical models are capable of describing the mean liquid-metal jet surface if adequate reconstruction schemes are used [6].
- A liquid-Na test loop has been successfully put into operation. The obtained results can be scaled to a liquid-Li loop. First calculations indicate, however, that the tensile strength of liquid-Li is not sufficient to withstand the high pressures induced by fast-extracted uranium pulses at FAIR [7].
- A new detection method for measuring online and non-invasively the free jet surface has been developed, tested and qualified for liquid-metal free-surface flows [8].

Beam catchers

The beam catchers are located at dedicated positions in the Pre-Separator [1] and will stop the non-reacting portion of the primary beam. They consist of a graphite front part to absorb efficiently the beam energy, and an iron back part to shield subsequent components of the separator from secondary radiation. As for the high-power target, the remote-handling concept of the beam catchers is based on a vertical plug system (see Figure 3).

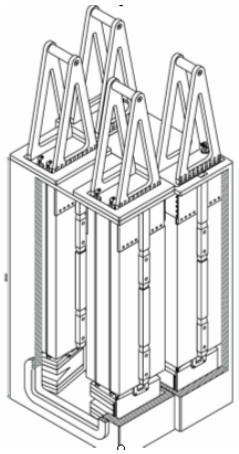

Figure 3: The remote handling of the beam catchers is assured by means of a vertical plug concept. The catchers consist of graphite (front part) and iron (back part).

Detector developments

In collaboration with the GSI Detector Laboratory a PCVD Diamond detector was tested in-beam at the FRS using $^{64}Ni^{26+}$ at 320 AMeV. The detector (30x30 mm^2, 360 µm thick) has 9 strips, each one equipped with a broadband amplifier [9]. The beam profile could be reconstructed by means of particle counting. In the future the application of optical-fibre cables and of optical transmitters/receivers is foreseen to preserve the properties of the fast signals and to perform time measurements up to count rates of 100 MHz.

Magnet developments

The Super-FRS will consist of normal-conducting radiation-resistant magnets which are required in the first dipole stage and of super-conducting magnets which are used in all other dipole stages.

Radiation resistant magnets

The production of a radiation-resistant prototype dipole magnet is performed in collaboration with BINP, Novosibirsk. The yoke production has been finished to a large extent. The radiation-resistant cable with mineral insulation has been produced by Tyco Ltd., Canada, and shipped to Novosibirsk where the winding of the coil is under progress. The design supports a dedicated remote concept for maintenance purposes.

Super-conducting magnets

The prototype of a super-ferric dipole magnet is being developed in collaboration with the FAIR China Group (IMP Lanzhou, ASIPP, Hefei, and IEE Beijing). The iron-yoke production has been finished; field measurements were performed using a normal-conducting test coil (see Figure 4). The SC coil was tested successfully using a prototype cryostat. Final magnet assembly, tests, and field measurements are planned for spring 2009 in Lanzhou.

Figure 4: Field mapping of the super-ferric dipole magnet at IMP, Lanzhou, using a normal-conducting 'test coil'.

Survey and alignment

To assure the survey and alignment of Super-FRS components in high-radiation areas, the R&D project RALF (**R**emote **AL**ignment on the **F**ly) was conducted in collaboration with FH Mainz. The measurement method is based on the principle of photogrammetry. Details are presented in [10].

[1] M. Winkler *et al.*, Nucl. Instr. Meth. B 266 (2008) 4183.
[2] M. Krause *et al.*, this report.
[3] M. Tomut *et al.*, this report.
[4] R. Wilfinger *et al.*, GSI Sci. Rep. 2007.
[5] C. Plate, Bachelor Thesis, TU Darmstadt (2008).
[6] S. Gordeev, PhD Thesis Univ. Karlsruhe-KIT (2008).
[7] An. Tauschwitz *et al.*, Nucl. Instr. Meth. A 591 (2008) 447.
[8] M. Hillenbrand, PhD Thesis, Univ. Karlsruhe (2008).
[9] P. Moritz *et al.*, Diamond and Related Materials 10 (2001) 1765.
[10] A. Marbs *et al.*, this report.

Magnet Alignment and the Super-FRS Resolving Power and Transmission*

J.S. Winfield[1#], D. Boutin[1], H. Geissel[1,2], S. Manikonda[3], J.A. Nolen[3], H. Weick[1], M. Winkler[1], M. Yavor[4]

[1]GSI, Darmstadt, Germany; [2]Justus-Liebig Univ., Gießen, Germany; [3]Argonne National Laboratory, Argonne, IL, USA; [4]Insitute of Analytical Instrumentation, RAS, St. Petersburg, Russia.

The ion-optical analysis program COSY-Infinity 9.0 [1] has been used to estimate the effect of magnet alignment on the transmission and momentum resolving power of the future Super-FRS [2,3] for FAIR. Possible alignment errors of the magnets involving horizontal and vertical offsets, tilts, and rotations about the optic axis were studied separately. The misalignments between one magnet and another were assumed to be uncorrelated (except when triplets as a whole were considered to be misaligned). The amplitude of the misalignment for a given magnet was a fixed factor multiplied by a random number between -1 and +1.

Effect on Transmission

For the transmission calculations, rectangular and circular apertures in front of and behind the dipole and multipole magnets are defined. A Monte-Carlo routine is then used to send test "particles" through the ion-optical lattice. The transmission is then simply the number of particles reaching the end of the High Energy Branch (FHF1 focal plane), compared to the initial number. Figure 1 shows an example of the loss of transmission as the magnets are offset from the proper alignment by increasing amounts.

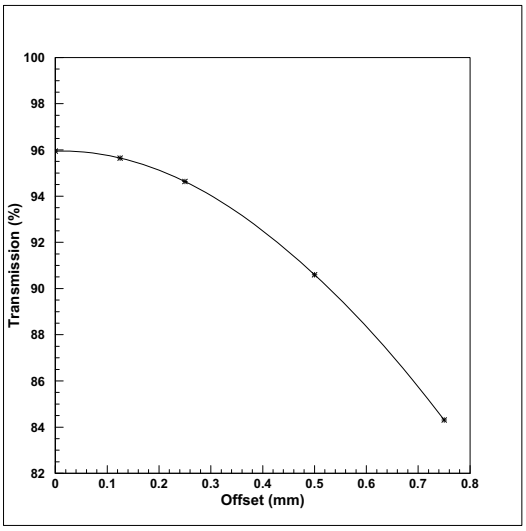

Figure 1: Transmission through the High Energy Branch of the Super-FRS with magnet offset misalignments.

The transmission was found to be rather sensitive to a possible tilt of the magnets. Further investigation showed that this effect owed principally to tilt misalignments of the quadrupoles, rather than the dipoles and hexapoles. By contrast, the transmission was quite insensitive to possible rotations about the optic axis.

Effect on Resolving Power

The resolving power was calculated at the dispersive focal planes of the Pre-separator (FPF2) and the Main Separator (FMF2) of the Super-FRS for different misalignments of the magnets. For these calculations, the COSY procedure AR [4] was used, except when the quadrupole triplets were misaligned as a whole. In the latter case, analytical formulae for the resolving power were used for quickness.

As found in the study of transmission losses, the tilt alignment is more important than the rotation alignment, especially for the quadrupole magnets.

Summary

The following summary table shows limits for only a few percent loss of transmission or momentum resolving power, while the phase space images at the focal planes are kept "reasonable".

	Transmission	Resolving Power
Offsets	≤0.5 mm	≤0.3 mm
Tilts	<0.05°	≤0.05°
Rotations	≤0.3°	<0.2°

References

[1] K. Makino and M. Berz, Nucl. Instr. Meth. A **558** (2005) 346.
[2] H. Geissel et al., Nucl. Instr. Meth. B **204** (2003) 71.
[3] M. Winkler et al., Nucl. Instr. Meth. B **266** (2008) 4183.
[4] M. Berz and K. Makino, COSY-Infinity Beam Physics Manual, MSU report MSUHEP 060804, 2006.

* Work supported by the EU under the FP6 DESIGN STUDY (contract No. 515873 – DIRACsecondary beams).
#j.winfield@gsi.de

Experimental Investigation of Microstructural Changes in Graphite Exposed to Fast-Extracted ^{238}U Beams *

M. Tomut[1,6,#], A. Keliç [1], K. H. Behr[1], A. Bruenle[1], R. Catherall[2], F. Cerutti[2], H. Geissel[1], D. H. H. Hoffmann[3], A. Hug[3], Ch. Karagiannis[1], B. Kindler[1], M. Krause[3], M. Kulish[4], J. Lettry[2], B. Lommel[1], J. Menzel[3], N. Müller[3], H. Richter[2], K. Sümmerer[1], N. Tahir[1], C. Trautmann[1], S. Udrea[3], D. Varentsov[1], H. Weick[1], R. Wilfinger [2], M. Winkler[1], and Y. Zhao[5]

[1]GSI, Darmstadt, Germany; [2]CERN, Geneva, Switzerland; [3]Technische Universität, Darmstadt, Germany; [4]IPCP, RAS, Chernogolovka, Russia; [5]Institute of Modern Physics, CAS, Lanzhou, China; [6] NIMP, Bucharest, Romania

The aim of experiment S334, performed at HHT area at GSI, is to investigate the response of different target materials to pressure waves generated by high instantaneous energy-deposition of fast-extracted ion beams [1]. The information on the magnitude of thermal stresses induced by short, intense ion pulses in graphite is vital for the foreseen use of a solid Super-FRS target in the fast-extraction regime [2]. We present results of the microstructural investigation on graphite samples (grade R 6650 SGL) exposed to multiple high-intensity ^{238}U spills.

Graphite cylindrical targets (10 mm diameter, 5 or 10 mm length) were bombarded with several ^{238}U spills, 300ns, intensity 2.25×10^9 ions/spill, $\sigma_{x,y}$=0.38 mm at 350 A MeV. Profilometry shows an overall increase of the roughness of the surface of the samples after ion bombardment. By SEM we observe that this is due to isolated beam-related features, like fractures (Fig.1) and craters formed on the surface of the samples. Fractures seem to develop from elongated pre-existing pores and small cracks related to machining process, acting as stress concentrators. Craters seem to form in areas with high porosity where loosely bound grains can detach under the action of pressure waves induced by the ion beam impact.

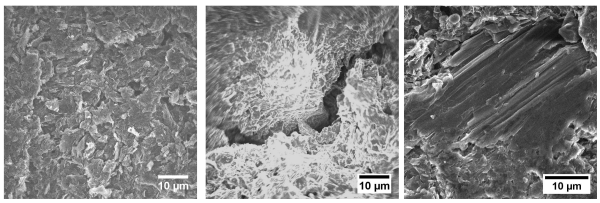

Fig. 1. SEM images of microstructure of fine-grained graphite exposed to fast-extracted U beams: (left) typical surface aspect of non-exposed sample, showing presence of pores; (center) an isolated crack (aprox. 100 µm length) on the surface of a sample exposed to 3 spills; (right) shear signs in the area of beam impact in a sample exposed to 50 spills.

A practical estimation of the upper limit of the size of the tolerated internal and surface defects for a fine-grained isotropic graphite grade, using a value of the fracture toughness of $K_{IC\infty}$=0.6 MPa$\sqrt{m}$ and σ_c=65 MPa - the critical flexural strength, gives a value of 250 µm [3]. The defects that we observed in graphite samples exposed to multiple fast-extracted beam spills are therefore sub-critical and unlikely to affect the integrity of the material. This is in agreement with the simulation results showing peak values of the thermal-induced tensile stresses lower than the critical flexural strength of graphite [2]. Fatigue aspects, irradiation- and temperature- induced modification of the thermo-mechanical properties of the material are not assessed in this simple estimation of the critical defect size. Another practical application of this calculated value is related to machined corners on the target wheel. They should be rounded to avoid stress concentrators and their rounding radius should be larger than the calculated 250 µm value.

To allow for an extended utilization of a solid Super-FRS target at the highest beam intensity in the fast-extraction regime, new materials more resilient to pressure waves are desirable. Figure 2 shows a comparison of candidate target materials based on a figure of merit which describes the resistance to thermal shocks induced by U beam. This parameter compares the bending strength of the material to the thermal stress induced by the ion beam energy deposition. Carbon materials remain the best choice for high temperature and high thermal stress applications. Although non-irradiated carbon-carbon composites (CFC) have a better response to transient thermal loads than graphite, further experimental studies at high level of radiation damage are necessary.

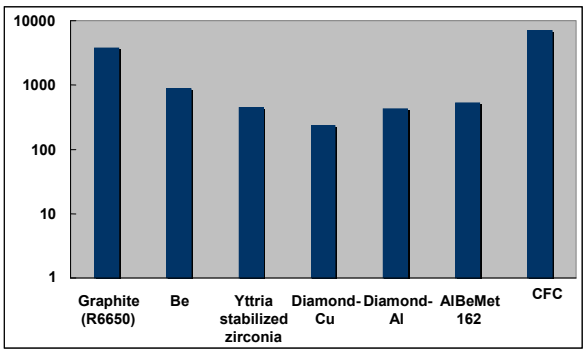

Fig. 2. Figure of merit for resistance of candidate target materials to ion beam-induced thermal stress

[1] R. Wilfinger *et al*., GSI Scientific Report (2007) 75.
[2] A. Keliç *et al.*, this report.
[3] R.Chavan, Int. report, CRPP/EPFL-Lausanne 195/99.

* Work supported by the European Community under the FP6 DESIGN STUDY (contract 515873 - DIRACsecondary-Beams).
#m.tomut@gsi.de

Simulations of a Solid Graphite Target for High Intensity fast Extracted Uranium Beams for the Super–FRS*

N.A. Tahir[1], H.Weick[1], A.Shutov[2], V.Kim[2], A.Matveichev[2], A.Ostrik[2], V.Sultanov[2], I.V. Lomonosov[2], A.R.Piriz[3], J.J.Lopez Cela[3], and D.H.H Hoffmann[4]

[1]GSI, Darmstadt, Germany; [2]IPCP, Chernogolovka, Russia; [3]UCLM, Ciudad Real, Spain; [4]TU Darmstadt, Germany

Extensive numerical simulations have been done to study, generation, propagation and decay of deviatoric stress waves induced by a high intensity uranium beam in a wheel shaped solid graphite Super–FRS production target. Maximum beam intensities that the target can tolerate using different focal spot sizes that are determined by requirements of good isotope resolution and transmission of the secondary beam through the fragment separator, have been calculated. A circular focal spot is superior to an elliptic one as the former generates minimum thermal stress in the material. The maximum spot size allowed by requirement of good isotope resolution is characterized with σ = 4 mm. Simulations have shown that the target will survive a beam intensity of 10^{11} ions per bunch. It is also to be noted that the yield strength of graphite increases with temperature. At 2000 K it becomes 100 MPa compared to 70 MPa at the room temperature. It has therefore been suggested that the target may be preheated by a defocused beam to a higher temperature before performing the experiments in order to take advantage of this effect [1]. Simulations show that at a temperature of 2000 K, the target will survive with a higher intensity of 2.0 $\times$ 10^{11}. However, for the full intensity of the uranium beam at the Super–FRS one would require an elliptic focal spot with σ_X = 4 mm and σ_Y = 11 mm.

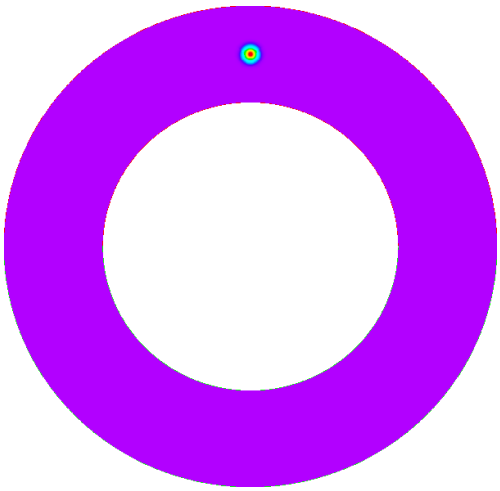

Figure 1: Target pressure at t = 50 ns, maximum value = 200 MPa.

The target has an inner radius = 13.5 cm and an outer radius = 22.5 cm. In Fig. 1 we present the target pressure at t = 50 ns for the case of 1 GeV/u uranium beam with an intensity of 10^{11} ions per bunch and a circular focal spot with σ = 4.0 mm.

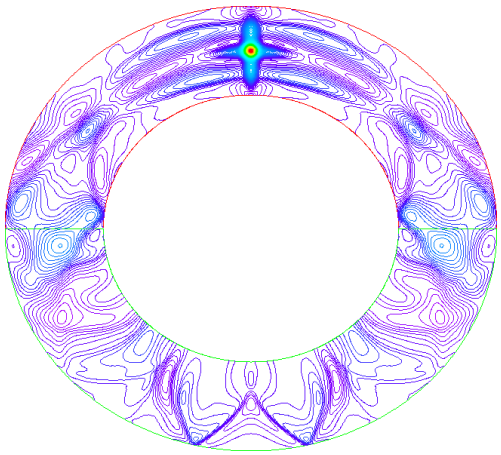

Figure 2: Same as in Fig. 1, but at t = 120 μs, maximum value = 39 MPa.

Fig. 2 presents pressure isolines at t = 120 μs that show the spread of the pressure waves in the entire target. The maximum value of pressure has been reduced to 39 MPa from an initial value of 200 MPa.

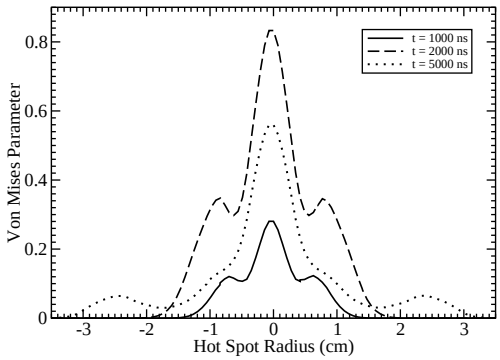

Figure 3: Von Mises Parameter at three different points (maximum value at t = 2000 ns).

In Fig. 3 we plot the corresponding von Mises parameter along the focal spot radius. It is seen that the maximum value achieved at t = 2 μs remains safely below 1 and therefore the material will remain elastic and the target will survive.

References

[1] N.A. tahir et al., Laser Part. Beams 26 (2008) 411

* Work supported by the BMBF and RFBR

Influence of Focal Spot Geometry on Stability of a Solid Graphite Super-FRS Production Target for a Fast Extraction Mode*

N.A. Tahir[1], V. Kim[2], A. Matveichev[2], A. Ostrik[2], A. Shutov[2], I.V. Lomonosov[2], A.R. Piriz[3], J.J. Lopez Cela[3], and D.H.H.Hoffmann[4]

[1]GSI, Darmstadt, Germany; [2]IPCP, Chernogolovka, Russia; [3]UCLM, Ciudad Real, Spain; [4]TU Darmstadt, Germany

The Super–FRS experiments will use highest intensities of the heaviest projectiles, namely, 5.0 $\times$ 10^{11} uranium ions delivered in a 50 ns long bunch. Survival of the production target over an extended period of time during this experimental campaign carried out at a repetition rate of 1 Hz, is a very important but difficult problem. One of the requirements necessary to achieve this goal is to keep the thermally induced material stress below a critical value so that the von Mises parameter remains less than 1 which implies that the target material remains in an elastic state. In this contribution we report 2D numerical simulations of interaction of a solid graphite cylindrical target that is irradiated with a 1 GeV/u uranium beam along the axis. The target radius is 5 cm while the beam intensity is 10^{10} ions per bunch with a bunch length of 50 ns. The main purpose of this work is to study the thermal stress generated by different focal spot geometries. We respectively consider a circular focal spot with σ = 1.69 mm and an elliptic focal spot with σ_X = 0.41 mm and σ_Y = 4.1 mm so that the focal spot area is the same in both cases.

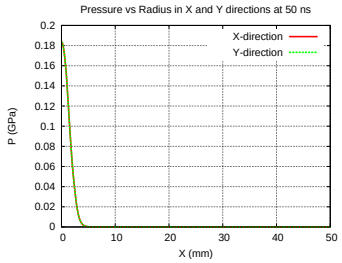

Figure 1: Pressure vs radius at 50 ns: circular spot.

In Fig. 1 we plot the pressure profile along radius in case of the circular focal spot at t = 50 ns, when the beam has just delivered its energy. It is seen that a maximum pressure of 180 MPa is generated at the target center.

The corresponding pressure profiles for the elliptic focal spot are shown in Fig. 2. It is seen that the maximum pressure in the two cases is the same, but the profile shapes are very different.

It is seen in Fig. 2 that the pressure gradient along the Y-direction is much steeper than that in Fig. 1. As a consequence, the stress level generated in the target irradiated with a perfectly circular focal spot is significantly less than that produced by an elliptic focal spot for the same specific energy. This is seen in Figs. 3 and 4 where we present the von Mises parameter in the two cases.

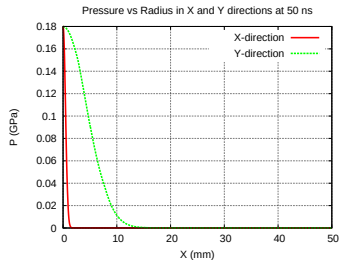

Figure 2: Pressure vs radius at 50 ns: elliptic spot.

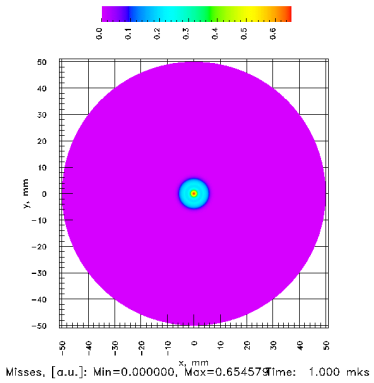

Figure 3: von Mises parameter: circular spot.

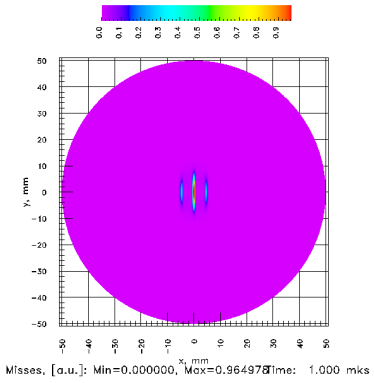

Figure 4: von Mises parameter: elliptic spot.

* Work supported by the BMBF and RFBR

Analysis of thermal stresses induced in the Super-FRS target in the fast-extraction regime *

C. Plate[1], R. Müller[1], B. Achenbach[2], K. H. Behr[2], A. Brünle[2], R. Catherall[3], F. Cerutti[3], H. Geissel[2], D. H. H. Hoffmann[1], A. Hug[1], Ch. Karagiannis[2], A. Kelić [2#], B. Kindler[2], M. Krause[2], M. Kulish[2], J. Lettry[3], B. Lommel[2], H. Richter[3], K. Suemmerer[2], N. Tahir[2], M. Tomut[24], Ch. Trautmann[2], S. Udrea[1], D. Varentsov[2], H. Weick[2], R. Wilfinger[3], M. Winkler[2]

[1]TU Darmstadt, Germany; [2]GSI, Darmstadt, Germany; [3] CERN, Geneva, Switzerland; [4]NIMP, Bucharest, Romania;;

In order to accommodate high intensities of fast-extracted primary beams that will be available at FAIR, new technologies for production targets at the projectile-fragment separator Super-FRS are mandatory. The key parameter for the stability of the target is the radial pressure induced by the beam – if this pressure is higher than the brittle-failure strength of the target material, the target will break even if the temperature stays below the melting or sublimation point. An experiment studying the impact of short high-intensity pulses of fast-extracted uranium beams on graphite [1] was analyzed and compared to finite-element (FE) calculations [2]. Here, a short overview of the obtained results is given.

Simulations

In Fig. 1, the measured time profile of the radial velocity is compared with the predictions of the finite-element model FEAP [3]. Two-dimensional simulations have been performed assuming axial symmetry. The case studied here corresponds to a ^{238}U beam at 350 *A*MeV, with a Gaussian time distribution (FWHM ≈ 300 ns), and a beam spot size of $\sigma_x = \sigma_y \approx 0.38$ mm; the intensity was $2.5 \cdot 10^9$ part/pulse. The first few oscillations in the measured surface-velocity profiles could be well reproduced by the calculations.

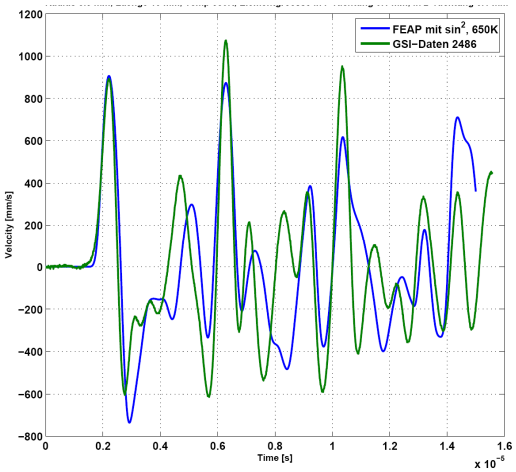

Figure 1: Calculated (blue) and measured (green) surface-velocity distribution of a graphite sample.

* Work supported by the European Community under the FP6 DESIGN STUDY (contract 515873 - DIRACsecondary-Beams).
#A.Kelic@gsi.de

For times larger than ~ 8μs, the simulated data start to deviate from the measured ones, due to the boundary conditions (e.g. sample support, or retro-reflective tape wrapped around the sample [1]), which were not considered in the present simulations.

In Fig. 2 are shown calculated tensile stresses (corresponding to the case considered in Fig. 1). According to the simulations, the largest stresses are created at the entrance and the exit point of the beam. The maximum values stay below 20 MPa which is well below the critical value for graphite of 60 MPa.

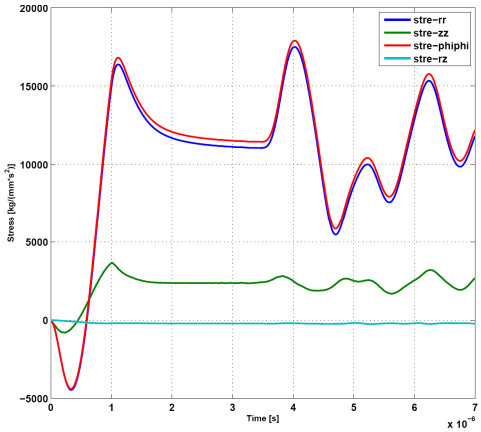

Figure 2: Time profile of the calculated tensile stress, corresponding to the case shown in Fig. 1.

The corresponding pressure peaks from the FEAP calculations were used to deduce the maximum target stress to be expected for fast-extracted FAIR uranium beams. These simulations have shown that Super-FRS graphite target can be operated with SIS100 design intensities, even in the fast-extraction operation mode. In order to stay within pressure limits that have already been tested at SIS18, for the SIS100 design intensity of $5 \cdot 10^{11}$ ^{238}U ions/pulse at 1 *A* GeV the beam spot has to be extended to $\sigma_x = 4$ mm and $\sigma_y = 6$ mm. As a consequence, the simulated transmission e.g. of ^{132}Sn into the collector ring will be reduced to approximately 65% compared to a beam with an ideal narrow spot size of ($\sigma_y = 2$mm).

References

[1] R. Wilfinger *et al*., GSI Scientific Report (2007) 75.
[2] A. Keliç *et al.*, this report.
[3] R.Chavan, Int. report, CRPP/EPFL-Lausanne 195/99.

Simulation Studies for p-Linac BPMs

P. Kowina[1], P. Forck[1], F. Wolfheimer[2], and T. Weiland[2]
[1]GSI, Darmstadt, Germany; [2]TU , Darmstadt, Germany

Motivation

The Beam Position Monitor (BPM) system presented in this contribution will be a part of the beam diagnostics for the new FAIR proton linac [1]. The CH accelerating cavities will be driven with a frequency of 325 MHz. A unique BPM type should be used for all 15 locations distributed over 30 meters of the p-Linac. The BPM design is challenging since the beam velocity varies along the p-Linac from $\beta = 0.08$ to $\beta = 0.37$ which strongly effects not only the BPM position sensitivity, but also the phase stability of the measured signal. Therefore, extensive numerical simulations were launched. A button type BPM geometry was chosen due to its compact mechanical realization and short insertion length to fit into the short inter-tank sections of the CH-cavities [2].

Simulation results

All numerical simulations were performed by means of CST PARTICLE STUDIO® [3] using the wake-field solver. As a source of excitation a pencil like beam was defined with a Gaussian-shaped longitudinal charge distribution. The length of bunches was $\sigma = 150$ ps corresponding to a bunch filling of 5 % at a frequency of 325 MHz. For the investigation of the position sensitivity, the position of the simulated beam was varied in 2 mm steps within the transverse plane in a range of ± 6 mm. The positions in vertical and horizontal direction were calculated from amplitudes of the signals induced in the opposite BPM electrodes using the 'delta over sum'-method (see. [4]). The response of the BPM was compared for the first three harmonics of the accelerating frequency, i.e. at 325 MHz, 650 MHz and 975 MHz. In Fig. 1 results obtained for $\beta = 0.3$ and $\beta = 0.1$ are shown. In the left part of the figure the nonlinearities of the position readings can be seen whereas the strength of distortions grows with the beam displacement. This is typical for button type BPMs and can be well

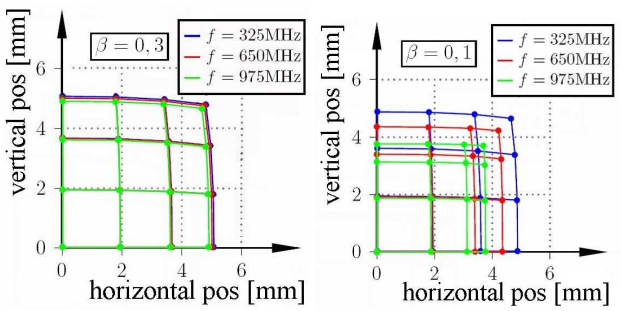

Figure 1: BPM response on variation of transverse beam position for $\beta = 0.3$ (left) and $\beta = 0.1$ (right). Due to its rotational symmetry only one BPM quarter is shown.

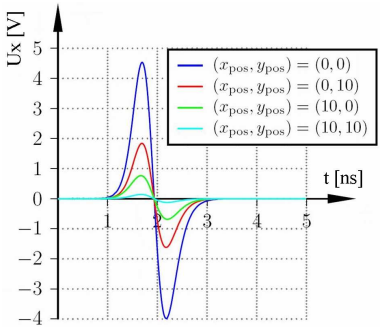

Figure 2: Signal induced in one BPM electrode for different transverse beam displacements.

described by a 2-dimensional analytical calculation of the proximity effect [5]. There is one additional effect that is more pronounced for slow beams with $\beta \leqslant 0.1$ (Fig. 1, right): Namely, the readings, especially for larger beam displacement, strongly depend on the evaluation frequency. For non relativistic beams the electromagnetic field propagation is much faster than the beam itself. Since the electric field distribution has a significant longitudinal component, the frequency composition of the signal induced in the BPM strongly depends on the distance between beam and BPM electrodes [5]. This has to be taken into account when installing BPMs in different locations along the p-Linac: for each location a separate table with the correction parameters specific for the given harmonic number and beam velocity have to be prepared.

The determination of beam energy can be performed using the time-of-flight (TOF) method i.e. by measuring the time duration the bunch needs to transverse a given distance as determined by two BPMs. Since the BPM signals are bipolar [5] usually the zero crossing is used for most precise time-of-flight determination. As mentioned above, the frequency spectrum of the signal strongly depends on the beam position. Therefore, the stability of the zero crossing as a function of beam position was investigated. As it can be seen in Fig. 2, although the signal amplitude varies by almost one order of magnitude, the zero crossing remains constant within 2 ps, corresponding to a phase stability of $0.2°$. However, it has to be kept in mind that such high accuracy has to be maintained by the signal processing and digitization which is presently in preparation.

References

[1] L. Groening et al., *Proc. LINAC06*, Knoxville (2006) p.186.
[2] "FAIR Baseline Technical Report", Vol. 2, GSI Darmstadt, Germany, 2006, p.335.
[3] www.cst.com
[4] P. Kowina et al., *Proc. DIPAC05*, Lyon (2005) p.114.
[5] P. Forck et al., *CAS "Beam Diagnostics"*, Dourdan (2008).

Prototype of a Novel DCCT for FAIR

A. Schlörit, H. Reeg
GSI, Darmstadt, Germany

Overview

The existing DCCT in the SIS18 is expected to not work correctly with the higher bunch current intensities in the prospective SIS100 [1]. This contribution gives a brief introduction to the prototype of the Novel DCCT for the SIS100, based on a GMR-sensor [2] and a split flux concentrator.

System Design

Figure 1 shows the preliminary system design. The magnetic field of the beam current I_S is concentrated with a slotted toroidal core. A sensor which detects the magnetic field in the air gap is read out by a differential preamplifier and filtered by a low pass. By a secondary winding, an AC transformer path is realized, and filtered by a high pass filter. Due to the concept of a flux compensated measurement system, the corrected and amplified signals compensate the magnetic field inside the toroid at a constant value, over an auxiliary winding. The voltage drop U_{out} across the resistor R_0 is proportional to the beam current I_S and the inverse number of the auxiliary winding.

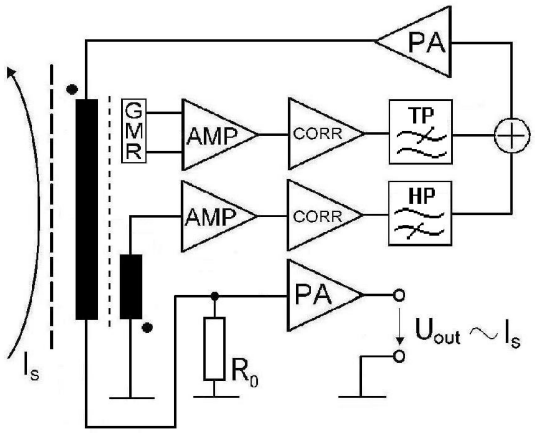

Fig. 1: Block diagram of the NDCCT.

Mechanical Construction

The mechanical design of the flux concentrator assembly is described in [3]. The concentrator is split into two parts, so the whole construction can be dismounted from the beam pipe during the bake-out process. The halves are fixed in a Mu-metal mounting frame to reduce external fileds. This frame can be adjusted in 3 dimensions. The sensor is fixated in the air gap of the split toroidal core.

Frequency behaviour of the GMR bridge

A magnetic field from DC to ~1 MHz is measured with a sensor based on the Giant Magnetic Resistance (GMR), type AA-0002 (Nonvolatile Electronics Co.). The sensor's frequency response was investigated up to 5MHz, using an amorphous laminated, and a ferrite material, at different premagnetization values respectively.

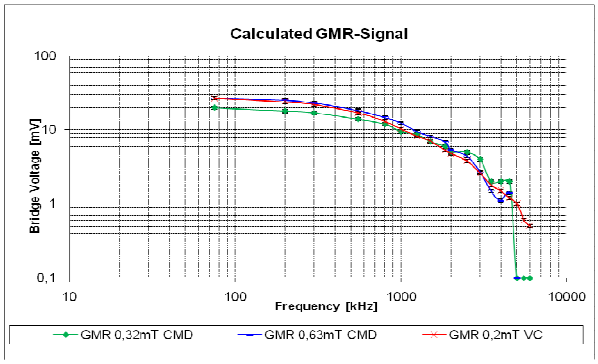

Fig. 2: GMR-Signal vs. frequency

It is evident that an inductive loop is spanned by the sensor IC's internal structures, whereby induced voltages falsify the GMR's frequency response.
Furthermore, the sensor bridge consists of 4 GMR elements, 2 of these buried under magnetic shields. The shielding efficiency decreases with rising frequency due to eddy currents in the NiFe-alloy. This in turn reduces the bridge's sensitivity. Fig. 2 shows the post processed GMR signal, exhibiting a -3 dB cut-off at 1 MHz.

Outlook

In a next step the measurement setup will be improved for operating frequencies above ~1 MHz. Applying a coaxial wave guide structure with a characteristic impedance of 50 Ohm and an outer diameter of 320 mm, a pulse excitation of the core/sensor device with fast rise-times will be possible, thus enabling the determination and optimization of the compensating loop parameters.

References

[1] H. Reeg „Performance Limitations of the DCCTs at GSI", CARE, Lyon, France 2004

[2] M. Häpe "Magnetische Strahlstrom-Messung hoher Dynamik mittels optimierter magnetoresistiver (MR) Sensortechnik im GSI-FAIR-Projekt", Final Report, University Kassel, 2007

[3] A. Schlörit „Entwurf, Auslegung und Aufbau von teilbaren, geschlitzten Flusskonzentratoren für Strahlstromsensorik", Diploma thesis, FH Wiesbaden, 2006

Magnetically Delayed Pseudospark Switch

B.J. Lee[1], I. Petzenhauser[2], U. Blell[2], M. Iberler[1], J. Jacoby[1] and K. Frank[3,]
[1]IAP, Univ. Frankfurt, [2]GSI, Darmstadt, Germany; [3]TexasTech University, Lubbock, U.S.A.

We have investigated the properties of a magnetically delayed pseudospark switch (PSS). One of the challenges of all low pressure gas discharge switches is the reduction of the lifetime due to commutation losses resulting in anode heating. This effect can be minimized by carefully dimensioning the saturating inductors. For many decades, this method has been successfully used for thyratrons. In principle, a saturating inductor prevents current flow until the end of the commutation phase. In contrast to thyratrons a PSS is based on a cold cathode electrode. To reach the low-resistive phase in a PSS, a significant current flow is necessary to allow self-heating of the cathode. A useful compromise has to be found to fulfill these opposing needs.

The test setup is shown in Figure 1. Different saturating inductors are connected in series with the PSS, on the anode side. Three different designs of the FINEMET (FT-3H) pulsed power core types were used. These cores use a thin ceramic insulation to provide a high break down voltage. The properties of the tested saturating inductors are summarized below.

Table 1: Properties of saturating inductors

Types	A	B	C
Inductance [µH]	50	250	350
ΔB_{max} [T]	1.7	1.7	1.7
ΔB_{min} [T]	0.8	0.8	0.8
μ_i	20000	30000	50000
Calculated Delay max./min. [ns]	62/29	213/100	213/100

The delay time is determined by Faraday's law with a voltage of 10 kV assuming that the voltage is linear with time.

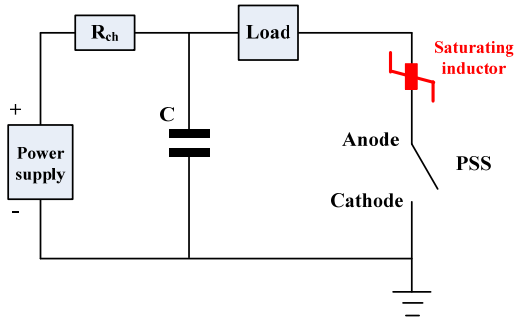

Figure 1: Test setup of the magnetically delayed PSS.

Since the impedance of the inducting cores is large, after closing the pseudospark switch, most of the voltage is present across the cores until they become saturated. As the cores become saturated, their impedance decreases drastically, allowing the discharging current to rise. Subsequently the current flow is delayed, minimizing the switching losses in the gas switch. As it can be seen in Table 1, there is a big difference between the maximum and the minimum delay we calculated. This would be unacceptable in most applications. The reason for the different values is that the cores were in an undefined state before the measurements depending on the previous experiments. To handle this problem, a reset system is needed, which pre-magnetizes the cores to a negative flux density before the pulse. Such a system was not available when the measurements were performed.

As shown in Figure 2, the commutation losses can be reduced by about a factor of six by the right choice of saturating inductors.

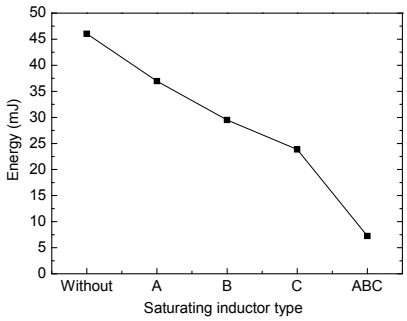

Figure 2: Commutation losses with different types of inductors.

In order to improve the lifetime of the switch by reducing commutation losses of a low pressure gas discharge switch, saturating inducting cores have been series integrated to pseudospark switch circuit. Two important results are observed. One is that the saturating inductor can be useful for the PSS in the same way it is useful for the thyratron switch. The other one is that in our setup the transition behaviour between the pseudospark discharge phases differs from its typical behaviour shown in [1]. This may lead to a better understanding of the physical properties of the pseudospark discharge. To investigate those physical phenomena, the optical investigation with fast shutter photography and some spectral observation will be required.

Further planned experiments of saturating inductors, including a reset-circuit, will be performed with a newly developed muti-gap pseudospark switch which is being tested at GSI and with a CX1671 thyratron.

References

[1] K. Frank et al."Spatial and time characteristics of high current, high voltage pseudospark discharges", IEEE Trans. Plas. Sci.,Vol. 25, No. 4, pp740-747, 1997.

Analysis of Several RF Control Loops using Control Theory Methods*

D. Lens[†1], H. Klingbeil[‡2], and J. Adamy[1]

[1]Technische Universität Darmstadt, Control Theory and Robotics Lab, Darmstadt, Germany; [2]GSI, Darmstadt, Germany

Overview

The possibilities of digital control systems for FAIR, based on digital signal processors (DSPs) and field programmable gate arrays (FPGAs), [1], raise questions concerning the optimal control algorithms for the RF control loops of heavy-ion synchrotrons. From a control theory point of view, the system comprising the RF cavity control loops and the longitudinal beam dynamics is a nonlinear and multivariable one. In order to to be able to damp the expected coherent longitudinal oscillation modes, the control algorithms should ensure stability of the RF system and the beam. Furthermore, they have to be efficient in means of computational time and deliver the control signals in a reasonable time.

In the scope of this work, two main scenarios are considered. In the following, an overview and the status of these projects is given.

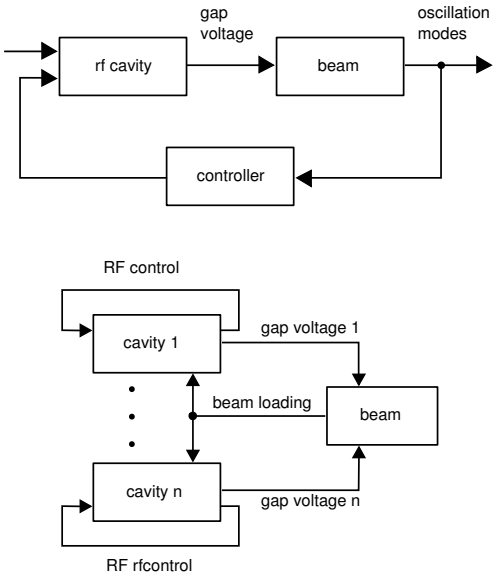

Figure 1: Longitudinal Feedback (top) and RF control for double-harmonic cavities (bottom).

Control of Coherent Longitudinal Modes

The principle of the Longitudinal Feedback system is shown schematically in figure 1 (top). Dipole, quadrupole and higher order modes are measured and fed back to the controller. The RF-cavity is used as an actuator to generate the appropriate corrections to the phase and the amplitude of the gap voltage. For the coherent dipole mode of oscillation, a controller design and implementation with experimental results was presented in [2]. In the scope of this project, a model was derived to enable a controller design for the quadrupole bunch mode, showing the dependencies of the input variables (amplitude and phase of the gap voltage) on the output variables (dipole and quadrupole mode) [3]. With this derivation the assumption could be confirmed that the quadrupol mode can be controlled and thus damped using the amplitude of the gap voltage and the dipole mode by adjusting the phase. Simulations were performed which were consistent with the analytic result. Currently, higher order modes are being analyzed.

RF Control for Double-Harmonic Cavities

As a second scenario, the RF control loops for a double-harmonic cavity system were investigated [4]. The cavity system which will be realized in the scope of the SIS18 upgrade program consists of a main broadband cavity and a second harmonic narrowband cavity. The cavities comprise both an amplitude and a phase feedback loop. In addition, the narrowband cavity includes a feedback loop which controls its resonance frequency to follow the main RF frequency. The beam acts back on each cavity via beam loading, as is shown in figure 1 (bottom). For high beam currents, the dynamics of the cavities depend on each other and the stability analysis has to consider the ensemble of cavities and beam. After modelling the system and the feedback loops, an analytic controller design was performed. Furthermore, longitudinal beam dynamics were added to the cavity system to allow a detailed simulation of the cavity-beam interaction. The results indicate that the acceleration of a beam with the planned beam intensity for FAIR is possible without beam loss.

References

[1] P. Zipf, et al., “Reconfigurable Computing Systems for Digital RF Closed-Loop Controls”, GSI Scientific Report 2006, p. 65, August 2007.

[2] H. Klingbeil, et al., “Digital Beam-Phase Control System for Heavy-Ion Synchrotrons”, IEEE Trans. on Nucl. Science, Vol. 54, No. 6, p. 2604-2610, December 2007.

[3] D. Lens, “Regelungstechnische Analyse verschiedener HF-/Strahlmanipulations-Regelkreise”, GSI Workshop FAIR-HF-Regelsysteme, Darmstadt, 13.03.2008.

[4] D. Lens, “Regelung von Kavitätensystemen unter Berücksichtigung von Strahleinflüssen”, TU Darmstadt, November 2008.

* Work partly supported by Deutsche Telekom Stiftung.

† dlens@rtr.tu-darmstadt.de

‡ h.klingbeil@gsi.de

Bipolar Power Supply for FAIR Emergency-Kicker

T. Wietoska TU Darmstadt, V. Hinrichsen TU Darmstadt, U. Blell GSI

For driving bipolar kicker-magnets you usually use circuits like in figure 1. This system has the disadvantage that two energy storage systems are required. In combination with long transfer cables it is extensive to get a low ripple, also the low-pass behaviour of the netwaork causes long rise times. The two connections of the kicker are both on high potential waht also can be problematic.

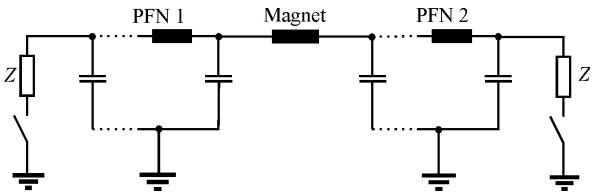

figure 1: conventional bipolar kicker drive unit

To work cost-effective by building the SIS100, a cicuit for driving bipolar kicker-magnets with only one energy-storage device was investigated. Such a circuit is shown in figure 2. The pulse-transformer transmits the pulse with selectable polarity and gives a insulation of the high potential. Only during the pulse the Kicker is on the high potential. This causes a much easier design of the bushing and the transfer cable.

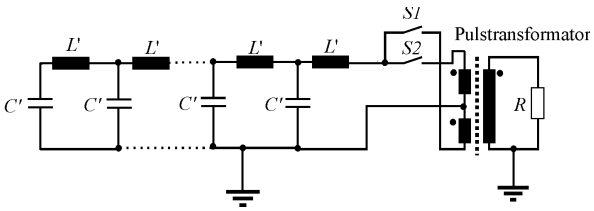

figure 2: bipolare kicker power-supply with pulse-transformer

In this configuration a complete isolation of primary and secondary side of the transformer is not needed, so instead of a three coil-transformer you can use a two coil autotransformer. This cost-saving configuration has the advantage that a positive pulse is not influenced by the pulse transformer (figure 3 top). In case of the emergency-kick (inverse polarity) the requirements are lower so it does not matter that the pulse is swayed a little bit by the transformer.
For further optimization of the circuit is a current-transformer layout of the circuit. For this circuit the pulse-transformer is connected behind the matching-resistor direct at the kicker-magnet (figure 3 bottom).

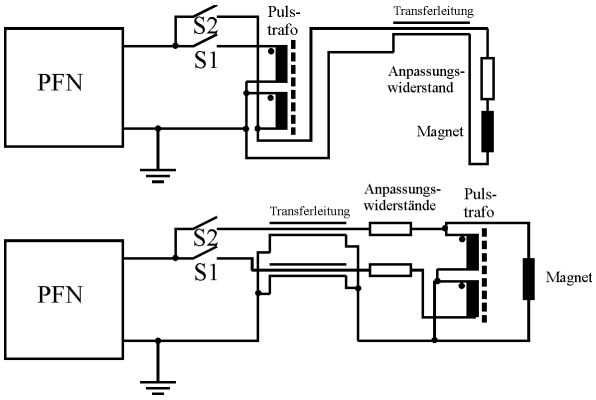

figure 3: circuit with autotransformer

In this circuit you have a much smaller voltage-time-area so the iron cross-section can be about 90 % smaller then by transfering the whole pulse in front of the matching-resistor. With this design you have lower stray-inductances in the transformer and the pulse quality is less influences by the transformer.
A low-voltage model of such a circuit was analyzed and the measurement results of a pulse with pulse-transformer and without faced to each other. The conclusion for a inverted pulse with a circuit like in figure 3 bottom is shown in figure 4. The results corroborate the qualification for the application at SIS100 and the company PPT in Dortmund calculates a offer for such a system.

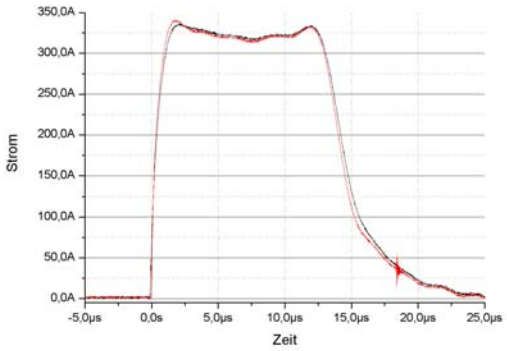

figure 4: inverted pulse (black) and pulse without transformer (red)

References

[1] T. Wietoska, Dissertation 2008

[2] GSI: Parameterliste SIS 100/300, U.Blell 25.10.2007

Development of a high voltage sealed of gas discharge switch

M. Iberler, K. Esser, A. Fedjuschenko, J. Jacoby, B.-J. Lee, J. Otto, T. Rienecker, J. Wiechula
Goethe University Frankfurt, Institut für Angewandte Physik, 60438 Frankfurt.

High voltage multi-gap gas discharge switches are very important tools for pulsed power applications in accelerator laboratories. They have applications for example in driving fast injection- and extraction magnets and beam dumps.

Basically, there are two different principles used to realise a high voltage switch. One is based on the use of several semiconductor switches, and the other is based on a triggered breakdown in gases or in vacuum. We introduce in this report a new type of high voltage gas discharge switch, which consists of multi-gap coaxial electrode geometry. Initially the inner electrode serves as anode, the outer electrodes as voltage divider for the applied high voltage. This switching device is called, based on its underlying effect, a multi-gap Lorentz Drift Switch (multi-gap LDS). For the initial investigations a two-gap LDS was designed (Fig.1).

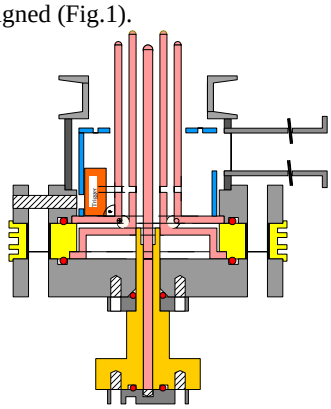

Figure 1: Schematic drawing of a two gap Lorentz Drift Switch.

The designed two-gap LDS is a low inductive, fast current, low pressure gas discharge switch, which functions on the left side of a Paschen voltage breakdown curve. The Lorentz force which interacts with the discharge is given by:

$$\vec{F} = \int dV\, J \times B \qquad (1)$$

Due to the magneto hydrodynamic motion mainly at the inner electrode gap the LDS has low electrode erosion and therefore a long lifetime [1].

By external triggering, a gas breakdown is initiated at the outer electrodes and forms a conductive plasma sheath and penetrates through holes to the inner electrodes.

During the trigger phase the ignition of the discharge occurs over the long distances of the radial cathode back space [2]. As a trigger we have used a semiconductor surface trigger [3]. For the experimental set-up one high voltage capacitor of 2.6 nF for each gap was used. Argon gas was used. The working pressure was adjusted between 10^{-3} mbar and 1 bar.

*Work supported by GSI, Darmstadt under contract F&E

For the first investigations the breakdown voltages depend on the product of the pressure and electrode distance of the two-gap LDS was measured. Figure 2 shows the voltage breakdown curve depending on the pressure which is similar to the characteristic of a Paschen branch. For low pressures in the range of several 10^{-2} mbar the breakdown voltage was increasing to a value of 30kV. The limitation of the achieved voltage was given by the experimental set-up, especially by the power supply. The maximum voltage drop for the switch was in the range of 0.25kV/ns.

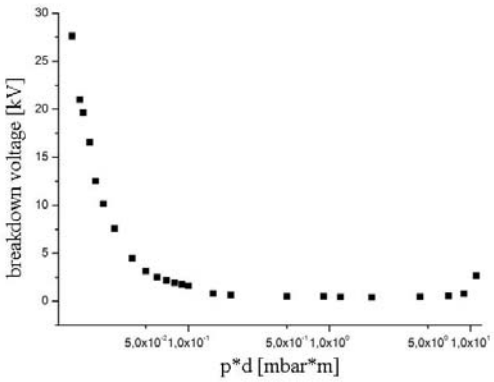

Figure 2: Breakdown voltage of the two-gap switch depending on the voltage.

For the future it is planed to develop a two stage sealed off LDS, which also requires the expertise of bake out and gas filling process. For this reason a bake out and gas filling system is on the University Frankfurt available. This experience we now possess we got by recycling three stage Thyratrons. For the next experiments it is also planned to develop a three stage LDS prototype to upgrade to voltages higher than 70kV.

References

[1] J. Jacoby, C. Bickes, D.H.H. Hoffmann, C. Hofmann, J. Philipps, Experimental Study to Accumulate, Accelerate and Focus a Massive Plasma Beam onto a Target Fusion Engineering and Design 44 (1999) 331.

[2] A. Görtler, “Untersuchungen von gepulsten Oberflächenentladungen an Dielektrika und deren Anwendung zur Triggerung eines Pseudofunkenschalters”, Diplomarbeit, Universität Erlangen-Nürnberg (1986).

[3] M. Iberler, R. Bischoff, K. Frank, I. Petzenhauser, A. Rainer, J. Urban, Fundamental investigation in two flashover-based trigger methods for low-pressure gas discharge switches, IEEE on Plasma Science, Vol 32 (1), 208-214, 2004.

Monte-Carlo Simulations for the Shielding of CR and RESR

A. Knapp, G. Fehrenbacher, T. Radon, K. Vogt
GSI, Darmstadt, Germany

In the following paper the concrete shielding for the CR and RESR is presented on the basis of several Monte-Carlo simulations for radiation transport with the FLUKA code [1].

CR and RESR

Two important storage rings of FAIR are the CR and the RESR, which are located together in the same building. The CR has to fulfill the following tasks: stochastic pre-cooling of antiprotons from the antiproton target at a fixed energy of 3 GeV and stochastic pre-cooling of secondary rare isotope beams from the Super-FRS at the energy of 740 MeV/u. The RESR accumulates the pre-cooled antiprotons, which can then be delivered to the HESR or the NESR. Figure 1 shows the shielding layout of the building including the two beamlines, 4 mazes, the transfer channel to the HESR (left corner) and the technical supplies room, which is inside the CR.

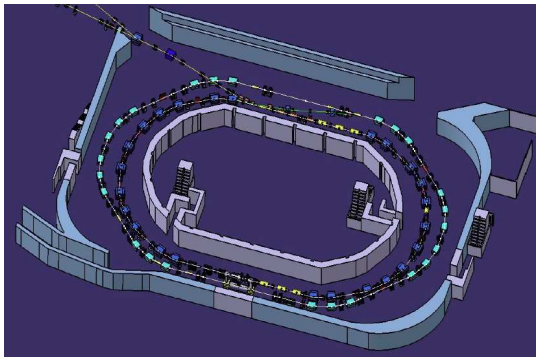

Figure 1: Sketch of the CR/RESR building, from [2].

Calculations

If the area outside the building and inside the CR (the technical supplies room) is to be freely accessible to the staff, a dose rate below 0.5 µSv/h must be ensured. GSI sets this dose rate as limit for the technical supplies room and the areas outside the building. All simulations were performed using the Monte-Carlo code FLUKA [3,4].

Due to the large shielding thickness of up to 3.75 m region importance weighting was applied for variance reduction. For all calculations a pencil-like beam was used, the beam losses occur mostly in the magnets, which are located in the arcs. The simulations are full 3D calculations, however the following plot (figure 2) shows a horizontal cut, which means the reader sees the horizontal dose rate distribution in the bird's eye view.

Results

Figure 2 displays the dose rate plot according to the following scenario: Normal beam operation of heavy ions in the CR: Uranium-238 beam, energy of 740 MeV/u and a total beam loss of 10^8 per second. Overall the design is quite good, but a closer look reveals weak points in the shielding. We find a dose rate near the arcs inside the technical room and near the mazes of up to 5 µSv per hour, which is too high according to the design goal.

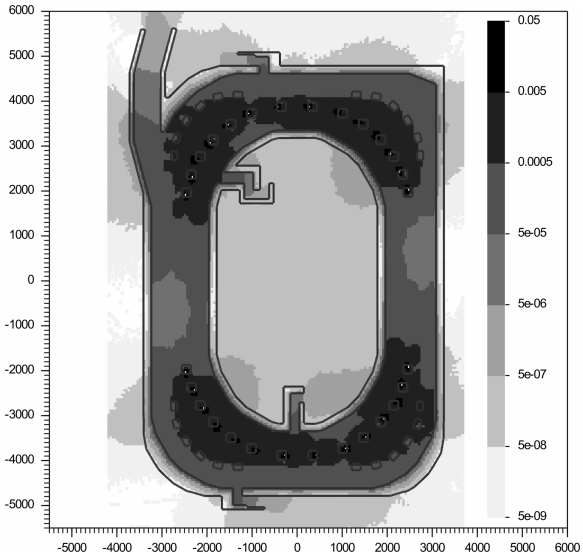

Figure 2: Dose rate plot of the CR/RESR building; the unit of the dose rate is Sv/h. The continuous beam loss is represented by 28 discrete beam loss positions. The unit of the horizontal and the vertical axis is cm.

The proposed improvements of the shielding are an increase of shielding thickness at the extraction to the HESR and near the inner arcs as well as a redesign of the mazes to reduce the number of scattered particles. These improvements are already partially included in the latest layout, however due to other modifications which were necessary the final layout needs to be calculated again.

References

[1] More information about this Monte-Carlo code can be found in http://www.fluka.org

[2] http://www-win.gsi.de/FAIR-EOI/PDF/TDR_PDF/TDR_RESR.pdf

[3] A. Fassò, A. Ferrari, J. Ranft, and P.R. Sala, "FLUKA: a multi-particle transport code", CERN Yellow Report (2005), INFN/TC_05/11, SLAC-R-773

[4] "The FLUKA code: Description and benchmarking" G. Battistoni, S. Muraro, P.R. Sala, F. Cerutti, A. Ferrari, S. Roesler, A. Fassò, J. Ranft, Proceedings of the Hadronic Shower Simulation Workshop 2006, Fermilab 6-8 September 2006, M. Albrow, R. Raja eds., AIP Conference Proceeding 896, 31-49, (2007)

Soil Activation Studies for the FAIR Project

K. Vogt, G. Fehrenbacher, and M. Haida
GSI, Darmstadt, Germany

For the planning of the shielding of the new FAIR accelerator facilities, as well as for the governmental approval procedures, we need to study the amount of radioactivity induced by the operation of the new accelerators in the soil surrounding the beam tunnels and especially in the groundwater. The latter is particularly important because radiation exposure to the general population can be caused by radioactive nuclei that are produced in the soil, then migrate to groundwater and subsequently are transported to inhabited areas.

Method

As a first step, soil activation experiments have been performed in order to get a rough estimate of the nuclides that will be produced in soil (see [1]). These experiments also served as a test for the accuracy of the Monte-Carlo code FLUKA [2] that is used for the estimation of the activity produced around the SIS100/300. Comparison between calculations and the measurements showed in general quite good agreement. In a second step the induced radioactivity around the beam tunnel of the planned SIS 100/300 accelerator ring was calculated.

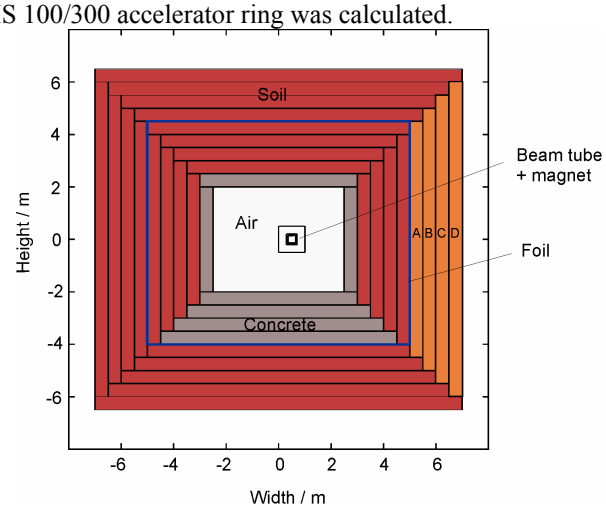

Figure 1: Input geometry for the FLUKA calculations

The input geometry used for the FLUKA calculations (see Fig. 1) is a straight rectangular tube. The walls and the surrounding soil were composed from layers with thicknesses of 50 cm. In order to prevent the radioactive nuclei produced around the tunnel walls from migrating to the groundwater, it was planned to insert a foil into the soil in a distance of 2 m around the tunnel walls, so that only the activation in the soil layers outside of the foil needed to be considered. For this calculation we assumed that all beam losses occur at the right side in Fig. 4. In the following we only considered the 4 layers marked with A, B, C and D because in this scenario they will have the highest activity concentrations. The calculations were performed for a ^{238}U beam with E=2.7 GeV/u, an intensity of 10^{12} / s and a total beam loss of 10% per second.

Results

In order to estimate the radiation exposure resulting from soil activation and subsequent ground water migration, several other aspects were investigated in addition to the actual activation, specifically the migration to groundwater (see Ref. 3), decay during transportation, and dilution within the groundwater.

Nuclide	**Half-live**	**irradiation- / decay-time**		
		10 a / 100 d	**10 a / 10 a**	**50 a / 10 a**
H-3	12.3 a	0.0174	0.0101	0.0221
Be-7	53.3 d	0.00565		
C-14	5730 a	$5.80 \cdot 10^{-4}$	$2.45 \cdot 10^{-4}$	$1.22 \cdot 10^{-3}$
Na-22	2.6 a	0.0560	0.00419	0.00450
Mn-54	312.2 d	$1.44 \cdot 10^{-3}$		
Fe-55	2.73 a	$5.25 \cdot 10^{-5}$	$4.42 \cdot 10^{-6}$	$4.82 \cdot 10^{-6}$
Co-60	5.27 a	$5.03 \cdot 10^{-5}$	$1.40 \cdot 10^{-5}$	$1.92 \cdot 10^{-5}$
Cs-134	2.06 a	$1.78 \cdot 10^{-5}$		
Eu-152	13.3 a	$6.49 \cdot 10^{-5}$	$3.94 \cdot 10^{-5}$	$9.07 \cdot 10^{-5}$
Sum		**0.0822**	**0.0146**	**0.0279**

Table 1: Specific activities in groundwater in units of the legal limits (StrlSchV Appendix VII, Table 4)

The resulting normalized activity concentrations of the most relevant nuclides are given in Table 2 for three different combinations of irradiation and decay times. For an estimate of the maximum real activity concentration, the last column with 50 years irradiation time and 10 years decay seems to be the most realistic scenario since the transportation time out of the FAIR facility will be about 5-15 years, and the total operating life of FAIR will be at the order of several decades. The last row of Table 2 gives the sum of the normalized activity concentrations for all nuclides. The value is far below 1 which means that the activity stays well below the legal limits.

References

[1] K. Vogt, M. Haida, and G. Fehrenbacher, GSI Scientific Report 2007, p. 249
[2] FLUKA: http://www.fluka.org
[3] X. Lin, Ch. Lierse von Gostomski, "Untersuchungen zur Freisetzung von Radionukliden aus Bodenproben in das Grundwasser", Lehrstuhl für Radiochemie, TU München.

Accelerator Operation Report

U. Scheeler, D. Wilms
GSI, Darmstadt Germany.

This report describes the operation statistics of the GSI accelerator facility in the year 2008. The presented information is based on the data of the GSI electronic operation logbook OLOG [1] which allows a detailed evaluation of operation statistics especially for the time-sharing operation mode of the accelerators.

General overview

From January till October 2008 four beam time periods were scheduled. Within the first block only beam for UNILAC experiments was provided. Altogether the SIS has been operated for 4712 hours and the UNILAC for 6272 hours, whereas beam for experiments was provided for 5968 hours and 304 hours were used for the commissioning of the accelerator after shutdown.

Two major activities were performed during the shutdowns. A new injection section in the SIS was installed and commissioned. The long break from October to December was used to organise an extensive maintenance of the first Alvarez cavity and the installation of new power supplies in this section.

In table 1 the total beam time of the whole facility is shown. Due to time sharing operation this number is higher than the 5968 hours operation time, used to provide beam for experiments.

Table 1: Overall beam time of the accelerator facility

	2008	2007
Integral target time for all experiments	**10123h**	11064 h
Time for retuning	**98 h**	90 h
Time of interruption	**2312 h**	2584 h
Total beam time	**12533 h**	13738 h

Altogether 10123 hours of beam-on-target-time was successfully delivered to the different physics experiments, especially ^{64}Ni for the SHIP Program and ^{36}S for Nuclear Chemistry Experiments, different Xe-isotopes to the FRS and protons to Hades. This amount of total target time is about 940 hours lower compared to 2007. The category 'retuning' shows the time necessary to improve the beam performance during the running experiment. The 'time of interruption' covers the categories ‘accelerator setup’ (898 h), ‘ion source service’ (273 h) and ‘unscheduled down time’ (1141 h). These are all events which lead to a break of the running beam for the corresponding experiment (for details see table 2 and table 3).

The ratio between target time and total beam time (availability of the facility) remained constant at 81% compared to 2007. The observed decrease of this key figure in 2007 has stopped. Nevertheless a long-term schedule of maintenance and service for the unreliable or old subsystems of the accelerator has to be organised.

Figure 1 displays the fraction of target time for each experimental program. The details corresponding to UNILAC and SIS beams are given in the next two sections.

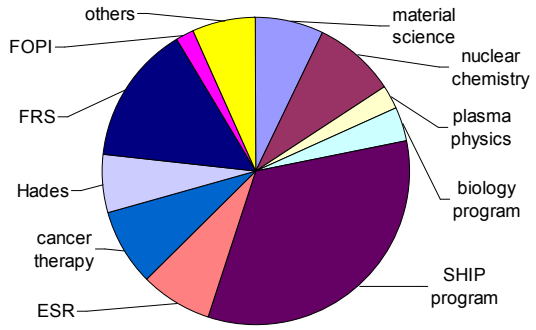

Figure 1: Distribution of target time to the different experiments.

UNILAC experiments

The beam time for the UNILAC experiments is shown in table 2. Altogether 14 different experiments were performed at the UNILAC with 5475 hours of target time. The target time was increased compared to the value of the year 2007 (4896 hours). The sharing of the beam to the different experiments is shown in figure 1. Main users of the UNILAC beam were the SHIP Program (3516 hours), Nuclear Chemistry Experiments (894 hours) and Materials Science (682 hours).

	Time	Fraction
Target time for experiments	5475 h	83,7%
Time for retuning	47 h	0,7%
Accelerator setup	357 h	5,5%
Ion source service	173 h	2,7%
Unscheduled down time	484 h	7,4%
Total beam time	6536 h	100%

Table 2: Beam delivered to UNILAC experiments.

SIS experiments

The heavy ion synchrotron has delivered beams to 24 fixed target experiments and to 6 experiments at the ESR.

The overall beam time of the SIS is shown in table 3. Altogether 4648 hours of target time have been achieved.

The distribution of the beam to different experiments is shown in figure 1. In 2008 the target time for cancer therapy was about 800 hours, 2 beam blocks were performed and this program ended up in this year. The target time for ESR (direct beam and beam via FRS) remained constant at about 1080 hours. For about 1567 hours beam was delivered to the FRS and for about 646 hours to the HADES experiment. The summary is given in table3.

	Time	Ratio
Target time for experiments	4648 h	77,5%
Time for retuning	52 h	0,9%
Accelerator setup	541 h	9,0%
Ion source service	99 h	1,7%
Unscheduled down time	657 h	11,0%
Total beam time	5997 h	100%

Table 3: Beam delivered to SIS/ESR experiments.

Accelerator operation

Figure 2 shows the total beam time for all accelerated isotopes during 2008. Over the year 18 different isotopes have been accelerated. The rare isotopes (^{6}Li, ^{36}S, ^{48}Ca, ^{64}Ni) were produced by the ECR ion source, which has been operated for 5349 h. This beam was mainly provided to UNILAC experiments. The Penning ion source was mainly used for ^{40}Ar, ^{22}Ne, ^{197}Au, and ^{58}Ni (in total 2550 hours). The high-current ion source operation lasted for 4887 hours. Especially ^{40}Ar, ^{124}Xe and proton beams were delivered from the MUCIS ion source. ^{238}U was accelerated from the MEVVA ion source for 972 hours.

	break down	No. of events
Power supplies	566 h	395
Vacuum and structures	130 h	70
Beam diagnostics	78 h	37
Operation	10 h	8
Safety-/ Interlock system	34 h	32
Ion Sources	278	138
RF system	252 h	450
Controls	67 h	54
Infrastructure	33 h	23
Others /	106 h	49
Total of unscheduled down time	1555 h	1258

Table 4: Statistics of all unscheduled down time events

In table 4 all unscheduled down time events are shown in more detail. Compared to 2007 about 500 hours more of down time events was recorded. Problems with power supplies and rf systems have been increased and provide about one half of the total unscheduled down time. A considerable number of the breakdowns were age related. This fact has to be considered for maintenance scheduling. A failure of the injection septum of SIS was the major breakdown event of this year. The repair of the fault and the following baking of the vacuum section lasted for about 12 days. By adapting the beam time schedule or by applying a different machine setup not all down time events led to an interruption of the experiment beams.

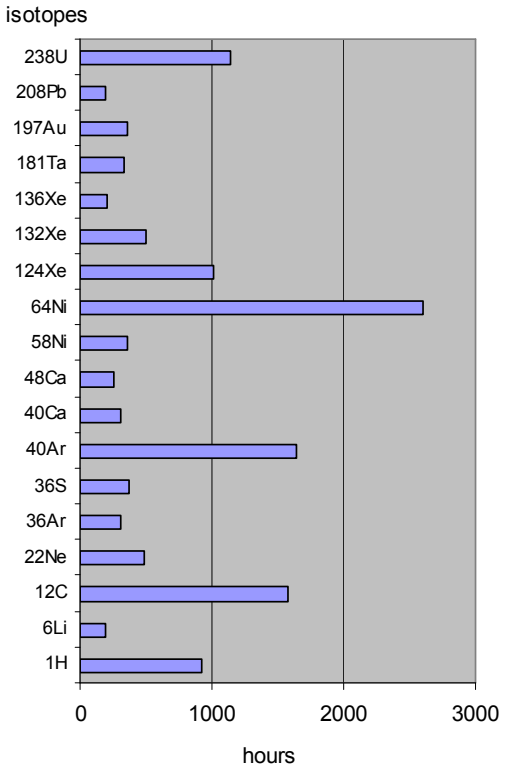

Figure 2: Total beam time for all different ion species.

In 2008 slightly more time for accelerator experiments were scheduled. Main topic was the improvement of High current operation to reach the FAIR injection parameters, the details are discussed in dedicated machine reports [2],[3]. At the UNILAC 191 hours and at ESR 136 hours beam were delivered. However for SIS the number dropped to 103 hours, because accelerator experiments had to be cancelled due to the above mentioned break down of the injection septum.

References

[1] OLOG GSI operation logbook
[2] W. Barth et al., UNILAC Status and Developments, see this GSI Annual Report
[3] P.Spiller et al., SIS 18 Status Report, see this GSI Annual Report

Ion Source Development and Operation

P. Spädtke, B. Gutermuth, F. Heymach, R. Hollinger, R. Lang, J. Mäder, K. Ochs, J. Roßbach, P. Schäffer, S. Schäffer, M. Stork, K. Tinschert, and C. Vierheller
GSI, Darmstadt, Germany

Two injector beam lines with up to three different ion sources (IS) are used to feed the accelerator simultaneously: the High Charge State Injector (HLI), equipped with a 14.5 GHz ECR Ion Source (ECRIS) of CAPRICE type [1], and the High Current Injector (HSI), equipped with two IS platforms. One is exclusively working with Penning IS [2], while the second one is dedicated to low duty cycle operation with one of the high-current IS MUCIS [3], CHORDIS [4], MEVVA [5], or VARIS [6].

ECR Ion Sources

Regular operation at the HLI was performed for the ion species listed in the table below:

Table 1: Ion beams delivered from the HLI in 2008.

Ion species	Auxiliary gas	Duration (days)	Analyzed intensity (eμA)
$^{6}Li^{+}$	He	5	30
$^{12}C^{2+}$	O_2	69	60 - 70
$^{36}S^{5+}$	O_2	17	70
$^{36}Ar^{7+}$	O_2	7	70
$^{48}Ca^{10+}$	He	48	70 - 80
$^{64}Ni^{9+}$	He	109	50
$^{136}Xe^{18+}$	O_2	9	40

In spring and in summer 2008 the last two blocks of beam time were provided for the cancer therapy program at GSI delivering $^{12}C^{2+}$ ions to the accelerator as it has been a standard procedure for more than 10 years now.

The vast majority of the beam time in 2008 served by the ECRIS at the HLI was dedicated to the research on Super Heavy Elements (SHE). Beams of $^{64}Ni^{9+}$, $^{36}S^{5+}$, $^{36}Ar^{7+}$, and $^{48}Ca^{10+}$, respectively, were shared between SHIP and experiments on nuclear chemistry. Furthermore, a beam of $^{6}Li^{+}$ was produced for an experiment at the SIS, and $^{136}Xe^{18+}$ was delivered to the local experimental area at the HLI.

Besides ^{12}C all ion beams were produced from highly enriched isotope materials which are transformed into ion beam with high efficiency and with low material consumption in the ECRIS.

According to the procedure of converting highly enriched (80 %) elementary ^{34}S to $^{34}SO_2$ [7] further sample material of ^{34}S and ^{36}S with an enrichment of 99 % has been converted in order to obtain highest efficiency of beam production [8].

$^{36}SO_2$ was used for the first time to provide an accelerator beam time delivering $^{36}S^{5+}$ for 17 days. Up to 70 eμA of $^{36}S^{5+}$ could be obtained. Fig. 1 shows a corresponding charge state spectrum of the analyzed ion beam. The average material consumption could be determined to be 420 μg of ^{36}S per hour which is an improvement with respect to the test run with ^{34}S in 2007. This corresponds to an efficiency of 23 % for the transformation of ^{36}S into ion beam distributed in the charge states 2+...8+. 4 % of the material are analyzed as ions of the requested charge state $^{36}S^{5+}$. The ion beam stability was excellent, deviations typically did not exceed $\pm$ 3 % of the nominal intensity.

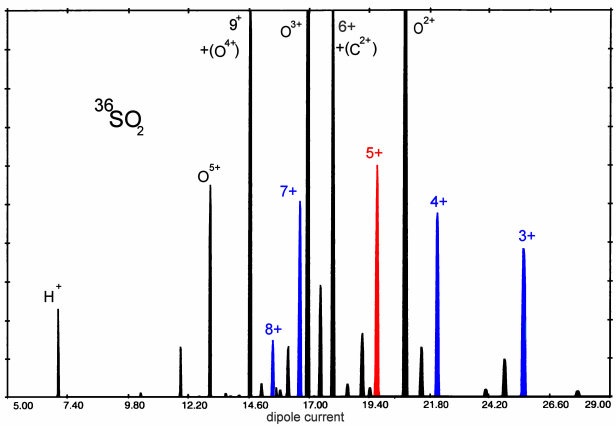

Figure 1: Charge state spectrum of the analyzed ion beam (^{36}S with mixing gas ^{16}O); full vertical scale: 100 eμA, horizontal scale: dipole current in A.

In the preceding year the ECR ion source injector setup (EIS) used as a test stand for ECRIS development had been prepared for the installation of the prototype of the fully superconducting MSECRIS operating at 28 GHz [9]. As the MSECRIS is not yet available because of technical problems, it was decided to provide an adaptation of the new mechanical support system in order to handle both ECRIS, either MSECRIS, or GSI's conventional ECRIS CAPRICE. First preparations have been performed for the reinstallation of CAPRICE. Furthermore, the implementation of cooling plates and shielding tubes into the beam line has been started to upgrade its cooling capacities in order to handle an increased power dissipation of intense ion beams. This includes modified or new beam diagnostic tools as well as an additional cooling shield for the vac-

uum chamber of the dipole spectrometer which provides the separation of the ion beam components.

High Current IS and Penning IS

Both terminals, for the high current IS as well as for the PIG IS, have been equipped with a new air circulation system to provide a lower air pressure inside the Faraday rooms, compared to the surrounding building. This modification was made to reduce the risk of contamination in case of any pollution of the building by an accidental event with an ion source. The system has been taken into operation without any problem.

Different ion sources were used for the required elements, see table 2 and 3, the Penning IS has been used for the following isotopes:

Table 2: PIG ion beams delivered from the HSI in 2008.

Ion species	Auxiliary gas	Duration (days)	Analyzed intensity (eμA)
$^{20}Ne^{1+}$	—	3	200
$^{22}Ne^{1+}$	—	14	200
$^{40}Ca^{3+}$	Ne	11	50
$^{58}Ni^{3+}$	Ar	15	200
$^{181}Ta^{7+}$	Ar	6	
$^{197}Au^{8+}$	Ar	9	20
$^{208}Pb^{9+}$	Ar	8	20
$^{238}U^{10+}$	Ar	24	50

Depending on the specific experimental requirements, the PIG IS can be operated with different duty cycles for the discharge. For lower duty cycle, usually higher particle intensities can be obtained. Further development work will be necessary to further improve the PIG IS for both operating modes.

The high current sources MUCIS (for gas ions) and MEVVA (for metal ions) have been operated for the following isotopes:

The housing of the single gap acceleration column for both Faraday rooms, separating the high voltage platform from ground potential, are in use since the very beginning of GSI [10] and have to be replaced. As the required maximum voltage was reduced from 320 kV to 130 kV when the Wideroe structure was replaced by a RFQ, it was decided to redesign this important ion optical element. Both designs are shown in Fig. 2. The required length has been minimized to reduce both the distance from the extraction system to the acceleration column as well as the distance from the column to the next optical element resulting in an increased acceptance. All internal electrodes are exchangeable for a final optimization with different electrode shaping. As in the present the electrode distance is remotely controlled. The column will be tested at the HOSTI test bench in the next year.

Table 3: High current ion beams delivered from the HSI in 2008.

Ion species	Auxiliary gas	Duration (days)	Analyzed intensity (emA)
$^{1}H_3^{1+}$	—	32	0.5
$^{36}Ar^{1+}$	—	6	15
$^{40}Ar^{1+}$	—	30	15
$^{58}Ni^{2+}$	—	17	4
$^{124}Xe^{3+}$	—	48	3
$^{132}Xe^{3+}$	—	19	0.5
$^{181}Ta^{3+}$	—	3	8
$^{238}U^{4+}$	—	38	15

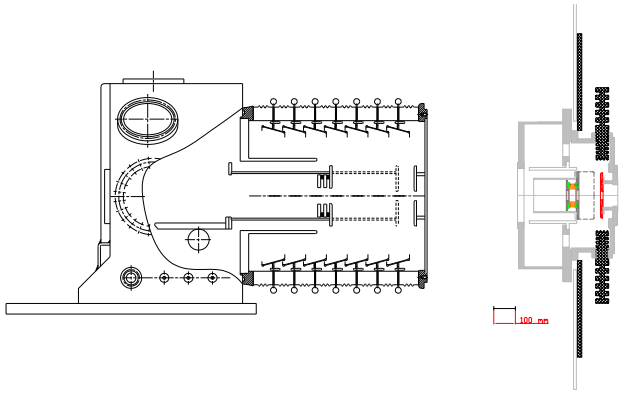

Figure 2: Old acceleration column design (left) and new design (right) showing the decreased required space. Beam direction from right to left.

References

[1] K. Tinschert, J. Boßler, S. Schennach, H. Schulte, Rev. Sci. Instrum. 69, 709 (1998).

[2] H. Schulte, W. Jacoby, B. H. Wolf, IEEE Trans. Nucl. Sci. 23, 1042, 1976

[3] R. Keller, K.-N. Leung, GSI Sientific Report 1987, GSI 88-1, 360

[4] R. Keller, P. Spädtke, H. Emig, Vacuum 36, 833(1986)

[5] B. H. Wolf, H. Emig, D. Rück, P. Spädtke, Rev. Sci. Instrum. 65 (10), (1994), 3091

[6] R. Hollinger, M. Galonska, P. Spädtke, Rev. Sci. Instrum. 75 (5), (2004), 1595

[7] P. Spädtke et al., GSI Sientific Report 2007, GSI Report 2008-1, 83

[8] K. Tinschert, R. Lang, J. Mäder, J. Roßbach, P. Spädtke, A. Yakushev, Proc. 18^{th} Int. Workshop on ECR Ion Sources, Chicago, 2008 (in print)

[9] K. Tinschert et al., GSI Sientific Report 2007, GSI Report 2008-1, 85

[10] P. Spädtke, GSI Report 83-9, 1983

UNILAC Status and Developments

W. Barth, L. Dahl, P. Gerhard, L. Groening, M. Maier, S. Mickat, M.S. Kaiser, H. Vormann, S. Yaramishev, GSI, Darmstadt, Germany

Status of Operation

For the treatment of patients a carbon beam from the Electron Cyclotron Resonance (ECR) ion source was accelerated via the high charge state injector (HLI) in the UNILAC for the SIS-injection (8 weeks) [1]. Additionally UNILAC experiments used the beam with a duty factor of up to 30 %. Furthermore the ECR source was in operation for the production of various isotopes (^{6}Li, ^{36}Ar, ^{36}S, ^{48}Ca, ^{64}Ni) as well. During a nine weeks block at the beginning of 2008 and a six week block in autumn a nickel beam was delivered to supply experiments for the Super Heavy Element synthesis (SHE). Besides a ^{48}Ca beam was used for one week by SHIPTRAP and two weeks of ^{36}S for nuclear chemistry experiments. Ion beams from the ECR (^{6}Li, ^{64}Ni) were also injected into the SIS 18 (for ESR-experiments). The Penning (PIG) ion source provided ^{20}Ne, ^{22}Ne, ^{40}Ca, ^{58}Ni, ^{197}Au and ^{208}Pb beams with medium intensity, especially while the ECR was used for the irradiation of patients. Mainly heavy ion beams (^{58}Ni, ^{197}Au, ^{238}U) from the PIG source were accelerated via High Current Injector (HSI) in the UNILAC with short pulses for the injection into the SIS 18. In addition, the beams were delivered especially for material research (heavy ions) and nuclear chemistry (^{22}Ne) experiments in the experimental hall. The MUlti Cusp Ion Source (MUCIS) provided high-current beams for different high-energy experiments with high intensities (H_2, ^{36}Ar, ^{40}Ar, ^{124}Xe, ^{132}Xe). The Metal Vapour Vacuum Arc (MEVVA) ion source delivered ^{181}Ta and ^{238}U for SIS-injection. Only two weeks the UNILAC was in operation for uranium machine studies as well as for regular uranium beam experiments. Machine experiments in preparation for the UNILAC as an injector for FAIR were performed with tantalum beams (medium intensity) and with high current argon beams. During shutdown time stronger power supplies for the Alvarez 1 inner tank quadrupoles were installed, enabling stronger beam focussing. The Alvarez tank revision program started in the winter shutdown with tank no. 1. Furthermore the connection to the new experimental branch for material science was integrated. In general the UNILAC operated with high reliability. [1]

Machine Experiments

Within three beam time blocks machine experiments in the UNILAC section were performed. In May high intensity Uranium beams could be used to investigate beam matching to the poststripper and to improve the UNILAC beam brilliance (max. 1.8 emA U^{73+}). In December high intensity argon beams were used to re-commission Alvarez 1 [2] and to perform emittance measurements with a dedicated test bench temporarily installed in the inter tank section. The new charge separator system was installed in the transfer line in December 2007. After tests (January 2008) of all components, beam commissioning was performed successfully with a medium intensity uranium beam and a high intensity argon beam. The measured beam transmission is close to 100 % for low and high current operation. For the high current heavy ion beam operation newly developed stripper foils of extended size are in use. The 'sweeper' operation was tested with a high intensity argon beam as well as with an uranium beam. In general emittance growth is not induced by the sweeper devices. The stripping efficiency measured with the charge separator as a spectrometer is as expected. The improved charge separation capability was confirmed. Simulated and measured emittance growth effects for low current operation are caused by small angle straggling. Additionally, the vertical emittance inside the charge state separator is increased by dispersion. Space charge forces act in the short drift length between stripper foil and charge separation – the space charge influenced emittance growth is 10 % (hor.) resp. 20 % (vert.). The measured high current emittance (ε_x =4 mm·mrad, 3.3 emA, Ar^{18+}) potentially meets the requirement defined by the FAIR project. [3]

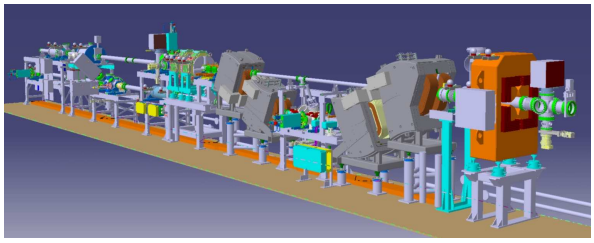

Fig. 1: The new charge separator

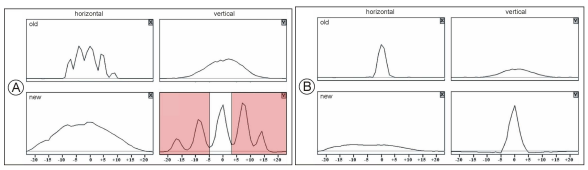

Fig. 2: Measured uranium beam profiles with opened (A) and closed (B) separation slits.

References

[1] U. Scheeler and D. Wilms, Accelerator Operation Report, (this report)
[2] H. Vormann, L. Groening, et. al., Unilac Upgrades 2008/2009 Status, (this report)
[3] W. Barth, et. al., Commissioning of the new charge state separator system for high current heavy ion beams, LINAC2008, Victoria, Canada (to be publ.)

SIS18 Status Report

P. Spiller, U. Blell, O. Boine-Frankenheim, G. Franchetti, P. Hülsmann, M. Kirk, H. Klingbeil, H.G. König, H. Kollmus, V. Kornilov, C. Omet, A. Parfenova, N. Pyka, H. Ramakers, H. Reich-Sprenger, P. Schütt, M. Schwickert and J. Stadlmann

GSI Darmstadt, Germany

INTRODUCTION

The heavy ion synchrotron SIS18 serves an extended experimental program at GSI and must in parallel be upgraded for the planned booster operation for FAIR [1]. To prepare the booster operation with highest intensities of intermediate charge state heavy ions, an extended upgrade program (*) [2] has been defined, including most of the major technical systems. The realisation of the upgrade program requires long shut downs and unavoidably causes extended interruption of the running experimental programs. Part of the defined upgrade measures could be completed in 2008. The further steps and the rearrangement of the existing and the positioning of the new technical systems have been carefully planned.

INJECTION SYSTEM

The major components of the beam injection system have been replaced by a new inflector magnetic, a new 300 kV electrostatic septum and a new vertical steerer magnet [3]. The new system provides the following advantages:

- Enhanced acceptance for an almost loss free injection of high intensity beams and better transverse matching,
- improved beam control by means of a profile grid at the entrance of the electrostatic septum,
- protection of the electrodes by means of a collimator system at the entrance of the septum and a new beam abort system,
- Injection at the standard energy of 11.4 MeV/u for heavy ion beams with intermediate charge states (e.g. U^{28+}), and thereby reduction of the effective cross section for charge changing processes,
- Simplified bake-out procedure of the inflector magnet by means of an embedded bake-out system.

UHV SYSTEM

The replacement of the dipole and quadrupole chambers by new, NEG-coated chambers has been continued. Meanwhile, most of the dipole chambers are exchanged. The manufacturing of the thin wall quadrupole chambers at BINP, Novosibirsk has been started and a first chamber has passed quality assurance tests at GSI. The surface and pumping properties of the NEG coating are continuously verified in collaboration with CERN and the bake-out procedure has been adapted to assure optimum pumping properties.

COLLIMATION SYSTEM

Two prototype collimators of the 'ion-catcher' system for the control of beam loss driven by ionization in the residual gas have been installed and tested with beam [4]. Both ion-catchers consist of a low desorption yield gold coated copper dump with adapted current measurement.

It could be shown that the effective desorption yield, seen by the revolving beam, is significantly reduced for both tested catcher geometries. However, since the desorption yield of the block catcher with perpendicular incidence was measured to be lower than the wedge catcher type, this geometry has been selected for the series production. The charge deposited by the lost ions impacting on the catchers could be measured both for ionisation and electron capture processes. Thereby, the first direct measurement of beam loss induced by charge changes and the energy dependence of the underlying electron capture and ionization process for U^{28+} ions could be performed (Figure 1).

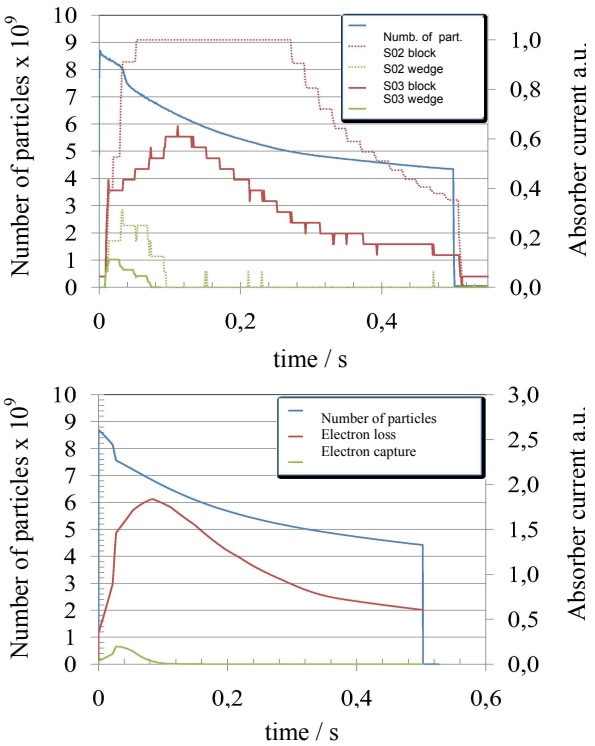

Figure 1: Beam current measured by the SIS beam transformer as a function of the cycle time (energy) (blue line). The red line shows the measured current (top) on the right scraper deposited by electron capture loss in comparison with the simulations (bottom). The green line shows the measured current and its simulated time (energy) dependence on the outer scraper for beam loss due to ionization.

OPERATION WITH INTERMEDIATE CHARGE STATE HEAVY IONS (FAIR BOOSTER OPERATION)

The machine experiments to prepare the booster operation for SIS100 with intermediate charge state heavy ions have been continued with high intensity U^{28+} and Ta^{24+} beams. Both

* Project funded by the European Community
DIRAC-PHASE-1 / SIS18 upgrade - Contract number: 515876

beams can be generated in the UNILAC with almost the same beam current in the order of 2-5 emA and have comparable cross sections for ionization. The progress in the SIS upgrade program as described before has enabled a major increase of the accelerated number of ions. In the frame of Ta^{24+} machine experiments, more than 10^{10} ions could be accelerated and extracted (see Figure 2). This result has been achieved with the following measures:

- increased acceleration ramp rate of 4 T/s for a rapidly increase of beam energy, resulting in a fast reduction of the ionization cross sections and shorter cycle times,
- increased injection energy of 11.4 MeV/u (instead of 6.8 MeV/u) by means of the new injection system to achieve a reduction of the integrated cross sections for ionization,
- careful setting of the multiturn injection parameters to minimize beam loss and to reduce initial pressure bumps,
- breaks between the machine cycles of 8 seconds for the recovery of the residual gas pressure,
- installation of two prototype ion catchers and a series of NEG coated vacuum chambers for a local increase of pumping power and a local suppression and control of desorption gases

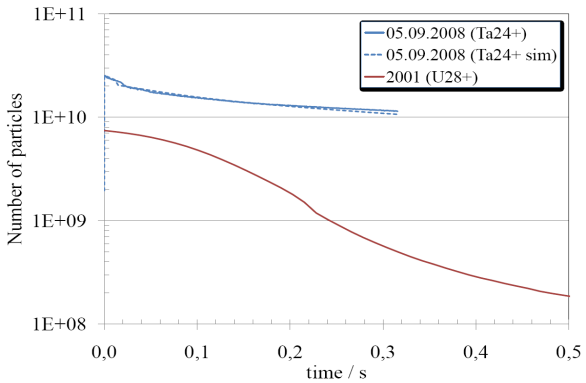

Figure 2: Comparison of the first machine experiments with high intensity intermediate charge state heavy ions in 2001, with the latest experiments performed in 2008. A significant reduction and stabilization of the ionization beam loss and the connected vacuum dynamics has been achieved.

The development of the STRAHLSIM code for the simulation of beam loss driven by charge changing processes under the influence of dynamic vacuum has been continued [5]. New effects and physical properties were added, e.g. the scrubbing effect and the pumping power of NEG surfaces as a function of adsorbed monolayers. Thereby, long term predictions of the number of extracted ions, the pumping power, the number of monolayers and the mean residual gas pressure have been enabled. In addition, first estimates for the life time of the new NEG surfaces were generated.

RF SYSTEMS

The RF bunch compression cavity has been successfully commissioned and the generation of short pulse gap voltages of 40 kV has been demonstrated [6]. In the first shut down 2008 the cavity has been installed in the synchrotron and recently first beam tests were performed. For the new h=2 acceleration cavity, the tendering process for the supply unit has been launched. A study with the goal to evaluate alternative ring core materials e.g. VITROPERM is being conducted. For the existing ferrite loaded RF systems, the preparations for a new beam phase control system have been continued.

POWER CONVERTERS

In order to provide higher flexibility for the correction of closed orbit distortions and for machine experiments, a replacement of all existing unipolar power converters of the horizontal correction coils and vertical steerers by bipolar power converters is planned - in 2008 four of these power converters have procured.

BEAM DYNAMICS AND HIGH CURRENT DEVELOPMENT

High current machine experiments, mostly with Ar-beams have been performed to confirm and prove the high current and high space charge modelling of SIS18 in connection with the nonlinear longitudinal and transverse beam dynamics and to explore the limits of beam stabilities given by the transverse and longitudinal impedances. BTF measurements are performed to determine the tune, the tune shift and the chromaticity. Measurements of the growth rate of instabilities under the influence of the transverse resistive wall impedance indicate that an operation with highest currents of coasting beams may be unstable. Studies of nonlinear transverse dynamics were dedicated to an extended experimental validation of the new method for reconstructing nonlinear errors [7] [8]. The aim of these measurements is to evaluate a resonance compensation strategy using the existing sextupoles taking into account the sextupole errors of the dipoles. At present, measurements for the reconstruction of 6 errors have been performed and the according data are now getting evaluated. This method will allow as well the reconstruction of the natural octupolar components. The outcome of this activity is relevant for high intensity beams suffering from potential trapping phenomena with associated long term beam loss.

Several runs of machine experiment have been used to improve the performance of the slow extraction process by means of a special optical setting which minimizes the momentum influence (Hard condition). First indications for lower beam loss and a reduced lateral movement at dispersive positions in the beam line have been observed.

REFERENCES

[1] P. Spiller and G. Franchetti, Nucl. Instr. and Methods, 561 (2006)305-309

[2] P. Spiller et al., Proc. of EPAC06, (2006)

[3] U. Blell et al., Proc. of PAC07 (2007), p. 167

[4] C. Omet, GSI-Dissertation 2009-01

[5] C. Omet et al., New Journal of Physics 8(11) (2006)284

[6] P. Hülsmann et al, this annual report

[7] G. Franchetti et al., Phys. Rev. ST Accel. Beams 11, 094001 (2008)

[8] A. S. Parfenova, G. Franchetti, I. Hofmann, Proc. of EPAC08 (2008), p. 3137

ESR Operation and Development

C. Dimopoulou, A. Dolinskii, O. Gorda, V. Gostishchev, S. Litvinov, F. Nolden, P. Petri, U. Popp, I. Schurig, M. Steck,[1] and A. Petrenko[2]

[1]GSI, Darmstadt, Germany; [2]BINP, Novosibirsk, Russia

The ESR provided stored beams to various internal experiments and decelerated ions with fast extraction for the commissioning of HITRAP. Machine development was performed on various aspects, in addition the stored beam during machine development periods was used for tests with the modified internal target set-up [1].

A period of more than two weeks was dedicated to measurements of the non-exponential nuclear beta decay of rare isotope beams. This experiment used an optimized combination of stochastic pre-cooling and final electron cooling. Single or very few stored ions of hydrogen-like $^{118}Sb^{50+}$ and $^{122}I^{52+}$ were injected at an energy of 400 MeV/u after isotopically pure separation in the fragment separator. A very good stability and availability of the whole accelerator system was achieved for this operational mode.

The commissioning of the HITRAP facility [2] with bare gold and nickel ions decelerated in the ESR to 4 MeV/u in two blocks of one week was continued. The standard ESR cycle included injection and stochastic cooling at 400 MeV/u, deceleration to 30 MeV/u with subsequent electron cooling, and further deceleration in a second step to 4 MeV/u. The efficiency of each of the two deceleration steps was about 50 %. However, for the lower energies strong beam losses were observed which were clearly attributed to electron capture processes of the beam particles in the residual gas. For minimum emittance of the extracted beam electron cooling at 4 MeV/u is beneficial. However, for highly charged ions like gold the gain was almost cancelled by the beam loss during the cooling time which at low energy was comparable to the beam lifetime.

The poor beam lifetime was confirmed in experiments with $^{238}U^{28+}$ at beam energies between 20 and 50 MeV/u. The beam lifetime of about 15 s was a factor of 3-4 shorter than in 2005. The localization of the leak was rather intricate. After various inspections it was found that a fore pump was malfunctioning which has to maintain good vacuum conditions in the sector with the feedthroughs of the stochastic cooling system.

Two unprecedented modes were used in a beamtime with uranium beam. For experiment at the internal target a beam of 380 MeV/u carbon-like $^{238}U^{86+}$ was stored, cooled and overlapped with the internal target operated with hydrogen. The uranium beam was also used to test the possibility to produce rare isotopes with the direct beam from SIS18 [3]. With a 10 mm beryllium target mounted in the standard stripping section more than 10^5 $^{237}U^{90+}$ ions at 183 MeV/u were injected into the ESR by a single injection, stored and cooled down by electron cooling and finally used to breed Li-like $^{237}U^{89+}$. Alternatively, also $^{234}Pa^{89+}$ could be injected in this mode. As these ions have lifetimes on the order of minutes a further increase of the beam intensity by a longitudinal accumulation method is feasible.

In machine experiments the ion optical properties of the ESR were studied. The goal is the achievement of a better ion optical model from beam based measurements. The response of the orbit to intentional local transverse kicks and the tune response to well defined changes of the focussing strength were measured. The measurements provide a large amount of information on higher order components due to imperfections of the magnets. This results in better knowledge of the actual ion optical functions (Fig. 1) and allows further optimization of the ring acceptance.

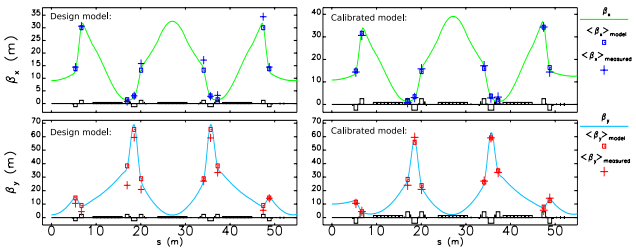

Figure 1: Comparison of measured horizontal and vertical beta function (crosses) with beta functions calculated for the design optics (left) and for the optical properties determined in a calibration procedure (right).

The experiments studying the longitudinal accumulation by a combination of rf potential and electron cooling were continued. A serious limitation in the ESR arises from time jitter of the injection kicker resulting in beam losses. The feasibility of the method could be clearly demonstrated [4].

In a first experimental approach slow resonance extraction of a decelerated beam was studied with $^{124}Xe^{54+}$ at 22 MeV/u. Although it could be verified, that the tune of the beam was adjusted to the value required for resonant extraction and the beam orbit was properly adjusted at the electrostatic septum which deflects the particles with large betatron amplitude into the extraction channel, no extracted particles could be observed. After careful analysis of the required tune value and sextupole strength, the possibility of resonant extraction will be further studied in beam experiments at higher energy.

References

[1] N. Petridis et al., contribution to this report.

[2] L. Dahl et al., contribution to this report.

[3] C. Brandau et al., contribution to this report.

[4] C. Dimopoulou et al., EPAC'08, THPP048.

The new UNILAC beamline for the Materials Research "M-Branch"

S. Mickat, L. Dahl, W. Barth, M. Bevcic, B. Franczak, P. Gerhard, D. Schäfer
GSI Helmholtzzentrum für Schwerionenforschung, Darmstadt, Germany

Introduction

The new UNILAC beamline "M-Zweig" was assembled in 2008 in the region of the former Z1 experimental area in the Experimental Hall (EH). The "M" in "M-Branch" stands for "Materials Research" and is a project, which is embedded in the programme of the BMBF named "Research of condensed matters at large scale plants". First activities for this project came along with the decision of the Helmholtz-Gemeinschaft (HGF) to close the Ion Beam Laboratory (ISL) of the Hahn-Meitner Institute (HMI) in Berlin in 2006. The construction of the new beamline was funded by the HGF and HMI to concentrate the materials research with ions at GSI and to continue the experiments at the meanwhile closed ISL.

Setup

The "M-Branch" comprises three experimental stations named M1, M2 and M3 (Fig. 1). At M1 the SEM of the University of Stuttgart and at M2 the x-ray diffractometer transferred from the ISL are ready for operation. At M3 an apparatus is mounted for investigations using different methods of spectroscopy and residual gas analysis by a cooperation of the GSI materials research group and the universities of Darmstadt, Jena, Dresden, Göttingen and Heideberg.One challenge during the setup of the beamline was not to disturb the UNILAC operation. Therefore the link to the UNILAC was established during the regular shutdowns only. The break through to the UNILAC tunnel and the installations of the magnets, vacuum and beam diagnostic elements and the necessary infrastructure inside the tunnel were performed within two weeks in May. The setup outside the tunnel could be performed independently from the UNILAC operation.

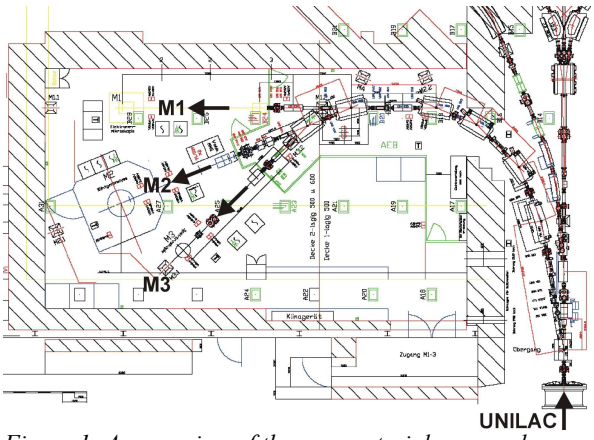

Figure 1: An overview of the new materials research cave. The new beamline coming from the UNILAC-tunnel branches out into the experimental stations M1, M2 and M3.

Commissioning

For the commissioning of the new beamline a parasitic sulphur beam ($^{34}S^{6+}$, 4,8 MeV/u) was available for nearly two weeks. It is mentionable that the new kicker magnet, placed behind the single resonators directly to switch the beam to the experimental stations M1, M2 and M3, could be operated without influence to other UNILAC beams passing through this kicker straight ahead. Also all the other new installed components have been tested successfully.

Furthermore the calculated beam dynamics design of all the three branches were confirmed among others by performing a final focus on the last grid of each branch. At M2 it was possible to shift the focus from such a grid (UM2 DG6) to a fluorescence screen placed in front of the vacuum chamber of the x-ray diffractometer and vice versa (Fig. 2). Additionally first functional tests of the former ISL setup at M2 were performed with beam successfully.

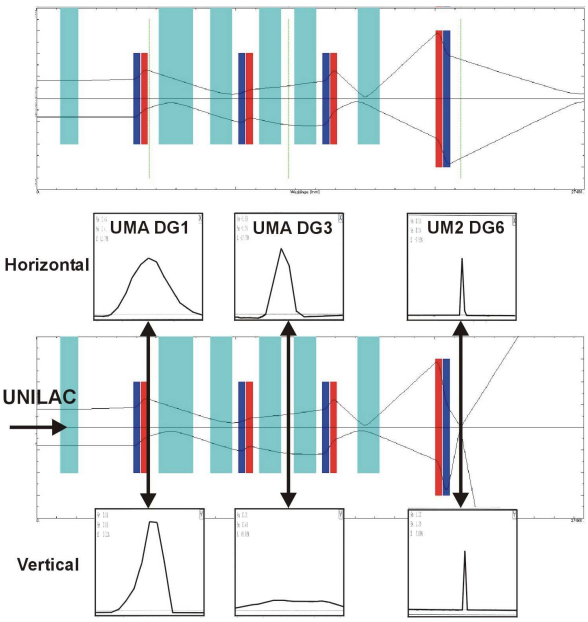

Figure 2: A Mirko beam dynamics simulation for M2 is shown. During the commissioning the focus behind the last quadrupole was shifted to the profile grid UM2 DG6. For that case the inserted beam profiles were measured as expected by simulations.

Currently about twenty experiment proposals applying for beamtime at the new "M-Branch" were submitted. Within the Materials Research Program Advisory Committee (Mat-PAC) an evaluation will take place in March 2009.

Unilac Upgrades 2008/2009 Status

H. Vormann, W. Barth, L. Dahl, L. Groening, A. Kolomiets*, S. Minaev*, S. Yaramyshev
GSI, Darmstadt, Germany; *ITEP, Moscow, Russia.

Unilac Upgrades Overview

In the future the UNILAC has to fulfil the requirements of FAIR (15 emA of U^{28+} with min. 70 µs pulse length to be injected into SIS18, corresponding to 18 mA U^{4+} at HSI-RFQ output), and furthermore has to deliver high current ion beams of different species in multi-beam operation for various experiments.

To achieve this goal, additional upgrade measures will be accomplished in several UNILAC sections: LEBT [1], HSI-RFQ [2] and Alvarez main linac (power supplies for the 168 focusing quadrupoles) [3], and high current beam diagnostics [4].

Status of Components

In 2008 planning and fabrication for the HSI-RFQ upgrade and commissioning for the Alvarez power supply upgrade have taken place.

HSI-RFQ Upgrade

The HSI-RFQ will be upgraded with new electrodes, based on a new particle dynamics design [2].This design, with larger aperture and higher voltage (155 kV instead of 125 kV at Uranium level), provides for a larger acceptance, keeping the max. surface peak field lower than the old design (<320 kV/cm). The new input radial matcher (IRM) design allows radial beam matching without emittance growth in the matching section.

Assuming an input beam current of 25 mA U^{4+} (assuming 280 mm mrad transversal emittance), a transmission of 80.6% can be expected.

The average aperture and the transverse shape of the electrode vanes are kept constant along the whole RFQ, as well as the dimensions of the electrode carrier rings, to keep the flat field distribution. From the comparison of preceding MWS simulations with measurement results of existing resonator sections, the correct resonance frequency (36.136 MHz) can be expected from simulations with geometry parameters as shown in table 1 (four fixed plungers).

HSI-RFQ	New Design	Existing Design
Electrode voltage / kV	155.	125.
Average aperture radius / cm	0.6	0.5245 – 0.7745
Electrode width / cm	0.846	0.9 – 1.08
Maximum field / kV/cm	312.0	318.5
Modulation	1.012 – 1.93	1.00 – 2.09
Synch. Phase, degrees	-90^0 - -28^0	-90^0 - -34^0
Minimum aperture radius, cm	0.410	0.381
Number of cells with modulation	394	343
Length of electrodes, cm	921.74	921.74

Table 1: Design parameters of the HSI-RFQ.

New electrodes (4 pieces for each of the 10 tank sections) and electrode carrier rings (100 pieces in total) have to be manufactured. All carrier rings were fabricated at FZ Karlsruhe (delivered to GSI in December 2008). Manual finishing is in progress. The electrode machining (GSI workshop) for tank sections no. 2-9 is finished, machining for no. 1 and 10 is in progress, too. 28 Electrodes for seven sections have been copper plated in November and December 2008 (GSI galvanics), twelve electrodes for the last three sections will follow.

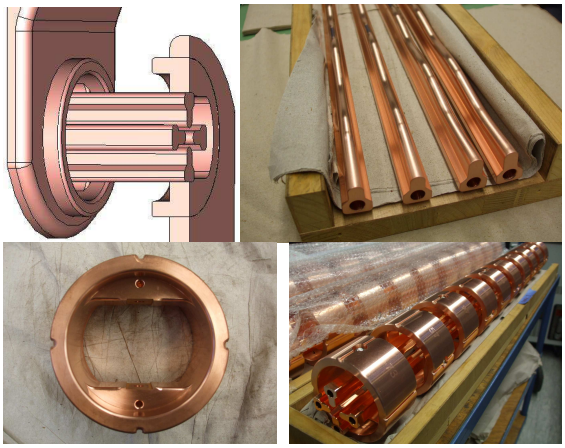

Figure 1 (from top left to bottom right): Regular HSI-RFQ resonator cell; electrodes after milling; carrier ring; pre-assembled electrode cage.

For the re-commissioning, emittance measurements behind of the RFQ are foreseen. Therefore, a temporary emittance measurement device has been built and tested.

New DC-Power Converters for the Alvarez Section

Previous experimental and theoretical investigations of the beam quality for low charged ions after the Alvarez section showed that the achievable beam quality is limited by the current limit of the power converters supplying the focusing magnets along the section [4]. In order to overcome this limitation new power converters have been procured. Their maximum current has been chosen such that the maximum power supplied to the quadrupoles is limited rather by the achievable water cooling rate. Additionally, the number of quadrupole families along the Alvarez section has been increased from 13 to 18 providing for more flexibility in the applied focussing scheme. In December 2008 the new converters for the first Alvarez tank have been commissioned successfully.

References

[1] L. Dahl et al., proc. Linac 2006, p. 183,
[2] A. Kolomiets, W. Barth et al., proc. Linac 2008,
[3] L. Groening et al., Phys. Rev. ST Accel. Beams **11** 094201, (2008)
[4] A. Peters, P. Forck et al., proc. Linac 2004, p.13.

Status of Construction and Commissioning of the HITRAP Decelerator

L. Dahl[1], W. Barth[1], P. Gerhard[1], F. Herfurth[1], M. Kaiser[1], O. Kester[1], H.-J. Kluge[1], S. Koszudowski[1], C. Kozhuharov[1], G. Maero[1], W. Quint[1], A. Sokolov[1], T. Stöhlker[1], W. Vinzenz[1], G. Vorobjev[1], D. Winters[1], B. Hofmann[2], J. Pfister[2], U. Ratzinger[2], A. Sauer[2], A. Schempp[2]
[1]GSI, D-64291 Darmstadt, Germany, [2]Goethe University, D-60438 Frankfurt, Germany

Status of Construction

After extraction from the ESR, highly charged heavy ion beams are decelerated down to 6 keV/u by a linear decelerator as part of the HITRAP project [1]. The first 108 MHz IH-type decelerator cavity and the matching section for the following RFQ were installed and commissioned in September 2008. Phase matching into the IH structure is prepared by a DDB (Double-Drift-Buncher combination) of λ/4-resonators working at frequencies of 108 and 216 MHz installed in 2007 and operating at design parameters. Magnet power converters and rf amplifiers are in operation as well as beam diagnostics and controls. The bunchers are fed by solid state amplifiers up to 5 kW pulse power and run reliable. The IH structure is fed by a 200 kW tube amplifiers.

The remaining component, a 4-rod-RFQ tank with integrated debuncher cavity for beam energy spread reduction is in house and ready for installation. The dedicated rf amplifiers are operational on-site.

The rf commissioning of the IH tank including bead pull measurements and high power conditioning was done in a rather short time. Fig. 1 shows the gap voltage distribution as calculated by MWS® (Micro Wave Studio) compared to the measured one. The drop corresponds to the position of the inner quadrupole triplet lens. The effective deceleration voltage is 10.5 MV.

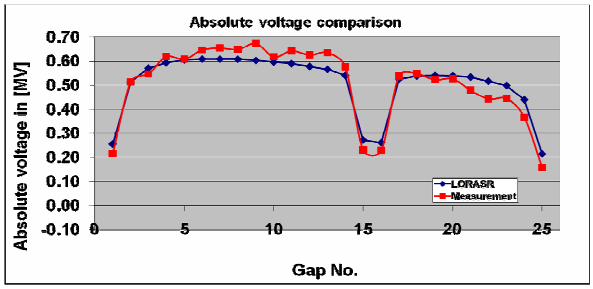

Fig. 1: Measured (red) and calculated (blue) field distribution of the IH decelerator

Beam Commissioning Measurements

During two commissioning periods in August and October 2008 [2] cooled $^{197}Au^{79+}$ and $^{64}Ni^{28+}$ beams at 4 MeV/u were provided by the ESR. To investigate the beam properties after deceleration the single-shot emittance meter and the diamond detector array were installed downstream of the IH. The working points of the DDB were determined by measuring the bunch width behind the IH tank (Fig. 2). Then rf power for the IH cavity was switched on and phase and amplitude settings

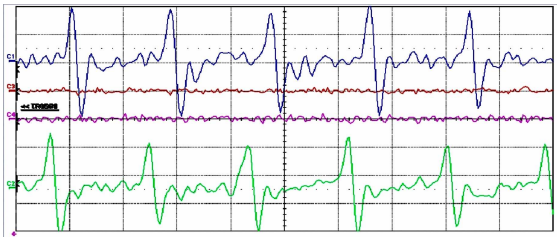

Fig. 2: Beam bunch signals generated by two capacitive pick-ups in front of the IH tank

were varied to determine the working point of this structure. As shown in Fig.1 the gap voltages in front of the inner quadrupole lens are higher and the gap voltages downstream are lower than calculated. Therefore the longitudinal acceptance for decelerated particles turned out to be reduced. The main beam fractions left the IH tank without deceleration or with the energy of around 2.4 MeV/u. Nevertheless, the expected particle energy of 500 keV/u could be observed using a steering magnet combined with a YAG scintillation screen and additionally a single crystal diamond detector (scCVD) for energy measurement of single ions (Fig. 3).

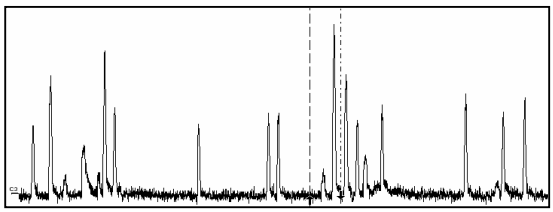

Fig. 3: Signals at the diamond detector. The strength is proportional to the energy of the single ions. The smallest peaks indicate the desired particles at 500keV/u.

In December 2008 the gap field distribution of the IH structure was retuned and adjusted according to theory by introduction of a copper block in the low energy section. Calculations show that the retuned structure captures 66% of the injected ions. High power conditioning started again. The next steps in 2009 are the final commissioning of the IH tank and the installation and commissioning of the RFQ.

References

[1] H.J. Kluge, et al., HITRAP: A Facility at GSI for Highly Charged Ions, Advances in Quantum Chemistry, Vol. 53, (2008) 83

[2] L. Dahl, et al., The HITRAP Decelerator Project at GSI – Status and Commissioning Report, Proc. of the LINAC08, Victoria, BC, Canada, (2008)

Numerical calculation of ring coupling impedance for synchrotron accelerators SIS-18 and SIS-100*

L. Hänichen[1], A. Al-khateeb[2], O. Boine-Frankenheim[2], W.F.O. Müller[1], and T. Weiland[1]

[1]Technische Universität Darmstadt, Institut für Theorie Elektromagnetischer Felder (TEMF), Schlossgartenstrasse 8, 64289 Darmstadt, Germany; [2]GSI, Darmstadt, Germany

Introduction

Coupling impedances are the source of coherent instabilities and corresponding beam intensity limits for the operation of high current accelerators such as the planned SIS-100 synchrotron for the GSI FAIR project. Alternative designs for the vaccuum chamber are discussed, demanding for means to calculate the distributed impedance of beampipe. The coupling impedances are defined as follows:

$$Z_{||}(\omega) = \frac{1}{q^2}\int d^3x E \cdot J_{beam}, \qquad (1)$$

$$Z_{x,y}(\omega) = \frac{i}{q^2\Delta}\int d^3x \rho_{x,y} \cdot (E_{x,y} \mp v B_{y,x}), \qquad (2)$$

where E is the longitudinal electric field and $E_{x,y}$ and $B_{y,x}$ are the transverse electric and magnetic fields excited by the beam.

Main objectives

The frequency domain approach includes solving the time-harmonic wave equation for multiple frequencies. This has been accomplished by B. Doliwa [1] for the localized impedance contributions of ferrite kickers. Given the FOURIER- correspondency between impedance and wake-function, a time domain approach can be used by calculating the wake-function and obtaining the impedance by applying the FOURIER-transform. For profiting from the advantages of the time domain approach, its applicability has been tested by calculating the impedance contribution of resistive beampipe and compared with the analytical reference given below.

Analytical description

It has been decided to use the analytical expressions derived by A. Al-khateeb et al. as reference. They are kept general with respect to all parameters to allow various parameter studies [2]. A particle beam with homogenous transverse profile is assumed. In frequency domain this is represented by an infinitely thin circular disc charge, which travels along the synchrotron orbit with $v = \beta c_0$. For the calculation of the longitudinal coupling impedance only the longitudinal electric fields are integrated over the beam cross section and along the circumference. For the transverse coupling impedance only the transverse electric and magnetic field components are taken into account.

* Work supported by GSI under contract DAWEI2.

Numerical description and simulation

When using a point beam for excitation, the corresponding limit has to be applied for the analytical expression as well. While this is possible for the resistive impedance contribution, the expression for the space charge impedance contribution gets singular. For this case the excitation has to be adapted. Another important difference between analytical and computational model is the integration path, which in the case of the latter is only a fraction of the circumference thus the results have to be scaled appropriately. These issues and the behaviour for low β particle beams are still subject to investigation.

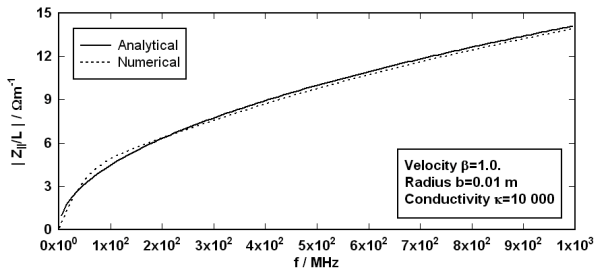

Figure 1: Longitudinal Coupling Impedance for a circular beampipe.

Results and outlook

Impedance calculation has been carried out using CST PARTICLE STUDIO® . Calculations for transverse coupling impedances are still pending, as well as the analysis of the results for a beam with finite transverse dimensions. This is to be achieved by approximating the circular beam profile by multiple point-like beams and superposition of the results. The calculation of resistive pipe impedance is finished so far and shows very good agreement in the medium and upper frequency range ($f > 100$ MHz). The deviation in the low frequency range ($f < 100$ MHz) needs further investigation and eventually represents a physical limitation for the applicability of this approach.

References

[1] B. Doliwa, H. De Gersem and T. Weiland, "Numerical calculation of coupling impedances for kicker modules.", FAIR report, March 2006, Darmstadt.

[2] A. M. Al-Khateeb, O. Boine-Frankenheim and R.W. Hasse "Comparison of the longitudinal impedance from different source terms.", Nucl. Instruments and Meth. in Physics Res. A, 2008.

Bunch Compressor System for the SIS 12/18 Upgrade

P. Hülsmann, R. Balß, T. Winnefeld

1. Compressor RF System

The **Bunch Compressor Cavity** is filled with 2x10 magnetic alloy ring cores and provides 42 kV gap voltage at an operating frequency of 0.8 and 1.2 MHz (harmonic number h=1 at extraction level) [1]. System challenges were for instance the very short rise time (< 10µs) of the RF voltage and thus the development of a very fast MOSFET switch for shortening the gap during acceleration (switching time ≤ 10µs).

The **RF-Power Amplifier** (PA, 600 kW) feeds the cavity in push-pull mode using two Siemens RS 2054 tubes. (tube working point 26kV; 19A, pulse duration 500µs).

The **Supply Unit** for the PA is located in a special supply room and contains the supply sub-devices like anode-, screen grid-, control grid-, and filament-supply. Amplitude- and phase control, the bunch compressor interface, the pre-amplifier and the programmable logic control (PLC) are also located here.

2. Commissioning phase

After finishing the test phase in the supply room successfully, cavity and power amplifier have been installed in the SIS-tunnel close to the SIS-acceleration-cavity S02BE1, as shown in Figure 1.

Fig. 1: Compressor cavity with power amplifier in the SIS 18 tunnel

During the commissioning phase various significant problems have been solved. One of the most impressive problems was an instability in the power amplifier. Some significant changes of the tube socket construction were necessary to eliminate the problem. The instability was caused by a screen grid shunt capacitance which becomes inductive at 2.2 MHz. Together with the intrinsic plate capacitance in the tube socket the shunt capacitor formed a tube socket resonator with a resonance frequency of 7.5 MHz. The oscillator was excited by fluctuations of the vacuum tube DC current.

Furthermore the performance of the tetrodes Siemens RS 2054 did not reach the target parameters. Fortunately, the cavity was equipped with 4 ring cores more than originally planned which allowed to fulfil the requirements in spite of the reduced tetrode performance.

3. First Measurements with beam

On January 16th 2009 first beam experiments with the compressor RF system have been performed with Ar^{18+} ions at injection level and harmonic number h=4. The beam energy and harmonic number were chosen in such a way to avoid sophisticated bunch merging (4 bunches into a single bunch) while keeping the RF frequency within the operating parameters of the bunch compressor.

During the experiment, the influence of different parameters as for example the amplitude and phase of the gap voltage as well as the pulse duration on the beam were evaluated.

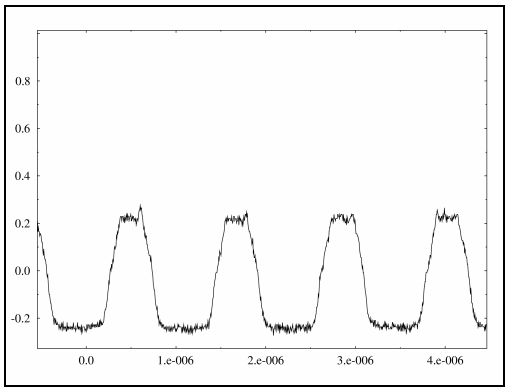

Fig. 2: beam signal before bunch-rotation

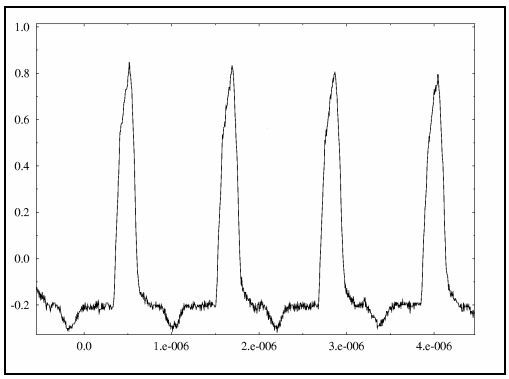

Fig. 3: beam signal after bunch-rotation

Figures 2 and 3 show the measured beam profile (Σ signal of a BPM) before (3kV gap voltage) and after the compression (30kV gap voltage, about 100µs RF pulse duration). A first preliminary evaluation of the measured data shows a compression factor of roughly 3 as expected for the mentioned ratio of gap voltages.

References

[1] P. Hülsmann, W. Vinzenz, G. Hutter: "The bunch compressor system for SIS18 at GSI", EPAC 2004 proceedings.

SIS18 Beam Experiments for the Verification of the RF Control System for Dual Harmonic Operation

H. Klingbeil, M. Kumm, U. Laier, M. Mehler, K.-P. Ningel
GSI, Darmstadt, Germany

Abstract

In the scope of the SIS18 upgrade, dual harmonic acceleration is an important requirement in order to reach the target beam intensities. Since about 6 years, the RF department has been developing digital low-level RF (LLRF) components that are flexible enough to allow various applications such as single-harmonic cavity synchronization, beam phase control, longitudinal feedback, etc. Therefore, it was now possible to use the new modular software and hardware components for first beam experiments on dual-harmonic operation.

Digital LLRF System

The following general-purpose hardware and software components developed in the RF department (see e.g. [1]) were used to perform dual harmonic machine development experiments (MDE):

- Mixer module converting RF (0.4...5.5 MHz) signals to an intermediate frequency (IF, 21.4 MHz)
- Offset LO (Local Oscillator)
- Microcontroller for automatic gain control
- FPGA (Field Programmable Gate Array) interface board (e.g. as interface to the control system)
- DSP (Digital Signal Processor) interface board
- Frequency generator module that produces clock and IF signals
- Direct Digital Synthesizer (DDS) module

The control loop is running on a commercial DSP system that also includes FPGAs (for glue logic and signal pre-processing) and analog-to-digital (ADC) and digital-to-analog (DAC) converters. Large software packages have been realized at GSI – also in collaboration with industrial partners and research institutes - for the DSP system, for microcontrollers, for FPGA components, and for diagnostics purposes (e.g. waterfall plot analysis).

Measurement Results

The dual harmonic overall system was tested during an MDE. The beam consisted of $^{238}U^{73+}$ ions with $3 \cdot 10^8$ particles at injection energy.

At the beginning, adiabatic bunching took place at h=4 using a final RF peak voltage of 10 kV. Afterwards, the second harmonic at h=8 produced by the other ferrite cavity was adiabatically ramped up to 5 kV. In order to analyze possible side-effects, the dual-harmonic bucket was only created temporarily (for ramping up, flat-top and ramping down, 200 ms were spent, respectively). All components mentioned above were used to generate the RF and IF signals and to synchronize the gap signals of both cavities (details see [2]).

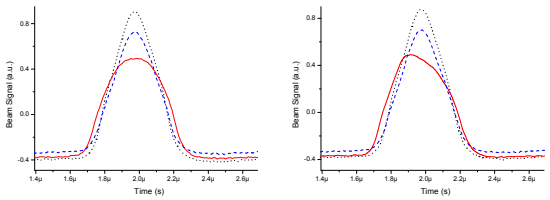

Figure 1: Beam signal for a target phase difference of -85° (diagram on the left) and -80° (diagram on the right)

The target phase difference between the two cavities that was used by the DSP system to control the slave cavity was one of the parameters that were varied during the MDE. The optimum result was reached for a set value of -85° (the deviation from the true value of -90° can be explained by length differences in the IF cables which will automatically be compensated in future by suitable calibration methods) which is shown on the left side in Fig. 1. The dotted black line shows the beam signal for the single-harmonic bucket before the manipulation. The solid red line refers to the flattened bunch in the dual-harmonic bucket (an increase of the bunching factor of about 40% is achieved). Finally, the dashed blue line shows the beam signal for the single-harmonic bucket after the manipulation.

On the right side in Fig. 1, the result for a target phase difference that deviates 5° from the optimum value is shown. One can see clearly that an accuracy of better than 5° is required which is fulfilled by the DSP system (current accuracy: ±1.5°). More details can be found in [2].

Conclusion and Outlook

The MDE showed that the digital LLRF system fulfills the requirements for dual-harmonic operation. Future experiments are prepared which will concentrate on the following aspects:

- Capturing higher intensity beams
- Dual harmonic acceleration with variable phase between the two harmonics
- Combination of dual harmonic operation with beam phase control

References

[1] H. Klingbeil, H. Damerau, M. Kumm, P. Moritz, G. Schreiber, B. Zipfel: “Commissioning of the SIS12/18 Cavity Synchronization System”, GSI annual report 2005.

[2] K.-P. Ningel, H. Klingbeil, M. Kumm, U. Laier: “Beam Experiment Dual Harmonic Operation”, GSI Internal Note No. 26052008.

Reduction of the Q-Loss-Effect in Ferrite-Loaded Cavities

H.G. Koenig, S. Schaefer
GSI, Darmstadt, Germany

Abstract

The performance of cavities loaded with Ni-Zn ferrites under parallel DC-biasing is often limited by the high-loss-effect (HLE) or quality-loss-effect (QLE) [1]. After some milliseconds at fixed frequencies, a sudden drop of the resonator's voltage occurs above a specific threshold level. The mechanism of this loss has not been fully understood yet. At GSI, a simple method has been found to work against this effect with the aid of mechanical damping of acoustical surface waves [2]. We are able to show that similar methods applied to full size rings lead to a significant increase of the onset voltage of the QLE. Most of the existing ferrite loaded accelerating cavities with QLE limitations can be improved in terms their accelerating voltage by this modification.

Investigations related to the QLE

Modal structure of the QLE

The sound fields within the ferrite core were analysed numerically by 2D-calculations. Some results are presented in figure 1. At higher frequencies there are mainly pure surface waves. The mode density is dominated by the largest physical dimension – that means by the outer circumference of the ferrite cores. Our results are summarised in table 1 where the mode density is roughly given in 'number of lines/10kHz'. The geometric influence is evident. The mode density could be measured as a corresponding subharmonic magnetic RF-response as shown in figure 2. In large rings, discrete modes seem to vanish at higher RF-levels as they can hardly be measured because of their overlapping.

Table 1: Acoustical Mode Densities of our Samples

Material Ni-Zn Ferrites	MAGNE-TON400 N	PHILIPS 8C12 std.	CMI CMD 5005	PHILIPS 8C12 mod.
Size: D x d x h	32x20x5	36x28x6	100x50x25	498x270x25
1st Resonance	57 kHz	54 kHz	26.4 kHz	4.5 kHz
calc. Density	2.4/10kHz	1.6/10kHz	28/10kHz	70/10kHz
meas. Density	3.4/10kHz	1.2/10kHz	28/10kHz	35/10kHz
Q@QLF	~ 500	~ 500	~ 2500	~ 5000

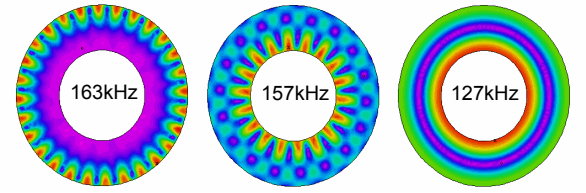

Figure 1: examples of circumferential- and shell-modes

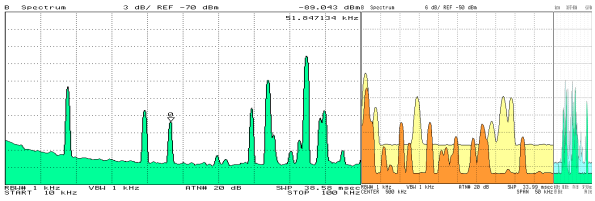

Figure 2: corresponding ½f_{RF} QLE signals

Suppressing the QLE with coatings

Two ring cores made of modified FXC8C12 by FERROXCUBE - treated with a thin bitumen coating - were measured at 1MHz with a DC-bias of 300A/m. The coating has a thickness of approx. 1mm. The QLE threshold is shifted from 180V_p to > 370V_p per ring (figure 3).

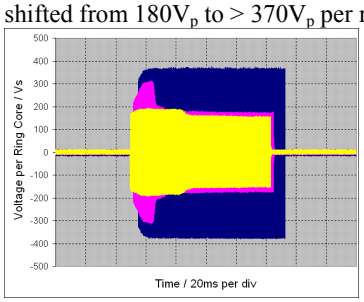

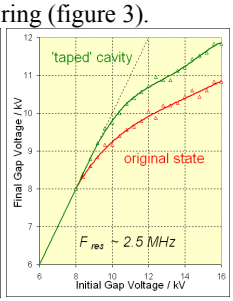

Figure 3 (l): QLE-suppression with bitumen coating
Figure 4 (r): Prototype - increase of the gap voltage

In order to verify the effect of mechanical damping, the SIS18 prototype cavity was covered with ordinary insulation tape on its accessible surface (less than 50%). A considerable increase by approx.10% of the final gap voltage was achieved – see figure 4.

Conclusion and Future Plans

Currently, the gap voltages reached in the SIS18 cavities are still limited by the QLE. But according to the described experimental results, one can expect a considerable increase just by coating the ferrites' surfaces with an adequate damping material. The Budker Institute of Nuclear Physics (BINP) developed a cavity, based on entirely encapsulated ferrite stacks [3]. On the basis of this assembly, we expect a sufficient suppression of the QLE.

References

[1] J. E. Griffin, G. Nicholls: 'A Review of Some Dynamic Loss Properties of Ni-Zn Accelerator RF System Ferrite';IEEE Trans.o.N.S., Vol. NS-26, 1979
[2] H. G. König, S. Schäfer: "Reduction of Q-loss-Effects in Ferrite-loaded Cavities", GSI, EPAC 2008
[3] V. S. Arbuzov et al.: 'Accelerating RF Station for HIRFL-CSR, Lanzhou, China ', BINP Novosibirsk, Proceedings of RuPAC XIX, Dubna 2004

A Space Charge Lens for Focusing Uranium Beams

K. Schulte, M. Droba, O. Meusel, and U. Ratzinger
IAP, Goethe University, Frankfurt am Main, Germany

Introduction

A promising approach for LEBT systems are Gabor Plasma Lenses using a stable space charge cloud [1]. The confinement of the electrons by external fields leads to focusing of ion beams at drastically reduced magnetic and electric field strength compared to conventional ion optics. Therefore in former experiments the fundamental properties of the electron cloud so called nonneutral plasma were studied.

To further investigate the performance of the Gabor Plasma Lens relating to focus low energy heavy ion beams a new experiment is under construction.

Application Requirements

To provide a good performance of the space charge lens besides a linear electric field also a high trapping efficiency is needed. The linearity of the selfelectric field involves a homogeneous electron density distribution. Not only the configuration of the external fields causes a homogeneous distribution in former measurements a strong dependancy of the electron density and distribution on the residual gas pressure has been investigated. Figure 1 shows the strong influence of the residual gas pressure on the measured average electron density.

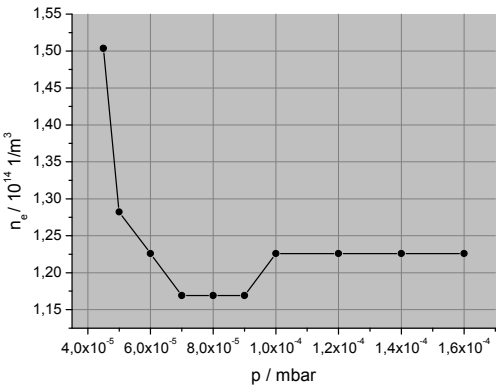

Figure 1: Dependancy of the measured average electron density on the residual gas pressure (He).

To transport a U^{4+} ion beam out of the HSI frontend at GSI a new space charge lens has to be designed (figure 1). The total length of this device will be about 0.4 m and the longitudinal confinement of the electrons will be provided by an anode with radius r_A = 0.085m. From numerical simulations results a required minimum potential of $\Phi_{A,max}$ = 30kV for the electrodes. Furthermore the magnetic field produced by a solenoid has to be about 12,6 mT to fulfill the main requirements for linear cylinder symmetric force on the beam particles.

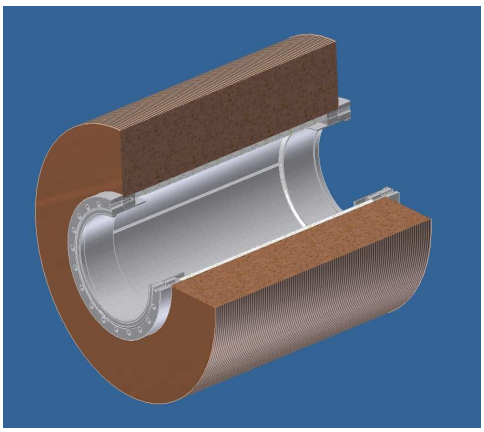

Figure 2: Design of the Gabor Plasma Lens.

Beam Transport Simulation

The transport of the uranium beam through the space charge lens was simulated using the code LINTRA (figure 3). The inital phase space distribution of the beam had to be generated referring to [2]. For the calculation a degree of space charge compensation of 100% was assumed.

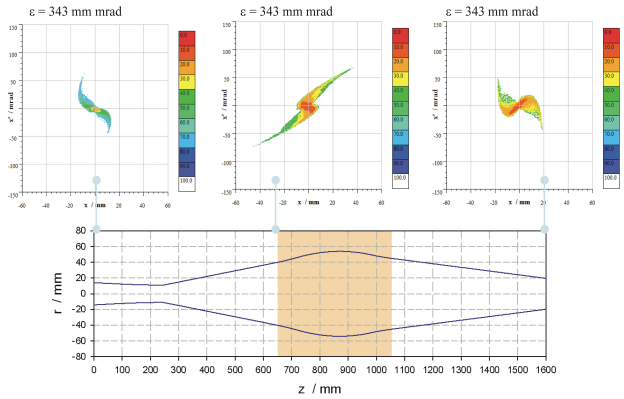

Figure 3: Beam transport simulation.

The simulation of the beam transport starts after the postaccelerating system of the ion source with a drift section. The focus of the lens given by the electron density is at 0,75m in the next drift section.

References

[1] O. Meusel, et al., “Low Energy Beam Transport Development at IAP”, GSI SCIENTIC REPORT (2003)
[2] P. Spätdke and R. Hollinger, et al., REVIEW OF SCIENTIFIC INSTRUMENTS 76, 063307 (2005)
[3] K. Schulte, et al., “Optical Diagnostic on Gabor Plasma Lenses”, EPAC’08, Genova, June 2008

Adaptive Control Unit for Digital Control of Power Converters for Magnets in GSI and FAIR Accelerators

H. Ramakers, A. Döring, D. Schupp, G. Schulz, H. Welker

GSI, Darmstadt, Germany

In 2004 the first generation of a digital control unit for power converters in GSI was developed. After successful prototype testing the system was decided to be implemented in the power converters of the Therapy Accelerator HIT in Heidelberg. Up to the end of 2007 nearly 150 power converters of HIT were put into operation and commissioned successfully.

At this time it became evident that for further applications in GSI and to comply with FAIR requiremets the system design flexibility should be improved to cover more power converter topologies. Therefore the second generation digital control unit was developed as an Adaptive Control Unit (ACU) which is a modular FPGA based system consisting of one core module and several satellite modules which allow the adaption to very different power converters. In the sense as used here adaptive does not mean the self learning process of regulation loops but the possibility of using different configurations of the satellite modules for different converter topologies.

Momentary the ACU system supports switch mode power converters in 1, 2 and 4 quadrant operation. Support for SCR (thyristor controlled) power converters and SCR power converters with active parallel filters in switch mode topology is in work. Further it supports power converters with one or two intermediate DC-links and its dynamic operation. It can be configured for current or field control with or without cascaded voltage control. Besides the control loops there is a fast feed forward path to compensate the effect of voltage changes in the intermediate DC link. The power converters can be operated in DC-mode, slowly pulsed mode (< 1Hz), fast pulsed mode (up to 25 Hz) and ramped mode.

Figure 1 gives an overview on the ACU and its standard implementation into a power converter. The ACU system consists basically of the Multifunction Module (core module), the Interlock & Control Module and the ADC Module (satellite modules). Further Special Function Modules can be added. All parts (except the Interlock & Control Module and Special Function Modules) are mounted into a 19´´ frame with the height of 3U.

All function specific parameters can be set or read by a local computer (via an USB cable) comfortably by using a specially developed Windows based graphical user interface or by an external accelerator control system. In either case the parameters can be written into a flash memory for long term configuration.

For manual operation there are several manual control elements and a graphical display on the front panel of the Multifunction Module. This display shows the graphical user interface (GUI) and it is also capable of displaying internal signals. Up to four analogue outputs can be configured to display various internal digital control signals on an external scope.

The components connected within an ACU system communicate by USI (Universal Serial Interface). This interface allows for further expansions and is easy to implement. Because of the ASCII based protocol structure the communication diagnosis is very simple. The various components can work with different communication speeds. Therefore USI discerns slow access and fast access. Eight slow speed components can be connected to one USI port. This number reduces according to the number of connected components with fast communication.

One or more ADC Modules allow to acquire fast analogue signals out of the power part with high precision for measuring and controlling purposes.

The Interlock and Control Module has inputs for up to 20 interlock signals. It also translates the commands of the Multifunction Module to the power part and generates appropriate activating signals into the power part.

At present 12 new power converters with ACU for the quadrupole chains of the Alvarez 1 section of the Unilac are in operation . Six other power converters for the sections 2, 3 and 4 of Alvarez are waiting for being commissioned.

In addition all new 23 power converters of the new M-branch of Unilac are equipped with ACU and have been commissioned successfully. There are power converters for a fast pulsed kicker magnet (25Hz, 1000A, 1200V), for dipole magnets, quadrupole magnets and vertical corrector magnets as well as two power converters with three-way load changers for supplying one out of three quadrupole dupletts.

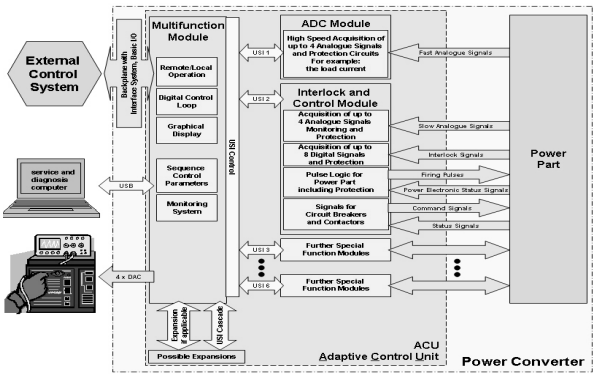

Figure 1: Overview on the ACU system and its implementation into a power converter

Evaluation of the Vacuum Performance of NEG Coated Chambers in the SIS18*

M.C. Bellachioma, J. Kurdal, H. Reich-Sprenger, A.Krämer, and G. Savino
GSI, Darmstadt, Germany

In the frame of the SIS 18 upgrade an intense research activity started in 2005 for the production and characterisation of Ti-Zr-V coated vacuum chambers.

Three new dedicated magnetron sputtering facilities were designed and commissioned to perform the coating on dipole, quadrupole and short straight chambers [1, 2].

The surface chemical composition and the activation behaviour of the produced thin films were studied at Cern by X-ray Photoelectron Spectroscopy (XPS). The H_2 and CO pumping speed were investigated at GSI by transmission measurement and by means of a Fischer-Mommsen dome [3].

Before proceeding to the installation of the NEG coated chambers in the accelerator, an additional study was performed to analyse the pressure evolution during bakeout and activation. For this purpose an experimental system equivalent to a SIS 18 vacuum sector was built in the vacuum laboratory. The set-up (see Fig. 1) consists of two pumping units, both equipped with two sputter ion pumps (IP) and two Ti sublimation pumps (TSP), a residual gas analyser and two gauges, mounted at the extremities of a coated SIS dipole chamber. A turbo molecular pump (TMP) is connected through a gate-valve to the system, and is valved-off at the end of the heating cycle, which follows the one typically used for the SIS18. After the bakeout of the uncoated parts of the system at 220°C for 157 hours, the temperature of the dipole chamber is raised from 120°C to 210°C, and kept at that temperature for 24 hours to perform the NEG activation. The pressures recorded before and after the heating cycle were respectively 6.1×10^{-8} mbar and 5.3×10^{-12}mbar in the first pumping unit and 1.4×10^{-7} and 6.3×10^{-12}mbar in the second pumping unit.

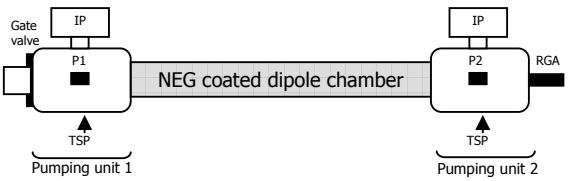

Figure 1: Schematic drawing of the experimental set-up.

The spectrum recorded after the activation process showed that the main residual gas in the system was methane, which is actually not pumped by the NEG.

By the end of 2007 the first coated dipole chambers were mounted in the SIS 18. The gauge S01 in the sector VII was chosen to follow the evolution of the pressure during the bakeout and activation procedure [4].

In Fig. 2 the variation of the pressure recorded during the heating cycle is shown and compared with the pressure value measured before venting the vacuum sector.

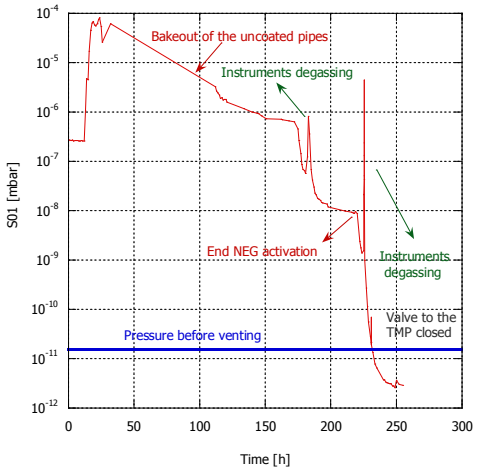

Figure 2: Variation of the pressure during the bakeout/activation cycle recorded by the gauge S01.

The final pressure recorded by the gauge S01 was about 3×10^{-12} mbar, 5 times lower that the one reached before venting the vacuum sector ($\approx 1{,}6 \times 10^{-11}$mbar) and therefore before the insertion of the coated chambers.

Conclusion

In the last three years three magnetron sputtering facilities were designed and commissioned at GSI. The performances of the thin film getter produced were analysed with different techniques and the good activation and pumping behaviour were proven. At present 14 coated dipole chambers have been mounted in the SIS 18, and the pressure variation measured is in agreement with the results obtained by means of the VAKTRAK [4,5] simulation.

For the accomplishment of the SIS 18 upgrade it is foreseen to mount the remaining coated dipole, quadrupole chambers and some straight pipes in the next shutdowns.

References

[1] M.C.Bellachioma et al., Vacuum 82 (2008) 435-439.
[2] M.C.Bellachioma et al., GSI Scientific Report 2007, GSI-ACCELERATORS-15 .
[3] M.C.Bellachioma et al., GSI Scientific Report 2005, FAIR-ACC-21.
[4] S.Wilfert et al., this GSI Scientific Report, ACC-16.
[5] V.Ziemann, Proc. PAC 1993, 3909-3911.

* Work supported by EU design study, DIRAC-PHASE-1 RP6 SIS18-2 contract No 515876.

Short-term outgassing measurements on special cryogenic stainless steel grade Bö P506

St. Wilfert[1], B. Garke[2], A. Krämer[1], and H. Reich-Sprenger[1]
[1]GSI, Darmstadt, Germany; [2] Otto-von-Guericke University Magdeburg, Germany

Abstract

Due to its excellent magnetic (μ_{rel} < 1.005) and mechanical properties even at cryogenic temperatures the newly-developed stainless steel grade Bö P506 (producer: CERN and Boehler Edelstahl Austria [1]) is a suitable material candidate for beam tubes of superconducting magnets for SIS100 in the FAIR project [2]. In order to analyze the usability of this special stainless steel grade as beam pipe material for room temperature applications, its short-term outgassing behaviour was investigated and compared with that of conventional UHV-compatible stainless steel grade AISI 304L.

Experimental setup

To investigate the outgassing behaviour of the stainless steel samples the difference method was used. The vacuum system consisted of two identical small vacuum chambers which are evacuated simultaneously via two small apertures. One of the chambers contains the sample and the other one is empty. To analyze the composition of the released gas, the partial pressures in both chambers were recorded as a function of time. The outgassing rates were calculated from the sample area and the difference of the partial pressures in both chambers. The experimental procedure is described in detail elsewhere [3,4].

Measurements

The results of the short-term outgassing measurements on unbaked Bö P506 samples are shown in Figure 1. The used samples were metallic blank with a typical surface roughness of some µm.

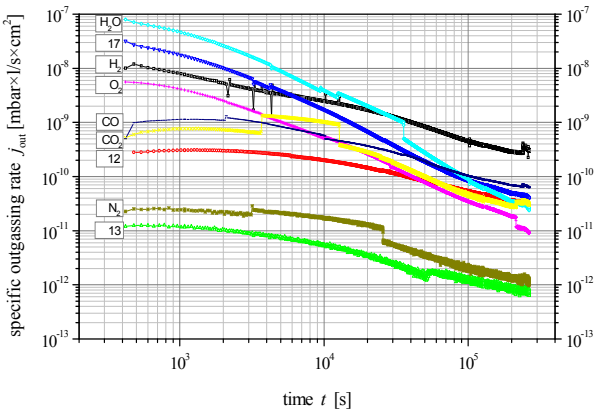

Figure 1: Short-term outgassing behaviour of the stainless steel grade Bö P506 in dependence of mass numbers.

During the first three hours after vacuum contact, the outgassing is mainly determined by water vapor which desorbs from the sample surface (desorption-controlled outgassing). The slope of the water vapour outgassing characteristic shows the typical $j_{out} \propto 1/t^{1.5}$ dependence. After this time, the main outgassing component is hydrogen. As expected, the outgassing rate of H_2 decreases slower with a $1/t^{0.5}$ dependence indicating a diffusion-controlled outgassing. Other gas species such as CO, CO_2 or O_2 play only a minor role in short-term outgassing behaviour, in long-term outgassing they may be even neglected. For the purpose of comparison the measurements were repeated with 304L samples. The results were absolutely comparable. In Figure 2 the total outgassing rates are diagrammed in dependence of time. As one can clearly see both steel grades have nearly identical j_{tot} vs. t curves.

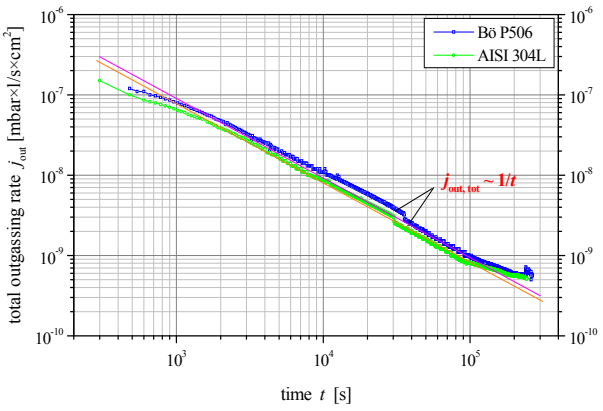

Figure 2: Comparison between short-term outgassing of conventional stainless steel grade AISI 304L and Bö P506

Conclusion

The results of the outgassing measurements seem to indicate that the new steel grade is UHV-compatible. Bö P506 shows a very similar short-term outgassing behaviour as the classical UHV stainless steel type AISI 304L. The investigation confirms that hydrogen is the dominant gas component with the highest outgassing rate after 3 hours of pumping. Furthermore, the measured outgassing rates are typical for unbaked stainless steel surfaces.

References

[1] http://www.boehler.at
[2] FAIR Technical Design Report (2008)
[3] N. Schindler, T. Riemann, Chr. Edelmann, J. Vac. Sci. Technol. **A 16(6)** (1998), 3569
[4] N. Schindler, et al. Vacuum **47(4)** (1996), 351

Simulation of pressure profiles for SIS18 upgrade using VAKTRAK code

St. Wilfert[1], C. M. Bellachioma[1], A. Krämer[1], J. Kurdal[1], M. Wengenroth[1], and H. Reich-Sprenger[1]
[1]GSI, Darmstadt, Germany

Abstract

Longitudinal pressure profile simulation for the Heavy Ion Synchrotron SIS18 upgrade program has been carried out using the VAKTRAK code [1,2]. Exemplary, static pressure profiles for SIS18 period VII were calculated in order to prove and verify the effectiveness of the linear pumping action of NEG (Ti-Zr-V)-coated vacuum chambers [3].

Simulations and results

The performed calculations base on the real dimensions and parameter of the vacuum components and UHV pumps assembled in period VII of the SIS18. The geometric structure of this period is shown in Figure 1. Since hydrogen is the dominant residual gas species (~ 80% H_2) in the SIS 18 the profile computations have been carried out only for a pure hydrogen atmosphere.

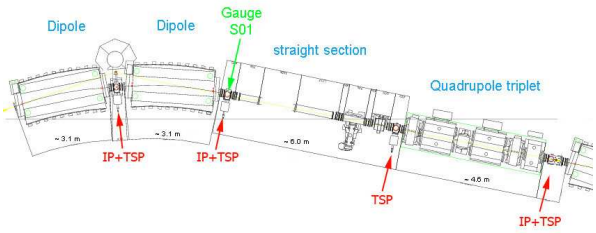

Figure 1: Structure of SIS18 period VII
(IP Sputter ion pump, TSP Titanium sublimation pump).

For the computation of the pressure profiles the following assumptions were made:

- Along the beam line section the beam pipe temperature is $T = 293\text{K} = \text{const.}$
- The UHV pumps (IP, TSP) have a pumping speed of S_{IP} = 100ℓ/s, and S_{TSP} = 900 ℓ/s for hydrogen. The NEG films show an uniform pumping action along the whole chamber length with a specific pumping speed of $(S/A)_{NEG} = 0.2\ \ell/\text{s}\cdot\text{cm}^2$.
- Approximately 99% of the released gas coming from the chamber walls is hydrogen, thus the outgassing is dominated by hydrogen. The outgassing rate for hydrogen was assumed to be $q_{H2} \sim 4\cdot10^{-13}$ mbar·ℓ/s·cm^2 (typical value [3]). Although CH_4 and CO are also detectable in the residual gas spectrum theses gas species are considered to be weakly released from the walls, hence the wall outgassing rate of these gases are neglected.

Four different cases for the positioning of NEG-coated chambers in period VII have been calculated. The results of the pressure profile calculations are displayed in Figure 2. Therein, the installation positions of the UHV pumps are marked with red arrows, the NEG-coated beam line components are labelled with dark grey bands, and the pressures measured at S01are marked with points.

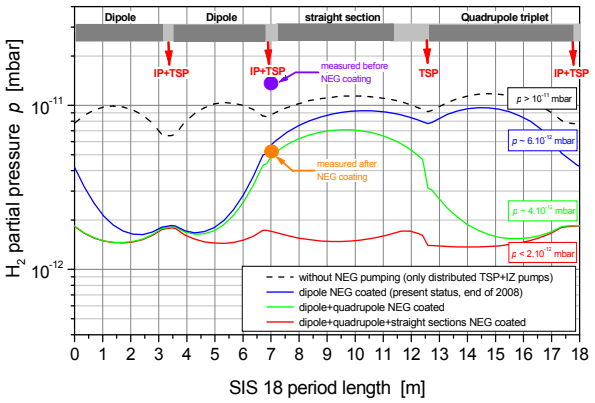

Figure 2: Static pressure profile for SIS18 period VII.

Conclusions

The results of the simulations are in sufficient good agreement with the pressures values recorded before and after the replacement of NEG-coated vacuum chambers in period VII (cf. Fig. 2). As expected, the investigations confirm that the NEG films influence considerably the pressure distribution in vacuum section of period VII. Depending on the installation position and the number of NEG-coated vacuum tubes, the pressure can be reduced locally of up to an order of magnitude. Without NEG-coated vacuum chambers, the average pressure in period VII was about ~ 10^{-11} mbar. If only both dipole chambers are NEG-coated (i.e. the present experimental conditions), the average pressure in period VII decreases to $6\cdot10^{-12}$ mbar. This was verified recently [4]. With additional NEG-coating of the quadrupole chambers an average pressure of $4\cdot10^{-12}$ mbar is expected. A nearly flat pressure profile in the lower 10^{-12} mbar range would be generated if the beam pipe chambers on the straight beam line section are NEG-coated, too.

References

[1] V. Ziemann, Proc. PAC 1993, 3909
[2] V. Ziemann, SLAC- PUB 5962 (Oct. 1992)
[3] V. Nemanič, T. Bogataj, Vacuum **50**(3) (1998), 431
[4] M.C. Bellachioma et al., this GSI Scientific report (ACC-13)

Investigations on the Activation- and Saturation Process of NEG Getters

M. Bender[1], H. Kollmus[2], M. C. Bellachioma[2], J. Kurdal[2], and W. Assmann[1]
[1]LMU, München, Germany; [2]GSI, Darmstadt, Germany

Non evaporable getter (NEG) coatings have become relevant in many particle accelerators during the last years. Beside RHIC at BNL, LHC and LEIR at CERN and others, also at GSI getter films are used in the heavy ion synchrotron SIS 18 [1, 2]. The applied films have established their full performance in the accelerators, however we have investigated the activation and saturation behavior as well as the aging of the getters in detail with a dedicated test bench and for the first time by ion beam analysis.

NEG getters consist typically of the elements Ti, Zr, and V. During pumping the metals are cumulatively terminated by oxides, carbides and nitrides, hence the pumping speed is decreasing. The reactivation of saturated NEG is done with high temperature, typically at the end of the UHV bake out. Here, the surface metal-gas-compounds dissolve and the gas is transferred to the inside of the layer.

To study the pumping performance of getter films in detail we have built up a test bench, consisting of a NEG coated DN-CF150 tube of 300 mm length. On one end a pumping post is connected to the tube and on the other side a gas inlet system, both by a conductance. The pressure in all three chambers is measured by extractor gauges. During gas injection the flux into and out of the NEG chamber is measured by $\Delta p \cdot C$ where C is the respective conductance. Dividing the difference of the gas fluxes by the pressure inside the coated tube we obtain the pumping speed of the NEG. Integrating the difference of the gas fluxes over time determines the capacity of the getter film since the coated area is well known. We have placed several square shaped coated samples inside of the NEG tube. Samples and tube were coated together giving equal film stoichiometry and thickness (roughly 1500 nm as measured by RBS). After activation the getter is saturated by CO. Then, the NEG tube is opened and one sample is extracted. Thus we obtain a series of samples activated once, twice, three times and so on. Typically one cycle of bake out, activation, saturation and dismounting takes one week.

We have obtained pumping speed and capacity values for eight cycles so far, whereas after four cycles the activation temperature was increased from 200°C to 250°C. The activation time was 24 h except for sample 8 that was activated 48 h. Fig. 1 shows values for the capacity in molecules per cm^2 and pumping speed in liters per second and cm^2. The decrease of the getter performance as well as the activation temperature shift are visible.

In addition to the aging measurements of the NEG films we have monitored the gettering process by ERDA. This ion beam analysis gathers element specific depth profiles by detecting sample atoms after they were elastically scattered by a heavy ion beam. Details are described elsewhere

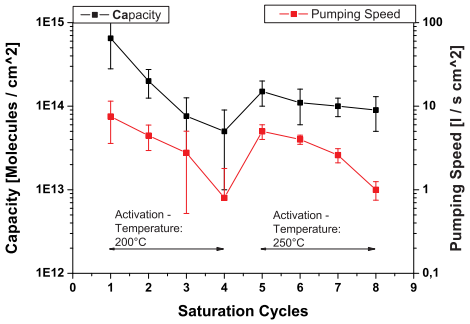

Figure 1: Aging of the NEG film: Capacity (black) and pumping speed (red) versus number of activation cycles.

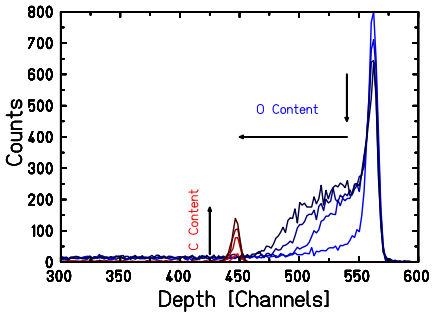

Figure 2: Element concentration vs. depth inside of the getter film

[3]. Since the saturation gas in our experiment is always CO we concentrate the ERDA examinations on the C and O amount inside of the metallic components. Fig. 2 shows the result of the first four samples. Oxygen (blue) and carbon (red) is plotted for the virgin sample and for three following activation / saturation cycles from light to dark color respectively. However the complete analysis is ongoing, it is already visible that carbon is augmented at the surface (at channel 450), while oxide (surface at channel 550) is incorporated into deeper layers, meaning lower channels as indicated by the arrows.

In future the results will be compared to XPS measurements and, depth dependant concentration profiles will be calculated.

References

[1] M. C. Bellachioma et al., Vacuum **82**, 435 (2008)

[2] M. C. Bellachioma et al., GSI Report **2007-1**, 91 (2008)

[3] W. Assmann et al., Nucl. Instr. Meth. B **89**, 131 (1994)

Base-Band Tune Measurements at SIS-18 using Direct Digitized BPM signals

U. Rauch[1,2], P. Forck[1], P. Kowina[1], and P. Moritz[1]
[1]GSI, Darmstadt, Germany; [2]Goethe University, Frankfurt, Germany

A clean determination of the tune value is important for stable SIS-18 operation, especially for intense beams. The new data acquisition system for Beam Position Monitors (BPM) based on fast signal digitization and digital signal processing [1] opens new possibilities for a sensitive tune measurement. In this system the broadband BPM signals are integrated bunch-by-bunch in order to get one position value (in vertical and horizontal plane) for each single bunch [2]. The measured position for the whole acceleration cycle is shown in Fig. 1 (right). Each point in the graph is an average over 1000 bunches. The obtained position resolution is better than 30 μm. For tune determination the so called "Base-Band tune measurement" method is used. The non-integer tune value q is obtained from position data by calculating a Fast Fourier Transform (FFT) typically over 2048 subsequent bunches. Since the FFT is calculated for equidistant points corresponding to the bunch positions, the frequency of the betatron oscillations is automatically normalized to the revolution frequency whereas no external parameter is required. Such frequency spectrum is expressed in units of q and ranges from $0 < q < 0.5$. The tune value measured over the whole acceleration cycle is shown in Fig. 1 (left). Each of the 153 points in the curve correspond to a peak position in the frequency spectrum described above. The observed tune value fluctuates within ± 0.013 around the mean value of 0.305. It has to be pointed out that the measured mean tune is shifted with respect to the preset value of 0.32. This may explain the discrepancies between predicted and measured resonance positions discussed in [3].

For a stable and well adjusted beam no coherent betatron oscillation can be observed. In order to measure the tune value the beam was slightly excited using a digital pseudo

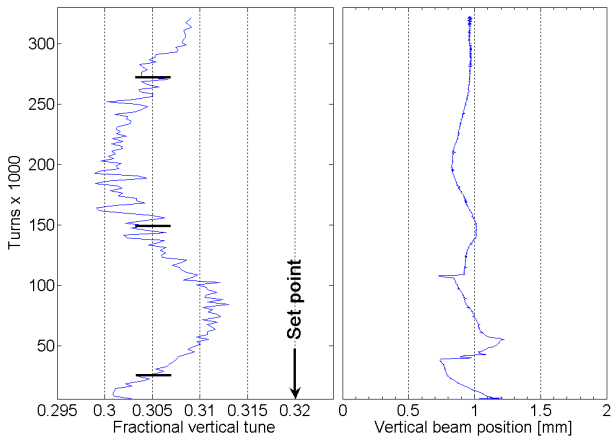

Figure 1: Vertical tune (left) and vertical position (right) of a beam of $3 \cdot 10^9$ Ar^{18+} ions accelerated from 11.4 to 450 MeV within 420 ms. Excitation at $q_{ex} = 0.32 \pm 0.025$ with $P_{ex} \simeq 3.5$ W. Three lines mark the data used for Fig. 2.

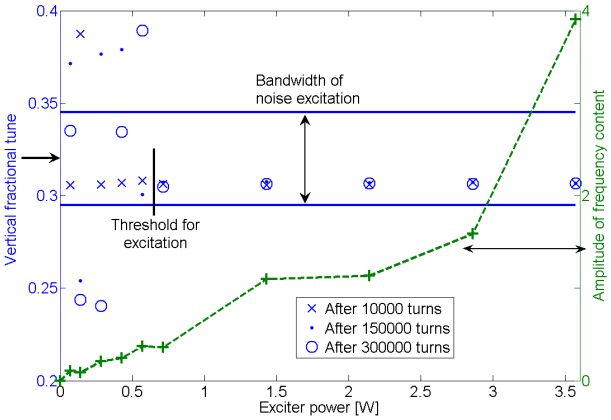

Figure 2: Beam response on noise excitation for turns indicated in Fig 1. Increasing excitation power leads to a repeatable tune value. The required power is lower than 1 W.

random noise generator (PRN). The PRN, connected to an exciter, produced white noise with an adjustable bandwidth on side bands of a carrier frequency f_c [4]. The white noise bandwidth was selected broad enough to cover the expected range of tune deviation i.e. usually $\Delta q_{ex} = 0.05$. The carrier frequency f_c is set by a frequency tracker connected to the SIS18 rf signal, for more details see [5, 6]. Since any beam excitation leads to emittance blow up, an important goal of the study was to determine the minimum exciter power required for precise tune evaluation. As depicted in Fig. 2 the value for the vertical tune strongly scatters at low exciter power which is an evidence for too weak beam excitation. On the contrary, above a threshold value of only 0.7 W the tune value is constant and reproducible. Moreover, for excitation power below 3.5 W no significant beam emittance blowup was observed.

Conclusions and Perspectives

We have shown that baseband digitization of BPM signals together with noise excitation of the beam allows precise tune determination on the synchrotron ramp. The measurements yield reproducible results even for low exciter power, thus preventing detrimental emittance blow-up. The system presented here is a promising prototype for tune measurements at FAIR.

References

[1] Hoffmann et al., contribution to this Report
[2] P. Kowina et al., GSI scientific Report 2007
[3] G. Franchetti et al., GSI-Acc-Note-2005-02-001 (Feb. 2005)
[4] K. Blasche et al., GSI Scientific Report 2000, p.184
[5] U. Rauch et al., Proc. of 5th CARE-HHH-ABI Workshop, Chamonix, Dec. 2007, p.58
[6] U. Rauch et al., DIPAC 09, Basel, to be published

A new Signal Treatment for SIS18 Beam Position Monitors

T. Hoffmann, P. Kowina, and K. Lang
GSI, Darmstadt, Germany

Introduction

Within the FAIR SIS18 upgrade the data acquisition hardware as well as the concept for signal treatment of the Beam Position Monitoring system (BPM) were renovated. The former BPM system was based on the analog narrow-band signal processing (see [1]). Since any information concerning an individual bunch is lost, observation in the turn-by-turn scale as well as tune measurement is impossible. Hence, a new data acquisition (DAQ) was developed. Acting as a prototype realization for the FAIR Control System, the software part of the DAQ is realized within the framework FESA [2], the Front-End Software Architecture developed by CERN. The programming is performed in cooperation with Cosylab [3].

System functionality

Fig. 1 shows the conceptual design of the system. The digitization of the analogue position signal, pre-evaluation and data transport is performed by FPGA based Libera stations [4]. Each of the four plates of one BPM Pick-up is connected to the analogue inputs of a Libera and sampled with 125 MHz by 14 Bit ADCs. For the position determination of one bunch, a broadband analysis of the bunch signals is realized by integration of the sum and difference signal over the bunch recorded in horizontal and vertical planes. Absolute position is calculated later on in the Concentrator Server (CS) including correction factors, i.e. position sensitivity and offset [5]. For the proper integration two things are required: i) window generation using the algorithm described in [6] and ii) a base line restitution, i.e. the reduction of the shift caused by AC coupling between beam and the Pick-up electrodes [7]. The maximum bit transfer for one position is 22 Bit. This exceeds the 14 bit resolution of the ADC since the maximum value of the integral is given by maximum signal amplitude (14 bit) and maximum expected bunch length (8 bit which corresponds to a bunch length of 2 μs). In addition to transversal positions, timestamps synchronized to the SIS18 RF signal are recorded. These timestamps are used to check the integration windows for errors and to synchronize the position data on the CS incoming from different BPM stations. Altogether an amount of 96 Bit of data is produced for one bunch at one BPM station. These data records are filled into jumbo Ethernet frames and sent with UDP out of the FPGAs Rocket IO which is used as a 1 GbE output. This results in a maximum data rate of about 580 MBit/s over Ethernet per BPM. To handle this high amount of data, produced by the twelve BPMs, a dedicated network was built by connecting the 1 GbE outputs of all Liberas to a switch with several 1 GbE and two 10 GbE ports. Tests have shown, that one single CS is not capable of handling the data of all twelve Liberas. So the switch merges the incoming data from the Liberas and splits them to two 10 GbE outputs, which are connected to two CSs. Once the data packages reach the CS the user can chose the way how the data will be evaluated. A basic operational mode is monitoring of the beam position in all 12 BPM stations and its evolution over an acceleration cycle. The beam behavior can be investigated in bunch-by-bunch manner as well as in the millisecond scale. Simultaneously, using the same data sets, the tune in vertical and horizontal planes can be measured for the selected BPM. This procedure bases on the FFT analysis of the bunch-by-bunch position information and is described in [8]. The BPM system can be easily extended by new functionalities without changing the hardware. It is foreseen, that the additionally stored RF signal will be used for the bunch marking. This allows the observation of the behavior of the given bunch through the BPM stations during acceleration, e.g. the phase advance between the subsequent BPM can be investigated. The commissioning of the system is planned for end of March 2009.

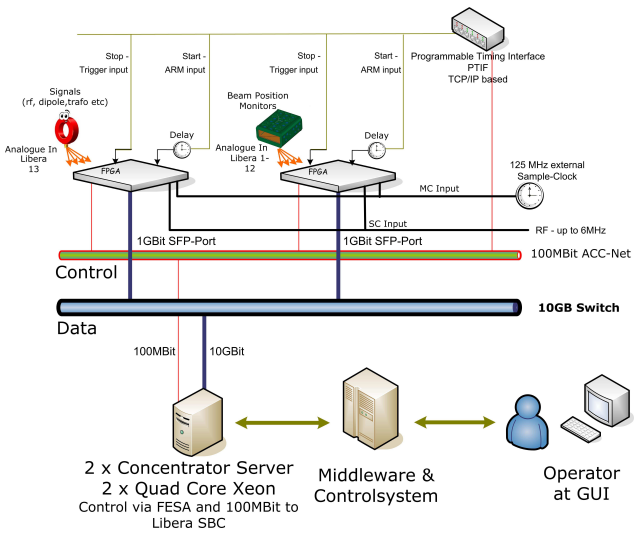

Figure 1: Layout of the BPM data acquisition system based on 10 GB network and Libera electronic.

References

[1] P. Forck et al., *CAS "Beam Diagnostics"*, Dourdan (2008).
[2] T. Hoffmann, *Proc. PCaPAC08*, Lubliana (2008) p.183.
[3] www.cosylab.si
[4] www.i-tech.si
[5] P. Kowina et al., *Proc. DIPAC05*, Lyon (2005) p.114.
[6] P. Kowina et al., *Ann. Rep. GSI 2007*, (2008), p. 78.
[7] A. Galatis et al., *Proc. EPAC06*, Edinburgh (2006) p.1019.
[8] U. Rauch et al., contribution to this Ann. Rep.

Commissioning of Beam Induced Fluorescence Monitor at Unilac

C. Andre, F. Becker, C. Dorn, P. Forck, H. Graf, R. Haseitl, K. Lang, M. Schwickert, B. Walasek-Höhne
GSI Darmstadt, Germany

Overview

Due to the high-current operation at UNILAC non-intercepting beam diagnostics is mandatory. In October 2008 a Beam Induced Fluorescent (BIF) monitor for transverse profile determination was set up in the UNILAC section US1. It serves as a prototype for the installation at 7 locations at UNILAC and the transfer channel to SIS. The comissioning and proof of functionality of the new installation was done in December 2008.

Hardware Setup

BIF basically consists of 2 custom designed intensified camera systems (Proxitronic, BV2582 TX-V 100N) installed perpendicular to achieve horizontal and vertical beam profiles simultaneously for each macropulse.

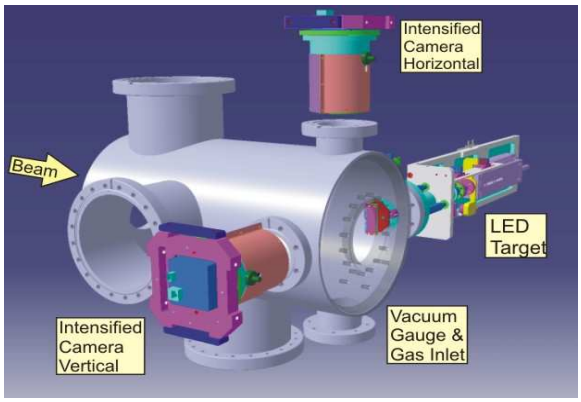

Fig. 1: Diagnostic chamber with BIF monitor

The intensified camera-system consists of a photocathode (S20), a double MCP and a phosphor (P46), fiber-coupled to a digital CCD camera (Basler 311f mono-chrome). With a magnification of up to 10^6, single photons can be detected, as emitted by fluorescence of atomic collisions between the heavy ion beam and residual or injected gas (N_2) molecules [1]. With a lens system of 16 mm focal length (Pentax C1416ER) mounted at a working distance of 195 mm, a resolution of 4.5 pix/mm and a depth of field of 30-40 mm could be achieved. All devices were optimized for the wavelength of N_2 transitions at about 400 nm. For the BIF monitor, a new chamber was designed with blackened walls and multiple flanges for cameras, gas inlet (Pfeiffer PKR 261), vacuum gauge (Pfeiffer EVR 116) and LED target. Additionally, the chamber (total length: 470 mm) contains a second diagnostic device (e.g. SEM grid, Faraday cup). The geometry of the LED target is designed to adjust both camera systems and to measure the resolution and depth of field within a single measurement. All devices of the BIF setup are remote controlled by a new Software 'BeamView' [2] and operated by a Windows PC from the main control room.

Results

First measurements with the new BIF Monitor were done with a high-current Ar^{1+} beam of 1.4 MeV/u, 4.5 mA and 10 µs. For validation, BIF images and profiles were compared to data of SEM grid US1DG1 (distance: 340 mm). They show good agreement in width and shape.

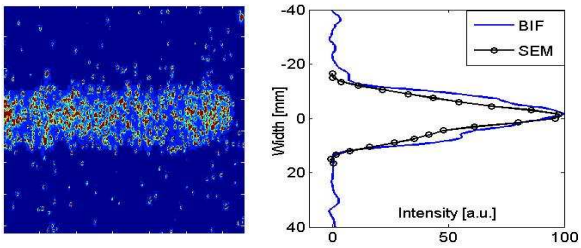

Fig. 2: BIF image (left); BIF and SEM horizontal profiles in horizontal direction (right); average of 5 single pulses

To estimate best settings for BIF, variations of the N_2 pressure were measured with a high current Ar^{1+} beam of 1.4 MeV/u, 3.5 mA and 15 µs.

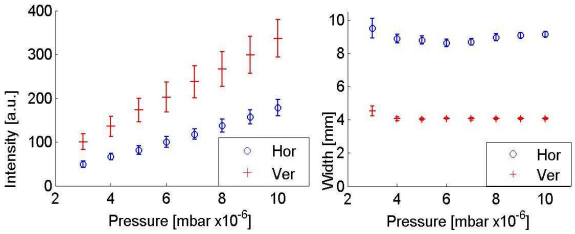

Fig. 3: BIF intensity and beamwidth during pressure variation: Mean value and error of 100 single pulses

A reasonable pressure for a high-current Ar^{1+} beam is at this location around $5 \cdot 10^{-6}$ mbar. The signal intensity is high enough to show a profile for a single shot and the measured beamwidth is constant. Less N_2 insertion seems to give a wider profile, due to transitions of other molecules (e.g. H_2O) [3]. This effect could be eliminated using optical filters, but only with a decrease in intensity.

Outlook

For high beam currents, BIF showed a good functionality and a reasonable signal, even in single shot operation. In 2009 further BIFs will be installed in TK and UNILAC. We will investigate in optimizing the system, e.g. by testing filters or spectroscopic measurements of other appropriate gases.

References

[1] P. Forck et al.,"Beam Profile Monitors on Residual Gas Interaction", DIPAC 2005
[2] R. Haseitl et al.,"BeamView- A Data Acquisition System for Optical Beam Instrumentation", PCaPAC 2008
[3] F. Becker et al.,"Beam Induced Fluorescence (BIF) Monitor for Transverse Beam Determination", DIPAC 2007

The new BeamView Software for Scintillator Screens*

R. Haseitl, C. Andre, P. Forck, and T. Hoffmann
GSI Accelerator Beam Diagnostics, Darmstadt, Germany

System Components

As optical beam instrumentation at GSI, mainly scintillator screens are used and read out with analogue cameras. This system is simple and cheap, but suffers from some disadvantages which are solved by the new, completely digital system: exact triggering, exposition control, histogram/projection calculation and picture storage for offline analysis. As prototype setups the HITRAP experiment, as well as a scintillator test installation have been equipped with digital FireWire cameras (AVT Marlin F033B).

The components of the new system are schematically shown in Fig. 1. The FireWire cameras are connected via fiber optical extenders to dedicated image processing hardware, acting as middle layer between the camera and the PC running the Graphical User Interface (GUI). For this purpose, the embedded system from National Instruments Compact Vision System 1456 (CVS) [1] is used running a LabView Real-Time application, implemented by an industrial partner [2]. Images from up to four active cameras can be compressed, mirrored, rotated, cropped and sent to a Windows or Linux PC. For timing purposes, a programmable timing decoder and trigger generator with network connection is used. The camera iris is connected to an Ethernet-controlled 'iris-control' device.

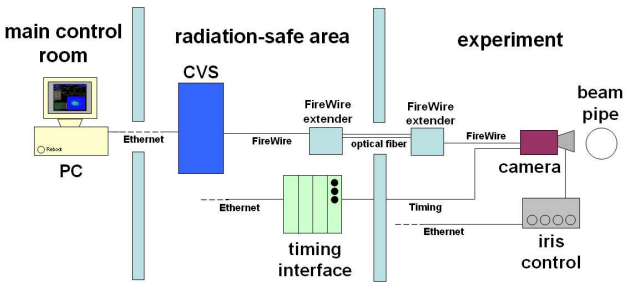

Figure 1: Overview of the controlled devices: CVS, FireWire camera, timing interface and iris control.

Software Design

On the control room PC the BeamView software receives images and projections from the CVS and presents it to the user. Furthermore, BeamView controls the timing and iris control hardware. A screenshot is depicted in Fig. 2. BeamView is written in C++ using Qt libaries [3] to guarantee platform independence. The connection to the CVS is implemented using standard TCP/IP sockets. An XML-based protocol is used for communication, to ensure compatibility for future extensions. More details on the system can be found in [4].

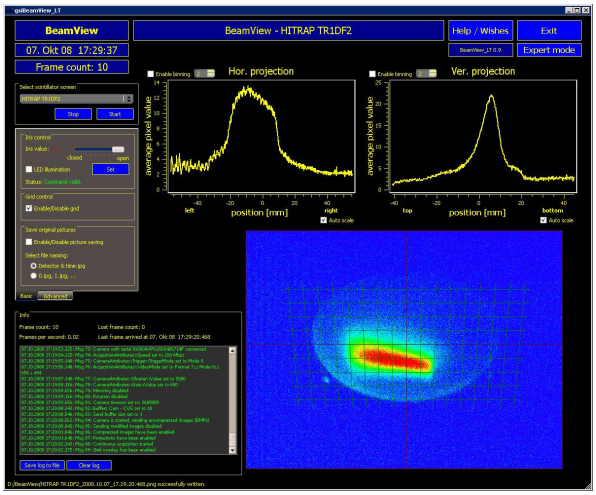

Figure 2: Screenshot of the BeamView software, showing a Ni beam on a YAG scintillator in false-color mode.

Performance and User Experience

For performance tests a camera, capable of delivering a maximum of 60 frames per second (fps) in VGA resolution (640x480 pixel), has been connected to the CVS. The bottleneck of the processing chain turned out to be the CVS CPU and its network performance. Uncompressed images can be sent to the PC with 16 fps, compressed images with 35 fps. Tests with many cameras are currently running. In daily operation, high frame rates are rarely required. BeamView has been used to collect data for different experiments, e.g. scintillator screen investigations with frame rates typically between 2 and 15 fps [5]. Over 28 GB of images have been stored without data loss during the whole measurement of six hours. The current version of BeamView is optimized for observations with a single camera. An upgrade for detector systems with multiple cameras like Beam Induced Fluorecence monitors is presently under development.

* Work supported by EU, project FP6-CARE-HIPPI

References

[1] Company National Instruments, www.ni.com
[2] Company Ingenieurbüro Hagel, www.ib-hagel.de
[3] Company Trolltech, www.trolltech.com
[4] R.Haseitl et al., Proc. PCaPAC'08, Ljubljana, (2008).
[5] E.Gütlich, P.Forck, R.Haseitl, "Scintillation Screen Investigations for High Current Ion Beams at GSI Linac", BIW'08, Lake Tahoe, (2008).

Scintillation Screen Investigations at UNILAC

E. Gütlich[1,2], P. Forck[1], C. Andre[1], F. Becker[1], W. Ensinger[2], R. Haseitl[1], H. Graf[1], P. Kowina[1]
[1]GSI, Darmstadt, Germany, [2]Technical University, Darmstadt, Germany

Scintillation screens are widely used since decades for qualitative beam profile measurement. Via scintillation screens one can obtain a direct and entire image of the transversal beam profile. Moreover, these screens are an essential part of a pepper-pot emittance system [1, 2] for which the imaged beam width σ is important. Therefore, we investigated the optical properties of 16 fluorescence materials with different beams delivered by the UNILAC [3-5]. The screens were irradiated with beams of C^{2+}, Ar^{10+}, Ni^{9+} and U^{28+} ions at energies between 5.5 and 11.4 MeV/u and different beam currents. Typical sizes for the focused beam were σ≈2mm. Sensitive scintillation screens, like YAG:Ce or ZnS:Ag were irradiated in addition with lower currents. Ceramic materials with less light yield, like BN, ZrO_2, ZrO_2 doped with Mg, pure Al_2O_3 and Al_2O_3 doped with Cr (Chromox) were also investigated and compared to Quartz-glass (Herasil 102) and Quartz-glass doped with Ce (M382), see Table 1.

Table 1: Compilation of investigated materials

Type	Material	Supplier
Crystal Scintillator	YAG:Ce, BGO, $CdWO_4$, CaF_2:Eu	Saint Gobain Crystals
Powder	ZnS:Ag	HLW
Ceramic	ZrO_2(Z700 20 A), ZrO_2:Mg (Z507), BN, Al_2O_3 and Al_2O_3:Cr (Chromox)	BCE Special Ceramics
Quartzglass	Pure: Herasil 102, Ce doped: M382	Heraeus Quartzglass

The experiments were carried out at cave X2 where a movable target ladder equipped with 6 different screens of diameter 30 mm was installed to allow undisturbed beam observations [4]. The scintillation light was detected with a digital CCD camera (AVT-Marlin) equipped with a FireWire interface. The image of each macro-pulse was stored and individually evaluated by a high performance data acquisition system [6]. As published in [3,4] the investigated materials have up to two orders of magnitude different light yield. For a medium current of 30µA and 100µs beam delivery of Ar^{10+} at 11.4 MeV/u, the light yield was nearly constant during 30 minutes of irradiation for Al_2O_3:Cr, ZrO_2:Mg, BN, Herasil, ZrO_2. However, the determined beam width differs in a reproducible manner between the materials. For the given beam parameters Herasil shows 22 % smaller width compared to ZrO_2:Mg. For three materials (BN, Al_2O_3:Cr and ZrO_2) the same width was recorded. Recent measurements at high currents (~310µA) revealed a more complicated behaviour of the screens due to the higher temperatures (~240°C @ 2.3W average beam power).

For comparison the properties of commonly used scintillators under low current irradiation were investigated. In Fig. 1 the results are shown for the 17 nA C^{2+} beam of 100 µs length and 12.6 Hz repetition rate. The light yield of the materials differs by one order of magnitude with YAG:Ce being a very efficient scintillator. However, even for these materials, quite different image widths were recorded. BGO showed the smallest value, while irradiation of YAG:Ce, $CdWO_4$ and CaF_2:Eu results in a ≈25% larger value for beam width σ.

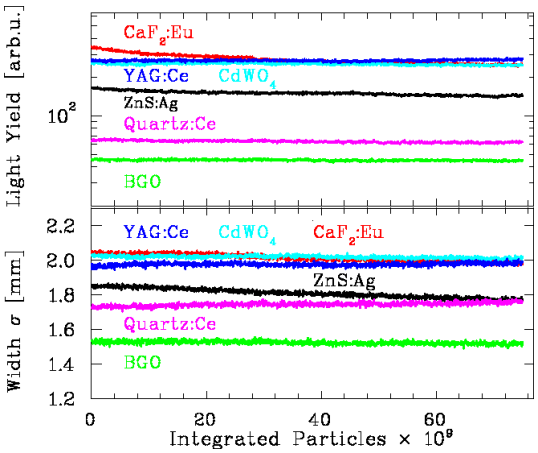

Figure 1: Light yield and beam width for different materials irradiated by 15000 macro-pulses of 12.6 Hz repetition rate with ≈5x10⁶ ppp C^{2+} at 11.4 MeV/u.

Conclusion

The investigated materials showed under the same beam parameters a difference in the imaged beam width of up to 25%. This is a critical issue for accurate measurements like the pepper-pot method. Moreover, it is remarkable that not only ceramics like ZrO_2:Mg and Al_2O_3:Cr showed this behaviour but also commonly used scintillators like YAG:Ce and BGO. This phenomenon is not fully understood by now and requires further investigations.

References

[1] T. Hoffmann et al, Proc. Beam Instrum. Workshop BIW, Cambridge, MA, AIP 546, p.432 (2000).
[2] J. Pfister et al., Proc. EPAC 2008, p. 3449 (2008).
[3] E.Gütlich, P.Forck et al., GSI-Scientific Report 2007, p.105.
[4] E. Gütlich, Diploma Thesis, University of Applied Science Wiesbaden (2008).
[5] E. Gütlich, P. Forck, et al., Proc. Beam Instrum. Workshop BIW, Lake Tahoe, CA 2008.
[6] R. Haseitl et al., Proc. PC@PAC, Ljubljana, p.180 2008.

A cw Heavy Ion Linac Based on Superconducting CH-Structures

H. Podlech[1], A. Bechtold[1], M. Busch[1], S. Minaev[1], U. Ratzinger[1], R. Tiede[1]
[1] Institut für Angewandte Physik , Goethe Universität, Frankfurt am Main.

Abstract

According to the Unilac upgrade program for the SHE research at GSI, a new high energy part of the High Charge State Injector (HLI) has to be worked out. One of the versions of this linac foresees the acceleration of the highly stripped ions with charge-to-mass ratio of 1/6 delivered from the existing HLI at 1.4 MeV/u. The output beam energy should allow experiments at the Coulomb barrier and is assumed to be variable from 3.5 MeV/u to 7.5 MeV/u. These capabilities would allow for a competitive research in the field of radiochemistry and for the production of super heavy elements (SHE).
Since high luminosities are strongly desirable on the target, the superconducting linac operated at 100% duty factor seems to be a very attractive solution for this machine. A preliminary linac design based on superconducting CH-cavities is presented.

Superconducting CH-Cavities

The CH-cavity is a multi-cell cavity suitable for the efficient acceleration of low and medium energy ions. It combines the advantages of more conventional multi-cell cavities like IH-structures and superconducting operation. Superconducting cavities can be operated at significant higher acceleration gradients especially with high duty cycles. A superconducting CH-prototype cavity has been developed and tested with gradients of 7 MV/m in cw operation [1],[2].

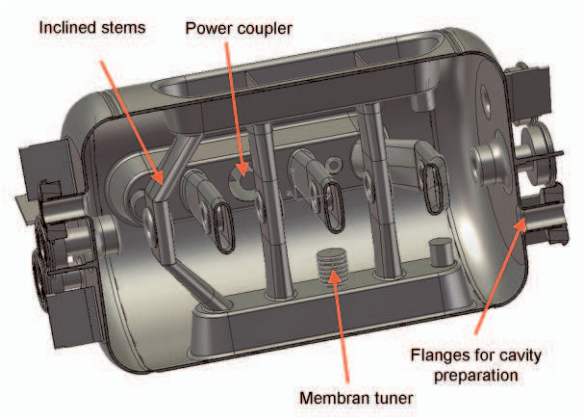

Figure 1: Optimized CH-cavity geometry.

Recently the cavity geometry has been optimized based on the experience with the prototype cavity. The new design has reduced drift sections in the end-cells which leads to very compact cavities with improved beam dynamics. Additionally, the new geometry is capable to handle more RF power and it has an innovative tuning concept using internal membrane tuners.
It is planned to build a 325 MHz prototype cavity optimized for a particle β of 0.15. This cavity will be fully equipped with cryo module, power coupler and tuner system. It is also planned to test this cavity with beam behind the Unilac at GSI. Figure 1 shows the new cavity which can be considered as the prototype for the cw heavy ion linac.

Linac Layout

The superconducting part of a dedicated cw heavy ion linac will consist of multi-cell CH-cavities. Nine CH-cavities are required to reach the maximum energy of 7.5 MeV/u. To simplify the production process of the cavities and to assure energy flexibility each cavity has a constant cell length. Beam dynamics simulations showed a good beam quality over the full energy range between 3.5 and 7.5 MeV/u. The RF frequency of the CH-cavities is 216.96 MHz which is twice as high as the frequency of the HLI. This frequency gives sufficient longitudinal acceptance and lead to the required cell length especially in the first superconducting cavities. Between the CH-cavities superconducting solenoids with fields of up to 10 T are foreseen. The use of solenoids and superconducting CH-cavities lead to a very compact linac design with a length of about 17 m including the matching section after the HLI. Figure 1 shows the schematic plot of the superconducting CH-linac.

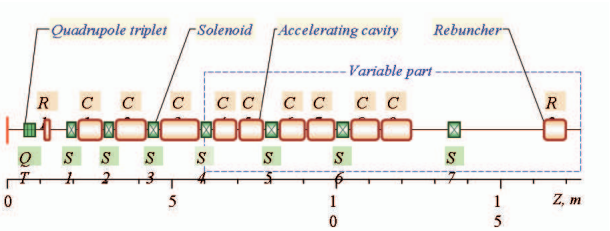

Figure 2: Layout of the sc CH-Heavy Ion Linac.

References

[1] H. Podlech et al., Phys. Rev. STAB, **10**, 080101(2007)
[2] H. Podlech, Habilitationsschrift, Goethe Universität Frankfurt, 2008.

Tuning of the Superconducting CH-Structure*

A. Bechtold[1], M. Busch[1], H. Liebermann[1], H. Podlech[1], U. Ratzinger[1]
[1]IAP, Universität Frankfurt, Germany.

Abstract

After the successful tests of the superconducting CH-prototype including the piezo tuners inside of a vertical cryostate, the CH-prototype is now beeing installed into a horizontal cryostate with a slow mechanical tuning device. In parallel a second generation is now beeing designed for dedicated high current projects such as IFMIF or EUROTRANS. The tuning concept has been innovated leading to an even more compact device.

Test of the CH-prototype Tuning System

All parts of the horizontal cryostat are now assembled and aligned. A first vacuum test of the inner cold mass has been performed successfully. The liquid nitrogen cooling system is prepared and closed now; it has been extended by an additional cooling loop at the pump port of the cavity. A first cold test is currently performed. A driver for the slow mechanical tuner has now been designed and constructed and allows either a manual or a computerized operation. This device has passed a first test run. The driving speed of the stepping motor can easily be changed and will be adjusted during the first performance test with the cavity. Before that there will be a cold test of the cryostat without cavity, to check for cold leaks and thermal issues.

Figure 1: Cold test of the horizontal cryostat with liquid nitrogen.

The New Superconducting CH Tuning Concept

The most obvious change is the inclining of the outermost stems to homogenize the field distribution along beam axis. That was realized at the prototype by lengthening the drifttubes which are embedded in the tank wall, with the acceptance of longer drifts which is rather disadvantageous especially at high beam currents where the next focusing element should not be to far away.

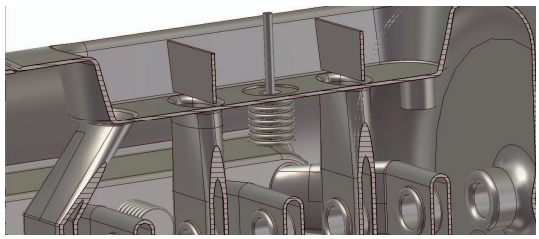

Figure 1: fast Membrane tuner for the new CH-structure at 325 MHz, $\beta = 0.154$.

The design of the stems has been changed in a second way: The ratio between logitudinal and transversal stem diameter has been inverted, giving more space inbetween to locate the power coupler and the new membrane tuners. This change has been done by accepting a slightly higher magnetic peak field at the basis of each stem. The magnetic peak fields are a limiting factor regarding the maximum achievable accelerating field.

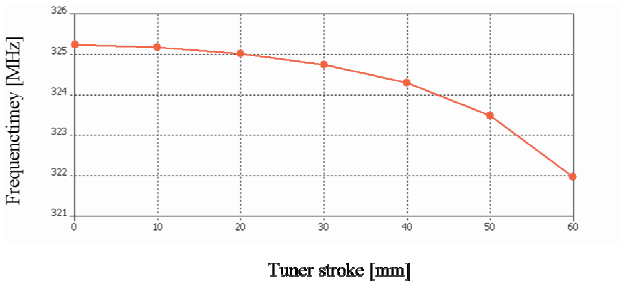

Figure 2: Performance of the membrane tuner.

References

[1] A. Bechtold, M. Busch, H. Liebermann, H. Podlech, U. Ratzinger, "A tuner for a Superconducting CH-Prototype Cavity", SRF2007, Peking.

[2] H. Podlech, A. Bechtold, M. Busch, H. Klein, H. Liebermann, U. Ratzinger, "Development of the superconducting CH-cavity and Applications to Proton and Ion Acceleration", SRF2007, Peking..

Neutron doses in the experimental halls TR, EX, TH

T. Radon[1], G. Fehrenbacher[1], Ch. Pöppe[1], J. Sauer[1], and M. Wengenroth[1]
[1]GSI, Darmstadt, Germany

Introduction

Ionising radiation is produced during the operation of heavy ion accelerators especially when substantial beam loss occurs. In order to protect persons from exposure to ionising radiation the efficiency of the shielding installations has to be checked by various measurements. The total dose outside the shielding of the accelerators and exp. areas comprises at GSI in most cases a major neutron component and a small photon component. We mainly focus here on the measurement of the neutron doses by a passive detection system. This detector system is based on thermoluminescence which makes it a reliable tool for dose measurements even for beams with complex spill-structures [1].

Annual doses in 2008, comparison with 2007

Figure 1 depicts the heavy ion synchrotron SIS and the adjacent experimental areas together with the positions of the neutron detectors. Similar to the previous years [2] it can be seen that the dose values are largest in the vicinity of the SIS extraction area. Due to an increase in the intensity of the ion beams leaving the SIS it was several times necessary to install (temporarily) controlled areas on top of the shielding near the SIS extraction, the FRS target and the beam dump HHD, because the measured dose rates were higher then 3 µSv/h which is the upper limit for uncontrolled areas. An analysis of the doses of the last two years shows that the overall integrated measured neutron-dose outside the shielding is more than 3.5 times larger in 2008, see Table 1. It should be noted that the detector with the highest dose value shown (40 mSv) is located inside a permanently controlled area, see Fig. 1. In addition another dose value is shown which is located inside of a cave (5 mSv). If these two values are removed from the list of doses, then still in 2008 a dose of more than a factor of 2 higher compared to 2007 was measured. If further on, all the values of the SIS and the FRS are subtracted from the total dose the dose-ratio between 2008 and 2007 is unity. As there were no major changes in the shielding, obviously a large intensity-upgrade has taken place in the last year. There is also an active method to detect the dose-rate providing the possibility to read the levels on an hour-base. The overall agreement between the measurements with active devices [3] and the TLD-based system is in the order of 10 to 30 % here, which is a good value for operational radiation protection.

Table 1: Measured neutron doses in the experimental halls outside the shielding, see Fig. 1 for explan. of * and **

position neutron-doses	2007	2008	fac.
total	19 mSv	70 mSv	3.6
total w/o * and **	11mSv	24 mSv	2.2
total w/o *, **, SIS, FRS	4 mSv	4 mSv	1.0

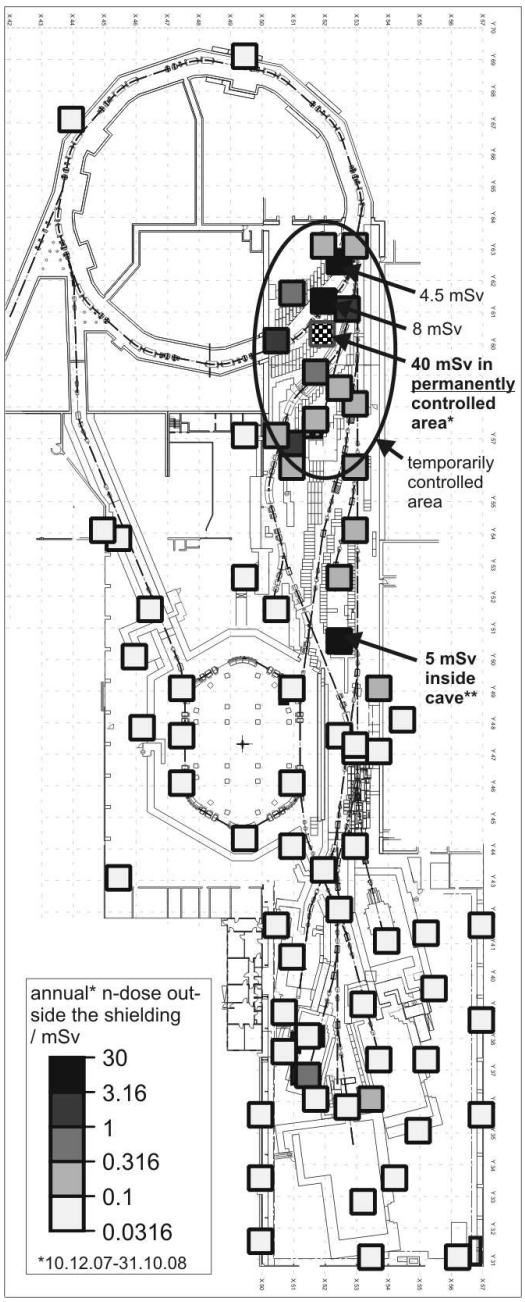

Figure 1: Measurement positions of the neutron doses (2008) in the experimental halls and their dose values.

References

[1] G. Fehrenbacher, F. Gutermuth, E. Kozlova, T. Radon, and D. Schardt, GSI-report 2005-1, p. 238.
[2] T. Radon, G. Fehrenbacher, S. Grosam, and Ch. Pöppe, GSI-report 2007, p. 248.
[3] F. Gutermuth, T. Radon, G. Fehrenbacher, and J.G. Festag, Kerntechnik (2003), 68, 4, pp. 172-179.

Probing Shell Effects at Z=120 and N=184

S. Hofmann[1,2], D. Ackermann[1], S. Antalic[3], V.F. Comas[4], S. Heinz[1], J.A. Heredia[4], F.P. Heßberger[1], J. Khuyagbaatar[1], B. Kindler[1], I. Kojouharov[1], M. Leino[5], B. Lommel[1], R. Mann[1], K. Nishio[6], A.G. Popeko[7], S. Saro[3], J. Uusitalo[5], M. Venhart[3], A.V. Yeremin[7]

[1]GSI Darmstadt, Germany, [2]University Frankfurt, Germany, [3]University Bratislava, Slovakia, [4]InSTEC Havana, Cuba, [5]University Jyväskylä, Finland, [6]JAEA Tokai, Japan, [7]FLNR-JINR Dubna, Russia

In a first attempt to confirm data on superheavy elements obtained in Dubna using hot fusion reactions [1] we studied the reaction ^{48}Ca + ^{238}U => ^{286}112*. Although the cross-section of (2.5+1.8−1.1) pb is not the highest one measured for hot fusion reactions at the Dubna gas-filled separator (DGFRS), the reaction with the relatively stable and easy to handle ^{238}U target was favored for technical reasons. Four events were measured in our SHIP experiment [2], which fully confirms the data measured at the DGFRS.

Another independent confirmation of the Dubna data was obtained by chemical means in the case of decay chains starting at the isotope ^{287}114 [3]. On the basis of the positive results from both confirmation experiments and consistent results of the various reactions (including cross bombardments) and decay chains up to element 118 measured in Dubna [1], we planned and performed an experiment to search for element 120 using the reaction ^{64}Ni + ^{238}U => ^{302}120*.

The main goal of this experiment was to probe the strength of the predicted closed neutron shell at N=184 and that of a subshell closure at Z=120. Various theoretical models predict different shell-correction energies of nuclei in this region, which cover a range from −6 MeV to −12 MeV, see e.g. [4] and references cited therein.

Using a shell-correction energy of ≈−7.0 MeV for the isotopes $^{299–302}$120, which converts into a fission-barrier height of ≈+7.0 MeV, a cross-section of 4.5 fb was obtained for the reaction ^{64}Ni + ^{238}U => ^{299}120 + 3n in a recent theoretical study [5]. However, using the rule of thumb that a change of the fission barrier by 1 MeV results in a change of the cross-section by one order of magnitude, we would obtain a cross-section of 4.5 pb at a fission-barrier height of 10 MeV, leaving the probabilities for capture in the entrance channel and formation of the compound nucleus unchanged.

The irradiations were performed in three periods in 2007 and 2008. Details of the experiment parameters and the obtained cross-section limits are listed in Table 1.

In the main part of the experiment a cross-section limit of 90 fb was reached at a mean excitation energy of 36.4 MeV where the cross-section maximum is expected. This cross-section limit converts into a lower limit of the negative shell-correction energies of the isotopes $^{299–302}$120 of −8.3 MeV using the estimation as described before. Unusual large shell-correction energies at Z=120 and N=184 thus can be excluded.

As a main activity of the continuation of our work on the synthesis and properties of superheavy elements we plan to systematically study hot fusion reactions based on ^{248}Cm targets. A first challenge will be the measurement of an excitation function for the synthesis of element 116 in the reaction ^{48}Ca + ^{248}Cm.

References

[1] Yu.Ts. Oganessian, J. Phys. G: Nucl. Part. Phys. 34, R165 (2007)
[2] S. Hofmann et al., Eur. Phys. J. A 32, 251 (2007)
[3] R. Eichler et al., Nature 447, 72 (2007)
[4] M. Bender et al., Phys. Lett. B 515, 42 (2001)
[5] V. Zagrebaev and W. Greiner, Phys. Rev. C 78, 34610 (2008)

Table 1: Parameters of the ^{64}Ni + ^{238}U => ^{302}120* experiment at SHIP.

date	days	target	d /µg	E* /MeV	dose /10^{18}	q	no. of events	ε /%	σ /pb
1. 16. 4. – 22. 4. 2007	6	U_{metal}	457	32.3	1.2	9^+	0	45	<1.6
2. 23. 4. – 21. 5. 2007	28	U_{metal}	447	37.4	5.0	9^+	0	45	
3. 20. 1. – 17. 3. 2008	54	U_{metal}	443	35.9	9.1	9^+	0	45	
4. 10. 9. – 20.10. 2008	34	U_{metal}	435	36.9	7.0	9^+	0	45	
mean/sum of 2. – 4.	116	U_{metal}	441	36.4	21.1	9^+	0	45	<0.09

Observation of ^{270}Hs in the complete fusion reaction ^{36}S+^{238}U*

R. Graeger[1#], A. Gorshkov[1], A. Türler[1], A. Yakushev[1], D. Ackermann[2], Ch. E. Düllmann[2], E. Jäger[2], F. P. Heßberger[2], J. Khuyagbaatar[2], J. Krier[2], D. Rudolph[2,3], M. Schädel[2], B. Schausten[2], J. Dvorak[4], M. Chelnokov[5], V. Chepigin[5], A. Kuznetsov[5], O. Petrushkin[5], J. Even[6], D. Hild[6], J. V. Kratz[6], J. P. Omtvedt[7], F. Samadani[7], K. Nishio[8] and Q. Zhi[9]

[1]TU München, Garching, Germany; [2]GSI Helmholtzzentrum für Schwerionenforschung GmbH, Darmstadt, Germany; [3]U Lund, Sweden; [4]LBNL, Berkeley, CA, USA;[5]FLNR, Dubna, Russia; [6]U Mainz, Germany; [7]U Oslo, Norway; [8]JAEA, Tokai-mura, Japan; [9]IMP, Lanzhou, China

Superheavy elements ($Z \geq 104$) exist only due to nuclear shell effects. Deformed shell closures at Z=108 and at N=162 have been predicted theoretically [1] and observed in recent experiments [2]. Three hassium isotopes $^{269\text{-}271}$Hs, have been produced in the complete fusion reaction ^{248}Cm(^{26}Mg, xn)$^{274\text{-}x}$Hs at the linear accelerator UNILAC at GSI [2,3]. The excitation function measurement at five different beam energies resulted in maximum cross sections of the 3n, 4n, 5n exit channels of a few pb [3].

Recent theoretical studies, analysing the formation of ^{270}Hs in the 4n channel, using a two-parameter Smoluchowski equation, predict even higher cross sections due to a lower reaction Q-value for the reaction ^{238}U(^{36}S,4n)^{270}Hs (24 pb) and ^{226}Ra(^{48}Ca,4n)^{270}Hs (30 pb) [4]. HIVAP [5] predicts a maximum cross section of 3.5 pb for the reaction ^{238}U(^{36}S,4n)^{270}Hs.

Here, we report on first results of an experiment aimed to study the nuclear fusion reaction ^{36}S + ^{238}U, leading to the compound nucleus ^{274}Hs*. For the experiment we used our highly efficient chemical separation and detection system COMPACT which was connected to a Recoil Chamber (RC) installed behind the ARTESIA target wheel in cave X1 [2]. A beam of $^{36}S^{5+}$ ions was accelerated by the UNILAC up to 7.13 MeV/u and impinged on a rotating ^{238}U target wheel. During the experiment, we used two different sets of ^{238}U targets. The beam passed through a 20.2 μm Be vacuum window, 6 mm of He/O_2 gas mixture (He:O_2 = 9/1), a 12.6 μm Be target backing before entering the ^{238}U target (3 segments of 1.8 mg/cm^2, 1.5 mg/cm^2 and 1.6 mg/cm^2). The second target set had a Be backing of 8.2 μm and 3 segments containing 1.0 mg/cm^2 of ^{238}U each. We assumed that only Hs nuclei with a minimum residual range after exiting the target of 10 mm in gas could be transported to the detection system, corresponding to an active layer of the target of 1.0 mg/cm^2. The energy of the ^{36}S ions was in the range of 175.0 MeV to 181.2 MeV within the first set of target and in the range of 190.4 MeV to 196.1 MeV in the second set [6], corresponding to excitation energies, E*, of 38±3 MeV and 51±3 MeV [7], near the predicted maxima of the 4n and 5n evaporation channel, respectively. Starting at E*= 38 MeV we irradiated the first target set with a beam dose of $5.74 \cdot 10^{17}$ ions. The second target set was irradiated with a beam dose of $1.03 \cdot 10^{18}$ ions at E*= 51 MeV.

We searched for correlated decay chains, which were defined as an α-decay ($8.0 \leq E_\alpha \leq 9.5$ MeV) followed within 300 s in the same or a neighbouring detector pair by an α-decay in the same energy range or by a SF-like event with at least one fragment above a threshold of 15 MeV. The data analysis revealed one chain at the higher E* of 51 MeV. A 9.02±0.05 MeV α-particle was observed in bottom detector #24 followed after 23 ms by one 41 MeV fission fragment measured in top detector #24. We attributed this decay chain to the decay of ^{270}Hs produced in the 4n evaporation channel [2].

Because of background from α-decay and SF of heavy nuclides from (multi) nucleon transfer pseudo correlated chains can be found with nonzero probability. We have calculated the probability to observe random decay chains of the types α·α·α·α, α·α·SF, and α·SF satisfying the criteria specified above. 351 and 771 α-particles have been registered in the first and the second run, respectively. They originated mainly from α-decays of ^{212}Po. Also, 6 SF-like events were registered in the first run and 13 events in the second run. None of these were coincident with each other. The results are shown in Table 1.

Table 1: Random rates for different decay chains

decay chain	E* = 38 MeV	E* = 51 MeV
α·α·α·α	$7.08 \cdot 10^{-4}$	$3.12 \cdot 10^{-3}$
α·α·SF	$4.61 \cdot 10^{-3}$	$1.67 \cdot 10^{-3}$
α·SF	$1.6 \cdot 10^{-2}$	$4.6 \cdot 10^{-2}$

At E*= 38 MeV the cross section limit for both channels is 2.9 pb. The cross section for the 4n channel at E*= 51 MeV based on the one event is $8_{-0.7}^{+2.6}$ pb and the cross section limit for the 5n channel is 1.5 pb. Errors and limits correspond to 68% confidence level. The measured cross section and limits are lower than those of the reaction ^{248}Cm(^{26}Mg,xn)$^{274\text{-}x}$Hs [3], in contrast to calculations from [4]. We plan to continue these measurements in the near future.

References

[1] Z. Patyk, A.Sobiczewski, Nucl.Phys.A533,132 (1991).
[2] J. Dvorak *et al.*, Phys. Rev. Lett. 97, 242501 (2006).
[3] J. Dvorak *et al.*, Phys. Rev. Lett. 100, 132503 (2008).
[4] Z. H. Liu, J.-D. Bao, Phys. Rev. C 74, 057602 (2006).
[5] W. Reisdorf, M. Schädel, Z. Phys. A 343, 47 (1992).
[6] J.F. Ziegler, Nucl. Instr. and Meth. A 219,1027(2004).
[7] G. Audi *et al.*, Nucl. Phys. A 729, 337 (2003)

* Work supported by BMBF project 06MP247I
#gra@rad.chemie.tu-muenchen.de

First Direct High-Precision Mass Measurements of Nobelium with SHIPTRAP

M. Block[1], D. Ackermann[1], K. Blaum[1,2], S. Eliseev[2,3], T. Fleckenstein[4], E. Haettner[1,4], F. Herfurth[1], F. P. Heßberger[1], S. Hofmann[1], J. Ketelaer[5], J. Ketter[5], H.-J. Kluge[1], G. Marx[6], M. Mazzocco[7], Yu. N. Novikov[3], W. R. Plaß[1,4], A. Popeko[8], S. Rahaman[9], D. Rodríguez[10], C. Scheidenberger[1,4], L. Schweikhard[6], P. G. Thirolf[11], G. K. Vorobjev[1,3], and C. Weber[9]

[1]GSI, Darmstadt, Germany; [2]MPI-K, Heidelberg, Germany; [3]PNPI, Gatchina, Russia; [4]Universität Giessen, Germany; [5]Universität Mainz, Germany; [6]Universität Greifswald, Germany; [7]University of Padova, Italy; [8]FLNR, Dubna, Russia; [9]University of Jyväskylä, Finland; [10]University of Huelva, Spain; [11]LMU München, Germany

The study of the structure evolution of exotic nuclei far away from stability is at the forefront of nuclear physics. The region of the superheavy elements is of particular interest since an enhanced stability due to shell effects is observed. Several new elements up to $Z = 118$ have been synthesized [1, 2] and worldwide efforts exist to reach the next spherical shell closures predicted around $Z \approx 114 - 120$ and $N \approx 184$. However, for a successful synthesis of new elements and an understanding of the structure of superheavy elements accurate data on the properties of nuclides in the region $Z > 100$ such as half-lives, masses, and energies of excited states are crucial.

High-precision mass measurements with Penning traps are a powerful method to investigate the nuclear structure of rare isotopes far away from stability [3]. In recent years the reach of Penning trap mass spectrometry has been extended towards more and more exotic nuclei by new technologies such as gas stopping of reaction products from fusion-evaporation reactions and fast-beam fragmentation in combination with radiofrequency quadrupole beam coolers for beam preparation. The very high mass resolving power of Penning traps suffices to resolve isomeric states and results in an unmatched accuracy for the mass determination. It can now be applied to rare isotopes of nearly all elements. With the Penning trap mass spectrometer SHIPTRAP at GSI elements even above $Z = 100$ are accessible.

Since 2005, SHIPTRAP has achieved high-precision mass measurements of about 60 rare isotopes contributing to nuclear astrophysics [4] and allowing for the first time an unambiguous determination of the proton drip line via direct mass measurements of proton-unbound nuclei [5]. In 2008, high-precision mass measurements of the nobelium isotopes $^{252-254}$No ($Z = 102$) have been performed with SHIPTRAP. A cyclotron resonance of ^{254}No is shown in Figure 1. These experiments are the first direct mass measurements in the region above uranium. Previously, the masses of ^{252,254}No were determined from Q_α measurements, whereas the ^{253}No mass was only known from extrapolations of systematic trends [6]. The experiments were very challenging due to the low production rates. Since ^{252}No has a production cross section of about 400 nb in the reaction ^{48}Ca(^{206}Pb,2n)^{252}No at 4.55 A MeV, less than one ion per second was entering the SHIPTRAP stopping cell. Mainly doubly charged nobelium ions were extracted from the stopping cell due to its high cleanliness, the low ionization rate by the incident ion beam, and an extraction time of few milliseconds. The new, directly measured nobelium masses provide reference points in this mass region and can be used to accurately determine the masses of heavier nuclides up to Ds ($Z = 110$) using α-decay links.

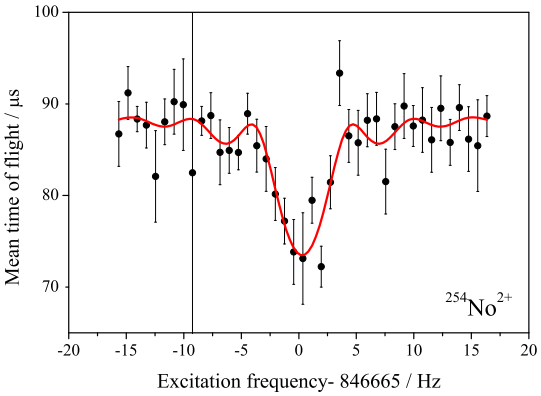

Figure 1: Cyclotron resonance of $^{254}No^{2+}$. The line represents a fit of the theoretical line shape to the data points.

The nobelium mass measurements with SHIPTRAP represent a major breakthrough in Penning trap mass spectrometry. Along with laser resonance ionization and trap-assisted decay spectroscopy they open up new perspectives for sensitive high-precision studies of very heavy elements at low energy utilizing ion traps. In the near future, further technical improvements such as a cryogenic stopping cell, for example, will be implemented and the experimental program will be extended to even higher Z.

References

[1] Yu. Ts. Oganessian, J. Phys. G **34**, R165 (2007).

[2] S. Hofmann and G. Münzenberg, Rev. Mod. Phys. 72, 733 (2000).

[3] K. Blaum, Phys. Rep. **425**, 1 (2006).

[4] C. Weber *et al.*, Phys. Rev. C. **78**, 054310, (2008).

[5] C. Rauth *et al.*, Phys. Rev. Lett. **100**, 012501, (2008).

[6] G. Audi, A. H. Wapstra, and C. Thibault, Nucl. Phys. A **729**, 327 (2003).

First direct mass measurement of the rp-nuclides ^{85,86,87}Mo and ^{87}Tc*

E. Haettner[1,2], D. Ackermann[2], K. Blaum[2,3], M. Block[2], S. Eliseev[3,4], T. Fleckenstein[1], F. Herfurth[2], F. P. Heßberger[2], S. Hofmann[2], J. Ketelaer[5], J. Ketter[5], H.-J. Kluge[2], F. Lautenschläger[1], G. Marx[6], M. Mazzocco[7], Yu. N. Novikov[4], W. R. Plaß[1,2], S. Rahaman[8], D. Rodríguez[9], C. Scheidenberger[1,2], L. Schweikhard[6], P. G. Thirolf[10], G. K. Vorobjev[2], C. Weber[8], and J. Werner[1]

[1]Universität Gießen; [2]GSI, Darmstadt; [3]MPI-K, Heidelberg; [4]PNPI, Gatchina, Russia; [5]Universität Mainz; [6]Universität Greifswald; [7]University of Padova, Italy; [8]University of Jyväskylä, Finland; [9]University of Huelva, Spain; [10]LMU, München

Mass measurements of proton-rich nuclides. The rapid capture of protons on seed nuclei, called the rp-process, has its pathway far away from the valley of stability through the territory of proton-rich nuclides. Nuclear properties in this region need to be known accurately in order to understand the origin of the elements and the observed abundances in the universe.

In August 2008 the masses of proton-rich nuclides in the vicinity of N=Z=43 were measured with the Penning trap mass spectrometer SHIPTRAP [1]. These nuclides were produced in the fusion-evaporation reaction ^{36}Ar+^{54}Fe at energies of 5.0 and 5.9 MeV/u and separated from the primary beam by the velocity filter SHIP.

The masses of ^{85}Mo and ^{87}Tc were measured for the first time (Fig. 1), and deviate from the extrapolated values of the 2003 Atomic Mass Evaluation [2] by up to 1.5 MeV. As a consequence the proton separation energy of ^{87}Tc has been determined to be only half of the value of the AME 2003. The masses of two other nuclides, ^{86,87}Mo, were measured and improved. The mass excess of these nuclides were previously only known from β^+ decay chains. Additionally, the masses of ^{86}Zr and ^{85}Nb were measured and found to be in agreement with the values obtained at JYFLTRAP [3].

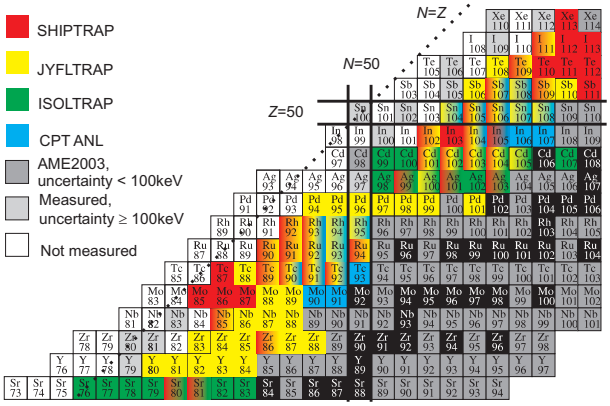

Figure 1: Section of the nuclear chart, showing mass measurements in the range $A = 80$ to 115 since the AME 2003.

Instrumental developments. Contaminant ions created in the gas-filled stopping cell and abundantly produced reaction products different from the nuclide of interest can significantly reduce the performance of SHIPTRAP. In order to remove the contaminant ions and thus to increase selectivity and efficiency of the experiment, additional separation steps are being implemented.

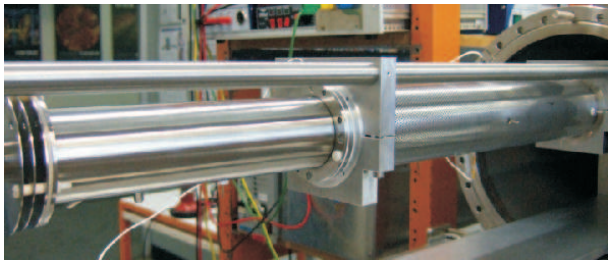

Figure 2: Photo of the RFQ cooler and mass filter system in its test setup at the University of Gießen.

(i) *Mass filter*: An RFQ mass filter [4] has been constructed and is currently being tested (Fig. 2). An improved resonance circuit, which will allow the mass filter to be operated at higher RF amplitudes and frequencies, is under development. An RFQ buncher matched to the RFQ cooler and mass filter has been designed and will be tested later this year.

(ii) *TOF separation and Bradbury-Nielsen-Gate*: Ion optical simulations of the ion transport from the SHIPTRAP buncher to the Penning traps were performed in order to implement a time-of-flight (TOF) analysis and separation. In a first step the ion optical elements were adjusted according to the simulations and a mass resolving power of 80 was achieved at the detector located 1.5 m downstream of the RFQ buncher. In a second step a Bradbury-Nielsen-Gate [5] was implemented. This separation method was investigated with a ^{223}Ra source [6] and the TOF analysis was applied in the two most recent SHIPTRAP beam times.

References

[1] M. Block et al., Eur. Phys. J. A 25 (2005) 49.

[2] G. Audi et al., Nucl. Phys. A 729 (2003) 337.

[3] A. Kankainen et al., Eur. Phys. J. A 29 (2006) 271.

[4] E. Haettner et al., GSI Scientific Report 2007 (2008) 210.

[5] N. E. Bradbury et al., Phys. Rev. 49 (1936) 388.

[6] J. Werner, Bachelor Thesis, JLU Gießen, 2008.

* Work supported by BMBF contract No. 06GI185I.

Decay of the 184 µs - isomer in ^{254}No

F.P. Heßberger[1], B. Sulignano[1,2], S. Hofmann[1,3], D. Ackermann[1], S. Antalic[4], S. Heinz[1], J. Khuyagbaatar[1,5], B. Kindler[1], I. Kojouharov[1], B. Lommel[1], R. Mann[1], K. Nishio[6], and M.Venhart[4]

[1]GSI, Darmstadt, Germany; [2]CEA Saclay, France, [3]Goethe-Universität, Frankfurt,Germany, [4]Comenius University Bratislava, Slovakia, [5]St.Petersburg University, Russia, [6]JAEA Tokai, Japan

Evidence for the existence of a 0.25 s - K-isomer in ^{254}No has been reported already in 1973 [1], but only recently first γ-spectroscopic studies were performed [2,3]. In these experiments in addition γ-rays from the decay of a so far unknown short-lived ($T_{1/2} \approx 180$ µs) K-isomer (^{254m2}No) were observed. While the long-lived isomer (^{254m1}No) was attributed to an $8^-\{9/2^+[624]_\pi x 7/2^-[514]_\pi\}$ located at $E^* \approx 1.295$ keV, only a rough value $E^* \approx 2.5$ MeV was estimated for ^{254m2}No, while spin and parity were controversial. In [2] it was assigned as $I^\pi = 16^+$, while in [3] $I^\pi = 14^+$ was preferred. Since no γ-rays that could be assigned to decays into or within the ground-state rotational of ^{254}No tentatively a decay of ^{254m2}No into ^{254m1}No was assumed.

To clarify the situation a more thourogh study was performed at SHIP. Thanks to a ^{48}Ca beam of high intensity (≈ 1pµA) about an order of magnitude higher counting statistics compared to [2,3] was obtained in a relatively short irradiation (≈20 h) of ^{208}Pb at E = 4.55 AMeV).

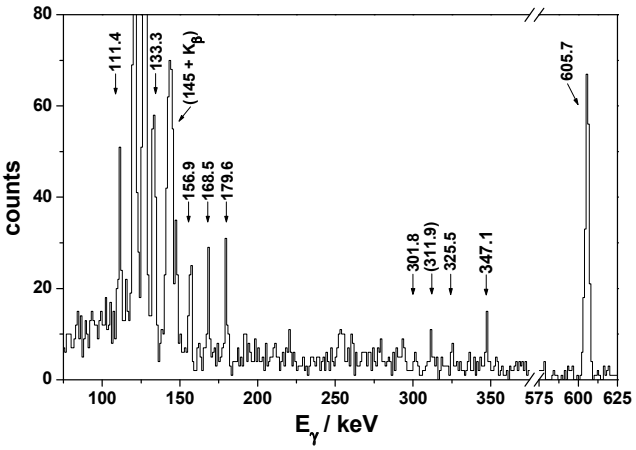

Figure 1: γ-decay spectrum of ^{254m2}No

The γ-spectrum from the decay of ^{254m2}No is shown in fig. 1. The γ-line at 605.7 keV is interpreted as decay of ^{254m2}No into the band built up on ^{254m1}No, while the lines at $E_\gamma < 350$ keV are assigned to intraband transitions. By prompt γ-γ- coincidences it could be shown that the 605.7 keV - line and the low energy lines indeed belong to the same decay cascade, while delayed γ-γ-coincidences proved the population of ^{254m1}No by decay of ^{254m2}No. Using $A = \hbar^2/2 \times \Theta = 6.01$ in $\Delta E = 2A \times (I+1)$, which is slighly higher than A = 5.81 suggested in [3] we fairly could reproduce the low energy γ-lines in fig. 1 leading to an assignment of $E_\gamma = 179.5$ keV as the transition $15^- \rightarrow 14^-$, which rather suggests a spin I = 16 ħ for the short lived isomer than I = 14 ħ. The intensity of the K X-rays a

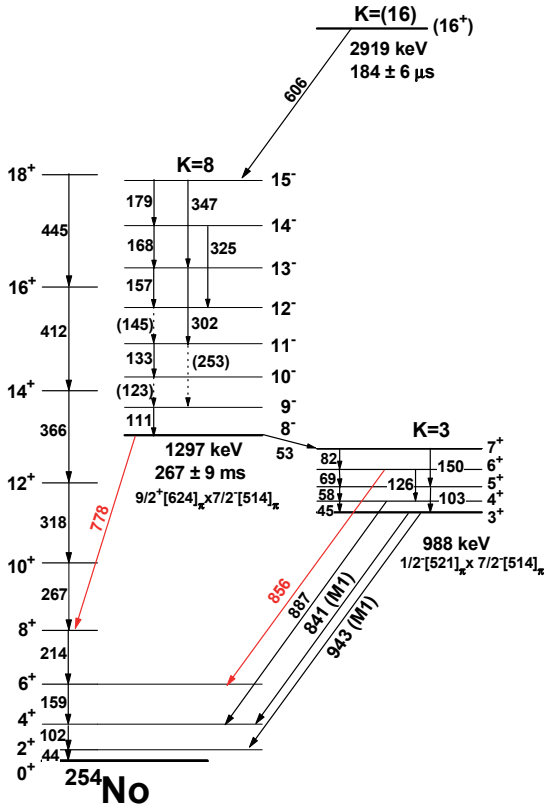

Figure 2: Decay schemes of ^{254m1,254m2}No dervived on the basis of the results from [2,3] and the present experiment.

within the error bars with that expected from K-conversion of M1 transitions of 156.9, 168.5 and 179.5 keV. Assuming the 605.7 keV line as an M1 transition a ≈20% K X-ray intensity would be expected. This can be regarded as a hint that the transition is rather E1 than M1, i.e. that the isomeric states have different parities. The relatively strong γ-lines at $E_\gamma = 179.5$ keV and $E_\gamma = 347.1$ keV ($15^- \rightarrow 13^-$) further suggest that no states of spins I > 15 ħ are populated by the decay of ^{254m2}No, i.e. it gives a hint that no transitions are missing and that E^* can be settled by adding the transition energies. We obtain a $E^* \approx 2919$ keV, which is about 300-400 keV higher than assumed in [2,3]. Our decay scheme is shown in fig. 3. It also includes the two new γ-lines (778, 856 keV) from the decay of ^{254m1}No, observed in this experiment.

References

[1] A. Ghiorso et al. PRC 7, 2032 (1973)
[2] R.-D.Herzberg et al. Nature 442, 896 (2006)
[3] S.K. Tandel et al. PRL 97, 082502 (2006)

Spontaneous fission of neutron-deficient fermium isotopes and the new nucleus ^{241}Fm

J. Khuyagbaatar[1], S. Hofmann[1], F.P. Heβberger[1], D.Ackermann[1], H.G. Burkhard[1], S. Heinz[1], B. Kindler[1], I. Kojouharov[1], B. Lommel[1], R. Mann[1], J. Maurer[1], K. Nishio[2]and Yu. Novikov[3]
[1]GSI Helmholtzzentrum für Schwerionenforschung, Darmstadt, Germany, [2]Japan Atomic Energy Agency (JAEA), Tokai, Japan, [3]PNPI, St. Petersburg, Russia

The neutron-deficient fermium isotopes with A≤244 were produced by the fusion-evaporation reactions of ^{40}Ar projectiles and targets of $^{204,206-208}$Pb [1].

Only spontaneous fission (SF) half-life of (3.12±0.08) ms. We deduced an upper limit of 0.01 and 0.02 for the α and EC branching of ^{244}Fm.

The isotope ^{243}Fm was produced in the reaction ^{40}Ar+^{206}Pb→^{243}Fm+3n, and an excitation function was measured using eight different beam energies (see fig. 1a). In our experiment a total of 2700 α events were observed with an energy of 8.55 MeV during the beam-on and beam-off periods. The excitation function deduced from these α decays is shown in fig. 1a by the solid circles. The measured cross-section values follow the shape of the curve calculated for the 3n channel with the statistical code HIVAP [1]. The half-life was determined by the time distribution of ER-α correlations. A value of (231±9) ms was determined.

The ER-SF correlations measured at the beam energy of 194 MeV revealed two components of similar intensity and with half-lives of (3.78±0.26) and (221±12) ms. The short-lived component was attributed to the isotope ^{244}Fm. The half-life of the long-lived component is within error bars in agreement with the value obtained from ER-α correlation for ^{243}Fm. Also the shape of the excitation function deduced from long-lived SF activity is similar to that of the 3n channel (triangles in fig. 1a). Therefore we attribute the long-lived SF activity to a hitherto unknown SF branch of ^{243}Fm. The branching ratios are b_α=(0.91±0.03) and b_{SF} =(0.09±0.01). An upper limit for an EC branch of ^{243}Fm is 0.1.

The fusion-evaporation reaction ^{40}Ar+^{204}Pb was applied to search for the new isotope ^{241}Fm. An excitation function was measured at beam energies in the range 187-206 MeV and ER-SF/ER-α correlations were evaluated. We observed a total number of 145 ER-SF events. The half-life (0.73±0.06) ms was determined. The measured excitation function is shown in fig. 1b together with the results of a HIVAP calculation. The experimental data follow convincingly the shape of the calculated curve for the 3n channel. Therefore we attribute this SF activity to the decay of the new isotope ^{241}Fm. Upper limits for an α and EC decay branch of ^{241}Fm were 0.14 and 0.12, respectively.

A previously made assignment of a 0.8 ms SF activity [3] to the isotope ^{242}Fm could not be confirmed.

From our studies and considering theoretical work on SF half-lives we conclude that the half-life of ^{242}Fm is less than 4 μs and thus below our detection limit.

Measured TKE values for ^{241,243,244}Fm are in agreement with the Viola systematics for SF along the elongated fission path.

Isomeric states were not observed in $^{241-244}$Fm.

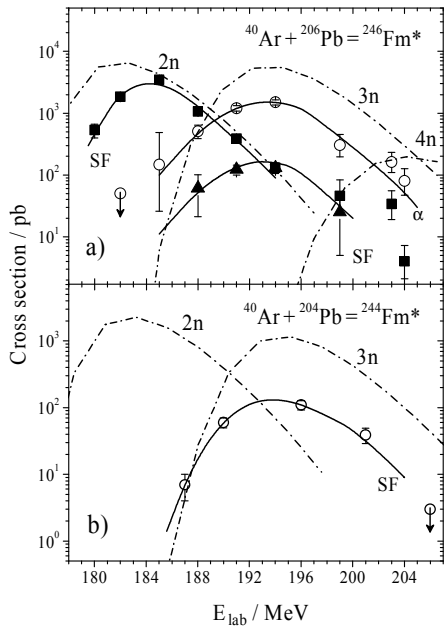

Figure. 1 Measured and calculated excitation functions for fusion-evaporation reactions of ^{40}Ar and ^{204,206}Pb. The results of HIVAP calculations are represented by dashed-dotted lines. The measured cross-sections are plotted with error bars representing statistical fluctuations only. These data points are connected by full lines to guide the eye. Upper cross-section limits are marked by arrows. The beam energies are given for the center of the targets. a) The reaction ^{40}Ar+^{206}Pb: The cross-sections for ^{244}Fm (2n channel) are marked by squares. The open circles denote the cross-sections deduced from α decays of ^{243}Fm (3n channel). The SF branch of this nucleus is represented by the triangles. No or SF events could be unambiguously attributed to ^{242}Fm (4n channel). b) The reaction ^{40}Ar+^{204}Pb: Open circles mark the excitation function of the SF events assigned to ^{241}Fm (3n channel). No unambiguous data for a production of ^{242}Fm (2n channel) were obtained.

References

[1] J. Khuyagbaatar et al., EPJ. A **37**, 137, 2008.
[2] W. Reisdorf, Z. Phys. A 300, **227,** 1981.
[3] G.M. Ter-Akopyan et al., Nucl. Phys. A **255**, 509, 1975.

Di-nuclear systems studied at the velocity filter SHIP

S. Heinz[1], V. Comas[2], S. Hofmann[1,3], D. Ackermann[1], J. Heredia[2], F.P. Heßberger[1], J. Khuyagbaatar[1], B. Kindler[1], B. Lommel[1], R. Mann[1], J. Maurer[1], K. Nishio[4]

[1]GSI, Darmstadt, Germany; [2]Institute of Technologies and Applied Sciences, Habana 10400, Cuba;
[3]Institut für Physik, Goethe-Universität Frankfurt, D-60054 Frnakfurt, Germany;
[4]Japan Atomic Energy Agency (JAEA), Tokai, Ibaraki 319-1195, Japan

The formation of a di-nuclear system (DNS) during the capture stage of two heavy nuclei can be regarded as the first step of a fusion process. However, with increasing Z of the reaction partners also their Coulomb repulsion is increasing. This can lead to the decay of the DNS before a compound nucleus is formed (quasi-fission (QF)). The velocity filter SHIP enables a background free identification of QF reactions and their study due to the following features:

1) Detection of heavy target-like reaction products at (0±2) degrees with respect to the beam direction.
2) Measurement of the velocity distributions of the reaction products.
3) Isotope identification via α decay recorded during the beam-off periods.

We investigated QF in ^{64}Ni + ^{207}Pb reactions at projectile energies of 5.9×A MeV [1]. Several reaction products in the range 83≤Z≤88 and 208≤A≤215 have been observed (nuclei with Z<83 are not α emitters and could therefore not be identified in this experiment). Isotopes beyond Ra (Z=88) were not observed. This might be due to the increasing fission probability for elements with Z>88 as described in ref. [2] for the reaction ^{58}Ni + ^{208}Pb.

In Fig. 1 the measured velocity spectra are shown, as an example, for ^{214}Ra and ^{213}Fr. For all isotopes we found pronounced maxima at velocities around $v = 1.7v_{cm}$ and further weak maxima around $v = 0.3v_{cm}$ (v_{cm} is the centre-of-mass velocity which is equivalent to the velocity of the DNS or compound nucleus ^{271}Ds, respectively). Both maxima are located symmetrically with respect to v_{cm} and their positions are determined by the proton number of the respective isotope. The total kinetic energies of the QF fragments are ≈20 MeV below the value expected from the Viola systematic [3] which is a typical signature for a deep inelastic process like QF (the total energy has been reconstructed from the velocity of the detected heavier fragment assuming a two-body break-up).

Due to the narrow acceptance of SHIP of (0±2) degrees only those products can be detected where the break-up takes place along the beam axis. Within the scenario described above the high-velocity component could be described as QF after a central collision where the lighter, projectile-like, fragment is emitted in backward direction and the heavier, target-like, fragment in beam direction (see illustration in fig. 1). Assuming that the velocity of the target-lke fragment after QF is v in the cm frame it will be detected with the velocity $v+v_{cm}$ in the laboratory

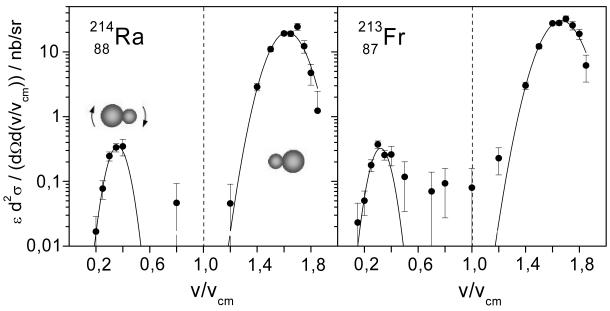

Figure 1: Velocity distributions of the isotopes ^{214}Ra and ^{213}Fr measured in the ^{64}Ni + ^{207}Pb reaction at 5.9×A MeV.

frame. Also the low-velocity component is consistent with the QF scenario if we assume that the DNS rotates around its centre-of-gravity in a non-central collision. A rotation of ≈180° brings the system again to an orientation parallel to the beam axis where, however, projectile and target have changed their positions with respect to the above discussed case of a central collision. Therefore, if the break-up occurs in this orientation the projectile-like fragment will be emitted in forward direction and the target-like in backward direction in the cm frame. In the laboratory frame the target-like nucleus is still emitted in beam direction, however, with a velocity $v–v_{cm}$. After approximately one full rotation the DNS would reach again the orientation leading to the high-velocity peak. The different peak intensities are reflecting the velocity dependence of the detection efficiency and the interaction time dependent non-isotropic angular distribution of the QF products.

The "visibility" (peak at $v-v_{cm}$) of the rotation of a DNS can be used to determine its rotation time. The rotation time t is given by $\varphi(t) = \omega t$, $\omega = \hbar L/\Theta$ (φ: rotation angle, L: angular momentum, Θ: moment of inertia). A lower limit for t can be obtained by assuming a grazing collision. In the case of ^{64}Ni + ^{207}Pb at 5.9×A MeV the grazing angular momentum is $L_{gr} = 190\hbar$. For Θ one can assume the DNS as composed of two spheres with radii R_1 and R_2 ($R=r_oA^{1/3}$). The time for a rotation by φ=180° which leads to the low-velocity component at $v-v_{cm}$ is then 2×10^{-21} s. This is a lower limit since closer collisions will lead to smaller L and therefore to longer rotation times.

References

[1] S. Heinz et al., EPJ A 38, 227 (2008).
[2] L. Corradi et al., Nucl. Phys. A 734, 237 (2004).
[3] V.E. Viola, Phys. Rev. C 31, 1550 (1985).

TASCA Commissioning Completed*

M. Schädel[1,#], D. Ackermann[1], L.-L. Andersson[2], J. Ballof[3], M. Block[1], R.A. Buda[3], W. Brüchle[1], I. Dragojević[4], Ch.E. Düllmann[1], J. Dvorak[4,5], K. Eberhardt[3], J. Even[3], J.M. Gates[4], J. Gerl[1], A. Gorshkov[5], P. Golubev[2], R. Graeger[5], K.E. Gregorich[4], E. Gromm[3], W. Hartmann[1], F.P. Heßberger[1], D . Hild[3], R. Hoischen[1,2], A. Hübner[1], E. Jäger[1], J. Khuyagbaatar[1], B. Kindler[1], I. Kojouharov[1], J.V. Kratz[3], J. Krier[1], N. Kurz[1], S. Lahiri[8], D. Liebe[3], B. Lommel[1], M. Maiti[8], M. Mendel[3], E. Merchán[2,9], H. Nitsche[4], D. Nayak[8], J. Nilssen[6], J.P. Omtvedt[6], K. Opel[6], P. Reichert[3], D. Rudolph[2], A. Sabelnikov[6], F. Samadani[6], H. Schaffner[1], B. Schausten[1], R. Schuber[5], E. Schimpf[1], A. Semchenkov[1,5,6], L. Stavsetra[4], J. Steiner[1], J. Szerypo[7], P. Thörle-Pospiech[3], A. Toyoshima[10], A. Türler[5], J. Uusitalo[11], N. Wiehl[3], H.-J. Wollersheim[1], T. Wunderlich[3], and A. Yakushev[5]

[1]GSI, Darmstadt, Germany; [2]University of Lund, Lund, Sweden; [3]University of Mainz, Mainz, Germany; [4]LBNL, Berkeley, CA, U.S.A.; [5]Technical University München, Garching, Germany; [6]University of Oslo, Oslo, Norway; [7]LMU München, Garching, Germany; [8]SAHA Institute of Nuclear Physics, Kolkata, India; [9]Universidad Nacional de Colombia, Bogota, Colombia; [10]JAEA, Tokai, Japan, [11]University of Jyväskylä, Jyväskylä, Finland

The **T**rans**A**ctinide **S**eparator and **C**hemistry **A**pparatus (**TASCA**) project [1], which is focusing on the separation and investigation of neutron-rich transactinide nuclides produced in actinide-target based reactions, has successfully finished its commissioning; see [2] for an interim report. TASCA is ready for the envisioned research program which includes both chemical investigations of transactinide or superheavy elements (SHE) after preseparation with the gas-filled separator and nuclear structure and nuclear reaction studies.

The central device of TASCA is a gas-filled separator in a DQQ configuration operated either in the "High Transmission Mode" (HTM, DQ_hQ_v) or in the "Small Image Mode" (SIM, DQ_vQ_h) [1-5]. In the HTM, the unsurpassed transmission of TASCA - at a relatively low dispersion - is exploited. In contrast, the SIM provides unique possibilities due to its small spot size in the focal plane (< 3 cm diam.) at a still relatively high transmission; see Table 1.

Table 1: Important parameters of TASCA, calculated for the reaction ^{48}Ca(^{244}Pu,3n)^{289}114, in comparison with other gas-filled separators operated in SHE research.

Separator	Configuration	Transmission %	Dispersion mm/%	Bρ (max) Tm
DGFRS	DQ_hQ_v	35	7.5	3.1
GARIS	DQ_hQ_vD	40	9.7	2.16
BGS	Q_vD_hD	49-59	20	2.5
TASCA	DQ_hQ_v	60	9	2.3
TASCA	DQ_vQ_h	35	1	2.3

Table 2 provides a compilation of all nuclear reactions and reaction products applied and detected in the course of the commissioning program together with the mode TASCA was operated in and the fill gas. Also listed are experiments to test and optimize the recoil transfer chambers (RTC) [6], the gas-jet transport of preseparated products into our Rotating wheel On-line Multidetector Analyzer (ROMA), and its performance, and the coupling and use of aqueous chemistry set-ups behind TASCA.

Table 2: Nuclear reactions and their products used to commission TASCA; H=HTM, S=SIM, TSp=TASISpec, R=ROMA, C=chemistry, catch=catcher foils.

Product	xn	Beam	Target	Mode	Gas	RTC +R/C
^{30}Si	--	^{30}Si	--	H,S	Vac	
^{173,175}Os	7n	^{40}Ar	^{nat}Ce	H	He	C
$^{180-182}$Hg	2-4n	^{40}Ar	^{144}Sm	H,S	He	C
^{188}Pb	4n	^{48}Ca	^{144}Sm	H,S	He	
^{188}Pb	4n	^{40}Ar	^{152}Gd	H,S	He	
$^{194-196}$Pb	4-5n	^{40}Ar	^{nat}Gd	H,S	He	R
$^{198-199}$Bi	4-5n	^{22}Ne	^{181}Ta	H,S	He	catch
$^{195-196}$Po	4-5n	^{48}Ca	^{152}Gd,	H	He	R
^{200}At	3n	^{64}Ni	^{nat}La	TSp	He	
^{200}Fr	5n	^{64}Ni	^{141}Pr	TSp	He	
$^{205-206}$Fr	5-6n	^{30}Si	^{181}Ta	H	He	
$^{208-211}$Ra	3-4n	^{54}Cr	^{nat}Gd	H,S	He	
$^{208-211}$Ra	3-6n	^{64}Ni	^{150}Nd	TSp	He	
^{210}Ac	5n	^{40}Ar	^{nat}Lu	H,S	He,N_2	
^{215}Ac	4n	^{22}Ne	^{197}Au	H,S	He,H_2	
$^{218-x}$Th	xn	^{64}Ni	^{154}Sm	TSp	He	
$^{224-x}$U	xn	^{64}Ni	^{nat}Gd	TSp	He,H_2	
^{245}Fm	3n	^{40}Ar	^{208}Pb	H,S	He	R
^{252}No	2n	^{48}Ca	^{206}Pb	H,S, TSp	He	R
^{253}No	2n	^{48}Ca	^{207}Pb	H, TSp	He	
^{254}No	2n	^{48}Ca	^{208}Pb	H,S	He,H_2	
^{255}No	5n	^{22}Ne	^{238}U	H,S	He,H_2	R
^{256}No	4n	^{22}Ne	^{238}U	H	He	
^{260}Rf	6n	^{22}Ne	^{244}Pu	H	He,H_2	
^{261a,261b}Rf	5n	^{22}Ne	^{244}Pu	H	He	R,C
^{262}Rf	4n	^{22}Ne	^{244}Pu	H	He,H_2	

Extensive studies have been performed in the HTM and SIM to obtain optimized parameter sets for (i) the target thickness and stability, (ii) the gas pressure and the gas filling (He, H_2, and mixtures), (iii) the dipole setting (Bρ) and quadrupole focusing, (iv) the RTCs (window material and thickness, support structures, and size and shape of the chamber), (iv) gas-jet transport of pre-separated products, and (vi) the coupling and performance of devices

* Work supported by BMBF (06MT247I, 06MT248, 06MZ223I) and GSI-F&E (MT/TÜR, MZJVKR)
#m.schaedel@gsi.de

like ROMA and the Automated Rapid Chemistry Apparatus (ARCA). Results of many of these parameter studies were compared with TASCA model calculations [7] and very good agreement was achieved. This agreement is of special importance as it allows for the selection of proper settings for magnetic rigidities (Bρ) in the dipole magnet and the quadrupole magnets for all nuclear reactions and for all gases and gas mixtures tested at various pressures. It is especially rewarding to see that not only Bρ values were properly chosen to centre product distributions on focal plane detectors (FPD) but also that the measured spatial distributions and, more importantly, the efficiencies were in very good agreement with model calculations. These results confidently demonstrate that we are able to perform trustworthy SHE experiments with TASCA. In the following, we mention a few concluding experiments, some of the highlights and new developments; see [2] for additional information on the parameter studies.

The first efficiency measurements with catcher foils behind the target and in the focal plane showed very good agreement with model calculations for the fairly asymmetric reaction ^{22}Ne(^{181}Ta,xn)^{198m,199}Bi [2]. To confirm this agreement in a more symmetric reaction, leading to a significantly heavier reaction product, and to obtain a standard reaction to test and check the TASCA performance, detailed studies were performed with well known reactions of ^{48}Ca with ≈ 0.5 mg/cm^2 thick targets of ^{206,207,208}Pb leading to ^{252,253,254}No. Assuming cross sections of 0.5 µb, 1.3 µb, and 2 µb [8] for the production of ^{252}No, ^{253}No, and ^{254}No, efficiencies of 54%, 56%, and 50%, respectively, were obtained for the HTM, using a He filling of 0.8 mbar, and a (80x36) mm^2 16-strip FPD. Taking into account uncertainties in cross sections and systematic errors of target thicknesses and beam current measurements, we observe an excellent agreement with model calculations [7] predicting 54%. Equally good is the agreement in the SIM, at a He pressure of 0.8 mbar, where a 30% efficiency was measured for the reaction ^{48}Ca(^{208}Pb,2n)^{254}No.

A new (140x40) mm^2 large, highly efficient FPD, consisting of double-sided silicon strip detectors (DSSSD) in the focal plane and SSSDs for the backward box detectors will further increase the TASCA efficiency; see [9] for details of the new detector.

As one of the crucial tests and one of the highlights finalizing the TASCA commissioning program, we studied the isotopes ^{260}Rf, ^{261a,261b}Rf, and ^{262}Rf synthesized in the very asymmetric reaction ^{22}Ne + ^{244}Pu; see [10] for details of the nuclear reactions, for TASCA parameters, and for the interesting nuclear decay results. In essence, the performance of TASCA was as anticipated; everything worked well, including the ^{244}Pu target wheel. Efficiencies and magnetic settings (Bρ=1.99 Tm at 0.4 mbar He, HTM) were as expected. As observed in previous experiments [2], it was again possible to reduce the background in the FPD by using a mixture of He and H_2. This part of the commissioning program showed clearly that TASCA can be applied efficiently for nuclear decay and nuclear reaction studies of neutron-rich nuclides of SHE synthesized in very asymmetric hot-fusion reactions. Rf isotopes were not only measured in the FPD but were also collected in an RTC and were transported either to ROMA for nuclear decay measurements [10] or to ARCA for chemical investigations [11].

An additional highlight of the experiment was the first transactinide chemistry behind TASCA designed as a proof-of-principle experiment. It was performed in ARCA with pre-separated 78-s ^{261a}Rf; details of the nuclear reaction and the Rf separation in TASCA are described in [10] while all chemical aspects are discussed in [11]. This successful experiment, which studied the formation of Rf-fluoride complexes and their adsorption behaviour on an anion-exchange resin, demonstrated that aqueous-phase transactinide chemistry behind TASCA can now be performed.

The new set-up termed *TA*sca *S*mall *I*mage mode *Spe*ctroscopy (TASISpec) [12] exploits advantages of the SIM, i.e. the fact that neutron-rich nuclides of SHE, produced in hot-fusion reactions, can be focused with high efficiency into an area of < 7 cm^2. This provides the unique possibility to build a compact Si-detector box for α-particle, electron, and fission-fragment measurements, and to pack composite Ge-detectors in very close geometry, resulting in an unprecedented, highly efficient set-up for multi-coincidence measurements with γ-rays and X-rays; see [12] for details. A prototype set-up has been commissioned successfully and first data have been collected for nuclides as heavy as ^{252,253}No.

In conclusion, the performance of TASCA as a separator is well understood and is perfectly under control. TASCA as a whole is presently the most versatile and highest efficient instrument in SHE research worldwide. It has entered the region of transactinides or superheavy elements, and is ready to explore the physics and chemistry of the "terra incognita" it was designed and built for.

References

[1] M. Schädel *et al.*, GSI Sci. Rep. 2005, GSI Report 2006-1, 2006, p. 262, and http://www.gsi.de/TASCA
[2] M. Schädel *et al.*, GSI Sci. Rep. 2007, GSI Report 2008-1, 2008, p. 152.
[3] M. Schädel, Eur. Phys. J. D 45 (2007) 67.
[4] A. Semchenkov *et al.*, Nucl. Instr. and Meth. in Phys. Res. B 266 (2008) 4153.
[5] Ch.E. Düllmann *et al.*, Nucl. Instr. and Meth. in Phys. Res. B 266 (2008) 4123.
[6] Ch.E. Düllmann *et al.*, GSI Sci. Rep. 2006, GSI Report 2007-1, 2007, p. 146.
[7] K.E. Gregorich *et al.*, GSI Sci. Rep. 2006, GSI Report 2007-1, 2007, p. 144.
[8] Yu. Ts. Oganessian *et al.*, Phys. Rev. C 64 (2001) 054606.
[9] A. Yakushev *et al.*, contribution to this report.
[10] A. Gorshkov *et al.*, contribution to this report.
[11] J. Even *et al.*, contribution to this report.
[12] L.-L. Andersson *et al.*, contribution to this report.

Measurements of $^{260-262}$Rf produced in ^{22}Ne + ^{244}Pu fusion reaction at TASCA*

A. Gorshkov[1#], R. Graeger[1], A. Türler[1], A. Yakushev[1], D. Ackermann[2], W. Brüchle[2], Ch. E. Düllmann[2], E. Jäger[2], F. Heßberger[2], J. Khuyagbaatar[2], J. Krier[2], M. Schädel[2], B. Schausten[2], E. Schimpf[2], L.-L. Andersson[3], D. Rudolph[3], K. Eberhardt[4], J. Even[4], J.V. Kratz[4], D. Liebe[4], P. Thörle[4], N. Wiehl[4], I. Dragojević[5], J.M. Gates[5], L. Stavsetra[5], J.P. Omtvedt[6], A. Sabelnikov[6], F. Samadani[6], J. Uusitalo[7]

[1]TU München, 85748 Garching, Germany; [2] GSI Helmholtzzentrum für Schwerionenforschung GmbH, 64291 Darmstadt, Germany; [3]Lund University, 22100 Lund, Sweden; [4]Mainz University, 55128 Mainz, Germany; [5]LBNL, Berkeley, CA 94720, USA; [6]Oslo University, 0315 Oslo, Norway; [7] University of Jyväskylä, 40014 Jyväskylä, Finland

As a final experiment in the commissioning phase of TASCA the transactinides (Z ≥ 104) were reached. Production and decay of ^{260}Rf, ^{261a,b}Rf and ^{262}Rf [1,2,3], produced in the asymmetric nuclear fusion reaction ^{244}Pu(^{22}Ne,xn) was studied. Separated reaction products were guided to a Focal Plane Detector (FPD) or into a Recoil Transfer Chamber (RTC), where they were available for transport to either the Rotating wheel On-line Multidetector Analyzer (ROMA) or to the Automated Rapid Chemistry Apparatus (ARCA) for chemical experiments [4].

TASCA was operated in the High Transmission Mode (HTM) [5]. The ^{22}Ne ion beam (average intensity: 0.8 μA_{part}) impinged on a rotating target wheel with 0.4 mg/cm^2 $^{244}PuO_2$ targets on 2.2 µm Ti backings. Three beam energies in the center of the target, $E_{c.o.t.}$, of 109 MeV, 116 MeV and 125 MeV, were used for the production of ^{262}Rf, ^{261}Rf and ^{260}Rf, respectively. The transmission of Rf has been optimized in He filling gas. The optimal pressure was 0.4 mbar. The magnetic rigidity, Bρ, was determined to be 1.99 T·m. To increase suppression of unwanted products, a He/H_2 (2:1) filling gas at a pressure of 1.5 mbar was used in experiments with the FPDs. Evaporation residues were implanted into a (80 x 36) mm^2 16-strip Position-Sensitive silicon Detector (PSD) or a (58 x 58) mm^2 Double-Sided Silicon Strip Detector (DSSSD). In other experiments, ^{261a,b}Rf passed a 1.2 µm thick (140 x 40) mm^2 Mylar window and was thermalized in 1.2 bar He in the RTC (depth: 17 mm). Rf atoms were then transported to ROMA by an He/KCl jet (gas flow rate: 3.45 L/min) through a 4 m long polyethylene capillary (inner diameter: 2 mm).

The measurement of ^{260}Rf, produced in the 6n evaporation channel at $E_{c.o.t.}$= 125 MeV yielded 15 time (Δt ≤ 200 ms) correlated EVR-SF events in the PSD. The correlation time analysis yielded a half-life of $21^{+7.3}_{-4.3}$ ms (errors are within the 68% confidence interval). A search for ^{262}Rf decays at $E_{c.o.t.}$ = 109 MeV yielded 7 position and time correlated EVR-SF events observed in the DSSSD, with EVR energies of 0.8 to 3.3 MeV and SF fragment energies of > 100 MeV. The measured $T_{1/2}$ for ^{262}Rf is 210^{+128}_{-58} ms (Fig. 1a), in contradiction with values from [1,2]. In addition, 9 short EVR-SF correlations were registered with Δt ≤ 1.5 ms and EVR energies of 7.5 ± 5.0 MeV. They were attributed to the decay of ^{244mf}Am ($T_{1/2}$ = 0.9 ms). Because of a relatively high counting rate of EVR-like events in the DSSSD a random event analysis was performed for EVR-SF correlations within a Δt of 1 s. The random event number, n_b, was calculated individually for each observed event. It varies between 0.035 and 0.11 and depends on the event position in the DSSSD.

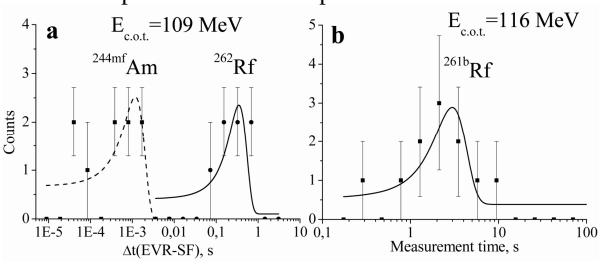

Figure 1: Time distributions of a) EVR-SF correlations from the DSSSD and b) SF decays from ROMA.

^{261}Rf was produced in the 5n channel at $E_{c.o.t}$ = 116 MeV and was detected in ROMA. Stepping times of 35 s (for ^{261a}Rf) and 2.5 s (for ^{261b}Rf) were used. 149 single α-particles (E_α = 7.8 – 8.5 MeV) from ^{261a}Rf and ^{257}No were registered; among these 28 α-α correlations. Also, 11 SF-events were registered and are attributed to ^{261b}Rf based on the measured $T_{1/2}$ of $2.2^{+0.9}_{-0.5}$ s. The SF activity assigned in [2] to ^{262}Rf likely originated from the then unknown ^{261b}Rf.

From our results and a cross section of 4.4 nb [6], a transmission of Rf through TASCA to a 140 x 40 mm^2 large area in the focal plane of 10% follows. For ^{261b}Rf, a cross section of $1.8^{+0.8}_{-0.4}$ nb was calculated, respecting decay during transport. With an estimated transmission of 6% to the area of the FPDs, preliminary cross sections for ^{260}Rf and ^{262}Rf of ≈ 1.2 nb and ≈ 250 pb, respectively, follow. ^{261b}Rf was observed for the first time as an EVR. The production ratio of ^{261a}Rf to ^{261b}Rf is about 2.5:1. The data analysis is still in progress.

References

[1] L. P. Somerville *et al.*, Phys. Rev. C **31**, 1801 (1985).
[2] M. R. Lane *et al.*, Phys. Rev. C **53**, 2893 (1996).
[3] Ch. E. Düllmann, A. Türler., Phys. Rev. C **77**, 064320 (2008).
[4] J. Even *et al.*, this Scientific Report.
[5] A. Semchenkov *et al.*, NIMB **266**, 4153 (2008).
[6] Yu. Lazarev *et al.*, Phys. Rev. C **62**, 064307 (2000).

* Work supported by BMBF project 06MT248.
# Alexander.Gorshkov@radiochemie.de

A new TASCA focal plane detector*

A. Yakushev[1#], R. Graeger[1], A. Gorshkov[1], A. Türler[1], D. Ackermann[2], Ch. E. Düllmann[2], E. Jäger[2], F.P. Heßberger[2], J. Khuyagbaatar[2], J. Krier[2], M. Schädel[2], B. Schausten[2], E. Schimpf[2], D. Rudolph[3], J. Even[4], J.V. Kratz[4], N. Wiehl[4], V. Chepigin[5], A. Fomichev[5], V. Gorshkov[5], S. Krupko[5], J. Bar[6], P. Grabiec[6], A. Panas[6], M. Wegrzecki[6], J. Dvorak[7], A. Semchenkov[8], J. Uusitalo[9]

[1]Technical University München, D-85748 Garching, Germany; [2] GSI Helmholtzzentrum für Schwerionenforschung GmbH, D-64291 Darmstadt, Germany; [3] Lund University, S-22100 Lund, Sweden; [4]University of Mainz, D-55128 Mainz, Germany; [5]FLNR, 141980 Dubna, Russia; [6]ITE, 02-668 Warsaw, Poland; [7]LBNL, Berkeley, CA 94720, U.S.A.; [8] University of Oslo, 0315 Oslo, Norway, [9]University of Jyväskylä, Jyväskylä, Finland

The new, highly efficient, gas-filled TransActinide Separator and Chemistry Apparatus (TASCA) has been recently put into operation at GSI with the aim to study chemical and physical properties of superheavy elements with Z≥104. Based on the results of magnetic field model calculations of the dipole and the quadrupoles, two modes of operation of TASCA, the "High Transmission Mode" and the "Small Image Mode" have been realized [1]. Two types of focal plane detector setups (FPD) were used during the TASCA commissioning phase: a (80 x 36) mm^2 16-strip position-sensitive silicon detector (PSD) and a (58 x 58) mm^2 double-sided silicon strip detector (DSSSD) as a prototype for a new TASCA focal plane detector. The test experiments showed that the image size in the HTM is larger than the detector size of both detector types, as it was expected according to ion transport calculations and Monte-Carlo simulations [1,2]. The nominal vertical position resolution of the PSD is ± 0.2 mm. However, a search for position correlated decay chain members usually occurs within ± 1 mm limits, corresponding to a pixel size area of (5 x 2) mm^2. The relatively large pixel size of the PSD negatively affects search limits for rare decay chains from long-lived isotopes of superheavy elements. The TASCA FPD working group has decided to build a detector setup based on a DSSSD as a stop detector and a backward array consisting of single-sided silicon strip detectors (SSSD). A *veto* detector for light fast ions that penetrate the DSSSD will be mounted behind the stop detector. The new setup will feature a (144 x 489 mm^2 large detector, which will accept > 90% of all evaporation residues reaching the focal plane. The geometrical detection efficiency for α-particles emitted from implanted nuclei will be > 70%. As compromise between a pixel size as small as possible and the number of spectrometric electronic channels as small as possible, a pitch width of 1 mm on the front and back side of the DSSSD has been chosen. To reduce the necessary number of ADCs the number of strips on each side of the DSSSD and on the SSSD should be a multiple of 8 when using 32-channel preamplifiers and 8 or 16-channel amplifiers with integrated multiplexers. A DSSSD structure with an active area of (72 x 48) mm^2 has 72 strips on the front side and 48 strips on the back side. The strip width and the interstrip distance on the both sides of the DSSSD are 900 μm and 100 μm, respectively. Two adjacent DSSSDs form the stop detector with an active area of (144 x 48) mm^2. A SSSD structure with an area of (72 x 48) mm^2 has 8 strips, which are 72 mm long. The strip width and the interstrip distance of the DSSSD are 5.65 mm and 100 μm, respectively. 8 SSSD detectors form the backward array with a depth of 72 mm. Two similar SSSD detectors are used as *veto* detector. Silicon wafer thicknesses of 300 μm and 500 μm have been chosen for the DSSSDs and SSSDs, respectively. These thicknesses will allow for the detection of conversion electrons in the backward array. A schematic design of the new TASCA detector array and first results from source measurements are shown in Fig. 1.

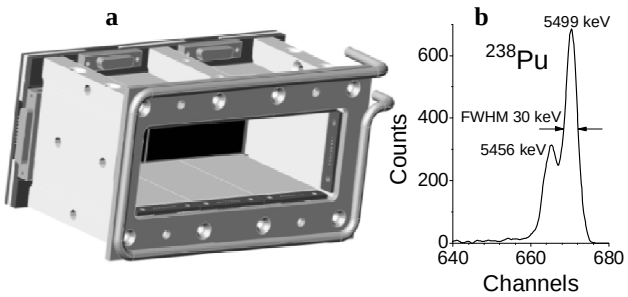

Figure 1: A drawing of the new TASCA FPD array (a) and an alpha particle spectrum from a DSSSD strip (b).

In total, the new TASCA detector array has to process the signals of 320 strips. The necessary spectrometric and data readout electronics, which are compatible with TASISpec [3], as well as the associated software, should be ready for experiments in spring 2009.

References

[1] A. Semchenkov et al. NIM B **266**, 4153 (2008).

[2] K. Gregorich et al. GSI Sci. Rep. 2006, 144 (2007).

[3] L.-L. Andersson et al., this report.

* Work supported by BMBF project 06MT248.

#Alexander.Yakushev@radiochemie.de

TASISpec - A new twist on spectroscopy of superheavy elements.

L.-L. Andersson[1], D. Rudolph[1], P. Golubev[1], R. Hoischen[1,2], E. Merchán[1,3], D. Ackermann[2], Ch.E. Düllmann[2], J. Gerl[2], F.P. Heßberger[2], E. Jäger[2], J. Khuyagbaatar[2], I. Kojouharov[2], J. Krier[2], N. Kurz[2], W. Prokopowicz[2], M. Schädel[2], H. Schaffner[2], B. Schausten[2], E. Schimpf[2], A. Semchenkov[2,4], H.-J. Wollersheim[2], A. Türler[4], A. Yakushev[4], K. Eberhardt[5], J. Even[5], J.V. Kratz[5], and P. Thörle-Pospiech[5]

[1]Department of Physics, Lund University, S-22100 Lund, Sweden; [2]GSI Helmholtzzentrum für Schwerionenforschung GmbH, D-64291 Darmstadt, Germany; [3]Universidad Nacional de Colombia, Bogotá, Colombia; [4]Technische Universität München, D-85748 Garching, Germany; [5]Universität Mainz, D-55128 Mainz, Germany

A new nuclear spectroscopy set-up called TASISpec (*TA*sca *S*mall *I*mage mode *Spec*troscopy) has been designed and commissioned. It exploits TASCA's specific small image focal mode, i.e. the fact that superheavy elements (SHE) produced in fusion-evaporation reactions can be focused into an area of less than 3 cm in diameter [1]. This provides the world-unique possibility to pack composite Ge-detectors in very close geometry, resulting in an unprecedented, highly efficient detection of γ-rays and X-rays in coincidence with implanted SHE.

The test set-up as used in 2008 is illustrated in Fig. 1. It comprised a focal plane made from a 58 mm $\times$ 58 mm large double sided silicon strip detector (DSSSD) complemented by four single sided silicon strip detectors (SSSD) mounted in the backward hemisphere and two Ge detectors: one cluster (7 crystals) downstream and one large VEGA clover (4 crystals) on one side. The final set-up foresees three additional clover detectors, while their implementation requires a dedicated holding structure to be built in 2009.

Conversion electron, γ-ray, and α-particle sources as well as evaporation residues from the reactions ^{206}Pb(^{48}Ca, $2n$)^{252}No, ^{207}Pb(^{48}Ca, $2n$)^{253}No, ^{244}Pu(^{48}Ca, $4n$)^{288}114, ^{150}Nd(^{64}Ni, xn)$^{214-x}$Ra, ^{154}Sm(^{64}Ni, yn)$^{218-y}$Th, and ^{nat}Gd(^{64}Ni, zn)$^{224-z}$U have been used to characterise the performance of TASISpec. Detection efficiencies of some 80% were measured for emitted α particles and extrapolated to more than 40% (absolute scale) for γ rays at an energy around 250 keV in the final set-up. In addition, energy thresholds of particle- and γ-ray detectors, dead times, and data rates of a first combined VME (up to 224 channels for Si-strip detector processing) and XIA-DGF (11 channels sampling the Ge-detector signals) data acquisition system were successfully tested as well as TASCA-SIM transmissions determined at different magnet settings.

In 2009 it is planned to establish the extraordinary $\gamma\gamma$-, γ-CE-, CE-CE, or even $\gamma\gamma$-CE-, multi-coincidence capabilities of the both segmented and compact TASISpec set-up by settling the decay scheme of K-isomeric states in ^{253}No [2, 3, 4, 5]. Despite of the underlying amount of data many question marks still remain regarding the structure of ^{253}No.

Following upon this ideal starting point to show the proof-of-principle of TASISpec, K isomers expected in neutron-rich SHE will be stepwise approached. Such a programme employs also the unique facets of both high UNILAC beam intensities, use of radioactive actinide targets, and high transmission of TASCA for rather asymmetric reactions. Last but not least, the unprecedented γ-efficiency of TASISpec may allow to identify SHE by means of characteristic X-rays.

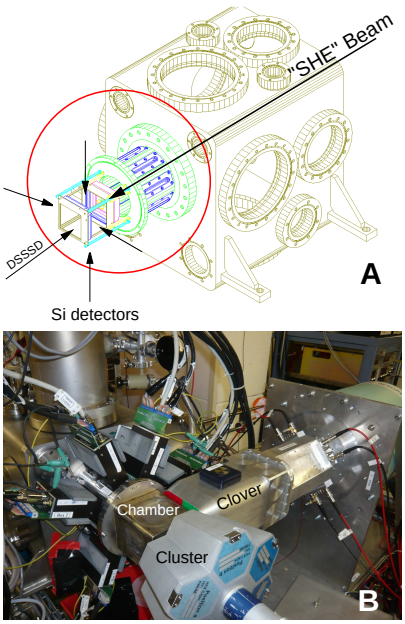

Figure 1: The TASISpec set-up installed at the focal plane of TASCA. Panel (A) illustrates a drawing of the focal-plane area of the TASCA separator. The TASISpec structure is encircled. Five silicon strip detectors are placed in a cube-like shape. Panel (B) shows a photograph of the commissioning set-up. The relative positions of the Ge-VEGA-clover and Ge-cluster detector is here visible.

References

[1] A. Semchenkov *et al.* Nucl. Instrum. Meth. Phys. Res. B **266**, 4153 (2008).

[2] F. P. Hessberger *et al.*, Eur. Phys. J. A **22**, 417 (2007).

[3] R.-D. Herzberg *et al.*, Eur. Phys. J. A **15**, 205 (2002).

[4] F. P. Hessberger, Physics of Atomic Nuclei **70**, 1445 (2007).

[5] A. Lopez-Martens *et al.*, Eur. Phys. J. A **32**, 245 (2007).

[6] J. Dvorak *et al.*, Phys. Rev. Lett **97**, 242501 (2006).

First Transactinide Chemistry Behind TASCA*

J. Even[1#], J.V. Kratz[1], J. Ballof[1], R.A. Buda[1], K. Eberhardt[1], E. Gromm[1], D. Hild[1], D. Liebe[1], M. Mendel[1], P. Reichert[1], P. Thörle-Pospiech[1], N. Wiehl[1], T. Wunderlich[1],W. Brüchle[2], Ch.E. Düllmann[2], E. Jäger[2], J. Krier[2], M. Schädel[2], B. Schausten[2], A. Semchenkov[2,5], D. Nayak[3], A. Toyoshima[4], A. Türler[5], A. Yakushev[5]

[1]Institut für Kernchemie, Johannes Gutenberg-Universität Mainz, Germany; [2]GSI, Darmstadt, Germany, [3]Saha Institute of Nuclear Physics, Kolkata, India; [4]Japan Atomic Energy Agency, Tokai, Japan; [5]Institut für Radiochemie, Technische Universität München, Germany

The final phase of the TASCA commissioning program [1] included a series of experiments with ^{260}Rf, ^{261a,b}Rf and ^{262}Rf produced in the ^{244}Pu(^{22}Ne,xn) reaction. One of the highlights was a proof-of-principle transactinide chemistry experiment with 78-s ^{261a}Rf. The Automated Rapid Chemistry Apparatus (ARCA) [2] was used to study the formation of fluoride complexes of Rf in diluted HF-solution by anion-exchange chromatography.

TASCA was operated in the High Transmission Mode (HTM) [3] at a pressure of 0.4 mbar He. After passing a 14 cm x 4 cm large Mylar window of 1.2 µm thickness, evaporation residues were thermalized in He at 1200 mbar in a newly designed recoil transfer chamber (RTC) of 1.7 cm depth. The RTC had two funnel shaped inlets at the right and left hand side for the He/KCl jet and a central outlet in the cover plate. The Rf was transported to ARCA by a He/KCl jet through a 10 m long PE capillary of 2 mm i.d. at a gas flow rate of 2.9 L/min. To monitor the gas-jet yield, a ^{227}Ac emanation source was connected to the RTC. Ar with a flow rate of 20 mL/min was passed through the source and transported ^{219}Rn into the RTC. The yield of its decay product ^{211}Bi was compared to the respective yield in ROMA [4]. The ^{211}Bi yield in ARCA including collection, dissolution in $7x10^{-4}$ M HF solution, and evaporation on a Ta disc was 50% of that in ROMA.

For the anion-exchange chromatography in ARCA, the column magazines were filled with the resin MCI GEL CA08Y from Mitsubishi Chemical Corporation, particle size 22±5 µm, which was transferred into the hydroxide form as described in [5]. In each chromatography experiment, two Rf fractions were collected. The first one was $7x10^{-4}$ M HF, which was also used for column loading, and the second one was 5 M HNO_3. The latter was used to strip the remainder of the Rf from the column. After around 18 h experiment, the concentration of the first solution was changed to $1x10^{-3}$ M HF and the experiments were continued for another 25 h.

The KCl clusters were collected in ARCA for 90 s. Within this time, the column for the next experiment was preconditioned for 65 s with the HF solution. After the collection, the products were dissolved in 200 µl of $7x10^{-4}$ M HF solution and were subsequently fed onto the anion-exchange column at a flow rate of 1.0 mL/min. The effluent of the column was collected on a Ta disk as fraction 1. The fraction of the products adsorbed on the resin was eluted with 250 µL of 5 M HNO_3 and collected on a second Ta disk. Both fractions were evaporated to dryness by infrared light and a hot helium stream. The two Ta discs were then subjected to α-spectroscopy. Counting of the first fraction started 60 s after the end of the collection interval, counting of the second fraction started 65 s after the end of the collection.

In total, seven α-events were detected which we attribute to 78-s ^{261a}Rf based on the measured α-energy and lifetime. All of them were observed in the HNO_3 fraction. Two of these events were detected during the experiments with $7x10^{-4}$ M HF, the other five events were detected while using $1x10^{-3}$ M HF. As no events were observed in the HF fractions, it is only possible to give a lower limit for the %ads value. As in Poisson statistics zero observed events are compatible with three events at 95% confidence level, 3 events were assumed for the first fraction and the remainder in the second fraction resulting in %ads ≥ 62.5 % in $7x10^{-4}$ M HF and %ads ≥ 72.5 % in $1x10^{-3}$ M HF. The sum of the α events is shown in Figure 1 indicating that the α spectra were very clean, also thanks to preseparation in TASCA.

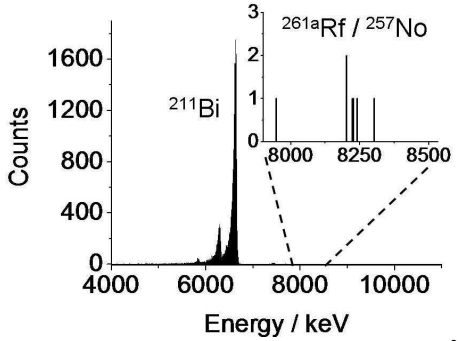

Figure 1: Sum spectrum of the α-particle events of ^{261a}Rf.

From a comparison with the number of ^{261a}Rf events in ROMA, we have to conclude that the chemical yield in ARCA was low, on the order of 30% only. This is in line with earlier observations indicating some sorption of transactinides from HF solutions on the Kel-F slider in ARCA.

References

[1] M. Schädel *et al.,* contribution to this report.
[2] M. Schädel *et al*., Radiochim. Acta **48**, 171 (1989).
[3] A. Semchenkov *et al.*, NIM B 266, 4153 (2008).
[4] A. Gorshkov *et al*., this report.
[5] A. Toyoshima *et al*., Radiochim. Acta **96**, 125 (2008)

* Work supported by BMBF (06MZ223I) and GSI-F&E (MZJVKR)
# evenj@uni-mainz.de

Calculation of Adsorption Energies of Elements 112 and 114, and their Homologues Mercury and Lead on Gold (111) Surface

J. Anton[1], T. Jacob[1], and V. Pershina[2]

[1]Institut für Elektrochemie, Universität Ulm, Germany; [2]GSI, Darmstadt, Germany

In the last decade the gas-phase thermography becomes the method of choice for studying the chemical behavior of super-heavy elements in nuclear-chemistry. In such experiments, however, the whole information about the adsorption process of a chemical element is reduced to a single number – the adsorption temperature. The adsorption on the other hand is a very complex process, which requires an adequate theoretical description for interpreting the experimental data.

Within our theoretical approach, which is based on fully-relativistic 4*c*-DFT [1], the substrate surface is represented by a cluster of atoms at fixed positions. The adsorption behaviour, i.e. binding energies and structures strongly depend on the size of the chosen cluster. Therefore a cluster size convergence studies are mandatory in order to be able to obtain accurate results.

In this report we present our calculations of the adsorption energies of elements 112 and 114 and their homologues Hg and Pb on a gold (111) surface for different cluster sizes. For all four possible adsorption positions – top, bridge, hollow1, and hollow2 – we first performed calculations for the smallest possible cluster, which for the on top site might even be a single atom only, for example. In the next step we added all atoms from the next coordination shell to our cluster and repeated the calculations. We continued this procedure until convergency was achieved in both the adsorption energy and adsorption distances. The results of this study are summarized in Figure 1, where the potential energy curves for elements 112 and 114, and mercury are presented. (Pb is not shown in the picture, because the binding energies are too large). The convergence of both the bond distance and the adsorption energy as function of cluster size was achieved with the largest clusters containing 95 (top), 94 (bridge), 120 (hollow1), and 107 (hollow2) gold atoms.

The results of the calculations show that the binding energies of each of the considered elements for the bridge and hollow2 positions are very similar. However, element 114 and Hg have a slight preference to adsorb in the bridge position, while element 112 and Pb - in the hollow2 one. Except for Pb, all the other three elements are weakly bound to the gold surface which is due to the strong relativistic effects in the outermost shells of these elements and a closed shell effect in Hg and element 112.

An interesting and important feature of the present calculations is that the binding energies change with both the adsorption position and cluster size in such a way that the adsorption strength order $E_b(E112) < E_b(Hg) < E_b(E114) \ll E_b(Pb)$ remains the same. This confirms our former qualitative predictions [2], which were based on calculations for dimers only. A detailed discussion of the presented results can be found in [3].

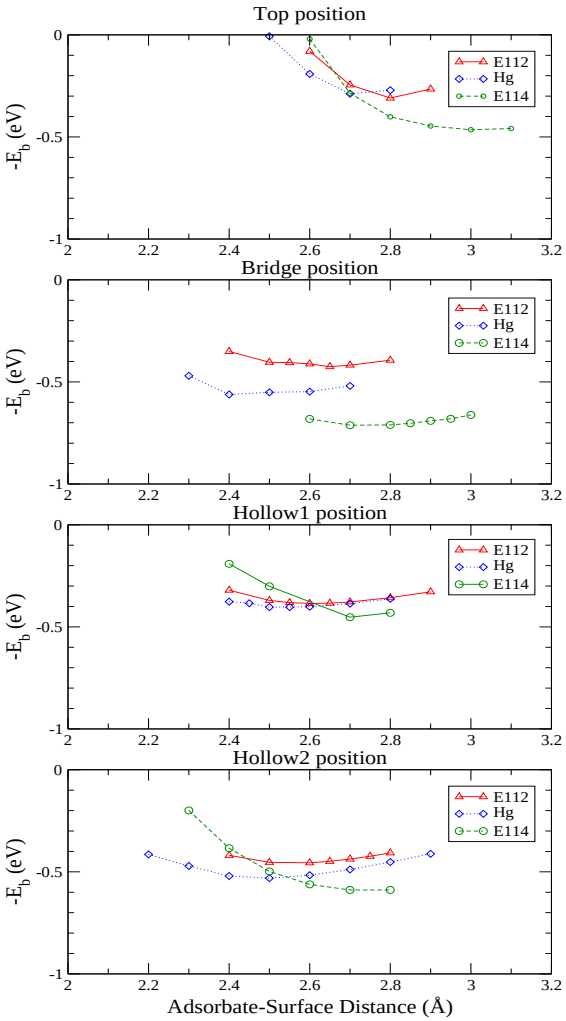

Figure 1: Adsorption energies of elements 112, 114, and mercury as function of the adsorbate-surface distance.

References

[1] J. Anton, B. Fricke, E. Engel, *Phys. Rev. A*, **69**, 012505 (2004).

[2] V. Pershina, J. Anton, and B. Fricke, *J. Chem. Phys.* **127**, 134310 (2007).

[3] J. Anton, T. Jacob, and V. Pershina, *PRL*, in preparation

Prediction of Adsorption of Element 113 on Inert Surfaces from *ab initio* Dirac-Coulomb Atomic Calculations

V. Pershina[1], A. Borschevsky[2], E. Eliav[2], and U. Kaldor[2]
[1]GSI, Darmstadt, Germany; [2]Tel Aviv University, Israel

Element 113 has an isotope (A=284) with $t_{1/2}=0.48^{+0.58}_{-0.17}$ s, which makes it suitable for chemical studies. The element is expected to be volatile. Its adsorption behaviour is to be investigated by gas-phase chromatography experiments using silicon detectors of the chromatography column covered with gold layers. Feasibility experiments are under way, studying the adsorption behaviour of the nearest homolog, Tl [1]. Prediction of the adsorption enthalpy, ΔH_{ads}, and temperature, T_{ads}, of element 113 on gold surface is very important for the planned experiments. Information about adsorption on inert surfaces such as Teflon and polyethylene (PE) is also valuable, as these materials are used as transport capillaries from the target chamber to the detection system in the experimental setup. In this work, we predict the adsorption behaviour of element 113 and its homolog Tl on Teflon and PE on the basis of very accurate results of *ab initio* calculations of their atomic properties.

The electronic structure calculations were performed using the DIRAC package [2]. In the Dirac-Coulomb (DC) *ab initio* method, the many-electron relativistic Dirac-Coulomb Hamiltonian

$$H_{DC} = \sum_i h_D + \sum_{i<j} 1/r_{ij} \qquad (1)$$

is employed, where

$$h_D = c\vec{\alpha}\cdot\vec{p} + \beta c^2 + V_{nuc}\,. \qquad (2)$$

The atomic orbitals (AO) are four-component spinors

$$\phi_{nk} = \begin{pmatrix} P_{nk}(r) \\ Q_{nk}(r) \end{pmatrix}, \qquad (3)$$

where $P_{nk}(r)$ and $Q_{nk}(r)$ are the large and small component, respectively. The Faegri uncontracted 26s24p18d13f5g2h basis set was used for both elements [3]. Electron correlation was taken into account at various levels of theory including the highest, the Fock-Space Coupled Cluster Single Double excitations, FS CCSD, for which the current results are presented.

The calculations of polarizability (α) were performed by the finite field method. The DC FS CCSD results for α are given in Table 1 along with the ionization potentials (IP) of Tl and element 113 calculated at best using the Dirac-Coulomb-Breit (DCB) FSCC method [4]. The van der Walls radii (R_{vdW}) were determined from a linear correlation with $R_{max}(np_{1/2})$-AOs of the group 13 elements. ΔH_{ads} were calculated using a model of physisorption given by eq. (8) of Ref. [5].

Table 1. Atomic properties of Tl and element 113: ionization potentials, IP (in eV), polarizabilities, α (in a.u.), van der Walls radii, R_{vdW} (in Å) and adsorption enthalpies, ΔH_{ads} on Teflon (T) and PE (in kJ/mol).

Property	Tl	Meth.	Ref.	113	Meth.	Ref.
IP	6.108	DCB	[4]	7.306	DCB	[4]
	6.110	exp.	[6]	-	-	
α	51.3	DC	this	29.85	DC	this
	51(7)	exp.	[6]	-	-	
R_{vdW}	1.90	corr.	this	1.84	corr.	this
$-\Delta H_{ads}$(PE)	22.22	calc.	this	15.83	calc.	this
$-\Delta H_{ads}$(T)	19.65	calc.	this	14.00	calc.	this

The obtained ΔH_{ads} on PE and Teflon for all group 13 elements are shown in Fig. 1, revealing a reversal of the trend beyond In due to the relativistic contraction of the $np_{1/2}$ AO. The very low $-\Delta H_{ads}$(113) on inert materials guarantees its transport to the chemistry set up.

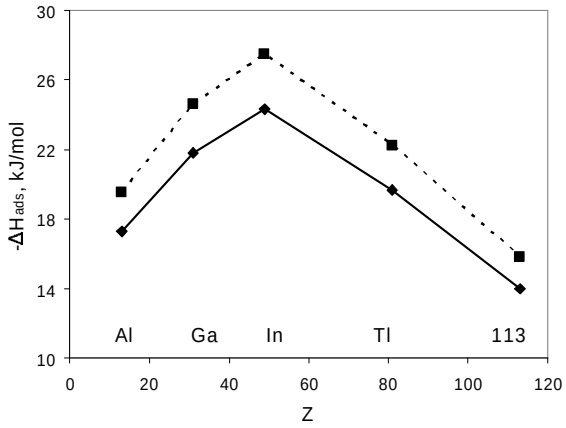

Fig. 1. Calculated adsorption enthalpies of group 13 elements on PE (dashed line) and Teflon (solid line).

References

[1] S. König *et al*. PSI Annual Report 2005, (http://lch.web.psi.ch/pdf/anrep05/03.pdf).
[2] DIRAC 04, written by H. J. Ja. Jensen *et al.* (2004).
[3] K. Faegri, Theor. Chim. Acta 105 (2001) 252 .
[4] E. Eliav *et al*. Phys. Rev. A, 53 (1996) 3926.
[5] V. Pershina *et al*. J. Chem. Phys. 122 (2005) 124301.
[6] CRC Handbook of Chemistry and Physics, 86th edition, ed. D. R. Lide (2005).

Relativistic *ab initio* Study of HgAu, Homologue of the Superheavy 112Au

A. Borschevsky[1], V. Pershina[2], E. Eliav[1], and U. Kaldor[1]
[1] Tel Aviv University, Israel; [2] GSI, Darmstadt, Germany

Predictions of the interaction of the superheavy elements with various surfaces are essential for their identification and separation. Recently, we have predicted the adsorption properties of the superheavy element 112 on inert surfaces [1]. The calculations were performed using the fully relativistic Dirac-Coulomb Hamiltonian combined with the coupled cluster method. The accuracy of the results was verified by performing the same calculations on mercury, which is a lighter homologue of element 112, and for which experimental data exist. For Hg, the results obtained were in excellent agreement with the experimental values, and we expect the same accuracy for its superheavy homologue. Similar investigations were performed on element 114 and Pb.

In this work we investigate the adsorption of superheavy element 112 and Hg on gold through the fully relativistic *ab initio* electronic structure calculations for the dimers 112Au and HgAu. The calculations have been completed for HgAu. Those for 112Au are under way.

The electronic structure calculations are performed using the DIRAC package [2]. In order to take relativity into account, we employ the 4-component Dirac–Coulomb Hamiltonian,

$$H_{DC} = \sum_i h_D + \sum_{i<j} 1/r_{ij}, \quad (1)$$

where

$$h_D = c\vec{\alpha}\cdot\vec{p} + \beta c^2 + V_{nuc}. \quad (2)$$

V_{nuc} is the nuclear attraction operator, and α and β are the four-dimensional Dirac matrices. In order to obtain computational efficiency, the interatomic SS-integral contributions were modeled by classical repulsion of small component atomic charges [3]. This is one of the most economical and accurate approximation to the full Dirac-Coulomb Hamiltonian. Electron correlation is taken into account using the Fock space coupled cluster (FS CC) method, which is considered to be one of the most powerful tools in quantum chemistry.

The basis set of Saue *et al* [4], consisting of 23*s*, 18*p*, 14*d*, and 8*f* orbitals, was used for the gold atom. For the mercury atom the basis set of Visscher [5] was used, with 20*s*, 18*p*, 12*d*, and 10*f* orbitals.

HgAu is an open shell system; hence we start our calculation with the closed shell reference state, $HgAu^-$. After solving the Dirac-Fock equations and correlating the closed shell reference state, one electron is removed, to give the neutral system. After recorrelation, an additional electron is removed, and the positive ion $HgAu^+$ is reached. Thus, in a single calculation we obtain the energies of HgAu, $HgAu^+$, and $HgAu^-$. The calculations were repeated for different values of the interatomic distance, to obtain the potential curves of the systems under study. The spectroscopic properties of interest were obtained from the potential energy curves, using the LEVEL program package [6].

To our knowledge, no experimental spectroscopic data exist for the HgAu molecule. However, this system has been extensively studied theoretically [7-11], mostly using relativistic DFT methods. A relativistic coupled cluster single doubles (triples) (RCCSD(T)) investigation was also performed [10]. A comparison with the other calculations is given in Table 1. One can see very good agreement with the 4*c*-DFT result for HgAu [11].

Table 1. Spectroscopic properties of HgAu, $HgAu^+$, and $HgAu^-$: equilibrium bond lengths R_e, (in Å), dissociation energies, D_e, (in eV), adiabatic ionization potentials, IP_{ad},(in eV), and vibrational frequencies, ω_e, (in cm^{-1})

Property	AuHg	$AuHg^+$	$AuHg^-$	Method, Ref.
R_e	2.657	2.553	2.854	DC FSCC, this
	2.711	2.581	2.967	RCCSD(T) [10]
	2.67	-	-	4*c*-DFT [11]
D_e	0.478	1.712	0.520	DC FSCC, this
	0.389	1.856	0.381	RCCSD(T) [10]
	0.495	-	-	4*c*-DFT [11]
IP_{ad}	7.374	-	1.995	DC FSCC, this
ω_e	116	156	79	DC FSCC, this
	103	139	64	RCCSD(T) [10]

Our results are expected to be more accurate than the RCCST(T) ones due to the larger basis set employed. The same degree of reliability may be expected for the heaviest homolog of HgAu, the 112Au molecule.

References

[1] V. Pershina, A. Borschevsky, E. Eliav and U. Kaldor, J. Chem. Phys **128**, 024707 (2008)
[2] DIRAC 04, written by H. J. Ja. Jensen *et al*. (2004)
[3] L. Visscher, Theor. Chem. Acc. **96**, 68 (1997)
[4] T. Saue, K. Fægri,T Helgaker, and O. Gropen, Mol. Phys, **91**, 937 (1997)
[5] L. Visscher, private communication.
[6] LEVEL 8.0, written by R.J. Le Roy (2007) (http://leroy.uwaterloo.ca/programs/)
[7] V. Pershina, T. Bastug, Chem. Phys. **311**, 139 (2005)
[8] Z.J. Wu, Chem. Phys. Lett. **406**, 24 (2005)
[9] A. Zaitzevskii *et al*, CEJP **4**, 448 (2006)
[10] R. Wesendrup and P. Schwerdtfeger, Angew. Chem. Int. Ed. **39**, 907 (2000)
[11] V. Pershina, T. Bastug, T. Jacob, B. Fricke, S. Varga, Chem. Phys. Lett. **365**, 176 (2002).

^{100}Sn and Nuclei in its Neighbourhood *

K.Eppinger[1], C.Hinke[1], M.Böhmer[1], P.Boutachkov[2], T.Faestermann[1#], H.Geissel[2], R.Gernhäuser[1], M.Górska[2], A.Gottardo[3], J.Gręboszˊ[4], R.Krücken[1], N.Kurz[2], Z.Liu[3], L.Maier[1], S.Pietri [2,5], Zs.Podolyák[5], H.Weick[2], P.J.Woods[3], N.Al-Dahan[5], N.Alkhomashi[5], A.Atac[6], A.Blazhev[7], N.Braun[7], L.Caceres[2], I.Čeliković[8], T.Davinson[3], I.Dillmann[1], C.Domingo-Pardo[2], P.Doornenbal [9], G.de France[10], G.Farell[5], F.Farinon[2], J.Gerl[2], N.Goel[2], T.Habermann[2], R.Hoischen[2], R.Janik[11], M.Karny[12], A.Kaskas[6], I.Kojouharov[2], Th.Kröll[1], M.Lewitowicz [10], Y.Litvinov[2], S.Myalski[4], F. Nebel[1], S.Nishimura[9], C.Nociforo[2], J.Nyberg[13], A.Parikh[1], A.Procházka[2], P.H.Regan[4], C.Rigollet[14], H.Schaffner[2], C.Scheidenberger[2], S.Schwertel[1], P.-A.Söderström[13], S.Steer [4], A.Stolz[15], P.Strmeň[11], H.J.Wollersheim[2], and the RISING collaboration

[1] TU München, [2]GSI, [3]U of Edinburgh, [4]IFJ PAN Krakow, [5]U of Surrey, [6]U of Ankara, [7]U of Köln, [8]Inst. Vinca Belgrade, [9]RIKEN, [10]GANIL, [11]U of Bratislava, [12]U of Warsaw, [13]U of Uppsala, [14]KVI - U of Groningen, [15]MSU

^{100}Sn is a unique case in the nuclear landscape, being doubly magic and the heaviest particle-stable N=Z nucleus. It had been produced and studied already in two FRS experiments [1,2] identifying together eight events. With the improved intensities from the SIS an experiment with good statistics became feasible.

We have produced ^{100}Sn and nuclei in its neighbourhood by fragmentation of a 1 A·GeV beam of ^{124}Xe on a Be target. Using rapid cycling of the SIS the average intensity on target was more than 10^9 ions/s. Redundant measurements of energy loss, magnetic rigidity, and flight time in the second half of the FRS allowed a unique identification of the fragments as shown in Fig. 1 for the 15 days of data taking in a ^{100}Sn setting of the FRS. In addition to 244 nuclei of ^{100}Sn we identified for the first time the nuclides ^{93}Ag, ^{95,96}Cd, ^{97}In and most probably ^{99}Sn. Although we see some events at the location of ^{103}Sb, its half life must be at least a factor of 10 shorter than the flight time through the FRS of 200 ns, in contrast to the literature[3]. The fragments were stopped in a stack of Si detectors. For the correlation of implantation position and time with subsequent decays we used three large area position sensitive Si strip detectors with a total of 7200 pixels. 10 1mm thick Si detectors in front and behind this implantation zone served as calorimeters to measure the β-spectrum and to determine its endpoint.

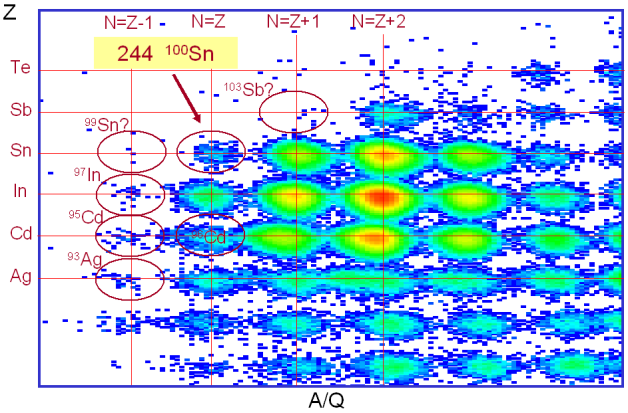

Figure 1: Nuclides identified in the FRS during the 15 days irradiation in the setting for ^{100}Sn.

The implantation detector was surrounded by the 105 Ge detectors of the RISING array to observe isomeric decays as well as the γ-deexcitation following β-decays. A number of isomeric states was observed. As an example Fig. 2 shows a delayed γ-spectrum for ^{102}Sn, where we found a new isomeric transition.

Analysis of the data for position-correlated β-decays is in progress to extract half-life, β-endpoint energy and decay γ information.

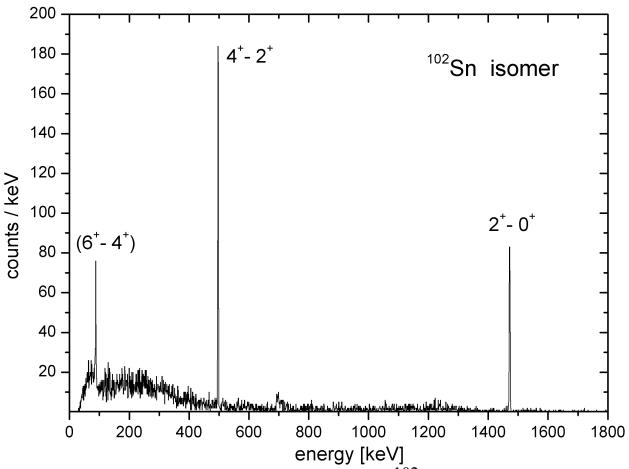

Figure 2: Delayed γ-spectrum for ^{102}Sn events. The low energy transition was hitherto unknown and could be interpreted as the 6^+- 4^+ transition.

References

[1] R. Schneider et al., Z.f. Phys. **A348** (1994) 241
[2] T. Faestermann et al., EPJ **A15** (2002) 185
[3] K. Rykaczewski et al., PR **C52** (1995) R231

* work supported by the MLL, BMBF(06MT238), DFG(EXC153), GSI(TM/KRUE), EPSRC, STFCUK, and EURONS

thomas.faestermann@ph.tum.de

N=82 shell gap below ^{132}Sn: core excited isomeric state in ^{131}In

M. Górska[1], L. Caceres[1,2], H. Grawe[1], M. Pfützner[3], A. Jungclaus[2], S. Pietri[4], E. Werner-Malento[3], D. Rudolph[5], Z. Podolyák[4], P.H. Regan[4], P. Detistov[6], S. Lalkovski[6,7], V. Modamio[2], J. Walker[2], P. Bednarczyk[1,8], P. Doornenbal[1], H. Geissel[1], J. Gerl[1], J. Grębosz[1,8], I. Kojouharov[1], N. Kurz[1], W. Prokopowicz[1], H. Schaffner[1], H.J. Wollersheim[1], K. Andgren[9], J. Benlliure[10], G. Benzoni[11], A.M. Bruce[7], E. Casarejos[10], B. Cederwall[9], F.C.L. Crespi[11], B. Hadinia[9], M. Hellström[5], R. Hoischen[5,1], G. Ilie[12], A. Khaplanov[9], M. Kmiecik[8], R. Kumar[13], A. Maj[8], S. Mandal[14], F. Montes[1], S. Myalski[8], G. Simpson[15], S.J. Steer[4], S. Tashenov[1] and O. Wieland[11], Zs. Dombrádi[16], P. Reiter[12], D.Sohler[16]

[1]GSI, Darmstadt, Germany; [2]Universidad Autónoma de Madrid, Spain, [3]IEP, Warsaw University, Poland, [4]University of Surrey, Guildford, UK, [5]Lund University, Sweden, [6]University of Sofia, Bulgaria, [7]University of Brighton, Brighton, UK, [8]The Henryk Niewodniczanski Institute of Nuclear Physics, Cracow, Poland, [9]KTH Stockholm, Sweden, [10]Universidad de Santiago de Compostela, Spain, [11]INFN, University of Milano and INFN sezione di Milano, Italy, [12]Universität zu Köln, Germany, [13]Inter University Accelerator Centre, New Delhi, India, [14]University of Delhi, New Delhi, India, [15]LPSC, Université Joseph Fourier Grenoble, CNRS/IN2P3, Institute National Polytechnique de Grenoble, France, [16]Institute of Nuclear Research of the Hungarian Academy of Sciences, Debrecen, Hungary

The Sn isotopes form the longest isotopic chain in the nuclear chart accessible to current experimental study covering a full major shell from ^{100}Sn [1] to ^{132}Sn [2, 3], and thus provide a stringent test ground for nuclear structure models. A remarkable analogy was found in the decay of the 8^+ isomers in $^{98}Cd_{50}$ [4] $^{130}Cd_{82}$ [3] which both have a pure $g_{9/2}^{-2}$ proton-hole configuration. The structure similarities in both regions of nuclei and the evolution of the *N=82* shell gap below ^{132}Sn are of key importance for the path of the rapid-neutron capture process. The persistence of the 8^+ isomer in the only *N=82* r-process waiting point nucleus known in excited states, ^{130}Cd [3], and the decay half-life suggested that no substantial shell gap reduction was present. A more direct measure of the size of the *N=82* shell energy gap can be obtained from the identification of core excited states in ^{131}In.

The experiment was performed using the standard FRS/RISING setup as described in Ref. [5]. The identified secondary beams were implanted at the final focal plane in a passive stopper.

From the half-life and reduced transition probability analysis [5] a tentative spin-parity of $(17/2^+)$ was assigned to the isomer implying a primary decay 3782 keV *E4* transition. A decay strength of *B(E4)= 1.48(14) W.u.* was inferred, similar to those reported in ^{132}Sn [6] and ^{98}Cd [7].

Shell-model calculations were performed in the proton $\pi(p_{1/2}, g_{9/2}, g_{7/2}, d_{5/2})$ and neutron $\nu(s_{1/2}, h_{11/2}, d_{3/2}, f_{7/2}, h_{9/2})$ model space using a ^{132}Sn core and experimental single-particle (hole) energies [6,8]. The two-body matrix elements of the residual interaction were inferred from a realistic interaction for ^{208}Pb [9]. Only *1p1h* excitations were allowed for each valence orbit. The multiplet monopoles were adjusted to fit level positions in the benchmark nucleus ^{132}Sn. The calculated energies of excited states in ^{131}In are compared to experiment in Fig.1. The shell-model level sequence supports the spin-parity assignments of the isomers in the present and previous work [6]. The *E4* strength of the $(17/2^+) \rightarrow (9/2^+)$ transition in ^{131}In is calculated to be 2.5 W.u. in fair agreement with experiment. The *N=82* shell gap for the even-even ^{130}Cd was

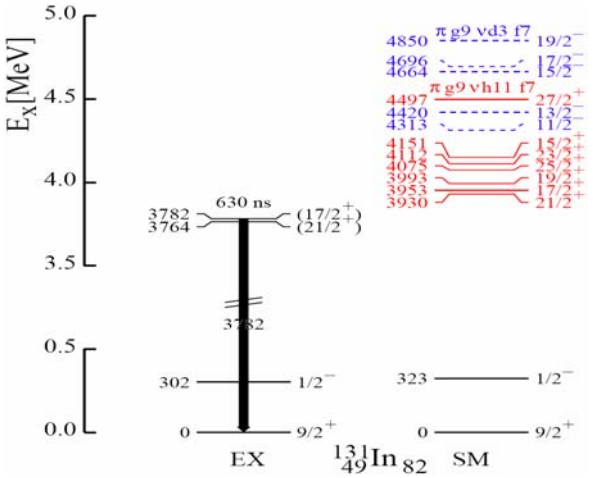

Fig. 1 Experimental level scheme and shell model calculation for ^{131}In

extracted from the calculated ground state binding energies of $^{129-131}$Cd employing the residual interaction which reproduced well the levels in ^{131}In and ^{132}Sn. The result is a considerable decrease of the ^{132}Sn neutron gap of 4.89(8) MeV by 610(100) keV which, however, is in the range of e.g. the reduction of the *Z=50* gap from *N=82* to *80* of 680 keV. It is therefore concluded that the shell-gap reduction does not need any quenching mechanism due to excessive neutrons but can be explained by ´´classical´´ monopole-driven shell evolution.

[1] H. Grawe et al., Eur. Phys. J. A **27**, s01, 257 (2006).
[2] A. Shergur et al., Eur. Phys. J A **25**, s01, 121 (2005).
[3] A. Jungclaus et al., P.R. Lett. **99**, 132501 (2007).
[4] M. Górska et al., Phys. Rev. Lett. **79**, 2415(1997).
[5] M. Górska et al., Phys. Lett. B **672**, (2009).
[6] ENSDF database, http://www.nndc.bnl.gov/ensdf/
[7] A. Blazhev et al., Phys. Rev. C **69**, 064304 (2004).
[8] H.Grawe, K.Langanke, G.Martinez-Pinedo, Rep. Progr. Phys. **70**, 1525 (2007).
[9] E.K. Warburton, Phys. Rev. C **44**, 233 (1991).

Spectroscopy of Cd isotopes approaching the proton drip line.

P. Boutachkov[1], N. Braun[2], T. Brock[3], B.S. Nara Singh[3], Z. Liu[4], A. Blazhev[2], R. Wadsworth[3], M. Górska[1], H. Grawe[1], S. Pietri[1], C.D. Pardo[1], J. Grębosz[5], S. Steer[6], T. Faestermann[7], Zs. Podolyak[6], L. Caceres[1], F. Farinon[1], C. Nociforo[1], A. Prochazka[1], J. Gerl[1], H. Weick[1], I. Kojuharov[1], N. Kurz[1], T. Engert[1], N. Goel[1], R. Hoischen[1,8], H-J. Wollersheim[1], L. Bettermann[2], F. Finke[2], K. Geibel[2], G. Ilie[2], H. Iwasaki[2], P. Reiter[2], C. Scholl[2], N. Warr[2], A. Gottardo[4], P. Woods[4], P. Regan[6], K. Eppinger[7], C. Hinke[7], R. Krücken[7], D. Rudolph[8], J. Nyberg[9], P-A. Söderström[9], M. Pfützner[10], S. Rinta-Antila[11], A. Atac[12], and E. Merchant[13]

[1]GSI, Darmstadt, Germany; [2]Univ of Köln, Köln, Germany; [3]Univ of York, York, UK; [4]Univ of Edinburgh, Edinburgh, UK; [5]Instytut Fizyki Jadrowej, Krakow, Poland; [6]Univ of Surrey, Surrey, UK; [7]Technical Univ of Munich, Garching, Germany; [8]Lund University, Lund, Sweden; [9]Uppsala Univ, Uppsala, Sweden; [10]Warsaw Univ, Warsaw, Poland; [11]Univ of Liverpool, Liverpool, UK; [12]Ankara Univ, Ankara, Turkey; [13]Univ Nacional de Colombia, Colombia

An experiment has been performed to study isomer and β decays in $N \sim Z$ Cd isotopes. These experiments provide information on the p-n interaction and the shell evolution around the N=Z=50 shell closure. It is expected that for N=Z nuclei the isospin mixing between T=0 and T=1 will be the largest, which will be reflected in the observed γ and β decays. There are many theoretical predictions for these nuclei, an example is the long standing prediction of 16^+ and $25/2^+$ spin gap isomers in ^{96}Cd and ^{97}Cd respectively [1]. The $N \sim Z$ region is also interesting from nuclear astrophysics point of view as it is involved in the *rp* process, e.g. Reference [2].

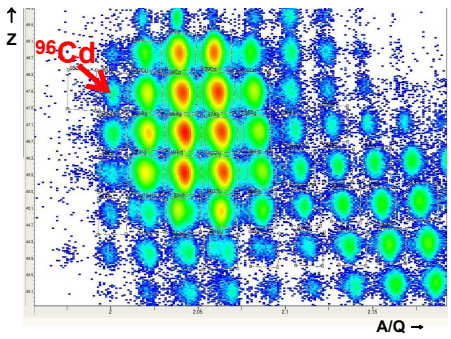

Figure 1: A preliminary Z vs A/Q plot.

In July 2008 we performed a measurement with the RISING setup at the GSI-FRS facility. Only part of the approved beam time of experiment S352 to study $^{96-98}$Cd and their decays was completed. Fragmentation of ^{124}Xe beam with energy of 850 MeV/u and intensity of $\sim 10^9$ pps on a ^{9}Be target of thickness 4 g/cm^2 was used for isotope production. Fragments were selected with the FRS [3]. After identification a degrader was used to slow down and implant $^{96-98}$Cd isotopes into a detector array of Double Sided Silicon Strip Detectors (DSSSD) [4]. This active stopper consisted of 3 rows of 3 DSSSDs each. The DSSSD was 5×5 cm and had 16 X-strips and 16 Y-strips. The stopper was surrounded by the RISING γ-ray spectrometer [5]. Time-correlated γ-decays following both isomer-decay and β-decay were recorded.

The ions identified in the experiment by time-of-flight and energy loss are shown on Figure 1. In the measurement Cd, Ag and Pd isotopes were implanted into the active stopper. A preliminary analysis of the data has revealed new results for some of the $N \sim Z$ nuclei in this region. For example, a spectrum of the γ-transitions from a new isomer in ^{94}Pd observed in this experiment is shown on Figure 2. More details can be found in Reference [6].

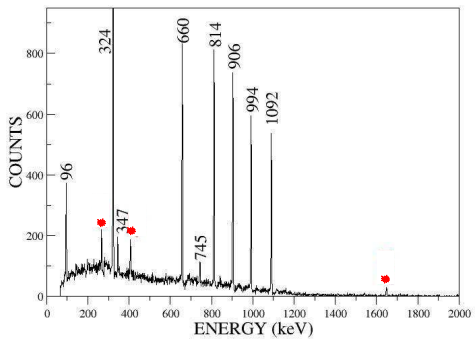

Figure 2: A preliminary γ-ray spectrum of ^{94}Pd isomeric decays. The transitions marked with dots were not reported in previous isomer studies of this nucleus but two of them were observed in β decay of the (21^+) isomer in ^{94}Ag[7].

Analysis of the data for further isomeric decay and $\beta-\gamma$ correlations is currently in progress. The remaining beam time will be key to the completion of the original goals of the experiment.

References

[1] K. Ogawa, Phys. Rev. C**28** (1983) 958.
[2] H. Schatz *et al.*, Phys. Rev. Lett. **86** (2001) 3471.
[3] H. Geissel *et al.*,Nucl. Instr. and Meth. B**70** (1992) 286.
[4] R. Kumar *et al.*, Nucl. Inst. and Meth. A**598** (2009) 754.
[5] S. Pietri *et al.*, Nucl. Inst. and Meth. B**261** (2007) 1079.
[6] R. Wadsworth *et al.*, Act. Pol. B**40** (2009) in press.
[7] M. La Commara *et al.*, Nucl Phys. A**708** (2002) 167.

Electron Screening and α-decay

A. Musumarra[3†], F. Farinon[2,4], C. Nociforo[2], G. Baur[1], K. Beckert[2], K.-H. Behr[2], A. Bonasera[3], F. Bosch[2], D. Boutin[2], A. Brünle[2], L. Chen[4], A. Del Zoppo[3], A. Di Pietro[3], T. Faestermann[5], P. Figuera[3], H. Geissel[2,4], K. Hagino[6], R. Janik[7], C. Karagiannis[2], Kienle[5,8], S. Kimura[3], R. Knöbel[2,4], I. Kojouharov[2], C. Kozhuharov[2], T. Kuboki[14], J. Kurcewicz[2], N. Kurz[2], K. Langanke[2], M. Lattuada[3], S.A. Litvinov[2], Yu.A. Litvinov[2], G. Martinez-Pinedo[2], M. Mazzocco[9], F. Montes[10], Y. Motizuki[11], F. Nolden[2], T. Ohtsubo[12], Y. Okuma[12], Z. Patyk[13], M.G. Pellegriti[3], W. Plaß[4], S. Pietri[2], Z. Podolyak[15], A. Prochazka[2,4], C. Scheidenberger[2,4], V. Scuderi[3], B. Sitar[7], M. Steck[2], P. Strmen[7], B. Sun[2], T. Suzuki[14], I. Szarka[7], D. Torresi[3], H. Weick[2], J. Winfield[2], M. Winkler[2], H.J. Wollersheim[2] and T. Yamaguchi[14]

[1]FZ Jülich, Germany; [2]GSI, Darmstadt, Germany; [3]INFN-LNS and University of Catania, Catania, Italy
[4]Justus-Liebig Universität, Giessen, Germany; [5]TU München, Germany
[6]Tohoku University, Senday, Japan; [7]Comenius University, Bratislava, Slovakia
[8]SMI, Wien, Austria; [9]INFN and University of Padua, Padua, Italy
[10]Michigan State University, East Lansing, U.S.A.; [11]RIKEN, Wako, Japan
[12]Niigata University, Japan; [13]Soltan Institute for Nuclear Studies, Warsaw, Poland
[14]Saitama University, Japan; [15]University of Surrey, Guildford, United Kingdom

As a first milestone of the E073 experiment, half-life measurements of neutral alpha-emitters including ^{214}Ra and ^{213}Fr have been performed at the FRS-S4-focal plane by using the implantation-decay technique with the RISING Silicon active stopper.

One of the major problems in nuclear astrophysics concerns the determination of the electron screening effects on nuclear reaction rates. At stellar energies, the effect of the electron clouds on reaction dynamics cannot be neglected, and a dramatic enhancement of the astrophysical S(E) factor shows up as a consequence of electron shielding [1]. Unambiguous determination of the electron screening energies by using astrophysically relevant two body reactions is quite difficult, since it is affected by several sources of systematic errors. In the E073 experiment we have proposed to investigate electron-screening effects on α-decay by looking at the modification of Q_α-values and half-lives of fully stripped, H-like and He-like α-emitters. The FRS-ESR facility at GSI offers a unique opportunity to perform such kind of studies [2,3]. In fact highly-charged alpha decaying nuclei can be produced by fragmentation of relativistic ^{238}U ions, selected by the FRS and injected in the ESR for in flight half-life and Q-value measurements.

^{214}Ra and ^{213}Fr have been put forward as good candidates for such an investigation. As a first step we performed very precise half-life measurements for neutral atoms by using the RISING silicon implantation-decay setup [4] installed at the FRS-S4 focal plane. It consisted of 6 DSSSD 1 mm thick with 16x16 strips.

Owing to the high selectivity of the FRS, a clear identification of the implanted ions is shown in Fig. 1, where characteristic Q_α-values peaks detected during 12 s inter-spill time are plotted. A decay curve shown in the upper left panel of Fig. 1 has been obtained after gating on the ^{214}Ra decay peak. A preliminary half-life of $T_{1/2}$=(2.485±0.025)s has been obtained by fitting of the corresponding decay events with the function const·exp(-t·ln2/$T_{1/2}$). The measurement is in agreement with the accepted value [5] and is more precise than any previous measurements, confirming the validity of the technique used. The presence of systematic errors will be estimated by extending the analysis to all the other implanted α-emitters.

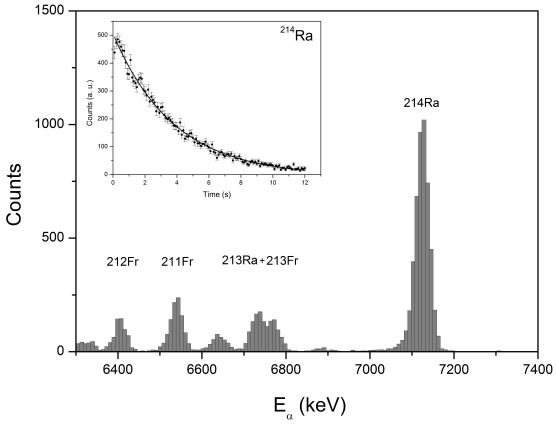

Figure 1: Q_α-value spectrum; upper left panel: ^{214}Ra decay curve.

References

[1] S. Engstler et al., Phys. Lett. B**202,** 179 (1980).
[2] H. Geissel et al., Nucl. Instr. and Meth. B**70**, 286 (1992).
[3] F. Bosch, J. Phys. B**36**,585 (2003).
[4]htpp://linux.gsi.de/~wolle/EB_at_GSI/STOPPED_BEAMS/ACTIVE_STOPPER/DOCUMENTS/DSSD-report.pdf.
[5] Y.A. Akovali, Nucl. Data Sheets **76,** 127 (1995).

†musumarra@lns.infn.it

One neutron removal from ^{24}O and the N=16 shell closure*

R. Kanungo[1#], C. Nociforo[2], A. Prochazka[2,3], T. Aumann[2], D. Boutin[3], D. Cortina-Gil[4], B. Davids[5], M. Diakaki[6], F. Farinon[2,3], H. Geissel[2], R. Gernhäuser[7], J. Gerl[2], R. Janik[8], B. Jonson[9], B. Kindler[2], R. Knöbel[2,3], R. Krücken[7], M. Lantz[9], H. Lenske[3], Y. Litvinov[2], B. Lommel[2], K. Mahata[2], P. Maierbeck[7], A. Musummara[10], T. Nilsson[9], T. Otsuka[11], C. Perro[1], C. Scheidenberger[2], B. Sitar[7], P. Strmen[7], B. Sun[2], I. Szarka[7], I. Tanihata[12], Y. Utsuno[13], H. Weick[2], M. Winkler[2],

[1]Saint Marys' University, Halifax, Canada; [2] GSI, Darmstadt, Germany; [3]University of Giessen, Giessen, Germany, [4]Universidad de Santiago de Compostela , Santiago de Compostella, Spain, [5]TRIUMF, Vancouver, Canada, [6]National Technical University, Athens, Greece, [7]TU München, Munich, Germany, [8]Comenius University, Bratislava, Slovakia, [9]Chalmers University of Technology, Göteborg, Sweden, [10]Catania University and LNS-INFN, Catania, Italy, [11]CNS, Tokyo, Japan, [12]RCNP, Osaka University, Osaka, Japan, [13]Japan Atomic Energy Agency, Tokai, Japan

The measurement of longitudinal momentum distribution for one-neutron removal from ^{24}O at 920*A* MeV is reported.

The change of shell structure for very neutron-rich nuclei has drawn considerable interest in recent times. Empirical evidences from one-neutron separation energy and beta decay Q-values have pointed out the existence of a new magic number at N=16 [1,2]. These evidences suggest that ^{24}O could be a new doubly-closed shell nucleus at the drip-line. The N=16 shell gap has been suggested to arise [3] due to an upward shift of the $1d_{3/2}$ orbital as an effect of the $\sigma\bullet\sigma\tau\bullet\tau$ interaction [4]. To confirm on a spherical shell closure in this nucleus, spectroscopic information on the ground state of ^{24}O is needed.

We performed the first measurement for one-neutron removal from ^{24}O at the FRS, GSI. The secondary beam of ^{24}O was produced from the fragmentation of a ^{48}Ca beam on a Be target and was identified using the first half of the fragment separator FRS based on the principle of energy-loss, magnetic rigidity and time-of-flight. The carbon reaction target was located at the dispersive mid-plane F2 of the FRS. The one-neutron removal fragment ^{23}O after reaction in the C-target was separated and identified at the final achromatic focus F4 using the second half of FRS in combination with multi-sampling ionization chamber for energy-loss measurement, time projection chambers for position measurement and plastic scintillators for time-of-flight measurement.

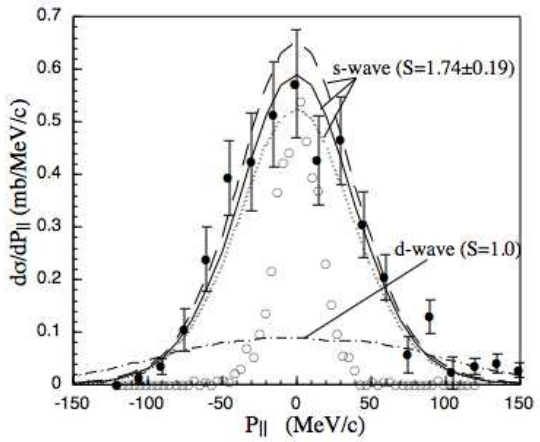

Figure 1: The one-neutron removal momentum distribution data for ^{24}O+C → ^{23}O at 920A MeV [6]. The open circles. The momentum resolution from ^{24}O+C → ^{24}O (open circles). The dashed-dotted line shows the calculated distribution for neutron knocked out from $1d_{5/2}$ orbital. The solid, dashed and dotted lines show calculated distributions for neutrons removed from $2s_{1/2}$ orbital with S=1.74,1.93,1.55 respectively.

The background originating from non-target materials, such as detectors placed in air at F2 and F4 was estimated by taking data for ^{23}O at F4 without a reaction target. The background-subtracted momentum distribution data is shown in Fig.1 (filled circles). The momentum resolution measured by transporting un-reacted ^{24}O after the C-target in a separate setting is shown as the open circles (Fig.1). The one-neutron removal cross section is measured to be 63±7 mb.

The curves in Fig.1 show eikonal model calculations for the configurations of $^{23}O_{gs}+n(2s_{1/2})$ (solid line) and $^{23}O_{gs}+n(1d_{5/2})$ (dashed line). It is seen that the data is well reproduced by the $^{23}O_{gs}+n(2s_{1/2})$ alone while the $^{23}O_{gs}+n(1d_{5/2})$ configuration is much wider. The experimental spectroscopic factor is obtained from a chisquare minimization of the $^{23}O_{gs}+n(2s_{1/2})$ eikonal model results to the data. The observed spectroscopic factor of 1.74±0.19 is in good agreement with shell model calculations using SDPF-M [3] and USDB [5] interactions that predict 1.769 and 1.81 respectively.

The pure s-wave nature of the valence neutron with almost complete s-wave strength of $2s_{1/2}$ orbital confirms the existence of a spherical shell closure in the nucleus, thereby establishing ^{24}O as a new doubly-magic nucleus.

References

[1] A. Ozawa et al., Phys. Rev. Lett. 84, 5493 (2000)
[2] R. Kanungo et al., Phys. Lett. B 528, 58 (2002).
[3] Y. Utsuno et al., Phys. Rev. C 60, 054315 (1999)
[4] T. Otsuka et al., Phys. Rev. Lett. 87, 082502 (2001).
[5] B.A. Brown and W.A. Richter, Phys. Rev. C 74, 034315 (2006).
[6] R. Kanungo et al., Phys. Rev. Lett. *submitted*

* Work supported by .Alexander von Humboldt Foundation
# ritu@triumf.ca.

Shell structure of neutron-rich titanium isotopes probed by one-neutron-knockout *

P. Maierbeck[1], R. Gernhäuser[1], R. Krücken[1], T. Kröll[1], H. Alvarez-Pol[2], F. Aksouh[3], T. Aumann[3], K. Behr[3], E. A. Benjamim[2], J. Benlliure[2], V. Bildstein[1], M. Böhmer[1], K. Boretzky[3], M. J. G. Borge[4], A. Brünle[3], A. Bürger[5,6], M. Caamano[2], E. Casarejos[2], A. Chatillon[3], L. V. Chulkov[3], D. Cortina Gil[2], J. Enders[7], K. Eppinger[1], T. Faestermann[1], J. Friese[1], L. Fabbietti[1], M. Gascon[2], H. Geissel[3], J. Gerl[3], M. Gorska[3], P. G. Hansen[†8], B. Jonson[9], R. Kanungo[3,10,16], O. Kiselev[3,12,17], I. Kojouharov[3], A. Klimkiewicz[3], T. Kurtukian[2], N. Kurz[3], K. Larsson[3,9], T. Le Bleis[3], K. Mahata[3], L. Maier[1], T. Nilsson[7,9], C. Nociforo[3], G. Nyman[9], C. Pascual-Izarra[4], A. Perea[4], D. Perez[2], A. Prochazka[3,11], C. Rodrigo-Tajes[2], D. Rossi[12], H. Schaffner[3], G. Schrieder[7], S. Schwertel[1], H. Simon[3], B. Sitar[11], M. Stanoiu[3], K. Sümmerer[3], O. Tengblad[4], H. Weick[3], S. Winkler[1], B.A. Brown[8], T. Otsuka[13], J.A. Tostevin[14], and W.D.M. Rae[15]

[1]E12, Physik Department, TU München, Germany; [2]USC, Santiago de Compostela, Spain; [3]GSI, Darmstadt, Germany; [4]CSIC, Madrid, Spain; [5]University of Oslo, Oslo, Norway; [6]CEA, Saclay, France; [7]TU Darmstadt, Germany; [8]MSU, East Lansing, USA; [9]Chalmers University of Technology, Göteborg, Sweden; [10]St Mary's University, Halifax, Canada; [11]Comenius University, Bratislava, Slovakia; [12]Johannes Gutenberg Universität, Mainz, Germany; [13]University of Tokyo, Tokyo, Japan; [14]University of Surrey, Guildford, United Kingdom; [15]Garsington, Oxfordshire, United Kingdom; [16]TRIUMF, Vancouver, Canada; [17]PSI, Villigen, Switzerland

One of the main topics of research in nuclear structure physics is the evolution of shell-structure for neutron-rich nuclei. Due to the residual interaction the well-established shell-structure at stability change in some regions. In shell-model calculations with the residual interaction GXPF1A [1], new (sub-) shell closures are predicted for 32 and 34 neutrons in neutron-rich calcium and titanium isotopes, while calculations with the residual interaction KB3G [2] only lead to a shell closure at N=32. The central nucleus of that region, ^{54}Ca, has not been reached yet with current facilities, therefore we currently have to rely on information from neighbouring nuclei.

Knockout reactions at relativistic energies are a tool to study single particle structure far away from stability by measuring inclusive cross sections and momentum distributions. Coincident gamma transitions show population of individual excited states at the same time [3]. This reaction was used for the first time for medium-mass nuclei at high beam energies to probe the structure of ^{55,56}Ti.

The experiment was performed in spring 2006 at the FRS [4]. In 8.5 days of beam time $1.65(4) \cdot 10^6$ incoming ^{56}Ti nuclei were produced and $1.33(1) \cdot 10^4$ knockout-reactions were measured leading to an inclusive cross-section of 84(12) mb. In the residual nucleus ^{55}Ti, a new gamma transition at 955(6) keV was found [4] and identified with the ground-state transition of a $3/2^-$ state predicted in shell-model calculations. This state was detected for the first time, and the transition was populated with 22(6) mb.

Figure 1 shows the momentum distribution obtained with the subtraction of a quasi-exclusive distribution of the inclusive one [6] leading to the ground state population in ^{55}Ti and calculated distributions [5]. The $L = 1$ distribution can reproduce the measured one. This leads to a ground-state spin in ^{55}Ti of $1/2^-$, in agreement with the prediction of shell-model calculations with the GXPF1A interaction. The KB3G interaction predicts a $5/2^-$ spin for the ground state. This is a confiramtion of a better description of shell structure in the vicinity of ^{54}Ca using the GXPF1A interaction and points to a new shell closure at N=34 in this region of the nuclear chart.

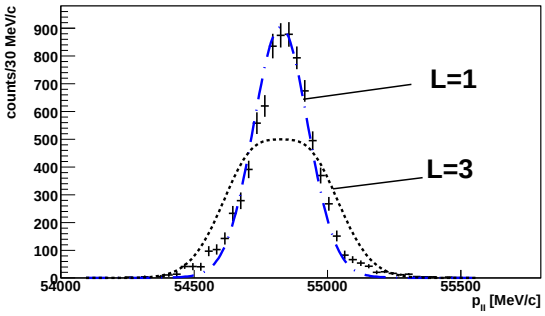

Figure 1: Quasi-exclusive momentum distribution identified with the ground-state population in ^{55}Ti. The calculated distribution correspond to $L = 1$ knockout (dash-dotted) and $L = 3$ knockout (dotted) [5].

References

[1] M. Honma et al., Eur. Phys. Jour. A25, 499, (2005)

[2] A. Poves et al., Phys. Rev. C72, 047302, (2005)

[3] D. Cortina-Gil et al., PRL93, 062501, (2004)

[4] GSI scientific report, 119, (2007)

[5] J.A. Tostevin, private communication

[6] P. Maierbeck et al., submitted to PLB

*Work supported by the BMBF (06MT238), by the DFG cluster of excellence 'Origin and Structure of the Universe', by the EC through I3-EURONS (RII3-CT-2004-506065) and the GSI R+D project (TMKRUE)

Charge Exchange of ^{11}C via Delta Excitation

H. Weick [1], D. Cortina-Gil [2], J. Enders [3], F. Farinon [1], H. Geissel [1], M. Holl [3], N. Iwasa [4], R. Janík [5], P. Maierbeck [6], C. Nociforo [1], A. Prochazka [1], C. Rodriguez-Tajes [2], H. Simon [1], B. Sitar [6], P. Strmeň [6], K. Sümmerer [1], V. Volkov [3], J. S. Winfield [1]

[1]GSI, Darmstadt, Germany; [2]Universidad de Santiago de Compostela, Spain; [3]TU Darmstadt, Germany; [4]Tohoku University, Sendai, Japan; [5]Comenius University Bratislava, Slovakia; [6]TU Munich, Germany;

During the FRS experiment S341 on breakup cross sections of carbon isotopes also charge-exchange reactions were investigated. From the momentum distributions the excitation energy in a charge-exchange reaction proceeding via a delta resonance can be obtained and the reactions via delta excitation of a nucleon can be distinguished from direct nucleon exchange.

A ^{11}C beam was produced from a 1300 AMeV ^{12}C beam hitting the 4 g/cm^2 Be production target at the entrance of the FRS. The ^{11}C then impinged on a 4.8 g/cm^2 Be-target in the midplane of the FRS at a rate of 10^5 ions per 8 sec spill. The reaction products where registered at F3 after the third dipole stage of the FRS. The identification of the incoming beam was done only by measuring the atomic number deduced from the energy deposition in a plastic scintillator in front of the reaction target. Due to the narrowed momentum acceptance from target to F2 it can be excluded that other carbon isotopes may reach this target. The identification behind the target was performed with two plastic scintillators at F3 for measuring the time-of-flight versus F2 and for measuring the charge. Together with the precise measurement of the magnetic rigidity the mass identification is obtained.

As we are only interested in the momentum distribution from the reaction at F2 and the FRS was used in a non-achromatic mode, the subtraction of the momentum spread of the incoming ^{11}C beam was done event by event in the analysis based on the measured positions in the object and image planes at F2 and F3, respectively. The resolution of this procedure was tested in settings with ^{11}C and ^{10}C beams going directly to F3 without second reaction. Also important is the position of the image plane at F3 which was determined by gating on different angles at S2 and measuring the corresponding position at F3. As the setup was optimized for transmission we need to extrapolate the position measured at F3 by a multi-wire proportional counter and a time-projection chamber to the image plane 0.8 m in front of the detectors, which due to straggling in the detector windows reduces the resolution.

The relative deviation in magnetic rigidity from a reference was deduced by scaling the FRS magnets by a defined factor and the absolute energy is given by the synchrotron energy after subtracting the small energy loss in the detectors in a setting without targets. With this we can calibrate the position spectrum in excitation energy. It is shown in Figure1 with a gate on ^{11}B after the reaction. Clearly two peaks can be seen, a narrow one for direct nucleon exchange and a broad one for going via the delta resonance. The two other cases investigated ^{9}Be(^{12}C,^{12}N) and ^{9}Be(^{12}C,^{12}B) show similar distributions.

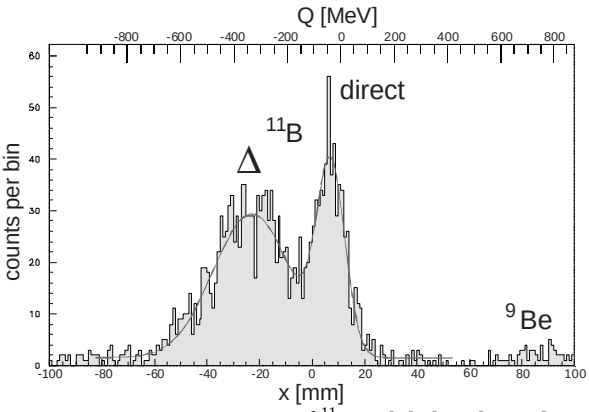

Figure 1: Position spectrum of ^{11}B and deduced Q-value.

An observation of a delta resonance in charge exchange of heavy ions has been done before at Saturne [1] and also at the FRS [2] but this is the first time it could be performed with a secondary beam of exotic nuclei.

Of particular interest is the difference between the direct and the delta peak, which assuming the mass of the free delta amounts to about 300 MeV. Investigations at Saturne using a ^{3}He beam [3] showed up to 70 MeV less for deltas produced on a heavy target of ^{12}C up to ^{208}Pb representing a dense nuclear medium compared to a proton target and also a difference for heavy ions. Theoretically this could be explained by delta-hole correlations [3,4]. However, the resulting mass shift in medium cannot be observed directly as also the mass of the excited nucleon becomes shifted and we observe only the difference.

More information lies in the peak widths. Whereas in our case the width of the direct peak is only slightly wider than the experimental resolution the width of the delta peak exceeds this by far and is much more than that of the free delta (Γ~120 MeV).

Another interesting aspect of this method could be the investigation of neutron and proton distribution in nuclei by measuring the charge-exchange cross sections as it was proposed by Benlliure et al. [5].

References

[1] M. Roy-Stephan et al., Nucl.Phys A447 (1985) 635c.
[2] A. Kelic et al., Phys.Rev. C 70, 064608 (2004).
[3] C. Gaarde, Ann.Rev.Nucl.Phys 41 (1991) 187.
[4] F. Riek, Dissertation TU Darmstadt (2007).
[5] J. Benlliure et al., GSI proposal S364 (2008).

Heaviest helium and lithium isotopes *

Yu. Aksyutina[1,2], T. Aumann[1], K. Boretzky[1], M.J.G. Borge[3], A. Chatillon[1], L.V. Chulkov[1,4], D. Cortina-Gil[5], U. Datta Pramanik[6], H. Emling[1], C. Forssén[2], H.O.U. Fynbo[7], H. Geissel[1], G. Ickert[1], H.T. Johansson[2], B. Jonson[2], R. Kulessa[8], C. Langer[1], M. Lantz[2], T. Le Bleis[1], A.O. Lindahl[9], K. Mahata[1], G. Münzenberg[1], T. Nilsson[2,10], G. Nyman[2], S. Paschalis[11], W. Prokopowicz[1], R. Reifarth[1], A. Richter[12], K. Riisager[7], G. Schrieder[12], H. Simon[1], K. Sümmerer[1], O. Tengblad[3], H. Weick[1], and M.V. Zhukov[2]

[1]GSI, Darmstadt; [2]Chalmers Tekniska Högskola, Göteborg; [3]Instito Estructura de la Materia, Madrid; [4]Kurchatov Institute, Moscow; [5]University of Santiago de Compostela, Compostela; [6]Saha Institute of Nuclear Physics, Kolkata; [7]Aarhus Universitet, Aarhus; [8]Universytet Jagielloński, Kraków; [9]University of Gothenburg, Göteborg; [10]CERN, Genève; [11]University of Liverpool, Liverpool; [12]Technische Universität, Darmstadt

Relativistic beams of the exotic nuclei ^{11}Li and ^{14}Be produced in fragmentation reactions were used to study nuclei beyond the drip line. From these ^{10}He and ^{13}Li nuclei which exhibit a multi-neutron halo were result of a proton removal reaction and represent experimental highlights. These nuclei provide a fertile testing ground for our understanding of drip-line nuclear structure. In addition, their unbound nuclear subsystems, ^{9}He and ^{12}Li, are key in order to study the validity of a three-body description for the ^{10}He and ^{13}Li nuclei.

Main components of the experimental setup were the large-area neutron detector with multi-hit capability, LAND, the large-gap dipole-magnet spectrometer, ALADIN, and a liquid-hydrogen target. The overall detection efficiency was determined from Monte-Carlo simulations using the experimental momentum distributions of the reaction products, the resolving power of the neutron-tracking routine and the acceptance of the setup. The probability for a neutron to be detected within the solid angle subtended by LAND is 85%. In the one-neutron case, the detection efficiency stays almost constant up to about 2 MeV of fragment+n relative energy and decreases at higher energies due to the finite solid angle of LAND and the acceptance of ALADIN. In case of two-neutrons, a decrease in efficiency is observed at low energy due to the limited resolving power for two adjacent neutrons. The efficiency also decreases at higher energies. All distributions shown in this report are corrected for the overall efficiency of the setup, the uncertainties are statistical. The experimental resolution in the relative-energy spectra was also obtained from Monte-Carlo simulations. All model calculations were folded with the experimental resolution and fitted to the experimental data by using the least-squares minimization method.

The three-body relative-energy spectra of ^{8}He+2n (^{10}He) and ^{11}Li+2n (^{13}Li) are shown in Fig. 1. The ^{10}He ground state was found at 1.63(11) MeV with a width of $\Gamma = 2.35(40)$ MeV and evidence was obtained for an excited state at 4.32(20) MeV ($\Gamma = 1.76(77)$ MeV). This preliminary result should be treated with some caution, possible ambiguities in the description are under investigation. The ^{13}Li ground state was found at an energy of 1.47(31) MeV [1]. The resonance-width parameter has large statistical uncertainty and was estimated to be in-between 1 and 3 MeV.

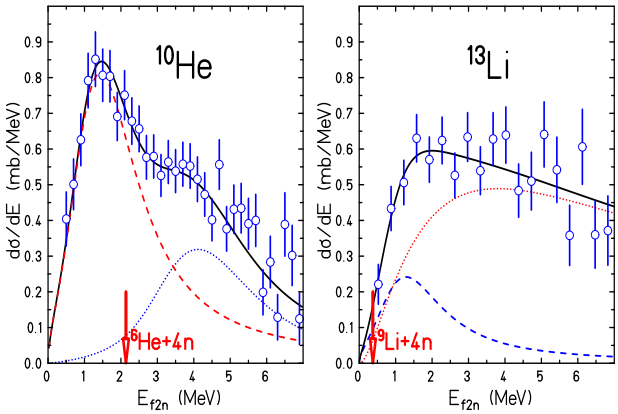

Figure 1: Left panel: Relative energy spectrum of ^{8}He+2n (^{10}He). Right panel: Relative energy spectrum of ^{11}Li+2n (^{13}Li).

The observed resonance parameters for the ground states of ^{10}He and ^{13}Li are the same within experimental uncertainties, in spite of very different binding energies of the core nuclei (^{8}He and ^{11}Li) when ^{10}He and ^{13}Li are considered as three-body systems. This results in very different thresholds for core-fragment+4n decays which are indicated in Fig. 1 by arrows.

The three-body correlation method [2] reveals the differences in their structure in a very pronounced way. The three-body configuration is determined by the angle θ between the Jacobi momenta $\mathbf{q}_{12}$ and $\mathbf{q}_{3-12}$, by the total energy of the three-body system E_{f2n} and by the energy shared by a pair of particles $\epsilon_{12} = q_{12}^2/E_{f2n}$. Here, in-

* Work supported by the BMBF, Contracts No. 06 DA 115, No. 06 OF 838 and No. 06 MZ 864 I, GSI, Contracts No. DA RICK, No. OF ELZ, No. MZ KRAK, Polish Committee of Scientific Research, Contract No. KBN/2P03B/144/10, CICYT, Contract No. FPA2005-02379 and CSD2007-00042 (MJGB,OT), RFBR, Contract No. 08-02-1224, EC, Contract No. ERBCHGE-CT92-0003 and the Knut and Alice Wallenberg Found ation.

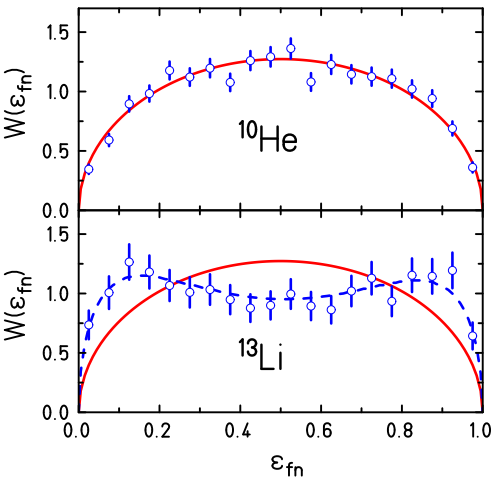

Figure 2: Projections of the probability distribution $W(\epsilon_{fn})$ in ^{8}He+2n (top panel) and ^{11}Li+2n (bottom panel) obtained for the 0-3 MeV region of the three-body relative energy. The solid line displays the phase-space distribution $W(\epsilon) = \frac{8}{\pi}\sqrt{\epsilon(1-\epsilon)}$.

dexes 1,2,3 refer to neutrons (n) or charged fragment (f). Finally, the energy and angular correlations in the f+n+n system can be described by a correlation function $W(\epsilon, \theta)$, representing the probability of finding the system in a configuration in vicinity of definite values ϵ and θ. The correlation function is normalized to unity. The $W(\epsilon, \theta)$ function was determined from the experimental data, and, as an example, its projections on the energy axis $W(\epsilon_{fn})$ are shown in Fig. 2 for the Jacobi configuration ($n - fn$). The distributions $W(\epsilon_{fn})$ were constructed from events restricted to the vicinity of the peak position ($0 < E_{f2n} < 3$ MeV) in the ^{10}He and ^{13}Li relative energy spectra. Experimental distributions are compared with a phase-space distribution function $W(\epsilon) = \frac{8}{\pi}\sqrt{\epsilon(1-\epsilon)}$ describing an ensemble of non-interacting particles. No essential correlation can be seen in the ^{10}He case while ^{13}Li demonstrates strong attraction between ^{11}Li and one of the neutrons. Similar distributions constructed in dependence on the relative energy between neutrons, $W(\epsilon_{nn})$, indicate attraction between neutrons in the ^{10}He case and repulsion in the ^{13}Li case. Thus, this simple comparison with the phase-space distribution function reveals alreday a qualitative difference between the three-body configurations in ^{10}He and ^{13}Li.

A preliminary analysis made by the expansion of $W(\epsilon, \theta)$ in a restricted set of hyperspherical harmonics, which are eigenfunctions of the orbital angular momentum in a three-body system, shows that the relative momentum $l_{fn} = 0$ is the dominant configuration in both cases. This method enables a quantitative analysis of the experimental distributions. The relative weights of the most important final-state configurations in the three-body decays can be derived by a least-squares fit to the experimental data.

Additional information was obtained by studying the properties of two-body systems. One-neutron events are those where only one neutron is detected in LAND while

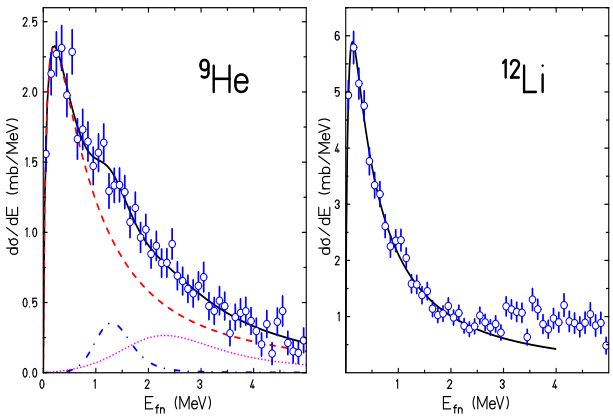

Figure 3: Left panel: Relative energy spectrum of ^{8}He+n (^{9}He). Right panel: Relative energy spectrum of ^{11}Li+n (^{12}Li).

the second neutron has a transverse momentum larger than $\approx$ 60 MeV/c and escapes detection. A possible final state interaction with the second neutron is therefore suppressed.

The ^{9}He spectrum (left panel in Fig. 3) reveals an obviously composite structure consisting of overlapping states: a s-wave virtual state with a scattering length of $a = -3.32(55)$ fm and resonances at 1.28(11) MeV and 2.4 MeV above the ^{8}He+n threshold. The relative-energy spectrum of ^{12}Li, shown in the right panel of Fig. 3, can be described as a single virtual state with $a = -13.7(1.6)$ fm [1]. Thus, s-wave interaction for ^{11}Li+n system is much stronger than for ^{8}He+n, in agreement with the observations using three-body correlations. The a values correspond to positions of S-matrix poles at $E_s = -0.077$ MeV for ^{11}Li+n and $E_s = -1.33$ MeV for ^{8}He+n. The low energy parts of the spectra were also analyzed by a conventional Breit-Wigner equation for s-wave scattering and resonance parameters found were $E_r = 0.38$ MeV ($\Gamma = 2.0$ MeV) and $E_r = 8.4$ MeV ($\Gamma = 49$ MeV) for ^{12}Li and ^{9}He , respectively. This result indicates that the virtual state can be interpreted as a very broad s-wave state with $\Gamma > 4E_r$, e.g. see Ref. [3]. The question naturally arises whether such low-energy asymmetric peaks should be classified as low-energy resonance states, as it is often accepted, or as a threshold phenomenon of an essentially different character.

The analysis indicates that the states observed in ^{10}He and ^{13}Li are likely to have more complex structure than ^{8}He+2n or ^{11}Li +2n. This assumption can be checked for the ^{13}Li ground state which has a very low threshold for emission of four neutrons, the binding energy of the core nucleus is only 0.376 MeV. The possibility to disentangle four-neutron events in LAND is now under investigation.

References

[1] Yu.Aksyutina et al., Phys. Lett. **B 666** (2008) 430.

[2] M.Meister et al., Phys.Rev.Lett. **91** (2003) 162504; L.V.Chulkov et al., Nucl. Phys. **A 759** (2005) 23.

[3] K.W. McVoy, P. Van Isacker, Nucl. Phys. **A 576** (1994) 157.

Quasifree Scattering with Relativistic ^{17}Ne Beams in Inverse Kinematics *

F. Wamers[1] for the R^{3}B collaboration
[1]GSI, Darmstadt, Germany

In 2007, relativistic beams of the proton dripline nucleus ^{17}Ne have been studied in a complete Inverse Kinematics (IK) setup at the "Cave C / LAND" experimental area. A key interest of the experiment is to solve the puzzle around ^{17}Ne's nuclear structure as a possible 2-proton-halo nucleus. Coulomb Excitation on a Pb target, Nuclear Knockout on a C target, and also Quasi-Free Scattering (QFS) on protons in a CH_2 target were employed. In this report, we present the status of the investigation of QFS of ^{17}Ne on CH_2, including the technical upgrades to the setup and a preliminary analysis of the ^{17}Ne(p,2p)^{16}F→Oxygen reaction channel, with resulting angular correlations between the observed QFS recoil protons.

In 'classical' IK knockout reactions, a valence nucleon is knocked/stripped off by peripheral scattering on a, e.g., C nucleus. The binding energy of the knocked out nucleon and its internal momentum are reflected in the remaining fragment's excitation energy and recoil momentum, which are measured. Thus, quantities as the main single-particle components of the wavefunction and associated spectroscopic factors can be determined. While such knockout reactions are sensitive mainly to the valence nucleons, the proton-induced quasifree knockout reaction allows also to probe more deeply bound nucleons [1]. Considering only the pure kinematics of our experiment, the two protons originating from ^{17}Ne(p,2p) reactions at 500 AMeV are expected in the lab frame within a range of 0° to 90° in polar on opposite sides with a polar opening angle around 80°. It was one the experimental goals to measure the energy and momentum distributions of those protons, as they carry information on the knocked out nucleon like the binding energy and intrinsic momentum distribution [2]. The fragment ^{16}F, resulting from the ^{17}Ne(p,2p) knockout reaction, is unbound and decays in flight to ^{15}O+p. To determine the momenta of the ^{15}O fragment and the proton also allows to reconstruct the excitation energy and the recoil momentum, and thus provides a redundant measurement.

To measure the (p,2p) protons, we have set up a new detection system consisting of 4 double-sided Si-strip detectors (DSSD) behind the reaction target in Cave C. The DSSDs measure the proton energy loss for identification and the position from which the angle is determined. The forward part of target-surrounding "Crystal Ball" (a 162-fold segmented 4 π NaI γ-detector) has been equipped with a second readout to detect the high-energy protons, keeping at the same time the sensitivity to gamma rays with lower energy. The Si-NaI covers the full azimuthal range and polar angles from 10° to 80°.

The new Crystal Ball energy readout had been gain-matched using cosmic muons and calibrated in energy versus the standard γ-energy readout. We investigated proton knockout with the CH_2 target: Events with initial ^{17}Ne projectiles and final oxygen fragments were identified and selected. Coincident protons were then analysed in the Crystal Ball. We defined a proton hit multiplicity as the number of seperated clusters of neighbouring crystals with a high energy deposit. Fig. 1 shows angular correlations for events with proton multiplicity "2", corresponding to the reaction channel ^{17}Ne(p,2p)^{16}F→Oxygen:

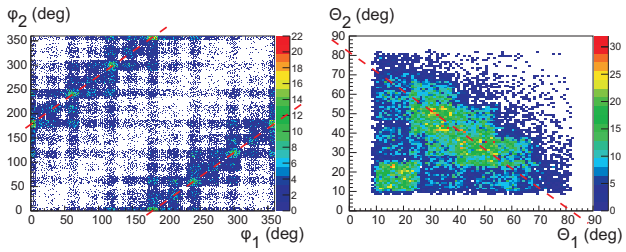

(a) φ_2 vs φ_1 (b) θ_2 vs θ_1, $\Delta\varphi = 180 \pm 15°$

Figure 1: Angular correlations between two protons in a ^{17}Ne(p,2p) reaction with CH_2. (a) Azimuthal correlation. A clear correlation is visible along $\Delta\varphi = 180°$. (b) Polar correlation for events with $\Delta\varphi = 180 \pm 15°$. The visible anti-correlation corresponds to an opening angle of $\theta_2 + \theta_1 = 82°$.

Part (a) of fig. 1 shows the azimuthal (φ) dependence of one versus the other proton. A strong correlation at $\Delta\varphi = 180°$ is observed as expected for quasifree scattering. Part (b) shows the polar (θ) angle dependence of protons with $\Delta\varphi = 180 \pm 15°$, i.e. back-to-back emitted corresponding to quasifree kinematics. A large number of events with a strong anti-correlation around $\theta_2 + \theta_1 = 80°$ is visible. The mean opening angle is in good agreement with the simulated result of $84°$ for quasifree proton knockout from ^{17}Ne.

The further analysis will concentrate on the determination of the total proton energy and will include as well the information from the Si-strip detectors in order to improve the angular resolution. The reconstructed momentum distributions can then be compared to the recoil momentum of the heavy fragment.

References

[1] G.Jacob and Th.A.J.Maris, Rev.Mod.Phys. 38 (1966) 121.

[2] L.V.Chulkov et al., Nucl.Phys.A. 759 (2005) 43.

* Supported through EURONS (European Commission contract no. 506065)

(p,2p) and (p,pn) quasifree knockout reactions with a ^{57}Ni radioactive beam*

S. Paschalis[1], K. Mahata[2], M. Chartier[1], R. Lemmon[3], and T. Aumann[2] for the R3B collaboration
[1]University of Liverpool, UK, [2]GSI, Darmstadt, Germany, [3]Daresbury Laboratory, UK

Knockout reactions using light nuclear targets, e.g., Be or C, have proven in the past to be very useful in gaining information on the wave function of the valence nucleons. However, the strong absorption concentrates the reaction probability at the surface. Similar arguments hold for transfer and Coulomb break-up reactions. Nucleon knockout reactions using protons, on the other hand, allow one to determine the spectral functions of protons and neutrons in a wide range from the weakly bound valence nucleons to the deeply bound core states. Thus, in neutron-rich nuclei one gains access to the hitherto unknown region of the strongly bound protons and simultaneously to the valence neutrons. Beside the single-particle shell-structure, nucleon-nucleon correlations may be investigated as well as cluster knockout reactions. For stable nuclei and in normal kinematics, (p,pN) reactions have been used in the past as spectroscopic tool.

The R3B collaboration intends to develop and apply the technique of quasi-free scattering at energies around 500-700 AMeV (which is high enough to ensure that the conditions for quasi-free scattering are met), where both outgoing nucleons have energies in the range where the nucleon-nucleon cross section is at a minimum, thus maximizing the transparency of the nucleus and minimizing final state interactions. Measurements such as (p,2p), (p,pn), (p,pα) etc. will become possible in a kinematically complete geometry, allowing for a background-free measurement and also for a better control of final state interactions. As a first step, pilot experiments have been performed to investigate the possibilities of employing quasi-free scattering in inverse kinematics at relativistic energies. In the first experiment, the ^{57}Ni(p,2p)^{56}Co and ^{57}Ni(p,pn)^{56}Ni reactions have been investigated at around 500 AMeV using the LAND-R3B setup. Additional detectors have been inserted to detect the nucleons from the quasi-free scattering process. Figure 1 shows a schematic drawing of the arrangement around the CH_2 target. The forward direction around the beam pipe was covered by a segmented CsI detector for detection of photons but also for the detection of energetic protons or neutrons. The figure indicates schematically a (p,2p) reaction. A 12-fold segmented plastic scintillator was placed between the beam pipe and the CsI detector to identify protons and trigger on quasi-free knockout events.

Protons have been identified clearly in coincidence with outgoing ^{56}Co or ^{56}Ni fragments. If ^{56}Co is identified after the reaction target, two protons are detected in coincidence exhibiting the typical angular correlations among them as expected for quasi-free scattering events. Figure 2 shows a correlation plot for events with ^{56}Ni in the outgoing channel, i.e., events associated to (p,pn) one-neutron removal reactions. The x and y axes correspond to the segment number of the hit in the plastic detector and the CsI detector, respectively. The plot was generated from the measurement with a CH_2 target after subtracting the contribution from carbon which was determined by a measurement with a C target. The diagonal line with equal segment numbers corresponds to coincident hits of protons in the plastic detector and in the CsI detectors following directly behind. Two more correlation lines appear where the plastic and CsI segment numbers differ by ±6, corresponding to a relative azimuthal angle of ~180° between the two segments. These correlations originate from a (p,pn) reaction where the proton leaves a signal in the plastic segment but the neutron only leaves a signal in the CsI segment. The angular correlations in such (p,pn) reactions are the same as observed for the two-proton events in (p,2p) reactions. This result demonstrates the feasibility to study also quasi-free neutron knockout reactions in a kinematical complete measurement. Corresponding momentum distributions of fragments and coincident γ rays are presently being analyzed.

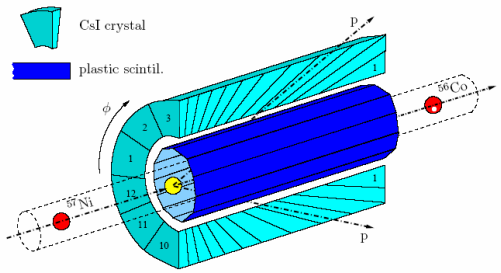

Figure 1: *Schematic drawing of the CsI detector array surrounding the beam pipe in forward direction with respect to the reaction target.*

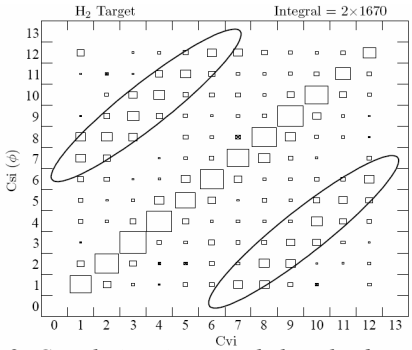

Figure 2: *Correlations in azimuthal angle observed in the plastic detector and the CsI array for the reaction ^{57}Ni to ^{56}Ni. Cvi and Csi refer to the module number of the 12-fold segmented plastic and CsI detectors, respectively [1].*

References

[1] S. Paschalis, PhD thesis, Univ. of Liverpool.

* Work supported by EU, EURONS contract No. 506065.

Dispersion of longitudinal momentum distributions in fragmentation reactions*

A. Bacquias[1], V. Föhr[1], V. Henzl[2], D. Henzlova[2], A. Kelic[1], M. V. Ricciardi[1,#], and K. –H. Schmidt[1]
[1]GSI, Darmstadt, Germany; [2]MSU, East Lansing, MI 48824, U.S.A.

In the last decade, a series of experiments devoted to systematically study fragmentation reactions were carried out at the FRagment Separator (FRS), GSI. The residual nuclei formed in the fragmentation of several relativistic primary beams were separated in-flight and identified before they decayed. The whole isotopic distribution was obtained for every element, and once the nuclides were identified their velocities could be evaluated precisely from their magnetic rigidities. This method yielded absolute and extremely accurate velocity values (resolution ~$5 \cdot 10^{-4}$), whose knowledge also permitted to disentangle fission and binary-decay events from fragmentation and multifragmentation events.

In this work we profit from the detailed overview on the velocity spectra of residual nuclei measured in several fragmentation reactions to revisit our understanding on the standard deviation ($\sigma_{P||}$) of the longitudinal momentum distribution of the final fragments of mass A_f. Please note that this work refers to fragmentation products only (fission and binary-decay products were discharged). Previous works on this topic date back to the theoretical work of Goldhaber (1974) [1] who calculated the influence of the abrasion stage, and to the empirical prescription of Morrissey (1989) [2], limited to rather peripheral collisions. We extended our study to light residual nuclei produced in mid-peripheral collisions. In this context, beside the contribution of abrasion, we considered additionally the effects on the width of the momentum distribution due to thermal break-up and the following sequential evaporation. The aim of the work was to determine a simple analytical formula which could satisfactorily describe $\sigma_{P||}$; this aim sometimes implied some simplifying assumptions in the description of the different processes.

In the abrasion process, we considered the nucleons as a Fermi gas and we assumed that each abraded nucleon contributed to the momentum of the fragment by its Fermi momentum, according to the idea of Golhaber [1].

During the sequential evaporation, each emitted particle introduces a recoil momentum to the corresponding compound nucleus. Since evaporation is an isotropic process, it will not change the mean velocity of the fragment; however it will increase the width of the distribution. The overall contribution from the recoil of evaporated particles to $\sigma_{P||}$ was calculated summing up all the individual contributions, assuming an average value of the mean momentum of the emitted particle.

According to what reported in ref. [3], in an approximate way one can establish if a certain final fragment underwent a break-up process. For these multifragmentation products, after abrasion, an additional sudden reduction of mass occurs. The corresponding change in momentum can be calculated in the frame of the Fermi gas model, providing that the Fermi momentum is reduced due to the increase of volume due to the thermal expansion and due to the thermal motion of the nucleons, according to ref. [4]. Finally, the Coulomb expansion of the emitting source at freeze-out is calculated as in ref. [5].

The results of the analytical formula are shown in figure 1 for three cases.

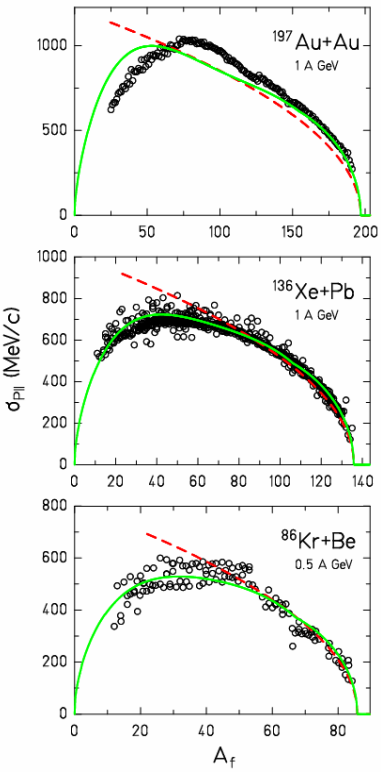

Figure 1: Standard deviation ($\sigma_{P||}$) of the longitudinal momentum distribution of the final fragments of mass A_f for three reactions: 1 *A* GeV ^{197}Au on Au [6], 1 *A* GeV ^{136}Xe on Pb [7], 0.5 *A* GeV ^{86}Kr on Be [8]. The dots are experimental data. The lines give the predictions of Morrissey's formula [8] (dashed) and of the analytical formula determined in this work (solid).

References

[1] A.S. Goldhaber, Phys Lett. B 53 (1974) 306
[2] D. J. Morrissey, Phys. Rev. C 39 (1989) 460.
[3] K.-H. Schmidt et al., Nucl. Phy. A 710 (2002) 157.
[4] W. Bauer, Phys. Rev. C 51 (1995) 803.
[5] K. C. Chung et al., Phys. Rev. C 36 (1987) 986.
[6] V. Henzl, PhD Thsis, TU Prague, 2001.
[7] D. Henzlova et al., Phys Rev. C 78 (2008) 044616.
[8] M. Weber, PhD Thsis, TU Darmstadt, 1993.

* This work forms part of A. Bacquias's PhD thesis.

m.v.ricciardi@gsi.de

Orbital electron capture decay of hydrogen- and helium-like ^{142}Pm ions.

N. Winckler[1,2], K. Beckert[1], F. Bosch[1], D. Boutin[1,2], C. Brandau[1], L. Chen[2], C. Dimopoulou[1], B. Fabian[2], T. Faestermann[3], A. Fragner[4], H. Geissel[1,2], E. Haettner[2], S. Hess[1], P. Kienle[3,4], R. Knöbel[1,2], C. Kozhuharov[1], S.A. Litvinov[1], Yu.A. Litvinov[1], M. Mazzocco[1], F. Montes[5], C. Nociforo[1], F. Nolden[1], W.R. Plaß[2], A. Prochazka[1], R. Reda[4], R. Reuschl[1], C. Scheidenberger[1,2], M. Steck[1], T. Stöhlker[1], S. Torilov[6], M. Trassinelli[7], B. Sun[1,8], H. Weick[1], and M. Winkler[1]

[1]GSI, Darmstadt; [2]JLU, Giessen; [3]TU, München; [4]SMI, Vienna, Austria; [5]MSU, East Lansing, USA; [6]PSU, St. Petersburg, Russia; [7]CNRS, Paris , France; [8]PKU, Beijing , China

We report on the measurement of the β^+- and orbital electron capture decay rates of fully ionized, hydrogen-like (H-like) and helium-like (He-like) ^{142}Pm ions. The motivations of these measurements arise from a recent experiment [1] showing a drastic increase of the orbital electron caputre decay rate of a Gamow-Teller transition in H-like ^{140}Pr ions with respect to He-like ions and neutral atoms.

Radioactive ^{142}Pm ions have been produced via projectile fragmentation of $\sim 10^8$ ^{152}Sm ions/spill, accelerated by the SIS to 607 MeV/u. A 2.5 g/cm^2 thick beryllium target has been used. The fully-ionized, H- and He-like ^{142}Pm ions were separated in-flight by means of the Bρ-ΔE-Bρ separation method in the FRS and subsequently injected into the ESR. Stochastic and electron cooling were applied to the ^{142}Pm^{61+}, ^{142}Pm^{60+} and ^{142}Pm^{59+} ions coasting in the ESR reducing the initial velocity spread to $\delta v/v \approx 5 \cdot 10^{-7}$ within about 5 seconds. The unambiguous identification of cooled ^{142}Pm^{61+}, ^{142}Pm^{60+} and ^{142}Pm^{59+} ions and their decay products has been achieved exploiting the time-resolved Schottky Mass Spectrometry. An example of measured decay- and growth curves is shown in Fig. 1.

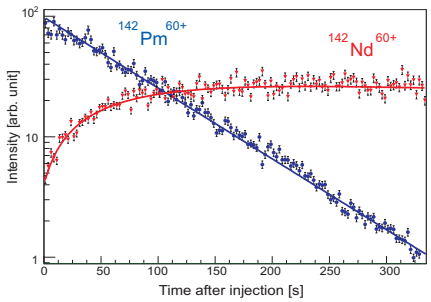

Figure 1: Intensities of ^{142}Pm^{60+} and ^{142}Nd^{60+} ions as a function of time. The data points are shown in the laboratory frame (Lorentz factor $\gamma = 1.43$) with a time resolution of 2.614 s per frame.

Several decay measurements of ^{142}Pm^{61+}, ^{142}Pm^{60+}, and ^{142}Pm^{59+} ions have been performed. Decay curves of the parent ions have been fitted with an exponential function:

$$N_{Pm}(t) = N_{Pm}(0) \cdot e^{-\lambda t}, \qquad (1)$$

where $N_{Pm}(t)$ and $N_{Pm}(0)$ are the number of parent ions at the time t after injection and at $t = 0$, the time of injection, respectively. For H-like and He-like ^{142}Pm ions, the decay constant λ is the sum of the EC decay constant λ_{EC}, the β^+ decay constant $\lambda_{\beta+}$, and the loss constant λ_{loss} due to collisions with residual gas atoms or pick-up of electrons in the electron cooler ($\lambda = \lambda_{EC} + \lambda_{\beta+} + \lambda_{loss}$). The bare ^{142}Pm^{61+} nuclei can only decay via the β^+- decay-mode. Hence, the measured decay constant is the sum $\lambda_{\beta+} + \lambda_{loss}$. The growth of the number of daughter ions from the EC decay of ^{142}Pm^{60+} into ^{142}Nd^{60+} nuclei and ^{142}Pm^{59+} into ^{142}Nd^{59+} ions is determined solely by the EC rate of ^{142}Pm, whereas the loss of stable ^{142}Nd ions is determined only by $\lambda_{loss} \sim 50\ (7) \times 10^{-5}\mathrm{s}^{-1}$. Therefore, we can express the number $N_{Nd}(t)$ of ^{142}Nd daughters as a function of the storage time t by :

$$N_{Nd}(t) = N_{Pm}(0) \cdot \frac{\lambda_{EC}}{\lambda - \lambda_{loss}} \cdot [e^{-\lambda_{loss} t} - e^{-\lambda t}] + N_{Nd}(0) \cdot e^{-\lambda_{loss} t} \qquad (2)$$

The averaged values for the λ_{EC} and $\lambda_{\beta+}$ decay constants converted to the rest frame of ions are presented in Table 1. All measurements show consistent results. In particular the ratio of the EC decay probability for H-like and He-like ^{142}Pm, respectively, $R = 1.44\ (6)$ (see Table 1) confirms the corresponding results obtained for ^{140}Pr [1], and is, furthermore, in good agreement to theoretical predictions ($R = 1.5$) [2].

Table 1: Measured decay constants obtained for fully-ionized, H- and He-like ^{142}Pm ions. The values are given in the rest frame of the ions.

Ion	$\lambda_{\beta+}$ $[s^{-1}]$	λ_{EC} $[s^{-1}]$
^{142}Pm^{61+}	0.01228 (70)	—
^{142}Pm^{60+}	0.01257 (32)	0.00514 (14)
^{142}Pm^{59+}	0.01393 (59)	0.00357 (10)

References

[1] Yu.A. Litvinov et al., Phys. Rev. Lett., 99:262501, (2007).

[2] Z. Patyk et al., Phys. Rev. C, 77, 014306, (2008).
A.N. Ivanov et al, Phys Rev.C 78, 025502 (2008).

Orbital Electron-Capture Decay of Stored Hydrogen-Like Ions

N. Winckler[1,2], K. Beckert[1], P. Beller[1], F. Bosch[1], D. Boutin[1], C. Brandau[1], L. Chen[2], C. Dimopoulou[1], H.G. Essel[1], B. Fabian[2], T. Faestermann[3], A. Fragner[4], H. Geissel[1,2], I. Hachiuma[5], E. Haettner[2], M. Hausmann[6], S. Hess[1], T. Izumikawa[7], P. Kienle[3,4], R. Knöbel[1,2], C. Kozhuharov[1], J. Kurcewicz[1], N. Kuzminchuk[2], S.A. Litvinov[1], Yu.A. Litvinov[1], L. Maier[3], R. Mao[8], R. Märtin[1], M. Mazzocco[1,9], F. Montes[1,6], G. Münzenberg[1], A. Musumarra[10,11], K. Namihira[5], C. Nociforo[1], F. Nolden[1], T. Ohtsubo[7], W.R. Plaß[1], A. Prochazka[1], R. Reda[4], R. Reuschl[1], C. Scheidenberger[1,2], U. Spillmann[1], M. Steck[1], T. Stöhlker[1,12], B. Sun[1], K. Suzuki[5], S. Torilov[13], M. Trassinelli[1,14], H. Weick[1], M. Winkler[1], D. Winters[1], and T. Yamaguchi[5]

[1]GSI, Darmstadt, Germany; [2]JLU Gießen, Germany; [3]TU München, Germany; [4]SMI Vienna, Austria; [5]Saitama Uni., Japan; [6]MSU East Lansing, U.S.A.; [7]Niigata Uni, Japan; [8]IMP Lanzhou, China; [9]INFN Padova, Italy; [10]INFN Catania, Italy; [11]Uni. Catania, Italy; [12]RKU Heidelberg, Germany; [13]St. Petersburg Uni., Russia; [14]CNRS, Paris, France

Time-modulated two-body weak decays have been observed in the orbital electron capture (EC) of hydrogen-like (H-like) $^{140}Pr^{58+}$ and $^{142}Pm^{60+}$ ions coasting in the ion storage ring ESR [1]. The expected exponential decay is modulated in time with a modulation period of 7.06(8) and 7.10(22) s (laboratory frame) for ^{140}Pr and ^{142}Pm ions, respectively. The average value of the modulation amplitude for these systems is 0.20(2).

The interpretation of the observed effect is broadly discussed in literature, see, e.g., recent Refs. [2-7]. Experiments with implanted ^{142}Pm [8] and ^{180}Re [9] (neutral) atoms do not show modulations. A clean two-body decay kinematics is, however, missing in these measurements.

Tentatively, we related our observations to the fact that the generated electron neutrino, being a *flavour* eigenstate of the weak hamiltonian, is composed of at least two coherent *mass* eigenstates m_1, m_2. For a parent state with mass M and momentum $\mathbf{P} = 0$ in the c.m. system, one obtains from momentum and energy conservation for the energy difference $\Delta E = E_2 - E_1$ of the two mass eigenstates of the electron neutrino [1][1]: $\Delta E = \Delta m^2/(2M)$, where $\Delta m^2 = m_2^2 - m_1^2$.

The periodic modulation could be a special kind of "quantum beat", caused by the tiny energy difference ΔE (in the order of 10^{-16} eV) of the two coherent mass eigenstates, suggested by almost the same modulation period for both decaying $^{140}Pr^{58+}$ and $^{142}Pm^{60+}$ ions with nearly the same mass M. From the observed period T_{Lab} (Lorentz factor $\gamma = 1.43$) of about 7 s, one derives according to: $T_{Lab} = h\gamma/\Delta E = h\gamma 2M/\Delta m^2$ a value $\Delta m^2 = 2.20(2) \cdot 10^{-4}$ eV^2, which is by a factor of 2.9 larger than the recently reported value of KAMLAND [10].

In order to test the M-dependence of T_{Lab} required by the "neutrino hypothesis" we investigated the EC decay of H-like $^{122}I^{52+}$ ions. Preliminary results from this experiment are shown in Fig. 1. They exhibit a well-pronounced modulation with a period of $T_{Lab} \approx 6$ s superimposed on the exponential decay. This period, being in perfect agreement to the predicted scaling with the mass of the parent ion M, corroborates the "neutrino hypothesis", if verified in the final data evaluation.

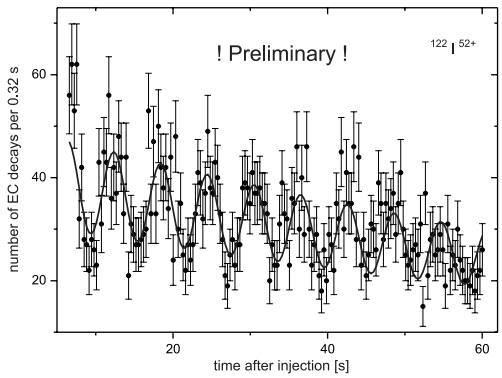

Figure 1: EC decay rate of H-like ^{122}I ions (preliminary) .

Three-body β^+ decays of H-like $^{142}Pm^{60+}$ ions recorded simultaneously with the corresponding EC decays are being analyzed. Preliminary results, based on a still small counting statistics, do not reveal any significant periodic modulation, in accordance with the expectation for a three-body β decay with a broad neutrino spectrum [1, 6].

References

[1] Yu.A. Litvinov et al., Phys. Lett. **B664** (2008) 162.

[2] A.N. Ivanov et al., *arXiv:0801.2121v6* [nucl-th].

[3] H. Lipkin, *arXiv:0805.0435v3* [hep-ph].

[4] A.G. Cohen et al., *arXiv:0810.4602v1* [hep-ph].

[5] H. Kleinert and P. Kienle, *arXiv:0803.2938v1* [nucl-th].

[6] A.N. Ivanov et al., Phys. Rev. Lett. **101** (2008) 182501.

[7] C. Giunti, Phys. Lett. **B665** (2008) 92.

[8] P. Vetter et al., Phys. Lett. **B670** (2008) 227.

[9] T. Faestermann et al., Phys. Lett. **B672** (2009) 196.

[10] S. Abe et al., Phys. Rev. Lett. **100** (2008) 221803.

[1]In the following we set *c*=1.

Numerical analysis of single-ion decays in the ESR

N. Winckler[1,2], F. Bosch[1], H. G. Essel[1], H. Geissel[1,2], C. Kozhuharov[1], A. Le Fevre[1], and Yu. A. Litvinov[1]

[1]GSI, Darmstadt; [2]JLU, Giessen

Time-resolved Schottky spectrometry has been successfully used at the ESR for life-time measurements of heavy, highly-charged ions. This method is non-destructive, non-instantaneous and can be sensitive to one single-ion. The high sensitivity at the ESR allows to observe one single ion. On this basis, a new approach for life-time measurements, the single-particle decay spectroscopy, has been developed which allows us to determine unambiguously the decay time of a single ion stored in the ESR [1]. However, the exact number of stored ions in the ESR can be only determined if we restrict it to a maximum of 3. The serious disadvantage of this method is its cumbersome counting statistics, since measurements have to be repeated several thousands times. A manual inspection of each spectrum is time-consuming and introduces individual ambiguities. Therefore, a numerical analysis has been developed for this purpose [2]. The goal of the analysis is to nail down as precisely as possible the time of an orbital electron capture decay. The signature of such events is the time correlation between the disapearance of one parent ion *and* the (somewhat delayed) appearance of the corresponding daughter ion at a well-defined close revolution frequency. However, due to fluctations of the strength of the Schottky amplitudes - that increase proportional to the number of ions - it is much easier to determine the appearance time of the daughter ion than the time of disappearance of the parent ion. This is particularly the case for injections with more than 3 parent ions, where the only clear evidence of a decay is the appearance of a daughter ion. The details of the numerical method which allows to detect the time of the appearance of a daughter ion are described in [2]. Restricting on a few stored parent ions ($N_p \leq 3$), the correlation of both decay time and appearance time can be figured out, allowing for an unambiguous determination of the decay.

For this purpose additionnal functions have been added to the software package described in [2]. The steps of the analysis consist in :

1. localizing the two traces.
2. filtering both time and frequency regions of the traces.
3. projecting the traces of the spectrum on the time axis.
4. analysing the correlation.

The filter consists in smoothing and enhancing the signal amplitude by means of a convolution product between the region of interest and a proper LoG function. Thresholds are adapted for the detection of one or two ions in the spectrum. It turned out that the mean value of both, the signal amplitude corresponding to a defined number of ions (1 or 2) and the background, are not constant over the several thousands of injections. Therefore adjustments depending on the mean value of the background have been performed

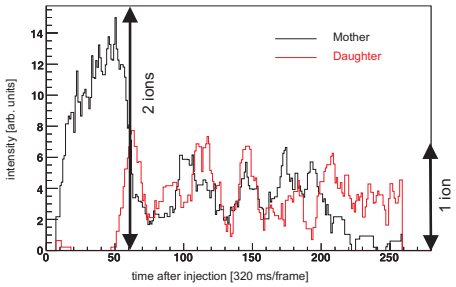

Figure 1: Projection of the parent and daughter traces.

to the thresholds. After the projection of the traces (see Fig. 1), a gaussian smoothing and a differentiation is applied. The resulting histograms indicate the variation of the traces. Large negative peaks indicate a decrease of the number of the parent ions and large positive peaks of the daughter histograms indicate an increase of them. A selection of the positive and negative values of the daughter and parent histograms, respectively, is applied. By multiplying the absolute values of these selections one obtains the histogram shown in Fig. 2. Due to the fluctuations, some spurious peaks may remain. Peaks corresponding to β^+ and EC decays are indicated in Fig. 2. The difference between the β^+ and EC decays is evaluated by means of a second correlation which determines the number of stored parent and daughter ions in the region of the peaks. This method has been applied on the ^{140}Pr and ^{142}Pm data of the experiment described in [1].

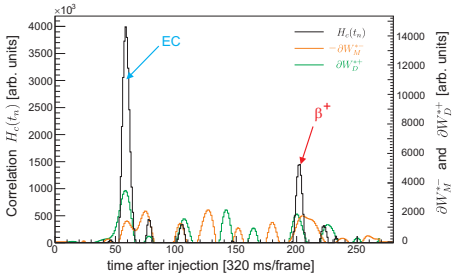

Figure 2: Histogram resulting from the correlation between the variations of amplitude in the parent and daughter traces

References

[1] Y. A. Litvinov et al., Phys. Lett. B664 (2008) 162168

[2] H.G. Essel, GSI scientific report 2006, 205

Schottky mass measurement of ^{208}Hg isotope: implication for the proton-neutron interaction strength around doubly-magic ^{208}Pb.

L. Chen[1,2], K. Beckert[1], F. Bosch[1], D. Boutin[1], L. Caceres[1], R.B. Cakirli[3,4], J.J. Carroll[5], R.F. Casten[4,6], R.S. Chakrawarthy[7], D.M. Cullen[8], I.J. Cullen[9], B. Franzke[1], J. Gerl[1], M. Gorska[1], G.A. Jones[9], A. Kishada[8], R. Knöbel[1], C. Kozhuharov[1], S.A. Litvinov[1], Yu.A. Litvinov[1], Z. Liu[9], S. Mandal[1], F. Montes[10], G. Münzenberg[1], F. Nolden[1], T. Ohtsubo[11], Z. Patyk[12], W.R. Plaß[1], Zs. Podolyák[9], R. Propri[5], S. Rigby[8], N. Saito[1], T. Saito[1], C. Scheidenberger[1,2], M. Shindo[13], M. Steck[1], P. Ugorowski[5], P.M. Walker[9], S. Williams[9], H. Weick[1], M. Winkler[1], H.-J. Wollersheim[1], and T. Yamaguchi[14]

[1]GSI, Germany; [2]JLU Gießen, Germany; [3]Uni. Istanbul, Turkey; [4]Uni. Köln, Germany; [5]Youngstown SU, USA; [6]Yale Uni., USA; [7]TRIUMF, Canada; [8]Uni. Manchester, UK; [9]Uni. Surrey, UK; [10]Michigan SU, USA; [11]Niigata Uni., Japan; [12]SINS Warsaw, Poland; [13]Uni. Tokyo, Japan; [14]Saitama Uni., Japan

The mass of the ^{208}Hg nucleus has been measured with time-resolved Schottky Mass Spectrometry [1] as part of a program on direct mass measurements of neutron-rich uranium projectile fragments in which the masses for about 30 neutron-rich nuclides have been obtained for the first time [2]. The mass excess value of ^{208}Hg has been determined and amounts to $ME = -13265(31)$ keV. The new precisely measured mass value of ^{208}Hg has been used to study the proton-neutron interaction around doubly magic ^{208}Pb nucleus, which is a subject of extensive discussion in the last few years as, e.g., presented in Refs. [4, 5]. There is one major gap in the data for δV_{pn} in the Pb region. The $p-n$ interaction is only known for three of four possible situations–there are no known values for protons filling just below Z=82 and neutrons just above N=126.

For even-even nuclei, the average $p-n$ interaction of the last two protons with the last two neutrons can be defined as [3]:

$$\delta V_{pn}(Z,N) = \frac{1}{4}[B(Z,N) + B(Z-2,N-2) - B(Z,N-2) - B(Z-2,N)], \quad (1)$$

where B is the binding energy of the nucleus.

Using the present mass measurement of ^{208}Hg, the $\delta V_{pn}(^{210}$Pb) point has been obtained in this work by using Eq. (1). This is the first δV_{pn} value for the region $Z \leq 82$, $N > 126$. The δV_{pn} value of ^{210}Pb is 165.2(10) keV which is about 2.5 times smaller than the δV_{pn} (^{208}Pb) value of 426.8(5) keV. This value and those for other nuclei in the ^{208}Pb region are shown in Fig. 1 , where δV_{pn} values for several isotopic sequences as a function of neutron number.

The $p-n$ interactions in this region have a characteristic and striking behavior that can be understood in terms of the spatial overlaps of the last valence nucleons [5]. The $^{208}_{82}$Pb$_{126}$ nucleus is in the symmetric hole-hole region, where both protons and neutrons fill low j high n orbits below the closed shell, and therefore it should (and does)

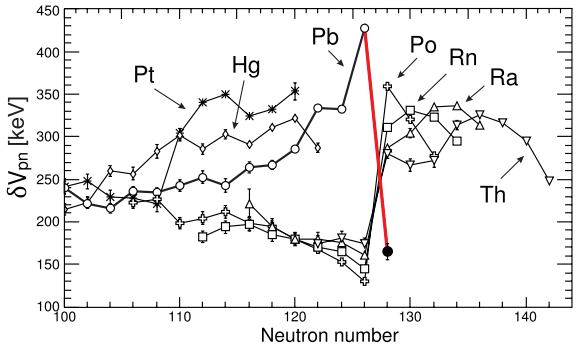

Figure 1: Experimentally known δV_{pn} values for isotopic chains below and above the $Z = 82$ proton closed shell. Only even-even nuclei are considered. If not shown the error bars are within the symbol size. The newly obtained δV_{pn} value for ^{210}Pb is emphasized by a filled symbol and the sharp drop from ^{208}Pb to ^{210}Pb is highlighted.

have a very large δV_{pn} value. In contrast, ^{210}Pb has two extra valence neutrons which occupy orbits just above the 126 closed shell, giving an asymmetric particle-hole case where one expects a low δV_{pn} value. The observed drop is such that, as seen in Fig. 1, the δV_{pn} value for ^{210}Pb is comparable to those in the other asymmetric group with $Z > 82$, $N \leq 126$. This drop vividly validates the sensitivity of the $p-n$ interaction to spatial overlaps of orbits in a crucial region and completes the evidence for a crossing pattern across closed shells.

References

[1] Yu.A. Litvinov et al., Nucl. Phys. **A756** (2005) 3.

[2] L. Chen, PhD Thesis, JLU Giessen, 2008.

[3] J.Y. Zhang et al., Phys. Lett. **B 227** (1989) 1.

[4] R.B. Cakirli et al., Phys. Rev. Lett. **96** (2006) 132501.

[5] D.S. Brenner et al., Phys. Rev. **C73** (2006) 034315.

The Advanced Atomic Mass Evaluation Project at GSI

B. Pfeiffer[1], Y.A. Litvinov[1], Z. Patyk[2], C. Scheidenberger[1], and K. Venkataramaniah[3]

[1]GSI, Darmstadt, Germany; [2]Soltan Institute for Nuclear Studies, Warsaw, Poland; [3]Sri Sathya Sai University, Prasanthinilayam, India

The ground-state binding energy, and thus the mass of a nucleus, is one its characteristic properties, revealing deep insight into the nuclear structure. Total binding energies and derived quantities such as proton or neutron separation energies, Q-values, etc., are needed for a basic understanding of the strong force, reaction kinematics and also for applications in medicine, energy generation, nuclear-waste transmutation, and nuclear astrophysics.

Ever since the beginning of modern chemistry and physics, compilations of masses have been undertaken [1]. The modern evaluations of atomic masses were initiated about 50 years ago by Aaldert H. Wapstra [2], and the most recent evaluations of atomic masses and decay properties, AME-2003 and NUBASE [3, 4, 5], respectively, were prepared by Wapstra and Audi. However, and despite of this work, in Europe there was a general decline of data collection and evaluation activities in the last decades [6]. Also the future of AME was somewhat uncertain. Therefore, almost two years ago, after consultation and in an agreement with G. Audi, GSI took the initiative to start working on the continuation of the atomic mass data collection and its evaluation. The first goal is to maintain and to update the existing data base. The success of radioactive beam facilities has lead to a notable increase in quantity and quality of mass data for exotic nuclides. Since the latest evaluation in 2003, a lot of new mass measurements are available from direct and indirect (e.g. Q_β) measurements and reaction studies.

The scientific literature has been scanned for publications containing information on nuclear masses, lifetimes of ground and/or isomeric states. The Nuclear Science References (NSR) data base [7] of the National Nuclear Data Center at Brookhaven National Laboratory was browsed from the year 2000 until present. In addition, the recent volumes of relevant journals as Physical Review A, C, Physical Review Letters, Nuclear Physics A, European Physical Journal, International Journal of Mass Spectrometry, Physics Letters, Journal of Physics G (London), Nuclear Instruments and Methods, Physics of Atomic Nuclei (Yadernaya Fizika), Physica Scripta, Pramana, Metrologia, Chinese Physics, Chinese Physics Letters are being scanned regularly.

Also data from non-refereed sources are collected, such as laboratory reports, preprints, diploma and PhD-theses and similar sources. More than 1000 data have been collected. Data previously available in the data base are checked for correctness and present validity. In parallel, the NUBASE data are updated: new data on masses and decay properties such as half-lives, excitation energies of isomeric states are examined and entered into compilatons for further use in evaluations. References are stored and archived electronically, links to existing data are stored. The activities are carried out in close contact with ENSDF editors.

Presently, each new data point is included into the master file of the evaluation for masses, decay properties and references. The consistency with existing data and the influence on the surrounding mass surface are checked by a local evaluation. In case of discrepancies, the relevant data and publications are scrutinized for hints pointing to possible problems. If necessary, the authors are contacted for clarification. A new evaluation is presently in preparation.

Measured masses are included in the AME as single equations related to one reference nucleus. Thus, the *many* correlations between *all* nuclides measured in FRS-ESR experiments – which is a strength of the method – are lost. Therefore, it is proposed to merge the original data from the FRS-ESR (i.e., frequency ratios) with data from other measuring techniques already contained in the AME into the Advanced Atomic Mass Evaluation (AAME).

For the mid-term future it is planned to make all data available via electronic media for broad dissemination of the original and the evaluated data, respectively. The creation of a web-site with interactive tools to serve the community of experimentalists, theorists, and for users in applied sciences is under development.

The project is conducted in collaboration with ISNSM in Orsay (France), and the Institute of Modern Physics of the Chinese Academy of Sciences in Lanzhou (China). The authors thank G. Audi, D. Lunney, H. Geissel, M. Wang for valuable discussions.

References

[1] J. Dalton, Memoirs and Proceedings of the Manchester Literary and Philosophical Society, Manchester, 6 (1805) 271.

[2] A.H. Wapstra, Physica 21 (1955) 367 + 385; J.R. Huizenga, Physica 21 (1955) 410.

[3] A.H. Wapstra, G. Audi C. Thibault, Nucl. Phys. A 729 (2003) 129.

[4] G. Audi, A.H. Wapstra C. Thibault, Nucl. Phys. A 729 (2003) 337.

[5] G. Audi, O. Bersillon, J. Blachot A.H. Wapstra, Nucl. Phys. A 729 (2003) 3.

[6] A.L. Nichols, Nuclear Physics News 19, 4 (2009).

[7] http://www.nndc.bnl.gov/nsr/

Neon Isotopes $^{17-22}$Ne studied in Fermionic Molecular Dynamics

T. Neff and H. Feldmeier
GSI, Darmstadt, Germany

In the Fermionic Molecular Dynamics (FMD) approach [1] nuclei are described using Gaussian wave-packets as single-particle states. Many-body basis states are Slater determinants which are projected on parity, angular momentum and total linear momentum to restore the symmetries of the Hamiltonian. The FMD basis is very flexible and contains harmonic oscillator and Brink-type cluster configurations as special limiting cases. The widths of the wave-packets are variational parameters which together with the possibility to superimpose two wave-packets in a single-particle states allows a successful description of extended halo states. An effective Hamiltonian derived from the realistice Argonne V18 interaction within the Unitary Correlation Operator Method (UCOM) is used for all nuclei.

Recent measurements of the charge radii of the Neon isotopes $^{17-22}$Ne by the COLLAPS group at ISOLDE triggered a study of the properties of these nuclei in the FMD approach and resulted in a joint publication [2]. Of particular interest here was the structure of ^{17}Ne. Whereas three-body cluster calculations found large s^2 components and therefore a halo-like structure, shell model calculations based on Coulomb displacement energies and magnetic moments predicted a small s^2 component.

FMD configurations for the neon isotopes were obtained in a variation after parity projection procedure. For ^{17,18}Ne two minima were found which are essentially ^{15,16}O cores plus two protons in either s^2 or d^2 configurations. Because of the missing centrifugal barrier the s-orbits are much more extended. A large s^2 component in the ground state wave function is therefore related to a large charge radius. The calculated s^2 admixture is about 42% for ^{17}Ne but only

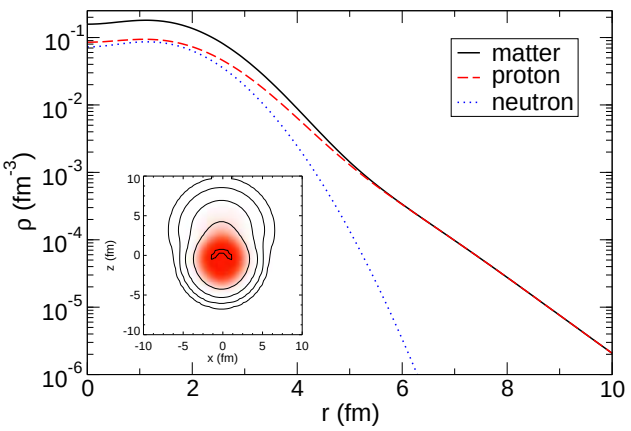

Figure 1: ^{17}Ne matter proton and neutron density distribution. The proton skin thickness is 0.45 fm. The probability to find a proton at $r > 5$fm is about 40%.

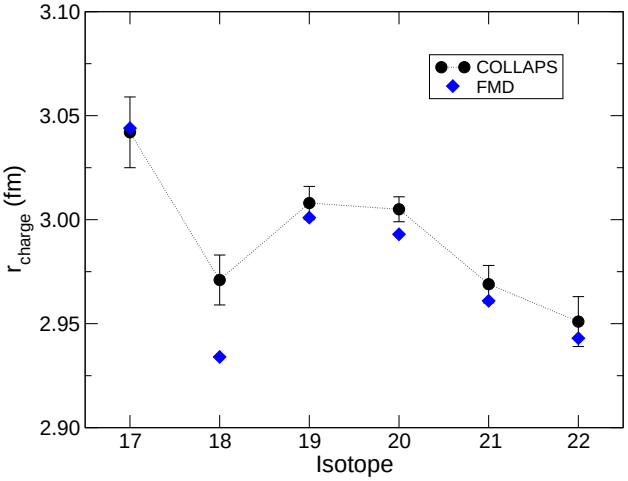

Figure 2: Experimental and FMD charge radii for the Neon isotopes $^{17-22}$Ne.

15% for ^{18}Ne which explains the large differences in the observed charge radii for these two isotopes. The halo-like nature of ^{17}Ne due to this large s^2 component in the wave function is clearly visible when comparing proton and neutron density distributions as shown in Fig. 1.

Whereas the natural parity for the Neon isotopes is positive the $1/2^-$ state in ^{19}Ne is almost degenerate with the $1/2^+$ ground state. We therefore include not only configurations optimized for positive parity but also states optimized for negative parity. The cluster thresholds for ^{16}O-^{3}He and ^{15}O-^{4}He are low in energy and the FMD configurations for positive and negative parity indicate a corresponding cluster nature. In addition to the FMD configurations where the parameters of all the single particle states are varied, we also included explicit cluster configurations with Oxygen and Helium clusters in their ground state configurations. These admixture of cluster configurations is responsible for the pronounced increase in the charge radius going from ^{18}Ne to ^{19}Ne as shown in Fig. 2. This is also true for ^{20}Ne, here the ^{16}O-^{4}He threshold is only 4.5 MeV and again the admixture of cluster configurations leads to a very large radius. For the heavier isotopes ^{21,22}Ne the admixture of cluster configurations is less important and smaller charge radii are observed.

References

[1] T. Neff and H. Feldmeier, Eur. Phys. J Special Topics **159** (2008) 69.

[2] W. Geithner, T. Neff, *et al.*, Phys. Rev. Lett. **101** (2008) 252502.

On ^{229}Th and time-dependent fundamental constants

E. Litvinova[1], H. Feldmeier[1], J. Dobaczewski[2,3], and V. Flambaum[4]

[1]GSI Helmholtzzentrum für Schwerionenforschung, Planckstr. 1, 64291 Darmstadt, Germany; [2]Institute of Theoretical Physics, University of Warsaw, Hoża 69, PL-00-681 Warsaw, Poland; [3]Department of Physics, P.O. Box 35 (YFL), FI-40014 University of Jyväskylä, Finland; [4]School of Physics, University of New South Wales, Sydney, NSW 2052, Australia

The electromagnetic transition between the lowest almost degenerate $5/2^+$ and $3/2^+$ states in ^{229}Th is deemed to be very sensitive to potential changes in the fine structure constant α [1]. We have investigated these two states of ^{229}Th employing Hartree-Fock and Hartree-Fock-Bogoliubov methods [2] based on the two very successful energy functionals SkM* and SIII [3]. A generalized Hellmann–Feynman theorem is proved including the use of density-matrix functionals. According to this theorem, the difference in Coulomb energies ΔV_C of the two states determines the amplification of variations in α into variations of the transition frequency $\delta\omega = \Delta V_C \delta\alpha/\alpha$.

The result is that for the SkM* functional the difference in Coulomb energy ΔV_C between excited and ground state ranges from 450 keV without pairing to -300 keV when pairing effects are included. On the other hand the SIII-HFB result gives $\Delta V_C = 1$ keV only. In SIII-HF and SIII-HFB the blocked states exhibit more concentration on the dominant Nilsson orbits $[633]$ and $[631]$. As both have the same nodal structure in z-direction ($N_z = 3$) one expects less difference in the density distribution than in the SkM* case where both states are superpositions of several Nilsson orbits with similar amplitudes. In the SkM* case the leading component of $|\frac{5}{2}^+\rangle$ is $[622]$ and of $|\frac{3}{2}^+\rangle$ is $[642]$, which implies a change in nodal structure in z-direction. In summary the polarization of the proton distribution due to the reoccupation of the level with the unpaired neutron has less effect in the SIII than in the SkM* case, see Fig. 1.

The kinetic energies are also calculated which reflect a possible variation in the nucleon or quark masses. The differences in neutron and proton kinetic energies are of similar size and also quite different for SkM* and SIII.

Altogether, the nuclear models we used predict amplification factors $A = \Delta V_C/\omega$, between the drift of the transition frequency $\delta\omega/\omega$ and the drift $\delta\alpha/\alpha$ in the fine structure constant, that have absolute values varying between about 10^2 and 10^4. We have pointed out and discussed the fact that the pairing correlations smooth out polarization effects exerted by the single-particle orbitals. Therefore, such correlations not only dramatically decrease the anticipated amplification factors but also make their determination very uncertain, due to dependence on very detailed properties of the mean-field and pairing effects. We have also performed spherical calculations and conclude that spherical models should not be consulted as they are too far from reality to provide serious numbers.

As even the sign of the amplification factor is uncertain, much more refined calculations are needed that include coupling to low-lying core excitations and projection on eigenstates with good total angular momentum and particle number. In any case the calculations must treat all nucleons (no inert core) because the whole effect comes from a subtle polarization of the core protons. Furthermore the model has to be of variational type in order to make use of the Hellmann–Feynman theorem. Without that one cannot be sure that the polarization effects caused by the strong interaction are treated consistently with the necessary accuracy. Rough estimates and simple minded models are not sufficient.

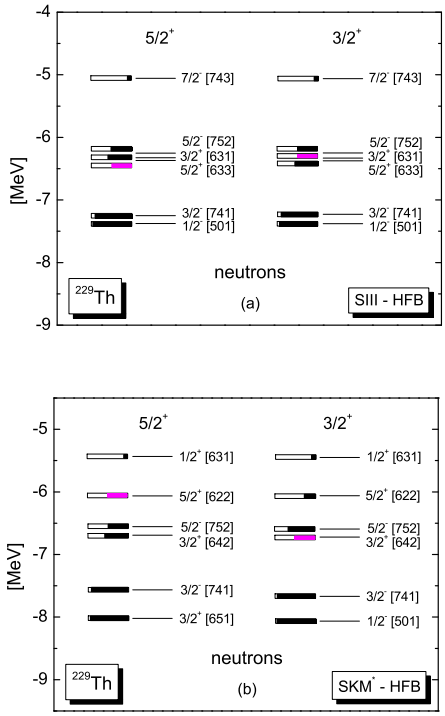

Figure 1: HFB mean-field neutron energies and occupation numbers v^2_ν labeled by the asymptotic Nilsson quantum numbers $\nu = \Omega^\pi[N, N_z, \Lambda]$ (a) for the SkM* energy functional and (b) for the SIII energy functional. Length of the bars indicates $v^2_\nu + v^2_{\bar\nu}$. Grey bars stand for blocked states with the occupation probabilities $n_\mu = 1,\ n_{\bar\mu} = 0$.

References

[1] V.V. Flambaum, Phys. Rev. Lett. **97**, 092502 (2006).

[2] J. Dobaczewski, J. Dudek, Comput. Phys. Commun. **102**, 166 (1997); **102**, 183 (1997).

[3] E. Litvinova, H. Feldmeier, J. Dobaczewski, V. Flambaum, arXiv:0901.1240.

Shell model description of isomers in mass A$\sim$95 region

K. Sieja[1,2], W. Urban[3], G. Martínez-Pinedo[1], and F. Nowacki[4]

[1]GSI-Helmholtzzentrum für Schwerionenforschung, Darmstadt, Germany; [2]Institut für Kernphysik, TU Darmstadt, Germany; [3]Institut Laue-Langevin, Grenoble Cedex 9, France; [4]Institut Pluridisciplinaire Hubert Curien, Strasbourg Cedex, France

Of the about 6000 atomic nuclei, expected to be bound, more than 2/3 are located on the neutron-rich side of the stability line. To provide an access to the very neutron-rich systems, radioactive ion beam facilities have been proposed delivering relevant new results in the near future. In the meantime, progress in this field is taking place thanks to the development of advanced gamma-ray detection instruments like EUROGAM [**?**] or GAMMASPHERE [**?**]. Such detectors allow to resolve of prompt gamma radiation following fission of actinides and providing information about the yrast structure of secondary fission fragments up to 20 units in spin [**?**]. Combined studies of prompt-gamma and isomeric-decays of the same secondary fission-fragment have been particularly successful.

Isomers help studying the structure of fission fragments in a number of ways. They usually result from coupling of nucleons occupying high-j, intruder or extruder orbitals, that do not mix with other orbits in the shell making the structure of these isomeric states rather simple and therefore easier to interpret and to calculate. They are usually located on the yrast line and have 'long' half-lives which helps in their detection following fission. From theoretical point of view, these states serve as nice testing cases for effective interactions, e.g. in the Large Scale Shell Model (LSSM) calculations.

Recently, we have established a new effective interaction for the model space outside the ^{78}Ni core, including $(1f_{5/2}, 2p_{1/2}, 2p_{3/2}, 1g_{9/2})$ orbitals for protons and $(2d_{5/2}, 3s_{1/2}, 2d_{3/2}, 1g_{7/2}, 1h_{11/2})$ for neutrons. Such a valence space enables the description of high-spin states, originating from deep proton holes and from neutron excitations to the $h_{11/2}$ intruder orbital. The latter are of a special interest, as the position of the $h_{11/2}$ centroid beyond N=59 remains experimentally unknown. In the spherical ^{95}Sr and ^{97}Zr nuclei, where one expects a $11/2^-$ level due to a pure $h_{11/2}$ neutron excitation, there is still no convincing experimental evidence for its presence. However, the $h_{11/2}$ intruder is expected to form two-quasiparticle configurations of yrast character. Observation and theoretical description of these states should help finding the exact position of this single-particle orbital.

The new effective interaction used here in LSSM calculations was derived from the CD-Bonn potential using G-matrix theory and adapted to the model space using many-body perturbation theory techniques. Monopole corrections were applied to reassure a correct propagation of the single-particle field between ^{91}Zr and ^{101}Sn and along the tin chain. The LSSM calculations were then performed using the m-scheme code ANTOINE [**?**].

We have located the unknown centroid of the $\nu h_{11/2}$ orbital by full digonalization calculation for the 17^- isomer in ^{92}Zr. This isomer of $[\pi(g^2_{9/2}) \otimes \nu(g_{7/2}h_{11/2})]_{17^-}$ configuration at energy 8041keV [**?**] was well reproduced in our calculation with respect to both its location (8301keV) and multiparticle configuration. This way, we have estimated the position of the $\nu h_{11/2}$ centroid in ^{91}Zr at 3.5 MeV. Further, we have calculated other isomeric states in the region of A$\sim$95. The 2μs 17^- isomer at 6603keV in ^{98}Zr was nicely reproduced at the energy of 6232 keV [**?**]. The wave function was dominated by the aligned $[\pi(g_{9/2})^2 \otimes \nu(g^1_{7/2}h^1_{11/2})]$ component, however strongly mixed with other configurations. A very good agreement between calculations and experiment was found for the 40ns isomer at 3523.9 in ^{96}Sr [**?**], supporting the 9^- spin and parity assignment and the predicted configuration originating from the $\nu(g_{7/2}, h_{11/2})_{9^-}$ coupling. In ^{95}Y, a 65ns isomer was detected at 5022keV with a proposed $27/2^-$ spin and parity assignment, originating mostly from $\pi g^1_{9/2} \otimes (\nu g^1_{7/2}h^1_{11/2})$ coupling. This is confirmed by the LSSM calculations [**?**]. Currently, calculations for recently observed isomeric states in $^{92-94}$Rb isotopes are under way and will provide new, rich information allowing to build a reliable set of s.p. excitation energies and two-body matrix elements for studies of the structure of neutron-rich nuclei outside the ^{78}Ni core.

References

[1] P.J. Nolan, F.A. Beck and D.B. Fossan, Ann. Rev. Nuc. Part. Sci. 44 (1994) 561.

[2] I.Y. Lee, Nucl. Phys. A520 (1990) 641c.

[3] I. Ahmad and W.R. Philips, rep. Prog. Phys. 58 (1995) 1415.

[4] E. Caurier and F. Nowacki, Acta. Phys. Pol. B30 (1999) 705.

[5] G. Korschinek et al., Proceedings of the International Conference on Nuclear Structure, Tokyo (1977).

[6] K. Sieja, K. Langanke, G. Martínez-Pinedo, F. Nowacki, in preparation.

[7] T. Rzaca-Urban et al.,Phys. Rev. C (2009), to be published.

[8] W. Urban, et al., submitted to Phys. Rev. C.

Shell model First Forbidden beta-decays for N= 82 nuclei

J. J. Cuenca-García[1,2], E. Caurier[4], K. Langanke[1,2,3], G. Martínez-Pinedo[1], F. Nowacki[4], and K. Sieja[1,3]

[1]GSI, Darmstadt, Germany; [2]FIAS, Frankfurt, Germany; [3]IKP, TU Darmstadt, Germany; [4]Institut Pluridisciplinaire Hubert Curien, Strasbourg, France

Introduction

The astrophysical r-process, a sequence of neutron capture interrupted by photodisotiation and followed by beta decay, is responsible of the synthesis of approximately half of the nuclei beyond the iron group. The estimate of the half-lives of the nuclei close to the neutron magic numbers are crucial to understand the dynamics of the process. Previous works [1, 2] used the shell model to estimate the half-lives of the nuclei in the magic neutron number N= 82 considering exclusively the contribution of the allowed Gamow-Teller transitions, mediated by the operator $\sigma\tau_-$. Here we present for the first time shell model calculations that include both the contribution of Gamow-Teller and First Forbidden (FF) transitions for the r-process N= 82 waiting point nuclei with charge number Z= 42 − 49.

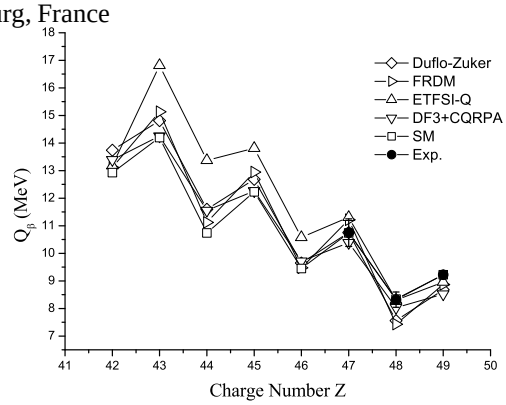

Figure 1: Comparison of shell model Q_β-values for the N= 82 isotones to the Audi-Wapstra systematics and to predictions of other models: FRDM, ETFS-Q, DF3 and Duflo-Zuker.

Results

The detailed theoretical formulation of the FF decay can be found in [3]. The contribution of the FF is represented by the mean values of eight operators that have been calculated using the shell model code NATHAN by E. Caurier. The configuration space used was composed of the orbits $0g_{7/2}$, $1d_{3/2,5/2}$, $2s_{1/2}$, $0h_{11/2}$ for neutrons and $0g_{9/2,7/2}$, $1d_{3/2,5/2}$, $2s_{1/2}$ for protons above a ^{80}Zr core. Fig. 1 shows the Q-values we have calculated compared to different mass models as FRDM, ETFIS-Q, and Duflo-Zuker together with the Audi-Wapstra systematics. Since our shell model Q-values reproduce the experimental values and are similar to those proposed by the mass models, we used them in our calculations. The total half-lives are shown in Fig. 2 compared to the available experimental values. Fig. 3 depicts the percentage of FF. As can be seen, the influence of the FF is less than 10% and plays a minor role in the N= 82 region. These results agree with calculations made by I. Borzov using the energy density-functional method [4]. Further studies of the FF transitions in the vicinity of ^{131}In have shown that those are consistent with the experimental data.

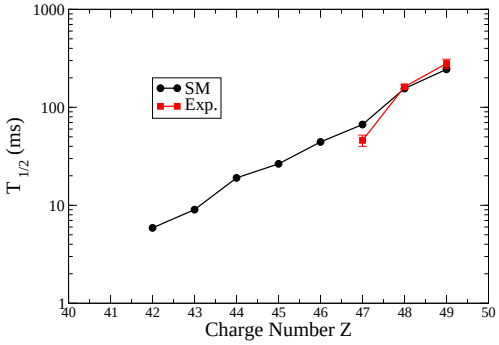

Figure 2: Shell model half-lifes including the FF contribution compared to experimental values.

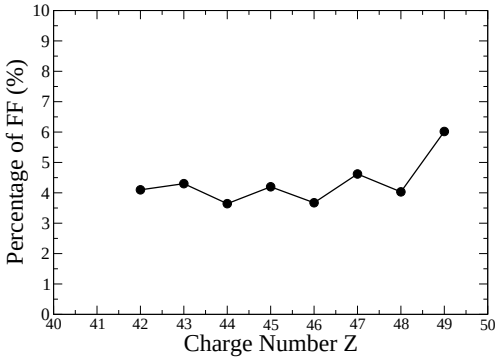

Figure 3: Influence of the FF in percentage.

References

[1] G. Martínez-Pinedo, K. Langanke Phys. Rev. Lett. **83**, 4502 (1999).

[2] J.J. Cuenca-García *et al.* Eur. Phys. J. A **34**, 99–105 (2007).

[3] H. Behrens and W. Bühring Nuc. Phys. A **162**, 111 (1971).

[4] I. Borzov, Phys. Rev. C **67**, 025802 (2003).

Scaling Laws in Coulomb Dissociation of Neutron Halo Nuclei*

S. Typel[1,2] and G. Baur[3]

[1]GSI, Darmstadt, Germany; [2]Excellence Cluster Universe, Technische Universität München, Garching, Germany;
[3]Institut für Kernphysik, Forschungszentrum Jülich, Germany

Exotic nuclei are available as secondary beams at many radioactive beam facilities around the world. These unstable nuclei are generally weakly bound with few, if any, excited states. A well developed method to study halo nuclei is Coulomb excitation. Halo nuclei are a low-energy phenomenon and can be described effectively in terms of a few low-energy parameters.

Let us consider the single-particle excitation of a neutron from a ground state $i = 0$ to a bound excited state $i = 1$ with neutron separation energies $E_i > 0$. The size of the single-particle wave functions is determined by the bound-state constants $q_i = \sqrt{2\mu E_i}/\hbar$ with the reduced mass $\mu = m_n m_c/(m_n + m_c)$ of the nucleon+core system. With the radius R of the core beyond which the nuclear interaction is assumed to vanish, it is possible to introduce dimensionless parameters $\gamma_i = q_i R$ that are a measure for the ratio of the core size to the size of the neutron wave functions. These parameters are small for halo nuclei, and can be used as convenient expansion parameters. In this spirit, we use this single-particle model in order to evaluate the matrix element for the $E1$ electromagnetic excitation. It is dominated by the exterior contributions.

We treat electromagnetic excitation in the semiclassical approximation. For high beam velocities v the classical trajectory can be taken as a straight line with impact parameter b. In the sudden approximation one can take higher-order effects into account. Like the related Glauber approximation it is applicable for high beam energies and low excitation energies. In the sudden approximation the dipole excitation amplitude from the ground state i to the final state f is given by

$$a_{\mathrm{sudden}} = \langle 1 | \exp\left(-i\vec{q}_{\mathrm{Coul}} \cdot \vec{r}\right) | 0 \rangle$$

where the transfered momentum is $\hbar\vec{q}_{\mathrm{Coul}} = (2\eta/b)\vec{e}_z$ with the Coulomb parameter $\eta = Z Z_{\mathrm{eff}}^{(1)} e^2/(\hbar v)$ depending on the charge number Z of the target and the effective dipole charge number $Z_{\mathrm{eff}}^{(1)} = Z_c m_n/(m_n + m_c)$.

This matrix-element can be evaluated analytically. It depends on the parameters q_0, q_1, q_{Coul} and R. We can expand the excitation amplitude in powers of $z = q_{\mathrm{Coul}} R/(\gamma_0 + \gamma_1)$. This leads to simple scaling laws for the excitation probabilities. Total cross sections are obtained by integration over the impact parameter, starting from a minimum impact parameter b_{min}. The sudden approximation fails for large impact parameters, and an adiabatic cutoff $b_{\mathrm{max}} = \gamma_{\mathrm{beam}}\hbar v/(E_1 - E_0)$ has to be introduced for the lowest-order result. We find for the lowest-order cross section

$$\sigma_{\mathrm{LO}} = \frac{8\pi}{27} \frac{\gamma_0(\gamma_0 + 2\gamma_1)^2}{(\gamma_0 + \gamma_1)^4} \left(\frac{2\eta m_n}{m_c + m_n}\right)^2 R^2 \ln \frac{b_{\mathrm{max}}}{b_{\mathrm{min}}}.$$

The next-to-leading order term is given by

$$\sigma_{\mathrm{NLO}} = -\frac{8\pi\gamma_0(\gamma_0 + 2\gamma_1)(\gamma_0 + 4\gamma_1)}{135(\gamma_0 + \gamma_1)^6} \times \left(\frac{2\eta m_n}{m_c + m_n}\right)^4 \frac{R^4}{b_{\mathrm{min}}^2}.$$

We define a reduction factor $R(v) = \sigma^{(\infty)}/\sigma_{\mathrm{LO}}$ of the total excitation cross section $\sigma^{(\infty)} = \sigma_{\mathrm{LO}} + \sigma_{\mathrm{NLO}} + \ldots$ caused by higher-order effects. This factor $R(v)$ can be used to take higher-order effects into account in an analysis of the experimental data. It is shown in Fig. 1 for the case of the $j_0^\pi = 1/2^+$ to $j_1^\pi = 1/2^-$ $E1$ transition in ^{11}Be from the s-wave ground state with $E_0 = 0.504$ MeV to the p-wave bound state with $E_1 = 0.184$ MeV. Higher-order effects reduce with increasing beam velocity v showing that the conditions for an experiment with a relativistic ^{11}Be beam at GSI would be favorable.

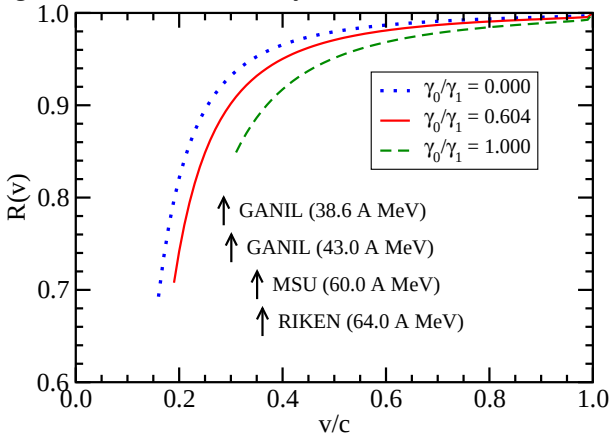

Figure 1: Reduction factor R(v) as a function of the beam velocity v for values of 0 (dotted line), 0.604 (solid line) and 1 (dashed line) of the ratio $\gamma_1/\gamma_0 = \sqrt{E_1/E_0}$. The beam velocities of the experiments at GANIL, MSU, and RIKEN are shown as arrows.

Our model is simple, realistic and appropriate for halo nuclei. The analytical results obtained are very useful for benchmark tests of more involved nuclear reaction theories and numerical calculations.

References

[1] S. Typel and G. Baur, Eur. Phys. J. A 38 (2008) 355.

* This research was supported by the DFG cluster of excellence "Origin and Structure of the Universe".

Hartree-Fock-Bogoliubov Calculations in the UCOM Framework*

H. Hergert and R. Roth
Institut für Kernphysik, TU Darmstadt, Schlossgartenstr. 9, 64289 Darmstadt, Germany

With the advent of new radioactive beam facilities like FAIR, the structure of exotic nuclei far beyond the valley of stability can be probed experimentally, providing a strong motivation for theoretical studies using ab initio approaches and interactions which provide a stringent link to QCD as the fundamental theory of the strong interaction.

To this end, we apply second-generation V_{UCOM} interactions [1] derived from the realistic AV18 interaction for the description of open-shell nuclei in a Hartree-Fock-Bogoliubov framework. To disentangle the effects of the particle-hole (ph) and particle-particle (pp) channels, we first use V_{UCOM} as a pairing force in conjunction with the Gogny D1S interaction providing the ph-mean-field. In Fig. 1, the resulting gaps Δ_μ of the canonical state with the lowest quasiparticle energy $\mathcal{E}_\mu = \sqrt{(\varepsilon_\mu - \lambda)^2 + \Delta_\mu^2}$, with the canonical single-particle energy ε_μ and Fermi energy λ, are compared to the odd-centered three-point formula $\Delta^{(3)}(N) = -\frac{1}{2}\left(E(N+1) - 2E(N) + E(N-1)\right)$, where $E(N)$ are experimental ground-state energies. The resulting gaps are stable over a wide range of UCOM interactions characterized by the parameter $\bar{\alpha}$. Only the long-ranged UCOM transformation with $\bar{\alpha} = 0.1$ fm^4 exhibits a significant reduction. While the relative $^1S_0$ matrix elements dominating the pairing remain almost unchanged from $\bar{\alpha} = 0.05$ fm^4 onward, they mix with higher partial waves due to a Talmi transformation from relative two-particle to decoupled single-particle states. These higher partial waves are predominantly repulsive, hence the reduction of the gap. We have also considered the effect of the commonly used one-body approximation to the intrinsic kinetic energy $\mathrm{T}_{\mathrm{int}} = \mathrm{T} - \mathrm{T}_{\mathrm{cm}}$ in Fig. 1, which produces significantly larger gaps, illustrating the sizable reduction caused by the repulsive two-body contribution of $\mathrm{T}_{\mathrm{int}}$ to the pairing field in an HFB scheme based on an intrisic Hamiltonian.

In line with our general goal, we now switch to a fully self-consistent approach, using V_{UCOM} in the ph and pp channels. In Fig. 2, we display the corresponding theoretical gaps for the tin isotopes. In these calculations, we check another approximation frequently used in HFB calculations, namely the restriction of the pairing interaction to the $^1S_0$ wave. This approximation produces gaps which are considerably larger than when the full interaction is used, irrespective of the parameter $\bar{\alpha}$.

We also observe important effects resulting from the tensor structure of V_{UCOM}. For the restricted pairing interaction, the canonical gaps are very similar to the average gap over paired states $\langle\, \Delta \,\rangle = \sum_\mu \Delta_\mu u_\mu v_\mu / \sum_\mu u_\mu v_\mu$, where u_μ, v_μ are the canonical occupation coefficients. When the full V_{UCOM} is used in the pp-channel, the canonical gaps are significantly reduced as the angular momentum of the nucleon increases. This effect is most visible for the $g_{7/2}$ and $h_{11/2}$ subshells which are filled over the tin chain, whereas the s- and $p-$subshells which are filled in the mid-shell tin isotopes are hardly affected.

* Supported by DFG through SFB 634 and the Helmholtz International Center for FAIR.

References

[1] R. Roth *et al.*, Phys. Rev. **C77**, 064003 (2008).

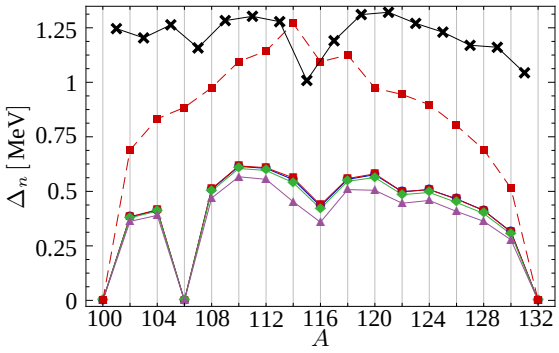

Figure 1: Canonical neutron gaps in the tin isotopes for Gogny D1S + V_{UCOM} with $\bar{\alpha} = 0.03$(●), 0.04(■), 0.06(♦), 0.1 fm^4(▲). Experimental $\Delta^{(3)}(N)$ are indicated by black crosses. Solid lines: full intrinsic kinetic energy, dashed line: one-body approximation.

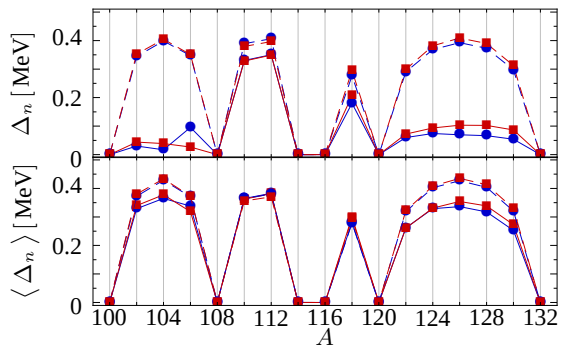

Figure 2: Canonical (top) and average (bottom) neutron gaps in the tin isotopes from fully self-consistent calculations using V_{UCOM} with $\bar{\alpha} = 0.04$(●), 0.1 fm^4(■). Solid lines: full interaction in the pp channel, dashed lines: restriction to relative $^1S_0$ wave.

UCOM Correlators Constructed from SRG Evolved Interactions*

S. Reinhardt, R. Roth, and H. Hergert
Institut für Kernphysik, Technische Univeristät Darmstadt, Germany

The Unitary Correlation Operator Method (UCOM) and the Similarity Renormalization Group (SRG) are two modern methods to derive universal effective interactions suitable for nuclear structure calculations in different many-body methods. Both approaches employ phase-shift conserving unitary transformations to tame an initial realistic interaction such that the transformed interaction induces less correlations and exhibits a superior convergence behavior.

In UCOM the unitary transformation is formulated via explicit correlation operators whose structure is motivated by the physics of short-range central and tensor correlations [1]. The UCOM transformation is characterized by correlation functions $R_+(r)$ and $\vartheta(r)$ which describe the radial dependence of the central and tensor correlations. For the first-generation of UCOM-transformed interactions, these functions were determined from an energy minimization in the two-body system [1]. In SRG a more generic idea is used. The unitary transformation is formulated in terms of a renormalization-group flow equation with a dynamical generator that drives the matrix elements of the Hamiltonian to a band-diagonal structure with respect to an uncorrelated basis. Solving the flow equations for momentum-space matrix elements leads to a transformed interaction that is band-diagonal in momentum space—similar to the matrix elements of the UCOM-transformed interaction.

Since both methods address the same physics of short-range correlations, we can connect them and use the SRG-evolution to construct correlation functions for UCOM [2]. For this we first construct an SRG-evolved interaction and solve the two-body problem in the different spin-isospin-channels. The lowest resulting two-body eigenstate is then used to define SRG-generated UCOM correlation functions by requiring, that the UCOM transformation should map the evolved two-body state onto the corresponding two-body eigenstate for the initial interaction. The resulting central and tensor correlation functions for the $(S,T) = (1,0)$ channel are depicted in Fig. 1 together with the first-generation variational correlation functions. The short-range behavior of the two sets of correlators is very similar, however, at intermediate ranges the SRG-generated UCOM correlators show a negative contribution which was not considered before.

Figure 2 summarizes the Hartree-Fock ground-state energies and charge radii obtained with the two types of UCOM interactions (variational and SRG-generated correlators, resp.) and a pure SRG interaction. Whereas the systematics of the binding energies is similar for the two UCOM interactions, the SRG interaction develops a severe overbinding for heavier nuclei. This systematic difference between UCOM and SRG interactions shows that three-body interaction play a very different role in the two approaches. This is also confirmed by the charge radii, which are significantly too small for the SRG interaction and best with the second-generation UCOM potential.

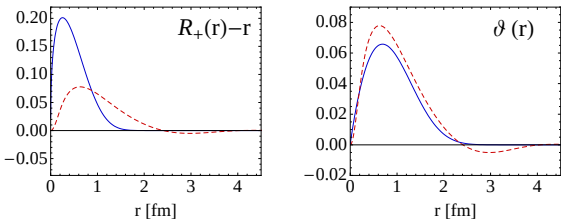

Figure 1: Variationally optimized (——) and SRG-evolved (– – –) central and tensor correlation functions $R_+(r) - r$ and $\vartheta(r)$ for $(S,T) = (1,0)$.

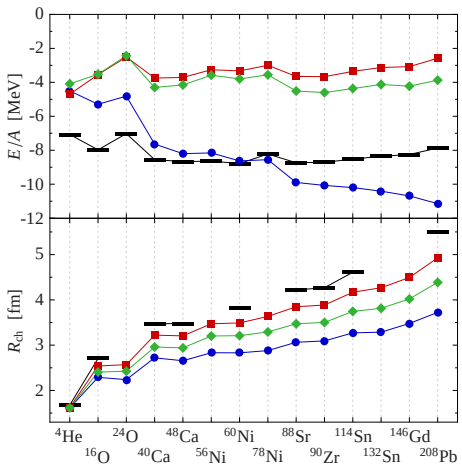

Figure 2: Hartree-Fock results for the SRG interaction for $\bar{\alpha} = 0.03$ fm^4 (●), the UCOM potential with $I_\vartheta = 0.09$ fm^3 (◆) and the SRG-generated UCOM potential with $\bar{\alpha} = 0.04$ fm^4 (■).

References

[1] R.Roth *et al.*, Phys. Rev. C 72, 034002 (2005)
[2] H. Hergert *et al.*, Phys. Rev. C 75, 051001(R) (2007)
[3] R.Roth *et al.*, Phys. Rev. C 77, 064003 (2008)

* Supported by DFG through SFB 634, the Helmholtz International Center for FAIR, and the GSI F&E Program.

Effective Three-Body Interactions in the UCOM Framework *

A. Günther, R. Roth, H. Hergert, and S. Reinhardt
Institut für Kernphysik, Technische Universität Darmstadt, Germany

We investigate the influence of phenomenological three-body forces supplementing unitarily transformed two-body potentials. For interactions constructed within the Unitary Correlation Operator Method (UCOM) the short-range central and tensor correlations induced by the nuclear interaction are treated explicitly by a unitary transformation. The character of the correlations is encapsulated in the operator structure of the correlation operators while the radial dependencies are described by correlation functions [1]. The Similarity Renormalization Group (SRG) also aims at the construction of a soft phase-shift equivalent interaction via a unitary transformation. But contrary to UCOM, the SRG leads to a pre-diagonalization of a matrix representation of the Hamiltonian by using a renormalization group flow evolution. The SRG can be used to extract correlation functions for the UCOM transformation [2]. For the following calculations, UCOM with SRG-generated correlation functions is employed to transform the Argonne V18 potential into a phase-shift equivalent correlated interaction $\mathrm{V_{UCOM}}$.

Investigations based on a pure two-body interaction show systematic deviations of different observables for heavier nuclei, e.g. charge radii are systematically too small. Therefore a phenomenological three-body interaction is introduced. Currently, we use a contact interaction with variable strength $C_{3\mathrm{N}}$ and an additional energy cut-off. The cut-off parameter is implemented in the calculation of matrix elements in harmonic-oscillator basis: $(2n_1 + l_1) + (2n_2 + l_2) + (2n_3 + l_3) \leq e_{3\max} = 10$. This simple three-body interaction is included in different many-body methods, for example in Hartree-Fock (HF) and many-body perturbation theory (MBPT).

One has two free parameters – the strength of the three-body interaction and the SRG flow parameter – which can be used to adjust the observables to experimental values. The strength of the three-body interaction is fixed to $C_{3\mathrm{N}} = 1200\ \mathrm{MeV\,fm^6}$ in order to reproduce the experimental charge radii while the SRG flow parameter is set to $\bar{\alpha} = 0.06\ \mathrm{fm}^4$. With this parameter set one can simultaneously reproduce the binding energies and the charge radii very well.

Figure 1 shows results from HF calculations (full symbols) and many-body perturbation theory (open symbols) for selected closed-shell nuclei from ^{4}He to ^{208}Pb. Differences between the calculated and experimental binding energies are depicted in the upper part and charge radii in the lower part. The different curves represent different model-space sizes, starting with $e_{\max} = 8$ (circles), $e_{\max} = 10$ (squares) up to $e_{\max} = 12$, $l_{\max} = 10$ (diamonds) and $e_{\max} = 14$, $l_{\max} = 10$ (triangles) with $e = 2n + l$. The perturbation theory corrections are calculated only for the two-body part of the interaction since the contributions for the three-body interaction are expected to be small. The charge radii and the HF energies are converged whereas the perturbed energies are not fully converged, but the missing $0.5\ \mathrm{MeV}$ can roughly be covered by an extrapolation to infinite basis size. The charge radii as well as the binding energies show a systematic agreement with experimental data which was not achieved with pure two-body interactions.

In summary, the repulsive three-body contact interaction in connection with the SRG-generated correlation functions yields nice agreement with experimental data for binding energies and charge radii. So far, the investigations were restricted to calculations on the level of HF and perturbation theory. Currently, we work on the construction of an effective two-body interaction out of the three-body force which can be included in several different many-body methods. In the near future, calculations in the framework of the No-Core Shell Model are envisioned.

* Supported by DFG through SFB 634 and the Helmholtz International Center for FAIR.

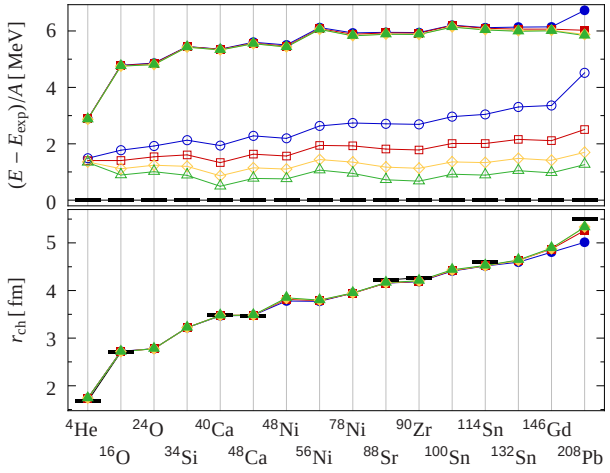

Figure 1: Differences between calculated and experimental binding energies and charge radii of selected closed-shell nuclei resulting from HF calculations (filled symbols) and MBPT (open symbols) for different basis sizes (see text). The bars indicate the experimental values.

References

[1] R. Roth et al., *Phys. Rev.* **C 72**, 034002 (2005).

[2] R. Roth et al., *Phys. Rev.* **C 77**, 064003 (2008).

Chiral Three-Nucleon Interaction and the ^{14}C Dating Beta Decay*

J. W. Holt†[1], N. Kaiser[1], and W. Weise[1]

[1]Physik Department, Technische Universität München, 85747 Garching, Germany

The anomalously long beta decay lifetime of ^{14}C, which makes possible the radiocarbon dating method, has long been a challenge to nuclear structure theory. The transition from the $J_i^\pi = 0^+$, $T_i = 1$ ground state of ^{14}C to the $J_f^\pi = 1^+$, $T_f = 0$ ground state of ^{14}N is of the allowed Gamow-Teller type, yet the known lifetime of $\sim 5730 \pm 30$ years is nearly six orders of magnitude longer than would be expected from typical allowed transitions in p-shell nuclei. The associated Gamow-Teller transition matrix element for the ^{14}C decay must therefore be accidently small, making this transition a sensitive test for both nuclear interaction models and nuclear many-body methods.

Very recently, it has been suggested [1] that the ^{14}C beta decay transition matrix element should be particularly sensitive to the density-dependence of the nuclear interaction. We study this problem systematically [2] from the perspective of in-medium chiral effective field theory, in which Pauli-blocked loop diagrams generated from the chiral three-nucleon force (3NF) give rise to a density-dependent correction, $V_{NN}^{\rm med}$, to the in-medium nuclear interaction. We have derived six unique contributions, represented by the diagrams in Fig. 1, to $V_{NN}^{\rm med}$ at one-loop order in the chiral 3NF.

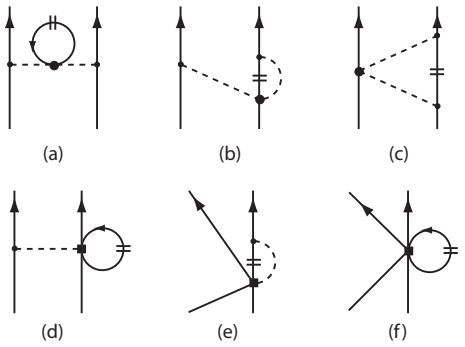

Figure 1: The six density-dependent contributions to the in-medium density-dependent NN interaction. The short double-line symbolizes the filled Fermi sea of nucleons in the in-medium nucleon propagator.

Together with the low-momentum NN interaction $V_{\rm low-k}$, we use $V_{NN}^{\rm med}$ (with low-energy constants c_D and c_E fitted to the binding energies of ^{3}H, ^{3}He, and ^{4}He) to calculate the states of ^{14}C and ^{14}N in the nuclear shell model. These states are treated as two $0p$-holes in an ^{16}O core, and we include the effects of higher-order configurations perturbatively in calculating the shell model effective interaction. The two-pion exchange component of the chiral 3NF generates the three diagrams (a)-(c) in Fig. 1. Evaluation of the Pauli-blocked pion propagator, term (a), and the Pauli-blocked vertex correction, term (b), shows that these two components are large, yet they enter with opposite sign and nearly cancel. Although much smaller in magnitude, the same is true for diagrams (d) and (e), which arise from the medium-range chiral 3NF proportional to the low-energy constant (LEC) c_D. This leaves diagrams (c) and (f) as the two most important contributions, and we discover that it is the latter (proportional to the LEC c_E) that drives a strong suppression of the ^{14}C decay rate at densities close to that of saturated nuclear matter.

In Fig. 2 we show the calculated Gamow-Teller transition strengths $B(GT)$ from the low-lying states of ^{14}C to the ground state (g.s.) of ^{14}N as a function of the nuclear density. Although most $B(GT)$ strengths are weakly density-dependent, there is a strong suppression of the g.s. to g.s. transition, reaching almost the experimental value at densities close to that of $A = 14$ nuclei. We conclude that in a chiral effective field theory framework, the addition of three-nucleon forces plays an essential role in describing the very long lifetime of ^{14}C.

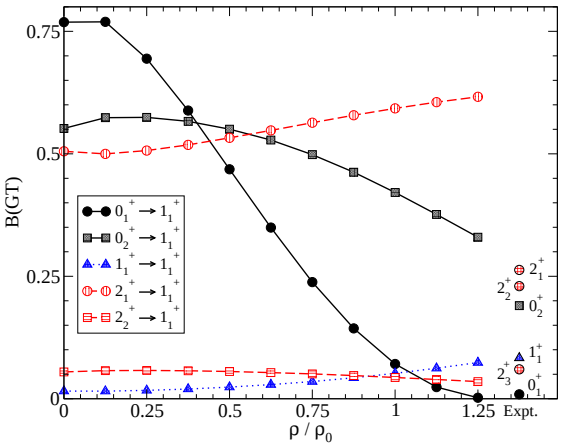

Figure 2: Caculated $B(GT)$ values for transitions from the states of ^{14}C to the ground state of ^{14}N as a function of the nuclear density. We show for comparison the experimental values determined in ref. [3].

References

[1] J. W. Holt, G. E. Brown, T. T. S. Kuo, J. D. Holt, and R. Machleidt, Phys. Rev. Lett. **100** (2008) 062501.

[2] J. W. Holt, N. Kaiser, and W. Weise, arXiv:0901.4750.

[3] A. Negret *et al.*, Phys. Rev. Lett. **97** (2006) 062502.

*Work supported in part by GSI, BMBF, and by the DFG cluster of excellence: Origin and Structure of the Universe.

† jholt@ph.tum.de

Low-lying dipole response in the relativistic quasiparticle time blocking approximation and its influence on neutron capture cross sections

E. Litvinova[1,2], H. P. Loens[1,3], K. Langanke[1,2,3], G. Martínez-Pinedo[1], T. Rauscher[4], P. Ring[5], F.-K. Thielemann[4], and V. Tselyaev[6]

[1]GSI Helmholtzzentrum für Schwerionenforschung, Germany; [2]Frankfurt Institute for Advanced Studies, Germany; [3]Technische Univeristät Darmstadt, Institut für Kernphysik, Germany; [4]Department of Physics, University of Basel, Switzerland; [5]Physik-Department, Technische Universität München, Germany; [6]Nuclear Physics Department, St. Petersburg State University, Russia

In order to evaluate the impact that a microscopic description may have in the calculations of (n,γ) cross sections, we have applied the statistical model [1] for the reactions on tin and nickel isotopes using four different models to describe the dipole strength function. Model A is the relativistic quasiparticle time blocking approximation (RQTBA) which, as demonstrated in [2], reproduces experimental photo absorption cross sections very well. In model B the centroid and the total strength are adjusted to the RQTBA strength using a Lorentzian with an energy dependent width taken from [3]. A comparison between models A and B allows to disentangle the influence of the low-energy strength on the neutron capture cross sections. Finally, we have performed calculations using the Lorentzian form but with the strength parameters determined as described in Ref. [3] (Model C) and calculations adopting the dipole strength functions of Ref. [4], which have been derived by a QRPA approach on top of a Hartree-Fock-BCS model (model D). The dipole γ-strength functions and the cross sections for (n,γ)-reactions for tin isotopes calculated within the models A-D are displayed in Fig. 1. For neutron captures on ^{105}Sn and ^{115}Sn the dominating γ transitions correspond to the energy of $E_\gamma \approx 3 + E_n$ MeV. We can see in Fig. 1 how the larger strength functions of the two parametrized descriptions (models B and C) result in larger cross sections than those obtained with the microscopic approaches RQTBA and QRPA (models A and D), until the predictions converge for E_n close to S_n. However, in ^{131}Sn the low level density of the doubly magic compound nucleus ^{132}Sn causes the dominance of γ transitions directly to the ground state, with $E_\gamma = S_n + E_n$. Up to $E_n < 1$ MeV the influence of the RQTBA pygmy peak yields the largest cross sections. Above that energy, the RQTBA γ strength drops below the strengths predicted by the other models and consequently the resulting cross section becomes the smallest. After another $2-3$ MeV the RQTBA predicts a larger γ strength again and consequently its respective cross section becomes the largest again. The level density description predicts a relatively low density of negative parity states at excitation energies around 9 MeV in ^{132}Sn. In consequence, magnetic dipole transitions to the low-lying positive parity states dominate. This is an example for the importance of the complete inclusion of parity-dependent level densities [5]. Except for the parity effect, the behavior of the ^{139}Sn(n,γ) cross section can be explained similarly to the one of ^{131}Sn. To estimate which impact the enhanced low-energy dipole strength could have on neutron capture rates under astrophysical conditions, we have calculated the stellar neutron capture rates for the tin and nickel isotopes. The computed neutron capture rates turn out to be sensitive to the fine structure of the low lying dipole strength, which emphasizes the importance of a reliable knowledge of this excitation mode.

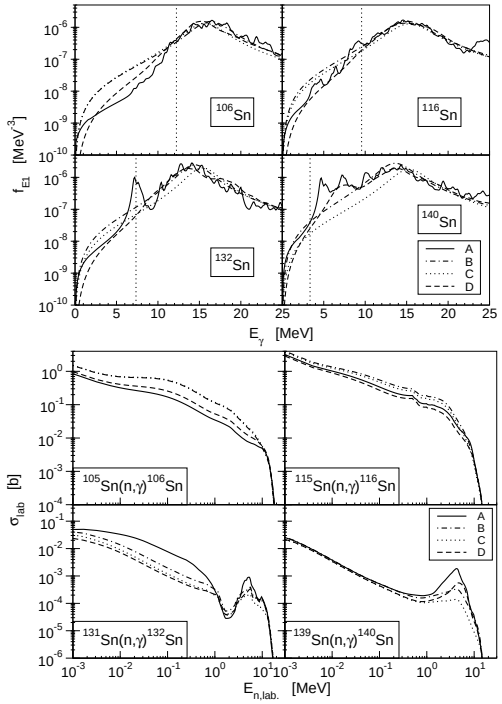

Figure 1: γ-strength functions f_{E1} and the respective cross sections σ_{lab} for (n,γ)-reactions on various tin isotopes for different models A-D, see text.

References

[1] W. Hauser, H. Feshbach, Phys. Rev. **87** (1952) 366.

[2] E. Litvinova, P. Ring, V. Tselyaev, Phys. Rev. C **78** (2008) 014312.

[3] J. J. Cowan, F.-K. Thielemann, J. W. Truran, Phys. Rep. **208** (1991) 267.

[4] S. Goriely, E. Khan, Nucl. Phys. A **706** (2002) 217.

[5] H. Loens, K. Langanke, G. Martínez-Pinedo, T. Rauscher, F.-K. Thielemann, Physics Letters B **666** (2008) 395.

Direct capture reactions and r-process

K. Otsuki[1], S. Typel[1], and G. Martinez-Pinedo[1]

[1]GSI Helmholtzzentrum für Schwerionenforschung, Planckstr. 1, Darmstadt, Germany

The r-process is the rapid neutron capture process which forms about half of the elements heavier than iron in nature. The astrophysical site of the r-process is still a mystery despite decades of study. Several astrophysical scenarios are considered as possible candidates. It is believed that the r-process proceeds in exotic neutron-rich regions of space and the reaction path is very close to the neutron drip line (e.g., cold r-process [4]). Nuclear physics input for theoretical calculations, such as masses, beta-decay rates and radiative capture rates have to be obtained in theoretical models since they cannot be measured in experiments.

There are two different contributions to neutron capture reactions, the direct capture process and the compound nuclear process. The rates of the latter are obtained in Hauser-Feshbach calculations (see, e.g., [3]), that are publicly available in archives. Since the level density of nuclei close to the neutron drip line is low, the statistical Hauser-Feshbach approach is inappropriate for estimating the radiative capture cross sections for these nuclei. Here, the direct capture contribution becomes substantial, however, it has been neglected in previous r-process studies though its importance has been pointed out [1].

We study the role of direct capture in r-process nucleosynthesis. For the calculation of the capture rates we employ an almost-analytical model based on [5] with single-particle levels that are adjusted to experimental data for stable nuclei. Both spherical and deformed nuclei can be considered in the approach. The basic parameters of the model are the mass number of the mother nucleus, the neutron separation energy and the deformation parameter that are taken from the FRDM model [6].

Our r-process calculations use a full dynamical network code [2] and adopt a supersonic wind model as the astrophysical environment. The entropy per nucleon is $250\ \mathrm{k_B}$, the dynamical timescale is 0.1 s, the initial electron fraction is 0.45 in this calculation.

Figure 2 shows final abundance of calculations with and without direct capture. The direct capture reactions change the final abundances drastically under such physical conditions. If direct capture is considered, the position of the third peak shifts to the left. It is more consistent with the solar r-process abundances. In addition, a significant amount of actinides is formed. They appear because direct capture reactions accelerate the flow of matter to the region above $N = 126$ and the r-process freeze-out is reached earlier than in the other case. This implies larger matter densities at freeze-out for the calculation with direct captures and consequently an r-process path that involves nuclei with smaller Z values for $N = 126$ than in the case where direct neutron captures are not included. This explains why the third peak is shifted to the left and becomes wider.

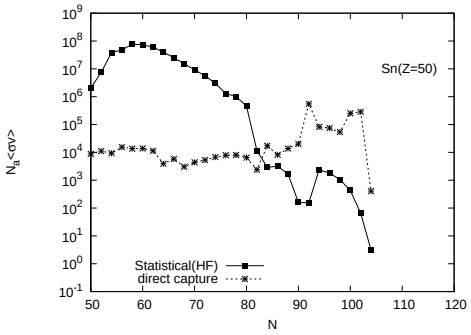

Figure 1: Comparison of neutron capture rates of Sn isotopes. The black squares are neutron capture rates computed using the Hauser-Feshbach model [3]. The stars are direct capture rates obtained in this study. At the neutron rich side, direct capture becomes the dominating contribution to the reaction rate.

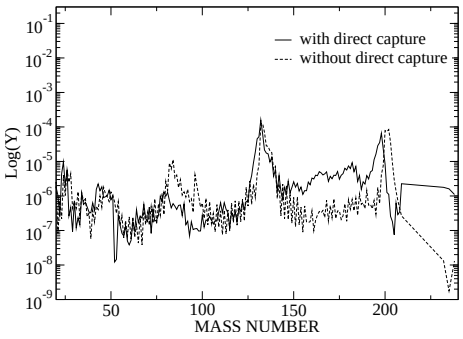

Figure 2: Results of r-process calculations with (solid line) and without (dashed line) direct capture.

References

[1] Mathews, G.J., Mengonni, A., Thielemann, F-K., & Fowler, W.A.
ApJ**270** 740 (1983)

[2] Otsuki, K., Mathews, G.J., & Kajino, T.
New Astronomy **8** 767 (2003)

[3] Rauscher, T. & Thielemann, F.-K.
ADNDT**75** 1 (2000)

[4] Wanajo, S. ApJ**666** L77 (2007)

[5] Typel, S. & Baur, G., Nucl. Phys. A 759, 247 (2005).

[6] Möller,P., Nix, J.R., Myers, W.D., & Swiatecki, W.J
ADNDT **59** 185 (1995)

R-process Nucleosynthesis

I. Petermann[1], A. Arcones[1,2], and G. Martínez-Pinedo[1,2]
[1]GSI, Darmstadt, Germany; [2]Institut für Kernphysik, TU Darmstadt, Germany

Elements heavier than iron are known to be made partly by the r-process, in a sequence of rapid neutron-captures and subsequent beta-decays in explosive scenarios with high neutron densities. Its astrophysical site has not yet been identified, despite the numerous works done in the last 50 years (see [2] for a review).

We have studied systematically the nucleosynthesis production in neutrino-driven winds and analyzed the influence of different factors like the nuclear physics input and fission.

Trajectories from long time supernova simulations ([1]) have been used as input in an explicit nuclear reaction network, which includes neutron capture, photodissociation, beta decay and fission. The conditions found in the supernova simulations (too low entropy and /or electron fraction) do not result in large enough neutron-to-seed ratio to produce elements heavier than A≈70. However by increasing slightly the entropy the neutron-to-seed ratio is large enough to produce r-process nuclei reaching A≈195. We have used the resulting trajectories to analyze the combined effect of uncertainties in the nuclear and astrophysical inputs. The later one includes the influence that the reverse shock may have in the matter expansion velocity.
We have performed nucleosynthesis calculations using four different mass models (FRDM, ETFSI-Q, HFB-14, Duflo Zuker) for which we have computed the relevant neutron-capture rates. The impact that the different mass models have in the final abundances is shown in Fig. 1.

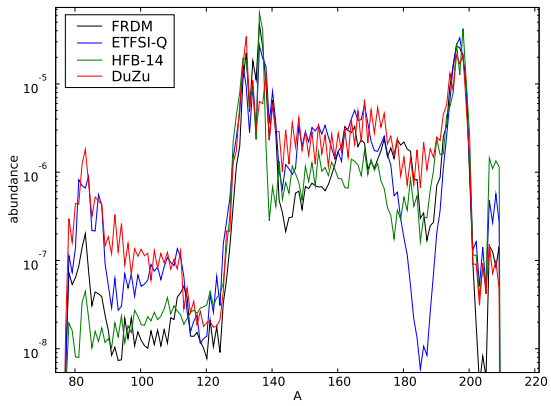

Figure 1: Comparison of final abundances obtained with different mass models.

Whenever the neutron-to-seed ratio in the r-process becomes larger than ≈140 fission will become important. We have developed [3] for the first time a complete database of reaction rates that in addition to neutron-capture rates and beta-decay half-lives includes all possible reactions that can induce fission (neutron-capture, beta-decay and spontaneous fission) and the corresponding fission yields. In addition, we have implemented these reaction rates in a fully implicit reaction network. We have performed r-process calculations for the neutrino-driven wind scenario to explore whether or not fission can contribute to provide a robust r-process pattern.

Our calculations show that neutron induced fission is the dominating channel with beta delayed fission having a slight influence (Fig. 2).

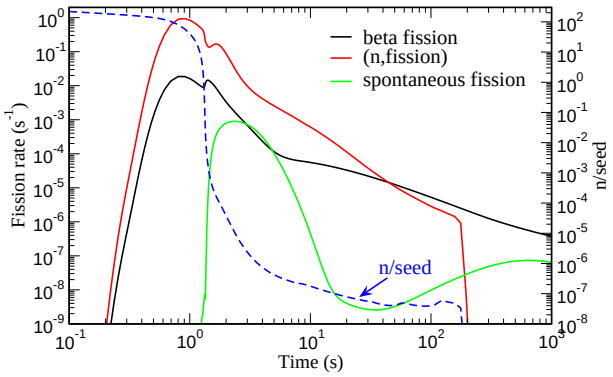

Figure 2: Evolution of the fission rate for the different channels for a calculation with initial neutron-to-seed ratio 295. The evolution of the neutron-to-seed ratio is also shown (dashed line, right y-axis scale.)

References

[1] A.Arcones, H.Th.Janka, and L.Scheck, Astron.& Astrophys. **467**,1227 (2007)

[2] M.Arnould, S.Goriely, K. Takahashi, Phys. Rep. **405**, 97 (2007)

[3] I. Petermann, A. Arcones, A. Kelić, K. Langanke, G. Martínez-Pinedo, K.-H. Schmidt, W. R. Hix, I. Panov, T. Rauscher, F.K. Thielemann, and N. Zinner ArXiv [0812.0968] (2008)

Black hole accretion disks as site for the νp-process

L. T. Kizivat[1] and G. Martinez-Pinedo[1]
[1]GSI, Darmstadt, Germany

Important questions like the definite astrophysical sites of the r- and p-process still remain unanswered. The puzzle concerning the origin of the light p-nuclides might have been solved recently with the discovery of the νp-process [1, 2]. The νp-process operates via antineutrino capture reactions on free protons in proton-rich environments with high neutrino and antineutrino fluxes such as the early ejected matter in core-collapse supernovae. Recent studies indicate that quite similar physical conditions also occur in the windlike outflows from the accretion disk surrounding a black hole in the collapsar model of gamma-ray bursts.

Once the ejected matter reaches cooler regions, i.e. with increasing distance from the neutron star surface or accretion disk, the nucleons assemble in nuclei and, without further neutrino reactions, the proton-rich matter freezes out with a significant production of $N = Z$ nuclei like ^{56}Ni and ^{64}Ge and some free protons left. However, antineutrino captures on these protons via

$$\bar{\nu_e} + p \rightarrow e^+ + n \qquad (1)$$

ensure a significant presence of free neutrons which can be captured on the $N = Z$ nuclei via (n,p) and (n, γ) reactions allowing for matter flow beyond ^{56}Ni and ^{64}Ge.

Our study is based on profiles from a windlike outflow model of refs. [3, 4] that are coupled to an extensive nuclear network. The disks studied in this work are all based on the model of Neutrino-Dominated-Accretion-Flows, "NDAF's" [5]. We have studied the nucleosynthesis in the accretion disk outflows varying different parameter values: the accretion rate $\dot{M}$, the acceleration parameter β, which determines the acceleration of the ejected matter, the radius R_0 at which the matter is ejected from the disk, and the entropy S of the ejecta [6].

Here we will discuss the influence of the velocity of the outflows, i.e. the acceleration parameter β, on the νp-process nucleosynthesis. Both models A and B assume the same physical conditions except for the outflow velocity. Model A has a relatively slow outflow velocity which corresponds to conditions for which one expects the outflows to be proton-rich as neutrino producing reactions occur with significant rates. A sequence of (n, p) and (p, γ) reactions allows for synthesis of elements upto the mass range $A \sim 80$–100 for the conditions of model A, as can be seen in Fig. 1, top. As a comparison we also show the abundance distribution obtained with the same nucleosynthesis network, however, switching off the neutrino and, importantly, antineutrino capture reactions once the freeze-out value of the electron fraction is reached. Strikingly the matter flow stops at the alpha seed nuclei with long halflives as in this scenario no free neutrons are available to carry the matter flow to larger mass numbers as it is guaranteed in the νp-process. Model B is expected to show only a rather weak νp-process as it has a relatively high outflow velocity. This is indeed borne out by our nucleosynthesis calculation, as can be seen in Fig. 1, bottom.

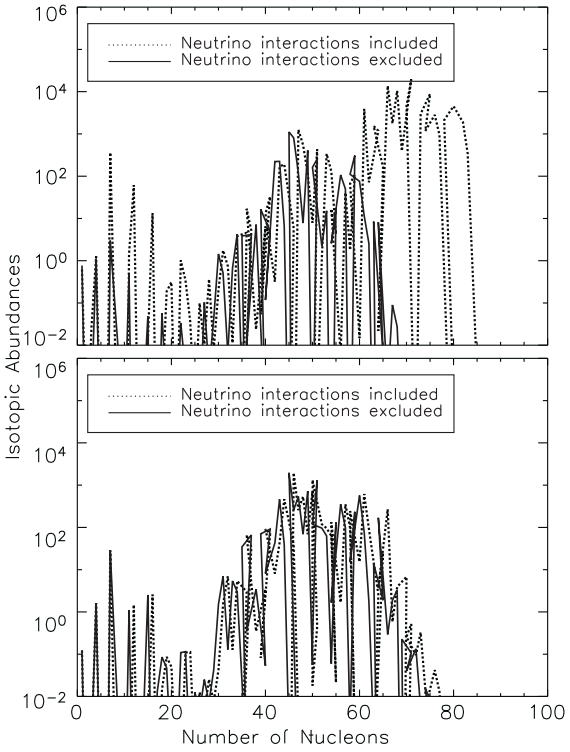

Figure 1: Final isotopic abundances normalized to solar abundances. On top the results for model A, at bottom the results for model B.

References

[1] G. Martinez-Pinedo, *et al.*, ArXiv Astrophysics e-prints (2006), astro-ph/0608490.

[2] C. Fröhlich, *et al.*, Physical Review Letters **96** (2006) (14) 142502, arXiv:astro-ph/0511376.

[3] R. Surman, G. C. McLaughlin, apj **603** (2004) 611, arXiv:astro-ph/0308004.

[4] R. Surman, G. C. McLaughlin, apj **618** (2005) 397, arXiv:astro-ph/0407206.

[5] R. Popham, S. E. Woosley, C. Fryer, Astrophys. J. **518** (1999) 356, arXiv:astro-ph/9807028.

[6] L. Kizivat, G. Martinez-Pinedo, R. Surman, G. McLaughlin, In preparation (2009).

Differential neutron-hydrogen squeeze-out

W. Trautmann[1], M. Chartier[2], Y. Leifels[1], R.C. Lemmon[2], Q. Li[3], J .Łukasik[4], A. Pagano[5], P. Pawłowski[4], P. Russotto[5], and P. Wu[2]

[1]GSI, Darmstadt, Germany; [2]University of Liverpool and STFC Daresbury Laboratory, United Kingdom; [3]FIAS, Universität Frankfurt, Germany; [4]IFJ-PAN, Kraków, Poland; [5]INFN-LNS and Universitá di Catania, Italy

The equation of state (EOS) of asymmetric nuclear matter is of fundamental importance to both nuclear physics and astrophysics. While considerable progress has been made recently in determining the symmetry energy around normal nuclear matter density [1], much more work is still needed to probe its high-density behaviour. This requires reaction studies at sufficiently high energies and probes sensitive to mean-field effects in the initial compressed stage of the reaction as, for example, the neutron-proton differential transverse and elliptic flows [2].

In two experiments at GSI using the LAND and FOPI detectors, both neutron and hydrogen collective flow observables from ^{197}Au + ^{197}Au collisions at 400, 600 and 800A MeV have been measured [3]. This data set is presently being reanalyzed in order to determine the optimum conditions for a dedicated differential flow experiment, but also with the aim to produce first results from a comparison with state-of-the-art transport models. In the following, we present results obtained with the UrQMD model which has recently been adapted to heavy ion reactions at intermediate energies [4].

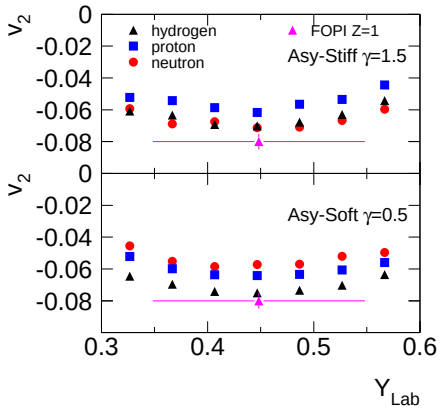

Figure 1: Elliptic flow parameter v_2 for mid-central ($5.5 < b < 7.5$ fm) ^{197}Au + ^{197}Au collisions at 400 AMeV as predicted by the UrQMD model for protons (squares), neutrons (circles), and hydrogen isotopes (triangles) as a function of the laboratory rapidity $Y_{\rm lab}$. The value measured for hydrogen by FOPI [5] is shown for comparison.

The predictions obtained for the elliptic flow of neutrons, protons and hydrogen isotopes for ^{197}Au + ^{197}Au at 400 A MeV are shown in Fig. 1. Two values are chosen for the power-law exponent describing the density dependence of the potential part of the symmetry energy, $\gamma = 1.5$ (asy-stiff) and $\gamma = 0.5$ (asy-soft). The neutron squeeze-out is found to be significantly larger in the asy-stiff case (upper panel) than in the asy-soft case (lower panel) while the proton and hydrogen flows respond only weakly to the variation of γ within the chosen interval. This observation persists after filtering the UrQMD outputs with the acceptance of the FOPI/LAND experiments.

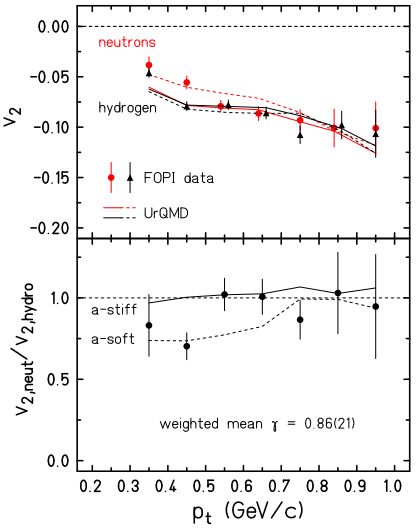

Figure 2: Differential elliptic flow parameters v_2 for neutrons and hydrogens (top panel) and their ratio (bottom) for central ($b < 7.5$ fm) ^{197}Au + ^{197}Au collisions at 400 A MeV as a function of the transverse momentum p_t. The symbols represent the experimental data, the UrQMD predictions for $\gamma = 1.5$ and $\gamma = 0.5$ are given by the full and dashed lines, respectively.

The comparison with the experimental data shows that the p_t dependence is well described by the UrQMD (Fig. 2, upper panel) and that the squeeze-out ratio is sensitive to the stiffness of the symmetry energy (lower panel). A linear interpolation yields $\gamma = 0.86 \pm 0.21$ which represents a moderately soft density dependence of the symmetry energy at supra-saturation densities. A more precise result can be expected from data with higher statistics.

References

[1] Bao-An Li et al., Phys. Rep. 464 (2008) 113.

[2] Bao-An Li, Phys. Rev. Lett. 88 (2002) 192701.

[3] Y. Leifels et al., Phys. Rev. Lett. 71 (1993) 963; D. Lambrecht et al., Z. Phys. A 350 (1994) 115.

[4] Q. Li et al., J. Phys. G 31 (2005) 1359.

[5] A. Andronic et al., Phys. Lett. B 612 (2005) 173.

Elliptic Flow of Light Fragments in Ru+Ru Collisions at 0.4 and 1.528 AGeV

Min Sang Ryu*[1,2], Byungsik Hong†[1], and the FOPI Collaboration
[1]Korea University, Seoul, Korea; [2]Physikalisches Institut, Universität Heidelberg, Germany

The measurement of elliptic flow of various particles can provide useful information on the nuclear equation of state and other properties of dense matter produced in heavy-ion collisions. Systematic measurements have shown that the elliptic flow is maximum at a beam energy around 400 AMeV and varies weakly between 250 and 800 AMeV [1].

The FOPI collaboration has measured Ru+Ru collisions at two beam energies, 0.4 and 1.528 AGeV. In the current analysis, the elliptic flow of the hydrogen isotopes (p, d, and ^{3}H) and the helium isotopes (^{3}He and ^{4}He) were studied. For the reconstruction of the reaction plane, the transverse momentum (p_t) method was employed [1, 2]. Because of multiplicity fluctuations [3] the orientation of the reaction plane can be reconstructed only with a limited precision in azimuthal angle. The corresponding correction factors for the v_2 values were 0.554 and 0.292 at 0.4 and 1.528 AGeV, respectively.

The collision centralities were estimated by applying the sharp-cut-off approximation model to the total charged particle multiplicity distributions. In the current analysis, we limited the data sample to semicentral collisions in which a maximum flow signal was expected: impact parameters between 2 and 4 fm and 3 and 5 fm were selected at 0.4 and 1.528 AGeV, respectively.

While at 0.4 AGeV the momentum spectra measured in the forward and the backward hemispheres could be used, at 1.528 AGeV only the spectra measured at the backward hemisphere were taken because of the limited particle identification capability in the forward region at this relatively high beam energy.

Figure 1 shows the differential v_2 distributions of the light fragments at 0.4 AGeV. Note that both the v_2 and the p_t of the light fragments are scaled by the number of the composite nucleons, n, in order to facilitate the comparison with the proton data. We find that the scaled v_2 distributions of all light fragments as a function of the scaled p_t agree well with the differential v_2 distribution of protons.

The same scaling phenomenon can be observed at 1.528 AGeV as demonstrated in Fig. 2. In this case, more statistics would be desirable to allow for a more detailed comparison of the ^{4}He data with protons in the range $p_t/n >$ 0.5 GeV. (The convention c=1 is adopted in this report.)

The observed scaling phenomenon of the light fragment elliptic flow at SIS18 energies will allow us to test the nucleon coalescence scenario in heavy-ion collisions [4]. Furthermore, we are also investigating the invariant spectra of light fragments for similar scaling phenomena.

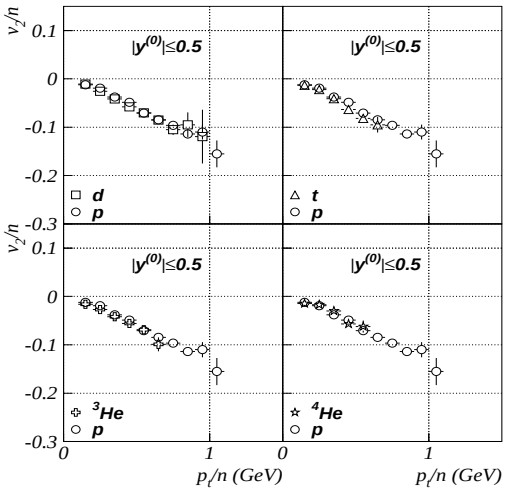

Figure 1: Scaled elliptic flow parameter, v_2/n, where n is the number of composite nucleons, as a function of the scaled transverse momentum, p_t/n, in Ru+Ru collisions at 0.4 AGeV.

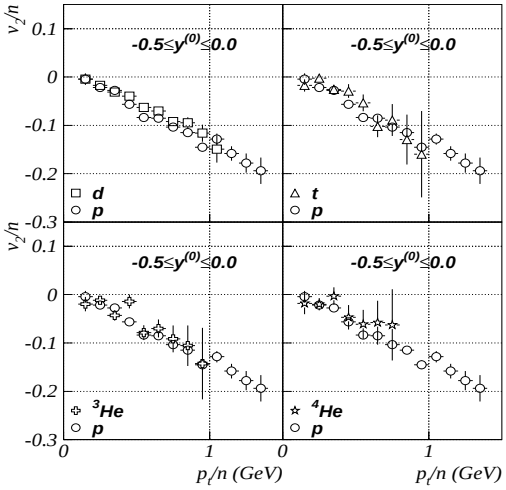

Figure 2: Same as Fig. 1, but at a beam energy of 1.528 AGeV.

References

[1] J.-Y. Ollitrault, Nucl. Phys. A 638 (1998) 195c.
[2] P. Danielewicz and G. Odyniec, Phys. Lett. B 157 (1985) 146.
[3] J.-Y. Ollitrault, nucl-ex/9711003 (1997).
[4] L. Csernai and J. Kapusta, Phys. Rep. 131 (1986) 223.

* dark93@korea.ac.kr
† bhong@korea.ac.kr

Status of the HADES physics program

The HADES collaboration

Introduction

In 2008 the analysis of dielectron spectra from our 2006 p+p and 2007 d+p runs at 1.25 GeV/u has been finalized. In these runs the elementary processes relevant for the understanding of the 1 GeV/u ^{12}C+^{12}C data [1, 2] were studied. The direct comparison of the pair spectra from p+p and d+p reactions allows to constrain the $\Delta \rightarrow Ne^+e^-$ and $N + N$ bremsstrahlung contributions which dominate the intermediate-mass region ($0.15 < M_{ee} < 0.50$ GeV/c^2) of the pair spectrum at this bombarding energy. In particular, information on the pn bremsstrahlung process has been obtained from $p + n \rightarrow p_{spec}e^+e^-X$ reactions selected by tagging the forward-going proton spectator p_{spec} in the HADES Forward Wall. These results indicate a strong isospin dependence of the pair emission, as was pointed out in earlier calculations [3, 4]. Indeed, NN bremsstrahlung had been considered as an important source of e^+e^- pairs since the first results from the DLS became public, although microscopic transport calculations including this contribution did not succeed to explain the experimental data satisfactorily.

High-statistics spectroscopy of the vector-meson region was started with the investigation of Ar+KCl collisions at 1.75 GeV/u in 2005. A dielectron invariant-mass distribution with $\sim 10^5$ signal pairs, showing for the first time a clear ω signal at SIS energies, is presented. The large statistics collected in this experiment also allowed to study various rare hadronic probes, like the K^+, K^-, K^0, and ϕ mesons, as well as the strange Λ and doubly-strange Ξ^- hyperons. The ω meson has furthermore been produced and identified in dedicated experiments, using in 2007 the p+p and in 2008 the p+Nb reactions at 3.5 GeV. These measurements combined provide the means to address directly in-medium effects on vector mesons in cold nuclear matter.

p+p and d+p reactions at 1.25 GeV/u

For a better understanding of the contribution of Dalitz decays and NN bremsstrahlung processes to dielectron production in heavy-ion collisions, HADES has studied p+p and d+p interactions at T_{kin}=1.25 GeV/u . The investigation of dielectron production in elementary reactions is also interesting in itself because it provides insight into the electromagnetic structure of hadrons in the time-like region. For example, the time-like $N - \Delta$ electromagnetic transition form factors [5], involved in the Δ Dalitz decay, have not been measured so far. In order to learn about this process, a dedicated exclusive measurement of the $pp \rightarrow p\Delta^+ \rightarrow ppe^+e^-$ reaction is required. Good knowledge of Δ resonance excitation in $pp \rightarrow \Delta^{++}n \rightarrow p\pi^+n$, $pp \rightarrow \Delta^+p \rightarrow n\pi^+p$ and $pp \rightarrow \Delta^+p \rightarrow p\pi^0p$ is a prerequisite for the in-depth understanding of the dielectron contribution resulting from the $\Delta^+ \rightarrow pe^+e^-$ Dalitz decay. Indeed, in the resonance model [6], pion production at T_{kin}=1.25 GeV/u is dominated by Δ excitation and decay into the above-mentioned channels. Isospin symmetry gives $\sigma(pp \rightarrow n\Delta^{++}) \sim 3 \cdot \sigma(pp \rightarrow p\Delta^+)$, furthermore the pion yields of the two reactions are related by $\sigma(pp \rightarrow pn\pi^+) \sim 5 \cdot \sigma(pp \rightarrow pp\pi^0)$.

Both, $pp \rightarrow pn\pi^+$ and $pp \rightarrow pp\pi^0$, exclusive cross sections have been measured with HADES, making use of the missing-mass technique where the non-detected neutral particle, namely the n or π^0, is identified with the help of energy and momentum conservation. Figure 1 presents a Dalitz plot (i.e. two-dimensional distribution of squared invariant masses of the two protons and the π^0) for the $pp\pi^0$ exit channel. The yield in each bin of this plot was obtained after subtraction of a background under the π^0 peak in the respective $p + p$ missing-mass spectrum taking into account reconstruction efficiencies. One can clearly see a prominent Δ^+ signal which can be quantitatively compared to the acceptance-filtered distribution from the resonance model (see Fig. 2). The absolute normalization was fixed by comparing the simultaneously measured elastic scattering yield to the known elastic cross section found by the EDDA experiment [7]. This analysis results in an exclusive π^0 production cross section of $\sigma_{\pi^0} = 4.5 \pm 0.5$ mb.

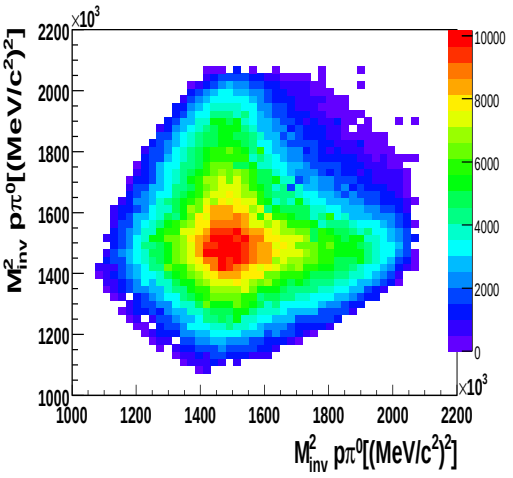

Figure 1: Invariant mass squared distribution of the protons and π^0 (Dalitz plot) of the $pp \rightarrow pp\pi^0$ reaction.

In the analysis of the $pp \rightarrow pn\pi^+$ channel, the background coming from misidentified protons and two-pion

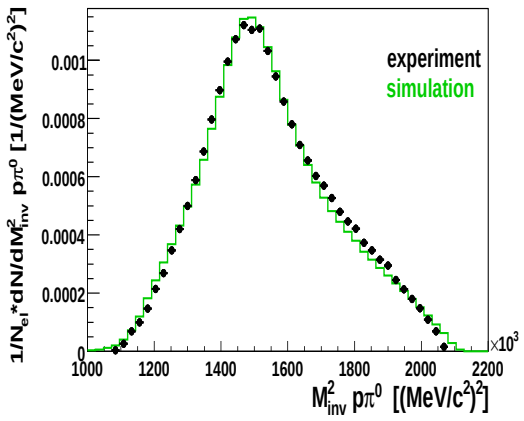

Figure 2: Projection of the Dalitz plot of Fig. 1 onto the $p-\pi^0$ invariant mass squared (black circles) compared to a simulation assuming the Δ^+ as intermediate resonance. Both distributions are normalized to the same number of $p+p$ elastic scattering events.

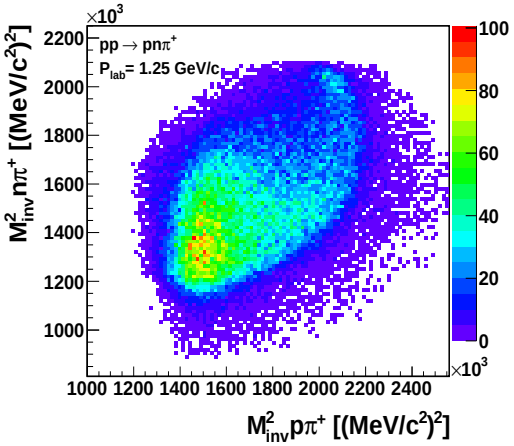

Figure 3: Dalitz plot of the $pp \rightarrow pn\pi^+$ reaction.

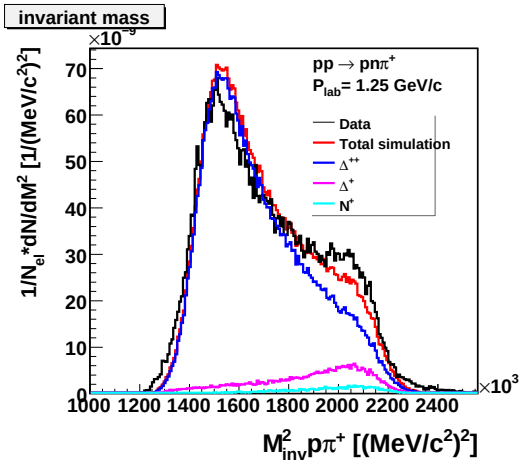

Figure 4: Projection of the Dalitz plot of Fig. 3 onto the $p-\pi^+$ invariant mass squared (black) compared to simulation: total contribution (red), Δ^{++} (blue), Δ^+ (pink), N^* (light blue).

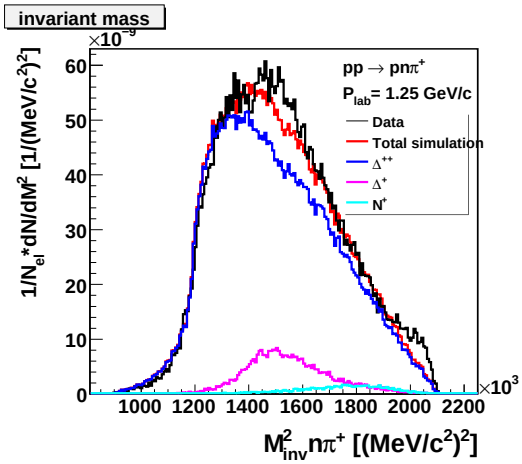

Figure 5: Projection of the Dalitz plot of Fig. 3 onto the $n-\pi^+$ invariant mass squared (black) compared to simulation: total contribution (red), Δ^{++} (blue), Δ^+ (pink), N^* (light blue).

contributions was efficiently suppressed by cuts on the $p-\pi^+$ missing mass. Figs. 3 (Dalitz plot), 4, and 5 (projections) clearly show the dominance of the Δ^{++} in this channel. All, the absolute yields and the respective yield of the Δ^{++} and Δ^+, are in agreement with the result from the simulation based on resonance-model predictions [6]. The contribution of the $N^*(1440)$ resonance seems also reasonable, although the sensitivity is much weaker. The spot appearing in the Dalitz plot (see Fig. 3) for invariant masses above 1400 MeV/c^2 can be attributed to the pn final state interaction which, however, has not yet been included into our simulation. The extrapolation of the cross section to 4π has been performed using the resonance model, and thus we find $\sigma(pp \rightarrow pn\pi^+) = 19.6 \pm 2.0$ mb. The ratio of both measured exclusive pion production cross sections is hence, within error bars, compatible with the isobar model. Our results are also consistent with previous (lower precision) data [8].

As already mentioned, in proton-proton reactions the most abundant source above the π^0 Dalitz-decay region is expected to be the Δ Dalitz decay. The large differences of dielectron production in the p+p and d+p systems observed by the former DLS experiment [9] suggested furthermore that in the $d+p$ system the pair yield is dominated by the quasi-free $n+p$ reaction. The main goal of our 2007 $d+p$ experiment was hence to understand the np bremsstrahlung component, namely by tagging explicitely the reaction channel $np \rightarrow npe^+e^-$. In this experiment, the $p+p$ and $n+p$ reactions could indeed be distinguished through a coincident measurement of a spectator proton in the HADES Forward Wall (covering polar angles between 0.5°and 7°).

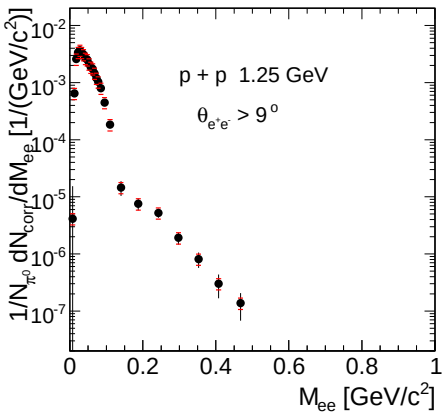

Figure 6: Measured invariant-mass distribution of e^+e^- pairs from the 1.25 GeV$p+p$ reaction within the acceptance of HADES. The data are corrected for detector and reconstruction efficiencies. Statistical errors are shown as vertical bars, systematic errors are indicated by horizontal ticks.

The dielectron yield measured in HADES was corrected for detection and reconstruction inefficiencies. Figs. 6 and 7 show the resulting e^+e^- invariant-mass distributions of true pairs normalized to the inclusive π^0 cross section, obtained by combining our own measurement of the exclusive channel (see above) with other inclusive channels [6]. The total systematic error of $\pm 30\%$ is determined by the uncertainty of the π^0 cross section in the dominant process $pp \rightarrow pp\pi^0$ ($\pm 20\%$) and uncertainties caused by the efficiency correction ($\pm 20\%$). An additional 10% error comes from the uncertainty in the pp elastic scattering correction and the extrapolation procedure.

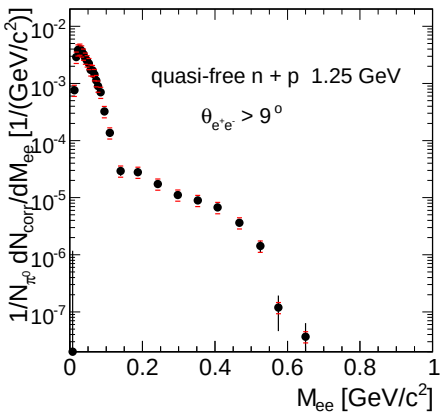

Figure 7: Measured invariant-mass distribution of e^+e^- pairs from tagged quasi-free $n+p$ interactions in the 1.25 GeV/u $d+p$ reaction. The data are corrected for detector and reconstruction efficiencies. Statistical errors are shown as vertical bars, systematic errors are indicated by horizontal ticks.

We observe a large enhancement of dielectron production in $n+p$ relative to $p+p$ reactions in the mass region above the π^0 Dalitz decay. In addition, a strong difference between the shapes of the $n+p$ and $p+p$ mass spectra is apparent. The $p+p$ mass spectrum is much steeper then the $n+p$ one, which can be partially explained by the smaller available energy in the proton-proton system (no Fermi motion!). The contributions of $N+N$ bremsstrahlung can now be investigated by comparison of the dielectron yields observed in $p+p$ and $n+p$ reactions with calculations of the OBE model [3]. Its detailed dependence on pair mass will be explored by the dielectron yield ratio $(\frac{dN}{dM_{ee}})^{np}$ / $(\frac{dN}{dM_{ee}})^{pp}$. With large statistics achieved, questions such as to the form factor and branching ratio of the Δ Dalitz decay, the $n+p$ bremsstrahlung as well as contributions from N* resonances and off-shell vector-meson contributions can be answered. Those results will provide stringent constraints to theoretical models of dilepton production. In particular, it is expected that the results of our analysis of the $p+p$ and $n+p$ interactions allow to exhibit additional sources, for instance higher-lying baryonic resonances [10].

Finally, our new data offer a possibility to directly compare the experimental cocktail based on $p+p$ and $n+p$ data to our ^{12}C+^{12}C data. This comparison will help in understanding the origin of the excess observed in ^{12}C+^{12}C collisions at SIS energies.

Ar+KCl collisions at 1.756 GeV/u

The main motivation for the Ar+KCl run was to perform for the first time high-resolution spectroscopy of the vector-meson region at SIS energies. Furthermore, an investigation of the medium-heavy Ar+KCl system also allows to study the dependency of the pair excess observed in ^{12}C+^{12}C reactions [1, 2] on the system size and centrality of the collision.

Ar+KCl collisions were measured in 2005 and provided one of the largest data samples collected so far by HADES ($\sim$ 7 Tbyte raw data). In this run 2.2×10^9 triggered (LVL1) events were acquired with the condition that at least 16 hits were registered in the TOF/Tofino detectors, with almost the complete HADES tracking system operational (two of the outermost MDC chambers were missing in this run). Fig. 8 shows an invariant-mass distribution of the pair signal after subtraction of the combinatorial background (CB), correction for detector and reconstruction inefficiencies, and normalization per triggered event and pion multiplicity. The CB was obtained by combining the like-sign and event-mixing techniques as explained in [1, 2]. The signal-to-CB ratio for pairs amounts to 20 in the π^0 region, to $\sim$1/5 at intermediate masses and to $\sim$1 at the omega pole mass. A total number of signal pairs of $\sim$86k was reconstructed, with more than 16k pairs above the π^0 Dalitz peak. Finally, a clear omega peak is visible for the first time at SIS/Bevelac energies, totalling about 50 pairs in the peak region [11, 12].

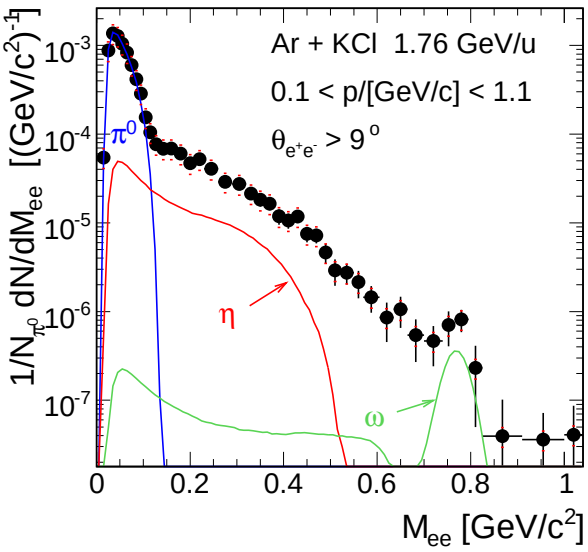

Figure 8: Reconstructed and efficiency-corrected dilepton mass spectrum from 1.756 GeV/u Ar+KCl. The pair yield is normalized to the number of LVL1 events and to the mean π^0 multiplicity. Various components of the PLUTO dilepton cocktail are shown as well.

The measured mass spectrum shown in Fig. 8 is compared with a pair cocktail generated with the PLUTO [13] event generator. This simulation is based on thermal particle sources with source parameters (multiplicities, temperatures, anisotropies) either taken from data (HADES, TAPS) or estimated with an $m_\perp$-scaling ansatz (see [2] for details). The cocktail accounts only for the emission from long-lived sources, i.e. those present at chemical freeze-out. It is hence evident that this type of calculation grossly underestimates the experimental pair yield at intermediate masses ($0.15 < M_{ee} < 0.60$ GeV/^{2}), stemming largely from short-lived resonances and NN bremsstrahlung. This is in line with our former findings from the ^{12}C+^{12}C system [1]. The excess above the η Dalitz is even stronger (by about a factor 2) than in ^{12}C+^{12}C at 2 GeV/u , from which its A_{part} dependence can be deduced to be about $N_{exc} \simeq A_{part}^{1.6}$. Clearly additional, non-trivial dilepton production mechanisms are needed to describe these findings.

In the Ar+KCl reaction at 1.765 GeV/u the production of strangeness has been studied as well. Particles containing strange quarks produced in this energy regime are mainly the K mesons, the Λ and Σ hyperons, as well as the ϕ meson. Except for the Σ, all of these hadrons could be reconstructed, resulting in the most comprehensive measurement of strangeness production at SIS energies in one and the same experiment. Besides the K$^+$ and the Λ, all other particles are produced below their respective NN threshold; they are hence rare and difficult to identify. On the other hand, due to the steepness of their excitation function, the observed multiplicities and inverse-slope parameters T_B are promising probes of predicted in-medium mass modifications [14]. The required selectivity of the particle identification (PID) was achieved by (1) a careful track selection, (2) the use of the combined dE/dx information from all drift chambers present in one sector [15] and (3) time-of-flght cuts optimized for the charged kaons.

About 250.000 K$^+$, spanning rapidities of $-0.85 \leq y_{cm} \leq -0.15$, and about 5500 K$^-$, at $-0.75 \leq y_{cm} \leq -0.25$, were reconstructed with a signal-to-background ratio of up to 36 for K$^+$ and up to 4 for K$^-$ [16]. Corrections for the detector acceptance and efficiency, as well as for the track-reconstruction efficiency were obtained from simulations and, for the latter, also from data.

With the help of Boltzmann fits to the corrected transverse-mass slices, rapidity distributions were obtained and extrapolated to the full phase space, yielding thus the particle multiplicities per triggered event, as well as the effective temperatures of the various particle species. The results obtained for charged kaons agree within error bars with the systematics of data published by the KaoS collaboration for the collision systems C+C, Ni+Ni and Au+Au [17].

The short-lived particles Λ, K^0_S and ϕ were reconstructed with the invariant-mass technique in the decay channels $\Lambda \rightarrow$ p π^-, K$^0_S \rightarrow \pi^+\pi^-$ and $\phi \rightarrow$ K$^+$ K$^-$. In each case the uncorrelated background was obtained by event-mixing and normalized to a peak-free region in the respective same-event distributions. For the reconstructed ϕ signal we find a pole mass of $M_\phi = (1017.8 \pm 0.9)$ MeV/c^2, a width of $\sigma_\phi = (6.2 \pm 0.8)$ MeV/c^2 and a total statistics of 168 ± 18 counts. Acceptance and efficiency corrections were obtained by embedding simulated ϕ tracks into real events. From the measured ϕ/K$^-$ multiplicity ratio of 0.34 ± 0.13 one can estimate that 17% of the produced K$^-$ stem from ϕ decays [16]. This indicates that, besides strangeness exchange, phi production and decay should be included in the description of K$^-$ production at SIS energies.

In the case of the Λ and K^0_S various cuts on the primary and secondary vertices strongly reduced the background of uncorrelated pairs, such that an excellent description of the remaining background was achieved in the event-mixing. Again track embedding provided realistic acceptance and reconstruction-efficiency corrections. The corrected transverse-mass spectra of reconstructed K^0_S mesons are shown in Fig. 9. The extrapolation of these spectra to $m_t = 0$ and $m_t \rightarrow \infty$ was performed by means of exponential functions fitted to each rapidity bin. The particle multiplicities in full phase space were then obtained from gaussian fits to the rapidity density distribution.

As in this experiment multiplicities of basically all particles with open strangeness could be determined, it is possible to constrain the missing fraction in the strangeness balance. This part represents mainly the undetected $\Sigma^{0,\pm}$ hyperons which be estimated from the following balance equation

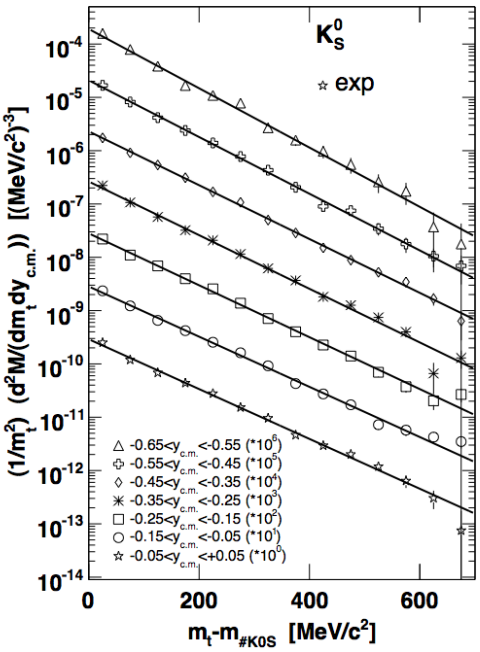

Figure 9: Transverse-mass spectra of reconstructed K^0_S mesons. The spectra are plotted for the laboratory rapidity bins and scaled by the factors indicated.

$$\Sigma^+ + \Sigma^- = K^+ + (K^0 + \bar{K^0}) - (\Sigma^0 + \Lambda) - 3K^- \quad (1)$$

yielding a total multiplicity of charged Σ hyperons of $(0.98 \pm 0.39) \cdot 10^{-2}$. This value is of the same order as the K^0_S multiplicity and only a factor four lower than the combined $\Lambda + \Sigma^0$ multiplicity.

p+p and p+Nb reactions at 3.5 GeV

Next we present a very preliminary result on inclusive and exclusive ω meson production from the 2007 run, performed with a 3.5 GeV proton beam on a liquid hydrogen target. The analysis of the omega in elementary $p+p$ interactions provides a reference for the line shape measurement in p+nucleus and π+nucleus reactions which ultimately aim at establishing medium effects of light vector-meson embedded in nuclei.

The analysis of inclusive electron-positron pair production yields a clear signal at the ω mass in the invariant-mass spectrum (not yet corrected for reconstruction efficiencies, see Fig. 10). More than 65k pairs have been obtained in the total mass range and 250 pairs for the ω peak, reconstructed with a mass resolution of σ =21 MeV/c^2.

A PLUTO simulation folded, with the detector acceptance and reconstruction efficiency, of the contributions to the pair spectrum from known sources is overlaid in Fig. 10. One can see that the peak shape is nicely described by this calculation, demonstrating that the detector

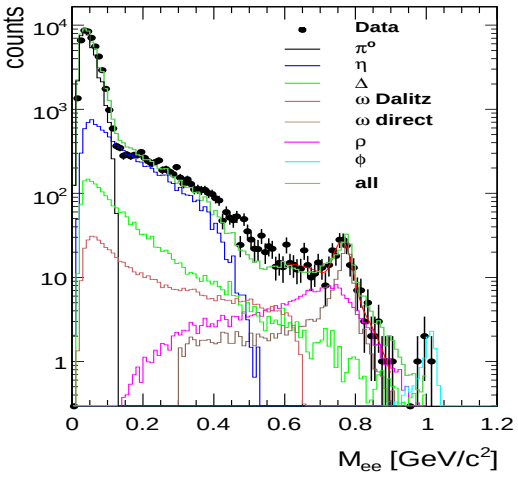

Figure 10: Invariant-mass distribution of e^+e^- pairs emitted into the acceptance of HADES in $p+p$ collisions at 3.5 GeV kinetic beam energy. Data are not corrected for detector efficiency. The contributions to the pair spectrum from a simulation which takes all known sources (see legend) and the detector characteristics into account are shown as well.

response is well understood. Note in particular the sizeable contribution to the peak width from the rho meson and underestimation of the experimental cocktail below the vector meson pole. The latter one might be due to the contribution of higher lying baryon resonances to the ρ meson production not included in the simulation. In a next step also the exclusive reconstruction of the $\omega/\rho \rightarrow e^+e^-$ reaction channel will be studied. It should shed more light on this important aspect which understanding is a prerequisite for the interpretation of the $p+A$ data.

The production of vector mesons off the nucleus has been measured in 2008 in $p+Nb$ collisions at the same bombarding energy. An on-line mass spectrum from this run is shown in Fig. 11. A clear ω peak with a very good signal-to-background ratio and comparable resolution is apparent. For this reaction we have obtained approximately twice the statistics of the $p+p$ run.

Taking the advantage of the powerful PID capabilities of the HADES detector we are also studying in the $p+p$ reaction various reactions channels involving hadrons.

The exclusive omega production channel $p+p \rightarrow p+p+\omega$ is studied in order to assess systematic errors and cross sections. In a first approach, the omega is identified in its hadronic decay channel $\omega \rightarrow \pi^+\pi^-\pi^0$, with the unobserved neutral pion being reconstructed with the missing-mass technique. Fig. 12 shows the invariant-mass spectrum of the 3-pion system with prominent ω and η signals.

The study of the resonance $\Lambda(1405)$ has recently attracted much attention [18], especially in an effort to achieve a better understanding of the K-N interaction, which plays an important role in predictions of possible

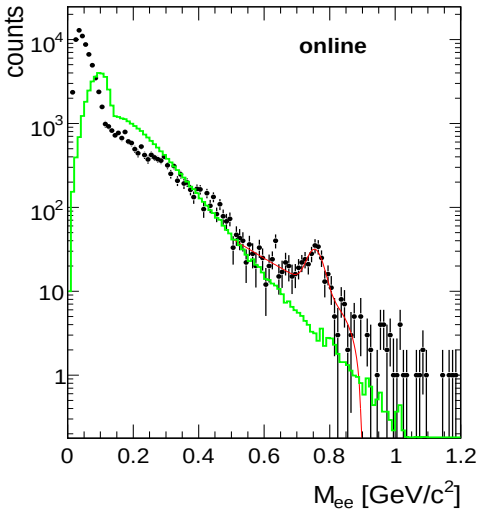

Figure 11: On-line dilepton mass spectrum of e^+e^- pairs from the 3.5 GeV p+Nb reaction. The solid histogram shows the combinatorial background.

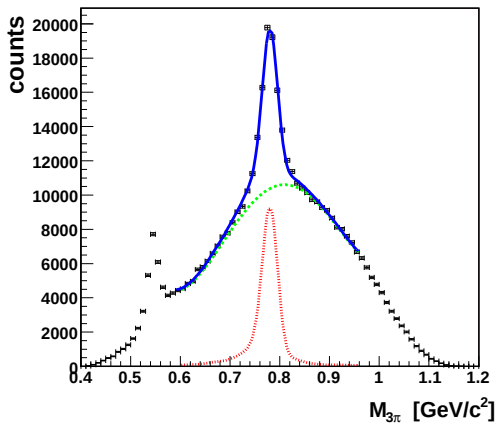

Figure 12: Three-pion invariant-mass spectrum obtained in the $p+p$ reaction at 3.5 GeV. Omega and eta peaks are visible. The non-resonant background is approximated with a polynomial fit.

kaonic clusters [19]. Taking advantage of the powerful PID capabilities of the HADES detector we have started to investigate this aspect of strangeness production in 3.5 GeV p+p reactions. Simulations were performed to estimate the expected yield of $\Lambda(1405)$ and the corresponding background in the measured data. The following reaction of interest was taken into account:

$$p + p \rightarrow \Lambda(1405) + K^+ + p \qquad (2)$$

With the $\Lambda(1405)$ decay channels, $\Lambda(1405) \rightarrow \Sigma^- + \pi^+ \rightarrow n + \pi^- + \pi^+, \Lambda(1405) \rightarrow \Sigma^+ + \pi^- \rightarrow p + \pi^0 + \pi^-, \Lambda(1405) \rightarrow \Sigma^+ + \pi^- \rightarrow n + \pi^+ + \pi^-, \Lambda(1405) \rightarrow \Sigma^0 + \pi^0 \rightarrow \Lambda(1116) + \gamma + \pi^0 \rightarrow p + \pi^- + \gamma + \gamma + \gamma$, one can see that the $\Sigma^0\pi^0$ channel is best suited to distinguish the $\Lambda(1405)$ from the overlapping $\Sigma(1385)$ resonance. Indeed, the $\Sigma(1385)$ decays like the $\Lambda(1405)$ into $\Sigma\pi$, but, due to isospin conservation, the decay $\Sigma(1385) \rightarrow \Sigma^0\pi^0$ is forbidden. This allows to disentangle experimentally the two resonances as already shown in [20]. Including in the simulations the geometrical detector acceptance as well as the efficiency of the trigger and track reconstruction, the amount of expected $\Lambda(1405)$ in the decay channel $\Sigma^0\pi^0$ has been estimated. In the statistics collected for the p+p at 3.5 GeV reaction we expect about 400 counts for this particular channel. These events are going to be reconstructed in an exclusive analysis.

As a first step of the data anaysis, the $\Lambda(1116) \rightarrow p\pi^-$ has been identified. Figure 13 shows the invariant-mass distribution of $p-\pi^-$ pairs reconstructed in $p+p$ at 3.5 GeV data. A clear peak is visible at the position corresponding to the Λ mass, with a signal-to-background ratio of about 1/4. The total statistics of reconstructed Λ hyperons amounts to 135.000 counts and represents a good starting point for the more sophisticated analysis of the $\Lambda(1405)$ signal.

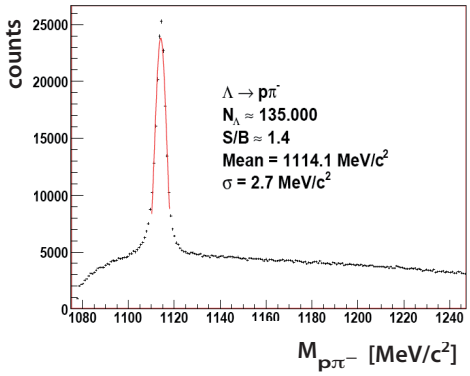

Figure 13: Invariant-mass distribution of $p-\pi^-$ pairs reconstructed in the $p+p$ data at 3.5 GeV.

Status of the upgrade project

During 2009 data taking is suspended in order to install and commission new detector components and to upgrade the digital part of the data acquisition system of HADES. With all new systems in place, HADES will be able to take data for Au+Au collisions at a rate of 20 KHz and up to a factor two faster for lighter collisions systems. Among the detector parts to be replaced are all six chambers of the inner tracking plane and the small-angle time-of-flight system (TOFINO) with high-granularity RPC modules [21].

The innermost tracking plane of HADES receives the same integral dose of radiation while having substantially smaller dimensions than the outer planes, although at same granularity. To guarantee stable operation at the much higher interaction rates and particle multiplicities anticipated in the upcoming runs, the collaboration decided to rebuild the MDC-I chambers by introducing several design

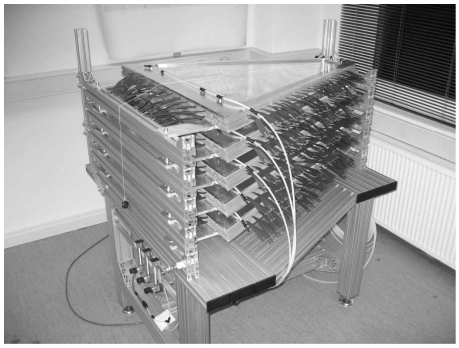

Figure 14: A stack of five (of the seven assembled) MDC-I chambers flashed with gas; the drift-chambers are ready for HV conditioning.

changes compared to the original concept and to replace the current ones after ten years of successful operation. Among those design changes are: (1) Cu/Be field wires providing less critical constraints on the mechanical wire tension and long-term stability, and (2) an optimized frame design. The redesign and construction of the new chambers was carried out in the detector laboratory of the Forschungszentrum Dresden-Rossendorf. The ambitious time schedule was kept and the assembly of seven new chambers (six + spare) was completed in November 2008 (see Fig. 14). Meanwhile, the first chamber has received its front-end electronics and the new read-out is being commissioned. This modified read-out system implements data transfer by means of Polymeric Optical Fibres (POF); it is described in detail in a separate report.

A major improvement of the spectrometer in terms of granularity and particle identification capability will be achieved after installation of the new RPC time-of-flight detectors. The assembly of the sectors is well progressing. All individual single shielded RPC cells are manufactured and four sectors assembled. A complete system, consisting out of one sector and the full read-out chain was successfully tested at GSI (see separate contribution to this annual report).

In the scope of the data acquisition upgrade, essentially all read-out controllers and trigger boards are replaced, introducing a modular system integrating trigger distribution, data transfer and slow-control data traffic to the same optical link. A generic protocol was developed, providing different channels for the different tasks to facilitate the communication (see separate report). The read-out and trigger distribution boards are based on the universal HADES-TRB board to which detector specific add-on boards are mounted. For all cases, prototype boards were produced and successfully tested. Meanwhile mass production of all board types was started.

According to the present planning, the commissioning of the fully upgraded spectrometer with parasitic beam will start in the late fall of 2009.

The collaboration gratefully acknowledges the support by BMBF grants 06MT238TP5, 06GI146I, 06F-140, 06DR135, and DFG EClust 153 (Germany), by GSI (TM-KRUE, GI/ME3, OF/STR), by grants MSTM LC07050 and GA AS CR IAA100480803 (Czech Republic), by grant KBN 1P03B 056 29 (Poland), by INFN (Italy), by CNRS/IN2P3 (France), by grants MCYT FPA2000-2041-C02-02 and XUGA PGID T02PXIC20605PN (Spain), by grant UCY-10.3.11.12 (Cyprus), by INTAS grant 06-1000012-8861 and by EU contract RII3-CT-2004-506078, and DIRAC-PHASE-1 contract 515876 .

References

[1] G. Agakichiev *et al.*, HADES Collaboration, Phys. Lett. B 663, 43 (2008).

[2] G. Agakichiev *et al.*, HADES Collaboration, Phys. Rev. Lett. 98, 052302 (2007).

[3] R. Shyam and U. Mosel, Phys. Rev. C67, 065202 (2003).

[4] L. P. Kaptari and B. Kämpfer, Nucl. Phys. A 764, 338 (2008).

[5] M. I. Krivoruchenko and A. Faessler, Phys. Rev. D 65, 017502 (2002).

[6] S. Teis *et al.*, Z Phys. A 356, 421 (1997).

[7] http://kaa.desy.de/edda/Edda.html.

[8] J. Bystricky *et al.*, J. Physique 48, 1901 (1987).

[9] W. Wilson *et al.*, Phys. Rev. C 57, 1865 (1998).

[10] K. Shekhter *et al.* Phys. Rev. C 68, 014904 (2003).

[11] S. Lang "Analyse der Elektronenpaarproduktion im Stoßssystem Ar+KCl bei 1.76 AGeV", Dissertation, Fachbereich Physik, U. Frankfurt, 2008.

[12] F. Krizek "Study of inclusive electron-positron pair production in collisions of Ar+KCl at 1.756 AGeV", Dissertation, Czech Technical U. in Prague, 2008.

[13] I. Fröhlich *et al.*, contribution to this Annual Report.

[14] I. N. Mishustin, J. Schaffner-Bielich, and B. Jakob, Nucl. Phys. A 625, 325 (1997).

[15] A. Schmah, "Seltsamkeit-Produktion in Ar+KCl Reaktionen bei 1.756 AGeV", Dissertation, Fachbereich Physik, TU Darmstadt, 2008.

[16] G. Agakichiev *et al.*, HADES Collaboration, arXiv:nucl-exp/0902.3487.

[17] A. Förster *et al.*, Phys. Rev. C 75, 024906 (2007).

[18] T. Hyodo et at, arXiv:nucl-th/0802.2212v2.

[19] Y. Akaishi and T. Yamazaki, Phys. Rev. C 65, 044005 (2002).

[20] I. Zychor *et al.* Phys. Lett. B 660, 167 (2008).

[21] D. Belver *et al.*, to be published in Nucl. Instrum and Meth. (http://dx.doi.org/10.1016/j.nima.2008.12.135).

Determination of the η form factor in p+p reactions at HADES*

B. Spruck for the HADES Collaboration[1]
[1]II. Physikalisches Institut, Universität Gießen

We report on the measurement of the electromagnetic transition form factor of the η meson in the $p + p \rightarrow pp\eta \rightarrow pp e^+e^-\gamma$ exclusive reaction channel at two different kinetic energies (2.2 GeV and 3.5 GeV, taken in 2004/2007 respectively). The particle identification has been obtained by the following methods: electrons and positrons by a corresponding ring in the Cherenkov counter, protons by using a two dimensional condition on the beta versus momentum plane. Background from the other reaction channels is reduced by exploiting the kinematic constraint of the missing γ in the $\eta \rightarrow e^+e^-\gamma$ decay via kinematic fit. The produced ηs are identified by the missing mass of the two protons. Suppression of conversion pairs is achieved by requiring an opening angle of the pair $\alpha_{e^+e^-} > 6^\circ$.

For acceptance and efficiency corrections a simulation of this channel with Pluto [1] was done and analysed under the same condition as the experimental data. A weighted distribution of the invariant pair mass was used to increase statistics in the high mass region.

The η signal in the missing mass of the two protons (fig. 1) is fitted in slices of the invariant mass of the e^+e^- pair with a signal plus background function. Every event is filled into these slices with a weight taken from the acceptance and efficiency correction. The obtained signal (fig. 2) is the measure of the yield in that specific bin of the invariant mass. Dividing the data points by the QED expectation results in the form factor $F(q^2)$ (fig. 3). The points are fitted by a one pole approximation $F\left(q^2\right) = \left(1 - M^2/q^2\right)^{-1} = \left(1 - bq^2\right)^{-1}$. A pole mass $M = 665^{+325}_{-55}\ MeV$ is obtained, which corresponds to a slope parameter of $b = 2.3^{+0.4}_{-1.3}\ GeV^{-2}$ at mass equal to zero.

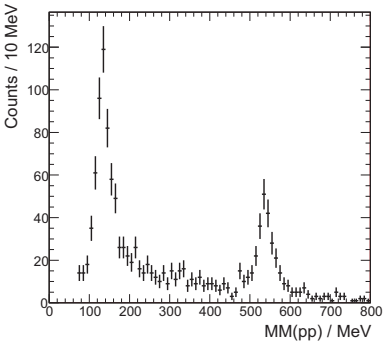

Figure 1: Missing mass of the two protons after kinematic fitting and cutting on opening angle $\alpha_{e^+e^-} > 6^\circ$ and e^+e^- invariant mass >50 MeV. Error bars are statistical errors.

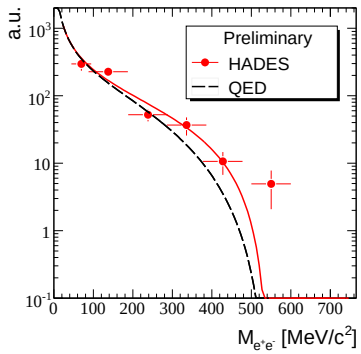

Figure 2: Invariant mass of the e^+e^- pair. The QED prediction is plotted as a dashed curve. Error bars are statistical errors only. The solid curve is a fit to the data, taking only points up to 500 MeV into account.

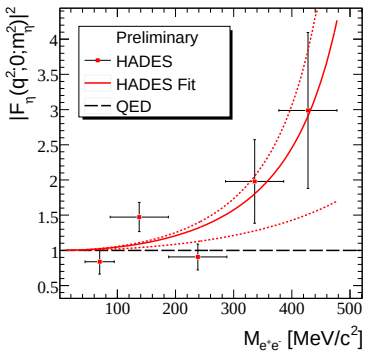

Figure 3: The $\eta \rightarrow e^+e^-\gamma$ transition form factor derived from p+p reactions at 2.2 GeV and 3.5 GeV data. Error estimates of the fit are indicated by dotted curves.

Result

Taking together both runs, the statistics of 200 events exceeds that of other published experiments in the e^+e^- channels [2,3]. In contrast to $\mu^+\mu^-$ results, which contain much higher number of decays, the full invariant mass range is covered.

Within error bars, this result is consistent with results obtained by other experiments and with expectations from the VMD model.

References

[1] I. Fröhlich et.al, arXiv:0708.2382v2

[2] L. G. Landsberg, Phys. Rep. 128, 301 (1985)

[3] M. N. Achasov et.al, PLB 504, 275 (2001)

* Work supported by BMBF 06GI146I and GSI

FOPI's Multi-strip Multi-gap RPC ToF Capability for Kaon Identification *

T. I. Kang[†1], N. Herrmann[2], K. Piasecki[2], K. D. Hildenbrand[3], A. Schüttauf[3], M. Kiš[3], M. S. Ryu[1,2], and the FOPI Collaboration[3]

[1]Korea University, Seoul, Korea; [2]Physikalisches Institut, Universität Heidelberg, Germany; [3]GSI, Darmstadt, Germany

The FOPI collaboration studies bulk properties of nuclear matter as well as in-medium effects on the properties of hadrons in a hot and dense environment by the measurement of the yields, the momentum distributions and the azimuthal emission pattern of hadrons with respect to the reaction plane. At SIS/GSI, $K^{\pm}$ are produced in nucleus-nucleus collisions at sub-threshold energies [1]. Theory suggests that the kaon effective masses would change in the medium, *i.e.* the K^+ mass increase slightly, while the K^- mass drops considerably with increasing baryon density. These changes can be understood as a consequence of the density-dependent kaon-nucleon potential. The measurement of the the flow of charged kaons can provide important information on the in-medium potential [2]. However, due to the low production rate of kaons such measurements are difficult and, in particular for K^-, limited by statistics.

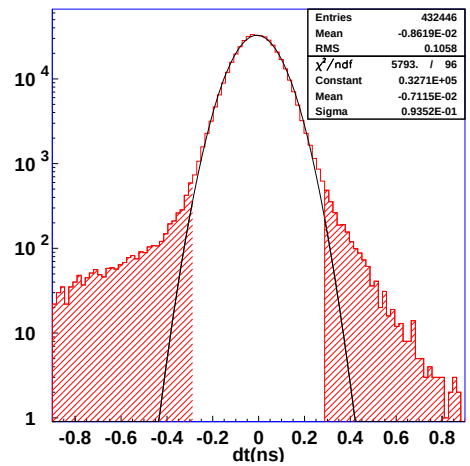

Figure 1: Time spectrum of the FOPI's MMRPC system for the whole system. The non-gaussian tail component is less than 1.2% in |dt| > 300 ps. The time resolution is σ_{ToF} = 94 ps.

To improve the charged kaon measurement, FOPI has successfully upgraded the Time-of-Flight detector system with a novel Multi-strip Multi-gap RPC (MMRPC) in 2007 [3]. In first experiments with this new device ^{58}Ni + ^{58}Ni collisions have been measured at 1.91 AGeV in September 2007 and April 2008. Figure 1 shows the Time-of-Flight resolution, σ_{ToF} = 94 ps, which was derived from fast pion tracks. The tail portion is partially coming from matching conditions, which indicate the intrinsic contribution of the RPC is clearly below 1.2%. The decomposition is under investigation. It should be noted that the σ_{ToF} = 94 ps corresponds to the full system time resolution including the start detector. With this improved time resolution, the charged kaon identification could be extended up to p $\simeq$ 1 GeV/c (K^+) and p $\simeq$ 0.8 GeV/c (K^-) [4].

Kaons are identified by matching tracks reconstructed in the central drift chamber (CDC) with hits recorded in the MMRPC. For the K^- mass spectrum shown in Figure 2, tracks corresponding to momentum up to 0.8 GeV/c were considered and strict matching quality cuts between the CDC and the RPC were applied.

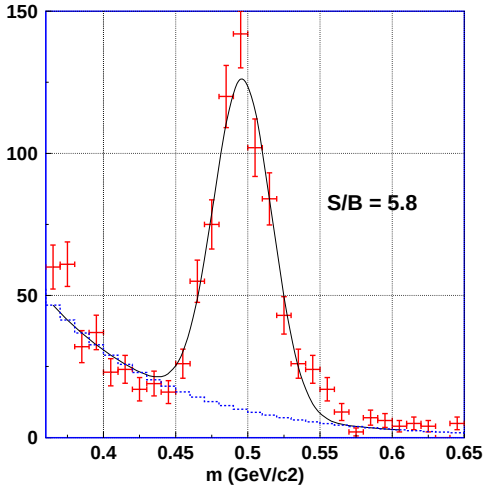

Figure 2: K^- mass spectra measured in ^{58}Ni + ^{58}Ni collisions at 1.91 AGeV.

In the September 2007 beam time, in total 1.76 $\times$ 10^7 events were recorded, correspoding to the most central 50 % of total geometric reaction cross section and about 600 K^-s are identified with a ratio of signal to background up to 5.8. Figure 2 demonstrate the excellent kaon identification as made possible by the new FOPI MMRPC system. From the kaon flow analysis which is in progress we expect to obtain further information on the in-medium effects of hadrons in dense baryonic matter.

References

[1] K. Wiśniewski *et al.*, Eur. Phys. Journ. A 9 (2000) 515.

[2] G. Q. Li *et al.*, Phys. Rev. Lett. 74, (1995) 235-238.

[3] A. Schüttauf *et al.*, Nucl. Phys. B Proc. Supp. 158 (2006) 52.

[4] M. Kiš *et al.*, GSI Scientific Report 2007 p. 226.

* Work supported by DFG 446 KOR 113/216/0-1, BMBF 06HD190I and EU/FP6 I3 HPcontract no. R113-CT-2004-506078.

† t.i.kang@gsi.de

Phi mesons from Ni+Ni collisions at 1.91A GeV measured by FOPI *

K. Piasecki† [1,2], N. Herrmann[1], P. Gasik[2], Z. Tymiński[2], and FOPI collaboration[1]

[1]Physikalisches Institut, Universität Heidelberg; [2]Institute of Experimental Physics, University of Warsaw, Poland

In heavy-ion collisions at 1-2A GeV the measurement of ϕ mesons can provide important insight into the physics of dense nuclear matter. Within the framework of thermal models, the measured ϕ meson production yield helps to quantify the temperature and baryo-chemical potential reached at freeze-out. In addition, the $\phi \rightarrow K^+K^-$ decay can substantially obscure the signatures of kaon interaction with the surrounding medium and of the related in-medium modification of kaon properties. It is therefore crucial to quantify the fraction of the total kaon yield, in particular the K^- yield, that originates from ϕ meson decays.

The S325 experiment was carried out in September 2007 and April 2008. The current report addresses the analysis of the 2007 data. ^{58}Ni ions from the SIS18 were incident on a ^{58}Ni target (shifted 40 cm upstream) at a beam energy of 1.91A GeV. $1.8{\cdot}10^7$ events were recorded with a trigger selecting a sample of 50±1% most central collisions. For the first time, FOPI made use of a new Multi-strip Multi-gap Resistive Plate Chamber (MMRPC) Time-of-Flight barrel, covering polar angles $36° < \vartheta < 67°$ with respect to the nominal target position and 81% of the full azimuth. An excellent ToF resolution of 100 ps was achieved [1].

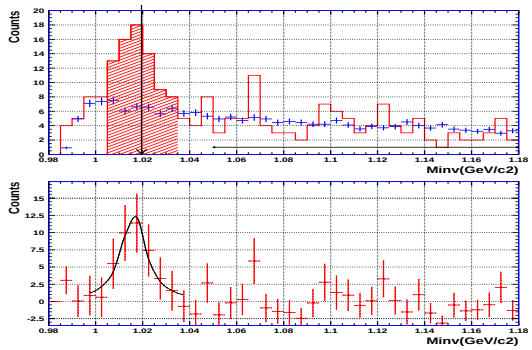

Figure 1: Invariant-mass distribution of K^+K^- pairs and combinatorial background obtained via event mixing (top). A distribution after background subtraction (bottom).

The ϕ mesons were reconstructed in theri K^+K^- decay channel (BR = 49.1%). Charged particle tracks were measured in the central drift chamber for transverse momenta $p_T > 0.1$ GeV/c, and were geometrically matched with hits in MMRPC. Kaon identification could be performed with good quality [2] up to maximum momenta of 1.0 GeV/c for K+ and 0.8 GeV/c for K^-, respectively, which is a significant improvement compared to previous measurements with a Plastic scintillator Barrel [3]. The invariant-mass distribution of K^+K^- pairs shown in Fig. 2 exhibits a clear ϕ-meson signal on top of a combinatorial background which was determined via the event mixing technique and which was normalized to the true pair mass distribution in the range $1.05 < m_{inv} < 1.18$ GeV/c^2. After background subtraction 35±6 ϕ mesons were observed.

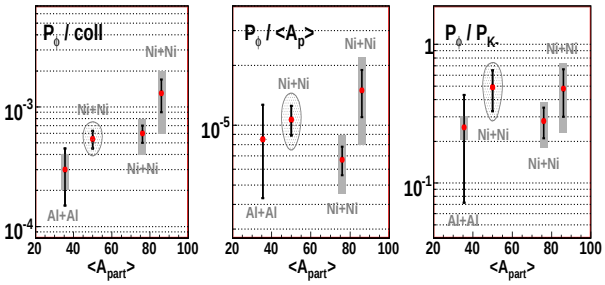

Figure 2: FOPI systematics on ϕ meson production yield (left), scaled with mean number of participants $<A_{part}>_b$ (middle), and ϕ/K^- ratio (right) as function of $<A_{part}>_b$. The results shown in the current report are marked.

The ϕ meson production probability per collision is calculated from

$$P_\phi = \frac{N_\phi}{N_{coll} \cdot BR(\phi \rightarrow K^+K^-) \cdot \varepsilon_\phi} \qquad (1)$$

where N_ϕ is the number of identified ϕ mesons, N_{coll} is the number of collisions, BR is the branching ratio, and ε is the detection efficiency. The efficiency was determined in a full GEANT simulation, including a realistic description of the new MMRPC detector. ϕ mesons were sampled from an isotropic thermal source using the Siemens-Rasmussen formula assuming T=100 MeV and β_{flow}=0.25 [1], and were embedded in UrQMD events. The resulting efficiency of 0.79% includes the geometric and momentum acceptances, kaon decays, tracking and matching efficiencies and internal MMRPC inefficiencies as taken from the experiment. With this value a ϕ meson production yield of $5{\pm}1{\cdot}10^{-6}$ was calculated which has been added to the existing FOPI systematics on ϕ-meson production, c.f. Fig. 2. A careful investigation of systematic uncertainties is ongoing.

References

[1] M. Kiš et al., GSI Scientific Report 2007, p. 226

[2] T.I. Kang et al., GSI Scientific Report 2008

[3] K. Wiśniewski et al., Eur. Phys. J. A9, 515 (2000)

[4] Z. Tymiński et al., NPD Ann. Rep. 2004, p. 13, Warsaw Univ.

* Work supported in part by BMBF 06HD190i and EU/FP6 I3 HP contract no. R113-CT-2004-506078

† kpiaseck@physi.uni-heidelberg.de

[1] based on T_{eff} = 120 MeV obseved for the same colliding system [4]

Centrality dependence of pion and kaon production at SPS energies

H. Beck[1], C. Blume[1], J. Book[1], P. Dinkelaker[1], V. Friese[2], M. Gaździcki[1], C. Höhne[2], D. Kresan[2], M. Mitrovski[1], M. Pohl[1], R. Renfordt[1], T. Schuster[1], H. Ströbele[1], R. Stock[1], and M. Utvić[1]

[1]IKF, Goethe Universtität, Frankfurt am Main, Germany; [2]GSI, Darmstadt, Germany – for the NA49 collaboration

Strangeness production in heavy-ion collisions has always been an important observable for probing the state of matter created in these collisions. A maximum in the relative strangeness yield in central Pb+Pb collisions was measured by NA49 at the CERN SPS at about 30A GeV beam energy [1]. The relative strangeness yield in p+p interactions is significantly lower than in central Pb+Pb collisions at all collision energies and it does not show any non-monotonic structure. Thus a study of the centrality and system size dependence of strangeness production at various energies should significantly improve our understanding of the phenomena observed in central Pb+Pb collisions.

In this report, first results from a reanalysis of the centrality dependence of pion and kaon production with the NA49 detector are presented. Minimum bias Pb+Pb collisions at 40A GeV and 158A GeV beam energy were divided into bins of centrality using information from the veto calorimeter which accepts nearly all beam particles and spectators. Corresponding values for the number of wounded nucleons are calculated from a Glauber model. Major particle identification devices for NA49 are four large volume TPCs providing a measurement of the specific energy loss dE/dx and a TOF wall with an acceptance around midrapidity. Raw yields of K^+ and K^- were extracted from a statistical unfolding of the dE/dx distribution and the time-of-flight measurement (where available) in narrow bins of momentum and transverse momentum. For pions at midrapidity the acceptance of the dE/dx and time-of-flight method is limited to the high p_t region, therefore yields of all negatively charged hadrons from the primary vertex were extracted in bins of rapidity and p_t assuming pion mass. The included background, i.e., contamination by K^-, $\overline{\mathrm{p}}$, e^-, negatively charged hadrons and from the decay of strange particles or from secondary interactions both reconstructed at the primary vertex, were determined by simulation and subtracted. All measured spectra are corrected for geometrical acceptance, in-flight decay of kaons, and reconstruction efficiency. The yield of π^+ is extracted for central Pb+Pb collisions from the π^+/π^- ratio from a dE/dx+TOF analysis assuming that π^- and π^+ have the same p_t and rapidity distributions. Extracted π^+/π^- ratios are 0.93 and 0.90 for 158A GeV and 40A GeV beam energy, respectively. We assume that this ratio is centrality independent.

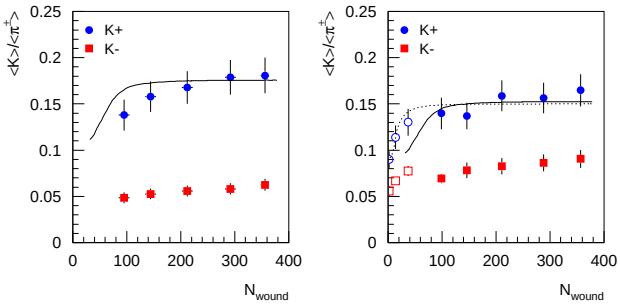

Figure 1: $\langle K^+\rangle/\langle\pi^\pm\rangle$ and $\langle K^-\rangle/\langle\pi^\pm\rangle$ dependence on the number of wounded nucleons for centrality dependent Pb+Pb collisions (filled symbols) at 40A GeV (left) and 158A GeV (right) beam energy ($\langle\pi^\pm\rangle = (\langle\pi^+\rangle + \langle\pi^-\rangle)/2$). Open symbols depict results from pp, semi-central C+C and Si+Si collisions. Lines correspond to calculations from a percolation model for top SPS energy for centrality dependent Pb+Pb collisions (solid) and central collisions of smaller systems (dotted).

Transverse momentum and rapidity distributions for K^+, K^-, and π^- were extracted in 5 bins of centrality and integrated for extracting particle yields in full phase space. Figure 1 shows the extracted dependence of the $\langle K^+\rangle/\langle\pi^\pm\rangle$ and $\langle K^-\rangle/\langle\pi^\pm\rangle$ ratios for 40A GeV and 158A GeV beam energy. The data are compared to results from semi-central C+C and Si+Si collisions [2]. A fast increase of relative strangeness production for small systems saturating at appr. 60 participants (158A GeV) is observed. The data seem to indicate that the saturation sets in somewhat later for the lower energy. Assuming that the $\langle K^+\rangle/\langle\pi^\pm\rangle$ ratio is approximately proportional to the total relative strangeness production, results from a percolation model can be compared to the data [3]. A good agreement is seen for top SPS data, however for centrality dependent Pb+Pb collisions a more peripheral measurement would be desirable in order to investigate the predicted difference between central collisions of small systems and peripheral Pb+Pb. The model assumes that the collisions can be integrated over the longitudinal direction which is a good approximation at higher energies. Whether this also holds for lower energies as e.g. 40A GeV is an open question and might explain the later saturation of the strangeness production in these collisions because of a longitudinal separation of percolation volumes currently not accounted for in the model.

References

[1] C. Alt et al. [NA49 coll.], Phys. Rev. C 77, 024903 (2008).

[2] C. Alt et al. [NA49 coll.], Phys. Rev. Lett. 94, 052301 (2005).

[3] C. Höhne, F. Pühlhofer, R. Stock, Phys. Lett. B 640, 96 (2006).

Two-particle correlations in Pb-Au collisions at 80A GeV beam energy*

S.Schuchmann[1], D.Antończyk[1], and H.Appelshäuser[1]
[1]Institut für Kernphysik, Goethe Universtität, Frankfurt am Main, Germany

In this report new results of a HBT analysis of Pb-Au collisions at 80A GeV beam energy are presented.

HBT parameters

The calibration scheme of the CERES TPC has been improved with respect to the data reconstruction used in [1], which leads to a remarkable decrease of the systematic error for the 80A GeV and 158A GeV data set. Figure 1 shows the new results of the HBT parameters for collisions at 80A GeV in the Bertsch-Pratt parametrization as a function of the transverse pair momentum $k_\perp$. The new values are compared to the published results as well as to the results obtained by the NA49 collaboration for the same beam energy. Systematic errors are depicted in filled boxes around the data points. For the error calculation effects due to finite momentum resolution, the fitting procedure, the Coulomb correction and the applied pair cuts are included. Regarding absolute values, the new analysis yields slightly larger R_{out} and R_{long} parameters in the low $k_\perp$ bins. In comparison to the NA49 results, the recent analysis entails a good agreement between both experiments.

Universal pion freeze-out

The slight growth of R_{long} at low $k_\perp$ consequently leads to an increase of the freeze-out volume, which was introduced in [2]. In Figure 2, showing the excitation function of the freeze-out volume, the recent CERES results for 80A GeV and 158A GeV are presented together with the previous results. The visible increase of the volume for these two energies leads to an increase of the mean free path of pions at freeze-out, which is defined by $V_f/(N\sigma)$. As it can be deduced from Fig 2, the mean free path features a general maximum at energies of $\sqrt{s_{NN}} \simeq 8-10$ GeV, which yields a 30% enhancement compared to the other energies with a mean free path of ~ 1 fm. The new CERES results suggest a confirmation of this enhancement, that could be interpreted as a modified freeze-out condition for pions in this small energy window.

However, at very low collision energies, the remaining discrepancy between CERES and NA49 as well as large errors of the AGS results do not yet allow further conclusions about an universal pion freeze-out scenario. In order to deduce a satisfactory interpretation from the excitation function of the freeze-out volume and the mean free path, a re-analysis of the 40A GeV data set remains as a mandatory task. Furthermore, new measurements in the AGS energy region would have an important impact on a confirmation of the indicated maximum mean free path around low SPS energies. Hence, we are looking forward to the future activities within the FAIR project at GSI and to the low energy run at RHIC, being performed soon.

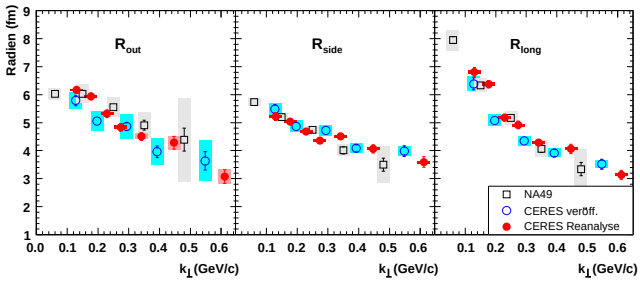

Figure 1: HBT radii vs. $k_\perp$ for 80A GeV from CERES (old: open circles, new: filled circles) and NA49 (open squares) [3]. Filled boxes indicate the systematic errors.

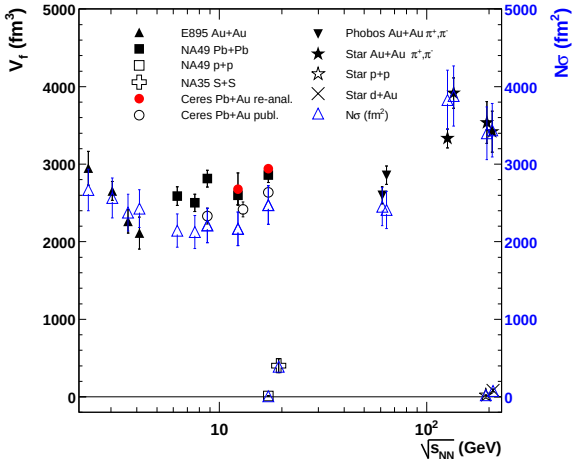

Figure 2: The Freeze-out volume V_f and the effective cross section for pion interactions in the medium $N\sigma$ (open triangles) vs. collision energy. For references see [2].

References

[1] H. Tilsner and H. Appelshäuser [CERES Collaboration], Nucl. Phys. A **715** (2003) 607.

[2] GSI scientific report 2007, NQMA-EXPERIMENTS-16, p.180

[3] C. Alt *et al.* [NA49 Collaboration], Phys. Rev. C **77** (2008) 064908

*Work supported by GSI Helmholtzzentrum für Schwerionenforschung GmbH and BMBF.

UNICOR - experiment independent two-particle correlation analysis

D. Miśkowiec
GSI, Darmstadt, Germany

Two-particle correlation functions provide experimental access to space-time extension of the particle source in nuclear collisions [1]. A typical correlation analysis involves i) looping over events, ii) looping over track pairs within the event, iii) calculating the momentum difference, iv) filling the pair histogram at the bin corresponding to this difference, v) repeating all the above but with a double loop over events and taking the two particles from different events (event mixing), and vi) dividing the true pair distribution by the mixed one to get the correlation function. The part related to reading events and applying experimental cuts is an order of magnitude less laborious (in terms of the number of lines of code) than pairing, event mixing, kinematics, and histogramming. A natural question arises whether the analysis software can be split into the experiment specific and the experiment independent pieces, such that the same analysis can be run on various data sets by changing only the interface part. I report here on a two-particle analysis package that was developed along these lines.

UNICOR is written in C++ and is strongly based on the ROOT data analysis framework [3]. It can be at present used to analyze data from CERES, ALICE, and CBM; interface to FOPI is to be added. The scheme is shown in Fig. 1. For each experiment an interface is implemented as a class inheriting from the event class with which the events were stored on one side, and from the `DEvent` class on the other, the latter being used by the subsequent analysis which calculates and histograms track pair variables. Some event and single track variables are being histogrammed as well. The only trace of the data source remains in the pseudorapidity range of the resulting histograms.

Multidimensional histograms are the second special feature of UNICOR. In a typical correlation analysis three-dimensional (three components of the momentum difference vector) correlation functions are produced for several pair-p_t and rapidity bins. Azimuthal analyses [4] require,

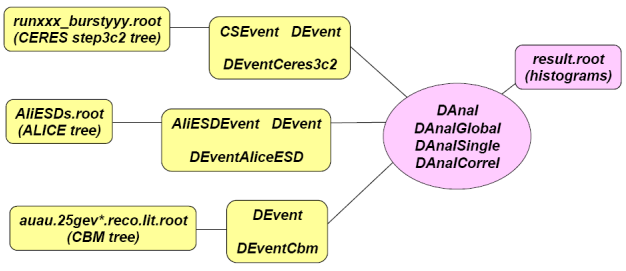

Figure 1: UNICOR scheme. Thin interfaces handle the data format of CERES, ALICE, and CBM. The subsequent correlation analysis is identical for all three experiments.

in addition, cuts on the emission angle. This results in a three-dimensional array of three-dimensional histograms, and the user has to keep track of the p_t, rapidity, and angle associated to each correlation function histogram. A six-dimensional histogram provides a much more elegant solution while requiring the same amount of memory. In the limit of small bin size this histogram would contain the full information about the two-particle correlations. In practice, the computer memory limits the maximum number of bins.

UNICOR was run on data from minimum bias Pb+Au collisions at 158 A GeV/c from CERES, pp collisions at $\sqrt{s}$=10 GeV simulated for ALICE, and central Au+Au at 25 A GeV/c simulated for CBM. Correlation functions for pairs of negative pions are shown in Fig. 2. The CERES

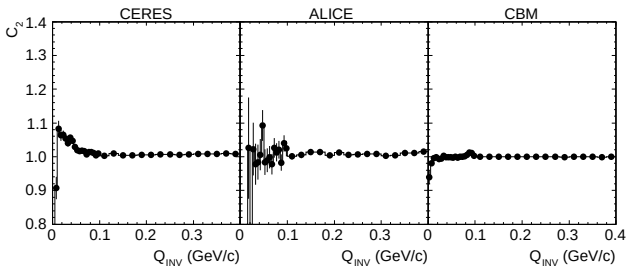

Figure 2: Two-pion correlation function for π^- from CERES, ALICE, and CBM (from left to right). ALICE and CBM data are simulated and their C_2 should be flat.

correlation function (left) was obtained with a rudimentary pion identification and without the two-track resolution cut; an enhancement originating from the Bose-Einstein quantum statistics is nevertheless clearly visible. The other two correlation functions are flat as expected for simulated data. While only one-dimensional projections are presented in Fig. 2, complete six-dimensional correlation functions are available as multidimensional histograms. Whether the variables chosen for the axes and the bin sizes are sufficient to study e.g. the out-side-long [5] radii in a system other that the pair rest frame remains to be verified.

References

[1] M.A. Lisa et al., Ann. Rev. Nucl. Part. Sci. 55, 357 (2005).

[2] `http://wiki.gsi.de/cgi-bin/view/Personalpages/UnitedGenerators`

[3] `http://root.cern.ch/`

[4] M.A. Lisa et al., Phys. Lett. B496, 1 (2000); J. Adams et al., Phys. Rev. Lett. 93, 012301 (2004); D. Adamová et al., Phys.Rev. C78:064901, 2008.

[5] G.F. Bertsch, Nucl. Phys. A498, 173c (1989); S. Pratt, Phys. Rev. D33, 1314 (1986).

Event-by-event Fluctuations of the Kaon to Pion Ratio in NA49

H. Beck[1], C. Blume[1], J. Book[1], P. Dinkelaker[1], V. Friese[2], M. Gaździcki[1], C. Höhne[2], D. Kresan[2], M. Mitrovski[1], M. Pohl[1], R. Renfordt[1], T. Schuster[1], H. Ströbele[1], R. Stock[1], and M. Utvić[1]

[1]IKF, Goethe Universtität, Frankfurt am Main, Germany; [2]GSI, Darmstadt, Germany – for the NA49 collaboration

Non-statistical event-by-event fluctuations are considered as an important signal for the critical endpoint of the QCD phase diagram. Event-by-event fluctuations of different observables are thus investigated in detail in current experiments.

The aim of this work is the centrality dependence of K/π fluctuations in Pb+Pb collisions at 158 AGeV. In this report we present first steps such as the energy (for validation of the analysis software) and centrality bin size dependence of the event-by-event kaon to pion yield ratio fluctuations measured with the NA49 experiment.

NA49 is a large acceptance hadron spectrometer at the SPS [1]. Its main particle identification detectors are four large volume TPCs, two of them located inside the magnetic field for momentum measurements. The specific energy loss dE/dx measured in the two large main TPCs outside the magnetic field was used for particle identification in this work. With a dE/dx resolution of 4% (100 points on the track) particles can only be identified on a statistical basis. Here a maximum likelihood method was used to measure relative particle yields event-by-event. For a detailed description of the method see [2].

The inclusive dE/dx spectrum was fitted in charge, momentum, transverse momentum and azimuthal angle bins. The parameters obtained from this fit are used to form Probability Density Functions (PDFs), which were then used for event-by-event fits. The stability of the fit with respect to different centrality selections was checked.

Minimum bias Pb+Pb collisions at 158 AGeV beam energy were divided into bins of centrality using information from the veto calorimeter which accepts nearly all beam particles and spectators.

Fluctuations from e.g. finite number statistics or detector resolution were estimated using the event mixing method which destroys all correlations present in one event. For this procedure, only events within the same centrality classes were mixed.

The energy dependence of dynamical fluctuations of the kaon to pion ratio is shown in figure 1 for two different momentum intervals showing little effect of the fluctuations on the selected range. An upper momentum cutoff of 40 GeV/c for beam momenta 20, 30 and 40 AGeV and 120 GeV/c for 80 and 158 AGeV was chosen as well as a common cutoff of 16 GeV/c for all beam energies. Results are shown for the 3.5% most central Pb+Pb collisions at beam momenta of 20, 30, 40, 80 and 158 AGeV. We observe an increase of the fluctuations towards lower SPS energies as already shown and discussed by NA49 [2].

A study of the centrality dependence of possible dynamical fluctuations is hampered by the need to select event samples in finite size centrality intervals in which seemingly dynamical fluctuations are in reality due to a trivial centrality dependence. A first step towards a centrality dependence, the centrality bin size dependence of the dynamical fluctuations of the kaon to pion ratio in Pb + Pb collisions at 158 AGeV is shown in figure 2. Different centrality selections create differences in the dynamical fluctuations on the order of two percent which means that the volume fluctuations to a large extend (1 - 2% remaining) are cancelled in the ratio. Different symbols on the figure correspond to different year and beam conditions of the data taking. This small dependence of dynamical K/π fluctuations on the bin width will now allow to extract the fluctuations in centrality steps of 5% to 10%.

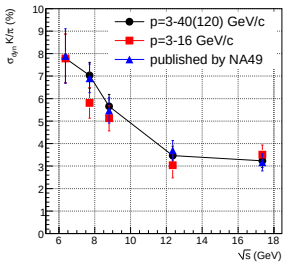

Figure 1: Energy dependence of dynamical fluctuations of the kaon to pion yield ratio in the 3.5% most central Pb+Pb collisions.

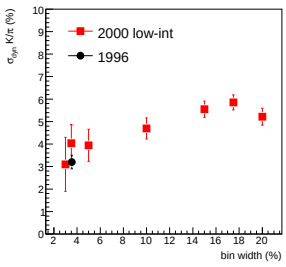

Figure 2: Centrality bin size dependence of dynamical fluctuations of the kaon to pion yield ratio in central Pb+Pb collisions at 158 AGeV.

References

[1] S.V.Afanasiev et al. Nucl. Instr. and Meth. A 430 (1999) 210 - 244

[2] C.Alt et al. arXiv:0808.1237 [nucl-ex]

Centrality dependence of (anti-)proton spectra in Pb+Pb collisions at 158A GeV measured at the CERN SPS

H. Beck[1], C. Blume[1], J. Book[1], V. Friese[2], M. Gaździcki[1], C. Höhne[2], D. Kresan[2], M. Mitrovski[1], R. Renfordt[1], T. Schuster[1], R. Stock[1], H. Ströbele[1], M. Utvić[1], and for the NA49 Collaboration

[1]IKF, Goethe Universität, Frankfurt am Main, Germany; [2]GSI, Darmstadt, Germany

The (anti-)proton yields in centrality selected Pb+Pb collisions at 158A GeV were measured by the NA49 Collaboration. The NA49 detector is a large acceptance spectrometer with particle identification capabilities. The detector is located at CERN, Geneva, where the Super-Proton-Synchrotron provides a beam of lead nuclei with energies up to 158A GeV, which are collided with a fixed lead target. Particle identification was possible in the c.m. rapidity interval -0.42 $<$ y $<$ 1.58 (corresponding to the laboratory momentum range 5 - 63 GeV/c) via the specific energy loss dE/dx in the TPC detector gas. It is done in bins of total and transverse momentum. The (anti-)proton yields are obtained in each bin from a fit to the dE/dx distributions. These yields are then corrected for acceptance, efficiency, and for feed-down from weak decays. The rapidity densities are calculated by integrating the measured transverse momentum distributions and applying a relatively small correction for losses in unmeasured regions. An earlier analysis of the same data set using a combined dE/dx-TOF method [1] provides a reference dn/dy measurement near midrapidity. The differences between the two results are below 5%.

Net-proton spectra are obtained from those of all protons by subtracting the distributions of anti-protons. The midrapidity net-proton yield normalized to the number of wounded nucleons N_W rises by a factor 1.3 from peripheral to central collisions (see Fig.1a). The spectra are compared with two model calculations. In contrast to UrQMD [2] (see Fig. 1b), the HSD [3] model describes the data well (see Fig. 1c). The difference in the rapidity distributions between HSD and UrQMD is due to a different definition of "formed" and "unformed" hadrons. In HSD a hadron is considered as "formed" only if the energy density (in the local cell) is less than a critical value, which is taken to be 1 GeV/fm^3 in line with lattice QCD. Otherwise, the hadron is accepted as "unformed" and can not interact with other hadrons until the energy density drops to the critical value. This energy density criterion is not included in UrQMD which leads therefore to a substantial overestimate of energy loss in collisions in which high energy densities are reached [3].

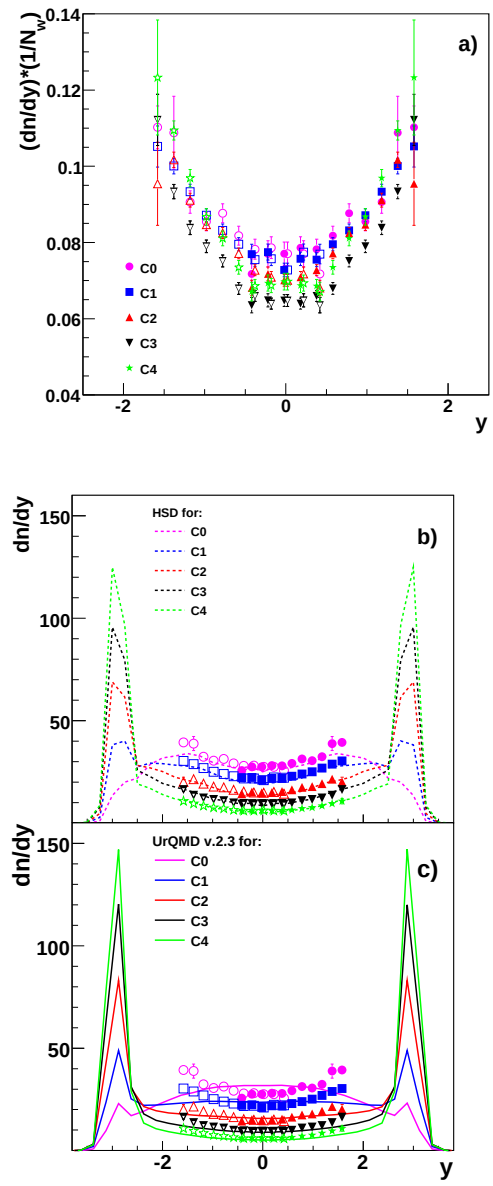

Figure 1: a) net-proton rapidity spectra in Pb+Pb collisions at 158A GeV for different centralities. The spectra are normalized by the average number of wounded nucleons N_W. b) shows the comparison with the HSD-model and c) with the UrQMD v2.3 model.

References

[1] C. Alt *et al.* [NA49 Collaboration], Phys. Rev. C **73**, 044910 (2006).

[2] H. Petersen, M. Bleicher, S. A. Bass and H. Stocker, arXiv:0805.0567 [hep-ph].

[3] H. Stoecker, Phys. Rev. C **66** (2002) 054903.

Study of the Measurement of Quarkonia in different ALICE Central Barrel Detector Configurations

A. Bernhard[1], F. Kramer[1], and C. Blume[1]

[1]Institut für Kernphysik, Goethe-Universität, Frankfurt am Main

Introduction

The measurement of quarkonia is a very promising observable for the study of the quark gluon plasma. The central barrel detectors of ALICE (ITS, TPC, TRD) will reconstruct heavy $q\bar{q}$ states, both in heavy ion collisions and in p+p collisions as reference, via their decay into an electron-positron pair. The TRD subdetector [1] will provide excellent electron identification for this purpose. However, in the first periods of data taking at the LHC the TRD will not yet be completely installed.

The Analysis

The expected performance for measuring quarkonia in $\sqrt{s} = 14$ TeV minimum bias p+p collisions via their decay into e^+e^- has been studied. Several different detector configurations have been simulated, all of them including the TPC and ITS: The fully installed TRD, the situation with two and with four installed TRD supermodules and, for comparison, the setup with no TRD. Fast simulations have been performed, using the event generator PYTHIA and a parameterization of the detector response.

Results of this analysis [2] are shown in Fig. 1. The invariant mass spectra of the e^+e^- pairs of two different cases are drawn. The upper part depicts the case including the complete TRD. The lower part represents the situation with four installed TRD supermodules, which is the minimum scenario for the first data taking period. In 10^8 min. bias events, 7241 entries for the setup including the full TRD and 7867 entries for the one comprising four TRD supermodules were registered. The high number of entries below 300 MeV/c^2 is due to Dalitz decays of π^0 and η particles. The maxima at 3.1 GeV/c^2 correspond to the J/Ψ, the others the ω (782 MeV/c^2), the ρ (775 MeV/c^2) and the ϕ mesons (1.02 GeV/c^2).

In the setup with only four TRD supermodules and especially at masses smaller than 2 GeV/c^2 a lot of misidentified pions make an entry in the spectrum, while these are suppressed by the fully installed TRD. The height of the signals above background is similar in both cases since the electron efficiency is set to 90% likewise. As can be seen in Fig. 1 the TRD becomes very important for precision measurements with a large S/B ratio, especially for masses in the Υ region. The Υ, however, will not be accessible within 10^8 min. bias reactions. For this a trigger on high momentum electrons will be necessary, which is the other main puprose of the TRD.

With a fully installed TRD the remaining main sources for uncorrelated background around the J/Ψ mass region are due to semileptonic decays of open heavy flavour particles. The simulation of the various TRD setups at first p+p data taking have shown that for a measurement with a high signal to background ratio within an incomplete TRD acceptance a minimum of four TRD supermodules are needed to find a significant signal in 10^8 min. bias events.

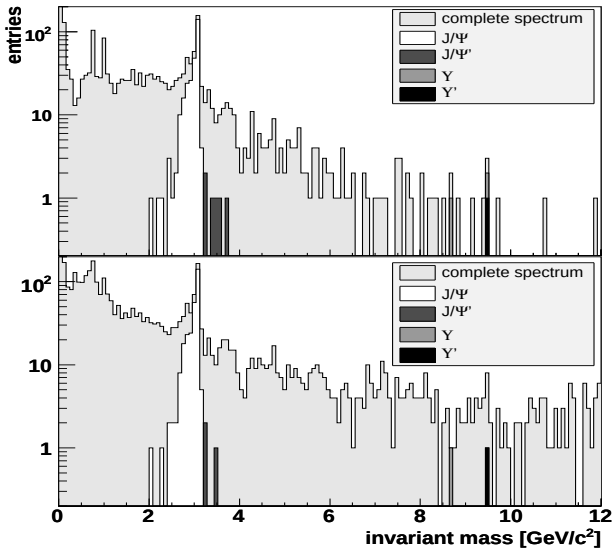

Figure 1: Invariant mass spectra of e^+e^- pairs in 14 TeV p+p collisions, for the scenarios with the full TRD (upper plot) and with four TRD supermodules (lower plot)

Summary and Outlook

Simulations of quarkonia measurements with realistic ALICE central barrel detector setups for first p+p data taking at LHC have been performed. As expected the TRD dramatically reduces the uncorrelated background from misidentified pions. A clear J/Ψ signal is visible within the simulated statistics. The measurement of the Υ family will require the complete TRD and an additional trigger.

Since the LHC startup schedule has changed additional TRD supermodules will be installed when the first collisions take place. This will be taken into account in future studies.

References

[1] The ALICE Collaboration, "TRD Technical Design Report", CERN/LHCC 2001-021, (2001).

[2] A. Bernhard, "Studie zur Messung von Quarkonia mit zentralen ALICE-Detektoren in 14 TeV p+p-Ereignissen", Bachelor thesis, Goethe University Frankfurt (2008).

Jet-Like Correlations in *pp* collision in the ALICE detector at the LHC*

J. G. Ulery[1] and H. Appelshäuser[1]
[1]Institut für Kernphysik, Goethe Universtität, Frankfurt am Main

Introduction

Jet-like correlations can provide insights into the physics of jets. Partonic jets are calculable in pQCD; however, jet fragmentation cannot be calculated through current methods. In *pp* collisions, jet-like correlations can be used to study jet fragmentation. Jet-like correlations in *pp* collisions also provide a reference for heavy-ion collisions. In heavy-ion collisions these correlations can be used to study the modification of the jet by the medium and the modification of the medium by the jet. The ALICE experiment will study jet-like correlations at the LHC. Data from *pp* collisions at $\sqrt{s_{NN}} = 10$ TeV is expected to be available first; therefore this report will primarily discuss jet-like correlations in *pp* collisions.

Jet-Like Correlations

In jet-like correlations a trigger particle is chosen to increase the selection of jets. All intermediate and high transverse momentum, p_T, particles are used as trigger particles. The trigger particles are binned according to their transverse momentum to give different jet selections and trigger biases. The associated particles are plotted using their angle relative to the trigger particle angle. For high p_T triggers the trigger particle p_T is approximately the jet p_T and the trigger particle direction is approximately the direction of the jet-axis.

In these correlations some particles may not be jet-like correlated with the trigger. These particles must be subtracted to obtain the true jet-like correlation. This background can be constructed by taking trigger particles and associated particles from different events. The level of the background from these mixed events may not be correct for two reasons. If minimum bias are used in the event mixing there is a trigger bias to the trigged events increases the multiplicity of these events. Secondly some of the particles in the triggered events are jet-like correlated so the background level should be lower then the average of the triggered events. An assumption must be made about the level of the background since the true level is unknown. A zero yield at minimum (ZYAM) assumption is used. Figure 1 shows the raw correlation in azimuth in circles. The mixed event distribution is shown in diamonds and the distribution normalized to ZYAM in is shown in squares. The final correlation is obtain by subtracting the normalized background distribution from the raw correlation. Alternatively Gaussian fits can be used in *pp* collisions; however in heavy-ion collisions this is not as helpful due to the complexity of the correlation function. The analysis code is written in ALIROOT and running on the GSI computer farm in the analysis train.

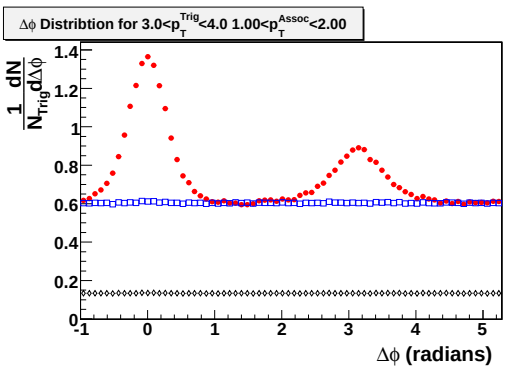

Figure 1: Two-particle jet-like correlation in azimuth for $3 < p_T^{Trigger} < 4$ GeV/c and $1 < p_T^{Associated} < 2$ GeV/c. Circles: Raw correlation. Diamonds: Background from mixed events. Squares: Normalized background. Reconstructed events in a simulation of the ALICE detector from the PYTHIA event generator of *pp* collisions at $\sqrt{s_{NN}} = 10$ TeV.

Results and Conclusions

The background subtracted correlation function can be obtained from Fig. 1 by subtracting the normalized mixed events from the raw distribution. Particles near $\Delta\phi = 0$ radians are from the same jet as the trigger particles, near-side peak. Particles around $\Delta\phi = \pi$ are from the other jet since the events are predominately di-jet events, away-side peak. There must be at least 2 jets due to momentum conservation. The difference in width of the near-side and away-side peaks is due to the initial transverse momentum of the partons within the colliding hadrons. This gives a broadening to the correlation as it is the average of many events where the center of the away-side peak can be shifted from π radians.

By changing the trigger and associated p_T ranges one can study the fragmentation by studying both the spectra, yields, and widths of these peaks. One should be able to perform this analysis using particles detected in the ALICE TPC. With only a few days of data taking this can be done to a moderately high trigger p_T of about 10 GeV/c. With additional statistics the p_T reach is increased. In heavy-ion collisions additional care must be taken on the background subtraction, but this method can be used to study the created medium though the modification of the jet-like correlations.

* Work supported by EMMI, GSI, and BorBF

QCD Phases and Thermodynamics of a $N_f = 3$ Nonlocal PNJL Model *

T. Hell, S. Rößner, M. Cristoforetti, and W. Weise
Physik Department, TU München, 85748 Garching, Germany

Low-energy QCD in its sector with $N_f = 3$ flavours of almost massless up and down quarks ($m_u \approx m_d \sim \mathcal{O}(5\,\mathrm{MeV})$) and a slightly heavier strange quark ($m_s \sim \mathcal{O}(100\,\mathrm{MeV})$) is known to have the following characteristic symmetry breaking pattern: the Goldstone bosons related to spontaneously broken chiral SU(3) × SU(3) symmetry are identified with the pions and kaons. Their masses originate from explicit symmetry breaking by the non-zero u-, d- and s-quark masses. The unusually large gap between η' and η mesons is understood as being a consequence of the axial anomaly in QCD, the breaking of the axial $U(1)_A$ symmetry, e. g. through instanton effects.

The present work extends a nonlocal version of the Nambu–Jona-Lasinio (NJL) model (developed in Ref. [1] for the two-flavour case) to $N_f = 3$ including the $U(1)_A$ breaking 't Hooft interaction terms. The model includes an effective gluon propagator which describes instanton effects in the low-momentum region, and asymptotic freedom at high-momentum scales. Altogether, this approach is able to reproduce the pseudoscalar meson spectrum, including the η-η' mass-splitting. Fundamental current algebra relations such as the Goldberger–Treiman- and the Gell-Mann–Oakes–Renner relations are exactly fulfilled.

This nonlocal PNJL model has been applied to QCD thermodynamics, incorporating the coupling to a gluonic background (Polyakov loop) field. The chiral condensates serve as order parameters for the chiral transition while the confinement-deconfinement transition is controlled by the Polyakov loop. The resulting approach is a consistent nonlocal, three-flavour extension of the previous PNJL model with local two-flavour couplings [2, 3]. As before, the dynamical entanglement of the fermionic and the gluonic sector is crucial in order to reproduce lattice results. While the transition temperatures for each individual sector differ significantly by roughly 100 MeV, the coupling of the fermions to the Polyakov loop intertwine these sectors so that chiral and confinement-deconfinement transitions coincide at a common transition temperature T_c close to 200 MeV (see Fig. 1).

Corrections beyond the mean field have also been investigated, in particular those concerning mesonic quark-antiquark correlations. Mesonic corrections turn out to be important below the transition temperature T_c and decrease rapidly above T_c (see Fig. 2). Below T_c mesonic contributions can be described roughly by those of an ideal meson gas.

* Work supported in part by GSI, BMBF, and by the DFG Excellence Cluster "Origin and Structure of the Universe".

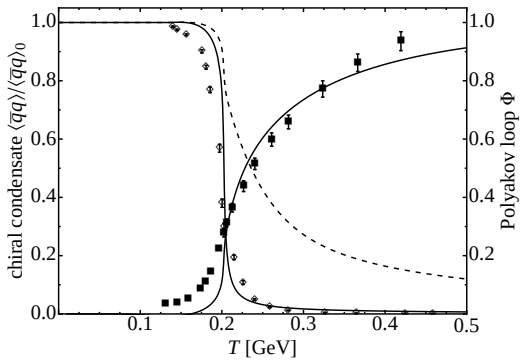

Figure 1: Temperature dependence of the up- and down quark condensates $\langle\bar{u}u\rangle = \langle\bar{d}d\rangle$ (full line) and the strange quark condensate $\langle\bar{s}s\rangle$ (dashed line) on the left hand side, and Polyakov loop Φ on the right hand side. The results are compared to lattice data of Ref. [4].

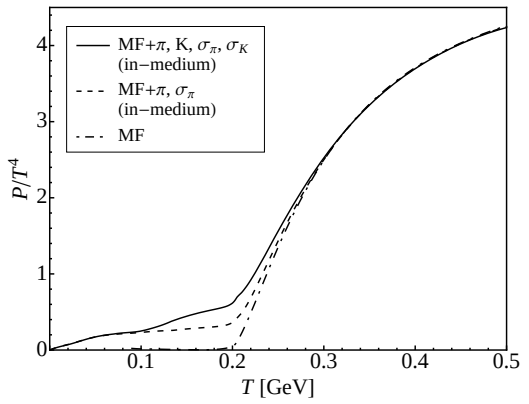

Figure 2: Temperature dependence of the pressure: The dashed-dotted line shows the mean field contributions, the dashed line the mean field result with addition of the contributions of the pions and the corresponding scalar $q\bar{q}$ mode (σ_π). The full result including contributions both from pions and kaons with corresponding sigma-fields is shown by the solid line.

References

[1] T. Hell, S. Rößner, M. Cristoforetti and W. Weise, Phys. Rev. **D79**, 014022 (2009).

[2] S. Rößner, T. Hell, C. Ratti and W. Weise, Nucl. Phys. **A814**, 118 (2008).

[3] S. Rößner, C. Ratti and W. Weise, Phys. Rev. **D75**, 034007 (2007).

[4] M. Cheng et al., Phys. Rev. **D77**, 014511 (2008).

The Chiral and Deconfinement Phase Transition in QCD

Bernd-Jochen Schaefer*[1], Mathias Wagner†[2], and Jochen Wambach[2,3]

[1]Institut für Physik, Karl-Franzens-Universität Graz, Austria; [2]Institut für Kernphysik, TU Darmstadt; [3]GSI, Darmstadt

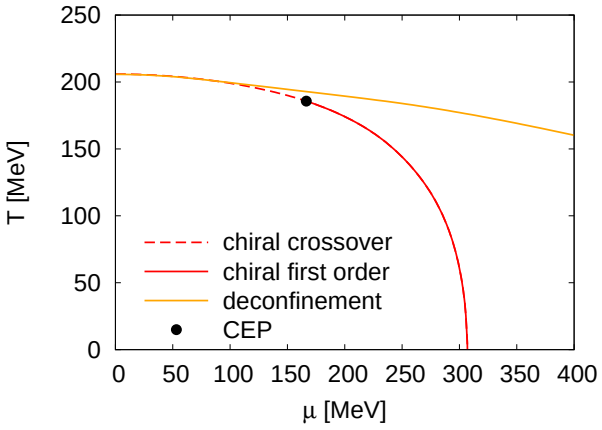

Figure 1: Phase diagram for the three flavor PQM model with a logarithmic Polyakov loop potential.

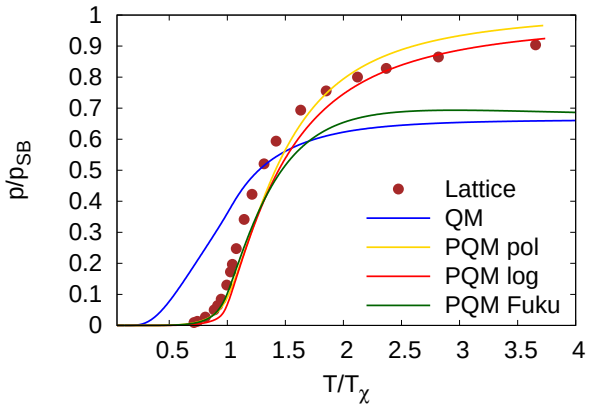

Figure 2: Scaled pressure for three different Polyakov loop potentials (labeled as pol, log, and Fuku) compared to $2+1$ flavor lattice data [3]. For comparison the pressure without the Polyakov loop is also shown (QM).

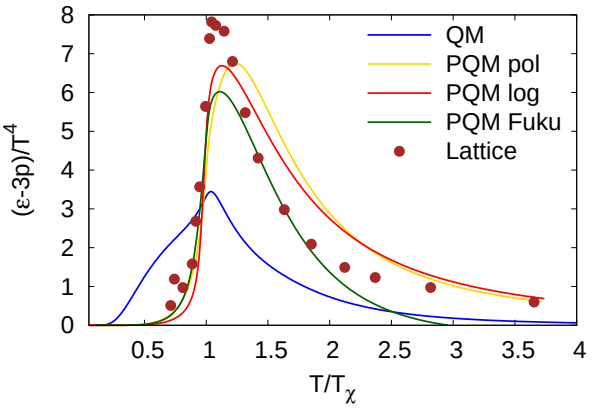

Figure 3: Similar to Fig. 2 but for the interaction measure $(\epsilon - 3p)/T^4$.

The phase diagram of strongly interacting matter is one of the most exciting subjects of modern particle physics. While QCD lattice calculations become more and more realistic at vanishing chemical potential, their predictive power at finite chemical potential is still very limited due to the fermion sign problem. Until now lattice calculations cannot provide insights on the existence of a possible QCD critical end point (CEP), where the chiral crossover pass into a first-order phase transition. By means of chiral effective models, such as the linear σ-model (LσM) with three quark flavors, one can access arbitrary regions in the phase diagram [1].

In general, chiral models do not incorporate explicit gluonic degrees of freedom and hence are unable to describe confinement properties of QCD. However, this can be cured by adding an effective Polyakov loop potential and embedding the Polyakov loop to the fermionic part of the LσM. In the framework of the resulting Polyakov-Quark-Meson (PQM) model both, the chiral and the deconfinement transitions can be investigated. Several possible choices for the Polyakov loop potential are available [2].

In Fig. 1 the phase diagram is shown for a logarithmic Polyakov loop potential. The model parameters have been adjusted such that both transitions coincide at $\mu = 0$. At some finite chemical potential both transition lines start to deviate and the emergence of a quarkyonic phase becomes possible.

The PQM model enables a more realistic description of the equation of state, which is demonstrated in Figs. 2 and 3 where the scaled pressure and the interaction measure for different Polyakov loop potentials are compared with recent lattice data [3].

* bernd-jochen.schaefer@uni-graz.at

† mathias.wagner@physik.tu-darmstadt.de

References

[1] B.-J. Schaefer and M. Wagner, Phys. Rev. **D79**, 014018 (2009).

[2] K. Fukushima, Phys. Rev. **D77**, 114028 (2008); B.-J. Schaefer, J. M. Pawlowski, and J. Wambach, Phys. Rev. **D76**, 074023 (2007); S. Roessner, C. Ratti, and W. Weise, Phys. Rev. **D75**, 034007 (2007).

[3] M. Cheng et al., Phys. Rev. **D77**, 014511 (2008).

Role of the tetraquark in the chiral phase transition

S. Strüber[1], F. Giacosa[1], A. Heinz[1], and D. Rischke[1,2]
[1]ITP, Frankfurt, Germany; [2]FIAS, Frankfurt, Germany

The Who is Who of Scalar Mesons — In the last 30 years theoretical and experimental work on the light scalar mesons with mass below ~ 1.8 GeV initiated an intense debate about their nature. The issue is that too many scalar resonances have been identified than can be accommodated in a naive quark-antiquark picture. For instance, in the scalar isoscalar channel there are five states: $f_0(600)$, $f_0(980)$, $f_0(1370)$, $f_0(1500)$, and $f_0(1710)$. In order to explain their nature, quarkonia, tetraquark and mesonic molecular assignments, as well as a scalar glueball state with mass around 1.5 GeV suggested by lattice studies of quantum chromodynamics (QCD), have been proposed and investigated in a variety of combinations and mixing patterns.

Nowadays evidence for a full nonet of scalars with mass below 1 GeV is mounting; these are the already mentioned isoscalars $f_0(600)$ and $f_0(980)$, as well as the isotriplet $a_0(980)$, and the two isodoublets of $K_0^*(800)$. A tetraquark assignment for these states can explain some puzzling properties, such as the mass ordering which is reversed compared to the expectation from a quark-antiquark picture, and the strong coupling of $a_0(980)$ and $f_0(980)$ to kaons. Within this context the lightest scalar resonance $f_0(600)$ is interpreted as a tetraquark state $\frac{1}{2}[u,d][\overline{u},\overline{d}]$ where the commutator indicates an antisymmetric flavor (as well as color) configuration of the diquark.

If the light scalars are (predominantly) tetraquark states, the question is how to identify the lightest quarkonium state $\overline{n}n = 1/\sqrt{2}(\overline{u}u+\overline{d}d)$: the broad resonance $f_0(1370)$ is the first candidate. This assignment is also supported by the fact that the scalar quarkonia are p-wave states, and thus expected to lie above 1 GeV together with other p-wave quarkonia such as axial-vector and tensor mesons. The two isoscalars of the quarkonia nonet and the scalar glueball can mix, forming the states $f_0(1370)$, $f_0(1500)$, and $f_0(1710)$.

The impact on the chiral phase transition — We consider the pion triplet $\vec{\pi}$, the bare quarkonium field $\sigma \equiv \overline{n}n$ and the bare tetraquark field $\chi \equiv \frac{1}{2}[u,d][\overline{u},\overline{d}]$. The potential defining our model emerges as the $SU(2)_r \times SU(2)_l$ limit of a more general $SU(3)_r \times SU(3)_l$ chiral invariant Lagrangian and reads explicitly:

$$V = \frac{\lambda}{4}(\sigma^2+\vec{\pi}^2-F^2)^2 - \varepsilon\sigma + \frac{1}{2}m_\chi^2\chi^2 - g\chi\left(\sigma^2+\vec{\pi}^2\right) , \quad (1)$$

where ε parametrizes explicit chiral symmetry breaking by nonzero quark masses and $g \geq 0$ is the interaction strength of the tetraquark field χ (which is a singlet under $SU(2)_r \times SU(2)_l$) with the quarkonia fields. g also determines the mixing of the scalar fields. When $g \to 0$ a simple linear sigma model for σ and $\vec{\pi}$ is left. In fact, the field χ, with mass M_χ, decouples in this limit. The minimum of the potential (1) is, to order $O(\epsilon)$, assumed for

$$\sigma_0 \simeq \frac{F}{\sqrt{1-2g^2/(\lambda m_\chi^2)}} + \frac{\varepsilon}{2\lambda F^2} , \quad \chi_0 = \frac{g}{m_\chi^2}\sigma_0^2 , \quad (2)$$

and $\vec{\pi} = 0$. The $\bar{n}n$ condensate σ_0 is identified with the pion decay constant $f_\pi = 92.4$ MeV. The vacuum expectation value χ_0 is proportional to σ_0^2. Thus, the tetraquark condensate χ_0 is induced by the spontaneous symmetry breaking in the quarkonium sector.

The calculation of the temperature dependent masses, the quarkonia and tetraquark condensate and the mixing angle between the scalar states are performed within the CJT-formalism at Hatree-Fock approximation (Fig. 1).

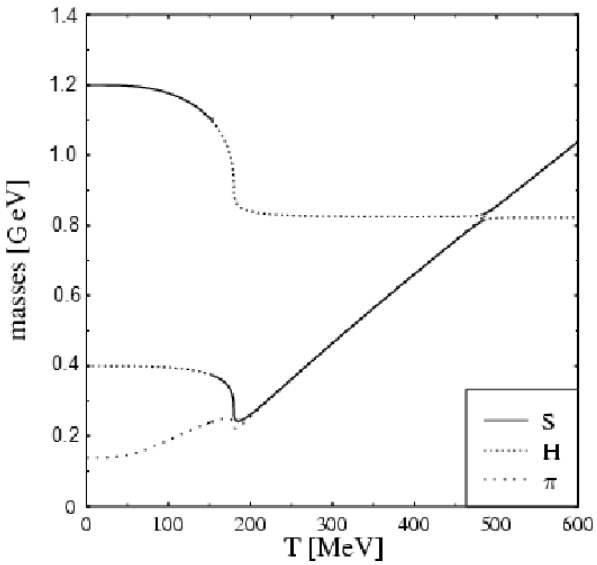

Figure 1: The coupling between χ and (σ,π) is chosen to $g = 3.4$ GeV, yielding a cross-over phase transition. The physical mass states $S := f_0(1370)$ and $H := f_0(600)$ behave discontinously as a function of temperature T, i.e., they interchange their mass eigenvalues at a critical step temperature T_s. At this temperaure, T_s, the states of the bare masses cross each other (level-crossing $\leftrightarrow$ level repulsion). For $T \to \infty$ the mixing vanishes and $f_0(1370)$ becomes a pure quarkonium, σ, and $f_0(600)$ becomes a pure tetraquark, χ, state.

References

[1] A. Heinz, S. Strüber, F. Giacosa and D. H. Rischke, "Role of the tetraquark in the chiral phase transition," arXiv:0805.1134 [hep-ph].

Evaluation of causal shear viscosity and relaxation time in QCD

E. Nakano[1], T. Koide[2], and T. Kodama[3]

[1]Extreme Matter Institute, GSI, Darmstadt, Germany; [2]Institut für Theoretische Physik, J. W. Goethe-Universität, Frankfurt, Germany; [3]Instituto de Física, Universidade Federal do Rio de Janeiro, Brasil

Analyses based on hydrodynamic equations for data accumulated from relativistic heavy ion collision (RHIC) has been an important task to see how closely the matter created behaves as an ideal fluid in a certain period of time after collisions. So far the analyses has been done entirely by ideal hydrodynamics

$$\partial_\mu T^{\mu\nu}(r,t)=0, \quad \text{and} \quad \partial_\mu N^{\mu}(r,t)=0, \tag{1}$$

where the first (second) equation represents energy-momentum (the number) conservation, and dissipative effects such as viscosities are completely neglected (the above set of equations is exact, but for the ideal hydrodynamics all the higher expansion parameters, transport coefficients, in $T^{\mu\nu}$ and N^{ν} are set to zero). Even though the ideal hydrodynamic simulations nicely coincides with experimental data, concluding that RHIC provided the most perfect ideal fluid we have ever got, there still remain a lot of ambiguities: hydro simulations depend much on the initial condition, equation of state used in the hydro simulation, effects from dissipative parts, and so forth.

In this work we rivet our eyes on the dissipation effects which are characterized by phenomenological transport coefficients in hydro equations, e.g., shear and bulk viscosities, and the particle number diffusion constant. The first step for the dissipative hydrodynamics should be the introduction of such transport coefficients, and add them to the ideal hydro equation. Since hydro equations describe a long range dynamics of the system in space time, one can expand the equation in terms of space-time derivatives of the flow velocity $u(x,t)$. The expansion begins with the lowest power of the derivatives, and the transport coefficients are these expansion coefficients, which are in principle derived from an underlying microscopic theory.

The introduction of only the first coefficients cause some problems in the relativistic case: acausality and instability. The former is related to instantaneous propagation of informations (e.g. sound velocity exceeds the speed of light), and the latter to time reversal in the equation. Both of them are due to the lack of relaxation time effects of the modes we are considering, and mathematically due to structure of the equation: difference in power of time and space derivatives, and the number of these terms. The relaxation time effect, for instance, for shear stress tensor T^{xy} which is responsible for diffusion of the shear flow created in the system, is categorized into the second order coefficient, compared to shear viscosity which is the first order one in derivatives. Thus, we need to incorporate the relaxation time effect in a consistent way.

The time evolution of spatial off-diagonal components of energy-momentum tensor $T^{\mu\nu}(\mathbf{k},t)$ is described, after the Markov approximation, by

$$\partial_t T^{yx}(k_y,t)=-ik_y(\varepsilon+P)R_{k_y}u^x(k_y,t)-\frac{1}{\tau_{k_y}}T^{yx}(k_y,t), \tag{2}$$

where $R_{k_y}=(T^{yx}(k_y),T^{yx}(-k_y))/(T^{0x}(k_y),T^{0x}(-k_y))$, and the inner product represents Kubo's canonical correlation $(X,Y)=\int_0^\beta d\lambda\beta^{-1}\mathrm{Tr}[\rho_{eq}e^{\lambda H}Xe^{-\lambda H}Y]$, with the Hamiltonian H and the inverse of temperature β. ε and P are the energy density and pressure, respectively. The noise term has been dropped. In this derivation, we have used the following replacement $T^{0x}=(\varepsilon+P)u^x(k_y,t)$ at the local rest frame. The introduction of the relaxation time τ_{k_y} is the main ingredient of this work, and it cures the problems mentioned above.

Hydrodynamics corresponds to the low momentum limit $k_y\to 0$: $\tau_{k_y}\to\tau_\pi$ and $R_{k_y}\to R_0$.

The important point here is that the equation (2) has been derived microscopically: starting from the general Heisenberg equation for the time evolution of $T^{\mu\nu}$ in the operator form, and coarse-graining it by the projection method [1]. So one can find that these coefficients can be expressed in terms of microscopic correlation functions. Comparing the phenomenological equation, we can identify the shear viscosity η and the relaxation time τ_π:

$$\tau_\pi=X^L_{22}(\mathbf{0},0), \quad \eta=(\varepsilon+P)R_{\mathbf{0}}\tau_\pi, \tag{3}$$

where $X^L_{22}(k_y,s)$ is the Laplace transform with respect to t of the shear correlation function,

$$X_{22}(k_y,t)=\frac{(T^{yx}(k_y,t),T^{yx}(-k_y,0))}{(T^{yx}(k_y,0),T^{yx}(-k_y,0))}. \tag{4}$$

With the above equations we have first shown a very interesting non-trivial relation between η and τ_π, and correlation functions can be cast into usual Kubo formula for the linear response theory. Its application to QCD, the chiral perturbation theory for Hadronic phase and perturbative QCD for high temperature plasma, has been implemented to evaluate η, τ_π and various physical ratios numerically, see [2] for detail.

References

[1] T. Koide and T. Kodama, arXiv:0806.3725 [cond-mat.stat-mech].

[2] T. Koide, E. Nakano and T. Kodama, arXiv:0901.3707 [hep-th].

Kurtosis and compressibility near the chiral phase transition

B. Stokić*[1], B. Friman[1], and K Redlich†[2]
[1]GSI, Darmstadt, Germany; [2]ITP, University of Wroclaw, Poland

Understanding the critical properties of the QCD medium and its phase diagram is a central problem in strong interaction physics [1]. Studies of QCD on the lattice at finite temperature and density show that the ratio of the quartic to quadratic fluctuations of the net quark number $R_{4,2}$ (kurtosis) is a valuable probe of deconfinement and chiral dynamics [2]. Furthermore, both model calculations [3] and LGT studies [4, 2] indicate that the inverse compressibility R_κ is a useful observable for identifying the position of the critical end point CEP in the QCD phase diagram.

We use universality arguments, relating QCD with chiral effective models, to explore the properties of the kurtosis and the inverse compressibility in hot and dense matter[5]. We study the dependence of $R_{4,2}$ and R_κ on the pion mass near the chiral transition. As an effective model of QCD we use the quark-meson Lagrangian coupled to the Polyakov loop in the mean field approximation [6].

Following the procedure in LGT studies, we use the Taylor expansion in μ/T to compute various observables. The expansion coefficients

$$c_n(T) = \left.\frac{\partial^n (p\,(T,\mu)/T^4)}{\partial(\mu/T)^n}\right|_{\mu=0} \qquad (1)$$

are generalized susceptibilities corresponding to moments of the net quark number [4, 2, 5]. In particular, the first two non-vanishing derivatives, c_2 and c_4 are the second and fourth order cumulants which are related to fluctuations of net quark number, $\delta N_q = N_q - \langle N_q \rangle$. For instance, $c_2 = \chi_q/T^2$, where χ_q is the quark number susceptibility. We focus on the kurtosis

$$R_{4,2} = \frac{c_4}{c_2}, \qquad (2)$$

and the dimensionless ratio of the inverse isothermal compressibility κ^{-1} and Gibb's free energy density μn_q,

$$R_\kappa = \frac{\kappa^{-1}}{\mu n_q} = \frac{n_q}{\mu \chi_q}\,. \qquad (3)$$

In Fig. 1 we show the temperature dependence of $R_{4,2}$. The kurtosis (2) is strongly dependent on the net quark content of the baryon number carrying degrees of freedom [4, 2]; at low temperatures, $R_{4,2} = (3B)^2$. Near the phase transition, the kurtosis exhibits a strong dependence on the pion mass, while at high and low temperatures, it rapidly approaches universal values. The ratio R_κ is also

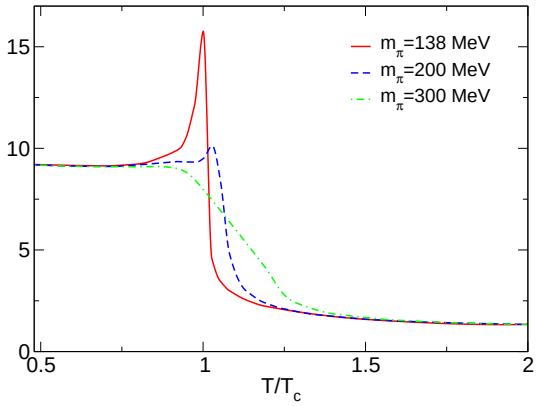

strongly dependent on the pion mass near the phase transition, while the high and low temperature behavior is universal for fixed μ/T. In Fig. 2 we show R_κ computed using the Taylor expansion for the density and the susceptibility. We note that the approximate R_κ, obtained using the Taylor expansion, deviates substantially from the full one, which vanishes at the critical end point.

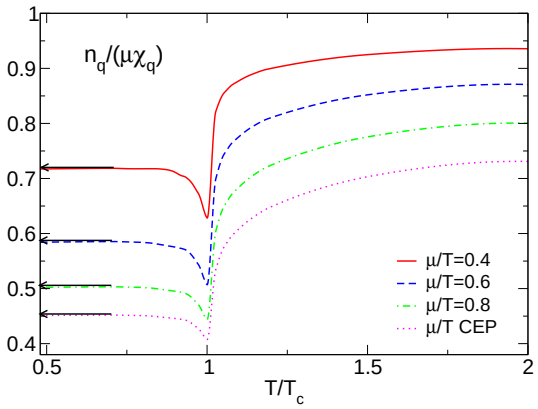

References

[1] See e.g. Proceedings of "Quark Matter 2008".

[2] S. Ejiri, F. Karsch and K. Redlich, Phys. Lett. B **633**, 275 (2006).

[3] C. Sasaki, B. Friman and K. Redlich, Phys. Rev. Lett. **99**, 232301 (2007).

[4] C. R. Allton, M. Doring, S. Ejiri, S.J. Hands, O. Kaczmarek, F. Karsch, E. Laermann and K. Redlich, Phys. Rev. D **71**, 054508 (2005).

[5] B. Stokić, B. Friman, K. Redlich, arXiv:0809.3129 (submitted to Phys. Lett. B)

[6] B. J. Schaefer, J. M. Pawlowski and J. Wambach, Phys. Rev. D **76**, 074023 (2007).

* Supported by the Helmholtz Research School on Quark Matter Studies

† Supported in part by the Polish Ministry of Science and by DFG under the Mercator Programme.

Dynamically generated mesons and chiral restoration

S. Leupold[1] and M. Wagner[1]

[1]Institut für Theoretische Physik, Universität Giessen, Germany

Spontaneous chiral symmetry breaking and its restoration in a QCD medium is one of the most interesting aspects of non-perturbative QCD [1]. One clear sign that chiral symmetry is broken in the QCD vacuum comes from a comparison of the spectra of two quark currents related by a chiral transformation, namely the isovector–vector and isovector–axial-vector current. If the vacuum obeyed chiral symmetry, both spectra would be the same. Instead one finds the ρ/a_1 meson in the vector/axial-vector channel [2]. Without much doubt the ρ meson is dominantly a quark-antiquark state [3]. In contrast, we have demonstrated recently [4] that the axial-vector spectrum can be well understood with the proposition [5] that the a_1 meson is a dynamically generated state, i.e. that it is dominantly a π-ρ "molecule" or correlation. This is demonstrated in Fig. 1.

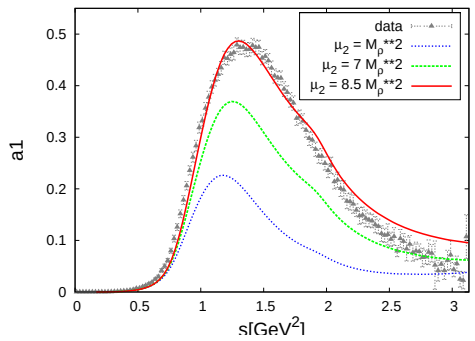

Figure 1: Three-pion part of the isovector–axial-vector spectrum and its description by a dynamically generated a_1 meson [4]. Data taken from [2].

It is expected that chiral symmetry is restored in a medium of sufficiently high (energy) density. The spectral information of the vector and the axial-vector current must become identical at this point of chiral restoration. There are various scenarios conceivable how this degenerate in-medium spectrum might look like [1]. Our picture for the vacuum case — where the lowest excitation in the vector channel is a quark-antiquark state, whereas the lowest excitation in the axial-vector channel is a meson-meson correlation — suggests that the melting scenario is realized: The ρ meson might dissolve already in hadronic matter instead of staying more or less intact as a single-particle state (at the level of hadrons). This can be understood as a precursor to deconfinement. Then also the a_1 meson should dissolve. In principle, this can be tested in our approach. In the following we present a very simple model: We increase the width of the ρ meson by a constant (by 50 or 100 MeV, respectively) and study what happens to the dynamically generated a_1. It must be stressed that this model should be regarded as a precursor to more serious calculations. In particular, an in-medium width of the ρ meson would not be independent of the momentum of the ρ meson relative to the medium. In addition, one also expects a strong in-medium effect on the pion and not only on the ρ meson (see [1] and references therein). These aspects are not covered by the simple model studied here. The result is shown in Fig. 2. The upper/lower two curves correspond to an increase of the ρ meson width by 50/100 MeV. The difference between the respective two curves close to each other is not relevant for the present purpose. (For one curve all vector-meson propagators in the rescattering process are changed, for the other only (the last) one.) Obviously, the

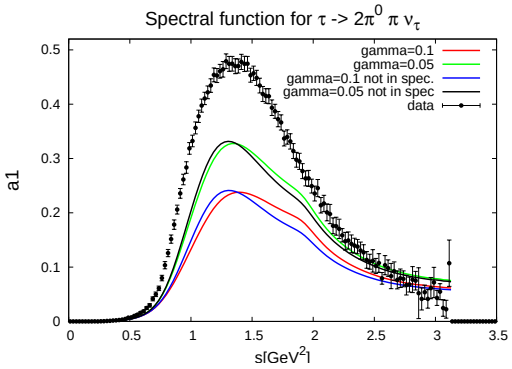

Figure 2: Simple model for the in-medium isovector–axial-vector spectrum. See main text for details. Vacuum data are added for comparison (taken from [2]).

a_1 meson also melts, if the ρ meson melts. This does not prove that the melting scenario is the correct approach to chiral restoration, but at least we obtained a consistent picture. One might say that the problem of the missing partner of the ρ meson on the single-particle level is solved by deconfinement. More sophisticated calculations, e.g., along the lines pointed out in [1], must be performed to check also quantitatively the melting scenario of chiral symmetry restoration.

References

[1] S. Leupold, M. F. M. Lutz and M. Wagner, J. Part. Nucl. Phys., in press, arXiv:0811.2398 [nucl-th].

[2] ALEPH Collab. (S. Schael *et al.*), Phys. Rept. **421**, 191 (2005).

[3] S. Leupold and M. Wagner, arXiv: 0807.2389 [nucl-th].

[4] M. Wagner and S. Leupold, Phys. Lett. B **670**, 22 (2008); Phys. Rev. D **78**, 053001 (2008).

[5] M. F. M. Lutz and E. E. Kolomeitsev, Nucl. Phys. A **730**, 392 (2004).

Pseudoscalar bosonic excitations in the color-flavor locked phase*

Verena Kleinhaus[1] and Michael Buballa[1]
[1]Technische Universität Darmstadt, Germany

The ground state of quark matter at asymptotically high baryon densities is the color-flavor locked (CFL) phase. In this phase up, down, and strange quarks are paired in a particularly symmetric way. Spontaneous breaking of baryon number and chiral symmetry leads to the emergence of one scalar and eight pseudoscalar Goldstone bosons. A ninth pseudoscalar Goldstone boson is expected due to the spontaneous breaking of the $U_A(1)$ symmetry, which is a symmetry of QCD at high density. These Goldstone bosons are the lowest lying excitations and should play an important role for the thermodynamics of strongly interacting matter at high density.

In Ref. [1] we have studied the properties of the flavored pseudoscalar Goldstone bosons in the CFL phase within an NJL-type model. The bosons have been constructed explicitly by solving the Bethe-Salpeter equation for quark-quark scattering in random phase approximation. In Ref. [2] this work was extended to the hidden-flavor sector.

In Fig. 1 the resulting masses of the Goldstone bosons at zero tempertature and $\mu = 500$ MeV are displayed as functions of the strange quark mass for $m_u = m_d = 30$ MeV. The numerical results for the Goldstone boson masses can be fitted nicely by parametrizations taken from the corresponding low-energy effective theory (LEET) [3].

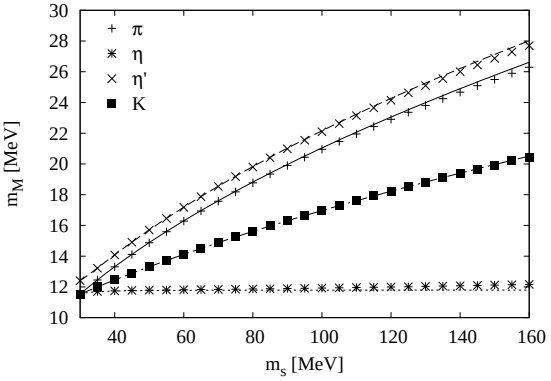

Figure 1: Masses of the pseudoscalar Goldstone bosons as functions of the strange quark mass m_s for $m_u = m_d = 30$ MeV. Points: numerical results, lines: LEET fit.

Besides the Goldstone bosons, there are also higher-lying pseudoscalar bosons, which stay massive in the chiral limit. In Fig. 2 the mass of the higher-lying pseudoscalar octet mesons in the chiral limit is displayed as a function of the chemical potential. For comparison, we also show the theshold 2Δ for decay into two quark quasiparticles. We find that the octet mesons are weakly bound. In addition, there is also a singlet mode, which is, however, unbound.

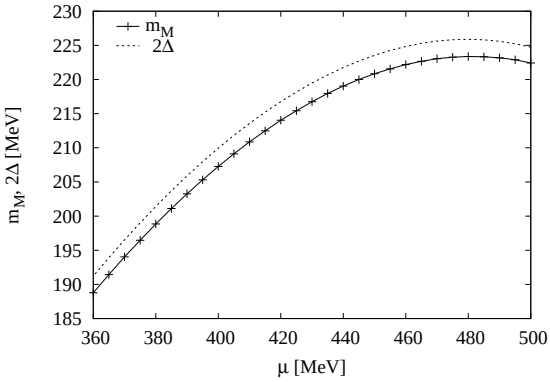

Figure 2: Mass of the higher-lying pseudoscalar octet mesons in the chiral limit as a function of the quark chemical potential μ. The dotted line indicates the decay threshold 2Δ.

Utilizing chiral Ward-Takahashi identities one can show that the decay constants of the higher-lying pseudoscalar excitations vanish in the chiral limit. This is confirmed by Fig. 3.

References

[1] V. Kleinhaus, M. Buballa, D. Nickel and M. Oertel, Phys. Rev. D 76 (2007) 074024.

[2] V. Kleinhaus and M. Buballa, Phys. Rev. D 79 (2009) 014016.

[3] T. Schäfer, Phys. Rev. D 65 (2002) 074006.

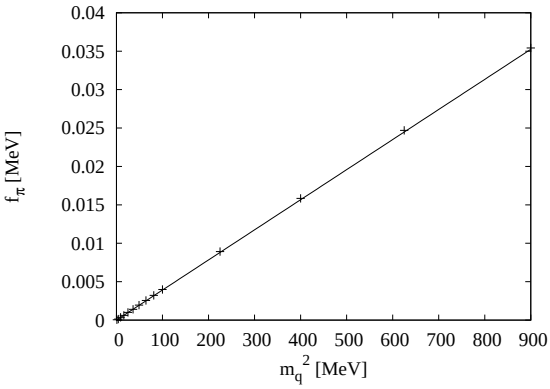

Figure 3: Decay constant of the higher-lying octet modes as a function of the squared common quark mass m_q. The points indicate the numerical results. The solid line is a linear fit.

* Work supported in part by BMBF under contract No. 06DA123.

Thermal description of hadron production in central nucleus-nucleus collisions

A. Andronic[1], P. Braun-Munzinger[1,2,3], and J. Stachel[4]

[1]GSI Darmstadt, Germany; [2]ExtreMe Matter Institute, GSI Darmstadt, Germany; [3]Technical University Darmstadt, Germany; [4]University of Heidelberg, Germany

The analysis of hadron yields measured in central heavy ion collisions from AGS up to RHIC energies has shown [2] that hadron multiplicities can be described very well with a hadro-chemical equilibrium approach which is governed by the chemical freeze-out temperature T, baryochemical potential μ_b, and the fireball volume V. The main result of these investigations was that the extracted temperature values rise rather sharply from low energies on towards $\sqrt{s_{NN}}$ $\simeq$10 GeV and reach afterwards constant values near T=160 MeV, while the baryochemical potential decreases smoothly as a function of energy. While in general all hadron yields are described rather quantitatively [2], a notable exception was up-to-now the energy dependence of the K^+/π^+ ratio which exhibits a rather marked maximum, "the horn" [3], near $\sqrt{s_{NN}} \simeq 10$ GeV [4].

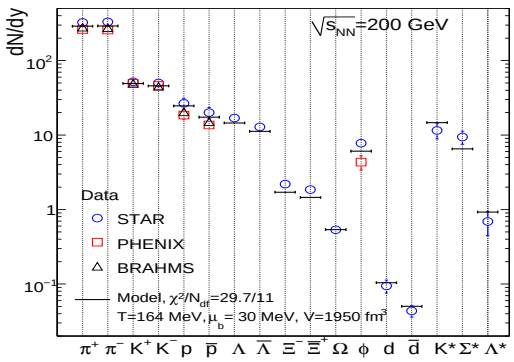

Figure 1: Experimental hadron yields and model fit at 200 GeV.

We have performed recently [1] a new analysis of hadron production in central nucleus-nucleus collisions, with the aim to explore the consequences of an improved hadronic mass spectrum in which the σ meson and many higher-lying resonances are included. An example of a fit to the data is shown in Fig. 1 for the energy of 200 GeV. The model is successful in reproducing the measurements and this applies to all energies, from 2 AGeV beam energy (fixed target) up to the top RHIC energy of $\sqrt{s_{NN}}$=200 GeV. The reduced χ^2 values are reasonable. In most cases the fit quality is improved compared to our earlier analysis [2], even though the experimental errors are now smaller. An important result of our analysis is that the resulting thermal parameters are close to those obtained earlier [2].

We employ parametrizations of T and μ_b to investigate the energy dependence of the relative production yields K^+/π^+ and Λ/π^-, shown in Fig. 2. The K^+/π^+ ratio shows a rather pronounced maximum at a beam energy

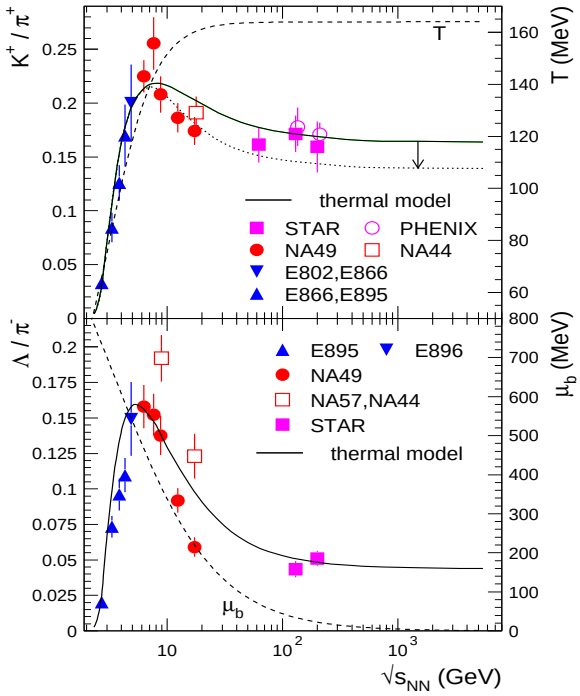

Figure 2: Energy dependence of the relative production ratios K^+/π^+ and Λ/π^-. The dashed lines show the energy dependence of T (upper panel) and μ_b (lower panel).

of 30 AGeV [4], and the data are well reproduced by the model calculations. In the thermal model this maximum occurs naturally at $\sqrt{s_{NN}}$ $\simeq$8 GeV [5]. It is due to the counteracting effects of the steep rise and saturation of T and the strong monotonous decrease in μ_b. The competing effects are most prominently reflected in the energy dependence of the Λ hyperon to pion ratio (lower panel of Fig. 2), which shows a pronounced maximum at $\sqrt{s_{NN}}$ $\simeq$5 GeV. This is reflected in the K^+/π^+ ratio somewhat less directly; it appears mainly as a consequence of strangeness neutrality, assumed in our calculations.

References

[1] A. Andronic, P. Braun-Munzinger, J. Stachel, Plys. Lett. B (2009), arXiv:0812.1186.

[2] A. Andronic, P. Braun-Munzinger, J. Stachel, Nucl. Phys. A **772** (2006) 167.

[3] M. Gaździcki, M.I. Gorenstein, Acta Phys. Polon. B **30** (1999) 2705.

[4] C. Alt et al. (NA49), Phys. Rev.C **77** (2008) 024903.

[5] P. Braun-Munzinger, J. Cleymans, H. Oeschler, K. Redlich, Nucl. Phys. A **697** (2002) 902.

Thermal production of multistrange hypernuclei in nucleus-nucleus collisions

A. Andronic[1], P. Braun-Munzinger[1,2,3], J. Stachel[4], and H. Stöcker[1]

[1]GSI Darmstadt, Germany; [2]Technical University Darmstadt, Germany; [3]ExtreMe Matter Institute, GSI Darmstadt, Germany; [4]University of Heidelberg, Germany

The analysis of hadron yields measured in central heavy ion collisions from AGS up to RHIC energies has shown [1] that hadron multiplicities can be described very well with a hadro-chemical equilibrium approach which is governed by the chemical freeze-out temperature T, baryochemical potential μ_b, and the fireball volume V. We have performed recently [2] a new analysis of hadron production in central nucleus-nucleus collisions, with the aim to explore the consequences of an improved hadronic mass spectrum in which the σ meson and many higher-lying resonances are included.

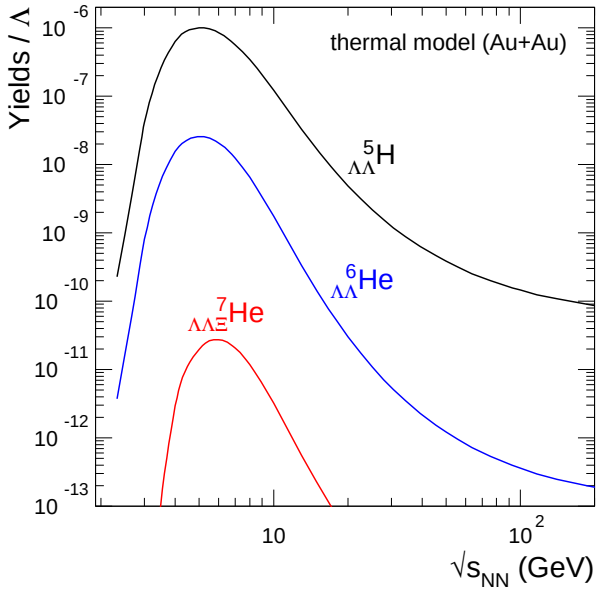

Figure 1: The energy dependence of multistrange hypernuclei yields relative to the yields of Λ hyperons at midrapidity for central nucleus-nucleus collisions.

In Fig. 1 we show a prediction within the thermal model [1] for the energy dependence of the production yield of multistrange light hypernuclei [3]. Shown is the yield relative to that of Λ hyperons, calculated using the parametrizations for the temperature (T) and baryochemical potential (μ_b) established in [1] based on fits of midrapidity data in central collisions. The production shows a pronounced maximum in the FAIR energy regime, which is the consequence of a competition between a strong increase (followed by saturation) of T and a strongly decreasing μ_b. In addition, the canonical suppression, arising from the condition of local strangeness conservation, leads to reduced yields at low energies.

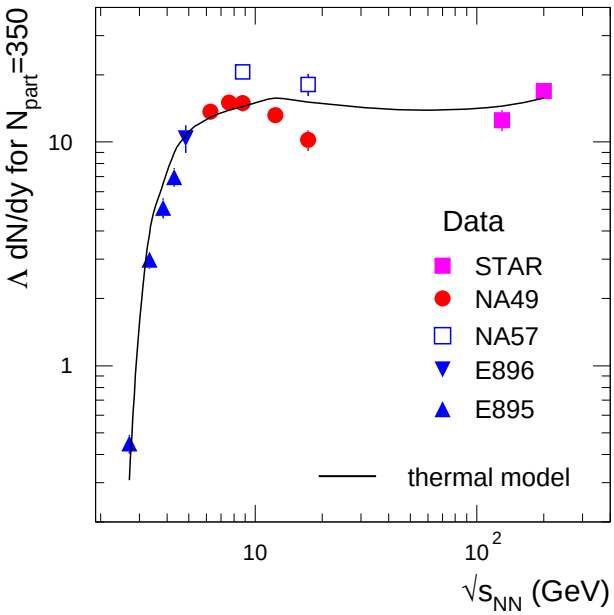

Figure 2: The energy dependence of Λ hyperon production yields at midrapidity for central nucleus-nucleus collisions.

Although even at the production maximum the yields of the multistrange hypernuclei relative to Λ are rather small, they could be measurable with the CBM detector, at least for the double-Λ hypernuclei. The measurement of the multi-hyperon nucleus $^{7}_{\Lambda\Lambda\Xi}He$ will be challenging. Considering the measured multiplicities of Λ hyperons at the SPS energies [4], shown in Fig. 2 as a function of energy in comparison to the thermal model prediction, production yields per collision in the range 10^{-6}-10^{-5} are expected for the double-Λ hypernuclei. The yields of multistrange hypernuclei predicted within the thermal approach are comparable to those predicted within a hybrid (transport-hydro) approach [5].

References

[1] A. Andronic, P. Braun-Munzinger, J. Stachel, Nucl. Phys. A **772** (2006) 167.

[2] A. Andronic, P. Braun-Munzinger, J. Stachel, arXiv:0812.1186.

[3] P. Braun-Munzinger, J. Stachel, J. Phys. G **21** (1995) L17 [nucl-th/9412035].

[4] C. Alt et al. (NA49), Phys. Rev.C **78** (2008) 034918 [arXiv:0804.3770].

[5] J. Steinheimer et al., arXiv:0811.4077.

Thermal description of hadron production in e^+e^- collisions revisited

A. Andronic[1], F. Beutler[2], P. Braun-Munzinger[1,3,4], K. Redlich[5,3], and J. Stachel[2]

[1]GSI, Darmstadt, Germany; [2]University of Heidelberg, Germany; [3]Technical University Darmstadt, Germany; [4]ExtreMe Matter Institute, GSI Darmstadt, Germany; [5]University of Wrocław, Poland

The analysis of hadron yields measured in central heavy ion collisions from AGS up to RHIC energies has shown [1] that hadron multiplicities can be described very well with a hadro-chemical equilibrium approach. The natural question arising here is whether this statistical behavior is a unique feature of high energy nucleus-nucleus collisions or whether it is also applicable in elementary collisions like, e.g., e^+e^-.

Usually a 5-flavor jet approach is used for the fits on multiplicities in e^+e^- collisions [4], with the fractions of the quark flavors in hadronic events [3] as external input values, unrelated with the thermal model. We have adopted this approach in our study, but we have also considered a purely thermal scenario in which the presence of the heavy-quark jets is neglected [2]. We are using the latest multiplicity measurements summarized and published by the Particle Data Group (PDG) [3]. Since the aim is a precision calculation for a small system we employ a fully canonical form of the statistical model conserving baryon number N, charge Q, strangeness S, charmness C, and bottomness B. To reach within the model a precision comparable to that of the data from the LEP collider (a few percent), we have performed computations including quantum statistics.

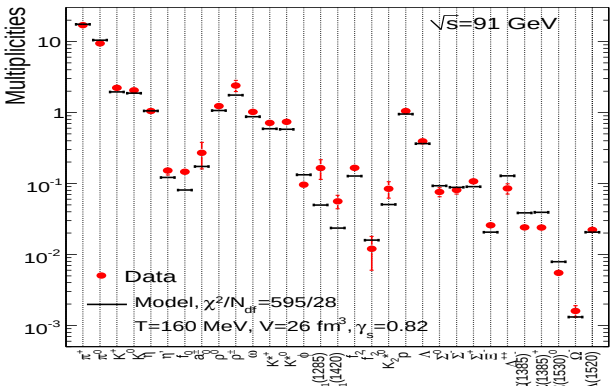

Figure 1: Thermal fit to hadron yields at the energy of 91 GeV.

The resulting best fit to the data at the energy $\sqrt{s}$=91 GeV is shown in Fig. 1 for the purely thermal scenario. We first note the overall behavior of the data, namely an approximately exponential decrease of particle yield with increasing particle mass. Such a behavior is expected in the hadron resonance gas model due to the Boltzmann factors, thus indicating the presence of statistical features of hadron production in elementary collisions. Clearly, the fit favors a strangeness suppression factor γ_s different than unity, at variance to the case in heavy-ion collisions.

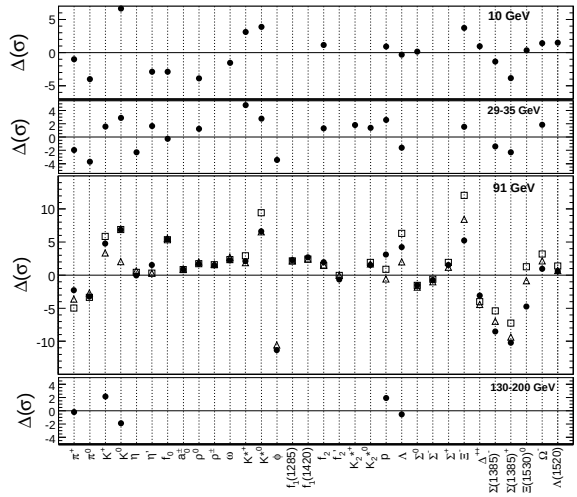

Figure 2: Difference (in units of experimental error) between experimental data and thermal model fits at four energies.

The quantitative description of the data with the statistical model is, however, rather poor and no improvement is visible for the case of subtracting charm and bottom contributions. The poor fit quality which is already visible in Fig. 1 becomes striking when, as in Fig. 2, we show for the four energies the difference Δ (in units of the experimental error) between the experimental data and the statistical model calculations for the best fit values. Typical χ^2 values per degree of freedom lie between 5 and 20 and discrepancies between single data points and fit values larger than 5 standard deviations are not rare. In particular, for all energies the yields of ϕ mesons and of hyperons are poorly reproduced. Large deviations are seen also for kaons. The case of the fit after subtraction of the contribution of the decays of charmed and bottom hadrons, explored at $\sqrt{s}$=91 GeV (open squares in Fig. 2), is characterized by a larger χ^2 value compared to the overall fit. The extracted fit parameters differ somewhat in the two cases. A third fit scenario, namely using a 5-flavor approach, shown by the triangles in Fig. 2, gives the lowest χ^2 value, although the value is still far from that of a good fit.

References

[1] A. Andronic, P. Braun-Munzinger, J. Stachel, Nucl. Phys. A **772** (2006) 167; Phys. Lett. B (2009), arXiv:0812.1186.

[2] A. Andronic et al., arXiv:0804.4132.

[3] C. Amsler et al., Phys. Lett. B 667 (2008) 1.

[4] F. Becattini et al., Eur. Phys. J. C **56** (2008) 493

Production of hypernuclei in heavy-ion collisions*

T. Gaitanos, U. Mosel, and H. Lenske
Institut für Theoretische Physik, JLU-Giessen, Germany

Hypernuclear physics is a useful tool to investigate the properties of the hyperon-nucleon (YN) and the hyperon-hyperon (YY) interaction [1]. The knowledge of the strangeness sector of the hadronic equation of state might be important for nuclear astrophysics, e.g., for the properties of neutron stars [2], and in exploring exotic states of finite nuclei, e.g., neutron-rich strange nuclei and exotic dibaryonic systems [3]. The experimental situation has so far been rather rare due to the short life time of hypernuclei, which impedes the detection of hypernuclei. However, the life time of hypernuclei seen in the laboratory is considerably enhanced in relativistic collisions. Thus concrete experimental proposals with high energy heavy-ion and proton beams at GSI (Darmstadt, Germany) and J-PARC (Japan), respectively, have been suggested by T. Saito [4]. Production of particularly double-strange ($s = -2$) hypernuclei will be also studied in antiproton-nucleus reactions by the PANDA collaboration [5].

In order to theoretically study hypernuclear formation in reactions the Giessen-BUU transport model [6] has been extended by including a statistical model of decay of excited nuclei (Statistical Multifragmentation Model, SMM) [7]. We have tested this hybrid approach in low-energy spallation reactions with success [6]. It has been therefore natural to extend it to the strangeness sector by including the formation of fragments with strangeness degrees of freedom. At the present level of investigation hypernuclei are formed by a phenomenological phase-space coalescence method.

We have applied the extended hybrid transport approach in collisions induced by light ^{12}C ions at incident energies of 2 AGeV and in proton-induced reactions at high relativistic energies ($E_{lab} = 50$ GeV). The particular choice of these reactions is related to the future experiments of the HypHI and PANDA collaborations.

Fig. 1 shows the theoretical results of the hybrid transport calculations in terms of inclusive rapidity spectra of different fragments and the corresponding light hypernuclei in spectator fragmentation, as indicated. The production cross section of light hypernuclei is very low, as expected for collisions between such light systems. In particular, the theoretical study predicts that the main contribution to the formation of hypernuclei originates from direct capture of fireball hyperons when spectator matter passes through the expanding fireball stage. The pionic contribution ($\pi B \rightarrow YK$) to hypernuclear production is negligible, since in reactions between light systems pion production with associated secondary re-scattering is rare. On the other hand, hyperons mainly produced in 3-body final states ($BB \rightarrow BYK$) in the fireball region are slow and thus can be easily captured by streaming spectator matter. The integrated rapidity distributions from projectile spectators lead to inclusive cross production sections in the order of only view $(0.8-2)\ \mu b$, a prediction close to earlier studies [8].

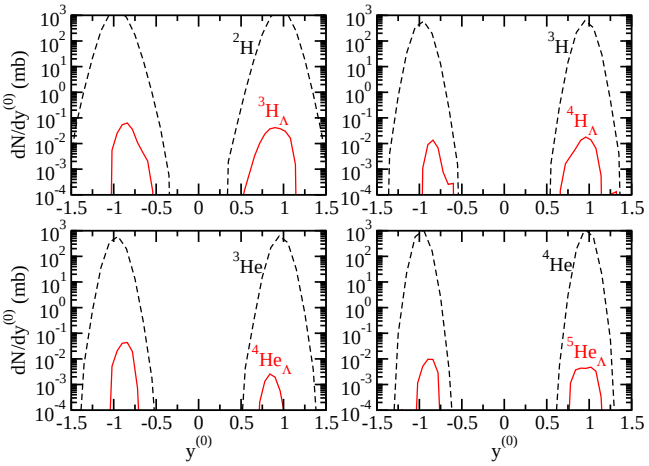

Figure 1: Rapidity distributions ($y^{(0)}$ is normalized to the projectile rapidity in the c.m. frame) of different particle types (as indicated) for the system $^{12}C + ^{12}C@2\ AGeV$.

The production of hypernuclei has been theoretically studied in the framework of a hybrid dynamical model which accounts properly for the non-equilibrium dynamics and the statistical decay of excited residual nuclei. Our predictions for light hypernuclei production cross sections might be helpful for the upcoming HypHI experiment, in which one intends to measure the properties of hypernuclei. An extension of the theoretical studies to antiproton-nucleus reactions, which are related to the PANDA experiment, are straightforward and under study.

* Work supported by BMBF

References

[1] A.D. Wroblewski, Acta Physica Polonica, B35 (2004) 901.

[2] J. Schaffner, I. Mishustin, Phys. Rev. C53 (1996) 1416.

[3] F. Hofmann, C.M. Keil, H. Lenske, Phys. Rev. C64 (2001) 025804.

[4] The HypHI collaboration: Letter of Intent (2005).

[5] J. Pochodzalla, Nucl. Phys. A754, 430c (2005).

[6] T. Gaitanos, H. Lenske, U. Mosel, Phys. Lett. B663 (2008) 197; Prog. Part. nucl. Phys. (2009) in press.

[7] J.P. Bondorf et al., Phys. Rep. 257 (1995) 133.

[8] M. Wakai, Nucl. Phys. A547 (1992) 89c.

Open and hidden charm in proton-nucleus and heavy-ion collisions *

O. Linnyk[1,#], E. L. Bratkovskaya[1], and W. Cassing[2]
[1]Frankfurt Institute for Advanced Studies, JWG Universität Frankfurt am Main, Germany; [2]Institut für Theoretische Physik, JL Universität Gießen, Germany

We present the results of our calcualtions on the collectivity and the suppression pattern of charmed mesons in heavy-ion collisions based on the microscopic Hadron-String Dynamics (HSD) transport approach for different scenarios of charm interactions with the surrounding matter..

Our findings suggest that the charmonium dynamics in heavy-ion reactions is dominantly driven by hadronic interactions in the SPS energy regime. Since energy densities above 1 GeV/fm^3 are reached in central nucleus-nucleus collisions at 158 A·GeV, our observation indicates that hadronic correlators (with quantum numbers of the familiar hadrons) still persist above the critical energy density for the formation of a QGP. In contrast, the study of the formation and suppression dynamics of charmonia within the HSD transport approach for Au+Au reactions at the top RHIC energy has demonstrated that the hadronic 'comover absorption and recreation model' fails severely at √s=200 GeV. This is found in the J/Ψ rapidity distribution, in the differential elliptic flow of J/Ψ and the charmonium nuclear modification factor R_{AA} as a function of transverse momentum p_T.

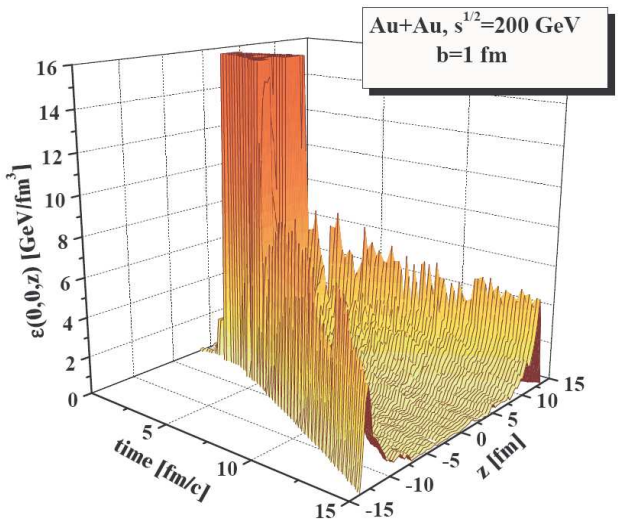

Fig 1. The energy density from HSD for a central Au+Au collision at √s =200 GeV. The time t is given in the nucleon-nucleon center-of-mass system. The figure is taken from Ref. [2].

Only when including pre-hadronic degrees in the early charm reaction dynamics, the general suppression pattern of charmonia may be reasonably described; though, the elliptic flow v_2 is still (slightly) underestimated. On the other hand, $R_{AA}(p_T)$ for J/Ψ mesons cannot be described appropriately in the comover approach even when incorporating the early pre-hadron interactions. The latter observable indicates that at least part of the final J/Ψ's are created by coalescence of c+cbar pairs in the hadronization phase. Our analysis demonstrates that the dynamics of c+cbar quarks in heavy-ion reactions at RHIC energies are dominated by partonic interactions in the sQGP.

More information on our research can be obtained from [3,4].

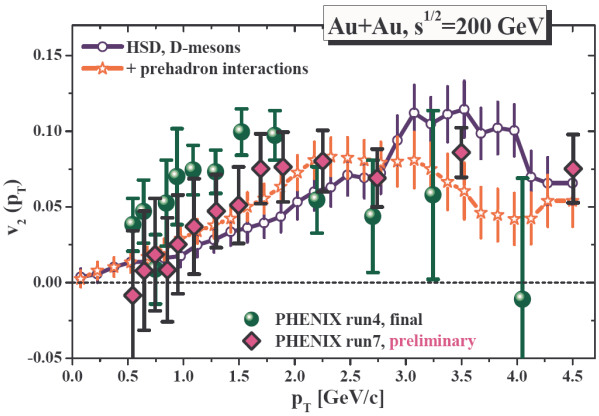

Fig 2. Elliptic flow of D mesons produced in Au + Au collisions at √s =200 GeV as a function of p_T from HSD (solid blue line with open circles) in comparison to the PHENIX data [2] on v_2 of non-photonic electrons. The red line with open stars shows the HSD result for the v_2 of D-mesons when including additionally pre-hadronic charm interactions. The figure is taken from Ref. [2].

References

[1] C. PHENIX, A. Adare et al., Phys. Rev. Lett. 98 (2007) 172301.
[2] O. Linnyk, E. L. Bratkovskaya, and W. Cassing, Nucl. Phys. A807 (2008) 79.
[3] O. Linnyk, E. L. Bratkovskaya, and W. Cassing, Int. J. Mod. Phys. E17 (2008) 1367.
[4] O. Linnyk, E. L. Bratkovskaya, and W. Cassing, arXiv:0810.4257, to be published in J of Phys. G.

* Work supported by BMBF. #linnyk@fias.uni-frankfurt.de

Hadronisation from the dynamical quasiparticle point of view

W. Cassing[1] and E. L. Bratkovskaya[2]
[1]Univ. of Giessen, Germany; [2]JWG Univ. of Frankfurt, Germany

The 'Big Bang' scenario implies that in the first microseconds of the universe the entire state has emerged from a partonic system of quarks, antiquarks and gluons – a quark-gluon plasma (QGP) – to color neutral hadronic matter consisting of interacting hadronic states (and resonances) in which the partonic degrees of freedom are confined. The nature of confinement and the dynamics of this phase transition has motivated a large community for several decades and is still an outstanding question of todays physics. A fundamental problem of models for hadronization is the conservation of 4-momentum and the entropy problem because by fusion/coalescence of massless partons to color neutral bound states of low invariant mass (e.g. pions) the number of degrees of freedom and, thus, the total entropy is reduced in the hadronization process. This problem - a violation of the second law of thermodynamics as well as of the conservation of 4-momentum - definitely needs a sound dynamical solution.

The present study is carried out within the Parton-Hadron-String Dynamics (PHSD) approach [1] and addresses the expansion dynamics of a partonic fireball at initial temperature $T = 1.7\ T_c$ (T_c= 0.185 GeV) with quasiparticle properties and 4-momentum distributions determined by the Dynamical QuasiParticle Model DQPM [2] at temperature T/T_c = 1.7 for quark chemical potential μ_q=0. The initial distribution in coordinate space is taken as a Gaussian ellipsoid with a spatial eccentricity $\epsilon = \langle y^2 - x^2\rangle / \langle y^2 + x^2\rangle$ in order to allow for the built-up of elliptic flow (as in semi-central nucleus-nucleus collisions at relativistic energies). Note that the dynamical evolution of the system is entirely described by the transport dynamics in PHSD incorporating the off-shell propagation of the partonic quasiparticles according to Ref. [3] as well as the transition to resonant hadronic states (or strings) in line with Lorentz-invariant off-shell transition rates (cf. [1]) for the fusion of quark-antiquark pairs to mesonic states or three quarks (antiquarks) to baryonic states. The latter rate equations are solved by Monte Carlo sampling on a time-depending expanding grid.

Since on average the number of hadrons from the resonance or string decays - formed by parton fusion - is larger than the initial number of fusing partons the hadronization process leads to an increase of the total entropy and not to a decrease as in case of coalescence models. This is a direct consequence of the finite quark and antiquark masses in PHSD which - by energy conservation - lead to hadron masses above 0.8 GeV (1.3 GeV) for meson and baryonic states, respectively; this solves the entropy problem in hadronization in a natural way!

It is, furthermore, interesting to have a look at the final particle ratios K^+/π^+, p/π^+, Λ/K^+ etc. (after hadronic decays) which are shown in Table 1. The latter ratios may be compared to the grandcanonical statistical hadronization model (SM) at baryon chemical potential $\mu_B = 0$ [4]. In this particular case the particle ratios only depend on temperature T. A respective comparison is given in Table 1 for T = 160 MeV and 170 MeV for the SM which demonstrates that the results from PHSD are close to those from the SM for $T \approx 170$ MeV.

	p/π^+	Λ/K^+	K^+/π^+
PHSD	0.086	0.28	0.157
$T = 160$ MeV	0.073	0.22	0.179
$T = 170$ MeV	0.086	0.26	0.180

Table 1: Comparison of particle ratios from PHSD with the statistical model (SM) [4] for T= 160 MeV and 170 MeV.

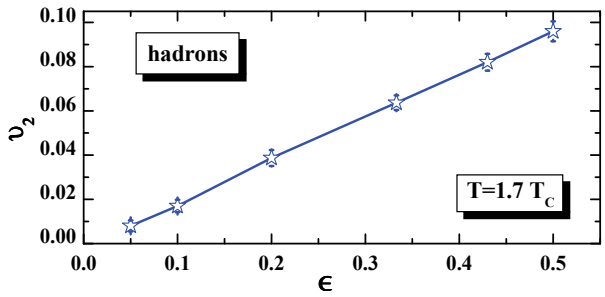

Figure 1: The elliptic flow v_2 versus the initial spatial eccentricity ϵ for an expanding partonic fireball.

Fig. 1, furthermore, shows the final hadron elliptic flow v_2 versus the initial eccentricity ϵ and indicates that the ratio v_2/ϵ is practically constant (≈ 0.2) as in ideal hydrodynamics. Accordingly the parton dynamics in PHSD are close to ideal hydrodynamics as expected from the low ratio of the shear viscosity η to the entropy density s in the DQPM which is on the level of $\eta/s \approx 0.2$ and thus rather close to the suggested limiting lower bound of $\eta/s = 1/(4\pi)$.

References

[1] W. Cassing, E. L. Bratkovskaya, Phys. Rev. C 78 (2008) 034919.

[2] W. Cassing, Nucl. Phys. A 795 (2007) 70.

[3] W. Cassing, S. Juchem, Nucl. Phys. A 672 (2000) 417.

[4] A. Andronic, P. Braun-Munzinger, J. Stachel, Nucl. Phys. A 772 (2006) 167 and private communication.

Fluctuations in A+A collisions within the HSD transport approach

E. L. Bratkovskaya[1] and V. P. Konchakovski[1,2]

[1]Frankfurt Institut for Advanced Studies, Goethe Universität, Frankfurt am Main; [2]Helmholtz Research School, University of Frankfurt, Frankfurt, Germany

An ambitious experimental program for the search of the QCD critical point has been started by the NA61 Collaboration [1] at the SPS, CERN (Geneva, Switzerland). The program includes a variation in the atomic mass number A of the colliding nuclei as well as an energy scan. This allows us to scan the phase diagram in the plane of temperature T and baryon chemical potential μ_B near the quantum chromodynamics (QCD) critical point. One expects to "locate" the position of the critical point by studying its "fluctuation signals". High statistics multiplicity fluctuation data will be taken for p+p, C+C, S+S, In+In, and Pb+Pb collisions at bombarding energies of E = 10, 20, 30, 40, 80, and 158 AGeV.

Our investigation is directly related to the future experimental program of the NA61 Collaboration at the SPS for a search of the critical point. The calculations were performed within the hadron string dynamics (HSD) microscopic transport approach [2].

Thus we have considered central C+C, S+S, In+In, and Pb+Pb collisions with the energy per nucleon in the lab frame E = 10, 20, 30, 40, 80, 158 AGeV. The HSD results shown in the figures correspond to full 4 acceptance (Fig. 1) and forward hemisphere, $y > 0$, (Fig. 2) what is supposed to be close to experimental acceptance. The influence of participant number fluctuations on hadron multiplicity fluctuations has been emphasized and studied in detail [3]. To make these "trivial" fluctuations smaller, one has to consider the most central collisions [4].

The influence of participant number fluctuations on hadron multiplicity fluctuations has been emphasized and studied in detail. To make these "trivial" fluctuations smaller, one has to consider the most central collisions. Indeed, one needs to make a very rigid selection 1% or smallerof the "most central" collision events. In addition, one wants to compare the event-by-event fluctuations in these most central collisions for heavy and for light nuclei. Under these new requirements different centrality selections are not equivalent to each other.

Our findings should be helpful for the optimal choice of collision systems and collision energies for the experimental search of the QCD critical point.

References

[1] M. Gazdzicki *et al.* (NA61 Collaboration), PoS **CPOD2006**, 016 (2006) [arXiv:nucl-ex/0612007].

[2] V.P. Konchakovski, B. Lungwitz, M.I. Gorenstein and E.L. Bratkovskaya, Phys. Rev. C **78** (2008) 024906.

[3] V.P. Konchakovski, S. Haussler, M.I. Gorenstein, E.L. Bratkovskaya, M. Bleicher and H. Stoecker, Phys. Rev. C **73** (2006) 034902.

[4] V.P. Konchakovski, M.I. Gorenstein and E.L. Bratkovskaya, Phys. Lett. B **651** (2007) 114.

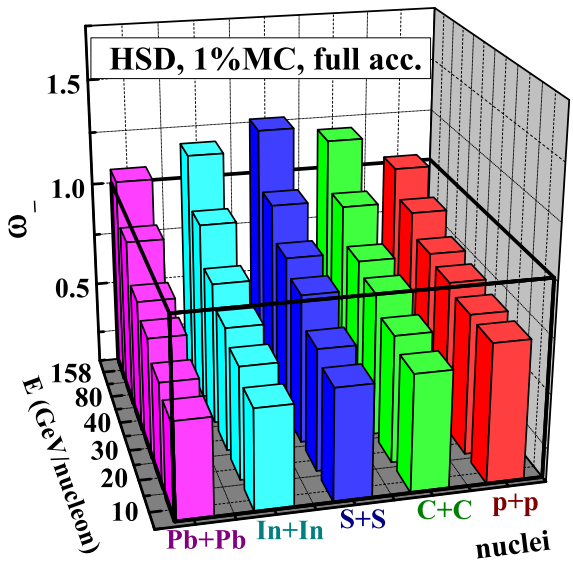

Figure 1: HSD results for multiplicity fluctuations in full acceptance for 1% most central A+A collisions at SPS energies.

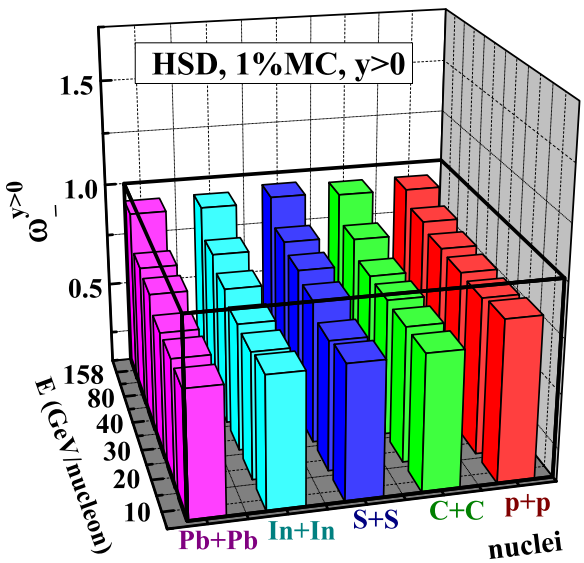

Figure 2: HSD results for multiplicity fluctuations in forward hemisphere, $y > 0$, for 1% most central A+A collisions at SPS energies.

Analytical potential for the elastic scattering of light halo nuclei in the Coulomb field of heavy targets *

L. Borowska† [1,2], K. Terenetsky[2], V. Verbitsky[2], and S. Fritzsche[3,4]

[1]University of Bonn; [2]KINR, Kyiv, Ukraine; [3]GSI, Darmstadt; [4]Frankfurt Institute for Advanced Studies

Light halo nuclei are exotic and weakly-bound systems that have attracted much interest during the past decades [1]. In particular neutron-rich nuclei near the dripline provide a new path for studying nuclear matter and correlations at low densities. In these nuclei, the halo is often formed by one or several loosely attached (valence) neutrons with binding energies of less than 1 MeV and with low angular momenta $(l = 0, 1)$.

To explore and understand the neutron-neutron correlations and their interaction with the (more or less) inert core of the nuclei, nuclear scattering and transfer reactions are the main experimental techniques available until today. Apart from enhanced reaction cross sections for the neutron transfer and rather narrow momentum distributions of the reaction products, these techniques also revealed sizeable cross sections especially for the elastic scattering and the Coulomb dissociation (break-up) of the halo nuclei in collisions with heavy targets below or near to the Coulomb barrier.

In order to describe the anomalous behaviour of these light (halo) nuclei, we have developed a theoretical model [2] for the projectile scattering below and near to the Coulomb barrier by assuming that the internal dynamics of the halo follows adiabatically the motion of the projectiles along a semi-classical trajectory. Emphasis was places on deriving an analytical expression for the (dynamic) polarization potential $\delta V(R)$. Apart from the elastic scattering of the projectiles, this potential enables us to describe the (electrical) polarization of the projectiles and, for a strong enough Coulomb field, also the breakup of the 'deuteron-like' projectile into its neutron and proton parts. In fact, this polarization potential can be applied for any system that has a 'di-neutron' configuration. Moreover, the expression obtained for $\delta V(R)$ displays a quite long-range behaviour, even though its modulus (of both, the real and imaginary part) remains rather small. This long-range behaviour of the potential is expected to be the main reason for the rather large (and unphysical) diffuseness parameter that occured in the work by Moro *et al.* [3] in their attempts to construct an optical potential for the elastic scattering.

As observed epxerimentally [4], a considerable decrease in the (elastic) scattering cross sections occur especially at large scattering angles. Using the analytical expression for $\delta V(R)$ from above, we calculated the differential cross-section for the elastic scattering of ^{6}He + ^{208}Pb at the sub-barrier energies of 14 and 16 MeV. Figure 1 displays these cross sections and compares them with experiment [4], taken relative to the differential cross sections for a pure Rutherford scattering of a projectile with mass m_d and charge Z_p. — From the good agreement with experiment, we may conclude therefore that a *di-neutron* configuration is very likely for the ground state of the ^{6}He halo nucleus. No additional parameters were required in the computations in order to explain the deviations from Rutherford's scattering cross sections.

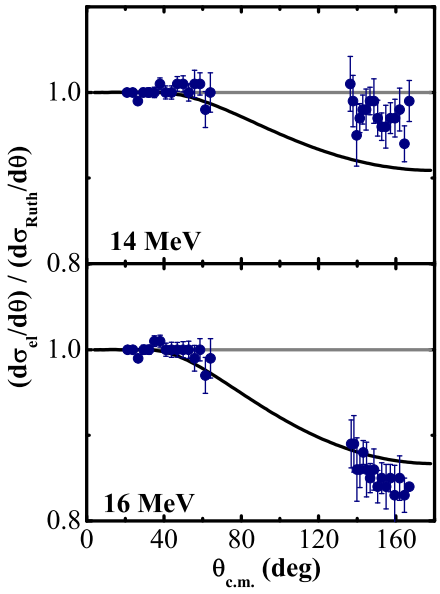

Figure 1: Elastic angle-differential cross sections for the collision of low-energy ^{6}He + ^{208}Pb nuclei as function of the scattering angle θ in the center-of-mass frame. The cross sections are taken relative to the cross sections of a pure Rutherford scattering for a projectile with mass m_d and charge Z_p and are shown for two collision energies as observed experimentally [4].

References

[1] I. Tanihata *et al.*, Phys. Rev. Lett. **55** (1985) 2676.

[2] L. Borowska, K. Terenetsky, V. Verbitsky and S. Fritzsche, Phys. Rev. C **76** (2007) 034606.

[3] A.M. Moro, K. Rusek, J.M. Arias, J. Gomez-Camacho, M. Rodriguez-Gallardo, Phys. Rev. C **75**, (2007) 064607.

[4] A.M. Sanchez-Benitez *et al.*, Nucl. Phys. A **803**, (2008) 30.

* Work supported by GSI under the Project KS-FRT.

† borowska@uni-bonn.de

Pion-cloud effects in light mesons*

Christian S. Fischer[1,2] and Richard Williams[2]
[1]GSI, Darmstadt, Germany; [2]TU Darmstadt, Germany

In hard scattering events mesons and baryons can be viewed as bound states built up from partonic constituents, i.e. quarks and gluons. This picture changes at low energies, where hadronic effects play a more prominent rôle in the nonperturbative structure of hadrons. Of particular importance are pion cloud effects which *e.g.* have a direct impact on the spin structure of the proton [1]. Thus they need to be incorporated in bound state calculations aiming at a realistic description of mesons and baryons.

The natural framework for this composite description of mesons in the continuum are the Schwinger-Dyson and Bethe-Salpeter equations (SDEs and BSEs). Such studies have been extensively performed in the Rainbow-Ladder approximation [2]. Although this approximation led to some phenomenological success, it generically misses out the pion cloud effects. Therefore in our work we improved upon this situation.

Based on an approximation scheme for the quark-gluon interaction developed in [3] and [4] we study the pion back-reaction on the quarks and light mesons thus taking into account pion cloud effects. The resultant system of SDEs and BSEs is depicted in Fig. 1. The first loop diagram of both pictorial equations relates to the usual rainbow-ladder, where the infrared suppressed gluon is enhanced by the vertex dressing, indicated by *YM*. To satisfy the axial-vector Ward-Takahasi identity, a prerequisite for all studies of light mesons, this enhancement is restricted to depend on the same momentum as the exchanged gluon; the two dressings are often combined into an effective gluon dressing which is consequently modelled. The second diagram that contributes to the quark-SDE and meson-BSE represents the back-reaction of the pion onto the quark, *i.e.* pion-cloud effects. This requires knowledge of the quark-pion vertex, which we parameterise in terms of the pion Bethe-Salpeter amplitude. Necessarily this couples the two equations into a highly non-trivial system which we solve numerically.

We calculated a range of meson observables, detailed in Table 1. We observe that the effect of the pion back-reaction has only a small impact on the pion mass itself, resulting in a small positive or negative shift depending upon the form of the interaction. The impact of including pion-cloud effects on the leptonic decay constant is fairly large, with effects of the order of 10%.

For the remaining heavier mesons, the common trend is that the inclusion of such an unquenching gives rise to negative mass shifts of 100–200 MeV. Most notable of these are for the rho, where we predict that unquenching from the pion-cloud yields a bound-state ~ 100 MeV lighter than in the quenched theory, in line with recent lattice simulations [6].

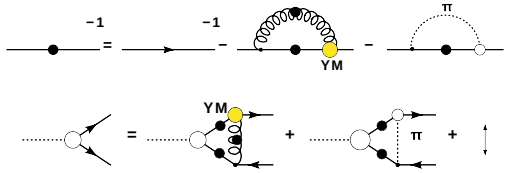

Figure 1: The approximated quark-SDE with effective one-gluon and one-pion exchange, together with the corresponding BSE. The up-down arrow indicates an averaging procedure of the pion-exchange diagram with respect to the dressed/undressed quark-pion vertex.

It is clear, however, that in order to reproduce the rich spectrum of light mesons that we need to include spin dependent contributions from the Yang-Mills part of the quark-gluon vertex. It is envisaged that this will indeed have a strong impact on the calculated masses of bound-states and is the object of future research.

	M_π	f_π	M_σ	M_ρ	f_ρ
w/o pi	125	102	638	795	159
inc. pi	138†	93.8†	485	703	162
Exp.	138	92.4	400–1200	776	156

	M_{a_1}	M_{b_1}	M_η	$M_{\eta'}$
w/o pi	941	879	493	949
inc. pi	873	806	497	963
Exp.	1230	1230	548	948

Table 1: BSE results for a range of mesons employed with ('incl.') and without ('w/o') the pion back-reaction.

References

[1] A. W. Thomas and J. Lab, Prog. Part. Nucl. Phys. **61** (2008) 219 [arXiv:0805.4437 [hep-ph]].

[2] P. Maris and C. D. Roberts, Int. J. Mod. Phys. E **12** (2003) 297 [arXiv:nucl-th/0301049].

[3] C. S. Fischer, D. Nickel and J. Wambach, Phys. Rev. D **76** (2007) 094009 [arXiv:0705.4407 [hep-ph]].

[4] C. S. Fischer, D. Nickel and R. Williams, accepted for Eur.Phys.J. C, arXiv:0807.3486 [hep-ph].

[5] C. S. Fischer and R. Williams, Phys. Rev. D **78** (2008) 074006 [arXiv:0808.3372 [hep-ph]].

[6] D. Leinweber et al, Talk given at the conference 'Tropical QCD' in Port Douglas, Australia, 27.7.-1.8.2008.

*Work supported by the Helmholtz-University Young Investigator Grant No. VH-NG-332.

U_A(1) anomaly and η' mass from an infrared singular quark-gluon vertex*

Christian S. Fischer[1,2], Reinhard Alkofer[3], and Richard Williams[2]
[1]GSI, Darmstadt, Germany; [2]TU Darmstadt, Germany; [3]Graz University, Graz, Austria

The $U_A(1)$ problem of QCD is inevitably tied to the infrared behaviour of quarks and gluons with its most visible effect being the η' mass. A dimensional argument of Kogut and Susskind showed [1] long ago that the mixing of the pseudoscalar flavour-singlet mesons with gluons can provide a screening of the Goldstone pole in this channel if the full quark-quark interaction is strongly infrared singular as $\sim 1/k^4$. A few years later Witten and Veneziano [2, 3] proposed their solution of the problem by considering an expansion of QCD in N_f/N_c, where N_f and N_c are the number of flavours and colours respectively. They showed that the correct pattern of the $U_A(1)$-symmetry breaking can be obtained if the anomalous mass of the η', m_A^2, is related to the topological susceptibility of the theory through the Witten-Veneziano formula

$$m_A^2 = 2\frac{N_f}{f_0^2}\chi^2\,, \qquad (1)$$

which includes the pion decay constant $f_0 \simeq 93$MeV. These two ideas, the Kugut-Susskind szenario of an η' driven by confinement and the Witten-Veneziano formalism are certainly not mutually exclusive. On the contrary, the same topologically non-trivial gauge field configurations could be responsible for both confinement and the resolution of the $U_A(1)$-problem.

In our work [4] we investigated the Kugut-Susskind idea taking into account nonperturbative information on the infrared behaviour of the gluon propagator and the quark-gluon interaction. We employ solutions to the Dyson-Schwinger equations for the propagators of QCD and the quark-gluon vertex to determine the anomalous mass of the η' in the chiral limit . To this end we evaluated the so called diamond diagram, given in Fig. 1. It provides for non-

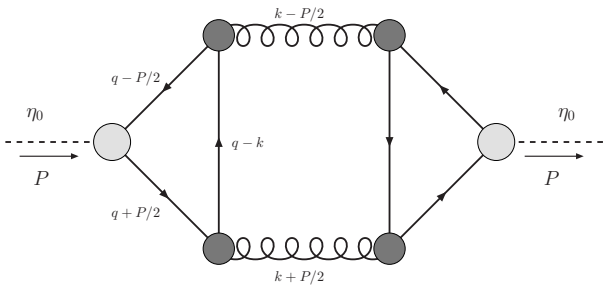

Figure 1: The diamond diagram $\Pi(P^2)$.

perturbative contributions to the meson masses which are only present in the flavour-singlet channel. The diagram is non-vanishing in the chiral limit if and only if it carries the $1/p^4-$singularity in both momenta of the gluons. These singularities, however, are not generated by the gluons alone as assumed in the Kogut-Susskind model. Instead by now we know that the momentum dependence of the gluon propagator function is given by $\frac{Z(p^2)}{p^2} \sim (p^2)^{-1+2\kappa}$ with a positive anomalous dimension κ. However, from the analysis of [5] we know that the quark-gluon vertex, $\Gamma^a_\mu = \frac{\lambda^a}{2}\Gamma_\mu$, should have the behaviour: $\Gamma \sim \left(p^2\right)^{-\kappa-1/2}$. Putting dressed propagators and vertices together we arrive at the necessary $\Gamma^2 Z \sim 1/p^4$ singularity as necessary for the Kogut-Susskind mechanism.

m_ρ MeV	m_A^2 GeV^2	χ^2 (MeV)^4	θ	m_η MeV	$m_{\eta'}$ MeV
747	0.56	169	-23.2	479	906

Figure 2: Numerical results.

Our numerical calculation of the diagram Fig. 1 and subsequent $\eta - \eta'$-mixing have been determined with input for the gluon propagator and the quark-gluon vertex as described in detail in [4]. The parameters are chosen such that the mass of the pion $m_\pi = 135$ MeV has been reproduced. Our results are shown in Fig. 2. They confirm the analytic analysis: we find a topological mass of the eta' and a topological susceptibility χ^2 in agreement with corresponding results from lattice gauge theory [6]. Taking into account $\eta-\eta'$-mixing we find values for the mixing angle θ and the masses of $\eta-$ and η'-mesons that are of the same order as the experimental values. This gives us confidence that the mechanism as such is correct and at work.

References

[1] J. B. Kogut and L. Susskind, Phys. Rev. D **10** (1974) 3468.

[2] E. Witten, Nucl. Phys. B **156** (1979) 269.

[3] G. Veneziano, Nucl. Phys. B **159** (1979) 213; P. Di Vecchia and G. Veneziano, Nucl. Phys. B **171** (1980) 253; G. Veneziano, Phys. Lett. B **95** (1980) 90.

[4] R. Alkofer, C. S. Fischer and R. Williams, Eur. Phys. J. A **38** (2008) 53 [arXiv:0804.3478 [hep-ph]].

[5] R. Alkofer, C. S. Fischer and F. J. Llanes-Estrada, Mod. Phys. Lett. A **23** (2008) 1105 [arXiv:hep-ph/0607293]; R. Alkofer, C. S. Fischer, F. J. Llanes-Estrada and K. Schwenzer, arXiv:0804.3042 [hep-ph].

[6] L. Del Debbio, L. Giusti and C. Pica, Phys. Rev. Lett. **94** (2005) 032003 [arXiv:hep-th/0407052].

*Work supported by the Helmholtz-University Young Investigator Grant No. VH-NG-332.

A General Purpose Trigger Distribution and Data Readout Network Protocol: TrbNet*

J. Michel[1], M. Böhmer[3], I. Fröhlich[1], M. Palka[4], J. Stroth[1,2], A. Tarantola[1], and M. Traxler[2]

[1]Institut für Kernphysik, Goethe-Universität Frankfurt, Germany; [2]GSI, Darmstadt, Germany; [3]Technische Universität München, Germany; [4]Jagiellonian University, Krakow, Poland

In the framework of the current upgrade of the HADES DAQ and Trigger System [1] a network protocol has been developed (Trigger and Readout Board Network - TrbNet) [2]. This protocol connects all entities of the system - including parts of the front-end-electronics - and provides all functionality needed to transport trigger information and data in parallel over the same physical connection.

Here, the main features are a fast and reliable data transport as well as a wide range of configuration options to adapt to the special needs of each subsystem. All boards will be accessible independently to allow for extensive controlling and monitoring features. As the trigger distribution requires a realtime behavior to keep the deadtime of the detector low the network has to guarantee the transmission of the information within a few microseconds.

To adapt to the unlike needs of the different kinds of data, the network is divided into virtual channels that share the physical connection only. Each channel uses distinct logic resources inside the FPGAs which keeps the interdependence of the channels to a minimum and gives the possibility to configure each channel individually.

The physical backbone of the network is formed by optical links, but depending on the specific setup of each subsystem, other types of connections are used as well. Hence, the implementation of the protocol using VHDL was done in a way that permits to exchange the interfaces to the media while the main control logic remains the same.

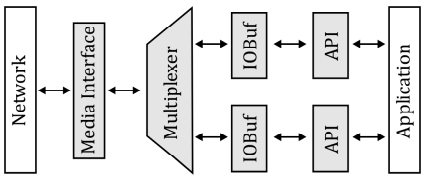

Figure 1: The logical parts of each network node.

This is sketched in Fig. 1. The application (which is a data or trigger source/destination) is hidden from the network via application interfaces (API). The media interface is exchangeable which makes the integration of various technologies possible.

Since the media is used by all channels at the same time, it is vital to be able to switch between them within a short amount of time without disturbing other running transfers. Hence, the data transport is organized in fixed sized packets of 80 Bit size, between which the source of data can be changed. The channels have different priorities to assure that the most important data is transported first.

Data loss or corruption is prevented by the input/output Buffers (IOBuf) which control the integrity all transfers in two ways: First, all receivers have a defined buffer size which is negotiated with the sender beforehand. After the buffer has been filled, sending is stopped until the reception of the data is acknowledged by the receiver. Second, for each buffer a checksum is calculated and checked by the receiver. If there is a mismatch data is marked as corrupted.

Via the API the data is equipped with a header containing an address before being sent and received data is presented to the application. One of the APIs special features is the locking behavior: It forces the sender of a data packet to wait until the replies from all network nodes have been collected before it is allowed to send data on this channel again. One of the reasons for this is the prevention of event mixing, i.e. the merging of data from different events.

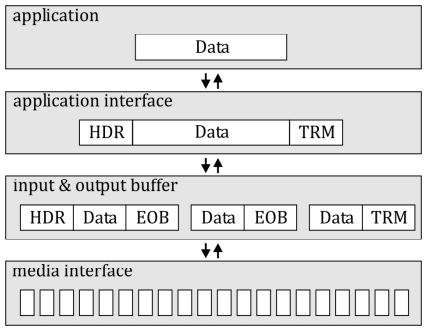

Figure 2: Data flow through network protocol levels.

Performance measurements and calculations have shown that the distribution time of a trigger information packet for the whole system with several layers of network hubs is about 2.1µs. This time is dominated by the time needed by the hardware serializers and deserializers of the optical links which cannot be influenced by the network design. The optical links themselves are working with a data rate of 2 GBit/s resulting in a data bandwidth of up to 1.24 GBit/s due to protocol overhead and the inherent 8b/10b encoding.

References

[1] S. Yurevich et al., Upgrade of the HADES DAQ/Trigger System, this volume.

[2] J. Michel, "Development of a Realtime Network Protocol for HADES and FAIR Experiments", diploma thesis, Univ. Frankfurt 2008.

* Work supported by EU grant 515876

Diamonds as timing detectors for MIPS: The HADES proton-beam monitor and start detectors

W. Koenig[1], and J. Pietraszko[1] for the HADES collaboration
[1]GSI, Darmstadt, Germany

Introduction

Diamond detectors are well known for their radiation hardness and high drift speeds of both electron and holes making them ideal as start detectors placed in the beam. However, due to the large effective energy needed to create electron hole pairs (13 eV) the charge created by minimum ionizing particles (MIPS) traversing the diamond is marginal (8000 pairs for a 300 µm thick diamond) [1]. In the following a dedicated, low noise readout scheme is described as well as its application as a start detector for protons in the HADES experiment.

Diamond Readout

Mono-crystalline diamonds with two different detector sizes of 3.5×3.5 mm² (4 segments) and 4.7× 4.7mm² (8 segments) were used with thicknesses of 300µm and 500µm, respectively. This results in both cases in a segment capacitance of 0.25 pF only. RF transistors with low input capacitance (0.2 pF) were closely attached to the diamond (see fig. 1). The bias current was reduced to an extremely small value leading to a relatively large input impedance of about 2 k Ω. This results in an integration of the primary charge signal.

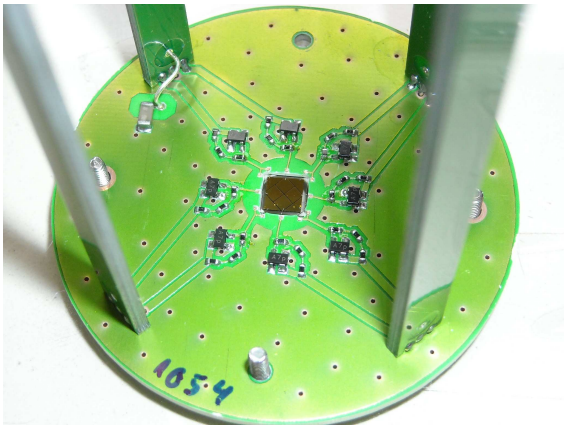

Figure 1: PC board (ϕ =50 mm) with the diamond (4.7× 4.7 mm²) in the centre surrounded by 8 amplifiers.

Final shaping is done by an external amplifier resulting in risetimes (10%-90%) of 1.2 ns (300µm) and 1.35 ns (500µm), respectively.
It should be mentioned that for such a design it is absolutely necessary to keep the stray capacitances at a minimum. E.g. the bias current is provided via 3 resistors in series in order to reduce their capacitive coupling.
The power consumption of a single amplifier amounts to slightly less than 5mW.

Results

The diamonds were exposed to proton beams with energies from 1.2 GeV to 3.5 GeV and rates of up to 3×10^6 /s /10mm². Fig. 2 shows the time resolution measured with leading edge discriminators between two diamonds. After correcting for the intrinsic resolution of the TDC's used and some walk correction, the single diamond resolution amounted to about 100 ps.

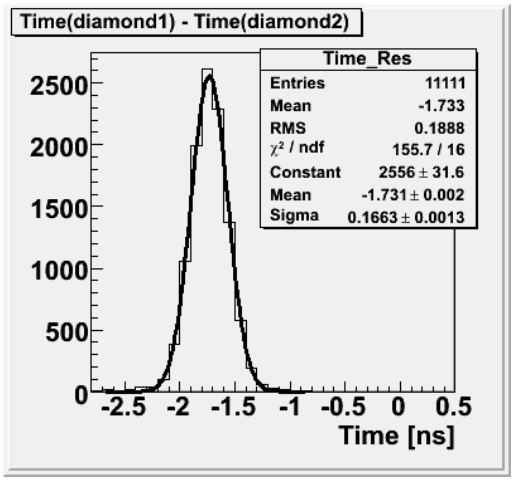

Figure 2: Time resolution for 1.8 GeV protons between two mono-crystalline diamonds without any correction.

From the signal to RMS-noise ratio of about 23 (300µm) and 27 (500µm) one expects a time resolution of about 65 ps for both thicknesses.
The detection efficiency was determined to be ≥ 95%.

Outlook

Due to continuous progress in the development of low noise transistors the signal to RMS-noise ratio can be improved by nearly 50% at 10% shorter risetime based on up to date SiGe:C technology (simulation result only). In particular, tiny housings provide less stray capacitance.
The total area of all components of such amplifier amounts to only 2 mm² including solder pads.

References

[1] Talks at the 4th NoRHDia Workshop, GSI, Darmstadt June 8 - June 10, 2008
http://www-norhdia.gsi.de/talks/4th/W_Koenig.pdf: HADES progress report on MIPS traversing single-crystal diamonds
http://www-norhdia.gsi.de/talks/4th/A_Schuettauf.pdf: Diamond detectors in FOPI

The Upgrade of the Multiwire Drift Chamber Readout of the HADES Experiment: the Optical End Point Board.*

A. Tarantola[1,2], M.Böhmer[6], I. Fröhlich[1], J. Hoffmann[2], B. W. Kolb[2], J. Michel[1], C. Müntz[1], M. Palka[2,3], P. Skott[2], H. Ströbele[1], J. Stroth[1,2], M. Traxler[2], Y. Wang[5], and J. Wüstenfeld[4]

[1]Institut für Kernphysik, Goethe-Universität, Frankfurt, Germany; [2]GSI Helmholtzzentrum für Schwerionenforschung GmbH, Darmstadt, Germany; [3]Smoluchowski Institut of Physics, Jagiellonian University, Krakow, Poland; [4]Institut für Strahlenphysik, Forschungszentrum, Dresden-Rossendorf, Germany; [5]Institute of Modern Physics, Lanzhou, China; [6]Technische Universität, München, Germany. For the HADES collaboration.

In the context of the HADES DAQ/Trigger upgrade [1], a new data acquisition for the 24 Multiwire Drift Chambers (MDCs) has been developed. The project is based on the Trigger and Readout Board (TRB) [2]. Specific add-on boards provide the interfaces to the detector Front End Electronic (FEE). The interface to the MDC FEE is the MDC optical add-on board (MDC-OptAddOn). The counterpart on the FEE side is the Optical End Point Board (OEPB) in Fig. 1. The OEPB will replace the currently used Driver Card (DC). The DC is equipped with two transceivers where the signals are converted (RS-485<->TTL).

The demands placed on the OEPB have to be matched with very strict space constraints and low power consumption. One FPGA (Lattice ECP2/M) will control and readout the TDCs on the FEE. Its large resources allow for the storage of several events close-to-front-end, in Fig. 2. With the employment of a Fibre Optical Transceiver (FOT, from Firecomms) the data transmission will be changed from a parallel copper bus to a serial optical fiber connection. The

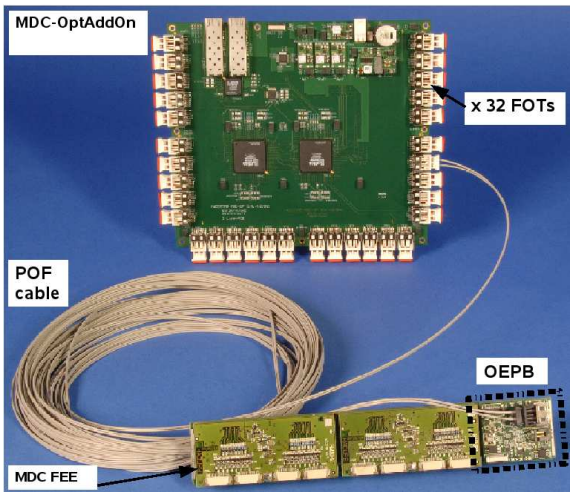

Figure 1: The MDC-OptAddOn with the FEE. The plastic optical cable (up to 30 meters) is connected to the OEPB, which is plugged onto one Motherboard. On the back side of the Motherboard are the TDCs.

* This work has been supported by GSI and the EU under the contracts CNI (construction) “DIRAC-PHASE-1” (515876) and “Hadron Physics” (RII3-CT-2004-506078), the BMBF, the Helmholtz Research School and the Polish MEEN (158/E-338/SPB/6.PR UE/DIE 455/2004-2007).

LVDS input/output of it is connected directly to the FPGA SERDES, which works down to 250 Mbit/s while the FOT works up to 250 Mbit/s. The principal advantage offered by Plastic Optical Fibre (POF) is its total electromagnetic immunity, simplicity in handling and low power consumption. Unlike copper cables, the POF does not induce noise into the very sensitive analog input of the MDC FEE. On the software level, data and trigger distribution over optical links is controlled by a media independent protocol (TRB-Net) [3]. The ability to remotely program the FPGA is required, as it is difficult to physically access these boards. Two flash memories placed on the board allow for a dual boot feature: a “golden” firmware is loaded in the first flash memory (which provides a safe communication but not all software features are included). A second firmware (fully featured firmware), which will change frequently, can be loaded remotely (via optical fiber) in the second flash memory. Additionally, the Lattice FPGA includes Single Event Upset (SEU) detection hardware, which is necessary because the OEPB will be operational in a radiation environment.

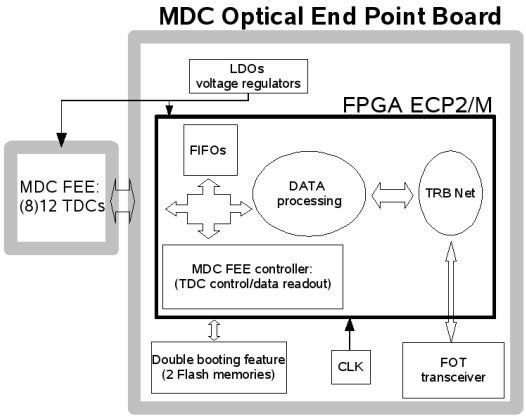

Figure 2: The block diagram of the MDC OEPB.

References

[1] S. Yurevich et al. this volume.

[2] I. Fröhlich et al, “A General Purpose Trigger and Readout Board for HADES and FAIR-Experiments.”, IEEE Trans.Nucl.Sci. 55 (2008) 59-66

[3] J. Michel et al. this volume.

New developments for the Pluto simulation framework

I. Fröhlich[1,3], R. Holzmann[2,3], J. Markert[1,2,3], and J. Stroth[1,2,3]

[1]Institut für Kernphysik, Goethe-Universität, Frankfurt, Germany; [2]GSI Helmholzzentrum für Schwerionenforschung GmbH, Darmstadt, Germany; [3]for the HADES collaboration

Recently, the Pluto event generator was re-designed in order to introduce a more modular, object-oriented structure [1], thereby making additions such as new particles, decays of resonances, new models up to complex customizations easily applicable. Particular attention was paid to define user-friendly interfaces allowing to extend Pluto to a comprehensive simulation framework.

The new model scheme

Architecture: Pluto uses distinct C++-classes for the description of particles and their production and decay properties. From these build-in classes Pluto creates the required instances for the calculations, which are called models. Each of these models, which describe the respective mass shape (e.g. a mass-dependent Breit-Wigner) and the partial/total decay width, can be accessed from all locations of the software package, as well as in user macros. The choice which of the offered physics models are actually used can be done inside the production ROOT macro via a distribution manager, which makes sure that only one "primary" model is selected per decay and particle, respectively. Pluto offers the user the freedom to attach user-defined models either based on its own sources or new classes at runtime, thereby replacing built-in models.

In the new scheme, our goal is to offer these models in a non-monolithic mode, mainly motivated by the HADES pp/dp measurements at 1.25 (A)GeV [2]. The above-indicated modularity of Pluto is realized by splitting the primary models into *secondary* models for all kinds of purposes in order to, e.g., exchange form factors or total cross sections. This is extremely valuable for incorporating different descriptions of the Dalitz decay $\Delta \rightarrow Ne^+e^-$ via a common interface and electromagnetic form factors, and to add parameterizations for the virtual bremsstrahlung process $NN \rightarrow NNe^+e^-$.

Generators and total cross sections: The event sampling generates spectra with a defined shape, but their normalization based on cross-sections and (mass-dependent) branching ratios are important as well. We included a normalization of elementary reactions as one of the main applications of weights, using the new feature of having seconday models. Total cross section models for elementary NN collisions at 1.25 (A)GeV have already been implemented. An additional feature is that sampling is done using an independent flat di-lepton distribution first and reweighted with the physics model. Finally, the distribution of the produced events represent the respective $d\sigma/dX$ on an absolute scale, which makes the comparison with data, in particular for cocktail simulations, more easy and save.

The event loop interface

After all models have been selected, an elementary reaction chain is defined with a character string containing the reaction products (which is e.g. for the Δ^+ production in the pp reaction at 1.25 GeV: `"p D+ [p dilepton [e+ e-] ]"`) and the event loop is started with the `Loop()` command. Here, user-defined as well as a number of pre-defined classes can interact with the event loop in order to modify the particle stream before writing to disk. This interface can be employed for a various number of features as decribed below. Like in the previous section, user classes can be compiled and added on-the-fly.

File access: Particle tracks might be added from (or written to) user files in any self-defined format.

Embedded particles: Test particles can be embedded into a background reaction. With the previous feature this allows for "track embedding", in order to embed particles into real events with an already reconstruced vertex.

Bulk decay: In addition to a well defined reaction chain, Pluto offers free "bulk" decays, i.e. the decay of (embedded) particles follo the calculated mass-dependent branching ratios.

Filters: The particles can be pre-filtered using a "detector acceptance" user class.

The histogram projector: The main aim of the "projector" is to offer a simplified analysis method following a similar idea as `TTree->Draw()` to project particles (and their correlations) into on-line histograms. However, it has more features, namely the composition of composite invariant masses, like e.g.:

```
_x=([e+] + [e-])->M2();
```

and inline rotations and boostings, e.g.:

```
p1->Rot([D+]); p1->Boost([D+]);
```

All browsable methods of the ROOT `TLorentzVector` class can be used on the resulting (composite) particles. This is much faster than (uncompiled) analysis macros and allows the user to stay very flexible. In addition, the connection to detector filter classes is already prepared and ready for implementation.

References

[1] I. Fröhlich *et al.*, PoS(ACAT)076 [arXiv:0708.2382].

[2] HADES collaboration, this volume.

Behaviour of the HADES-RPC counters under highly ionizing particles

P. Cabanelas[1], M. Morales[1], D. Gonzalez-Diaz[2], A. Gil[3], J. A. Garzon[1], D. Belver[1], E. Casarejos[1], W. Koenig[2], M. Palka[2], J. Pietraszko[2], M. Traxler[2], M. Weber[4], and the HADES collaboration

[1]USC, Santiago, Spain; [2]GSI, Darmstadt, Germany; [3]CSIC-IFIC, Valencia, Spain; [4]TUM, Munich, Germany

The energy loss dependence in tRPCs is poorly known, being the only available data subject to strong controversy [1]. All in all, there are theoretical evidences [2], [3] that the intrinsic behaviour of a tRPC with the average energy loss (ΔE) can be approximated by the relations:

$$\bar{t}(\Delta E) = \frac{t_{rise}}{\ln 9} \ln \frac{\Delta E_{mips}}{\Delta E} + t_{off}(v_{th}, t_{rise}) \quad (1)$$

$$\sigma_{_T}(\Delta E) = \frac{t_{rise}}{K_1 \ln 9} \sqrt{\frac{\Delta E_{mips}}{\Delta E}}$$

$$\varepsilon(\Delta E) = 1 - \exp\left[-n_o(1 - \frac{\eta}{\alpha} + K_2 \frac{\alpha}{g}) \frac{\Delta E}{\Delta E_{mips}}\right]$$

$\bar{t}$ refers to the average and $\sigma_{_T}$ to the rms of the time response distribution, v_{th} is the physical threshold, t_{rise} the signal rise-time, n_o is the number of primary ionizations, g the gap size, α and η the multiplication and attachment coefficients and K_1 and K_2 are functions of order unity. Eqs. 1 are obtained under the assumption that the signal is still exponential at the threshold level, and the very complex Space-Charge effects can be neglected there. Due to that it is perhaps no surprise that there is no analytical way so far for obtaining either the average prompt $\bar{q}_p(\Delta E)$ or total $\bar{q}_{_T}(\Delta E)$ charge in tRPCs. This is indeed of paramount importance for subtracting the drifts of $\bar{t}(\Delta E)$ through slewing corrections in plots of the kind $\bar{t}(\Delta E)$ vs $\bar{q}(\Delta E)$.

Data recently taken at GSI-SIS using RPC cells from HADES [4] under direct C^{12} and p irradiation ($E_K \simeq 1.8$ GeV/A) has provided for the first time access to these observables, in a clear way. Fig. 1 shows the behaviour of the average time-of-flight with respect to mips ($\Delta\bar{t} = \bar{t}_{mips} - \bar{t}$) and the resolution $\sigma_{_T}$, together with $\bar{q}_p$ (right axis). Remarkably, the behaviour of $\Delta\bar{t}$ coincides with eq. 1, for $t_{rise} \simeq 350$ps (close to the experimental value). Contrary, the time resolution $\sigma_{_T}$ is pretty much independent on ΔE and very close to the measured system-value $\sigma_{_T} = 73$ ps [5]. If the predicted scaling of [2] is taken seriously this would be a strong indication that for strip-like detectors the signal transmission, noise and electronics have a prominent role in the measured $\sigma_{_T}$, rather than primary ionization. The existence of a very strong Space-Charge is illustrated by the fact that $\bar{q}_p \propto \sqrt{\Delta E/\Delta E_{mips}}$ that would be linear, otherwise. Finally, the dependence of $\varepsilon(\Delta E)$ cannot be easily explored, being $\simeq 100\%$. Indeed, if a system is to be built aiming at ion detection for $Z > 2$, the 'multi-gap' seems to be unnecessary [6].

The 'soft' dependence of $\bar{q}_p$ and $\bar{q}_{_T}$ with ΔE has the benefit of providing a much higher rate capability than otherwise expected, since it depends linearly on $\bar{q}_{_T}$ ([7], for instance). With nominal tRPC fields ($E = 100$kV/cm) we see that operation under C^{12} up to fluxes $\phi = 100$ Hz/cm^2 at $\sigma_{_T} < 100$ ps is possible while for mips the practical limit is around 500 Hz/cm^2, as previously reported in [8].

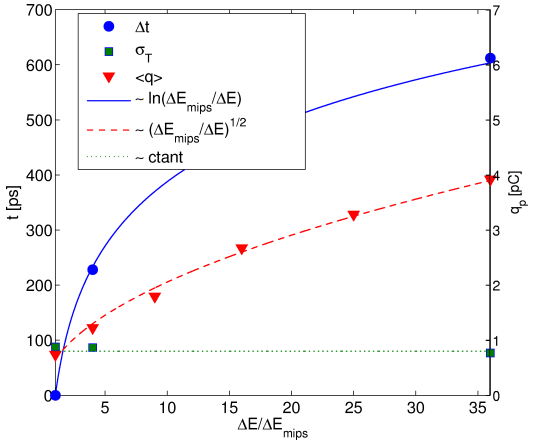

Figure 1: Average time, charge and resolution as a function of the energy loss in mips-equivalent.

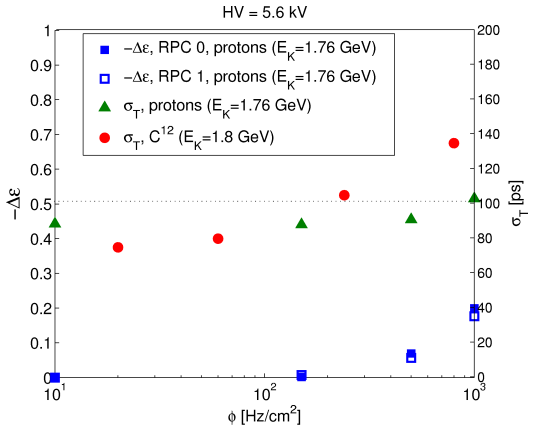

Figure 2: Efficiency and time resolution for mips and C^{12} as a function of the flux of particles ϕ.

References

[1] V. Ammosov et al., JINST 3(2008)P01002.

[2] A. Mangiarotti, P. Fonte, A. Gobbi, NIM A 533(2004)16.

[3] W Riegler, C. Lippmann, NIM A, 518(2004)86.

[4] P. Cabanelas et al., NIM A, to be submited.

[5] A. Blanco et al., doi:10.1016/j.nima.2008.12.091.

[6] E. Casarejos et al., GSI report 2008.

[7] D. Gonzalez-Diaz et al., Nucl. Phys. B(Proc. Suppl.), 158(2006)111.

[8] H. Alvarez-Pol et al., NIM A. 535(2004)277.

Upgrade of the HADES DAQ/Trigger System*

S. Yurevich[1], M. Böhmer[2], I. Fröhlich[3], M. Kajetanowicz[4], J. Michel[3], M. Palka[6,1], P. Salabura[6,1], P. Skott[4], J. Stroth[3,1], H. Ströbele[3,1], A. Tarantola[3,1], M. Traxler[1], R. Trebacz[6], and E. Usenko[7]

[1]GSI Helmholtzzentrum für Schwerionenforschung GmbH, 64291 Darmstadt, Germany; [2]Technische Universität, 80333 München, Germany; [3]Institut für Kernphysik Goethe-Universität, 60486 Frankfurt, Germany; [4]Nowowczesna Elektronika 30-109 Krakow, Poland; [5]GSI Helmholtzzentrum für Schwerionenforschung GmbH, 64291 Darmstadt, Germany; [6]Jagiellonian University, 30-059 Krakow, Poland; [7]Institute for Nuclear Research RAS, 117312 Moscow, Russia

The new HADES DAQ/Trigger system is designed to collect and analyze the detector information at DAQ rates up to 100 kHz (at 20 kHz in Au-Au collisions). Fig. 1 shows a general overview [1] of the architecture of the upgraded DAQ system.

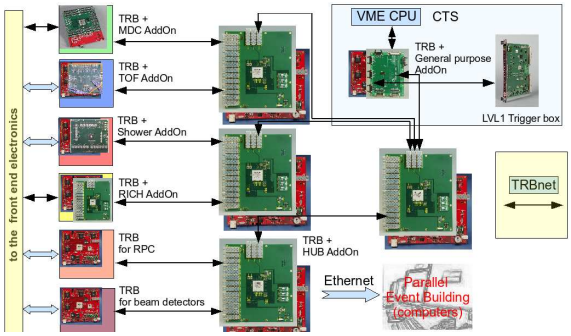

Figure 1: Architecture of the new DAQ/Trigger system.

The "Trigger and Readout Board" (TRB) [2] was successfully used for the data taking during several beam-time periods and can be directly used as a readout board for the Resistive Plate Chamber and beam detectors. Detector specific functions for other detectorsare performed by detector dependent add-on boards (AddOn) which can be mounted on the TRB using a very high data rate digital interface connector.

The AddOn board for the Time of Flight detector is a 128-channel leading edge discriminator plus charge to width converter. The AddOn provides excellent timing performance (less than 10 ps internal time jitter) and a power dissipation of less than 10 mW per channel.

The Shower-AddOn is a 96-channel ADC board with 10-bit resolution.

The RICH detector readout is performed by ADC modules (ADCM). The ADCM contains two ADCs (12 bit, 40 MHz) and provides the connections to 16 front-end cards with up to 128 analog channels. The analog front-end cards connected to the ADCM use the APV25S1 preamplifier ASIC. The APV25S1 has 128 analog input channels, each one connected to a 192 cell analogue pipeline. Online baseline-restoration is done on a large FPGA (Lattice ECP2M100). The board has a low power consumption of approximately 10 W. The data is transported via an optical link with 2 Gbit/s full duplex data transfer capability. The RICH-AddOn modules equipped with 16 optical links will handle the task of receiving and concentrating the data streams.

The complete digital readout of the Multi-wire Drift Chamber (MDC) is replaced by the Optical End Point Board [4] (OEPB) on the Front End Electronics (FEE) side. The OEPB is equipped with a Lattice FPGA (ECP2M20) chip and a fibre optical transceiver. An employment of optical signals generated right after the digitization of the analog signals leads to a reduction of noise in the system and an increased data transport bandwidth. The interface to the detector FEE of the MDC is provided by the MDC optical AddOn board. Two Lattice FPGAs (ECP2M100) placed on the board combine the data to events and can possibly perform a first fast on-line tracking.

The media independent Trigger and Readout Board Network [3] protocol (TRBNet) will substitute the current bus-like trigger distribution system. The main feature of the TRBNet is the "concurrent" transmission of data/trigger and slow-control data on the same line (typically optical fibre). The protocol guaranties low latency (below 3 μs) and no data loss due to the included back pressure feature. The distribution of data in the network is performed by optical hubs.

To accumulate 300 MB/s data rate at 20 kHz LVL1 trigger rate, a parallel event building concept will be used. A successful test of the event building scheme with 90 data sources showed a stable operation with the data rates even exceeding the expected. Several schemes of mass storage such as direct recording to the tape via RFIO mechanism and transmitting data to the Lustre file system have been tested. A central control and monitoring system required by the distributed event building and a graphical user interface have been also developed based on the EPICS software.

References

[1] M. Palka et al, Proceedings of IEEE NSS, October 2008, Dresden, Conference Record N06-6

[2] I. Fröhlich et al, "A General Purpose Trigger and Readout Board for HADES and FAIR-Experiments.", IEEE Trans.Nucl.Sci. 55 (2008) 59-66

[3] J. Michel et al, this volume

[4] A. Tarantola et al, this volume

* Work supported by EU grant 515876

Improvement of the HADES track reconstruction

J. Markert[1], V. Pechenov[2], A. Rustamov[2], C. Müntz[1], and J. Stroth[1,2]
[1]Goethe-University, Frankfurt, Germany; [2]GSI, Darmstadt, Germany

The track reconstruction algorithms of the HADES software have been continuously improved during the last years and successfully applied for the analysis of elementary and light collision systems like C+C and Ar+KCl. Currently we are working to cope with the track multiplicity of central heavy ion collisions like Au+Au which are scheduled for the year of 2010 and beyond.

The reconstruction of the particle trajectories in the tracking system of HADES is accomplished in several steps: the spatial correlation of fired drift cells in the drift chambers (MDCs) is performed by a *track candidate* search based on the identification of so-called *wire clusters*. The wire clusters constructed by using the geometrical positions of the fired drift cells together with the target position and define *track segments*. *Track candidates* are finally obtained through the matching of track segments in the inner and outer drift chambers within one sector. The corresponding space positions of the track candidates are fitted by a model function taking into account the drift time information of the cells. The particle momentum is determined by various algorithms making use of the bending of its trajectory inside the magnetic field region.

The up to now used candidate search reaches an efficiency close to 100 % at multiplicities of about 20-30 charged particles per event inside the acceptance, with a few percent contribution of fakes. For higher multiplicities it turned out, that the fake suppression algorithm causes a loss of efficiency of about 20-30 %, especially at the low polar angle region, where the track density is highest. Without applying the fake suppression the efficiency comes back close to 100 %, at the price of 3-4 times more of fake candidates as compared to real tracks (Fig. 1).
This fact indicates that for the tracking software a dedicated filtering algorithm has to be developed which reduces the number of fakes before proceeding to the track fitter. A first version of filter algorithm has been implemented and tested. The filter builds candidates in an iterative procedure out of wires which have the highest probability to originate from a real track. The current version of the filter rejects up to 70 % of the fakes at a high efficiency in Au+Au collisions at 1 AGeV. Furthermore some work has been done to improve the initial position of the candidates by taking into account the measured drift time signals during the projection of the wire volumes. Only the bins on the projection plot which satisfy the condition $\Delta d < \Delta d_{cut}$, where $\Delta d = |d_{exp} - d_{calc}|$ (d_{exp} - measured distance, d_{calc} - distance between wire and line target - project plot bin) are filled (Fig. 2). For d_{cut} = 1.5 mm the initial track position is improved by a factor $\sim$ 2 along the x-coordinate, still at a high efficiency. At the same time the number of tracks contributing to a candidate is substantially reduced yielding an improved input to the track fitting.

The current status of the reconstruction software represents an intermediate step towards high track density tracking, which we will reach at the beginning of 2010.

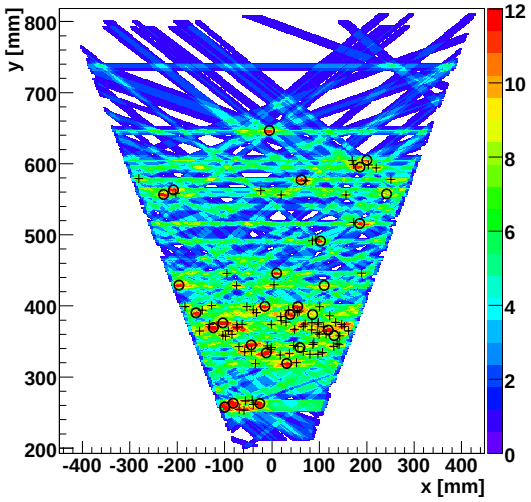

Figure 1: Candidate search in the MDC projection plane for one event Au+Au at 1 AGeV. Black circles indicate the position of candidates belonging to a real track position, black crosses to found fake candidates. The fake suppression is disabled.

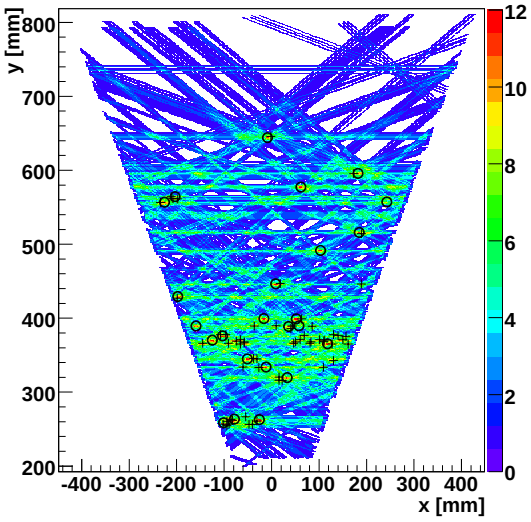

Figure 2: As in fig. 1, but making use out of the information from the drift time measurement. The fake suppression is disabled.

Status of the HADES RPC Time Of Flight Wall*

D.Belver[1], A. Blanco[2], P. Cabanelas[1], J. Diaz[3], P. Fonte[2], J. A. Garzon[1], A. Gil[3], D. Gonzalez-Diaz[4], W. Koenig[4], L. Lopes[2], M. Traxler[4], and the HADES RPC group[1]

[1]USC, Santiago, Spain; [2]LIP, Coimbra, Portugal; [3]CSIC-IFIC, Valencia, Spain; [4]GSI, Darmstadt, Germany

Year 2007 was crowned with the test of a complete RPC sector equipped with 400 FEE channels [1]; a very important mile-stone, indeed, in order for HADES to explore extreme heavy ion collisions in the years 2009-2010. Despite the success, specially regarding the overall detector performance, there were nevertheless concerns regarding the minimum threshold, grounding, system stability, discharge protection and FEE production yield, so efforts were driven to introduce modifications in the FEE design in order to overcome these potentially troublesome limitations.

The FEE of the HADES RPC wall consists of two boards: the DB (Daughter-Board) performing the amplification and digitization of 4 channels, and the MB (Mother-Board) providing the DBs with the regulated power, test signals, a fast sum signal for trigger, threshold setting and monitoring, and a very precise 100 Ω routing for the output LVDS signals. Each MB houses 8 DBs connected through a 16-differential-pin-pairs SAMTEC connector at 90°.

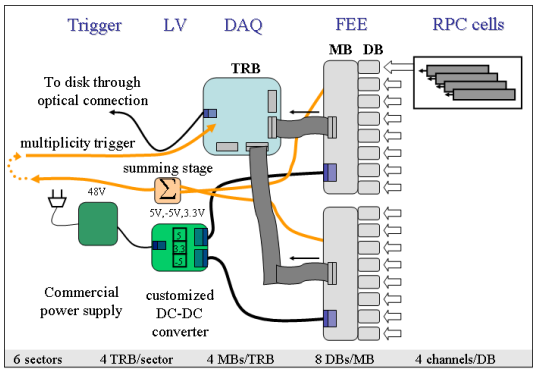

Figure 1: Sketch of the HADES FEE system.

Each of the 6 sectors of the wall is equipped with 108 6-layer DBs providing 35.5 dB power gain at 1 GHz (31 dB amplitude gain up to 2.2 GHz bandwidth), 15 ps jitter per channel, 40 ns built-in dead time and charge-to-width (QtoW) conversion codified in an LVDS output signal. The DBs are connected to 16 8-layer MBs while all the boards in a sector are fed by 2 custom DC-DC switching converter boards [2] (Fig.1). The data acquisition is based on the general purpose TRBs (Trigger and Readout Boards) [3]. Each TRB is equipped with 4x32 HPTDC channels [4] and driven by an ETRAX integrated processor.

After the latest modifications, the FEE stability was increased when operated at a typical 'physical' threshold of

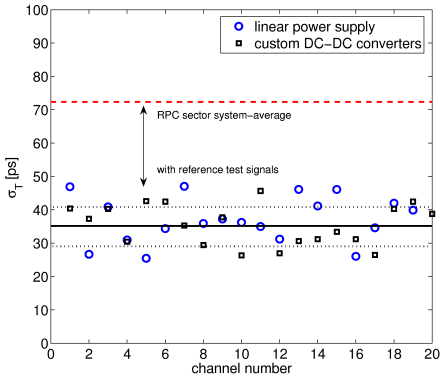

Figure 2: Mean-time resolution for 2 random samples of 20 FEE pairs of channels, using linear power supplies (circles) and custom DC-DC boards (squares). The average system resolution for a full instrumented sector as measured in [5] is indicated with a dashed line.

1.25 mV, being limited to a minimum value of 0.2-0.4 mV (likely due to noise). Fig. 2 shows the FEE jitter, with an average value $\sigma_T = 35 \pm 7$ ps, for the mean-time $T = 1/2(t_{left} + t_{right})$ of 2 FEE channels, as measured with reference test signals. Based on these results the FEE layout has been frozen and mass production started at GSI in late 2008. In total 800 DBOs and 130 MBOs will be produced, enough for feeding 7 sectors. At the time this report is being written, $\sim$ 600 DBOs have been produced and fully assembled, with 216 (2 sectors) of them already tested and validated at USC, at an acceptance rate higher than 95%. As much as 1000 RPC cells (5/6 of the total) have been produced and 4 sectors already mounted at LIP-Coimbra and will be delivered to GSI within short notice, to proceed with a cosmic ray pre-commissioning, before final assembly in the HADES spectrometer. With the main software infrastructure already existing and being regularly used, we are concentrating efforts on the Slow Control software mainly for threshold and HV control (operative), LV, temperature and gas monitoring (under development).

References

[1] D. Belver et al., doi:10.1016/j.nima.2008.12.135.

[2] A. Gil et al., 'Distributed Low Voltage System for the Front-End of the HADES timing RPC wall', accepted in IEEE, Trans. Nucl. Sci.

[3] M. Traxler et al., 128 channel high resolution TDC with integrated DAQ-system, GSI Scientific Report 2005.

[4] HPTDC, J. Christiansen, Digital Microelec. Group, CERN.

[5] A.Blanco et al., doi:10.1016/j.nima.2008.12.091.

*This work was supported by the EC FP6-Hadron Physics No. RII3-CT-2004-506078, EC DIRAC RII3-CT-2005-515876, MEC grants Nos. FPA2006-09154 and FPA2006-12120-C03-02, XUGA grant No. PGIDIT06PXIC20601PM and FCT CERN/FP/83560/2008.

Energy loss measurement with the HADES drift chambers using the Time-over-Threshold method

J. Markert[1], A. Schmah[2], C. Müntz[1], and J. Stroth[1,2]
[1]Goethe-University, Frankfurt, Germany; [2]GSI, Darmstadt, Germany

The signals of the HADES drift chambers [1] are readout and digitized by means of dedicated, customized boards. The sense wires are connected to the analog boards [2], housing ASD8 chips [3] for differential amplification, shaping and discrimination. These chips deliver logical signals with variable width, equivalent to the time the shaped signal exceeds the given threshold. From the width of the drift time signal (***T**ime **o**ver **T**hreshold* (ToT)) an unambiguous measure of the energy loss of the particle can be extracted. The measured ToT depends on the gas mixture, on the reduced electric field E/P, on the track geometry, on the drift cell size and on the threshold setting of the ASD8 chip. Special attention was paid to the unfolding of these dependencies to allow for averaging over all drift cell measurements contributing to a particle track.

For the following discussion the particle tracks are parameterized via minimum distance of the track to the sense wire and the impact angle with respect to the wire plane. To calibrate the measured ToT of the single drift cells the correlation of the ToT with the particle energy loss is fitted by the function

$$ToT = f(dE/dx) = c_0 + c_1 \cdot [log_{10}(dE/dx + c_3)]^{c_2}, \quad (1)$$

with the parameters c_0, c_1, c_2 and c_3. Knowing the value of the momentum and the particle nature from the other detectors, the energy loss of the particle can then be calculated using the Bethe-Bloch formula [8]. The procedure is performed for intervals of 5° impact angle and 100 μm distance from the sense wire for all 4 MDC types. The correlation between the measured ToT and the energy loss of the particles track is non linear. This compression of the correlation is most pronounced for strongly ionizing particles. The shape of the correlation curve depends on the shape of the signal and thus on the arrival time of the drifting electrons on the sense wire and also on the signal shaping performed in the readout electronics.

To allow for averaging over all drift cell measurements, all contributing measurements are normalized to one reference measurement employing the inverse correlation function of eq. (1). Finally a truncated mean method has been applied to improve the resolution. After the truncation method, on average 18 cells out of 24 remain, corresponding to a 20 % cut of all measurements.

The ToT resolution has been studied by making Gaussian fits in each 25 MeV wide momentum bin. The ToT resolution for different particle species is depicted in Fig. 1. For minimum ionizing particles, an energy loss resolution of around 7 % has been achieved. A better resolution of about 4 % can be found for stronger ionizing particles.

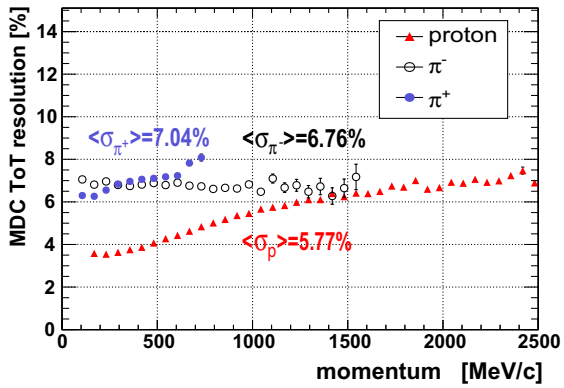

Figure 1: ToT resolution versus particle momentum. The merging of the π^+ line into the proton line at high momentum is due to the increase of the wrongly identified protons

The resolution strongly depends on the number of drift cell measurements contributing to a particle track. Taking into account the varying thickness of the detector and the number of measurements per track, one can demonstrate that the method described here yields similar results regarding the dE/dx resolution as compared to the drift chambers of Belle [6] and BABAR [7]. It fits also nicely with the empirical formula given in [8].

At present the energy loss measurement of the MDCs is heavily used by the HADES collaboration in addition to the time of flight of the particles and the energy loss measured in the TOF detectors to improve the signal to background ratio (S/B) in the detection of rare strange hadrons like K^+, K^- and ϕ. For the K^+ signal a S/B ratio of ~ 36 has been reached, correspondingly $S/B_{K^-} \sim 4$ and $S/B_\phi \sim 1.1$. The K^- and ϕ signals could be extracted only due to the additional background rejection power of the MDC energy loss measurement.

References

[1] C. Müntz et al. Nucl. Instr. Methods, A 535:242, 2004.
[2] E. Badura et al. Particles and Nuclei, No.1[98]:73, 2000.
[3] F. M. Newcomer. IEEE Transactions on Nuclear Science, 40(4):630, 1993.
[4] L. Ratti et al. VCI 2004, Vienna, talk 2004.
[5] A. H. Walenta et al. Nucl. Instr. Methods, 161(45), 1979.
[6] A. Abashian *et al.*, Nucl. Instr. Meth. A479 (2002) 117.
[7] B. Aubert et al. Nucl. Instr. Methods, A(479):1–116, 2002.
[8] W.M. Yao *et al*, J. Phys. G33 (2006) 1.

Low resistivity materials for the low polar angle of the CBM-TOF wall

L.A. Diaz[1], J. A. Garzon[2], D. Gonzalez-Diaz[3], L.Lopes[4], M. Morales[2], and C. Pecharroman[5]
[1]CINN-CSIC, Oviedo, Spain; [2]USC, Santiago, Spain; [3]GSI, Darmstadt, Germany; [4]LIP, Coimbra, Portugal; [5]ICMM-CSIC, Madrid, Spain

Avalanches in timing RPCs release an average charge $\bar{q} \simeq 1.5 - 3$ pC per gap, slightly depending on the geometry, gas and field [1]. An RPC must be therefore able to evacuate the charge from the system at a rate $1/\tau$ comparable to the avalanche rate r (τ is the relaxation time of the resistive material). The dependence with r can be evaluated after the initial transitory phase by resorting to the Ohm law in electrostatic equilibrium (DC situation):

$$V_{gap} = V - IR = V - \bar{q} r R = V - \bar{q}\phi\rho d \qquad (1)$$

with ϕ being the avalanche flux and d the resistive plate thickness per gap. For 1 mm thin float glass tRPCs ($\rho_{20} \simeq 6000$ GΩcm [2] with one order of magnitude decrease in 25 K [3]) a voltage drop of nearly 1-2 volts/Hz/cm^2 can be inferred at ambient T. This is the reason why float glass tRPCs work only up to some 100's Hz/cm^2. In practice, operation up to almost 500 Hz/cm^2 was proved with a defocused beam in stationary (DC) conditions [4] and even up to 1000 Hz/cm^2 but in the transitory region [5] (short spills). Eq. 1 can be re-expressed as a function of the relevant time scales and the ratio of the nominal voltage to the voltage drop created by each individual avalanche V_{aval}:

$$r\tau \ll \frac{V}{V_{aval}} \qquad (2)$$

and a simple derivation based on eq. 1 shows that in first order the rate capability of an RPC can be expressed as [6]:

$$\phi_{max} \propto \frac{\bar{q}}{\rho d} \qquad (3)$$

so one can linearly increase the rate capability of the chamber by decreasing ρ and/or d. The 20 kHz/cm^2 at the low polar angle region of the CBM-TOF wall therefore impose a 20/40-fold decrease with respect to float glass for any of these variables, of which ρ is the more natural candidate.

Modelling the material as a simple RC circuit, the transitory regime prior to the aforementioned DC situation can be characterized by a transient time t_{eq} given by [7]:

$$t_{eq} \simeq \frac{\tau}{d\bar{q}/dV\phi\rho d} \ln\left(1 + d\bar{q}/dV\phi\rho d\right) \qquad (4)$$

Nonetheless, a realistic description requires to implement via MC the material response function $\Psi(t)$. Fig. 1 shows the accuracy of such an approach at describing the transients in $\bar{q}$ ($I \propto \bar{q}$) arising from X-ray illumination [2].

The high CBM rates pose new questions regarding ageing. Taking a working time equivalent to 5 years operation at 50% duty cycle, a density of total transported charge $Q/A \simeq 1.5{-}3$ C/cm^2 must be furnished. While low ageing for $Q/A = 20$ mC/cm^2 has been proved for glass tRPCs over 2 years operation [8], the almost 100-fold increase for

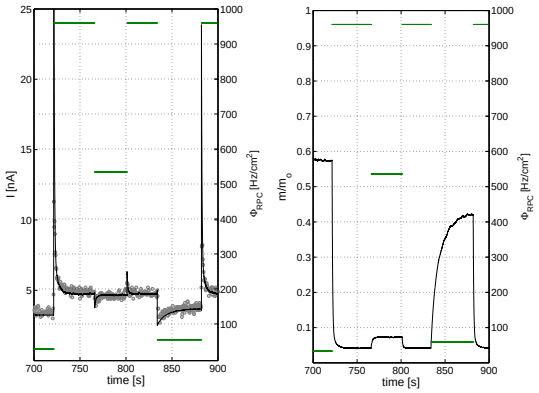

Figure 1: Left: Transients in the measured current (the flux steps are indicated on the right axis). Right: behaviour of $\bar{q}$ in adimensional units as obtained from the model.

CBM requires of similar studies yet. In particular, the material itself should keep the integrity of its electrical properties for such a high Q/A and total dose.

Through a collaboration USC/CSIC/GSI we recently started an effort to produce low resistive materials able to withstand the required amount of transported charge. Four samples of a ceramic-metal composite were produced via the novel SPS technique for different metal concentration f close to the percolation limit f_c, where the electrical properties of the composite roughly scale like:

$$\rho = \rho_{cer}(f_c - f)^p \quad \epsilon = \epsilon_o(f_c - f)^{-q} \qquad (5)$$

In particular, the 88/12 (ceramic/metal) sample, with 2 cm diameter and 3 mm thickness, showed $\rho_{20} = 25$ GΩcm and $\epsilon_{r,\infty} = 32$, with a breakdown field higher than 3 kV/cm and just a small degradation of the resistivity for $Q/A = 20$ mC/cm^2 (attributed to the experimental setup). We plan to build chambers with the different samples soon in order to explore the typical CBM rates and higher.

References

[1] P. Fonte, V. Peskov, NIM A, 477(2002)17.
[2] D. Gonzalez-Diaz et al., doi:10.1016/j.nima.2008.12.133.
[3] D. Gonzalez-Diaz et al., NIM A. 555(2005)72.
[4] H. Alvarez-Pol et al., NIM A. 535(2004)277.
[5] A. Akindinov et al., NIM A. 533(2004)74.
[6] D. Gonzalez-Diaz et al., GSI Report(2007), FAIR-EXP-09.
[7] D. Gonzalez-Diaz et al., Nucl. Phys. B(Proc. Suppl.), 158(2006)111.
[8] S. Gramacho et al., doi:10.1016/j.nima.2008.12.133.
[9] A. L. Efros et al., Phys. Status Solidi B 76(1976)475.

A Swift High Resolution Pixel Sensor for the CBM MVD *

M. Winter[1], J. Baudot[1], A. Besson[1], A. Brogna[1], G. Claus[1], C. Colledani[1], R. De Masi[1], A. Dorokhov[1], G. Dozière[1], W. Dulinski[1], M. Goffe[1], A. Himmi[1], Ch. Hu-Guo[1], K. Jaaskelainen[1], F. Morel[1], I. Valin[1], and G. Voutsinas[1]

[1]IPHC, Strasbourg, France

Introduction

Swift, high resolution CMOS pixel sensors are being developed for the CBM Micro Vertex Detector (MVD), allowing for high density particle tracking. Designed at IPHC, the sensors are manufactured by the CMOS industry and can be thinned down to $\leq 50\ \mu m$.

To accommodate the data rate, the signals delivered by the sensors are discriminated before being filtered by an integrated zero-suppression logic. A fast read-out is achieved by grouping the pixels composing the sensitive area in columns read out in parallel. The development of this architecture relies on two parallel tasks. One of them addresses the upstream part of the signal conditionning chain, including the pixel array and the discriminators ending the columns. The other concerns the downstream part, combining a zero-suppression logic with output memories.

Pixel array with binary outputs

Small prototypes were fabricated and tested in previous years to develop the upstream part of the sensor architecture [1]. *MIMOSA-22* is the final prototype of this R&D line supported by the European project EUDET [2]. Two complementary versions were designed and fabricated. They were both characterised in 2008, first at IPHC with an ^{55}Fe source and next at the CERN-SPS, mounted on a silicon-strip beam telescope.

The sensor features 136 columns read out in parallel, each containing 576, 18.4 μm pitch, pixels. 128 columns are ended with a discriminator, while 8 columns have analog outputs for test purposes. The chip incorporates a JTAG controller. The frame read-out time is 92.5 μs. Various pixel designs were integrated in the chip, allowing to explore different sensing diode sizes, amplification schemes, ionising radiation tolerant designs, etc.

A modest noise value was found for most pixel designs, ranging from about 10 to 14 e$^-$ENC, with a mild operating temperature dependence. The 128 discriminators exhibited a modest threshold dispersion ($\pm$ 4 % standard deviation) and contributed marginally to the total noise. No significant non-uniformity was found over the sensitive area of any of the 6 sensors tested.

When exposed to a 120 GeV π^- beam at the CERN-SPS, a signal-to-noise ratio in the range 17–21 (most probable value) was observed, depending on the pixel design. Table 1 illustrates the measured detection performances.

Threshold	Detection eff.	Fake rate	Resolution
3 mV	99.8 $\pm$ 0.05 (stat) %	$\sim 4{\cdot}10^{-4}$	$\sim 3.7\ \mu m$
4 mV	99.7 $\pm$ 0.05 (stat) %	$\sim 7{\cdot}10^{-5}$	$\sim 3.5\ \mu m$

Table 1: Detection efficiency, average fake hit rate and single point resolution measured at the CERN-SPS with MIMOSA-22 for two discriminator threshold values.

The observed detection efficiency remains > 99.5 % for threshold values high enough to keep the fake hit rate $< 10^{-4}$, a value ensuring that the signal processing micro-circuits will not be saturated by pixel noise fluctuations. The single point resolution is $< 4\ \mu m$, well below the MVD requirement of $\lesssim 5\ \mu m$. These results validate the architecture for its integration in the complete sensor.

Zero-suppression micro-circuit

SUZE-01 incorporates the zero-suppression micro-circuit and output memories composing the downstream part of the sensor architecture. Fabricated in 2007 within the EUDET project, it was tested extensively at IPHC until Spring 2008 with millions of patterns at its nominal clock frequency (100 MHz) and above. No failures were spotted for frequencies $\leq$ 115 MHz. This guarantees that the architecture is suited to the complete sensor specifications.

Towards a complete sensor

A complete, full scale, sensor (called *MIMOSA-26*) was designed in 2008 within the EUDET project and sent for fabrication. It combines the architecture of *MIMOSA-22* and *SUZE-01* in a comprehensive charge sensing and signal read-out chain, providing discriminated signals in a binary mode including the pixel address. It features 1152 columns of 576 pixels, read out in $\sim 100\ \mu s$. It will be extensively tested in 2009 and equip the final version of the EUDET telescope. If satisfactory, this architecture will next be evolved progressively to shorter read-out time, aiming for the target value of $\sim 10\ \mu s$ required for the MVD.

References

[1] M.Winter et al., "Achievements of CMOS Pixel Sensors for the CBM Micro-Vertex Detector", GSI Scientific Report 2007.

[2] EUDET collaboration, "Detector R&D towards the International Linear Collider", supported by the E.U. within FP6, http://www.eudet.org/.

* Work supported by the European project EUDET(FP6).

Software development for CBM readout controller board

N. Abel[1], J. Adamczewski-Musch[2], H.G. Essel[2], U. Kebschull[1], S. Linev[2], and S. Müller-Klieser[1]
[1]KIP, Heidelberg, Germany; [2]GSI, Darmstadt, Germany

Readout controller

The readout controller (ROC) is an FPGA-based board, developed at the Kirchhoff Institute for Physics (KIP), University of Heidelberg, for configuration and reading out data from nXYTER chips [1]. Basic readout features of ROC are implemented in VHDL. For high-level functionality (configuration, control, data transport to host PC) a hard-core PowerPC avaiable on the Virtex-4 FX FPGA is used. Communication with host PC is performed via a 100 Mbit Ethernet link.

PowerPC program

The PowerPC program is written in plain C. It runs standaone, without any operating system. Therefore all tasks are handled in a common application loop: data taking from FPGA; storing data into a ring buffer; sending data from ring buffer to the PC; serving control requests from the PC. The main loop is designed such that each task runs not more than few ms at once. Otherwise small FPGA queues would run out of memory and data would be thrown away. The big size of the ring buffer ($\sim$110 MB) allows to decouple two major tasks - data taking and data sending. So, the PowerPC can fill the buffer during several seconds without sending data immediately to host PC.

Data transport protocol

The reliable transport of data from ROC to the PC is very important. Due to performance reasons UDP/IP as transport layer is used. It is very simple and does not consume many CPU resources. On the other hand, UDP does not guarantee the delivery of packets and one should implement a retransmission logic.

The designed protocol is fully based on a request-reply scheme - the ROC never sends data without request from host PC. This allows to implement a back pressure logic easily: if the host PC is not able to process data in time, it will not request new data from ROC.

The host PC is protocol master and takes care that no more than 30-40 UDP packets ($\sim$1.5 KB size) are requested at once, otherwise the Linux socket buffer would overflow and some of the packets would be lost. To check for a packet loss each packet has a unique id. So the host PC can easily detect missing packets and can request their retransmission.

ROClib library

The C++ based ROClib library provides an API to configure and monitor ROC states via reading/writing (peek/poke logic) of virtual registers on the ROC. It also implements the transport protocol and offers blocking and non-blocking methods to readout data from ROC in user application. The current ROClib implementation achieves data transfer rate up to 12.3 MByte/s with very low CPU usage.

The ROClib also provides a ROOT [2] dictionary for all classes. Therefore one can use the ROClib within CINT scripts and easily develop controlling and configuration scripts for ROC.

Integration with DABC

The Data Acquisition Backbone Core (DABC) [3] is a general purpose data aquisition framework which allows to integrate experiment specific front-end components. Special device and transport classes were implemented to integrate ROClib functionality into DABC. This allows to configure ROC and take its data directly into DABC modules. To perform ROC-specific data transformations and analysis, two special module classes were written: a combiner of data from several ROCs into one event, and a module for time calibration.

All these components were used in a CBM test beam time in September 2008 to read and store data from 3 ROCs. Special DABC application class was introduced to configure and run all necessary components during beam time. Monitoring of the running DAQ was possible with a Go4 analysis, connected to DABC via socket channel.

Status and outlook

The developed software allows to configure and control ROC from any Linux PC. Data taking with DABC is implemented and was used during September 2008 beamtime. With latest improvements $\sim$7 MB/s sustained rate of data taking is achieved. Further developments are required to reach the possible maximum of 12 MB/s. Implementation of a data transport via optical channel is planned. Information and latest news on http://cbm-wiki.gsi.de

References

[1] A.S. Brogna et al., "N-XYTER, a CMOS read-out ASIC for high resolution time and amplitude measurements on high rate multi-channel counting mode neutron detectors", Nucl. Instrum. Methods A 568 (2006), pp. 301-308

[2] ROOT - object oriented analysis framework, http://root.cern.ch

[3] J. Adamczewski, H.G. Essel, N. Kurz, S. Linev, "Data Acquisition Backbone Core DABC", IEEE Trans.on Nucl. Science, Vol.55, No.1, February 2008, pp. 251-255

Ultra-Fast Timing with Plastic Scintillators

R. Hoischen[1,2], S. Pietri[1], W. Prokopowicz[1], J. Gerl[1], N. Kurz[1], H. Schaffner[1], H.J. Wollersheim[1], P. Golubev[2], and D. Rudolph[2]

[1]Helmholtzzentrum für Schwerionenforschung GmbH, D-64291 Darmstadt, Germany;; [2]Department of Physics, Lund University, S-22100 Lund, Sweden

As precursor to HISPEC, the upcoming PreSPEC campaign incorporates the commissioning of the first version of the LYCCA (Lund-York-Cologne-CAlorimeter) detector system called LYCCA-0. The LYCCA detector is a Time-of-Flight (ToF), ΔE, E set-up designed to unambigiously identify nuclear reaction products by their mass A, and charge Z. For this to be possible up to masses around $A = 100$, the total time resolution of the ToF measurement should be on the order of 100 ps FWHM or better [1]; comprised of 50 ps and 80 ps FWHM for the start and stop detctor, respectively. Mainly two timing options are deemed viable; polycrystaline CVD diamond detectors and fast plastic scintillators. In the LYCCA-0 set-up the diamond detectors are to be tested as ToF-start detector, while a large-area fast plastic scintillator is to give the ToF-stop signal. This report outlines first results from proof of principle tests of the fast plastic scintillator investigated both in the laboratory using a laser and in-beam during a test experiment at the FRS [2].

The LYCCA-0 ToF-stop detector will have to cover an area of about 25x25cm^2. The most convenient way to achieve this coverage is to use a large plastic membrane read-out from four or more sides. Early tests performed on such a system with four large active-area photomultiplier tube (PMT) read-outs indicated a good performance of around 80 ps FWHM. In this test a 1 mm thick BC-420 membrane was pulsed with a laser at very low repetition rates, and the raw signals were processed by Philips Scientific constant fraction discriminators (CFDs) before being fed into a 21-bit CAEN V1290A Multihit TDC with 25 ps per step. During this test it was observed that measuring with just two of the four PMTs effectively worsened the time resolution by a factor of $\sqrt{2}$, which is expected from a purely statistical point of view. Thus, to further improve the time resolution one needs either PMTs with a larger active area, collecting more photons, or more PMTs. A similar test was carried out with a BC-422Q (quenched) plastic membrane. Although this material has a significantly faster rise-time the results were not convincing. Indeed, its high light attenuation coefficient does not fit for membranes of this size.

To test the system under realistic circumstances and to be able to interpret and extrapolate obtained laboratory data correctly, an in-beam experiment was conducted with a ^{64}Ni beam in the S4 area of the FRS. A 25x10 cm^2, 1 mm thick BC-422Q membrane, read out by 2x2 small and fast Hamamatsu R7400U PMTs on the short sides showed the time resolution of 162 ps FWHM displayed in Figure 1. This is significantly better than the performance of the exact same set-up measured in the laboratory. The difference is explained by the quenched plastics used in this case. With BC-420 a time resolution of 90 ps was obtained in the laboratory. The BC-422Q / R7400U system was tested at high beam intensities and showed no signs of signal deterioration at particle rates of up to 100 kHz.

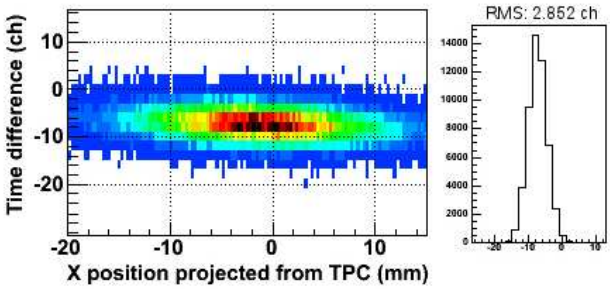

Figure 1: *The left-hand side shows a position corrected spectrum of the time difference measured between the PMTs. The right-hand spectrums displays the projection of the left spectrum onto the time axis. With a binning of 24.2 ps this corresponds to around 162 ps FWHM.*

From the tests we conclude that a high performance ToF detector indeed can be built based on a large BC-420 plastic scintillator with R7400U read-out. Utilizing 32 PMTs instead of four on a BC-420 membrane should yield a much improved time resolution of about 50 ps FWHM, while particle rates of up to 100 kHz are possible. We plan to confirm this concept in 2009 during another in-beam test.

References

[1] The LYCCA Technical Design Report. Can be found at: http://wwwnsg.nuclear.lu.se/lycca/lycca-TDR.pdf

[2] H. Geissel *et al.*, Nucl. Instr. Meth. B70, 286 (1992).

A position sensitive γ-ray scintillator detector with enhanced spatial resolution, linearity and field of view

N.Goel[1], C.Domingo-Pardo[1], T.Engert[1], J.Gerl[1], M.Isaka[2], I.Kojouharov[1], and H.Schaffner[1]
[1]GSI, Darmstadt, Germany; [2]Hokkaido University, Japan

State of the art small position sensitive γ-ray detectors (PSDs) are normally made from a relatively thin scintillation crystal, which is optically coupled to a position sensitive photomultiplier tube (PSPMT). A frequently used PSPMT is based on a crossed wire anode structure e.g. the Hamamatsu R2486/3292 family. The anode of the R2486 consists of two orthogonal layers of 16 wires in the X axis and 16 in the Y axis, on a pitch of 3.75 mm. In order to simplify the readout process, the wires within each layer are often connected to a resistive charge dividing network such that only 4 outputs are required to determine the centroid of the electron cloud reaching the anode. However, we showed that a substantial improvement in the intrinsic position linearity and thus in the useful field of view (FoV) of the detector can be achieved by individual multi-anode readout (IMAR) method[2] as compared to the resistive network(RN) aprroach. Our detector system consists of a cylindrical LYSO crystal with 76 mm diameter and 3 mm thickness, optically coupled to a Hamamatsu R2486 PSPMT. Using the IMAR method, it is possible to calibrate the gain of individual anodes. From the calibrated charge distributions measured along X and Y anodes, the interaction position (x,y) is determined via several algorithms as shown in Fig.1. The first panel (top-left) in Fig.1 represents the conventional centroid method of the RN-based devices, which here for sake of simplicity has been reproduced via software instead of using a real division circuit. The top-right panel shows the performance of the Gauss-fitting approach. These two approaches work relatively well in the central region of the photocathode, where the charge distributions are still rather symmetric. However, towards the border of the photocathode two additional effects take place. On one hand, part of the scintillation light cone is outside the active photocathode area, which makes the mean of the charge distribution to be different from its maximum. On the other hand, light reflections at the edge region of the scintillation crystal contribute also to the measured charge profile. These two effects can be properly taken into account by using a realistic description of the light distribution, like the one reported by Lerche [1]. The bottom-left panel of Fig.1 illustrates the improvement obtained in the determination of the (x,y) coordinates, when the formula of Lerche is fitted on an event-by-event basis. We have implemented an alternative approach[2]. Instead of fitting an analytical expression we have obtained an average pattern of the charge distribution, which is well defined from the average of a large number of charge distributions corresponding to interactions at the same place, in the center of the photocathode. Now only one parameter, which is a distance or the relative position of this pattern, is varied until the pattern matches with the measured "problem" charge distribution. The procedure becomes about 100 times faster than fitting the analytical expression. The system becomes remarkably linear with an enhanced FoV using the IMAR method. Our system behaves linear 50 mm along the photocathode, in both X and Y directions. The FoV with the IMAR technique is about $19\,cm^2$ assuming a circular FoV.Requesting the same linearity would yield a FoV of only $\approx 4\,cm^2$ for a RN-based system.

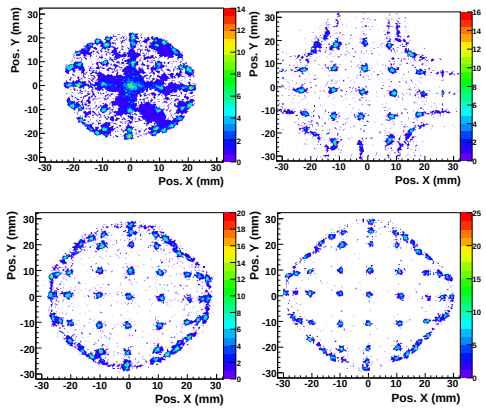

Figure 1: (Top left) Centroding approach (Top Right) Gaussian fitting approach (Bottom left) Lerche Model fitting approach (Bottom-Right) Pattern-Position fitting approach.

On average, along the X and Y axis of the PSPMT, we have measured position distributions with an equivalent FWHM $= 0.91 \pm 0.08$ mm and FWHM $= 0.98 \pm 0.08$ mm for positions along the X- and Y- axis respectively (see Fig.2). With the large FoV and the excellent position resolution of our detector we obtain an effective image resolution of ≈1900 pixels[2].
The average efficiency of the PSD for 511 keV γ-rays was experimentally determined as $\varepsilon_\gamma^{FE} = 7.5 \pm 1.5\%$ for full energy events, which is in agreement with the value expected for a LYSO scintillation crystal. These qualities make this system very attractive for many γ-ray imaging applications.

References

[1] C.W Lerche,et al.,Nucl. Instr. Meth. A, vol 537, pp. 326-330, Jan.2005.

[2] C.Domingo-Pardo et al."A position sensitive γ-ray scintillator detector with enhanced resolution,linearity and field of view", submitted to IEEE on 19th Dec,2008.

Surface characterisation of Germanium detectors

T. Engert[1,2], I.Kojouharov[1], M. Krause[1], J. Kunkel[1], K.O. Voss[1], J.Gerl[1], P.Nolan[2], Th. Krings[3]
[1]GSI, Helmholtzzentrum für Schwerionenforschung GmbH, Germany;
[2] University of Liverpool, UK; [3] SEMIKON Detector GmbH, 52428 Juelich, Germany

Germanium-detectors are the most sensitive high-resolution γ detectors available and are the instrument in nuclear structure physics which allows important information about the structure of atomic nuclei to be obtained. The technology of High purity Germanium detectors is presented in [1]. The reported work is motivated by the needs for a new mechanical treatment procedure within the manufacturing methods in order to obtain better quality of the Germanium surfaces and increased cost-efficiency. Seven germanium crystals with different surface qualities due to varying mechanical treatment were employed for the characterisation of their surfaces. Five of the crystals were fully processed to obtain working detectors. In a first step surfaces were investigated with a Scanning Tunnelling Microscope and a Profiler.

The crystals have a size of 8×8×10 mm^3 and are fixed in special housings. A Germanium crystal installed in its housing is shown in Figure 1. These housings are optimized for all used microscopes as well as for a newly developed detector cryostat.

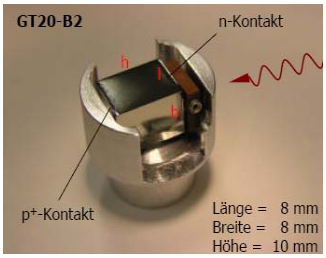

Figure 1: HPGe crystal installed in the housing

These two non-detector crystals are only for the mechanical characterisation. One was only grinded while the other one was lapped in addition. This treatment status corresponds to the status of usual detectors before chemical processing.

A sample of the results from the profiler and from the Scanning Tunnelling Microscope (STM) is shown in Figure 2 and 3.

For the mechanical treatment of germanium crystals, a fixing device has been developed which enables safe mounting of AGATA-type crystals on machines for grinding and lapping.

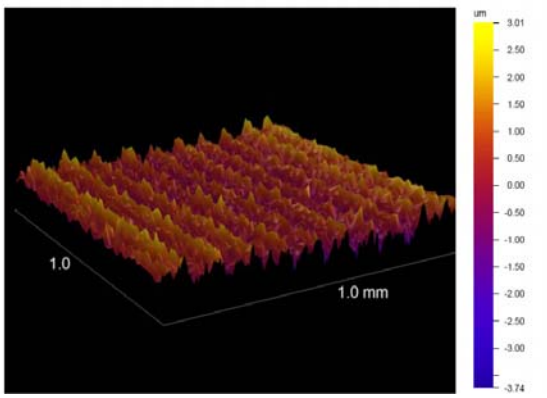

Figure 2: Profiler scan of grinded surface.

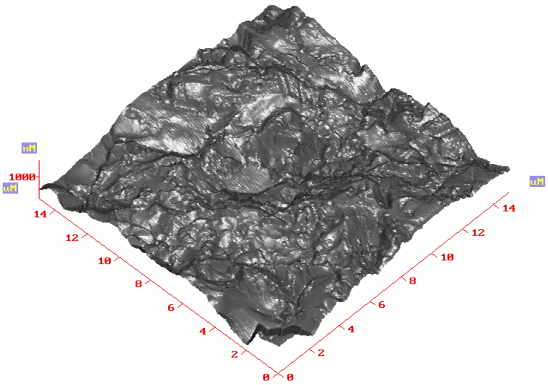

Figure 3: STM scan of lapped surface.

Germanium treatment and shaping tests with a new ultrasonic grinding machine have been carried out and the results have shown very fine surface structures with tight tolerances of 2 µm. Qualitatively the degree of roughness achieved is a factor of 3.9 times better than with standard grinding techniques, while being a factor of 1.8 times better compared to standard lapping processes. This kind of sophisticated mechanical treatment allows also complicated shapes to be achieved. On the basis of these results novel types of planar Ge detectors are planned.

References

[1] GeLab at GSI, I.Kojouharov, T.Engert, J.Gerl, Gamma Net, Padova, 10-11.05.2007

Simulation and Real-Time Analysis of Pulse Shapes from HPGe Detectors *

M. Schlarb† [1], R. Gernhäuser[1], and R. Krücken[1]
[1]Technische Universität München, Garching, Germany

The capabilities of future Germanium (HPGe) detector arrays consisting of large volume segmented crystals like AGATA [1] will depend heavily on the performance of γ-ray tracking. The most crucial component in the whole concept is the pulse shape analysis (PSA). The efficiency of tracking algorithms hinges on the ability of the PSA to reconstruct the interaction locations accurately, especially for multiple γ-interactions in one detector segment. For the typical hexagonal shaped coaxial closed end detectors the currently most successful working principle of PSA is to compare the experimental signal shape with signals available from a basis set with known interaction locations. Considering size, rate capabilities and resolution of the arrays, the PSA algorithm must operate in real-time.

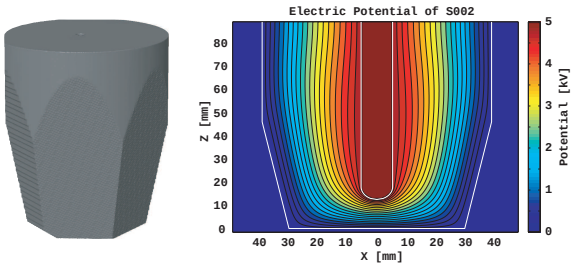

Figure 1: Geometry definition of a typical HPGe crystal (left) and the calculated electrical potential (right).

A prerequisite to a successful PSA is an accurate knowledge of the detectors response. To avoid time consuming 3D scanning of the individual detectors a precise simulation of the detector response provides a basis of signals for each possible interaction point on a 1 mm grid inside the detector with all the current signals induced on each segment, digitized in time slices of only 1 ns. For this purpose a ***J**ava based **A**gata **S**imulation for **S**ignals* (JASS) was developed. Here the geometry of the detector is given with numerical precision, electric fields are calculated by solving the Poisson equations constraint by the electrodes on the detector (see Fig.1). The anisotropic mobilities of the charge carriers in Germanium [2] are used to calculate the trajectories of electrons and holes inside the detector. The pulse shapes of the transient and net-charge signals are calculated using weighting potentials on a finite 0.5 mm grid. Special care was taken on the interpolation routine to reproduce the configuration close to the segment boundaries with diverging gradients. Experimental signals from a coincidence scan and a pencil beam experiment reproduced faithfully the result from the JASS simulation.

The goal of Pulse shape Analysis is to reconstruct position and energy of each individual interaction of a gamma ray inside the detector volume with maximum accuracy. The particular challenge lies in the binomial growth of the search space making an intelligent search algorithm compulsory. In order to reduce the number of dimensions of this search space, the starting time t_0 of the pulse shapes can be determined independently before the search starts. We have developed a neural network algorithm with only one hidden layer that recovers the t_0 with a precision of 2 ns (FWHM) consuming only computing times of a few microseconds on a standard PC. Using only the energy signal of the core of each crystal this method is also extremely robust and insensitive to noise.

For the search of interaction points the so-called "Fully Informed Particle Swarm" has proven to be very efficient to speed up the grid search and determine all interaction positions. The algorithm is loosely imitating the behavior of a flock of birds looking for food. In this case a small number of randomly chosen test particles dynamically moves to the direction of the one with the best fitting conditions converging typically after few iterations. For a photon absorbed in a single interaction the position is reconstructed with an accuse of 2 mm (FWHM) in 300 μs on a standard CPU. The reconstruction of two interactions in one segment is accomplished in 2-5 ms with an average resolution of 5 mm (FWHM). A full grid search on the same machine needs about 8 ms and 300 s respectively improving the position resolution only by about 20%.

The codes have been tested with full simulations of a (d, p) reaction in inverse kinematics, using a ^{48}Ti beam at an energy of 100 MeV, impinging on a deuterated Titanium target where the achieved energy resolution after Doppler correction is used to judge the capabilities of the developed PSA algorithms.
After the first commissioning phase of the AGATA spectrometer currently set up at the Legnaro (Italy) accelerator facility, these codes which are of particular interest for the AGATA experiment campaign planned at GSI will be implemented to the online computing system in 2009.

References

[1] AGATA technical design report, http://www-w2k.gsi.de/agata/Publications/TDR_EUJRA.pdf .

[2] Characterization of large volume HPGe detectors, B. Bruyneel, Nucl. Instr. Meths A, Vol.569 p764 (2006).

* Work supported by the GSI R+D project (TMKRUE), MLL, BMBF-06MT238, EU, EURONS No. 506065. and the AGATA collaboration
† Michael.Schlarb@ph.tum.de

Progress on the Time-of-Flight detectors for the HypHI project*

S. Bianchin[†1], O. Borodina[‡1,2], P. Achenbach[2], S. Ajimura[3], M. Kavatsyuk[4], F. Maas[1,2], S. Minami[1], T. Mochizuki[5], T. Nagae[6], D. Nakajima[1,7,8], A. Okamura[6], B. Özel[1], R. Pleskac[1], J. Pochodzalla[2], C. Rappold[1,9], T.R. Saito[1,2], A. Sakaguchi[5], M. Sako[6], H. Sugimura[6], K. Tanida[6], and W. Trautmann[1]

[1]GSI, Darmstadt, Germany; [2]Mainz University, Mainz, Germany; [3]RCNP, Osaka University, Ibaraki, Japan; [4]KVI, Groningen, The Netherlands; [5]Osaka University, Toyonaka, Japan; [6]Kyoto University, Kyoto, Japan; [7]KEK, Tsukuba, Japan; [8]Tokyo University, Tokyo, Japan; [9]Strasbourg University, Strasbourg, France

The Phase 0 experiment of the HypHI project [1] planned in September 2009 at GSI is devoted to demonstrate the feasibility of a precise hypernuclear spectroscopy by using heavy ion collisions. In the experiment, we will concentrate on studying light hypernuclei such as ${}^{3}_{\Lambda}$H, ${}^{4}_{\Lambda}$H and ${}^{5}_{\Lambda}$He produced by collisions of a ^{6}Li and a ^{12}C beam at 2 A GeV with an intensity of 10^7 particles per second on a thick carbon target (8g/cm^2).

The setup of Phase 0 experiment shown in Fig. 1 consists of the large acceptance dipole magnet ALADiN, the start detector in front of the target, three arrays of scintillating fiber tracking detectors (TR0, TR1 and TR2), the existing ALADiN TOF-wall for the detection of π^- and the TOF+ wall, which is currently under construction, for detecting positively charged particles. In addition, two drift chambers from KEK will be placed in front of and behind the magnet in order to increase the tracking redundancy.

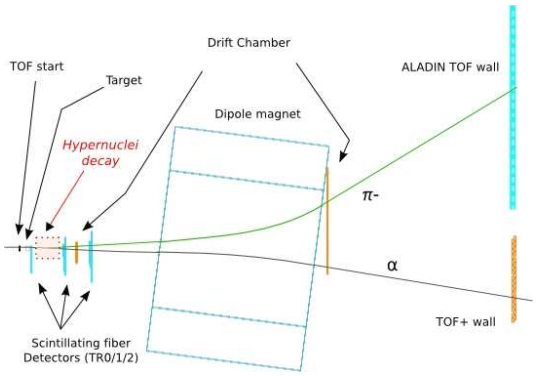

Figure 1: Experimental setup for the phase 0 experiment

The TOF+ wall [2] consists of two layers of 16 plastic scintillator bars BC408. Each bar is veiwed by two Hamamatsu H7415 photomultiplier tubes attached to its two end faces. The active area of the TOF+ wall is about 1 m^2. There is a hole (7.5×6.5 cm^2) to allow the passage of the beam trough the detector without damaging the plastic scintillators. Series of tests have been performed with a prototype of the TOF+ wall and a time resolution of 350 ps (FWHM) as well as an energy resolution of 18% (FWHM) in the case of minimum ionizing particles have been achieved.

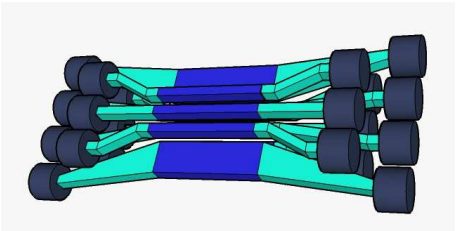

Figure 2: Start detector

In order to precisely measure the time of flight of the particles produced by the decay of hypernuclei, the time difference between a *stop signal* in the TOF-walls and the *start signal* in the start detector has to be measured. For this purpose, a start detector (Fig. 2) consisting of 10 plastic scintillating fingers made of BC420 is currently being developed. Hamamatsu R7400U-06 photomultipliers are used to read out scintillation signals from both ends of each finger. The detector is arranged in three layers with overlapping of adjacent fingers of 1 mm. The width of the fingers around the beam center region is 4 mm in order to accept a high beam intensity of 10^7 particles per second over the detector. This detector has an active area of 50×53 mm^2. Along with the tests performed on the TOF+ prototype, prototypes of the start detector have been tested as well. Two scintillator plates of BC420 with a thickness of 5 mm with PMTs on both ends were tested with a ^{6}Li beam and with cosmic rays. The obtained energy resolution is of the order of 30% (FWHM) in the case of ^{6}Li beam particles and the time resolution is $\sigma \sim 200$ ps which is in accordance with the requirements of the Phase 0 experiment.

References

[1] A proposal of the HypHI Phase 0 experiment, the HypHI collaboration, submitted to GSI PAC EA33 with a realization as S319.

[2] Rappold, C. *et al.* (2006) Design studies on Time-Of-Flight walls for the HypHI project, GSI Scientific Report 2006, GSI, Darmstadt

* The HypHI project is funded by GSI-darmstadt and Helmholtz Association as Helmholtz-University Young Investigators Group VH-NG-239.

† s.bianchin@gsi.de

‡ o.borodina@gsi.de

Scintillating fiber detectors for Phase 0 experiment of HypHI project *

D. Nakajima[†1,9,10], B. Özel[‡1], P. Achenbach[2], S. Bianchin[1], O. Borodina[1,2], T. Fukuda[4], Y. Hayashi[5], T. Hiraiwa[5], J. Hoffmann[1], M. Kavatsyuk[6], K. Koch[1], N. Kurz[1], F. Maas[1,2], S. Minami[1], Y. Mizoi[4], T. Mochizuki[8], M. Moritsu[5], T. Nagae[5], A. Okamura[5], W. Ott[1], R. Pleskac[1], J. Pochodzalla[2], C. Rappold[1,11], T.R. Saito[1,2], A. Sakaguchi[8], M. Sako[5], H. Sugimura[5], K. Tanida[5], W. Trautmann[1], and S. Voltz[1]

[1]GSI, Darmstadt, Germany; [2]Mainz University, Mainz, Germany; [3]RCNP, Osaka University, Ibaraki, Japan; [4]Osaka Electro-Communication University, Neyagawa, Japan; [5]Kyoto University, Kyoto, Japan; [6]KVI, Groningen, The Netherlands; [7]Tohoku University, Sendai, Japan; [8]Osaka University, Toyonaka, Japan; [9]KEK, Tsukuba, Japan; [10]Tokyo University, Tokyo, Japan; [11]Strasbourg University, Strasbourg, France

The main idea of the HypHI project is to perform precise hypernuclear spectroscopy with stable and unstable heavy ion beam at GSI and FAIR[1]. The HypHI collaboration plans the first experiment Phase 0 in 2009 to investigate the feasibility of hypernuclear spectroscopy with heavy ion beams.

In the Phase 0 experiment, three sets of Scintillating Fiber (SciFi) detectors (TR0, TR1 and TR2) will be mounted in front of the ALADiN magnet to track charged particles and to produce a trigger signal for the data acquisition system by selecting events with decay vertices outside the target, which are induced by decay of hypernuclei and hyperons. Energy deposit of charged particles will also be measured by TR0 to separate particles with Z=1 and 2 from the target in order to reduce the background [1].

Scintillating fibers, SCSF-78 (Kuraray), have an outer diameter of 0.83 mm and a core diameter of 0.73 mm. The readout of scintillating photons is performed with H7260KS MOD (Hammamatsu) 32 channel multi-anode photomultiplier tubes (PMT).The SciFi detector consists of quadruple-layer of fibers, which is aligned at a pitch of 0.59 mm. Fibers aligned perpendicularly to the detection plane are combined together into one channel of the PMT. Analog signals from PMT are processed by a double-threshold discriminators (DTDs) from the Kaos spectrometer at MAMI. LVDS logic signals from the DTD are guided to a logic module (VUPROM) with FPGA and DSP, which is developed for the HypHI project at GSI. An additional analog readout is performed by CAEN VME QDC for only TR0.

Table 1: The width, length, number of channels of SciFi

Detector	x layer [mm]	y layer [mm]	Channels
TR0	39	39	128
TR1	132	76	352
TR2	245	113	608

Three sets of the SciFi detectors with capabilities of charged particle measurements in horizontal and vertical axes have been built. The width, length, number of channels of SciFi are listed in Table 1. They have been tested by using light projectile fragments with Z=1, 2 and 3 particles from ^{58}Ni and ^{12}C beams at Cave B in September 2007, by ^{6}Li beams at Cave A in August 2008 [2].

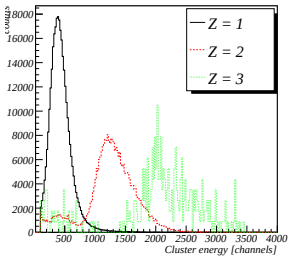

Figure 1: Energy deposition for Z=1, 2 and 3 particles

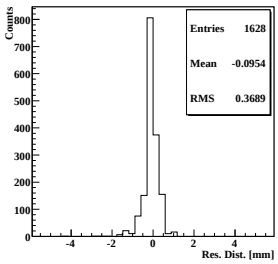

Figure 2: Residual distribution for TR1

The response for energy deposition measurement of TR0 is studied by light projectile fragments. A hit in the SciFi detector is defined as a hit cluster which is a group of neighboring hit channels. Figure 1 shows the distribution of energy deposition of Z=1, 2 and 3 particles. This shows reasonable separation for particle with Z=1 and 2, which fulfill the requirement. The position resolution is measured by ^{6}Li beams. The hit position is calculated from the center of gravity of the hit cluster. The position resolution is defined as the residual distribution which is the distance between measured hit position and the track determined by the other two planes. Figure 2 shows the residual at TR1 for straight-line tracks extrapolated by TR0 and TR2. A position resolution of 0.37 mm in RMS is achieved for the dominant ^{6}Li projectiles.

References

[1] T.R. Saito *et al.*, Proposal of the HypHI Phase 0 experiment submitted to the G-PAC 33 in October 2006.

[2] T.R. Saito *et al.*, in these reports.

* The HypHI project is supported by the Helmholtz Association as Helmholtz University Young Investigators Group VH-NG-239 and by DFG with the research grant SA 1696/1-1.

† d.nakajima@gsi.de

‡ b.oezel@gsi.de

Encapsulated Germanium Detector with Electromechanical Cooling

I.Kojouharov[1], H.-J. Wollersheim[1], [2]J.Kojouharova, J.Gerl[1], M.Wolf[1], T.Engert[1]
[1]GSI, Darmstadt, Germany; [2]Consulting Bureau FDHM, Zornheim, Germany

Detector Design

A detector, based on large volume encapsulated Ge [1] crystals and cooled by electromechanical cooling engine X-Cooler II (ORTEC) [2], has been developed at GSI aimed at utilization as isomer tagging detector at FRS Super-FRS at GSI [4], Fig.1. The encapsulated Ge-crystal is installed in the cryostat ensuring maximal heat transfer capability of the cooling structure – very few thermal joints and thick cold finger. The flexible section of the cold finger, which serves as vibrations absorber, has been produced by new technology that improves the thermal transfer through it.

The capsule, as a rule, has rough and oxidized, non-polished, surface, which has high absorption capability (emissivity), thus increasing the radiative transfer from the outer (at room temperature) components of the cryostat to it. Since polishing of the capsules is not possible due to the danger to damage the crystal, which is inside, a special thermal shield has been applied in order to reduce the radiative transfer of energy toward the cold structure.

The complexity of the design requires optimization of the components and therefore a careful thermal analysis and simulation by COMSOL MULTIPHYSICS package has been performed [3].

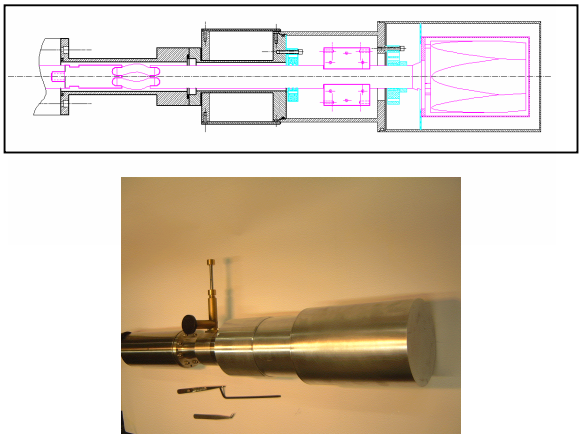

Figure 1: Electromechanically cooled encapsulated detector – the design (up) and assembly (down)

Result and Discussion

Encapsulated detector HEX146 has been installed in the cryostat and after the vacuum conditioning needed for the proper operation of the detector has been cooled. The temperature of the detector reached approx. -160 ºC which is typical for the HPGe detectors. After biasing the detector energy resolution was measured with ^{60}Co source at various shaping times and the result is shown on Fig.2. Since the same capsule installed in LN2-cooled cryostat has shown energy resolution of 1.96 keV for 1332 keV line, the best achieved resolution in electromechanically cooled cryostat of 2.03 keV seems to be consistent. The rapid increasing of the FWHM at low shaping times and high energy (1332 keV) compared with the more constant behaviour at low energy (122 keV) also demonstrates low leakage current of the detector.

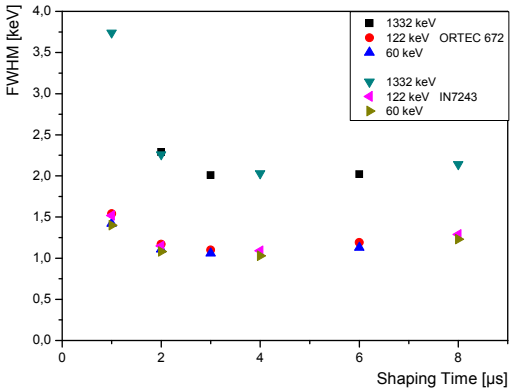

Figure 2: Energy resolution of the detector vs. shaping time at different energies

The energy resolution of the detector was scanned also along the axis of the detector using ^{241}Am source. The energy of the γ-radiation of the source is low and the absorption of the photons occurs close to the surface of the detector. Therefore the charge is being collected in very limited volume and the signal produced may be affected by the temperature effects. The energy resolution was scanned with 5 mm step and was found (within the statistical error) to be constant which indicates that constant or close to that is the surface temperature of the Ge-crystal. Further information about the temperature effects and their impact on the spectroscopy properties and the performance of the detector is to be obtained by more precise scanning of the crystal.

References

[1] J.Eberth, H.G.Thomas, et al. NIM A369 (1996), 135-140.
[2] ORTEC. X-Cooler™ II - Mechanical Cooler for HPGE Detectors User Manual. http://www.orteconline.com.
[3] M. Wolf, J. Kojouharova, I. Kojouharov, T. Engert, J. Gerl, J. Groß, and H.-J. Wollersheim, Temperature distribution study of composite germanium detectors, Proceedings CD of the COMSOL Users Conference 2007 Grenoble, P1-P4 and Diploma Thesis, Hochschule Darmstadt.

Tests with slowed down beams at GSI.*

P. Boutachkov[1], M. Górska[1], N.A. Kondratjev[2], S. Pietri[1], F. Naqvi[1], J. Gerl[1], H. Weick[1], W. Prokopowicz[1], H. Schaffner[1], C. Nociforo[1], H. Geissel[1], I. Kojouharov[1], M.A.G. Alvarez[3], I. Mukha[3], K. Hadynska[4], P. Napiorkowski[4], and D. Pietak[4]

[1]GSI, Darmstadt, Germany; [2]FLNR, JINR, Dubna, Russia; [3]Seville University, Seville, Spain; [4]Warsaw University, Warsaw, Poland.

The NuSTAR HISPEC slowed down beams project at GSI/FAIR aims to produce rare isotopes with energies of 10 MeV/u and less, to be used for spectroscopy and reactions studies.

The radioactive beams produced at the NuSTAR FAIR facility of sufficient intensity to perform Coulomb excitation, resonance or transfer reactions studies are included in the nuclear chart shown on Figure 1. There is limited or no information on the excited sates of many of these nuclei. The high production rates of slow down beams at FAIR will allow detail studies of these systems.

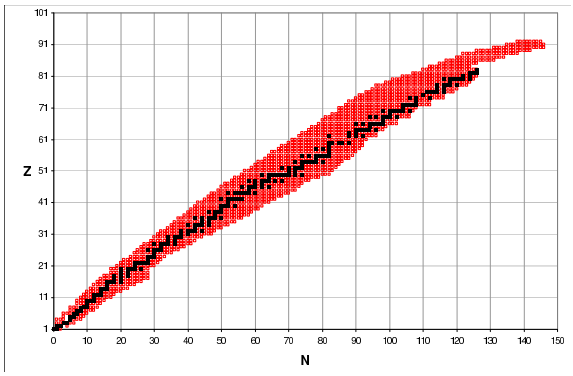

Figure 1: Radioactive beams which are expected to have sufficient intensity for reaction studies after slowing down. The simulation includes expected production rates at Super FRS.

The slowed down beam setup at the FRS utilizes a thick degrader positioned after the fragment separator. The ions of interest are tracked and identified before the slowing down with the detectors available at the FRS [1]. After the degrader the fragments enter an evacuated tube and are detected in a transmission position sensitive Time Of Flight (TOF) detector, positioned 1.5 m down stream. The measured TOF and position are used to determine the ion velocity and trajectory on event-by-event basis. Simulation of this setup were discussed in Reference [2].

To remove the uncertainty due to the energy loss in the TOF detector, two thin transmission detectors based on Micro Channel Plates(MCP) were constructed. The detectors were tested with alpha source and fission fragment source. The measured time resolution with alpha particles between the two MCP detectors was ΔT(FWHM) $\sim$ 140 ps. The position resolution for alpha particles was ΔX_{α}(FWHM) $\sim$ 3 mm and ΔX_{fr}(FWHM) $\sim$ 1.5 mm for fission fragments.

In September-October 2008 a test experiment with slowed down ^{64}Ni was performed at the FRS. The experiment utilized the MCP-TOF detectors described above, 2 DSSSD detectors and NaI detectors surrounding a gold target. The averaged beam intensity on target was about 10^5 pps. The rate was limited by the response of the scintillator used for start of the TOF measurement, positioned in front of the degrader. The test provided information on the performance at high rates of the auxiliary FRS detectors (TPC, MUSIC and scintillator detectors) used for beam tracking before the degrader.

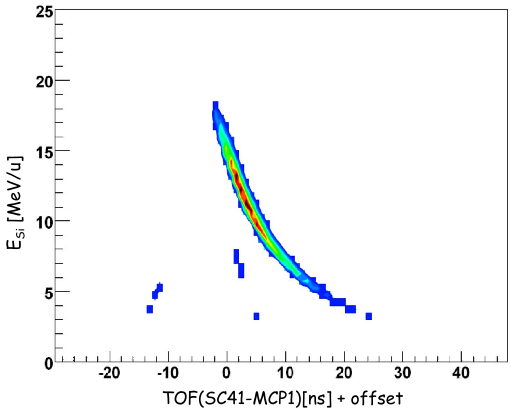

Figure 2: Energy of ^{64}Ni after slowing down, determined with a thick Silicon and a thin MCP-TOF detector.

In Figure 2 the energy spectrum after slowing down is shown. It was measured with a 300 μm Si detector and a TOF between the scintillator in front of the degrader and a the first MCP detector up stream from the target position. The energy spread in Figure 2 is smaller compared to the analogous measurement shown in Reference [2]. In the latter the energy distribution is broader due to the straggling in the TOF detector, a 100 μm scintillator.

The data is presently under analysis, which will provide an answer to the feasibility of Coulomb excitation experiments with the proposed approach.

References

[1] H. Geissel *et al.*,Nucl. Instr. and Meth. B **70** (1992) 286

[2] P. Boutachkov *et al.*, "Simulations and first tests of slowed down beams project at GSI.", Annual report 2007, GSI, Darmstadt

*Work supported by EU, EURONS contract No. 91606 and Spanish MEC, FPA2006-13807-C02-01.

Reliability improvement of the DCS Board used in the ALICE Experiment

T. Krawutschke[1] and G. Hartung[1]
[1]Cologne University of Applied Sciences, Köln, Germany

The DCS Board is an Embedded System that is part of the ALICE Detector Control System and employed as interface layer between detector hardware and control environment. One hardware design is used in multiple applications and adapted based on a combination of a dedicated processor and configurable hardware to special detector needs. 1040 pieces of the DCS Board are produced for 9 detectors and used in 18 variants. This report summarizes our work to improve the reliability of the DCS board. A full description may be found in the article presented at FPL08[2].

Architecture

The DCS Board is based on reconfigurable hardware with a CPU combined in one package. The PLD as a layer in between real hardware and software in combination with an embedded Linux Operating System with a small memory footprint permits the flexible adaption to different detectors.

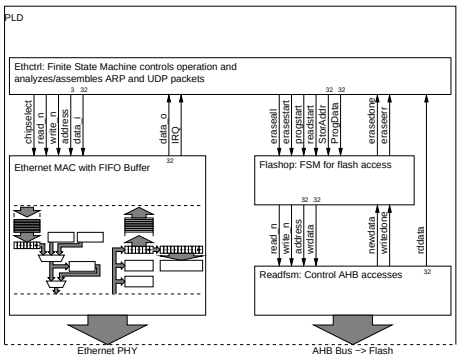

Figure 1: Schematic of the reconfiguration logic

A communication and configuration link to a neighboring DCS Board is used for boundary scan and power control. It is used for reprogramming the flash of a neighbor board, which is in an error state due to e.g. faults produced by radiation. A normal reprogramming is conveniently possible with a running operating system, but it must be possible to write the flash contents to a board that does not start up anymore (s. fig. 1). Physical access to the boards is impossible because of the layered architecture of the detector, so standard programming tools are not usable. Several DCS Boards are grouped together in a ring structure, so every device has a controlling neighbor as sketched in Figure 2.

With JTAG Boundary Scan (IEEE 1149.1) the controlling board can read or set every pin status and internal signals of the devices part of the JTAG chain which enables a versatile remote diagnosis tool.

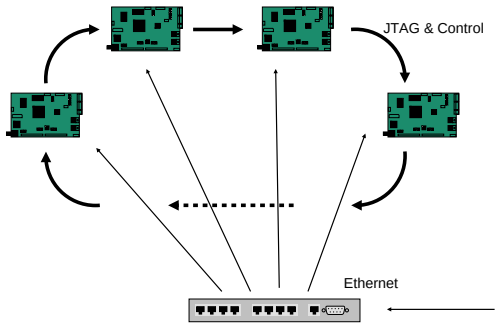

Figure 2: Communication and control

Radiation induced memory errors

The expected failure rate due to Single Event Upsets in memory was measured during the development phase in radiation tests. The mean time for an error to occur is approximately three days (all values are for worst case, see [1])

An additional diagnostic tool was developed to monitor memory errors online: The Online Memory Selftest (OMS) fills unused memory with a test pattern and regularly checks for failures. An advantage is the maximization of the tested memory without interfering with running software. This system runs in kernel space and interacts with the memory management of the Linux kernel. The OMS utilizes kernel caches (called *slabs*) to work on memory that can be reused anytime. If the system is low on memory it frees parts of the unused slabs and the OMS has to differentiate between real memory errors and the loss of memory by slab deallocation. It is done by comparing two lists. Should a memory region be altered, but still be marked as part of the slab it is considered to be a memory failure due to an SEU and be reported to a central system collecting the failure data.

The knowledge and experience to build a self-monitoring DCS will be transferred to further DCS systems in new detector experiments.

References

[1] Tsiledakis, G.: Scale Dependence of Mean Transverse Momentum Fluctuations at Top SPS Energy measured by the CERES experiment and studies of gas properties for the ALICE experiment, 2005, TU Darmstadt

[2] Krawutschke, T.: A flexible and reliable embedded system for detector control in a high energy physics experiment, FPL 2008, Heidelberg

The FOPI GEM-TPC – Design studies, prototyping and set up

B. Voss, J. Hehner, A. Heinz, M. Henske, J. Kunkel, C.J. Schmidt, S. Schwab, D. Soyk, J. Weinert
GSI, Darmstadt, Germany.

The Project

In 2008 the construction and building of the **T**ime **P**rojection **C**hamber (TPC) [1] to be installed at FOPI/GSI has been continued. The design is based on **G**aseous **E**lectron **M**ultipliers (GEM) as amplification stages. A sketch of the cut of the detector alongside the beam axis is show in fig. 1. The detector system is built completely modular with respect to its components and various functions like supplies, particle detection, amplification, signal mapping and electronic processing

Status & Outlook

The 'Spider', a hollow, light-weight 3D **C**arbon **R**einforced **P**lastic (CRP) structure serving e.g. as a support of the TPC has been built (fig. 2) and successfully installed at FOPI.

The mechanical parts of the detector have been produced and the GSI workshop did a good job in producing parts of the seamless cooling structure working with oil under pressure. The set up of the detectors infrastructure e.g. cooling plant, HV- and gas-supply systems as well as testing rigs has been started. Tests of the material properties like HV-resistance, outgasing and aging have been performed and are still ongoing. Especially the latter have been found to be important. As an example fig. 3 exhibits unwanted deposition of material on the signal wires of a detector after intense x-ray irradiation. The detector was flooded with gas which was washing around a piece of **G**las-fiber **R**einforced **P**lastic (GRP) material under test.

Several designs for the cooling structures as well as the GEM foils (fig. 4, right) and read-out planes with hexagonal, arc and mixed pad-shapes have been investigated and ordered. FEM simulations with ANSYS with regard to heat-transfer and the electrical field configuration have been performed. The latter revealed that the inhomogeneities of the electrical drift field for a double-sided staggered potential-strip arrangement were inacceptable especially considering the very unfavourable aspect ratio (100:650) of the drift volume (fig. 5). Alternative solutions for the design are currently investigated.

The layout of the readout-electronic intended is based on the nXYTER ASIC. It locally requires 50 µm structures which are at the cutting-edge of state-of-the-art PCB production capabilities. So far, only a few samples of 2-chip versions have been produced by CERN TS-DEM and were successfully tested in the laboratory. Several alternatives to cope with these problems are under investigation.

Manufacturing, final assembly of ≈ 1000 main parts and laboratory-test operation are planned for mid of this year. Nevertheless, quite a lot of work is still to be done with a rather low budget and low man power before the setup can be implemented into FOPI were a production run has been approved for autumn this year.

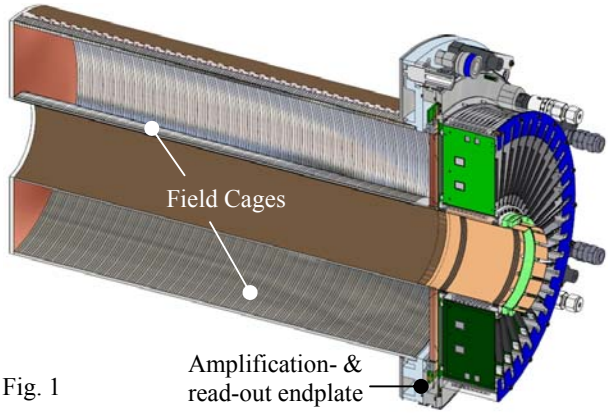

Fig. 1

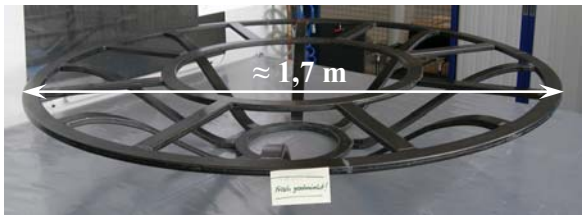

Fig. 2

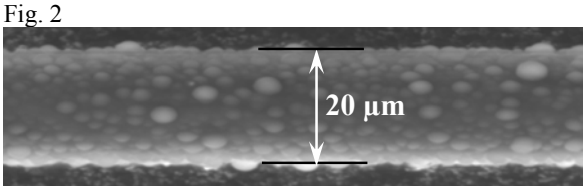

Fig. 3

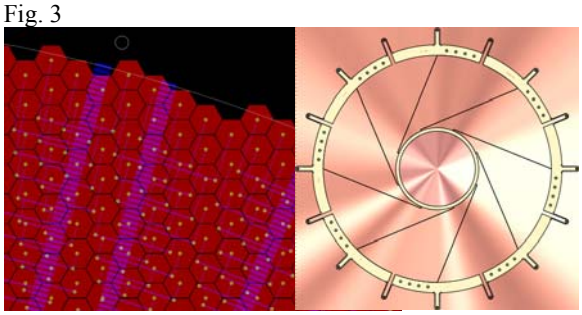

Fig. 4

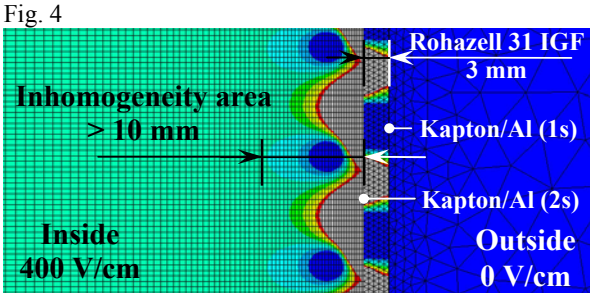

Fig. 5

References

[1] Voss B. et al., GSI Scientific Report 2007, GSI Report 2008-1, p.228.

Trigger Logic for FOPI Experiment

J. Frühauf, Y. Leifels, J. Hoffmann, W. Ott, N. Kurz, P. Koczon and C. Wandji
[1]GSI, Darmstadt, Germany

In the FOPI experiment at GSI an accelerated ion beam of the SIS hits a target inside the detector. As a consequence of the collisions of the two nuclei many particles are emitted and pass through the FOPI setup. These particles are registered by various detectors and their electronic signals are digitized and recorded by a data acquisition system. The readout of these detectors starts if an event is recognized. A trigger system decides which event is potentially interesting. The trigger decision consists of one trigger pulse and two bit patterns based on the information delivered by subdetectors. To generate this trigger decision up to 16 different logical signals have to be logically connected, enabled or disabled, and downscaled, rerouted and prioritized. Scalers counting the occurrence of each signal are installed in different parts in the logic.
The aim was to replace the existing "Trigger Logic" built out of conventional NIM and CAMAC modules by a single VME–FPGA programmable module (VULOM3 [1]). The functionality of the previous modules (2x LMU, 2x Trigger Box (TB8000 [2]), 1x Priority Encoder, 3x internal pulse generators, 2x Switch) is programmed in VHDL code and combined into one package running on the VULOM3´s FPGA.

Figure 1: VME – Logic Module (VULOM3)

Parameters necessary to control the trigger system have to be defined in a configuration file which gets loaded over a front end processor (RIO2) into the registers of the FPGA. There are also registers foreseen for the different scalers and bit pattern for readout over the VME interface. The generated trigger pulse as well as two bit patterns are available at the front panel of the VULOM3.

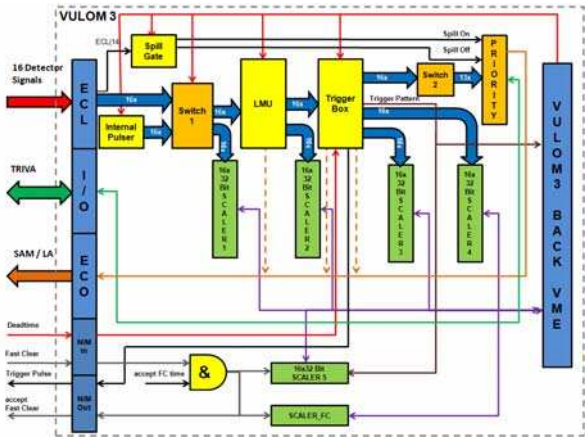

Figure 2: Block Diagram Trigger Logic VULOM3

The 16 input signals are send into "Switch 1" of the logic, which allows to chose individually for each channel whether the connected input signal or an internally generated pulse is send to the "LMU". Out of the "Spill Gate Signal" two triggers are generated ("Spill On" and "Spill Off"). In the "LMU" the signals are logically connected. Each of the 16 outputs of the "LMU" has one valid input bit pattern. The outputs of the "LMU" are connected to the "Trigger Box" where signals can be enabled or disabled, downscaled by factors of 2^0 to 2^15 and blocked during the dead time of the system. The "Trigger Box" generates a trigger pulse, which is sent out on the front panel of the VULOM3, and it stores the output bit pattern for readout via VME. The outputs of the "Trigger Box" are sent over the "Switch 2" to the "Priority Encoder". In "Switch 2" each signal can be routed to any input of the "Priority Encoder" where, according to the input bit pattern, two output bit patterns are generated, one for the TRIVA Module and one for the SAM. The TRIVA generates a dead time for the system during the readout of the DAQ. Besides this dead time the "Trigger Logic" has an additional external dead time input. Two versions are available
In version 1 the scaler values are latched and reset each time a trigger occurs and in version 2 the scaler values are latched and reset each "Spill On" and Spill Off" trigger.
It is also possible to latch and reset these scalers via the VME interface in both versions.

References

[1] http://www.gsi.de/informationen/wti/ee/elekt_entwicklung/vulom3.html

[2] http://www.gsi.de/onTEAM/grafik/1130845854/TB8000.pdf

Performance of the FOPI Λ-Trigger *

M. Berger[1], L. Fabbietti[1], O. Hartmann[1], R. Münzer[1], and the FOPI Collaboration
[1]Excellence Cluster of Universe TU München, 85748 Garching

Recently, the search for deeply bound nuclear states with antikaons has attracted large interest. It was recently found [1] that the p+p reaction might be well suited for the production of (K^-pp) nuclear bound states. We have proposed to perform an exclusive measurement using the FOPI detector [2] exploiting the reaction p+p at 3.5GeV and to build for this purpose a dedicated trigger device.
The final state of the pp→(K^-pp)K^+ → ΛpK^+ reaction involves Λ hyperons which can be detected using their decay into p + π^- (64% branching ratio). Thus, the FOPI detector has been extended by a Λ trigger system, in order to enrich events containing Λ candidates.
The scheme of the Λ trigger (SIΛVIO – SIlicon Λ Vertexing and Identification Online) is shown in figure 1. It consists of two detector layers downstream of the target with distances such that the bulk part (about 60%) of the produced Λs decay in between the two layers. The first layer

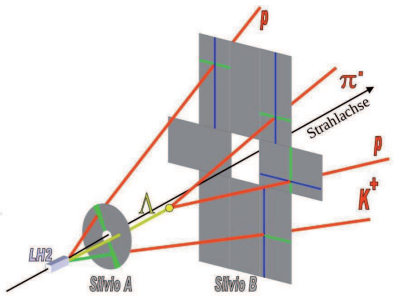

Figure 1: Schematic view of the trigger concept.

(SIΛVIO A) is a single-sided, 1mm thick annular detector segmented in 32 slices, while the second layer (SIΛVIO B) consists of a patch-work of 8 rectangular double-sided, 1 mm thick, $40x60mm^2$ with 1 mm pitch for each side. The event selection is performed requiring online that the hit multiplicity on the second silicon layer is higher (1 or 2 hits more) than the hit multiplicity on the first layer. This operation is taken care by the Mesytec analog electronics that reads out the annular and the n side of the 8 rectangular detectors. The Mesytec shaper provide a trigger signal according to the hit multiplicity on each detector and can be set such to realize the above mentioned trigger condition. The p-side of the rectangular detectors has been read out with an APV-25 chip which allows a compact readout of all the channels. The assembled detector system is shown in figure 2, where the boards on which SIΛVIO A and B are hosted and the APV-25 cards are visible. A test has been carried out at GSI to test the performance of the trigger system. A proton beam at 3GeV with an intensity of

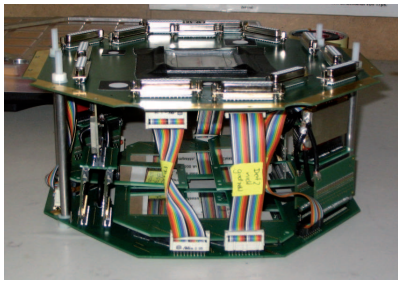

Figure 2: Assembled SIΛVIO system.

10^5 particles/sec has been focused on a plastic target and the full FOPI spectrometer, together with the Λ-trigger, has recorded data under different trigger condition. The main trigger (LVL1) has been set requiring at least one charge particle to cross the FOPI-RPC and the FOPI-PLAWA, the time of flight detectors situated at mid- and forward rapidity in the laboratory reference system respectively. The Λ trigger has been set such to accept events with one or more particle hits on SIΛVIO A in coincidence with two ore more hits on SIΛVIO B. Figure 3 shows the particle multi-

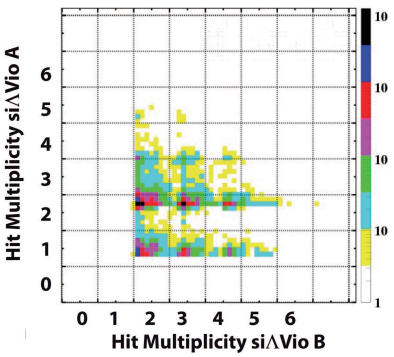

Figure 3: Offline particle multiplicity of SIΛVIO A versus the particle multiplicity on SIΛVIO B.

plicity obtained via an offline calibration for events which fullfil the Λ trigger condition. One can see how clean the required multiplicity condition is selected by the trigger. In overall a reduction of a factor 14 respect to the LVL1 trigger has been obtained applying the Λ trigger condition.

References

[1] Yamazaki et al, arXiv:0810.5182v1 nucl-ex.
[2] http://www.gsi.de/documents/DOC-2007-Mar-168-1.pdf

* Work supported by HGF and DFG-Excellence Cluster Universe

PANDA Grid Activities

D. Protopopescu[1], A. Amoroso[2], P. Bühler[3], R. Dosdall[4], P. Gianotti[5], C. Grigoraş[6], J. Messchendorp[7], V. Mitsyn[8], D. Pantea[9], F. Ronchetti[5], P. Saiz[6], K. Schwarz[10], M. Al-Turany[10], F. Uhlig[10], and J. van der Weele[7]

[1]University of Glasgow, UK; [2]University Department of Physics and INFN Torino, Italy; [3]SMI Vienna, Austria; [4]Forschungszentrum Jülich, Germany; [5]INFN Frascati, Italy; [6]CERN, Geneva, Switzerland; [7]KVI Groningen, The Netherlands; [8]JINR Dubna, Russia; [9]IFIN-HH Bucharest, Romania; [10]GSI, Darmstadt, Germany

Abstract

PANDA Grid is the present computing infrastructure of the PANDA@FAIR experiment, but concerted efforts are put into evolving it beyond that, into a complete and transparent solution for physics simulation, reconstruction and analysis, right at the fingertips of the physicist.

PANDA Grid

Experiments with very high data acquisition rates like PANDA [1] could not be thought to stand a chance without a Grid model for their computational needs. The PANDA collaboration established PANDA Grid as its computing infrastructure [2].

PANDA Grid uses as middleware AliEn [3], developed by ALICE@CERN and used outside CERN now, besides PANDA, by other FAIR experiments, like CBM. The software is centered on PandaROOT [4], developed partly within the PANDA collaboration, partly within the larger FAIR community. Grid monitoring and data production supervision are done via MonALISA [5].

PANDA Grid encompasses now 16 sites from 12 institutes in 8 countries, including EGEE sites integrated via the VOBox tools. The last three sites were added during 2008. While being an up and running system, PANDA Grid is continually growing, with 3 new institutes having already announced their intention to join in 2009.

A Tool for Physics

During the last year, through concerted efforts from a heterogeneous team of physicists and computer scientists, we brought PANDA Grid beyond mere 'computing infrastructure'. Our aim is to transform it into a *'tool for physics'*, that is a *complete and transparent solution for physics simulation, reconstruction and analysis*, with minimal overhead for the user (*i.e.* the physicist).

All the PANDA software for data simulation, reconstruction and analysis is based on PandaROOT. In our computing model, the 'user' software is based on ROOT macros using modular precompiled libraries from PandaROOT. The PANDA Grid infrastructure is used for software distribution via the package manager service (PackMan) provided by the middleware layer. We set up in 2008 a completely automatic system for package installation, compilation and testing, supervised directly by the PandaROOT developers, in such a way that the user has to customize only a couple of scripts before pursuing his/her own physics.

AliEn is the perfect tool for the job, as it already provides advanced data production tools at the middleware level (various mechanisms for job split and merging, catalogue tags and triggers, file collections have been implemented [3]). But the addition of the MonALISA integration layer allowed us to develop in 2008 a range of supervision tools and command mechanisms that made PANDA Grid easy to administer and easy to use for large productions.

Close contact between the subgroups participating in this effort is maintained by numerous ad-hoc meetings as well as via dedicated workshops [7], hosted in turn by various participant institutes. Two PANDA Grid workshops were hosted in 2008, in Rome, Italy and Sinaia, Romania.

In 2008 we also had two data challenges [6], during which large quantities of data were produced via a full chain of simulation, digitization and reconstruction. This data will be analysed and used to improve the design of the PANDA detector. The GSI and JINR sites are at the time being our largest contributors in terms of computing power.

Since this is a crucial ingredient for creating the complete solution we aim for, during 2008, significant effort has been dedicated to perfecting the organizational framework for administration and usage of PANDA Grid. A *production management* scheme has been set in place (and tested during the data challenges), complete with user, data storage and scheduling schemes. An official participation document - a so-called statement of service (SoS) - has been drafted to formalize the participation process in PANDA Grid. There is now a mutually beneficial collaboration in terms of software development and Grid deployment between ALICE and the FAIR experiments using AliEn, with several joint meetings in 2009 [8].

References

[1] http://www.gsi.de/panda

[2] http://panda-wiki.gsi.de/cgi-bin/view/Computing/PandaGrid

[3] http://alien.cern.ch

[4] http://panda-wiki.gsi.de/cgi-bin/view/Computing/PandaRoot

[5] http://monalisa.cern.ch

[6] see 'Data Challenges' links in [2]

[7] http://nuclear.gla.ac.uk/grid-workshop/

[8] M. Al-Turany *et. al, Grid Activities at GSI, GSI Scientific Report 2008*

GEM-Trackers for the PANDA Target Spectrometer – Design studies

B. Voss, J. Kunkel
GSI, Darmstadt, Germany

The Project

In 2008 the design of the large area planar GEM-Trackers to be installed inside the target spectrometer of PANDA has been started. These detectors are based on large-area planar **G**aseous **E**lectron **M**ultipliers (GEM) as amplification stages.

The Setup

The detector system will be operated inside the 2 T magnetic field of the PANDA magnet. A sketch of the proposed setup cut alongside the beam axis is show in fig. 1. It consists of four detector stations with principally identical buildup. Some of the preliminary mechanical parameters are given in the table below.

Station no.	1	2	3	4
Weight (kg)	≈ 20	≈ 20	≈ 30	≈ 40
Distance to target (mm)	810	1170	1530	1890
Outer diameter (mm)	900	900	1120	1480

The 'Riddle' as shown in fig. 2 (left), a light-weight (< 3 kg) and still very stiff CRP (**C**arbon **R**einforced **P**lastic) structure with a wall thickness of only ≈ 0,4 mm, may serve as a common support. The detector assembly is sketched in figs. 3 and 4. They are built completely modular with respect to their components and various functions like supplies, particle detection, amplification, signal mapping and electronic processing. Mechanical FEM-simulations (fig. 2, right) reveal that a totally symmetric overall-layout and a fully circular shape is a prerequisite to keep the shape stability in the required region of ○ (100 µm). Each detector will deliver the position of the passing particles in four projections. For this purpose e.g. polygon-pixel, radial+cylindrical, tilted or curved strips as well as hybrids are investigated as electrode structures of the large-area double-sided read-out planes. The front-end electronic (FEE) will be arranged on the perimeter of each detector.

For a set of four (%)	Active (Ar/CO_2)	Absorber (no backing)	Supply	Support	Front-End Electronic
Weight Contribution	0,5	4	≈33	≈34	≈28
Radiation Length design goal	0,09	1,4	not evaluated		
Radiation Length status-quo technique	0,09	3,6			

One of the major challenges of this project is the required highly-sectioned large-area GEMs and read-out planes as well as the requested low overall material budget (see table above). These R&D issues will also be addressed in the FP7 framework under I3HP 'JointGEM'.

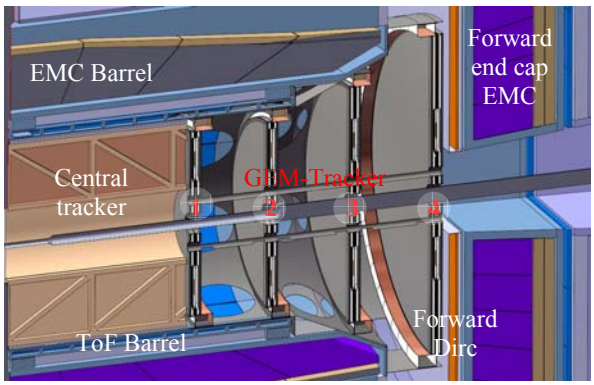

Fig.1

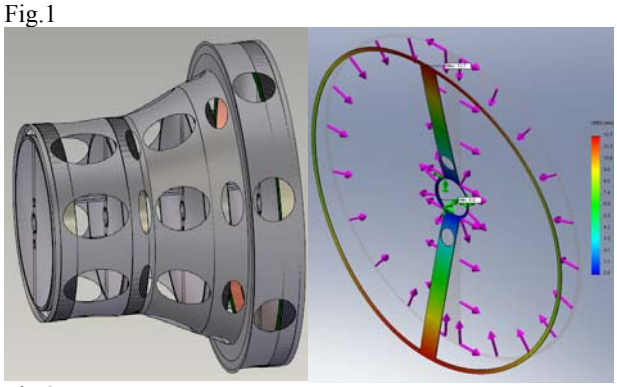
Fig.2

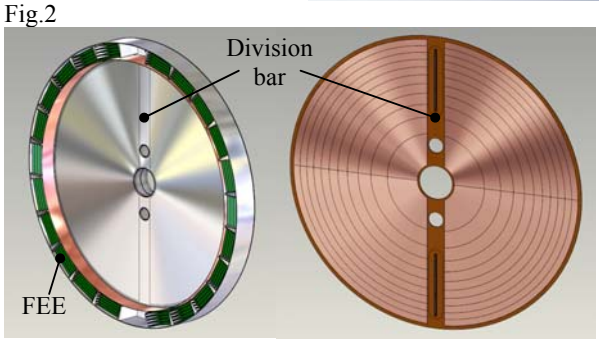

Fig.3

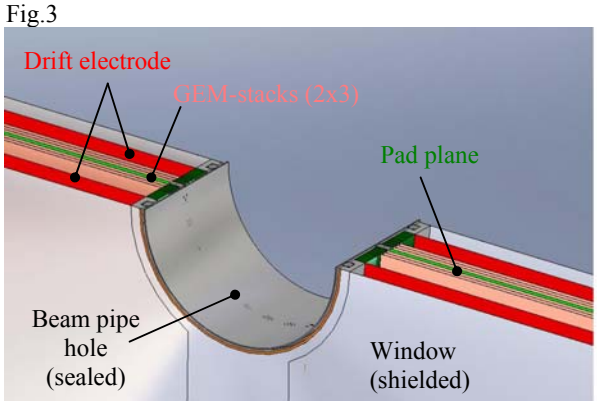

Fig.4

Radiation hardness of SiPM in the PANDA radiation environment

S. Sánchez Majos*, P. Achenbach†, A. Sanchez Lorente, and J. Pochodzalla
Inst. für Kernphysik, Joh. Gutenberg-Universität, Mainz,Germany

Silicon photomultipliers (SiPM) consist of a pixelized array of micrometric avalanche photodiodes (APD) connected in parallel. Their small size and low voltage operation allows the construction of very compact detectors. The price to pay is the megahertz dark count rate at room temperature. These events are generated by thermal electrons within the pixel and are undistinguishable from real signals what complicates low light level detection.

The use of SiPM as read-out devices has been discussed as an option for a time-of-flight start detector in the hypernuclear programme of PANDA [1] or as a candidate for the DIRC photon detectors in the experiment. The radiation hardness of the SiPM is a major issue due to the close proximity of the detector to the target area and the low light levels in these detectors. There is very little information in the literature about SiPM performance in the long term when operated in high radiation environments. It is well known for silicon detectors that generating centers are created during irradiation which increase the leakage current. The bulk leakage current is multiplied in APD by the gain factor and the resulting pulses are undistinguishable from photon generated events. Consequently, an increasing rate of dark pulses as a function of the radiation dose is expected in SiPM. Other effects might also appear due to the specific geometry and operation mode of these devices.

Radiation hardness studies have been performed at the MAMI accelerator facility of the Joh. Gutenberg-Universität, Mainz, by exposing a sample of 1 mm^2 SiPM (SSPM-0701BG-TO18) manufactured by Photonique and composed of 500 APD to a beam of 14 MeV electrons. The electrons crossed a 0.3 mm thick aluminum window at 15 cm distance from the active area of the SiPM. Fluences on the SiPM were calculated taking into account multiple Coulomb scattering in the thin exit window and ranged from $3.1 \cdot 10^9$ to $3.8 \cdot 10^{10}$ electrons/ mm^2. Heat generation and damage on the transparent epoxy layer protecting the silicon material was proved to be negligible. The low light level detection under reproducible conditions was realized by exciting a BC-408 plastic scintillator with a fast pulsed UV laser. Blue scintillation light was attenuated by a neutral density filter. The laser intensity could be regulated so that only few photons arrived to the SiPM. Fig 1 shows ADC spectra before and after irradiation for a fixed light intensity. A Monte Carlo simulation was used in order to extract the changes in the characteristic parameters of the SiPM [2]. The results show that the spectra of irradiated SiPM can only be reproduced with an increased noise rate and a reduced gain uniformity. A small gain reduction and increased after-pulsing probability were also observed.

* sanchez@kph.uni-mainz.de
† patrick@kph.uni-mainz.de

A possible time-of-flight start detector realized as a fibre barrel would be composed of 500 scintillating fibres read out in the backward angle direction by SiPM. This arrangement is demanded by the forward peaked character of the proton and neutron background [3].

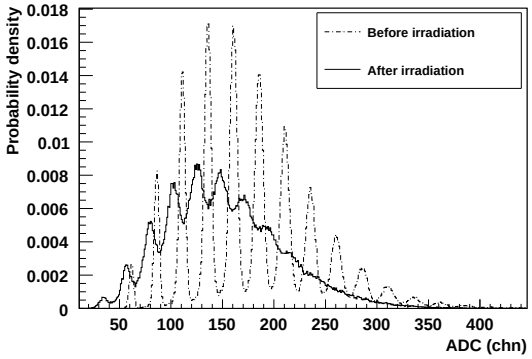

Figure 1: ADC spectra for low amplitude signals from green sensitive Photonique SiPM before and after irradiation with $3 \cdot 10^9$ electrons.

A simulation code originally written for the background radiation in the germanium detectors [3] has been used to calculate an integrated irradiation fluence at the SiPM location of $2.3 \cdot 10^4$ n+p/s with an average nucleon kinetic energy of 25 MeV. Radiation damage on the 500 SiPM devices can be predicted using the electron irradiation results by considering the non-ionizing energy loss (NIEL) of protons and neutrons distributed according to the simulated spectra. The resulting mean value of $7 \cdot 10^{-3}$ MeVcm^2/g (almost equal for both hadrons) has to be compared to $1.1 \cdot 10^{-4}$ MeVcm^2/g for electrons implying that hadronic damage will be 64 times stronger. A fluence of $8 \cdot 10^7$ (12 days of operation at $5 \cdot 10^6$ collisions/s) will result in a degradation as shown in Fig 1. Annealing recovery was studied by heating the irradiated SiPM at 80° during two weeks. Only a partial recovery was observed. No further improvement was obtained by longer heating periods. In conclusion, the use of this specific type of SiPM is not recommended for an application in the PANDA radiation environment.

References

[1] Technical progress report for Panda: strong interaction studies with antiprotons, Jan. 2005.

[2] S. Sánchez Majos, P. Achenbach, J. Pochodzalla, *Characterisation of radiation damage in silicon photomultipliers with a Monte Carlo model*, Nucl. Instr. and Meth. in Phys. Res. A 594 (2008) 351–357.

[3] A. Sanchez Lorente, et al., *Particle background simulation for a triple germanium Cluster detector at PANDA*, in: *Scientific Report 2007*, GSI, Darmstadt, 2008, p. 36.

Design Studies of an Antiproton Production Target*

N.A.Tahir[1], K.Knie[1], S.Richter[1], D.Kraemer[1], A.Shutov[2], V.Kim[2], A.Matveichev[2], A.Ostrik[2], V.Sultanov[2], I.V. Lomonosov[2], and A.R. Piriz[3]

[1]GSI, Darmstadt, Germany; [2]IPCP, Chernogolovka, Russia; [3]UCLM, Ciudad Real, Spain

We present numerical simulations of thermodynamic and hydrodynamic response of a proposed production target (see Fig. 1) for generation of antiprotons at the FAIR. As seen in Fig. 1, it consists of a Ni cylinder which has a radius of 0.15 cm and a length of 10 cm that is enclosed in solid graphite casing which is followed by an aluminum layer. One face of the cylinder is irradiated by a beam of

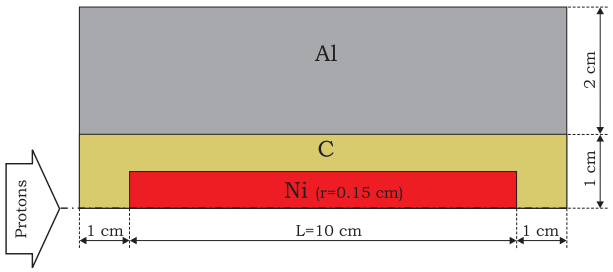

Figure 1: Target configuration

29 GeV protons that are delivered in a single bunch, 50 ns long. The beam intensity is considered to be 2×10^{13} and two different radial intensity distributions have been considered. In one case we consider a rectangular distribution with a focal spot radius = 1 mm while in the second case we use a Gaussian distribution with σ = 1 mm.

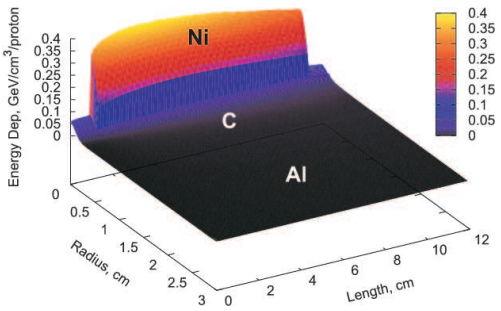

Figure 2: Energy loss by a single proton per unit volume calculated by FLUKA for a Gaussian intensity profile, leads to about 0.14 kJ/g specific energy in Ni.

The protons interact with the target material, thereby generating cascade particles. These processes are treated using the FLUKA code [1] and the energy loss data is shown in Fig. 2. This data is converted into specific energy deposition (kJ/g) which is used as input to a 2D computer code BIG2 [2] to study beam–target interaction. .

* Work supported by the BMBF and RFBR

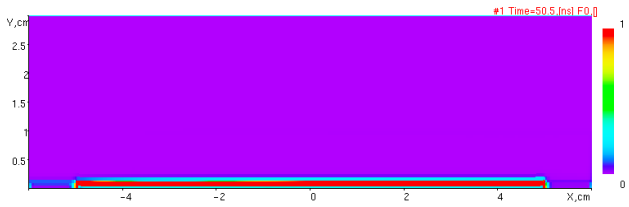

Figure 3: von Mises parameter at t = 50 ns for the Gaussian distribution.

In case of the rectangular intensity distribution, a maximum specific energy deposition of 0.27 kJ/g is achieved in the Ni part while the corresponding temperature and pressure are 940 K and 2.6 GPa, respectively. For the Gaussian distribution, the maximum specific energy is 0.14 kJ/g, the temperature is 629 K and the pressure is 2.4 GPa. It is to be noted that the target temperature remains safely below the melting temperature of Ni (1726 K) so the target will remain in the solid state. However, the high pressure in the target launches an outgoing radial compression wave which generates stress in the material that could lead to plastification of certain parts of the target. In Fig. 3 we plot the von Mises parameter, M, on a length–radius plane in case of the Gaussian distribution at t = 50 ns which shows that M = 1 in the Ni region which indicates material plastification. Figure 4 presents M at t = 1 μs which shows that the plastification wave has entered into the graphite by this time. Calculations at later points in time show that the aluminum region remains in an elastic regime. These calculations indicate that although plastification occurs in the interior, the target will still remain in tact.

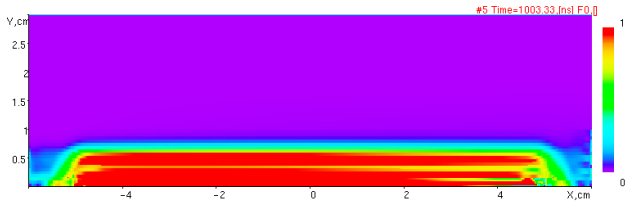

Figure 4: Same as in Fig. 3, but t = 1 μs.

References

[1] A. Fasso et al., "FLUKA: A Multi-Particle Transport Code", CERN-2005-10, INFN/TC-05/11, SLAC-R-773 (2005).

[2] V.E Fortov *et al.*, Nucl. Sci. Eng. 123, 169 (1996)

p-CVD diamond heavy-ion beam detector with integrated electronics

M. Kiš[1,2], M. Ciobanu[1,2], N. Herrmann[2], K.D. Hildenbrand [1], Y. Leifels[1], A. Schüttauf[1], and FOPI Collaboration[1]

[1]GSI,Darmstadt, Germany; [2]Physikalisches Institut, Heidelberg, Germany

For the new ToF Barrel of FOPI, [1], a new beam detector based on polycrystalline-CVD diamond was developed. The new device replaces the existing beam monitoring system which comprise a ToF Start detector and a beam-halo detector, both built from plastic scintillator material. However, since the employed diamonds are not sensitive to minimum ionizing particles the new device can be used efficiently only for heavy-ion beams. The layout of the detector foresees a single electrode for a start signal in the center and four adjacent electrodes to facilitate the focusing of beam and to serve as an additional beam-halo detector (see Fig. 1). The size of the electrodes was optimized such that

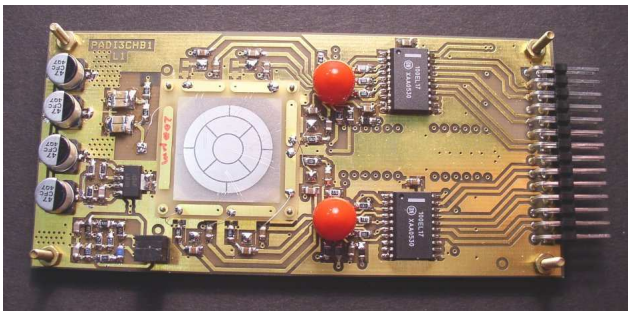

Figure 1: PCB with the p-CVD diamond mounted together with electronics. PADI chips (bellow red caps) are bonded directly to the PCB. The electrode layout is clearly visible on the diamond.

the central circle matches the expected beam diameter and all electrodes have similar surface sizes in order to keep their capacitances similar as well. The layout is completed by four additional electrods that together form a guard ring around the start and halo other electrodes.

Two diamonds of the same surface size (2×2 cm^2) but with different thicknesses (150 and 300 μm) were obtained from Element Six Ltd. The electodes (500 nm thick) were produced out of pure aluminum by shadow-mask metalization in the GSI Target Laboratory. The substrate side of the diamonds was used to metalize the readout electrodes, while the growth side was metalized with a single circle electrode to which common biasing voltage was applied. Tests in the GSI Detector Laboratory demonstraded a very good leakage current behavior, such that diamonds could be operated in a biasing field of more than 2 V/μm.

Previous measurements have shown [2] that the signal path between diamond and preamplifier has to be minimized in order to suppress reflections due to an unavoidable impedance missmatch. Since the detector has to be mounted in the vacuum of the beam pipe at the position of the existing start detector of FOPI it is also crucial to minimize the space occupied by the readout electronics. Therefore, we decided to employ the newly developed ASIC chip PADI [3] which was developed for the readout of small and fast RPC signals. The chip was already used in a similar application [4] with a single-crystal CVD diamond detector in a carbon beam. Since the PADI chip has a fixed gain of $\sim$60, for our application the diamond signals had to be attenuated in order to keep the input signal within the working range of the chip.

The setup consisting out of two diamond detectors and one reference plastic scintillator detector was tested in a Ni beam of 1.9 AGeV. One of the diamond detectors suffered from reflections that were attributed to the signal traces of the PCB, in particular due to the PADI chips that were directly bonded to the PCB. With the second diamond a stable operation point was reached with a rather high signal threshold. A measured time difference spectrum between two diamonds is shown in Fig. 2. A time resolution res-

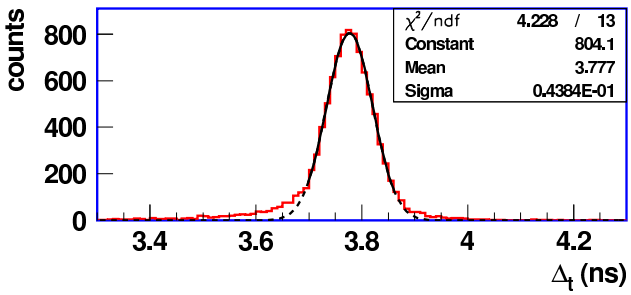

Figure 2: Time difference Δ_t between two diamonds. A gaussian fit is shown as an estimate of resolution. The tail to the left is due to reflections and extends out of the shown region for a few ns.

olution of better than 50 ps was obtained, as estimated by shown fit. This result confirms our previous measurements and demonstrates the capabilities of the PADI chip.

For the future we plan to improve the detector concept by a different PCB layout and a new version of the PADI chip that was developed particularly for the readout of diamond detectors.

References

[1] A. Schüttauf et al., Nucl. Phys. B (proc.Supp.) 158 (2006) 52

[2] M. Kiš et al., GSI Sci. Rep. 2005 269

[3] M. Ciobanu et al., IEEE NSS Conf. Rec., N30-18 (2008) 2018

[4] M. Ręþisz et al., GSI Sci. Rep. 2007 374

Investigations of new samples of single-crystal CVD-diamond detectors*

E. Berdermann[1], M. Ciobanu[1], W. de Boer[2], R. Lovrincic[3], J. Morse[4], M. Pomorski[1,5], M. Traeger[1]
[1]GSI Darmstadt; [2]University of Karlsruhe; [3]KIP, University of Heidelberg; [4]ESRF, France; [5]CEA Saclay, France

In 2008, we continued investigating a series of sensors of 3.5mm x 3.5mm area, which were thinned (for the first time) to thicknesses ≥ 50µm applying different treatments. Aiming to define the best surface preparation protocols, we correlated the detectors characteristics with peculiarities of AFM pictures, 'white-beam' X-ray-diffraction topographs and birefringence images.

Surface- and Bulk Defects of the Crystals

Single-crystal CVD diamond (scCVDD) for detector applications is grown on best quality HPHT single-crystal diamond substrates of (100) crystallographic orientation, because the incorporation of stacking faults or the creation of twin crystals is hereby more suppressed than, e.g., in the (111) growth direction. Any imperfection of the substrate may hand over in the CVD diamond film either as isolated bundle of threading dislocations or as an extended cluster defect. Both cases lead to crystal stress. After growth, the CVD plates are separated by laser cutting from the substrates and polished on both sides. In case of samples treated with diamond-coated scaife- or resin-wheels (Fig. 1, top-row), the AFM images of opposite surfaces (left and centre) show significant differences in morphology and roughness, e.g., 4-6nm rms and 15-30nm rms, respectively. This is due to the initial brazing of the diamonds to the sample holder during polishing and the following chemical removal. The last fixed side remains amorphous (centre), whereas the opposite surface shows typical scratch line patterns (left). In contrast, ion-beam polished plates (Fig. 1, bottom-row) have almost atomically flat surface with roughness of ~ 0.5nm rms on both sides (left).

The morphology and the 'reconstruction' of the diamond surface are important issues. Specific surface defects capable of accommodating excess electrons or holes by charge exchange between surface and bulk material [1] may be the reason of different and altering electronic properties of the electrodes, which lead to polarization of mechanically polished scCVDD detectors. Due to the unsaturated dangling bonds of the last atomic layer (two per C-atom) the 'clean, unreconstructed' CVD diamond surface is unstable [1]. In a last preparation step just before metallization, the diamond plates are oxygenated by wet chemistry and oxygen-plasma treatment [2].

'White-beam' X-ray topography (Fig. 1, top-right and bottom-centre) visualizes regions of defect-free crystal structure by homogeneous bright areas, and structural defects or strain by dark figures. Also excellent CVD diamond contains presently a few isolated bundles of threading dislocations originating from the HPHT substrate, which are easily identified in birefringence images as bright crosses (Fig. 1, bottom-right) within the homogeneous dark area indicating optically isotropic diamond.

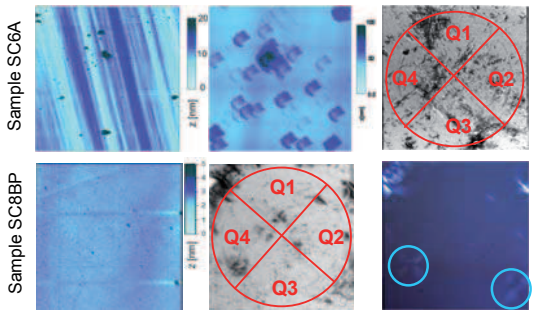

Figure 1: (top-row) 4x4µm² AFM images (opposite sides) of a resin-wheel polished sample, and full-size X-ray topograph (right). (bottom row) 4x4µm² AFM image (left), X-ray topograph (centre), and birefringence image (right) of an ion-beam polished sample. The electrode layouts used for characterization are indicated in the topographs.

Dark Conductivity

All tested samples reveal very low dark conductivity. The IV characteristics of samples SC6A and SC8BP are shown in the top and bottom plots of Figure 2, respectively. Negligible current is measured over the whole bias range in the defect-free sector Q2 of sample SC6A, whereas the cluster defect in Q4 leads to polarization and memory effects. A smooth decrease of the resistivity in Q1 and Q4 is obtained at fields E_D > -2V/µm, and an erratic increase of the leakage current at a relatively low breakdown field of E_D ~ ± 1.2 V/µm in Q3, due to a threading dislocation at the border of that electrode.

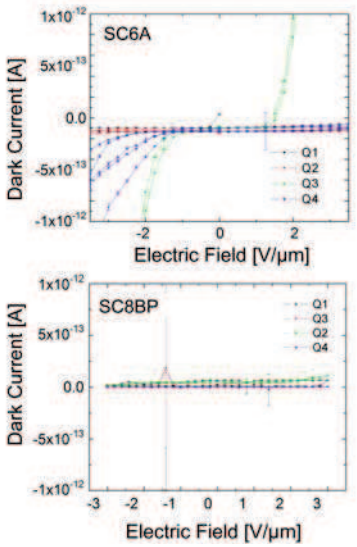

Figure 2: Dark current behaviour in sectors Q1-Q4 of the resin-wheel (SC6A, top graph)- and the ion-beam polished sample (SC8BP, bottom graph). (see text)

In contrast, homogeneous low conductivity (dark currents < 0.1 pA) was obtained in all sectors of sample SC8BP up to $E_D = \pm 3V/\mu m$. The erratic dark currents expected from the threading dislocations [3] were not observed. Most likely is that they appear in conjunction with structural surface defects, which were not detected in the ion-beam polished diamond sensors. A decisive parameter may be also the main inclination angle between dislocations bundles and the (100) direction.

The majority of the investigated samples show two distinguished IV ranges: the detectors safe bias range of negligible leakage current and the E_D region where smoothly increasing currents obey a single power low $I_D \propto E_D^a$ [2]. The exponents are ranging from a = 2.2 for defect-free diamond plates up to a = 5-7 for defective and stressed samples. The onset of the 'soft breakdown' varies by two orders of magnitude.

Timing and Spectroscopy Properties

The insert of Figure 3 demonstrates the homogeneity of the α-induced e-drift Transient Current (TC) signals in all sectors of sample SC8BP, and thus, the homogeneity of the electric field and of the e-drift velocity (~100μm/ns at E_D = -1.5 V/μm). The commonly observed leading peak (i.e. the holes contribution to the TC before absorption in the next electrode) is more pronounced in thin sensors.

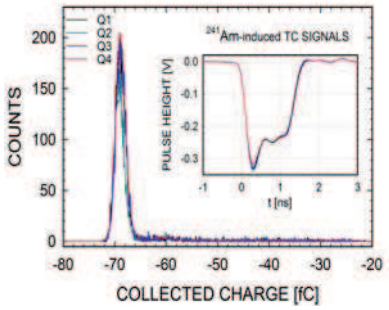

Figure 3: Overlay of the collected-charge spectra obtained from ^{241}Am-α-particles in all sectors of detector SC8BP using DBA amplifiers. (Insert) Corresponding average electron-drift signals. (see text)

The collected-charge spectra recorded with broad-band electronics reveal a mean value which corresponds to the expected 67fC of a ^{241}Am-alpha particle. The energy resolution measured at room temperature with spectroscopy amplifiers was δE ~ 15 keV (δE/E = 0.27%).

First Radiation Hardness Studies

In 2008, Michal Pomorski completed successfully his PhD thesis [2], in which the aspects of the results described above are discussed in more detail. First radiation-hardness studies are concluded as a worst scenario of the radiation tolerance of scCVDD, which can be optimized in future developments. Eight samples of 400μm thickness were irradiated with 26 MeV protons and 20 MeV neutrons up to a highest integral fluence $\Phi = 1.18 \times 10^{16}$ particles/cm^2. In both cases, the optical absorption spectra showed a Zero-Phonon Line (ZPL) at 1.638eV, indicating the dominance of the neutral mono-vacancy defect V^0 in the absence of complex defects. No space charge is found in p-irradiated detectors confirming the neutral state of the created defects. The V^0 concentrations estimated by integration of the ZPL revealed a defect-production rate after proton irradiation, which was about one order of magnitude lower than expected from the Non-Ionizing Energy Loss (NIEL) hypothesis, suggesting diamond self-annealing. Furthermore, the six times higher defect concentration expected from NIEL calculations after p-irradiation is in contradiction to the identical defect-production rates found for both, p- and n-irradiation. Different self-annealing processes or the different irradiation conditions applied during neutron irradiation (biased sensors) must be considered.

The inverse effective deep-trapping time $1/\tau_{e,h}$ increases linearly with Φ. The corresponding Charge Collection Distance (CCD) is plotted in Figure 5 versus Φ for the unprimed (open and checked circles) and the primed (lined and full dots) case, respectively. A permanent increase of the CCD by a factor of ~2.3 is achieved after priming with ^{90}Sr electrons.

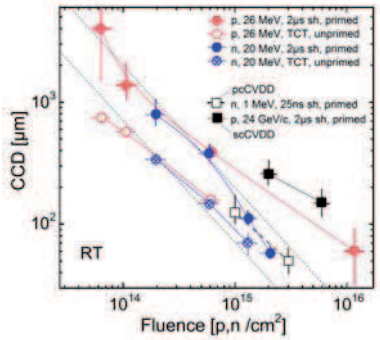

Figure 5: First radiation-hardness data of GSI (circular symbols) and some measurements of the RD42 Collaboration (squares).

In contrast to silicon sensors, the leakage current is suppressed in damaged diamonds - most likely due to the compensation of shallow traps by deep states of neutral mono-vacancies. Irradiated diamond detectors work without special treatment at high electric fields approaching the saturation velocity range. The influence of the contacts to the radiation hardness data is not completely understood yet. Improved electrodes could be prepared on top of a thin, highly boron-doped diamond interface layer.

References

[1] C. Nebel and J. Ristein in 'Thin-Film Diamond II' edt. by R. K. Willardson and E. R. Weber
[2] M. Pomorski, PhD Thesis, Univ. of Frankfurt, 2008
[3] J. Yang et al., Proc. of MRS 2005, 0905-DD06-09

* This work was supported by the EC *I3 Hadron Physics*, Project RII3-CT-2004-506078. We express our gratitude to J. Härtwig from the ESRF for the X-ray topographs and to the GSI Target Laboratory for the diamond metallizations.

Influence of substrate temperature on electrical conductivity of thin metal films on single crystal diamond*

Robert Lovrinčić, Sebastian Noebel, and Annemarie Pucci
Kirchhoff-Institut für Physik der Universität Heidelberg

The growth of thin metal films on single crystal diamond (SCD) was studied by means of infrared (IR) spectroscopy, aiming to support the development of diamond detectors for particle physics.

Our findings on the growth of chromium (Cr) thin films on SCD have been published here [1, 2] and will be published in more detail elsewhere [3]. Additionally, we investigated the growth of aluminum (Al) on SCD, see [4] for details. In this short report we want to emphasise the importance of the substrate temperature for the electronic conductivity of metal films on SCD.

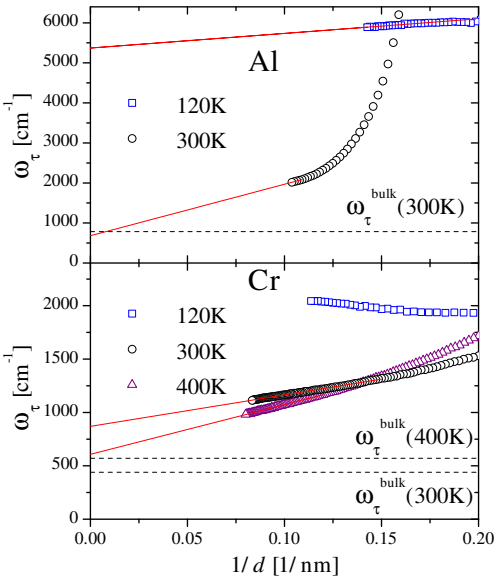

Figure 1: $\omega_\tau(d)$ versus inverse film thickness as calculated from IR spectra for Al and Cr on diamond at different substrate temperatures. The continuous lines are linear extrapolations for $d \to \infty$.

By IR spectroscopy the dynamic conductivity of thin films can be determined in the inspected spectral range. Assuming the validity of the Drude model in this range, the two Drude parameters plasma frequency ω_p and relaxation rate ω_τ can be calculated from the measured spectra, allowing an extrapolation to the static conductivity σ which is given by $\sigma = \epsilon_0 \frac{\omega_\mathrm{p}^2}{\omega_\tau}$. While ω_p is not expected to deviate from its bulk value for film thicknesses d above a few nanometers, the relaxation rate in films with d in the range of several $10\mathrm{nm}$ can be significantly higher due to two effects. First, scattering at defects inside the film enhances ω_τ by ω_τ^d, which depends on the crystalline quality of the layer. Second, the conduction electrons may scatter on rough surfaces, increasing ω_τ by $\omega_\tau^\mathrm{s} \propto d^{-1}$ (for constant surface roughness), giving the total relaxation rate for a thin film:

$$\omega_\tau(d) = \omega_\tau^\mathrm{bulk} + \omega_\tau^\mathrm{s}(d) + \omega_\tau^\mathrm{d}(d). \qquad (1)$$

Typically, from a certain thickness on, the film structure and morphology does not change anymore, resulting in a constant ω_τ^d and a linear behaviour for $\omega_\tau(d)$ over d^{-1}. An extrapolation for $d \to \infty$ can then yield information on ω_τ^d and hence on the number of defects. Fig. 1 shows the obtained development of $\omega_\tau(d)$ for Cr and Al at different temperatures. See references for experimental details.

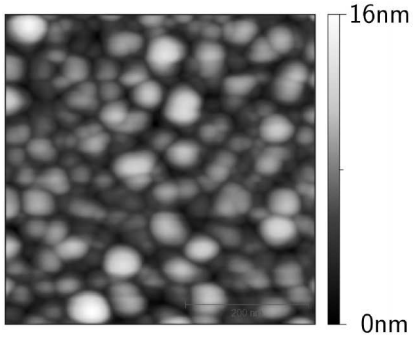

Figure 2: AFM measurement $(500 \times 500\mathrm{nm}^2)$ of an Al layer with a average thickness of $8\mathrm{nm}$, deposited on diamond at room temperature.

The main results are that for Cr a substrate temperature of $400\mathrm{K}$ is necessary for a high crystalline quality, while for Al ω_τ already at room temperature reaches $\omega_\tau^\mathrm{bulk}$. Consequently, Cr growth on SCD should be performed at $T = 400\mathrm{K}$, if the bulk value for σ is required.

However, in the case of Al a strong island growth could be detected by atomic force microscopy (AFM), as shown in Fig. 2, requiring high film thicknesses for a full coverage of the diamond, whereas Cr forms a closed film already at small d [3].

The authors gratefully acknowledge a fruitfull collaboration with Elèni Berdermann.

References

[1] R. Lovrincic and A. Pucci, GSI Scientific Rep., p. 197 (2006).
[2] R. Lovrincic and A. Pucci, GSI Scientific Rep., p. 207 (2007).
[3] R. Lovrincic and A. Pucci, submitted to Phys. Rev. Let.
[4] S. Noebel, Diplomarbeit, Universität Heidelberg (2008).

* Work supported by EU, project RII3-CT-2004-506078.

In-Beam Test Results of the Pestov Glass Resistive Plate Counter Prototypes *

D. Bartoş[1], G. Caragheorgheopol[1], F. Dohrmann[2], K.D. Hildenbrand[3], B. Kaempfer[2], R. Kotte[2], L. Naumann[2], M. Petriş[1], M. Petrovici[1], V. Simion[1], D. Stach[2], C. Williams[4], and J. Wuestenfeld[2]

[1]NIPNE, Bucharest, Romania; [2]FZ Dresden - Rossendorf, Dresden, Germany; [3]GSI, Darmstadt, Germany; [4]CERN, Geneva, Switzerland

The Compressed Baryonic Matter (CBM) experiment foresees a time-of-flight (TOF) wall equipped with resistive plate chambers (RPC) 10 m downstream from the target. The inner part of the TOF covers 50-100 mrad around the beam axis with an estimated flux densities of charged particles up to 20 kHz/cm^2. The rate capability of the present RPC based on comercial float glass ($\sim 10^{12}\Omega\cdot$cm) as electrodes is limited at about 1 kHz/cm2.

We designed and built two new prototypes of multi-gap, multi-strip RPCs based on Pestov glass of $10^{10}\Omega\cdot$cm bulk resistivity: one with standard readout - single-ended and the other one with differential readout.

The experiment has been performed at the electron linac ELBE at the Forschungszentrum Dresden-Rossendorf following the procedure described in [1]. Results of the in-beam tests of these two prototypes are presented in the following.

In the first part of the measurements a standard multi-strip, multigap RPC architecture [2, 3]) based on Pestov glass [4] was used. The counter was operated at 5.8 kV using standard gas mixture (85% $C_2H_2F_4$+5% iso-C_4H_{10}+10% SF_6). The signals of four strips read-out at both sides have been recorded. For the signal amplification we used the first generation of fast amplifier/discriminator (called FEE1) developed for FOPI RPCs at GSI [5] providing both timing and charge information for each channel. The time of flight distribution, for each measured strip, was obtained as the mean of the time information at both ends (t_{left} + t_{right})/2 . The obtained time resolutions, after

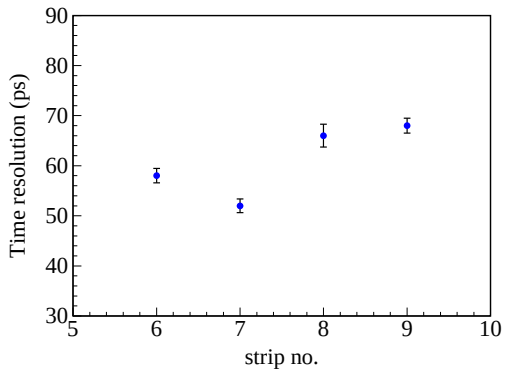

Figure 1: Time resolution of four neighbouring strips.

walk correction and selection of the events with the maximum charge on the analyzed strip, for the four measured strips, can be followed in Fig. 1. The observed variation of the time resolution for different strips quite probable is due to different intrinsic resolution of the corresponding electronic channels.

It should be stressed that these results have been obtained under a uniform illumination of the counter at a particle flux density of 1 kHz/cm^2 in contrast with tests performed with collimated MIP hadron beams when only a small part of the active area is exposed.

A second prototype that was tested is the four gaps Pestov glass RPC with a differential readout architecture. The applied voltage was 5.45 kV for all the performed measurements. An 8-channel differential amplifier/discriminator based on NINO ASIC chip, developed within the ALICE Collaboration [6], provided the timing information and the time over threshold as a measure of the input charge for slewing correction. Due to the limitation of the available electronic channels of the DAQ system, the signals of only two strips, readout at both ends, were recorded. The results obtained for time resolution at

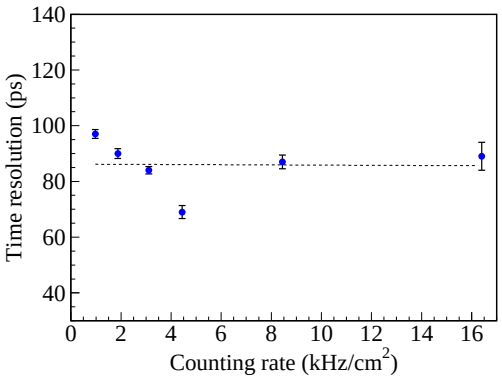

Figure 2: Time resolution as a function of counting rate.

different counting rate can be followed in Fig.2. Hardly any degradation of the time resolution up to about 16 kHz/cm^2 was observed. The larger value of the time resolution obtained for lowest rates can be due to some temperature instabilities during longer acquisition times needed at lower rates.

References

[1] R. Kotte et al. Nucl. Instr. and Meth. A 564(2006), 155.

[2] M. Petrovici et al., Nucl. Instr. And Meth. A 487(2002), 337.

[3] M. Petrovici et al., Nucl. Instr. And Meth. A 508(2003), 75.

[4] M.Petrovici et al., CBM Progress Report 2006, 43

[5] M. Ciobanu et al., IEEE Vol.54, Issue 4 (2007), 1201.

[6] F. Anghinolfi et al., Nucl. Instr. And Meth. A 533(2004), 183

* Work supported by JRA12-I3HP contract no.506078 finaced by EU-FP6 and CORINT/EU-RO contract no.58 financed by Romanian NASR and BMBF contract 06 DR 135.

Ion beam microstructure measurement.

P. Koczoń[1], C.J. Wandji[1], J. Hoffmann[1], N. Kurz[1], and W. Ott[1]
[1]GSI, Darmstadt, Germany

Abstract: A VHDL program for FPGA on VULOM3 has been developed which allows to perform measurements of time microstructure of the heavy ion beam.

Introduction

The intensity of heavy ion beam shoot into the experimental setup can vary periodically with time scale of microseconds. In order to identify those unwished microstructures the intensity of heavy ions within short periods of time (below microseconds) over the length of the spill should be measured. A simple approach based on counting heavy ions within a short period of time (say 100 ns) over a time comparable to the spill length (10 s) would produce an immense amount of data. Another solution, which statistically evaluates the incomming data sorting them immediately into histograms has been chosen. In case of presence of the microstructure at least two distinct peaks in the frequency distribution of the beam intensity should be observed. The histogram content, which is a moderate amount of data, can be transferred easily once per spill or per predefined number of seconds to a dedicated slow control computer.

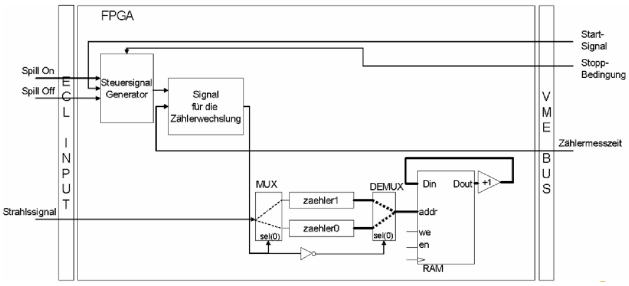

Figure 1: The principle of dead time free scaler shown schematically.

Dead time free scalers

Two scalers alternately counting incoming signals have been programmed in Virtex4 FPGA of the VULOM3 [1] using VHDL. The first scaler keeps counting for a predefined period of time (i.e. 100 ns). At the end of the time period it launches the second scaler, stores its own data in an array and resets itself Fig.1. The second scaler repeats exactly the same procedure so that the counting continues without any breaks over either predefined amount of time or whole length of the spill. The collected data is read out via VME bus by a controlling processor for further distribution.

Measuring procedure

Beam intensity up to 10^6 ions/s can easily be measured with a simple, thin scintillating detector like a start detector, which is available in almost every HI experiment. Logical signals in ECL standard of at least 10 ns length have to be delivered to the input of the dedicated VULOM3 module. Additional signals informing about the start and the end of the spill can be delivered as well to assure the synchronous data transport to a VME processor installed in the same crate as the VULOM3. This controlling CPU (RIO3/CES [2] in the test measurement) reads out and distributes the measured data and is also used to load the FPGA programm into the VULOM3. System configuration (measurement period and time) is done in a LabView application running on a standard WindowsXP PC which communicates with the VME processor. This programm displays also the incoming data in form of histograms and archives them for further analysis.

Test measurements

After succesfull tests in the laboratory the system has been used for beam diagnostics in two experiments: FOPI and FRS. The results are shown in Fig. 2 and prove the absence of the significant beam microstructure during the measurements.

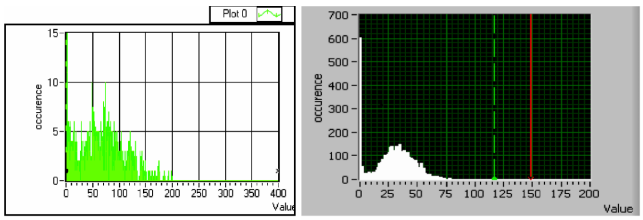

Figure 2: Each of the histograms shows one pronounced peak (around 75 and 30) - no microstructure. Values of exactly 0 appear when there is no beam intensity for a certain time of the spill.

References

[1] J. Hoffmann `http://www.gsi.de/informationen/wti/ee/elekt_entwicklung/vulom3_e.html`

[2] Creative Electronic Systems `http://www.ces.ch`

Characterization of detector systems for single-photon counting applications in laserspectroscopy experiments at GSI*

R. Jöhren[†1], D. Anielski[1], W. Buglak[1], V. Hannen[1], W. Nörtershäuser[2,3], and C. Weinheimer[1] for the SPECTRAP collaboration

[1]Westfälische Wilhelms-Universität Münster, Institut für Kernphysik, Wilhelm-Klemm-Str. 9, 48161 Münster; [2]Johannes Gutenberg-Universität Mainz, Institut für Kernchemie, Fritz-Straßmann-Weg 2, 55128 Mainz; [3]GSI Helmholtzzentrum für Schwerionenforschung GmbH, Planckstr. 1, 64291 Darmstadt

The Institut für Kernphysik in Münster participates in the SPECTRAP experiment and related ESR measurements within the framework of an R&D contract with GSI. The task in Münster is the characterization and setup of detector systems capable of single-photon counting and suitable for the use at the experiments just mentioned.

The measurements presented in this report were performed with a special test setup. A small vacuum chamber provides a vacuum up to 10^{-7} mbar. The detector mount inside the chamber can cryogenically be cooled to near LN2 temperature and is equipped with a LabVIEW based temperature control to hold the detector temperature at any value between room temperature and -160°C. It can also be used to bake out the detectors at temperatures of up to 100°C. To minimize the noise contribution from external sources a low noise preamplifier board tailored to operation at low temperatures inside the vacuum has been developed based on the AMPTEK A250 chip.

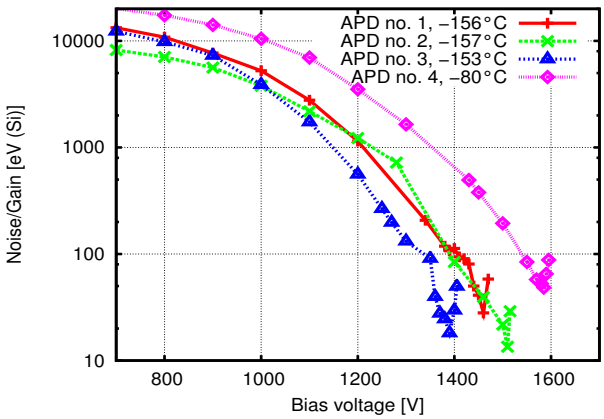

Figure 1: Noise to gain ratio of several RMD type S1315 APDs at different temperatures. Different APDs show some variation in performance.

Characterization of Avalanche Photo Diodes

With high quantum efficiencies (QE) in the visible region and a QE of 20% near 1064 nm, Avalanche Photo Diodes (APDs) of the type S1315 manufactured by Radiation Monitoring Devices Inc. (RMD) are a possible candidate for measurements of the hyperfine transition in $^{207}Pb^{81+}$ at SPECTRAP and for ESR measurements in the visible and NIR regime [1]. The tested RMD APDs have an active area of 13 mm x 13 mm and stand bias voltages up to 1.8 kV. Additional tests with RMD APDs of the types S0223 (2 mm x 2 mm activ area) and S0814 (8 mm x 8 mm active area) are ongoing.

By determining gain and noise as a function of bias voltage at different temperatures we determined an ideal operating point at each temperature. The noise to gain ratio drops with temperature as shown in Fig. 1. For example, APD no. 3 shows the best noise to gain ratio at 1390 V bias at -153°C. At this operation point a gain of about 3000 was achieved.

To determine the sensitivity to low single-photon rates the electronic noise rate in the region of the single-photon signal in the APD was investigated. For a quantitative determination of the single-photon counting sensitivities, additional measurements with a dedicated single-photon source are required. In addition the charge sensitive preamplifier will be further optimized.

Channel Photomultipliers

Another detector type under investigation are Channel Photomultipliers (CPM) manufactured by PerkinElmer [2]. With a QE of about 12% near 244 nm, a large active area of about 180 mm^2, and a very low dark count rate of about 20 Hz they are suitable for measurements from the UV region up to about 700 nm wavelength. They fit the requirements for measurements of the hyperfine transition in $^{209}Bi^{82+}$ at SPECTRAP and might also be suitable for the measurements at the ESR, where the wavelength of photons from, e.g, the $^{209}Bi^{80+}$ hyperfine transition are Doppler shifted to 640 nm in forward direction.

Detectors used at the SPECTRAP setup have to stand high magnetic fields of the superconducting magnets. The dependence of the CPM countrate on magnetic field strength has been determined. At 60 Gauss the CPM count rate is 50% compared to the value without magnetic field.

References

[1] http://www.rmdinc.com/products/p006.pdf

[2] http://optoelectronics.perkinelmer.com

* Work supported by an R&D contract with GSI

† rjoehren@uni-muenster.de

Development of a H*(10)-Photon Dosemeter

G. Fehrenbacher[1], J.G. Festag[1], S. Grosam[1], and K. Vogt[1]
[1]GSI, Darmstadt, Germany

Introduction

At accelerator facilities radiation fields containing photon radiation arise and can cause serious dose rate levels. One task for the radiation safety is the reliable measurement of the magnitude of the radiation dose rate. The quantity to be measured is the ambient dose equivalent H*(10). This quantity gives an estimate for the effective dose. The energy range to be considered ranges from 10 keV to several MeV. At high energy accelerators even higher energies of photon radiation can occur. Because of the lack of commercial photon dosemeters for the low energy range, the aim of this work is the development of a dosemeter for the measurement in the energy range from 10 keV to several MeV. Basis of the dosemeter is the use of thermoluminescence detectors (TLD) which contain ^{7}LiF elements. The whole dosemeter consists of a TLD card (type Harshaw TLD-700) with four elements (see fig. 1), a polyethylene cylinder absorber and copper foils for the upper elements.

Figure 1: GSI cylinder dosemeter for the measurement of photon radiation.

Readout and Response of TL Detectors

The irradiated TL cards are evaluated by a reader (type Harshaw 6600) which measures the emission of light during the heating process. The signals of the four elements are evaluated in pairs. The averaged signal of the two elements covered by copper foils is weighted with the corresponding averaged signal of the bare elements (signal weighting is 45% and 55%). For the reliable measurement of the ambient dose equivalent the energy and angular dependence of the response of the dosemeter must be determined. Monte Carlo calculations have been performed using the code FLUKA [1]. The geometry of the whole dosemeter was modelled. The response, relative to the signal for the radiation of a ^{137}Cs source was computed for the energy range from 10 keV to 10 MeV. The calculations were carried out for both types of elements. The results are shown in fig. 2 for the perpendicular incidence of the radiation to the TLD card (0°). The solid line gives the results of the FLUKA calculation, the symbols with error bars give the measured values [2, 3].

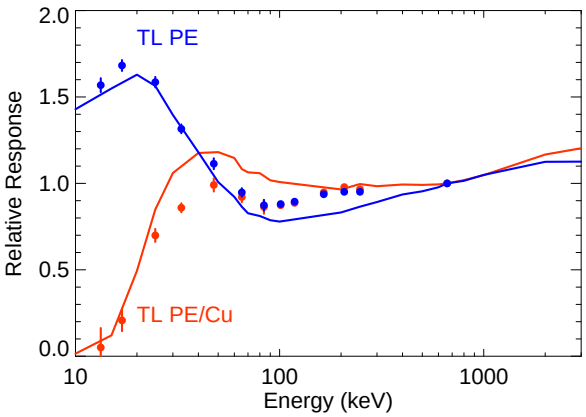

Figure 2: Response of the two types of elements of the GSI cylinder dosemeter for 0° irradiation (TL PE – signal of bare elements in PE cyl., TL PE/Cu signals of copper foil covered elements in PE cyl.).

In fig. 3 the resulting response – the weighted sum of the signals - of the dosemeter is shown. It can be seen that the reading of the dosemeter agrees with the measured dose values with an accuracy of about 25% in the whole energy range from 10 keV to 3 MeV or higher energies.

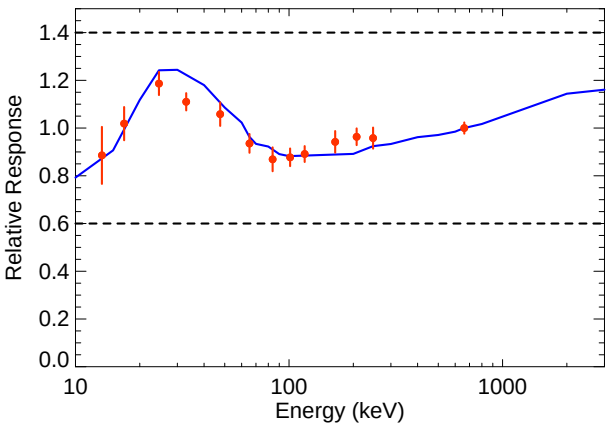

Figure 3: Resulting response of the GSI cylinder dosemeter for 0° irradiation.

References

[1] FLUKA: http://www.fluka.org
[2] S. Grosam, Diploma thesis, BA Karlsruhe, 2007.
[3] Forschungszentrum Karlsruhe, Jahresbericht der Hauptabteilung Sicherheit 2007, p. 74.

Absorption and scattering lengths of high density silica aerogels with $n = 1.07$

L. Debenjak[1,2], P. Achenbach*[2], J. Pochodzalla[2], T. Saito[2,3], and S. Širca[1]

[1]IJS, Ljubljana, Slovenia; [2]KPH, Joh. Gutenberg-Universität, Mainz, Germany; [3]GSI, Darmstadt, Germany

Charged particle identification at the PANDA experiment will be performed over a wide range of momenta by Čerenkov detectors. One option to identify higher momentum charged particles under small polar angles could be the use of silica aerogels as radiator. Simultaneously, an aerogel Čerenkov counter is being designed for the Kaos spectrometer at the Mainz Microtron MAMI for the discrimination between kaons and pions of momenta $\geq$ 1GeV/c. For the simulation of such detectors, the optical properties of the aerogel are needed as input data.

We have measured the wavelength dependence of the transmittance (T) and reflectivity (R) of high density aerogel with $n \approx 1.07$, made by Chiba U. in Japan. The characteristic absorption length (Λ_{abs}) and scattering length (Λ_{scat}) were extracted by fitting Λ_{abs} and Λ_{scat} to T.

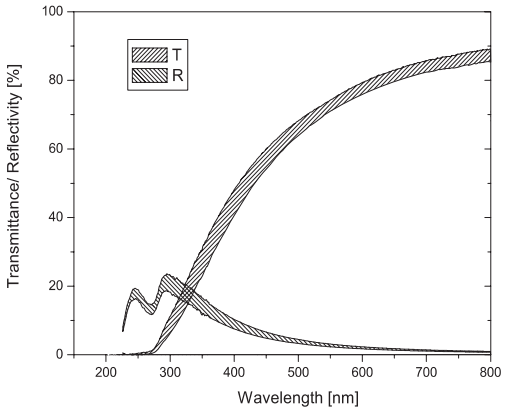

Figure 1: Transmittance (T) and reflectivity (R) as a function of the wavelength for silica aerogel with $n \approx 1.07$.

The transmittance between 200 nm and 800 nm of two aerogel tiles has been measured at different positions on the surface to scan for potential inhomogeneity and to obtain averaged values, see Fig. 1. From these measurements the scattering length, the absorption length and the attenuation length have been deduced by applying the following relation

$$T(\lambda) = (1 - R(\lambda)) \exp\left(-\frac{a}{\lambda^2}d - \frac{b}{\lambda^4}d\right). \qquad (1)$$

Here, d is the thickness of the aerogel tile. The parameters a and b are related to the absorption and scattering length:

$$\Lambda_{abs} = \lambda^2/a, \quad \Lambda_{scat} = \lambda^4/b. \qquad (2)$$

The fit yields:

$$\begin{aligned} a &= (2.48 \pm 0.04) \times 10^{-10}\,\text{cm}, \\ b &= (5.76 \pm 0.07) \times 10^{-19}\,\text{cm}^3. \end{aligned}$$

Table 1: The absorption and scattering lengths at different aerogel thicknesses (at $\lambda = 500$ nm). Deviations of values at different thicknesses may indicate that the simple power-law dependance assumed in Eq. (2) is inappropriate, as also established by [2].

d	2 cm	4 cm	9 cm
Λ_{abs}	10.1 cm	9.1 cm	7.9 cm
Λ_{scat}	10.8 cm	13.7 cm	13.5 cm

The results are in fair agreement with the values obtained by [1]. These parameters have also been measured at different thicknesses of the aerogel by selecting different tile orientations. The corresponding absorption and scattering lengths at the wavelength seen by PMTs ($\lambda \approx 500$ nm) are shown in Table 1. Such high losses in the aerogel lead to a very low number of deteced photons.

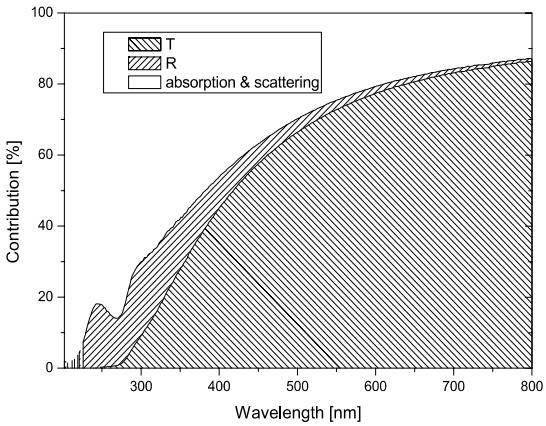

Figure 2: Relative contributions of the optical effects in the aerogel. The probability of transmittance $T(\lambda)$ and reflection $R(\lambda)$ are shown. The remainder corresponds to the absorbtion and scattering (white area). The sum of all the probabilities is normalised to 100%.

While measuring the transmittance, a part of the light is reflected, a part is transmitted and the remainder is absorbed or scattered. The breakdown into individual contributions can be seen in Fig. 2.

References

[1] R. Siudak et al., Nucl. Instr. and Meth. in Phys. Res. A 596 (2008) 311.

[2] E. Aschenauer et al., Nucl. Instr. and Meth. in Phys. Res. A 440 (2000) 338.

* patrick@kph.uni-mainz.de

Charge Breeding with Dresden EBIS/T systems

A. Silze*[1], G. Zschornack[1], S. Geyer[2], O. Kester[2], A. Sokolov[2], G. Vorobjev[2], and F. Ullmann[3]

[1]Institut für Angewandte Physik, Technische Universität Dresden, Germany; [2]Gesellschaft für Schwerionenforschung mbH, Darmstadt, Germany; [3]Dreebit GmbH, Dresden, Germany

Electron Beam Ion Sources and Traps (EBIS/T) of the Dresden EBIS/T type have been proven to be efficient and reliable sources of highly charged ions in many applications [1]. At GSI, a Dresden EBIT named SPARC-EBIT is currently being installed as an ion injector at the HITRAP facility. It will serve as an off line ion source for test runs and experiments. Plans for the future also envision the application of the SPARC-EBIT or other Dresden EBIS/T systems for charge breeding purposes. In this regard, the project presented here focuses on testing the performance of these sources as charge breeders.

Charge breeding with EBIS/T facilities using superconducting solenoid coils for the compression of the electron beam has been achieved successfully with breeding efficiencies into one charge state of more than 10 % [2]. The Dresden EBIS/T concept, however, is based on the usage of permanent magnets. The absence of refrigeration technology or liquid cooling gases results in many advantages such as low initial and running costs, easy operation, and a compact design which allows for transportation of the sources. On the other hand, their relatively short ion trap regions, shallow trap potentials, and low magnetic field strengths create challenges in trapping injected ions.

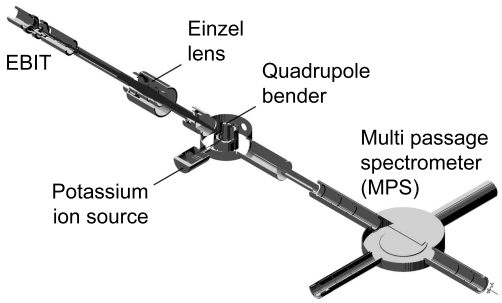

Figure 1: Main setup of the GSI MAXEBIS test bench including a SIMION simulation of the K^{1+} beam injected into the SPARC-EBIT.

The main components of the GSI MAXEBIS test bench which had been redesigned for charge breeding experiments with the SPARC-EBIT are shown in figure 1. The injection of externally produced singly charged potassium ions into the EBIT was realized with the help of a quadrupole bender and an einzel lens. After extraction from the source the ions were guided straight through the quadrupole to the multi passage spectrometer (MPS) where various beam analysis techniques could be performed. SIMION [3] simulations of the K^{1+} ion beam as well as Field Precision TriComp calculations of the fields and ion trajectories inside the source were carried out predicting an achievable capture efficiency of 1-2 %. Therefore, with the equipment available at the test facility, charge breeding was forecast to be difficult but possible.

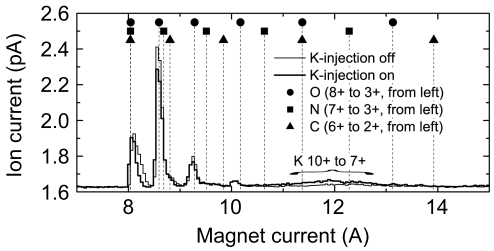

Figure 2: Extraction spectra of the beam from the EBIT without and with potassium injection measured with the MPS used as a 90° bending magnet.

In fact, the corresponding experiments showed that for charge breeding with the Dresden EBIT precision is essential. X-ray spectroscopy as well as time-of-flight spectroscopy and 90° magnetic scanning were used to identify the ion species trapped inside and extracted from the source. Hints on potassium reaching the trap region were found, as presented in figure 2. Herein, it is shown how an extraction spectrum changed when K^{1+} was injected into the EBIT. The peaks referring to the residual gas mainly consisting of oxygen, nitrogen, and carbon decreased in height. The light ions acted as a cooling gas for the heavier potassium. Meanwhile, a weak signal was detected where one would expect potassium peaks to appear in the spectrum. However, a clear identification or investigation of charge bred potassium ions could not be achieved.

A new setup for further attempts is currently under construction at GSI's HITRAP facility. In Dresden, a test facility for charge breeding will be assembled as soon as ongoing tests of its components will have finished. The plans of this facility include the application of a pepperpot emittance measurement system for advanced ion beam characterization which recently has been taken into operation.

References

[1] See www.dreebit.com for a list of publications.

[2] D. Voulot et al., Nucl. Instr. and Meth. in Phys. Res. B 266 (2008) 4103

[3] D. A. Dahl, Int. J. Mass Spectrom. 200 (2000) 3

* a.silze@fzd.de

Data Acquisition Backbone Core DABC v1.0*

J. Adamczewski-Musch[1], H.G. Essel[1], N. Kurz[1], and S. Linev[1]
[1]GSI, Darmstadt, Germany

DABC purpose The DABC [1] addresses requirements of FAIR experiments like CBM [2] for detector and data acquisition test beds. As it is implemented it also provides a general purpose DAQ framework for experiments in production. DABC is able to handle any kind of front-end systems and provides event building over fast networks using commodity hard- and software. Especially a mixture of commonly used MBS (daq.gsi.de) based front-ends and time stamped data streams is supported.

The DABC software written in C++ is developed on Linux. Arbitrary front-end systems (FES) can be connected to standard PCs (by hardware or network). Application specific software plug-ins for handling the front-ends have to be provided by the application programmers.

DABC components The DABC consists of a core system providing the data flow and processing, and a control environment providing state machines, task controls, monitoring and setup/configure mechanisms. The controls environment uses DIM servers (dim.web.cern.ch) and a generic Java written GUI for control and monitoring. Fig.1 shows the main components of the core. *Modules* (application

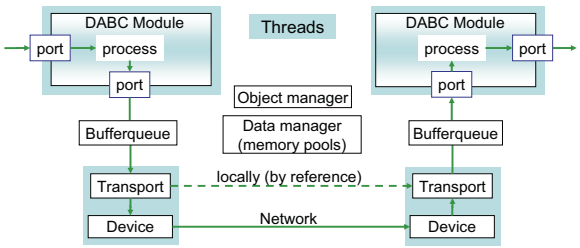

Figure 1: Data flow model with software components.

plug-ins) process the data which is kept in buffers of smart memory pools. *Transport* and *Device* classes handle data sources, networking, data storage, or data servers. *Transports* connect *Modules* via buffered *Ports*, either locally or remotely. The components may run in separate threads to utilize multi core PCs. Central managers organize all objects.

DABC applications Some applications implemented:
1. MBS event builder. MBS front-end systems are connected via TCP to DABC nodes for event building. The MBS DIM servers provide control and monitoring by the DABC GUI, also in a stand-alone mode.
2. PCI express board [3]. All plug-ins have been implemented. Data rates between 400 MBytes/s (reading) and 700 MBytes/s (writing) have been measured.
3. CBM readout board [4]. Three boards were used in a test beam time to read out front-end boards equipped with nXYTER chips. They were sending the data via Ethernet with a UDP based protocol to a PC. The DABC plug-ins did some processing and storage. Through a data server (MBS stream server protocol) standard analysis programs Go4 [5] has been used to perform some more detailed monitoring on-line.

Controls and monitoring Parameters and commands can be specified in the application plug-ins. The GUI builds up displays from all services provided by the DIM servers. Special parameters like rates or states are visualized.

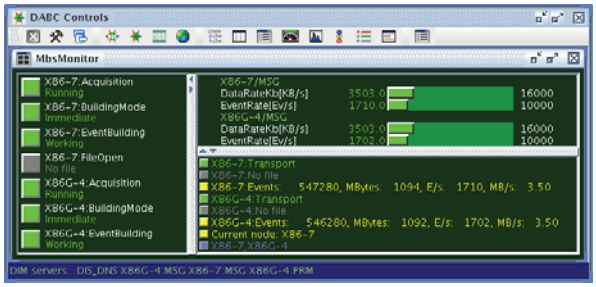

Figure 2: MBS rate meters and status displays.

Status and outlook DABC version 1.0 will be published begin of 2009 (see [6]). The plug-in API has been implemented after a redesign. No more external packages except DIM are needed. In 2008 DABC was used in a first test beam time to test CBM detectors and front-end components. More complex testings will follow in 2009.

References

[1] J. Adamczewski, H.G. Essel, N. Kurz, S. Linev, "Data Acquisition Backbone Core DABC", IEEE Trans.on Nucl. Science, Vol.55, No.1, pp. 251-255, Feb. 2008

[2] "CBM progress report 2007", GSI, February 2008

[3] J.Adamczewski et al. "Data Communication Tests on Active Buffer Board", GSI report 2007

[4] S.Linev "Software Development for CBM Readout Controller Board", GSI report 2008 (this report)

[5] J. Adamczewski-Musch, H.G. Essel, S. Linev, "Go4 Analysis Framework v4", GSI report 2008 (this report)

[6] Web site: dabc.gsi.de

* Work supported by EU-RP6 HadronPhysics, RII3-CT-2004-506078

Front-End-Device - Application Programming Interface *

R. Keidel[1], S. Bablok[2], and E.S. Conner[1]

[1]ZTT, University of Applied Sciences, Germany; [2]Institutt for Fysikk og Teknologi, Universitetet i Bergen

The Front-End-Device - Application Programming Interface (FED-API)[1] has been designed and developed to supervise and control FED with versatile programming interfaces to support different detector systems while reducing the amount of data per time unit up to a distinct level to prevent the Process Visualization System from malfunctioning.

Software Architecture

The FeeCom (Front-End-Electronics Communication) chain consists of three layers: the FedClient which is part of the PVSS on the supervisory layer, the InterComLayer (ICL) on the control layer and the FeeServers with their ControlEngines (CE) connected to the Front-End-Electronics (FEE) on the field layer. The FED-API constitutes the upper part of the FeeCom chain (FedClient and the FedServer module of the ICL) and is responsible for the communication between the Supervisory Layer and the Control Layer. In addition the ICL comprises of the following modules: the ApplicationLayer module, which hosts the database access of the ICL and the CommandCoder, and the FeeClient module controlling the FeeServers (see figure 1). The database provides the detector parameters which are in turn assigned by the CommandCoder to the individual field devices. [2] The communication between PVSS and ICL and ICL and FeeServers is done by means of the high-performance and fail safe DIM protocol[3].

Results of the Test Run of the ALICE Experiment

During 2008 the TPC and four supermodules of the TRD operated continuously for more than six months at the ALICE Experiment at Cern. The FED-API was used extensively to supervise and control these detectors. Several software bugs were found and fixed. The runtime behavior of the FED-API can now be considered stable. During the field test the following unforeseen issues were found:

- The initialization of the field devices is performed more often than expected. Thereby the initialization time becomes an issue. Shorter initialization times are mandatory.
- Some detector messages are more important than others. This depends on the state of the detector system. Important messages need to be delivered first. A configurable priority queue for important messages is mandatory.
- The CPU load of the InterComLayer hardware has an undocumented impact on the timing of the message delivery and thereby delays the delivery of the messages unnecessarily under heavy CPU load. An adaptive control optimization needs to be implemented.

Summary and Outlook

All aforementioned topics are of high economic and functional importance for an efficient run of the experiment and will be implemented in the next period. After succeeding with the adaptations the FED-API will be a versatile DCS middleware which will be used by several detector systems (TPC, TRD, PHOS FMD, EMCal) and can be easily adapted to upcoming physical detector systems. An adaptor to CSS[4] and EPICS[5] is planned.

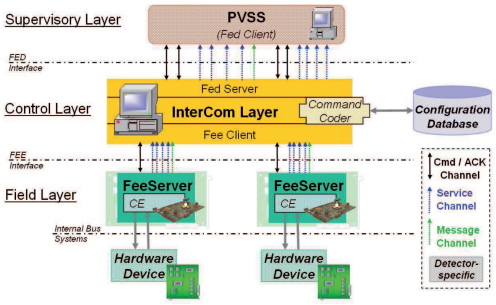

Figure 1: Three layers of the FED-API and the modules of the InterComLayer.

References

[1] S. Bablok, E.S. Conner, et al: Front-End-Electronics Communication software for multiple detectors in the ALICE experiment, Nuclear Instruments and Methods in Physics Research Section A: Accelerators, Spectrometers, Detectors and Associated Equipment Volume 557, Issue 2, 15 February 2006

[2] S. Bablok: Heterogeneous Distributed Calibration Framework for the High Level Trigger in ALICE, PhD Thesis, University of Bergen (Norway), 30 October 2008 (to be published in February 2009)

[3] C. Gaspar, M. Doenszelmann, Ph. Charpentier: DIM, a Portable, Light Weight Package for Information Publishing, Data Transfer and Inter-process Communication, Presented at: International Conference on Computing in High Energy and Nuclear Physics 2000, Padova (Italy), February 2000

[4] http://css.desy.de/content/index_eng.html

[5] http://www.aps.anl.gov/epics/

* Work supported by GSI; Vorhaben: ALICE Softwareanwendung zur Modellierung von Prozesssteuerungsschnittstellen / EPICS; WOKEI

MBS v5.1 and DABC

J. Adamczewski-Musch[1], H.G. Essel[1], N. Kurz[1], and S. Linev[1]
[1]GSI, Darmstadt, Germany

MBS controls upgrade MBS v5.1 can optionally be built with DIM (dim.web.cern.ch) control. All MBS nodes then provide DIM services for monitoring. MBS prompter is still command dispatcher to the other nodes but gets commands from any DIM client. Command definitions in XML format are provided to DIM clients like the DABC Java GUI (dabc.gsi.de [1][3]) to build up command panels as can be seen on top in Fig.1. Commands to set the execution node (`set dispatcher`) and to execute MBS scripts found on the working directory are added. The middle

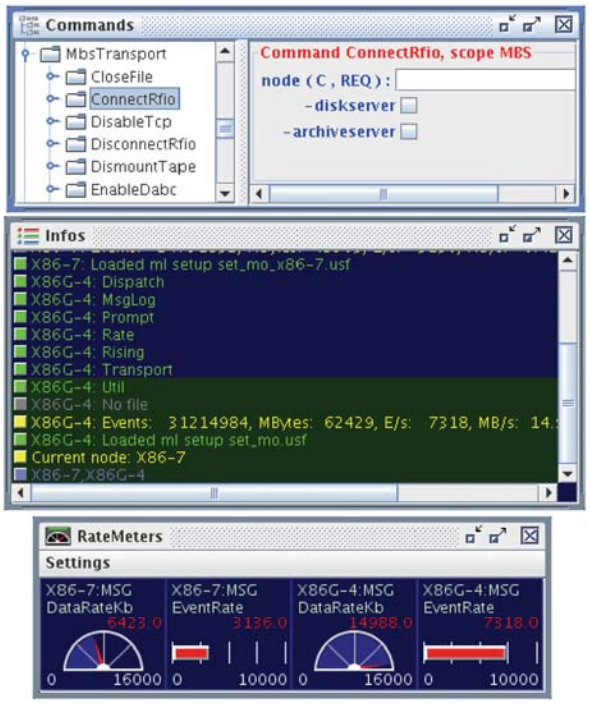

Figure 1: MBS command tree and info panel.

window in Fig.1 shows some info lines like the node list, the current command execution node, the active tasks, the setup loaded, and the data rates. The bottom window shows rate meters. Attributes of rate meters can be specified in a file on the working directory. Other windows show running states and the MBS logger output. MBS can be fully controlled by that GUI.

MBS buffer size limit Due to historical reasons there was a limitaion in the buffer size to 32K. This limitation has been lifted and buffers may have larger size. The number of buffers per stream can be set to one avoiding event spanning. A new version of the event API library (v5.1) is required to handle these large buffers on- and off-line (already used in Go4 [2]).

MBS with DABC as event builder The DABC [1] is a general purpose DAQ framework for experiments in production. The software written in C++ is developed on Linux. DABC is able to handle a mixture of commonly used MBS based front-ends and time stamped data streams. For pure MBS front-ends a plug-in is included in the distribution. Fig.2 shows the connection between MBS and

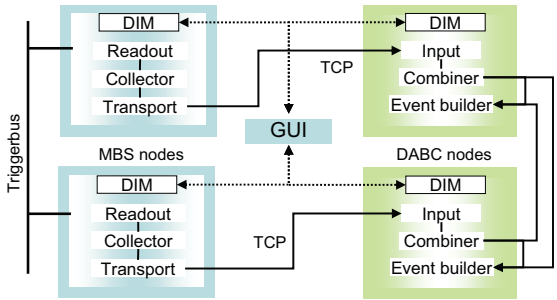

Figure 2: MBS with DABC event building.

DABC, both controlled by DIM. The MBS nodes run as in stand-alone mode except that each node has a *Transport*. DABC event builder nodes connect to these *Transports* and build the events over a network. Running with DABC the *Transports* are blocked by DABC and send variable length buffers. The *Combiner* module may merge subevents from several *Transports* connected to the same node. DABC stores the data in a new file format overcoming the 2 GB limit and with random event access (already supported in Go4 [2]). It also provides a *Stream Server* for connection of standard stream server clients like Go4.

Status and outlook DABC version 1.0 will be published begin of 2009. MBS v5.1 is available and installed at GSI. Remote installations must also install DIM (distributed with MBS).

References

[1] J. Adamczewski, H.G. Essel, N. Kurz, S. Linev, "Data Acquisition Backbone Core DABC", IEEE Trans.on Nucl. Science, Vol.55, No.1, pp. 251-255, Feb. 2008

[2] J. Adamczewski-Musch, H.G. Essel, S. Linev, "Go4 Analysis Framework v4", GSI report 2008 (this report)

[3] J. Adamczewski-Musch, H.G. Essel, N.Kurz, S. Linev, "Data Acquisition Backbone Core DABC v1.0", GSI report 2008 (this report)

PCI-express Optical Receiver, PEXOR.

J.Hoffmann, N.Kurz, S.Minami, W.Ott, S.Voltz
GSI, Darmstadt, Germany.

A PCI Express (PCIe) to optical link interface (***PEXOR***: ***P***ci-***EX***press ***O***ptical ***R***eceiver) was developed to connect front end boards to standard PCs. The center of the PEXOR is a high performance Lattice FPGA connecting three main components together: 1) A four lane PCIe endpoint device (4*2.5 Gbits/s). 2) Four high speed optical transceivers (4*2 GBits/s, SFP [1]) as inputs for front end electronics. 3) A second generation RLDRAMII, serving as intermediate data buffer between SFPs and PCIe. Its capacity is 576 Mbytes and it can be accessed with up to 1 Gbits/s per pin. Effectively 16 pins are available.

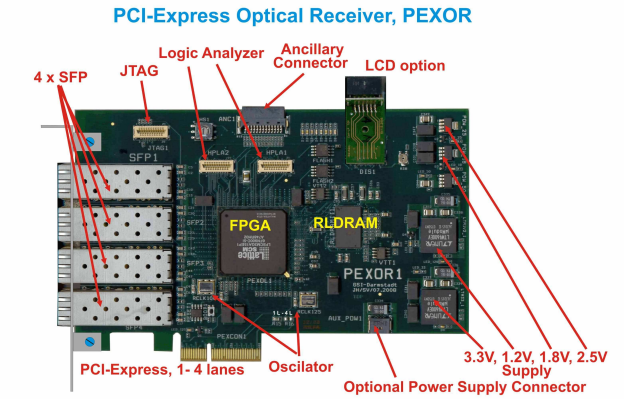

Figure 1: Photograph of PEXOR

The PCIe interface of the PEXOR module is realized completely in FPGA logic. An intellectual property (IP) core from the manufacturer of the FPGA covers all PCIe layers up to the basic transaction layer. The processing of the transaction layer packets (TLPs) has to be supplied by the user and was implemented utilizing sources of a demo PCI express board. The separate modules of the design are interconnected through Wishbone interfaces [2]. To achieve maximum data throughput, a DMA engine was developed. The DMA engine is able to copy data from e.g. the internal RAM to the PC memory. The performance of the DMA engine with a burst size of 128 bytes is shown in Fig. 3 and reaches up to 560 Mbytes/s for a transfer size of 16 Kbytes. In addition interrupt handling with the PC has been established with latencies of 500 ns for notification in the interrupt service handler of a device driver and below 6 us for notification in user applications.

Data transmission through the SFP interfaces has been tested by connecting each FSC to the other one with a fibre optic cable. The 8b10b block code was adapted to encode for serial data transmission which can be easily implemented using a IP core provided by the manufacture. The data transmission worked with maximum clock frequency for the SFP, 2GHz, which corresponds to 1.6GBits/sec by taking 20% of overlap by 8b10b code into account.

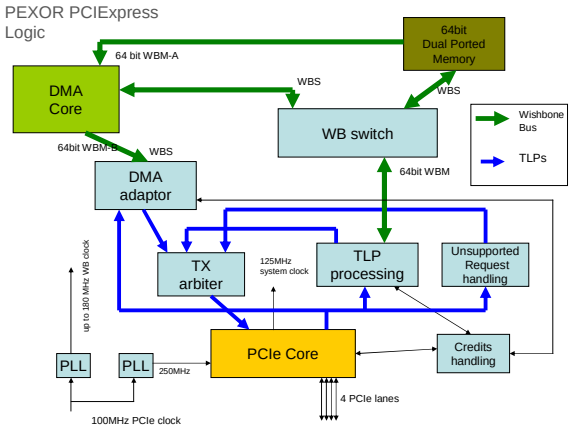

Figure 2: Schematic View of PEXOR FPGA logic

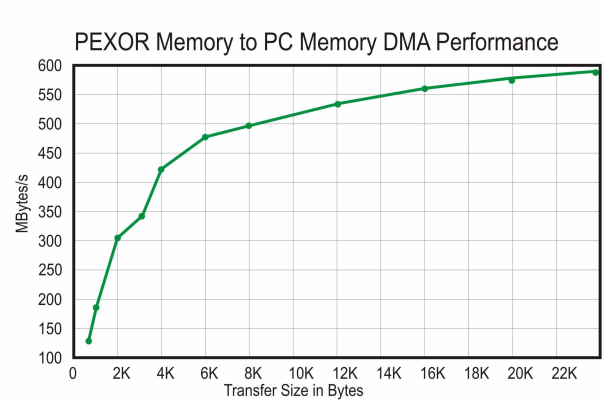

Figure 3: DMA performance of PEXOR card

References

[1] http://de.wikipedia.org/wiki/Small_Form factor Pluggable
[2] WISHBONE System-on Chip (SoC) Interconnection Architecture for Portable IP Cores, www.opencores.org

Go4 Analysis Framework v4

J. Adamczewski-Musch[1], H.G. Essel[1], and S. Linev[1]
[1]GSI, Darmstadt, Germany

Overview

Go4 (**G**SI **O**bject **O**riented **O**nline **O**ffline) is established as standard GSI analysis framework for several experiments of atomic and nuclear structure physics, e.g. FRS, SHIP, and RISING. Go4 is based on ROOT [1] and is available for download under GPL at the Go4 homepage [2]. Go4 is installed and maintained for all users on the GSI linux cluster.

A new major release Go4 v4 was published in 2007, supporting the Qt 4 graphics library [3]. Additionally, a monitoring tool for the new GSI DAQ system DABC [4] was introduced both for Go4 v3 and v4. Both source releases now support to build Go4 with gcc 4.3.x on *Linux*, and CC 5.x on *Solaris* platform, resp.

Support for Qt 4

Go4 v3 has become a stable production version since 2006, but its graphical user interface is based on the deprecated version 3 of the Qt framework [3]. Because this will not be supported anymore in the near future, it was necessary to port the Go4 GUI to the current Qt version 4. This task included an adjustment of the GSI qt-root interface (with some Go4 specific extensions), and a redefinition of all Go4 GUI elements.

In February 2008 a first release of Go4 v4.0 was published, supporting Qt versions 4.3.x. Due to continuous developments in the Qt4 API, the Go4 version 4.1 had to follow already in October 2008, supporting also Qt 4.4.x. The most recent Go4 v4.1.1 was released in November 2008.

In parallel to this, Go4 version 3 is also being maintained, still with a GUI for Qt v3, but containing all other improvements of Go4 version 4. Changes in Linux distributions and ROOT versions require a continuous maintenance of both branches. The most recent Go4 v3.4.1 was thus also released in November 2008.

New DIM monitor tool for DABC

When working with the new GSI Data Acqusition Backbone Core framework (see [4] and contribution in the current report), a new Go4 toolwindow can monitor the published DIM services [5] of the DABC control system. It is available if the Go4 installation was build with an existing DIM environment `$DIMDIR`.

Figure 1 shows the Go4 main window with the DABC monitor tool at the bottom and some histograms filled with monitored data. Any node that exports a DABC state service to the DIM name server will show up in the *DABC Nodes* table in the middle. The current state of the DABC node (or the MBS acquisition status, resp.) is displayed by colour and name in this table. The user can select to subscribe for all DABC rate meters of the corresponding node. The subscribed rate meters will show up in the *Ratemeter View* table on the right.

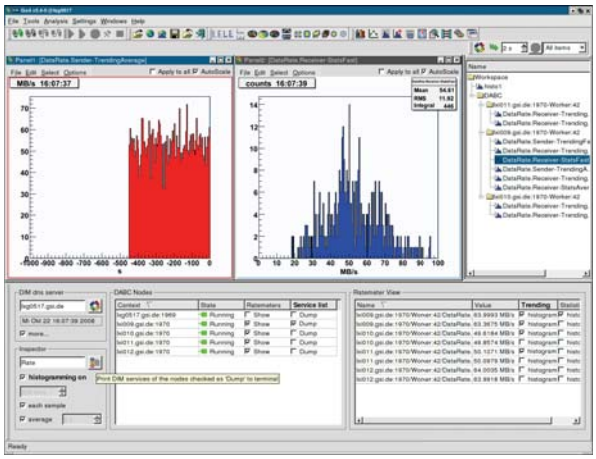

Figure 1: DABC monitor tool with histograms.

The table information is refreshed by means of the DIM mechanism whenever a rate service is updated. Additionally, each rate variable may be filled in a trending histogram, and a statistics histogram. The histogram's properties, like bin size, axis range, etc., can be defined before accumulation. For each rate variable there may be a "fast" histogram, filled at each DIM update; and an "average" histogram, accumulated during a user defined time interval. All these histograms appear in the workspace folder of the Go4 browser, so one may display, rename, or save them as usual.

Moreover, the tool allows to print the current values of any DIM service on the observed nodes to the `stdout` of the GUI terminal. It is also possible to dump such services only if their name matches a wildcard expression; thus filtering out some of the variables on the DAQ cluster.

References

[1] R. Brun et al., "The ROOT System Homepage", http://root.cern.ch,

[2] H.G. Essel et al., "The Go4 web page", http://go4.gsi.de,

[3] Nokia corporation, "Qt software web page", http://www.qtsoftware.com/,

[4] J. Adamczewski, H.G. Essel, N. Kurz, S. Linev, "Data Acquisition Backbone Core DABC", IEEE Trans.on Nucl. Science, Vol.55, No.1, pp. 251-255, February 2008.

[5] C. Gaspar, "Distribution Information Management system DIM", http://dim.web.cern.ch/dim/

The HGF* Base Class Library based on LVOOP

H. Brand, D. Beck
GSI, Darmstadt, Germany

LabVIEW provides its own approach to object oriented programming since version 8.2 consequently following the dataflow paradigm. Most well known object oriented design patterns [1] have to be reinvented with respect to dataflow. The HGF Base Class Library is a first attempt to provide general purpose classes to deal with LabVIEW objects as entities in multithreaded and distributed applications.

Motivation

Object oriented concepts were introduced in native LabVIEW with version 8.2 (LVOOP). Contrary to conventional programming languages, like C++ or JAVA, LabVIEW follows the data flow paradigm. This is also true for LVOOP. LabVIEW does not treat objects as entities, but LabVIEW classes define new wire types. Data objects flow through wires from a data source to data sinks and become cloned at wire forks, which causes problems if the object refers to unique resources, e. g. files, sockets, physical devices, etc. Objects cannot be referenced. This fact has serious consequences for LVOOP design and well known object oriented design patterns have to be reinvented with respect to data flow. The HGF Base Class Library addresses the most important design patterns that enable the treatment of LabVIEW objects as entities. It is extending a feasibility study [2] we did earlier and proposed to be used for LVOOP based next generation automation and control system applications for FAIR experiments.

Design Patterns for LVOOP

The following design patterns are necessary to implement event driven and distributed automation and control system applications relevant for FAIR. The prime features of the HGF Base Class library are the following. A detailed technical description was published in [3].

- A **Factory** provides a *constructor* to create initialized and named objects to be used as entities. Initialization data are provided as *Variant* attributes. The *destructor* is used to release acquired resources.
- **Reference** and **Singleton** can be used to prevent unintended copying of objects at wire forks. Both patterns are using a single element queue that also enables mutual exclusion. (The object is in the queue or not.)
- An **ObjectManager** provides *new* and *delete* operators and maintains a unique **Reference** object database. Objects created with the ObjectManager can be referenced by name.
- A **Functioal Global Variable** is another possibility to create object databases. In this case the contained objects must have inherited from **Visitable** and are only accessible via **Visitors**.
- The separation of passive LabVIEW data objects and active threads demands for a **ThreadPool** dealing with active **ThreadWorkers** that execute functions defined by **ThreadTasks** on **Visitable** objects triggered by **Events** which carry the **Visitors**.
- Internal (Wait, NextMultiple, Rendezvous), triggered (Occurrence, Notifier, Queue) and network (DIM [4], SharedVariable) **Events** were implemented.
- **ProcessVariable**, publisher and subscriber, and corresponding data converter classes are available.

LVOOP Restrictions

- **Aggregation** must be used instead of multiple inheritance
- The **Delegation** pattern must be used to overcome the missing support for interfaces.
- **Variant** data type can be used to overcome missing overloading.

Status & Outlook

The HGF Base Class project is still under development, but already available# under the terms of the GPL. It contains some simple demo applications to illustrate the usage and extension of the base classes. Further developments will investigate the usability for Mobile Agent systems.

References

[1] Erich Gamma, Richard Helm, Ralph Johnson, John Vlissides, “Design Patterns - Elements of Reusable Object-Oriented Software”, Addison-Wesley, 1994
[2] D. Beck and H. Brand, “Control System Design Using LabVIEW Object Oriented Programming”, Proceedings of ICALEPCS07, Knoxville, Tennessee, USA
[3] H. Brand, “Object oriented programming with LabVIEW”, SEI-Herbsttagung 2008, HMI-B623 Berlin, Dez. 2008, Seiten 217–256, ISSN-0936-0891
[4] C. Gaspar, M. Dönszelmann, Ph. Charpentier, International Conference on Computing in High Energy and Nuclear Physics (Padova, Italy, 1-11 February 2000), http://www.cern.ch/dim.

*used as prefix in this context: Helmholtz, GSI, FAIR
#http://wiki.gsi.de/cgi-bin/view/NIUser/HGFBaseClassLibrary

Grid Activities at GSI*

M. Al-Turany, A. Kreshuk, P. Malzacher, A. Manafov, V. Penso, C. Preuss, K. Schwarz, F. Uhlig, and M. Zynovyev

GSI, Darmstadt, Germany

Abstract

This article describes the work of the GSI Grid Group with the aim to enlarge and operate an ALICE tier2 centre within the global environment of the LHC Computing Grid and to prototype a possible FAIR grid environment.

ALICE tier2 centre

The deployment of the ALICE tier2 centre has been finished in time for the planned startup of the Large Hadron Collider at CERN. The focus of the work moved to operating, customising, and upgrading the new infrastructure.

The disk space of about 300 TB bought for ALICE up to 2008 is distributed among an xroot[1] cluster and Lustre[1], a distributed parallel file system. The xroot cluster is configured as a Grid Storage element and globally accessible, while Lustre is used for local data storage. The performance of various storage strategies (local disks, xrootd, Lustre, GlusterFS[1]) is still being investigated.

Also the CPU capacity has been increased up to 1500 cores corresponding to a compute power of about 2400 KSI2K. All compute nodes have been moved to a new computing room in the accelerator building. This new facility has been interconnected to the main computing centre with the storage and service facilities using an aggregate bandwidth of 80 Gb/s.

Throughout the whole year GSI participated in all centrally managed ALICE Grid production and data analysis activities. The overall job share of GSI and Forschungszentrum Karlsruhe have been 15% of all ALICE jobs worldwide. Through the fact that the GSI cluster is used for local production by the GSI ALICE group as well as by Grid jobs from outside and interactive PROOF analysis processes the machines are well utilised all the time. For PROOF[1]analysis a dedicated cluster - GSIAF - is maintained where a user can start up to 160 parallel workers. The stability of the GSIAF cluster has been increased by introducing automatic maintenance utilities.

The whole infrastructure of the ALICE tier2 centre is monitored in detail by using MonaLisa[1].

The EGEE project

GSI is participating in EGEE III as partner of the distributed Swiss German Regional Operations Centre (ROC) and the German Joint Research Unit (JRU). Within EGEE[1] the main tasks of GSI are to operate a functioning Grid site and to support users and applications from ALICE and FAIR. In this context GSI participated also with courses in interactive data analysis in the GridKa School 2008[1] and in various Grid trainings for the Panda experiment. Moreover GSI operates a pre production testbed for gLite[1].

D-Grid

Within work package 3 of the HEP community Grid distributed analysis tools are being developed at GSI. Within this context the gLitePROOF package[1], now "PROOF on Demand" has been released. Herewith a user can dynamically combine the resources of several Grid centres to create a distributed PROOF cluster for immediate use. PROOF on Demand, originally developed for the usage with a gLite based Grid has been extended by plugins for the ALICE Grid middleware AliEn[1] and for the batch system LSF as it is used at GSI. The software package enjoys an increasing popularity and support is provided via a download site and a ticketing system.

Also 2008 significant amounts of compute resources have been bought from D-Grid fundings to enlarge the local cluster (storage and cpu). To be able to use the resources with D-Grid methods the machines have been equipped with supported middleware including Globus Toolkit 4 and added to the D-Grid information system.

Preparation for FAIR tier0

PANDA-Grid[1] has been extended to 19 sites. In a second data challenge the full chain of simulation, digitization, reconstruction, and data analysis has been exercised. The jobs have been computed on 12 sites with GSI and Dubna being the largest contributors.

The central Grid services for CBM have been set up at GSI. First small productions have been running successfully at GSI using the CBM Grid infrastructure.

After the ALICE FAIR meeting[1] in April 2008 the collaboration between ALICE and the FAIR experiments has been intensified. It has been agreed upon to work together in various areas of software development, e.g. Virtual Monte Carlo (VMC)[1] as well as in the context of Grid computing. ALICE, Panda, and CBM experienced successful synergy effects in the development of AliRoot and FAIRROOT as well as in the usage and ongoing development of AliEn.

* Work supported by BMBF - Förderkennzeichen 01AK802G (D-Grid) and 06GSI0011I (ALICE-Tier2) - and European Commission - contract number INFOSO-RI-031688 (EGEE II) and INFSO-RI-222667 (EGEE III))

[1] a list of related links: http://wiki.gsi.de/cgi-bin/view/Grid/Links

The GSI Mass Storage

H.Göringer, M.Feyerabend, S.Sedykh
GSI, Darmstadt, Germany.

Overview

The GSI mass storage systems provide safe, reliable, and redundant long term storage of all user and experiment data. Fast and highly parallel access to the data is available for 24 hours a day and 7 days a week.
Backup/Archive functionalities are provided with the commercial Tivoli Storage Manager (**TSM**).
Access to **experiment data** is enabled with **gStore,** the GSI made client server system. gStore is based on data mover nodes with disk cache and automatic tape libraries (ATL) connected via **S**torage **A**rea **N**etwork (SAN). Design principles and functionality are described in more detail in previous reports (e.g. [1]) and in a paper [2].

gStore Status and Enhancements

In 2008 the migration from older tape media has been completed. All experiment data are stored now on modern IBM 3592 tape media in the IBM 3494 ATL, which has been enhanced with two new tape drives. Nearly 80 TB of valuable raw data are stored twice to prevent from data loss in case of media damage.

All older data movers running with Windows have been removed from operation. The current eight data movers are running with SuSe Linux. The current status of gStore can be seen in table 1.

experiment data volume	360 TB	max 1.6 PB
overall data mover characteristics	disk cache 30 TB	max. bandwidth: 800 MB/s to tape 800 MB/s to user

Table 1: Status GSI Mass Storage December 2008

gStore has been used heavily in 2008. Overall 4.5 million files (490 TB) have been moved between tape and data mover disk cache or between disk cache and user.

Backup Enhancements

The migration of backup/archive data from LTO1 media to LTO2 has been completed in 2008. Therefore all components handling backup/archive to LTO1 have been removed from operation, especially the old LTO1 tape library and the related Windows TSM servers.

Lustre Connection to gStore

In 2008 first portions of a high performance lustre file system have been implemented at GSI as cache for experiment data. To provide fast access from gStore the lustre file systems are mounted on all gStore data movers. The gStore software has been enhanced enabling direct file copy operations with data rates of the order of 100 MB/s between lustre and the gStore servers running on the data movers. Such copy processes can be initiated by any gStore client, e.g. running on desktops where lustre is not mounted. Immediately after availability this fast connection was heavily used by the Hades collaboration for the beam-time in autumn 2008.
Taking into account the xrootd connection which has been tested successfully for Alice Tier2 the GSI storage landscape for experiment data looks in principle as shown in figure 1.

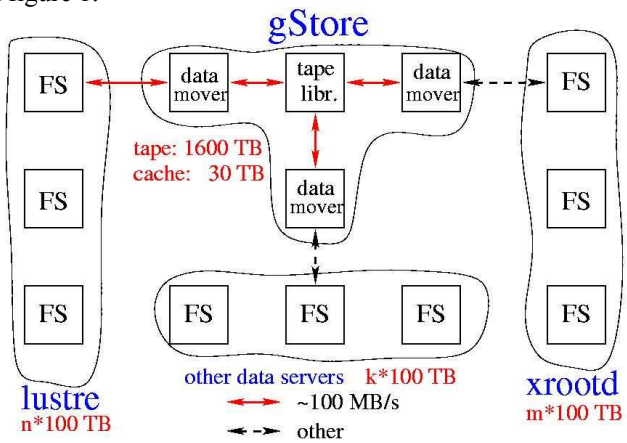

Figure 1: The GSI Storage Landscape

Future DAQ Connection to gStore

For running experiments there are two conflicting tasks to fulfil. The on-line experiment data must be copied for long term storage as fast as possible to gStore (write cache). On the other hand, the experiment data buffers must be available as soon as possible for monitoring purposes. For experiments with low data rates below 10 MB/s, large files of ~1GB are available from gStore after minutes, depending on the client bandwidth. However, this delay is not acceptable.

To overcome this unsatisfactory situation the high performance lustre file system will also be utilized during on-line data storage of a running experiment. In case of lower data rates, data buffers sent to gStore data movers will be written in parallel to gStore write cache and to lustre. In case of higher data rates, immediately after completion each file in gStore write cache will be copied to lustre. Migration to tape takes place if the copy to lustre is finished. In both cases the first data buffers of a file are available in lustre very quickly, and the data streams from the DAQ event builders are automatically stored.

References

[1] H.Göringer et al: The GSI Mass Storage System for Experiment Data, GSI Report 2008-1, p. 269
[2] Experiences with gStore, a scalable mass storage system with tape backend. J.Phys.: Conf. Ser. 119 Volume 119 (2008) 052018 (7pp)
see also: http://www-aix.gsi.de/computing/expdv/gStoreChep07JournalofPhysics.pdf

Status of the FairRoot Simulation and Analysis framework

M. Al-Turany[1] and F. Uhlig[1]
[1]GSI, Darmstadt, Germany

Introduction

The FairRoot framework [1, 2], is an object-oriented simulation, reconstruction and data analysis framework based on ROOT [3], and the Virtual Monte-Carlo (VMC) interface [4]. It includes core services for detector simulations and offline analysis.

Event Display

The event display in FairRoot is based on the Eve (Event Visualization Environment) package in ROOT [3]. Combined with trajectory visualization in FairRoot, the event display can be used directly from macro to display TGeoTracks (MC Tracks), Monte Carlo points and hits, together with the detector geometry. The FairEventManager implemented in FairRoot deliver an easy way to navigate through the event tree and to make cuts on e.g. energy, pt or particle PDG in user events. However the drawback of this ansatz is that the tracks has to contain some visualization information in order to be displayed. In the following we describe a solution where the track information is created at visualization level without the need to store track information during the simulation. This is achieved using Geane.

Geane

GEANE [5, 6] is a package to calculate the average trajectories of particles through dense materials and to calculate the transport matrix as well as the propagated errors covariance matrix in a given track representation. GEANE has been fully integrated in FairRoot as a package. The framework defines the basic classes relevant for track following, i.e. configuration, geometry description (from the Monte Carlo, parameters files) and the magnetic field map definition. The exact geometry and field used in the simulation can be taken into account by the track follower.

Event Display with Geane as track propagator

The fact that both Eve and Geane uses the root geometry description for detector geometry make it natural to integrate Geane as a track propagator for the event display. With this integration reconstructed tracks and/or monte carlo tracks can be visualized to a good accuracy. The main advantage of this integration is that any set of reconstructed or simulated tracks can be visualized without the need of special visualization modes. Moreover only selected tracks will be propagated on the fly which enhance the performance of the display. Figure 1 shows a schematic diagram of the interface to Geane.

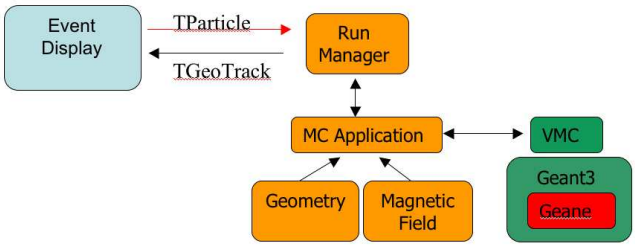

Figure 1: Event Display and Geane

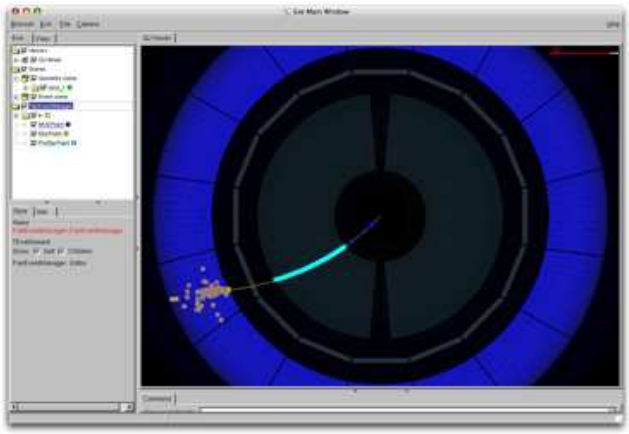

Figure 2: Event display example: Panda inner tracker and EMC

References

[1] M. Al.-Turany FairRoot: http://fairroot.gsi.de.

[2] D. Bertini, M. A-Turany, I. Koenig, and F. Uhlig. The fair simulation and analysis framework. In *International Conference on Computing in High Energy and Nuclear Physics (CHEP'07)*, volume 119 of *Conference Series*. IOP Publishing, 2008.

[3] R. Brun and F. Rademakers. Root - an object oriented data analysis framework. *Nuclear Instruments and Methods in Physics Research A*, 389:81–86, Sep. 1997.

[4] R. Brun, F. Carminati, I. Hrivnacova, and A. Morsch. Virtual Monte-Carlo. In *Computing in High Energy and Nuclear Physics*, pages 24–28, La Jolla, California, 2003.

[5] V. Innocente, M. Maire, and E. Nagy. *GEANE: Average Tracking and Error Propagation Package*. CERN, Geneva, 1994.

[6] A. Fontana, P. Genova, L. Lavezzi, A. Panzarasa, A. Rotondi, M. Al-Turany, and D. Bertini. Use of geane for tracking in virtual monte carlo. *Journal of Physics*, 119(032018), 2008.

ALICE data analysis with the GSI computing resources

The ALICE Group at GSI[1]
[1]GSI, Darmstadt, Germany

Introduction

During the year 2008, the ALICE experiment at CERN acquired real data from cosmic rays and was prepared for the first proton-proton collisions at the LHC. The data volume expected from ALICE represents a substantial challenge for storage and data processing: 10^9-10^{10} events of approximately 5 MBytes each, are expected every year. A proper planning of the computing infrastructure is essential to guarantee a fast data quality assessment, a prompt detector calibration, and the development of the analysis tools to produce the first physics results.

Data Storage

The available disk space of about 300 TB is organized in 2 systems: an xrootd cluster as GRID storage element, and the lustre [1] file system for local storage. The latter, planned to be scalable to the PB scale, was intensely tested for stability and speed, being the candidate solution for mass storage GSI wide, possibly also for the FAIR computing. Speed performance in writing and reading data files scales well with the number of file servers included (at the moment 33 servers for a total of 170 TB).

The PROOF Cluster

A subset of the available compute nodes is used as a PROOF [2] cluster (GSIAF - GSI Analysis Facility) for data analysis. This system enables the parallel processing of events and is especially aimed at the prototyping phase of analyses that need a high number of development iterations with short response time. GSIAF consists of 160 PROOF workers (CPU cores) and has been extensively used for detector calibration and several physics analyses.

Performance Tests

The structure chosen at GSI consists in keeping data on dedicated file servers remote from the compute nodes. The available 1500 cores are connected to the disk storage via several switches and links with an aggregate bandwidth of about 80 Gb/s. We performed large scale tests to verify the stability of the system, the homogeneous routing of the data flow (to avoid any link saturation), and measure the effective speed in a realistic physics analysis scenario. The tests for standard batch processing involved about 150 compute nodes (for about 1200 cores), 30×10^6 simulated events stored on lustre (about 50 TB) and the whole network structure in between. Analysis jobs were run in the form of an analysis train (packing 10 full physics analyses in a framework which optimizes the data I/O). Roughly 20,000 jobs were run, analyzing the data volume equivalent to 1 year of pp data taking in ALICE. Fig. 1 (top) shows the total number of events analyzed per second, depending on the number of parallel batch jobs. GSIAF was benchmarked by analysing 1.5×10^6 simulated pp events stored on lustre. The analysis performed in this test was rather I/O than CPU intensive. The obtained average event processing rate is above 1000 events/s (Fig. 1 bottom).

These tests allow to identify possible weak spots of the global computing system, suggest the correct balance between compute nodes, disk storage servers and relative network. This is the crucial input to plan the further growth of the GSI Tier2 center. The current overall performance for batch and PROOF processing is highly satisfactory: GSI offers excellent capability for the first physics data analysis in ALICE.

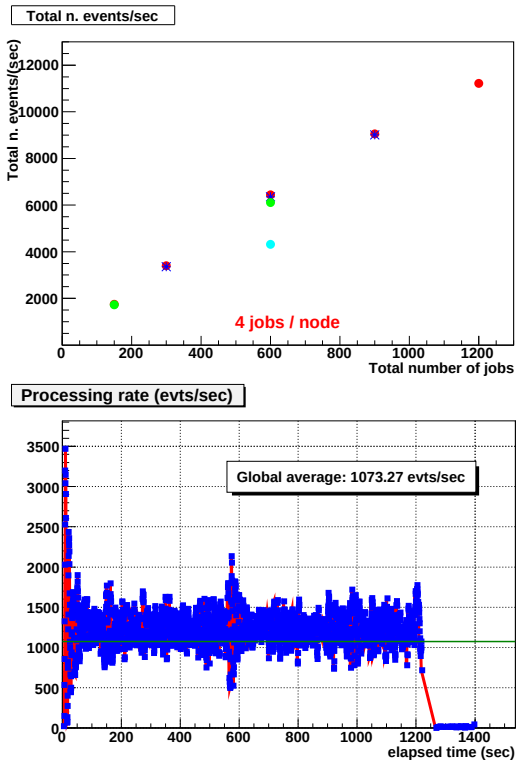

Figure 1: Event processing rate as a function of parallel analysis batch jobs (upper plot). Event processing rate obtained with GSIAF (lower plot).

References

[1] "Lustre File System", http://www.clusterfs.com
[2] "PROOF: the Parallel ROOT Facility", http://root.cern.ch/

The status of the ALICE TRD project

The ALICE TRD collaboration*

During the year 2008 the Transition Radiation Detector project of the ALICE experiment at LHC has accomplished important milestones and has progressed towards readiness for data taking. We will review the status of the project and the various ongoing activities.

The chamber production was completed in 2008, so that now all 540 individual readout chambers (ROC) of TRD are ready. The chambers are equipped with front-end electronics (manufactured in industry based on our own design and tested in Heidelberg) and the readout functionality tested in Frankfurt and at GSI (on a newly setup test stand). The chambers are then shipped to Münster, where they are assembled in supermodules (each containing 30 chambers). Extensive measurements with cosmic-rays are undertaken at this stage. As the individual readout chambers are no longer accessible once the super-module is assembled, rigorous testing is necessary at this stage. For this purpose, all necessary infrastructure for the operation of super-modules has to be available in Münster and as similar as possible to the conditions found in the final installation in the ALICE pit. This includes low- and high-voltage power supplies, gas and cooling as well as computers for slow control and data aquisition. In addition, a trigger system for cosmic rays has been developed to acquire data for a first calibration pass.

The assembly of a supermodule starts with the assembly of the supermodule hull including distribution of low voltage and cooling water. Afterwards, the readout chambers are installed layer by layer. Each layer undergoes tests of electronics, gas tightness, high-voltage distribution and cooling. The integration of a supermodule is concluded by several days of cosmics data taking to produce a calibration data set.

The tightness of the gas volume is tested by flushing the ROCs of one layer with a mixture of argon and carbon dioxide while the pressure is regulated by a fan. The oxygen content at the outlet of the layer is a measure for the leaks in the layer. Separate tests at over- and underpressure of 1 mbar allow for the distinction of diffusive and high resistity viscous leaks. The average leak conductance per chamber is less than 1 Nl/bar·h[1], consistent with single ROC tests performed at GSI and well below the limit of 3 Nl/bar·h set by the cost of xenon.

A large acceptance trigger for cosmic rays is used to acquire data for supermodule testing and calibration. The trigger consists of two arrays of scintillators above (40 scintillators, 220×173 cm) and below (50 scintillators, 550×66 cm) the supermodule. The setup is shown in Fig. 1. While the lower layer covers the full length, the upper layer limits the acceptance to about one third of a supermodule and has to be moved along it. The scintillator signals are discriminated and the logical OR of the upper and lower layers are generated. A coincidence of signals from the upper and lower layers triggers the readout of the super-module. Depending on the positioning of the upper layer, between 60 and 90 events are triggered per second.

Figure 1: Cosmic ray setup in Münster .

To overcome the limited acceptance of the upper layer, the trigger logic was modified to take advantage of the trigger capabilities of the TRD: the logical OR from the scintillators in the lower layer is provided as a pretrigger to start the read-out, store the raw data in the event buffer and calculate the tracklets for the Global Trigger Unit (GTU). The GTU generates a L1 trigger if it finds tracklets in four layers of one stack, otherwise the event is rejected. In this configuration, eleven hundred pretriggers per second yield three hundred events recorded on disk. Apart from reducing the time to collect calibration data, this setup also provides a more realistic test for the front-end-electronics.

The reconstructed point resolution in pad direction has been determined by applying a straight line fit to the clus-

*The list of members and institutions is available at `http://www-alice.gsi.de/trd`

[1] 1 Nl/bar·h corresponds to a leakage of 1 ml of gas under normal conditions per hour at a differential pressure of 1 mbar

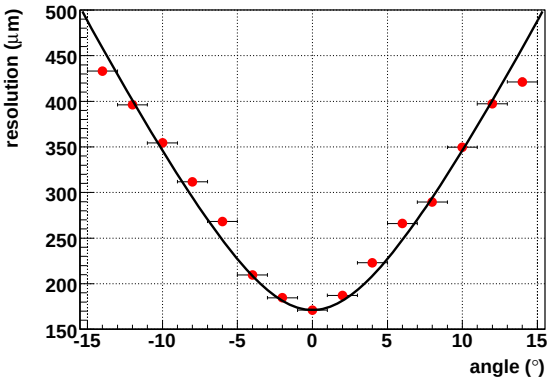

Figure 2: Residuals of cluster with respect to a straight line fit within one chamber.

ters in one chamber, constituting the so-called tracklet. For tracks perpendicular to the pad plane, the residuals of the clusters with respect to the tracklet determine the detector resolution. Inclination of the tracks leads to a contribution of the resolution in drift direction according to $\sigma = \sqrt{\sigma_{pad}^2 + \sigma_{drift}^2 \tan^2 \alpha}$ and widens these residuals. The residuals are shown in figure 2 and indicate a resolution in pad direction of 170 μm.

The residuals with respect to tracks crossing several ROCs, which are shown with the red data points in Fig. 3, are wider than in the case of a tracklet within one chamber mainly because the ROCs are not perfectly aligned. When the chamber misalignment is accounted for, employing the ALICE Alignment Framework, the resolution becomes comparable with that obtained with respect to tracklets (green points in Fig. 3). Fig. 4 shows the alignment values, which are typically below 1 mm.

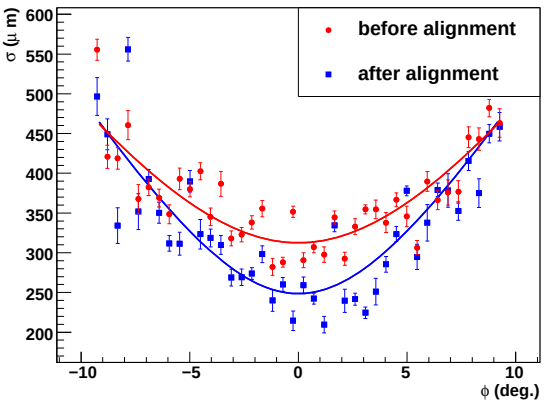

Figure 3: Residuals of clusters with respect to a track before (red) and after (green) alignment.

After delivery to CERN, each supermodule undergoes functionality and gas tightness tests on the surface, before being inserted in the ALICE setup. The delicate procedure of insertion lasts about one day and is followed by several

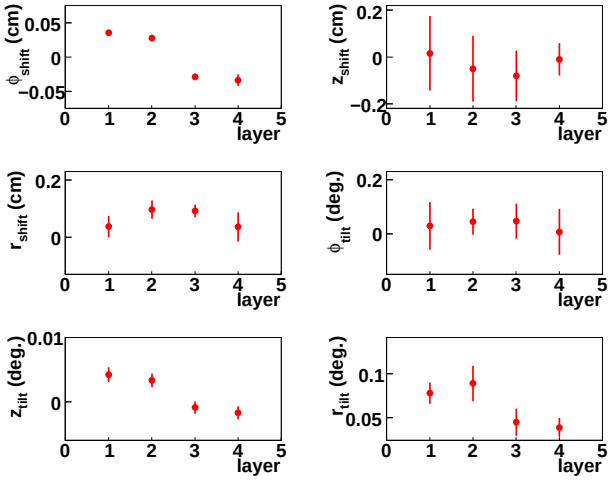

Figure 4: Alignment parameters of the inner four chambers in stack 2 of super-module III.

days of connecting all the cables. Four supermodules were present in the ALICE setup in 2008 with the full data readout chain and participated in the cosmic-ray data taking. A display of a cosmic-ray event is shown in Fig. 5. During the cosmic-ray data taking, the TRD was operated with an Ar-CO_2 [82-18] gas mixture to replace the more expensive nominal (Xe-based) mixture.

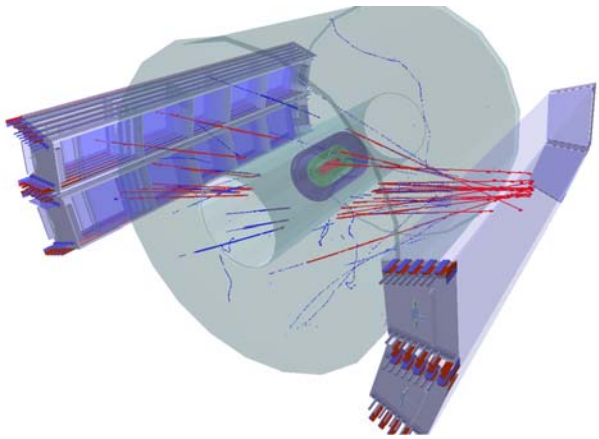

Figure 5: A cosmic-ray event display with the TPC and the 4 supermodules of the TRD.

During data taking, the Transition Radiation Detector requires a trigger signal within 500 ns after the interaction. This is 1 μs before the first trigger decision by the ALICE experiment is made. The design of the TRD pretrigger, using 88 analogue inputs from the V0 and T0 detector and interfacing an additional 576 digital input from TOF via an external unit, has been developed and is now installed in the L3-magnet of the ALICE experiment. All input information from the fast V0 and T0 detectors is processed by 27 FPGAs, which are mounted at a distance of 1.5 m to

4.5 m around the interaction point. The pretrigger system was successfully commissioned during several data taking periods with ALICE using cosmic events and a first circulating proton beam at LHC injection energy in September 2008. Trigger signals have been provided to the Central Trigger Processor of ALICE. The system is highly flexible to account for different physics conditions in $p+p$ and Pb + Pb collisions. A sophisticated client-server software which implements a finite state machine and provides a graphical interface for user friendly operation is under development.

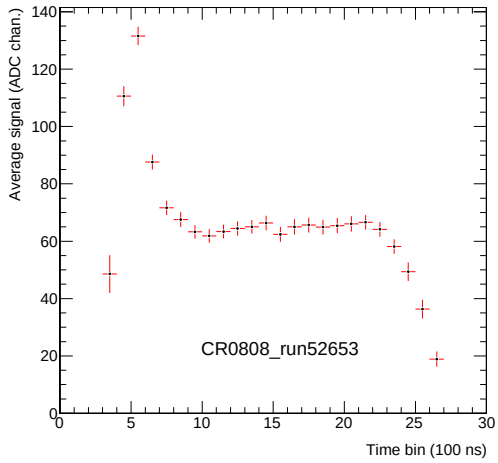

Figure 6: Average signal as a function of time.

The completion of the pretrigger system, realized in summer 2008, allowed for a readout of the complete detector signal and enabled for the first time the track reconstruction in real operation. The signal as a function of time averaged over all detectors is shown in Fig. 6. During the cosmic-ray data taking in ALICE in the fall of 2008 a total of about 50k tracks were recorded in the TRD. This was made possible due to the successful operation of the TRD Level 1 trigger, allowing a fast and efficient track decision at the GTU level.

The tracking and PID algorithms of the TRD rely on the knowledge of several calibration constants depending on temperature and pressure, the gas composition and the chamber geometry. These are the drift velocity of the electrons, the time-offset of the signal, the gas gain and the width of the Pad Response Function. They will be calibrated using the raw signal of the detector or the signal from reconstructed tracks in $p + p$ and Pb+Pb collisions. During the data taking, a first calibration is performed on the online systems, the Data Acquisition (DAQ) and High Level Trigger (HLT). The software was tested on DAQ with so-called "black events" and with cosmic-ray events taken in the ALICE setup. With the assumption that the cosmic rays are uniformly distributed over the detector, a gas gain variation of about 16 % was found over the chambers. Fig. 7 shows the gain factors as function of the detector number for the four supermodules operated in ALICE in 2008.

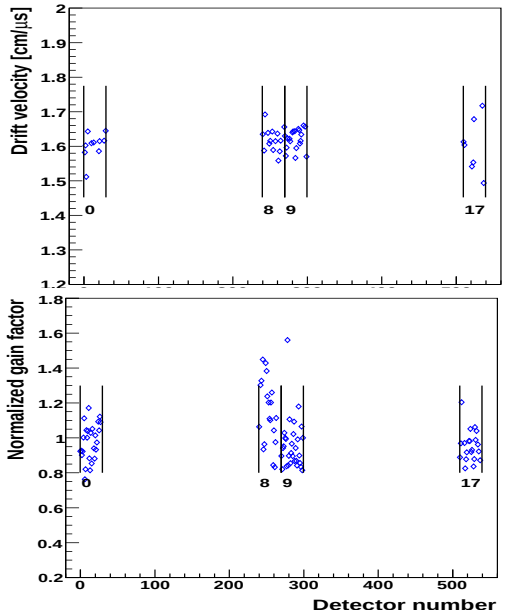

Figure 7: Drift velocity and normalized gain factor as a function the detector number.

The drift velocity and time offset are determined with the average signal as function of time shown in Fig. 6. The results obtained online were consistent with those obtained offline after the tracking in a second pass calibration. The extracted drift velocity values had a variation of 3.3% over the chambers.

Figure 8: Screenshot of the DCS system for TRD. This example shows the status of the front-end electronics of all 30 chambers within one TRD supermodule.

The running of a complex system as the TRD is facilitated by an efficient and user-friendly detector control system (DCS) which ensures safe and stable operation and monitoring of the detector. It is built on a SCADA system, allowing modelling, supervising and operating the detector via finite state machines, which also provide easy scalability. It models and realizes the complex TRD FEE communication architecture in the supervisory control layer. The TRD DCS is realized as a large distributed system

scattered over ten computers. It integrates about a quarter million embedded processors mounted on the detector chambers that implement complex on-detector controls with massive use of ethernet for both interprocess communication and device control. The DCS monitors about three thousand parameters read out by the FEE. The TRD low- and high-voltage systems implement all together more than twelve hundred channels that are controlled and monitored independently. All parameters relevant to off-line analysis are archived by means of dedicated mechanisms implemented in the TRD DCS. The data read from the detector is archived on an ORACLE datbase cluster. A special emphasis has been put on making the TRD DCS graphical user interfaces intuitive and user-friendly for non-expert operation. An example is shown in Fig. 8. The TRD DCS has been commissioned during runs within the ALICE experiment in the cosmic-ray data taking in 2008.

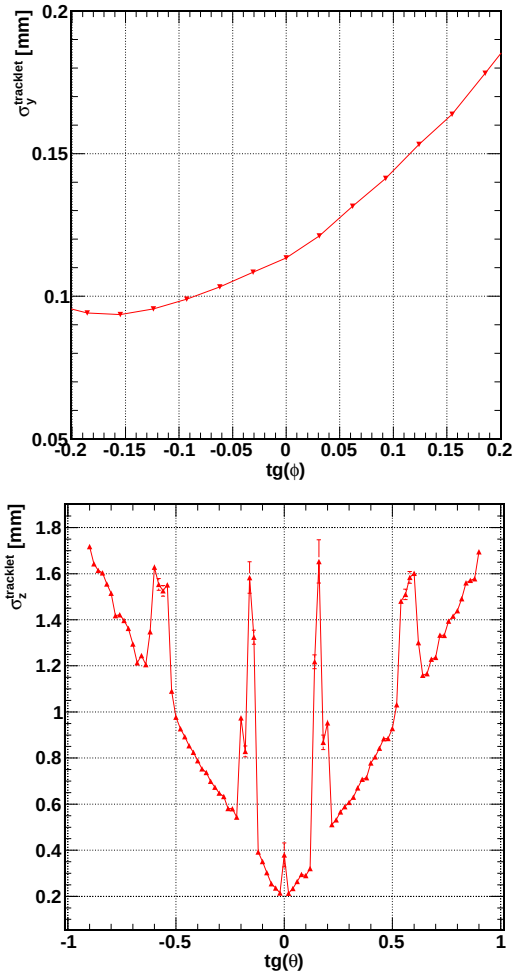

Figure 9: The spatial resolution in the transverse (bending) plane (upper panel) and in the beam direction for tracks crossing pad rows (lower panel).

To achieve the ambitious design values for the TRD performance [1] we continuously develop the algorithms to reach the theoretical limit for spatial resolution as well as those for particle identification. We briefly describe the status of the reconstruction within the TRD. The TRD reconstruction comprises the steps of point and tracklet reconstruction as welll as track prolongation. The first two steps are applied independently from the other barrel detectors while the third is highly correlated with the reconstruction in the TPC. Besides the quality of the reconstructed values like spatial, momentum and charge resolution, the reconstruction code has to fullfill also criteria of flexibility, speed and low memory usage (in particular for usage in the High Level Trigger, HLT).

The code had been developed as a modular structure with two main components: the ”Clusterizer” for point reconstruction and the ”Tracker” for tracklet construction and track prolongation. Additionally, all algorithms used for data reconstruction have been made parametric and the corresponding set of parameters have been calibrated and saved to a database. Sets of parameters have been thus obtained which can provide dynamical response of the reconstruction algorithms to the particularities of the data (for instance track multiplicity).

The results for the spatial resolution obtained with the present algorithms on simulated data are summarized in Fig. 9. Shown is the tracklet resolution with respect to the Monte Carlo information. A minimum of approx 90 μm is obtained in the transverse plane for the azimuthal angle corresponding to the Lorentz angle (the angle under which the electrons are drifting due to $\mathbf{E}\times\mathbf{B}$ coupling). The expected linear dependence of the resolution on the tangent of the dip (polar) angle is seen, together with the 5-fold TRD segmentation in the beam direction. The best resolution of about 200 μm is reached around θ=0. Only about half of all tracks do cross the pad rows of the detectors and are characterized by such a good resolution.

The complexity of the TRD project did lead to several challenging issues. We have fortunately discovered in time a leak problem in our detectors and we were able to rectify this for all the chambers, in a concerted effort of our teams at CERN and in particular in the detector laboratory of GSI. Unexpected complications with the manufacturing in industry of our front-end electronics boards, occuring after successful preseries, have caused a delay in the supermodule assembly. Despite this, eight out of the total 18 supermodules of the TRD will be ready in the ALICE setup when cosmic-ray data taking resumes in June 2009 and will contribute to physics results with beams expected to start in fall 2009. The TRD will be completed during the next shutdown period.

References

[1] ALICE Transition Radiation Detector Technical Design Report, ALICE TDR 9, CERN/LHCC 2001-021.

A DCS-Offline Communication Framework for the ALICE TRD

F. Kramer[1], C. Blume[1], T. Dietel[2], and K. Oyama[3]

[1]Institut für Kernphysik, Goethe-Universität, Frankfurt am Main; [2]Westfälische Wilhelms-Universität, Münster;
[3]Physikalisches Institut, Ruprecht Karls-Universität, Heidelberg

Introduction

The Transition Radiation Detector (TRD) of the CERN LHC experiment ALICE [1] has been designed to provide excellent electron identification, tracking and a level-one trigger on different event signatures. To meet these requirements, the front-end electronics (FEE) of the TRD performs complex data processing like online tracking, particle identification and a fast evaluation of trigger conditions. The detector control system (DCS) is used for operating and monitoring this electronics. For the purpose of data reconstruction and quality assurance the configuration, operation status and various run-specific counters of each TRD module are to be stored in the ALICE offline calibration database.

Data Flow and Communication

To transport data from the TRD FEE to the DCS data storage a special proxy program called "fxsproxy" has been developed. It runs permanently on one of the Linux PC within the ALICE TRD online network. Upon start and end of each run the experiment control system (ECS) sends signals to the "fxsproxy" through the TRD DCS in order to trigger the readout process.

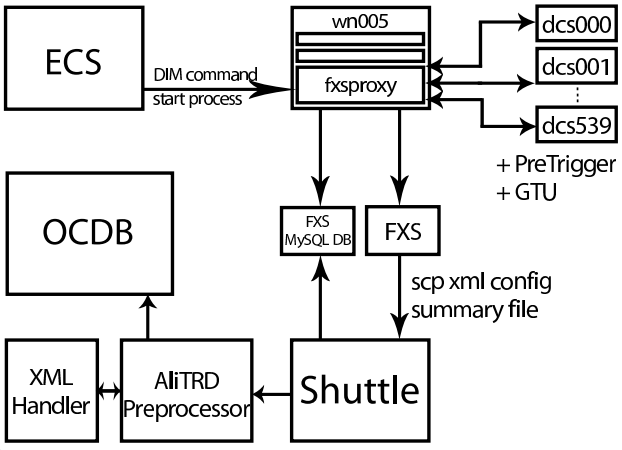

Figure 1: Scheme of data flow and communication

During this process the fxsproxy forwards the requests to send the run condition data to all active TRD modules; whether a module is in an active state or not is permanently monitored by the proxy. The software running on the FEE has been modified to assemble the necessary information into well-formed XML [3] and to send it back to the proxy. The received data is stored in one file which is sent and registered to the file exchange server (FXS) for subsequent offline processing.

After each run the Shuttle system collects the files from the FXS and passes them to the detector's preprocessor. The TRD preprocessor has been adjusted to parse the XML data files and store the information therein in special ROOT objects. These are then copied to the ALICE offline calibration database (OCDB) which is the designated place for such data and which can be accessed via the grid.

The data flow is summarized in Fig. 1. The described architecture of the framework applies existing systems and is therefore lightweight. Another advantage is its flexibility and extensibility.

The Distributed Information Management System (DIM) [2] is used for the online data transfer and all communication between the involved systems.

Data Monitoring

Two ways of data monitoring have been implemented. The first is realized with an XML transformation via XSL (Extensible Stylesheet Language), where a digest of the data is displayed in a browser window. This method is primarily intended for fast online quality assurance and debugging. The second way is realized with a ROOT macro which analyzes the final OCDB object. The User can run this tool locally or via the grid.

Summary and Outlook

A procedure for the readout of the configuration, operation status and various run-specific counters of each TRD module and for the communication between the systems involved has been implemented. Further, tools have been developed for online and offline data monitoring. The discussed software is in use since summer 2008.

After the successful implementation of the framework and the readout of the FEE now the system is to be extended by the acquisition of data from two other system components in the TRD, the pretrigger and the global tracking unit (GTU).

References

[1] The ALICE Collaboration, "TRD Technical Design Report", CERN/LHCC 2001-021, (2001).

[2] C. Gaspar et al., "DIM", International Conference on Computing in High Energy and Nuclear Physics (Padova, Italy, 1-11 February 2000).

[3] T. Bray et al., "Extensible Markup Language (XML) 1.0 (Fourth Edition)", W3C Recommendation 16 August 2006, http://www.w3.org/TR/2006/REC-xml-20060816.

Measurement of the gas amplification of ALICE-TRD chambers at the IKF

P. Reichelt*, M. Hartig and H. Appelshäuser
for the ALICE collaboration, Institut für Kernphysik, Goethe - Universität Frankfurt am Main, Germany

Before integration in the ALICE experiment, the readout chambers of the ALICE-Transition-Radiation-Detector (TRD) [1] are tested at the Institut für Kernphysik Frankfurt (IKF), including measurements of their gas amplification factor. In this report, we describe the revisal of these test-procedures by introducing additional measurements to ensure a self-consistent determination of the absolute gas gain.

Determination of the gas gain

In the laboratory of the IKF, a ^{109}Cd-source is used to create ionization in the chamber gas, as the source is in the energy range of the transition radiation. The energy spectrum of the source, as recorded by reading out the anode wire current, shows two peaks at energies of about 8 and 22 keV. The spectrum is shown in figure 1. While the 22 keV peak is the sum of the Cadmium-K_α and K_β lines, it turns out that the low energy peak originates from the copper surface of the cathode pads inside the TRD-chamber, which are ionized by the primary radiation of the source [2]. This known, the spectrum can be calibrated and its mean energy used to calculate the gas gain. At an anode voltage of 1600 V, the gain of a typical chamber reaches a value of 11500. Figure 2 shows the exponential dependence of the gas gain on the anode voltage.

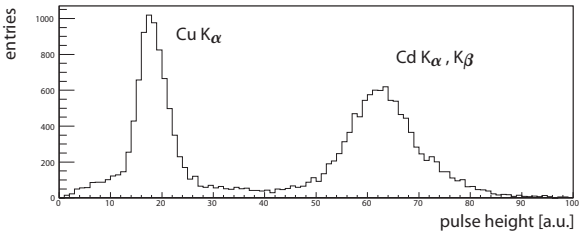

Figure 1: Energy spectrum of a cadmium source, recorded with a TRD readout chamber. The peaks correspond to 8 and 22 keV. [2]

Pressure Dependency of the gas gain

It is further tested how the gain changes with variations of the pressure. A rise of one mbar in atmospheric pressure causes the gas gain to decrease by about 0.8 %. This dependence is consistent with expectation [3]. Also the effects of differential pressure are studied. The change of the gain, resulting from the slight deformation of the chamber, is recorded and compared to the calculations in [1]. According to these measurements, the performance of the chambers is slightly more stable than predicted.

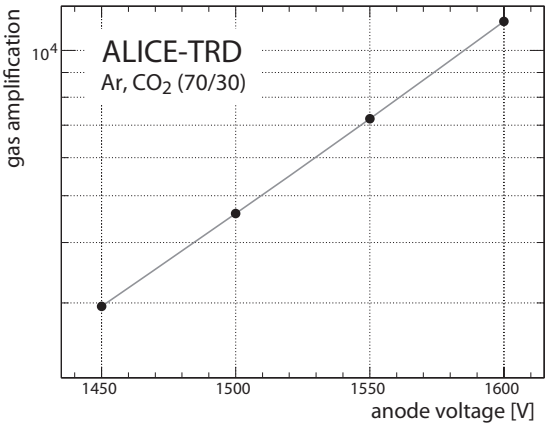

Figure 2: Gas amplification of a TRD-chamber as a function of the anode wire voltage. [2]

Outlook

The photons of the cadmium source belong to the energy range of the transition radiation. The detection of TR-photons is decisive for separation of electrons from pions. As shown in figure 1, the ionization of the cathode pads, produced by photons that were not absorbed in the chamber gas, contribute significantly to the total energy deposited in the detector. This effect will be studied and considered to be exploited for future detectors like the CBM-TRD.

References

[1] ALICE Collaboration: *Technical Design Report of the Transition Radiation Detector*. CERN/LHCC 2001-021, (2001).

[2] P. Reichelt: *Bestimmung der Gasverstärkung der ALICE-TRD-Auslesekammern.* Bachelorarbeit Goethe-Universität Frankfurt (2008).

[3] W. Blum, W. Riegler, L. Rolandi: *Particle Detection with Drift Chambers, Second Edition*. Springer, 2008.

* preichelt@ikf.uni-frankfurt.de

Ongoing activities of mass test of the ALICE TRD front end electronics at IKF*

P. Lüttig†, A. Arend‡, M. Hartig and H. Appelshäuser
for the ALICE collaboration, Institut für Kernphysik, Goethe - Universität Frankfurt am Main, Germany

In the process of constructing the detector chambers for the ALICE - Transition-Radiation-Detector [1] at IKF the Read Out Chambers (ROC) are equipped with Front End Elektronics (FEE). In this report, we describe the ongoing activities of tests for these FEE.

Recent updates on the FEE-tests

Two types of tests are performed for every ROC. Tests via the control engine (CE-tests) are used to check the general functionality of the multi chip modules (MCM). These tests are described in [2]. The experience gained by testing the supermodules 2 to 5 in the year 2007 has been transferred to the tests developing experts and has been used to improve and upgrade single components of the CE-tests. These new versions and the required updates in the framework have been implemented in the test setup.
After the CE-tests have been performed successfully, the connection between the read out pads and the MCM is tested. Therefore the electronic noise characteristics are recorded and rehashed graphically [3]. In addition to the verification of the low and homogeneous distribution of this intrinsic noise of the MCM, we use a pulse generator to inject a rectangular signal into the cathode wire and read out the response of read out pads. Therefore an especially for this purpose developed displaying tool based on ROOT provides multiple features to simplify the workflow, like a zooming feature, automatic spotting of candidates for bad channels and the possibility to display recorded data resolved by time. By using the pulsed signal and the displaying of the read out data in a time resolved way, it is possible to identify and distinguish between unconnected and shorted read out pads in a very convenient way. An example for this display is given in figure 1.

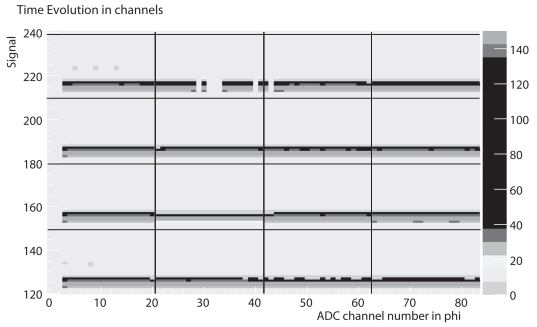

Figure 1: Time evolution of a picked up pulser signal in one read out board (ROB) on position 3 (zoomed in). The signal height is color coded. The second MCM in the uppermost row shows several not connected pads.

PVSS based testing panel

With testing panel (figure 2) based on PVSS, a common interface has been developed to run and display the results of the FEE - testing procedure. The interactions to the CE-tests are done via standardized DIM protocols, the configuration and read out procedures are done via self developed scripts, which are activated out of the testing panel.

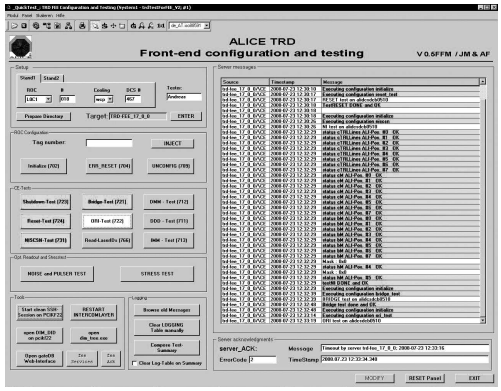

Figure 2: Standard view of the FEE testing panel.

Summary and outlook

In 2008 all available ROBs have been equipped to read out chambers and have performed the testing procedure. To improve the testing procedure we constantly keep on developing and upgrading single components of the tests in close collaboration with University of Muenster, University of Heidelberg and the GSI.

References

[1] ALICE TRD, *Technical Design Report*, CERN / LHCC, 2001-021.

[2] A. Fick, *Entwicklung einer Prozessvisualisierung zur Qualitätskontrolle der Front End Elektronik des ALICE - Übergangsstrahlungsdetektors*, Diplomarbeit, September 2008

[3] P. Lüttig, *Entwicklung einer Testumgebung für TRD-Auslesekammern*, Bachelorarbeit, August 2008

* Work supported by BMBF and GSI
† luettig@ikf.uni-frankfurt.de
‡ andreas@ikf.uni-frankfurt.de

Analyse of TRD test beam data 2007 at PS-accelerator at CERN*

M. Kliemant , H. Appelshäuser , and M. Hartig
Institut für Kernphysik Universität Frankfurt

The Transition Radiation Detector (TRD) is one of the main detectors in the ALICE experiment, the dedicated heavy ion experiment at the Large Hadron Collider (LHC) at CERN Ref. [1]. This detector consists of 18 super modules, each of them containing 30 TRD chambers. Each chamber has a 4.8 cm thick radiator, which is attached to a gas chamber with a 3 cm long drift region and a 0.7 cm amplification gap. The induced charge is read out at the back via copper pads .

In November 2007 a test of one fully integrated TRD super module(final electronic and cooling set-up) at the CERN PS - accelerator with a mixed electron - pion beam (1, 2, 4 and 6 GeV/c) was performed Fig. 1.

With this data set it is feasible to investigate the PID and tracking performance of the detector. The major aspect is to improve the electron PID performance taking into account the correlations between the different detector layers due to Bremsstrahlung.

One effective PID strategy for electron/pion separation in TRDs is the likelihood calculation on total deposited charge. In Fig. 2 the spectra of charge, integrated over drift time for electrons are shown. In this spectrum it is visible that the detected charge is higher for detectors far from the incoming beam, this is an indication for Bremsstrahlung in the TRD detector. One task in the analysis of the data is to clean up the data sample from events with double tracks which coming from the beam line. If this double pion tracks are to close then the charge deposit in the TRD and in the Pbglas detector is increased. An increased charge deposit we then identify as one electron. With the likelihood method we can combine the information from six layers and get as an result the overall probability of one track to be an electron or an pion . With the average charge spectra we calculate the likelihood as follows:

$L = \frac{P_e}{P_e+P_\pi}$
with
$\prod_{i=1}^{N} P_\pi = P(X_i|\pi)$ for the pion probability and
$\prod_{i=1}^{N} P_e = P(X_i|e)$ for the electron probability.

The product is running over the six layers , N. At this point it is possible to combine the likelihood with the Pbglas and Cherenkov detector PID information and get an value for the pion efficiency.

*This work is supported by BMBF FSP201, the GSI F&E and the Helmholtz Gemeinschaft

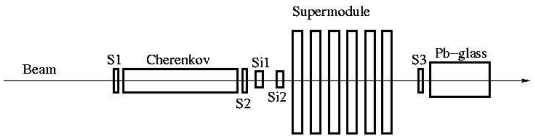

Figure 1: Setup for the TRD-Supermodul test in the T10 line of the PS accelerator at CERN .

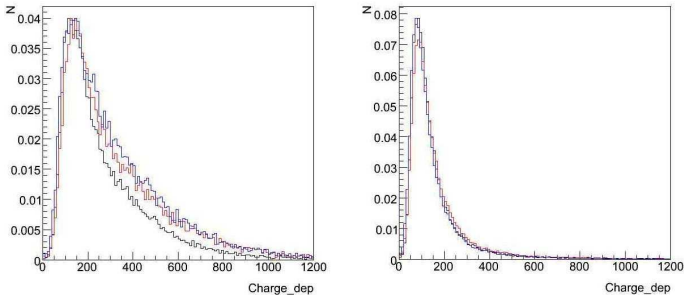

Figure 2: Comparison of charge distribution for electrons at right and pions at left, in camber L0(black), L2(red) and L4(blue).

References

[1] ALICE TRD, Technical Design Report 9, CERN/LHCC 2001-021.

Commissioning and Calibration of the ALICE TPC

L. Bozyk[3], P. Braun-Munzinger[1], J. Castillo[1], U. Frankenfeld[1], C. Garabatos[1], S. Gärtner[3], M. Ivanov[1], A. Kalweit[3], M. Mager[3], R. Renfordt[2], H.R. Schmidt[1], D.Vranic[1], J. Wiechula[1], and the ALICE collaboration

[1]GSI, Darmstadt, Germany, [2]University of Frankfurt, Frankfurt, Germany, [3] Technical University of Darmstadt, Darmstadt, Germany

Overview

The TPC was moved to its final underground location in the L3 magnet by the end of 2006 after a phase of pre-commissioning at surface level. In 2007,the TPC and all auxiliary systems like the cooling plants, the gas system, and the control systems(DCS) were setup, brought into operation and thoroughly tested. During 2008 several long cosmic data taking runs (> 10^7 events in total) were carried out. Examples of a cosmic shower measured in the TPC can be seen in Fig. 1. In addition, a run using a radioactive Krypton source as well as laser runs were performed. The goal of these runs was to calibrated or correct the TPC's response in respect of the differential energy loss of particles (dE/dx), the gain of individual pads, the ExB effect, space point and momentum resolution, drift time and temperature in-homogeneities and to optimize the noise performance.

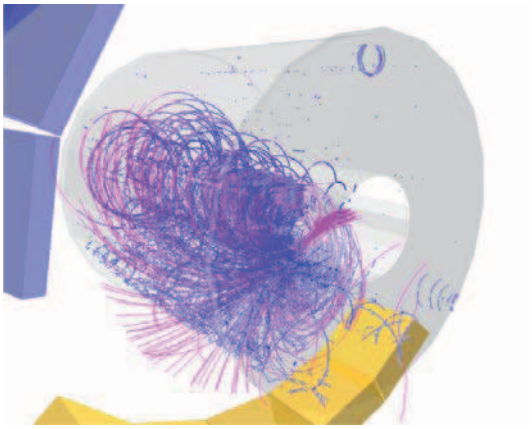

Figure 1: Example of a cosmic shower measured in the TPC.

Detector Calibration and Performance

Noise Performance

While noise figures close to the theoretical limit (given by the ADC and the PASA noise as well as the capacitance of pads and signal lines) were achieved already during the pre-commissioning [1], the realistic experimental environment within the L3 magnet required a careful revision of the noise optimization including an upgrade of the low voltage power supplies. Fig. 2 shows the final L3-area noise figures, which are on average below 1 ADC count and thus in accordance or even better than the specifications laid out in the TPC Technical Proposal [2]. The somewhat higher noise number for the outer readout chambers (OROCs) can be explained by the larger capacitance of the larger pads as together with the longer traces from the pad to the readout electronics.

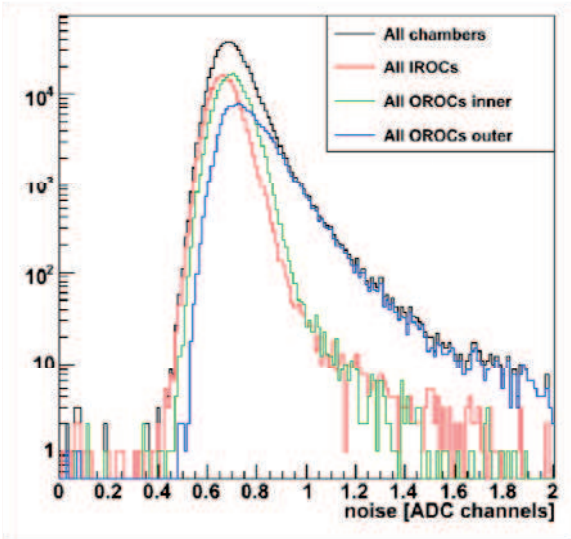

Figure 2: Histogram of the noise of individual pads of the TPC separated by chamber type.

Gain Calibration Krypton

Krypton calibration is one of the standard ways of doing TPC gain calibration. It was developed by the ALEPH collaboration [3] and has been used by many experiments, e. g. the DELPHI , NA49, and STAR to calibrate their TPCs and has also been employed to calibrate the ALICE TPC [4]. A ^{83}Rb source with an initial activity of 5 MBq is deposited on a thin Kapton foil at the CERN ISOLDE facility. A brass cylinder containing the 83Rb sample is connected to the ALICE TPC gas system via a bypass. ^{83}Rb decays to gaseous ^{83m}Kr, which is distributed homogeneously in the TPC volume by the gas circulation system. As the decays are not predictable, a random trigger is used for data taking. The maximum range of electrons produced in Krypton decays is roughly 3.2 cm and therefore the charge is collected on several readout pads. A benefit of the gaseous ^{83m}Kr is its short half-life of 1.83 h, which ensures that the Krypton activity reaches quickly a

negligible level after the calibration data have been accumulated .Fig. 3 shows the map of relative gains of all 278784 pads of one TPC readout plane as determined from the accumulated 41.6 keV Krypton decay. The overall gain variation is of the order ±15% and agrees with the variations expected from the chamber production tolerances. The gain calibration map is a key ingredient for the determination of the differential energy dE/dx of particles traversing the TPC (see below).

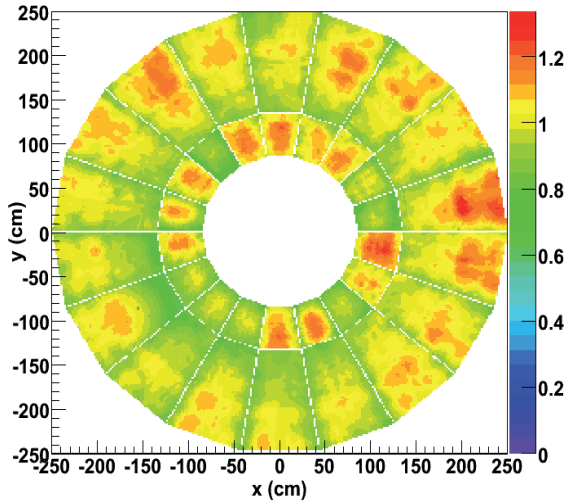

Figure 3: Map of the relative gain of the all pads of one TPC readout plane (C-side)

Temperature Homogenization and Drift Velocity Calibration

Besides the gas composition, the drift velocity depends also strongly on the gas density, i.e., the ratio of gas pressure and temperature [5].To ensure minimal corrections to the drift velocity it is thus mandatory to homogenize the temperatures within the TPC's fiducial volume. The major heat source close to the TPC drift volume is the TPC front-end readout. A cooling strategy has been developed [6] to minimize temperature gradients across the TPC caused by residual heat dissipated from the readout electronics. The cooling system is divided into 47 loops with individual high precision temperature control. The temperatures of these loops are tuned to have no heat transfer to the sensitive volume of the TPC, which is verified by 5 temperature probes on each sector. To homogenize the temperature inside the TPC the chamber body cooling temperature is set to minimize the temperature gradient inside the TPC measured by 36 sensors inside the gas volume (cf. Fig. 4). As can be seen from the Figure, the temperature variations in the TPC volume can be limited to σ<100 mK, as required in the TPC Technical Proposal. The outliers on the high side are due to cooling loops with insufficient flow, which will be fixed before the LHC restart by rerouting some cooling lines.

The remaining gradients and a variation of the drift velocity with time can be determined by analyzing data taken from laser induced tracks. From the arrival time of the signals from the know position of the laser tracks the residual drift velocity variations can be extracted. The variations during the test period have shown that a calibration of the drift velocity every hour in-between data taking will lead to a stability of better then 0.6‰.

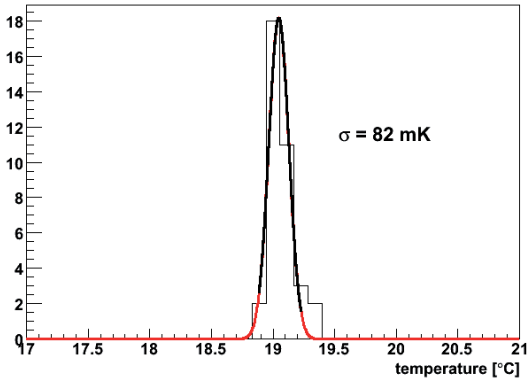

Figure 4: Histogram of temperatures measured within gas volume by 36 Pt-1000 sensors.

E ×B Calibration

The central detectors of ALICE are located inside the L3 magnet. The magnetic field B of the L3 magnet and the electric field E of the TPC are only to first order parallel, i.e., the magnetic field (it measures about 11.6 ×11.2 m^2) is not perfectly homogenous. In the region where the TPC is located these inhomogeneities are on the order of 1%.The distortions cause a displacement of tracks, which is proportional to the drift length and parameter $\omega\tau$. The parameter $\omega\tau$itself is given by the magnetic field $\omega=(e/m)|B|$) and a characteristic time τ of the TPC drift gas. Integrating over the full drift length of the ALICE TPC (250 cm), these displacements are of the order of one centimeter and have to be corrected.

The E×B effect in the ALICE TPC was calibrated using the ALICE laser, which produces 336 widely spaced laser tracks within the TPC fiducial volume. The displacement of the reconstructed laser beam position with respect to surveyed position was determined for different magnetic field setting (B_z= -0.5, -0.5,-0.2, 0, 0.2, 0.4 and 0.5 T).

Subtracting the displacement values for the setting without magnetic field reduced the effect of geometrical distortions, e.g., misalignment of readout chambers.
The measured L3 magnetic field map serves as additional input source for the calibration procedure. The parameter $\omega\tau$was adjusted by fitting the laser track distortion at different magnetic field intensity.

The precision of the constructed E×B distortion map is on the level of about 0.35 mm. Additional improvement was obtained by adding constant B-field components on top of the measured B field map.

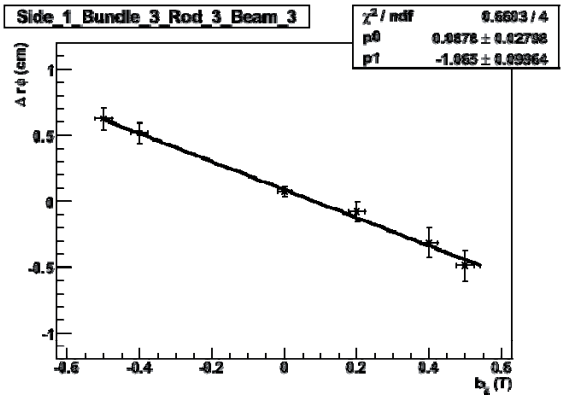

Figure 5: Example of the displacement of the reconstructed laser beam position with respect to surveyed position for different magnetic field settings.

dE/dx Calibration with Cosmics

Charged particles traversing the TPC fill gas lose a certain amount of energy per unit path length depending on their momentum and rest mass. By this different particle species can be identified over a broad momentum range. Figure 6 shows a dE/dx spectrum of cosmic rays measured with the ALICE TPC during the cosmic runs in 2008. Muons, protons, electrons and deuterons can be clearly identified. The dE/dx resolution of 5.7% for minimum ionising particles is close to the expected value showing the precision of the underlying gain calibration .The mean energy loss as a function of momentum can be described by the Bethe-Bloch curve. As can be seen from the lines in Figure 6, a parameterization of this curve gives a good description of the data. In conclusion, the particle identification of the ALICE TPC can already be used for physics with the first beam data.

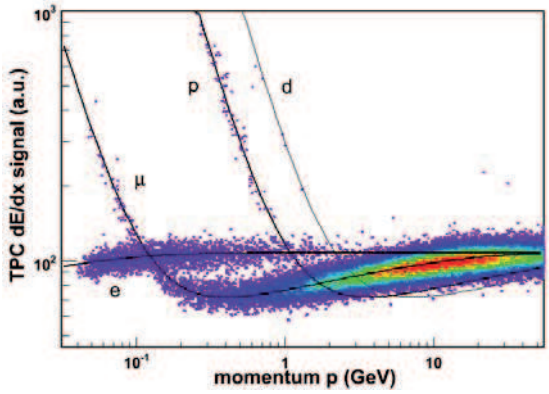

Figure 6: Differential energy loss in the TPC as a function of momentum for particles from cosmic ray events. The red lines are parameterized Bethe-Bloch estimates of the energy loss for different particles species.

Space-Point Calibration

The accuracy of the space-point coordinate measurement, i.e. the position determination of induced charge clusters on the pad plane, is a key ingredient for the tracking precision and hence the momentum resolution.

The space-point resolution is a function of many parameters but for the ALICE TPC the dominant ones are the diffusion, track inclination angle and deposited charge.

The space point resolution was extracted from cosmic data in bins of these variables and is shown in Fig. 7. As can be seen the space-point resolution for tracks emerging at small angles and large drift length, corresponding to high p_t tracks from nuclear collisions, feature a resolution between 300 and 800 μm. This experimentally determined resolution agrees well with the accuracy expected from simulations.

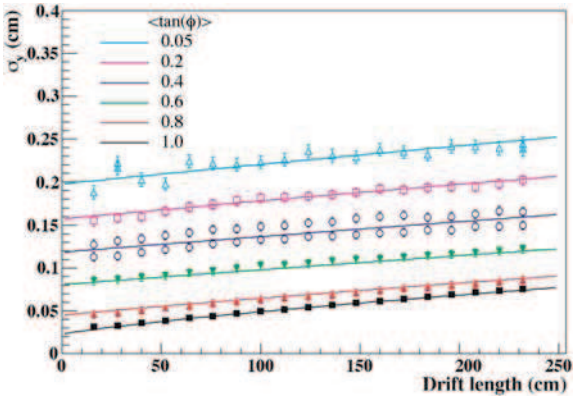

Figure 7: Space point resolution in y direction as function of the drift length and the inclination angle. The lines cover the range from 0° to 55° (bottom to top)

Momentum Calibration and Resolution

The TPC performance was studied using cosmic tracks. Hereby a cosmic track is reconstructed independently in the top and bottom halves of the TPC. The TPC fiducial volume was restricted. Only track topologies similar to the primary tracks were used. Both semi-tracks are propagated independently to the DCA (Distance of Closest Approach) to the nominal vertex (point {x,y,z}={0,0,z}). The tracks parameters are compared at the DCA point. The performance in impact parameter, angular and p_t resolution were studied as function of particle momenta and are summarized in Tables 1a and 1b.

	A_{side}	C_{side}
σ_x	0.15 cm	0.20 cm
σ_z	0.05 cm	0.08 cm
σ_ϕ	2.0 mrad	4.0 mrad
σ_ϑ	0.5 mrad	1.0 mrad
$\sigma_{1/pt}$	0.007 (1/GeV)	0.008 (1/GeV)

Table 1a: Impact parameter, angular and p_t resolution integrated over the full p_t range.

	A_{side} $(1/p_t \approx 1)$	A_{side} $(1/p_t \to 0)$
σ_x	0.17 cm	0.14 cm
σ_z	0.10 cm	0.04 cm
σ_ϕ	2.6 mrad	2.0 mrad
σ_ϑ	2.0 mrad	0.3 mrad
$\sigma_{1/pt}$	0.011 (1/GeV)	0.007 (1/GeV)

Table 1b: Impact parameter, angular and p_t resolution for high $(1/p_t \to 0)$ and low $(1/p_t \approx 1)$ momentum tracks.

For high momenta cosmic tracks the p_t-resolution $\Delta p_t/p_t$ is ~ 6-7% at 10 GeV/c (see Fig. 8) and thus, at present, about a factor ~1.5 worse than estimated for an ideally calibrated and aligned TPC [7]. For low momenta tracks (below 1 GeV) the observed resolution is in agreement with the expectation. The resolution on the C side (muon spectrometer side) is somewhat worse due to the multiple scattering in the absorber.

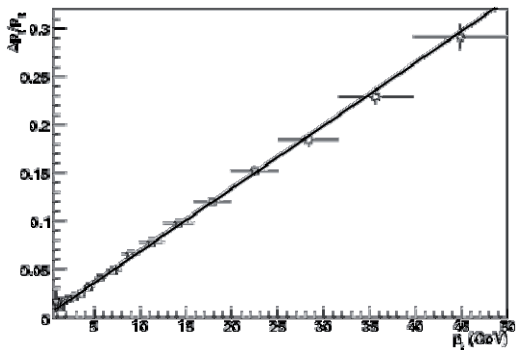

Figure 8: p_t resolution as a function of p_t.

Summary

In preparation for the LHC start-up in September 2008 the ALICE TPC has been fully commissioned and calibrated employing both cosmic as well as laser induced tracks. Data have been taken in running continuously for over 2 month. The gain map of all 557568 pads has been obtained with a krypton source calibration and is well within the specified gain variations. The performance parameters of the TPC after calibration in terms dE/dx, momentum and vertex resolution is close the design values. It has been demonstrated that the goal of an overall temperature homogenization with gradients smaller than 0.1 K can be obtained with active cooling. The TPC is thus ready for first collisions at the LHC restart presumably in fall 2009.

References

[1] J. Wiechula, PhD Thesis, University of Frankfurt, 2008
[2] ALICE Technical Proposal, ALICE TDR 7, CERN/LHCC 2001
[3] D. Decamp et al., Nuclear Instruments and Methods in Physics Research A294 (1990) 121.
[4] S.A. Gärtner, Diploma Thesis, TU Darmstadt, 2008
[5] J. Wiechula et al., NIM A 548 (2005) 582
[6] S. Popescu, U. Frankenfeld, H.R. Schmidt (ALICE collaboration) IEEE Transactions on Nuclear Science, Volume 52 (2005) 2879
[7] ALICE Collaboration et al., J. Phys. G: Nucl. Part. Phys. 30 (2004)1517
ALICE Collaboration et al., J. Phys. G: Nucl. Part. Phys. 32 (2006)1295

Interaction of the CERN LHC Beam with Collimators and Absorbers*

N.A. Tahir[1], R. Schmidt[2], M. Brugger[2], A. Shutov[3], I.V. Lomonosov[3], A.R. Piriz[4], and D.H.H. Hoffmann[5]

[1]GSI, Darmstadt, Germany; [2]CERN, Geneva, Switzerland; [3]IPCP, Chernogolovka, Russia; [4]UCLM, Ciudad Real, Spain; [5]TU Darmstadt, Germany

Carbon collimators and beam absorbers are installed in many locations around the LHC to absorb beam losses, since carbon is the material that is most suitable to absorb the beam energy without being damaged. Because collimators and absorbers are close to the beam, it is very likely that they are hit first when the beam is accidentally deflected. In this contribution we present the results of two-dimensional hydrodynamic simulations of heating of a solid carbon cylinder with a radius = 2.5 cm and a length = 10 m which is facially irradiated by one LHC beam with nominal parameters.

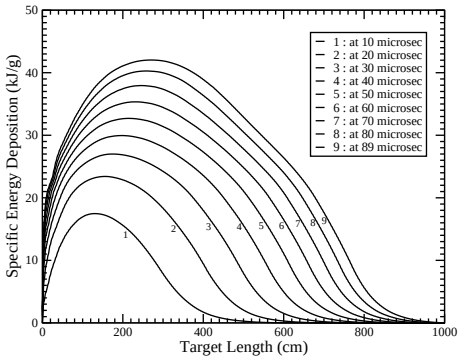

Figure 1: Specific energy deposition vs target axis at different times during irradiation.

Fig. 1 shows specific energy deposition along target axis at different times. It is seen that at 10 μs a specific energy of about 15 kJ/g is deposited. The magnitude of the peak increases with time while its position shifts rightwards. It is seen that at the end of the pulse, at 89 μs, a maximum specific energy deposition of about 40 kJ/g is achieved.

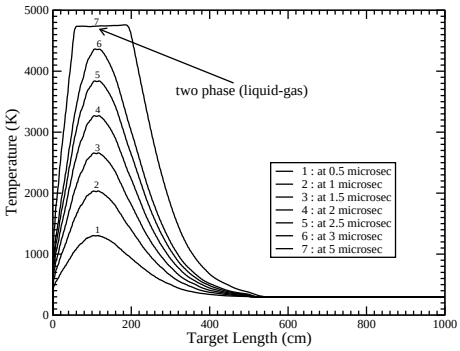

Figure 2: Temperature vs target axis at different times.

Fig. 2 shows the temperature evolution along the target axis during early stages of heating. It is seen that the temperature increases as more and more energy is deposited by the beam and at 5 μs it becomes constant. This is because the target enters into a two-phase liquid–gas state.

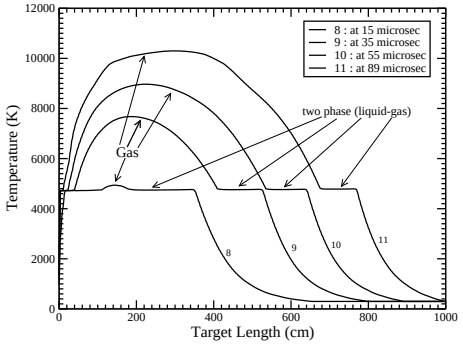

Figure 3: Temperature vs target axis at different times up to 5 μs.

Fig. 3 shows temperature evolution at later times. It is seen that at 15 μs, a small region of the target becomes gaseous. Following curves show that the two–phase region moves rightwards while the temperature in the gaseous part increases to about 10000 K.

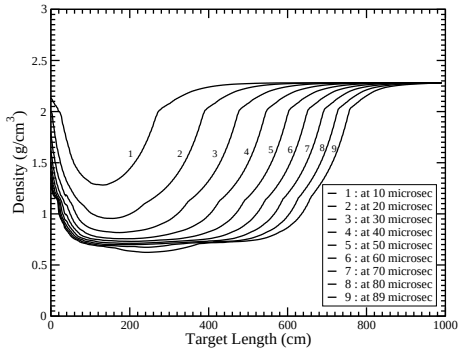

Figure 4: Density along target axis at different times after 5 μs.

Figure 4 shows the density change along the target axis at different times. It is seen that at the end of the pulse, at 89 μs, the beam has penetrated about 9 m into solid carbon and the density in the beam heated region has been reduced to about one third of the solid density (2.28 g/cm^3).

* Work supported by the BMBF

Dielectronic Recombination of Heavy Radioisotopes

C. Brandau *[1,2], C. Kozhuharov[2], A. Müller[3], F. Bosch[2], D. Boutin[2], H. Bräuning[2], F.J. Currell[4], C. Dimopoulou[2], Th. Faestermann[1], B. Franzke[2], R. Krücken[1], Yu.A. Litvinov[2], F. Nolden[2], B.E. O'Rourke[2,4], S. Schippers[3], M. Steck[2], Th. Stöhlker[2,5], and D. Winters[2]

[1]TU München; [2]GSI Darmstadt; [3]Universität Gießen; [4]Queen's University, Belfast, U.K.; [5]Universität Heidelberg

Isotope shift (IS) and hyperfine experiments that extract the information about nuclear ground state parameters such as radius R, nuclear spin I and magnetic moment μ_I from the resonance spectra of dielectronic recombination (DR) are a promising novel approach with large potential beyond to what is achieved with established methods. The general concept of DR-IS experiments was demonstrated by our collaboration for the two stable isotopes A=142 and A=150 of Li-like $^{A}Nd^{57+}$ [1]. The possibility to study few-electron ions with a high experimental precision is a decisive advantage of the DR method since it allows for a theoretical treatment on a full QED level [1,2]. Here we report on preliminary results from a two-day pilot experiment at the ESR in May 2008 where we measured for the first time DR spectra with in-flight synthesized radioisotopes.

The exotic nuclides were produced from a ^{238}U primary beam with 381.5 MeV/u hitting a 1 cm thick (1.85 g cm^{-3}) Be-foil located in the stripping area of the direct transfer beam line between the synchrotron SIS and the ESR. The resulting ion energies after the target are about 185 MeV/u, depending on the isotope. The isotope cocktail was injected into the ESR and cooled for about 5 min. Concurrently, the initially He-like ions of the desired isotopes ^{234}Pa and ^{237}U were charge-state bred yielding Li-like ions as required for our DR experiment. Typical intensities of about 2-3 $\cdot 10^4$ $^{234}Pa^{88+}$ and 3-4 $\cdot 10^5$ $^{237}U^{89+}$, respectively, were obtained. The beam was centered by synchronous increase of the ring magnets' B-field corresponding to a momentum change of $\delta B\rho = 1.1$ %. The separation of the isotopes was accomplished by inserting scrapers from both sides into the ring acceptance. Thus, we utilized the well-known capability of the ESR as a high resolution device for isobaric/isomeric separation [3]. After preparation of the beams in the ring data taking for the DR measurement was started. Preliminary results for the DR of $^{234}Pa^{88+}$ and $^{237}U^{89+}$, respectively, are displayed in Fig. 1, proving the feasibility of DR studies of exotic ions with intensities as low as 10^4 ions. Based on these experiences we can estimate that already at the present GSI installations for any element between the primary beams ^{238}U or ^{232}Th down to the stable ^{209}Bi a long range of isotopes is accessible for DR-IS studies, e.g., ^{227}U - ^{238}U. Feasibility studies suggest that long-lived isomers can be addressed as well.

Besides the obvious impact in nuclear physics for heavy elements charge radii and isotope effects are also crucial for precision atomic physics experiments. For example, for future PNC studies the list of candidates comprises different isotopes of Eu/Gd, Fr and U [4-6]. Detailed knowledge on nuclear parameters is essential to disentangle nuclear effects and sought-after contributions. As a benefit, isotope effects can also be utilize for the fine tuning of the energy separation of atomic levels with opposite parity [6]. In view of the expected high intensities at FAIR, unstable isotopes provide an appealing new degree of freedom also for atomic physics experiments. Due to its high sensitivity even at low beam intensities DR is well-suited as a precursor of this upcoming new class of measurements.

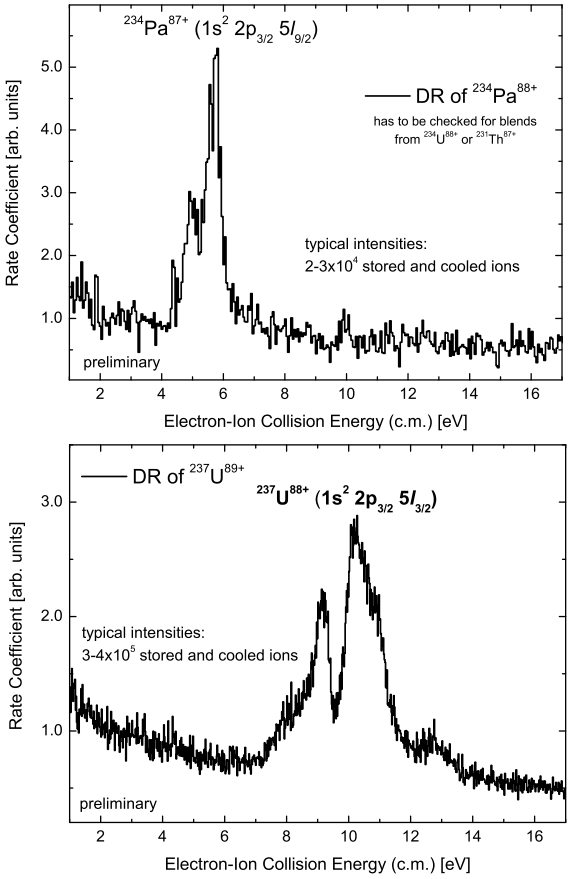

Figure 1: DR of the two Li-like radioisotopes $^{234}Pa^{88+}$ (upper panel) and $^{237}U^{89+}$ (lower panel).

* C. B. acknowledges support by GSI Darmstadt (F&E) under contract number TM/KRUE.

[1] C. Brandau et al., Phys. Rev. Lett., **100**, 073201 (2008).
[2] Y.S. Kozhedub et al., Phys. Rev. A **77**, 032501 (2008).
[3] C. Scheidenberger et al., Hyp. Int. **173**, 61 (2006).
[4] V.M. Shabaev et al., Phys. Rev. A **72**, 062105 (2005).
[5] V.M. Shabaev, private communication.
[6] M. Maul et al., Phys. Rev. A **53**, 3916 (1996).

Linear polarization and angular distribution of Lyman-α_1 radiation following from the REC process in collisions of bare uranium ions with H_2

G. Weber[1,2], H. Bräuning[1], S. Hess[1,3], U. Spillmann[1,3], S. Fritzsche[2], S. Geyer[1,3], R. Märtin[1,3], R. Reuschl[1,3], A. Surzhykov[2], S. Trotsenko[1,3], D. Winters[1], and Th. Stöhlker[1,2]

[1]GSI, Darmstadt, Germany; [2]University of Heidelberg, Germany; [3]University of Frankfurt, Germany

For high-Z systems the elementary process of photoionization is studied best in inverse kinematics by utilizing its time-reversed reaction, namely the radiative electron capture (REC) in energetic ion-atom collisions. In case of capture into the $2p_{3/2}$ state the REC process leads to a non-statistical population of the magnetic sublevels, the so-called alignment, resulting in an anisotropic distribution of the emitted Lyman-α_1 (Ly-α_1) radiation, which is characterized by the parameter β_A. For H-like uranium it was previously shown that the M2 branch of the transition into the ground state gives rise to a significant modification of the angular distribution, namely a 28 % increase in the alignment parameter compared to the pure E1 decay channel, even so it only contributes by about 1 % to the total transition rate [1]. In addition, calculations predict that the same effect should lead to a significant decrease in the degree of the linear polarization of the Ly-α_1 radiation [2]. While previous measurements were mainly restricted to study the spectral and angular distribution of the emitted radiation, the recent development of energy, time and position sensitive X-ray detectors, which can be used as efficient Compton polarimeters, now allows for measurements of linear polarization in the energy region above 50 keV [3].

The experiment was performed at the internal gasjet target of the ESR by interacting bare uranium ions at an energy of 96.6 MeV/u with H_2 molecules. The emitted photons were detected by an array of standard solid state X-ray detectors at 60°, 90°, 120° and 150° and two novel-type double-sided segmented X-ray detectors at 35° and 90° with respect to the beam axis. The down-charged ions were separated from the main beam by a dipole magnet and afterwards detected by a particle detector located at the outer site of the ring. This allows for coincidence measurements between X-rays and down-charged ions in order to suppress background radiation.

While the standard X-ray detectors were used to obtain the angular distribution of the emitted radiation, the segmented detectors were used to detect the linear polarization. The latter is done by exploiting the polarization sensitivity of the Compton effect described by the Klein-Nishina equation:

$$\frac{d\sigma}{d\Omega} = \frac{{r_e}^2}{2}\left(\frac{E'}{E}\right)^2\left(\frac{E'}{E}+\frac{E}{E'}-2\sin^2\vartheta\cos^2\varphi\right), \quad (1)$$

with E denoting the energy of the incident photon and E' denoting the Compton scattered photon. According to equation 1, the degree of the linear polarization and the orientation of the polarization plane of the incident photons can be obtained by measuring the angular distribution of the scattered photons with respect to the azimuthal angle φ. In contrast to standard Compton polarimeters consisting of a scatterer and one or more separated detectors for the scattered photons, the detectors applied here act simultaneously as scatterer and scattered photon detector [3]. Preliminary results for the Ly-α_1 line are shown in Fig. 1.

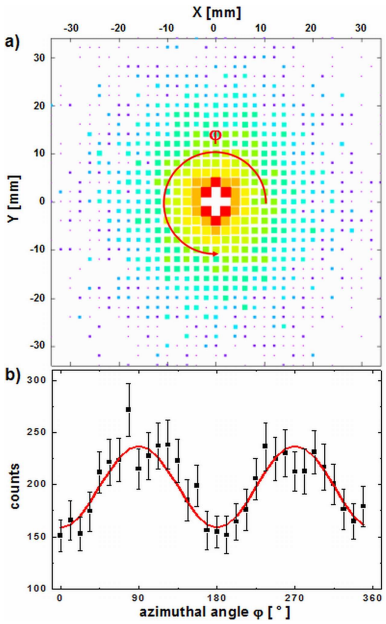

Figure 1: a) Position distribution of the Compton scattered photons with respect to the scattering position on the double-sided segmented X-ray detector at 90°. b) Projection on the φ-axis; the red line results from a fit of the Klein-Nishina equation to the experimental data.

Summarizing, in the presented experiment we studied the angular distribution as well as the linear polarization of the Ly-α_1 radiation arising from collisions of U^{92+} with H_2. Each of the two measurements lead to an independent determination for the anisotropy parameter β_A, and consequently probe our understanding of the atomic structure at high-Z as well as the REC process. Detailed analysis of the obtained data is still ongoing.

References

[1] A. Surzhykov, et al., Phys. Rev. Lett. **88**, 153001 (2002).

[2] A. Surzhykov, et al., Hyperfine Interact. **146-147**, 35 (2003).

[3] U. Spillmann, et al., Rev. Sci. Instrum. **79**, 083101 (2008).

Energy Distribution of the $2^1S_0 \rightarrow 1^1S_0$ Two-photon Transition in Heliumlike Tin

S. Trotsenko[1,2], A. Kumar[1,5], A. Volotka[6,7], D. Banas[3], H. Beyer[1], H. Bräuning[1], A. Bräuning-Demian[1], A. Gumberidze[4], S. Hagmann[1,2], S. Hess[1,2], P. Jagodziński[3], C. Kozhuharov[1], M. Nofal[1], R. Reuschl[1,2], S. Salem[1,2], U. Spillmann[1,2], M. Trassinelli[4], L. Tribedi[5], G. Weber[1,8], Th. Stöhlker[1,8]
[1]GSI, Darmstadt, Germany; [2]IKF, Univ. of Frankfurt, Germany, [3]Swietokrzyska Academy, Kielce, Poland; [4]École Normale Supérieure, CNRS, Univ. Pierre et Marie Curie-Paris 6, France; [5]Tata Institute of Fundamental Research, India; [6]ITP, TU Dresden, Germany, [7]Department of Physics, St. Petersburg State Univ., Russia; [8]Univ. of Heidelberg, Germany

Two-photon decays have been extensively studied, both theoretically and experimentally, since the 1930s. However many of the experiments aiming for the determination of the spectral shape of the two-photon decay in high-Z ions were suffering from a substantial background [1]. These measurements usually involved photon/photon coincidences between two x-ray detectors, and therefore suffered from the detector efficiencies. So far, none of these measurements reached the necessary level of precision to test fully relativistic calculations [2].

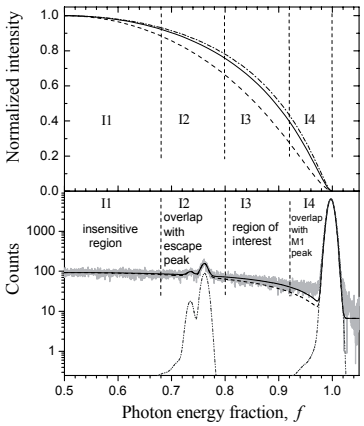

Figure 1: *Top*: Higher energy half of the calculated fully relativistic two-photon energy distribution for He-like Ni (dash-dot line), Sn (solid line), and U (dashed line). *Bottom*: Preliminary comparison of the measured two-photon spectral distribution of He-like tin and fully relativistic calculations for heliumlike Sn (solid line), and U (dashed line), together with the simulated detector response function for the $M1$ line (dotted line).

Recently, a novel experimental technique was applied to selectively produce K-shell vacancies in heliumlike heavy ions [3, 4, 5, 6]. This method allows the use of only a single x-ray detector, which offers substantial advantages as compared to the conventional photon/photon coincidence technique.

Here, we present the results of the two-photon decay studies of the 2^1S_0 state in He-like tin. The experiment was performed at the ESR (GSI) with 300 MeV/u Li-like tin ions colliding with a gas jet target (N_2) [6,7].

For the analysis of the energy distribution of the 2^1S_0-1^1S_0 two-photon decay, the higher energy half of the calculated (Fig. 1: top) and measured (Fig. 1: bottom) was chosen (see [6, 7] for the explanation). In this region the two-photon distribution is affected by only events from the $M1$ decay of the 2^3S_1 state. In order to estimate the influence of the $M1$ events on the two-photon spectral shape, the detector response for the $M1$ transition was simulated with the EGS4 package (bottom part of Fig.1).

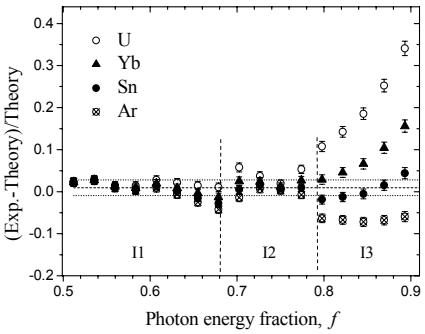

Figure 2: Preliminary (Experiment-Theory)/Theory intensity ratio with theoretical values for Ar, Sn, Yb, and U plotted as a function of the photon energy fraction f.

The measured energy distribution was compared with the theoretical one using the MINUIT minimization code by requiring the best agreement between the theoretical and the measured spectral shapes. In Fig. 2, our preliminary results are presented, i.e. the fraction (Exp.-Theory)/Theory. We compare the measured energy distribution with the relativistic calculations of line shapes for different Z. In the region of interest I3 the influences of relativistic and correlation effects on the spectral shapes are most pronounced (top part of Fig. 1), therefore this region was considered for the experiment-theory comparison. We can preliminary conclude: a) the method allowed for a background free (I3) measurement of the two-photon spectral shape; b) the Sn data points are in the agreement (within ±3σ of the average values) with the theory, in contrast to the data points of the other elements (Ar, Yb, U) which substantially deviate. The data analysis is in progress.

The support by the DAAD (A.K., No.: A/05/52927), the A. von Humboldt Foundation (M.T.) and by I3 EURONS (EC contract no. 506065) is gratefully acknowledged.

References

[1] P. H. Mokler and R. W. Dunford, Physica Scripta 69, C1 (2004).
[2] A. Derevianko and W. R. Johnson, Phys. Rev. A 56 (1997) 1288.
[3] J.Rzadkiewicz et al., Phys. Rev. A 74 (2006) 012511.
[4] D. Banas et al., Nucl. Instrum. and Methods B 235 (2005) 326.
[5] Th. Stöhlker et al., Phys. Rev. A 58 (1998) 2043.
[6] S. Trotsenko et al., GSI Scientific Report (2006) 246.
[7] A. Kumar et al., GSI Scientific Report (2007) 274.

Polarized tunable monoenergetic X-rays produced by REC into Xe^{54+}

S. Hess[1], H. Bräuning[1], U. Spillmann[1], S. Geyer[1], S. Hagmann[1], C. Kozhuharov[1], T. Krings[2], A. Kumar[1], R. Märtin[1], B. O'Rourke[1], D. Protic[2], R. Reuschl[1], S. Trotsenko[1], G. Weber[1,3], D. Winters[1], and Th. Stöhlker[1,3]

[1]GSI, Darmstadt, Germany; [2]Forschungszentrum Jülich, Germany; [3]Universität Heidelberg, Germany

Many physical effects like bremsstrahlung, synchrotron radiaton and radiative recombination produce polarized X-rays. However for technical purposes only a few facilities like highly specialized synchrotron light sources are able to deliver tunable high quality beams of almost completely polarized X-ray radiation to the user. In our novel approach, we used radiative electron capture (REC) into the K - shell of bare xenon to produce tunable and highly polarized X-ray radiation, even in a storage ring environment. Although former theoretical investigations [1] already showed this potential feature of the REC process, the polarization of X-rays, produced by capture transitions, could hardly be detected with traditional polarimeters due to a low efficiency in this energy regime. The recent development of novel 2D semiconductor Compton polarimeters [2,3] opens up the low energy regime for efficient polarization measurements for the very first time.

In an experiment performed in March 2008, we used the internal gasjet target of the ESR and a beam of 155 MeV/u Xe^{54+} ions to produce polarized X-ray radiation and a novel 2D Si(Li) type Compton polarimeter to detect the polarization of the radiation. The feasibility of the polarimeter for such investigations has been demonstrated in an earlier experiment [4]. The polarimeter has been positioned at 90° with respect to the ion beam axis and events have been measured in coincidence with down-charged ions behind the first dipole magnet (see Fig. 1). Molecular hydrogen has been chosen as a target due to several advantages such as a very narrow Compton-profile and therefore small REC linewidths. To measure the polarization we made use of the anisotropy of the Compton scattering process. In this incoherent scattering process, energy is transferred from an incident photon to a free or quasi-free recoil electron. Both, the recoil electron as well as the scattered photon can be detected within the detector crystal. To separate between Compton scattering and photoabsorption events, we used the detector's optimal combination of energy and spatial resolution as well as timing and multihit capability.

The scattering geometry within the detector crystal is shown on the left side in Fig. 2. Since the polarimeter is capable of detecting scattering into all directions, but is most sensitive for scattering into $\vartheta = 90° \pm 10°$ this angle has been selected via an energy condition corresponding to the kinematical relation between recoil electron energy and scattering angle ϑ. While the energy of the recoil electrons is determined by the scattering angle, it is the anisotropy of the angular distribution along φ perpendicular to the photon beam direction, which determines the degree of the polarization. This φ distribution is shown on the right side of

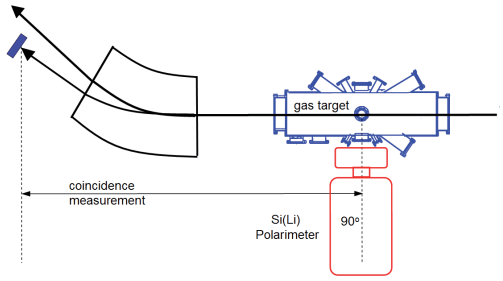

Figure 1: Sketch of the experiment. REC - photons have been measured in coincidence with down-charged Xe ions behind the first dipole magnet of the ESR.

Fig. 2 for the K-REC into bare xenon. This is a direct image of the Compton scattering process and compares well to the Klein Nishina differential cross section for fully polarized light. In fact a fit of a modified Klein Nishina function for arbitrary polarization reveals a polarization value of roughly 97%. Hence, the REC process seems to be the ideal tool to produce highly polarized, energetically tunable X-ray radiation in a storage ring environment.

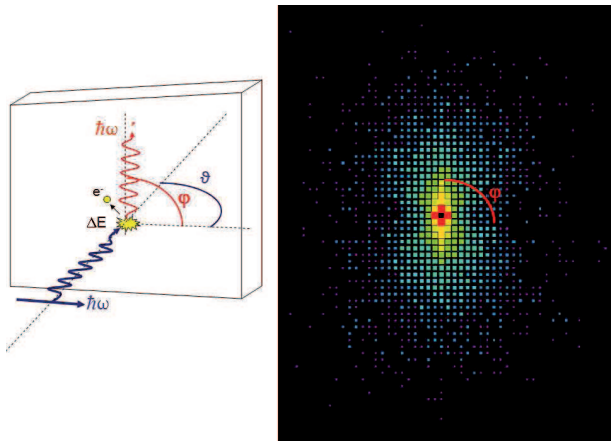

Figure 2: The geometry of the Compton scattering effect in the crystal of the 2D Si(Li) polarimeter (left) and a direct image of the compton scattering process of the highly polarized X-ray emission of the K-REC into bare xenon at a Compton scattering angle of $\vartheta = 90°$

[1] A. Surzhykov et al., Phys. Rev. Lett. 94 (2005) 203202
[2] U. Spillmann et al., Rev. Sci. Inst. 79 (2008) 083101
[3] D. Protic et al. , NSSMIC IEEE Vol.2 (2004) 943-944
[4] S. Hess et al. , GSI Scientific Report (2007)

Simultaneous ionization and excitation of He-like uranium ions

S. Salem[1, 2], Th. Stoehlker[1, 3], A. Bräuning-Demian[1], F. Bosch[1], H. Bräuning[1], A. Gumberidze[1], S. Hagmann[1, 2], Ch. Kozhuharov[1], D. Liesen[1, 3], S. Hess[1, 2], R. Reuschl[1, 2], U. Spillmann[1, 2], S. Trotsenko[1, 2], G. Weber[1, 2].

[1]GSI, Darmstadt; [2] IKF, Frankfurt Univ., [3] Heidelberg Univ., Germany.

The study of the simultaneous ionization and excitation of helium-like heavy ions with neutral target atoms offers the opportunity to investigate the two-electron transitions, where one electron ends up in the continuum while the other electron ends up in a hydrogen-like final state. The present work provides a complement to the existing experimental data [1] for the domain of strong Coulomb fields and for energies, where relativistic effects play an important role.

The process of simultaneous ionization and excitation was experimentally studied in He-like uranium ions colliding with an atomic xenon gas target at 220 *MeV/u*. The measurement was performed at the gas-jet target of the ESR. The Ly-α radiation has been measured by x-ray germanium detectors mounted at different observation angles of 35°, 60°, 90°, 120° and 150° with respect to the beam direction.

Fig.1 shows the x-ray spectrum measured at 35° in coincidence with up-charged (U^{91+}) ions. As seen from Fig.1, the uranium *K*α and Ly-α lines and the Xe characteristic radiation can be easily distinguished. The strong Xe x-ray transition lines are due to the ionization of Xe atoms by the energetic projectiles during the collision. In order to distinguish the four transition lines shown in Fig.1, conditions on the coincidence time spectrum were used yielding the Ly-α1 and Ly-α2 lines (*see Fig.*2a). The other two lines can be also distinguished by subtraction the Ly-α line from the four transition lines yielding the *K*α1 and *K*α2 lines of He-like uranium ions as shown in Fig.2b. The spectra were corrected for the x-ray detection efficiency [2] and for the Doppler shift.

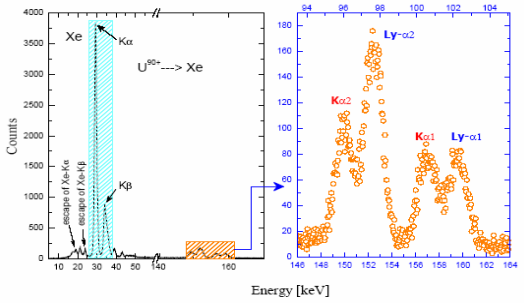

Figure 1: X-ray energy spectrum as observed by the germanium detector located at 35^0.

The present measurement gives the possibility to investigate the impact parameter characteristic of two different processes, namely the process of simultaneous ionization-excitation and the single excitation process. Experimentally, it can be investigated by finding out the alignment parameter A_{20} which reflects the relative weights of the population of the magnetic sub-states of a certain level by the excitation process. Generally, the angular distribution of photons, in the emitter frame, can be expressed as [3]:

$$W(\theta) \propto 1 + \alpha \cdot A_{20}\left(1 - \frac{3}{2} \cdot Sin^2\theta\right) \qquad (1)$$

where α depends only on the total angular momentum of the initial and final ionic state, respectively. The value of the alignment parameter can be deduced by a fit of Eq.1 to the experimental angular distribution of the x-rays. The predicted results are shown in Fig.3.

From the dependence of the alignment parameter on the collision impact parameter ***b***, theoretically performed by Ludziejewski [1], it is possible to find out the impact parameter for the process of simultaneous ionization and excitation ($b^{exp} = 700$ *fm*). A good agreement between the experiment and the theory in which the collision is found only at small impact parameter ($b^{theory} = 550$ *fm*). This allows for the conclusion that the experimental results can support the theoretical predictions for the validity of first-order perturbation theory at relativistic energies.

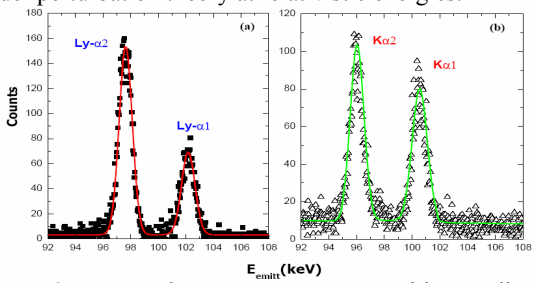

Figure 2: Ly-α and *K*α x-ray energy transitions collected in coincidence with up-charged H-like uranium ions (a) and for He-like uranium ions (b), respectively.

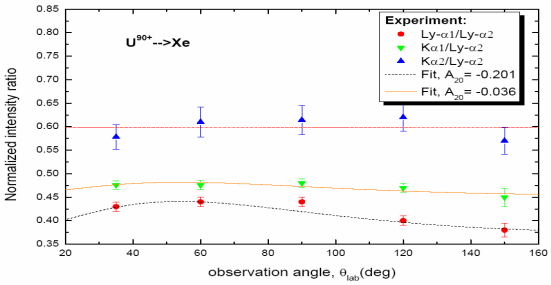

Figure 3: The intensities of *K*α1,*K*α2 *and Ly*-α1 lines normalized to the Ly-α2 as function of the observation angle.

References

[1] T. Ludziejewski et al., Phys. Rev. A 61, (2000).

[2] S. Salem, Ph.D. Thesis, (2009), submitted.

[3] J. Eichler, Phys. Rev. A, 2128 (1998).

Observation of the rate enhancement in K-shell radiative recombination of bare uranium ions with cooling electrons*

D. Banaś[1], M. Pajek[1], Th. Stöhlker[2,3], A. Surzhykov[2,3], H. F. Beyer[2], S. Böhm[4], F. Bosch[2], C. Brandau[2], M. Czarnota[1], S. Chatterjee[2], J.-Cl. Dousse[5], S. Fritzsche[2], A. Gumberidze[2], S. Hagmann[2], C. Kozhuharov[2], D. Liesen[2], P. H. Mokler[2], A. Müller[4], A. Kumar[2], R. Reuschl[2], E. W. Schmidt[4], D. Sierpowski[6], U. Spillmann[2], J. Szlachetko[1,5], S. Tashenov[2], S. Trotsenko[2], P. Verma[2], and A. Warczak[6]

[1]Institute of Physics, Jan Kochanowski University, 25-406 Kielce, Poland; [2]Gesellschaft für Schwerionenforschung, D-64291 Darmstadt, Germany; [3]Physikalisches Institut der Universität Heidelberg, D-69117 Heidelberg, Germany; [4]Institut für Kernphysik, Justus-Liebig Universität, D-35390 Giessen, Germany; [5]Department of Physics, University of Fribourg, CH-1700 Fribourg, Switzerland; [6]Institute of Physics, Jagiellonian University, 30-059 Cracow, Poland

We report here results of a state selective radiative recombination experiment in which the K-shell radiative recombination (K-RR) rates for U^{92+} ions interacting with low-energy electrons in electron cooler were measured for a different relative (off-cooling) energies in the range 0-1000 meV. The experiment has been performed at the ESR storage ring at the GSI facility. Details of the experiment can be found elsewhere [1].

The measured K-RR radiative recombination rates were compared with predictions of nonrelativistic dipole approximation [2, 3] and fully relativistic treatment [4]. Within the nonrelativistic approach, in the low energy limit, the differential K-shell recombination cross section is described by the well-known dipole term $\mathrm{d}\sigma_{K-RR}/\mathrm{d}\Omega = \sigma_{1s}\sin^2\vartheta$. This formula, being symmetric with respect to the angle $\vartheta = 90^\circ$ between the directions of incoming electron (in the ion frame) and emitted photon, results in a differential RR rate which is symmetric with respect to relative energy E_{rel} = 0 eV. However in the experiment the asymmetry in the differential K-RR rate coefficient is observed (see Fig. 1). Such an asymmetry can be understood within the fully relativistic calculations which account for the non-dipole electric and magnetic terms in the electron-photon interaction (see Refs. [5, 6]). These terms lead to a departure of the K-RR differential cross section from the Stobbe's prediction and, in turn, to the asymmetry in the rate coefficient $\alpha_{RR}(\theta)$. As seen from Fig. 1, the K-RR rates, which were calculated within the fully relativistic treatment and next corrected for a variation of the relative electron energy in the cooler due to a drift tube voltage drop, reproduce very well the energy dependence of the measured K-RR rates for off-cooling energies ($E_{rel} \neq 0$) and clearly indicate a presence of the rate enhancement for the cooling condition (E_{rel} = 0 eV) [7]. By normalization of the measured rates to the theoretical predictions we estimated, for the first time, a magnitude of the recombination enhancement for the lowest n=1 state at the cooling condition, which is factor of two.

Summarizing, the radiative recombination of U^{92+} ions with cooling electrons observed for the K-shell in the state-selective x-ray radiative recombination experiment performed at the ESR storage ring gives the first experimental evidence of the recombination enhancement for the low n-states. This experimental finding is important for explanation of a nature of the enhancement effect, since the existing theoretical models emphasize a role the recombination to very high Rydberg states as a main source of the observed enhancement in total radiative recombination rates.

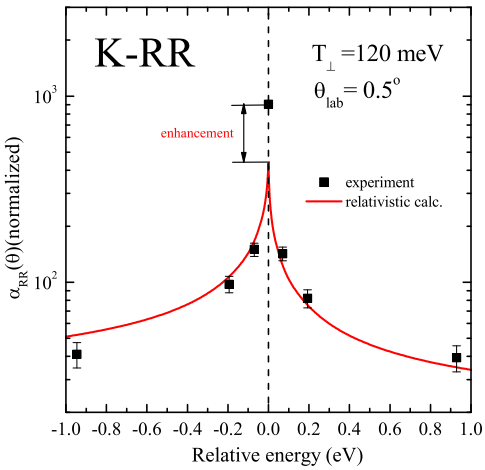

Figure 1: The K-shell RR rate coefficient measured by detector placed at 0.5^o versus the relative electron energy. The data are compared with the predictions of the relativistic calculations [4] assuming the electron beam transverse temperature $kT_\perp$ = 120 meV.

References

[1] M. Pajek *et al.*, *Proc. of ICPEAC-2005*
[2] M. Stobbe, Ann. Phys. 7, 661 (1930)
[3] M. Pajek and R. Schuch, Phys. Rev. A 45, 7894 (1992)
[4] A. Surzhykov *et al.*, Comput. Phys. Com. 165, 139 (2005)
[5] R. H. Pratt *et al.*, Rev. Mod. Phys. 45, 273 (1973)
[6] J. Eichler and T. Stöhlker, Phys. Rep. 439, 1 (2007).
[7] D. Banaś *et al.*, Eur. Phys. J. ST, accepted

*Work supported by EURONS contract No. 506065 and Polish Ministry of Science and Higher Education under Grant No. N20215931/3048

Data Analysis of the Test Experiment for Lamb Shift Measurements on Hydrogen-Like Lead Ions $^{208}Pb^{81+}$ with Low Temperature Calorimeters

V. Andrianov[1,2,3], K. Beckert[1], P. Beller[1,†], A. Bleile[1,2], Ch. Chatterjee[1], P. Egelhof[1,2], A. Gumberidze[1], S. Ilieva[1,2], O. Kiselev[1,2], C. Kilbourne[4], H-J. Kluge[1], S. Kraft-Bermuth[1,2], D. McCammon[5], J.P. Meier[1], R. Reuschl[1], T. Stöhlker[1] and M. Trassinelli[1]

[1]GSI, Darmstadt, Germany; [2]Univ. of Mainz, Germany; [3]Lomonosov Moscow State Univ., Moscow, Russia; [4]NASA/Goddard Space Flight Center, Greenbelt, USA; [5]Department of Physics, Univ. of Wisconsin, Madison, USA.

In the framework of the program on the precise test of QED by determining the ground state Lamb shift in hydrogen-like heavy ions the next generation of high resolution X-ray spectrometers has been developed at GSI [1]. In this report, the results of a test run with the calorimetric low temperature detector are communicated.

The experiment was carried out at the ESR. The beam of the bare $^{208}Pb^{82+}$ ions with an energy of 218.54 MeV/u (β=0.58647(2)) and with a momentum spread of less than 10^{-5} interacted with the Kr-gas target. The nuclei captured one electron and promptly emitted Lyman X-rays. Lyman X-rays and X-rays from calibration sources ^{241}Am and ^{133}Ba were detected by the calorimetric detector mounted under Θ=145° relative to the ion beam.

The detector modules were designed on the basis of silicon microcalorimeters [2]. The prototype detector array consisted of 8 pixels with Sn and Pb absorbers with a total active area of 2.9 mm^2. The array was placed inside a ^{3}He/^{4}He-dilution refrigerator with an operation temperature of about 60 mK. The detector performance was tested under laboratory conditions with 59.6 keV photons. An energy resolution of ΔE_{FWHM}=65 eV was obtained.

The experimental run lasted about 10 days, and 6 good data sets (12-24 h each) were recorded. The 3 detector pixels with the best performance were selected for the present data analysis. The detector signals were digitized, and digital filtering and time correction of line drift were applied. The pulse height spectrum for a pixel with a Sn absorber is displayed in Fig. 1. The Lyman lines and the calibration lines are unambiguously visible. Under running conditions the energy resolution was of the order of 150-200 eV due to worsened signal to noise ratio and Doppler broadening due to the size of the gas target. Each spectrum was used for the energy calibration and the determination of the energy of the Lyman lines. The nonlinear calibration curve was fitted by a 3-rd order polynomial. As a result the Ly line energies in the Lab system were obtained for each pixel (Fig. 2).

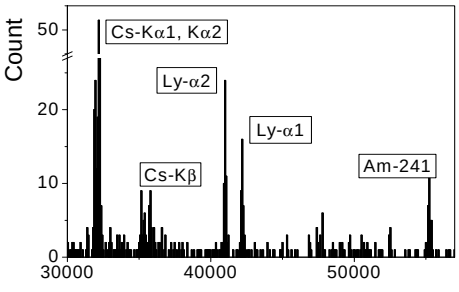

Figure 1: Spectrum obtained with the calorimetric detector pixel with a Sn absorber.

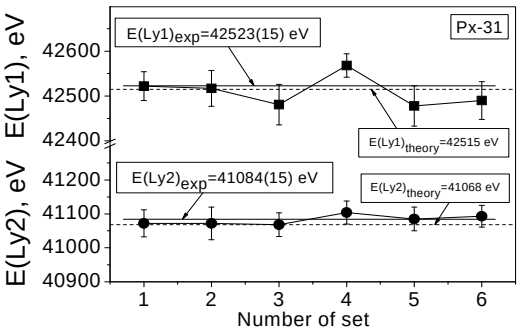

Figure 2: The energy of Ly α1 and α2 lines in the Lab system (the experimental data for one pixel).

The positions of the detector pixels with respect to the experimental setup were determined by topographic measurements and in a separate experiment by using a moveable collimated ^{241}Am source scanning across the cryostat window. These measurements are used for the calculation of the Ly-line energies in the emitter frame.

After averaging the data for 3 pixels the energy of the Ly α1 line in the emitter frame was obtained, $E(Ly_{\alpha 1}\ ^{208}Pb^{81+})$=77950±16±12 eV. The first error is the statistic one. The second error is the systematic one due to uncertainty in the positions of the gas target and the detector array. The obtained value coincides with theoretical prediction $E(Ly_{\alpha 1})$=77934.4±0.5eV. [3].

In summary the present work represents the first successful measurement of Lyman lines by calorimetric detectors. For the next experimental run the setup of a detector array with a total amount of 32 pixels is in progress. In order to improve the energy calibration the use of sources with energies located close to the Lyman-α lines is planned. Uncertainties in the Doppler correction will be reduced by choosing beams with lower energies and by more accurate determination of pixel and target positions.

References

[1] A. Bleile et al., AIP Conference Proc. 605 (2002)409.
[2] C. Stahle et al., Nucl. Instr. Meth. A310 (1996) 173.
[3] W.R. Johnson and G. Soff, At. Data and Nucl. Data Tables 33 (1985) 405.

Charge radius determination of ^{7,9,10}Be and the one-neutron halo nucleus ^{11}Be by high-resolution collinear laser spectroscopy*

Ch. Geppert[1,2], D. Tiedemann[3], M. Zakova[3], J. Krämer[3], Z. Andjelkovic[1,3], A. Krieger[3], R. Neugart[3], M. Nothhelfer[3], R.M. Sanchez Alarcon[1], M. Bissell[4,6], D. T. Yordanov[5,6], M. Kowalska[6], F. Schmidt-Kaler[7], C. Zimmermann[2] und W. Nörtershäuser[1,3]

[1]GSI, Darmstadt, Germany; [2]Universität Tübingen, Germany; [3]Universität Mainz, Germany; [4]Katholieke Universiteit Leuven,Belgium; [5]MPI f. Kernphysik, Heidelberg, Germany; [6]CERN, Genf, Suisse; [7]Universität Ulm, Germany

The region of the lightest elements is very much of interest due to the appearance of halo nuclei. However since they demand high-resolution measurements of the isotope shifts and highly accurate theoretical calculations of the mass shift contribution [1,2,3] they are extremely challenging and could not be performed until a few years ago. Charge radii measurement of short-lived isotopes have been performed by means of high-resolution laser spectroscopy in the isotopic chains of lithium at GSI and TRIUMF [4,5] and for helium isotopes at Argonne [6] and GANIL [7]. We focused now on the charge radius measurement of the beryllium isotopes ^{7,9,10}Be and the lightest one-neutron halo nucleus ^{11}Be.

We performed the charge radius investigation at the existing COLLAPS beamline at ISOLDE, CERN. A scheme of the experimental setup is shown in fig. 1 (left). Here the experimental setup was improved by simultaneous collinear and anti-collinear laser spectroscopy in order to be insensitive to any uncertainties or instabilities in the knowledge of the ions acceleration potential [8]. This is only possible if the laser frequency determination is performed with a relative accuracy $\delta\nu/\nu$ in the order of 10^{-9}. This has been achieved by locking the applied laser systems on a fibre-laser based frequency comb and by frequency-modulation saturation spectroscopy of iodine. The iodine spectroscopy setup has been calibrated and cross checked by measurements of the molecular iodine transitions with the frequency comb system as well. Two second-harmonic generation cavities have been applied in order to produce the required 313 nm UV wavelength for the D1 transition in the Be^+ ion. In order to assign the corresponding fluorescence peak to collinear or anti-collinear excitation, the anti-collinear and the collinear laser beam, respectively, were remotely blocked by fast beam blockers. Each of these individual subsequent scan was performed within 2-10 seconds, depending on the ion production rate.

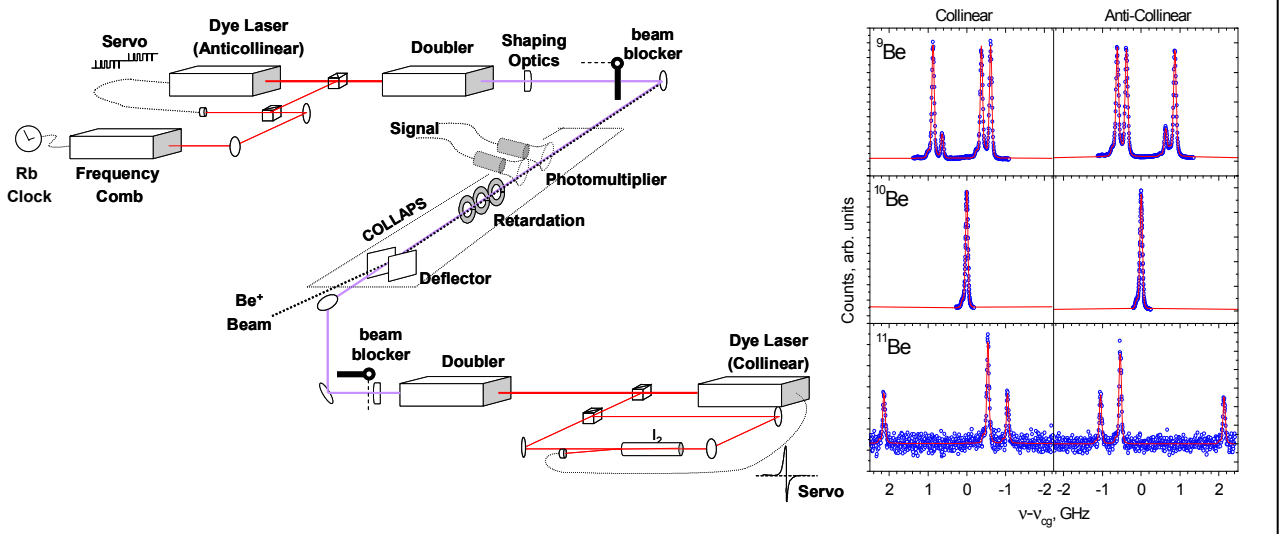

Figure 1: Schematic drawing of the experimental setup using two laser systems for simultaneous collinear and anti-collinear laser spectroscopy at COLLAPS, ISOLDE (left) and typical on-line spectra (right).

The spectroscopy of the stable and radioactive beryllium ions was performed by collinear spectroscopy on a 60 keV ion beam. To determine the charge radii of the beryllium isotopes with an accuracy of better than 1 %, a precision in the order of 1 MHz in the isotope shift measurement is required. With the standard approach of collinear laser spectroscopy such accuracy for light isotopes is not achievable.

* this work is supported by BMBF Contract Nos. 06TU263I, 06UL264I, and 06MZ215/TP6, and by the Helmholtz Association under Contract VH-NG-148.

	$\delta\nu_{IS}^{9,A}$ /MHz	$\delta\nu_{MS}^{9,A}$ /MHz	$\delta\langle r_c^2\rangle^{9,A}$ / fm^2	$\mathbf{r_c}$ **/ fm**	A_{2s} /MHz	A_{2p} /MHz	μ / μ_N
^{7}Be	-49 236,81(88)	-49 225,757(19)	0,65(5)	**2,646(15)**	-742,90(25)	-140,17(18)	-1,3995(5)
^{9}Be	0	0	0	**2,519(12)**	-624,97(4)	-118,00(4)	(1,177432(3))*
^{10}Be	17 323,8(13)	17 310,44(6)	-0,79(8)	**2,357(21)**	0	0	0
^{11}Be	31 564,96(93)	31 560,100(15)	-0,29(5)	**2,461(17)**	-2677,36(77)	-505,41(50)	-1,6813(5)

Table 1: Measured isotope shifts $\delta\nu_{IS}^{9,A}$ in the D1 line of the beryllium ion and theoretical calculations for the mass shifts $\delta\nu_{MS}^{9,A}$ [2] for ^{A}Be - ^{9}Be and the extracted change in rms charge radius $\delta\langle r_c^2\rangle^{9,A}$. Uncertainties for the absolute charge radius r_c are taking the uncertainty in the reference radius $r_c(^9\text{Be}) = 2.519(12)$ fm [10] into account. From fits to the hyperfine structure splitting of the odd isotope in the 2s- and 2p-level, the magnetic dipole moment has been extracted. *Here the magnetic moment for ^{9}Be taken from [16] has been used as reference.

In an off-line run the contributions of possible systematic effects have been investigated. There it has been observed that the dominant contribution originates from possible laser to ion beam misalignment (500 kHz) and the uncertainty of the frequency comb reference rubidium clock (400 kHz).

Examples for typical scans in the on-line beamtime are shown in fig. 1 (right). From these measurements the charge radii ^{7,9,10,11}Be have been extracted [9]. Table 1 shows the measured isotopes shifts and the calculated mass shift contribution [2]. As isotope shift measurements can only yield information on the change in charge radii along the isotopic chain, the charge radius for ^{9}Be from electron scattering experiments [10] was used as reference to determine the absolute charge radii. Results are shown in fig. 2 (solid circles) and are compared with the predictions of theoretical models. All models describe the observed trend of charge radii very well. The charge radii extracted from measurement with Glauber calculations (open circles) [11] strongly overestimated the charge radius of ^{11}Be, which emphasizes the necessity for model-independent experimental approaches.

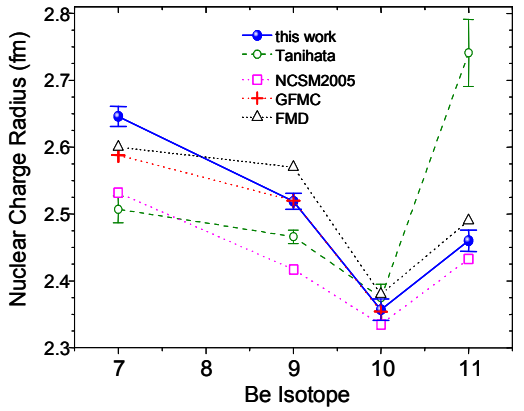

Fig. 2: Charge radii development along the beryllium isotopic chain. Experimental results of this work (solid circles) in comparison with model dependent results from earlier experiments (open circles) [11] and theoretical predictions from the no-core-shell model (NCSM) [12], fermionic molecular dynamic (FMD) [13] as well as Greens function Monte Carlo (GFMC) [14].

If the increase in charge radius from ^{10}Be to ^{11}Be is solely ascribed to the center of mass motion of the ^{10}Be core, a distance of the halo neutron to the center of mass of 7.0 fm is required. This is in excellent agreement with the expectation from the earliest model of halo nuclei where the binding energy of the nucleon determines the degree of tunneling into the classical forbidden region [15].

The investigation of ^{12}Be is planned for 2010 applying the ISOOL cooler and buncher at ISOLDE. Current production rates of ^{14}Be at ISOL facilities are by far not sufficient to perform similar measurements. Experimental approaches to study ^{14}Be with at an in-flight facility are under consideration.

References

[1] Z.-C. Yan et al., Phys. Rev. A 61 (2000) 0022504
[2] Z.-C. Yan et al., PRL 100 (2008) 243002
[3] K. Pachucki et al., Phys Rev A 78 (2008) 052511
[4] G. Ewald et al., PRL 93 (2004) 113002
[5] R. Sanchez et al., PRL 96 (2006) 033002
[6] Wang L.-B. et al., PRL 93 (2004) 142501
[7] P. Müller et al., PRL 99 (2007) 252501
[8] G. Borghs et al., Optics Comm. 38 (1985) 101
[9] W. Nörtershäuser et al., arXiv: 0809.2607 v2 and accepted by Phys. Rev. Lett.
[10] J.A. Jansen et al., Nucl. Phys. A 188 (1972) 337
[11] I. Tanihata, Phys. Lett. B 206 (1988) 592
[12] C. Forssen, Phys. Rev. C71 (2005) 044312 and priv. comm.
[13] R. Torabi, priv. comm. (2008)
[14] S. Pieper, PRC 66 (2002) 044310
[15] P.G. Hansen et al., Europhys. Lett. 4 (1987) 409 (1987)
[16] W. M. Itano, Phys. Rev. B 27 (1983) 1906

Fragmentation of ethylene in collisions with 3.6 MeV/u Xe $^{21+}$- and Xe^{38+}-ions

U. Werner[1], B. Siegmann[2], and R. Mann[3]
[1]Universität Bielefeld, Bielefeld, Germany; [2]TU Dortmund, Dortmund, Germany; [3]GSI, Darmstadt, Germany

The multiple ionization and fragmentation of ethylene was studied in collisions with 3.6 MeV/u Xe^{21+}- and Xe^{38+}-ions provided by the UNILAC at GSI. The slow electrons and ions generated in the collision process are separated by a weak homogeneous electric field. Electrons are detected by a channeltron at one side of the interaction region; positive ions are accelerated towards the position- and time-sensitive multi-particle detector at the other side [1] which records the position and flight time of each ion relative to the electron signal. Due to the crossed-wire structure of the detector anode particles arriving "at the same time" on different wires can be resolved, which is particularly useful in case of hydrocarbons where several correlated fragments with equal mass-to-charge ratio occur [2].

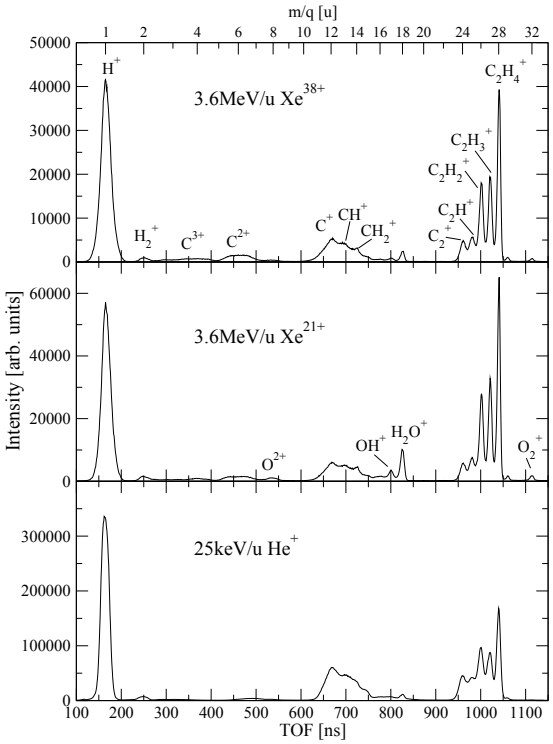

Figure 1: Time-of-flight spectra from collisions of 25 keV/u He^+, 3.6 MeV/u Xe^{21+} and 3.6 MeV/u Xe^{38+} with C_2H_4.

The time-of-flight spectra in Fig. 1 give an overview over the different reaction channels observed in collisions of 3.6 MeV/u Xe^{21+}- and Xe^{38+} with C_2H_4; for comparison the bottom spectrum shows the results for 100 keV He^+-impact. Although the full complexity of the observed fragmentation patterns are only revealed by the multi-particle coincidence spectra some indications appear in fig. 1. As expected for the comparatively slow He^+ ions only few multiply charged C^{q+} ions occur, whereas their abundance increases with the charge of the swift Xe-ions. In all collision systems H_2^+-ions appear which can not be produced by a simple bond-breaking; an analysis of the coincidence data shows, that they arise from the $(C_2H_4)^{*2+} \rightarrow C_2H_2^+ + H_2^+$ channel. There is a comparatively large contribution of fragmentation processes which leave the C-C structure intact. Furthermore, the relative intensity of these reactions seems to be larger in the collisions with the highly charged Xe-ions.

If all fragments from a particular fragmentation are detected, a kinematically complete study of the molecular breakup process is possible [3] and the kinetic energy release as well as angular correlations can be derived for each individual event. In this measurements only the complete two-particle fragmentations into $H^+ + C_2H_3^+$, $H_2^+ + C_2H_2^+$, and $CH_2^+ + CH_2^+$ were observed (Fig. 2). In contrast to the fragmentation of acetylene and ethane no significant contributions of complete three-particle fragmentations, as e.g. $H^+ + H^+ + C_2H_3^+$, were found. Here the appearance of 3 charged fragments preferable seems to involve the complete destruction of the molecule. The statistics achieved in this exploratory measurement is not sufficient to draw conclusions about 6 particle fragmentations.

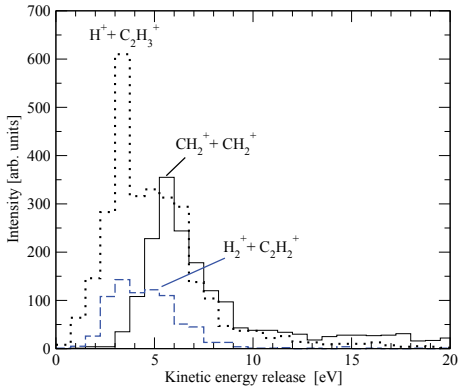

Figure 2: Kinetic energy released in two-particle fragmentations of C_2H_2 after collisions with 3.6 MeV/u Xe^{21+}.

References

[1] J. Becker, K. Beckord, U. Werner, and H.O. Lutz, Nucl. Instr. and Meth. A337, (1994) 409.

[2] B. Siegmann, U. Werner, and R. Mann, Nucl. Instr. and Meth. B233 (2005) 182.

[3] B. Siegmann, U. Werner, H. O. Lutz, and R. Mann, J. Phys. B: At. Mol. Opt. Phys. 35, (2002) 3755.

Low-Energy Electrons Emitted from Solid-State Targets in Ion-Atom Collisions

Natalia Lineva[1], C. Kozhuharov[1], M. Krämer[1], S. Hagmann[1,2], and G. Kraft[1]
[1]GSI Darmstadt, Germany; [2]Institut für Kernphysik, Universität Frankfurt am Main, Germany

We have continued our studies of the energy and angular dependence of low-energy electron emission pertinent to the needs of the radiobiology. In our previous report [1], we described briefly our method of accounting for the properties of the solid-state targets, both bulk and surface: We use dedicated TRAX Monte Carlo simulations to analyze the measured angular and energy distributions of electrons emitted after the impact of 1 keV and 500 eV electrons on thin carbon targets. Such analysis allows us to account quantitatively for the inhomogeneity of the target thickness and for its roughness. The TRAX code [2] treats each basic interaction of an electron or a heavy ion separately and does not require models for multiple scattering, angular straggling, etc. as an input. The basic processes taken into account for electrons are: elastic scattering, excitation, and ionization. This bottom-up approach in simulating the emission and transport phenomena of electrons makes the TRAX code very well-suited for our purposes. An elaborated treatment of the problems, the descriptions of our experimental set-up and of the performed experiments can be found in Ref. [3].

Based on the findings for the electron beam, we analyzed the spectra of electrons emitted in collisions of 3.6 and 11.4 MeV/u carbon ions impinging on the same carbon target. Additionally, we bombarded Ni, Ag, and Au targets. In Fig. 1, we compare our results with common simple conventional theory and with the results of our TRAX simulations. We used the modified Rutherford formula as described in Ref. [4], which according to the authors 'works remarkably well for both soft-collisions and binary-encounter electrons.' As usual, we took solely the 'active' electrons (those with velocities smaller than the projectile velocity) into account. We calculated the evolution of projectile charge states within the targets with the Etacha code [5], and we used the numbers to weigh the square of the charge state needed to calculate the cross sections. We used the average charge state after the target to obtain the number of projectiles from the measured Faraday cup current. We would like to emphasize that the effective charge state can vary quite strongly with the fluctuations of the target thickness.

The measured and calculated energy distributions are displayed in the left part of Fig. 1. The discrepancies between the theory and experiment are large. Even more important, the measured and calculated cross sections show different sequences, i.e. a different scaling with the atomic number of the target. Apparently, the electron transport phenomena play an important role. In the right part of the figure we compare the measured data for the carbon target with our TRAX simulations. For the simulations, we did not include the electrons stripped from the projectile that move predominantly with velocities close to that of the projectile itself. The lower right part shows that the TRAX simulation for He-like C-projectiles reproduces the measured data very well if the proper projectile charge state is accounted for. The structures visible in the measured spectra are C and O-Auger lines, which we did not include in the simulations. They can be attributed to adsorbents from the residual gas of the vacuum chamber. Only a fraction of the carbon Auger electrons from the carbon target is emitted from the target itself [3]. Although the C-Auger electrons from the other targets and the O-Auger electrons are emitted from the target surfaces, the lines exhibit very long low-energy tails that demonstrate the role of the back diffusion processes.

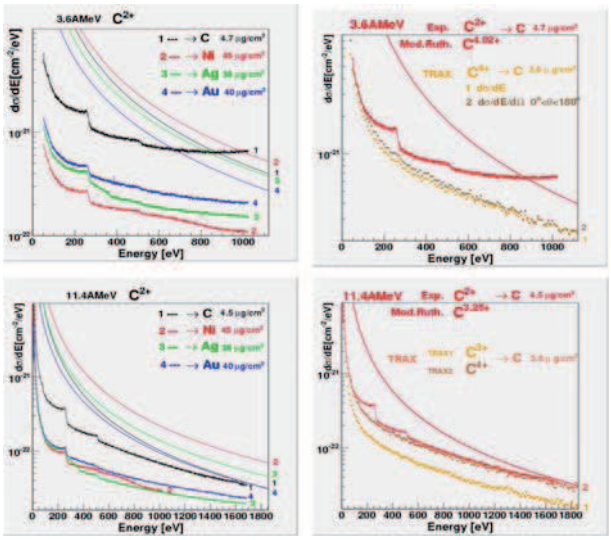

Figure 1: Electron emission yields for 3.6 and 11.4 carbon beam on various thin targets (cf. text for details).

Based on the present results, we have developed a detailed program for further investigations [3].

References

[1] N. Lineva et al. GSI Annual Report 2007

[2] M. Krämer Nucl. Instr. Meth. B **105** (1995) 14

[3] N. Lineva, PhD Thesis, TU Darmstadt, 2008
http://www.gsi.de/documents/DOC-2008-Aug-25-1.pdf

[4] N. Stolterfoth et al. *Electron...*, Springer, 1997, p.18ff

[5] J.P. Rozet et al. Nucl. Instr. Meth. B **107** (1996) 67

A High-Resolution Reaction Microscope for Storage Rings

D. Fischer*[1], K. Schneider[1], R. Moshammer[1], and J. Ullrich[1]
[1]Max-Planck-Institut für Kernphysik, Heidelberg, Germany

Reaction Microscopes (REMI) [1] enable kinematically complete experiments on atomic and molecular fragmentation processes by coincident and momentum resolved detection of recoiling target ions and emitted electrons. Thus, these devices represent the ideal tool to study with highest possible detail the many-particle dynamics in collisions of fast highly-charged ions with atoms or molecules. The implementation of Reaction Microscopes into ion storage rings like the ESR at GSI or the TSR at the MPI in Heidelberg (MPIK), which provide ion beams of unprecedented quality with respect to beam intensity, ion temperature, and emittance, offers completely new and unique possibilities. The combination of both techniques will, for the very first time, enable highly differential measurements of reaction channels with very small cross-sections.

In spring 2009 a Reaction Microscope equipped with a supersonic gas-jet target - a setup that has been operated before inside the ESR - will be inserted into the TSR and first experiments will be performed. Here, in particular the dynamics of electron-transfer reactions in ion-atom collisions will be of interest. The goal is to obtain first data on radiative electron capture (REC) differential in the projectile deflection angle. In addition, the kinematics of non-radiative capture shall be measured in coincidence with characteristic photons emitted from the outgoing, generally highly excited projectile in order to obtain spectroscopic information of highly-charged ions.

Furthermore, a new Emmy-Noether Junior Research Group - the 'PRIOC' group ('PRecision studies of IOn Collisions') headed by D. Fischer - will be launched at the MPIK, the University of Heidelberg, and the GSI in 2009. The work of this group will be devoted to the physics of ion-atom collisions and to electronic structure studies of highly charged ions in highest possible detail. To achieve that goal it is planned to install a Reaction Microscope equipped a laser-cooled, ultra-cold lithium target, provided by means of a magneto-optical trap (MOT), into the ESR storage ring. This will lead to an improvement in the momentum resolution of up to a factor of 10 compared to previous experiments using conventional supersonic gas-targets.

In the planned experiments, fully differential cross sections for singly ionizing ion-atom collisions shall be obtained. The high quality of the target, as well as its electronic structure, very much mimicking a H-like system, will help to unambiguously disentangle previously troubling discrepancies between experiment and theory. These issues have been prevalent in the past several years, and were partly traced back to electronic correlation in the initial state, as well as to the limited experimental resolution that could not be significantly improved with conventional gas-targets [2]. Additionally, kinematically complete information on double and triple ionization processes shall be gained for the first time for a three-electron target. The goal is the detailed investigation of the correlated five-particle Coulomb dynamics.

Finally, within the proposed research program, the development of a completely novel experimental approach is planned exploiting kinematic information of the collision in order to obtain high-precision spectroscopic data of highly charged projectiles. By observing collisions with projectile electronic excitation and by precisely determining the momenta of the involved particles, the excitation energy of the projectile can be derived with an accuracy, which will finally be limited only by the beam velocity uncertainty. Depending on the collision velocity and the observed reaction the achievable resolution can be by a factor of 2-10 higher than with conventional germanium detectors. If successful, this innovative kinematical method allows one to obtain precision spectroscopy data between ground state and excited levels of any ion species that can be stored in the ring with an accuracy comparable or even superior to all other optical or cooler recombination methods.

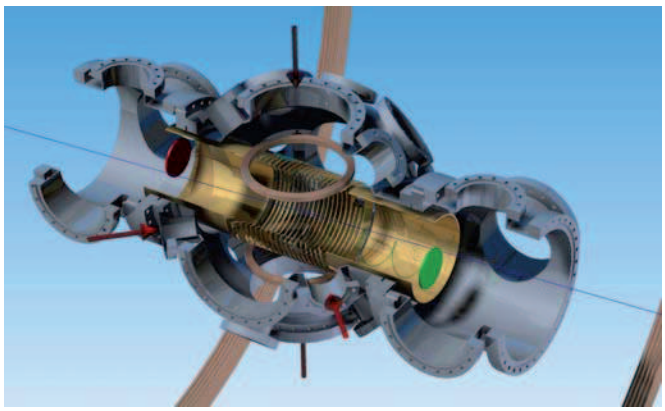

Figure 1: Design of the new MOTREMI setup. The ion beam (blue line) is intersected with the atomic lithium cloud in the center of the chamber. Recoiling lithium ions and electrons are extracted in opposite directions (red and green lines resp.) and detected by position-sensitive detectors.

References

[1] J. Ullrich et al., Rep. Prog. Phys. **66**, 1463 (2003)
[2] M. Schulz et al., Nature **421**, 48 (2003)

* fischer@mpi-hd.mpg.de

Towards a fully 3D spatial readout of a 2D-µstrip detector system

U. Spillmann[1,2], H. Bräuning[1], S. Heß[1,2] and Th. Stöhlker[1,3]
[1]GSI, Darmstadt, Germany; [2]IKF, University of Frankfurt, Germany; [3]PI, University of Heidelberg, Germany.

The x-ray spectroscopy program of the SPARC collaboration strongly relies on the availability of two-dimensional, time and energy sensitive Si(Li)- and Ge(i)-strip-detectors with their inherent advantages concerning spectroscopy and imaging capabilities as well as polarization sensitivity [1].

During the last years we successfully used this kind of detectors in combination with standard analog electronics in several experiments at the ESR [2]. The experience gathered in these experiments also showed that there is a need to measure the interaction depth of an incoming photon within the detector crystal which will help to avoid errors due to parallax. A second demand especially if the detector is to be used with the crystal spectrometer FOCAL is to reach a spatial resolution below 100µm. Here we will report on first tests to explore these additional features in planar microstrip detectors by employing analog readout electronics as well as digital pulse readout.

To estimate the depth resolution of our 2D microstrip Ge(i) detector (see [3] for a detailed description of the detector) one strip on each side of the detector was readout by conventional analog electronics. The preamplifier signal was split and amplified by a Buspla1600 Amplifier (GSI-development). The timing signal was filtered by a custom made bandpass filter and feed into a CFD followed by a TDC. The energy signal was amplified by a spectroscopy amplifier with a 3µs shaping time. The interaction depth can be derived from the drift time difference between the electron and holes to their respective contacts. Figure 1 shows the number of absorbed photons from a combination of Am-241 and Co-57 sources as function of this time difference, i.e. the interaction depth in the crystal. In addition the events which belong to the most prominent lines of the Am-241 (60 keV) and the Co-57 (122 keV) sources are shown. The exponential decline with the penetration depth as well as the shorter absorption length of the lower energetic line is clearly visible.

In our case the planar crystal has a thickness of 11 mm which leads to a drift velocity of roughly 10ns/mm. The resolution of the depth measurement may be estimated from the edges of the distributions. It was found that the error in the drift time measurement corresponds to a spatial resolution between 0.5 mm and 1.0 mm depending on the deposited energy.

To overcome present limitations of the analog readout electronics there is a strong trend in developing fully digital readout schemes. For first tests a preamplifier signal from a 16-fold Ge(i)-pixel detector was filtered, linear amplified and digitized by a PC-based Flash-ADC card (100Ms/s). The data was analyzed with an adapted Moving Window Deconvolution Algorithm (MWD). The result is shown in figure 2. With this setup a resolution of 1.7 keV at 60 keV as well as at 122 keV was obtained. For comparison the readout was also performed with an analog setup which gave an almost identical result of 1.6 keV at 60 keV.

Further developments of the digital readout together with a pulse shape analysis of signals induced on neighbouring strips are expected to result in an improvement of the position resolution better then the current strip width of 250µm.

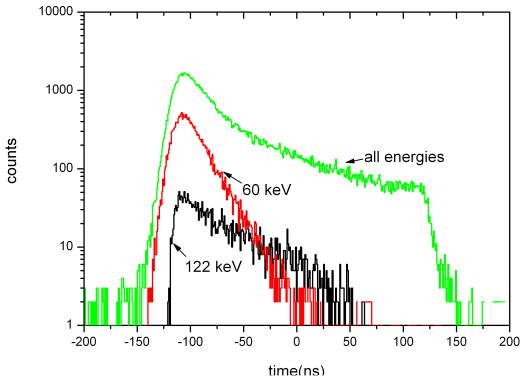

Figure 1: Absorption of x-rays for two different energies as function of depth in the detector represented by the drift time.

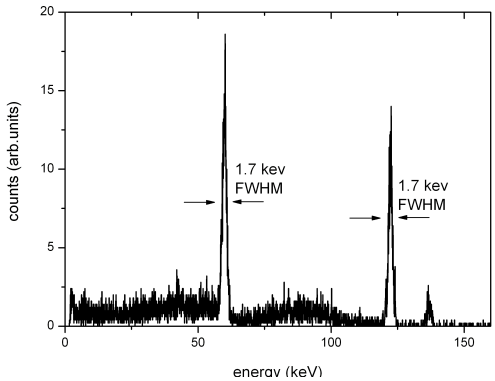

Figure 2: Energy spectrum derived from digitized preamplifier signals by use of a Moving Window Deconvolution Algorithm.

References

[1] Technical Report of the SPARC collaboration http://www.gsi.de/fair/experiments/sparc/index_e.html

[2] see for example G. Weber at al. and S. Heß et al., this report

[3] D. Protić, Th. Stöhlker, T. Krings, I. Mohos, U. Spillmann, IEEE TNS (2006) .

Tests with a cryogenically cooled target beam source at the ESR

N. Petridis[1,#], M. Kühnel[1], U. Popp[2], A. Kalinin[1], R. Dörner[1], T. Stöhlker[2,3] and R. E. Grisenti[1,*]
[1]IKF, J.W.G.-University Frankfurt; [2]GSI, Darmstadt; [3]Physikalisches Institut, Ruprecht-Karls-University, Heidelberg.

For the future storage-ring experiments at the FAIR facility besides a large target area density (10^{13}-10^{15} cm^{-2}) a small interaction length (<5 mm) is also required, especially for the low-*Z* gases hydrogen and helium. State-of-the-art internal targets are realized by producing a supersonic gas jet, i.e., by expanding a gas through a nozzle into vacuum, providing a target with a thickness < 10^{13} cm^{-2} spreading out over several millimeters in the interaction region. Recent experiments suggested that significantly higher target densities could be achieved by expanding the liquid at significantly lower temperatures [1]. In particular, a liquid discharged into vacuum delivers a uniquely functional target in the form of a droplet beam, where the droplet size, which can be as large as few micrometers, is univocally set by the source parameters, pressure and temperature. The larger the droplet size, the smaller the beam divergence because of mass conservation, and thus the higher the target density. The use of very small (≤ 5 µm) orifices is here mandatory in order to make the liquid target beam compatible with the high-vacuum conditions in a storage ring.

In order to verify the above predictions we have installed a cryogenically cooled liquid beam source at the current internal target station at the ESR at GSI [2]. This required a substantial modification of the main expansion chamber [3]. The source consists essentially of a compact (about 400 mm long) continuous flow cryostat, providing temperatures down to 4 K, mounted onto an x-y translational stage to allow a precise adjustment of the target beam axis.

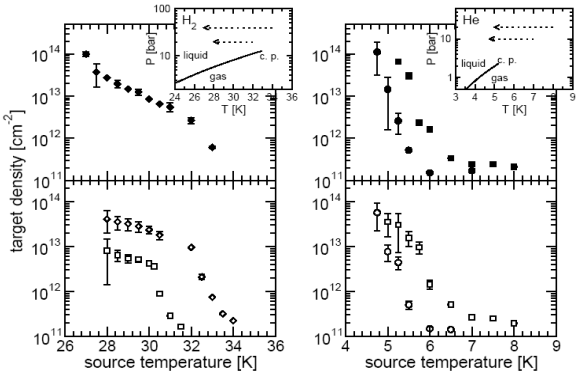

Fig. 1: Area densities of the hydrogen (left) and helium (right) liquid beams determined from dump pressure data as a function of the source temperature T_0 at P_0 = 10 bar (circle), 20 bar (square), and 40 bar (diamond). The nozzles had a nominal orifice diameter of 3 (closed symbols) and 5 µm (open symbols). The pictures in the right upper corners are the pressure-temperature phase diagrams of hydrogen and helium, respectively, showing the two-phase boundary line ending at the critical point (c. p.). The dotted arrows indicate the stagnation source conditions investigated during the present experiments.

The target area density has been determined from the pressure increase in the target dump [2] recorded in a wide range of source pressures and temperatures. To verify the reliability of the present method we additionally determined the target density from the radiative electron capture rate measured during collision with 150 MeV/*u* Xe^{54+} ions [3]. The good agreement between the two sets of data confirmed the validity of the present method for target density determination. Fig. 1 summarizes the measured area densities for the hydrogen and helium targets. The rapid increase in the density with decreasing source temperature is consistent with the expected exponential narrowing of the liquid beam as a function of the source temperature [1]. The highest area density achieved here is comparable with previous results for hydrogen [4] and represents an improvement of several orders of magnitude for the helium target. For all the stagnation source conditions the interaction length was constant and equal to about 5 mm as set by the current skimmer geometry [2,3].

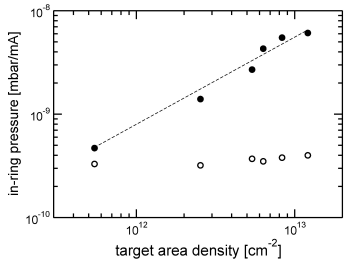

Fig.2: In-ring pressure measured as a function of the hydrogen area density prior to ion-beam injection (open symbols) and during the interaction with 150MeV/u Xe54+ ions (closed symbols). The dashed line is a fit to the experimental data (see text for details). The H_2 liquid beam was produced at P_0 = 40 bar and T_0 = 29.7 − 33K.

To address the crucial issue on the gas load in the interaction region during ion beam-target beam collisions we measured the in-ring pressure as a function of the target density. The results are shown in Fig. 2. The observed pressure increase is attributed to droplet fragmentation upon collision with the ion beam. This represents a major drawback and will necessarily require a differentially pumped interaction chamber.

References

[1] R. E. Grisenti and J. P. Toennies, Phys Rev. Lett. **90**, 234501-1 (2003)
[2] H. Reich *et al.*, Nuc. Phys. A626, **417c** (1997)
[3] M. Kühnel *et al.*, Nucl. Instr. And Meth. A (2009), doi:10.1016/j.nima.2008.12.212
[4] A. Khoukaz, T. Lister, C. Quentmeier, R. Santo, C. Thomas, Eur. Phys. J. D 5, (1999) 275

[#]petridis@atom.uni-frankfurt.de

*This research has been funded by the Helmholtz society under grant Nr. VH-NG-331, and by the BMBF under grant 06FY152I

Heavy, highly-charged ions at rest - The HITRAP facility

F. Herfurth*[1], W. Barth[1], M. Bevcic[1], M. Block[1], K. Blaum[2,3], L. Dahl[1], S. Eliseev[1,2], R. Fischer[1], P. Forck[1], M. Kaiser[1], O. Kester[1,4], H.-J. Kluge[1], C. Kozhuharov[1], S. Koszudowski[1], G. Maero[1], W. Quint[1], U. Ratzinger[5], A. Sauer[5], A. Schempp[5], A. Sokolov[1], T. Stöhlker[1,3], W. Vinzenz[1], G. Vorobjev[1], and D. Winters[1]

[1]GSI, Darmstadt, Germany; [2]MPI-K, Heidelberg, 69117 Heidelberg, Germany; [3]Ruprecht-Karls-Universität, 69120 Heidelberg, Germany; [4]NSCL/MSU, East Lansing, USA; [5]Goethe-Universität, Frankfurt, Germany

The HITRAP facility will deliver heavy, highly charged ions at very low energy and very well defined to precision experiments. These range from measurements with stored singe particles through stored clouds of particles to the interaction of a beam of highly charged ions with atomic or solid target. Examples are the measurement of the g-factor of the bound electron in hydrogen like system, very precise mass measurements to determine the electron binding energies, laser spectroscopy for a precise determination of the hyperfine structure of highly-charged ions or highly-charged-ion-surface interactions.

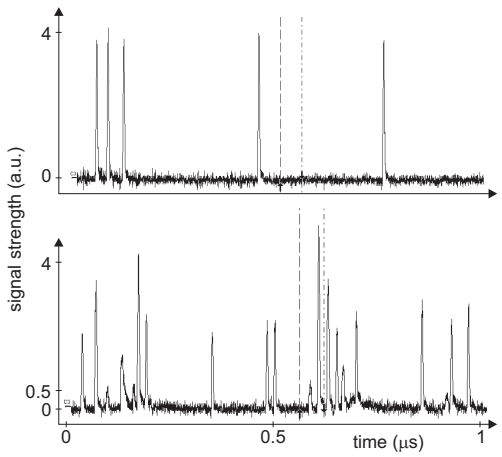

Figure 1: Signal detected at the diamond detector. The signal strength is proportional to the energy of the detected single particles. In the upper figure the IH structure is switched off so all the particles detected have an energy of 4 MeV/u. In the lower figure the IH is switched on and decelerated ions are visible.

The only way to produce intense low energy beams and samples of highly-charged ions up to bare uranium is to strip the inner electrons passing through a target at relativistic velocities. For that, the ions are first accelerated by the UNILAC and the SIS up to 400 MeV/u, sent through a stripper foil and then captured in the ESR. Here the first deceleration accompanied by electron cooling will take the beam from about 400 MeV/u down to 4 MeV/u. The beam is extracted in a single bunch and fed into the HITRAP linear decelerator. The linear decelerator consists of two decelerating structures, a radio-frequency quadrupole (RFQ) and an inter-digital H-type (IH) structure, and several bunchers for longitudinal phase space matching. The beam is decelerated in the IH structure from 4 MeV/u to 0.5 MeV/u and in the RFQ from 0.5 MeV/u to 6 keV/u. Then it is sent to a Penning trap for final deceleration and cooling.

HITRAP has been set up in the last years and most components have been installed by now. In detail, the first part of the decelerator, the IH-structure, has been installed in 2008 and the RFQ has been produced. It will be installed in the beginning of 2009. The installation's commissioning has been started and in 2008 two on-line tests of the IH structure were performed. It could be shown, that the IH decelerates particles from 4 MeV/u to 0.5 MeV/u. Figure 1 shows the measured signal on a diamond detector. A small fraction of the beam is decelerated.

The Penning trap electrodes, made from oxygen-free, high-conductivity copper, have been manufactured in the GSI workshops. They have been assembled to test the fitting accuracy of all parts. The test assembly of the inner electrodes is shown in fig. 2. After adaptation of all parts, the electrodes were gold plated and are in the final assembly stage.

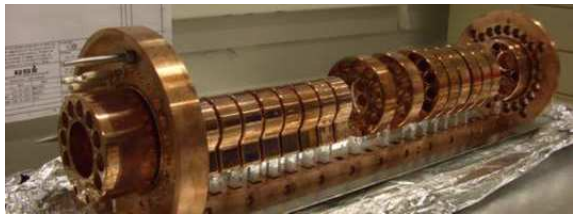

Figure 2: Electrodes of the cooler Penning trap.

After the ions enter the cooler Penning trap they will collide with simultaneously stored electrons and loose most of their energy. At about 10 eV the ions and electrons shall be separated before resistive cooling takes over. The source for the electrons has been built at the MPI-K in Heidelberg and the coils for the magnetic guiding field into the trap center are produced at GSI.

Extensive calculations have come to an end in 2008 and it was shown that the resistive cooling process also works for a large cloud of highly-charged ions, as for instance U^{92+}. However, the cooling process might take longer than anticipated until the ions reach the ultimative temperature, the environmental temperature of the trap, i.e. 4 K.

* F.Herfurth@gsi.de

Development of the SPECTRAP experimental setup for laser spectroscopy of cold & trapped HCI*

Z. Andjelkovic[1], B. Sommer[2], W. Nörtershäuser[1,2], M. Vogel[5], V. Hannen[3], R. Jöhren[3], D. Church[4], S. Bharadia[5], D. M. Segal[5], R. Thompson[5], G. Birkl[6], and the HITRAP collaboration[2]

[1]Institut für Kernchemie, Johannes Gutenberg-Universität, Mainz, Germany; [2]Gesellschaft für Schwerionenforschung, Darmstadt, Germany; [3]Westfälische Wilhems-Universität, Münster, Germany; [4]Texas A&M University, USA; [5]Imperial College London, UK; [6]TU Darmstadt, Germany

Several precision experiments are under development within the framework of the HITRAP facility at GSI Darmstadt. One of them is SPECTRAP, which aims to trap highly charged heavy ions in a Penning trap, cool them to cryogenic temperatures and measure their hyperfine structure by means of laser spectroscopy. The peculiarity of the setup is the split coil arrangement of the superconducting magnet which allows direct radial optical access to the trap center. Additionally, the setup can be used for electron capture cross-section measurements at low energies [1], g-factor measurements [2] or laser cooling [3].

Since the equipment experienced damage during transport from Lawrence Berkeley National Laboratory to GSI, both repair and modification of the SPECTRAP setup have been necessary. It was decided to replace the existing hyperbolic trap with a new open-endcap cylindrical Penning trap developed in collaboration with Imperial College London. Starting already in 2006, off-line tests of the trap electrode structure were performed at Mainz University. Work on the development of the spectroscopy laser system is done by the group of Gerhardt Birkl at TU Darmstadt, while the corresponding detectors are going to be provided by the University Münster.

In close cooperation with Stahl Electronics the work on designing the new electronic measurement and control system has begun. The main parts are high-Q induction coils for the tuned LRC circuit, ultra low noise amplifiers and various filters, all of them compatible with cryogenic temperatures and with low heat emittance. An overview is given in Fig.1. Testing of those components under cryogenic conditions is currently being performed, preparing them for final implementation underneath the trap. The trap itself experienced some modifications as well in order to house the newly designed components, and to fit into the superconducting magnet central bore.

A lot of effort was made to reduce the thermal load of the liquid helium container as much as possible. All the cables representing the only direct contact with the "outer world" were designed to have low thermal conductance. The internal structure of the magnet housing was covered with an additional layer of high reflectivity aluminium foil. Finally, a great deal of attention was directed towards achieving good vacuum inside the system, equally important also for the experiment and the measurements. At the moment the pressure is $4 \cdot 10^{-8}$ mbar and is expected to decrease by several orders of magnitude after cooling down.

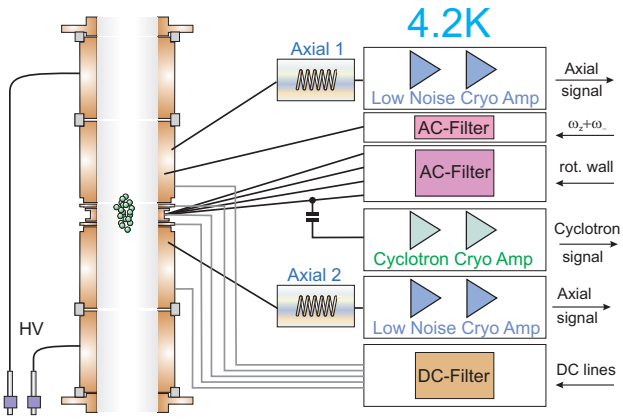

Figure 1: Overview of the cryogenic electronic parts and signal connections for operation of the Penning trap

Attachment of the SPECTRAP experimental setup to the HITRAP beam line is predicted for the coming year. Part of the beam line connecting directly to the magnet was constructed and tested with an off-line ion source. It comprises several ion optic, beam steering, analysis and detection components as well as supporting pumps and power supplies. Its integration to the magnet system is foreseen for the near future, after the first (successful) tests of the superconducting magnet and implementation of the trap and the cryo-electronics.

References

[1] G. Weinberg, B.R. Beck, J. Steiger, D.A. Church, J. McDonald, and D. Schneider, Phys. Rev. A **57**, 4452 (1998)

[2] W. Quint, D.L. Moskovkhin, V.M. Shabaev, M. Vogel, Phys. Rev. A **78**, 032517 (2008)

[3] M. Vogel and W. Quint, New Journal of Physics, in print (2009)

*Work supported by HGF under contract VH-NG-148 and the GSI F&E program.

Double-electron transfer with an ultra-cold atom target as a preparation for experiments at HITRAP

S. Götz[1], I. Blank[2], G. Hasan[2], R. Hoekstra[2], T. Mullins[1], W. Quint[1,4], A. Sokolov[1,4], R. Wester[3], and M. Weidemüller[1]
[1]Universität Heidelberg, Germany, [2]KVI Groningen, The Netherlands,
[3]Universität Freiburg, Germany, [4]GSI Darmstadt, Germany

We have set up an ultra-cold target of rubidium atoms combined with a recoil ion momentum spectrometer for kinematically complete scattering experiments at the GSI-HITRAP facility. First experiments will focus on multiple electron-transfer reactions in collisions of highly charged ions with many-electron atoms such as U^{92+} + Rb. In particular, we want to investigate correlation effects in multi-electron transfer which will serve as a model for dynamics in quantum mechanical many-particle systems.

Multiple-electron transfer has so far been investigated in many targets, where the initial momenta of the atoms limit the resolution on the recoil ion momentum. Laser-cooled targets, where temperatures down to a few hundreds of microkelvin can be reached, provide a stationary target which allows to measure the differential cross-sections in multiple charge transfer with very high accuracy [1]. Furthermore, full control over the internal state of the target can be obtained easily with optical pumping.

The ultra-cold target that we developed for the HITRAP experiments consists of an ultra-cold gas of rubidium atoms which are stored in a magneto-optical trap (MOT) in dark-SPOT configuration, reaching densities of 10^{11} cm^{-3} in a volume of 0.8 mm diameter. The temperature of the captured gas is around 100 μK which corresponds to momentum uncertainties of the individual target atoms of 0.01 a.u. The trap captures atoms of the isotope ^{85}Rb with nearly 100% isotope selectivity, and can, if desired, be changed to store ^{87}Rb. Furthermore, the dark-SPOT configuration allows storing the target atoms in a single hyperfine state of the electronic ground state with an efficiency of 99%.

The trap has been combined with a recoil ion momentum spectrometer. Classical over-the-barrier models [2] show that in collisions of U^{90+} and Rb(5s) at 9 keV/amu transfer of up to four electrons can be measured. Results of theoretical calculations are shown in figure 1 [3].

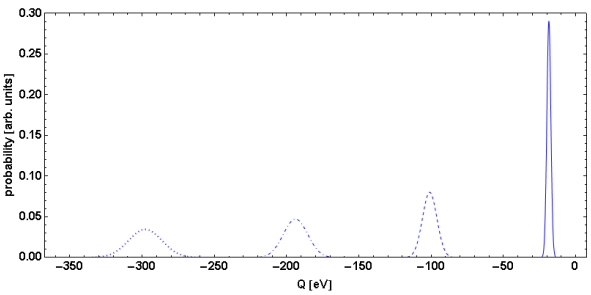

Fig. 1: From right to left: Q-Values for single, double, triple and quadruple electron transfer in collisions of U^{90+} and Rb(5s) at 9 keV/amu calculated with the classical over-the-barrier model.

The whole setup is fully transportable and can be implemented into various setups at GSI [4]. In preparation of the planned experiments at HITRAP we performed energy dependent experiments on double electron transfer in the system O^{6+} + Na in collaboration with the KVI Groningen. The results show two distinguished channels, where the dominant channel corresponds to sequential double capture of two electrons into asymmetric final channels with different principal quantum numbers (3lnl', n>4) [5]. A second channel populating the symmetric final states 3l3l' via correlated double electron capture has also been observed. The measured partial cross section ratio show the remarkable result that, despite the large difference in binding energies between the valence electron and the inner electron, about 15% of the double electron transfer takes place via correlated capture. In the energy range investigated, we could not observe any dependence on energy and thus on the interaction time. For further experiments we plan to increase the range of the collision energy.

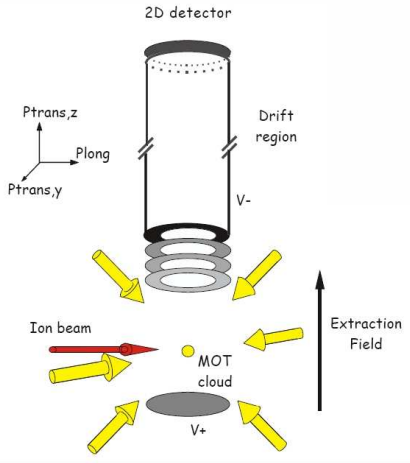

Fig 2: MOTRIMS setup where experiments on the energy dependence of double-electron transfer have been performed [6].

This work is supported by BMBF and the GSI F&E Programme.

References

[1] B. DePaola *et al*, Ad. in Atomic, Molecular and Optical Physics **55**, 139 (2008)
[2] A. Niehaus, J. Phys. B **19**, 2925 (1986)
[3] I. Blank, Diplomarbeit, Universität Freiburg (2008)
[4] W. Salzmann, Dissertation, Universität Freiburg (2007)
[5] S. Knoop *et al*. Europhys. Lett. **74** (6), pp. 992 -998 (2006)
[6] S. Knoop, Dissertation, Rijksuniversiteit Groningen (2006)

The ISOLTRAP Penning trap mass spectrometer*

G. Audi[1], D. Beck[2], K. Blaum[3,4], M. Breitenfeldt[5], R.B. Cakirli[6], R.F. Casten[7], S. Eliseev[3], S. George[3], F. Herfurth[2], A. Herlert[8], A. Kellerbauer[3], M. Kowalska[8], D. Lunney[1], E. Minaya-Ramirez[1], S. Naimi[1], D. Neidherr[9], M. Rosenbusch[5], S. Schwarz[10], L. Schweikhard[5], U. Warring[3], Ch. Weber[3], Yu. Novikov[11]

[1]CSNSM-IN2P3-CNRS, Orsay, France [2]GSI, Darmstadt, Germany, [3]MPI für Kernphysik, Heidelberg, Germany, [4]Ruprecht-Karls-Universität Heidelberg, Germany, [5]Ernst-Moritz-Arndt-Universität, Greifswald, Germany, [6]Istanbul University, Turkey, [7]WNSL, Yale University, New Haven, USA, [8]CERN, Geneva, Switzerland, [9]Johannes Gutenberg-Universität, Mainz, Germany, [10]NSCL, Michigan State University, East Lansing, USA, [11]PNPI, St. Petersburg, Russia.

The year 2008 was very successful for the ISOLDE Penning trap mass spectrometer ISOLTRAP [1]. The addressed physics topics included halo nuclei, the residual neutron-proton interaction, as well as nuclear astrophysics and neutrino-mass determination.

The final analysis was performed on data from many isotopic chains. To these belong masses of neutron-deficient Ne isotopes, including the two-proton halo candidate ^{17}Ne, used to derive precise charge radii with the ISOLDE collinear-spectroscopy setup. Both, the binding energies and the radii are very well described by theory and reveal a wealth of phenomena in the studied region. Additionally to the possible 2-proton halo structure of ^{17}Ne, a closed neutron shell is visible for ^{18}Ne, whereas ^{19}Ne and ^{20}Ne show clustering [2].

For application in nuclear astrophysics we completed the analysis of the ^{80,81}Zn [3] and ^{132,134}Sn [4] measurements, which restore the N=50 and 82 shell closures and allow refined calculations for the astrophysical process of rapid-neutron capture (r process). On the neutron-deficient side the analysis and the astrophysical calculations were finalized for the $^{99-110}$Cd isotopes, which have implications on the reaction path of the rp process (rapid proton capture) in stellar X-ray bursts.

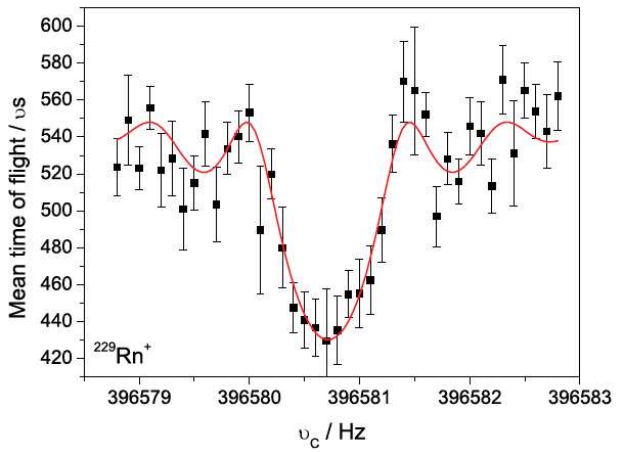

Figure 1: Time-of-Flight ion-cylotron-resonance of ^{229}Rn, a nuclide observed for the first time ever. The solid line is a fit of the expected line shape to the data points.

Measurements in 2008 yielded the masses of $^{143-146}$Xe and $^{223-229}$Rn, 11 of which were determined for the first time. We used those data to investigate the residual neutron-proton interaction, reflected in the so called dVpn values, far from stability. A unique pattern in the dVpn values was revealed in the Rn chain, which might be connected to octupole deformation known to exist in this region of the nuclear chart. In addition, a new nuclide, ^{229}Rn, was identified for the first time in a Penning trap, the production of which was enhanced by the use of a new, highly-efficient arc-discharge ion source [5].

In 2008 we also investigated the mass of ^{126,128}Cd with relevance for astrophysical questions and the N=82 shell closure. Masses of the orbital electron-capture nuclides ^{194}Hg and ^{202}Pb and their daughters were also studied with the goal to determine their Q-values accurately. These values are expected to be some of the smallest among a great variety of known electron-capture precursors. Therefore, they are possible candidates for a new approach to determine the electron neutrino mass.

On the technical side, the experimental setup was maintained thoroughly and improved considerably in 2008. The latest version of the control system was implemented, which automates many activities. A new alkali reference source was installed, and the carbon-cluster laser ion source was remodelled. Using these two ion sources investigations of systematic uncertainties for mass determinations were started, with the aim to push down the present residual systematic limit of $\delta m/m = 8 \cdot 10^{-9}$. Also, different excitation schemes in the purification Penning trap were performed. Towards the end of the year, first trial towards trap-assisted decay spectroscopy was undertaken.

In 2009 we plan to continue the activities started in 2008, including the investigation of the masses of ^{202}Pb/Tl and ^{130}Cd, and mass measurements assisted by decay spectroscopy. Two new proposals will be presented to the INTC committee, devoted to masses of short-lived rare-earth nuclides and noble gases.

[1] M. Mukherjee et al., Eur. Phys. J. A 35, 1 (2008)
[2] W. Geithner et al., Phys. Rev. Lett. 101, 252502 (2008)
[3] S. Baruah et. al, Phys. Rev. Lett. 101, 262501 (2008)
[4] M. Dworschak et al., Phys. Rev. Lett. 100, 072501 (2008).
[5] L. Penescu et al., Nucl. Instrum. Methods B 266, 4415 (2008)

* Work supported by EU, EURONS contract No. 506065.

TRIGA-TRAP: A Penning trap mass spectrometer at the nuclear research reactor TRIGA Mainz*

Sz. Nagy[1], K. Blaum[1], K. Eberhardt[2], M. Eibach[2], F. Herfurth[3], J. Ketelaer[1], J. Ketter[4], K. Knuth[4], W. Nörtershäuser[2], and C. Smorra[5]

[1]Max-Planck-Institut für Kernphysik, Saupfercheckweg 2, D-69117 Heidelberg; [2]Universität Mainz, Institut für Kernchemie, Fritz-Strassmann Weg 2, D-55128 Mainz; [3]GSI Helmholtzzentrum für Schwerionenforschung, Planckstraße 1, D-64291 Darmstadt; [4]Universität Mainz, Institut für Physik, Staudingerweg 7, D-55128 Mainz; [5]Universität Heidelberg, Physikalisches Institut, Philosophenweg 12, D-69120 Heidelberg

The mass is one of the most primary properties of a nucleus, a key input to understand the nuclear structure of rare isotopes, in particular of exotic nuclei far away from stability. The research reactor TRIGA Mainz provides access to a large variety of neutron-rich nuclides produced by thermal-neutron induced fission of an actinide target. Recently, the double-Penning trap mass spectrometer TRIGA-TRAP has been installed to perform high-precision mass measurements on these fission products on-line, and on actinides off-line [1]. Important experimental data will be provided for tests of mass models, and for astrophysical calculations on nucleosynthesis processes. Samples of actinides from uranium to californium are available for off-line mass measurements. Masses of most transuranium nuclides have not been determined directly, but are deduced from alpha-decay energies and systematic trends. TRIGA-TRAP will provide several anchor points to link alpha-decay chains to the mass scale in the actinide region. Besides the physics program, TRIGA-TRAP also serves as a test setup for the development of new ion-detection techniques [2] which will be implemented either at SHIPTRAP (GSI, Darmstadt) [3] or at future facilities like MATS at FAIR.

Assembling of the Penning trap setup in a 7 T superconducting magnet has been completed in the beginning of 2008. For commissioning the experimental setup, a surface ion source providing $^{133}Cs^{+}$ ions is installed. For calibration purposes, a non-resonant laser ablation ion source, recently developed in our group, has been set up, which provides a large variety of absolute mass references via carbon cluster ions up to C_{24}^{+}. Beside carbon clusters the same source can be used to produce ions of certain transuranium elements. Fig. 1 shows a time-of-flight resonance for C_{20}^{+} ions recorded by employing the Ramsey-technique. To avoid damping by the residual gas, a total excitation time of only 300 ms was used. The center frequency, which is related to the mass via $\nu_c = qeB/(2\pi m)$ has been determined to be 447837.860 ± 0.007 Hz.

TRIGA-TRAP is the only on-line Penning trap mass spectrometer where in addition to the destructive time-of-flight detection, a non-destructive ion detection system is implemented, based on the detection of image currents with single-ion sensitivity [2]. Its major part is a superconducting coil with a quality factor of about 1000 when connected to the trap setup. In order to reduce the thermal noise and to improve the vacuum conditions in the Penning traps, the trap system is operated at a temperature of 77 K.

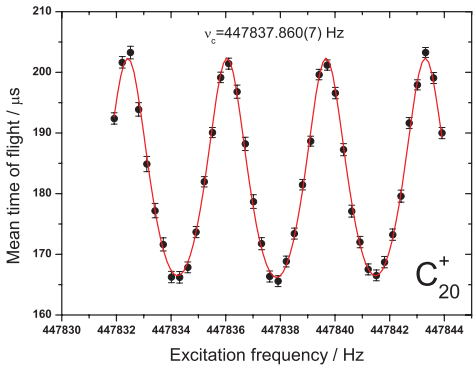

Figure 1: Time-of-flight cyclotron resonance of C_{20}^{+} obtained with a 300 ms Ramsey excitation at TRIGA-TRAP.

For the on-line coupling of the mass spectrometer to the TRIGA reactor, an ECR ion source will be installed in combination with a helium gas jet and a carbon aerosol arrangement, carrying the fission products from the target chamber at the reactor core to the ion source. First fission products have been already transported from a test target and analysed by a gamma detector. Presently, the high-voltage platform for the ion source and the ion optics to the experiments including a 90- degree high-resolution mass separator magnet are under construction.

TRIGA-TRAP, the only Penning trap mass spectrometer installed at a research reactor, has become operational in the second half of 2008 and all systematic checks are completed using carbon cluster ions. First precision mass measurements on rare-earth nuclides have been performed at the end of 2008. The first neutron-rich nuclides will be investigated after the on-line coupling is commissioned by the end of 2009.

References

[1] J. Ketelaer *et al.*, Nucl. Instr. Meth. A **594** (2008) 162

[2] R. Ferrer *et al.*, Eur. Phys. J. Special Topics **150** (2007) 347348

[3] M. Block *et al.*, Eur. Phys. J. A **25** (2005) 49

*Work supported by HGF contracts No. VH-NG-037 and No. VH-NG-148, BMBF contract No. 06MZ215, and Stiftung Rheinland-Pfalz für Innovation contract No. 854

Status of the *g*-Factor Experiment on Highly-Charged Calcium*

A. Wagner† [1], K. Blaum,[1], W. Quint[2], B. Schabinger[3], S. Sturm[3], and G. Werth[3]

[1]MPI für Kernphysik, D-69117 Heidelberg, Germany; [2]GSI, D-64291 Darmstadt, Germany; [3]Institut für Physik, Johannes Gutenberg-Universität, D-55099 Mainz

High-precision measurements of the gyromagnetic factor (*g*-factor) of the electron bound in highly-charged ions allow for a stringent test of bound-state quantum electrodynamics (BS-QED) calculations [1]. Therefore, it is planned to measure the *g*-factor of lithium- (Ca^{17+}) and hydrogen-like (Ca^{19+}) calcium in a triple Penning trap setup. In the last year substantial progress was achieved: after major technical developments including new cryogenic low-noise amplifiers, first frequency measurements on single ions have been performed.

Target

The setup is completely closed and operated at liquid-helium temperature (T=4.2 K) in order to obtain an excellent vacuum ($p \simeq 10^{-15}$ mbar) for long storage times of the ions and to keep the Johnson noise of the detection electronics as low as possible. Therefore, the ions are produced inside the trap by a miniature EBIT/S [2]. Since only a few calcium ions could be produced in the trap with the formerly used CaF_2-target, it was exchanged against a metallic calcium target.

Axial amplifier

A new axial amplifier with a significantly improved noise performance (400-800 pV/$\sqrt{\text{Hz}}$ at 4 K) compared to the previous system (3-6 nV/$\sqrt{\text{Hz}}$ at 4 K) has been designed (see Fig. 1). Accordingly, and due to a stronger coupling to the resonator, the signal-to-noise ratio for the ion detection will improve and it is expected to be able to detect ions without any excitation corresponding to an ion temperature of 4.2 K instead of previously required 60 K. Furthermore, the power consumption is reduced from 12-14 mW to 4-5 mW, resulting in a much lower helium evaporation rate.

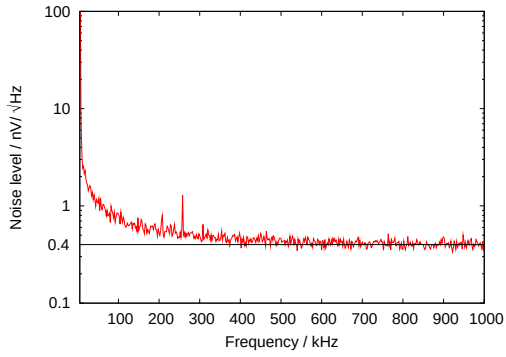

Figure 1: Noise level of the new axial amplifier at a temperature of 77 K and with a power consumption of 9 mW. The small peaks are not caused by the amplifier but by the test setup. The higher noise level at low frequencies is due to the $1/f$-noise.

Frequency measurements on single ions

The axial frequency and the reduced cyclotron frequency have been measured with single ions by the single- and double-dip-technique [3], respectively (see Fig. 2), as well as with direct methods. Knowing these two frequencies, the free cyclotron frequency was calculated, which again was used to determine the magnetic field.

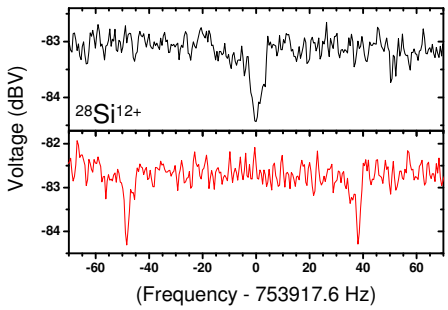

Figure 2: Single and double axial frequency dips in the precision trap on $^{28}Si^{12+}$ ions. Being in resonance with the detection tank-circuit, the ion in the trap short-cuts the Johnson noise of the tank-circuit and a dip in the noise-spectra can be detected. The axial frequency can be obtained by determining the position of the minimum. The cyclotron motion (ω_+) of the ion can be coupled to its axial motion (ω_z) by irradiating $\omega_+ - \omega_z$. The axial signal then splits into two dips (lower panel). Knowing the axial frequency, one can extract the cyclotron frequency from the position of the two dips for different detunings.

References

[1] G. Werth *et al.*, Int. J. Mass Spectrom. **251**, 152-158 (2006)

[2] B. Schabinger *et al.*, J. Phys. **58**, 121-124 (2007)

[3] H. Häffner *et al.*, Eur. Phys. J. D **22**, 163-182 (2003)

* Work supported by HGF under contract VH-NG-037 and DFG under contract Vo-980-1.

† ankewag@uni-mainz.de

Towards a measurement of the (anti)proton g-factor*

S. Kreim†[1], K. Blaum[2], H. Kracke[1], A. Mooser[1], C. Mrozik[1], W. Quint[3,4], C. C. Rodegheri[1], S. Ulmer[4], and J. Walz[1]

[1]Institut für Physik, Johannes Gutenberg-Universität, 55099 Mainz, Germany; [2]Max-Planck Institut für Kernphysik, Saupfercheckweg 1, 69117 Heidelberg, Germany; [3]Helmholtzzentrum für Schwerionenforschung GmbH, 64291 Darmstadt, Germany; [4]Ruprecht Karls-Universität, 69047 Heidelberg, Germany

This experiment is aimed at measuring the magnetic moment or g-factor of a single, isolated proton stored in a cylindrical Penning trap with a relative uncertainty of below 10^{-9} [1]. It will be conducted in a double Penning trap and constitutes the first direct and self-contained measurement ever performed. Besides the proton g-factor, future experiments aim at determining the antiproton g-factor. Comparison of the two experimental values will provide a stringent test of CPT invariance on the baryonic sector.

The g-factor results from an accurate measurement of its cyclotron (ν_c) and spin precession frequency (ν_L): $g = 2\,\nu_L/\nu_c$. The former being deduced from the eigenfrequencies (ν_i) of the particle motion in the trap using the relation $\nu_c^2 = \nu_+^2 + \nu_z^2 + \nu_-^2$ [2], where the eigenfrequencies will be measured by detecting the image currents induced in the trap electrodes. Since the spin motion is an internal degree of freedom, a magnetic bottle is exploited to imprint the spin state information onto an external degree of freedom, namely the axial eigenmotion of the particle. This so-called continuous Stern-Gerlach effect is used to detect the resulting frequency shift and thus the spin state non-destructively [3]. The value of the frequency shift scales with the magnetic moment of the particle and the strength of the magnetic bottle. Thus, a novel trap design was developed, which we call *hybrid Penning trap* [4], to increase the axial frequency jump to a detectable range.

To realize a high-precision experiment, long storage times are required which is realized by performing the experiment in a closed horizontal setup at cryogenic temperatures yielding an extremely low background pressure ($p < 10^{-13}$ mbar). The double Penning trap installed in a 1.8 T superconducting magnet is housed in the trap chamber, in which a temperature of 3.9 K is reached using a low vibrational Gifford-MacMahon pulse tube cooler. Protons are created from a black polyethylene target inside this sealed system by electron beam impact ionization. The experimental environment bears great challenges for the electronics needed to non-destructively detect the trapped proton, however, it leads to a low electronic noise. To obtain a high signal-to-noise ratio (SNR), a detection system with a high quality factor Q is required. For the detection of the axial frequency at $\nu_z = 680$ kHz a Q-value of $Q_z = 5500$ is reached using a resonator with coil and shield made out of type II superconducting NbTi. This permits placing the detector near the trap in the high magnetic field thus reducing parasitic capacitances and further increasing the SNR. The detection system further consists of a low noise cryogenic FET amplifier ($\epsilon_n^z = 1.9\,\mathrm{nV}/\sqrt{\mathrm{Hz}}$) and an amplifier at 300 K. A Q-value of $Q_+ = 1039$ is achieved for the cyclotron frequency at $\nu_+ = 29$ MHz. The resonator made out of copper is placed inside the trap chamber together with the cryogenic amplifier ($\epsilon_n^+ = 0.7\,\mathrm{nV}/\sqrt{\mathrm{Hz}}$). To render possible a high-precision measurement, a highly accurate voltage source with a stability of 1 ppm/K feeds the trap electrodes.

Commissioning experiments with the complete setup were performed and the control system was put into operation. The performance of the trap tower and the thermal behavior of electronic components were examined. We are now able to produce, store, and detect particle clouds. Undesired species are removed by lowering the trap potential while applying a strong dipolar axial excitation. A single proton is prepared by successively removing particles via cyclotron excitation from an anharmonic trap. Fig. 1 shows the noise spectrum of the cyclotron detection circuit after the proton has been excited in the precision trap.

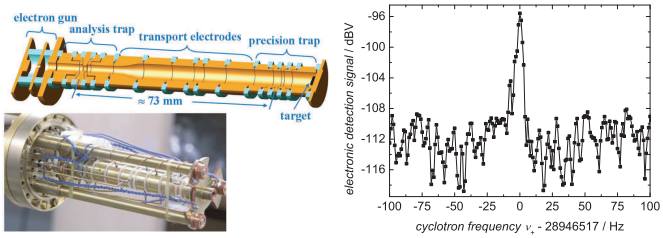

Figure 1: Double Penning trap and noise spectrum of the cyclotron detection unit with a single proton.

Future advancement consists in adiabatic transport between the traps, inducing spin-flip transitions, and detecting the axial frequency shift. Furthermore, the hybrid trap design enables a variety of new experiments such as investigating the magnetic moments of the antiproton and other bare light nuclei like ^{3}He or tritium.

References

[1] W. Quint *et al.*, NIM B **214**, 207-210 (2004)

[2] L. S. Brown and G. Gabrielse, Rev. Mod. Phys., **58**, 233-311 (1986)

[3] H. G. Dehmelt, Proc. Natl. Acad. Sci. USA, **83**, 2291 (1986)

[4] J. Verdú *et al.*, New J. Phys. **10**, 103009 (2008)

* Work supported by DFG, QU 122/3, HGF, VH-NG-037, and Alβan, no. E06D101305BR.

† kreim@uni-mainz.de

Design of an Asymmetric Cylindrical Penning Trap for Bound-Electron g-Factor Measurements

N.P.M. Brantjes[1], D. von Lindenfels[2], D.L. Moskovkin[3], W. Quint[1,2], V.M. Shabaev[3], and M. Vogel[1,4]

[1]GSI, Darmstadt, Germany; [2]Univ. Heidelberg, Germany; [3]Department of Physics, St. Petersburg State University, Russia; [4]Department of Physics, Imperial College London, UK

In the current contribution, we present recent experimental developments for bound-state QED tests and/or fundamental constants via double-resonance laser spectroscopy, in combination with trapped hydrogen-like heavy ions. We here present the experimental design for accurate measurements of the g_F factor of a high–Z hydrogenlike ion (nucleus with spin) [1, 2, 3].

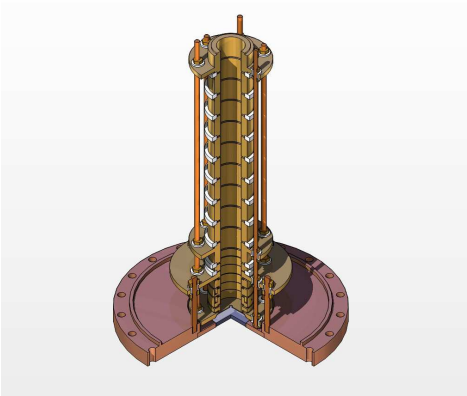

Figure 1: Penning trap design for double-resonance spectroscopy. The capture trap is on top, the precision trap is on the bottom.

Briefly, a mass and charge-state selected ensemble of cooled and bunched highly charged ions from the HITRAP facility will be injected into a cryogenic Penning trap (Figure 1) designed for laser and microwave spectroscopy. The ions will remain cooled at a motional temperature of 4 K and excited by a combination of laser and microwave irradiation. The fluorescence signal will be detected axially.

We consider a hydrogenlike ion of high nuclear charge, whose nucleus has a spin, in a magnetic field. In this case, every hyperfine sublevel splits up into individual Zeeman components. The double-resonance scheme in this case involves (i) microwave transitions among the Zeeman sublevels of the hyperfine level, and (ii) laser-induced, optical transitions among the hyperfine levels of the hydrogen-like ion. The g_F factor of the electron can thus be determined with unprecedented accuracy.

As an example, the case of bismuth $^{209}Bi^{82+}$ is depicted in Figure 2. The level scheme allows a population of states with extremal m_F by optical pumping.

An initial population of the ($F = 4$, $m_F = -4$) state

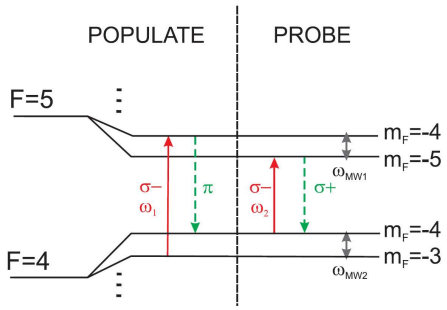

Figure 2: Scheme of the Zeeman-split hyperfine energy levels in the ground state of a hydrogen- like ion with $I = 9/2$. Solid arrows indicate excitation lasers or microwaves. Note the inverted m_F level ordering due to the negative g_F-factor of the $F = 4$ level.

can be obtained by irradiation of σ^- light at a frequency ω_1. When the population is reached, the corresponding fluorescence including the π-fluorescence light is maximum. When microwave radiation at frequency ω_{MW2} comes into resonance with the ($F = 4, m_F = -4 \leftrightarrow -3$) transition as shown in Figure 2, the σ^+ fluorescence disappears. Thus, from a scan of the $\sigma+$-fluorescence as a function of ω_{MW2} the corresponding g_F-factor can be inferred. By combining the Zeeman splitting for two different hyperfine levels of the ion's ground state, the electronic as well as the nuclear g-factor can easily be disentangled.

An experiment using a double-resonance scheme will thus allow precise determinations of g-factors in the ion of interest. This allows sensitive tests of corresponding calculations of the transition energy and lifetime, especially of contributions coming from bound-state QED. As compared to the continuous Stern–Gerlach effect, we expect much better statistics and envisage accurate measurements on an accuracy level of 10^{-9} and beyond.

This work is supported by the IMPRS School on Quantum Dynamics and the EU INTAS Programme.

References

[1] V.M. Shabaev, J. Phys. B **27**, 5825 (1994).

[2] V.M. Shabaev *et al.*, Phys. Rev. A **56**, 252 (1997).

[3] D.L. Moskovkin *et al.*, Phys. Rev. A **70**, 032105 (2004).

Multipole-mixing effects on the angular distribution of the dielectronic satellite lines from high-Z ions

S. Fritzsche*[1,2], N. M. Kabachnik[2,3], Th. Stöhlker[2,4], and A. Surzhykov†[2,4]

[1]Frankfurt Institute for Advanced Studies; [2]GSI, Darmstadt; [3]Institute of Nuclear Physics, Moscow State University; [4]University of Heidelberg

In the dielectronic recombination (DR), a free (or quasi-free) electron is resonantly captured by an ion under the excitation of one or several bound electrons, and is stabilized afterwards due to photoemission. For many years, this resonant capture process has attracted much interest, both by experiment and theory, since it helps to explore relativistic and quantum electrodynamical (QED) effects on the electronic structure of heavy atomic systems. In order to investigate these effects, a number of DR experiments have been carried out recently by applying relativistic collisions of highly-charged projectile ions. At the GSI storage ring ESR, for example, the $K-LL$ resonant transfer and excitation of (finally) helium-like uranium U^{90+} ions and their subsequent radiative decay have been studied in detail [1]. While most of the measured data are generally well understood within the framework of Dirac's relativistic theory, a considerable discrepancy was found for the angular distribution of the $K\alpha_1$ hypersatellite radiation following the $K-L_{1/2}L_{3/2}$ resonant electron capture [2].

In all previous theoretical investigations, however, only the electric-dipole (E1) radiation has been taken into account in analyzing the angular distribution of the Kα_1 lines. To understand the role of the higher, non–dipole terms in the electron–photon interaction we re–investigated the angular properties of the characteristic radiation following the DR of high-Z ions. By making use of the density matrix theory, we derived in particular a general expression for the angular distribution of the hypersatellite HS photons emitted in the $|\alpha_d J_d\rangle \rightarrow |\alpha_f J_f\rangle + \gamma^{HS}$ decay [3]

$$W^{\rm dec}(\theta) \;=\; \frac{\Gamma_{df}}{4\pi}\left(1+\sum_{k=2,4,..}\beta_k P_k(\cos\vartheta)\right)\,, \quad (1)$$

and wherein the anisotropy parameter

$$\beta_k \;\equiv\; \beta_k(\alpha_d J_d, \alpha_f J_f) = f_k(\alpha_d J_d, \alpha_f J_f)\,\mathcal{A}_{k0}(\alpha_d J_d)$$

depends both on, the alignment $\mathcal{A}_{k0}$ of the excited ionic states as produced by the resonant capture as well as the structure function f_k, which accounts for the interference between the allowed decay channels. In Eq. (1), moreover, $\Gamma_{df} \;\equiv\; \Gamma_{\alpha_d J_d \rightarrow \alpha_f J_f}$ denotes the decay rate of this HS transition, while $P_k(\cos\vartheta)$ is the Legendre polynomial of order k.

Our computations, based on Eq. (1) and the explicit form of the structure function (cf. Ref. [3]), clearly show that the interference between the multipole components can strongly decrease or enhance the anisotropy of the individual fine-structure transitions, including changes up to a factor of 6. Figure 1, for example, displays the angular distribution of the two HS lines $2s_{1/2}2p_{3/2}\ (J=2) \rightarrow 1s_{1/2}2s_{1/2}\ (J=1)$ (left panel) and $2s_{1/2}2p_{3/2}\ (J=1) \rightarrow 1s_{1/2}2s_{1/2}\ (J=1)$ (right panel) for helium-like uranium following the DR into (initially) $U^{91+}\,(1s_{1/2})$ ions. While, within the E1 approximation (dashed lines), an anisotropy of $\beta_2(2s_{1/2}\,2p_{3/2}\ J=2 \rightarrow 1s_{1/2}2s_{1/2}\ J=1) = -0.373$ and $\beta_2(2s_{1/2}\,2p_{3/2}\ J=1 \rightarrow 1s_{1/2}2s_{1/2}\ J=1) = 0.324$ was found, this becomes -0.479 and 0.046, respectively, if the magnetic-quadrupole (M2) contributions are taken into account. For the latter transition, we therefore expect an almost isotropic emission despite of the rather strong alignment $A_{20} = -0.918$ of the $2s_{1/2}2p_{3/2}\ (J=1)$ resonance.

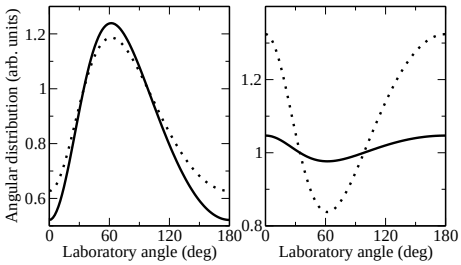

Figure 1: Angular distribution of the $2s_{1/2}2p_{3/2}\ (J=2) \rightarrow 1s_{1/2}2s_{1/2}\ (J=1)$ (left panel) and $2s_{1/2}2p_{3/2}(J=1) \rightarrow 1s_{1/2}2s_{1/2}\ (J=1)$ (right panel) transitions of helium-like uranium ions following the $K-LL$ DR. Calculations are performed within the electric-dipole approximation (dotted line) and by taking into account all allowed multipoles (solid line).

Up to the present, unfortunately, a direct comparison of the calculated angular distribution with measured data is difficult to be carried out for the K$\alpha_{1,2}$ (fine-structure) HS lines because of the unsufficient experimental resolution. We therefore suggest experiments with higher resolution in the x-ray spectra and with the excitation of just *one* of the $K-LL$ resonances in order to better understand the effects of higher multipoles and relativity on the (DR) population and decay mechanisms of high-Z ions.

References

[1] X. Ma et al., Phys. Rev. A **68** (2003) 042712.

[2] S. Zakowicz et al., Phys. Rev. A **68** (2003) 042711.

[3] S. Fritzsche et al., Phys. Rev. A **77** (2008) 032703.

* Support by GSI under the project No. KS-FRT.

† Work supported by the Helmholtz Gemeinschaft (VH-NG-421).

Polarization correlation in the two–photon decay of heavy ions

A. Surzhykov[1,2], S. Fritzsche[2,3], T. Radtke[4], and Th. Stöhlker[1,2]

[1]University of Heidelberg; [2]GSI, Darmstadt; [3]Frankfurt Institute for Advanced Studies; [4]University of Kassel

Since the early days of quantum mechanics, the two–photon transitions in hydrogen–like ions have been the subject of intense experimental and theoretical studies. For many years, these studies have mainly dealt with the two–photon decay rates, energy and angular distributions. More recently, moreover, interest was focused on the polarization–resolved analysis of the two–photon emission. For example, a number of experiments have been performed in order to analyze the polarization correlations between the photons emitted in the decay of neutral hydrogen or low–Z ions [1]. In contrast, much less attention has been previously paid to the high–Z domain. A first step towards the two–photon polarization studies with heavy, few–electron ions is likely to be carried at the GSI facility where significant progress has been recently achieved in development of x–ray polarization detectors [2]. By making use of these detectors it becomes possible today to measure both (i) the correlated spin state of two photons (polarization entanglement) and (ii) the polarization of only one of the photons measured in coincidence with the other one.

To better understand the polarization effects in the two–photon emission from heavy ions we have recently re–investigated the decay of metastable hydrogenic states in view of the photon spin properties [3]. The theoretical analysis has been performed within the framework of the Dirac's relativistic equation and the density matrix approach. By making use of such an approach we were able to obtain an "angle–polarization" correlation function which characterizes the *linear polarization* of one of the photons if measured in coincidence with the second one whose spin states remain unobserved. For the well–known $2s_{1/2} \rightarrow 1s_{1/2}$ two–photon transition, for example, we found a simple analytical expression for the (degree of) linear polarization of the emitted radiation:

$$P_L(\theta) = -\frac{\sin^2\theta}{1+\cos^2\theta}\,, \qquad (1)$$

where θ is the angle between the photon directions (opening angle). Eq. (1) has been obtained, however, within the electric dipole (2E1) approximation for the interaction between the electron and the radiation field. This dipole approximation is known to be valid for analyzing the polarization properties of light emitted in the two–photon decay of low–Z ions. It has to be questioned though, whether this approximation also applies for the medium– and high–Z domain where rather large contributions are expected from the retardation in the electron-photon interaction. For the two–photon angle–angle correlations, for example, a significant change is known to arise from the higher multipoles and may lead to quite sizeable deviations when compared with the dipole approximation [3].

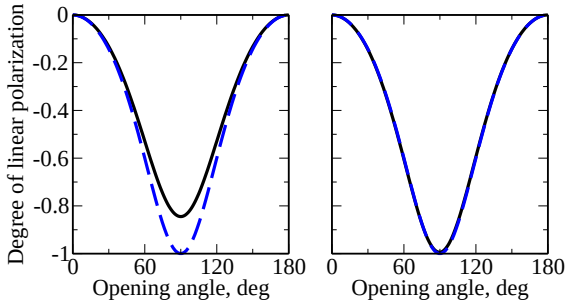

Figure 1: Degree of linear polarization of the photons emitted in the $2s_{1/2} \rightarrow 1s_{1/2}$ two–photon decay of hydrogen–like uranium U^{91+} as function of the opening angle θ. Results are presented for the exact relativistic theory (solid line) as well as the non–relativistic dipole approximation (dashed line) and for the energy sharing x = 0.1 (left panel) and x = 0.3 (right panel). From Ref. [3].

For the $2s_{1/2} \rightarrow 1s_{1/2}$ two–photon transition in hydrogen–like U^{91+} ions, we have applied both, the electric-dipole approximation (1) and an exact relativistic treatment which accounts for a full multipole decomposition of the radiation field in order to calculate the polarization properties of emitted x–rays. Fig. 1 displays the degree of linear polarization of the *low–energy* photon measured in coincidence with the *high–energy* one. As seen from the figure, the higher non–dipole terms may result in a reduction of the photon linear polarization; the effect which can be observed however only, if the major fraction of the (two–photon) transition energy is carried away by a single photon. For the energy sharing $x = 0.1$ and for the perpendicular photon emission (θ = 90°), for example, the degree of linear polarization decreases from P_L = -1 to almost P_L = -0.8 if the higher multipoles are taken into account. In contrast, when the parameter x increases towards the value x = 0.5 which refers to an equal energy sharing of two photons the non–dipole effects almost disappear. Since the emission of two photons with equal energies is known to be most probable our results imply that the simple analytical expression (1) can be used for the analysis of the forthcoming experiments on polarization properties of two–photon x–ray emission from high–Z ions.

Work is supported by GSI and Helmholtz association under the project VH–NG–421.

References

[1] H. Kleinpoppen *et al.*, Phys. Scr. **T72**, 7 (1997)

[2] S. Tashenov *et al.*, Phys. Rev. Lett. **97**, 223202 (2006)

[3] A. Surzhykov *et al.*, Eur. Phys. J.: ST, *in press*

Parity nonconservation effects with polarized beams of highly charged ions*

A. Bondarevskaya[1], L. Labzowsky[1,2], G. Plunien[3], D. Liesen[4], and F Bosch[4]

[1]St.Petersburg State University, St. Petersburg, Russia; [2]Petersburg Nuclear Physica Iinstitute, 188300 Gatchina, St.Petersburg, Russia; [3]Technische Universität Dresden, Germany; [4]GSI Darmstadt, Germany

Testing of the Standard Model (SM) at the low energies remains an important problem in spite of the existence of very accurate experiment on the neutral Cs atom [1], where the parity nonconservation (PNC) effect of optical dichroism (difference in transition rates for right- and left-circularly polarized emitted photons) was observed: $W = W_0[1 + P(\vec{s}\,\vec{\nu})]$. Here W_0 is the basic transition probability, $\vec{s}$ is the photon spin, $\vec{\nu}$ is the direction of the photon emission. The pseudoscalar $\vec{s}\,\vec{\nu} = \pm 1$ defines the photon chirality (equivalent to the circular polarization). In case of the neutral Cs atom the coefficient P defining this PNC effect is of about $P \simeq 10^{-4}$.

However, the extraction of the electroweak interaction constant from the experimental data in [1] requires very accurate theoretical calculations, since the short-range weak interaction occurs actually at the nuclear surface while electron-correlation effects are crucial, too. Although latest theoretical investigations [2] show the agreement with the high-energy SM predictions, yet another low-energy atomic experiment with simpler systems is highly desirable.

In [3] a PNC experiment with polarized He-like HCI was proposed utilizing the crossing of two levels with opposite parity (2^3P_0 and 2^1S_0). Considered as functions of the nuclear charge Z, unique level crossings occur at $Z = 32$ (Ge), $Z = 64$ (Gd) and $Z = 92$ (U). Level crossing enhances essentially the PNC effect, so that the coefficient P becomes as large as in case in neutral Cs.

For experimental reasons it appeared to be more convenient to employ polarized He-like Eu ions (Z=63). However, the observation of the optical dichroism is not realistic for the X-ray photons characteristic for HCI. Therefore, it was proposed in [3] to observe yet another PNC effect associated with the asymmetry of the photon emission with respect to the ion beam polarization direction ($\vec{\zeta}$), i.e. $W = W_0[1 + P(\vec{\zeta}\vec{\nu})]$. Again the coefficient P appears to be of the order 10^{-4}. The task of the production of a polarized HCI beam still remains, which up to now is only available for electrons, muons, protons or neutrons [4]. An idea how to polarize a one-electron HCI beam (longitudinally with respect to the beam axis) via selective laser excitation of the Zeeman sublevels of the excited hyperfine level $|FM_F\rangle$ (total ion angular momentum F and projection M_F) and the subsequent radiative polarization of the ground hyperfine level was discussed in [5]. The important question about preservation of the ion beam polarization in the magnetic system of the storage ring arises. In [6] it was demonstrated, that the polarization of H-like ions, being once introduced in the storage ring, can be preserved during the entire beam lifetime. Moreover, the degree of polarization $\lambda_F = \frac{1}{F}\sum_{M_F} n_{FM_F} M_F$, defined in terms of the occupation numbers n_{FM_F} of the Zeeman sublevels of the hyperfine level, is affected neither by the magnetic fields of the ring nor by the process of radiative decay of the excited hyperfine level to the ground one. However, in view of the large magnetic moment of an ion the key problem seems to be the preservation of the longitudinal direction of the polarization for all the ions. Nevertheless, potential depolarization can be avoided with the aid of a "Siberian snake", i.e. a magnet which rotates the direction of polarization by an angle π around the direction of the beam axis. After an even number of revolutions around the ring the longitudinal direction of the polarization for every ion will be restored.

Finally, the options for monitoring the ion beam polarization in the ring need to be investigated [7]. A recent approach [8] concerns directly the polarization in He-like ions, required for the PNC experiments. These ions should be in the excited electronic states 2^1S_0, 2^3P_0 [3] and can be prepared by a H-like ion beam, which penetrates a dressing foil. Since the total angular momentum is zero, the ion polarization for the states 2^1S_0, 2^3P_0 reduces to the pure nuclear polarization λ_I (nuclear spin I). In [6] this value was evaluated to be $\lambda_I = 0,93$ for the $^{151}_{63}\mathrm{Eu}^{61+}$ ($I = 5/2$) ions, provided that the ion polarization $\lambda_F = 1,0$. The proposal [8] consists of the measurement of the difference in the hyperfine-quenched transition rates from the excited 2^1S_0, 2^3P_0 levels to the ground state in the presence and in the absence of an external magnetic field. This difference is defined by the expression $W = W_0[1 + Q(\vec{\zeta}\vec{H})]$. Here $\vec{H}$ represents the external magnetic field and W_0 is the transition probability in the absence of the magnetic field. The parity-conserving scalar $(\vec{\zeta}\vec{H})$ defines the effect and the coefficient Q for a field of typical order $H \simeq 1T$ was found to be of the order $Q \simeq 10^{-4}$ [8], i.e. of the same order as the coefficient P in the PNC effect.

References

[1] C.S. Wood et al., Science **275**, 1759 (1997)
[2] V.M. Shabaev et al., Phys. Rev. Lett. **94**, 213002 (2005)
[3] L.N. Labzowsky et al., Phys. Rev. **A63**, 054105 (2001)
[4] S.R. Mane et al., Rep. Progr. Phys. **68**, 1997 (2005)
[5] A. Prozorov et al., Phys. Lett. **B574**, 180 (2003)
[6] A. Prozorov et al., GSI-report 2008-03
[7] A. Surzhikov et al., Phys. Rev. Lett. **94**, 203202 (2005)
[8] A. Bondarevskaya et al., Phys. Lett. **A372**, 6642. (2008)

* Work supported by DFG and INTAS-GSI.

Hyperfine splitting and g factors of heavy few-electron ions*

A. V. Volotka[1,2], D. A. Glazov[1,2], I. I. Tupitsyn[2], G. Plunien[1], and V. M. Shabaev[2]
[1]Technische Universität Dresden, Germany; [2]St. Petersburg State University, Russia

High-precision measurements of the ground-state hyperfine structure of heavy highly charged ions [1-4] and the g factor of H-like carbon [5] and oxygen [6] have triggered a great interest to related theoretical calculations. In particular, the 2002 CODATA value for the electron mass is derived mainly from the experimental and theoretical g factor values for H-like carbon and oxygen and it is 4 times better than that of the 1998 CODATA value. An extension of these experiments to highly charged Li- and B-like ions presently being prepared [7, 8] will provide tests of the magnetic sector of quantum electrodynamics (QED) in strong fields in the specific differences between H-, Li-, and B-like ions [9, 10]. For the hyperfine structure in H- and Li-like ions the limitation of the total accuracy is set by the Bohr-Weisskopf correction. This uncertainty is considerably reduced in the specific difference between the ground-state hyperfine structure values of H- and Li-like ions with the same nucleus [9]. Similarly, the accurate knowledge of the experimental and theoretical values of a specific difference between the g factors of H- and B-like highly charged ions could also lead to an independent determination of the fine structure constant α [10]. The achievement of the required theoretical accuracy is a very interesting and demanding challenge for theory. As a further step toward this goal we have performed *ab initio* QED calculations of the ground-state hyperfine structure of the H-, Li-, and B-like sequences in the middle-Z region [11]. Similar calculations have been carried out for the g factor of heavy few-electron ions. Below we report briefly on our recent improvments in the predictions for the hyperfine splittings.

For an ion with one electron (e.g., ns or $np_{1/2}$ state) over closed shells the hyperfine splitting can be written in the form

$$\begin{aligned}\Delta E^{(a)} &= \frac{\alpha(\alpha Z)^3}{n^3}\frac{g_I}{m_p}\frac{2I+1}{(j+1)(2l+1)}\frac{1}{(1+\frac{m}{M})^3} \\ &\times \Big[A(\alpha Z)(1-\delta)(1-\varepsilon)+\frac{1}{Z}B(\alpha Z) \\ &+\frac{1}{Z^2}C(Z,\alpha Z)+x_{\rm rad}\Big], \qquad (1)\end{aligned}$$

where $A(\alpha Z)$ is the one-electron relativistic factor, δ and ε are the corrections for the distributions of the charge and magnetic moment over the nucleus, respectively. The functions $B(\alpha Z)$ and $C(Z,\alpha Z)$ determine the corrections for the electron-electron interaction of first and higher orders in $1/Z$, respectively, and $x_{\rm rad}$ denotes the QED correction. The Bohr-Weisskopf correction ε originates from the spatial distribution of the magnetic moment inside of the nucleus. The approximation of the nuclear single-particle model has been used for the evaluation of the Bohr-Weisskopf correction. Within this model the nuclear magnetization is determined by the total angular momentum of the unpaired nucleon. The term $B(\alpha Z)/Z$ describes the interelectronic-interaction correction of the first order in $1/Z$. Its rigorous QED treatment utilizes the two-time Green's function method. Since the total $1/Z$ interelectronic-interaction correction is gauge independent, calculations were performed in the Coulomb and Feynman gauges, which serve as an accurate check of the numerical results. The interelectronic-interaction correction of higher orders $C(Z,\alpha Z)/Z^2$ has been calculated within the framework of the large-scale configuration-interaction method in the basis of Dirac-Fock-Sturm orbitals. The configuration-interaction matrix contained all single, double, and triple positive-energy excitations. Single-electron excitations to the negative-energy spectrum have been accounted for in the many-electron wavefunction employing perturbation theory. The one-loop radiative corrections have been evaluated to all orders in αZ employing an effective local screening potential. The one-loop radiative contribution appears as the sum of vacuum-polarization and self-energy corrections. In order to account simultaneously for many-electron effects in Li- and B-like ions, we have introduced an effective spherically symmetric potential that partly takes into account the interelectronic interaction between the valence electron and the core electrons.

As the result of the improvements made in [11], we obtain the most accurate predictions for the hyperfine splitting in H-, Li-, and B-like ions with a level of accuracy better than 0.01%. Accurate knowledge of the hyperfine structure lines of middle-Z multicharged ions is also of great interest in connection with observations of these lines from hot rarefied astrophysical plasmas [12].

References

[1] I. Klaft *et al.*, Phys. Rev. Lett. **73**, 2425 (1994).
[2] J. R. C. López-Urrutia *et al.*, Phys. Rev. Lett. **77**, 826 (1996).
[3] P. Seelig *et al.*, Phys. Rev. Lett. **81**, 4824 (1998).
[4] P. Beiersdorfer *et al.*, Phys. Rev. A **64**, 032506 (2001).
[5] H. Häffner *et al.*, Phys. Rev. Lett. **85**, 5308 (2000).
[6] J. L. Verdú *et al.*, Phys. Rev. Lett. **92**, 093002 (2004).
[7] D. F. A. Winters *et al.*, Can. J. Phys. **85**, 403 (2007).
[8] M. Vogel *et al.*, Eur. Phys. J. Special Topics **163**, 113 (2008).
[9] V. M. Shabaev *et al.*, Phys. Rev. Lett. **86**, 3959 (2001).
[10] V. M. Shabaev *et al.*, Phys. Rev. Lett. **96**, 253002 (2006).
[11] A. V. Volotka *et al.*, Phys. Rev. A **78**, 062507 (2008).
[12] R. A. Sunyaev and D. Docenko, Astron. Lett. **33**, 67 (2007).

* Work supported by DFG and INTAS-GSI.

Multi-Electron Continua in Strongly Perturbing Ion-Atom Collisions

S. Hagmann[1,2,3] and C. Liao[3]
[1]Institut f. Kernphysik, Univ. Frankfurt, [2]GSI, Darmstadt, Germany, [3] J.R. Macdonald Lab., Dept. of Physics, KSU, Manhattan, Ks 66506, USA

Ion-atom collisions characterized by a strong perturbation, i.e. a Sommerfeld parameter $s=q_{proj}/v_{proj} >>1$, produce multiply ionized target ions with a very high cross section [1,2]. To shed light on the underlying poorly understood yet efficient multi-electron excitation and transfer mechanisms we have measured coincident doubly differential cross sections (DDCS) for continuum electron emission of electrons coincident with the recoiling ion charge state. These DDCS show that for high s the $v_e=v_{proj}$ forward cusp eclipses all other features in the continuum. This becomes evident as these DDCS cover for the first time contiguously the entire relevant phase space, the complete range of emission angles from 0^0 to 180^0 and electron velocities from threshold to near twice the projectile velocity.

Beams of p, $F^{8+,9+}$ and $I^{23+,25+}$ from the EN Tandem of the J.R. Macdonald Laboratory at KSU traversed the target zone inside an electrostatic toroidal electron analyzer; recoil ions were extracted from the target zone using a fast pulsed extraction [3]. In Fig. 1 we present for a weakly perturbing system s=0.15 in the DDCS for electrons emitted all simultaneously visible constitutive features: the slow electron emission (SEE) cusp dominating the DDCS at small s, the electron capture to continuum cusp (ECC) and the arc of target KLL Auger electrons.

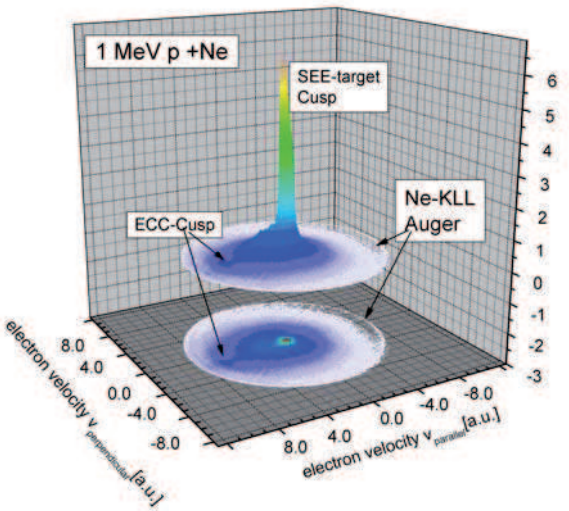

Figure 1: Relative DDCS ($d^2\sigma /d\Omega_e dv_e$) for electron emission in 1 MeV p on Ne collisions in momentum space. The beam direction is defined by both, $v_{parellel}=v_{perpendicular}=0$ and the ECC cusp location (at $v_e=v_{projectile}=6.3$.a.u.). The spectrum shown corresponds to electron kinetic energies extending up to ≈900eV slightly beyond the Ne KLL Auger energy

We find that the perturbation strength s and the number of electrons lost by the He target entirely determine the features in the DDCS of coincident electrons emitted for single and double ionization of He.

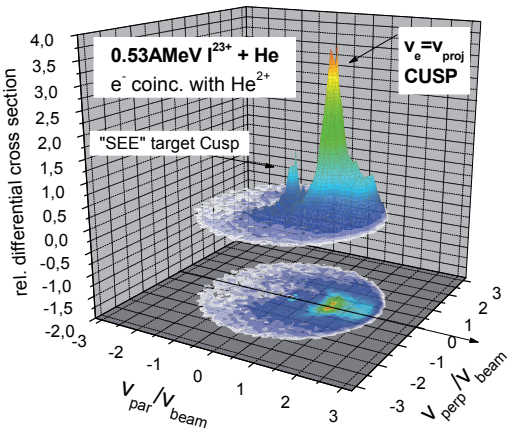

Figure 2: Relative DDCS ($d^2\sigma/d\Omega_e dv_e$) for electron emission coincident with the He^{2+} recoil ion in strongly perturbing 0.53A MeV I^{23+} on He collisions.

For a strong perturbation s, the $\vec{v}_e = \vec{v}_{Proj}$ cusp (ECC in the 1-electron case) prevails; moreover, it is here dominantly arising from *double electron removal* from He (Fig.2), not anymore from single electron transfer to the projectile continuum as for weak perturbations. For s>>1 severe constraints appear in reaction phase space for 2-electron loss by the target: a key characteristic for double ionization of the target is the propensity for emission of electrons preferably into a narrow forward cone culminating in the very *low energy electron projectile continuum* around the $\vec{v}_e = \vec{v}_{Proj}$ cusp, and the concomitant acute attenuation of the *low energy target continuum* SEE cusp (fig.2). We interpret this preponderance of the 2-electron over the 1-electron channel as evidence for considerable electron correlation in the electron transfer [4] to the continuum. Further experiments with heavier projectiles and multi-electron targets are in progress.

We gratefully acknowledge support by US-DOE, Div. of Chem. Sciences, Fundam. Interactions Branch

References

[1] S. Datz et al. Phys. Rev. **A41** (1990) 3559
[2] R. Moshammer et al. Phys. Rev.**A65**(2002) 042727
[3] S. Hagmann et al., to be submitted to Phys. Rev. A
[4] G. Tanner et al. Rev. Mod. Phys. **72**(2000) 497

Ionization of K-shell electrons by electron or positron impact*

A.I. Mikhailov[1], A.V. Nefiodov[1,2], and G. Plunien[2]

[1]PNPI, 188300 Gatchina, St. Petersburg, Russia; [2]TU Dresden, Mommsenstr. 13, D-01062 Dresden, Germany

The single ionization of inner-shell electrons by electron or positron impact are the fundamental processes, which still attract considerable interest in collision theory, experimental studies, and various applications. To predict the ionization cross sections, one usually employs either sophisticated numerical approaches or empirical and semi-empirical formulas. Significant efforts have been also devoted to investigations of the scaling behavior of ionization cross sections with respect to the energy of the incident particles.

We have deduced a universal scaling behavior for the cross sections of the single K-shell ionization of hydrogen-like ions with moderate values of the nuclear charge Z by electron or positron impact [1, 2]. The study is performed to leading order of non-relativistic perturbation theory with respect to the electron-electron interaction. Accordingly, it is assumed that $\alpha Z \ll 1$ and $1/Z \ll 1$, where α is the fine-structure constant. The energy of the projectiles E is considered to be within the range $I \le E \ll m$, where $I = m(\alpha Z)^2/2$ is the Coulomb ionization potential and m is the electron mass ($\hbar = 1$, $c = 1$).

The total cross section for the single ionization of a K-shell electron can be cast into the following form

$$\sigma_{\rm K} = \pi a_0 Z^{-4} Q_{\pm}(\varepsilon)\,, \qquad (1)$$

where $\varepsilon = E/I$ and $a_0 = 1/(m\alpha)$ is the Bohr radius. The dimensionless function $Q_{\pm}(\varepsilon)$ describes the universal scaling behavior, which does not depend on the particular value of Z (see Figs. 1 and 2). The subscript plus (minus) corresponds to the incident positron (electron). Near the ionization threshold, the exact functions $Q_{\pm}(\varepsilon)$ strongly deviate from the Born predictions, which completely neglect the interaction of projectiles with the nuclear field (as well as the exchange interaction in the case of electron impact).

For the high-energy domain $\varepsilon \ge 10$, the functions $Q_{\pm}(\varepsilon)$ are given by

$$Q_{\pm}(\varepsilon) = \varepsilon^{-1}(A \ln\varepsilon + B + C_{\pm}\varepsilon^{-1})\,, \qquad (2)$$

where the coefficients are equal to $A = 1.126$, $B = 5.067$, $C_- = -11.19$, and $C_+ = -7.636$. At asymptotic high energies, the total cross sections for the K-shell ionization by electron and positron impact exhibit the same behavior.

If the K shell is filled, the universal scaling functions $Q_{\pm}(\varepsilon)$ still remain the same. However, the cross section (1) should be multiplied by the factor 2, which takes into account the number of K-shell electrons. In addition, one needs to simulate the screening effect of the passive electron(s) on the active K-shell electron, participating in the ionization process. This can be done by replacing the true nuclear charge Z by an effective value $Z_{\rm eff}$. The latter can be defined by equating the experimental potential for the single ionization of a K-shell electron and the effective one, that is, $I_{\rm exp} = m(\alpha Z_{\rm eff})^2/2$. Accordingly, the energy of the incoming particle E is measured in units of the experimental value $I_{\rm exp}$.

The universal scaling laws turn out to be applicable for a wide family of atomic targets (multicharged ions and neutral atoms) with the moderate values of the nuclear charge Z.

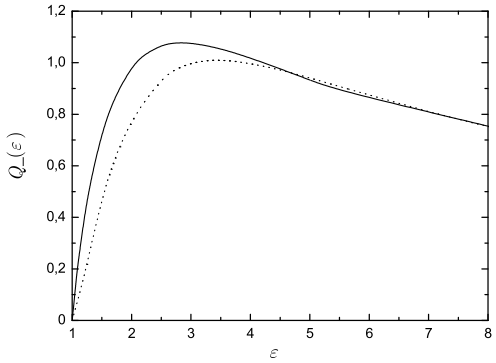

Figure 1: K-shell electron ionization by electron impact: dotted line, calculation within the Born approximation; solid line, exact calculation.

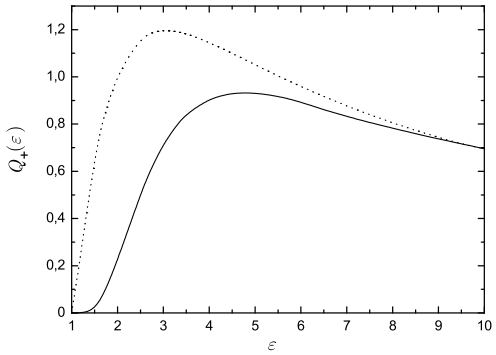

Figure 2: K-shell electron ionization by positron impact: dotted line, calculation within the Born approximation; solid line, exact calculation.

References

[1] A.I. Mikhailov, A.V. Nefiodov, and G. Plunien, Phys. Lett. A 372 (2008) 4451.

[2] A.I. Mikhailov, A.V. Nefiodov, and G. Plunien, Phys. Lett. A 372 (2008) 5171.

* Work supported by BMBF, DFG and INTAS-GSI.

Electron Cooling of highly charged ions in HITRAP*

G. Zwicknagel
Institut für Theoretische Physik, Universität Erlangen, Germany

In previous simulation studies [1, 2, 3] of electron cooling of highly charged ions in HITRAP we have investigated the time evolution of the energy distribution of the ions, the related cooling times and the surviving probability of the initially injected ion species with respect to losses by ion-electron recombinations. In these studies an isotropic velocity distribution of the trapped electrons during their heating by the ions was assumed. But our detailed considerations of the energy loss of ions by collisions with magnetized electrons in a strong magnetic field (like the 6T-field in HITRAP), showed that the ion energy is almost solely transfered into the electrons' degree of freedom parallel to the magnetic field [2]. On the other hand, the synchrotron radiation emitted by the gyrating electrons reduces only the energy in their transverse degrees of freedom. This should result in a strong anisotropic velocity distribution of the electrons.

To estimate and model the effects due to such an anisotropy in the heating and cooling of the electrons and their feedback to the energy loss of the ions, we extended our previous model [1, 2, 3] by considering now two electron temperatures $T_{e,\parallel}, T_{e,\perp}$ and the following rate equations:

$$\frac{dT_{e,\parallel}}{dt} = \frac{-2}{N_e k_B} \sum_{\mu}^{N_i} \frac{dE_\mu}{dt} - 2\nu_{\rm iso}\left(T_{e,\parallel} - T_{e,\perp}\right) \quad (1)$$

$$\frac{dT_{e,\perp}}{dt} = \nu_{\rm iso}\left(T_{e,\parallel} - T_{e,\perp}\right) - \frac{1}{\tau}\left(T_{e,\perp} - T_0\right) \quad (2)$$

Here the term containing the energy loss of the ions dE_μ/dt reflects the heating of the N_e trapped electrons by the N_i trapped ions which is calculated by following the individual trajectories of the ions. The cooling of $T_{e,\perp}$ by synchrotron radiation to an ambient temperature of $T_0 = 4$ K is modeled by the time constant τ (which is about 0.1 s for $B = 6$ T). The isotropisation between $T_{e,\parallel}$ and $T_{e,\perp}$ is given in terms of the rate $\nu_{\rm iso}$ which has been taken from Refs. [4, 5].

In Fig.1, the changes in the time evolution of the mean ion energy $\langle E_i \rangle$ for different ion species in the cases of isotropic and anisotropic distributions are compared for a cloud of $N_e = 10^9$ trapped electrons of a density of $n_e = 10^8$ cm^{-3} and an ensemble of 500 ions, representing (after proper scaling) $N_i = 10^5$ trapped ions. As the major effect of the anisotropy we found an enlargement of the cooling times by about 30%...40% common to all ion species, see Fig.1.

But the isotropisation rate $\nu_{\rm iso}$ given in Refs. [4, 5] was derived under the assumption that $T_{e,\parallel} \approx T_{e,\perp}$, which is clearly not met in the present scenario where $T_{e,\parallel}$ and $T_{e,\perp}$ may often differ by orders of magnitude. Investigations how much this will alter the predictions of the outlined calculations are in progress.

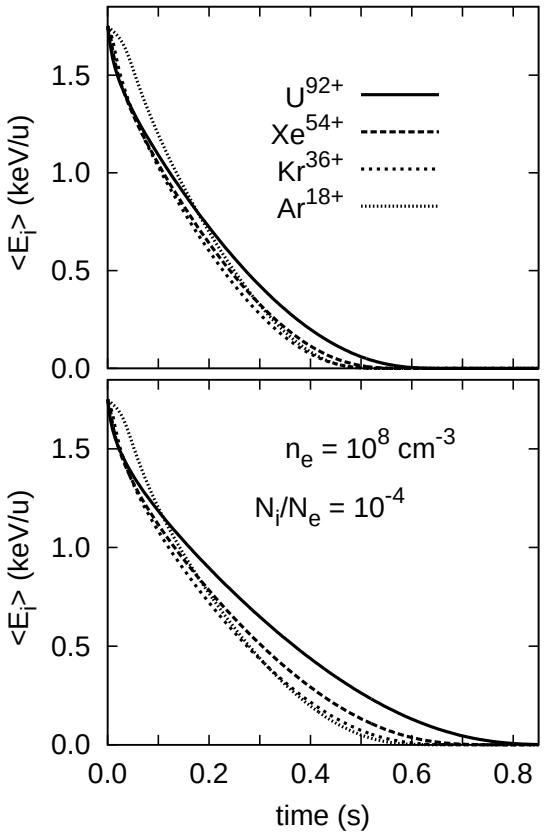

Figure 1: Temporal evolution of the mean energy of the ions $\langle E_i \rangle$ for different highly charged ions at $B = 6$T, $n_e = 10^8$ cm^{-3}, $N_e = 10^9$ and $N_i = 10^5$. The upper figure shows the case of an isotropic velocity distribution of the electrons (see Refs. [1, 2, 3]), the lower one represents the results for an anisotropic distribution modeled by the rate equations (1) and (2).

References

[1] G. Zwicknagel, in *AIP Conference Proceedings*, vol 862, (AIP, New York 2006) pp 281–291

[2] H. Nersisyan, C. Toepffer, G. Zwicknagel, *Interactions Between Charged Particles in a Magnetic Field* (Springer, Berlin Heidelberg New York 2007)

[3] B. Möllers, PhD-thesis, University Erlangen 2007, `www.opus.ub.uni-erlangen.de/opus/volltexte/2007/547/`.

[4] M.E. Glinsky *et al.*, Phys. Fluids B **4**, 1156 (1992)

[5] T.M. O'Neil, P.G. Hjorth, Phys. Fluids **28**, 3241 (1985)

*Work supported by the BMBF (06ER145)

Developments at the Interface between Accelerator Sciences and Atomic Physics within the QUASAR Group

S. Artikova[2], J. Egberts[2], J. Harasimowicz[1,2], A. Intermite[1,2], T. Junginger[2,3], K.-U. Kühnel[2], A. Papash[1-3], M. Putignano[1,2], P. Schmid[1,2], C. Schömers[2,5], M. Schuh[2,3], and C.P. Welsch[1,2,6-8]
[1]GSI, [2]MPI-K, [3]also: CERN, [4]also: JINR, [5]also: Heidelberg Ionenstrahl-Therapie (HIT), [6]University of Heidelberg, [7]University of Liverpool, [8]Cockcroft Institute

Particle accelerators have proven to be indispensable tools to understand nature at smaller and smaller scales. The QUASAR group started at the Max Planck Institute for Nuclear Physics in 2008 and combines developments in accelerator sciences with measurements on quantum systems, with a particular focus on antimatter research. The group's international structure and close collaboration with partners from around the world provides a fruitful ground for beyond state-of-the-art developments in a number of different fields.

THE ULTRA-LOW ENERGY STORAGE RING (USR)

Antiprotons stored and cooled at low energies in a storage ring or at rest in traps are highly desirable for the investigation of a large number of basic questions on fundamental interactions, on the static structure of exotic antiprotonic atomic systems or of (radioactive) nuclei as well as on the time-dependent quantum dynamics of correlated systems. In addition, low-energy antiprotons are the ideal and perhaps the only tool to study in detail correlated quantum dynamics of few-electron systems in the femto and sub-femtosecond time regime.

To enable the efficient investigation of these important questions, a novel electrostatic cooler synchrotron and a state-of-the-art in-ring spectrometer are under development in close collaboration between the QUASAR group, the Max-Planck Institute for Nuclear Physics, the GSI Atomic Physics Division, and groups from the University of Heidelberg with the aim of slowing down antiprotons as well as possibly highly charged ions (up to bare uranium) to low energies between 20 and 300 keV/q at FLAIR. This will provide world-wide unique conditions for both in-ring studies with an intensity of up to 10^{12} cooled and stored antiprotons or highly charged ions per second, as well as for experiments requiring extracted slow beams and will therefore push the limits in all fields concerned.

Ring Layout

In order to be adjustable to the different needs of the experimentalists, the storage ring has to be set to different operation modes. Apart from the basic cooling and deceleration schemes, internal experiments ask for short bunches in the ns-range while external experiments have to be provided with extracted beams of most different pulse duration.

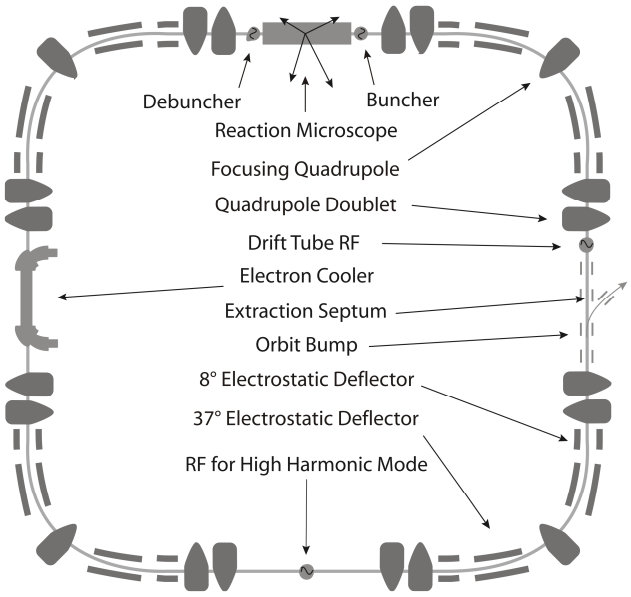

Figure 1: Layout of the ultra-low energy storage ring.

The synchrotron has been completely re-designed in 2008. The ring has a four-fold symmetry and an overall circumference of 42.6 m. The bending sections of the ring are designed in a novel "split-achromat" geometry. The total deflection of the beam by 90° in each of the corner section is realized by a combination of 8°-37°-37°-8° electrostatic cylinder deflectors. For the transverse modulation of the beam quadrupole doublets placed at the entrance and exit of every experimental straight section are used. An additional focusing quadrupole, placed in between the two 37° deflectors, is included to control the dispersion of the beam.

Beam Extraction

As different types of experiments using antiproton beams are planned within the FLAIR project, the extraction scheme of the USR needs to be highly flexible. Experiments requiring single short pulses per deceleration cycle, like e.g. trap experiments, a fast extraction scheme needs to be provided while nuclear-physics type experiments require a continuous beam during one machine cycle and thus slow extraction. For fast extraction the beam will be moved adiabatically towards the electrostatic septum, located in one of the straight sections, by a local orbit bump. To allow for high flexibility during this process, the bump is created by four dedicated electrostatic deflectors, located symmetrical

around the electrostatic extraction septum. As soon as the beam moves along the orbit bump, an additional "kicking voltage" is applied to one of the bump electrodes, pushing the beam over the septum wall into the extraction transfer line in a single turn. Simulations with SIMION showed that the required electrode potentials are below +/- 800 V, which can be easily realized. Slow extraction on the other hand requires a resonant extraction scheme using a third order resonance. To drive this resonance, a dedicated sextupole will be installed, working on the $3 \cdot Q = 8$ resonance. This leads to a distortion of the stable elliptical trajectories (in un-normalized phase-space) and the available phase-space is split into stable and unstable regions by the separatrices that define the stable triangle. It should be pointed out that this is the first time ever such a combined fast/slow extraction scheme has been designed for an electrostatic storage ring.

Short Bunches

In order to reach a high resolution in the envisaged experiments with the novel in-ring reaction microscope, presently being developed in the QUASAR group in collaboration with the Ullrich group at MPIK, ultra-short pulses of 20 keV antiprotons with a time structure of only a few nanoseconds have to be provided. It is clearly impossible to create ultra-short bunches of a few ns duration in one step from a coasting beam: With a revolution period of 20 μs the required buncher voltage to provide a 2 ns time focus would exceed 10 kV and thus the induced energy spread by the phase compression would simply destroy the beam circulating in the ring.

The following procedure was developed in 2008 to provide ultra-short bunches: Once the beam has been slowed down to 20 keV, the coasting beam of antiprotons is cooled down to a momentum spread of $\sim 10^4$. Then the cooled beam is adiabatically captured into $\tau \sim 50$ ns stationary buckets formed by a 20 MHz cavity operating at a high harmonic mode of the ring revolution frequency h_{RF}=400-500. The desired ultra-short pulses of τ=2ns duration will then be formed in the symmetry point of the straight section where the reaction microscope is located. The focus will be provided by an additional $3\beta\lambda/2$ double drift buncher, placed at the beginning of the straight section. Once the experimental section is crossed, a debuncher will provide phase decompression and limit the growth of the equilibrium momentum spread. Otherwise the increasing energy spread introduced by the phase compressor would cause a beam blow up in the bending sections of the ring.
As it was already pointed out, the phase compression will lead to an additional energy spread. This requires that any manipulation of the beam towards short pulses needs to be limited to the straight sections of the ring, where the dispersion function needs to be zero. To allow for this special operation mode, the USR lattice was recently modified substantially, as described in the previous section.

Beam Diagnostics

The USR puts very high demands on the beam instrumentation as most conventional techniques will not work. Ultra-short bunches (1-2 ns) on the one hand and a quasi-DC beam structure on the other, together with a variable very low beam energy, ultra-low currents (from 1 μA down to 1 nA, or even less for a non-circulating beam) require the development of new diagnostic methods. A set of diagnostics devices, ranging from fully destructive monitors to non-perturbing ones, is under development for the USR. This includes a highly sensitive resonant beam position monitor based on capacitive pick-ups, Shottky pick-ups, specially adapted Farraday cups, and different kinds of beam profile monitors.

In addition, a neutral supersonic gas jet target shaped into a thin curtain combined with bi-dimensional imaging of the gas ions created by impact with the projectiles is being developed as an interesting alternative to profile monitors based on secondary electron emission and/or luminescent screens. A study of the intrinsic sensitivity and resolution of the monitor depending on its geometrical design has been carried out, and optimisation of it proposed, therewith highlighting the importance of the curtain geometric width.

We identified as relevant variables to be monitored the first maximum Mach number in the expansion and its coordinates, the maximum Mach number in a plane further away from the skimmer (and in particular at 70% distance in our simulation domain), and finally the geometry of the curtain itself.

By in-detail analysis of the simulation results, we achieved a powerful optimization method for highly variable gas jets. A test vacuum chamber has been designed and optimized for testing the validity of the numerical simulation on the behaviour of the jet curtain and will be built up in 2009.

RF ACCELERATORS

Benchmarking OPERA/SOPRANO

Rebunching cavities are today routinely used for matching a beam of charged particles between different accelerator structures, and thus optimizing the overall transmission and beam quality. At low resonance frequencies, unnecessary large dimensions of these cavities can be avoided by using spiral-loaded cavities. The optimization of these structures is a complicated process in which a wide range of different parameters have to be modified essentially in parallel. We investigated in detail the characteristics of a model structure with the 3D code OPERA/SOPRANO. This includes the optimization of the structure in terms of the spiral geometry for a given resonance frequency, the

investigation of power losses on the inner surfaces, and the possibility of cavity tuning by means of a tuning cylinder.

It is now planned to develop a fully parameterized model where the simulation and evaluation is automated using OPERA's internal script environment.

Power Dissipation in Higher Order Modes

In pulsed high power superconducting H^- linacs different resonances can be triggered by the beam pulses. To ensure machine operation even at high currents the influence of Higher Order Modes (HOM) on beam motion has to be understood in detail. If HOM were triggered next to one of the resonances frequencies, high voltages might be induced, leading to additional power dissipation and negative impact on beam stability.

In order to estimate the additional power consumption from HOMs for the superconducting proton linac (SPL) at CERN, simulation studies with rescaled cavities at different operation frequencies (704 Mhz and 1408 MHz) and beta values were started. On the basis of these results HOM damping requirements will be defined to efficiently limit the power dissipation to a few watts per cavity.

MEDICAL ACCELERATORS

Therapy-synchrotrons, like the HIT-facility, operate in a fast pulse-to-pulse mode, where beam energy and intensity are switched in every new cycle. Furthermore, efficient tumor treatment requires a high precision of both, the beam position and the spill structure.

Hysteresis effects or eddy currents that occur in fast ramped synchrotron dipole and quadrupole magnets are in contradiction to those requirements. The standard (current-based) magnet control cannot handle these effects, demands additional time and increases the overall energy consumption. A field-based magnet control, however, could. This requires, among others, an improved magnetic field measurement with an accuracy of 10^{-4}.

It was decided to first measure the magnetic field with a Hallsensor at injection level (50-100 mT) of each synchrotron cycle. As the HIT-synchrotron is operated in 24/7 mode and thus not accessible for systematic studies, an external test bench for tests and measurements was installed. It consists of a former GSI dipole magnet and the corresponding power supply to simulate the field of interest. In addition, the lattice design of the HIT synchrotron and in particular its extraction mechanism has been studied in detail.

HIGH DYNAMIC RANGE BEAM PROFILE MEASUREMENTS

A thorough understanding of halo formation and its possible control is highly desirable for essentially all particle accelerators. Limiting the number of particles in the halo region of a beam would allow for minimizing beam losses and maximizing beam transmission, i.e. the experimental output. Measurements based on either optical transition radiation (OTR), synchrotron radiation (SR) or on light from luminescent screens at low energy accelerators like the USR provide an interesting opportunity for high dynamic range measurements of the transverse beam profile, since the signal is linear with the beam charge. In order to approximate a typical beam distribution as it is found in an accelerator we use a conventional laser beam in a small lab setup. Its profile was then analyzed by a charge injection device (CID) camera system. By covering at least five orders of magnitude in dynamic range, the CID-camera is the perfect tool for said measurements. Another option under investigation in parallel is the so-called "core masking technique". If it were possible to blank out the intense light from the beam core, a normal camera could be used to monitor the halo without saturation and overexposure. A strong limitation in earlier tests at CERN with the core masking technique was the fixed shape of the mask itself. In our setup, we thus aim for realizing a flexible mask by using a Micro-Mirror-Array (MMA). A test setup was built up and we are currently automating the overall process: profile acquisition - mask definition - reacquisition of halo profile.

DITANET

Beam diagnostics is a rich field in which a great variety of physical effects are made use of and consequently provides a wide and solid base for the

training of young researchers. Moreover, the principles that are used in any beam monitor or detector enter readily into industrial applications or the medical sector which guarantees that training of young researchers in this field is of relevance far beyond the pure field of particle accelerators. Without an appropriate set of diagnostic elements, it would simply be impossible to operate any accelerator complex let alone optimize its performance. DITANET - **DI**agnostic **T**echniques for particle **A**ccelerators - a European **NET**work" - covers the development of advanced beam diagnostic methods for a wide range of existing or future accelerators, both for electrons and ions. DITANET is the largest ever coordinated EU education action for PhD students in the field of beam diagnostic techniques for future particle accelerators with a total budget of 4.2 M€. The network was initiated and is coordinated by the QUASAR group.

ACKNOWLEDGEMENTS

The QUASAR Group is grateful for the fruitful cooperation with our partners at CERN (E. Bravin, F. Gerigk, T. Lefèvre, W. Weingarten), HIT (E. Feldmeier, A. Peters, R. Steiner). The generous support of the Helmholtz Association of National Research Centers (HGF) under contract number VH-NG-328 and of the GSI Helmholtzzentrum für Schwerionenforschung GmbH is acknowledged. Finally, we would like to thank the MPI-K for hosting the QUASAR group.

Performance of PHELIX in 2008

K. Witte[1], V. Bagnoud[1], A. Blazevic[1], S. Borneis[1], C. Bruske[1], J. Caird[2], S. Calderon[3], D. Eimerl[4], U. Eisenbarth[1], J. Fils[1,5], R. Fuchs[1], S. Götte[1], T. Hahn[1], G. Klappich[1], F. Knobloch[1], Th. Kühl[1,6], S. Kunzer[1], M. Kreutz[1], R. Lotz[1], T. Merz-Mantwill[1], E. Onkels[1], D. Reemts[1], M. Roth[1,5], A. Roussel[7], T. Stöhlker[1], A. Tauschwitz[1], R. Thiel[1], U. Thiemer[1], B. Zielbauer[1,8], D. Zimmer[1,6]

[1]GSI Darmstadt; [2]Lawrence Livermore National Laboratory/USA; [3]Pegasus Design, Inc., Pleasanton, Cal./USA; [4] EIMEX, Livermore, CA/USA; [5]Technische Universität Darmstadt; [6]Universität Mainz; [7]Commissariat à l'Energie Atomique, Le Barp/France; [8]Université Paris-Sud 11, Orsay/France

PHELIX is a Petawatt high-energy laser for heavy-ion experiments that can deliver 1-10 ns long pulses at 1053 nm with energies up to 1 kJ to the ion beam target chamber at the Z6 experimental area or 200 TW in subpicosecond pulses to the target chamber in the laser bay. Near-term upgrades comprise frequency doubling of the ns pulses to 527 nm and a power increase of the short pulse to 500 TW with the larger compressor gratings obtained from the **L**awrence **L**ivermore **N**ational **L**aboratory (LLNL) in the USA PHELIX was built in close cooperation with LLNL and the **C**ommissariat à l'**E**nergie **A**tomique (CEA) in France.
In the following, the major achievements in 2008 are reported.

First combined operation of PHELIX and the UNILAC ion beam at the measuring site Z6

The most important achievement in 2008 were the activation of the beam line connecting the exit of the PHELIX main amplifier chain to the Z6 experimental area and the subsequent experiments which have started in May 2008. These experiments study the stopping of argon and sulphur ion bunches accelerated by the UNILAC in hot plasma generated from thin carbon foils irradiated with long PHELIX pulses focused to a spot of about 1-mm diameter.
As a prerequisite the installation of all beam tubing and optics in a clean room 100-environment, the commissioning of the nanosecond front end (nsFE, see details below) as well as the full functionality of the PHELIX interlock system PILS had to be completed. Likewise, the PHELIX nanosecond pulse had to be synchronized to the UNILAC ion bunches.

Shot statistics

The shot log file of PHELIX documents more than 600 shots already, most of them served for the characterization of the laser system. The first experimental campaign was conducted from May 11 to May 14. In this time, 21 high-energy shots were fired onto foil targets in the Z6 chamber with typical pulse energies between 100 and 300 J investigating the ion beam interaction with hot plasma [1]. These experiments were continued in another campaign from August 14 to 29 with a shot count of 27. In addition to these combined ion-laser beam experiments, five PHELIX-stand-alone campaigns were executed using the target chamber in the laser bay (see Fig. 1). Two campaigns were related to a new pumping scheme for x-ray lasers, two others to the development of multi-keV backlighter sources [2]. The fifth experiment was devoted to the proton acceleration from thin metal foils [3].

Synchronization PHELIX-UNILAC

Since May 2008, the UNILAC and PHELIX running in the ns-mode of operation may be synchronized by employing the proven scheme and hardware as is in use to synchronize nhelix to the UNILAC. The nhelix facility is a 100-J Nd:glass laser system (1064 nm) set up at the Z6 area. It delivers 5 to 10-ns long pulses that can be frequency-doubled and frequency-tripled. The timing accuracy of PHELIX with respect to a selectable 3-ns micropulse from the UNILAC ion beam is 1ns. In this scheme, PHELIX provides additional timing signals for the Z6 area. These were used to fire the nhelix front-end. The frequency converted nhelix pulses allow to conduct interferometric measurements of the plasma.

The PHELIX nanosecond front end (nsFE)

Significant progress was achieved with respect to the operation of the nsFE. After many issues with its fiber-based part had been solved, we were able to use it for the first time on the Z6 shot campaign in May.
The nsFE can deliver pulses at 1053nm with a freely programmable temporal pulse shape whose duration can be chosen between 3 and 20 ns. Typical output energies are around 20 mJ at the repetition rate of 0.5 Hz. Like with the femtosecond front end (fsFE), these pulses can be amplified by the PHELIX pre-amplifier up to 5 J. The nsFE consists of two parts: A fiber-based system comprising a continuous wave (cw) fiber oscillator, an acousto-optical modulator, a double-pass amplifier, and a fast optical gate delivering pulses up to 10 nJ and a flash lamp pumped ring regenerative Nd:glass amplifier that amplifies the 10-nJ pulses to the 20-mJ level.
Some components of the fiber part installed by LLNL several years ago showed aging-related degradation.

These include pump diodes, fibers, and the cw-oscillator which had to be replaced. The latter component was substituted for a state-of-the art commercial system (Koheras BASIK Module) delivering a very stable output beam up

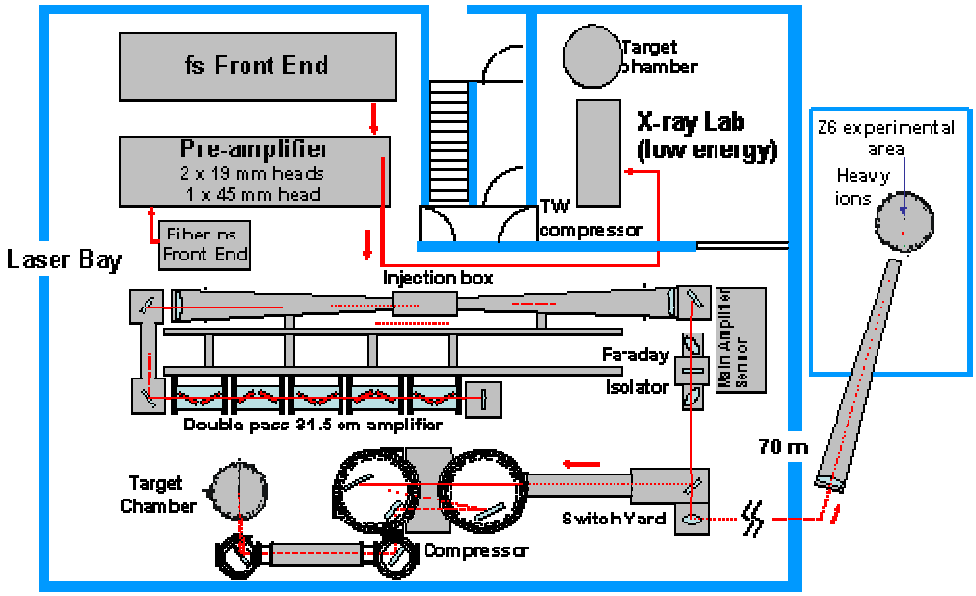

Figure 1: Schematics of PHELIX in 2008

to 15 mW at 1053 nm. Due to significant transmission losses, the fast optical gate also had to be replaced. The regenerative amplifier was equipped with new laser amplifier rods as well. The output section including near/far-field and energy measurements as well as energy control (variable attenuation) was completely rebuilt. The nsFE can now be remotely controlled by the PHELIX Control System (*PCS*).

By the turn of the year, all the individual components of the nsFE had been extensively studied and characterized. We now have a good understanding of the potential and limitations as well as a clear view for improvements of the nsFE. In the future, we will mostly concentrate on a better contrast ratio which is currently of the order of 10^{-4} and an optimized ring-resonator design for a higher stability of the TEM_{00} mode.

The femtosecond front end (fsFE)

The fsFE was rearranged to provide space for the upgraded stretcher. The two regenerative amplifiers and the oscillator had to be moved to new positions on the optical table. The magnification of the fsFE output beam was optimized with respect to the input aperture of the pre-amplifier yielding a higher fill factor at the pre-amplifier exit, i. e., a more rectangular fluence profile ("top hat"). Additional effort has been put into temporal contrast improvement of the stretched pulse in the frame 2-10 ns ahead of its peak. By design, the fsFE comprises three resonator cavities with periods of 12, 9, and 14 ns. Because of the finite extinction ratio of the optical switches (Pockel cells), pre-pulses are present with delays equal to the resonator period differences. In order to reduce these pre-pulses, an additional Pockels cell was introduced between the two regenerative amplifiers. Further, the Pockels cell downstream the second regenerative amplifier is now driven by a fast pulsed driver. We measured optical rise times of 450 ps (10 to 90%) and 800 ps (1 to 99%), respectively, which are nearly 10 times faster than those achievable with conventional drivers. These measures improved the contrast at the output of the fsFE by a factor of ~1000.

The existing Mach-Zehnder interferometer (MI) incorporated into the beam line downstream the stretcher allows the generation of two pulses with adjustable intensities and relative delay but equal pulse durations. The operational capacity of this MI was extended by placing a compressor in one of its arms to enable the production of two pulses of different duration on the target. The maximally achievable difference in the compression ratio is 50 ps/mm enabling the generation of a 250-ps long pre-pulse ahead of the compressed main pulse (the second). The delay is continuously adjustable between 0 and 2 ns.

Other subsystems

The PHELIX control system (*PCS*) was updated to LabVIEW™ version 8.2 and *CS* version 3.1 [4]. The next goals are an improved data recording system to document each PHELIX shot and to solve problems related to the GSI intranet.

Pre-amplifier. In the course of the year, the PHELIX pre-amplifier has evolved into a reliable workhorse for the generation of laser pulses with energies up to 5 J. In this time, the system delivered about 300 shots with a fairly low maintenance effort. Due to the precise and stable input and output diagnostics, the time needed for routine beam alignment could be reduced to 30 minutes limited

by the warm-up time of the front end. The beam leaving the pre-amplifier still carries some astigmatism arising mainly from the polarizers of the 45-mm Faraday isolators. These devices need to be replaced in the future.

Beam-profile shaping. In between experimental campaigns, we concentrated on the improvement of the fill factor which is a measure for the uniformity of the beam profile. This parameter is particularly important for the maximum extractable energy without exceeding the damage threshold of the optical components. In a first step, a robust computer algorithm has been developed for the automatic calculation of the fill factor using a measured near-field beam profile. In the future, this code will be implemented in the *PCS* in order to automatically detect unacceptable beam profiles caused by system misalignment or damaged optical components. Immediate correction will greatly improve the machine safety. In a second step, the diameter of the beam seeding the pre-amplifier was reduced to an optimum value in order to compensate for the radial gain profile of the rod amplifiers used in the pre-amplifier. This way we achieved fill factors up to 72% which comes close to the theoretical limit for an 8^{th}-order super-Gaussian beam profile.

Main amplifier (MA). It can now be completely remotely controlled due to further automation of the bridge telescope, the injection section, and an improved implementation of the mirror controls. The precise input and output diagnostics and the improved support by the *PCS* has reduced the daily alignment time and allows an easy verification of the beam position from the control room; a complete realignment of the full beam path can be done in three hours.

In conjunction with the MA, the MA beam sensor was further developed and characterized. Although not completed yet, the techniques used to accomplish large beam-size reductions and large-scale energy attenuations will also be applied at the compressor sensor and the Z6 areas.

The pulse compressor and target areas have been developed further with the main emphasis on beam transport and beam focusing. The preliminary, in-air beam line was replaced by two in-vacuum beam turning boxes. The second box houses an all-metal, 90-degree off-axis focusing parabola. A 15-cm clear-aperture transparent valve separates the target chamber from the compressor and beam line vacuum systems offering a high degree of flexibility in operation.

New parabola. A new copper parabola of 30-cm diameter and 1.5-m focal length with improved performance was installed. The amendment was achieved by two measures. Firstly, the rigidity of the substrate was increased by enlarging its thickness and using a honeycomb structure. Thereby the substrate could be made effectively twice as thick as previously but at reduced weight. Secondly, excessive irregularities in the centre part of the parabolic surface could be avoided during manufacture. As a result, the PHELIX pulses could be focused to spots of less than 20-µm diameter at estimated on-target intensities above 10^{19} W/cm² (see Fig. 2) and were successfully applied to ion acceleration from the rear side of thin metal foils [3].

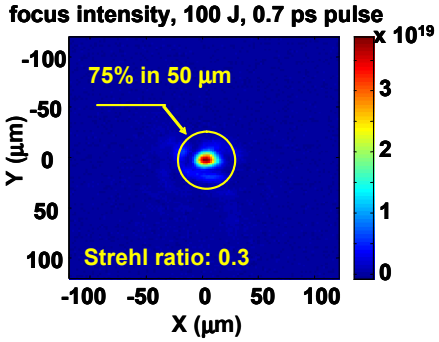

Figure 2. Fluence profile of a 100-J PHELIX pulse in the focus of the new parabola. 75% or 75 J of the total energy of 100 J is found within the spot of 50-µm diameter. The Strehl ratio is the quotient of the actual peak intensity and the peak intensity obtained from a beam with a perfect top-hat profile.

The 10°-beam transport and focusing system was completed (Fig. 3) and its performance characterized. Stiffening of the support structures in the mirror towers north and south by installing additional I-beams reduced the horizontal and vertical beam pointing stabilities down to 5 and 10 µrad, respectively (2σ values, see Fig. 4). These measurements were conducted with a dual-axis lateral effect diode and the cw YLF alignment laser beam injected into the laser chain upstream the pre-amplifier. Signal sampling rates of 500 Hz and a 4-second acquisition time allow determination of low to subsonic vibration

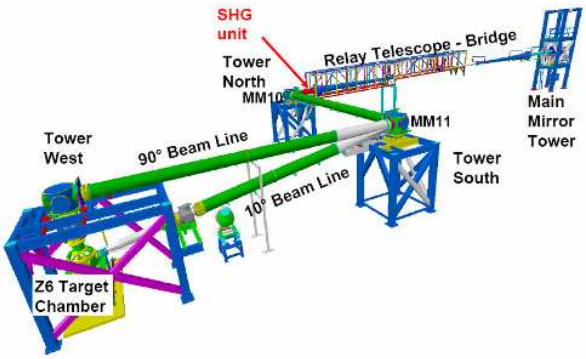

Figure 3. 10°- and 90°-beam lines for the transport of the 1ω- and 2ω-pulses, respectively, to the Z6 target chamber.

frequencies and noise, typically found in large-size structures and buildings. The measurements are consistent with data taken with a CCD camera operating at a sampling rate of a few 10 Hz.

2ω-beam line to Z6. For the planned hohlraum experiments at the measuring area Z6, frequency doubling of

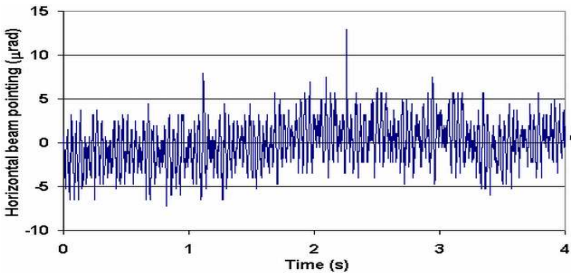

Figure 4. Horizontal beam pointing in the focal plane of the f=4 m focusing lens with a dual-axis lateral effect diode at the sampling rate of 500 Hz.

Figure 5. Frequency-doubling DKDP crystal of 25-mm thickness and 310-mm diameter.

the PHELIX pulses to 527 nm is indispensable. The size of the hohlraums require pulses as short as 1-2 ns. The 25-mm thick DKDP crystal of 310-mm diameter (Fig. 5) will be placed at a position between the exit lens of the bridge telescope to Z6 and the turning mirror MM10 in the North Tower such that it is safe versus ghost focii resulting from the lens, the DKDP crystal, and the window of the housing containing the DKDP crystal. Important issues concerning the sensitivity of the conversion efficiency versus the ambient temperature, beam pointing fluctuations, fluence modulations, and the degree of polarization of the fundamental beam were carefully analyzed. Given the present PHELIX performance and with losses resulting from the 1ω-suppression and 2ω-beam transport taken into account, conversion efficiencies of more than 50% appear feasible, yielding more than 200 J of 527-nm light energy on target for an infrared pulse of 450-J energy. The 2ω-beam will be focused with a lens of 1.5-m focal length located under the Tower West above the Z6 target chamber. Most of the required optics are already delivered and validated. The complex design of the DKDP crystal mount is completed and will be manufactured soon.

References

[1] Confer contr. by A. Blazevic et al. in this Report
[2] Confer contr. by O. Rosmej et al. in this Report
[3] Confer contr. by I. Alber et al. in this Report
[4] “Improving the usability od the CS framework”, D. Beck, H. Brand, M. Feldmann, M. Kugler, and A. Schwinn, GSI Science Report 2007, p. 25

Phelix at Z6 - Extended possibilities for combined ion-laser experiments

A. Blažević[1], V. Bagnoud[1], S. Borneis[1], U. Eisenbarth[1], A. Frank[2], J. Fils[1], S. Götte[1], M. Günther[2], T. Hahn[1], T. Heßling[1], M. Kreutz[1], S. Kunzer[1], J. Menzel[2], T. Merz-Mantwill[1], E. Onkels[1], A. Pelka[2], D. Reemts[1], O. Rosmej[1], M. Roth[2], M. Schollmeier[2], D. Schumacher[2], T. Stöhlker[1], A. Tauschwitz[1], H. Wahl[1], K. Witte[1]

[1]GSI, Darmstadt, Germany; [2] TU Darmstadt, Germany

Since May 2008 the Phelix laser has become operational at the plasma physics experimental area Z6. This area now has become a unique facility offering ion and laser beams for combined experiments. Targets can be heated by the Phelix laser, diagnosed by up to three laser beams from the nhelix laser and with a synchronisation of about 1 ns probed by an ion beam coming from the Unilac. In detail the following laser and ion beams can be used in the target chamber of Z6.

The Unilac ion beam: The accelerator is providing the experimental areas with any projectile between Li and U and any energy up to 13 MeV/u ($\Delta E/E<10^{-4}$). The pulses, with a pulse length of 40 µs – 5 ms, have a substructure of 36 MHz resp. 108 MHz, depending on the ion source. This means the long ion pulse consists of short micro bunches with a width of about 3 ns (FWHM) probing the target each 27 ns resp. 9 ns, which is essential for investigation of short living states of matter like a hot expanding plasma.

The Phelix laser beam: At the moment one of three planned beam lines is finished delivering a laser beam almost anti-parallel to the ion beam ($\varphi = 9°$). Laser pulses at a wave length of 1053 nm and pulse length of 1 – 15 ns with an energy of up to 500 J can be focused by a lens (f = 4 m) on target. In 2010/2011 two additional beam lines will be finished. The first one is planned to deliver a laser pulse at 2ω perpendicular to the ion beam line, focused by a 1.5 m focusing lens, whereas the second will transport a compressed short pulse at 1ω with a power of 100 TW for, e. g., laser acceleration experiments.

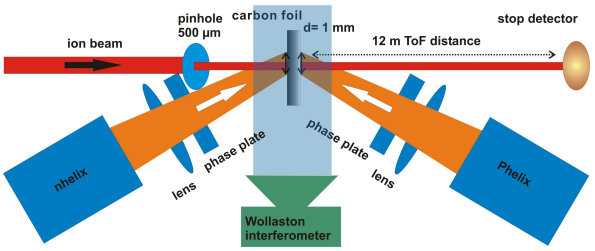

Figure 1: Experimental setup at Z6 using an ion and three laser beams for ion-plasma interaction studies

The nhelix laser beams: The nhelix laser will be used furthermore for heating and especially diagnostics. Three laser beams with timing better than 1 ns among each other can be used simultaneously in the target area: a high energy laser beam for heating, an amplified shorter pulse for Thomson scattering or backlighting, and a low-energy beam at 2 or 3 ω for laser interferometry measurements of an expanding plasma. Figure 1 illustrates an experimental setup we used for the investigation of the interaction of swift ion beams with laser heated plasma.

Following is an overview of the laser and ion parameters available at Z6:

- **Unilac ion beam: probing**
  3<Z<92, E = 3 -13 MeV/u
  f=108/36 MHz, Δ_{tion} = 3 ns (FWHM)
- **Phelix laser beam: heating**
  E < 0.5 kJ @ 1 - 15 ns, λ = 1053 nm (2ω in 2010)
  50 J @ 0.5 - 2 ps, λ = 1053 nm =>100 TW (2011)
  300 J @ ~ ns (broad spectral width)
- **nhelix laser beam: diagnostics**
  100 J @ 6 -14 ns, λ = 1064 nm
  5 J @ 0.5 ns, 2ω (e.g. Thomson scattering)
  <1 mJ @ 0.5 ns, 3ω (interferometry)

Furthermore a wide range of plasma diagnostic tools have been developed and are ready to be used, like laser interferometry, X-ray streak spectrometer, visible streak camera, VUV-, XUV-, X-ray spectrometers, pinhole cameras or Thomson scattering measuring time or space resolved the most important plasma parameters like free electron density or temperature. A first experiment on energy loss of Ar ions in a carbon plasma generated by the Phelix laser (E = 80-90 J) has been performed. Fig. 2 shows some results. As with the nhelix [1] laser right at the beginning of the laser heating the energy loss decreases. Once reaching the max. laser intensity, the plasma homogenizes and the energy loss increases again. Due to the higher plasma temperature and a faster expansion, the energy loss does not exceed that in the solid foil (100%).

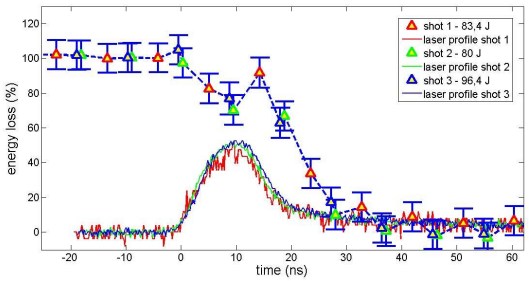

Figure 2: Energy loss results of Ar (E=4 MeV/u) in a carbon plasma generated by the Phelix laser at Z6.

References:

[1] A. Frank et al., this annual report

A theoretical description for heavy ion beam stopping in hot and dense plasma

A. Frank[1], A. Blazevic[2], P.L. Grande[3], G. Schiwietz[4], V.V. Vatulin[5], O.A. Vinokurov[5], and M. Roth[1]

[1]TU Darmstadt, Germany; [2]GSI, Darmstadt, Germany; [3]Helmholtz-Zentrum Berlin für Materialien und Energie, Germany; [4]Universidade Federal do Rio Grande do Sul, Porto Alegre, Brazil; [5]RFNC-VNIIEF, Sarov, Russia

The stopping power of heavy ions in matter is a field of research that has been addressed for about a century. The understanding of the interaction of charged particles with cold matter has continuously evolved, however for ionized matter it is not yet fully understood. This report presents a new theoretical ansatz to a consistent microscopic description for the energy loss of argon in a laser-generated carbon plasma covering a huge parameter regime in density and temperature. This approach to the stopping in plasma does not use any effective charge description of the projectile as for example the commonly used Bethe formula. The theoretical description of the energy loss was carried out with the results of the CasP code [1]. A modified version of the code allows the calculation of the projectile energy transfer with a defined charge state to bound electrons of ionized carbon and to free electrons as well. The plasma's charge state distribution is taken into account by solving the Saha equation. The energy transfer to free electrons is modeled by a single oscillator with an excitation energy equal to the plasmon energy according to the free electron density. This approach leads to stopping cross sections for argon of a defined charge state for any set of plasma parameters needed. The results are shown using the example of Ar^{18+} at 4 MeV/u in figure 1. For high temperature and low ion density the stopping cross sections are considerably larger (up to a factor of 2) than for high density and low temperature. For intermediate temperatures between 30 and 60 eV at moderate densities there is a plateau due to the stable configuration of C^{4+}. For higher temperatures electrons from the target's K-shell are ionized which makes the biggest contribution to the increased stopping cross section in the plasma since the differences in the excitation energies are very huge. The resulting stopping cross sections from the CasP calculations can be combined with the Monte-Carlo simulation described in [2]. This allows to determine the energy loss of each projectile at its current charge state. No effective charge description of the projectile is needed in this method. However projectile excitation is currently neglected in the stopping power calculation. The results for a 0.5 μm carbon foil irradiated by a laser pulse are plotted in figure 2 as well as the experimental data [3]. The plasma is modeled by MIMOZA-2D [4] hydrodynamic simulations. For the first 10 ns after the beginning of laser-matter interaction, experimental and theoretical data differ due to the until now not fully explained experimentally observed decrease in the energy loss. As soon as the plasma is sufficiently heated there is a good agreement between experimental and theoretical data. Please note that the error bars of the code only include the straggling due to different projectile charge state evolutions of the argon ions. Errors due to charge exchange cross sections and hydrodynamic profiles are not considered.

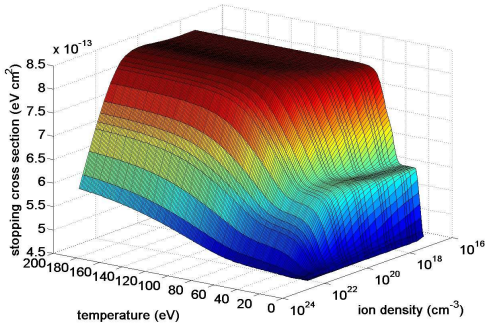

Figure 1: Stopping cross sections for $^{18+}$Ar in carbon plasma at 4 MeV/u regarding the contributions of bound and free electrons calculated by the CasP code.

In conclusion there is a huge difference between the energy loss of heavy ions in carbon plasma and the one in solid/gaseous state, strongly depending on the plasma parameters. For the investigated projectile-target configuration the differences stem from two effects, most importantly the more efficient excitation of free electrons which make a contribution of 90 % to the energy loss increase in the considered target. The higher projectile charge states in this case only make a contribution of 10 %.

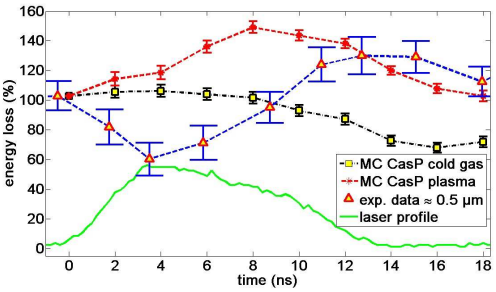

Figure 2: Comparison between experimental and theoretical energy loss data of argon in carbon plasma.

References

[1] P. L. Grande and G. Schiwietz, Phys. Rev. A 58, 3796, 1998

[2] A. Frank, A. Blazevic et al, GSI annual report 2007, 306

[3] A. Blazevic, A.Frank et al, GSI annual report 2007, 305

[4] I. Sofronov et al., Ser. Mat. mod. of phys. proc. 1, 25 (2000)

* supported by ISTC 2264

Spectral distribution of laser-driven hohlraum radiation

T. Heßling[1], A. Blažević[1], D. Kraus[2], M. Roth[2], G. Schaumann[2], D. Schumacher[2], and D.H.H. Hoffmann[2]

[1]GSI, Darmstadt, Germany; [2]TU Darmstadt, Darmstadt, Germany

Introduction

The plasma physics group at GSI investigates among other issues the energy loss of heavy ions in laser produced plasma [1]. The current experimental setup consists of an ion beam from the UNILAC accelerator that penetrates a thin carbon foil which is irradiated by an intense laser beam, e.g. the *nhelix* or PHELIX laser. The foil is turned into a hot plasma while the ions pass through it and the change in energy loss is measured by the time of flight.

The laser cannot penetrate the foil and heats only the surface. This results in temperature as well as density gradients, complicating the analysis and theoretical description of the experiment. An advanced setup utilizes gold cavities which convert the monochromatic laser light into thermal black body radiation in the soft X-ray regime. A carbon foil is placed into a secondary cavity which is attached to the converter and will be heated by the X-rays volumetrically and homogeneously.

As a preparation towards this setup the thermal radiation has to be characterized. The latest results are presented in this report.

Experiments

The temperature was measured with an absolutely calibrated VUV spectrometer [2]. The maximum radiation temperature was found to be $(73 \pm 8)\ eV$, or about $8.4 \cdot 10^5 K$. In Figure 1 the time-dependent temperature is depicted, the laser hits the target at $t = 0$. In the grey area the temperature can no longer be deduced due to the disintegration of the cavity and the unknown increase of the radiation source size, whose knowledge is essential for the analysis.

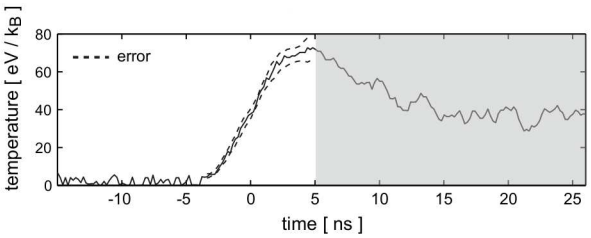

Figure 1: Time-resolved measurements of the radiation temperature in a laser heated hohlraum

The spectrometer measures the radiation at distinct wavelength intervals from 120 nm to 360 nm. The black body radiation of this high temperature, however, peaks at wavelengths in the soft X-ray regime of a few nanometres. To verify the time-resolved measurement an X-ray spectrometer covering this region was used in recent experiments to record an overall spectrum. Due to the time-integration only the maximum temperature can be extracted from the measurements. The intensity of thermal black body radiation increases with the temperature to the power of 4 and thus the time-integrated spectrum shows mostly this part of the radiation. From this the temperature can be deduced by Wien's displacement law.

In Figure 2 such a spectrum is presented. Two curves are shown: the upper line is the spectrum of a gold foil and the lower line the spectrum of a hohlraum. The radiation emanating from the cavity shows a much smoother distribution due to the transition from line-dominated radiation to thermal black body radiation, as expected. Additionally the thermal radiation shows a peak at about 3.7 nm (the grating's first diffraction order is almost not visible, the spectra are shown in the second diffraction order). This corresponds to a radiation temperature of 68 eV and fits remarkably well with the previous time-resolved measurement.

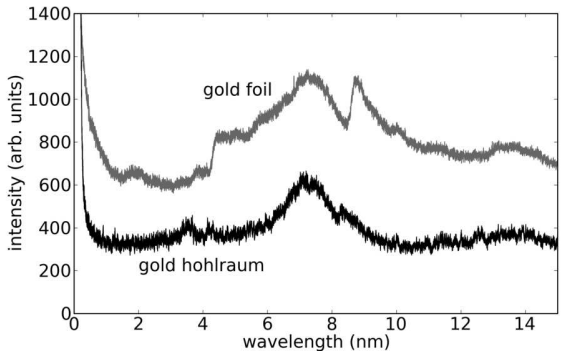

Figure 2: Time-integrated spectra of a gold foil and a hohlraum

References

[1] M. Roth *et al.*, "Energy loss of heavy ions in laser-produced plasmas", Europhys. Lett. **50** (2000), p. 28

[2] G. Schaumann, "Experimente mit lasergeheizten Hohlräumen für die Untersuchung der Wechselwirkung von Schwerionen mit ionisierter Materie", PhD thesis, 2007

Radiation Temperature of a Gold Hohlraum Heated by PHELIX

O. N. Rosmej[1], Y. Zhao[1, 2], N. Miski-Oglu[1], N. Zhidkov[3], A. Kunin[3], N. Suslov[3], V. Vatulin[3], Borisenko[4], Yu. Merkuliev[4], I. Burenkov[5], S. Zajac[6], Th. Stoehlker[1], D. H. H. Hoffmann[1, 7]

[1]GSI-Darmstadt, Germany; [2]IMP, Lanzhou, China; [3]VNIIEF, Sarov, Russia; [4]LPI, Moscow, Russia; [5] Moscow State University, Russia; [6]IPPLM, Warsaw, Poland; [7]TU-Darmstadt, Germany

Interaction of heavy ions with ideal and non-ideal plasmas is the key research activity of plasma physics at the Z6 experimental area. The plasma can be either created by direct laser irradiation of the target or indirectly by using a two-steps heating scheme. While the direct method provides ideal-plasma conditions, the indirect heating allows the creation of non-ideal plasmas which are homogeneous over the time scale of several nanoseconds. In the proposed scheme [1] a main cylinder of 1-2 mm length filled with low-density CH foam is directed along the ion–beam axis. The laser heats directly the walls of the first target section, the so called converter, separated from the main target by a thin foil. Soft X-ray radiation in the energy range of 0.3-2 keV with a spectral distribution close to the thermal equilibrium produces a volumetric heating of the foam up to T_e = 20-30 eV at a particle density of 10^{20} cm^{-3}.

The present experiments use PHELIX pulses of up to 250-J energy and investigate the spectrum of the X-ray radiation emitted from the gold converter and transmitted through the thin gold foil of 0.12 μm thickness.

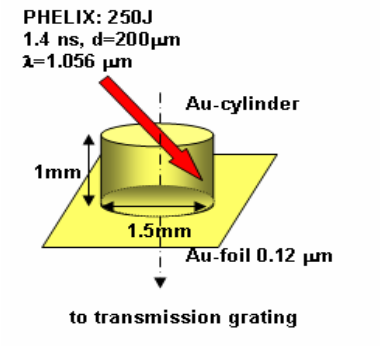

Fig. 1 Gold converter target

The laser pulse of 1.4 ns duration is focused to a 150-200 μm spot on the wall of 1mm height and 1.5mm in diameter gold cylinder covered from one side with a thin gold foil (see fig. 1). The converter radiation is then diffracted by a free standing gold transmission grating of 70 μm height and a period of 1.4 μm and finally recorded by a VUV-film. In order to obtain sufficient spatial resolution, two slits of width w_1= 93 μm and w_2= 197 μm are used respectively. The moderate spectral resolution of the spectrometer of 25 Å is defined by the 1.5 mm size of the X-ray source. For the photon energies of 0.1, 0.25 and 0.5 keV, the spectral resolution amounts to 10, 50 and 100%, respectively. The last can be improved by reducing the source size. Fig. 2 shows the obtained VUV- spectra of the gold converter transmitted through the thin gold foil.

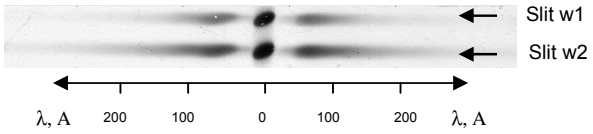

Fig. 2 Measured VUV-spectra obtained from the gold converter target for two different slit widths of 93 (top) and 197 μm (down), respective.

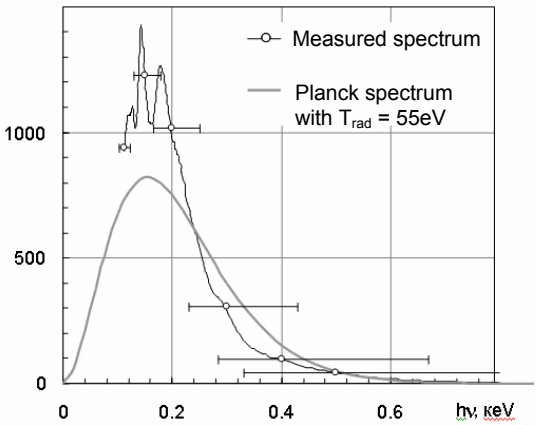

Fig. 3 Measured and calculated spectral distribution I_ν (keV/ster/cm^2) of the gold plasma.

The measured spectral intensity distribution was fitted with a Planck spectrum (see fig. 3). The best fit is obtained for a black-body temperature of 55 eV. In the upcoming experiments, the parameters of CHO triacetate foams [2] heated by the radiation flux from the gold converter will be measured. For the current laser parameters one expects an electron temperature of 10 eV and an electron density of 5.10^{20} cm^{-3}. The indirect heated foams serve as interaction plasma targets for the UNILAC heavy ion beam.

This work is supported by the ISTC# 2264 project.

References:

1. E. Vasina et al, GSI Report, 2001
2. A. M. Khalenko et al, LPB24 (2006), 283-290

Transport of laser-accelerated proton beams with pulsed high-field solenoids

I. Alber[1], K. Harres[1], M. Schollmeier[1], F. Nürnberg[1], M. Günther[1], J. Schütrumpf[1], A. Tauschwitz[2], A. Blazevic[2], M. Tampo[3], H. Daido[3], V. Bagnoud[2], and M. Roth[1]

[1]TU Darmstadt, Germany; [2]GSI, Darmstadt, Germany; [3]Kansai Photon Science Institut, Japan

The interaction between an ultra-intense laser pulse ($I > 10^{18}$ W/cm^2) and a thin target foil leads to an acceleration of protons up to kinetic energies of several tens of MeV. In the short acceleration time of a few picoseconds up to 10^{13} protons and ions are accelerated. Well-defined, smooth beams with transverse emittances more than hundred times smaller than in conventional accelerators are observed in experiments [1]. This remarkably good beam quality motivates the injection into conventional accelerators. However, such an application requires further investigations to reduce the half-opening angle of the beam which is up to 40° and to minimize the energy spread. An external magnetic field as a collimation and energy filtering method decouples the acceleration process and the transport providing the opportunity of independent optimisation of both processes.

In a previous experiment two permanent magnet quadrupoles were used to focus protons with the kinetic energy of 14 MeV. In a small area of 200 μm diameter, proton flux increase by a factor of 75 was achieved in comparison to an unfocused beam [2]. Since a single quadrupole only focuses the beam in one direction and defocuses the beam in the perpendicular one, at least two quadrupoles are necessary to focus the beam whereas the second quadrupole cuts most of the beam.

We report on an experiment carried out at the PHELIX laser-system at GSI using a pulsed high field solenoid to collimate and focus the proton beam and further increase the proton flux density. Collimation or focusing is achieved by the Lorentz force generated by the particles when crossed into the radial and axial magnetic field components of the solenoid. Since the solenoid focuses the beam in all transverse directions, it can be used as a compact single device. Thus, higher transmission of protons through the solenoid can be achieved in comparison to the quadrupoles. The current needed to generate the strong magnetic flux densities of up to 15 T were provided by discharging some of the capacitors normally used to power the flash lamps of PHELIX. The solenoid was placed 17 mm behind the target to make sure that all protons enter the solenoid's aperture of 44 mm.

The simulation with CST Particle Studio in figure 1 shows the behavior of the proton beam in the magnetic field. An on axis magnetic flux density of 8 T leads to a collimation of protons with the kinetic energy of 2.5 MeV.

Figure 2 shows the measured particle numbers detected behind the solenoid at a magnetic flux density of 8 T in comparison to the initial particle numbers. The detector was placed 240 mm behind the target and had a size of (5×5) cm. As the simulation suggests, the 2.3

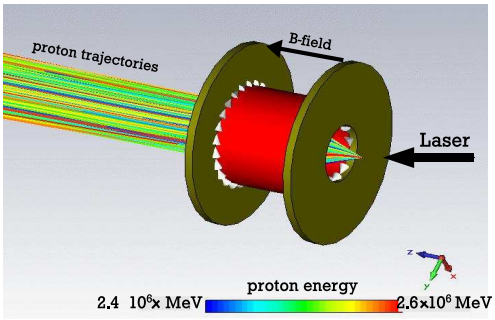

Figure 1: The figure shows a simulation with CST Particle Studio. A magnetic flux density of 8 T in the solenoid collimates protons with an energy of 2.5 MeV.

MeV protons are slightly focused, so that the beam diameter behind the solenoid is smaller than the detector size. About (95^{+5}_{-19})% of the initial particles can be detected. In comparison in laser-proton-acceleration without beam parallelization by the solenoid only 23% of the initial protons can be detected in the RCF due to the strong divergence of the beam. Since the magnetic field is not strong enough to

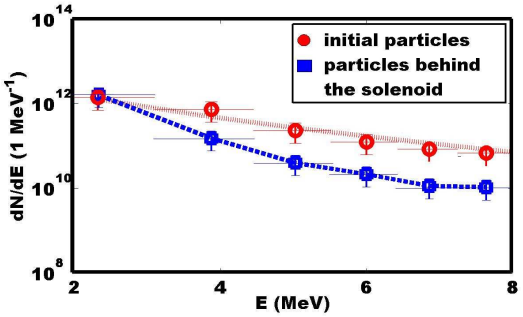

Figure 2: The figure shows the particle numbers detected behind the solenoid (squared data points) in comparison to the initial particle numbers (circular data points).

collimate protons with energies higher than 2.5 MeV, the amount of detected particles in comparison to the initial particles decreases strongly with increasing proton energy.

In summary, we have demonstrated collimation of laser-accelerated proton beams with a pulsed high-field solenoid. Behind the target (95^{+5}_{-19})% of the initial particles with the kinetic energy of 2.3 MeV can be detected.

References

[1] T. Cowan *et al.* Phys. Rev. Lett. **92**, 204801 (2004).

[2] M. Schollmeier *et al.*, Phys. Rev. Lett. **101**, 055004 (2008).

X-ray diagnostic of a Ti-plasma created by a PHELIX nanosecond pulse

O. N. Rosmej[1], Y. Zhao[1, 2], T. Kuehl[1], N. Miski-Oglu[1], N. Zhidkov[3], N. Suslov[3], A. Kunin[3], N. Andreev [4], M. Povarnitsyn[4], I. Burenkov[5], S. Zajac[6], Th. Stoehlker[1], D. H. H. Hoffmann[1,7]

[1]GSI-Darmstadt, Germany; [2]IMP, Lanzhou, China; [3]VNIIEF, Sarov, Russia; [4] Joint Institute for High Temperature, Moscow, Russia; [5]Moscow State University, Russia; [6]IPPLM, Warsaw, Poland; [7]TU-Darmstadt, Germany

The Nd:glass PHELIX-laser operating at Z6 experimental area provids an opportunity for heavy ion – laser crossing experiments. The laser is capable to deliver up to 300J energy focused at the target in 100-150 µm spot in the nanosecond pulse regime. The experimental task was the characterization of the plasma parameters obtained at maximum possible laser intensity of 10^{15} W/cm^2. For these purposes the characteristic radiation of the highly ionized target plasma was used. Preliminary 1-D calculations of the plasma hydrodynamic expansion were carried out in order to estimate the temporal and spatial distribution of the plasma temperature and density as well as the charge states of highly ionized target material. Calculations carried out for a Fe bulk target irradiated by the PHELIX laser (250J, 1.4 ns, 150 µm focal spot) estimated the maximum electron temperature up to 3 keV and demonstrated transient behavior of the Fe-plasma charge state evolution.

In the experiments thick Ti-foils were chosen as a target material, in order to reach a more stationary plasma charge distribution and to show up keV´s electron temperature. In this temperature region Ti atoms are highly ionized up to H-, He-, and Li-charge states whose characteristic radiation is very suitable for the determination of the plasma parameters using methods of X-ray spectroscopy [1]. Titanium X-ray spectra were registered by means of two focusing spectrometers providing high spectral ($\lambda/d\lambda \sim 2000$) and spatial resolution [1, 2]. Spherically bent mica crystals with a curvature radius of 150 mm were used as dispersive elements.

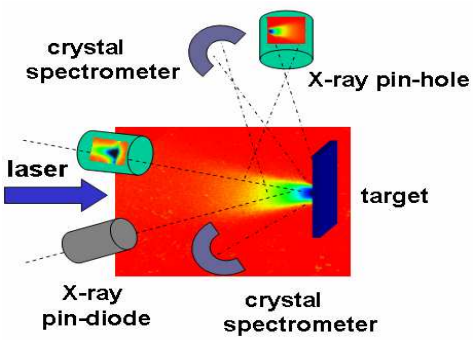

Fig. 1 Experimental setup.

One spectrometer was placed perpendicular to the direction of the plasma expansion giving a possibility for a spatially resolved analysis of the characteristic Ti-spectra. The second one observes the plasma radiation perpendicular to the target surface. X-ray pin-hole images and X-ray pin-diode signals with nanosecond temporal resolution were used in order to complete the X-ray diagnostics with spatially and temporarily resolved information (see fig.1). The registered characteristic spectra (see Fig.2) show a transient feature of the Ti - ion charge state evolution and the presence of a non-thermal component in the plasma electron energy distribution.

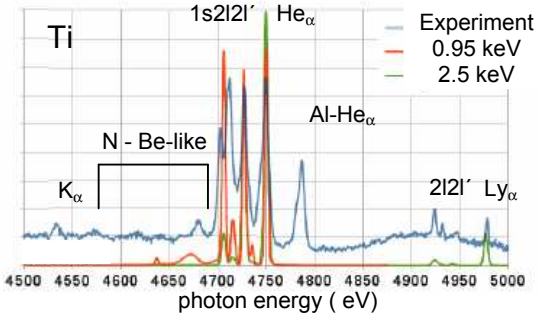

Figure 2: X-rays of a Ti-foil heated by PHELIX-laser.

The spectra analysis was carried out using the code "Flychk" [NIST, 3] providing the time dependent collisional - radiative population kinetics of the ion ground and excited states with a possibility of including a fraction of non-thermal electrons. K-shell transitions in cold and low ionized Ti (4500-4700 eV in fig. 2) reveal the plasma charge state distribution at the beginning of the ionization process. The relative intensities of the radiative transitions in He-like Ti ions and the Li-like dielectronic satellites 1s2l2l´-1s^{2}2l (4700-4750eV) show the plasma at a bulk electron temperature of 1 keV. Further evolution of the plasma temperature during the target heating leads to the formation of H-like ions with an ionization potential of 6 keV. The electron temperature estimated from the relative intensities of the Ly$_\alpha$ and 2l2l´-1s2l transitions from double excited states (4975-5000 eV) gave the value of 2.5 keV.

Summarizing the experimental results we can say, that the PHELIX–laser with nanosecond pulse duration is capable to heat the mid Z targets up to 2.5 keV

This work was supported by the ISTC#2264 project

References

[1] A.Ya. Faenov et al, Phys. Scripta, **50**, 333 (1994)
[2] O. N. Rosmej et al, Phys. Rev. A **72**, (2005), 1-8.
[3] H.-K.Chung et al, HEDP **1** (2005) 3-12

Characterization of a 10Hz double-pulse non-normal incidence pumped transient collisional Ni-like molybdenum soft x-ray laser for applications

D. Zimmer*[1,2,3], B. Zielbauer[1], O. Guilbaud[1], J. Habib[1], S. Kazamias[1], M. Pittman[1], D. Ros[1], V. Bagnoud[2], B. Ecker[2,3], D. Hochhaus[2,3], and T. Kuehl[2,3]

[1]Université Paris-Sud 11, Orsay, France; [2]GSI, Darmstadt; [3]Johannes Gutenberg-Universität Mainz, Germany

Stable and reliable operation demonstrated and studied with a 10 Hz Ti:sapphire laser system proves the suitability of the double-pulse non-normal incidence pumping geometry for table-top high repetition soft x-ray lasers (SXRL) on the way to applications.
In this experiment a nickel-like molybdenum $4d^1S_0 - 4p^1P_1$ transient collisional soft X-ray laser at 18.9 nm is investigated which is pumped in a double-pulse non-normal incidence geometry [1] at a 10Hz laser system facility [2]. The two pumping pulses are generated in the front-end of the Ti:sapphire laser system in a Mach-Zehnder type setup. The stretched pulse is distributed into the two arms with an adjustable ratio via the combination of a wave plate and a polarizing beam splitter. One of the arms incorporates a delay line adjustable between 0.8 and 2.6 nanoseconds. The two pulses are then amplified through the chain of the Ti:sapphire CPA system which includes a regenerative amplifier, a 4-pass pre-amplifier and two 4-pass cryogenic power amplifiers. After the compression adjustment two pulses of equal duration between 2 and 16 picoseconds are formed and then sent to the experiment chamber. The focussing system consisting of a flat 45 degree mirror and a spherical mirror with a focal length of 500 mm off the normal incidence produces a line focus of 3.8 mm length and $50\,\mu m$ width with an intrinsic traveling wave speed of 1.2 c. Both pulses hit the target at the same grazing incidence angle Φ of 19 degrees. For the pump laser wavelength of 805 nm the electron density at which the energy is absorbed amounts to $n_{e,abs} \approx 2.3 \times 10^{20}\,cm^{-3}$, following $n_e = n_c \cdot \sin^2 \Phi$ with the critical density n_c. The line foci optimization is done in the infra-red with a high resolution imaging device (RILF).

The applied diagnostic consists of a monochromatic near-field imaging system that shows the soft-x-ray laser source size and position relative to the target surface and a far-field imaging system to provide information about the divergence and the coherence of the soft x-ray laser beam. The near-field is imaged by a spherical multi-layer mirror and a flat multi-layer mirror onto on a 16-bit back-thinned CCD camera behind a $2\,\mu m$ Al filter. A typical near-field image of the source, with its limitation in resolution of the $13\,\mu m$ camera pixel size, is shown in the upper part of Fig. 1. The measured source size is $4\,\mu m \times 12\,\mu m$. The far-field beam profile is recorded by another 16-bit back-thinned CCD camera after a deflection by a flat multi-layer mirror and a total propagation path of 1 m. A typical far-field image using a $0.3\,\mu m$ Al filter is shown in the lower part of Fig. 1. The beam has a horizontal and vertical divergence of 3 mrad and 8 mrad respectively. The strong fringes in the vertical axis give additional information about the coherence of the soft x-ray laser beam [3].

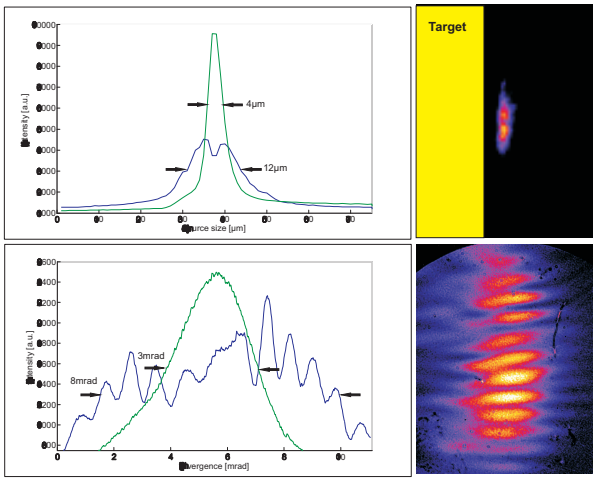

Figure 1: Near- and far-field beam profiles of the SXRL.

A characterization of the soft x-ray laser output is done in a extensive three parameter scan of double-pulse energy balance, time delay and pulse duration. Strongest lasing is found at a pre-pulse to main pulse ratio of $1:6$, a time delay of 1.6 ns and a pulse duration of 10 ps. Additionally a fourth parameter, the focus width, is varied from $30\mu m$ to $120\mu m$ and an optimal regime at $50\mu m$ is identified. The highest measured x-ray laser energies reach up to $0.7\,\mu J$ for a total pump laser energy of $0.7\,J$ on the target.
The introduction of the double-pulse non-normal incidence pumping geometry improves the reliability and stability of efficient table-top high-repetition soft x-ray lasers: we were able to obtain x-ray laser emission for several hours at 10 Hz repetition-rate without re-alignment.

References

[1] Zimmer D et al. 2008 Opt. Express. **16** 10398

[2] Kazamias S et al. 2006 J. Phys. IV France **138** 13

[3] Guilbaud O et al. 2006 Europhysics Letters **74**, 823

* d.zimmer@gsi.de

Double-pulse non-normal incidence pumping geometry for transient collisionally excited short-wavelength x-ray lasers

D. Ros[1], D. Zimmer*[1,2,3], V. Bagnoud[2], B. Ecker[2,3], U. Eisenbarth[2], J. Habib[1], D. Hochhaus[2,3], D. Javorkova[2], S. Kazamias[1], T. Kuehl[2,3], D. Ursescu[4], B. Zielbauer[1], and the PHELIX-Team[2]

[1]Université Paris-Sud 11, Orsay, France; [2]GSI, Darmstadt; [3]Johannes Gutenberg-Universität Mainz, Germany; [4]National Institute for Laser, Plasma and Radiation Physics , Bucharest, Romania

On the way to reaching shorter wavelength x-ray lasers (XRL) great progress was achieved towards lowering the necessary high pump laser energy required for the preparation of the lasing medium. For this, two pulses in two independent beam-lines with different duration and at different angles of incidence were applied. This is a non-trivial complication, since the delivery of high-energy pulses require the use of large beam diameters. With the concept presented here, the set-up is simplified tremendously. Since the double pumping pulse scheme uses only one beam-line to generate the x-ray laser gain medium, numerous advantages i.e. improved stability, reproducibility and not least cost decrease are apparent.
In the front-end of the driving chirped pulse amplification (CPA) laser system, the double pumping pulse is generated in a standard Mach-Zehnder type set-up. The stretched pulse is distributed into the two arms with an adjustable energy ratio. One of the arms incorporates a delay line adjustable between 0 and 3 nanoseconds delay. The two pulses are then amplified through the chain of the CPA system which includes regenerative Ti:Sapphire and Nd:Glass amplifiers. After compression, the two short pulses are sent to the experiment chamber [1]. For this experiment an additional adjustable compressor is installed in the pre-pulse arm, which allows to produce a pre-pulse duration between 100 and 200 picoseconds.

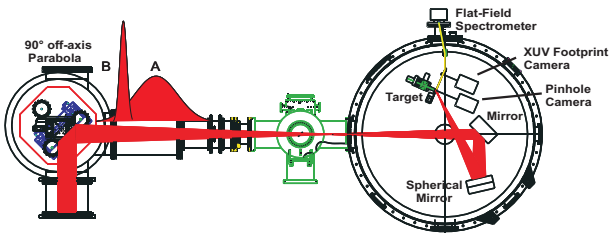

Figure 1: Double-pulse focussing system and diagnostics.

In the experiment the nickel-like samarium $4d^1S_0 - 4p^1P_1$ transient collisionally excited x-ray laser at 7.3 nm was either recorded by a XUV far-field camera via a 45 degree XUV mirror optimized for that wavelength or by a grazing incidence reflection on a silver coated glass substrate which guided the XRL beam into a flat-field gold grating spectrometer with 1200 lines/mm. The experimental set-up in the target chamber is shown in Fig. 1: The focusing system produces a line focus with an intrinsic traveling wave speed of 1.5 c by using a combination of a 90 degree off-axis parabolic mirror and an on-axis spherical mirror. The beam from the compressor is deflected by a 30 cm diameter copper parabola with a focal length of 2 m via a flat folding mirror onto the 20 cm diameter spherical mirror with a focal length of 675 mm which is aligned off the normal incidence by 12 degrees. The line focus on the Sm-slab target was $8\,mm \times 100\,\mu m$ FWHM. Both pulses hit the target at the same non-normal incidence angle of 50 degrees. The double-pulse delay was varied from 100 ps to 200 ps, values which are described as optimal in [2],[3]. The intensity of the pre-pulse was changed between 5% and 50% of the total energy. The contrast level could not be measured better than 10^{-3} at the time of the experiment. The resulting irradiance on the target were $\sim 2.5 \times 10^{13}\,W/cm^2$ for the pre-pulse and $\sim 5 \times 10^{15}\,W/cm^2$ for the main pulse respectively.

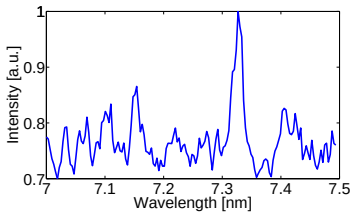

Figure 2: Sm x-ray laser line at 7.3 nm.

The output of the samarium x-ray laser at 7.3 nm was identified via the spectrum. Figure 2 shows the lineout of the spectrum of the region of interest. The peak of lasing at 7.3 nm is visible, but due to the strong x-ray background of the much hotter plasma the contrast to background is not as high as for soft XRL. Optimized pumping pulse parameters and the pump laser contrast improvement can enhance the short wavelength x-ray laser output, as reported by [2].
The work was supported through the Laserlab Europe Integrate Infrastructure Initiative.

References

[1] Zimmer D et al. 2008 Opt. Express. **16** 10398
[2] King R E et al. 2001 Phys. Rev. A **64** 053810
[3] Pert G J 2007 Phys. Rev. A **75** 063814

* d.zimmer@gsi.de

Tuning of high-order harmonics seeding plasma-based x-ray laser*

J. Seres[1], D. Zimmer[2,3], D. Hochhaus[2,3], B. Ecker[2,3], C. Spielmann[1,4], T. Kühl[2,3#]
[1]Julius Maximilians Universität, Würzburg, Germany; [2]GSI, Darmstadt, Germany; [3]Johannes Gutenberg Universität, Mainz, Germany; [4]Friedrich Schiller Universität, Jena, Germany.

Seeding x-ray lasers with high-order harmonic (HH) radiation has been successfully demonstrated a few years ago [1] and it is under extensive investigation nowadays [2]. The HH spectrum consists of discrete spectral lines at the odd multiples of the frequency of the driving laser pulses. Unfortunately, most of the harmonic lines do not coincide exactly with the wavelength of potential x-ray laser transitions. Using a Nd:glass laser system such as PHELIX at GSI for pumping an x-ray laser, the wavelength of the fundamental laser beam can not be tuned. However, harmonic lines can be shifted [3]. The magnitude of the shift can be controlled e.g. with the gas backing pressure. However, the obtainable shift is not sufficient to cover the whole wavelength range. The number of possible x-ray laser transitions can be increased by using the two-colour scheme for HH generation. Using pulses at the fundamental laser frequency mixed with pulses at the second harmonic, it is possible to generate odd and even harmonics [4,5]. With this schema we generated strong even and odd harmonics in a wide spectral range in Ar gas suitable for seeding Ni-like x-ray lasers.

The HH source was pumped by the fs-front-end of the PHELIX laser system at GSI. The 15 mJ pulses have duration of 300 fs at 10 Hz repetition rate and were focused into the gas jet with a lens with focal length of 400 mm. A 0.3-mm-long BBO crystal was placed into the focused beam for second harmonic generation. Under optimized conditions the measured conversion efficiency was up to 40%. The generated XUV radiation was characterized by using a flat-field grating (1200 l/mm) and a CCD camera. The required low background gas pressure has been ensured by applying a pulsed gas jet.

In the experiment we varied the Ar gas pressure for tuning the HH and rotated the BBO crystal to adjust second harmonic intensity (Fig. 1). Using only the fundamental beam, only odd harmonics were generated (Ar) and the spectrum extends to photon energies up to 70 eV. Converting some part (approx. 40%) of the infrared laser light into the green and using the mixed beam for HH generation, even and odd harmonic lines were observed in the measured spectra (Ar 2c). The ratio between the even and odd harmonics decreases at larger photon energies [5] and is strongly affected by the tilting angle of the BBO. Extending the two-colour HH spectrum to higher photon energies needs further systematic investigation and using Ne instead of Ar. In the applicable pressure range, the harmonic lines can be shifted by 0.2 harmonic orders to shorter wavelengths. The shift is proportional to the pressure, and can be explained as an adiabatic shift.

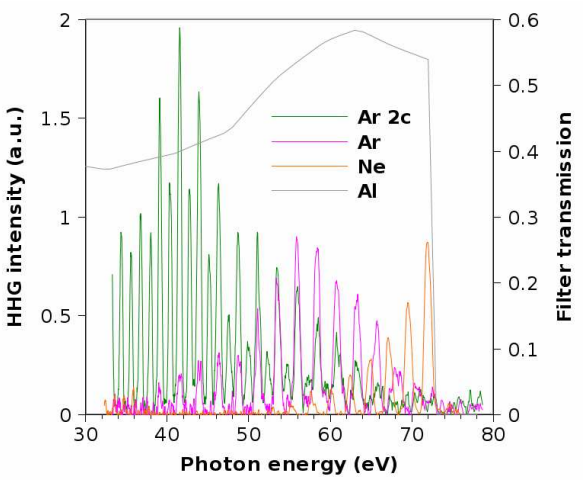

Figure 1: Generated harmonics in Ar with (Ar 2c) and without (Ar, Ne) applying two-colour pump. The spectra are cut at the short wavelength side by an Al filter (Al).

Summary

The generated HH lines in combination with pressure tuning overlap with the Ni-like Kr at 37.8eV (32-order), Y at 51.7eV (44-order) and Zr at 56.3eV (48-order) x-ray laser transitions. With the seeded x-ray laser currently developed it will be possible to substantially improve the spatial beam profile and the energy stability. With the improved parameters, high resolution spectroscopy on highly charged ions such as Li-like Uranium, as available at GSI, are in reach.

References

[1] Ph. Zeitoun, et al., Nature 431, 425 (2004)
[2] Y. Wang et al., Nature Phot. 2, 94 (2008)
[3] S. C. Rae et al., Phys. Rev. A 50, 3438 (1994)
[4] I. J. Kim et al., Appl. Phys. B 78, 859 (2004)
[5] L. Misoguti et al., Phys. Rev. A 72, 063803 (2005)

* Supported by the grants of DFG SP 687/1-3, and BMBF 06WU266I.
#t.kuehl@gsi.de

First reflectivity measurements of ion-beam heated refractory metalls*

A. Hug[1,2], S. El Moussati[2], A.D. Fertman[4], V.E. Fortov[3], A.A. Golubev[4], D.H.H. Hoffmann[2], M.I. Kulish[3], J. Ling[2], J. Menzel[2], V.B. Mintsev[3], N. Müller[2], D.N. Nikolaev[3], A. Pyalling[3], B.Yu. Sharkov[4], N.S. Shilkin[3], V.Ya. Ternovoi[3], V.I. Turtikov[4], S. Udrea[2], A. Ulrich[5], D. Varentsov[1], J. Wieser[6], and M. Zhukova[7]

[1]GSI, Darmstadt, Germany; [2]TUD, Darmstadt, Germany; [3]IPCP, Chernogolovka, Russia; [4]ITEP, Moscow, Russia; [5]TUM, Munich, Germany; [6]Coherent, Munich, Germany; [7]TPU, Tomsk, Russia

Experiments at the HHT experimental area of GSI employ intense heavy ion beams from SIS-18 to generate warm dense matter (WDM) states with fairly uniform physical conditions.

One of the main activities of the WDM experiments at HHT in 2008 (see also [1, 2]) was the direct reflectivity measurements with a laser-diode based reflectometer, embedded in the fast multi-channel pyrometer [3].

The pyrometer consists of an achromatic light collecting system and two spectral analysers with six narrow channels each in the visible and near infra-red spectral regions. The thermal emission from two spots at the target surface is guided via quartz optical fiber from the experimental area to the analysers. The spatial resolution is defined by the fiber diameter and can be as high as $50\,\mu\mathrm{m}$. The absolute calibration of the pyrometer allows to determine the brightness (radiance, "black body") temperatures for each channel. The brightness temperature is however always lower than the physical temperature of a real sample. In order to estimate the emissivity $\epsilon < 1$ and thus the surface temperature, the grey body model can be applied, where the multi-colour temperature $T_{\mathrm{fit}}(t)$ and the grey-body emissivity $\epsilon(t,\lambda) \equiv \epsilon_{\mathrm{fit}}(t)$ are fitting parameters.

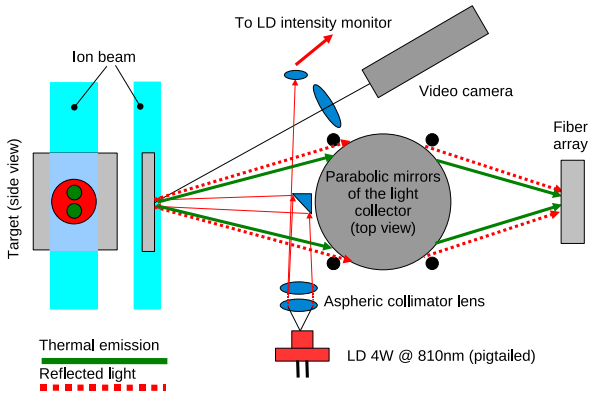

Figure 1: Reflectometer embedded in multi-channel pyrometer.

Recently a set-up for direct reflectivity measurements embedded into the pyrometer has been developed. The schematic is shown in Fig. 1. An intense laser-diode ($4\,\mathrm{W}$ at $810\,\mathrm{nm}$) illuminates the region of the target surface that is imaged by the pyrometer optics. The reflected light is then collected by the same system and recorded in a dedicated channel of the spectral analyser in which the intensity of the laser-diode completely outshines the thermal emission.

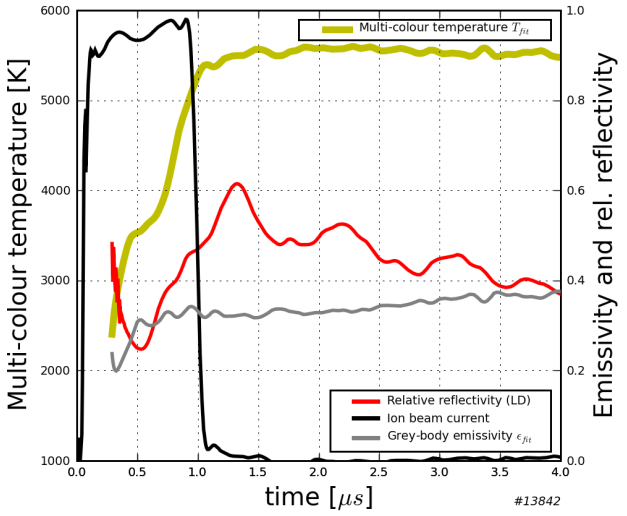

Figure 2: Multi-colour temperature and grey-body emissivity along with relative reflectivity record for a tungsten target

The relative reflectivity signal of tungsten is plotted in Fig. 2. One can clearly see a feature on the signal during melting. However, the estimated grey-body emissivity and the recorded reflectivity signals are not fully consistent which may be related to a change of the reflection character (specular to diffusive). This can also explain a strong decrease of the reflectivity signal at later times, while the thermal emission is still present.

For the next experiments, it is planned to improve the absolute calibration of the reflectivity channel, to increase the acceptance of the light collector, to install a detector for diffusively reflected light and to extend the system for reflectivity measurements at multiple wavelengths.

References

[1] D. Varentsov *et al.*, this report.

[2] S. Udrea *et al.*, this report.

[3] P. Ni *et al.*, GSI Scientific Report 2004, 237.

* Supported by GSI-INTAS grants 03-54-4254, 06-1000012-8707 and the BMBF.

Measurements of the Electrical Conductivity of Ion–Beam Generated WDM *

S. Udrea[1], S. El Moussati[1], A.D. Fertman[4], V.E. Fortov[3], A.A. Golubev[4], D.H.H. Hoffmann[1], A. Hug[1,2], M.I. Kulish[3], J. Ling[1], J. Menzel[1], V.B. Mintsev[3], N. Müller[1], D.N. Nikolaev[3], A. Pyalling[3], B.Yu. Sharkov[4], N.S. Shilkin[3], V.Ya. Ternovoi[3], V.I. Turtikov[4], A. Ulrich[5], D. Varentsov[2], J. Wieser[6], and M. Zhukova[7]

[1]TUD, Darmstadt, Germany; [2]GSI, Darmstadt, Germany; [3]IPCP, Chernogolovka, Russia; [4]ITEP, Moscow, Russia; [5]TUM, Munich, Germany; [6]Coherent, Munich, Germany; [7]TPU, Tomsk, Russia

Over the past few years, a series of measurements of the electrical resistivity of heavy-ion beam generated warm dense matter (WDM) has been performed at the HHT experimental area of GSI. These measurements [1, 2] have mostly been based on the well known four-point method. Recently, first attempts at non-contact measurements by induced eddy currents have been performed as well [3].

In this report we present the developments of the four-point as well as the non-contact experimental setups as achieved during 2008.

The last year's experimental campaign also aimed at combined measurements of thermophysical and transport properties and a shift towards establishing a reliable set of benchmark experimental results [4]. To achieve these goals a new target design for the four-point electrical conductivity measurements was necessary. As a result a **H**-

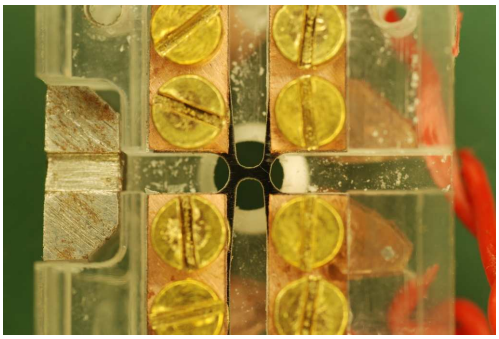

Figure 1: **H**-shaped target for combined four-point and thermophysical measurements.

shaped foil target has been developed, which allows for both measurements of the electrical conductivity and diagnostic of the thermodynamic state (Fig. 1). The first targets of this kind employed laser-cut, $100\ \mu$m thick tungsten and tantalum foils and have been irradiated by $5 \cdot 10^9$ intense $^{124}Xe^{48+}$ pulses with a duration of 900 ns.

Another improvement of the four-point setup was a redesign of the pulsed current source, by the introduction of an intermediate inductive storage with an inductance of about 4.5 mH and appropriate modifications to the circuitry layout. This allowed for a compact, battery-driven device able to deliver more than 10 A peak current in a $50\ \Omega$ load with a decay time of about $90\ \mu$s.

* Supported by GSI-INTAS grants 03-54-4254 and 06-1000012-8707 and the BMBF

The first proof of principle experiments for non-contact measurements of the electrical conductivity of ion-beam generated WDM have been conducted in 2006 by means of wide-band pulses [3]. The analysis of the results showed that it would be advantageous to use a setup with narrow-band signals. Thus a new setup has been realised which employs a frequency synthesizer and a double directional coupler, to allow for acquiring of both the direct (reference) and reflected signals. Lead wires with a length of 5 mm and

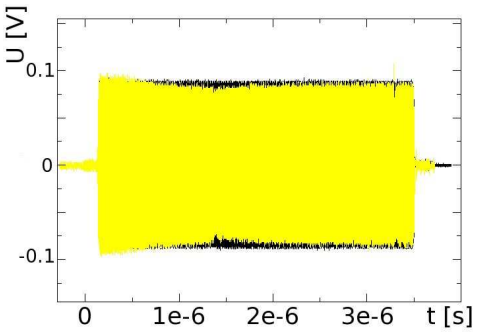

Figure 2: Non-contact measurement of the electrical conductivity. Reflected signal (yellow) is superimposed on the the reference signal (black). The frequency of the signals is 200 MHz.

0.25 mm diameter placed on the axis of quarz capillaries of 1 mm outer diameter and 0.1 mm wall thickness have been used as targets. The eddy currents in the WDM layer accumulated on the capillary's inner surface have been induced by a 3-turn coil, wound on the capillary's outer surface. A typical experimental signal with a frequency of 200 MHz is displayed in Fig. 2. The reflected signal shows a reduction in amplitude which qualitatively agrees with the presence of an conductive layer on the inner side of the capillary. A detailed analysis is ongoing for relating this signal feature with the electrical conductivity of the layer.

References

[1] S. Udrea et al., J. Phys. IV France 133 (2006) p. 1089.

[2] S. Udrea et al., J. Phys. A: Math. Gen. 39 (2006) p. 4743.

[3] J. Ling et al., GSI Report 2007-2 (2007) EP-08.

[4] D. Varentsov et al., this report.

Progress in WDM experiments with intense heavy ion beams at GSI*

D. Varentsov[1], S. El Moussati[2], A.D. Fertman[4], V.E. Fortov[3], A.A. Golubev[4], D.H.H. Hoffmann[2], A. Hug[1,2], M.I. Kulish[3], J. Ling[2], J. Menzel[2], V.B. Mintsev[3], N. Müller[2], D.N. Nikolaev[3], A. Pyalling[3], B.Yu. Sharkov[4], N.S. Shilkin[3], V.Ya. Ternovoi[3], V.I. Turtikov[4], S. Udrea[2], A. Ulrich[5], J. Wieser[6], and M. Zhukova[7]

[1]GSI, Darmstadt, Germany; [2]TUD, Darmstadt, Germany; [3]IPCP, Chernogolovka, Russia; [4]ITEP, Moscow, Russia; [5]TUM, Munich, Germany; [6]Coherent, Munich, Germany; [7]TPU, Tomsk, Russia

The primary goal of the ongoing warm dense matter (WDM) research by intense heavy ion beams at GSI is to develop essential diagnostic instruments and methods for future HEDgeHOB experiments at FAIR. This is being done in the frame of the experiment S331 fielded at the HHT area of GSI (see Fig. 1).

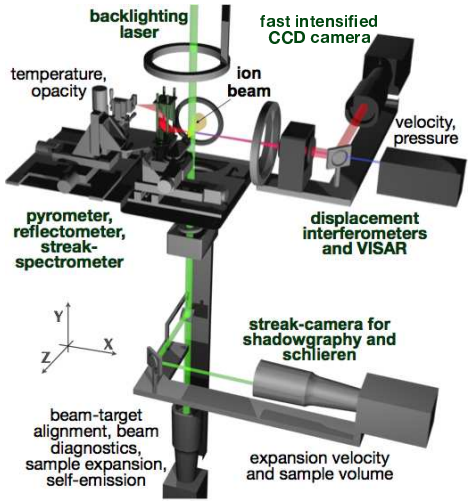

Figure 1: Schematic of the S331 setup at HHT.

During the year 2008, the fast multi-channel radiation pyrometer has been complemented with an embedded laser-diode reflectometer [1]. This allows one to obtain direct information about optical properties of the target surface such as emissivity and to advance toward physical temperature determination with the pyrometric technique. Going in the same direction, first attempts to study emission characteristics of ion-beam heated metals using flat hohlraum configurations have been made as well. This technique however requires quite high beam intensity in order to achieve uniform heating of a macroscopic hohlraum.

An important aspect of the WDM experiments is the transverse diagnostics of intense focused beams [2]. A significant progress has been achieved here due to detailed spectroscopic studies of beam-induced fluorescence of Ar and N_2 in the pressure range of $10 - 900\,\mathrm{mbar}$ as well as systematic measurements of transverse fluorescence profiles and shock waves in the gas with high temporal and spatial resolutions. In addition, a *post mortem* analysis of irradiated metallic foils provided a mean to relate the dimensions of a macroscopic melted zone to the transverse beam sizes at the focal plane [3].

Further developments include improved targets for four-contact electrical conductivity measurements [4] which are now fully integrated with thermodynamic state diagnostics, first tests of non-contact conductivity measurement techniques and measurements of time-resolved spectral opacity of thin WDM layers (C, Al, Au; $9-100\,\mu\mathrm{g/cm^2}$) in visible and near-infrared spectral regions, along with their thermal emission.

Two experimental runs have been carried out at HHT in 2008 using 350 AMeV ions of $^{238}\mathrm{U}^{73+}$ ($N \approx 1.2 \cdot 10^9$) and $^{124}\mathrm{Xe}^{48+}$ ($N \approx 5 \cdot 10^9$). The main physics objective of these S331 runs was to study thermodynamic, transport, and optical properties of refractory metals, namely tungsten and tantalum, at melting and in hot expanded liquid states. In particular, to simultaneously measure surface reflectivity, thermal light emission and electrical conductivity. The key idea was to avoid excessive boiling and consequent fast expansion of the target material, and thus to secure a well-defined emitting/reflecting surface. This also means no "record-breaking" in terms of maximal achieved temperature and pressure but quality of experimental data that should provide reliable and rigorous benchmarks for testing simulation codes. Therefore a better heating uniformity and measurement precision have been achieved by using defocused and coasting (900 ns long flat-top) ion beam pulses. Another highlight of these experiments was to move from the "single-shot philosophy" towards reproducibility and statistics. For this purpose, many identical targets have been shot compromising variations in target material and/or beam-target geometries.

An important event was founding in 2008 a Helmholtz-Russia Joint Research Group [5] *"Experimental Study on WDM by Intense Heavy Ion Beams"* which will provide a solid framework for this research at the HHT area of GSI for the following three years.

References

[1] A. Hug et al., this report.

[2] D. Varentsov et al., Contrib. Plasma Phys. **48** (2008) 586.

[3] M. Zhukova et al., GSI Student Program Reports 2008, 159.

[4] S. Udrea et al., this report.

[5] `http://www.helmholtz.ru/doc/index/HRJRG_ENG_20102008.pdf`

* Supported by GSI-INTAS grants 03-54-4254 and 06-1000012-8707.

Investigation of the properties of a MHD plasma valve*

W. Schweizer, C. Teske, J. Schunk, J. Jacoby.
Inst. für Angewandte Physik, Goethe-Universität, D-60438 Frankfurt am Main, Germany

An ion beam has quite different vacuum requirements in different sections of an accelerator. Behind a stripper gas or after interaction with a gas target the vacuum conditions are poor, whereas in an accelerator module or especially in a storage ring the residual gas pressure has to be orders of magnitude better. As a new device to allow an ion beam to enter sections of different pressure we investigate a new kind of plasma valve [1,2].

The basic principle of the MHD (magnetohydrodynamic) valve uses the Lorentz force acting upon an ionized gas between an ultra high vacuum chamber and a gas reservoir up to a pressure of several mbar. When activated, the MHD valve is composed of a discharge plasma that fills a chamber with crossed electric and magnetic fields. Gas flowing from the gas tank into the UHV chamber is ionized by the discharge. The Lorentz force acts now upon the charged particles due to the crossed electromagnetic fields and repels them back into the gas chamber. By proper adjustment of the Lorentz force, the valve can allow any desired gas flow between the two chambers, or fully block any exchange of gas. The MHD valve can even act as an efficient vacuum pump to improve the vacuum conditions in the high vacuum section. High energy particles reaching the valve from the high vacuum side will penetrate the fields and the plasma. For heavy ion beams the MHD valve would therefore act like a window.

The following Figure 1 shows one of the latest measurements of the pressure gradient between two gas chambers.

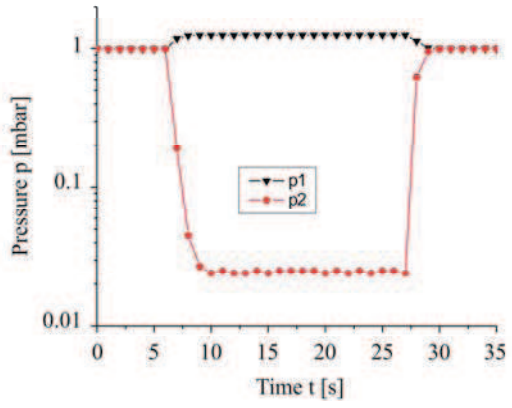

Fig.1: Pressure p_1 and p_2 as a function of the time t. For this measurement Ar-H_2-Gas was used. At a discharge current above 18 A the pressure gradient between two gas chambers is achieved.

In comparison with the plasma window of *A. Hershcovitch* [3,4], which establishes a vacuum-air separation by means of a viscosity change due to a temperature gradient induced by an arc discharge, the MHD valve needs ionized gas as a result of its basic principle of operation.

After the setup has been established the MHD plasma valve was tested. The electrical power necessary to operate the device was more than 1 kW. A plasma current higher than 18 A was required to block any exchange of gas allowing a pressure drop down to 0.045 mbar inside the test chamber while maintaining approximately 1 mbar inside the gas discharge chamber. The opening between the two chambers was 1 cm².

In addition the pumping speed of the MHD valve was determined. By measuring the time scale of the pressure build up the pumping speed could be estimated to about 2 liter/seconds.

Future projects will include a pulsed version of the MHD valve. In this case we expect a very dense highly ionized plasma by means of low frequency inductively excited discharge [2,5]. Through induced $\mathbf{j}\times\mathbf{B}$–fields it is possible to build a plasma flow against a pressure gradient during the pulse duration.

* Acknowlegement: This work was partially funded by BMBF under contract No. 06FY155.

References

[1] C. Teske, M. Iberler, J. Jacoby, "Magneto-Hydrodynamisches Plasmaventil", Patent Pending, J50063, 30. June 2006.

[2] W. Schweizer, "Entwicklung, Aufbau und Untersuchung eines MHD-Plasmaventils", Diplomarbeit, Goethe-Universität Frankfurt am Main, Nov. 2008.

[3] Hershcovitch et. al., "The Plasma Window: A Windowless High Pressure-Vacuum Interface for Various Accelerator Applications", Proceedings of the 1999 Particle Accelerator Conference, New York, 1999.

[4] A. Hershcovitch, "A plasma window for vacuum-atmosphere interface and focusing lens of sources for nonvacuum ion material modification", Review of Scientific Instruments", Volume 69, Number 2, Feb. 1998.

[5] C. Teske, J. Jacoby, "Pulsed Low Frequency Inductively Coupled Plasma Generator and Applications". IEEE Transactions on Plasma Science, Vol. 36, Issue 4, pp. 1930-1936, 2008.

Hole Boring in Dense Plasmas and Fast-Ion Ignition of Precompressed Fusion Targets with Ultraintense Laser Pulses*

N. Naumova[1], T. Schlegel †[2], and V. Tikhonchuk[3]

[1]Laboratoire d'Optique Appliquée, UMR 7639 ENSTA, École Polytechnique, CNRS, 91761 Palaiseau, France; [2]GSI Helmholtzzentrum für Schwerionenforschung GmbH, Planckstrasse 1, D-64291 Darmstadt, Germany; [3]Centre Lasers Intenses et Applications, Université Bordeaux 1 - CEA - CNRS, 33405 Talence Cedex, France

Recently achieved high intensities of short laser pulses open new prospects of their application to hole boring in inhomogeneous overdense plasmas and for ignition in precompressed DT fusion targets. Simple analytical estimates and numerical simulations demonstrate that pulses with intensities exceeding 10^{22} W/cm^2 may penetrate deeply into the plasma as a result of efficient ponderomotive acceleration of ions in the forward direction. Results of the quasi-stationary model of a laser piston (or double layer), introduced in the previous contribution and in references therein, are shown in Fig. 1.

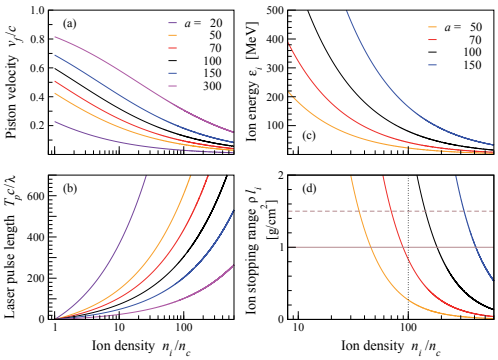

Figure 1: (a) Piston velocity in a deuterium plasma for circularly polarized laser light and several values of the dimensionless vector potential $a = (I/m_e n_c c^3)^{1/2}$. (b) Density dependence of time T_p required for the laser pulse to traverse a plasma layer $[n_{i\,\min}, n_{i\,\max}]$ with an exponential density profile, $L = 20\lambda$, where $\lambda = 0.8\,\mu$m. (c) Ion energy. (d) Stopping range of ions, $\rho l_i \simeq 10^{-3}\varepsilon_i^{1.8}$, with energies shown in panel (c). Dashed line represents the maximum areal density in the core of the fusion pellet.

Knowing the piston velocity v_f and the scale length of the inhomogeneous plasma layer, one can determine the duration of a laser pulse with intensity I necessary to reach a dedicated point on the density profile, $T_p = 2L\,(m_i c/I)^{1/2}\left(n_{i\,\max}^{1/2} - n_{i\,\min}^{1/2}\right)$. Here we supposed the case of an exponential density distribution with the constant scale length L. Since the ions are pulled by the charge separation field of the double layer, their energy follows as $\varepsilon_i = 2m_i v_f^2 \gamma_f^2$. The ion fluence from the density region $[n_{i\,\min}, n_{i\,\max}]$ will be $F_i \simeq (2IL/c)\ln(n_{i\,\max}/n_{i\,\min})$, supposing a nonrelativistic piston motion.

Results of 2D particle-in-cell simulations, shown in Fig. 2, demonstrate an efficient hole boring in the overcritical plasma, a clean and a stable channel. The major part of the accelerated ions has a narrow angular distribution with the opening agle less than 6°.

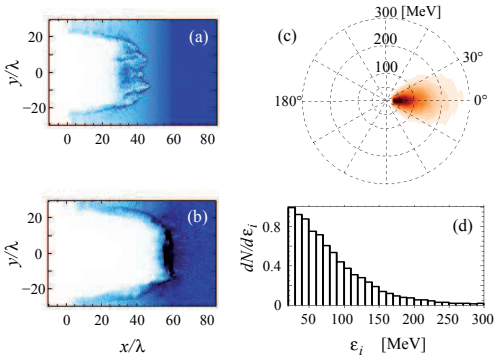

Figure 2: Channel formation in plasma and ion acceleration in the laser piston regime. Ion density distribution at instants (a) 90 λ/c and (b) 190 λ/c. (c) Angular and energy distribution of accelerated ions and (d) the energy distribution of ions in a cone with 6° divergence. Simulation parameters: $I = 4\times10^{22}$ W/cm^2, $L = 20\lambda$, flattop transverse laser profile with the width of 20λ and exponential wings.

Scaling laws for fast ignition of the precompressed fuel with a maximum density of 400 g/cm^3 give a necessary energy flux $F_{ig} \simeq 1.5$ GJ/cm^2 and an ignition spot radius 15 μm. Accounting for the ion beam divergence of 6° and a propagation length of $\approx 50\,\mu$m, an ion energy fluence $F_i \simeq 2\,F_{ig} \simeq 3$ GJ/cm^2 must be provided. The maximum energy of fast ions fully stopped in the core with its areal density of ~ 1.5 g/cm^2 is limited by the value ~ 60 MeV. A laser pulse with the amplitude $a = 70$ ($I \simeq 2\times10^{22}$ W/cm^2) would accelerate ions to energies less than 60 MeV at plasma densities larger then $n_{i\,\min} = 70\,n_c$. The upper density value $n_{i\,\max} \simeq 200\,n_c$ of the plasma acceleration layer can be found with the ion beam fluence relation shown earlier. With an estimated laser pulse duration of 0.75 ps for the ion acceleration phase, we evaluate a laser fluence of 15 GJ/cm^2. For the focal spot area 3×10^{-6} cm^2, we find the laser energy to be 45 kJ. In addition, the hole boring up to the acceleration zone requires a laser fluence of about 7 GJ/cm^2. The overall energy need is of the same order of magnitude as in other schemes of fast ignition. However, no additional target arrangements are necessary in this approach.

* Work supported by the ANR under the contract BLAN07-3-186728

† t.schlegel@gsi.de

Ponderomotive Ion Acceleration in Bulk Dense Plasmas *

T. Schlegel[†1], N. Naumova[2], and V. Tikhonchuk[3]

[1]GSI Helmholtzzentrum für Schwerionenforschung GmbH, Planckstrasse 1, D-64291 Darmstadt, Germany; [2]Laboratoire d'Optique Appliquée, UMR 7639 ENSTA, École Polytechnique, CNRS, 91761 Palaiseau, France; [3]Centre Lasers Intenses et Applications, Université Bordeaux 1 - CEA - CNRS, 33405 Talence Cedex, France

Laser ponderomotive force at super-high intensities provides an efficient ion acceleration not only in thin foils but also in bulk dense targets, thereby evacuating a channel which enables further laser beam propagation. A quasi-stationary model of a laser piston – a double layer structure supported by the radiation pressure – predicts the general parameters of the acceleration process in homogeneous and inhomogeneous overdense plasmas. Particle-in-cell simulations confirm the estimated characteristics in a wide range of laser intensities and ion densities and show advantages of circularly polarized laser pulses. Figure 1 displays the double layer structure in the rest frame of the piston (R frame) moving with the velocity $v_f = \beta_f c$.

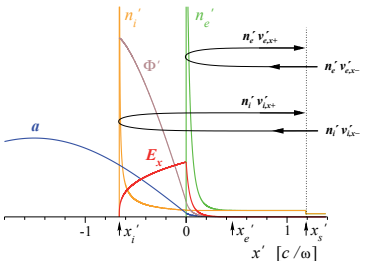

Figure 1: Double layer structure composed of an ion charge separation layer $[x_i', 0)$ and the electron sheath $[0, x_e')$ shown in the R frame. Curves: Electron density – green, ion density – orange, laser field amplitude – blue, scalar potential – brown, electrostatic field – red. Data (in arbitrary units along the vertical axis) are taken from the theory developed in [2].

The momentum flux deposited by the laser photons in the piston frame has to be balanced by the momentum flux of the particles coming from the upstream region of the plasma, $x' > x_s'$, and reflected elastically as shown in Fig. 1. We find the relation for the front velocity

$$\frac{I}{\rho c^3}\,\frac{1-\beta_f}{1+\beta_f} = \gamma_f^2 \beta_f^2, \qquad (1)$$

with the incident laser intensity I in the laboratory frame (L frame), the mass density $\rho = m_a n_{0i}$, where $m_a = m_i + Z m_e$ is the atomic mass and Z the ion charge number, with the upstream ion density n_{0i} in the L frame and the piston relativistic factor $\gamma_f = (1-\beta_f^2)^{-1/2}$. Solving Eq. (1), we get the relation $\beta_f = B/(1+B)$, where the parameter B is proportional to the square root of the laser pulse intensity divided by the plasma mass density: $B = (I/\rho c^3)^{1/2}$. In terms of the dimensionless vector potential of a circularly polarized laser pulse we have: $B = a_0\sqrt{n_c m_e/\rho}$, where $n_c = m_e\omega^2\epsilon_0/e^2$ is the critical plasma density and ω is the laser frequency in the L frame. From the piston velocity v_f we deduce the ion velocity in the L frame and the ion energy

$$\varepsilon_i = m_i c^2(\gamma_i - 1) = 2 m_i c^2 \gamma_f^2 \beta_f^2 = 2 m_i c^2 \frac{B^2}{1+2B} \qquad (2)$$

as well as the energetic efficiency of the laser driven ion acceleration: $1 - R = 2\beta_f/(1+\beta_f) = 2B/(1+2B)$, where we assume that no energy is deposited to electrons.

Knowing the density dependence of the piston velocity and of the ion energy, we are able to describe also the acceleration process in an inhomogeneous plasma. For an exponential density increase in laser propagation direction, we obtain analytical results for the ion energy distribution function and for the laser pulse duration needed to reach a certain region on the given density profile. More information can be found in Refs. [1, 2].

Assuming a quasi-stationary piston motion and the full evacuation of the charge separation layer from electrons by the laser ponderomotive force, we may solve the set of governing equations for both layers – ion layer and electron sheath – separately, with well-known boundary conditions. Figure 2 shows results for the charge separation layer. A comprehensive description is given in [2].

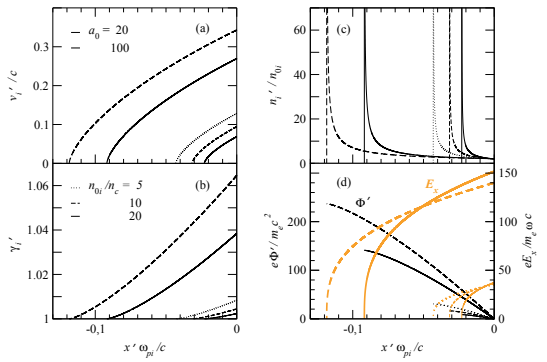

Figure 2: Spatial profiles in the R frame of: (a) ion velocity, b) ion gamma factors, c) ion density normalized to the density of the unperturbed plasma, d) normalized electrostatic potential and field. Circularly polarized laser light with amplitudes $a_0 = 20, 100$ and different deuteron densities are supposed. The spatial coordinate is normalized to the ion inertia length.

References

[1] N. Naumova et al., Phys. Rev. Lett. 102 (2009) 025002.

[2] T. Schlegel et al., Phys. Plasmas submitted (2009).

* Work supported by the Region Aquitaine, project No. 34293

† t.schlegel@gsi.de

LHC at CERN: Beams for Generating High Energy Density Matter *

N.A. Tahir[1], R. Schmidt[2], A. Shutov[3], I.V. Lomonosov[3], A.R. Piriz[4], V.E. Fortov[3], D.H. Hoffmann[5], and C. Deutsch[6]

[1]GSI, Darmstadt, Germany; [2]CERN, Geneva, Switzerland; [3]IPCP, Chernogolovka, Russia; [4]UCLM, Ciudad Real, Spain; [5]TU Darmstadt, Germany; [6]LPGP, University Paris–Sud, Orsay, France

Each of the two beams of the Large Hadron Collider (LHC) at CERN consist of 2808 bunches with an intensity of 1.15×10^{11} protons per bunch so that the total number of protons per beam is about 3×10^{14} that corresponds to a total energy of 362 MJ. The bunch length is 0.5 ns and two successive bunches are separated by 25 ns, while the power distribution in the radial direction is Gaussian with a standard deviation, σ = 0.2 mm. The total duration of the beam is about 89 μs. The energy stored in each beam is sufficient to melt 500 kg of copper.

In this contribution we report numerical simulation results of the hydrodynamic and thermodynamic response of a solid copper target that is facially irradiated with one LHC beam. The cylinder radius is 5 cm and its length is 10 m. The energy loss of protons in solid copper is calculated using the FLUKA code and this data is used as input to a 2D hydrodynamic code, BIG2.

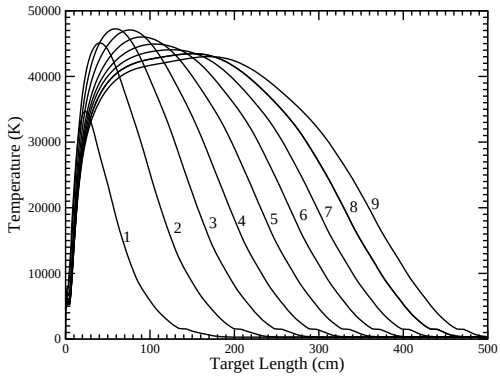

Figure 1: Target temperature along the axis (at r=0.0) at different times during irradiation; the time interval between two consecutive lines is 1 μs; line 1 is at 500 ns.

Temperature profiles along the cylinder axis (r=0.0) at different times are shown in Fig. 1. It is seen that at t = 500 ns, when about 20 bunches have been delivered, a maximum temperature of 3500 K is generated in the target. At later times, the temperature peak moves inwards and the temperature becomes uniform within 3 m length of the cylinder (at t = 8500 ns). Due to the radial shock wave generated by the high pressure in the deposition region, the target density decreases that leads to deeper penetration of the protons. This corresponds to a specific energy deposition of 25 kJ/g in the target.

Corresponding pressure profiles are plotted in Fig. 2. It is seen that a maximum pressure of about 30 GPa is generated at t = 500 ns and the pressure peak moves deeper into the target at later times while the the maximum value of pressure decreases.

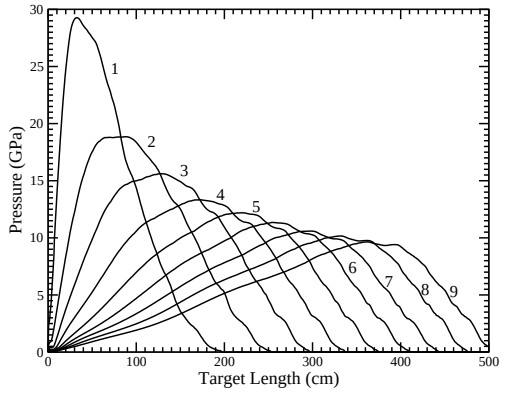

Figure 2: Target pressure along the axis (at r=0.0) at different times during irradiation; the time interval between two consecutive lines is 1 μs; line 1 is at 500 ns.

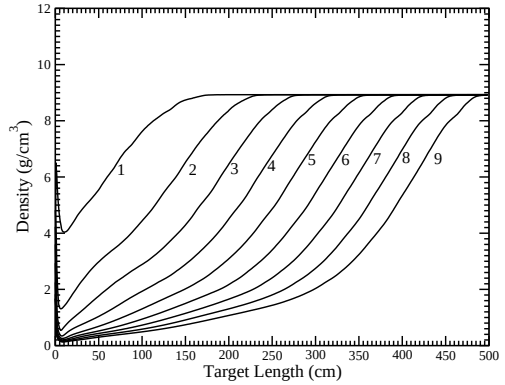

Figure 3: Target density along the axis (at r=0.0) at different times during irradiation; the time interval between two consecutive lines is 1 μs; line 1 is at 500 ns.

Density profiles along the target axis at different times are shown in Fig. 3. It is seen that at t = 8.5 μs, the beam has penetrated about 5 m and the penetration wave is traveling with a fairly uniform speed of 0.35 m/μs. This means that the protons will penetrate about 35 m during the pulse time of 89 μs and the target will be severely damaged. However it is interesting to note that high energy density (HED) matter is generated in the heated part of the target. HED matter studies can therefore be an additional important application of the LHC. Detailed about these simulations will be published in PRE.

* Work supported by the BMBF

Simulations of Future Experiments at HiRadMat Facility at the SPS at CERN*

N.A. Tahir[1], R. Schmidt[2], M. Brugger[2], A. Shutov[3], I.V. Lomonosov[3], V.E. Fortov[3], A.R. Piriz[4], D.H.H Hoffmann[5], and C. Deutsch[6]

[1]GSI, Darmstadt, Germany; [2]CERN, Geneva, Switzerland; [3]IPCP, Chernogolovka, Russia; [4]UCLM, Ciudad Real, Spain; [5]TU Darmstadt, Germany; [6]LPGP, Universite Paris–Sud, Orsay, France

We present numerical simulations of the interaction of a 450 GeV/c proton beam that is generated by the Super Proton Synchrotron (SPS) at CERN, with a solid copper cylindrical target. This study has been done to assess the damage caused by these highly relativistic protons to equipment including collimators, absorbers and others in case of an uncontrolled accidental release of the beam. A dedicated experimental facility named HiRadMat is under construction at CERN that will allow to study these problems experimentally.

The SPS is used as an injector to the LHC. Several SPS cycles are required to fill the LHC while in one cycle, a batch of 288 bunches can be accelerated whereas each bunch comprises of about 1.1×10^{11} protons. The bunch length is 0.5 ns and two neighboring bunches are separated by 25 ns so that the duration of the entire beam is about 7 μs. Three different focal spot sizes that correspond to σ = 0.088 mm, 0.28 mm and 0.88 mm, respectively, have been used. The target length is assumed to be 2 m and the radius = 1 cm. The proton energy loss in solid copper is calculated using the FLUKA code and this data is used as input to a 2D hydrodynamic code, BIG2.

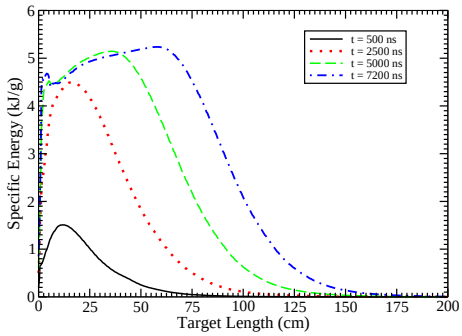

Figure 1: Specific energy deposition vs target axis at different times, beam σ = 0.088 mm.

In Fig. 1 we plot the specific energy deposited by the beam with a spot size characterized with σ = 0.088 mm. It is seen that at the end of the pulse at 7.2 μs, a maximum specific energy of about 5 kJ/g is achieved. Penetration of the projectile particles due to density reduction at the target center is also clearly seen. Fig. 2 shows a maximum temperature of the order of 8000 K generated in the beam heated region while Fig. 3 shows a corresponding pressure of 2.5 GPa. Fig. 4 shows that the projectile particles penetrate up to 1.5 m in Cu and generate HED matter.

* Work supported by the BMBF

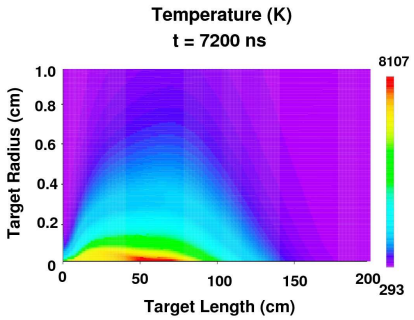

Figure 2: Temperature on length–radius plane at t = 7.2 μs.

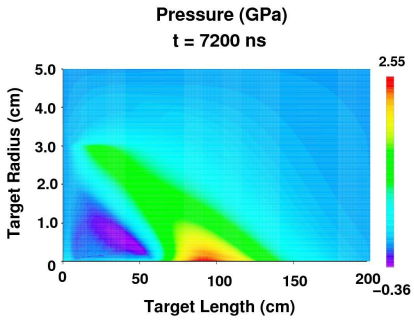

Figure 3: Pressure on length–radius plane at t = 7.2 μs.

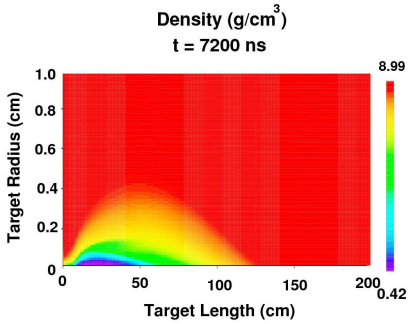

Figure 4: Density on length–radius plane at t = 7.2 μs.

Studies of Uranus and Neptune Interiors in LAPLAS Experiment Simulations*

N.A. Tahir[1], A.Shutov[2], I.V.Lomonosov[2], V.E. Fortov[2], N.Nettelmann[3], M.French[3], R.Redmer[3], A.R. Piriz[4], D.H. Hoffmann[5], and C. Deutsch[6]

[1]GSI, Darmstadt, Germany; [2]IPCP, Chernogolovka, Russia; [3]Rostock University, Rostock, Germany; [4]UCLM, Ciudad Real, Spain; [5]TU Darmstadt, Germany; [6]LPGP, Universite Paris–Sud, Orsay, France

Two–dimensional hydrodynamic simulations have been performed using a circular focal spot to compress solid water using a uranium ion beam that will be available at the future FAIR facility at Darmstadt. This work has been done to study the possibility of studying planetary physics by generating extreme states of matter which are expected to exist in the interiors of the giant planets [1].

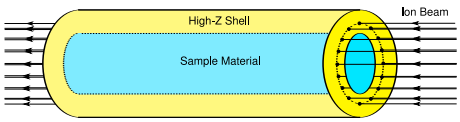

Figure 1: Beam–target geometry for LAPLAS experiment

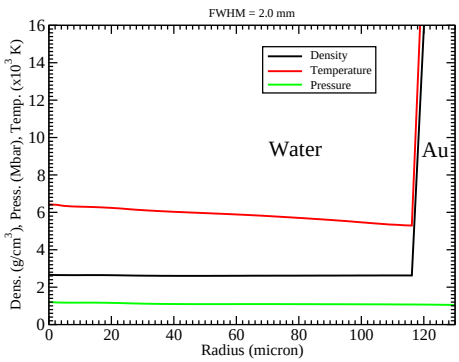

Figure 2: ρ, T and P vs radius in the water layer at the time of maximum compression for a beam FWHM = 2 mm

In this study we consider an intensity of 10^{11} 1 GeV/u uranium ions that are delivered in a single bunch, 50 ns long. A circular focal spot is considered with a Gaussian intensity distribution.The target is a cylinder of frozen water having a radius = 200 μm that is enclosed in a Au shell (see Fig. 1). The target length is 5 mm which is shorter than the length of the projectile particles so that the energy deposition is uniform in the longitudinal direction. In these simulations we use a semi-empirical equation of state model [2] for Au and data based on Quantum Molecular Dynamic (QMD) simulations for water [4].

In Fig. 2 we plot the density, temperature and pressure along the radius (in the water layer) using a beam FWHM = 2 mm at the time of maximum compression. It is seen that a density of 2.6 g/cm^3, a pressure of 1.2 Mbar and a temperature of about 5000 K is achieved.

* Work supported by the BMBF

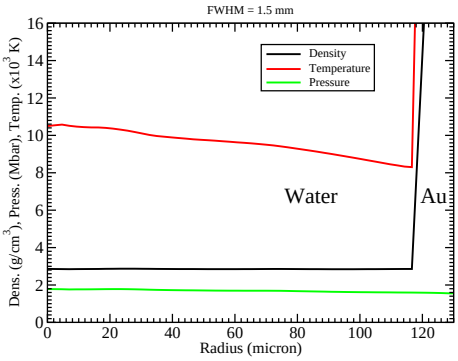

Figure 3: Same as in Fig. 2, but for a beam FWHM = 1.5 mm

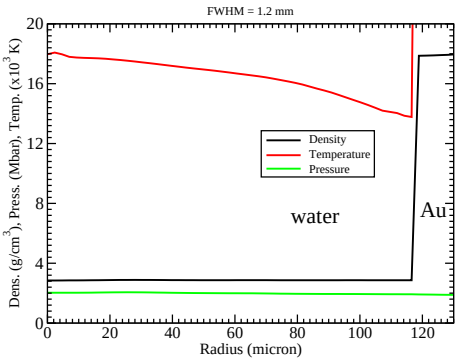

Figure 4: Same as in Fig. 2, but for a beam FWHM = 1.2 mm

Fig. 3 shows the same variables as Fig. 2, but using beam FWHM = 1.5 mm. In this case we achieve a water density of 2.8 g/cm^3, a pressure of 1.8 Mbar and a temperature on the order of 10000 K. Fig. 4 shows the results for a beam FWHM = 1.2 mm and one achieves a density of 3 g/cm^3, a pressure of 2 Mbar and a temperature of about 16000 K. These parameters correspond to the plasma state of water.

Further calculations are planned using higher beam intensities that will allow one to access higher densities corresponding to the superionic state in which the protons become mobile in the oxygen lattice [3, 4].

References

[1] N. Nettelmann et al., Astrophysics J. 683 (2008) 1217.

[2] I.V. Lomonosov, Laser and Part. beams 25 (2007) 567.

[3] T.R. Mattsson and M. Desjarlais, PRL 97 (2006) 017801.

[4] M. French et al., Phys. Rev. B 79 (2009) 054107.

Determination of the ion track structure in amorphous SiO_2 using small angle x-ray scattering

P. Kluth[1,#], C.S. Schnohr[1], O.H. Pakarinen[2], F. Djurabekova[2], D.J. Sprouster[1], R. Giulian[1], M.C. Ridgway[1], A.P. Byrne[1], C. Trautmann[3], K. Nordlund[2], M. Toulemonde[4]

[1]Australian National University, Canberra, Australia; [2]University of Helsinki, Helsinki, Finland; [3]GSI, Darmstadt, Germany; [4]Centre interdisciplinaire de recherche sur les Ions, les MAtériaux et la Photonique (CIMAP), Caen, France

In amorphous SiO_2 (a-SiO_2), a technologically most important material, average structural properties of ion tracks have been inferred from macroscopic measurements, yet details of the track structure and inner morphology are difficult to retrieve due to the lack of sufficient contrast inherent with most techniques. Here we report on measurements of a fine structure in ion tracks in a-SiO_2 using small angle x-ray scattering (SAXS) [1].

The ion tracks were produced in 2-µm thick a-SiO_2, thermally grown on Si(100) substrates, by irradiation with 1.4 and 0.6 GeV Xe ions at the UNILAC accelerator. The fluence was limited to 3×10^{11} ions/cm^2 to avoid significant track overlap. Thin SiO_2 layers were utilized to achieve a uniform energy loss over the extent of the layer and hence uniformity of the tracks along the ion paths.

The track structure was studied using synchrotron SAXS in transmission geometry performed at beamline 15ID-D of the Advanced Photon Source, Argonne National Laboratories, USA. The x-ray wavelength was 1.1 Å (~10.27 keV) and the distance between the sample and the CCD detector was 555 and 1894 mm. All measurements were performed with the sample surface aligned normal to the x-ray beam, i.e. parallel to the ion tracks. The resulting isotropic images were radially integrated around the beam center. Scattering from an unirradiated SiO_2 standard was subtracted from all spectra. Figure 1 shows the scattering intensities of the samples.

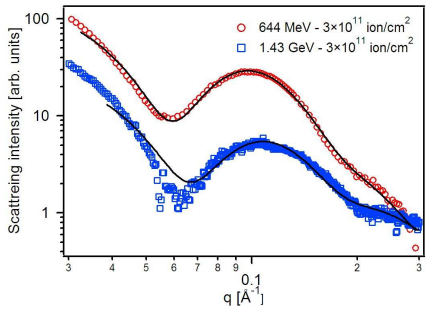

Figure 1: SAXS spectra of a-SiO_2 irradiated with Xe ions. The solid lines show the corresponding fits to the core-shell cylinder model.

For the analysis, we assumed a cylindrically symmetric density distribution within a track, consistent with continuous track formation and approximately constant energy loss throughout the SiO_2 layer. This is further substantiated by measurements of the tracks tilted with respect to the x-ray beam [2]. The simplest model that adequately fits the experimental data requires a cylindrical core surrounded by a shell of different density indicating the presence of a fine structure in the ion track radial density distribution. The fits to the core shell model are plotted as solid lines in Fig. 1. In agreement with molecular dynamics (MD) simulations [1], the results are consistent with a lower density core and a higher density shell as compared to unirradiated material. Figure 2 shows the total track radii measured by SAXS as a function of electronic stopping power, including the results from irradiation with Au ions at energies below 200 MeV and track radii evaluated from MD simulations [1].

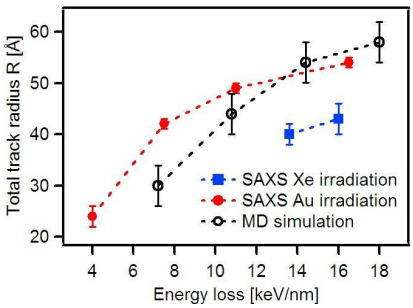

Figure 2: Total track radii as a function of electronic energy deposition measured by SAXS and obtained from MD simulations.

The track radii from the Xe irradiations are approximately 10 Å smaller than those from the Au irradiations at the same stopping powers. This result is ascribed to the difference in the associated energy densities (so-called "velocity effect").

The measurements are also in good agreement with thermal spike calculations where the total track radii and the track core radii concur with cylinders where the temperature exceeds the melting temperature and the boiling temperature, respectively [1]. This supports the simplistic view of a frozen-in pressure wave originating from the centre of the track with a dilatation in the hot track core.

References

[1] P. Kluth *et al.*, Phys. Rev. Lett. 101 (2008) 175503
[2] P. Kluth *et al.*, Nucl. Instr. and Meth. in Phys. Res. B 266 (2008) 2994

Patrick.kluth@anu.edu.au

Irradiation of $Gd_2Zr_2O_7$ with 2.6-GeV Uranium Ions

J. Zhang[1,#], M. Lang[1], J. Lian[1,2], C. Trautmann[3], R.C. Ewing[1]
[1]University of Michigan, Ann Arbor, USA.; [2]Rensselaer Polytechnic Institute, Troy, USA.; [3]GSI, Darmstadt, Germany

The radiation response of isometric pyrochlore, $A_2B_2O_7$, has received great attention because it is considered as a potential host phase for the incorporation of actinides, e.g., for nuclear waste forms [1]. A large number of ion-irradiation studies have been completed in order to simulate α-decay damage in pyrochlores with a wide variety of compositions [2-4]. By ion irradiation, material with the ideal pyrochlore structure, such as Ti-rich pyrochlore, is initially transformed to a disordered, defect-fluorite structure and finally becomes fully amorphous at a rather low fluence (i.e., 2.5×10^{14} ions/cm^2 with 1.0 MeV Kr^+ irradiation [3]). However, most zirconate pyrochlores are highly "resistant" to ion-beam induced amorphization. For example, $Gd_2Zr_2O_7$ cannot be amorphized with 200-keV Ti ions even at fluences as high as 1×10^{17} ions/cm^2. Instead, $Gd_2Zr_2O_7$ forms a disordered, defect-fluorite structure [4].

Most of the previous irradiation experiments were conducted at relatively low ion energies (keV-MeV), where elastic collisions dominate the damage creation process (nuclear energy loss). This paper presents experimental results showing that even 2.6-GeV U ions with very high electronic energy loss of 52 keV/nm are not able to amorphize $Gd_2Zr_2O_7$ but instead induce a transformation from the ordered pyrochlore to the disordered-fluorite structure .

Fig. 1a shows a bright-field TEM image in cross-sectional view of $Gd_2Zr_2O_7$ irradiated with 2.6-GeV uranium ions. On top of the sample surface, hillock-like structures can be found, and below the surface, a ~70 nm thick damage layer is formed. Beyond this layer, individual ion tracks can clearly be identified as homogeneous parallel damage trials (Fig. 1b.), with a mean track diameter of ~6 nm. The SAED pattern from surface area exhibits a polycrystalline, disordered-fluorite structure (data not shown here), whereas below the damaged layer the structure remains ordered pyrochlore (data not shown here); no diffuse scattering of the amorphous phase was observed. The HRTEM image reveals that the damaged surface region consists entirely of the disordered, defect fluorite-structure with some evidence of polygonization of larger crystalline areas and the formation of low-angle grain boundaries (Fig. 1c). Two defect-fluorite structured hillocks from the near-surface region shows that all ion-induced hillocks consist entirely of the defect-fluorite structure, and no amorphous phase was evident in any of the hillocks.

In conclusion, individual tracks together with surface hillocks were obtained in $Gd_2Zr_2O_7$ after the irradiation with swift ^{238}U ions. Similar to low-energy projectiles in the elastic collision regime, swift heavy ions produce extremely ionizing conditions that are not able to induce amorphization, but rather, only disordering into the defect-fluorite structure. This study highlights the exceptional radiation stability of zirconate pyrochlore even for the extremely high energy density induced by swift heavy ions.

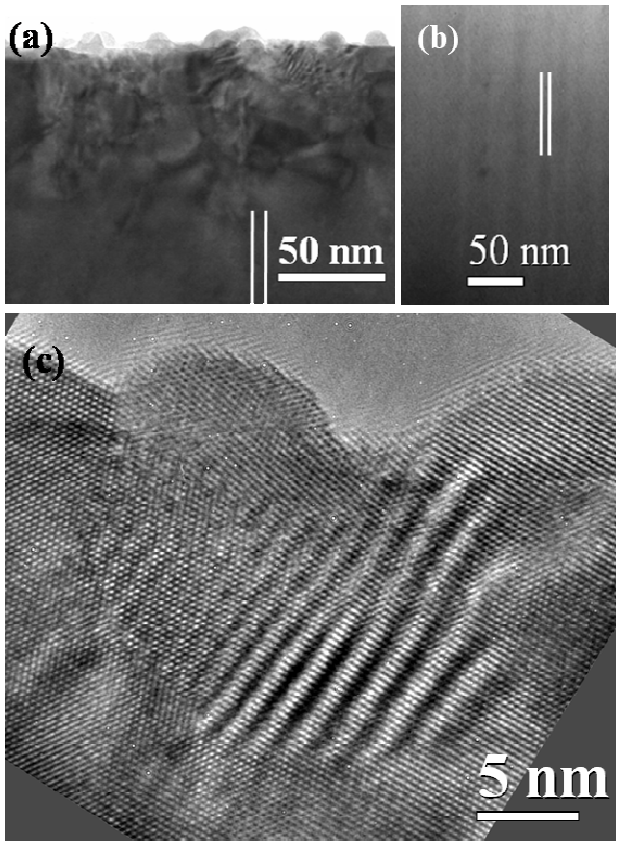

Figure 1: (a) Cross-sectional TEM image of $Gd_2Zr_2O_7$ irradiated with 2.6-GeV U ions. (b) Ion tracks found in the matrix. (c), (d) SAED patterns from the surface and matrix. (e) HRTEM image from the damaged surface.

M. L. acknowledges support from the German Science Foundation DFG.

[1] K.E. Sickafus, et al., Science **289**, 748 (2000).
[2] R.C. Ewing, et al., J. Appl. Phys. **95**, 5949 (2004).
[3] S.X. Wang, et al., J. Mater. Res. **14,** 4470 (1999).
[4] J. Lian, et. Al., Phys. Rev. B **66**, 054108 (2002).

* Work supported by DOE contract No. DE-FG0297ER45656.
# zhangjia@umich.edu

Damage Creation in Ion-Irradiated CeO_2

N. Ishikawa[1], K. Ohhara[1], O. Michikami[2], Y. Kimura[2], M. Lang[3], R. Neumann[4]
[1]JAEA, Tokai, Ibaraki 319-1195, Japan; [2]Iwate Univ., Morioka, Iwate 020-0066, Japan, [3]Univ. of Michigan, Ann Arbor, USA; [4]GSI, Darmstadt, Germany

Introduction

It is known that high-energy fission products create serious damage in the crystal structure of nuclear fuel ceramics (UO_2), leading to swelling and degradation of thermal properties. The damage process, being particularly important in the high-energy region, is investigated in this study. Cerium dioxide, CeO_2, is one of the ceramics that have the same (fluorite) structure as UO_2 and also a similar melting temperature. Therefore, in this study CeO_2 functioning as a simulation material is irradiated with high-energy projectiles.

It is already known that ion tracks are formed in CeO_2 by 210-MeV Xe irradiation [1]. The ion track has typically a diameter of several nanometers. The crystal lattice inside the track is not amorphized. The purpose of our study is to analyze the change in crystal structure which reflects the formation of ion tracks. X-ray diffraction (XRD) is used to evaluate the crystal structure modification.

Experimentals

Thin films of CeO_2 were prepared on sapphire substrates by dc sputtering. The film thickness was about 300 nm. The films were irradiated at room temperature with 1.5-GeV Xe from the UNILAC accelerator at GSI and with 200-MeV Au from the tandem accelerator at Tokai Research and Development Centre, Japan Atomic Energy Agency (JAEA-Tokai). XRD profiles were measured before and after the irradiation.

Results and Discussion

As shown in Fig.1, after the irradiation with 200-MeV Au, the (002) XRD peak becomes asymmetric in the fluence range of less than $1x10^{12}$ ions/cm^2. In an even higher fluence range, the asymmetric profile gradually becomes symmetric as the fluence increases. These changes of the XRD profile can be interpreted as follows [2]. The XRD profile can be regarded as a sum of two peaks; the original peak corresponds to the matrix, and the new peak which appeared after the irradiation corresponds to the crystal structure inside the ion track. The new XRD peak can be recognized as a shoulder at the low-angle side of the main (002) peak. This new peak reflects the crystal structure with relatively larger lattice spacing. The position of the new peak ranges at around $2\theta = 32.8^0$-32.9^0. The fact that the lattice spacing is larger than that of the matrix can be explained by the creation of oxygen deficiency inside ion tracks.

An asymmetric peak profile is also found for CeO_2 irradiated with 1.5-GeV Xe ($5x10^{12}$ ions/cm^2). As shown in Fig. 2, the asymmetric peak can be again fitted by assuming that the peak profile is the sum of the main peak and the new peak. In this case, the new peak is observed at the position of $2\theta = 33.05^0$ which is a somewhat higher angle than that observed for 200-MeV Au irradiation. The above results can be summarized as follows. Although both irradiations exhibit a new XRD peak, the corresponding lattice spacings are different, suggesting different densities of oxygen deficiency.

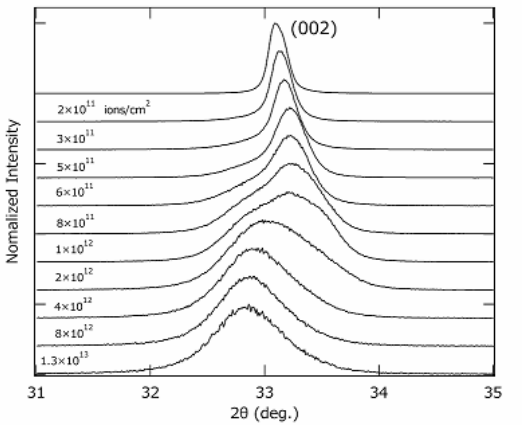

Figure 1: XRD profiles of CeO_2 irradiated with 200-MeV Au at different fluences. Top curve represents unirradiated sample.

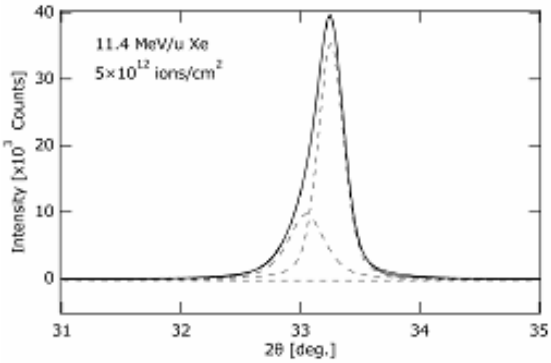

Figure 2: XRD profiles of CeO_2 irradiated with 1.5-GeV Xe at a fluence of $5x10^{12}$ ions/cm^2. The dashed lines correspond to the main peak and the new peak.

References

[1] T. Sonoda, M. Kinoshita, Y. Chimi, N. Ishikawa, M. Sataka, and A. Iwase, Nucl. Instr. and Meth. B 250 (2006) 254.

[2] N. Ishikawa, Y. Chimi, O. Michikami, Y. Ohta, K. Ohhara, M. Lang, R. Neumann, Nucl. Instr. and Meth. B 266 (2008) 3033.

Vickers Microhardness Measurement for AlCu Alloy Irradiated with Swift Heavy Ions

A. Iwase[1], I. Kobayashi[1], and R. Neumann[2]
[1]Osaka Prefecture University, Sakai, Osaka, Japan, [2]GSI Darmstadt Germany.

Introduction

Irradiation-induced hardening is an important phenomenon concerning the nuclear reactor safety, because it induces the embrittlement of reactor pressure vessel steels. This phenomenon, however, can also be applied for the modification of hardness of alloys. In the case of FeCu alloys, we have reported that GeV heavy-ion irradiation remarkably increases the hardness [1]. Volkov et al. have explained the phenomenon as originating from the nano-precipitate nucleation of solute atoms, which is induced by the thermal spike in the track of swift heavy ions [2]. In this report, we show the result of microhardness measurements for AlCu alloy irradiated with 11.4 MeV/u Ni ions.

Experimental procedure

Specimens used in the present study were Al-based alloys with the following element compositions: Cu: 4 wt.%, Mn: 0.5 wt.%, Si: 0.5 wt.%, Fe: 0.7 wt.%, Zn: 0.2 wt.% and Cr: wt. 0.1%. The specimens of size 10x10x1mm^3 were solution-annealed at 520 ºC for 4 hours and were quenched into water of 0 ºC. This process induced supersaturated dissolution of Cu and other additive elements in the Al lattice. Using the UNILAC accelerator of GSI, the specimens were then irradiated at room temperature with 11.4 MeV/u (0.66 GeV) Ni ions, applying fluences of 5x10^{11},, 1x10^{12}, and 2x10^{12} ions/cm^2. Before and after irradiation, Vickers microhardness was measured with a load of 25 and 100 gf, where the indent depth was about 4 and 9 μm, respectively.

Results and Discussion

Figure 1 shows the Vickers microhardness for AlCu specimens irradiated with 11.4 MeV/u Ni ions as a function of fluence. The value of microhardness for the unirradiated specimen is 138-140. Even after the irradiation, we can hardly observe any remarkable change in hardness. For Fe-1.2% Cu alloy irradiated with 26 MeV/u Xe ions, the Vickers microhardness increases by about 40 after applying a fluence of 2x10^{12} ions/cm^2 [1]. The irradiation temperature for Fe-1.2% Cu alloy is, however, not room temperature but 250 ºC. In addition, the value of the electronic stopping power for 26 MeV/u Xe ions is much smaller than that for 11.4 MeV/u Ni ions. In conclusion, to observe the effect of electronic excitation on hardness in AlCu alloys, it will be necessary to irradiate the specimens with heavier GeV ions, for example, Pb or Au, under elevated temperatures.

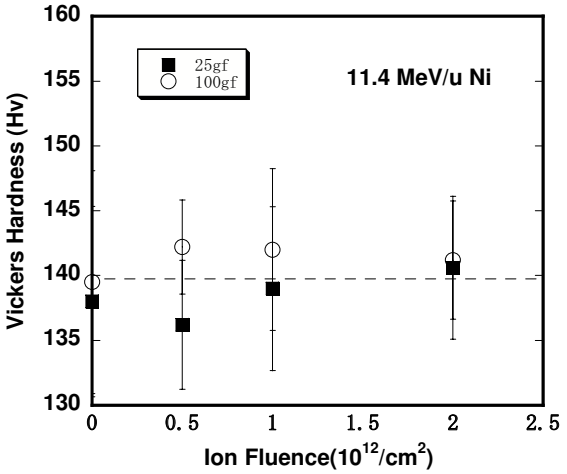

Fig. 1. Ion-fluence dependence of Vickers microhardness for AlCu alloy irradiated with 11.4 MeV/u Ni ions. Values of indent load are 25 and 100 gf.

References

[1] A. Iwase, T. Hasegawa, Y. Chimi, T. Tobita, N. Ishikawa, M. Suzuki, T. Kambara, S. Ishino, Nucl. Instr. Meth.B 195 (2002) 309-314.

[2] A.E. Volkov, D.N. Korolev, Nucl. Instr. Meth. B 195 (2003) 98-102.

Modifications of Yttria Fully Stabilised Zirconia Thin Films by Ion Irradiation in the Inelastic Collision Regime

A. Lamperti[1], A.P. Caricato[2], P. Ossi[3,#] , C. Trautmann[4], L. Vanzetti[5]
[1]Durham University, Durham, U.K.; [2]Universita' di Lecce, Lecce, Italy; [3]Politecnico di Milano, Milano, Italy; [4]GSI, Darmstadt, Germany; [5]Fondazione Bruno Kessler, Povo (Tn), Italy

Radiation tolerance of Yttria Fully Stabilised Zirconia (FSZ) [1-3] to ion beams in the *elastic* collision regime has been investigated with respect to material structure, microstructure, and nature and distribution of defects. FSZ cannot be amorphised by exposure to heavy ions [4] and shows excellent thermal stability, making it particularly attractive as inert matrix for nuclear fuel elements and for the containment of high activity nuclear wastes. However, understanding the material response in the *inelastic* collision regime is needed, because such matrices are exposed to neutrons *and* heavy fission fragments with energies in the 100 MeV range, where the interactions are dominated by inelastic processes including ionisation and electronic excitations. Such a radiation damage can be simulated by irradiations performed at large accelerator facilities using ion beams of energy between MeV and GeV.

Experimental

By pulsed laser deposition both at room temperature (RT; series 15) and at 673 K (series 13) we produced FSZ films (12%at.Y_2O_3) preserving the target stoichiometry and avoiding the porosity and contamination typical of sintered FSZ. Films were irradiated at the GSI-UNILAC using uranium ions of specific energy 11.4 MeV/u. To avoid sample heating, the beam flux was limited to ~10^8 ions cm^{-2} s^{-1}. Irradiations were performed at RT and normal beam incidence, at fluences of 2 (L), 5 (M), 8 (H), and 12 (VH) $\times 10^{11}$ ions cm^{-2}. As-deposited and irradiated samples were characterised by ex-situ GIXRD (Cu K_α at 8047 eV, 0.5° incidence angle) and XPS (Al K_α at 1486.6 eV).

Results and Discussion

XPS shows that both Zr 3d and O 1s core levels are shifted towards higher binding energy by ~0.4 eV with respect to literature values. After irradiation, the line shape of Zr 3d and Y 3d did not change, but fluctuations in the energy peak positions were observed. From the *chemical* point of view, irradiation induces a shift towards lower binding energies in the Zr 3d and O 1s core levels of sample 13L and 13H, but the value remains close to that of sample 13A and to the literature value**.** On the contrary, in samples 15L and 15H, the same two core levels shift in opposite directions at a value lower than for sample 15A and literature. Such effects are due to *small* differences in the chemical environment of O and Zr depending on the crystalline or amorphous matrix structure.

* Work partially supported by EU, ULTRASMOOTH contract No. 504462. - #paolo.ossi@polimi.it

GIXRD indicates (Fig. 1) that RT and 673 K depositions lead to films with an amorphous (15A) or polycrystalline single-phase cubic FSZ structure (13A), respectively. GIXRD of initially crystalline films exposed to a fluence of 2×10^{11} (13L) and 5×10^{11} ions cm^{-2} (13M) show surprisingly no diffraction reflexes: within the detection limit of our technique (~1.5 nm), these samples are completely amorphised. In contrast, GIXRD of the film irradiated at 8×10^{11} ions cm^{-2} (13H) exhibits broadened reflexes suggesting partial reversion to the FSZ cubic structure. These reflections become evident for the highest fluence of 1.2×10^{12} ions cm^{-2} (13VH). No features in GIXRD of films which are amorphous before ion irradiation (15L, 15M, 15H, 15VH) indicate that they remain amorphous.
The observed amorphisation of our initially crystalline

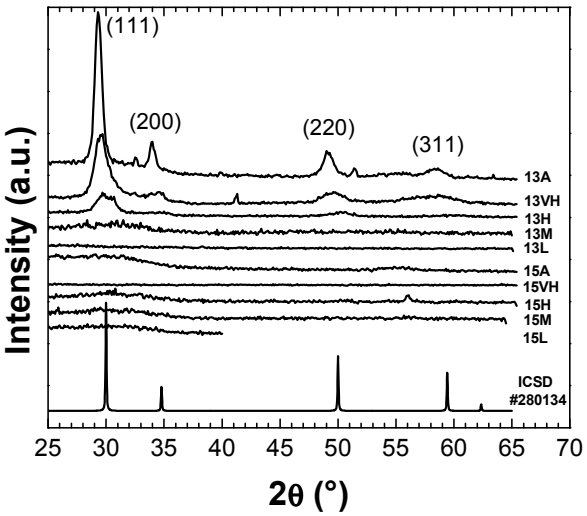

Figure 1: GIXRD patterns of samples with reference.

FSZ films is surprising in two respects: (i) The fluence is rather low and far from a situation where significant track overlapping occurs; (ii) Amorphisation at low fluence is followed by re-crystallisation progressing with increasing fluence. The reduced radiation tolerance of polycrystalline films with respect to amorphous ones can indicate higher radiation sensitivity.

References

[1] K.E. Sickafus, Hj. Matzke et al., J. Nucl. Mater. 274 (1999) 66
[2] J. Cheng and F.B. Prinz, Nucl. Instr. Meth. B 227 (2005) 577
[3] P.M.G. Damen, Hj. Matzke et al., Nucl. Instr. Meth. B 191 (2002) 571
[4] A. Gentils, L. Thomé et al., Nucl. Instr. Meth. B 218 (2004) 457

Optical absorption spectroscopy of color centers produced in yttria-stabilized zirconia by swift heavy ion irradiation

J.-M. Costantini[1, #], C. Trautmann[2], K. Schwartz[2], F. Beuneu[3]
[1]CEA, DEN, SRMA, Saclay, France; [2]GSI, Darmstadt, Germany; [3]LSI, Palaiseau, France.

Cubic zirconia (ZrO_2) is considered to be a suitable refractory host (T_m≈3000 K) for actinide confinement used for transmutation or high-temperature reactor projects. Literature data on radiation damage of this material are rather limited concerning studies with heavy ions [1]. Moreover, point defects were investigated only in the case of pure electronic excitations with photons [2].

This study is focusing on defect creation in cubic-stabilized zirconia exposed to energetic heavy ions, in particular on the characterization of defects and the role of the irradiation temperature on the damage process.

Zirconia single-crystals stabilized by yttrium in the cubic fluorite structure (ZrO_2: Y, with 9.5 mol% Y_2O_3) were used. Samples with <100> orientation were exposed to ions with energy of 11.4 MeV amu^{-1} (1.44-GeV ^{132}Xe, 2.24-GeV ^{197}Au, 2.37-GeV ^{208}Pb, and 2.7-GeV ^{238}U) at the UNILAC (GSI, Darmstadt). On-line optical absorption measurements in the UV-visible range were performed at 8 K and at room temperature (RT) for various fluences. Thermo-stimulated luminescence (TSL) was also recorded during heating up of the samples from 8 K to RT. After annealing to RT, all irradiated samples were characterized again by optical absorption and electron paramagnetic resonance (EPR) spectroscopy, which is highly sensitive for color centers in dielectrics. The EPR spectra of all samples (irrespective of the mode of irradiation) exhibited the same main resonance lines assigned to F^+-type centers and to the so-called T (trigonal) centers (i.e. Zr^{3+} centers) [2, 3]. Finally, surface profilometry measurements were carried out on some U and Pb ion irradiated samples.

The EPR data show a strong indication of the dominant role of elastic collisions in the F^+-type center production process [3, 4]. In contrast, the T centers that can be generated by single electronic excitations with energetic photons [2] are produced by the inelastic collisions of ions or electrons [3, 4].

Optical spectra exhibit a broad and asymmetrical absorption band peaked at about 2.5 eV (~500 nm) (Fig. 1), regardless of the irradiation features, which was already found with heavy ion irradiations in the 100-MeV energy range [3]. This band can be de-convoluted into two Gaussian-shaped sub-bands at about 2.4 eV and 3.1 eV corresponding to F^+-type centers [3] and T-centers [2] respectively. In the case of Au irradiation, the spectra can be resolved into six sub-bands including the latter ones. No clear temperature effect is seen on the band widths, in agreement with our previous results [3].

However, a strong increase of the defect production yield (slope of the optical density growth curve) is found for both color centers at low irradiation temperature (8 K) with respect to RT irradiations. Moreover, annealing the samples from 8 K to RT does not restore the defects to the level of RT irradiations (Fig. 1). The TSL data exhibit weak peaks at about 90 K that we have associated to this partial annealing effect. These results show the impact of dynamic annealing on the defect production mechanism.

The out-of-plane expansion as measured by surface profilometry is rather low (< 0.2%) and is proportional to the F^+-type center concentration deduced from the EPR data averaged over the projected range of the ions, in agreement with our previous results [5].

Further experiments using intermediate irradiation temperatures and lighter ions with lower stopping powers are in preparation.

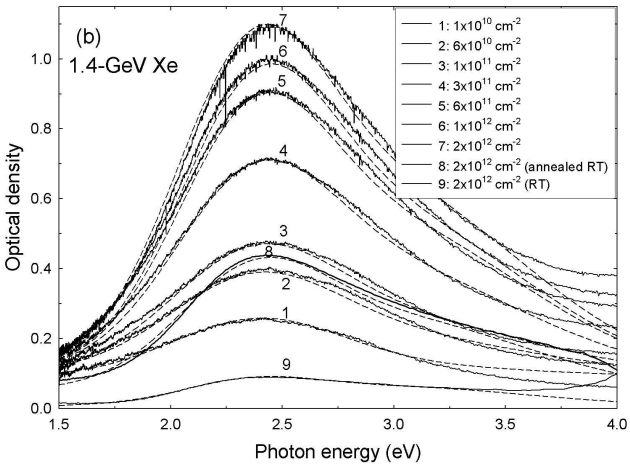

Fig. 1: Optical absorption spectra of yttria-stabilized zirconia recorded after irradiation with 1.44-GeV ^{132}Xe at various fluences and temperatures.

References

[1] K.E. Sickafus, Hj. Matzke, Th. Hartmann, K. Yasuda, J.A. Valdez, P. Chodak III, M. Nastasi, R.A. Verall, J. Nucl. Mater. **274** (1999) 66

[2] V.M. Orera, R.I. Merino, Y. Chen, R. Cases, P.J. Alonso, Phys. Rev. B **42** (1990) 9782

[3] J.M. Costantini, F. Beuneu, D. Gourier, C. Trautmann, G. Calas, M. Toulemonde, J. Phys.: Condens. Matter **16** (2004) 3657

[4] J.M. Costantini, F. Beuneu, Phys. Stat. Sol. (c) **4** (2007) 1258

[5] J.M. Costantini, C. Trautmann, L. Thomé, J. Jagielski, F. Beuneu, J. Appl. Phys. **101** (2007) 073501

jean-marc.costantini@cea.fr

Influence of Irradiation Temperature on Structure of Ion Tracks in Polycarbonate

P.Yu. Apel[1,#], I.V. Blonskaya[1], T.W. Cornelius[2,3], R. Neumann[2], R. Spohr[2], K. Schwartz[2], V.A. Skurtov[1], C. Trautmann[2]

[1]FLNR JINR, Dubna, Russia; [2]GSI, Darmstadt, Germany; [3]present address: ESRF, Grenoble, France

Studying track etching in polymers irradiated with charged heavy particles at different temperatures is of interest for two main reasons. First, reproducible fabrication of precisely defined nanostructures via etching of ion tracks requires the detailed knowledge of factors determining the properties of the initial stage of pore growth. Second, the track etching is a tool that can help to shed light on the track formation mechanisms which are still not completely understood. One of the most prominent track formation models is the thermal spike, which is a process that should depend on the irradiation temperature.

Polycarbonate foils Makrofol KG (10 μm thick) were irradiated with U, Sm, and Ni ions (initial energy 11.1 MeV/u) at the UNILAC (GSI, Darmstadt), both at room temperature (RT) and at 15 K. The irradiation at low temperature (LT) was performed in a cryostat installed at the beamline X0. Irradiation with Kr ions (energy 2.5 MeV/u) was carried out at the U-400 cyclotron (FLNR, Dubna) at RT and liquid nitrogen temperature. Track densities in the samples ranged from 10^5 to 10^6 cm^{-2}. The ion-irradiated samples were sensitized with ultraviolet light for 1h and etched in a conductometric cell with 5M NaOH at 40ºC. LabView-controlled HIOKI RCL-meter was employed to monitor ohmic resistance of the cell in the range of 10^{10} down to 10 Ohm [1]. The effective pore diameter d_{eff} as a function of the etching time t was calculated assuming cylindrical geometry of the etched pores.

The evolution of d_{eff} is characterized by three successive regions which we interpret as the track core, track halo, and bulk etching, respectively. We define the diameter of the track core d_c and the halo d_h as the point of inflection of the d_{eff} –t curve at the respective transition [1, 2]. The typical track diameters as a function of energy loss dE/dx are presented in Fig. 1. The correlation of the diameters and dE/dx clearly indicates that the d_{eff} –t curve reflects structural features of latent tracks. The data are well described by a power-law fit:

$$d_{c,h} = A\,(dE/dx)^b.$$

The halo diameters, d_h, are on the average smaller for samples irradiated at LT (see Fig.1). This effect can be associated with the suppression of temperature-dependent secondary reactions in the zone where the electron cascade occurs. At the same time, the d_h data exhibit significant scattering suggesting some uncontrolled factors which may influence processes in the track periphery.

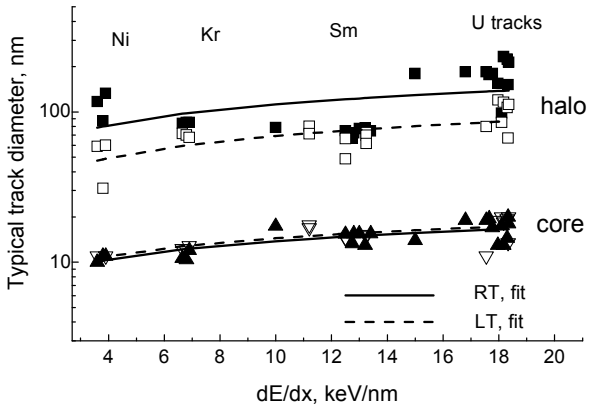

Figure 1: Diameter of track core d_c (triangles) and track halo d_h (squares) of various ion species as a function of the energy loss dE/dx. Solid symbols: irradiation at RT; open symbols: irradiation at low temperature (LT).

In contrast to d_h, no significant dependence of the irradiation temperature on the core diameters d_c is observed. Using the thermal spike model, the track temperature in a polymer was estimated to be ~1400 K at a radius of 7 nm for an ion with dE/dx = 10 keV/nm [3]. When irradiating at low temperatures, the track core diameter should reduce by about 2 nm. This contradicts our observation that within a few percent accuracy, no shifts in the d_c values were registered. The independence of d_c on irradiation temperature suggests that there is no thermal degradation of the polymer at larger radii of 5-10 nm. This can be explained based on known pyrolysis reaction rate constants and taking into account that thermal degradation requires both temperature and time. Since the temperature peak is very short (< 10^{-10} s) [3], the pyrolytic decay is negligible in the zone heated up to ~1500 K. However, degradation of polymer in the track core of r < 3-4 nm, where temperature as high as 3000-4000 K can be attained, cannot be ruled out.

References

[1] P.Yu. Apel et al., Nucl. Instr. Meth. B245 (2006) 284
[2] T.W. Cornelius et al., Nucl. Instr. Meth. B265 (2007) 55
[3] M. Skupinsky et al., Nucl. Instr. Meth. B240 (2005) 681

#apel@nrmail.jinr.ru

Self-Aligned Structures Created by Swift Heavy Ion Irradiation*

H.-G.. Gehrke[1#], A.-K.Nix[1], J. Krauser[2], C. Trautmann[3], A. Weidinger[4], and H. Hofsäss[1]
[1] II. Physikalisches Institut, Universität Göttingen, Germany; [2] Hochschule Harz, Wernigerode, Germany; [3] GSI, Darmstadt, Germany; [4] Helmholtz-Zentrum Berlin für Materialien und Energie, Berlin, Germany

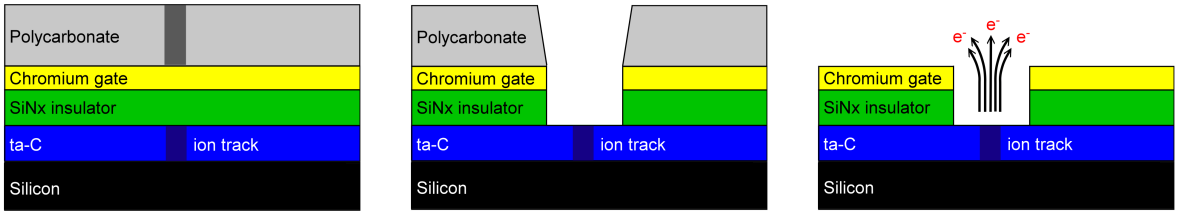

(a) Ion-irradiated multilayer structure with etchable track in polymer and conducting trail in carbon film.

(b) Self-aligned access to conducting track by etching and sputtering.

(c) Final field emission structure.

Figure 1: Schematics of fabrication process of ion-track based device.

The irradiation with swift heavy ions provides a powerful tool to fabricate structures with high aspect-ratio and diameters in the nanometer range. In most cases, ion tracks are not used directly but in combination with chemical etching which dissolves the damaged track material and creates nano- or micro-channels. Ion-track membranes, mainly produced from polymer foils, are suitable as filters or as templates to grow nanowires. Track-etched pores in a resist can also be used as mask for structuring subjacent substrate layers. This lithographic method was applied earlier [1] but has not been developed much since then.

In the present experiment, we combine ion irradiation and different etching steps to build an advanced structure for application e.g. as field emitter. The production process, schematically shown in Fig. 1, uses a multilayer sample consisting of a thin film of polymer resist (mask), chromium (electrode), SiN_x (insulator), tetrahedral amorphous carbon (ta-C), and a thick n-type Si wafer. The stack is irradiated with uranium ions of 1-GeV energy provided at the UNILAC. Due to this high kinetic energy, the beam passes through all layers and finally stops deep inside the Si substrate. Along the path of each individual ion, a damage trail is created in the polymer and in the ta-C film, whereas the Cr, SiN_x, and Si layers are sparsely or not at all affected. As described earlier, tracks in ta-C represent conducting graphitic nanowires with diameters in the order of 8 nm [2,3]. Such a conducting filament is the main device component and needs to be gated if e.g. applied as nanosized field emitters. Since the track in the resist and the conducting filament in the ta-C layer are induced by the same ion, both structures are self-aligned. Track etching of the resist gives access to the subjacent layers which can be opened by applying adequate etching or sputtering processes (Fig. 1b). Finally, the resist is removed and the Cr layer can be contacted as gating electrode without tedious alignment procedures.

Fig. 2 shows the final structure produced so far. The individual fabrication steps are adequate but layer quality and process parameters require further optimisation. Also the field emission properties of the device have to be tested.

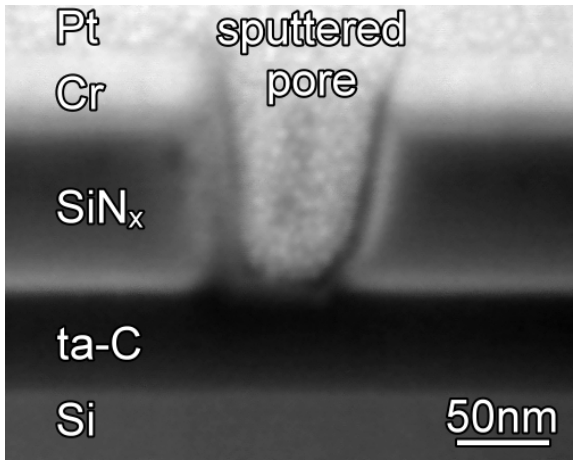

Figure 2: Cross-sectional SEM image of irradiated and etched multilayer sample. The aperture etched in the Cr- and SiN_x-layer has a diameter of about 50 nm and gives access to the conducting track in the ta-C layer (not visible due to limited resolution). For better imaging contrast, the opening was filled with Pt. The cross-section was produced by focused ion beam cutting.

[1] A.F. Bernhardt et al., J. Vac. Sci. Technol. B 18 (2000) 1212
[2] M. Waiblinger et al., J. Appl. Phys. 69 (1999) 239
[3] J. Krauser, J.-H. Zollondz, A. Weidinger, C. Trautmann. J. Appl. Phys. 94 (2003) 1959
[4] J.-H. Zollondz, D. Schwen, A.-K. Nix, C. Trautmann, J. Berthold, J. Krauser, H. Hofsäss, Mat. Sci. Eng. C 26 (2006) 1171
[5] J. Krauser, A.-K. Nix, H.-G. Gehrke, H. Hofsäss, C. Trautmann, A. Weidinger, F. Wünsch, J. Bruns, J. Vac. Sci. Technol. B 26 (2008) 2468

* supported by DFG (Ho1125/17-1) and BMBF (05 KK4MGA/9)
# hans-gregor.gehrke@phys.uni-goettingen.de

Dielectric strength of ion irradiated polyimide and epoxy/fiber composites

T. Seidl[1,#], W. Ensinger[1], E. Floch[2], A. Golubev[3], R. Lopez[4], E. Mustafin[2], A. Plotnikov[2], D. Severin[1], A. Smolyakov[3], D. Tommasini[4], C. Trautmann[2]

[1]Technische Universität Darmstadt, Germany; [2]GSI, Darmstadt, Germany; [3] ITEP, Moscow, Russia; [4]CERN, Geneva, Switzerland

During long-term operation of the new FAIR facility, parts of the superconducting magnets will be exposed to high radiation levels, cryogenic temperatures, and dynamic mechanical loads (Lorentzian forces during pulsed operation). Depending on the position of the different components, the radiation due to beam losses consists of a cocktail of gammas, neutrons, protons, and heavier particles [1]. Although the number of heavy fragments of the initial projectiles is small compared to neutrons, protons, or light fragments (e.g. α particles), their large energy deposition can induce extensive damage at rather low fluences (dose calculations show that the contribution of heavy ions to the total accumulated dose can reach 80% [2]). In the MeV to GeV energy regime, beam-induced radiation damage strongly depends on the specific sensitivity of the material and scales with fluence and electronic energy loss of the ions. In particular, organic polymers to be used e.g., as cable insulation for the superconducting FAIR magnets, may undergo severe degradation accompanied by outgassing of small volatile radiolysis products [3,4].

This study tackles the dielectric strength of polyimide (Kapton) as electrical insulation and G11-type epoxy/glassfiber composites as structural support material. Kapton foils of thickness 12, 25, and 50 µm were irradiated with 21 and 800 MeV protons (ITEP) and with various heavy ions of MeV-GeV energy (UNILAC, GSI). In addition, three types of 1-mm thick epoxy/glassfiber sheets were exposed to 180-MeV/u Xe ions (SIS, GSI). The irradiation experiments with protons and Xe ions took place in air, while the UNILAC irradiations were performed in vacuum.

To test degradation of the insulating properties, breakdown voltage measurements were carried out using a current-limited 20-kV high voltage tester available at CERN. The ramping speed of the DC voltage was 1.3 kV/s. The location of breakdown events was inspected by means of optical microscopy and typically occurred inside the Rogowski-type stainless steal electrodes having a diameter of 10 mm. Any significant geometric influence on the electric field is therefore excluded. The tests took place in air, at room temperature, and at a humidity of 24-30%. No systematic errors due to temperature and/or humidity fluctuations were found.

For Kapton, the measurements show an overall decrease of the breakdown voltage with increasing dose (Fig. 1). For light projectiles, such as protons and C ions of rather small electronic energy loss (dE/dx between 0.03 and 0.5 keV/nm), the decrease of the breakdown voltage becomes significant at doses above 1 MGy. In the case of heavy ions (dE/dx > 16 keV/nm), the breakdown voltage changes at a much lower dose (note the semi-log presentation of Fig. 1). The expected maximum voltage in the superconducting coils of the FAIR magnets is about 3 kV. In the tested dose regime up to ~80 MGy, the degradation due to light ions is insignificant for the operation voltage. The situation is much more crucial for heavy ions, where already a dose of a few kGy results in a severe decrease of the breakdown voltage. At around 0.1 MGy, the values are close to the voltage requirement for the FAIR magnets. These results give a first indication that individual tracks completely passing through the Kapton insulation may represent a serious security risk for the insulation of the FAIR magnet coils.

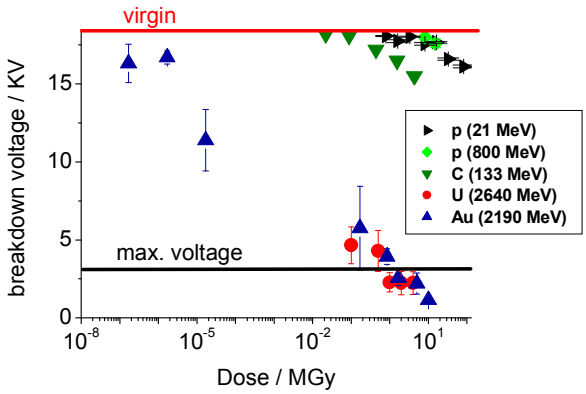

Fig. 1. Breakdown voltage of 50-µm thick Kapton foils as a function of dose for various irradiations.

We also tested the dielectric strength of pristine and irradiated epoxy/glassfiber composites, but the 20-kV high voltage tester was not powerful enough to reach breakdown limits. Although future measurements require higher voltages, this result is at least an indication that the ion-induced decrease of the breakdown voltage is less dramatic for the epoxy/glassfiber composites than for Kapton films.

References

[1] L. Latycheva et al., Proc. 9th Europ. Particle Accelerator Conf. 2004, Lucerne, Switzerland (2004) 1408

[2] L. Latycheva, "Irradiation experiment in Cave HHD: Numerical estimates of the energy deposition into the samples", GSI internal note: DOC-2009-Jan-47

[3] D. Severin et al., Nucl. Instr. Meth. B 236 (2005) 456

[4] V. Picq et al., Nucl. Instr. Meth. B 151 (1999) 76

Radiation hardness of Kapton exposed to swift heavy ions

D. Severin[1,#], W. Ensinger[1], T. Seidl[1], C. Trautmann[2]
[1]Technische Universität Darmstadt, Germany; [2]GSI, Darmstadt, Germany.

This research project focuses on the radiation hardness of Kapton under extreme conditions (high dose, low temperature) and is motivated by the application of this polyimide as insulator in the new superconducting FAIR magnets. The FAIR facility is expected to deliver protons and heavy ions of extreme energies (10 GeV/u) and unprecedented intensities (10^{12} ions/pulse). Reliable data of the radiation hardness of polymers exposed to energetic particles are important with respect to mechanical, electrical, and outgassing properties as well as for long-term reliability estimations. The results are also of interest for other high-current facilities such as the Large Hadron Collider (LHC) of CERN.

To study ion-beam induced modifications, Kapton foils were irradiated at the UNILAC using different projectiles (e.g. Ti, Mo, Au, and U) within a broad fluence regime (10^{10} – 5×10^{12} ions/cm^2). The irradiated Kapton foils were analysed by infrared (FTIR) and UV/Vis spectroscopy, tensile strength measurements, mass loss analysis, and dielectric relaxation spectroscopy (DRS) [1]. For testing the radiation stability of Kapton at the cryogenic operation temperature of the superconducting magnets, additional experiments were dedicated to low temperature (5-10 K) irradiations performed at the GANIL (Caen, France) focusing on outgassing processes of small volatile degradation fragments using online residual gas analysis.

All results obtained by optical spectroscopy, tensile strength measurement, and mass loss analysis show a similar trend and can be scaled by the irradiation dose given by the product of fluence and energy deposited along the ion trajectory. Critical material degradation appears above a dose of about 1 MGy.

In contrast, the electrical properties analysed by DRS exhibit a rather different behaviour for light and heavy ions: high fluence irradiations with light ions (e.g. Ti) lead to a slight increase of the conductivity, whereas drastic changes are already observed for heavy ions (e.g. Sm, Au) in a moderate fluence regime (non-overlapping tracks) of 5×10^{10} ions/cm^2.

Online residual gas analysis during irradiation at cryogenic temperatures shows the release of a variety of small gaseous molecules (e.g. CO, CO_2, and short hydro carbons). Also a small amount of large polymer fragments is identified and confirms the degradation mechanism of Kapton proposed earlier. Simultaneous in-situ infrared spectroscopy gives evidence of accumulation of these small molecules inside the bulk polymer at cryogenic temperatures. During heat-up cycles, these fragments outgas in specific temperature zones.

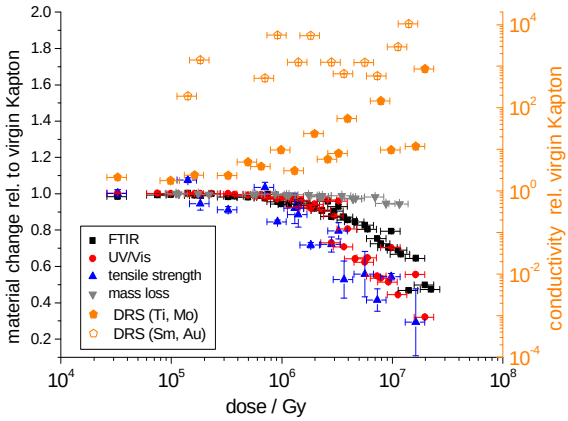

Figure 1: Relative material change referred to virgin Kapton as a function of irradiation dose (product of applied fluence and dE/dx of the different ion species). Data from various analytical methods indicate the same critical degradation above ~1 MGy, except the clear deviation for low-fluence heavy ions (open symbols) concerning electrical property analysed by DRS

The results obtained for Kapton by applying different analytical techniques allow the following conclusions [2]:

i) Kapton exposed to high-energetic particle radiation undergoes severe material degradation above a critical dose of 1 MGy.

ii) The critical dose deduced from tensile strength tests is in good agreement with optical spectroscopy data. This correlation allows the prediction of mechanical degradation from rather simple, non-destructive infrared spectroscopy measurements.

iii) Dielectric relaxation spectroscopy indicates a dramatic increase in the conductivity when Kapton is exposed to heavy ions. We assume that above a critical energy loss, tracks of individual ions represent trails of significant increased conductivity. This phenomenon needs to be investigated in more detail, because heavy ions of rather low fluences may strongly reduce the breakdown voltage.

iv) Outgassing of small degradation fragments has to be considered even at cryogenic irradiation temperatures. Below 20 K, some of the small molecules accumulate in the bulk material, inducing additional gas evolution during heat-up cycles.

[1] D. Severin, W. Ensinger, R. Neumann, C. Trautmann, G. Walter, I. Alig and S. Dudkin, NIM B, 236 (2005) 456-460.
[2] D.Severin, Dissertation, Philipps-Universität Marburg, 2008.

Microstructural changes of graphite irradiated with swift heavy ions

M. Krause[1,2], M. Tomut[2,3], S. Amirthapandian[2,4,5], R. Neumann[2], C. Trautmann[2], W. Ensinger[1]
[1]Technische Universität Darmstadt, Germany; [2]GSI, Darmstadt, Germany; [3]NIMP, Bucharest, Romania;
[4]IHFG, University of Stuttgart, Germany; [5]MSD, IGCAR, Kalpakkam, India

Several methods, such as electron microscopy, scanning tunnelling microscopy (STM), X-ray diffraction, and decoration technique can be used to observe radiation damage in materials. In this work, we report microstructural changes and defect clusters induced by swift heavy ions (SHI) on graphite surfaces, visualized by scanning electron microscopy (SEM). Our studies have been performed on fine-grained polycrystalline graphite (grade R6650, SGL Carbon) which is proposed as material for beam catchers and rotating target at the Super-FRS of FAIR [1]). In addition, we extended our investigations to highly oriented pyrolytic graphite (HOPG, ZYB, NT-MDT company) as model material consisting of layered graphite sheets.

SEM images of polycrystalline graphite irradiated with 11.1 MeV/u U ions at high fluences show a decrease of the crystallite size in comparison to the pristine samples (Fig. 1). New irregular crystallites form on the surface in a non-linear manner. This "milling" effect of swift heavy ion beams has been previously inferred from the evolution of Raman spectra as a function of fluence [2]. High-magnification SEM images of the irradiated grain surface, in the secondary electron imaging (SEI) mode, show the presence of many point-like features with bright contrast and characteristic diameters of about 10 nm. Fig. 2 illustrates these features on a surface grain irradiated at a fluence of 5×10^{12} U-ions/cm^2 in comparison to the smooth defect-free surface of the pristine sample. The counted density of the features is one order of magnitude smaller than the ion track density, therefore we would rather attribute them to defect clusters than to single ion tracks.

To better understand the nature of these defects, high-resolution images of HOPG samples irradiated with Pb-ions at low (5×10^{10} ions/cm^2) and high (5×10^{12} ions/cm^2) fluences are shown in Fig. 3. In both cases, similar bright-contrast defect structures appear. They are larger for the low fluence sample and have a higher number density and smaller size for the large fluence sample. There are several reports on the formation of prismatic dislocation loops of interstitial nature in neutron irradiated graphite [3] and vacancy prismatic loops in quenched graphite annealed at 1300 ºC [4]. This type of defects was observed by TEM [4] and STM [5]. Given by the similarity, we attribute our SEM observations in SHI-irradiated graphite to interstitial prismatic dislocation loops. They are smaller for the high fluence samples due to the higher nucleation rate at supersaturated point-defect concentrations when tracks overlap. In the low-fluence sample, the nucleation rate is lower and the defects tend to aggregate into larger clusters. Also shear as shown by the large loop with bright edges in Fig. 3a or dissociation into two loops showing stacking fault contrast (as seen in the upper left corner of Fig. 3) takes place. Additional STM on oxidized irradiated samples will be performed to support these SEM observations. Prismatic dislocation loops are sessile defects and responsible for irradiation-induced hardening by preventing dislocation movement via pinning, as seen in graphite irradiated at high fluence [6].

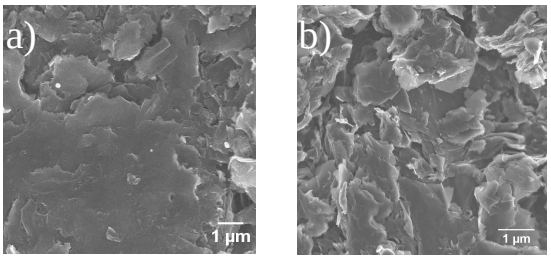

Fig. 1. Low-magnification SEM images of polycrystalline graphite sample: (a) pristine and (b) irradiated with 5×10^{12} U ions/cm^2.

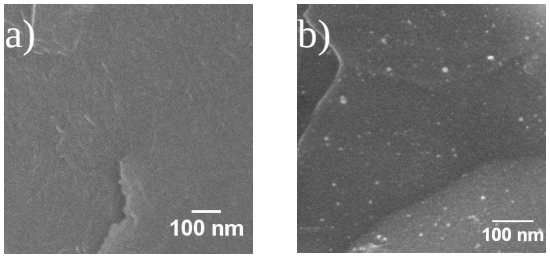

Fig. 2. High-magnification SEM images of the grain surface topography of polycrystalline graphite: (a) pristine and (b) irradiated with 5×10^{12} U ions/cm^2.

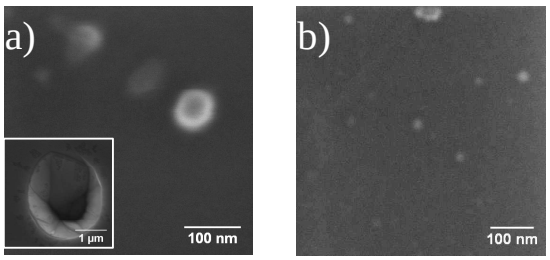

Fig. 3. High magnification SEM images of defect clusters formed in HOPG irradiated with (a) 5×10^{10} Pb/cm^2 and (b) 5×10^{12} Pb/cm^2. The inset shows a large annular defect formed by superposition of two concentric defect loops.

References

[1] H.Geissel et al., NIM B 204 (2003) 71.
[2] M. Tomut et al., GSI Scientific Report (2007) 336.
[3] P. A. Thrower, Brit. J. Appl. Phys. 15 (1964) 1153.
[4] S. Amelinckx et al., Phys. Rev. Let. 5 (1960) 50.
[5] P. J. Ouseph, Phys. Stat. Sol. 169 (1998) 25.
[6] M. Tomut et al., GSI Scientific Report (2007) 69

Heavy ion irradiation of crystallographically oriented cordierite

C. Weikusat[1,#], U.A. Glasmacher[1], R. Miletich[1], R. Neumann[2], C. Trautmann[2]
[1]Institut für Geowissenschaften, Univ. Heidelberg, Germany; [2]GSI, Darmstadt, Germany

The mineral cordierite is a framework silicate with corner-sharing six-membered rings of SiO_4-tetrahedra, forming channels along the crystallographic c-axis. During crystal growth, these channels incorporate alkali atoms and various volatiles (e.g., Na, K, CO_2, H_2O, CH_4).

Natural cordierite single crystals from Madagascar were oriented with optical and X-ray methods and cut normal to the crystallographic a-axis. Irradiations were performed at the UNILAC with Pb ions of 8 MeV/u, applying fluences between 7×10^{11} and 2×10^{12} ions/cm^2. The penetration depth of the ions (75 µm) and the electronic energy loss (dE/dx) at the sample surface (25 keV/nm) were calculated with the SRIM2008 code, assuming the standard chemical composition ($(Mg,Fe^{2+})_2Al_4Si_5O_{18}$) and a density of 2.65 g/cm^3.

Colour change of the irradiated layer and cracking beyond the penetration depth of the ions were observed in all samples, becoming more pronounced with increasing fluence. As has already been reported for unoriented samples [1], the loss of H_2O and CO_2 content and a simultaneous increase of CO are easily detectable in the Raman spectra.

A comparison of the Raman spectra of pristine and irradiated cordierite is shown in Figure 1. Band broadening and a loss of intensity increase with increasing fluence.

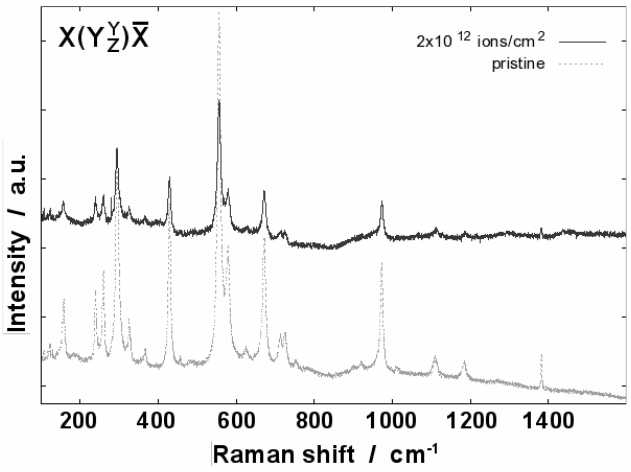

Figure 1: Typical Raman spectra of cordierite, pristine and irradiated with 2×10^{12} Pb-ions/cm^2. Spectra are slightly stacked.

The results of a linescan perpendicular to the irradiated surface (e.g., *E || [100]*) are shown in Figure 2. The automated xy-stage was used to acquire a full Raman spectrum every 5 µm on a line along the ion trajectory.

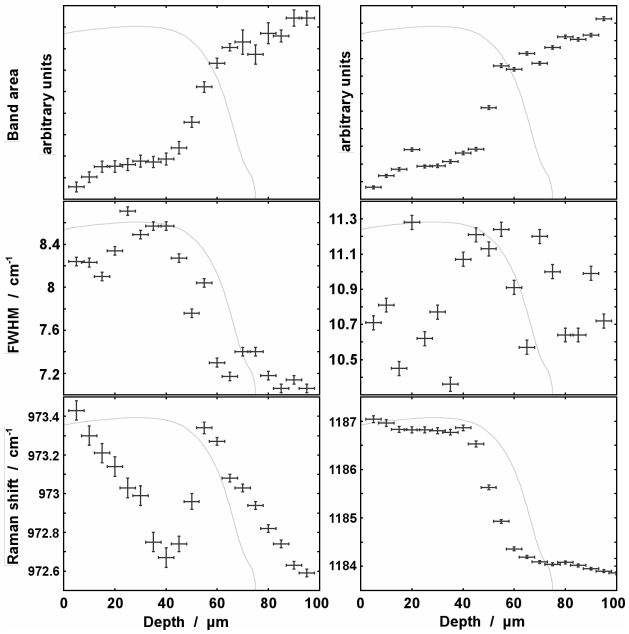

Figure 2: Raman spectroscopy results of cordierite irradiated with 8-MeV/u Pb ions of fluence 1×10^{12} ions/cm^2. Band area, FWHM, and peak position of the Raman band at ~973 cm^{-1} (left) and at ~1184 cm^{-1} (right) as a function of sample depth. The electronic energy loss of the incident ions (estimated with SRIM08) is indicated in grey.

The mapped parameters include *band areas*, *FWHM* (probing the crystallinity of the sample and the order/disorder distribution in the lattice) as well as the *peak positions* (sensitive to internal stresses due to various lattice defects). For some bands, the evolution of these parameters as a function of sample depth suggests a close correlation with (dE/dx), however, this does not hold true for all bands. The luminescent background, which increases significantly with increasing fluence, also seems to be correlated with(dE/dx). The exact nature of the luminescent centers and the mechanisms of defect production are subject to ongoing research.

References

[1] C. Weikusat et al., Nucl. Instr. Meth. B 266, 2990 (2008)
[2] W.C.-K. Poon et al., J.Phys: Condens. Matter, 2, 6361 (1990)

#weikusat@min.uni-heidelberg.de

Ion irradiation under pressure using the Paris-Edinburgh press: first results

M. Burchard[1], C. Weikusat[1], U.A. Glasmacher[1], S. Klotz[2], R. Miletich[1], C. Trautmann[3], R. Neumann[3]

[1]Inst. für Geowissenschaften, Univ. Heidelberg, Germany, [2]Univ. P&M Curie, Paris, France, [3]GSI, Darmstadt, Germany

In the recent past, diamond anvil cells (DAC) have been used for experiments exposing samples to swift heavy ions at nonambient pressures. Diamonds as anvils allow spectroscopic measurements inside the cell, but they have the drawback that the maximum size of the sample is typically limited to less than 200 µm. In order to provide larger volumes of irradiated material in particular to be able to apply various other analytical techniques, we performed first irradiation tests using a multi-anvil Paris-Edinburgh cell (PEA) (Fig. 1.). This apparatus was originally developed for neutron scattering experiments and offers a defined radiation pathway as well as relatively high pressure limits.

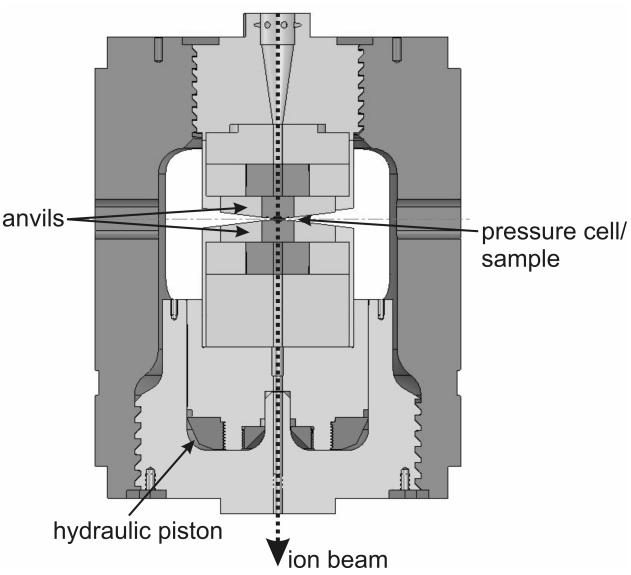

Figure 1: Scheme of multi-anvil Paris-Edinburgh press. The dotted line indicates the ion beam passgae. Dark gray outer parts and light gray inner parts consist of hardened steel. Dark gray parts next to the pressure cell are made of hard metals (tungsten carbide, cubic boron nitride (cBN)).

To avoid severe ion-induced activation of the material within the central pressure cell, the design of the PEA had to be modified by using ultrapure silver as secondary pressure medium and capsule material. The sample chamber was directly drilled into the silver and has a thin hBN-plate on the bottom and a silver foil on top (Fig. 2.). For the first test irradiation, we used a zircon crystals and silicone paste as primary pressure medium to avoid chemical reactions. Zircon was chosen because of its well documented ion-induced radiation damage, which can easily be detected by Raman spectroscopy [1]. Because the PEA is a "simple-squeezer" type pressure cell, it had to be sealed by using a mechanically rigid CuBe-gasket and surrounded by cBN-anvils (Fig.3). For the first experiment, a pressure of ~6 GPa was applied. The irradiation was performed with Xe ions of 300 MeV/u initial energy applying a fluence of 1.5×10^{12} ions/cm^2. The deactivation time until the cell could be handled was ~5 month mainly due to tungsten carbide cell components.

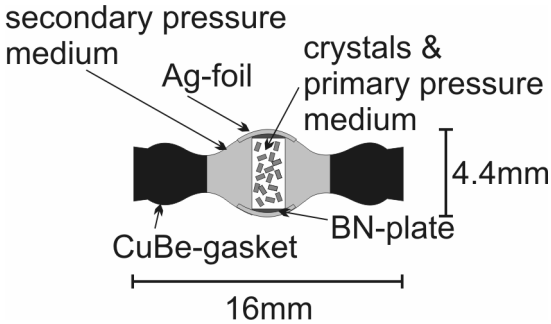

Figure 2: Schematic cross section of sample chamber of size ~20 mm^3.

After the irradiation, the silver sample chamber was carefully opened and the zircon crystal was extracted. The Raman spectrum of the high-pressure irradiated zircon compared to a non-irradiated reference sample revealed a significant decrease of band intensity as recorded in earlier experiments and characteristic of radiation damage [2].

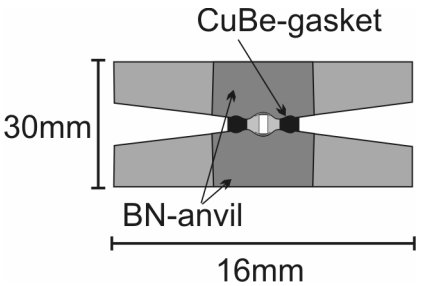

Figure 3: Scheme of sample chamber between cBN anvils.

References

[1] U.A. Glasmacher, M. Lang, H. Keppler, F. Langenhorst, R. Neumann, D. Schardt, C. Trautmann, G.A. Wagner, Phys. Rev. Lett., **96**, 195701 (2006).

[2] M. Zhang, E.K.H. Salje, I. Farnan, A. Graeme-Barber, P. Daniel, R.C. Ewing, A.M. Clark, H. Leroux, J. Phys.: Condens. Matter, **12**, 1915 (2000).

New phase of ZrO_2 created by swift heavy ion irradiation at high pressure

B.Schuster[1,2], R. Neumann[1], and C. Trautmann[1]
[1]GSI, Darmstadt, Germany; [2]Technische Universität Darmstadt, Germany

Zirconia (ZrO_2) is a commonly used ceramic which is known for its thermal and mechanical resistance and its radiation hardness. Because of these properties it is often used as inert fuel matrix in nuclear reactors [1].

At ambient conditions the material is in its monoclinic form which it changes to tetragonal at ~ 1200°C and to cubic at ~2400°C. High pressure forms are known to be orthorhombic. None of these polymorphs is quenchable to ambient conditions [2].

But previous irradiation experiments [3] showed that ZrO_2 can transform to its high temperature polymorph (tetragonal) and will remain stable at ambient conditions, if the fluence exceeds values of 5×10^{12} Pb- or U-ions/cm^2, or higher values for lighter ions [4].

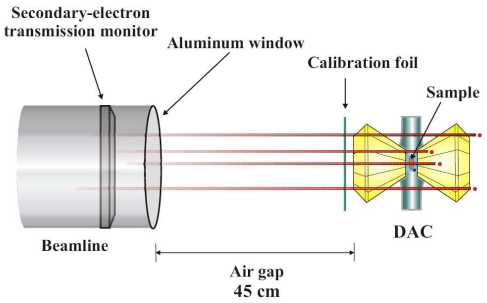

Figure 1: Schematic of ion irradiation of samples pressurized in diamond anvil cell (DAC) at the SIS (Cave A)

Irradiation experiments at high pressures open up the possibility to study new effects that can only be caused by simultaneous exposure to swift heavy ions and high pressure. These pressures are realized by using a diamond anvil cell (DAC), in which the sample is squeezed in between two diamonds. Irradiations were performed at the heavy-ion synchrotron SIS of GSI where the kinetic energy of the ions is sufficiently large (~200MeV/u) to completely pass through the first diamond (Figure 1).

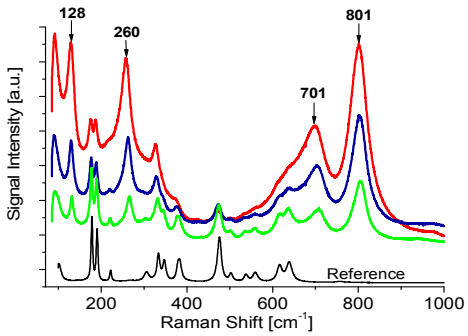

Figure 2: Raman spectra of irradiated ZrO_2 at various sample positions. The three upper spectra show different degrees of transformation to a possible new phase

Recent experiments showed that irradiations at about 11 GPa can cause a phase transition from monoclinic to tetragonal already at a fluence of ~2×10^{11} Pb/cm^2 which can be stabilized to ambient conditions. This behaviour was tested up to 13 GPa [3]. Here we present new experiments performed at 25 GPa using U ions of 214 MeV/u and a fluence of 2×10^{11} cm^{-2}.

All Raman spectra in Figure 2 were acquired after opening the DAC so the sample was not exposed to external no pressure. The recorded spectra correspond to none of the Raman spectra of known polymorphs of ZrO_2. The degree of this phase transformation varied throughout the sample. Figure 3 compares the Raman spectra of ZrO_2 polymorphs that are well known, representing from bottom to top: ambient conditions (monoclinic), a sample that has been pressurized up to 25 GPa (orthorombic), high-temperature polymorph created by ion irradiation with 2×10^{11} U/cm^2 at 11 GPa (tetragonal), and the possible new polymorph with Raman bands appearing at 91, 128, 260, 701, and 801 cm^{-1}.

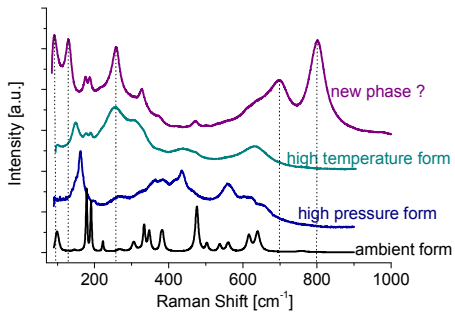

Fig. 3: Raman spectra of known ZrO_2 phases and of samples irradiated at 25 GPa (2×10^{11} U/cm^2) with new bands.

Irradiation of ZrO_2 at pressures around 25 GPa can obviously provoke a transformation to a possible new phase which can also be quenched to ambient temperature and pressure. The measured Raman Spectra correspond to none of the known polymorphs. Future XRD measurements will be needed to identify the structure of this new phase

References

[1] V.M. Oversby, C.C. McPheeters, C. Degueldre, J.M. Paratte, J. Nuc. Mat. 245 (1997) 17.
[2] O. Ohtaka, H. Fukui, T. Kunisada, T. Fujisawa, Phys. Rev. B 63 (2001) 174108.
[3] B. Schuster, M. Lang, R. Kein, C. Trautmann, R. Neumann, A. Benyagoub, Nucl. Instr. Meth. B (2009) in press
[4] A. Benyagoub, Phys. Rev. B 72 (2005) 094114.

Swift Heavy Ion Irradiation of Pressurized Boron Nitride

R. Klein[1], L. Dubrovinsky[2], R. Miletich[3], and R. Neumann[1]

[1]GSI, Darmstadt, Germany; [2]BGI, University of Bayreuth, 95440, Germany; [3]University of Heidelberg, 69120, Germany

Introduction

Recently, it has been shown that irradiation with swift heavy ions can trigger [1] or also prevent [2] phase transitions in oxides at static high pressure and outside the equilibrium stability field [3]. At GSI, several experiments were conducted in order to probe the influence of applied pressure of up to 25 GPa on the irradiation behaviour of various materials [2, 3].

We decided to study effects of elevated pressure and simultaneous ion irradiation on boron nitride (BN), the reason being its simple structure, the structural relationship to the carbon allotropes, the existing knowledge about polymorphism, and the technical relevance of this material class. Transformations between hexagonal, cubic, rhombohedral and wurtzitic BN (hBN, cBN, rBN, wBN) in the pressure-temperature parameter space are well established [4, 5]. Our focus is the transformation of hBN to wBN, which is supposed to be quenchable only in nanostructured material [4].

Experimental

Commercial hBN powder was pressurized in dedicated self-made diamond anvil cells (DACs) using rhenium gaskets and ruby pressure markers. The latter serves as luminescence gauge to be read out via Raman fluorescence spectroscopy. Since we worked at pressures higher than 20 GPa and the specimens to be investigated were microcrystalline powders, no pressure transmitting medium was used. The ion irradiation was performed with a beam from the SIS heavy-ion synchrotron of GSI. All cells were exposed to Pb ions with primary energies of 175 - 250 MeV/u, which are necessary to penetrate the front diamond of the DAC and to ensure maximal energy loss within the sample. Furthermore, one load of non-pressurized hBN was irradiated directly behind a diamond in order to have a reference with possible influences from the anvil. After irradiation the cells were highly activated and needed to decay for several weeks. For ex-situ X-ray diffraction studies as well as Raman spectroscopy, the pressure was released, and the quenched phases were probed outside the DACs.

Results and Conclusions

Due to the obvious difference between specimens that were only pressurized and those that were treated with the same pressure but with additional heavy-ion irradiation, we conclude that the energy loss of the ions triggers significant alterations within the crystal structure. Ex-situ X-ray measurements revealed that irradiation of hBN at ambient pressure conditions caused amorphization. However, irradiation of pressurized hBN resulted in nearly pure wBN, whereas pressurization alone generated a polymorph material (Fig. 1). Decelerating charged particles thus can trigger phase transitions via recrystalliziation of molten ion tracks. In conlusion, the additionally applied pressure prevents amorphization of the material and deters BN from reverting to its hexagonal structure. In order to obtain further insight in these processes, it is planned to investigate irradiated and pressurized BN samples in-situ via synchrotron X-ray diffraction.

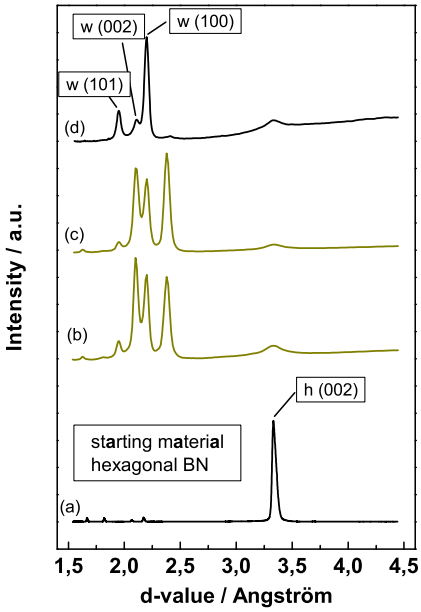

Figure 1: X-ray diffraction (CuKα, rotating anode) patterns of BN: (a) pristine BN, (b) and (c) diffractograms recorded at ambient pressure subsequent to pressurization to 13 and 21 GPa without ion irradiation. (d) nearly pure wBN after irradiation with 4.5×10^{11} ions/cm^2 at 21 GPa and initial energy of 225 MeV/u.

References

[1] A. Benyagoub; Nucl. Instr. Meth. B **245** (2006) 225.
[2] M. Lang et al.; Earth Planet. Sc. Lett. **269** (2008) 291.
[3] U.A. Glasmacher et al.; Phys. Rev. Lett. **96** (2006) 195701.
[4] S. Saha et al.; Chem. Phys. Lett. **421** (2006) 86.
[5] F.P. Bundy, R.H. Wentorf; J. Chem. Phys. **38** (1963) 1144.

Biomolecule writing using nanopens fabricated by ion-track etching*

P. Kohli[1,#], R.R. Pradeep[1], J. Wolff[1], R. Zakeri[1], C. Patel[1], K. Tadinisa[1], S. Aouadi[1], H. Wang[1], C. Trautmann[2]

[1] Southern Illinois University, Carbondale IL, USA; [2] GSI, Darmstadt, Germany

Patterning at submicron/nanometer resolution has a wide range of applications in a variety of fields. On this length scale, it is difficult to make patterns with conventional photolithography and it usually involves expensive and complex instrumentation. Some of the present techniques involve Atomic Force Microscopy (AFM), Dip Pen Lithography (DPN) [1], or Nanofountain Pen (NFP) [2] electron beam based patterning. Here we present a relatively simple and inexpensive method using an electric potential to force charged molecules through a submicron or nano-scale "pen" embedded in a glass chip [3].

Figure 1 shows a fabricated conical aperture (pen) in a glass chip which was fabricated by ion irradiation using 11.1 MeV/u Au ions and subsequent track etching. For the etching process we used HF on one side and a calcium ion blocking solution on the other side of the glass chip. This resulted in a conical pore whose small and large opening diameter can be tuned by the etching parameters to 400 nm and many tens of microns, respectively.

The glass chip containing the pen is mounted on a home-assembled piezoelectric (PZT) motor stage which is computer-controlled (Fig. 2). For deposition of DNA molecules in a given pattern, the charged biomolecules are pulled through the pen onto a glass substrate by applying a voltage. Two examples of biomolecule patterns are illustrated in Fig. 3, showing dots of size of 10-13 µm (Fig. 3 top) and a line which has a width of 4 µm (Fig. 3 bottom). In future, we plan to increase to the resolution and speed of the molecular and nanoparticle patterning.

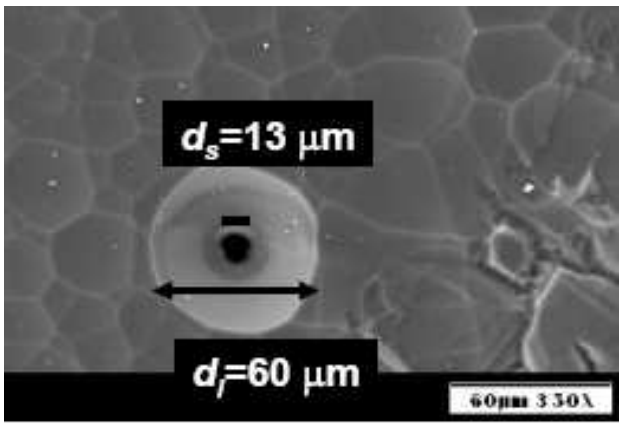

Fig. 1. Scanning electron microscopy image of conical pen produced in glass chip by etching of single ion track.

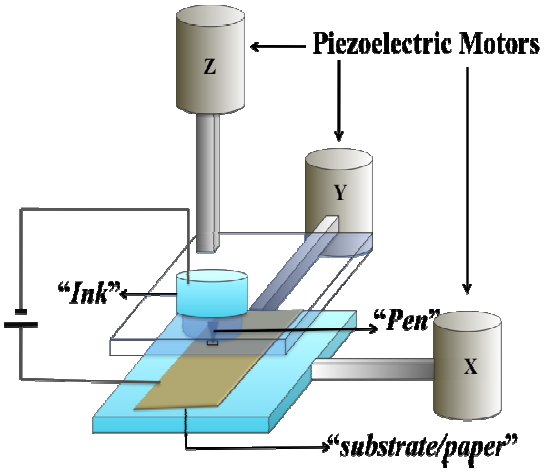

Figure 2. Schematic of nanopen patterning system.

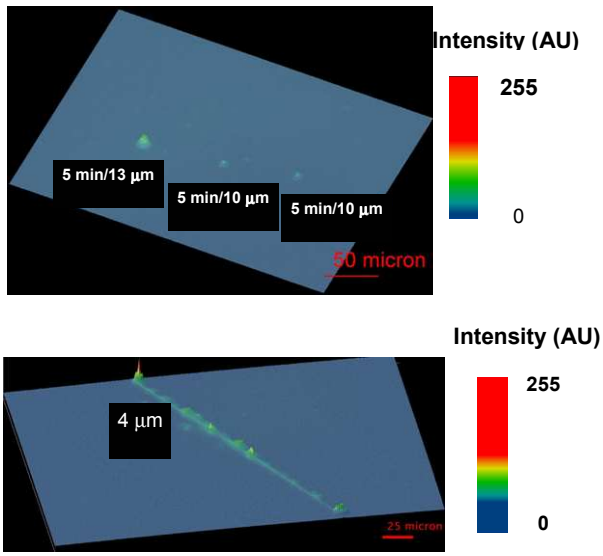

Fig. 3. Oligonucleotide dot (top) and line (bottom) pattern produced by pen writing.

References

[1] Mirkin, C. *et al*. Science, 283 (1999) 661

[2] Loh, O.Y., Ho, A.M., Rim, J.E., Kohli, P., Patankar, N.A., Espinosa, H.D. "*Electric-field Induced Direct Delivery of Proteins by a Nanofountain Probe*" *PNAS* 105 (2008) 16438

[3] Pradeep, Ramiah Rajasekaran; Wolff, J.; Zakeri, R.; Mitrovic, B.; Aouadi, S.; Trautmann, C.; Kohli, P. "Lithography using Nanotubes", *JACS* (in preparation)

* Work supported by National Science Foundation through a Career award and CMMI 0609349.

pkohli@chem.siu.edu

Gating of Single Synthetic Nanopores by DNA Molecular Switching *

W. Guo[1], C. Trautmann[2], R. Neumann[2], and Y. Wang[1, #]
[1]Peking University, Beijing, China; [2]GSI, Darmstadt, Germany.

Switchable ion channels that are made of membrane proteins play crucial role in cellular circuits. Thereby synthetic nanofluidic channels attract great interest owing to the novel ion transport properties that are helpful for understanding the biological ion channels and for the promising applications on ultrasensitive molecular detection and separation [1]. Here we report a synthetic nanopore-DNA system where single solid-state nanopores are reversibly gated by switching DNA motors immobilized inside the nanopores. High- (on-state) and low- (off-state) conductance states are found within the nanopore-DNA system corresponding to the single-stranded and i-motif conformation of the DNA motors.

The nanopores were fabricated by the ion-track technique. Chemical etching of the single-ion irradiated foils leads to the formation of conical single nanopore membranes. The large opening (base) was several hundred nanometers, and the narrow opening (tip) was 5-44 nm. The pH-responsive DNA molecules, which have been extensively studied in the field of nucleic acid nanodevices, were immobilized onto the inner wall of the nanopore by a two-step chemical reaction. The motor DNA molecules (C4-DNA) undergo pH-responsive conformational change between four-stranded i-motif structure (at pH 4.5) and random single-stranded structure (at pH 8.5) (Scheme 1) [2]. The gating performance of the nanopore-DNA system was evaluated by measuring the ionic current across the channel in solution with variant pH.

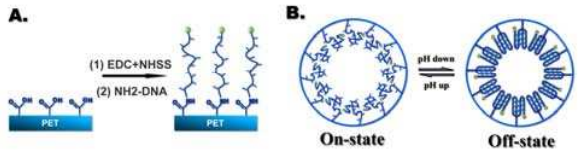

Scheme 1. (A) Immobilization of DNA molecules by a two-step chemical reaction. (B) The conformations of the DNA motor are responsive to pH, leading to the on and off states.

In low-pH solution, the motor DNA folds into a densely packed rigid quadruplex i-motif structure that partially decreases the effective diameter of the nanopore. In high-pH solution, the motor DNA relaxes to a loosely packed single-stranded and more negatively charged structure that enhances the total ion conductivity inside the nanopore [3]. Control experiments were also conducted with poly-A-DNA whose conformation is not sensitive to pH. The current ratio obtained in such nanopores is slightly higher than the bare nanopores and much lower than the C4-DNA-modified nanopores. Therefore, we consider the low and high conductive states as the off and on states of the nanopore-DNA hybrid system. The difference in ionic conductance provided by the DNA molecular conformational change is much higher than that contributed by the carboxyl groups on the bare nanopore surface as well as the non-responsive DNA molecules (Figure 1).

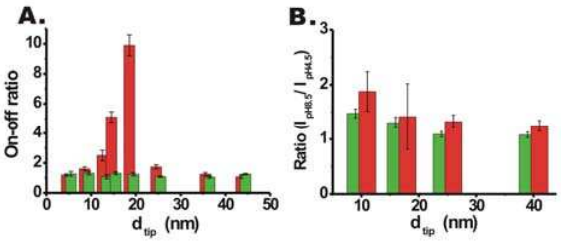

Figure 1. (A) Current ratio of on state versus off state (on-off ratio) calculated in the C4-DNA modified nanopores for the potential of -200 mV (red columns) and (B) Current ratio obtained in the poly-A-DNA modified nanopore systems (red columns). Control results obtained in bare nanopore are also shown (green columns).

The highest gating efficiency is found when the length of the attached DNA molecules matched the tip diameter of the nanopore (Figure 1). This novel nanopore-DNA system set up an artificial counterpart of switchable protein-made biological channels. A remarkable paradigm is the acid-sensing ion channels (ASICs) found in nature, which are cation-selective ligand-gated ion channels that activated by protons and are implicated in many physiological processes such as pain perception, learning, and memory [4]. Since DNA molecular switching have been successfully applied to gating the synthetic nanopore, in the near future, molecules with complicated functions, such as polypeptides and protein enzymes, may be utilized to build novel, biologically inspired nanopore machines.

References

[1] Z. Siwy, *Adv. Func. Mater.* 16 (2006) 735.
[2] F. Xia, W. Guo, Y. Mao, X. Hou, J. Xue, H. Xia, L. Wang, Y. Song, H. Ji, Q. Ouyang, Y. Wang, and L. Jiang, *J. Am. Chem. Soc.* 130 (2008) 8345.
[3] Z. Siwy, E. Heins, C. Harrell, P. Kohli, C. Martin, *J. Am. Chem. Soc.* 126 (2004) 10850.
[4] J. Jasti, H. Furukawa, B. Gonzales, E. Gouaux, *Nature* 449 (2007) 316.

* Work supported by National Nature Science Foundation of China No. 10634010, 10675009, 50703020, 20125102, 90306011, 20421101.
# ygwang@pku.edu.cn

High-sensitivity ion track-etching of poly(vinylidene fluoride) membranes

T. Yamaki[1,#], M. Asano[1], H. Koshikawa[1], Y. Maekawa[1], R. Neumann[2], C. Trautmann[2], K.-O. Voss[2]
[1]Japan Atomic Energy Agency (JAEA), Takasaki, Gunma 370-1292, Japan; [2]GSI, Darmstadt, Germany.

Quite recently, ion-track membranes of poly(vinylidene fluoride) (PVDF) have attracted a renewed interest for their applications to next-generation electrochemical devices such as fuel cells [1,2]. In order to produce track-etched pores in PVDF films, several kinds of etching solutions were previously employed. In most cases [3], a highly concentrated aqueous KOH solution with a $KMnO_4$ additive was maintained at a high temperature (85ºC). These severe etching conditions provided irreversible chemical damage all over the film including the non-irradiated part, thereby destroying some distinctive properties of PVDF. Therefore, in this study, we attempted to prepare PVDF ion-track membranes of up to a few hundred nm thickness without any oxidant additives in the alkaline etching solution. Instead of the $KMnO_4$ induced activation, ion irradiation with high linear energy transfer (LET) was considered to enhance the etching sensitivity even under milder conditions [4,5].

A 25-μm thick PVDF film was irradiated at room temperature by swift heavy ions from the TIARA cyclotron of JAEA and the UNILAC linear accelerator of GSI. The fluence ranged from 3×10^6 to 3×10^{11} ions/cm^2. Further irradiation conditions are listed in Table 1. Track etching was then performed in a 9 mol/dm^3 KOH aqueous solution at 80˚C. After depositing a gold coating, the surface of the 24-hour etched membranes was imaged by scanning electron microscopy (SEM). In order to measure the track etch rate, V_T, the etching was performed in an electrolytic conductivity cell. A bulk etch rate, V_B, was estimated to 0.46 nm/h by taking the decrease in film thickness during long-time etching. Using the ratio V_T / V_B, we obtained the track etching sensitivity, Q, according to

$$Q = (V_T / V_B) - 1. \quad (1)$$

First of all, as an advantage of the no-oxidant alkaline etching, it must be noted that V_B was extremely small, suggesting very mild etching conditions for PVDF, in marked contrast to a few hundred nm/h for etching in the $KMnO_4$ containing solution [3]. In a strong alkaline medium at high temperatures, virgin PVDF undergoes deprotonization and the consecutive elimination of fluorine to afford –CH=CF- or –CH=CF$_2$. In the absence of the additives, however, these modifications should be restricted to the outermost film layer because there is basically no wetting at the polymer/solution interface.

All results, including the LET evaluated by a TRIM code, as well as the Q value and pore diameter, are shown in Table 1. This table roughly indicates that the higher-mass ion irradiation led to enhanced etching in both the track-core and -halo; V_T and pore diameters measured by SEM increased by about a factor of 3 between ^{58}Ni and ^{208}Pb ions. Such a large V_T enabled us to obtain very high etching sensitivity for the preparation of cylindrical through-pores. A similar effect on the etching behavior was quite recently observed when performing ion-track etching of poly(*p*-phenylene terephthalamide) [6].

The change of V_T for the different beams is ascribed to a LET effect, because the bombardment with high-LET ions produces more severe molecular damage in each latent track. Interesting is that from ^{129}Xe to ^{208}Pb, we found a sharp increase in pore diameter, while the difference in LET between these ions is similar to that between the other nearest-mass ions. Thus, the LET does not seem to be the only significant factor in this case. The so-called "velocity effect" might be manifested for the present etched tracks. High-LET irradiation will be most suitable for preparing, in an effective way, PVDF-based ion-track membranes with a pore diameter of nm to sub-μm.

Table 1. Irradiation conditions and results

Ion	Energy (MeV/n)	LET (MeV/μm)	V_T (μm/h)	Q	Pore diameter (nm)
^{208}Pb	11.1	19.0	2.3	5000	305±31
^{129}Xe	3.5	13.0	1.6	3500	118±11
^{84}Kr	6.2	8.0	1.4	3000	109±14
^{58}Ni	6.7	5.4	0.82	1800	93±8

References

[1] T. Yamaki, Y. Kozone, A. Hiroki, M. Asano, H. Kubota, M. Yoshida, E*CS Transactions* 3 (2006) 103
[2] T. Yamaki, Y. Kozone, A. Hiroki, K. Hosoi, M. Asano, H. Kubota, M. Yoshida, *Electrochemistry* 75 (2007) 175
[3] C. Daubresse, T. Sergent-Engelen, E. Ferain, Y.-J. Schneider, R. Legras, *Nucl. Instr. Meth. B* 105 (1995) 126
[4] T. Yamaki, R. Rohani, H. Koshikawa, S. Takahashi, S. Hasegawa, M. Asano, K.-O. Voss, R. Neumann, Y. Maekawa, *Kobunshi Ronbunshu*, 65 (2008) 273
[5] R. Rohani, T. Yamaki, H. Koshikawa, S. Takahashi, S. Hasegawa, M. Asano, Y. Maekawa, K.-O. Voss, C. Trautmann, R. Neumann, *Nucl. Instr. Meth. B*, in press
[6] Y. Suzuki, T. Yamaki, H. Koshikawa, M. Asano, K.-O. Voss, R. Neumann, M. Yoshida, *Nucl. Instr. Meth. B* 260 (2007) 693

yamaki.tetsuya@jaea.go.jp

Incorporating Amphoteric Groups in Ion Track-etched Single Conical Nanochannels

M. Ali[1#], P. Ramirez[2], V. Bayer[3], R. Neumann[3] and W. Ensinger[1]
[1]Technische Universität Darmstadt, Germany; [2]Universidad Politécnica de Valencia, Spain; [3]GSI, Darmstadt, Germany.

Nanochannels fabricated in polymer membranes have a great range of applications in biotechnology, where they are suitable for sensing biomolecules[1], and act as stimuli-responsive devices[2] and molecular filters of high selectivity.[3]

The surface of ion track-etched nanochannels in polymer membranes bear carboxyl (-COOH) groups which were chemically reacted with a variety of different molecules having variable size and polarity. Previously, gold coated nanochannels were used for the incorporation of amphoteric groups into the nanochannels via the chemisorption of cysteine molecules.[4]

Here, we report a facile and straight-forward approach to incorporate amphoteric groups inside the single conical nanochannels. This was realized by direct chemical modification of the surface carboxyl groups with L-lysine chains whose positive and negative charges are very sensitive to the external *pH*. The chemically functionalised channels were characterized both theoretically and experimentally. The single nanochannel constitutes a *universal* nanofluidic diode in the sense that the amphoteric chains attached at its surface allow for a broad set of rectification properties. Briefly, the selective functionalization of lysine with surface carboxyl groups was accomplished by blocking the amino group and carboxyl group bonded to the α-carbon with Cu^{2+} ion to form a copper-chelate complex. This process leaves an unprotected ε-amino group which was covalently attached with the carboxyl group created during track-etching via EDC/PFP coupling chemistry.[5]

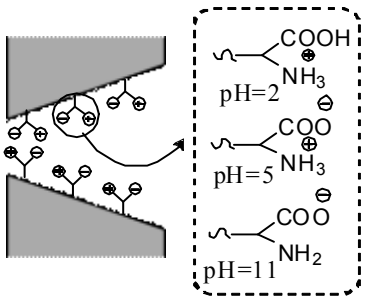

Figure 1: Schematic illustration of amphoteric groups inside the single conical nanochannel.

The polymer foil, containing a single channel modified with lysine, was mounted in the conductivity cell and current-voltage (*I-V*) curves were measured at different pH values. At low *pH* = 2, the ionized amino groups (–NH_3^+) are positively charged due to protonation, while the protonated carboxyl groups (–COOH) are neutral. The nanochannel is then selective to anions and shows the rectification properties characteristic of conical channels with positive fixed charges. Conversely, at high *pH* = 11, the deprotonated amino groups (–NH_2) are in neutral form, while the carboxylate groups (–COO^-) are ionized. The net channel fixed charge is then negative, and the nanochannel is now selective to cations. The transition between these two rectification regimes occurs at *pH* = 5, which is close to the isoelectric point *pI* = 5.6 of the lysine chain attached to the channel surface. At this *pH* value, the α-carboxylic and the α-amino groups are charged, but the nanochannel net charge is zero, and the *I-V* curve shows a linear, ohmic behavior.

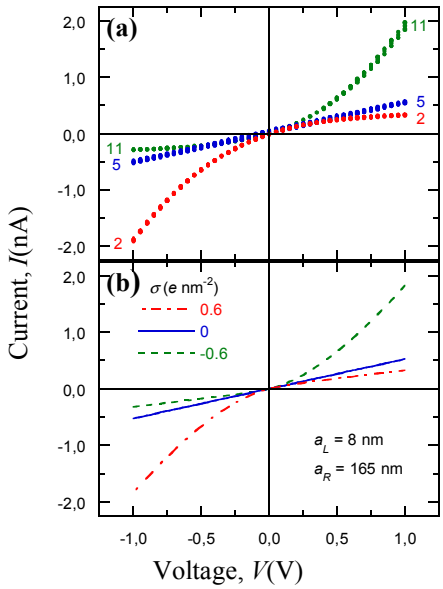

Figure 2: Current-voltage curves of a single conical channel modified with L-lysine. **a)** Experimental, and **b)** theoretical.

The above experimental results can now be described theoretically in terms of a continuous model based on the Poisson and Nernst-Planck (PNP) equations.[6]

In conclusion, the amphoteric chains functionalized on the conical nanochannel surface form the basis of a nanofluidic diode allowing universal, *pH*-tunable rectification properties. The results demonstrate that virtually any characteristics required in practical applications can be accomplished with the same device by simply changing the *pH* of the external solutions.

References

[1] M. Ali *et al., J.Am.Chem.Soc.* (2008), **130**, 16351
[2] B. Yameen *et al., J.Am.Chem.Soc.* (2009), In press
[3] E. N. Savariar *et al*., *Nat.Natechnol.* (2008), **3**, 112
[4] S. B. Lee *et al.*, *Anal.Chem*., (2001), **73**, 768
[5] M. Ali *et al.*, *Nanotechnology* (2008) **19**, 485711
[6] J. Cervera *et al., Europhys. Lett.* (2005), **71**, 35

M.Ali@gsi.de

Resistive-Pulse Detection of Short Double-Stranded DNAs Using a Chemically Functionalized Conical Nanopore Sensor

K. Kececi, L.T. Sexton, F. Buyukserin, and C.R. Martin
Department of Chemistry and Center for Research at the Bio/Nano Interface, University of Florida, Gainesville, U.S.A.

Current work in the Martin group has focused on utilizing single conical nanopores prepared by the track-etch method [1] to detect short DNA molecules via the resistive pulse sensing technique. In resistive pulse sensing i-t traces are recorded through a single pore. When an analyte passes through the pore translocation events are observed in the i-t trace. In this work, we recorded translocation events for 50 and 100 base-pair (bp) DNAs. We then analyzed the difference between the translocation events for the two lengths of DNA.

Membranes containing single nanopores were prepared by irradiating 12-μm thick polyethylene terephthalate (PET) foils with individual heavy ions (e.g. Au, Pb, U of 11.4 MeV/u) from the UNILAC. Through a chemical track etching process, using 9M NaOH and 1M formic acid, the single track was developed into a conical pore [1]. The base diameter of the resulting conical pore was ~520 nm, and the small diameter opening after etching was ~35 nm. The pore-etching procedure generates carboxylate groups on the pore walls and membrane faces [2]. EDC chemistry was used to attach ethanolamine to these $-COO^-$ groups via amide bond formation [3]. Attachment of the ethanolamine is necessary to mitigate electrostatic repulsion of the negatively charged DNAs. After this step, the base and tip diameters remained approximately the same diameter because the ethanolamine deposited monolayer is very thin.

To obtain current-pulse data, the membrane sample was mounted between the two halves of the conductivity cell, and each half-cell was filled with 3.5 mL of 1M KCl in 10 mM Tris, 0.1 mM EDTA. A Ag/AgCl electrode was placed on each side of the cell and connected to an Axopatch 200B (Molecular Devices Corporation, Union City, CA) patch clamp amplifier which was used to apply the desired potential (1000 mV) and measure the resulting ionic current flowing through the nanopore.

We attempted to detect the 50- and 100-bp DNAs with an unmodified PET nanopore, and no current-pulses were observed. We hypothesized that this was due to electrostatic repulsion between the anionic DNA molecules and the carboxylate groups on the pore walls. In order to overcome this problem, ethanolamine was attached to the carboxylate groups to remove the anionic surface charge. Ethanolamine attachment was confirmed by using XPS

In the absence of DNA, a steady-state ion current (no current-pulse events) of 11.6 nA was observed for the ethanolamine-modified nanopore with tip diameter of 35 nm. When either the 50- or 100-bp DNA was added to the tip side, current-pulse events were observed. These current-pulse events can be characterized by the event amplitude (Δi) and the event duration (τ).

Histograms of the Δi data for the 50- and 100-bp DNAs are shown in Figure 1. Average Δi values of 50 ± 12 pA and 115 ± 32 pA were observed for the 50- and 100-bp DNAs, respectively. These data show that our ethanolamine-modified nanopore sensor can discriminate between the 50- and 100-bp DNAs on the basis of the current-pulse amplitude. Analogous histograms of the current-pulse amplitude data yielded average τ values of 1.3 ± 1 ms and 1.7 ± 1 ms for the 50- and 100-bp DNAs, respectively. These data show that current-pulse duration cannot be used to discriminate between these two short ds-DNAs.

We have shown that a chemically modified nanopore can be used as a resistive-pulse sensor for the detection of short ds-DNAs. This sensor can distinguish between a 50-bp DNA and a 100-bp DNA on the basis of the magnitude of the current pulses produced by these DNAs. There are no prior examples of distinguishing between such closely sized DNAs using a synthetic nanopore sensor. In contrast, a biological nanopore sensor based on the protein α-hemolysin has been used to distinguish between such short DNAs [4]. However, the α-hemolysin-based sensor can only detect ss-DNA, not ds-DNA as reported here.

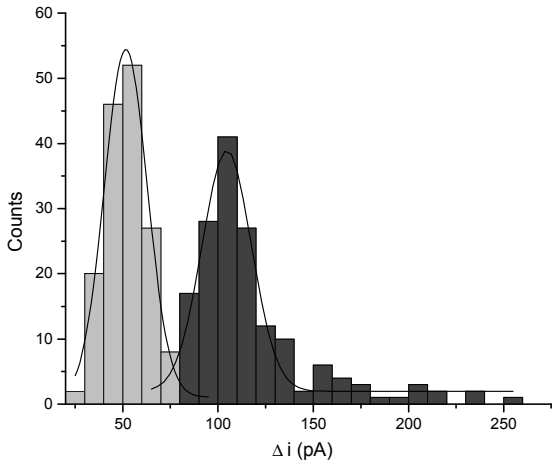

Figure 1: Histograms of DNA current-pulse-amplitude data for 50 (light gray) and 100 (dark gray) bp DNAs.

References

[1] P.Y. Apel, Y.E. Korchev, Z. Siwy, R. Spohr, M. Yoshida, Nucl. Instr. Meth. B 184 (2001) 337
[2] A. Wolf, N. Reber, Y.P. Apel, B.E. Fischer, R. Spohr, Nucl. Instr. Meth. B 105 (1995) 291
[3] Z. Grabarek, J. Gergely, Anal. Biochem. 185 (1990) 131
[4] S. Howorka, S. Cheley, H. Bayley, Nature Biotechnology 19 (2001) 636

Surfactant-Assisted Etching of Nanochannels

V. Bayer[1], M. Ali[2], Q. H. Nguyen[2], R. Neumann[1], and W. Ensinger[2]
[1]GSI, Darmstadt, Germany; [2]TU Darmstadt, Germany

Motivation

The fabrication and functionalization of synthetic nanochannels has in the last years become of increasing interest for basic research as well as for applications. Nanochannels have an especially high surface-to-volume ratio which makes them ideal for handling very small amounts of liquid in nanofluidic devices or for designing highly sensitive sensing elements. In contrast to their biological counterparts like e.g. α-hemolysin, synthetic channels are more robust towards external conditions. At GSI Materials Research, nanochannels are fabricated by wet chemical etching of latent tracks in thin polymer membranes induced by heavy-ion irradiation. This technique permits the production of various channel geometries and facile control over the resulting channel diameter.

Surfactant-assisted etching

Nanochannels with conical longitudinal profiles in polyethyleneterephthalate (PET) are usually etched in an electrochemical cell, where an etching solution is applied on one side and a neutralizing solution on the other side of the membrane. The diameter of the small aperture of these channels can be as narrow as 2 nm. However, this etching technique is inhomogeneous and slow (etching times range between 1 and 2 h) due to insufficient wetting of the membrane and the need to employ a neutralizing medium. A way to solve these problems is provided by adding small amounts of a surfactant (in this case Dowfax 2A1 from Dow Chemicals) to the NaOH etching solution, into which the ion-track membranes are immersed. For achieving asymmetrical channel profiles, the membranes are sensitized on one side for 30 h with UV light. The resulting channels have bullet-shaped profiles (Fig. 1a) and rather large diameters which are usually not smaller than $\approx$ 20 nm. Surprisingly, these large channels exhibit very pronounced current rectification, which is probably due to a highly tapered geometry at the channel tip. In order to obtain narrower channel openings and thereby sustain the good rectification properties, the surfactant-assisted etching technique described in [1] was modified. Instead of immersing the samples in a bath of etching solution, an electrochemical cell was employed, where the etching process can be monitored online. The etching was performed at 60°C. In order to increase the asymmetry of the channels, pure etchant was added in the compartment adjoining the UV sensitized side of the PET membrane. Application of 6 M NaOH in one compartment and a mixture of 6 M NaOH and 0.03% (v/v) surfactant on the other side leads to the most pronounced rectification. Subsequent to etching, the membranes were washed with 3 M HCl and left overnight in deionized water.

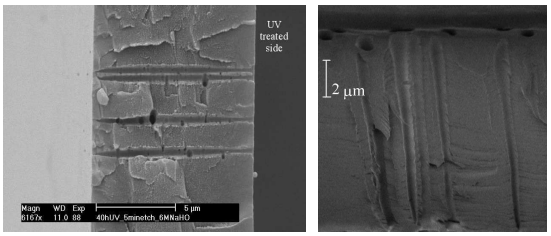

(a) (b)

Figure 1: Channels in PET membrane etched with surfactant in (a) bath, (b) electrochemical cell.

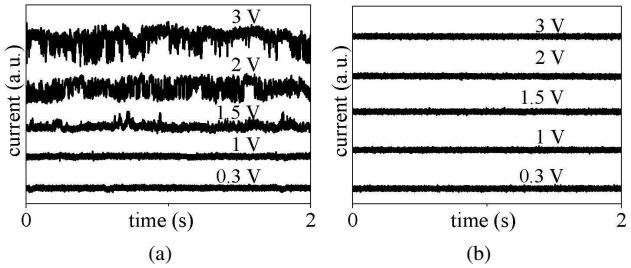

Figure 2: Current through nanochannels etched with (a) neutralizing solution, (b) surfactant.

Results

The diameter d_s of the small aperture of single channels of length L was calculated by means of

$$d_s = (4L/d_L\lambda\pi R)^{1/2}$$

resulting in approximately 2 nm at minimum. For this purpose, the resistance R of the channel was measured with 1 M KCl solution of conductivity λ. The large diameter d_L was determined with scanning electron microscopy. Longitudinal cross-sections of these channels exhibit a more conical geometry than channels etched in a bath containing surfactant (Fig. 1).

In contrast to equally narrow channels etched with the aid of a neutralizing solution (Fig. 2a), with these samples no current fluctuations were observed (Fig. 2b), which makes them ideal for application in resistive pulse sensing. Additionally, rapid sample preparation is possible due to etching times ranging between 0.5 and 5 min.

References

[1] P. Yu. Apel, I. V. Blonskaya, S. N. Dmitriev, O. L. Orelovitch, A. Presz, and B. A. Sartowska, "Fabrication of nanopores in polymer foils with surfactant-controlled longitudinal profiles", Nanotechnology **18**, 305302 (2007)

Separation of Organic Molecules through Track-Etched Nanopores in PET Membranes

Q. H. Nguyen[1*], M. Ali[1], W. Ensinger[1] and R. Neumann[2]
[1]Technische Universität Darmstadt, Germany; [2]GSI, Darmstadt, Germany

Chemical separations play an important role in most chemical, pharmaceutical, and petrochemical processes. Membrane-based separations are potentially important because they can be less energy intensive and more economical than conventional separation methods [1]. By controlling the pore diameter of track-etched nanoporous polymer membranes, they can be used as nanofilters for the separation of molecules based on their size. Nanopore surfaces have been gold-plated electroless and subsequently modified via chemisorption of a variety of different thio-molecules to control the surface properties, e.g., charge or hydrophobicity [2,3].

In this contribution, we report the direct chemical modification of the surface carboxylic groups (–COOH) with desired molecules. Our work focuses on the fabrication and modification of track-etched nanopores (10^8 pores/cm^2) in 12-µm thick polyethylene terephthalate (PET) membranes. During the etching process, carboxylic groups are formed on the surface and walls of nanopores. These groups were converted into terminated amino groups by reaction with ethylenediamine via N-(3-dimethyl-aminopropyl)-N-ethylcarbodiimide hydrochloride (EDC) / pentafluorophenol (PFP) coupling chemistry [4].

The unmodified (carboxylated) and modified (aminated) membranes were used for the separation of two charged organic molecules: methyl viologen (MV^{2+}) and 1,5-disulfonate naphthalene (NDS^{2-}) which possesses divalent positive and negative charges, respectively. The membrane was mounted between the two halves of the conductivity cells. The feed half-cell contains 10 mM of an analyte in electrolyte solution, the permeate half-cell contains only pure electrolyte solution. The electrolyte solutions were prepared in phosphate buffer saline pH = 7, and both solutions were continuously stirred during the whole process. After the preset time, the concentration of analyte in the permeate half-cell was determined by measuring the UV absorbance (Figure 1).

If the pore is small enough, molecules with a charge matching that of the pore surface will be electrostatically repelled and thus prevented from entering the nanopore. Conversely, molecules with a charge of opposite sign will be electrostatically attracted into the nanopore and transported across the membrane more efficiently [5]. The results from Fig. 1 show that, before modification at pH = 7, the carboxylic groups are deprotonated ($–COO^-$), and therefore the positively charged molecule (MV^{2+}) passes through the membrane more favorably than the negatively charged molecule (NDS^{2-}) (Fig. 1a).

After modification, the amino groups are protonated ($–NH_3^+$) at pH 7 and as a consequence, the membrane

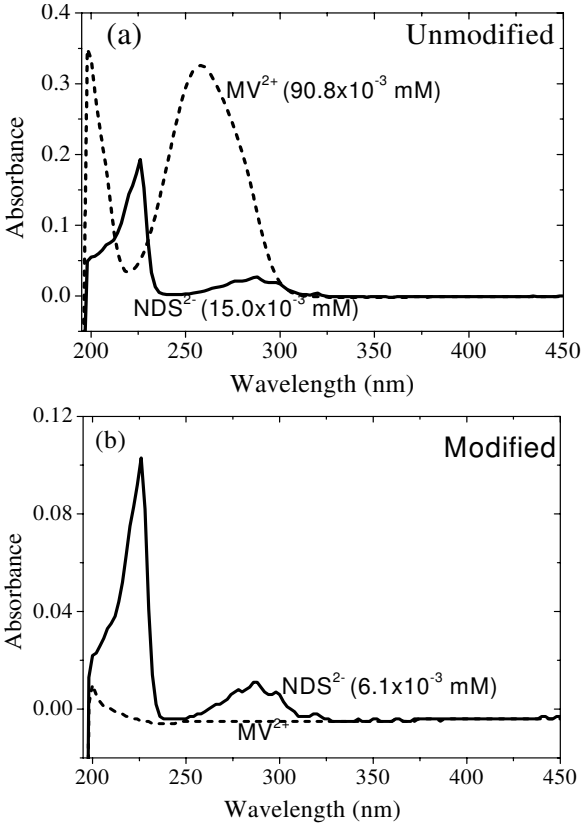

Figure 1: UV absorbance of permeate solution after 5 h of diffusion before (a) and after (b) modification with ethylenediamine.

transports negatively charged molecules (NDS^{2-}) and reject positively charged molecules (MV^{2+}) (Fig. 1b). It can be concluded that the ion-transport properties of the membrane can be switched by changing the surface charge of nanopores. These results also demonstrate that the mobility of organic molecules through the nanoporous membranes is based on their surface charges rather than on their size.

Acknowledgment

Q.H. Nguyen gratefully acknowledges financial support from the Daimler-Benz Foundation.

References

[1] K. Jirage and C. R. Martin, Trends in Biotechnology (1999), 17, 197
[2] C. R. Martin et al., Adv. Mater. (2001), 13, 1351
[3] S. B. Lee and C. R. Martin, J. Am. Chem. Soc. (2002), 124, 11850
[4] M. Ali et al., Nanotechnology (2008), 19, 485711
[5] L. A. Baker and S. P. Bird, Nature Nanotechnology, (2008), 3, 73

*q.h.nguyen@gsi.de

Apex angle controlled fabrication of Cu nanocones

J.L. Duan[1], J. Liu[1], T.W. Cornelius[2], O. Picht[2], M. Rauber[2], C. Trautmann[2], R. Neumann[2]

[1] Institute of Modern Physics, CAS, China; [2] GSI, Darmstadt, Germany.

As a special case of 1D nanostructures, conical nano-objects have attracted increasing interest stimulated by their potential applications. For example, conical nanopores can serve as DNA detectors, and conical diamond tips are ideal field emitters. Here, we report that vertically aligned Cu nanocones with controlled apex angle were successfully fabricated in ion track-etched templates.

The nanocones were produced by filling the conical nanopores of ion track-etched polycarbonate (PC) templates with Cu. For this purpose, PC foils (Makrofol N, Bayer Leverkusen) of thickness 30 µm were irradiated at the UNILAC linear accelerator with fluence 10^6 ions/cm^2. To obtain conical nanopores, the asymmetric-etching method was employed [1], using etchants of various volume ratios of 9 M NaOH and methanol. Subsequently, Cu nanocones were electrochemically deposited at 50°C by applying a constant voltage of -200 mV. The electrolyte consisted of 75 g/l $CuSO_4 \cdot 5H_2O$ and 30 g/l H_2SO_4. A thin sputtered Au layer reinforced by an electroplated Cu layer was used as cathode. After dissolving the host PC template with dichloromethane, the cone morphology was analyzed by scanning electron microscopy (SEM).

Figure 1 shows a representative SEM micrograph of the base opening of conical nanopores that were etched by 9 M NaOH and methanol with volume ratio 1:9 for 1 h. All pores display a conical shape with a base diameter of 4.5 µm.

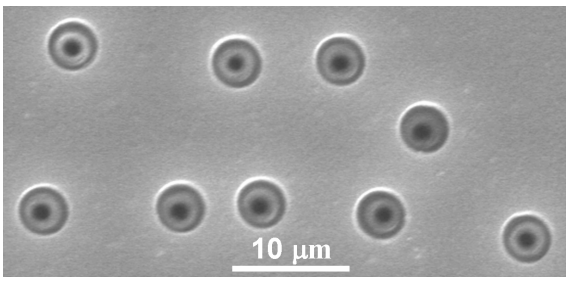

Figure 1: SEM micrograph of track-etched PC foil with conical channels.

The Cu nanocone arrays with controlled apex angle are shown in Fig. 2. With decreasing volume ratio of 9 M NaOH and methanol from 10:0 to 0.5:9.5, the apex angle increases from 0.3° to 6.5°. All cones possess a homogeneous and smooth contour. It is well-established that two etching rates coexist in the etching process, namely, bulk etching rate (v_b) and track etching rate (v_t). By varying the ratio of these two rates, several shapes such as cylindrical, "bow-tie", and cigar-like pores have been obtained in the past [1]. If v_t is far larger than v_b, cylindrical pores can be achieved [2]. By adopting asymmetric etching conditions, conical pores are produced when v_b is comparable to v_t. In the present work, methanol, a solvent suitable for dissolving PC, was employed to enhance v_b.

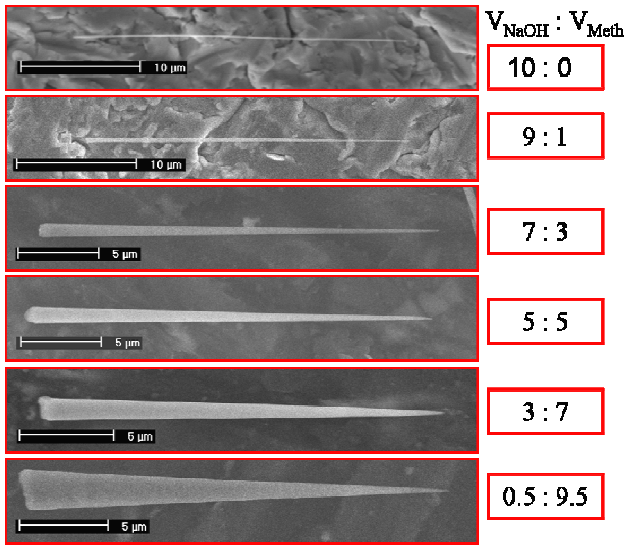

Figure 2: SEM images of Cu nanocones with different apex angle controlled by the etching solution used for the template.

In addition, we have observed that the mechanical stability of Cu nanocones depends on their apex angles when they have similar tip diameters and heights. Three representative SEM pictures of nanocone arrays are displayed in Fig. 3. In the case of apex angle 0.3° (Fig. 3a), the cones collapsed into aggregates, whereas for an apex angle of 6.5° (Fig. 3c), all cones are vertically aligned, indicating a better mechanical stability.

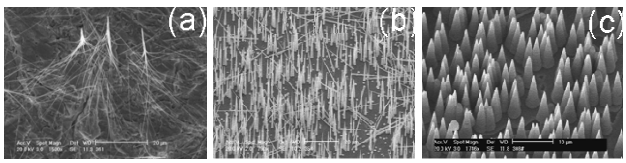

Fig. 3: SEM micrographs of vertically aligned Cu nanocones with apex angles (a) 0.3°; (b) 2°; and (c) 6.5°.

In summary, we have fabricated Cu nanocone arrays based on the technique of asymmetric etching of PC templates. Using these arrays as field emitters is currently being investigated.

References

[1] P. Apel, Radiat. Meas. 34 (2001) 559-566.
[2] J.L. Duan et al., Mat. Sci. Eng. B 147 (2008) 57-62.

Efficient field emission from structured gold nanowire cathodes

A. Navitski[1], V. Sakharuk[1], G. Müller[1,*], T.W. Cornelius[2], and C. Trautmann[2], S. Karim[3]
[1]Physics Department, University of Wuppertal; [2]GSI, Darmstadt, Germany; [3]PINSTECH, Islamabad, Pakistan

Based on last years field emission (FE) results achieved with randomly distributed free-standing gold nanowires (NW) [1], cathodes with regular arrays of Au-NW patches (50 µm diameter) were fabricated by means of a shadow mask during heavy ion irradiation of polycarbonate foils [2-3]. The number density, diameter *Ø*, and length *L* of the NW were controlled by the ion fluence *f*, foil etching time, and electrochemical deposition time, respectively. Various patch structures were obtained as summarized in Tab.1. The dimensions and aspect ratio *AR* of the Au-NW were determined from SEM images. Pyramidal clustering of the NW was observed for $f > 10^7$ cm^{-2} and $AR > 200$.

Table 1: Fabrication parameters of structured cathodes.

f [cm^{-2}]	10^6		10^7		10^8		
Pitch P [µm]	150	100 150	100 150	100 150	100		
Ø [nm]	300	311	270		270		
L [µm]	10	25	8	28	7	10	28
AR	67	161	60	207	52	74	207

The emitter distribution of all samples was measured with the field emission scanning microscope (FESM). The efficiency and alignment of the FE sites strongly depend on the type of nanostructures in the patches. Patches with solitary NW were less efficient than those with NW clusters. The best aligned and most homogeneous FE sites were achieved for wide-spaced patches with NW clusters as shown in Fig. 2, where about 90 % of the patches emit at 30 V/µm. Patches with 100 µm pitch and multiple clusters also showed high efficiency but less alignment [3].

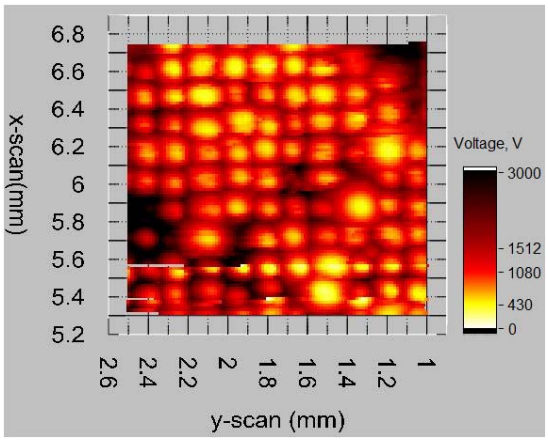

Figure 1: FE map (regulated voltage for 1 nA) of a Au-NW patch array ($f = 10^7$ cm^{-2}, P= 150 µm, L = 28 µm) measured with a W-tip of Ø 30 µm at a gap of 40 µm.

* contact: gmueller@uni-wuppertal.de

The current-voltage curves and maximum FE current I_{max} were locally measured for 10-30 NW patches of each structure. The effective field enhancement factor β_{eff}, which depends not only on the *AR* but also on the distance between the anode tip and the actual emitter [3], were derived from the corresponding Fowler-Nordheim plots assuming a work function of 5 eV for Au. As shown in Fig. 2a, the highest β_{eff} of 630 was achieved for a patch with high *AR* and multiple NW clusters. In contrast, the highest I_{max} of 100 µA was obtained for a patch with dense short NW (Fig. 2b). The lowest spread of both values, however, is shown by patches with short solitary Au-NW. In conclusion, these results provide valuable hints for the optimization of patch-structured NW cathodes for triode applications.

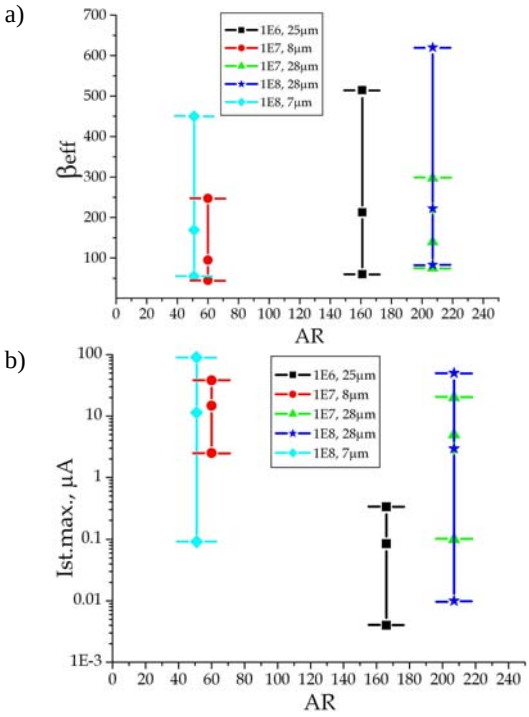

Figure 2: Mean value (dots) and range (bars) of the field enhancement (a) and maximum stable FE current (b) measured for all types of Au-NW patches.

References

[1] A. Dangwal, C.S. Pandey, G. Müller, S. Karim, T.W. Cornelius, C. Trautmann, Appl. Phys. Lett. 92 (2008) 063115, and A. Dangwal, PhD thesis 2007-08.
[2] A. Navitski, G. Müller, T. Cornelius, C. Trautmann, Techn. Digest IVNC08, Wroclaw, 2008, ISBN: 83-914886-2-4, p. 75.
[3] A. Navitski, G. Müller, V. Sakharuk, T. Cornelius, C. Trautmann, S. Karim, subm. to J. Vac. Sci. Techn. B.

Controlled Synthesis of Nanowire Networks by Ion Track Template Electrodeposition

M. Rauber[1], T.W. Cornelius[2,3], W. Ensinger[1], D. Huzel[2], S. Müller[2], R. Neumann[2] and O. Picht[2]
[1]Technische Universität Darmstadt, Darmstadt, Germany; [2] GSI, Darmstadt, Germany; [3]ESRF, Grenoble, France

One-dimensional nanostructures have been studied intensively because of their interesting properties, which hold great promises for various applications [1]. However, to realize devices based on nanostructures, efficient methods that can translate a multitude of nanoscale components into micro/macroscale dimensions are needed. Controlled assembly is of particular importance for nanostructures used for catalysis, not only because loss of active surface area should be minimized, but also because the efficiency of a catalyst is related to the distribution of the material [2]. One of the most suitable techniques to achieve this aim is the direct synthesis of nanowire networks. These complex structures can be produced by templateless or templating techniques, the use of a template often allowing the better structural control [3]. However, none of the hard templates reported so far can precisely adjust the integration level and degree of connectivity.

We recently developed a new approach to synthesize nanowire networks (NWNs) by a modified template electrodeposition method using track-etched polycarbonate membranes (Fig. 1). The membranes are irradiated at different angles in several steps with energetic heavy ions and subsequently etched in an aqueous NaOH solution. Filling the resulting 2-D or 3-D nanochannel network with a metal by electrodeposition leads to the formation of well-defined interconnected nanowires. The arising structure consists of numerous nanowires that are interconnected to a macroscopic network with dimensions up to several square centimetres and a typical height of 30 µm. After removing the template in an organic solvent,

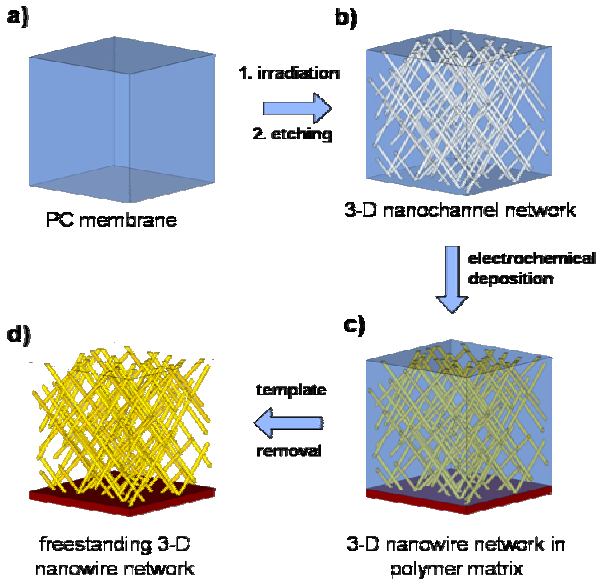

Fig. 1: Schematic of the template fabrication and the formation of a 3-D nanowire network by electrodeposition.

the samples were imaged by field-emission electron scanning microscopy (FESEM, Fig. 2a-b) and transmission electron microscopy (TEM, Fig. 2c). As shown in the micrographs, the wires are tightly attached to each other providing a high mechanical stability. Due to this strength, the orientation defined by the matrix is maintained to a very large degree after template removal, and no aggregation or loss of contact is observed. Thus, excellent accessibility and easy catalyst recovery are assured.

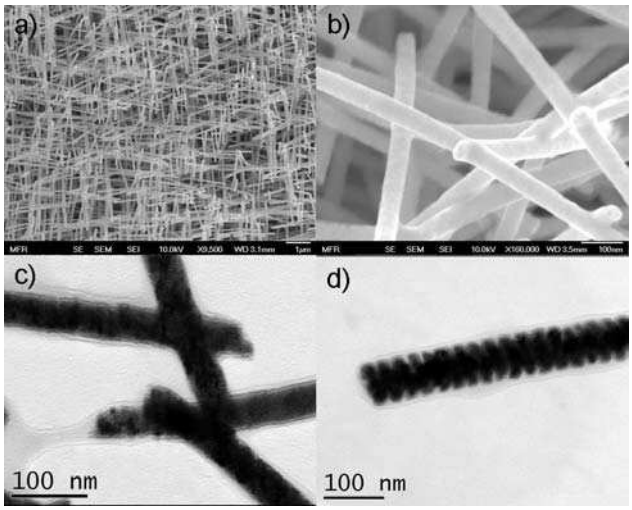

Fig. 2: a) and b) FESEM images of a nanowire network (nanowire diameter is 45 nm), c) TEM image of interconnected nanowires, d) TEM image of a segmented wire.

Because of the dimensions and the high stability the networks are suitable for direct system integration in microstructured systems. The method allows easy adjustment of nanowire diameter, integration level, and complexity of the network. Determination of the electrochemical active surface area (ECSA) of platinum nanowires (PtNWs) by hydrogen adsorption reveals that they exhibit a large catalytic surface area without the need for a support material. The ECSA can even be increased by using reverse pulsed deposition to produce segmented nanowires (Fig. 2d). Because all nanowires are electrically interconnected, PtNWNs could be also of great potential for electrocatalysis or other applications that require intensive interwire communication. Adjustable degree of networking and high surface area of these unique network structures makes them a potential candidate for catalysis, sensitive sensing, and filtering.

References

[1] A. K. Wanekaya et al., *Electroanalysis* **2006**, *18*, 533
[2] H.-M. Zhang et al., *Chem. Commun.* **2003**, 3022
[3] D. Wang et al., *Chem. Mater.* **2006**, *18*, 4

Micro- and nanorods of potassium acid phthalate grown in ion-track templates*

M. Enculescu[1,#], C. Trautmann[2], and R. Neumann[2]
[1]National Institute for Materials Physics, Magurele-Bucharest, Romania; [2]GSI, Darmstadt, Germany.

Micro- and nanorods of potassium acid phthalate (KAP) with diameters ranging from a hundred nanometers to tens of microns were obtained by solution crystallization in the channels of ion-track membranes. The template consists of a polymer foil irradiated with energetic heavy ions and subsequently track-etched to dissolve the tracks and create open cylindrical channels. The pores are then filled with the desired material by electrochemical or electroless methods (see, e.g. [1]. The solution crystallization method which we employ in the present study was already used for the growth of KCl or NaCl nanorods [2].

This project focuses on KAP as material which is very soluble in water and easily crystallizes under ambient conditions. Dye-doped KAP crystals show extremely interesting luminescence behaviour with exceedingly high and fast nonlinear optical response [3]. Their performance is linked to the good optical quality, which depends on the crystal structure and morphology. The size and density of nanorod assemblies in templates can easily be controlled, and they can directly be incorporated into devices.

As template we used 100 and 30 µm thick polycarbonate (PC) foils and irradiated them at the UNILAC with heavy ions of 11.1 MeV/nucleon energy and fluences between 10^5 and 10^9 ions/cm^2. The ion tracks were etched in an aqueous solution of 6M NAOH at 50°C. For these etching conditions the pore diameter increases with ~2µm/h. For crystal growth, the track-etched membranes were placed on top of the growth solution and left floating in ambient conditions for several days. The solution consisted of KAP dissolved in water up to 80% of the saturation solubility. Due to evaporation, the crystallization occurs in the solution as well as inside the pores and on the surface of the membrane.

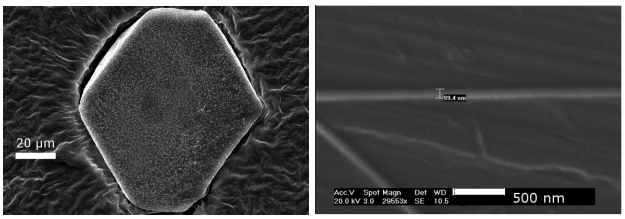

Figure 1. (left) KAP microcrystal on the membrane surface; (right). KAP nanorods (100 nm diameter, 30 µm length) grown inside track-etched pores after dissolving the PC template.

Figure 1 (left) shows a scanning electron microscopy (SEM) image of a large KAP microcrystal grown on the membrane surface. The facetted shape results from the orthorhombic symmetry of KAP. Crystals grown at the same time inside the pores are limited by the channel diameter and thus form extended nanorods (Fig. 1 right).

Figure 2 presents KAP microrod assemblies at low and high magnification. The crystallization process is highly efficient, indicated by the fact that each pore is filled.

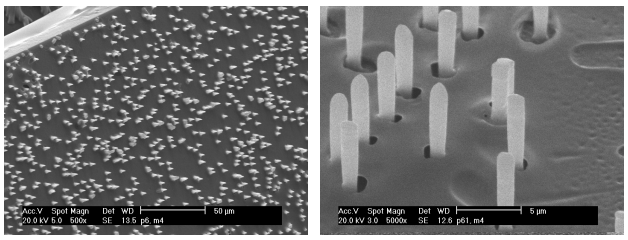

Figure 2. Arrays of KAP rods grown from solution, embedded in partially dissolved membranes.

In order to release the nano- or microrods, the polymer matrix is dissolved. During this process, some of the rods are mechanically deformed and coagulate by bending into clusters (Fig. 3 left). In some cases, we observed hollow structures probably due to morphological instabilities of the crystal growth (Fig. 3 right).

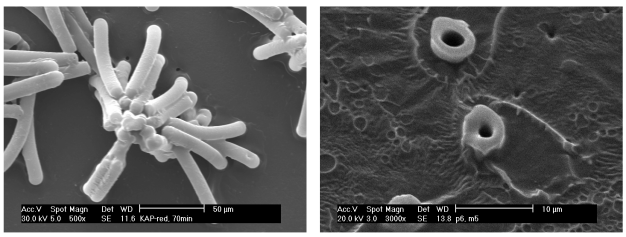

Figure 3. (left) cluster of bent KAP microrods, and (right) hollow microtubuli.

In conclusion, using solution growth in combination with the ion-track templates represents a suitable method to fabricate micro- and nanorods of potassium hydrogen phthalate crystals. Their length and diameter can be adjusted by controlling the membrane thickness and pore diameter, respectively. The growth process shows a strong tendency towards single-crystalline structures. The bending properties of such small high-aspect-ratio rods exhibit higher flexibility than stiff larger crystals. Dye-doped KAP rods produced by this technique have potential impact as components for micro- and nano-lasers.

References

[1] B. Bercu, I. Enculescu, R. Spohr, Nucl. Instr. Meth. B 225 (2004) 497
[2] M. Enculescu, I. Enculescu, M. Sima, R. Neumann, C. Trautmann, J. Optoelec. Adv. Mat. 9 (2007) 1561
[3] J.B. Benedict, P.M. Wallace, P.J. Reid, S.H. Jang, B. Kahr, Adv. Mater. 15 (13) (2003) 1068

* Partially supported by Romanian Ministry of Education and Research (contract IDEI 30/2007)
#mdatcu@infim.ro

Ion-track lithography for thermoelectric applications *

E. Koukharenko[1], X. Li[1], I. Nandhakumar[1], S.P. Beeby[1], M.J. Tudor[1], B Schiedt[2], C. Trautmann[2], and N.M. White[1]

[1]University of Southampton, Southampton, UK; [2]GSI, Materialforschung, Darmstadt, Germany

This work presents a novel process to fabricate nanostructures for thermoelectric applications by a combination of a traditional silicon microfabrication techniques, electroplating, and submicron ion-track nanolithography. Polyimide (Kapton HN, PI2731), and PMMA (polymethyl methacrylate) were ion-track irradiated and wet etched. Bi_2Te_3 nanowires (80 and 120 nm diameter) were electroplated with preferential orientation in the (110) crystallographic planes and fine-grained microstructure.

An increased need of powering low-power wireless systems and portable electronics requires an alternative source of electrical energy to replace batteries, which have limited shelf life and are bulky. One of the existing alternatives is thermoelectric power, which offers several advantages over other energy harvesting techniques: the devices are wholly solid-state, have no moving parts, long life and high reliability [1]. Drawbacks of existing thermoelectric generators are low efficiency and large size. Recent theoretical studies have predicted that efficiency is increased if the thermoelectric element diameter can be decreased to a size at which quantum confinement and interface scattering effects occur [2]. There are different approaches to miniaturize thermoelectric materials, e.g. by growth in porous alumina templates, and e-beam or micro-photolithography. These methods have limitations in size, density of thermoelectric elements, complexity, and high cost and they are not compatible with silicon microfabrication processes. Ion-track technology can overcome mentioned issues and produce low-cost templates for nanowires with high-aspect-ratio [3,4]. This work is aimed to develop a new generation of thermoelectric generators with high-aspect-ratio and high density nanoelements to target power harvesting from small temperature gradients.

As templates we used polyimide and PMMA polymer samples and irradiated them with Pb, U, or Au projectiles of MeV to GeV kinetic energy and fluences of 5×10^8 or 5×10^9 ions/cm^2 at the UNILAC. Track etching was studied in polyimide PI2731 photoresists (HD Microsystems), dry films (12.7 and 20 µm thick) of Kapton HN (Dupont), PMMA foils and PMMA 950A11 photoresist (Goodfellow Microchem). Polyimide samples were pre-etched in H_2O_2 solution at 60°C and subsequently etched in sodium hypochlorite (NaClO, 13%, pH~12.6) solution at 60°C, resulting in pore diameters between 30 and 120 nm for different etching times. Two etch solutions were used to fabricate PMMA nanotemplates: methyl-iso-butyl-ketone (MIBK/IPA) and GG developer (15% water, 60% butoxyethoxyethanol, 20% morpholin, 5 % aminoethanol). For the PMMA photoresist, these etching conditions resulted in pore diameters of <30 nm for the MIBK:IPA solution and ranging from 30 to 50 nm for the GG solution.

Electroplating of Bi_2Te_3 and $Bi_{0.5}Sb_{1.5}Te_3$ nanowires into polymide templates was carried out by cathodic electrochemical co-deposition of Bi, Sb, and Te powder dissolved in the aqueous nitric acid using a three-electrode cell with an Autolab potentiostat/galvanostat. For a range of applied potentials from -0.22 to 0.03 V vs a Saturated Calomel Electrode (SCE), the resulting Bi_2Te_3 compounds showed a stoichiometric composition with a grain size of the order of tens nanometers (Figure 1). X-ray Diffraction Spectroscopy (XRD) spectra revealed that the deposited nanowires are monophased polycrystalline Bi_2Te_3 of rhombohedral structure, $R\bar{3}m$.

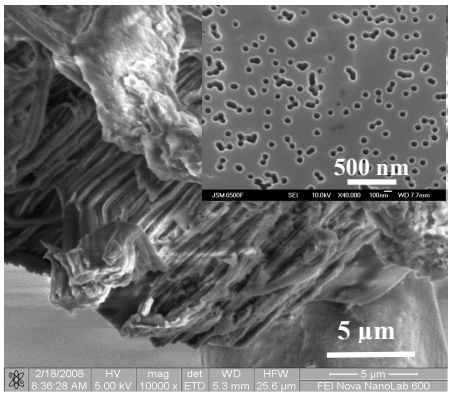

Figure 1: Cross section of Bi_2Te_3 nanowires deposited at –0.2 V vs SCE at room temperature into polyimide template (20 µm thick, 5×10^9 pores/cm^2) with a pore diameter between 80 and 120 nm

References

[1] A.F. Ioffe, "Semiconductor Thermoelements and Thermoelectric Cooling" Infosearch Limited, London (1957)

[2] L.D. Hicks, M.S. Dresselhaus, "Thermoelectric figure of merit of a one-dimensional conductor", Physical Review B 47 (1993) 16631

[3] M. Lindeberg, K. Hjort, "A comprehensive study of ion track enabled high aspect ratio microstructures in flexible circuit boards", Microsystem Technologies 10 (2004) 608

[4] E Koukharenko, X Li, I Nandhakumar, N Frety, SP Beeby, D Cox, MJ Tudor, B Schiedt, C Trautmann, A Bertsch and NM White, Towards a nanostructured thermoelectric generator using ion-track lithography, J. Micromech. Microeng. 18 (2008) 104015

* Work supported by the EPSRC, UK (EP/D076250).

Seebeck Measurements on Arrays of Embedded Bi Submicron Wires

S. Müller[1], T. W. Cornelius[1,2], D. Huzel[1], O. Picht[1], M. Rauber[1], and R. Neumann[1]
[1]GSI, Darmstadt, Germany; [2]ESRF, Grenoble, France

The transport properties of nanoscaled objects can be very different from those of the corresponding bulk material due to the influence of finite-size and quantum-size effects in low-dimensional structures. In 1993, Hicks and Dresselhaus published theoretical investigations on transport properties of one-dimensional conductors, predicting a significantly enhanced thermoelectric efficiency [1]. Because of large effective masses and mean free path of the conduction electrons, Bi is an ideal material for studying the transport properties of nanowires. The electrical conductivity of Bi nanowires was already intensively investigated [2]. Here, a simple method for the measurement of another thermoelectric material property, the Seebeck coefficient S, of arrays of embedded submicron wires is presented.

S is defined as proportionality factor between the potential difference $\mathrm{d}U$ and the temperature difference $\mathrm{d}T$ at zero current. Hence,

$$S(T) := \frac{\mathrm{d}U}{\mathrm{d}T}.$$

Experimental Setup

Wire arrays are deposited electrochemically in ion track-etched polycarbonate foils. The deposition parameters were chosen as room temperature and a voltage of -50 mV for polycrystalline growth, and 60°C and -18 mV for single-crystalline wires. Afterwards, the template with the embedded wire array is clamped between the two copper plates of a specially designed sample holder. On each plate, a thermal sensor and a lead to a nanovoltmeter is attached. While the sample holder is being cooled down in a gas evaporation cryogenic refrigerator, the voltage and the temperature gradient are being monitored as a function of temperature.

Results

In Fig. 1, S of poly- and single-crystalline wire arrays is shown as a function of wire diameter d and temperature. For both types of wires, the absolute value of S is decreasing with shrinking d. Furthermore, it is diminishing with decreasing temperature. In the case of polycrystalline growth, the slope of S between 50 and 200 K is -0.17 and -0.20 µV·K^{-2} for $d = 330$ and 1080 nm, respectively, whereas for bulk bismuth the slope is -0.51 µV·K^{-2} for temperatures between 50 and 100 K (cf. Fig. 1a). For temperatures below about 150 K, the curves of single-crystalline wires show a linear relationship with constant slopes of $+0.02$, -0.15, and -0.18 µV·K^{-2} for 205, 830, and 1080 nm thick wires, respectively (cf. Fig. 1b).

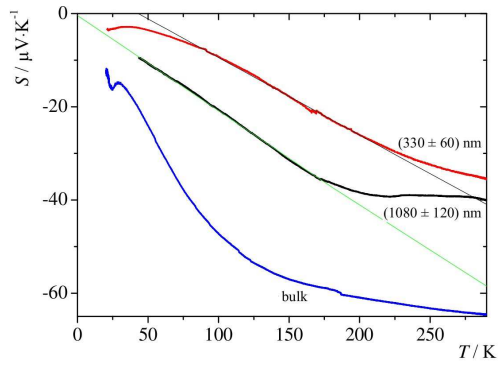

(a) polycrystalline wires

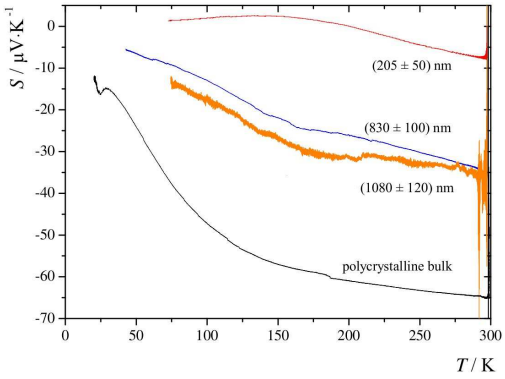

(b) single crystalline wires

Figure 1: Seebeck coefficient of Bi wire arrays for various wire diameters as a function of temperature.

The main systematic error is due to an unknown thermal resistance between the copper plates and the sample itself. Therefore, $|S|$ is systematically underestimated. Nevertheless, the wire arrays show n-type conduction like the bulk sample that was also measured using the same setup except for the single-crystalline sample with $d = 205$ nm which is p-type below 200 K.

Further measurements on nanowires with smaller diameters will be performed on an improved setup. Additionally, S and the thermal conductivity of individual lithographically contacted nanowires will be determined on microchips designed by the group of F. Völklein (FH Wiesbaden/Rüsselsheim) [3].

References

[1] L. D. Hicks et al., Physical Review B 47 (1993), 16631
[2] T. W. Cornelius et al., Physical Review B 77 (2008), 125425
[3] F. Völklein et al., Nanotechnology (2008) (accepted)

A New LED Illumination System for the Bio-Endstation of the GSI Microbeam

B. Merk*, B. E. Fischer, R. Neumann, K.-O. Voss
GSI, Darmstadt, Germany

Introduction

In collaboration with GSI Biophysics, the microbeam, operated with ions from the UNILAC linear accelerator of GSI, is routinely employed for targeted irradiation of living cells in culture [1]. An online fluorescence microscope is used both for beam targeting [1] and for cell observation after irradiation via fluorescent dyes [2].

Fluorescence microscopy requires an intense light source at a set of specific wavelengths that excite the fluorescent dyes. For this purpose, we used to employ a high-pressure mercury arc lamp with a number of bandpass filters on a mechanical filter changer along with a mechanical shutter.

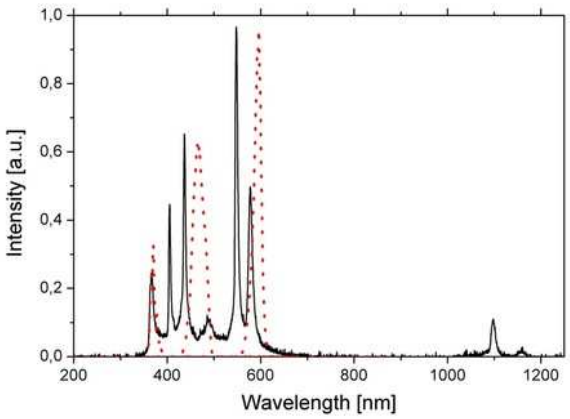

Figure 1: Comparison of the full spectrum of the Hg arc lamp (full line) and the spectra of three LED modules (dotted line).

However, such a solution, though common in conventional microscopes, does introduce a number of imperfections when employed at the microbeam: Firstly, the Hg arc lamp tends to heat the optical setup, resulting in thermal drifts that in turn negatively affect the targeting accuracy of the microbeam by shifting the microscope optics relative to the ion beam optics. Secondly, switching the light on and off and switching between different filters is a slow mechanical process. In the case of the mechanical shutter, switching time even introduces unnecessary photobleaching due to superfluous light exposition of the stained cells. Additionally, even very good bandpass filters show less than perfect blocking in spectral regions outside their passband, resulting in a somewhat decreased contrast in fluorescence images.

* b.merk@gsi.de

The New Illumination System

To circumvent these problems, we decided to install a new light emitting diode illumination system (Colibri, Carl Zeiss MicroImaging GmbH, Germany). This system comprises up to four bright and narrow-band LEDs (fig. 1) coupled into a single optical light path (fig. 2). Each of these LEDs can be rapidly adjusted to the necessary intensity, making obsolete any type of electro-mechanical switching of filters or shutters in the excitation light path.

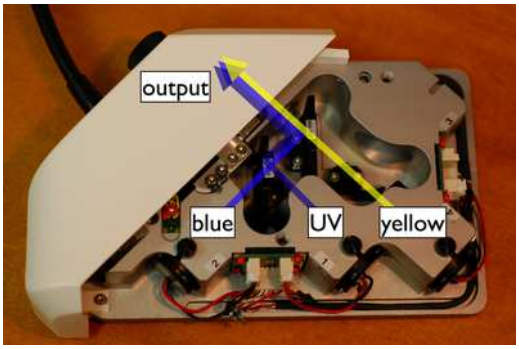

Figure 2: Photograph of the opened LED system with three LED modules combined into one light path.

Integration into the Irradiation System

To facilitate and speed up the irradiation, all recurring procedures have been automated as a plug-in to the commercial image processing package ImagePro Plus (Media Cybernetics Inc., USA). Thus, we needed to replace the old software interface to the filter and shutter mechanics, used in combination with the Hg lamp, with one that connects to the Colibri LED system via a Zeiss-supplied relay software package.

Outlook

With the new illumination system, we expect a further reduction of the thermal drift of the optical setup. Additionally, very rapid interleaved excitation of up to four fluorochromes has been added to the experimental toolbox of the microbeam.

References

[1] M. Heiß, B.E. Fischer, B. Jakob, C. Fournier, G. Becker, and G. Taucher-Scholz, Radiation Research 165 (2006) 23

[2] G. Du, B.E. Fischer, K.-O. Voss, G. Becker, G. Taucher-Scholz, G. Kraft, and G. Thiel, Radiation Research 170 (2008) 3

The M-Branch, a new UNILAC irradiation facility with in-situ analytical techniques for materials research

D. Severin, C. Trautmann, R. Neumann
GSI, Darmstadt, Germany.

The new M-Branch is installed in the former Z1 area of the UNILAC experimental hall and has three new beamlines which are presently in the commissioning phase. The M-Branch will provide ion beams up to 11.4 MeV/u specific energy for materials research and will partially compensate the former access to ion beams at the Ionenstrahllabor (ISL) existing until the end of 2006 at the Hahn-Meitner-Institut (HMI). The facility with state-of-the-art in-situ instrumentation and analytical tools was financed by combining funds from partially transferred research budget of ISL and from the GSI, the Helmholtz Association (Impuls- und Vernetzungsfond), and a BMBF project of several German universities (Verbundprojekt "Hochauflösende in-situ Charakterisierung struktureller Veränderungen in Festkörpern induziert durch hochenergetische Schwerionenstrahlung").

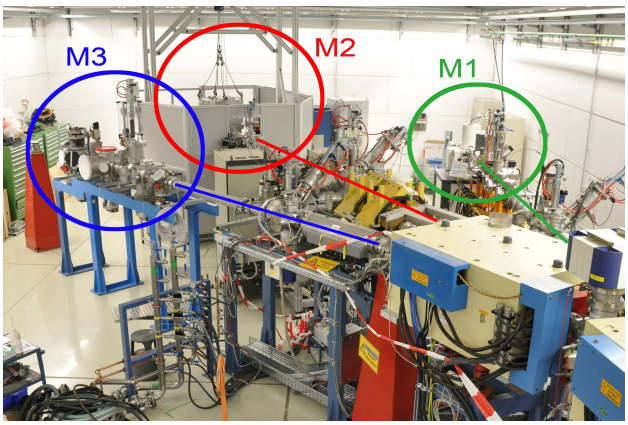

Figure 1: New M-Branch with beamlines M1, M2, and M3 equipped with different in-situ analytical tools such as scanning electron microscopy (M1), x-ray diffractometry (M2), and spectroscopy (M3).

M1 Beamline – Scanning electron microscope

Beamline M1 is connected to a high-resolution scanning electron microscope (HRSEM) installed and operated by the University of Stuttgart (W. Bolse). The HRSEM (Zeiss, SUPRA 40, 30 kV, magnification 12 – 900000×) is equipped with a thermal field-emission cathode and a secondary electron detector. It also houses a 5-axes motorised eucentric sample stage permitting the irradiation under tilted ion beam incidence or of a rotating specimen. For imaging, the stage is tilted into the electron beam without exposing the irradiated sample to air. The facility offers in-situ investigations of surface modification such as the formation of nanocracks, surface defects, and nanostructures.

M2 Beamline – X-Ray diffractometer

Beamline M2 is equipped with a standard 4-circle x-ray diffractometer (Cu-K_α) which was transferred from ISL (S. Klaumünzer). The instrument operates in vacuum and is equipped with a position sensitive detector (simultaneous measurement of $2\theta = 2°$). Investigation under any angle of incidence enables the quantitative analysis of structural modifications such as amorphisation or other phase transitions, internal stresses, and textural changes.

M3 Beamline – In-situ spectroscopy

Beamline M3 is equipped with two irradiation chambers. The first one houses a high-temperature stage (up to 900°C) installed by the University of Göttingen (H. Hofsäss). The second chamber is equipped with a closed-cycle He-cryostat and with several state-of-the-art analytical techniques. The combination of the cryostage, a residual gas analyser, and a gas flow controller allows irradiations under controlled temperature and gas atmosphere conditions. The set-up is important, e.g., when measuring outgassing yields of ion-bombarded polymers. The chamber is also equipped with an infrared spectrometer (TU Darmstadt, W. Ensinger) and an UV/Vis spectrometer (University of Heidelberg, U. Glasmacher) and will allow in-situ monitoring of optical absorption indicating e.g. degradation of organic insulators or creation of color centers as a function of irradiation fluence. Furthermore, the facility houses a luminescence spectrometer (University Dresden, J. Weber) to investigate time, temperature, and wavelength-resolved ion-stimulated luminescence for instance of semiconductors. In-situ observation of stress will be possible by means of curvature measurement using laser reflection in combination with an on-line long-distance microscope (University of Jena, W. Wesch).

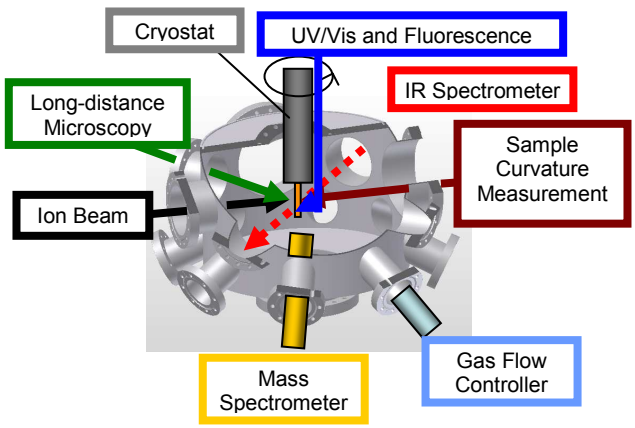

Figure 2: Scheme of the M3 multi-purpose chamber housing a large variety of in-situ analytical methods.

Live cell microscopy analysis of radiation-induced DNA double-strand break motion after charged particle irradiation*

B. Jakob[1], J. Splinter[1], A.L. Leifke[1], M. Durante[1,2] and G. Taucher-Scholz[1]
[1]GSI Biophysik, Darmstadt, Germany; [2] TU Darmstadt, Institut für Festkörperphysik, Darmstadt, Germany

We studied the spatiotemporal organization of DNA damage processing by live cell microscopy analysis of GFP-tagged 53BP1in human cells after the exposure to charged particles. The inhomogeneous dose deposition along the ion trajectories facilitates studies on the dynamics of radiation-induced protein foci [1,2]. In unirradiated U2OS osteosarcoma cells, a fast Brownian-like motion of DNA repair protein foci confined to an area below 1 μm^2 was observed, which was not altered by radiation (Fig. 1).

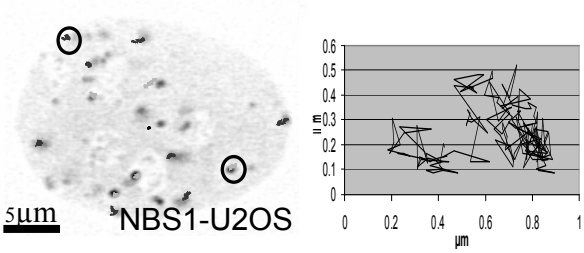

Figure 1.Left: U2OS-cell expressing NBS1-GFP. Overlaid tracks represent the motion of foci during the observation time of 30 min after irradiation with Ca-ions. Right. Magnified motional track of a single NBS1 focus showing the fast confined Brownian-like motion.

By analyzing the motional activity of GFP-53BP1 foci in live cells up to 12 hours post-irradiation after high LET (3430 keV/µm) Ni irradiation (Fig.2), we detected an additional slower mobility of damaged chromatin sites showing a mean square displacement of around 0.6 µm²/h (Fig2. inset). This motion was also observed after sparsely ionizing radiation and is most likely driven by normal diffusion of chromatin.

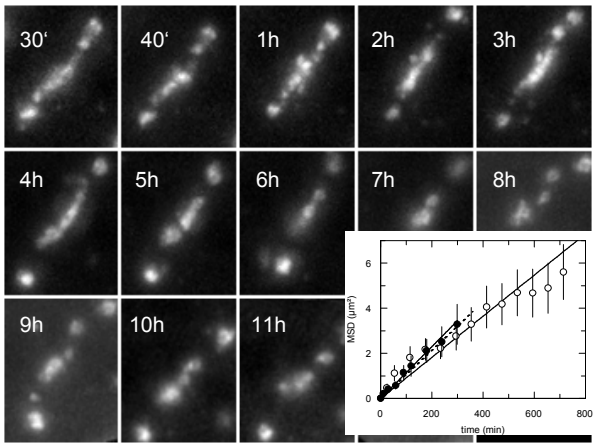

Figure 2: Motion of foci in a streak of 53BP1 generated by traversing Ni-ions. Inset: Summarized data showing the Mean Square Displacement (MSD) of repair foci of around 0.6 µm²/h.

Only occasionally, larger translational motion connected to morphological changes of the whole nucleus or the (transient) formation of repair clusters (Fig. 3) could be observed in the cells irradiated with charged particles.

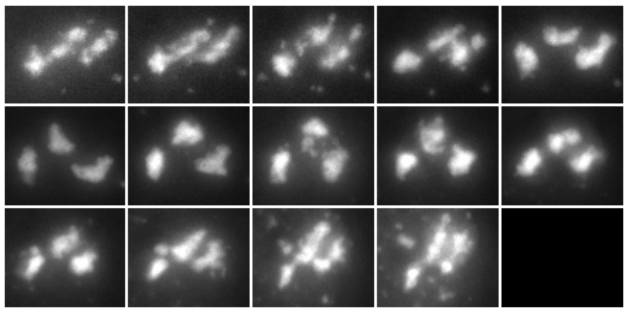

Figure 3 Motion of foci in streaks of 53BP1 generated by traversing Ni-ions showing a transient compaction or cluster formation.

We conclude that long range displacements of damaged chromatin domains do not generally occur during DNA double-strand break repair after introduction of multiple damaged sites by charged particles. The occasional and in part transient appearance of cluster formation of radiation-induced foci may represent a higher mobility of chromatin along the ion trajectory (Fig.4). These new observations support the hypothesis that spatial proximity of DNA breaks is required for the formation of radiation-induced chromosomal exchanges.

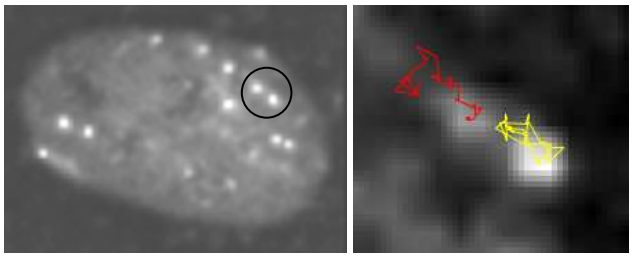

Figure 4: Motion of selected foci of NBS11 generated by traversing Kr-ions. The higher mobility along the path of the traversing ion is indicated by the overlaid motional tracks (left) of the encircled foci (right). Total observation time was 5h.

References

[1] B. Jakob et al., Rad. Res. (2009), in press
[2] B. Jakob et al., PNAS (2009), in press

This work was partly supported by BMBF Grant 03NUK001A

A new experimental setup allows studying protein turnover at DNA damage sites

F. Tobias, A.L. Leifke, G. Becker, M. Durante, B. Jakob and G. Taucher-Scholz
GSI, Darmstadt, Germany

Introduction

For each cell and consequently each organism, efficient DNA repair is essential to maintain genome integrity and thus to prevent mutations which might cause cancer. Hence understanding the molecular mechanisms of DNA repair is of enormous interest, but also a great challenge because of its high complexity. Within the last years great advances have been made by analysing the accumulation and interaction of repair proteins in foci at DNA damage sites. Most of these studies consider the nuclear repair proteins without differentiating between compartments. Fluorescence recovery after photobleaching (FRAP) is a technique which allows to measure the dynamics of fluorescently tagged proteins in subcompartments of living cells. Here a new experimental FRAP setup is introduced which provides insights into the turnover of DNA repair proteins at local DNA damage sites after heavy ion irradiation.

Experimental Setup and Results

Experimental Setup

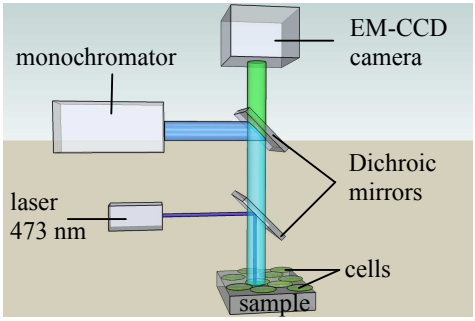

Figure 1: Schematic drawing of the optical path in the experimental FRAP setup.

A schematic drawing of the optical path in the experimental setup is shown in figure 1. Cells growing on glass slides express proteins tagged with the green fluorescent protein (GFP). This fluorescence is excited by light of a monochromator with a selected wavelength of 488 nm. The fluorescent light passes through both dichroic mirrors and is detected by a highly sensitive electron multiplying charge-coupled device (EM-CCD) camera. A 473 nm laser is mounted into the microscope. The fluorophores of the tagged proteins within small regions of the cell nucleus can be irreversibly bleached by intense and short laser pulses. The position, size, shape and number of these bleach spots can be freely chosen as the whole setup is operating on the soft- and hardware of a Leica Microdissection Microscope.

Results

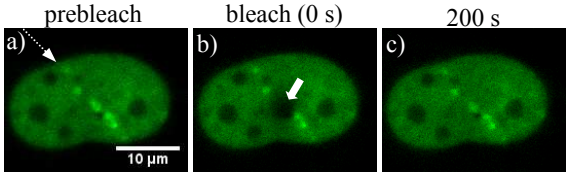

Figure 2: Selected pictures of a typical FRAP experiment. U2OS-MDC1-GFP cells after ^{12}C irradiation.

Heavy ion irradiation causes highly localized DNA damage along the ions-trajectories [1]. The fluorescently tagged repair proteins accumulate in foci at these sites (figure 2a). To measure the repair protein turnover some of these foci are bleached with a short laser pulse (figure 2b). Due to normal exchange over time, the bleached proteins will be released from the DNA damage binding sites and unbleached proteins form the surrounding will bind. This process causes fluorescence recovery in the bleached spot (figure 2c). The speed of this recovery directly reflects the protein turnover at DNA damage sites (figure 3). Quickly exchanging proteins will show a fast replacement while others, firmly bound, will show less or no recovery. First results indicated high turnover rates of early repair proteins.

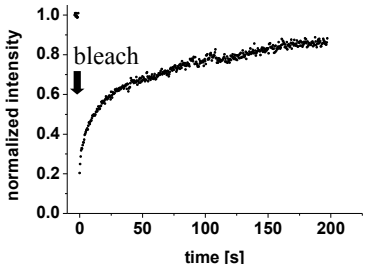

Figure 3: Measured fluorescence of GFP tagged MDC1 proteins in a bleached spot.

Conclusion

The combination of heavy ion irradiation and this new FRAP setup allows to study the dynamic behaviour of many different repair proteins at the sites of damaged DNA. In such a way this technique will help to analyse repair mechanisms at clustered lesions.

Acknowledgment

This work was funded by BMBF grant 03NUK001A.

References

[1] Taucher-Scholz, G.; Jakob, B., Genome Integrity, Ed. D.H. Lankenau, (2007) Springer, 453-78.

DNA Damage after High-LET Exposure

M. Ensminger[1], S. Conrad[1], G. Taucher-Scholz[2], A. Krempler[1] and M. Löbrich[1]
[1]Darmstadt University of Technology, Germany; [2]GSI, Darmstadt, Germany

The number of tumor patients treated with carbon ions is increasing worldwide and even new therapy centres are planned. Therefore it is important to get a better understanding of high-LET particle induced DNA damage. It has been known for several years that DNA double strand breaks (DSBs) evoked by particle radiation are generally more slowly repaired than breaks induced by photon irradiation. Moreover, the fraction of residual breaks after prolonged repair incubation correlates with the cell killing capacity of high-LET radiation.

Owing to the high ionisation density of high-LET particles, it seemed possible that heavy ion irradiation evoke DSBs that are generally more complex with additional lesions in very close proximity to the DSBs. These breaks would require processing before repair. In this context, the nuclease Artemis may play a decisive role. Recently we have reported that ATM and Artemis operate in a common repair pathway. Cells deficient in one of these factors are specifically defective in the repair of DSBs with slow repair kinetics and the level of unrepaired breaks seems to depend upon the complexity of the DSB ends. After α-particle irradiation a higher proportion of DSBs is repaired in an ATM and Artemis dependent manner. By contrast this process is dispensable for the repair of DSBs induced by etoposide, an inhibitor of topoisomerase II that causes "clean" DSBs [1].

To investigate the relationship between LET and complexity of a break, we analyzed the fraction of those DSBs that require Artemis after various radiation qualities. First, we determined whether X-rays of different energies would produce varying amounts of complex lesions. In an energy range from 25 keV X-ray to γ-rays (660keV) no difference in the level of unrepaired DSBs in Artemis cells was observed [2]. We next applied ultra-soft X-rays (carbon K shell radiation, 280eV) that deposit a large proportion of the energy within a very short distance. Here, an elevated level of Artemis dependent DSBs was observed compared to X-ray irradiation. This supported our notion that high energy deposition within a very short distance results in complex lesions [3].

To determine the amount of complex DSBs after heavy ions, we irradiated stationary wildtype (82-6 hTert) and Artemis cells (CJ hTert) with different fluences of ^{12}C (LET: 170keV/µm) or ^{64}Ni (LET: 3430keV/µm) ions using the UNILAC at the GSI. The repair of the DSBs was observed by PFGE analysis and compared to the repair after similar X-ray doses. Although preliminary, the data suggest that DSBs induced by ^{12}C ions were more slowly repaired than breaks after X-ray irradiation. Moreover, the level of unrepaired DSBs in Artemis cells compared to wildtype cells appeared significantly elevated after ^{12}C ions (Fig.1A). First experiments after ^{64}Ni irradiation suggest an even bigger amount of Artemis dependent DSBs (Fig.1B) consistent with the notion that the high biological effectiveness of high-LET radiation may result from the high proportion of complex DSBs.

In the future, we aim to get a better view on the pathways chosen to repair high-LET damage. We suppose that homologues recombination may be important to repair these complex breaks. Therefore, further PFGE-experiments and additional techniques like γH2AX immunofluorescence will be conducted.

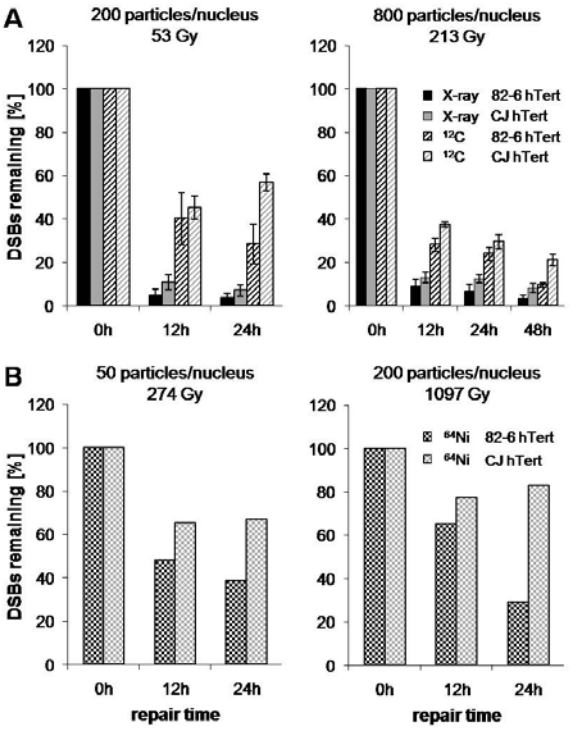

Fig.1: PFGE analysis in 82-6 hTert (wildtype) and CJ hTert (Artemis) after (A) X-ray and ^{12}C ions or (B) ^{64}Ni ions respectively.

References

[1] E. Riballo, M. Kühne, N. Rief, A. Doherty, et al., Molecular Cell 16 (2004) 715-724
[2] P. Kegel, E. Riballo, M. Kühne, P.A. Jeggo, M. Löbrich et al., DNA Repair 6 (2007) 1692-1697
[3] M. Ensminger, G. Taucher-Scholz, M. Löbrich, A. Krempler, GSI report 2008

DNA Double-Strand Break Quantification and Localization in Mouse Tissues

A. Raths[1], S. Grudzenski[1], and M. Löbrich[1,]
[1]Darmstadt University of Technology, Germany

DNA double-strand breaks (DSBs) are the most deleterious form of ionizing radiation (IR) induced DNA damage. Several *in vitro* studies accentuate the enormous effect of efficient DSB response systems on cell survival after exposure to IR. However, only little is known about the induction and processing of IR induced DSBs in tissues under the physiologic conditions of living organisms. For many years, the analysis of DSB repair was based on techniques such as pulsed-field gel electrophoresis that require high irradiation doses and consequently were restricted to *in vitro* studies. The finding that the histone H2AX is phosphorylated in the DSB surrounding chromatin and can be visualized by immunofluorescence microscopy as γH2AX foci allowed the investigation of DSB induction and repair in single cells after physiologically relevant low doses. A further sensitive marker for DSBs is the 53BP1 protein, which is recruited to DSBs sites within several minutes after IR and also forms discrete nuclear foci which colocalize with γH2AX.

Now, in collaboration with the group of C. Rübe we established a method of γH2AX and 53BP1 foci staining in mouse tissues after *in vivo* x-ray irradiation. Figure 1 shows the staining of discrete 53BP1 foci in nuclei of mouse heart, small intestine and kidney 10 minutes after *in vivo* irradiation with 1 Gy. To verify the sensitivity of this technique we counted 53BP1 foci in different organ tissues 10 minutes after doses of 10mGy, 100mGy and 1 Gy. As expected, we found a linear dose relationship which was identical in all organs (Figure 2). This demonstrates that we are able to reliably quantify the number of DSBs *in vivo* after IR with very low doses as well as their location in the nucleus.

Ataxia telangiectasia mutated (ATM), a protein defective in the hereditary disorder ataxia telangiectasia (AT) is activated after IR and phosphorylates proteins involved in cell cycle checkpoint control and DNA repair. It is known that AT cells reveal a DSB repair defect *in vitr*o, which has now been illustrated in tissues of AT mice [1]. In a recent publication it has been demonstrated that in ATM-deficient cells the DSBs that remain unrepaired over a long time are preferentially located at heterochromatic regions [2]. These finding indicate a participation of ATM in the repair of heterochromatin associated DSBs. Mice are a suitable cell system to distinguish between euchromatic and heterochromatic regions because of the assembly of heterochromatin in chromocenters. Thus, we plan to extend previous *in vitro* studies to mouse tissue *in vivo*. Thereby, we plan to identify the localization of DSBs in the nuclei of different mouse tissues and compare wild type mouse strains with ATM-deficient mouse strains. First experiments demonstrate the ability to mark 53BP1 foci as well as a heterochromatic marker- trimethylated K9 of histone 3- in a mouse kidney after IR with 1 Gy (Figure 3).

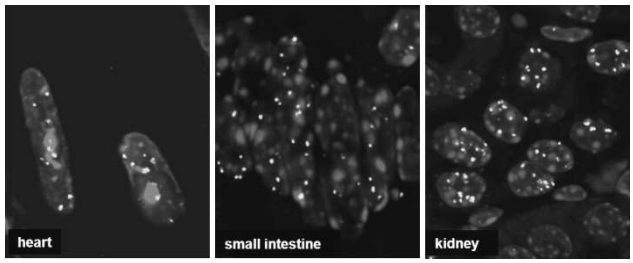

Figure 1: Immunofluorescence staining of 53BP1 (bright foci) in nuclei of mouse heart, small intestine and kidney 10 minutes after *in vivo* irradiation with 1 Gy.

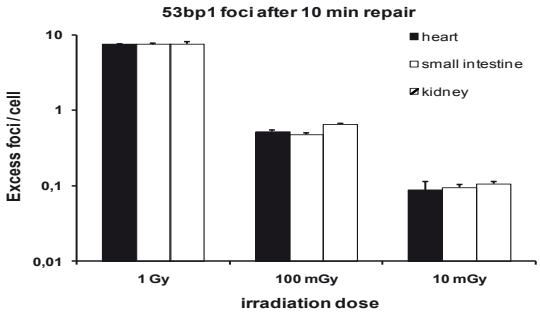

Figure 2: 53BP1 foci quantification in cells of mouse heart, small intestine and kidney 10 minutes after *in vivo* irradiation with 1 Gy, 100 mGy and 10 mGy.

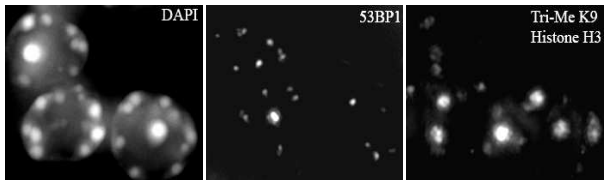

Figure 3: Localisation of 53BP1 foci in euchromatic and heterochromatic (trimethylated K9 of histone 3) regions in nuclei (DAPI) of a mouse kidney after *in vivo* irradiation with 1 Gy.

References

[1] C.E. Rübe, S. Grudzenski, et al., Clin Cancer Res. 2008; 14 (20) 6546-55.
[2] A.A. Goodarzi, A. T. Noon, et al., Mol. Cell 2008; 31, 167-177.

Structure and positional stability of damaged protein domains in mammalian cells after high LET exposure*

B. Jakob[1], J. Splinter[1], M. Herrlitz[1], K. Knoop[1], G. Becker[1] M, Durante[1,2] and G. Taucher-Scholz[1]
[1]GSI Biophysik, Darmstadt, Germany; [2] TU Darmstadt, Institut für Festkörperphysik, Darmstadt, Germany

Exposure of mammalian cell nuclei with charged particles leads to the spatially defined production of damaged chromatin domains along the particle trajectories. Analysis of track morphology facilitates studies on the dynamics of radiation-induced protein foci associated with lesion processing. Recently we described the discrete formation of γ-H2AX foci and the recruitment of repair related proteins along ion trajectories over a LET range from 200 to 14300 keV/µm in human fibroblasts and in HeLa cells (Fig. 1)[1].

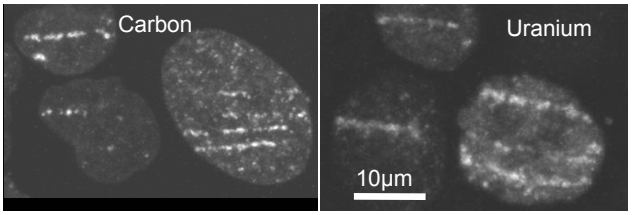

Figure 1: Low-energy particle irradiation leads to linear tracks of γ-H2AX. Hela cell nuclei 10 min after irradiation with carbon ions (LET: 200keV/µm; left) or uranium ions (LET 14300 keV/µm; right).

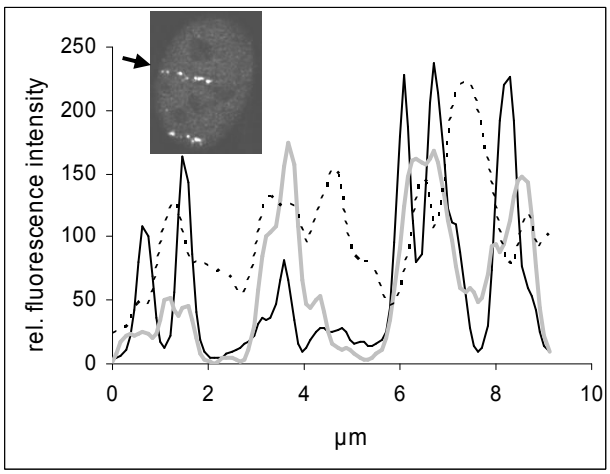

Figure 2: Intensity line scans along the respective trajectories marked by the arrows are displayed in the profiles. Correlation of RPA (black), 53BP1(grey) and chromatin stained by TOPRO3 (dotted) in AG1522 fibroblast cell nuclei 1h after low angle irradiation with uranium ions.

We could demonstrate, that the irradiation induced γ-H2AX formation colocalized with other proteins involved in DNA repair like 53BP1 (macrofoci) or RPA, which stains only microcompartments probably more directly related to the actual site of ongoing repair. Interestingly, the signals of the repair proteins e.g. 53BP1 (Fig. 2, grey line) and RPA (black line) as well as γ-H2AX (not shown) can be either detected at chromatin peaks or, more often adjacent to the DNA maxima (dotted line).

After Carbon irradiation, repair of DSBs was evident, indicated by loss of foci at later times (Fig. 3; 18h). Repair was less pronounced after higher LET. The stained DSBs exhibited a limited mobility independent of the LET pointing to a relatively stable positioning of the damaged chromatin domains during repair, especially in normal human fibroblasts (Fig. 3). In a small fraction of HeLa cells significant changes in the streak patterns during incubation (Fig. 4, arrow) could be observed, suggesting slightly higher mobility during local processing of DSBs in this tumor cell line. Nevertheless, we have to point out that deduction of dynamic behaviour is difficult in fixed cells and can be address in live cell experiments more easily.

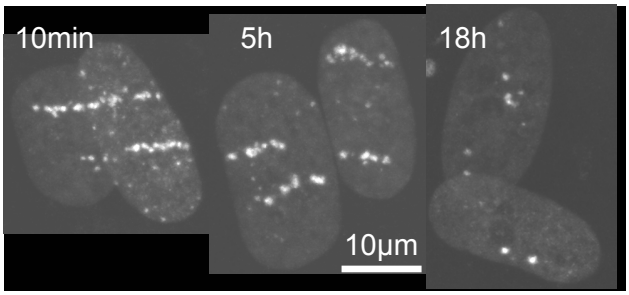

Figure 3: γ-H2AX in human fibroblasts irradiated with carbon ions (LET: 200keV/µm).

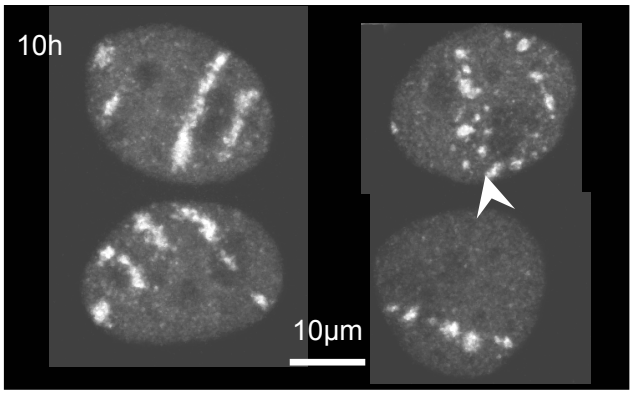

Figure 4: Hela cells irradiated with uranium ions (LET 14300 keV/µm). γ-H2AX signal 10h after exposure.

Our data indicate that the presence of multiple DSBs is not associated with a significantly altered potential for the movement of damaged chromatin. We infer that the repair of high-LET radiation-induced DSBs in mammalian cells is not coupled to an increased motional activity of lesions enhancing the probability of translocations.

References

[1] B. Jakob et al., Rad. Res. (2009), in press
Figures are taken and modified from [1]

The Chromatin Remodeller TIP60 Is Involved in Repair of Radiation-Induced DNA Double Strand Breaks

N. Averbeck, K. Knoop, F. Knauf, A. Leifke, G. Becker, M. Durante, and G. Taucher-Scholz
GSI Helmholtzzentrum für Schwerionenforschung GmbH, Darmstadt, Germany

Abstract

Ionizing radiation is harmful for living organisms. The most sensitive target within a cell is the DNA molecule, as it carries the genetic information. Therefore, the cell has sophisticated DNA repair mechanisms.

Repair of DNA double strand breaks (DSBs) requires numerous factors. The lesions need to be recognized and labeled so that repair proteins will be recruited. Further, as the DNA is embedded in a higher order structure (the chromatin) this structure needs to be altered to allow repair to occur.

We study processing of DSBs induced by heavy ions, which produce discrete regions of high-density DNA lesions within the nucleus.

Here we present data on DSB recruitment of TIP60, a histone acetyl transferase involved in chromatin remodeling.

Results

TIP60 is found at heavy ion induced DSBs

To find out whether TIP60 is recruited to DSBs induced by heavy ions, we performed immunofluorecence staining of human cells exposed to ^{132}Xe (4.5 MeV/n). TIP60 clearly localizes at DSBs, thus suggesting its possible involvement in post-irradiation repair of DSBs (Fig. 1).

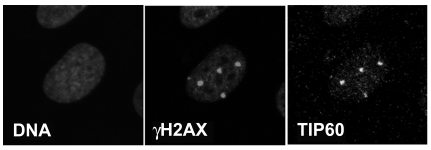

Figure 1: TIP60 colocalizes with the DSB marker γH2AX. Nucleus of a human fibroblast 1 h after irradiation with ^{132}Xe (4.5 MeV/n; LET: 8900 keV/µm; 2 x 10^6 p./cm^2). The fixed cells where immunostained with γH2AX- and TIP60 antibodies. DNA was stained with TOPRO3.

DNA damage caused by heavy ions induces histone H4 acetylation

In a next step we wanted to find out whether TIP60 that is recruited to DSBs is involved in their repair via chromatin decondensation, which allows repair factors to reach the lesions. Therefore, we studied the acetylation status of histone H4, which is the main acetylation substrate of TIP60 within its function in chromatin decondensation. Fig. 2 demonstrates that the fraction of H4 that is acetylated after ^{12}C irradiation (9.8 MeV/n) is significantly increased 15 min after irradiation and back to the level of non-irradiated cells 1 h after irradiation. These data suggest that following heavy ion irradiation TIP60 is indeed involved in chromatin decondensation to facilitate DNA repair.

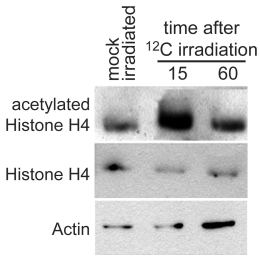

Figure 2: Histone H4 acetylation is increased after ^{12}C irradiation (9.8 MeV/n; LET: 170 keV/µm; 3 x 10^6 p./cm^2). Western analysis of human fibroblasts. Actin is shown as loading control.

Recruitment of TIP60 to DSBs depends on the chromatin acetylation status

If TIP60's main function at DSBs is to de-condense chromatin, it might be that artificial chromatin decondensation decreases the need of TIP60 at lesions. Thus, we examined the appearance of TIP60 at DSBs in cells that were treated with Trichostatin A (TSA), a histone deacetylase inhibitor causing histone hyperacetylation. We found less TIP60 recruited to DSBs in TSA-treated cells (Fig. 3). This result supports the idea that one of TIP60's key functions at DSBs is to de-condense chromatin, and thus enables repair factors to reach the lesion.

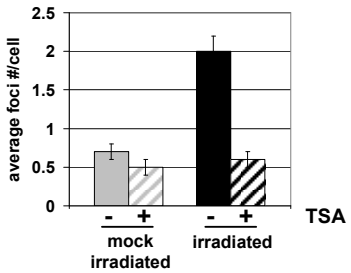

Figure 3: Histone hyperacetylation reduces TIP60 recruitment to DSBs. Human fibroblasts were treated 20 h with 200 ng/µl TSA prior to ^{12}C ions exposure.

Discussion

Our data suggest that TIP60 acts as a chromatin remodeller at heavy ion induced DSBs in order to allow repair factors to approach the break. Our future research will focus on whether TIP60 that is recruited together with ATM to DSBs is able to acetylate histone H4 or whether this task is performed by TIP60 within the NuA4 complex.

Acknowledgements

This work is supported by BMBF grand 03NUK001A.

No formation of γH2AX foci or micronuclei in bystander cells

C. Fournier,[a] P. Barberet,[a] T. Pouthier,[a] S. Ritter[a] B. Fischer,[a] K. O. Voss,[a] T. Funayama,[b] N. Hamada,[b,c] Y. Kobayashi[b,c] and G. Taucher-Scholz[a]

[a]GSI, Darmstadt, Germany; [b] JAEA, Takasaki, Japan; [c] Gunma University, Maebashi, Japan

Introduction

In previous studies we have observed a transient cell cycle arrest as well as an altered expression and activation of cell cycle regulating proteins in bystander cells after exposure to heavy ions. In general, damage to the DNA in bystander cells is considered as a possible mechanism triggering the observed effects.

Here we address whether heavy-ion induced DNA and cytogenetic damage is detectable in bystander cells. For this purpose, we evaluate both the formation of γH2AX foci and micronuclei as markers for damaged DNA. In the course of this study, and to our knowledge for the first time worldwide, parallel experiments at two heavy-ion microbeams (GSI, JAEA) using parallel cultures of the same cell strain, duplicate conditions, and irradiation protocols have been conducted [1].

Experiment

Normal human fibroblasts (AG1522) were thawed and cultivated to confluence at GSI. One part of this culture was flown to JAEA, the other remained at GSI. Both parts were kept at identical culture conditions until the respective irradiation. Microbeam irradiation was performed at GSI (targeted exposure, UV excited nuclear dye, 1%, 3% proliferating cells hit) and JAEA (geometrical micro pattern of exposure, no UV, 1% confluent cells hit). The quantitative assessment of γH2AX foci (only GSI) was performed by immunofluorescence staining and semi-automatic detection and quantification. The formation of micronuclei (GSI and JAEA) was investigated using two different protocols: According to protocol 1, the proliferating cells were incubated for 72h in medium supplemented with 1µg/ml Cytochalasin B directly after microbeam irradiation. The treatment corresponding to protocol 2, confluent cells were incubated in conditioned medium for 24h after irradiation, and then reseeded at low density in fresh medium with 1µg/ml Cytochalasin B and incubated for 24h. In both cases, bi-nucleated cells containing micronuclei were identified by microscopy using a set of morphological criteria (blinded samples, three independent researchers).

Results

Regarding γH2AX analysis in bystander populations, Fig. 1 depicts the percentage of cells exceeding the average number of foci per control cell. The kinetics of the foci formation shown in Fig. 2 does not give any hint to an effect at earlier time points. No significant elevation of the number of foci in bystanders was observed. The formation of micronuclei is depicted for the different protocols and facilities in Fig. 3. Although a clear dependence of the frequency of cells with micronuclei on the protocol was observed, no significant difference was detected after exposure.

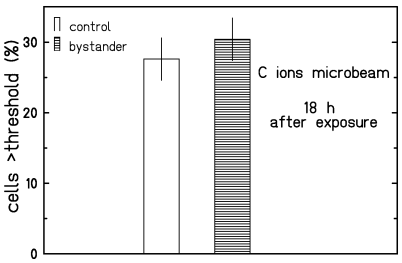

Fig.1: Percentage of cells containing more γH2AX foci than control mean plus 1.5 standard deviations. More than 1000 cells scored.

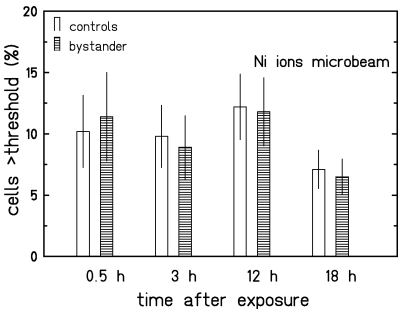

Fig.2: Same criterion as in Fig 1. No effect at earlier time points (one experiment).

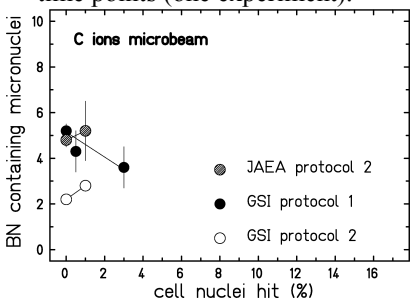

Fig.3: Percentage of bi-nucleated cells containing micronuclei for two protocols and at two microbeam facilities. No bystander effect at this endpoint visible.

In conclusion no significantly elevated formation of γH2AX foci or micronuclei was observable in bystander cells [1].

References

[1] C. Fournier, P. Barberet, T. Pouthier, S. Ritter, B. Fischer, K. O. Voss, T. Funayama, N. Hamada, Y. Kobayashi, and G. Taucher-Scholz, Radiat Res accepted for publication

Analysis of chromosome aberrations in peripheral blood lymphocytes of prostate cancer patients: an update *

C. Hartel[1], C. Fournier[1], P. Hessel[1], R. Lee[1], M. Durante[1], E. Nasonova[1,2], S. Sommer[1,3]
P. Virsik[4], J. Debus[5], R. Haselmann[5], A. Nikoghosyan[5] and S. Ritter[1]
[1]GSI, Darmstadt, Germany; [2]JINR, Dubna, Russia, [3]ICHTJ, Warsaw, Poland, [4]University Göttingen, Germany,
[5]Clinical Radiology, Heidelberg, Germany.

Encouraging clinical results applying C-ions have been obtained at the heavy ion synchrotron (SIS) at GSI, Darmstadt. Most patients that have been treated at GSI had chordoma or low grade chondrosarcoma of the skull base. In 2006 a clinical phase I/II trial has been started treating patients with locally advanced prostate cancer using a combination of C-ions as boost-irradiation (6x3GyE) and photon-IMRT (30x2Gy). In parallel to this study chromosome aberrations in blood lymphocytes of patients are analysed. Blood is unavoidably exposed during radiotherapy and the analysis of chromosome aberrations in lymphocytes is considered as a sensitive method to estimate the dose to which an individual has been exposed. Furthermore, since aberrations are a potential biomarker of carcinogenesis, their frequency can be used to estimate the risk of secondary cancer induction after therapeutic irradiation [1 and references therein].

For cytogenetic analysis blood samples from prostate cancer patients irradiated with C-ion boost and photon-IMRT are drawn before, during, at the end and one year after therapy. Lymphocytes are isolated and cultivated in vitro for 48h. Chromosomes are prepared and aberrations are analyzed by Giemsa staining to detect unstable aberrations and by multiplex fluorescence in situ hybridization (mFISH) to quantify stable aberrations as well as complex exchanges. To gain information on differences in individual radio-sensitivity, an aliquot of the pretreatment blood sample is exposed *in vitro* to 3 Gy X-rays. For comparison, blood samples from prostate cancer patients treated solely with IMRT (total dose >76 Gy) are studied.

To date 21 patients entered our study. Cytogenetic analysis of patients' lymphocytes before therapy revealed only slight individual differences which are comparable to those observed in healthy donors [2]. As expected the number of chromosome aberrations increases during radiotherapy. The data obtained so far indicate that at given time the aberration yield is slightly higher in patients treated solely with photon-IMRT, i.e. we have no indication of an enhanced toxicity of heavy particles in normal tissue in the short course of particle therapy (figure 1).

Till now only a few blood samples have been obtained one year after therapy. Our preliminary data suggest that the aberration yield declines slightly within the first year after treatment. Interestingly, first results obtained for patients treated with a larger IMRT field (not fitting to study conditions) suggest that the field size has a prominent effect on the aberration yield (figure 1).

Furthermore, the yield of complex aberrations was analyzed. *In vitro* experiments and modelling studies suggest that complex aberrations (see figure 2) are a signature of high LET exposure. However, our data as well as results reported by others reveal that their numbers are low in lymphocytes of patients, i.e. this aberration type does not represent a practical biomarker of radiation quality *in vivo*.

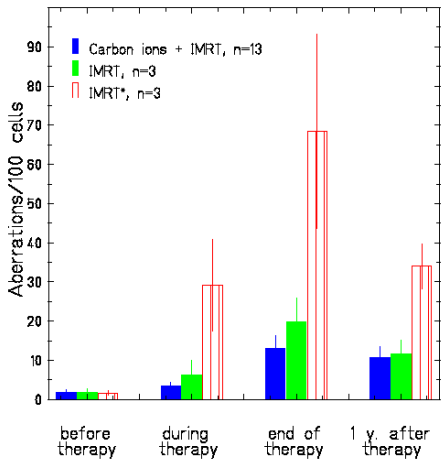

Figure 1: Chromosome aberrations in lymphocytes of prostate cancer patients as detected by Giemsa-staining (mean ± SD). Patients were treated with C-ion boost and photon IMRT or solely IMRT. Additionally, data from patients treated with a larger IMRT field are shown (IMRT*).

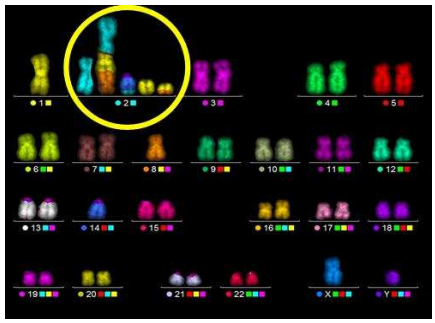

Figure 2: Complex aberration (indicated by a yellow circle) detected by mFISH in a lymphocyte of a prostate cancer patient. This complex aberration involves 4 chromosomes.

References

[1] S. Bonassi and W.W. Au, Mutation Res. 511, 2002, p. 73-86.
[2] C. Hartel et al., GSI Scientific Report 2007, GSI Report 2008-1, p. 361.

* Work supported by BMBF, Bonn, under contract 02S8497.

Characterization of human thyroid cells exposed to heavy ions

D. Pignalosa[1,2], S.P. Paone [1], M. Durante[2] and S. Ritter[2]
[1]Federico II University, Italy; [2]GSI, Darmstadt, Germany

Introduction

Chromosomal aberrations (CAs) are useful biomarkers for radiation exposure, as their frequencies are related to absorbed dose and they are related to an increased risk of cancer induction [1]. Epidemiological studies of the population exposed during Chernobyl accident demonstrate that thyroid cancer is a typical radiation induced tumour. These data provide risk estimates of thyroid cancer induction for low LET radiation exposure. No data are available for heavy ions irradiation. Gene analysis of papillary thyroid carcinomas in children of the Chernobyl area [2] show in more than 87% a characteristic family of CAs, the RET/PTC family, involving the RET gene mapped on chromosome 10 and other gene located mostly on the same chromosome (intrachanges, CAs produced from DNA breaks on the same chromosome).

The aim of our project is to examine aberrations in chromosome 10 after high and low LET irradiation to obtain a biological estimate for the different efficiency in intrachange induction (RBE). Characterization of the cell line selected for this study (H-Tori 3 cells) is necessary. Here we present the data concerning the delayed reproductive death, an index of radiation-induced genomic instability [3]. H-Tori 3 cells have been exposed to different doses of Fe ions and subcultivated for a long time in order to measure their clonogenic capability many generations after exposure. We also present early data from cytogenetic analysis on unirradiated sample.

Materials and methods

H-tori 3 are human thyroid epithelial cells immortalized with an origin defective SV40 virus genome. Weekly subcultivation was performed in RPMI 1640 complete medium supplemented with 10% fetal bovine serum. Cells were irradiated with different doses (0, 50, 100, 150 and 200 cGy) of Fe ions (1 GeV/n) at BNL (Upton, NY), with 5.5 and 11 Gy of Ni ions (6 MeV/n) and with X rays (2 and 4 Gy) at GSI. Early survival assay was conducted on cells irradiated with Ni ions and X rays. To assess delayed reproductive death colony formation assay was performed on cells sub-cultivated 7 times after exposure to Fe ions.

Results and conclusions

Survival data are shown in Fig. 1. Early survival curves (panel A) show LET and dose dependence as expected. Since no LET dependence has been observed for delayed reproductive death we can compare early survival curve with late measurements In late effect analysis no dose dependence has been observed (panel B), and no significant difference with the unirradiated sample. Our results demonstrate that H-Tori 3 cells do not show radiation induced delayed reproductive death. This could be explained considering the high background genetic instability of this cell line.

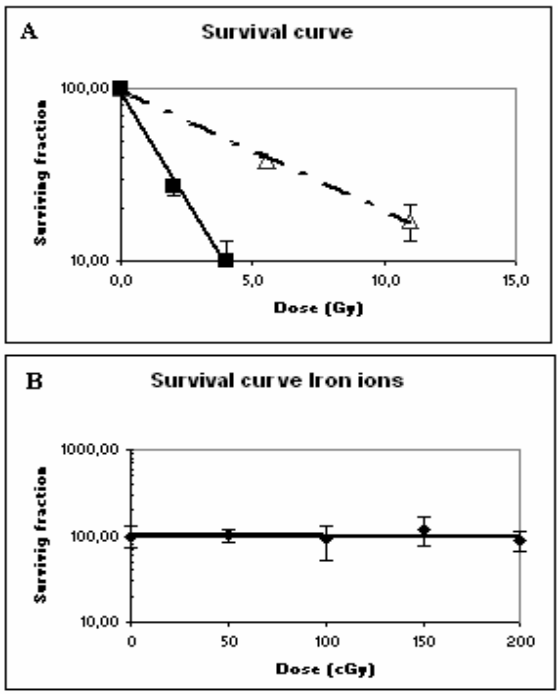

Figure 1: Dose dependence for the surviving fraction of H Tori 3 cells. Panel A: Ni ions (triangles) and X rays (squares) exposure. Panel B : Fe ions irradiated samples

These cells have a karyotype ranging from 44 to 76 chromosomes and they carry many structural chromosomal rearrangements. Early results from cytogenetic analysis performed with mBAND technique give a frequency of aberrant chromosome 10 equal to 0.9 ± 0.2 in the control. Our data (not reported) show that there is a decrease in plating efficiency with number of sub-cultivation procedures (passage), from 46% to less than 20% after 9 passages. Any radiation effect is therefore going to be hidden by the high rate of instability already present in this cell line.

References

[1] M. Durante and F. Cucinotta 2008 Nat. Rev. Cancer 8 : 465-472.
[2] Y. E. Nikiforov et al. 1997 Cancer Res. 57 : 1690-1694.
[3] C. B. Seymour et al. 1986 Int .J. Radiat. Biol. 50 : 167- 169

Dose rate effect on cytogenetic damage in cells exposed to relativistic protons

D. Pignalosa.[1,2], M. Durante[2], T. Friedrich[3] and S. Ritter[2]
[1]Federico II University, Italy; [2]GSI, Darmstadt, Germany, [3]Metasystems, Germany

Introduction

Astronauts in space are chronically exposed particularly to high energetic protons [1]. However most of the data concerning biological effects of ionizing radiation come from studies in vitro and in vivo under acute conditions. To obtain a correct estimation of risk related to space radiation, it is necessary to compare biological damage obtained after acute and chronic irradiation. The aim of this project is to examine differences in cytogenetic damage induced by relativistic protons through the analysis of chromosomal aberrations (CAs). CAs are a useful indicator of biological risk [2]. During chronic exposure a lower frequency is expected compared to acute exposure, since intra-track effect will predominate in CA formation. The spectrum of aberrations should also be different. After acute exposure the inter-track effect should prevail, so more complex exchanges (derived from 3 or more breaks involving two or more chromosomes) are expected compared to chronic condition.

Materials and methods

Blood samples were drawn from a healthy donor and irradiated (0 to 200 cGy) with 1 GeV proton beam (LET 0.2 keV/µm,) at NSRL (Brookhaven National Laboratory, Utpon, NY). Acute and chronic irradiations (100 and 8 cGy/min respectively) were performed under controlled conditions (37°, 5% CO_2) with an online incubator. After irradiation, blood samples were cultured in PHA-enriched medium and kept in incubator for 48 h. Chromosome harvest was performed following established procedures. Slides were hybridized with 24 colour labelling probes. This technique allows the simultaneous detection of all human chromosomes. Image acquisition was performed at Metasystems (Altlussheim, Germany). Metaphase analysis was performed at GSI with ISIS software.

Results and conclusions

Our data indicate that there is no difference in the frequency of aberrant cells after chronic and acute exposure at least in our experimental conditions (Fig. 1). Previous low LET studies have shown a pronounced curvature in the dose response curve for chromosomal aberration. This shape was interpreted as the consequence of the simultaneous presence of multiple damages, induced by multiple tracks, interacting with each other with the increase of dose.

In our study, the shape of the dose-response curve is linear up to the highest dose (200 cGy). This is in accordance with previous results on human fibroblasts [3] were linearity could be observed until 360 cGy of gamma rays.

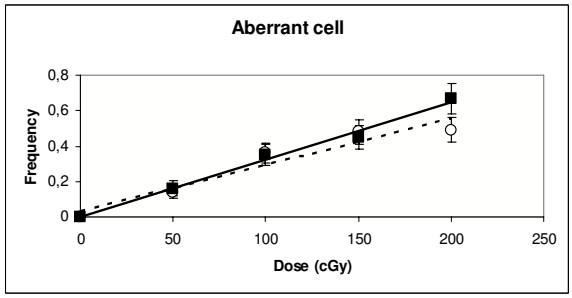

Figure 1: Frequency of aberrant cells after exposure to acute (square) and chronic (open circle) proton beam.

It was also stated that most of complex exchanges arises from interaction between chromosomes damaged by different tracks (inter-track effect). As it could be observed from our (Fig. 2) and previous results [3] complex exchanges are also observed in chronic irradiated samples, even at low doses. It means that this kind of aberration are produced also by intra-track action.

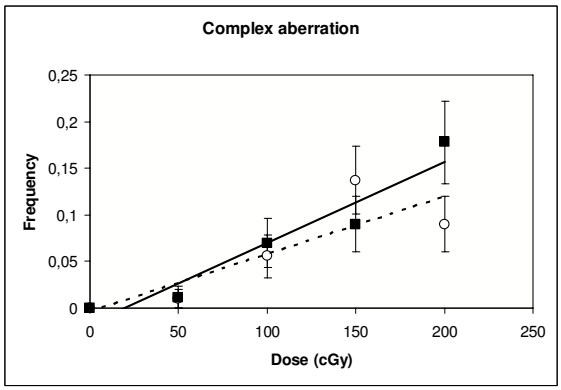

Figure 2: Complex aberrations in high (square) and low (circle) dose rate (square) exposed samples.

This could explain why we did not find differences in aberrant cells and in the complex exchange frequency between our samples. Probably, the delivered doses are not sufficiently high to make inter-track effect efficient enough to significantly enhance the aberration formation rate.

References

[1] M. Durante and F. Cucinotta 2008 Nat. Rev. Cancer 8 : 465-472.
[2] M. Durante 2005 Rad. Res. 164 : 467-473.
[3] B.D. Loucas et al. 2004 Rad. Res. 162 : 339- 439.

Intra- and inter-chromosome aberrations in human lymphocytes exposed to radiation *in vivo* and *in vitro* detected by mBAND *

R. Lee[1], S. Sommer[1,2], C. Hartel[1], P. Hessel[1], M. Durante[1], A. Nikoghosyan[3] and S. Ritter[1,#]
[1]GSI, Darmstadt, Germany; [2]ICHTJ, Warsaw, Poland; [3]Clinical radiology, Heidelberg, Germany

Identification of a cytogenetic signature that allows distinguishing high from low LET exposure is a long-standing goal in radiobiology. High LET particles deposit the energy in a narrow region around their trajectory, while γ-rays or X-rays deposit the dose uniformly in cell nuclei. Thus, it has been predicted that high LET radiation preferentially produces multiple breaks within a given chromosome which will result in intra-chromosomal aberrations [1]. In contrast, after low LET exposure many chromosomes will be damaged, favouring the formation of inter-chromosome aberrations.

Until recently the detection of intra-chromosomal exchanges was hampered by the low resolution of the available staining techniques such as G- or R-banding. With the advent of multicolour banding (mBAND) this limitation has been overcome, i.e. breakpoints can be unequivocally identified, even if highly complex rearrangements are induced (see fig 1 c, d).

In the present study we report first results obtained by mBAND for human lymphocytes exposed *in vitro* or *in vivo*. For *in vitro* experiments, lymphocytes of a healthy volunteer were irradiated with 2 Gy of 11.4 MeV/u C-ions (LET = 175 keV/µm) or 4 Gy X-rays. Cells were cultured in medium containing BrdU. After 48-72 hr the lymphocytes were fixed and chromosome spreads were prepared. Slides were hybridized with an mBAND probe specific for chromosome 2 (XCyte 2, MetaSystems, Germany) according to the manufacturer's protocol. Aberrations were analysed in first cycle metaphases identified by BrdU-incorporation [2]. Additionally, lymphocytes from a prostate cancer patient treated with photon-IMRT were analysed. Cells were obtained at the end of therapy (38 fractions × 2 Gy) and processed as described above.

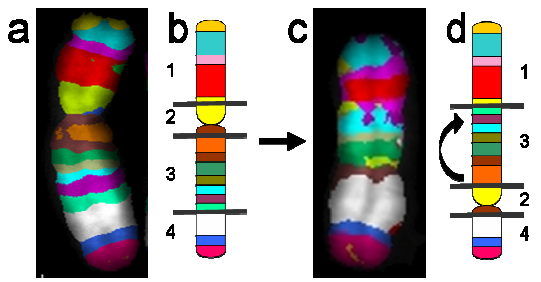

Figure 1: Example of a normal (a,b) and aberrant (c,d) chromosome 2 with 16 pseudocolor bands. Radiation exposure induces three breaks indicated by lines in scheme b. As a result a complex intra-chromosome exchange was formed (d).

* Work supported by BMBF, Bonn, under contract 02S8497.
#s.ritter@gsi.de

Aberrations were categorized as I) terminal deletions in chromosome 2, II) inter-chromosome exchanges between painted and unpainted chromosomes, III) intra-chromosome exchanges in a chromosome 2, and IV) chromosomal rearrangements involving both inter- and intra-changes. Terminal deletions are induced by a chromosome break. Inter-chromosome exchanges result from 2 breaks (simple-type) or ≥3 breaks (complex-type) in ≥2 chromosomes. Intra-chromosome exchanges originate from 2 breaks (simple-type) or ≥3 breaks (complex-type) in an mBAND chromosome.

Aberrations were analysed in 110-350 metaphases per sample. In all three samples scored, inter-chromosome aberrations dominate, while only a small number of intra-chromosome aberrations has been found as reported by [3]. Furthermore, only C-ions induce a high frequency of aberrations involving both inter- and intra-chromosome exchanges in the same cell. Since our current database is too small for firm conclusions on radiation quality dependent changes in the proportion of intra- vs. inter-chromosomal exchanges, a larger number of cells will be examined. Finally, the analysis of chromosome aberrations revealed that C-ions induce more complex-type aberrations than X-rays or photon-IMRT (i.e. 0.67, 0.34 and 0.10, respectively) in line with data reported by others [3, 4]. This effect is reflected in the frequency distribution of breaks in chromosome 2. As shown in figure 2, after C-ion exposure up to 10 breaks in a chromosome 2 were found, while the maximum break numbers after X-irradiation and photon-IMRT treatment were 4 and 3, respectively.

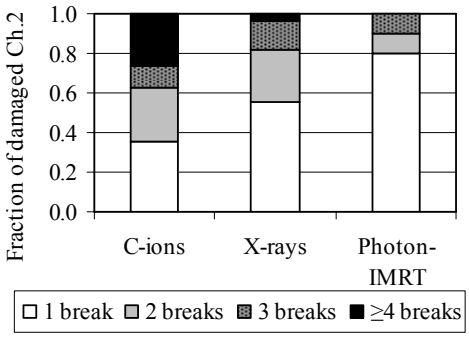

Figure 2: Number of breaks per aberrant chromosome 2 in lymphocytes after irradiation with C-ions, X-rays, or following IMRT-treatment.

References

[1] R.K. Sachs *et al.*, Rad Res 148, 1997, p. 330-40.
[2] J.J.W.A. Boei *et al.*, Mut Res 349, 1996, p. 127-135.
[3] C. Johannes *et al.*, Rad Res 161, 2004, p. 540-548.
[4] M. Hada *et al.*, Rad Res 168, 2007, p. 98-105.

Clonogenic survival and apoptosis of prostate cancer cells irradiated with X-rays or carbon ions*

P. Virsik[1], A. Gregus[1], P. Hessel[2], R. Lee[2] and S. Ritter[2]
[1] Dept of Environmental Medicine, University of Göttingen, Germany; [2] GSI, Darmstadt, Germany

Prostate cancer is the most frequent solid tumour in men in Europe. When recognized in a late, possibly metastasized state, these tumours appear to be rather radioresistant. Knowledge of the effects of C-ions on these tumours as well as on normal prostate cells is of fundamental interest for the optimal application of C-ion therapy. Apart from clinical studies, there is little detailed knowledge about the effects of C-ions upon various prostate tumour cells characterized by different individual genetic profiles [1].

To contribute to a better understanding of the effects of C-ions on prostate cancer, we will investigate the radiation response of two radio-resistant cancer cell lines, i.e. PC-3 cells derived from a bone metastasis and DU-145 cells originating from a brain metastasis. In particular cell inactivation and apoptosis will be measured. Further, we will investigate the oxidative status, anti-oxidative defence and repair of oxidative DNA damage in both cell lines. As a marker of the oxidative DNA damage, 8-oxoguanine will be used. Finally, for a more global picture, we will study structural and numerical chromosomal instability in surviving short-term and long-term cultures with respect to selected chromosomes, i.e. chromosome 3 carrying a gene involved in repair of the oxidative DNA damage (hOGG1) and chromosome 17 carrying a gene involved in polyploidization (Aurora B).

In our first experiments, cell inactivation and apoptosis were measured in both cell lines. Confluent cells were irradiated in G1-phase with 200 kV X-rays or with carbon ions. Clonogenic survival was measured by standard colony assay. Apoptosis was measured 24h, 48h and 72h after irradiation by a morphological assay (acridine orange plus Hoechst 33342 staining) applying fluorescence microscopy [2] and by a caspase-3 activity assay (ELISA).

Cell inactivation measurements performed so far indicate that the X-ray sensitivity of both cells is similar. Carbon ions (extended Bragg peak) were more effective than X-rays in inducing cell killing. RBE values for 10% survival were 1.9 and 2.4 for PC-3 and DU-145 cells, respectively (see figure 1).

Additionally, apoptosis was measured in PC-3 cells after exposure to 11 MeV/u carbon ions and X-rays (figure 2). Our first experiments revealed an increased efficiency of carbon ions, and in contrast to X-rays, practically no dose-dependence up to 4 Gy. These results were confirmed by caspase-3 activity measurements using ELISA (data not shown). Further experiments with carbon ion irradiation combined with sodium selenite pre-treatment inducing an increased oxidative stress, are in progress.

* Work supported by BMBF, Bonn, under contract 02S8497.

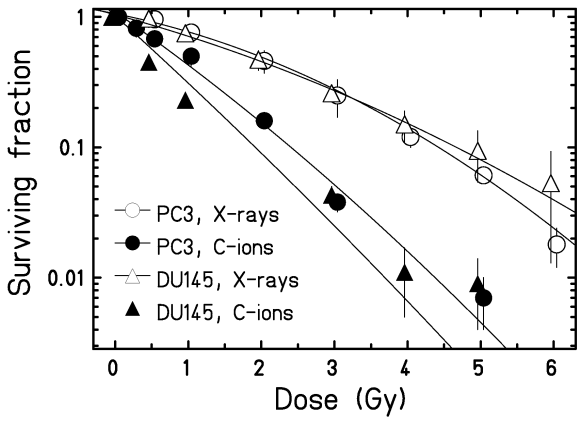

Figure 1: Clonogenic cell survival of PC-3 and DU-145 cell lines irradiated in plateau-phase with X-rays or C-ions (extended Bragg peak).

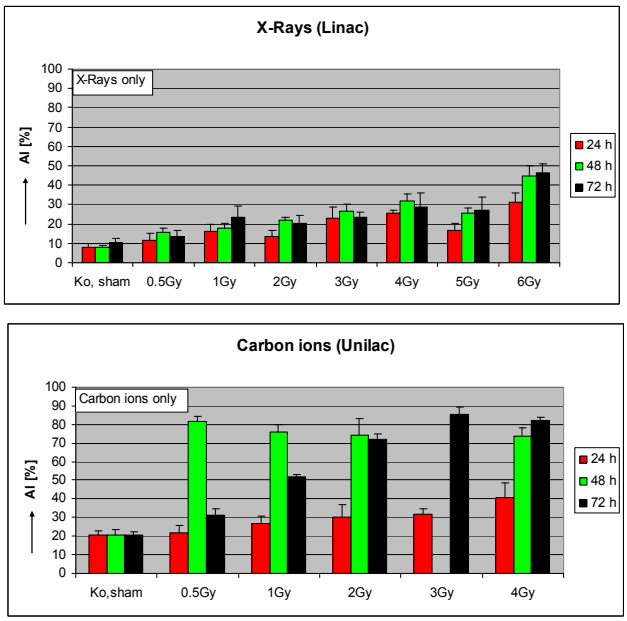

Fig.2. Percentage of apoptotic cells induced by X-rays or 11 MeV/u carbon ions as determined 24h, 48h and 72h after irradiation.

References

[1] V. Nwosu et al., Human Molecular Genetics 10 (2001) 2313.
[2] A.E. Meijer et al., International Journal of Radiation Biology 73(1998) 169.

In vitro co-culture experiments on prostate cancer and small intestine cells irradiated with carbon ions and x-rays

C. von Neubeck, W. K. Weyrather and M. Durante
GSI, Darmstadt

Introduction

In 2006 a study was started at GSI to treat prostate cancer patients with a boost irradiation of carbon ions in combination with an intensity modulated radiotherapy (IMRT) treatment administered at the Uniklinikum Heidelberg. The carbon ions are delivered in two opposing fields whereas IMRT uses many small fields. So IMRT irradiation includes more normal tissue than carbon ion treatment but even here parts of the rectum and the bladder are in the irradiated field. This raises the question whether the irradiated tumor cells influence the normal cells (irradiated/ unirradiated) but also whether the normal irradiated cells influences normal tissue in a different way for carbon and photon irradiation.

To study this problem, we established an *in vitro* co-culture model of prostate cancer and small intestine cells of the rat to simulate the patient treatment situation for analyzing tissue reaction exemplary. For characterization of the cells lines the parameters alpha and beta (linear quadratic model) for clonogenic survival were determined for x-rays and for carbon ions of different energies. For co-culture experiments unirradiated and irradiated cells were seeded together and the survival was analyzed.

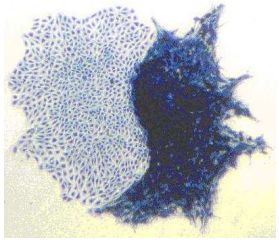

Figure 1: IEC-6 (left) and RAT-1 (right) colonies.

Material and methods

The Dunning prostate adenocarcinoma cell system of the rat is well studied and broadly accepted as a prostate cancer progression model. We worked with the line R 3327 AT-1 (RAT-1) [1] which can grow *in vitro* as well as *in vivo*. We combine this cell line with the intestinal epithelium cell line 6 (IEC-6): an accepted model for studying tissue reactions in the healthy small intestine [2].

For carbon irradiation at the heavy ion synchrotron at GSI (100 MeV/u, 270 MeV/u) as well as for 250 kVp x-ray irradiation the cells were seeded in culture flasks. For carbon irradiation at the linear accelerator of the GSI (11.4 MeV/u) the cells were seeded in Petri dishes. The cell survival was determined in a colony forming assay. The relative biological effectiveness (RBE) was calculated. For co-culture experiments the cells were irradiated with 100 MeV/u and 11.4 MeV/u carbon ions as well as 250 kVp x-rays. Instead of full survival curves three survival levels were chosen and the required doses were adapted according to beam and energy. Mono-cultures of unirradiated and irradiated cells served as controls.

To determine an influence of the co-culturing on the clonogenic survival, the cell lines were seeded together in culture flasks. The plating efficiency (PE), the colony size and the survival level of the co-cultures were compared to mono-cultures of unirradiated and irradiated cells.

Results

The radio resistance of RAT-1 cells against 250 kVp x-rays stayed stable over the whole experimental period whereas the radio resistance of the IEC-6 cells increased with ongoing passage number. The measured data show that RAT-1 cells are more radio resistant to carbon ions than IEC-6 cells.

Although in co-culture the colonies arising from different cell types could be easily distinguished according to their morphology (Fig. 1). The colony size of RAT-1 cells was unaffected but the colony size of unirradiated IEC-6 cells increased in co-culture. Figure 2 shows exemplary the influence of the co-culture when both cell lines were unirradiated or irradiated with 6 Gy (RBE). IEC-6 cells show independent of the irradiation modality a benefit of the co-culturing whereas RAT-1 cells were not affected.

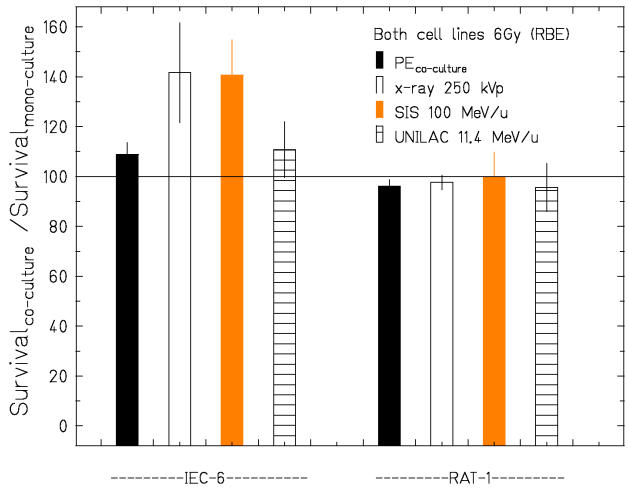

Figure 2: Influences in co-culture: IEC-6 cells (left) show a benefit and RAT-1 cells (right) no effect in survival. Error bars are standard error of the mean for PE (n= 7) and x-ray (n=5), carbon ions 10% error estimation

References

[1] Isaacs JT et al. The Prostate 9:261-281 (1986)
[2] A. Quaroni et al. J. Cell Biology, 80:248-265 (1979)

Induced apoptosis in tumour cells with different p53 status after X-ray and carbon ion exposures*

A.E. Meijer[1], M.R. Edgren[1], B.S. Eriksson[1], G. Alphonse[2], M. Maalouf[2], C. Rodriguez-Lafrasse[2], G. Becker[3], C. Fournier[3] and G. Taucher-Scholz[3]

[1]KI, Stockholm, Sweden; [2]Molecular and Cellular Radiobiology Laboratory, Lyon-Sud, France, [3]GSI, Darmstadt, Germany.

Introduction

Knowledge of the molecular pathways involved in cell death in tumour cells after exposure to accelerated ions could contribute to an improved prognosis of patients with malignant resistant tumours.

The aim of this study was to investigate the cellular and molecular responses induced by carbon ions at different linear energy transfer (LET) in human tumour cells with different p53 status. As previously reported, the tumour cell line with wild type (*wt*) p53; AA, is more radiation sensitive than the cell line with a p53 mutation; U-1690 [1].

Here we report on the levels of apoptosis, p53 and ceramide at comparable survival levels.

Materials and methods

Human melanoma cells (AA) with *wt* p53, and the small cell lung cancer cells (SCLC; U-1690) with a p53 point-mutation [2], were exposed to 30, 80 or 170 eV/nm ^{12}C-ions. As reference radiation low LET X-rays were used. Cell survival curves were established as basis for these studies on levels of apoptosis, p53 and ceramide. Morphological alterations were analyzed microscopically after dual staining with acridine and Hoechst 33342 [3]. The levels of p53 were determined by ELISA analysis and the levels of ceramide after HPLC analysis.

Results and conclusion

Apoptosis was induced after both X-rays and ^{12}C-ions (all data not shown). Low levels of apoptosis occurred early (1-10 h) in a dose dependent manner in both the AA and U-1690 cell line and increased with time (Figure 1) and LET.

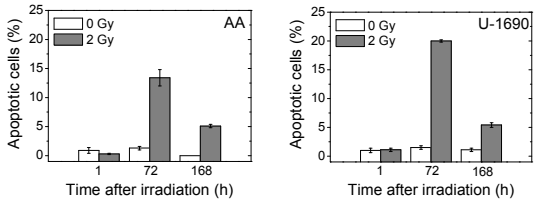

Figure 1: Percent apoptotic cells after exposure to 170 eV/nm ^{12}C-ions.

Exposures to X-rays and ^{12}C-ions increased the levels of p53 in both cell lines in a time (Figure 2) and dose dependent manner (all data not shown).

* Work supported by the Swedish Cancer Society, the Stockholm Cancer Society, the King Gustaf V Jubilee Found and Founds of the Karolinska Institutet.

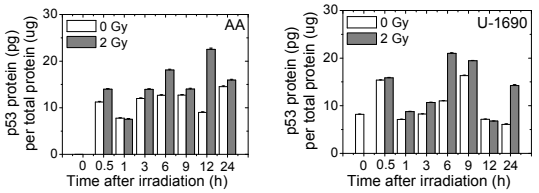

Figure 2: Levels of p53 after exposure to 170 eV/nm ^{12}C-ions.

The levels of ceramide increased with time in the U-1690 cells but not in the AA (Figure 3).

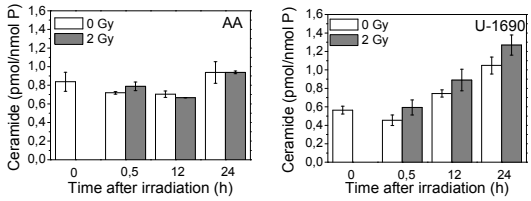

Figure 3: Ceramide levels after exposure to 170 eV/nm ^{12}C-ions.

In conclusion, we here show that apoptosis could be induced after exposures to accelerated carbon ions regardless the p53 status of the cells. However, since high LET radiation causes clustered damage it is most likely that there are several pathways in the process of apoptosis. When having a p53 mutation this pathway often is less pronounced and other pathways, as shown here, the ceramide pathway may be triggered.

References

[1] Meijer *et al.,* Annual GSI report 2006.
[2] Bergqvist *et al*, Anticancer Res 23:1207 (2003)
[3] Meijer *et al,* Int J Radiat Biol 81: 261 (2005)

Gene expression of angiogenic factors in A549 cells after carbon-ion and photon irradiation

F. Kamlah[1], A. Arenz[1], R. Engenhart-Cabillic[1], C. Fournier[2], J. Hänze[3], J. Juricko[1], F. Rose[1], M. Scholz[2], and G. Taucher-Scholz[2]

[1]Dept. of Radiotherapy and Radiooncology, University of Marburg, Germany; [2]GSI, Darmstadt, Germany; [3]Department of Internal Medicine II/V, University of Gießen, Germany

Radiation therapy is an integral part of the multi disciplinary therapy of lung cancer. Genetic changes and the specific tumor microenvironment favour therapy resistance of tumor cells. Clinical studies suggest that particle irradiation with carbon ions may improve the therapy response of solid tumors compared to photon radiation [1]. Occurrence of therapy resistance is related to secretion of growth and angiogenic factors that stabilize and promote the tumor vasculature [2]. Thus, we analyzed the effects of either carbon ion or photon irradiation on the gene expression of vascular endothelial growth factor (VEGF) and placental growth factor (PlGF). VEGF is a well established factor that promotes angiogenesis (extension of existing vessels) and PlGF is a factor that initiates de novo angiogenesis by recruitment of stem cells (vasculogenesis) [3].

Values for relative biological effectiveness after exposure to photon (6 MV-X) or carbon ion (11.4 MeV/u) irradiation were calculated from clonogenic survival experiments according to Puck and Marcus [4].

From these preliminary results we selected 6 Gy for photon- and 2 Gy for carbon ion irradiation for the further analyses of the expression of angiogenic factors.

The effect of irradiation was confirmed by the typical induction of CDKN1A mRNA in A549 cells (4 h and 24 h) that is observed by both photon- and carbon ion irradiation. Quantification of mRNAs for CDKN1A, VEGF and PlGF was performed by realtime RT-PCR (Figure 1).

Interestingly, carbon ion irradiation (4 h and 24 h) caused a significant induction of VEGF-mRNA and PlGF-mRNA. After photon irradiation a significant increase of VEGF-mRNA and PlGF-mRNA was observed after 4 h whereas no more changes could be demonstrated after 24 h. CDKN1A-mRNAs were significantly increased after photon- and carbon ion irraditation at both time points.

The expression levels of mRNAs are presented by the ΔCt values ΔCt = Ct (gene of interest) – Ct (house keeping gene). As a house keeping gene porphobilinogen deaminase mRNA was used, a gene that is constitutively expressed and not changed after irradiation. A lower ΔCt indicates a higher mRNA level (a difference of -1 corresponds approximately to a twofold increase between treated and control group).

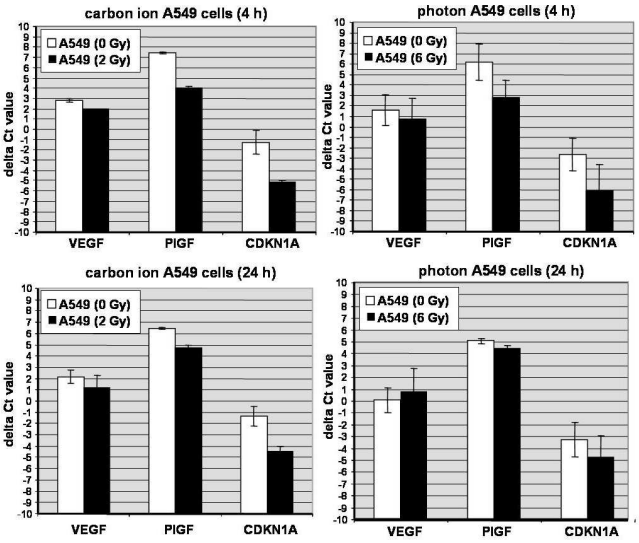

Figure 1. Realtime RT-PCR of VEGF-, PlGF- and CDKN1A-mRNAs after carbon ion and photon irradiation (4 h and 24 h).

In further experiments, we plan 1) to characterize the effects of irradiation on the protein levels of VEGF and PlGF, 2) to investigate whether the induction of VEGF and PlGF by irradiation is relevant in functional angiogenesis (matrigel plug assay).

References

[1] Hamada, N. (2008) *J Radiat Res (Tokyo)*

[2] Dewhirst, M. W., Cao, Y., and Moeller, B. (2008) *Nat Rev Cancer* **8**, 425-437

[3] Semenza, G. L. (2008) *N Engl J Med* **358**, 2066-2067

[4] Puck, T. T. (1955) *PNAS* **41,** *432-437*

Neoplastic Transformation Induced by Carbon Ions*

D.Bettega, †1, M.Catalano[1], P.Calzolari[1], P.Hessel[2], and W.K.Weyrather[2]
[1]Dept.Physics, Univ. of Milan and INFN, Italy; [2]GSI, Darmstadt, Germany

Besides the effect of the primary carbon ions, secondary beam fragments like neutrons and lighter ions which are produced by the primary beam have to be taken into account in risk calculation of carbon ion therapy [1]. This plays a major role in the fragmentation tail behind the Bragg peak. Though the absolute dose is low, a contribution to transformation can be expected, due to the high transformation efficiency of single high LET particles [2]. Regarding the promising results in the treatment of pediatric patients [3], this problem is of special interest. A series of experiments, which have been completed during the last year, have therefore been performed to investigate the oncogenic potential of a therapy-like carbon ion beam with special regard to the nuclear fragments effects.

Materials and Methods

An extended volume, simulating a tumor in a depth between 60 mm and 100 mm, was irradiated with an absorbed isodose of 0.75 Gy. Survival, neoplastic transformation and micronuclei induction were measured in CGL1 human hybrid (Hela X skin fibroblast) cells placed at 6 different positions, three in the entrance channel, one in the middle of the target volume and two beyond the target volume. Details on the protocol used for the transformation assay have been reported elsewhere [2]. Micronuclei induction was determined in binucleated cells 24 and 48 h after the irradiation using the standard cytochalasin based technique [4].

Results

The results are reported in Fig.1. For survival as well as for transformation induction the effect compared to the entrance channel is enhanced close to the tumor border and highest in the tumor volume. In the low dose range behind the target the effect on these endpoints is different: whereas survival is close to the control level, indicating no appreciable cytotoxic effects, neoplastic transformation exceeds the control level by a factor of about 3 and reaches nearly the effect in the entrance channel. The induction of micronuclei follows the transformation induction, indicating to be a probable alternative to the time and material consuming transformation measurements.
Comparison of the results of the present study to corresponding results after photon and proton irradiation with isotoxic doses to the same target volume would be a resonable basis to determine the relative risk of secondary cancers of these three different radiotherapy modalities.

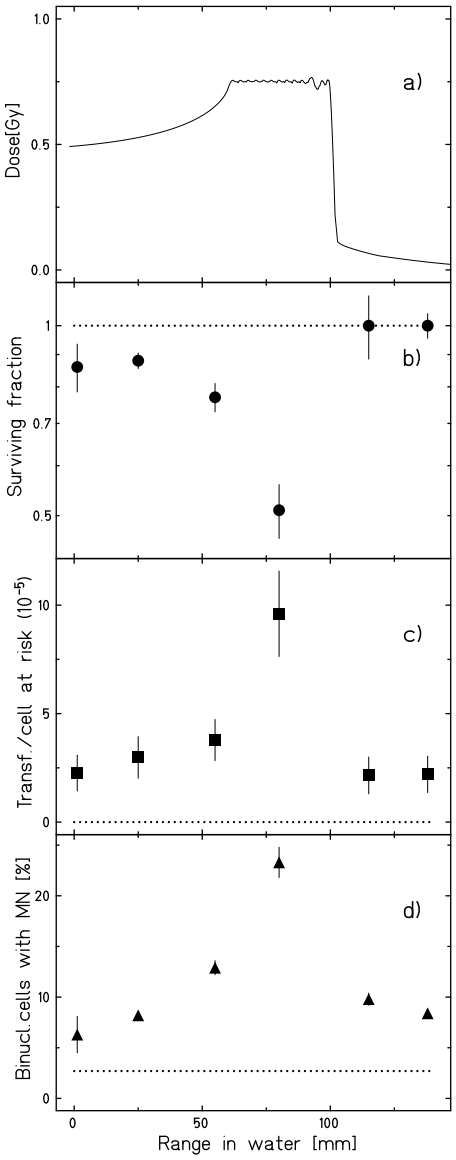

Figure 1: Doseprofile (a), clonogenic survival (b), transformation frequency per cell at risk (c), and frequency of micronuclei in binucleated cells (d). Data are the results of two independent experiments. Dotted lines show the control level.

References

[1] Gunzert-Marx et al., *New J. Phys.* 2008; 10 :075003-(21pp)

[2] Bettega et al., *Int J Radiat Oncol Biol Phys*in press

[3] Combs at al., *Cancer* 2009 Jan 20. [Epub ahead of print]

[4] Fenech et al., *Mutation Research* 2007; 600:58-66

* Work supported by EU, EURONS contract No. 506065.
† I3-EURONS (European Commission contract no. 506065)

Oxidative stress and telomere shortening in normal human fibroblasts after irradiation with X-rays*

S. Zahnreich[1], P. Boukamp[2], M. Colindres[1], N. Dencher[3], M. Durante[1], C. Fournier[1], M. Frenzel[3], D. Krunic[2], S. Ritter[1]

[1]GSI, Darmstadt, Germany, [2]DKFZ, Heidelberg, Germany, [3]TU Darmstadt, Germany

Introduction

Irradiation of normal human fibroblasts with X-rays has been reported to cause an intracellular accumulation of reactive oxygen species (ROS) [1]. The enhanced production of ROS is hypothesised to correlate with a continuous damage to cellular molecules, especially the DNA. In this context, the end-protecting structures of the linear human chromosomes are of particular interest, playing a major role in preserving genomic stability. Telomeres are very susceptible to oxidative damage and show a deficiency in the repair of single strand breaks, preferentially caused by ROS [2,3]. For our experiments normal human fetal fibroblasts originating from the lung were chosen because cells from that tissue have to cope with a relative high pO_2 and might dispose on well developed defence mechanisms. For X-rays and carbon ions a persistent increase of intracellular oxidative stress could be shown for several days after the irradiation in the descendants of the initially irradiated cells [1,4]. Interestingly this response was more pronounced in lung compared to other fibroblast cell strains.

Materials and Methods

To confirm these results in a second cell strain WI-38 fibroblasts were exposed to doses of 6 or 8 Gy of X-rays (250kV). The cells were harvested at different early time points or subcultivated in two-weekly intervals for long term cultivation. ROS were measured using the Dichlorofluorescein Assay for flow cytometry [2,5]. For the assessment of telomere length, fluorescence in situ hybridization, 3D image acquisition, deconvolutional microscopy and image processing were performed as described elsewhere [6].

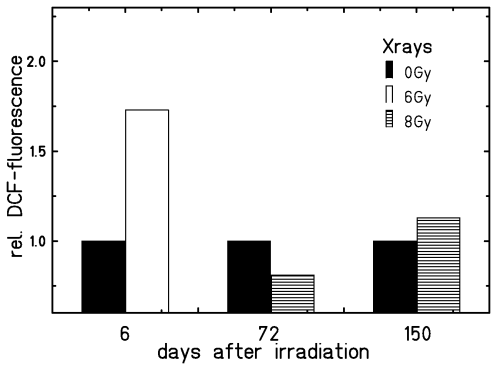

Figure 1: DCF-fluorescence indicating the intracellular ROS measured in WI-38 fibroblasts as a function of dose and time after irradiation (mean values from one to three independent experiments).

Results and Conclusion

In repeated experiments irradiated WI-38 cells showed a maximum response in ROS induction at 6 days after irradiation (Fig. 1). A higher, dose-dependant level of ROS was persisting even for 9 days after irradiation (data not shown). However, when the cells had already reached replicative senescence (72 and 150 days after exposure), no significant increase in the intracellular level of ROS could be observed in the progeny of 8Gy-irradiated cells compared to unirradiated senescent controls (Fig.1). However, most likely the level of intracellular ROS is higher in the senescent populations than in the young cells because this has been observed in other fibroblast cell strains [7]. A comparable accumulation of ROS in WI-38 cells remains to be shown.

An important effect that is considered to lead to the onset of senescence is the continuous shortening of telomeres correlated with an increased level of ROS. In order to find out whether this applies to WI-38 cells, we measured the mean telomere length in senescent compared to young cells (both unirradiated). As telomere shortening was observed (Fig.2) we plan to investigate the telomere length and functionality in the progeny of irradiated WI-38 cells.

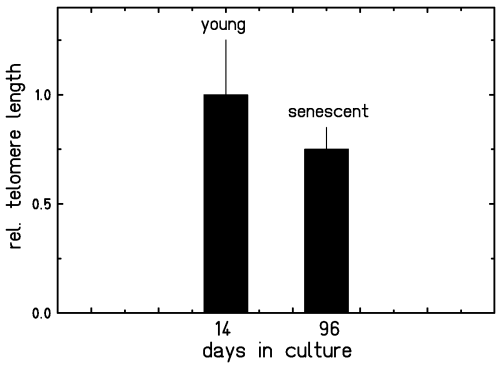

Figure 2: Mean telomere-signal intensities after IQFISH-staining for non-irradiated aging WI-38 fibroblasts.

References

[1] Rugo R. E. *et al.*, Rad. Res. 158, 2002, 210-219
[2] Oikawa S. & Kawanishi S., FEBS Letters 1999, 453, 365 -368
[3] Petersen S. *et al.*, Exp. Cell Res. 1998, 239, 152-160
[4] Colindres M. *et al.*, GSI Annual Report 2007, 365
[5] Hafer K. *et al.*, Rad. Res. 2008, 169, 460-468
[6] Ermler S. *et al.*, Eur. J. Cell Biol. 83, 2004, 681-690
[7] Frenzel, M. *et al.*, GSI Annual Report 2008,
[8] Fournier C. *et al.*, Radiotherapy and Oncology 83, 2007, 277-282

* Work supported by BMBF (Bonn), grant 02S8497

Radiation induced apoptosis in CD34+ hematopoietic stem cells after exposure to x-rays or carbon ions

D. Becker[1,3], M. Durante[1], C. Fournier[1], R. Marschalek[2], S. Ritter[1], T. Tonn[3]
[1]GSI, Darmstadt, Germany; [2] Faculty of Pharmacology, Johann Wolfgang von Goethe University, Frankfurt, Germany;
[3]Institute for Transfusion Medicine and Immunohaematology, Frankfurt, Germany

In multicellular organisms stem cells are involved in tissue regeneration, which is regulated by apoptosis (programmed cell death). An early event of apoptosis is the externalisation of membrane phospholipids to the extracellular environment, on which Annexin-V is able to bind with a high affinity. The later stages of apoptosis are characterized by the loss of plasma membrane integrity, DNA fragmentation, and chromatin condensation (overview in [1]). DNA fragmentation can be measured using the TUNEL assay (terminal deoxynucleotidyl transferase-mediated dUTP nick end-labeling), in which labeled nucleotides are incorporated into the 3'OH recessed termini of radiation induced DNA breaks. The occurrence of radiation induced apoptosis is in particular in proliferating cells an important factor in assuring the correct transmission of genetic information, because damaged cells are eliminated from the population [2].

To investigate the occurrence of apoptosis hematopoietic stem and progenitor cells (HSPCs) were collected by apheresis of healthy, G-CSF treated donors. Following CD34+ enrichment by immunomagnetic separation, HSPCs were exposed to either x-rays (16mA, 250kV) or carbon ions (100MeV/u, 29keV/µm). The Annexin-V and TUNEL assays were used to measure radiation induced apoptosis by microscopic or flow cytometric analyses (Annexin-V-FLUOS and In Situ Cell Death Detection Kit, Fluorescein, Roche).

In first experiments on the protective role of cytokines [3], the cells were cultured in serum-free expansion medium, supplemented or not with different cytokines (StemCell Technologies Inc.). Without cytokines we observed apoptosis in unirradiated HSPCs, with an increasing frequency with progressing culture time (figure 1).

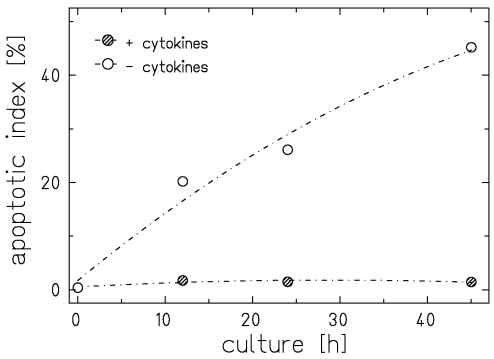

Figure 1: The percentage of apoptotic HSPCs at different time points (up to 48h) in expansion medium, (-) without cytokines or (+) supplemented with cytokines (TUNEL, microscopic analysis).

In the following irradiation experiments we focused on the induction of apoptosis in HSPCs compared to lymphocytes, comparing the effects of carbon ions and conventional photon irradiation. We observed a radiation induced, dose-dependent increase in apoptotic cells with time (not shown), but no pronounced difference in kinetics for x-rays and carbon ions. Comparable data were obtained in preliminary experiments for lymphocytes [4]. In figure 2 the increase in apoptotic cells 24h after exposure to 1Gy x-rays or carbon ions is exemplarily shown. The observed induction of apoptosis was comparable for both methods (TUNEL and Annexin-V) indicating a slightly higher apoptotic index for carbon ions compared to x-rays. Furthermore we compared the induction of apoptosis after exposure to 1Gy x-rays in HSPCs (cultured with cytokines) and lymphocytes (stimulated with PHA), which were isolated from the same donor. The apoptotic response was similar in both cell types.

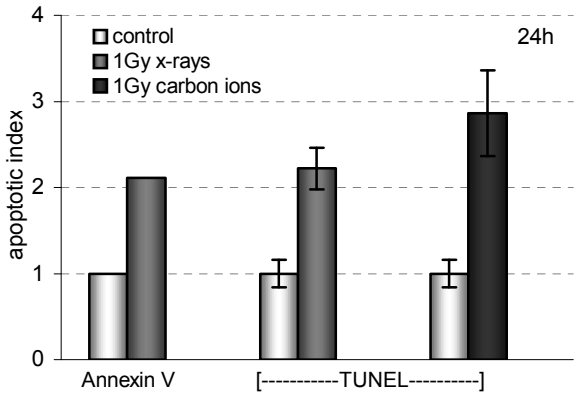

Figure 2: Apoptotic index of HSPCs 24h after exposure to 1Gy x-rays or carbon ions (Annexin-V n=1, TUNEL assay, n= 3).

Taken together, the results confirm that cytokines are essential for cell survival and cell expansion of HSPCs. The amount of apoptotic cells increases dose-dependently and with time. Carbon ions are only slightly more efficient than x-rays in inducing an apoptotic response. This is in line with results obtained on clonogenic survival [5].

References

[1] Granville D. J., Carthy C. M., Hunt D., McManus B. M., Laboratory Investigation, Vol. 78, No. 8 (1998)
[2] Amenomori, T. et al (1985), Int. J. Cell Cloning 3, 133-142.
[3] Drouet M., Mathieu J., Grenier N., Multon E., Sotto J.-J. and Herodin F., Stem Cells 17:273-285 (1999)
[4] Lee R., Nasonova E., Ritter S., Advances in Space Research 35:268-275 (2005)
[5] D. Becker, C. Fournier, S. Ritter, R. Marschalek, T. Tonn, Annual GSI report (2007)

Reactive oxygen species are involved in senescence of human cells independently from irradiation exposure

M. Frenzel[1], N. A. Dencher[1], C. Fournier[2], S. Ritter[2] and S. Zahnreich[2]
[1]Technische Universität Darmstadt; [2]GSI, Darmstadt, Germany

Introduction:
Increasing evidence is provided that during ageing reactive oxygen species (ROS) accumulate in cells (1). Upon irradiation, cells undergo senescence earlier compared to the non-irradiated controls. Exposure to X-rays or heavy ions induces an increase in the intracellular level of ROS over several days (2). To assess whether ROS accumulation leads to genetic instability in the progeny of irradiated human fibroblasts, several cell strains of different origin were irradiated with X-rays and carbon ions. The ageing process and the effect of oxidative stress will be studied for each cell-line. Besides cell-line specific differences, also the effect of X-rays compared to heavy ions will be analysed.

Materials and Methods:
Confluent normal human dermal fibroblasts (NHDF) were irradiated with X-rays (8 Gy). The cells were subcultured the first day after irradiation and thereafter every second week. At different time points cells have been harvested for various measurements. The intracellular ROS-levels in the progeny of irradiated cells were analysed (25 µM 2´,7´-Dichlorodihydrofluorescein in PBS, 37°C, 30 min; 4 µM Dihydroethidium in PBS, 10 min, flow cytometry) at intermediate and late time points.

Results and Conclusions:
NHDF cells were subcultured for 179 days after X-ray exposure (fig. 1). No significant radiation induced changes in population doubling occures.

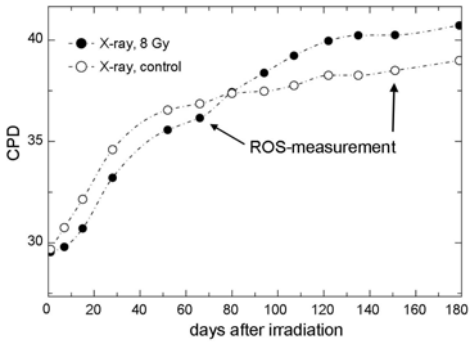

Fig. 1: Growth curve of irradiated (filled circle) and control (open circle) NHDF cells. Cell population doubling (CPD) is blotted versus culture days after irradiation.

During the first two weeks after irradiation the intracellular ROS is increasing till 6 days after exposure (2). To study the long-term effect of irradiation, ROS-levels were measured after 66 and 151 days (fig. 2).

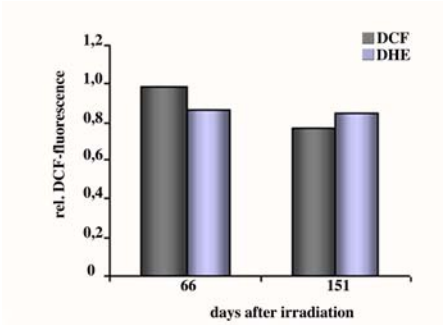

Fig. 2: Intracellular ROS-level in NHDF cells 66 and 151 days after irradiation with X-rays as compared to control.

No significant changes were observed in progeny of irradiated cells compared to the control. To reveal if there is an age-related increase of ROS in long-term cell culture, the mean DCF-fluorescence of non-irradiated young (14 days in culture) and aged progeny of irradiated (8 Gy) and control (164 days in culture) NHDF cells were compared (fig. 3).

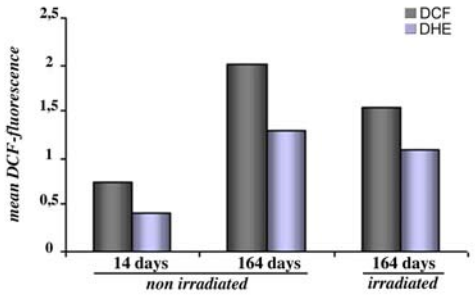

Fig. 3: ROS-level in non-irradiated young (14 days in culture) and in aged progeny of irradiated (8 Gy) and control (164 days in culture) NHDF cells.

Comparison of ROS-levels in long-time subcultured progeny of irradiated and control NHDF cells (fig. 2, 3) demonstrate, that there is an age-related increase of ROS indepently of irradiation exposure.
To clarify why irradiated cells undergo early senescence, NHDF cells have been irradiated with X-rays and afterwards harvested at different times. Samples for different cellular responses have been collected. Changes in mitochondrial proteome, telomere length, chromosomal aberration frequency, differentiation pattern and the level of apoptosis will be analysed.

References:
[1] R. S. Balaban *et al.*, Cell, 2005, 483-495
[2] M. Colindres *et al.*, GSI-report 2007

The apoptotic response following low and high LET radiation involves production and release of ceramide*

M. Maalouf[1], G. Alphonse[1], M. Durante[2], C. Fournier[2], G. Taucher-Scholz[2] and C. Rodriguez-Lafrasse[1]

[1]Laboratory of Molecular and Cellular Radiobiology, EA3738, Lyon, France; [2]GSI, Darmstadt, Germany

Although mutations in the p53 gene can lead to resistance to radiotherapy, high linear energy transfer (LET) radiation induces apoptosis independently of p53 gene status in cancer cells (1). However the mechanisms involved in high LET radiation-induced apoptosis are not well characterized. Our laboratory and others (2) have demonstrated that ceramide generation is a key and determining event in X-ray radiation induced p53-independent apoptosis. However nothing is known about the putative implication of this lipid second messager in high LET ions induced-cell death.

We have previously reported (3) that carbon irradiation is more efficient in inducing clonogenic cell death than X-rays in two head and neck squamous carcinomas (HNSCC) cell lines which are both p53 mutated. In one of the cell lines, SCC61 (sensitive to X-rays) we observed an early p53-independent apoptosis after X-ray and carbon ion irradiation. In contrast, the SQ20B cells (resistant to X-rays) underwent a cell cycle arrest followed by a delayed cell death at 120h after carbon exposure. The aim of this study was to clarify the mechanisms involved in high LET radiation-induced p53-independent apoptosis. Thus the role of ceramide has been investigated after carbon ion irradiation in three cell lines with different p53 status and different radiosensitivities.

Two HNSCC cell lines (SCC61 and SQ20B, both p53 mutated) and one glioblastoma cell line (U87, p53 wild type) were irradiated with X-rays and carbon ions (9,8 MeV/n). Ceramide levels were measured by High Performance Liquid Chromatography (HPLC). For apoptotic cell death studies, the activity total caspases was analysed by flow cytometry.

In the SCC61 cells (p53 mutated), an increase in the level of ceramide was observed 48h after irradiation (Fig.1).

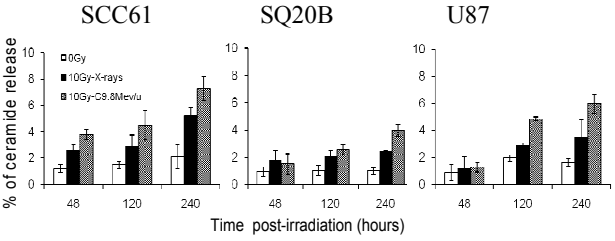

Fig.1: Kinetics of ceramide levels after irradiation

The ceramide production was time and LET dependent (Fig.1) and occurred concomitantly with the induction of apoptosis (Fig.2).

In SQ20B cells (p53 mutated), the ceramide levels increased starting from 120h similar to that of apoptosis and were higher after carbon exposure compared to X-rays. Interestingly, in U87 cells (p53 wild type) ceramide was also produced in a time and LET dependent manner, concomitantly with apoptosis, starting from 120 hours following carbon ions. Thus, high LET irradiation enhances ceramide production independently of the p53 status.

On the other hand, following X-ray irradiation we have observed that the inhibition of the ceramide production in SCC61, SQ20B and U87 cells led to a suppression of apoptosis (data not shown). Thus ceramide appears to be a determining factor in the process of apoptosis following irradiation.

Moreover, we analysed the onset of apoptosis in more detail by measuring the activation of the caspases, a key event in the apoptotic process.

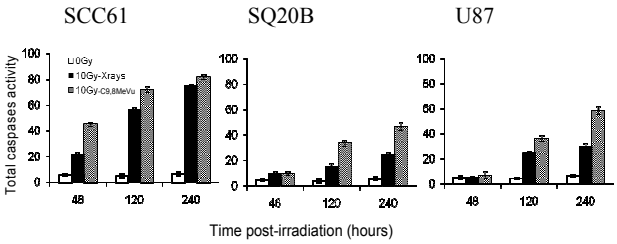

Fig.2: Total caspases activity following irradiation

As shown in Fig. 2, carbon irradiation increased the total caspases activity compared to X-rays, starting from 48 hours for SCC61 cells and from 120 hours for SQ20B and U87 concomitantly to the ceramide release.

Taken together these results suggest that comparable to the observation upon X-ray irradiation, carbon ion irradiation leads to apoptosis via the release of ceramide and the activation of the caspases. Moreover it seems that this apoptotic pathway occurres independently of the p53 status. These studies can provide new insights into the role of ceramide following heavy ion irradiation. Further experiments are in process in order to investigate the contribution of ceramide following carbon exposure.

[1] Yamakawa *et al.* Cancer Sci. 2008
[2] Alphonse *et al.* Int. J. Radiat. Biol 2002.
[3] M Maalouf *et al*. Int. J. Rad. Oncol. Biol. Phys. 2009.

* Work supported by Contract de Plan Etat-Region-ETOILE and EU, EURONS contract No. 506065.

Biological Dose Optimization Using the Levenberg-Marquardt Method

M. Horcicka, A. Gemmel, M. Durante, and M. Krämer
GSI, Darmstadt, Germany

Introduction

The treatment planning software TRiP98 [1, 2, 3] is successfully used in the ion therapy project at GSI. A crucial part of the treatment planning is the particle number optimization in order to achieve a target dose distribution as close as possible to the prescribed biological dose distribution. The optimization task can be expressed mathematically by the minimization of a multidimensional objective function by means of the least squares method. In this contribution we examine the Levenberg-Marquardt method (LMM), used to handle the optimization problem.

Materials and Methods

The objective function is defined as follows:

$$X^2(\vec{N}) = \sum_{i \in Target} \frac{(D_{pre} - D^i_{bio}(\vec{N}))^2}{\Delta D^2_{pre}} + \sum_{i \in OAR} \frac{(D_{max} - D^i_{bio}(\vec{N}))^2}{\Delta D^2_{max}} \cdot \Theta(D^i_{bio}(\vec{N}) - D_{max}) \; .$$

$\vec{N}$: vector that contains the particle numbers
D_{pre} : prescribed dose within the target
D_{max} : maximum dose within OAR (Organ-At-Risk)
D^i_{bio} : actual biological dose at voxel i
Θ : Heaviside function

Due to the nonlinearity of $D^i_{bio}(\vec{N})$ in the parameters $\vec{N}$ the equation $\vec{N}_{opt} := \nabla X^2(\vec{N}) = \vec{0}$ can only be solved with numerical methods. We tested the LMM which is a standard algorithm for nonlinear least squares problems. Various versions exists of the LMM. We implemented a version which is described in detail in [6]. The number of voxels i and the dimension of the vector $\vec{N}$ are several tenthousands. Therefore, iterations are time-consuming and require a lot of memory.

Results and Discussion

Last year we reported about the examination of three other numerical algorithms used to minimize $X^2(\vec{N})$ [4]. The results showed, that the method of steepest descent (SD) [6] has the best numerical properties. But computation times are still an issue.

The results of the LMM in comparison with the results of the SD are illustrated in figure 1 and figure 2. The data were taken from the patient plan #135 and performed on a reference device, a single 1.2 GHz Power4 CPU of an IBM p630 server. The LMM shows a very good convergence speed in terms of iteration steps. However, due to the handling of huge systems of linear equations the computation times of the LMM are very long.

Examinations showed that the coefficient matrices of the systems of linear equations have a sparse pattern [5]. Hence, the matrices would be better organized as a list and the systems of equations could be solved with Krylow-Subspace methods. Currently we are working on this issue.

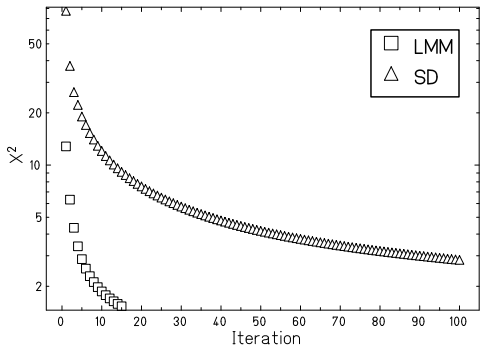

Figure 1: Convergence speed as a function of iterations.

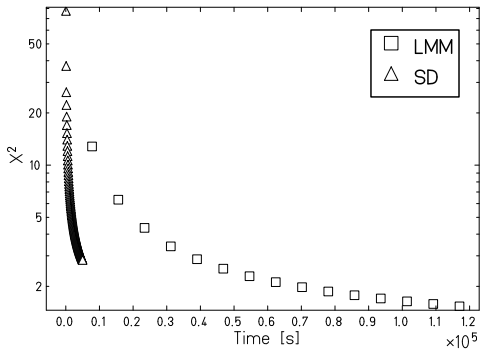

Figure 2: Convergence speed as a function of time.

References

[1] M. Krämer et al, Phys. Med. Biol., 45/11 (2000) 3299.
[2] M. Krämer et al, Phys. Med. Biol., 45/11 (2000) 3319.
[3] O. Jäkel et al, Phys. Med. Biol., 46/4 (2001) 1101.
[4] M. Horcicka et al, GSI Scientific Report 2007, 376.
[5] M. Horcicka, *Mehrfelderoptimierung für die biologisch effektive Dosis in der Schwerionentherapie: Nichtlineare Methoden und numerische Analyse*, Dipl.-Thesis, GSI (2008).
[6] B. P. Flannery et al, *Numerical Recipes in C - The Art of Scientific Computing*, Cambridge University Press, Second Edition (1992).

Different track structure representations as input for the Local Effect Model

Th. Elsässer, R. Cunrath, M. Durante, M. Krämer, and M. Scholz
GSI, Darmstadt, Germany

Introduction

Treatment planning for ion therapy requires precise knowledge about the biological effectiveness of particle beams, which is strongly determined by the microscopic radial energy deposition around individual ion tracks. Therefore, we applied the Local Effect Model (LEM) to investigate the dependence of the relative biological effectiveness (RBE) on different representations of the radial dose distribution.

Track Structure

We used three different classes of models for the radial dose distributions, namely amorphous descriptions with a core radius r_{min} independent of the ion energy (CR), with core radii that are energy-dependent (EDR, KC) and dose distributions generated with a Monte Carlo (MC) code [1]. The CR representation is used in the first two versions of the LEM I,II assuming a constant track center of 10nm (CR10) and 0,3 nm (CR03), respectively. The latest model implementation LEMIII acknowledges the energy dependence of the track core and assumes a maximum core radius of 40nm (EDR40). Additionally, we use the Kiefer-Chatterjee (KC) track structure recently introduced in the framework of the Microdosimetric Kinetic Model (MKM) [2]. The MC calculations are performed with the TRAX code, which was developed at GSI [3].

In Figure 1 we show the different dose distributions around 11 MeV/u carbon ions after convolution with a two-dimensional Gaussian function accounting for radical diffusion. Whereas the dose in the outer track region is similar in all cases, the differences in the track core amount to more than an order of magnitude.

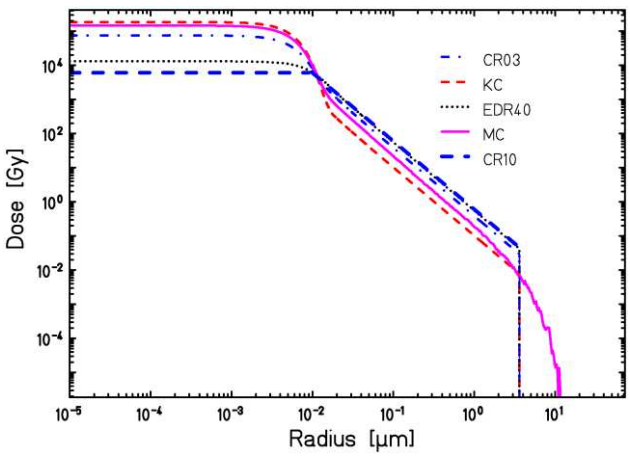

Figure 1. Radial dose distributions around 11 MeV/u carbon ions for different track structure models.

RBE calculations

Based on the dose distributions presented in the previous section, we applied the Local Effect Model to experimental data for cell inactivation of HSG cells after carbon ion irradiation for different linear energy transfers (LET). As depicted in Fig. 2, the RBE is extremely sensitive to the inner part of the track, since the RBE values correlate with the dose in the track center. In this case, the semi-free model parameter D_t was adjusted to give the best results for LEM II (CR03). For other values of D_t, the theoretical results are in better agreement with other model versions. However, the differences arising from track structure representations remain.

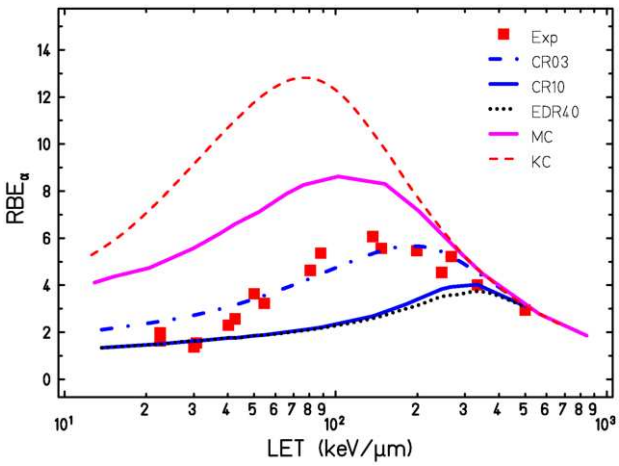

Figure 2. RBE of the initial slope for cell inactivation of HSG cells after carbon ion irradiation. Experimental data by [4].

Conclusion

We compared different amorphous track structure representations and showed that they nearly coincide at large distances from the trajectory, whereas they significantly differ at small radii in the track centre. We found that the RBE calculations are very sensitive to that inner part of the dose distribution. Therefore, it is of utmost interest to further study ion-matter interaction at low distances from the ion path over the entire range of therapy-relevant specific energies between 1 MeV/u and 400 MeV/u theoretically and experimentally.

References

[1] Elsässer et al. 2008 *NJP* **10** 075005
[2] Kase et al. 2008 *Phys.Med.Biol.* **53** 37-59.
[3] Krämer et al.1994 *Radiat.Env.Biophys.* **33** 91-109
[4] Furusawa et al. 2000 *Radiat.Res.* **154** 485-496

Effect of cell migration on space radiation leukemia risk

Th. Elsässer[1], M.Y. Kim[2,3], F. Cucinotta[3]
[1]GSI, Darmstadt, Germany; [2]USRA, Houston, USA; [3] NASA Johnson Space Center, Houston, USA

Introduction

The leukemia risk associated with solar particle events constitutes a major hazard for astronauts on missions in deep space. In recent years experimental work has been largely increased to elucidate the mechanisms of leukemia induction. Here, we report on the application of a leukemia risk model that was successfully applied in the framework of conventional radiotherapy in order to estimate the leukemia risk for an energy spectrum like the 1972 solar particle event. We additionally investigate the possible effect of cell migration on the risk predictions.

Model of leukemia risk

The biologically motivated model of Shuryak et al. [1] assumes that hematopoetic stem cells are the main target for leukemia induction. These cells undergo the processes of inactivation, initiation, repopulation and migration. Whereas cell killing and initiation occur immediately during radiation exposure, repopulation and migration may take up to several months. The number of premalignant stem cells at that time is matched with atomic bomb survivor data to estimate the leukemia risk.

Application to solar particle events

In addition to the parameters describing the biological processes, the dose distribution in the active bone marrow needs to be known as accurately as possible. Therefore, we simulated the effective dose in the blood forming organs in the MAX phantom after exposure to the energy spectrum of the solar particle event of 1972 behind 5g/cm^2 shielding and grouped it in six compartments (see Table 1) [2]. In Figure 1, the dose dependence of the excess relative risk (ERR) is depicted for three different scenarios calculated by the leukemia model. The first assumes a homogeneous dose distribution among the bone marrow compartments and no migration, the second acknowledges the dose distribution of Table 1, and the third curve takes cell migration between different compartments into account. The ERR dependence on the average dose in the bone marrow for a homogeneous dose distribution is mainly governed by the linear-quadratic initiation term, whereas the dose distribution of Table 1 increases the leukemia risk due to the contribution of the high-dose skull compartment. Most interestingly, the effect of cell migration between bone marrow compartments drastically reduces the risk. Intuitively, the high-dose compartments will be mainly repopulated by healthy stem cells from other compartments, effectively suppressing repopulation of premalignant stem cells that eventually develop cancer. The average dose deposition in blood forming organs for the SPE 1972 was about 330mSv behind 5g/cm^2 shielding material and a corresponding excess relative risk of 1. As a consequence more shielding needs to be considered in order to protect astronauts from SPE, since the acceptable risk of 3% probability of cancer death corresponds to an ERR of 0.13. However, for all realistic scenarios in space shielding material on the order of 15-20 g/cm^2 is projected.

bone marrow compartment	active bone marrow [%]	effective dose [mSv]
spine	42,3	172
ribs	24	370
pelvis	17,5	119
skull	8,4	1483
arms	1	247
legs	6,8	307

Table 1. Dose distribution in different bone marrow compartments and the corresponding precentage of active bone marrow

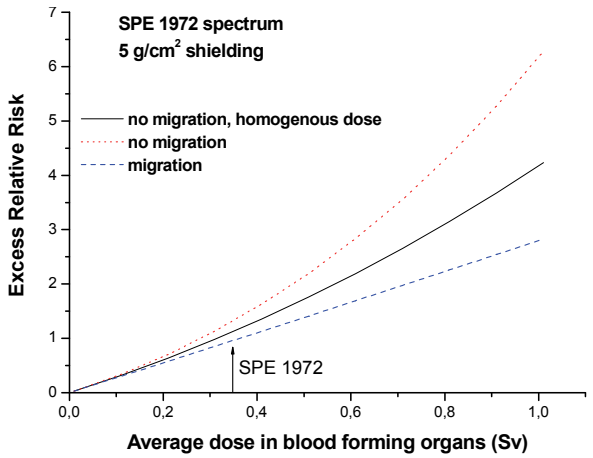

Figure 1. Excess relative risk (ERR) for leukemia induction for astronauts exposed to radiation with an energy spectrum of the 1972 SPE.

Conclusion

We calculated the ERR for leukemia induction following a solar particle event with a spectrum of the SPE of 1972 and found that the consideration of cell migration significantly alters the risk estimation for astronauts. In future calculation for the design of radiation shelters, migration of hematopoetic stem cells should be considered when estimating the leukemia risk.

References

[1] Shuryak et al. 2006 J.Natl.Cancer Inst. 98 1794-1806.
[2] Kim et al. 2009, sumbitted to Advances in Space Research

TRAX simulations

M. Krämer[1], M. Fernandez[1], T. Elsässer[1], M. Scholz[1], and M. Durante[1]
[1]GSI, Darmstadt, Germany

The successful outcome of the GSI radiotherapy pilot project is owed to a significant extent to the realistic predictions of radiobiological modelling (Local Effect Model, LEM). With more widespread use of ion radiotherapy the necessity of more sophisticated and more accurate predictions arises, which most certainly will involve more detailed knowledge about basic interactions of ions and electrons with living matter.

The Monte Carlo track structure code TRAX [1], developed at GSI Biophysics over several years [2], seems to be the right tool for this task. Its design point is the simulation of ion-matter interaction on the microscopic scale to obtain quantities like radial dose profiles, microdosimetric distributions or stochastic energy deposition patterns across tiny structures like a cell nucleus. Various enhancements have been made, in order to support improvements of radiobiological modelling.

Cross sections

The most important ingredients for MC calculations are the cross sections for the elementary interactions the model desires to describe. In our case these are on one hand the basic cross sections governing electron transport (elastic scattering, excitation, ionization). However, the initial distribution of δ-electrons will play an important role as well for the microscopic dose distribution around an ion's path. For one of our main goals, i.e. improving radiobiological modelling with the Local Effect Model (LEM), the inner part of the ion track is currently of particular interest. Thus the double differential δ-electron emission cross sections deserve more attention at low electron energies. In order to allow comparative calculations with different sets of initial cross sections, TRAX is now enabled to cope with external tables of total, single and double differential cross sections. In Fig.1 we compare radial dose distributions based on different sets of cross sections [3]. CDW-EIS based cross sections are expected to be superior to BEA at low energies and hence low distances (Fig. 2), and indeed the dose deposition is reduced by about 30%. Independent radiobiological observations suggest this to be the right direction. The curve identified as "empirical" is based on BEA angular distributions together with the empirical energy differential cross sections according to Rudd [4]. This curve shows best agreement in this case, but the Rudd model is based on available experimental data and thus has a limited range of validity. The CDW-EIS calculations seem to overestimate the dose deposition at larger radii (corresponding to higher electron energies), hence further checks are necessary. Systematic investigations with heavier projectiles and higher energies will follow in the future.

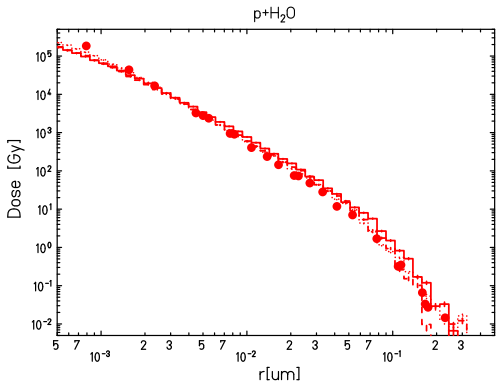

Figure 1: Radial dose distributions in water vapour scaled to liquid density. Symbols: experiment [5]. Curves are calculations based on CDW-EIS [6] (solid), BEA (dotted), empirical (dashed, see text)

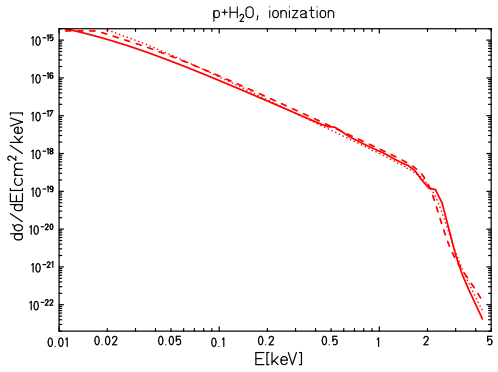

Figure 2: Energy differential cross sections for 1 MeV p on water. Curves are calculations based on CDW-EIS [6] (solid), BEA (dotted), Rudd (dashed)

References

[1] http://bio.gsi.de/DOCS/trax.html

[2] Krämer M., Kraft G. Calculations of heavy-ion track structure Radiat. Environ. Biophys. , 33 (2) :91-109 (1994)

[3] GSI Report 2007

[4] M. E. Rudd et al., Rev. Mod. Phys., 64/2 (1992) 441

[5] C.L. Wingate, J.W. Baum, Radiat. Res. 65:1-19 (1976)

[6] DSF Crothers, JF McCann Journal of Physics B: Atomic and Molecular Physics, 1983

Angular distribution of hydrogen- and helium-fragments produced by 200 MeV/u ^{12}C beams stopping in water

H. Iwase[1] and D. Schardt[2]
[1]KEK, Radiation Science, Tsukuba, Japan; [2]GSI/Biophysics, Germany

The characteristics of secondary fragments produced by high-energy ^{12}C beams stopping in water was investigated in earlier experiments [1,2] in Cave A, providing benchmark data for the physical model of the treatment planning system of the therapy pilot project at GSI. Light charged fragments produced along the penetration path of the primary ions are of particular importance as they have long ranges and form the main part of the long dose tail behind the Bragg peak which is a typical feature of the depth-dose profile of heavy ions.

The aim of this work was to study the angular distribution of light fragments (mainly protons and α-particles) for a wide angular range from 0° to 120°. A sketch of the experimental setup is shown in Fig.1. Secondary light charged fragments escaping the water phantom were identified with a ΔE-E telescope detector (see Fig.2). The data were normalized to the number of incident ^{12}C ions monitored by a parallel-plate ion chamber (IC).

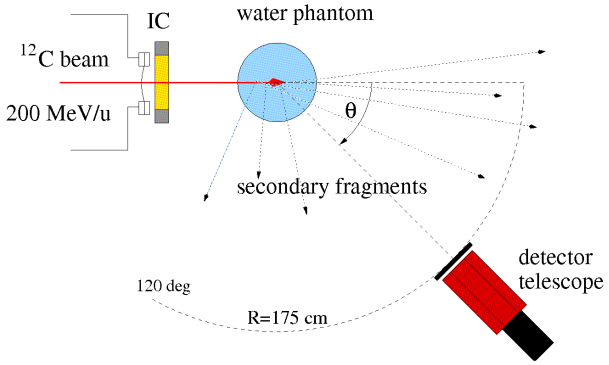

Figure 1: Experimental setup used for detecting light fragments produced by a primary ^{12}C beam in a cylindrical water phantom of 15 cm diameter. The range of the primary beam in water is 8.57 cm.

The resulting angular distributions (Fig.3) are in good agreement with previous data taken for 0° – 30° [1] and with calculations with the Monte-Carlo code PHITS.

Helium fragments are emitted in a sharp forward cone within about 10°, while hydrogen fragments exhibit a broader distribution, decreasing by three orders of magnitude from 0° to 90°. These data confirm the steep lateral dose fall-off [3] which is an advantage of ion therapy, in particular for the treatment of deep-seated tumors.

Potential applications of promptly emitted secondary radiation for in-vivo imaging of dose delivery in particle therapy will be investigated in the frame of the ENVISION-project (EU FP7-program). First experiments [4,5] on prompt photon emission show a clear correlation of the measured depth-profile of the photon intensity with the Bragg curve. Similarly, promptly emitted light fragments emerging from the patient's body might be utilized for imaging and verification of the treatment dose delivery.

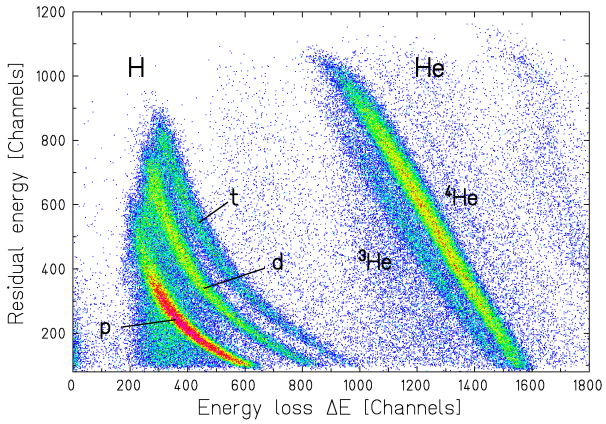

Figure 2: Correlation of energy loss ΔE and residual energy E measured with the telescope detector (θ = 5°). Secondary protons (p), deuterons (d), tritons (t), ^{3}He and ^{4}He can be identified.

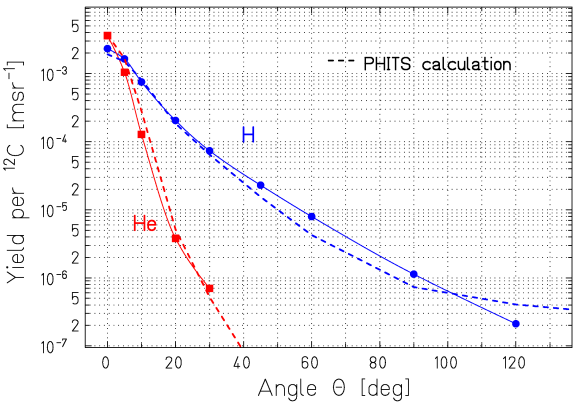

Figure 3: Measured angular distribution of hydrogen- and helium fragments (solid points) compared to calculations with the Monte-Carlo code PHITS (dashed lines).

References

[1] K. Gunzert-Marx et al., New J. Phys. 10 (2008) 075003
[2] E. Haettner et al., Rad.Prot.Dosim. 122, 485 (2006)
[3] G. Martino et al., contribution to this report
[4] C.H. Min et al., Nucl. Instrum. Meth. A580, 562 (2007)
[5] E. Testa et al., Appl. Phys. Lett. 93, 093506 (2008)

Microdosimetric characterization of 300 MeV/u ^{12}C beams in water

G. Martino, M. Durante, O. Kavatsyuk, and D. Schardt
GSI, Darmstadt, Germany

Microdosimetry measurements have been carried out in Cave A to investigate the radiation field produced by ^{12}C pencil-like beams stopping in water and to study the dose fall-off as a function of distance from the beam axis [1]. For this purpose, a water phantom was irradiated by a 300 MeV/u ^{12}C beam with 2 mm spot size. Microdosimetric spectra were recorded moving a Tissue-Equivalent-Proportional-Chamber (TEPC) to 50 different positions inside the water phantom, along the beam axis and on the lateral side. As the lateral spread of heavy ions is very small the main contribution to the lateral dose comes from secondary fragments which are produced in nuclear reactions.

The TEPC is a proportional counter that employs a spherical chamber with an inner diameter of 12.7 mm and a wall thickness of 1.27 mm. The detector has tissue equivalent wall and filling gas. Its purpose is to measure the dose to small volumes of human tissue replacing it by a larger cavity filled with gas of lower density. A density of 0.21 mg/cm^3 simulates a diameter of 2.7 μm of biological tissue. The TEPC is equipped with a built-in ^{244}Cm α source used for the lineal energy calibration. The off-axis lineal energy spectra are characterized by peaks around 5 keV/μm (Fig.1).

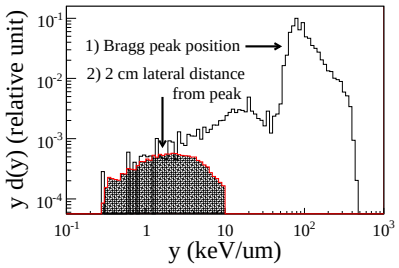

Figure 1: Two lineal energy spectra: 1) measured in the Bragg peak position along the beam axis; 2) measured at 2 cm lateral distance from the Bragg peak.

Absorbed doses were obtained by integration of microdosimetric spectra. They are normalized to the number of incident particles measured with an ionizing chamber (IC) (Fig.2). Along lines parallel to the beam axis (Fig.3) the dose curves, as a function of depth, show a typical grow-in part due to the build-up of secondary fragments including neutrons. The dose characteristics along lines perpendicular to the beam axis (Fig.4) show a steep fall-off. At larger distances from beam axis the fall-off is slower. Here the main contribution comes from light secondary fragments, such as protons and neutrons, which have much broader angular distributions than the heavier fragments.

The measured doses were found to be in good agreement with a similar study at HIMAC (Japan) [2].

These results confirm that the lateral dose characteristics of carbon ion beams used in radiotherapy shows an extremely steep decrease with distance from the beam axis.

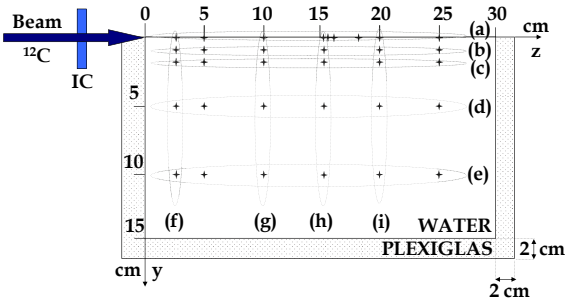

Figure 2: Schematic view of measurement positions in a horizontal section of the water phantom half side.

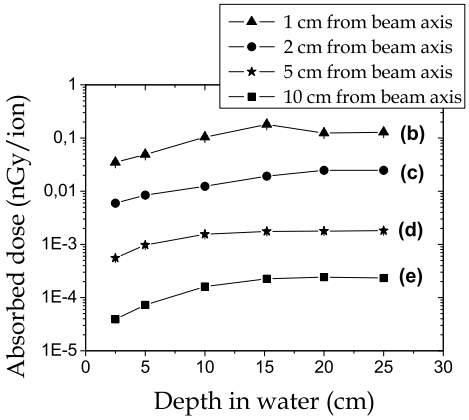

Figure 3: Absorbed dose parallel to the beam axis.

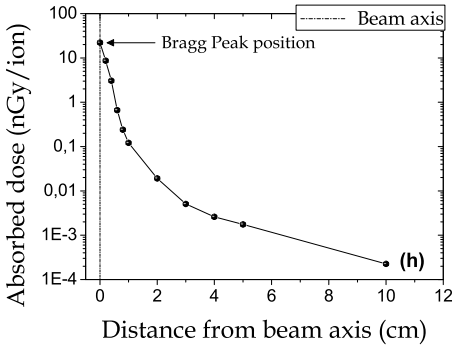

Figure 4: Absorbed dose perpendicular to the beam axis.

[1] S. Tsuda *et al.*, GSI Report 2006, p. 367.
[2] S. Endo *et al.*, Med. Phys. 34(9), Sep. 2007, p. 3571.

On the accuracy of range determination from in-beam PET data *

F. Fiedler[1], G. Shakirin[1], J. Skowron[1,4], H. Braess[3], P. Crespo[1,2], D. Kunath[1,5], J. Pawelke[1,5], F. Pönisch[1,6], and W. Enghardt[1,5]

[1]FZD, Forschungszentrum Dresden-Rossendorf; [2]now with: LIP, University of Coimbra, Portugal; [3]Siemens Health Care, Particle Therapy; [4]now with: IBA Dosimetry GmbH; [5]also with: Oncoray - Center for Radiation Research in Oncology; [6]now with: The University of Texas MD Anderson Cancer Center

Introduction

At present in-beam positron emission tomography (PET) is the only method for in-vivo and in-situ range verification in ion therapy [1]. In this report a first quantitative study on the accuracy of the in-beam PET method to detect nonconformities between planned and applied treatment in clinically relevant situations using simulations based on clinical data is presented.

Materials and Methods

The study is based upon calculated β^+-emitter distributions derived from real patient treatment plans using a dedicated simulation package [2]. The original and artificially range-modified β^+-emitter distributions corresponding to the treatment plan were compared with each other. For each patient a range difference of $\pm$ 6 mm in water was applied and compared to simulations without any changes (cf. Fig. 1). The 6 mm in water is equivalent to 3.2 mm in bone and 5.1 mm in soft tissue. This is of clinical interest, since the uncertainty for the particle range calculation is 2 - 3 %, increased potentially further by setup errors of the patient [3].

The range and consequently the energy of the beam was increased or decreased, respectively, in the shape of a frustum of a pyramid. This design was used to perform a realistic simulation along the beam path. Such modifications usually do appear as a smooth function included in the model. From the edge to the center the energy of the beam was modified by one step, i.e. 1 mm range in water, for each 1.67 mm of distance. The plateau of the modification with an extension of $(2\,\mathrm{cm})^2$ was centred at the central beam. All pencil beams crossing this region were changed according to the intersection of the pencil beam and the isocentric plane perpendicular to it. The comparison was performed by 6 experienced evaluators for data of 81 patients. The number of patients required for the study was calculated using results of a pilot study.

Results

The results indicate a sensitivity of $(91 \pm 7)\,\%$ and a specificity of $(96 \pm 3)\,\%$ for detecting an overrange, a reduced range is recognized with a sensitivity of $(92 \pm 6)\,\%$ and a specificity of $(96 \pm 3)\,\%$. The positive and the negative predictive value of this method are 94 % and 87 %, respectively. The interobserver coefficient of variation is between 3 and 8 %.

* Work supported by Siemens AG

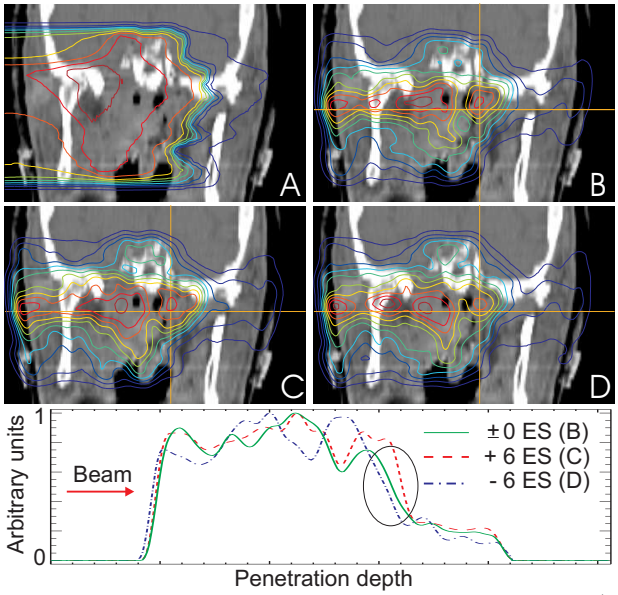

Figure 1: Top: Dose distribution and reconstructed β^+-activity distributions of a patient superimposed on the patient CT. The isodose and isoactivity lines are decoded in rainbow colors and denote levels of 5 % (blue), 15 %, ..., 95 % (red) of the maxima. A: dose distribution, B: reference image, C: β^+-activity distribution with an increased range by 6 energy steps (ES), D: β^+-activity distribution with a reduced range by 6 energy steps. Bottom: Profiles of the reconstructed β^+-activity distributions. The profiles are taken in beam direction crossing the isocenter, i.e. along the horizontal orange line. The range deviations can be observed inside the ellipse.

Conclusions

The in-beam PET method demonstrated a high sensitivity and specificity for the detection of range deviations. As the range is a most indicative factor of deviations in the dose delivery, the promising results shown in this report confirm the in-beam PET method as an appropriate tool for monitoring ion therapy.

References

[1] W. Enghardt, P. Crespo, F. Fiedler, et al, “Charged hadron tumour therapy monitoring by means of PET”, Nucl. Instr. Meth. A 525 (2004) pp. 284-8.

[2] F. Pönisch, K. Parodi, B.G. Hasch, W. Enghardt “The modelling of positron emitter production and PET imaging during carbon ion therapy”, Phys. Med. Biol. 49 (2004) pp. 5217-32.

[3] C.P. Karger, O. Jäkel, “Current Status and New Developments in Ion Therapy”, Strahlenther. Onkol. 6 (2007) pp. 295-300.

Optimum Voxel Size for the Reconstruction of In-Beam PET Data

G. Shakirin[1], P.Crespo[1,2], F. Fiedler[1], A. Wagner[1], and W. Enghardt[1,3]
[1]FZD, Dresden, Germany; [2]now with University of Coimbra, Portugal; [3]OncoRay - Technische Universität Dresden

Introduction

At the experimental heavy ion therapy facility at the GSI Darmstadt the in-beam PET scanner BASTEI is operated for quality assurance monitoring simultaneously to the therapeutic irradiation [1-3]. Due to the relatively short irradiation time, low number of positron emitters production rate and limited-angle geometry in-beam PET data are characterized by very low counting statistics. The important requirement for in-beam PET is fast availability of reconstructed images for analysis in order to make conclusions about performed irradiation and propose corrections for further treatment as soon as possible. Therefore, the parameters of reconstruction algorithms must be optimized in order to achieve maximum speed keeping the image quality on the acceptable level. In this work we propose an optimum size for the imaging element (voxel). The small voxel size increases the resolution but may produce high fluctuations of the signal (noise) in low statistics case. In contrast, large voxel produces homogeneous images, however, with low resolution. Increasing the voxel size also allows to speedup the reconstruction keeping the image quality on the acceptable level which is very important for fast availability of in-beam PET images.

Method

Different voxel sizes were tested using NEMA-like phantoms and the patient data collected during irradiation at GSI. The reconstruction was performed with the ML-EM algorithm:

$$x_j^{(n+1)} = x_j^{(n)} \frac{1}{\sum_{i'} a_{i'j}} \sum_i \frac{a_{ij} y_i}{\sum_{j'} a_{ij'} x_{j'}^{(k)}}, \qquad (1)$$

where $x_j^{(n)}$ is the activity distribution after the n-th iteration, y_i are the measured projections for the i-th channel, a_{ij} are the elements of the system matrix. The image quality was evaluated by means of the root mean square error (RMSE), contrast recovery for NEMA-like phantoms, and visual analysis of the patient images.

Results

Figure 1 shows central slices of the NEMA-like phantom reconstructed with different voxel sizes. The background becomes less noisy with increasing the voxel size. However, images corresponding to voxels larger than (3 mm)^3 do not show the important information about location of small hot inserts. The contrast recovery for the hot inserts reduces with the increasing the voxel size and increases with the increasing the hot insert size. The contrast recovery for the cold inserts is stable (around 50 %) for all voxel sizes smaller than (5 mm)^3. RMSE reduces with increasing the voxel size both for NEMA-like phantom and patient data reconstructions. Voxels with size less than (3 mm)^3 were tested in reconstruction of the patient data. The finally selected optimum voxel size is 2 × 2 × 3 mm^3. Reconstructions performed with voxels of this size recovered all important details in patient images, i.e. the resolution is high enough. At the same time the reconstruction speed increases by factor of 2 in comparison with the standard (1.6875 mm)^3 voxel.

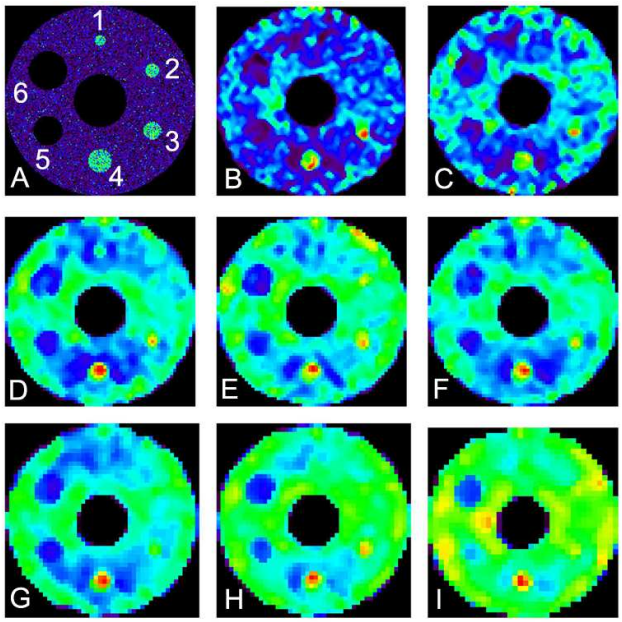

Figure 1: The distribution of annihilation points for the NEMA-like phantom (A). Spheres 1 – 4 represent hot inserts, spheres 5 and 6 represent cold inserts. The standard ML-EM reconstructions were performed for the following voxel sizes (mm^3): 1.6875 × 1.6875 × 1.6875 (B), 2 × 2 × 2 (C), 3 × 3 × 3 (D), 3 × 3 × 4 (E), 3 × 3 × 5 (F), 4 × 4 × 4 (G), 4 × 4 × 6 (H), 5 × 5 × 5 (I).

References

[1] W. Enghardt, et al., "Charged hadron tumour therapy monitoring by means of PET", Nucl. Instr. and Meth. in Phys. Research, vol. 525, pp. 284-288, 2004.
[2] W. Enghardt, et al., "Dose quantification from in-beam positron emission tomography", Radiother. Oncol. vol. 73, suppl. 2, pp. S96-S98, 2004.
[3] W. Enghardt et al., "Positron emission tomography for quality assurance of cancer therapy with light ion beams", Nucl. Phys. A, vol. 654, pp. 1047c-1050c, 1999.

Prompt gamma profile induced by carbon ions in water in view of real time ion therapy monitoring*

M. Bajard[1], M. Chevallier[1], D. Dauvergne[1], N. Freud[2], P. Henriquet[1], S. Karkar[3], F. Le Foulher[1], J.M. Létang[2], R. Plescak[4], C. Ray[1], D. Schardt[4], E. Testa[1#], M. Testa[1].

[1]IPNL, Université de Lyon, F-69003 Lyon; Université Lyon 1 and CNRS/IN2P3, UMR 5822, F-69622 Villeurbanne, France ; [2] Laboratoire de Contrôles Non Destructifs par Rayonnements Ionisants, INSA-Lyon, F-69621 Villeurbanne cedex, France ; [3] CPPM, Aix-Marseille Université, CNRS/IN2P3, Marseille, France ; [4]GSI, Darmstadt, Germany.

Online monitoring of the dose is a key issue for quality control during ion therapy. Up to now, the Positron Emission Tomography (PET) has been the only tool to control the dose deposition inside the patient during therapy[1]. However, this control is provided *a posteriori*, due to the relatively long acquisition time requested by the lifetimes of the radioactive β^+ emitters. Besides PET, prompt gamma emission, also induced by nuclear fragmentation reactions, is regarded as a promising tool to provide real time monitoring of the deposited dose.

Previous studies at GANIL have shown that, using a collimated detection system and Time Of Flight (TOF) to discriminate between direct gammas issued from a target and scattered particles (mainly neutrons), the gamma emission profile is strongly correlated to the ion range. Moreover, the absolute detected gamma yield makes this method compatible with a control setup to be used in clinical conditions [2,3].

In order to validate the TOF-based prompt gamma detection system for carbon ion therapy, the following questions still needed to be answered: i) is the spatial correlation between prompt gamma emission and ion range kept at the high energies requested for tumour therapy? ii) is the TOF technique still efficient to eliminate the background of scattered particles with the time structure of the beam extracted from a synchrotron?

A first test experiment was undertaken in 2008 in cave A. 300 MeV/u ^{12}C ions were extracted from the SIS, with a pulse duration of 8-10 s. The intensity was kept at a low value (a few 10^5 ions/s at maximum instantaneous current) to allow ion per ion triggering with a set of two plastic scintillators inserted in the beam in front of the target. The beam was stopped in a thick water tank used as a target. The photon detection system consisted in a 20 cm thick lead collimator, with 1 cm wide vertical aperture perpendicular to the beam direction, and a 10 cm diameter, 15 cm thick BaF_2 scintillator placed at 1m from the beam axis. The target was translated in front of the collimator to scan the prompt radiation yield as a function of the longitudinal ion path. The photon energy and TOF between the BaF_2 and the plastic scintillators signals were recorded event by event.

Figure 1 presents the result for the prompt radiation yield as a function of penetration depth, obtained after a selection of the BaF_2 energy signals above 2.5 MeV.

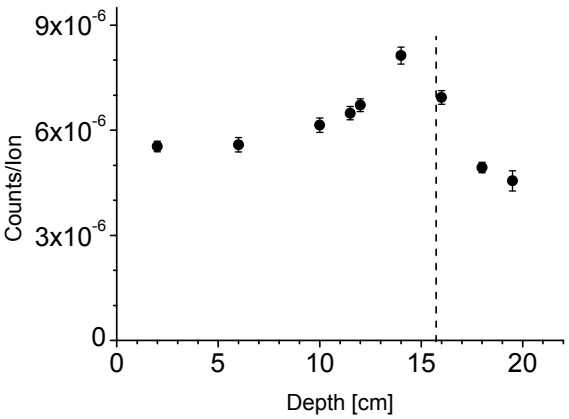

Figure 1: Prompt radiation yield above 2.5 MeV, with TOF selection of gamma rays. The vertical line represents the calculated position of the Bragg peak for 292 MeV/u carbon ions penetrating the water target.

A sharp selection of the prompt gammas emerging directly from the target could be performed with a TOF window of 2 ns. The corresponding yield, shown in Fig. 1, exhibits a clear correlation with the ion range. The signal to noise ratio is about 1, when comparing the yield before and beyond the Bragg peak. This ratio depends strongly on the energy and TOF selections, and certainly also on the experimental configuration used.

The absolute measured yield confirms that, with suitable detection efficiency and collimation, prompt gamma can be used to monitor the Bragg peak position during ion treatments. A dedicated high rate capability ion trigger system is being designed to match the intensities requested during therapy. These developments will be performed in the frame of ENVISION project (EU-FP7 program) within the ENLIGHT framework.

References

[1] W. Enghardt, P. Crespo, F. Fiedler, R. Hinz, K. Parodi, J. Pawelke, and F. Pönisch, Nucl. Instrum. Methods Phys. Res. A **525** (2004) 284.

[2] E. Testa, M. Bajard, M. Chevallier, D. Dauvergne, F. Le Foulher, N. Freud, J.-M. Létang, C. Ray, M. Testa, Applied Physics Letters, **93** (2008) 093506

[3] E. Testa et al., to be published in Nuclear Instruments and Methods B. Preprint available online at http://hal.archives-ouvertes.fr/hal-00283936/fr/

* Work partly supported by Région Rhône-Alpes.

#e.testa@ipnl.in2p3.fr

Scattering implementation in TRiP *

G. Iancu[1] , D. Schardt[1] and M. Krämer[1]
[1]GSI, Darmstadt, Germany

TRiP

One of the most important aims of each treatment planning system is the ability of delivering a target conformal dose distribution. Developed and successful used within the heavy ion therapy pilot project, the TReatment plannIng for Particles (TRiP)[1] is characterised by the capability of delivering exact results in relatively short time, making it possible to rapidly verify and, if necessary, recalculate the therapy plans.

Scattering

The scattering of charged particles, travelling with velocities corresponding to energies above the Coulomb barrier potential, consists mainly of two processes: multiple scattering and scattering as a result of fragmentation. The elastic scattering of the slow stopping ions remains small in comparison with the two processes described above and can be neglected.

Both processes of interest are known of having several theoretical approaches. Some of the models require the use of Monte Carlo simulations that are inappropriate due to the long run time which reduce the flexibility of fast recalculation.

The models chosen for implementation are the formula of Moliere [2] for multiple scattering and the Morrisey [3] approach of the Glauber theory, describing the momentum distribution of fragments in a nuclear reaction.

Moliere method is known to give exact results for the region of interest for therapy and also to be easily extensible to include the calculation of mixed targets. Measurements of H ions beams incident on several targets have shown very good agreement with Moliere model calculations [4].

Morrisey theory for the momentum distribution of the resulting fragments in a nuclear reaction is also known to be in excellent agreement with measurements of longitudinal energy distribution of these. Nevertheless for lateral distribution several authors have reported a systematic underestimation, up to a factor of two, between measured data and calculations [5]. This deviation becomes increasingly important for deep seated targets. Newly measured data will therefore be used to estimate for the correction factor.

Results

Figure 1 is showing the angular distribution of the C beam ions for an incident energy of 400 AMeV. The calculations are in very good agreement with the experimental data.

Figure 2 show a typical treatment situation for irradiating deep seated tumours like the prostate. The solid line represent the physical dose calculation with the new implemented algorithms compared with the old one (dashed line)

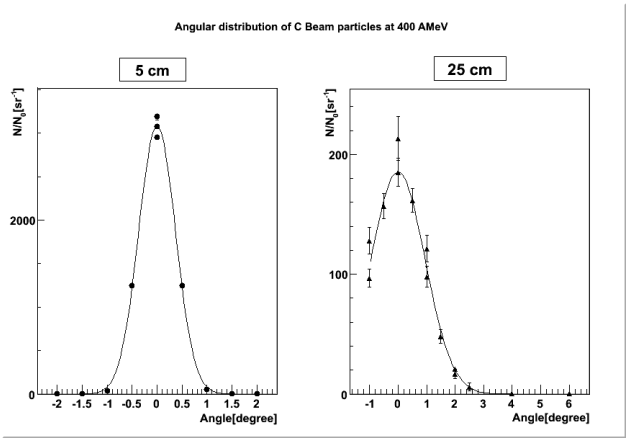

Figure 1: Angular distribution of beam particles incident at 400 AMeV for 2 different depths: 5 cm and 25 cm

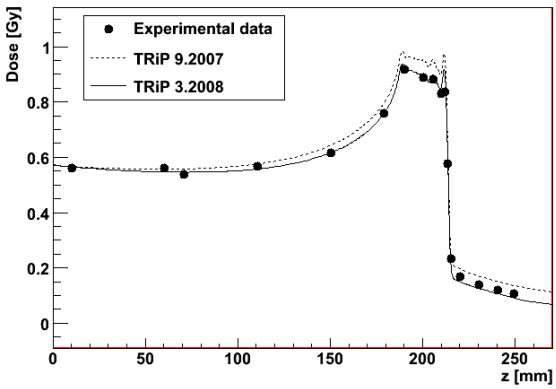

Figure 2: Comparison of different TRiP implementations for a treatment like irradiation.

References

[1] M. Krämer et al. , “Treatment planning for heavy ion radiotherapy: physical beam model and dose optimisation”, Phys. Med. Biol. 45 (2000) 3299-317.

[2] G. Moliere, “Theorie der Sreuung schneller geladener Teilchen”, Z. Naturforschung 3a (1948) p. 78

[3] D.J. Morrisey, Phys. Rev. C39 (1989) p.460

[4] B. Gottschalk et al., "Multiple coulomb scattering of 160 MeV protons", Nucl. Instr. and Meth. B74 (1993) p. 467-490

[5] J. Dreute, W. Heinrich, G. Rusch and B. Wiegel „Fragmentation of gold projectiles with energies of 200-980 MeV/nucleon. I. Experimental method, charge yields and transverse momenta“

Short-term electrophysiological monitoring of ^{12}C carbon therapy of skull base tumors *

S. Carozzo [1], S. Combs [3], L. Narici [2], D. Schardt [4], D. Schulz-Ertner [3], W.G. Sannita [1]

[1] Dept. of Motor Science, University, Genova, and [2] INFN, Roma2, Roma, Italy; [3] Clinical Radiology, University, Heidelberg, and [4] GSI Abteilung Biophysik, Darmstadt, FRG.

The short-term effects on brain visual structures of the ^{12}C ions therapy delivered by intensity-controlled raster scanning with pulse-to-pulse energy variation [1,2] were investigated by electrophysiological techniques allowing inference about neuronal function. Thirty patients with tumors of the skull base were studied at GSI. Electroencephalogram (EEG) and the retinal (ERG) and cortical (VEP) responses to contrast stimulation of the retina fovea were recorded following the IFCN international guidelines [3]. Recordings were performed before the first ^{12}C treatment and at the end of therapy. Patients were informed in full detail about the study purpose and procedures; the ethical principles of the Declaration of Helsinki (World Medical Association, 1964) concerning human experimentations were followed. Recording setting and procedures were neither invasive nor caused the patients any pain or significant physical/emotional discomfort; recordings were cancelled or discontinued when full compliance was/became inadequate or upon the patient's request. Due to the setup procedures, ^{12}C therapy tight schedule and the patients' clinical conditions, EEGs were recorded at baseline in all patients, but ERGs and VEPs were obtained from only 14 patients. Only 27 patients accepted the follow-up EEG recordings and 10 the ERG/VEP tests.

The electrophysiological tests were abnormal by the conventional criteria in most patients at baseline and improved after treatment in over 50% of them. EEGs were normal in 7 cases (23.3%) and showed transient abnormalities of differing morphology, scalp topography and predominance, or severity in 23 patients (76.7%). The ERG was normal in 1 patient and abnormal in both eyes in 9 cases (64.3%) or in one eye in 4 cases. VEPs were normal in three (21.4%) and abnormal in 11 (78.6%) cases (unilateral in two). After therapy, a worsening of the EEG was observed in four (57.1%) of the 7 subjects with normal EEG at baseline and in five (25.0%) of the 23 patients with abnormal EEGs at baseline; among the latter group, improvement was observed in 8 patients (40.0%) and no significant change in 7 (35.0%). Normal ERGs at baseline did not worsen. Four of the 9 patients with bilateral abnormal ERG improved and 2 did not change. Two patients with monocular retinal abnormalities improved; two refused follow-up measurements.

* within the frame of the ALTEA project on the effects of heavy particles in space supported by ASI(MoMa)

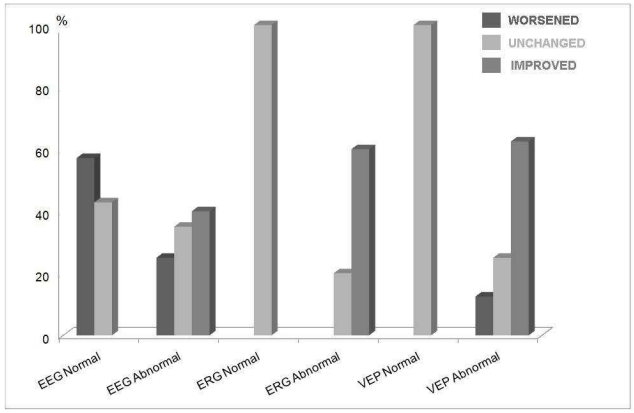

Two of the patients with normal VEPs at baseline showed no change and one refused measurement after therapy. Six of the 9 patients with bilaterally abnormal VEPs accepted follow up measurements: 3 had improved (50%), two did not change and 1 worsened. Both patients with unilateral VEP abnormalities improved.

Clinical symptoms and electrophysiological abnormalities rank differently as side effects, particularly in the treatment of conditions threatening survival; cautious interpretation is therefore warranted. The EEG, ERG and VEP abnormalities observed before therapy conceivably reflect direct/indirect compression by tumor or oedema; improvement/worsening after therapy should depend to a considerable extent on the reduction of the tumor mass or ^{12}C local effects, respectively.

REFERENCES

[1] Schulz-Ertner D, Nikoghosyan A, Didinger B, Münter M, Jäkel O, Karger CP, Debus J. Therapy strategies for locally advanced adenoid cystic carcinomas using modern radiation therapy techniques. Cancer. 2005, 104(2):338-44.

[2] Schulz-Ertner D, Karger CP, Feuerhake A, Nikoghosyan A, Combs SE, Jäkel O, Edler L, Scholz M, Debus J. Effectiveness of carbon ion radiotherapy in the treatment of skull-base chordomas. Int J Radiat Oncol Biol Phys. 2007, 68(2):449-57. Epub 2007 Mar 23.

[3] Deuschl G, Eisen A. Recommendations for the practice of clinical neurophysiology: guidelines of the International Federation of Clinical Neurophysiology, EEG Suppl 52, Elsevier Science, Amsterdam, 1999

Experimental evaluation of beam tracking for 3D motion *

N. Chaudhri[1], N. Saito[1], A. Gemmel[1], R. Lüchtenborg[1], M. Durante[1], E. Rietzel[1,2] and C. Bert[1]
[1]GSI, Darmstadt, Germany; [2]Siemens AG, Particle Therapy, Erlangen, Germany.

Introduction

The beam delivery system of the carbon ion therapy at GSI has been modified to perform beam tracking [1,2]. Beam tracking is achieved by monitoring the target motion and by adapting the pencil beam in lateral (magnetically) and in longitudinal direction (motorized wedge absorbers). The updated integrated system was experimentally tested for left-right target motion with depth changes that were induced by a ramp shape absorber positioned in front of the moving target [2].

We report on experiments that evaluated the tracking accuracy for 3D target motion in water.

Material and Methods

Two types of 3D motions were introduced: 1) A robotic arm moved the detector in the target volume on an elliptical trajectory in a water tank (fig. 1A). 2) A translational sliding table moved the detector diagonally to the beam axis up and down in water. Both setups induced a maximum change of ±15 and ±9 mm lateral and depth in the beam axis respectively. Target motion period was ~ 3.8 s.

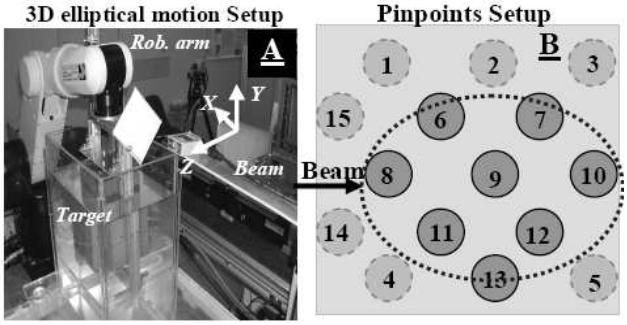

Figure 1: A: Motion setup using a robotic arm for 3D elliptical motion. B: Pinpoint ionization chamber arrangement in the target volume. The dotted elliptical contour indicates the target; the dark shaded circles the chambers within the target. Chambers are positioned in different heights to avoid shadowing effects.

A radiographic film stack (in a light- and water tightened box) and a set of pinpoint ionization chambers (arrangement in figure 1B) were used as detectors in the target volume. While radiographic films have a high spatial resolution from which e.g. the dose homogeneity can be determined, ionization chambers yield the absolute dose. The ionization chamber array is an established dosimetry system used for verification of treatment plans at GSI [3].

A homogeneous dose delivery was planned for an elliptical target of size 30x40x32 mm^3. The target was irradiated under three conditions: no motion (Stationary), target motion without adaptation (Moving) and target motion with beam adaptation (Tracking). Relative root mean square (RMS) deviation was calculated from measured doses for Moving and Tracking with respect to Stationary. Films were processed and analyzed as reported in [4].

Results

Each setup condition was measured only once with slight inaccuracies in repositioning of the detector array. The film homogeneity distribution results show good agreement between Stationary and Tracking, details were reported in the [5]. The measured doses for the ionization chamber array for Stationary, Moving and Tracking for the Robot setup are shown in Figure 2. The relative RMS deviation for Tracking within the target (Figure 2, middle) is ~6% for the Robot setup and 2% for the 3D Translation motion. The Moving condition resulted into 50% and 21% RMS deviation for Robot and 3D Translational motion respectively.

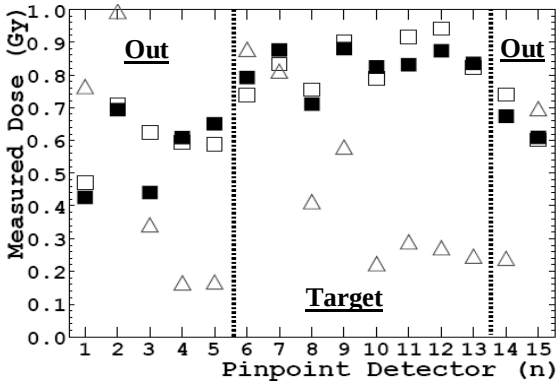

Figure 2: The measured dose for Stationary (filled squares), Moving (triangles), and Tracking (empty squares) conditions are shown for Robot setup. Numbering of detectors is according to figure 1B.

Conclusion

Despite slight inaccuracies in the detector repositioning, the dose delivered with tracking is in a close agreement with doses measured for stationary irradiations. Upcoming experiments will include an improvement in experimental setup and multiple measurements per irradiation condition to decrease random uncertainties.

References

[1] S. Grözinger et al., (2008)
[2] C. Bert et al., Med. Phys. 34 (2007) 4768
[3] C. Karger et al., Med Phys. (1999)
[4] B. Spielberger et al., NIM B209 (2003)
[5] N. Chaudhri et al., Conf. Proceeding, DGMP 2008

* Work is in part supported by Siemens AG, Particle Therapy

Extension of In-Beam PET to 4D for QA of motion-mitigated ion therapy

K. Parodi[1], N. Saito[2], N. Chaudhri[2], C. Richter[3], K. Laube[3], W. Enghardt[3], E. Rietzel[2,4], and C. Bert[2]
[1]HIT, Heidelberg; [2]GSI, Darmstadt; [3]OncoRay and FZD, Dresden; [4]Siemens AG, Erlangen

Introduction

More than 10 years of clinical operation of in-beam PET at GSI have proven its positive contribution to quality assurance (QA) of ^{12}C ion therapy [1]. Due to promising clinical results of ion therapy of e.g. lung tumors which are influenced by respiratory motion, investigations on the potential of time-resolved 4D in-beam PET have been started.

Material and Methods

The in-beam PET camera has been operated in combination with beam tracking [2]. A homogeneous PMMA phantom was placed in the center of the field of view of the scanner and moved parallel to the two detector heads (left-right in beam's eye view with 3 cm peak-to-peak amplitude and ≈ 3 s period). The prescribed dose was a two-dimensionally spread-out Bragg-peak (SOBP) of 5×5 cm^2 extension, centered at a depth of 10 cm in the central plane of the phantom. The list-mode PET acquisition was performed during the 6 min of beam delivery and for 25 min after irradiation (*MOV*). The data stream was synchronized with the time course of the dynamic beam application and with the motion monitor [2]. Additional 18 min of decay were acquired with the activated phantom kept steady (*STAT*), for comparison with a separate measurement of the same treatment field without motion (*REF*).

For time-resolved reconstruction, the reconstruction algorithm [3] has been extended to distribute events to the different phases of the motion trajectory, including attenuation and solid angle corrections for moving geometries.

Results

Reconstruction of the static acquisitions (*STAT*) yielded comparable activation patterns for beam tracking and stationary irradiation (*REF*).

Time-resolved activation patterns in the SOBP for representative motion-phases of *MOV* are shown in fig. 1, together with the corresponding attenuation maps. The depicted lateral activity profiles cleary reflect the different positions of the target in the selected motion-phases. The benefit of the 4D reconstruction is illustrated in fig. 2, where all the phase-resolved reconstructions are co-registered and summed up to a reference central phantom position (phase # 10 of fig. 1). Whereas the 3D-reconstruction of the data acquired with the moving target is obviously distorted in the direction of motion, the 4D activity distribution is found in good agreement with the reference irradiation of the same dose without motion.

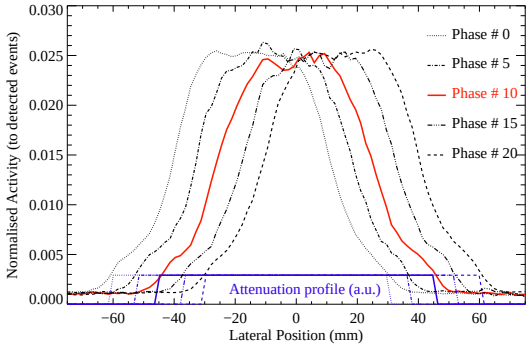

Figure 1: Lateral activity profiles reconstructed in different motion phases (largest displacement in # 0 and # 20, reference in # 10) during/after beam tracking (*MOV*). Phase-resolved attenuation data are shown at the bottom.

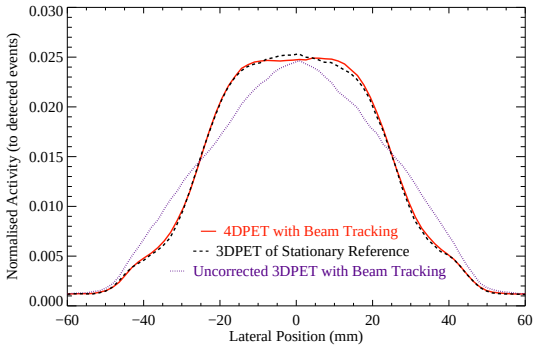

Figure 2: Lateral activity profiles for *MOV* (4D reconstruction: solid; 3D reconstruction: dotted) and *REF* (dashed).

Conclusion

4D in-beam PET is capable to recover the volumetric extension of the delivered treatment in the presence of target motion. Following this initial experiment, thorough investigations [4] have been started to address the role of 4D in-beam PET for in-vivo assessment of tumor miss or unwanted involvement of nearby critical structures for ion beam tracking in the presence of motion.

References

[1] W. Enghardt et al., *NIM* **A525** (2004) 284–288
[2] C. Bert et al., *Med. Phys.* **34** (2007) 4768–4771
[3] F. Pönisch et al., *Phys. Med. Biol.* **48** (2003) 2419–2436
[4] K. Laube et al., contribution to this Annual Report

On-line compensation of dose changes caused by tumor motion*

R. Lüchtenborg[1], N. Saito[1], N. Chaudhri[1], M. Durante[1], E. Rietzel[1,2], and C. Bert[1]
[1]GSI, Biophysics, Darmstadt, Germany; [2]Siemens AG, Particle Therapy, Erlangen, Germany

Introduction

Treating tumors that are subject to intrafractional motion (e.g. lung tumors) with scanned particle beams leads to deterioration of the deposited dose distributions. One possible technique to mitigate motion effects is beam tracking [1].

In case of rotational motion the beam path and thereby the dose deposition in the plateau region proximal of the Bragg peak position changes despite adaptation of the Bragg peak position by tracking (see Figure 1). Adequate on-line compensation of these effects will be required for tumors that rotate remarkably during respiration. [2].

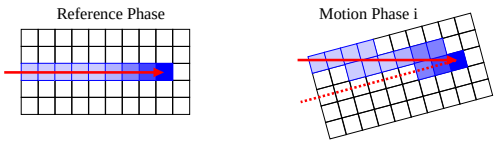

Figure 1: Comparison of the reference phase and an arbitrary motion phase i where the beam position is adapted according to tracking parameters. Rotation changes the deposited dose distribution (shade of color). The beam path is indicated by arrows (dashed line: beam path in reference phase) ([2]).

Materials and Methods

Functionality to compensate dose changes caused by target motion has been implemented in the treatment control system (TCS) and treatment plans have been extended by a dose compensation Lookup Table. This Lookup Table provides a precalculated database from that, depending on the measured target positions during irradiation, dose compensation parameters can be determined. Nominal rasterpoint fluences are adapted accordingly during irradiations.

To test the implemented functionality, two treatment plans have been designed. One, referred to as HOMPLAN, consists of a square with a constant fluence per rasterpoint yielding a homogenous dose distribution while for the other plan, called STRIPEPLAN, the target area was divided into four stripes with different fluences. A Lookup Table has been created to deliver the stripe pattern while using HOMPLAN. This offers the possibility to test the dose compensation functionality without moving the target. Three different irradiations on radiographic films have been performed:

- HOM: HOMPLAN has been irradiated without dose compensation,
- STRIPE: STRIPEPLAN has been irradiated without dose compensation,
- COMP: HOMPLAN has been irradiated using the Lookup Table to obtain the pattern of STRIPEPLAN.

The films have been developed and digitized according to [3]. Normalized film responses S/S_0 are reported.

Results

Despite some artifacts caused by poor beam quality during this experimental beamtime, the different film responses show good agreement between STRIPE and COMP (see Figure 2). This result can be quantitatively confirmed by horizontal S/S_0-profiles that also show good agreement between STRIPE and COMP (see Figure 2).

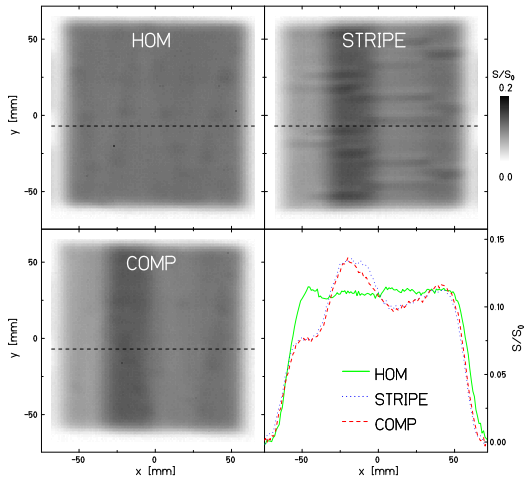

Figure 2: Normalized optical densities S/S_0. Dashed lines indicate the positions of the profiles.

Conclusion

In COMP the rasterpoint fluences of HOMPLAN were successfully adapted to deliver STRIPEPLAN. Thus it was shown that the upgraded TCS offers the possibility to individually adapt rasterpoint fluences during irradiation.

Further tests with moving targets and more complex geometries are currently in preparation.

References

[1] C. Bert et al., *Med. Phys.* **34** (2007), pp. 4768–4771.
[2] C. Bert, PhD Thesis, TU Darmstadt, 2006.
[3] B. Spielberger et al., *NIM* **B209** (2003), pp. 277–282.

* This work is in part supported by Siemens AG, Particle Therapy.

Rescanning to mitigate the impact of motion in scanned particle therapy*

Ch. Bert[1], A. Gemmel[1], N. Chaudhri[1], R. Lüchtenborg[1], N. Saito[1], M. Durante[1], and E. Rietzel[1,2]
[1]GSI, Biophysics, Darmstadt, Germany; [2]Siemens AG, Particle Therapy, Erlangen, Germany

Introduction

Treatment of targets that move during the irradiation with a scanned particle beam leads to deterioration of the dose distribution [1]. This dose deterioration results from interference of target motion and scanned beam, so called interplay. Apart from beam tracking [2] and gating [3] rescanning [4] can be used to mitigate the impact of motion.

Rescanning mitigates interplay effects by multiple re-irradiations of the target with proportionally less dose during a single scan and margins that cover the motion extent. In principle, local mis-dosage averages out over several re-irradiations.

Rescanning was implemented at GSI, initial results are presented.

Material & Methods

Radiographic films (Kodak X-Omat V) moved up-down in beam's eye view free in air (motion amplitude: 10 and 15 mm), a target area was planned to be irradiated homogeneously ($90 \times 60\,\mathrm{mm}^2$, single energy 244.21 MeV/u, $3 \times 3\,\mathrm{mm}^2$ grid, 9.2 mm beam full width at half maximum, scan-path: horizontal lines). To account for target motion, 10 mm (15 mm) margins were added in the motion direction. Irradiations were performed with up to 21 rescans.

Films were developed, digitized with 12 bit intensity resolution and 1 mm spatial resolution [5]. Normalized film responses S/S_0 are reported ($S_0 = 4.1$). Interplay patterns on the films were analyzed by visual inspection and homogeneity $H = 1 - \sigma/\mu$ relative to a stationary irradiation with standard deviation σ and mean film response μ within the target area. The experimental data were fitted to $H(r) = 1 - a\,\exp(-b\,r)$ with number of rescans r and free variables a, b .

Results

Figures 1 and 2 show the film responses and the influence of the number of rescans on the relative homogeneity H. Interplay leads to a distinct interference pattern for a standard irradiation (1 rescan) of the moving film. For a small number of rescans, interplay is not reduced for 10 mm motion amplitude and results in a decreased homogeneity with a minimum at 5 rescans. For different motion conditions different outcomes can be expected because interplay is in principle random. With a sufficiently large number of rescans, homogenous target coverage is achieved. Less rescans are required for 10 mm motion amplitude in comparison to 15 mm. The exponential fit yields 12 scans (15 scans) for 10 mm (15 mm) target motion amplitude to reach 97 % relative homogeneity.

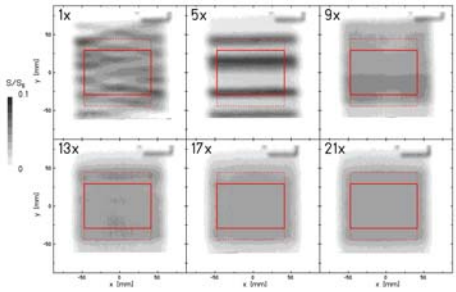

Figure 1: Normalized film response as a function of the number of rescans for 15 mm target motion. (target area: solid line; margins: dashed line)

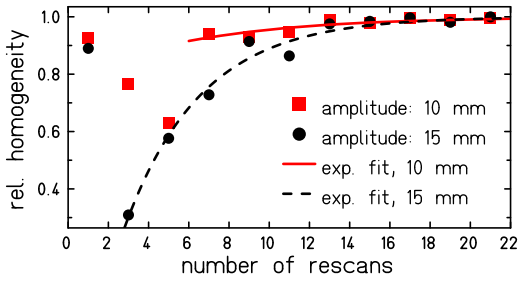

Figure 2: Relative homogeneity $H/H_{\mathrm{stationary}}$ within the target area as a function of the number of rescans r.

Conclusion

Rescanning has been successfully implemented in the therapy control system at GSI. Initial experiments demonstrated the expected dose averaging effect if margins cover the target motion extent and 15 rescans are used for 15 mm motion amplitude. Further experiments will focus on absolute dosimetry, more complex setups, and implementation at the Heidelberg Ion Therapy Center.

References

[1] C. Bert et al., *Phys. Med. Biol.* **53** (2008) 2253–2265
[2] P. Keall et al., *Phys. Med. Biol.* **46** (2001) 1–10
[3] S. Minohara et al., *Int. J. Radiat. Oncol. Biol. Phys.* **47** (2000) 1097–1103
[4] M. Phillips et al., *Phys. Med. Biol.* **37** (1992) 223–234
[5] B. Spielberger et al., *NIM* **B209** (2003) 277–282

* This work is in part supported by Siemens AG, Particle Therapy

Technical status of the real-time beam tracking system*

N. Saito[1], C. Bert[1], N. Chaudhri[1], M. Durante[1], A. Gemmel[1], R. Lüchtenborg[1], D. Schardt[1], and E. Rietzel[2]

[1]GSI, Darmstadt, Germany, [2]Siemens AG, Particle Therapy, Erlangen, Germany

Introduction

For intra-fractionally moving tumours such as lung cancer, treatments with scanned particles [1] without motion compensation can cause unacceptable local under- or over-dosage due to interplay effects of sequential dose delivery and target motion [2]. In order to treat moving tumours with scanned particle beams, a beam tracking system, 3DOMC system, was developed [3] and upgraded [4,5]. The beam tracking system employs the raster scanner for lateral beam tracking and a range shifter to adapt the Bragg peak position longitudinally. The upgraded system components and the achieved speed were reported previously [5]. In 2008 experiments to assess the system accuracy, an interlock feature, an implementation to overcome delay times, and real-time dose compensation [6] have been performed. Here we report studies related to the accuracy of the system in detail.

Material and Methods

Beam tracking performance was measured for both lateral and longitudinal target motion compensation. Lateral beam tracking accuracy was analysed in a time resolved manner with millisecond resolution by comparing nominal and measured beam positions for each raster point for a sinusoidal target motion (left-right motion, period: 3.5 s, peak to peak amplitude: 30 mm). The nominal beam position on the moving target was obtained by adding the displacement monitored with a beam tracking unit to the originally planned beam position for each raster point. The actual beam position was measured with the position detector of the beam monitoring system. In order to analyse the accuracy of fast longitudinal tracking, the response of the range shifter was measured every few milliseconds for various range shifts up to 14.7 mm water equivalence (WE). Time windows of length $10 \leq T_w \leq 50$ ms were set before and after the reference time defined as the middle of the range transition. The time window represents an assumed irradiation time for individual raster points. Within the time window, the measured range shift data were interpolated and sampled every 0.25 ms, and the deviation of the measured range shift from the required full shift (nominal) was determined from the samples. The analysis was applied to many transitions to obtain statistics for the deviation distributions.

Results

Figure 1 shows time-resolved lateral beam tracking data for an irradiation sequence with approximately 6000 raster points over 100 s total irradiation time. Positional differences between nominal and measured data showed a mean value of 0.04 mm with a standard deviation of 0.16 mm. Figure 2 shows longitudinal deviations as a function of assumed raster-point irradiation times T_w and magnitude of range shifts. Longer time windows T_w result in less deviation since the range shifter can reach the required position within the time window. Deviations for a 5 mm WE range shift within time windows of 10 and 50 ms were 1.08 and 0.48 mm WE, respectively.

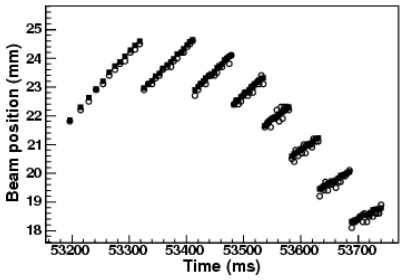

Figure 1: Horizontal beam positions for lateral tracking: measured (open circles) and nominal (filled squares).

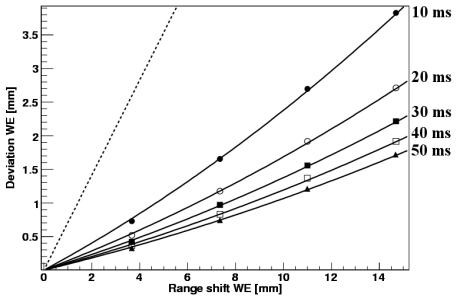

Figure 2: Deviations of the required range shifts (solid line, polynomial fits). The calculated deviation curve for uncompensated motion is shown with a dashed line.

Conclusion

The real-time beam tracking system to irradiate moving tumours with scanned particle beams has been improved and implemented into the treatment control system. Temporal as well as geometrical accuracy of the system were measured to confirm appropriate functionality. Further improvements of the system are currently in progress [7].

References

[1] G. Kraft, Nucl. Instr. and Meth. A 454 (2000) 1
[2] C. Bert et al., Phys. Med. Biol. 53 (2008) 2253
[3] S. Grözinger et al., Radiat. Oncol. 3 (2008) 34
[4] C. Bert et al., Med. Phys. 34 (2007) 4768
[5] N. Saito et al., GSI Sci. Rep. 2007 (2008) 385
[6] R. Lüchtenborg et al., GSI Sci. Rep. 2008 (2009)
[7] N. Chaudhri et al., GSI Sci. Rep. 2007 (2008) 382

* This work in part supported by Siemens AG, Particle Therapy

Two approaches for calculation of the absorbed dose in the presence of target motion — a comparative study based on patient data*

A. Gemmel[1], Ch. Bert[1], and E. Rietzel[1,2]

[1]GSI, Darmstadt, Germany; [2]Siemens AG, Particle Therapy, Erlangen, Germany

Introduction

In the course of scanned carbon ion beam cancer treatment at GSI, 437 patients were successfully treated at sites that could be immobilized. With the upcoming facilities in Heidelberg, Marburg, and Kiel one major task is the expansion of the rasterscan technique [1] to moving tumors, e.g. lung cancer. This requires an extension of the treatment planning software TRiP [2] by 4D functionalities. In a first step, TRiP was extended by the possibility to calculate the absorbed dose in the presence of motion (linear method (LM)) [3, 4]. Recently, calculation of the RBE-weighted dose was implemented in TRiP using a different calculation scheme. As part of the new approach, that is capable of taking nonlinear dose dependencies into account and therefore referred to as non-linear method (NLM), the absorbed dose is determined in a different way than in the LM but should lead to the same results. LM and the NLM were compared based on 4D data from three lung-cancer patients.

Materials and methods

Both calculation schemes are based on 4D-CT, deformable registration, and a reference treatment plan that is distributed to the motion phases based on data from the target motion trajectory and the irradiation progress.

LM: The dose is calculated in each motion phase independently. The total dose distribution is determined by first, mapping the dose distribution of each phase to the reference phase using deformable registration and second, by summation of the transformed dose distributions. Interpolation is needed to map the dose distributions to the calculation grid of the reference phase.

NLM: Each point of the calculation grid of the reference phase is mapped to each other motion phase via deformable registration and the contributions for the dose calculation are stored in a parameter list. Consecutively, the list is used to compute the total dose.

For comparison of LM and NLM dose distributions for beam tracking were simulated for 12 different motion trajectories per patient. Resulting dose distributions were subtracted from each other ($D_{\mathrm{LM}} - D_{\mathrm{NLM}}$) and statistically analyzed (mean difference and standard deviation). The mean of the mean differences and the mean of the standard deviations from the 12 simulations per patient are reported. Additionally, dose-volume-histograms (DVHs) were inspected.

Results

Figure 1 depicts the DVHs. Table 1 shows the results of the statistical analysis.

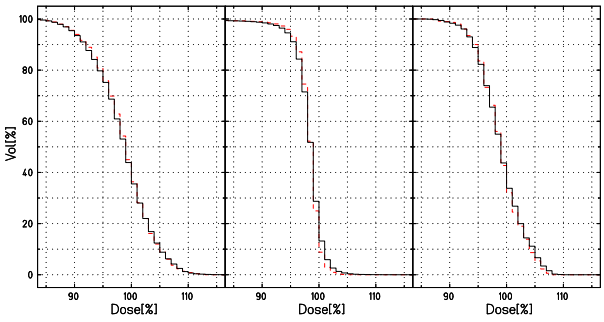

Figure 1: Target dose volume histograms for three patients computed with NLM (solid line) and LM (dashed line).

	Target		Total	
Patient	Mean	StDev	Mean	StDev
A	-0.2	1.7	0.0	0.6
B	-0.0	1.2	-0.1	2.2
C	-0.0	0.9	0.0	0.5

Table 1: Statistical analysis of differential dose distributions $D_{\mathrm{LM}} - D_{\mathrm{NLM}}$. Values are reported relative to the planned target dose of 1 Gy.

Discussion

Results of the linear and non-linear dose calculation methods are almost identical. Differences are negligible and arise most likely from the interpolation that is used in the LM. Experimental validation of the calculations especially with respect to the RBE-weighted dose is currently in progress.

References

[1] Th. Haberer et al., *NIM* **A330** (1993) 296-305

[2] M. Krämer et al., *PMB* **45** (2000) 3299-3317

[3] Ch. Bert, PhD-thesis, TU Darmstadt, 2006

[4] Ch. Bert und E. Rietzel, *Med. Phys.* **34** (2007) 4768-4771

* This work is in part supported by Siemens AG, Particle Therapy.

4D in-beam PET of moving targets for different irradiation scenarios

K. Laube[1], C. Bert[2], N. Chaudhri[2], F. Fiedler[1], K. Parodi[3], E. Rietzel[4], N. Saito[2], and W. Enghardt[1,5]
[1]FZD, Dresden; [2]GSI, Darmstadt; [3]HIT, Heidelberg; [4]Siemens Medical Solutions, Erlangen; [5]OncoRay, TU Dresden

Introduction

Ion therapy allows a high precision, tumor conformal dose application but it is very sensitive to density changes along the beam path. Intra-fractional tumor motion due to respiration increases the risk of an incorrect irradiation and thus requires a reliable dosimetry as it was done by means of 3D in-beam PET for more than 400 patients at the experimental heavy ion treatment facility at GSI Darmstadt. A new beam delivery system for tracking moving targets with the scanned ion beam has been developed at GSI [1] and first experiments have shown the feasibility to correct the in-beam PET measurements for target motion [2]. Now the potential of this new 4D in-beam PET method for detecting possible malfunctions of the motion compensated dose application is under investigation.

Materials and Methods

For this experiments the new research beam delivery system for tracking moving targets was used which records the target motion and instantaneously adapts the beam's direction and, if necessary, its energy. A monoenergetic pencil beam of ^{12}C ions has been rescanned on a horizontal line in a moving target ($80\times35\times30\,\mathrm{mm}^3$) in front of a stopper ($100\times100\times30\,\mathrm{mm}^3$), both of polymethyl methacrylate $(C_5O_2H_8)_n$. The target performed a one dimensional periodic motion perpendicular to the beam direction (left-right in beam's eye view) and parallel to the scanning direction with a period of 3.7 s and a peak-to-peak amplitude of 20 mm. The lateral parts of the 50 mm long rescanned line are not stopped in the target but in the stopper because of the target width of only 35 mm.

The measurement of the ion beam induced β^+-activity in the target and stopper was realized by the PET camera at the medical treatment site at GSI consisting of two detector heads of bismuth germanate block detectors from the commercial ECAT EXACT PET scanner [3]. The listmode data acquisition was performed during the irradiation and for additional 5 min with continuous target motion. The detected decay events were separated into nine motion phases due to the current elongation of the target, reconstructed by a backprojection algorithm with correction of attenuation and detector efficiency and finally coregistered onto the same target position as described in [4]. Four different cases of target irradiation with constant energy have been investigated to compare the general impact of possible errors of the motion compensation on the reconstructed β^+-activity distribution: 1) the stationary target, the moving target with 2) correct motion compensation, 3) phase shifted motion compensation (worst case scenario: when target moves to the right the beam was directed to the left), and 4) without any motion compensation.

Results

Figure 1 shows the cross sections along the motion and beam scanning direction through the target and stopper of the reconstructed β^+-activity distribution at the depth of the Bragg peak. An impact on the target's activity cross section (thin lines) occures only for the phase shifted motion compensation (dashed dotted line), because the motion amplitude is of the same order as the lateral size of the activity generated in the stopper. The irradiation scenarios can be better distinguished by the stopper's activity. As expected, the activity behind the target increases whenever the target is moving, but is almost independent from the compensation method. Compared to the stationary target irradiation (thin solid line) the lateral fall off is similar for the case without motion compensation (dotted line) and most expanded to the left and right for the correct motion compensation (thick solid line).

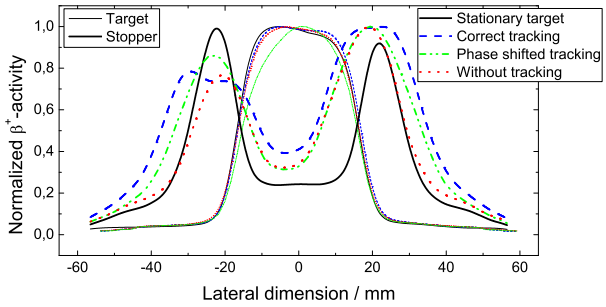

Figure 1: Measured β^+-activity profiles along motion direction of the target at the depth of the Bragg peak in the target (thin) and stopper (thick) for different target tracking scenarios. Each curve is normalized to its maximum.

Conclusion

It has been shown by systematic experiments that in-beam PET is capable to distinguish different irradiation scenarios and therefore to detect possible malfunctions of target tracking. It can be expected that in-beam PET will become a valuable tool for quality assurance also for the irradiation of intra-fractional moving targets.

References

[1] C. Bert et al., Medical Physics 34, 2007, pp. 4768–71

[2] K. Parodi et al., IEEE NSS-MIC Conference Record, 2008, pp. 4520–24

[3] W. Enghardt et al., Nucl. Instr. Meth. A 525, 2004, pp. 284–8

[4] K. Parodi et al., contribution to this Annual Report

Heavy Ion Tumor Therapy at GSI closed

G. Kraft[1], J. Debus[2], W. Enghardt[3], T. Haberer[4], D. Schardt[1], M. Krämer[1], H. Eickhoff[1], O. Jäkel[5], C.P. Karger[5], P. Heeg[4], S. Brons[4], K. Parodi[4], J. Pawelke[3], M. Scholz[1] and D. Schulz-Ertner[2]

[1]GSI, Darmstadt, Germany; [2]Department of Radiation Oncology, University Hospital of Heidelberg, Heidelberg, Germany; [3]Insitute of Radiation Physics, Forschungszentrum Dresden-Rossendorf, Dresden, Germany; [4]Heidelberger Ionenstrahl Therapiezentrum, Heidelberg, Germany; [5]Department of Medical Physics in Radiation Oncology, German Cancer Research Center, Heidelberg, Germany

July 26 the last patient was treated with carbon ions at GSI. This day marks the end of the first heavy ion therapy in Europe. With the construction of dedicated facilities at Heidelberg, Marburg Pavia and Kiel particle therapy will now enter its clinical phase.

The pilot project for heavy ion therapy was started at GSI with the first two patients in Dec. 2 1997 .This treatment was proceeded by two decades of scientific research and development, and a four year construction period of the therapy rooms, beam lines, annex building and by the necessary accelerator modifications.

The major differences of the GSI pilot project to all other particle therapies operating before were:

- the novel type of beam delivery using the rasterscan system to direct a fine pencil beam to thousands of pixels of the target volume resulting in a 3D intensity modulated particle therapy IMPT.

- the biology based therapy planning calculating for each target pixel the number of required carbon ions based on RBE calculation using the Local Effect Model LEM.

- the in-beam PET system measuring the range of the ion beam on the basis of the positron emitting carbon isotopes produced inside the patient.

- the novel accelerator flexibility producing 250 energies, 10 intensities and 7 different beam diameters in any combination from pulse to pulse on demand.

These innovations have been the result of a long standing research and development in radiobiological and physical experiments, design and construction of a dedicated fast magnetic deflection system and its electronic control , treatment planning and accelerator developments. From the beginning of the pilot project all these innovations were available and used without any major restriction. Treatment plans were biologically optimized, simultaneously for two or three fields. The PET data were taken normally for each field and analysed for range deviations that occurred in a few patients. In these cases treatment planning was repeated based on a new CT image.

Treatment started with slowly growing tumors in head and neck with the intension of a full course of curative care. Although the head and neck area has a very complex geometry, difficult to plan and sensitive to positioning error, the fixation of the head by external means is rather safe and reproducible. In addition slowly growing tumors such as chordomas, chordrosarcomas are normally very resistant against normal radiotherapy but become sensitive to carbon irradiation.

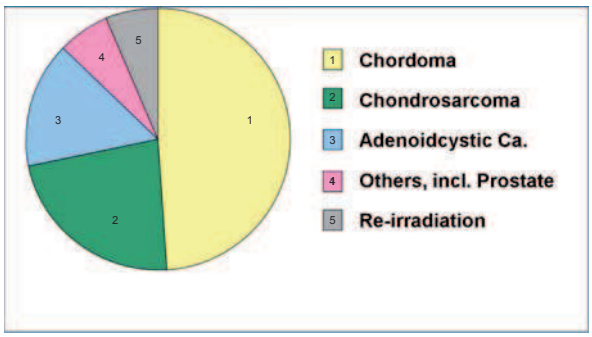

Figure 1: Total distribution of the 440 Patients treated at GSI for 1997-2008.

Later on the therapy was extended to targets along the spinal cord and into the pelvic region, because of the reduced motion and the possibility of the external fixation.

The full spectrum of tumors treated at GSI is given in Fig. 1. Most of these patients received a full treatment of 20 fractions at 20 consecutive days.also at the weekend. A minor part of salivary gland tumors and prostate cancer received a boost treatment of 6 fractions of 18 Gye replacing a part of an IMRT treatment. In these boost treatments the 5 year control rate could be increased from around 30% to 80%, for the salivary gland tumors. For the prostate tumors the data are not yet analysed because of the short time since treatment.

Also for the other treatments 5-year local control could be always increased close to 80%. For chondrosarcoma this rate could be increased to 100% based on a dose escalation which was possible because of the small side effects. (Fig. 2)

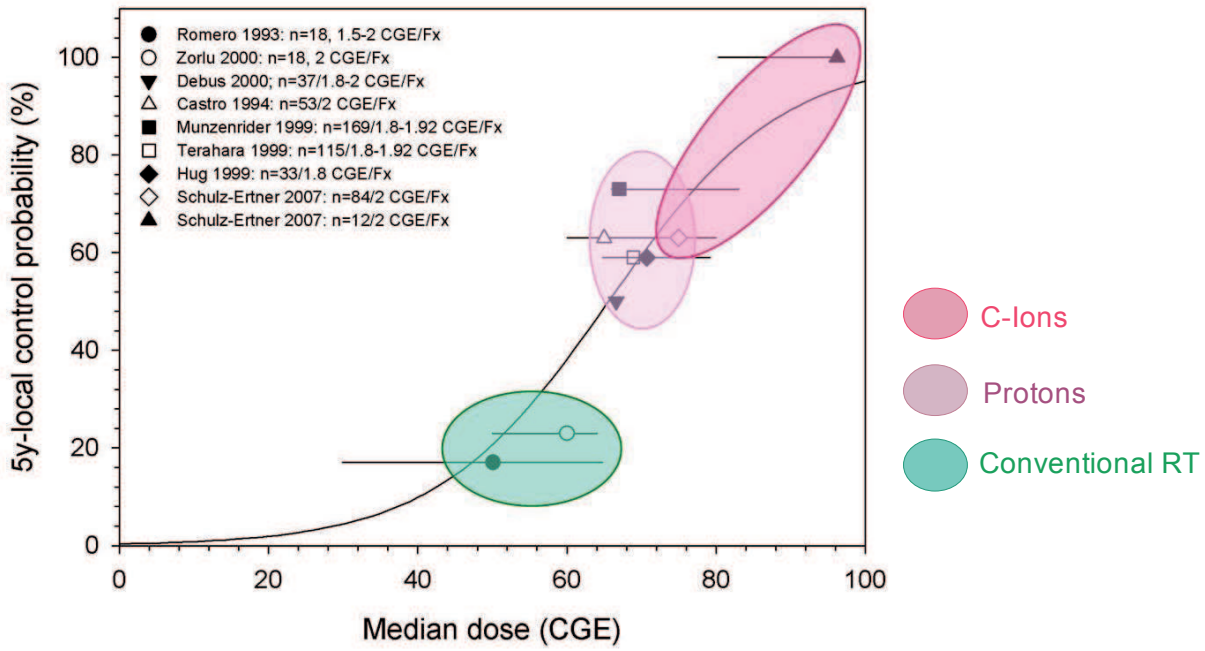

Figure 2: 5 year tumor control for chondrosarcomas treated with different techniques. For the intensity modulated Carbon therapy 100% control rate could be reached.

Although the patient statistics with 440 patients treated in total at the GSI pilot project is not large but the success rate is significantly better than other therapy modalities. In addition, the incidence and the severity of side effects are much smaller. Therefore the public pressure to make this treatment modality available to the public is strong and yields the projects at Heidelberg, Pavia, Marburg and Kiel where thousands of patients will be treated per year instead of the small annual number of 50 patients at the GSI pilot project. At these new therapy centers the spectrum of tumor types to be treated can be extended because of the larger availability of beam for patient treatment. Candidates are prostate and lung cancer. But for the lung cancer the scanning system has to be adapted to treat also moving targets. This is one of the maior topics of the present research to be continued at GSI after therapy has been terminated.

The Heidelberg facility will start operation in spring 2009 and the Marburg and Pavia facilities in 2010. The new heavy ion therapy at Kiel started with the construction phase and is supposed to be completed in 2012. Other facilities are in preparation as shown in Fig. 3.

Also taking into account only the facilities that are under construction, the heavy ion therapy developed at GSI represents the largest transfer from basic research to industry that the Helmholtz community had up to now.

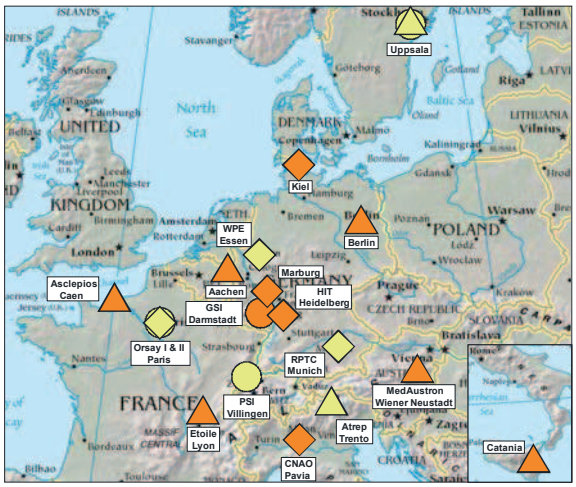

Figure 3: Particle therapy centers in Europe: Circles are running facilities, diamonds under construction and triangles planed. The yellow color is assigned to protons, the orange to combined carbon proton centers.

References

[1] G. Kraft, "Tumor Therapy with Heavy Charged Particles", Progress in Part. and Nucl. Phys. 45 (2000) S473-S544

[2] D. Schulz-Ertner and H. Tsujii, "Particle radiation therapy using proton and heavier ion beams", J Clin Oncol 25 (2007) 953–964

The Status of the HE-Cave for the BIOMAT and the SPARC Collaborations

R. Pleskač[1], M. Durante[1], F. Hinterberger[2], D. Liesen[1] and D. Schardt[1]
[1]GSI, Darmstadt, Germany; [2]HISKP, University of Bonn, Germany

The future high-energy (HE) cave at FAIR will house the SPARC collaboration having its installations in the front part of the cave and the BIOMAT collaboration having its high-quality irradiation facility at the end of the cave. The BIOMAT laboratory is dedicated to biophysical experiments (mainly for space research) and to experiments of ion-induced changes in solids [1]. During the last time major progress was achieved regarding the design of ion optics and beam preparations for the target stations for BIOMAT and SPARC [2], planning of the civil construction, beam diagnostics specific for irradiation experiments and also preparative work for the scanning target system.

The beam transfer line from SIS18 to the HE-cave has been changed several times and at the moment its design is not yet completely fixed. The last section of this beam line is identical with the SIS100-HE-cave beam line. Therefore, we assume that the ion-optical design will be the same in this last part for both beam lines. The ion optics of the transfer line is characterized by a non-regular FODO structure and the beam is achromatic in the front as also in the last part. The emittance of the SIS100-HE-cave transport line is ϵ_x = 50 mm mrad and ϵ_y = 25 mm mrad.

Altogether three different target stations are planned: TP1 of SPARC and TP2 and TP3 of BIOMAT. The target station TP1 is located between the scanning magnets in front of the cave and the magnetic spectrometer of SPARC (see Figure 1) and the beam preparation allows either sharp or shallow beam waists there. Target stations TP2 and TP3 are located very close to each other at the end of the HE-cave and both require a similar shallow pencil beam. Therefore, the beam preparation for TP2 and TP3 (dedicated to very high-intensity beams) is practically identical. The distance between the exit of the last scanner magnet and the target station TP2 amounts to 28.0 m. Maximum horizontal and vertical deflections of a 100 Tm beam amount to ± 131.4 mm and ± 70.7 mm, respectively. The horizontal and vertical beam emittance is 2.5 mm mrad. All ion-optical calculations were performed either with MIRKO or TRANSPORT code.

Apart of the beam scanning system mentioned above the preparative works on the target scanning system are in progress. In this case, the stationary beam will irradiate different targets which will be fixed on a moving table to assure required quality of irradiation.

[1] BIOMAT, Technical Proposal, April 2005
[2] F. Hinterberger, internal report, 2008

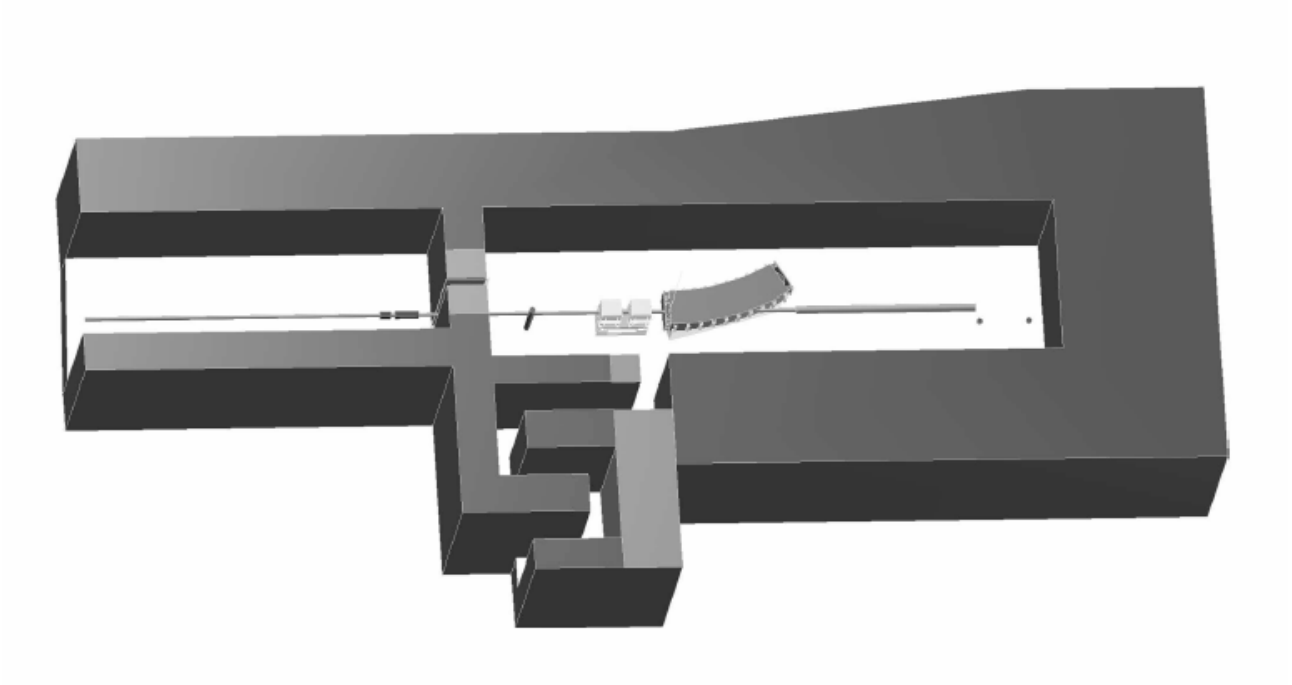

Figure 1: The BIOMAT cave at FAIR.

European space radiation research program at GSI

M. Durante[1], D. Schardt[1], S. Metzger[2] and O. Angerer[3]
[1]GSI, Darmstadt, Germany, [2]Fraunhofer Institute, Euskirchen, Germany, [3]ESA-ESTEC, Nordwijk, The Netherlands

Introduction

Space radiation has long been acknowledged as a potential showstopper for long duration manned interplanetary missions (Fig. 1). Our knowledge of biological effects of cosmic radiation in deep space is almost exclusively derived from ground-based accelerator experiments with heavy ions in animal or *in vitro* models [1]. In an effort to gain more information on space radiation risk and to develop countermeasures, NASA initiated several years ago a Space Radiation Health Program, which is currently supporting biological experiments performed at the Brookhaven National Laboratory. The European Space Agency (ESA) has recently established human space exploration beyond Low Earth Orbit as one of its goals, and in this frame, new space radiation activities have been initiated. Europe has a long tradition in radiobiology research at accelerators, generally focussing on charged-particle cancer therapy. This expertise can be adapted to address the issue of space radiation risk.

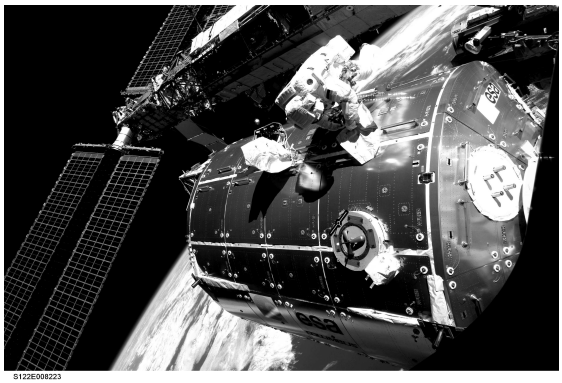

Figure 1: ESA astronaut Hans Schlegel works on Columbus exterior during the second spacewalk of the STS-122 mission. The astronauts are exposed to radiation plus many other stressors (including microgravity) during spaceflights (Official credit: ESA/ NASA)

Space radiobiology

A preparatory studied funded by ESA in 2006 made a careful review of the current knowledge in space radiation effects, gaps in knowledge, and ground-based facilities where radiobiology studies could be performed in Europe. The main conclusion of this study [2] was that more research is needed in the field of cancer and noncancer late effects induced by heavy ions and that GSI is the ideal facility for this kind of research in the energy range 100-2000 MeV/n, while GANIL in France can supply beams at lower energies. Based on these recommendations, ESA has issued in 2008 an announcement of opportunity (AO) for investigations into biological effects of cosmic radiation using the GSI accelerator facility. Over 30 proposals have been submitted in response to the AO, and 13 have been selected by an independent review panel for implementation at GSI. The projects include studies on the effects of heavy ions on DNA, central nervous system, retina, mucositis, bone, heart, as well as physics studies on low energy electrons and organ dose measurements.

Radiation damage to microelectronics

In addition to the health risk for manned missions, cosmic rays are of concern because it is well known that these energetic particles can damage integrated circuits (IC) in spacecrafts electronics [3]. The main effect associated with a hit of a heavy ion is the generation of electrical charges along their track through the semiconductor material inside the ICs (Fig. 2). In some cases it can lead to catastrophic failures when the deposited charge is high enough, such as latchup. Heavy ion testing at accelerator facilities is routinely used to study mechanisms of single-event effects (SEE). ESA has recognized that these tests must be also performed at high-energy accelerators, because range effects and nuclear interactions can modify the damage to microelectronics. For these very reasons, ESA is now supporting a study on the impact of relativistic heavy ions on different electronic devices (including MOSFET and SDRAM) led by the Fraunhofer Institute for Technological Trend Analysis using the GSI accelerator. The results of this study will be used to clarify the risk to electronic devices from very high energy cosmic rays, and to plan future testing of spaceflight hardware.

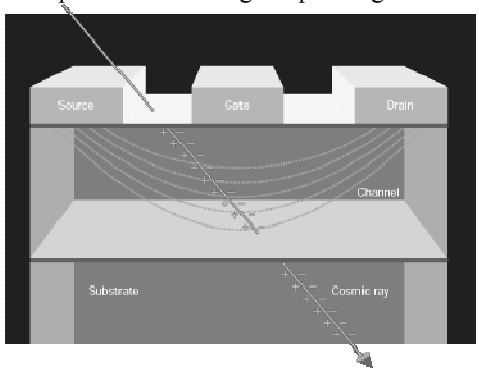

Figure 2: Effect of cosmic rays in electronic chips.

References

[1] M. Durante and F.A. Cucinotta, *Nat. Rev. Cancer* **8** (2008) 465-472
[2] M. Durante *et al.*, *Adv. Space Res* **39** (2007) 1082-1086
[3] A. Holmes-Siedle and L. Adams, *Handbook of Radiation Effects*, Oxford Univ. Press, 2002.

Status Report of the HIT Project

U. Weinrich for the GSI therapy accelerator team

Abstract

During the year 2008 the accelerator settings of the Heidelberg Ion Therapy Center (HIT) were finalized for patient treatment with carbon and proton beam for three fixed horizontal beam stations. For the worldwide first carbon gantry the beam commissioning reached a point that good carbon beam performance could be shown for a dedicated set of beam diameters, beam energies and gantry angles. The accelerator was handed over from GSI to the HIT GmbH, the operating company of the facility. The GSI project phase ended officially in September 2008.

Beam commissioning for fixed beam stations

The beam commissioning covered the 'patient ready' beam performance both for proton and carbon ions with about 60000 beam parameter set values for the two horizontal treatment places H1, H2 and the experimental QA-place [1,2]. Table 1 summarizes the library (LIBC) now available for request by the treatment technique systems for these places.

Table 1: Beam parameter set values (LIBC)

Parameter	Steps	Protons	Carbon
Energy	255	48 – 221 MeV/u	88 – 430 MeV/u
Penetration	255	20 - 300 mm	20 - 300 mm
Beam Size	4	8 – 20 mm	4 – 12 mm
Intensity	10	$8{\cdot}10^7$ - $2{\cdot}10^9$ 1/s	$2{\cdot}10^6$ - $8{\cdot}10^7$ 1/s
Ions / Spill	10	$4{\cdot}10^8$ - $1{\cdot}10^{10}$	$1{\cdot}10^7$ - $4{\cdot}10^8$
Place	3	H1, H2, QA	H1, H2, QA

Another implemented option is that the beam delivery to the treatment station can be interrupted and switched on again several times within one synchrotron cycle, without significant losses and with a rather homogeneous spill pattern. The reached performance is shown in Figure 1

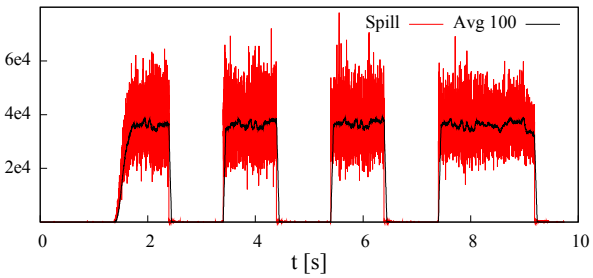

Figure 1: Particles per 500 µs intervall during a spill with three interruptions.

The level of extracted intensity during interruptions was reduced below $5{\cdot}10^{-4}$ of the nominal intensity. Red and black curve represent particle number in 500 µs intervals and a 50 ms average and were measured with ionisation chambers delivered by GSI[3;4].

Figure 2 displays the horizontal width and position at the isocenter for four beam-width steps F1 through F4 as a function of energy step, measured with a viewing screen. The deviation from the requested LIBC set values is smaller than ±15%. The deviation of the beam position from the exact location of the isocenter remains in a band of ±15% of the corresponding width value, too.

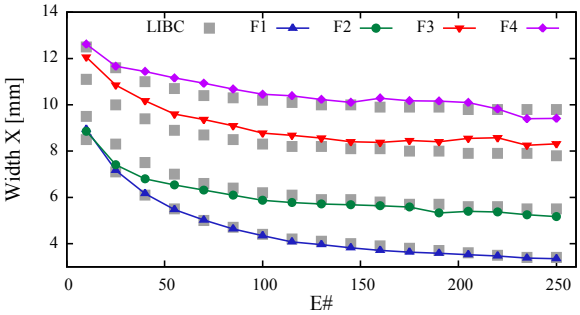

Figure 2: Measured horizontal beam-width in the isocenter.

The stability of transversal beam parameters during the spill is very good, as can be seen from Figure 3, showing horizontal position and width as a function of time measured by the treatment monitoring system.

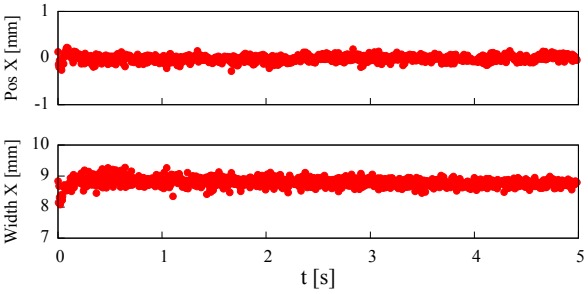

Figure 3: Horizontal position and width over the spill.

Commissioning of the Gantry

The assembly of the Carbon Gantry was finished in 2008 with some major problems to overcome[5]. In March 2008 severe problems on cable isolation in the flexible cable tray of the gantry occurred, leading to modifications that

had to be performed before the system could be used again in November 2008.
During the short time of beam commissioning in 2008 it was, however, possible to reach good beam performance for different carbon beam parameters[6]. It was possible to establish a procedure to achieve beam size stability within 25% of the nominal beam size over all gantry angles without any change of focusing. A typical result of such a procedure is shown in Figure 4.

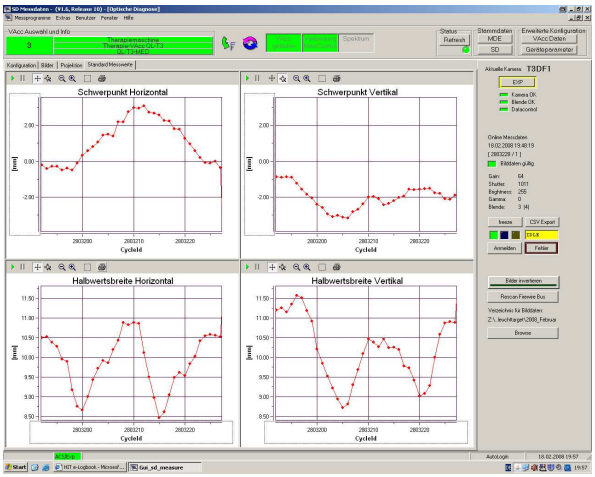

Figure 4: Beam position (upper figures) and focus behaviour (lower figures) over a full gantry rotation.

It was possible to use this procedure at maximum and at minimum energy for all different beam sizes. The result ist shown in the following table. If needed it will be possible to further improve these results by gantry angle dependent interpolation of the quadrupole settings. This was foreseen in the concept right from the beginning.

Table 2: Achieved carbon beam focus performance

Energy step	Target Focus [mm]	Horizontal Focus [mm]	Vertical Focus [mm]
1	9.8	9.6 - 10.0	9.6 - 10.0
1	10.7	10.2 - 11.0	10.2 - 11.4
1	12.1	11.7 - 12.9	11.9 - 13.1
1	13.4	12.6 - 14.4	12.2 - 14.8
255	3.4	3.1 - 4.1	2.9 - 3.9
255	5.5	4.7 - 6.5	5.1 - 6.1
255	7.8	6.9 - 8.9	7.2 - 8.8
255	9.8	8.5 - 10.9	8.7 - 11.7

The next step which was aimed at was to establish a similar procedure for the beam position optimisation. Unfortenuatly practically no further beam time was available for the gantry commissioning. All available was instead dedicated to prepare the treatment technique for patient treatment.

Conclusion and outlook

In addition to the described commissioning activities training of the HIT staff took place and various documentation was provided by the GSI team to HIT GmbH in order to operate the accelerator in a reliable manner. After the GSI contract for the project ended officially in September the staff members of the GSI therapy accelerator team had been directed to other GSI tasks.
In addition to a service and maintenance contract for the beam diagnostic systems a support contract was signed between GSI and the University Clinics of Heidelberg which allows further GSI consultations and labour. Within this contractual frame the continuation of the Gantry commissioning will be performed and a strategy to improve the linac beam transmission will be realized in cooperation with the HIT GmbH [7].

GSI has successfully demonstrated with large engagement of many GSI members the ability to realize a new accelerator facility for cancer treatment at the University Clinics of Heidelberg, covering all steps from the design upto beam commissioning.

References

[1] D.Ondreka et al., "THE HEIDELBERG ION THERAPY (HIT) ACCELERATOR COMING INTO OPERATION", EPAC 2008 Genoa

[2] C.Kleffner et al., "THE HEIDELBERG ION THERAPY (HIT) ACCELERATOR COMING INTO OPERATION", CAARI 2008 Fort Worth

[3] M.Schwickert et al., "BEAM DIAGNOSTIC FOR COMMISSIONING THE HEBT AND GANTRY SECTIONS OF THE HIT MEDICAL ACCELERATOR", EPAC 2008 Genoa

[4] A.Peters et al., "SPILL STRUCTURE MEASUREMENTS AT THE HEIDELBERG ION THERAPY CENTRE ", EPAC 2008 Genoa

[5] R.Fuchs et al., "ASSEMBLY OF THE CARBON BEAM GANTRY AT THE HEIDELBERG ION THERAPY (HIT) ACCELERATOR", EPAC 2008 Genoa

[6] U.Weinrich et al., "COMMISSIONING OF THE CARBON BEAM GANTRY AT THE HEIDELBERG ION THERAPY (HIT) ACCELERATOR", EPAC 2008 Genoa

[7] M. Maier et al.: HIT Linac upgrade, this annual report

Completion of HIT Beam Diagnostics Project

A. Reiter, R. Boywitt, C. Dorn, H. Graf, T. Hoffmann, C. Müller, H. Reeg, M. Witthaus and M. Schwickert

GSI, Darmstadt, Germany

Introduction

In 2008 GSI Beam Diagnostic (BD) department successfully finished the project of supplying beam diagnostic devices for the HIT (Heidelberg Ion Therapy) accelerator facility. After signing of the contract in June 2003, beam diagnostic department was responsible for the layout, construction and commissioning of the devices on site. The delivery included the complete set of 95 diagnostic devices (mechanics, detectors and electronics), the data acquisition system (DAQ) and, in close collaboration with the industrial partner Eckelmann AG, the implementation of the DAQ software. After completion of the accelerator commissioning GSI officially handed over the medical therapy accelerator to the Heidelberg university clinics. In this report we briefly outline some of the beam diagnostics topics that had to be addressed throughout the past year.

Beam Diagnostics Issues

BD group provided continuous support for the on-going accelerator commissioning. The beam parameters for the already commissioned two horizontal treatment places were carefully verified and adjusted, gantry and quality assurance place completed the beam time schedule. The work on the BD software and hardware aimed to facilitate day-to-day operation of the machine and to include the long-term requirements of a medical accelerator:

- Implementation of therapy protocols (section 1)
- Integration of stray field correction for DC transformers (section 2)
- Display and tests of patient monitors (section 3)
- System checks and storage of reference data for BD detectors
- Automated monitoring of stripper foil quality
- Upgrade of LabView RT software to version 8 on all DAQ systems

An in-depth software upgrade became necessary in order to implement missing features and hence a considerable amount of time had to be spent on software tests. As one of the major results reliability issues with the firewire network were resolved which links the CCD cameras for readout of scintillating screens to the DAQ system. Problems with the previous LabView driver caused unreliable camera connections on the network.

1. Therapy protocols

During commissioning mandatory therapy protocols were established. These protocols are fully automated sequences of beam requests to monitor the stability of the machine and are executed every day in preparation of the treatment. The data acquired with BD devices are analysed and displayed in standardised protocols that quickly allow operators to determine whether the beam quality is acceptable for patient treatment.

2. Synchrotron transformer

Due to the very compact design of the HIT synchrotron (65 m circumference) the available space for BD components impedes a sufficient magnetic shielding for susceptible devices like DC transformers. Interference had been foreseen for the near-by synchrotron dipole ramping at 1.5 T/s, but a second hall probe had to be added to correct the transformer signal also for the fringe field of the following sextupole. The energy-dependent correction was derived and introduced in the accelerator control system, see Figure 1. Similar measures might follow for the two DC-transformers in the low-energy beam lines.

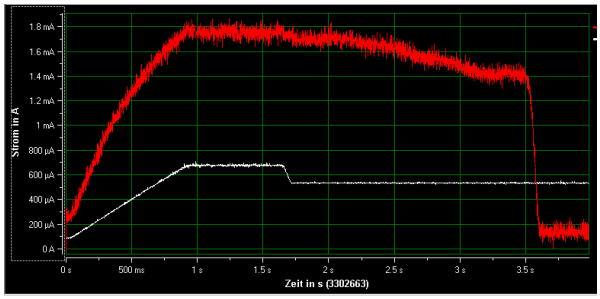

Figure 1: Synchrotron beam current (top). The bottom line shows the interference due to magnetic stray fields.

3. Patient monitor

Patient treatment at HIT is controlled by the beam application and monitoring system (BAMS), delivered by Siemens AG. A BAMS consists of ionisation and multi-wire chambers. The ionisation monitor outputs were duplicated via real-time Ethernet hardware and integrated into the AC current measurement system. Intensity and structure of the spill can now be monitored up to the end of the beam lines even in treatment mode, where the usage of other intercepting BD devices is prohibited. Thus the operators in the HIT control room receive important online information of successful beam delivery to the treatment places.

Conclusion

In 2008 the BD project in Heidelberg was successfully completed. All systems are now operated by the HIT operating company, but GSI beam diagnostics group still acts as technical advisor in the frame of a service and maintenance contract with HIT.

HIT Linac upgrade

M. Maier, W. Barth, A. Orzhekhovskaya, H. Vormann, S. Yaramyshev

GSI, Darmstadt, Germany

Introduction

The overall achieved transmission for carbon ions through the injector linac at the Heidelberg ion therapy HIT did not ecxeed 30 % due to a mismatch of the beam at the RFQ entrance [1]. Thus a detailed upgrade programm has been started to exchange the RFQ with a new input radial matcher (IRM) design, to correct the misalignment and to optimize beam transport to the IH-DTL. The aim is to achieve a sufficient overall linac transmission above 60%.

Design and production

The design of the IRM based on particle distributions generated from emittance measurements behind the LEBT at HIT was done using the Dynamion simulation code [2] and is shown in Figure 1. Also shown is the original design which requires a beam size and convergence that the existing solenoid, used for the beam matching to the RFQ, is not able to provide.

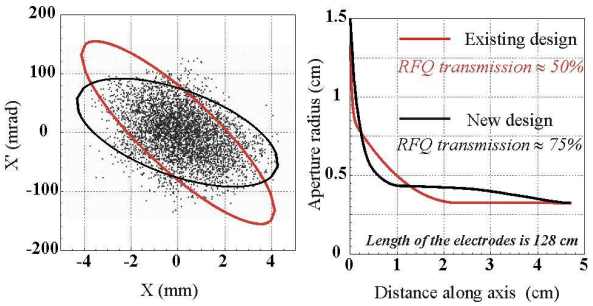

Figure 1: Dynamion simulation of the transmission improvement through the old and the new input radial matcher design.

Figure 2: Final test piece (right), of the RFQ radial matcher section and a plastic model (left) to check the production procedures.

The assembly, alignment and RF tuning of the RFQ was done at IAP Frankfurt in summer 2008.

Measurements

The new RFQ design was tested at a test setup in Risø, Denmark for adjusting the Rebuncher voltage [3]. A test bench comprising a full ion source and LEBT branch to commission the RFQ had been installed by Danfysik.

Results

The beam commissioning at Risø took place in autumn 2008. In summary the results were, that the power consumption of the RFQ is above 200 kW and thus too high for operation in Heidelberg,. The steering of the RFQ depending of the rf-power is stronger than tolerable. The rebuncher voltage was not adjustable within the geometrical limits. Additionally the measured RFQ energy, depending on the rf-power, shows a 'wavy' structure (Figure 3). Furthermore, it was not possible to determine the transmission of the RFQ due to insufficiently defined beam parameters at the RFQ entrance.

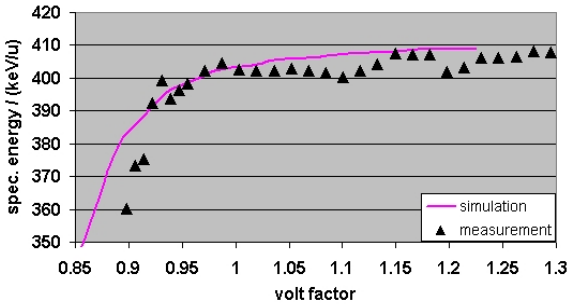

Figure 3: Measurement of the RFQ beam energy versus the volt factor (corresponds to rf-voltage).

The suspected reasons for this unexpected and intolerable behaviour are a misalignment of the electrodes, a too strong influence of the modified rebuncher section on the field distribution and not sufficiently defined beam parameters from the LEBT at Risø.

End of 2008 the RFQ was transported to IAP and there its mechanical and rf-properties will be revised. Depending on the results the whole structure might be reassembled and finally a new location and time has to be found for commissioning of the RFQ and adjusting the rebuncher.

References

[1] M. Maier et al., Proc. PAC 2007, p. 2734
[2] S. Yaramishev et al., NIM A, 2005.
[3] C. Kleffner et al., GSI annual report 2005.

Status of the Linac for the Italian Hadrontherapy Centre CNAO

B. Schlitt[1], R. Boywitt[1], G. Breitenberger[1], J. Cavaco[1], G. Clemente[1], H. Graf[1], M. Hörr[1], N. Kischnik[1], M. Pilz[1], A. Reiter[1], G. Riehl[1], G. Schulz[1], D. Schupp[1], J. Trüller[1], W. Vinzenz[1], H. Vormann[1], A. Alpegiani[2], D. Bianculli[2], E. Vacchieri[2], S. Vitulli[2], C. Roncolato[3], and G. Venchi[4]
[1]GSI, Darmstadt, Germany; [2]CNAO Foundation, Pavia, Italy; [3]INFN-LNL, Legnaro, Italy; [4]Univ. of Pavia, Italy

Introduction

The italian hadrontherapy centre CNAO (Centro Nazionale di Adroterapia Oncologica) in Pavia, Italy, is designed for the treatment of tumours with proton and carbon ion beams and is presently under commissioning [1][2][3]. The accelerator consists of a 7 MeV/u injector linac and of a 400 MeV/u synchrotron. The linac is a copy of the linac of the Heidelberg Ion-beam Therapy centre HIT and consists of a 400 keV/u RFQ and a 20 MV IH-type drift tube linac (IH-DTL) [4]. GSI delivers technical support for manufacturing, assembly, RF tuning, tests, and on-site installation and commissioning of the CNAO linac and its technical systems [5][6][7]. GSI has also delivered various beam diagnostics components to CNAO for LEBT, linac, and MEBT [8].

Linac Status

After completion of assembly, RF tuning, and vacuum tests at GSI early in 2008 [7], the IH-DTL and some further components were shipped to Pavia in April. Various low-level RF and vacuum tests were performed successfully in Pavia with the RFQ and the IH-DTL to check the cavities performances after transportation. Since these tests, the structures were kept under vacuum until installation in the accelerator complex.

The complete electronics, data acquisition systems, and cables for the beam diagnostics devices delivered by GSI were installed and tested in Pavia in 2008. The beam current and profile measurement systems installed in the LEBT and on a subsequent test bench were tested successfully with ion beams in September and were used for systematic beam measurements in January 2009 (Fig. 1).

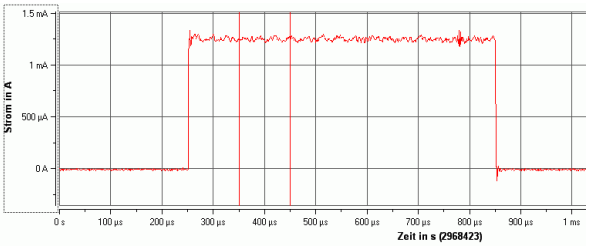

Figure 1: H_3^+ beam pulse (1.2 mA, 600 µs) measured during LEBT commissioning in front of the solenoid for focusing the beam into the RFQ.

During 2008, all linac control system components were delivered by ECKELMANN and were installed and tested on site in Pavia. First magnet power supplies delivered by JAEGER as well as the high-voltage supply for the LEBT beam chopper were commissioned and tested successfully. Commissioning and on-site acceptance tests of all linac RF amplifiers (pulse powers of 200 kW, 1400 kW, and 4 kW) delivered by THOMSON B&M were successfully performed on dummy load.

In November 2008, the RFQ was temporarily installed close to its final position and first on-site RF conditioning was done in December 2008 and January 2009. Final installation of the RFQ started end of January 2009. RF tests are ongoing. A special beam diagnostics test bench including an emittance measurement device loaned from GSI was designed for RFQ beam commissioning and was installed behind of the RFQ (Fig. 2).

Commissioning of LEBT and ion sources was finished by CNAO successfully in January 2009. Design ion beam currents and emittances were reached [1][2][3]. The correct matching conditions at the position of the RFQ entrance were checked by beam emittance measurements.

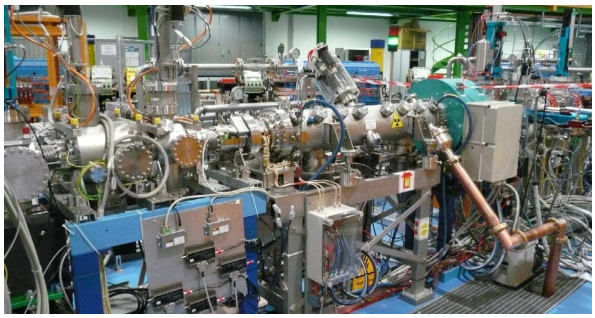

Figure 2: RFQ at final position (centre) and beam diagnostics test bench for RFQ commissioning (left).

Outlook

RFQ beam commissioning is planned for March 2009, followed by installation and commissioning of the IH-DTL from April to June 2009. The GSI services fixed in the CNAO GSI contract will be finished in summer / autumn 2009 with the commissioning of the last beam diagnostics components from GSI and a debuncher cavity installed in the MEBT. We would like to thank all involved colleagues from CNAO, GSI, and the suppliers for their support and for the great hospitality at CNAO.

References

[1] M. Pullia et al., EPAC08, p. 982.
[2] G. Ciavola et al., EPAC08, p. 415.
[3] J. Bosser et al., EPAC08, p. 1071.
[4] B. Schlitt, LINAC08, in print.
[5] B. Schlitt et al., GSI Sci. Rep. 2006, p. 383.
[6] B. Schlitt et al., GSI Sci. Rep. 2007, p. 395.
[7] H. Vormann et al., EPAC08, p. 1833.
[8] A. Reiter et al., EPAC 2006, p. 1028.

GSI publications to the programme 'Physics of hadrons and nuclei': Accelerator Research & Development published in 2008

1. Reviewed publications

001 Al-Khateeb, A.*; Hasse, R. W.*; Boine-Frankenheim, O.*; Hofmann, I.*: **Screening of the resistive-wall impedance by a cylindrical electron plasma.** *New Journal of Physics* **10**: 083008. DOI:10.1088/1367-2630/10/8/083008 OPEN ACCESS. HANU:Accelerator.

002 Al-Khateeb, A. M.*; Hasse, R. W.*; Boine-Frankenheim, O.*: **Comparison of the longitudinal coupling impedance from different source terms.** *Nuclear instruments & methods in physics research, Section A, Accelerators, spectrometers, detectors and associated equipment* **593**(3): 171–176. DOI:10.1016/j.nima.2008.05.011 HANU:Accelerator.

003 Al-Khateeb, A. M.*; Hasse, R. W.*; Boine-Frankenheim, O.*; Hofmann, I.*: **Longitudinal coupling impedance for a smooth resistive cylindrical pipe of two conducting layers of finite thicknesses.** *Nuclear instruments & methods in physics research, Section A, Accelerators, spectrometers, detectors and associated equipment* **587**(2): 236–242. DOI:10.1016/j.nima.2008.01.074 HANU:Accelerator.

004 Belov, A. V.; Belyakova, T. F.; Gornikel, I. V.; Kuchinsky, V. G.; Kukhtin, V. P.; Lamzin, E. A.; Semchenkov, A. G.*; Shatil, N. A.; Sytchevsky, S. E.: **3D field simulation of complex systems with permanent magnets and excitation coils.** *IEEE transactions on applied superconductivity* **18**(2): 1609–1612. DOI:10.1109/tasc.2008.920816 HANU:Accelerator.

005 Bezshyyko, O.; Dolinskii, A.*; Bezshyyko, K.; Kadenko, I.; Yermolenko, R.; Ziemann, V.: **PETAG01: A program for the direct simulation of a pellet target.** *Computer Physics Communications* **178**(2): 144–155. DOI:10.1016/j.cpc.2007.07.013 HANU:Accelerator.

006 Boine-Frankenheim, O.*; Kornilov, V.*; Paret, S.*: **Measurement and simulation of transverse Schottky noise with space charge.** *Physical Review Special Topics - Accelerators and Beams* **11**(7): 074202. DOI:10.1103/physrevstab.11.074202 OPEN ACCESS. HANU:Accelerator.

007 Brandau, C.*; Kozhuharov, C.*; Harman, Z.; Müller, A.; Schippers, S.; Kozhedub, Y. S.; Bernhardt, D.; Boehm, S.; Jacobi, J.; Schmidt, E. W.; Mokler, P. H.*; Bosch, F.*; Kluge, H.-J.*; Stöhlker, T.*; Beckert, K.*; Beller, P.*; Nolden, F.*; Steck, M.*; Gumberidze, A.*; Reuschl, R.*; Spillmann, U.*G; Currell, F. J.; Tupitsyn, I. I.; Shabaev, V. M.; Jentschura, U. D.; Keitel, C. H.; Wolf, A.; Stachura, Z.: **Isotope shift in the dielectronic recombination of three-electron ^{A}Nd^{57+}.** *Physical review letters* **100**(7): 073201. DOI:10.1103/physrevlett.100.073201 PNI.HANU:Accelerator.

008 Celona, L.; Ciavola, G.; Consoli, F.; Gammino, S.; Maimone, F.; Mascali, D.; Spädtke, P.*; Tinschert, K.*; Lang, R.*; Mader, J.*; Roßbach, J.*; Barbarino, S.; Catalano, R. S.: **Observations of the frequency tuning effect in the 14 GHz CAPRICE ion source.** *Review of scientific instruments* **79**(2): 023305. DOI:10.1063/1.2841694 HANU:Accelerator.

009 Ciavola, G.; Gammino, S.; Barbarino, S.; Celona, L.; Consoli, F.; Gallo, G.; Maimone, F.; Mascali, D.; Passarello, S.; Galata, A.; Tinschert, K.*; Spädtke, P.*; Lang, R.*; Maeder, J.; Roßbach, J.*; Koivisto, H.; Savonen, M.; Koponen, T.; Suominen, P.; Ropponen, T.; Barue, C.; Lechartier, M.; Beijers, J. P. M.; Brandenburg, S.; Kremers, H. R.; Vanrooyen, D.; Kuchler, D.; Scrivens, R.; Schachter, L.; Dobrescu, S.; Stiebing, K.: **A status report of the multipurpose superconducting electron cyclotron resonance ion source.** *Review of scientific instruments* **79**(2): 02A326. DOI:10.1063/1.2812336 HANU:Accelerator.

010 De Gersem, H.; Koch, S.; Shim, S. Y.; Fischer, E.*; Moritz, G.*; Weiland, T. KV: **Transient finite-element simulation of the eddy-current losses in the beam tube of the SIS-100 magnet during ramping.** *IEEE transactions on applied superconductivity* **18**(2): 1613–1616. DOI:10.1109/tasc.2008.921230 HANU:Accelerator.

011 Dolinskii, A.*; Demyanov, A.; Dolinska, M.; Kolosov, A.; Valkov, A.: **Design study of the KINRIS isotope separator with a 270^{o} wide aperture magnet.** *Nuclear instruments & methods in physics research, Section B, Beam interactions with materials and atoms* **266**(19): 4188–4191. DOI:10.1016/j.nimb.2008.05.025 HANU:Accelerator.

012 Dolinskii, A.*; Dolinska, M.; Valkov, A.; Gorda, A.*; Rudenko, T.: **Influence of second order abberations on**

mass-separations with 270^o analyzing magnet. (5): 77–80. URL HANU:Accelerator.

013 Dolinskii, A.*; Geissel, H.*; Litvinov, S.*; Nolden, F.*; Steck, M.*; Weick, H.*: **The CR storage ring in an isochronous mode operation with nonlinear optics characteristics.** *Nuclear instruments & methods in physics research, Section B, Beam interactions with materials and atoms* **266**(19): 4579–4582. DOI:10.1016/j.nimb.2008.05.082 HANU:Accelerator.

014 Fabbricatore, R.; Alessandria, F.; Bellomo, G.; Farinon, S.; Gambardella, U.; Kaugerts, J.*; Marabotto, R.; Musenich, R.; Moritz, G.*; Sorbi, M.; Volpini, G.: **Development of a curved fast ramped dipole for FAIR SIS300.** *IEEE transactions on applied superconductivity* **18**(2): 232–235. DOI:10.1109/tasc.2008.922291 HANU:Accelerator.

015 Franchetti, G.*; Parfenova, A.; Hofmann, I.*: **Measuring localized nonlinear components in a circular accelerator with a nonlinear tune response matrix.** *Physical Review Special Topics - Accelerators and Beams* **11**(9): 094001. DOI:10.1103/physrevstab.11.094001 OPEN ACCESS. HANU:Accelerator.

016 Franzke, B.*; Geissel, H.*; Münzenberg, G.*: **Mass and lifetime measurements of exotic nuclei in storage rings.** *Mass Spectromtery Reviews* **27**(5): 428–469. DOI:10.1002/mas.20173 HANU:Accelerator.

017 Groening, L.*; Barth, W.*; Bayer, W.*; Clemente, G.*; Dahl, L.*; Forck, P.*; Gerhard, P.*; Hofmann, I.*; Riehl, G.*; Yaramyshev, S.*; Jeon, D.; Uriot, D.: **Benchmarking of measurement and simulation of transverse rms-emittance growth.** *Physical Review Special Topics - Accelerators and Beams* **11**(9): 094201. DOI:10.1103/physrevstab.11.094201 OPEN ACCESS. HANU:Accelerator.

018 Hedlund, E.; Westerberg, L.; Malyshev, O. B.; Leandersson, M.; Friden, C.-J.; Edqvist, E.; Kollmus, H.*; Bellachioma, M. C.*; Reich-Sprenger, H.*; Krasnov, A.: **A new test stand for heavy ion induced gas desorption measurements at TSL.** *Nuclear instruments & methods in physics research, Section A, Accelerators, spectrometers, detectors and associated equipment* **586**(3): 377–381. DOI:10.1016/j.nima.2007.12.020 HANU:Accelerator.

019 Hollinger, R.*; Galonska, M.*; Gutermuth, B.*; Heyrnach, F.* Krichbaum, H.*; Leible, K. D.*; Ochs, K.*; Schäffer, P.*; Schäffer, S.*; Spädtke, P.*; Stork, M.*; Wesp, A.*; Mayr, R.: **Status of high current ion source operation at the GSI accelerator facility.** *Review of scientific instruments* **79**(2): 02C703. DOI:10.1063/1.2801623 HANU:Accelerator.

020 Hollinger, R.*; Spädtke, P.*: **High current ion beam transport using solenoids.** *Review of scientific instruments* **79**(2): 02B704. DOI:10.1063/1.2801351 HANU:Accelerator.

021 Koch, S.; De Gersem, H.; Weiland, T.; Fischer, E.*; Moritz, G.* KV: **Transient 3D finite element simulations of the SIS100 magnet considering anisotropic, nonlinear material models for the ferromagnetic yoke.** *IEEE transactions on applied superconductivity* **18**(2): 1601–1604. DOI:10.1109/tasc.2008.921892 HANU:Accelerator.

022 Koivisto, H.; Suominen, P.; Ropponen, T.; Ropponen, J.; Koponen, T.; Savonen, M.; Toivanen, V.; Wu, X.; Machicoane, G.; Stetson, J.; Zavodszky, P.; Doleans, M.; Spädtke, P.*; Vondrasek, R.; Tarvainen, O.: **Ion beam development for the needs of the JYFL nuclear physics programme.** *Review of scientific instruments* **79**(2): 02A303. DOI:10.1063/1.2804866 HANU:Accelerator.

023 Kornilov, V.*; Boine-Frankenheim, O.*; Hofmann, I.*: **Stability of transverse dipole modes in coasting ion beams with nonlinear space charge, octupoles, and chromaticity.** *Physical Review Special Topics - Accelerators and Beams* **11**(1): 014201. DOI:10.1103/physrevstab.11.014201 OPEN ACCESS. HANU:Accelerator.

024 Kreidi, K.; Jahnke, T.; Weber, T.; Havermeier, T.; Grisenti, R. E.*; Liu, X.; Morisita, Y.; Schössler, S.; Schmidt, L. P. H.; Schöffler, M.*; Odenweller, M.; Neumann, N.; Foucar, L.; Titze, J.; Ulrich, B.; Sturm, F.; Stuck, C.; Wallauer, R.; Voss, S.; Lauter, I.; Kim, H. K.; Rudloff, M.; Fukuzawa, H.; Prümper, G.; Saito, N.*; Ueda, K.; Czasch, A.; Jagutzki, O.; Schmidt-Böcking, H.; Semenov, S. K.; Cherepkov, N. A.; Dörner, R.: **Localization of inner-shell photoelectron emission and interatomic Coulombic decay in Ne_2.** *Journal of physics B, Atomic, molecular and optical physics* **41**(10): 101002. DOI:10.1088/0953-4075/41/10/101002 HANU:Accelerator.

025 Nolden, F.*; Dimopoulou, C.*; Dolinskii, A.*; Steck, M.*: **Storage rings for radioactive ion beams.** *Nuclear instruments & methods in physics research, Section B, Beam interactions with materials and atoms* **266**(19): 4569–4574. DOI:10.1016/j.nimb.2008.05.103 HANU:Accelerator.

026 Schnizer, P.*; Kiesewetter, H. R.*; Mack, T.*; Knapp, T.*; Klos, F.*; Manderla, M.; Rauch, S.*; Schonecker, M.; Werkmann, R.* KV: **A mole for measuring pulsed superconducting magnets.** *IEEE transactions on applied superconductivity* **18**(2): 1648–1651. DOI:10.1109/tasc.2008.921250 HANU:Accelerator.

027 Schnizer, P.*; Schnizer, B.; Akishin, P.; Fischer, E.* KV: **Magnetic field analysis for superferric accelerator magnets using elliptic multipoles and its advantages.** *IEEE transactions on applied superconduc-*

tivity **18**(2): 1605–1608. DOI:10.1109/tasc.2008.920636 HANU:Accelerator.

028 Semchenkov, A.*; Brüchle, W.*; Jäger, E.*; Schimpf, E.*; Schädel, M.*; Mühle, C.*; Klos, F.*; Türler, A.; Yakushev, A.; Belov, A.; Belyakova, T.; Kaparkova, M.; Kukhtin, V.; Lamzin, E.; Sytchevsky, S.: **The TransActinide Separator and Chemistry Apparatus (TASCA) at GSI - Optimization of ion-optical structures and magnet designs.** *Nuclear instruments & methods in physics research, Section B, Beam interactions with materials and atoms* **266**(19): 4153–4161. DOI:10.1016/j.nimb.2008.05.132 HANU:Accelerator.

029 Sidorov, A.; Dorf, M.; Zorin, V.; Bokhanov, A.; Izotov, I.; Razin, S.; Skalyga, V.; Roßbach, J.*; Spädtke, P.*; Balabaev, A.: **Multiaperture ion beam extraction from as-dynamic electron cyclotron resonance source of multicharged ions.** *Review of scientific instruments* **79**(2): 02A317. DOI:10.1063/1.2805640 HANU:Accelerator.

030 Spaedtke, P.*: **The physics of ion beam extraction from an electron cyclotron resonance ion source.** *IEEE transactions on plasma science* **36**(4): 1569–1573. DOI:10.1109/tps.2008.928716 HANU:Accelerator.

031 Spädtke, P.*; Tinschert, K.*; Lang, R.*; Mader, J.*; Roßbach, J.*; Stetson, J. W.; Celona, L.: **Prospects of ion beam extraction and transport simulations (invited).** *Review of scientific instruments* **79**(2): 02B716. DOI:10.1063/1.2823968 HANU:Accelerator.

032 Stafiniak, A.*; Floch, T.; Hahne, P.*; Heß, G.*; Kauschke, M.*; Klos, F.*; Marzouki, F.*; Moritz, G.*; Mueller, H.*; Rebscher, M.*; Schnizer, P.*; Schroeder, C.*; Walter, G.*; Walter, F.*; Welker, H.* KV: **Commissioning of the prototype test facility for rapidly-cycling superconducting magnets for FAIR.** *IEEE transactions on applied superconductivity* **18**(2): 1625–1628. DOI:10.1109/tasc.2008.922289 HANU:Accelerator.

033 Struckmeier, J.*; Redelbach, A.*: **Covariant Hamiltonian field theory.** *International journal of modern physics E, Nuclear physics* **17**(3): 435–491. DOI:10.1142/S0218301308009458 HANU:Accelerator.

034 Tahir, N. A.*; Spiller, P.*; Piriz, A. R.; Shutov, A.; Lomonosov, I. V.; Schollmeier, M.; Pelka, A.; Hoffmann, D. H. H.; Deutsch, C.: **Studies of high-energy density states using isochoric heating of matter by intense heavy ion beams: the HEDgeHOB Collaboration.** *Physica scripta* **T132**: 014023. DOI:10.1088/0031-8949/2008/t132/014023 PNI.HANU:Accelerator.

035 Tinschert, K.*; Iannucci, R.*; Lang, R.*: **Electron cydotron resonance ion sources in use for heavy ion cancer therapy.** *Review of scientific instruments* **79**(2): 02C505. DOI:10.1063/1.2805226 HANU:Accelerator.

036 Volpini, G.; Alessandria, F.; Bellomo, G.; Fabbricatore, P.; Farinon, S.; Gambardella, U.; Kaugerts, J.*; Moritz, G.*; Sorbi, M.; Wilson, M. N. KV: **Low-loss NbTi Rutherford cable for application to the SIS-300 dipole magnet prototype.** *IEEE transactions on applied superconductivity* **18**(2): 997–1000. DOI:10.1109/tasc.2008.922516 HANU:Accelerator.

037 Willering, G. P.; Verweij, A. P.; Kaugerts, J.*; ten Kate, H. H. J. KV: **Stability of Nb-Ti Rutherford cables exhibiting different contact resistances.** *IEEE transactions on applied superconductivity* **18**(2): 1263–1266. DOI:10.1109/tasc.2008.920560 HANU:Accelerator.

038 Winkelmann, T.; Cee, R.; Haberer, T.; Naas, B.; Peters, A.; Scheloske, S.; Spädtke, P.*; Tinschert, K.*: **Electron cyclotron resonance ion source experience at the Heidelberg Ion Beam Therapy Center.** *Review of scientific instruments* **79**(2): 02A331. DOI:10.1063/1.2823952 HANU:Accelerator.

039 Winkler, M.*; Geissel, H.*; Weick, H.*; Achenbach, B.*; Behr, K. H.*; Boutin, D.*; Brünle, A.*; Gleim, M.*; Hüller, W.*; Karagiannis, C.*; Kelic, A.*; Kindler, B.*; Kozlova, E.*; Leibrock, H.*; Lommel, B.*; Moritz, G.*; Mühle, C.*; Münzenberg, G.*; Nociforo, C.*; Plaß, W.; Scheidenberger, C.*; Simon, H.*; Sümmerer, K.*; Tahir, N. A.*; Tauschwitz, A.*; Tomut, M.*; Winfield, J. S.*; Yavor, M.: **The status of the Super-FRS in-flight facility at FAIR.** *Nuclear instruments & methods in physics research, Section B, Beam interactions with materials and atoms* **266**(19): 4183–4187. DOI:10.1016/j.nimb.2008.05.073 HANU:Accelerator.

040 Zhao, W. J.; Müller, M. W. O.*; Janik, J.; Liu, K. X.; Ren, X. T.: **DUHOCAMIS: A dual hollow cathode ion source for metal ion beams.** *Review of scientific instruments* **79**(2): 02B315. DOI:10.1063/1.2823894 HANU:Accelerator.

2. Further publications [1]

001 Aleksandrov, A. V.; Hofmann, I.*; Lagniel, J.-M.: **Summary Report of the Working Group B: Beam Dynamics in High Intensity Linacs.** In: *42nd ICFA, Advanced Beam Dynamics Workshop on High-Intensity, High-Brightness Hadron Beams,* 2;p. OPEN ACCESS HANU:Accelerator

002 Al-Khateeb, A. M.*; Boine-Frankenheim, O.*; Hasse, R. W.*; Shobaki, J. M.;: **On the Longitudinal Coupling Impedance and Transmission Coefficient from Uniform and Hollow Ring Sources.** In: *EPAC'08, 11th European*

[1] Unproved announcements of the scientific and technical divisions.

Particle Accelerator Conference, 23-27 June 2008, Genoa, Italy, OPEN ACCESS HANU:Accelerator

003 Araz, A.; Bonnes, U.; Eichhorn, R.; Konrad, M.; Platz, M.; Richter, A.; Laier, U.*; Stassen, R.: **Development of a New Low-Level RF-Control-System for the S-DALINAC.** In: *EPAC'08, 11th European Particle Accelerator Conference, 23-27 June 2008, Genoa, Italy,* OPEN ACCESS HANU:Accelerator

004 Baartman, R. A.; Franchetti, G.*; Metral, E.: **Summary of Group A: Beam Dynamics in High Intensity Circular Machines.** In: *42nd ICFA, Advanced Beam Dynamics Workshop on High-Intensity, High-Brightness Hadron Beams,* 3;p. OPEN ACCESS HANU:Accelerator

005 Benedetti, C.; Turchetti, G.; Franchetti, G.*; Hofmann, I.*: **Transverse Mismatch Oscillations of a Bunched Beam in Presence of Space Charge and External Nonlinearities.** In: *EPAC'08, 11th European Particle Accelerator Conference, 23-27 June 2008, Genoa, Italy,* OPEN ACCESS HANU:Accelerator

006 Boine-Frankenheim, O.*: **High Intensity Challenges of the FAIR Project.** In: *42nd ICFA, Advanced Beam Dynamics Workshop on High-Intensity, High-Brightness Hadron Beams,* 1;p. OPEN ACCESS HANU:Accelerator

007 Bousonville, M.*; Meissner, P.: **RF Reference Signal Distribution System for FAIR.** In: *EPAC'08, 11th European Particle Accelerator Conference, 23-27 June 2008, Genoa, Italy,* OPEN ACCESS HANU:Accelerator

008 Ciavola, G.; Celona, L.; Gammino, S.; Maimone, F.; Mascali, D.; Koivisto, H. A.; Lang, R.*; Maeder, J.*; Rossbach, J.*; Spaedtke, P.*; Tinschert, K.*: **Status of the Multipurpose Fully Superconducting ECR Ion Source.** In: *EPAC'08, 11th European Particle Accelerator Conference, 23-27 June 2008, Genoa, Italy,* OPEN ACCESS HANU:Accelerator

009 Clemente, G.*; Groening, L.*; Minaev, S.; Ratzinger, U.; Tiede, R.: **Beam Dynamics Layout and Loss Studies for the FAIR P-Injector.** In: *EPAC'08, 11th European Particle Accelerator Conference, 23-27 June 2008, Genoa, Italy,* OPEN ACCESS HANU:Accelerator

010 Clemente, G.*; Groening, L.*; Ratzinger, U.; Tiede, R.: **Investigation of the Beam Dynamics Layout of the FAIR Proton Injector.** In: *42nd ICFA, Advanced Beam Dynamics Workshop on High-Intensity, High-Brightness Hadron Beams,* 3;p. OPEN ACCESS HANU:Accelerator

011 Dimopoulou, C.*; Franzke, B.*; Katayama, T.*; Nolden, F.*; Schreiber, G.*; Steck, M.*; Möhl, D.: **Experimental Demonstration of Longitudinal Ion Beam Accumulation with Electron Cooling.** In: *EPAC'08, 11th European Particle Accelerator Conference, 23-27 June 2008, Genoa, Italy,* OPEN ACCESS HANU:Accelerator

012 Dolinskii, A.*; Gorda, O. E.*; Litvinov, S. A.*; Nolden, F.*; Peschke, C.*; Schurig, I.*; Steck, M.*; Obradors-Campos, D.: **The CR-RESR Storage Ring Complex of the FAIR Project;.** In: *EPAC'08, 11th European Particle Accelerator Conference, 23-27 June 2008, Genoa, Italy,* OPEN ACCESS HANU:Accelerator

013 El Ghazaly, M. O. A.; Alzeanidi, A. A.; Aleksandrov, V.; Papash, A. I.; Welsch, C. P.*: **Design of a Versatile Injector for a Low-energy Experimental Platform at KACST.** In: *EPAC'08, 11th European Particle Accelerator Conference, 23-27 June 2008, Genoa, Italy,* OPEN ACCESS HANU:Accelerator

014 Fabbricatore, P.; Farinon, S.; Musenich, R.; Alessandria, F.; Bellomo, G.; Volpini, G.; Gambardella, U.; Kaugerts, J. E.*; Moritz, G.*; Marabotto, R.; Sorbi, M.: **R&D Activities Aimed at Developing a Curved Fast Ramped Superconducting Dipole for FAIR SIS300.** In: *EPAC'08, 11th European Particle Accelerator Conference, 23-27 June 2008, Genoa, Italy,* OPEN ACCESS HANU:Accelerator

015 Fischer, W.; Ahrens, L.; Brown, K. A.; Gardner, C. J.; Glenn, J. W.; Huang, H.; Mapes, M.; Morris, J.; Schoefer, V.; Smart, L.; Thieberger, P.; Tsoupas, N.; Unger, K. L.; Zeno, K.; Zhang, S. Y.; Omet, C.*; Spiller, P. J.*: **Injection and Acceleration of Au^{31+} in the BNL AGS.** In: *EPAC'08, 11th European Particle Accelerator Conference, 23-27 June 2008, Genoa, Italy,* OPEN ACCESS HANU:Accelerator

016 Franchetti, G.*: **The S317 Experiment on High Intensity Beam Loss and Emittance Growth.** In: *42nd ICFA, Advanced Beam Dynamics Workshop on High-Intensity, High-Brightness Hadron Beams,* 3;p. OPEN ACCESS HANU:Accelerator

017 Franchetti, G.*; Hofmann, I.*; Zimmermann, F.;: **Incoherent Effects of Space Charge and Electron Cloud.** In: *EPAC'08, 11th European Particle Accelerator Conference, 23-27 June 2008, Genoa, Italy,* OPEN ACCESS HANU:Accelerator

018 Franchetti, G.* Zimmermann, F.: **Electron-cloud Intrabunch Density Modulation.** In: *EPAC'08, 11th European Particle Accelerator Conference, 23-27 June 2008, Genoa, Italy,* OPEN ACCESS HANU:Accelerator

019 Gerhard, P.*; Barth, W.*; Dahl, L. A.*; Tinschert, K.*; Schempp, A.: **Status of the UNILAC-upgrade Programme for the Heavy Element Research at GSI-SHIP.** In: *EPAC'08, 11th European Particle Accelerator Conference, 23-27 June 2008, Genoa, Italy,* OPEN ACCESS HANU:Accelerator

020 Gorda, O. E.*; Dimopoulou, C.*; Dolinskii, A.*; Nolden, F.*; Steck, M.*: **Field Interference of Magnets in the Large Acceptance Storage Ring CR of the FAIR**

Project. In: *EPAC'08, 11th European Particle Accelerator Conference, 23-27 June 2008, Genoa, Italy,* OPEN ACCESS HANU:Accelerator

021 Groening, L.*; Barth, W.*; Bayer, W. B.*; Clemente, G.*; Dahl, L. A.*; Forck, P.*; Gerhard, P.*; Hofmann, I.*; Riehl, G.*; Yaramyshev, S.*; Jeon, D.-O.; Tiede, R.; Uriot, D.;: **Simulation of Experiments on Transverse RMS-Emittance Growth Along an Alvarez DTL.** In: *42nd ICFA, Advanced Beam Dynamics Workshop on High-Intensity, High-Brightness Hadron Beams,* 5;p. OPEN ACCESS HANU:Accelerator

022 Heine, R. G.*; Dimopoulou, C.*; Laier, U.*;: **The High Harmonics Cavity System for the New Experimental Storage Ring at FAIR.** In: *EPAC'08, 11th European Particle Accelerator Conference, 23-27 June 2008, Genoa, Italy,* OPEN ACCESS HANU:Accelerator

023 Hofmann, I.*: **Space Charge Resonances in High-Intensity Beams.** In: *42nd ICFA, Advanced Beam Dynamics Workshop on High-Intensity, High-Brightness Hadron Beams,* 5;p. OPEN ACCESS HANU:Accelerator

024 Jeon, D.-O.; Franchetti, G.*; Groening, L.*; Hofmann, I.*: **Prediction of the 4ν=1 Resonance of a High Intensity Linac.** In: *42nd ICFA, Advanced Beam Dynamics Workshop on High-Intensity, High-Brightness Hadron Beams,* 4;p. OPEN ACCESS HANU:Accelerator

025 Kester, O.*; Becker, R.; Pfister, J.; Sokolov, A.*; Vorobjev, G.*; Vogel, M.*; Winters, D.*: **The MAXEBIS at GSI as a test ion source for charge breeding and for HITRAP.** In: *Review of Scientific Instrument* **79***(2),* 02A705p. DOI:10.1063/1.2823900 HANU:Accelerator

026 Koenig, H. G.*; Schaefer, S.*: **Reduction of Q-loss-effects in Ferrite-loaded Cavities.** In: *EPAC'08, 11th European Particle Accelerator Conference, 23-27 June 2008, Genoa, Italy,* OPEN ACCESS HANU:Accelerator

027 Kornilov, V.*; Boine-Frankenheim, O.*;: **Simulation Study of Transverse Coherent Instabilities in Intense Bunches with Space Charge and Image Currents.** In: *42nd ICFA, Advanced Beam Dynamics Workshop on High-Intensity, High-Brightness Hadron Beams,* 3;p. OPEN ACCESS HANU:Accelerator

028 Kovalenko, A. D.; Agapov, N. N.; Alfeev, A. V.; Bychkov, A. V.; Gromov, A. V.; Khodzhibagiyan, H. G.; Kuznetsov, G. L.; Starikov, A. Y.; Fischer, E. S.*; Moritz, G.*; Spiller, P. J.*; Shabunov, A. V.: **Full Size Prototype Magnets for Heavy Ion Superconducting Synchrotron SIS100 at GSI: Status of Manufacturing and Test at JINR.** In: *EPAC'08, 11th European Particle Accelerator Conference, 23-27 June 2008, Genoa, Italy,* OPEN ACCESS HANU:Accelerator

029 Liakin, D. A.; Barabin, S. V.; Orlov, A. Y.; Forck, P.*; Giacomini, T.*: **A Counting Module for an Advanced Ionization Profile Monitor.** In: *EPAC'08, 11th European Particle Accelerator Conference, 23-27 June 2008, Genoa, Italy,* OPEN ACCESS HANU:Accelerator

030 Liakin, D. A.; Forck, P.*; Hoffmann, T.*: **An Emittance Evaluation Toolbox.** In: *EPAC'08, 11th European Particle Accelerator Conference, 23-27 June 2008, Genoa, Italy,* OPEN ACCESS HANU:Accelerator

031 Möller, S. P.; Andersen, T.; Bödker, F.; Baurichter, A.; Budde, M.; Elkiaer, P. A.; Hansen, C. E.; Hauge, N.; Holst, T.; Jensen, I.; Kruse, L. K.; Madsen, S. M.; Schmidt, M.; Blasche, K.*; Franczak, B. J.*: **Status of the Particle Therapy Accelerator System Built by DANFYSIK A/S.** In: *EPAC'08, 11th European Particle Accelerator Conference, 23-27 June 2008, Genoa, Italy,* OPEN ACCESS HANU:Accelerator

032 Nolden, F.*; Dolinskii, A.*; Franzke, B.*; Jandewerth, U.*; Katayama, T.*; Peschke, C.*; Petri, P.*; Steck, M.*; Möhl, D.: **Stochastic Cooling in the Framework of the FAIR Project at GSI.** In: *EPAC'08, 11th European Particle Accelerator Conference, 23-27 June 2008, Genoa, Italy,* OPEN ACCESS HANU:Accelerator

033 Omet, C.*; Kollmus, H.*; Reich-Sprenger, H.*; Spiller, P. J.*: **Ion Catcher System for the Stabilisation of the Dynamic Pressure in SIS18.** In: *EPAC'08, 11th European Particle Accelerator Conference, 23-27 June 2008, Genoa, Italy,* OPEN ACCESS HANU:Accelerator

034 Ondreka, D.*; Weinrich, U.*: **The Heidelberg Ion Therapy (HIT) Accelerator Coming into Operation.** In: *EPAC'08, 11th European Particle Accelerator Conference, 23-27 June 2008, Genoa, Italy,* OPEN ACCESS HANU:Accelerator

035 Paret, S.*; Boine-Frankenheim, O.*; Kornilov, V.*; Weiland, T.: **Transverse Schottky Noise and Beam Transfer Functions with Space Charge.** In: *EPAC'08, 11th European Particle Accelerator Conference, 23-27 June 2008, Genoa, Italy,* OPEN ACCESS HANU:Accelerator

036 Parfenova, A. S.*; Franchetti, G.*; Hofmann, I.*: **Measuring Ring Nonlinear Components via Induced Linear 'Feed-down'.** In: *EPAC'08, 11th European Particle Accelerator Conference, 23-27 June 2008, Genoa, Italy,* OPEN ACCESS HANU:Accelerator

037 Peters, A.; Cee, R.; Haberer, T.; Winkelmann, T.; Hoffmann, T.*; Reiter, A.*; Schwickert, M.*: **Spill Structure Measurements at the Heidelberg Ion Therapy Centre.** In: *EPAC'08, 11th European Particle Accelerator Conference, 23-27 June 2008, Genoa, Italy,* OPEN ACCESS HANU:Accelerator

038 Pfister, J.; Hofmann, B.; Ratzinger, U.; Schempp, A.;:

A Decelerator for Heavy Highly Charge Ions at HITRAP. In: *EPAC'08, 11th European Particle Accelerator Conference, 23-27 June 2008, Genoa, Italy,* OPEN ACCESS HANU:Accelerator

039 Plotnikov, A. B.*; Mustafin, E.*; Pyka, N.*; Spiller, P. J.*;: **Investigation of Lifetime of the Electronics and the Fiber Optics inside the Niche and the Tunnel in the Slow Extraction Area of SIS100.** In: *EPAC'08, 11th European Particle Accelerator Conference, 23-27 June 2008, Genoa, Italy,* OPEN ACCESS HANU:Accelerator

040 Pyka, N.*; Blell, U. B.*; Spiller, P. J.*; Stadlmann, J.*: **Design of the Beam Extraction System of the New Heavy Ion Synchrotrons SIS100 and SIS300 at FAIR.** In: *EPAC'08, 11th European Particle Accelerator Conference, 23-27 June 2008, Genoa, Italy,* OPEN ACCESS HANU:Accelerator

041 Ratschow, S.*; Hagenbuck, F.*; Spiller, P. J.*: **The High Energy Beam Transport System for FAIR.** In: *EPAC'08, 11th European Particle Accelerator Conference, 23-27 June 2008, Genoa, Italy,* OPEN ACCESS HANU:Accelerator

042 Schnizer, P.*; Fischer, E. S.*; Akishin, P. G.; Kurnyshov, R. V.; Schnizer, B.; Shcherbakov, P. A.; Sikler, G.; Walter, W.: **Magnetic Field Characteristics of a SIS 100 Full Size Dipole.** In: *EPAC'08, 11th European Particle Accelerator Conference, 23-27 June 2008, Genoa, Italy,* OPEN ACCESS HANU:Accelerator

043 Schnizer, P.*; Fischer, E. S.*; Akishin, P. G.; Schnizer, B.;: **Theoretical Field Analysis for Superferric Accelerator Magnets Using Elliptic Multipoles and its Advantages.** In: *EPAC'08, 11th European Particle Accelerator Conference, 23-27 June 2008, Genoa, Italy,* OPEN ACCESS HANU:Accelerator

044 Schwickert, M.*; Reiter, A.*;: **Beam Diagnostics for Commissioning the HEBT and Gantry Sections of the HIT Medical Accelerator.** In: *EPAC'08, 11th European Particle Accelerator Conference, 23-27 June 2008, Genoa, Italy,* OPEN ACCESS HANU:Accelerator

045 Smolyakov, A.; Mustafin, E.*; Pyka, N.*; Spiller, P. J.*: **Radiation Damage Studies for the Slow Extraction from SIS100.** In: *EPAC'08, 11th European Particle Accelerator Conference, 23-27 June 2008, Genoa, Italy,* OPEN ACCESS HANU:Accelerator

046 Spiller, P. J.*: **The Superconducting SIS100 Synchrotron for High Intensity Proton and Heavy Ion Beams.** In: *42nd ICFA, Advanced Beam Dynamics Workshop on High-Intensity, High-Brightness Hadron Beams,* 4;p. OPEN ACCESS HANU:Accelerator

047 Spiller, P. J.*; Blell, U. B.*; Boine-Frankenheim, O.*; Fischer, E. S.*; Franchetti, G.*; Hagenbuck, F.*; Hofmann, I.*; Kaugerts, J. E.*; Kauschke, M.*; Kirk, M.*; Klingbeil, H.*; Kraemer, A.*; Krämer, D.*; Moritz, G.*; Omet, C.*; Pyka, N.*; Ramakers, H.*; Ratschow, S.*; Saa-Hernandez, A.*; Kovalenko, A. D.: **Design Status of the FAIR Synchrotrons SIS100 and SIS300 and the High Energy Beam Transport System.** In: *EPAC'08, 11th European Particle Accelerator Conference, 23-27 June 2008, Genoa, Italy,* OPEN ACCESS HANU:Accelerator

048 Stöcker, H.*: **FAIR: Challenges Overcome and Still to be Met.** In: *EPAC'08, 11th European Particle Accelerator Conference, 23-27 June 2008, Genoa, Italy,* OPEN ACCESS HANU:Accelerator

049 Stadlmann, J.*; Franchetti, G.*; Franczak, B. J.*; Kirk, M.*; Pyka, N.*; Saa-Hernandez, A.*; Spiller, P. J.*: **Ion Optical Design of SIS100 and SIS300.** In: *EPAC'08, 11th European Particle Accelerator Conference, 23-27 June 2008, Genoa, Italy,* OPEN ACCESS HANU:Accelerator

050 Steck, M.*; Dimopoulou, C.*; Dolinskii, A.*; Gorda, O. E.*; Gostishchev, V.*; Knie, K.*; Litvinov, S. A.*; Nesmiyan, I.*; Nolden, F.*; Obradors-Campos, D.*; Peschke, C.*;: **Advanced Design of the FAIR Storage Ring Complex.** In: *EPAC'08, 11th European Particle Accelerator Conference, 23-27 June 2008, Genoa, Italy,* OPEN ACCESS HANU:Accelerator

051 Strasik, I.*; Hofmann, I.*; Kozlova, E.*; Mustafin, E.*; Latysheva, L. N.; Sobolevskiy, N.; Pavlovic, M.; Smolyakov, A.: **Residual Activity Induced by High-energy Heavy Ions in Stainless Steel and Copper.** In: *EPAC'08, 11th European Particle Accelerator Conference, 23-27 June 2008, Genoa, Italy,* OPEN ACCESS HANU:Accelerator

052 Tahir, N. A.*; Assmann, R. W.; Brugger, M.; Schmidt, R.; Fortov, V. E.; Lomonosov, I.; Shutov, A.; Hoffmann, D.; Piriz, R.: **Simulation Studies of Impact of SPS Beam with Collimator Materials.** In: *EPAC'08, 11th European Particle Accelerator Conference, 23-27 June 2008, Genoa, Italy,* OPEN ACCESS HANU:Accelerator

053 Tiede, R.; Podlech, H.; Ratzinger, U.; Zhang, C.; Clemente, G.*: **KONUS Beam Dynamics Designs Using H-Mode Cavities.** In: *42nd ICFA, Advanced Beam Dynamics Workshop on High-Intensity, High-Brightness Hadron Beams,* 8;p. OPEN ACCESS HANU:Accelerator

054 Vormann, H.*; Kleffner, C. M.*; Reiter, A.*; Schlitt, B.*; Clemente, G.; Ratzinger, U.: **Status of the Linac Components for the Italian Hadrontherapy Centre CNAO.** In: *EPAC'08, 11th European Particle Accelerator Conference, 23-27 June 2008, Genoa, Italy,* OPEN ACCESS HANU:Accelerator

055 Weinrich, U.*; Fuchs, R.*; Sust, E.: **Assembly of the Carbon Beam Gantry at the Heidelberg Ion Therapy (HIT) Accelerator.** In: *EPAC'08, 11th European Parti-*

cle Accelerator Conference, 23-27 June 2008, Genoa, Italy, OPEN ACCESS HANU:Accelerator

056 Weinrich, U.*; Kleffner, C. M.*: **Commissioning of the Carbon Beam Gantry at the Heidelberg Ion Therapy (HIT) Accelerator.** In: *EPAC'08, 11th European Particle Accelerator Conference, 23-27 June 2008, Genoa, Italy,* OPEN ACCESS HANU:Accelerator

057 Welsch, C. P.*: **DITANET–A European Training Network on Novel Diagnostic Techniques for Future Particle Accelerators.** In: *EPAC'08, 11th European Particle Accelerator Conference, 23-27 June 2008, Genoa, Italy,* OPEN ACCESS HANU:Accelerator

GSI publications to the programme 'Physics of hadrons and nuclei': Experiments published in 2008

1. Reviewed publications

001 Aamodt, K.; Abrahantes Quintana A.; Achenbach, R.; Acounis, S.; Adamova, D.; Adler, C.; Aggarwal, M.; Agnese, F.; Aglieri Rinella, G.; Ahammed, Z.; Ahmad, A.; Ahmad, N.; Ahmad, S.; Akindinov, A.; Akishin, P.; Aleksandrov, D.; Alessandro, B.; Alfaro, R.; Alfarone, G.; Alici, A.; Alme, J.; Alt, T.; Altinpinar, S.; Amend, W.; Andrei, C.; Andres, Y.; Andronic, A.*; Anelli, G.; Anfreville, M.; Angelov, V.; Anzo, A.; Anson, C.; Anticic, T.; Antonenko, V.; Antonczyk, D.*; Antinori, F.; Antinori, S.; Antonioli, P.; Aphecetche, L.; Appelshäuser, H.; Aprodu, V.; Arba, M.; Arcelli, S.; Argentieri, A.; Armesto, N.; Arnaldi, R.; Arefiev, A.; Arsene, I.; Asryan, A.; Augustinus, A.; Awes, T. C.; Äysto, J.; Danish Azmi, M.; Bablock, S.; Badala, A.; Badyal, S. K.; Baechler, J.; Bagnasco, S.; Bailhache, R.*; Bala, R.; Baldisseri, A.; Baldit, A.; Ban, J.; Barbera, R.; Barberis, P.-L.; Barbet, J. M.; Barnäfoldi, G.; Barret, V.; Bartke, J.; Bartos, D.; Basile, M.; Basmanov, V.; Bastid, N.; Batigne, G.; Batyunya, B.; Baudot, J.; Baumann, C.; Bearden, I.; Becker, B.; Belikov, J.; Bellwied, R.; Belmont-Moreno, E.; Belogianni, A.; Belyaev, S.; Benato, A.; Beney, J. L.; Benhabib, L.; Benotto, F.; Beoe, S.; Berceanu, I.; Bercuci, A.*; Berdermann, E.*; Berdnikov, Y.; Bernard, C.; Berny, R.; Berst, J. D.; Bertelsen, H.; Betev, L.; Bhasin, A.; Baskar, P.; Bhati, A.; Bianchi, N.; Bielcik, J.*; Bielcikova, J.; Bimbot, L.; Blanchard, G.; Blanco, F.; Blanco, F.; Blau, D.; Blume, C.*; Blyth, S.; Boccioli, M.; Bogdanov, A.; Boggild, H.; Bogolyubsky, M.; Boldizsar, L.; Bombara, M.; Bombonati, C.; Bondila, M.; Bonnet, D.; Bonvicini, V.; Borel, H.; Borotto, F.; Borshchov, V.; Bortoli, Y.; Borysov, O.; Bose, S.; Bosisio, L.; Botje, M.; Böttger, S.; Bourdaud, G.; Bourrion, O.; Bouvier, S.; Braem, A.; Braun, M.; Braun-Munzinger, P.*; Bravina, L.; Bregant, M.; Bruckner, G.; Brun, R.; Bruna, E.; Brunasso, O.; Bruno, G. E.; Bucher, D.; Budilov, V.; Budnikov, D.; Buesching, H.; Buncic, P.; Burns, M.; Burachas, S.; Busch, O.; Bushop, J.; Cai, X.; Caines, H.; Calaon, F.; Caldogno, M.; Cali, I.; Camerini, P.; Campagnolo, R.; Campbell, M.; Cao, X.; Capitani, G. P.; Romeo, G. C.; Cardenas-Montes, M.; Carduner, H.; Carena, F.; Carena, W.; Cariola, P.; Carminati, F.; Casado, J.; Casanova Diaz, A.; Caselle, M.; Castillo Castellanos, J. C.; Castor, J.; Catanescu, V.; Cattaruzza, E.; Cavazza, D.; Cerello, P.; Ceresa, S.; Cerny, V.; Chambert, V.; Chapeland, S.; Charpy, A.; Charrier, D.; Chartoire, M.; Charvet, J. L.; Chattopadhyay, S.; Chattopadhyay, S.; Chepurnov, V.; Chernenko, S.; Cherney, M.; Cheshkov, C.; Cheynis, B.; Chochula, P.; Chiavassa, E.; Barroso, V. C.; Choi, J.; Christakoglou, P.; Christiansen, P.; Christensen, C.; Chykalov, O. A.; Cicalo, C.; Cifarelli-Strolin, L.; Ciobanu, M.*; Cindolo, F.; Cirstoiu, C.; Clausse, O.; Cleymans, J.; Cobanoglu, O.; Coffin, J.-P.; Coli, S.; Colla, A.; Colledani, C.; Combaret, C.; Combet, M.; Comets, M.; Conesa Balbastre, G.; Conesa del Valle, Z.; Contin, G.; Contreras, J.; Cormier, T.; Corsi, F.; Cortese, P.; Costa, F.; Crescio, E.; Crochet, P.; Cuautle, E.; Cussonneau, J.; Dahlinger, M.*; Dainese, A.; Dalsgaard, H. H.; Daniel, L.; Das, I.; Das, T.; Dash, A.; Da Silva, R.; Davenport, M.; Daues, H.*; De Caro, A.; de Cataldo, G.; De Cuveland, J.; De Falco, A.; de Gaspari, M.; de Girolamo, P.; de Groot, J.; De Gruttola, D.; De Haas, A.; De Marco, N.; De Pasquale, S.; De Remigis, P.; de Vaux, D.; Decock, G.; Delagrange, H.; Del Franco, M.; Dellacasa, G.; Dell'Olio, C.; Dell'Olio, D.; Deloff, A.; Demanov, V.; Denes, E.; D'Erasmo, G.; Derkach, D.; Devaux, A.; Di Bari, D.; Di Bartelomen, A.; Di Giglio, C.; Di Liberto, S.; Di Mauro, A.; Di Nezza, P.; Dialinas, M.; Diaz, L.; Diaz Valdes, R.; Dietel, T.; Dima, R.; Ding, H.; Dinca, C.; Divia, R.; Dobretsov, V.; Dobrin, A.; Doenigus, B.; Dobrowolski, T.; Dominguez, I.; Dorn, A.; Drouet, S.; Dubey, A. E.; Ducroux, L.; Dumitrache, F.; Dumonteil, E.; Dupieux, P.; Duta, V.; Dutta Majumdar, A.; Dutta Majumdar, M.; Dyhre, T.; Efimov, L.; Efremov, A.; Elia, D.; Emschermann, D.; Engster, C.; Enokizono, A.; Espagnon, B.; Estienne, M.; Evangelista, A.; Evans, D.; Evrard, S.; Fabjan, C. W.; Fabrid, D.; Faivre, J.; Falchieri, D.; Fantoni, A.; Farano, R.; Fearick, R.; Fedorov, O.; Fekete, V.; Felea, D.; Feofilov, G.; Fernandes Tellez, A. F.; Ferretti, A.; Fichera, F.; Filchagin, S.; Filoni, E.; Finck, C.; Fini, R.; Fiore, E. M.; Flierl, D.; Floris, M.; Fodor, Z.; Foka, Y.*; Fokin, S.; Force, P.; Formenti, F.; Fragiacomo, E.; Fragkiadakis, M.; Fraissard, D.; Franco, A.; Franco, M.; Frankenfeld, U.*; Fratino, U.; Fresneau, S.; Frolov, A.; Fuchs, U.; Fujita, J.; Furget, C.; Furini, M.; Girard, M. F.; Gaardhoje, J.-J.; Gabrielli, A.; Gaido, L.; Gallas Torreira, A. G.; Gallio, M.; Gadrat, S.; Gagliard, M.; Gag, A.; Gandolfi, E.; Ganoti, P.; Ganti, M.; Garabatos, J.*; Lopez, A. G.; Garizzo, L.; Gaudichet, L.; Gemme, R.; Germain, M.; Gheata, A.; Gheata, M.; Ghidini, B.; Ghosh, P.; Giolu, G.; Giraudo, G.; Giubellino, P.; Glasow, R.; Glässel, P.; Ferreiro, E. G.; Gutierrez, C. G.; Gonzales-Trueba,

L. H.; Gorbunov, S.; Gorbunov, Y.; Gos, H.; Gosset, J.; Gotovac, S.; Gottschlag, H.; Gottschalk, D.; Grabski, V.; Grassi, T.; Gray, H.; Grebenyuk, O.; Grebieszkow, K.; Gregory, C.; Grigoras, C.; Grion, N.; Grigoriev, V.; Grigoryan, A.; Grigoryan, C.; Grigoryan, S.; Grishuk, Y.; Gros, P.; Grosse-Oetringhaus, J.; Grossiord, J. Y.; Grosso, R.; Grynyov, B.; Guarnaccia, C.; Guber, F.; Guerin, F.; Guernane, R.; Guerzoni, M.; Guichard, A.; Guida, A.; Guilloux, G.; Gulkanyan, H.; Gulbrandsen, K.; Gunji, T.; Gupta, A.; Gupta, V.; Gustafsson, H.-A.; Gutbrod, H.*; Hadjidakis, C.; Haiduc, M.; Hamar, G.; Hamagaki, H.; Hamblen, J.; Hansen, J. C.; Hardy, P.; Hatzifotiadou, D.; Harris, J. W.; Hartig, M.; Harutyunyan, A.; Hayrapetyan, A.; Hasch, D.; Hasegan, D.; Hehner, J.; Heine, N.; Heinz, M.; Helstrup, H.; Herghelegiu, A.; Herlant, S.; Corral, G. H.; Herrmann, N.; Hetland, K.; Hille, P.; Hinke, H.; Hippolyte, B.; Hoch, M.; Hoebbel, H.; Hoedlmoser, H.; Horaguchi, T.; Horner, M.; Hristov, P.; Hrivnacova, I.; Hu, S.; Guo, C. H.; Humanic, T.; Hurtado, A.; Hwang, D. S.; Ianigro, J. C.; Idzik, M.; Igolkin, S.; Ilkaev, R.; Ilkiv, I.; Imhoff, M.; Innocenti, P. G.; Ionescu, E.; Ippolitov, M.; Irfan, M.; Insa, C.; Inuzuka, M.; Ivan, C.; Ivanov, A.; Ivanov, M.; Ivanov, V.; Jacobs, P.; Jacholkowski, A.; Jancurova, L.; Janik, R.; Jasper, M.; Jena, C.; Jirden, L.; Johnson, D. P.; Jones, G. T.; Jorgensen, C.; Jouve, F.; Jovanovic, P.; Junique, A.; Jusko, A.; Jung, H.; Jung, W.; Kadija, K.; Kamal, A.; Kamermans, R.; Kapusta, S.; Kaidalov, A.; Kakoyan, V.; Kalcher, S.; Kang, E.; Kapitan, J.; Kaplin, V.; Karadzhev, K.; Karavichev, O.; Karavicheva, T.; Karpechev, E.; Karpio, K.; Kazantsev, A.; Kebschull, U.; Keidel, R.; Khan, M. M.; Khanzadeev, A.; Kharlov, Y.; Kikola, D.; Kileng, B.; Kim, D.; Kim, D. S.; Kim, D. W.; Kim, H. N.; Kim, J. S.; Kim, S.; Kinson, J. B.; Kiprich, S. K.; Kisel, I.; Kiselev, S.; Kisiel, A.; Kiss, T.; Kiworra, V.; Klay, J.; Bosing, C. K.; Kliemant, M.; Klimov, A.; Klovning, A.; Kluge, A.; Kluit, R.; Kniege, S.; Kolevatov, R.; Kollegger, T.; Kolojvari, A.; Kondratiev, V.; Kornas, E.; Koshurnikov, E.; Kotov, I.; Kour, R.; Kowalski, M.; Kox, S.; Kozlov, K.; Kralik, I.; Kramer, F.; Kraus, I.; Kravcakova, A.; Krawutschke, T.; Krivda, M.; Kryshen, E.; Kucheriaev, Y.; Kugler, A.; Kuhn, C.; Kuijer, P.; Kumar, L.; Kumar, N.; Kumpumaeki, P.; Kurepin, A.; Kurepin, A. N.; Kushpil, S.; Kushpil, V.; Kutovsky, M.; Kvaerno, H.; Kweon, M.; Labbe, J.-C.; Lackner, F.; Ladron de Guevara, P.; Lafage, V.; La Rocca, P.; Lamont, M.; Lara, C.; Larsen, D. T.; Laurenti, G.; Lazzeroni, C.; Le Bornec, Y.; Le Bris, N.; Le Gailliard, C.; Lebedev, V.; Lecoq, J.; Lee, K. S.; Lee, S. C.; Lefevre, F.; Legrand, I.; Lehmann, T.; Leistam, L.; Lenoir, P.; Lenti, V.; Leon, H.; Monzon, I. L.; Levai, P.; Li, Q.; Li, X.; Librizzi, F.; Lietava, R.; Lindegaard, N.; Lindenstruth, V.; Lippmann, C.; Lisa, M.; Listratenko, O. M.; Littel, F.; Liu, Y.; Lo, J.; Lobanov, V.; Loginov, V.; Noriega, M. L.; Lopez-Ramirez, R.; Torres, E. L.; Lorenzo, P. M.; Lovhoiden, G.; Lu, S.; Ludolphs, W.; Lunardon, M.; Luquin, L.; Lusso, S.; Lutz, J. R.; Luvisetto, M.; Lyapin, V.; Maevskaya, A.; Magureanu, C.; Mahajan, A.; Majahan, S.; Mahmoud, T.; Mairani, A.; Mahapatra, D.; Makarov, A.; Makhlyueva, I.; Malek, M.; Malkiewicz, T.; Mal'Kevich, D.; Malzacher, P.*; Mamonov, A.; Manea, C.; Mangotra, L. K.; Maniero, D.; Manko, V.; Manso, F.; Manzari, V.; Mao, Y.; Marcel, A.; Marchini, S.; Mares, J.; Margagliotti, G. V.; Margotti, A.; Marin, A.*; Marin, J. C.; Marras, D.; Martinengo, P.; Martinez, M. I.; Martinez-Davalos, A.; Martinez Garcia, G. M.; Martini, S.; Marzzari Chiesa, A. M.; Marzocca, C.; Masciocchi, S.*; Masera, M.; Masetti, A.; Maslov, N. I.; Masoni, A.; Massera, F.; Mast, M.; Mastroserio, A.; Matthews, Z. L.; Mayer, B.; Mazza, G.; Mazzaro, M. D.; Mazzoni, A.; Meddi, F.; Meleshko, E.; Menchaca-Rocha, A.; Meneghini, S.; Meoni, A.; Perez, J. M.; Mereu, P.; Meunier, O.; Miake, Y.; Michalon, A.; Michinelli, R.; Miftakhov, N.; Mignone, A.; Mikhailov, K.; Milosevic, J.; Minaev, Y.; Minafra, F.; Mischke, A.; Miskowiec, D.*; Mitsyn, V.; Mitu, C.; Mohanty, B.; Moisa, D.; Molnar, L.; Mondal, M.; Mondal, N.; Montano Zetina, L.; Monteno, M.; Morando, M.; Morel, M.; Moretto, S.; Morhardt, T.*; Morsch, A.; Moukhanova, T.; Mucchi, M.; Muccifora, V.; Mudnic, E.; Muller, H.; Müller, W.*; Munoz, J.; Mura, D.; Musa, L.; Muraz, J. F.; Musso, A.; Nania, R.; Nandi, B.; Nappi, E.; Navach, F.; Navin, S.; Nayak, T.; Nazarenko, S.; Nazarov, G.; Nellen, L.; Nendaz, F.; Nianine, A.; Nicassio, M.; Nielsen, B. S.; Nikolaev, S.; Nikolic, V.; Nikulin, S.; Nikulin, V.; Nilsen, B.; Nitti, M.; Noferini, F.; Nomokonov, P.; Nooren, G.; Noto, F.; Nouais, D.; Nyiri, A.; Nystrand, J.; Odyniec, G.; Oeschler, H.; Oinonen, M.; Oldenburg, M.; Oleks, I.; Olsen, E.: **The ALICE experiment at the CERN LHC.** *Journal of Instrumentation* **3**: S08002. DOI:10.1088/1748-0221/3/08/S08002 OPEN ACCESS.

002 Ablikim, M.; Bai, J. Z.; Ban, Y.; Cai, X.; Chen, H. F.; Chen, H. S.; Chen, H. X.; Chen, J. C.; Chen, J.; Chen, Y. B.; Chu, Y. P.; Dai, Y. S.; Diao, L. Y.; Deng, Z. Y.; Dong, Q. F.; Du, S. X.; Fang, J.; Fang, S. S.; Fu, C. D.; Gao, C. S.; Gao, Y. N.; Götzen, K.*; Gu, S. D.; Gu, Y. T.; Guo, Y. N.; Guo, Z. J.; Harris, F. A.; He, K. L.; He, M.; Heng, Y. K.; Hou, J.; Hu, H. M.; Hu, J. H.; Hu, T.; Huang, G. S.; Huang, X. T.; Ji, X. B.; Jiang, X. S.; Jiang, X. Y.; Jiao, J. B.; Jin, D. P.; Jin, S.; Lai, Y. F.; Li, G.; Li, H. B.; Li, J.; Li, R. Y.; Li, S. M.; Li, W. D.; Li, W. G.; Li, X. L.*; Li, X. N.*; Li, X. Q.*; Liang, Y. F.; Liao, H. B.; Liu, B. J.; Liu, C. X.; Liu, F.; Liu, F.; Liu, H. H.; Liu, H. M.; Liu, J.; Liu, J. B.; Liu, J. P.; Liu, J.; Liu, Q.; Liu, R. G.; Liu, Z. A.; Lou, Y. C.; Lu, F.; Lu, G. R.; Lu, J. G.; Luo, C. L.; Ma, F. C.; Ma, H. L.; Ma, L. L.; Ma, Q. M.; Mao, Z. P.; Mo, X. H.; Nie, J.; Olsen, S. L.; Peters, K. J.*; Ping, R. G.; Qi, N. D.; Qin, H.; Qiu, J. F.; Ren, Z. Y.; Rong, G.; Ruan, X. D.; Shan, L. Y.; Shang, L.; Shen, C. P.; Shen, D. L.; Shen, X. Y.; Sheng, H. Y.; Sun, H. S.; Sun, S. S.; Sun, Y. Z.; Sun, Z. J.; Tang, X.; Tong, G. L.; Varner, G. S.; Wang, D. Y.; Wang, L.; Wang, L. L.; Wang, L. S.; Wang, M.; Wang, P.; Wang, P. L.; Wang, W. F.; Wang, Y. F.; Wang, Z.*; Wang, Z. Y.*; Wang, Z.*; Wei, C. L.; Wei, D. H.; Weng, Y.; Wu, N.; Xia, X. M.; Xie, X. X.; Xu, G. F.; Xu, X. P.; Xu, Y.; Yan, M. L.; Yang, H. X.; Yang, Y. X.; Ye, M. H.; Ye, Y. X.; Yu, G. W.; Yuan, C. Z.; Yuan, Y.; Zang, S. L.; Zeng,

Y.; Zhang, B. X.; Zhang, B. Y.; Zhang, C. C.; Zhang, D. H.; Zhang, H. Q.; Zhang, H. Y.; Zhang, J. W.; Zhang, J. Y.; Zhang, S. H.; Zhang, X. Y.; Zhang, Y. Y.; Zhang, Z. X.; Zhang, Z. P.; Zhao, D. X.; Zhao, J. W.; Zhao, M. G.; Zhao, P. P.; Zhao, W. R.; Zhao, Z. G.; Zheng, H. Q.; Zheng, J. P.; Zheng, Z. P.; Zhou, L.; Zhu, K. J.; Zhu, Q. M.; Zhu, Y. C.; Zhu, Y. S.; Zhu, Z. A.; Zhuang, B. A.; Zhuang, X. A.; Zou, B. S.: **Search for the rare decays J/$\psi \to \mathbf{D}_{-}^{S}\pi^{+}$, J/$\psi \to \mathbf{D}^{-}\pi^{+}$, and J/$\psi \to \bar{D}^{0}\bar{K}^{0}$.** *Physics letters B* **663**(4): 297–301. DOI:10.1016/j.physletb.2008.04.028

003 Ablikim, M.; Bai, J. Z.; Ban, Y.; Cai, X.; Chen, H. F.; Chen, H. S.; Chen, H. X.; Chen, J. C.; Chen, J.; Chen, Y. B.; Chu, Y. P.; Dai, Y. S.; Diao, L. Y.; Deng, Z. Y.; Dong, Q. F.; Du, S. X.; Fang, J.; Fang, S. S.; Fu, C. D.; Gao, C. S.; Gao, Y. N.; Götzen, K.*; Gu, S. D.; Gu, Y. T.; Guo, Y. N.; Guo, Z. J.; Harris, F. A.; He, K. L.; He, M.; Heng, Y. K.; Hou, J.; Hu, H. M.; Hu, J. H.; Hu, T.; Huang, G. S.; Huang, X. T.; Ji, X. B.; Jiang, X. S.; Jiang, X. Y.; Jiao, J. B.; Jin, D. P.; Jin, S.; Lai, Y. F.; Li, G.; Li, H. B.; Li, J.; Li, R. Y.; Li, S. M.; Li, W. D.; Li, W. G.; Li, X. L.; Li, X. N.; Li, X. Q.; Liang, Y. F.; Liao, H. B.; Liu, B. J.; Liu, C. X.; Liu, F.; Liu, F.; Liu, H. H.; Liu, H. M.; Liu, J.; Liu, J. B.; Liu, J. P.; Liu, J.; Liu, Q.; Liu, R. G.; Liu, Z. A.; Lou, Y. C.; Lu, F.; Lu, G. R.; Lu, J. G.; Luo, C. L.; Ma, F. C.; Ma, H. L.; Ma, L. L.; Ma, Q. M.; Mao, Z. P.; Mo, X. H.; Nie, J.; Olsen, S. L.; Peters, K. J.*; Ping, R. G.; Qi, N. D.; Qin, H.; Qiu, J. F.; Ren, Z. Y.; Rong, G.; Ruan, X. D.; Shan, L. Y.; Shang, L.; Shen, C. P.; Shen, D. L.; Shen, X. Y.; Sheng, H. Y.; Sun, H. S.; Sun, S. S.; Sun, Y. Z.; Sun, Z. J.; Tang, X.; Tong, G. L.; Varner, G. S.; Wang, D. Y.; Wang, L.; Wang, L. L.; Wang, L. S.; Wang, M.; Wang, P.; Wang, P. L.; Wang, W. F.; Wang, Y. F.; Wang, Z.; Wang, Z. Y.*; Wang, Z.*; Wei, C. L.; Wei, D. H.; Weng, Y.; Wu, N.; Xia, X. M.; Xie, X. X.; Xu, G. F.; Xu, X. P.; Xu, Y.; Yan, M. L.; Yang, H. X.; Yang, Y. X.; Ye, M. H.; Ye, Y. X.; Yu, G. W.; Yuan, C. Z.; Yuan, Y.; Zang, S. L.; Zeng, Y.; Zhang, B. X.; Zhang, B. Y.; Zhang, C. C.; Zhang, D. H.; Zhang, H. Q.; Zhang, H. Y.; Zhang, J. W.; Zhang, J. Y.; Zhang, S. H.; Zhang, X. Y.; Zhang, Y.; Zhang, Z. X.; Zhang, Z. P.; Zhao, D. X.; Zhao, J. W.; Zhao, M. G.; Zhao, P. P.; Zhao, W. R.; Zhao, Z. G.; Zheng, H. Q.; Zheng, J. P.; Zheng, Z. P.; Zhou, L.; Zhu, K. J.; Zhu, Q. M.; Zhu, Y. C.; Zhu, Y. S.; Zhu, Z. A.; Zhuang, B. A.; Zhuang, X. A.; Zou, B. S.: **First observation of J/ψ and ψ(2S) decaying to ${}_{n}\mathbf{K}_{S}^{0}\,\bar{\Lambda}$ + c.c.** *Physics letters B* **659**(4): 789–795. DOI:10.1016/j.physletb.2007.11.087

004 Achenbach, P.; Gayoso, C. A.; Bernauer, J. C.; Böhm, R.; Distler, M. O.; Doria, L.; de la Paz, M. G. R.; Merkel, H.; Müller, U.; Nungesser, L.; Pochodzalla, J.; Majos, S. S.; Schlimme, B. S.; Walcher, T.; Weinriefer, M.; Debenjak, L.; Potokar, M.; Sirca, S.; Kavatsyuk, M.*; Lepyoshkina, O.*; Minami, S.*; Nakajima, D.*; Rappold, C.*; Saito, T. R.*; Schardt, D.*; Träger, M.*; Iwase, H.; Ajimura, S.; Sakaguchi, A.; Mizoi, Y.: **In-beam tests of scintillating fibre detectors at MAMI and at GSI.** *Nuclear instruments & methods in physics research, Section A, Accelerators, spectrometers, detectors and associated equipment* **593**(3): 353–360. DOI:10.1016/j.nima.2008.05.017 Also part of: 'Health: Cancer research'.

005 Adamczewski, J.*; Essel, H. G.*; Kurz, N.*; Linev, S.*: **Data Acquisition Backbone Core DABC.** *IEEE transactions on nuclear science* **55**(1): 251–255. DOI:10.1109/tns.2007.913938

006 Adamian, G. G.*; Antonenko, N. V.*; Scheid, W.; Zubov, A. S.*: **Possibilities of production of neutron-deficient isotopes of U, Np, Pu, Am, Cm, and Cf in complete fusion reactions.** *Physical review C, Nuclear physics* **78**(4): 044605. DOI:10.1103/physrevc.78.044605

007 Adamova, D.; Agakichiev, G.; Andronic, A.*; Antonczyk, D.; Appelshäuser, H.; Belaga, V.; Bielcikova, J.; Braun-Munzinger, P.*; Busch, O.; Cherlin, A.; Damjanovic, S.*; Dietel, T.; Dietrich, L.; Drees, A.; Dubitzky, W.; Esumi, S. I.; Filimonov, K.; Fomenko, K.; Fraenkel, Z.; Garabatos, C.*; Glässel, P.; Hering, G.*; Holeczek, J.; Kalisky, M.; Kniege, S.; Kushpil, V.; Maas, A.*; Marin, A.; Milosevic, J.; Miskowiec, D.*; Ortega, R.; Panebrattsev, Y.; Petchenova, O.; Petracek, V.; Ploskon, M.; Radomski, S.; Rak, J.*; Ravinovich, I.; Rehak, P.; Sako, H.*; Schmitz, W.; Schuchmann, S.; Schukraft, J.; Sedykh, S.*; Shimansky, S.; Soualah, R.; Stachel, J.; Sumbera, M.; Tilsner, H.; Tserruya, I.; Tsiledakis, G.*; Wessels, J. P.; Wienold, T.; Wurm, J. P.; Yurevich, S.*; Yurevich, V.: **Azimuthal dependence of pion source radii in Pb plus Au collisions at 158A GeV/c.** *Physical review C, Nuclear physics* **78**(6): 064901. DOI:10.1103/physrevc.78.064901

008 Adamova, D.; Agakichiev, G.*; Antonczyk, D.*; Appelshäuser, H.; Belaga, V.; Bielcikova, S.; Braun-Munzinger, P.*; Busch, O.*; Cherlin, A.; Damjanovic, S.*; Dietel, T.; Dietrich, L.; Drees, A.; Dubitzky, W.; Esumi, S. I.; Filimonov, K.; Fomenko, K.; Fraenkel, Z.; Garabatos, C.*; Glässel, P.; Holeczek, J.*; Kushpil, V.; Maas, A.*; Marin, A.*; Milosevic, J.; Milov, A.; Miskowiec, D.*; Panebrattsev, Y.; Petchenova, O.; Petracek, V.; Pfeiffer, A.; Ploskon, M.*; Radomski, S.*; Rak, J.; Ravinovich, I.; Rehak, P.; Sako, H.*; Schmitz, W.; Sedykh, S.*; Shimansky, S.; Stachel, J.*; Sumbera, M.; Tilsner, H.; Tserruya, I.; Tsiledakis, G.*; Wessels, J. P.; Wienold, T.; Wurm, J. P.; Xie, W.; Yurevich, S.; Yurevich, V.: **Scale-dependence of transverse momentum correlations in Pb-Au collisions at 158A GeV/c.** *Nuclear physics A, Nuclear and hadronic physics* **811**(1): 179–196. DOI:10.1016/j.nuclphysa.2008.07.014

009 Adamova, D.; Agakichiev, G.*; Antonczyk, D.; Appelshäuser, H.*; Belaga, V.; Bielcikova, J.; Braun-Munzinger, P.*; Busch, O.; Cherlin, A.; Damjanovic, S.; Dietel, T.; Dietrich, L.; Drees, A.; Dubitzky, W.; Esumi, S. I.; Filimonov, K.; Fomenko, K.; Fraenkel, Z.; Garabatos, C.*; Glässel, P.; Holeczek, J.; Kushpil, V.; Maas, A.*; Marin, A.*; Milosevic, J.; Milov, A.; Miskowiec,

D.*; Panebrattsev, Y.; Petchenova, O.; Petracek, V.; Pfeiffer, A.; Rak, J.; Ravinovich, I.; Rehak, P.; Sako, H.*; Schmitz, W.; Sedykh, S.*; Shimansky, S.; Stachel, J.*; Sumbera, M.; Tilsner, H.; Tserruya, I.; Wessels, J. P.; Wienold, T.; Wurm, J. P.; Xie, W.; Yurevich, S.; Yurevich, V.: **Modification of the ρ meson detected by low-mass electron-positron pairs in central Pb-Au collisions at 158A GeV/c.** *Physics letters B* **666**(5): 425–429. DOI:10.1016/j.physletb.2008.07.104

010 Adamova, D.; Agakichiev, G.; Antonczyk, D.*; Appelshäuser, H.*; Belaga, V.; Bielcikova, J.; Braun-Munzinger, P.*; Campagnolo, R.; Cherlin, A.; Damjanovic, S.*; Dietel, T.; Dietrich, L.; Drees, A.; Dubitzky, W.; Esumi, S. I.; Filimonov, K.; Fraenkel, Z.; Garabatos, C.*; Glässel, P.*; Hering, G.*; Holeczek, J.*; Kushpil, V.; Marin, A.*; Milosevic, J.; Milov, A.; Miskowiec, D.*; Musa, L.; Panebrattsev, Y.; Pechenova, O.; Petracek, V.; Pfeiffer, A.; Rak, J.; Ravinovich, I.; Richter, M.; Sako, H.; Schäfer, E.; Schmitz, W.; Schukraft, J.; Seipp, W.; Sharma, A.; Shimansky, S.; Stachel, J.; Sumbera, M.; Tilsner, H.; Tserruya, I.; Wessels, J. P.; Wienold, T.; Windelband, B.; Wurm, J. P.; Xie, W.; Yurevich, S.; Yurevich, V.: **The CERES/NA45 radial drift Time Projection Chamber.** *Nuclear instruments & methods in physics research, Section A, Accelerators, spectrometers, detectors and associated equipment* **593**(3): 203–231. DOI:10.1016/j.nima.2008.04.056

011 Agakishiev, G.; Agodi, C.; Alvarez-Pol, H.; Balanda, A.; Bassini, R.; Bellia, G.; Belver, D.; Belyaev, A.; Blanco, A.; Bohmer, M.; Bortolotti, A.; Boyard, J. L.; Braun-Munzinger, P.*; Cabanelas, P.; Castro, E.; Chernenko, S.; Christ, T.; Destefanis, M.; Diaz, J.; Dohrmann, F.; Dybczak, A.; Eberl, T.; Fabbietti, L.; Fateev, O.; Finocchiaro, P.; Fonte, P.; Friese, J.; Fröhlich, I.; Galatyuk, T.; Garzon, J. A.; Gernhäuser, R.; Gil, A.; Gilardi, C.; Golubeva, M.; Gonzalez-Diaz, D.*; Grosse, E.; Guber, F.; Heilmann, M.; Heinz, T.*; Hennino, T.; Holzmann, R.*; Lerusalimov, A.; Iori, I.; Ivashkin, A.; Jurkovic, M.; Kampfer, B.; Kajetanowicz, M.; Kanaki, K.; Karavicheva, T.; Kirschner, D.; Koenig, I.*; Koenig, W.*; Kolb, B. W.*; Kotte, R.; Kozuch, A.; Krasa, A.; Krizek, F.; Krücken, R.; Kuhn, W.; Kugler, A.; Kurepin, A.; Lamas-Valverde, J.; Lang, S.*; Lange, J. S.; Lapidus, K.; Lopes, L.; Maier, L.; Mangiarotti, A.; Marin, J.; Markert, J.; Metag, V.; Michalska, B.; Mishra, D.; Moriniere, E.; Mousa, J.; Münch, M.*; Müntz, C.*; Naumann, L.; Novotny, R.; Otwinowski, J.; Pachmayer, Y. C.; Palka, M.*; Parpottas, Y.; Pechenov, V.; Pechenova, O.; Cavalcanti, T. P.; Pietraszko, J.*; Pleskac, R.; Pospisil, V.; Przygoda, W.; Ramstein, B.; Reshetin, A.; Roy-Stephan, M.; Rustamov, A.*; Sadovsky, A.; Sailer, B.; Salabura, P.; Schmah, A.*; Schroeder, C.*; Schwab, E.*; Simon, R. S.*; Sobolev, Y. G.; Spataro, S.; Spruck, B.; Strobele, H.*; Stroth, J.*; Sturm, C.; Sudol, M.*; Tarantola, A.; Teilab, K.; Tlusty, P.; Toia, A.; Traxler, M.*; Trebacz, R.; Tsertos, H.; Veretenkin, I.; Wagner, V.; Weber, M.*; Wen, H.; Wisniowski, M.; Wojcik, T.; Wüstenfeld, J.; Yurevich, S.*; Zanevsky, Y.; Zhou, P.; Zumbruch, P.*: **Study of dielectron production in C+C collisions at 1 A GeV.** *Physics letters B* **663**(1): 43–48. DOI:10.1016/j.physletb.2008.03.062

012 Aggarwal, M. M.; Ahammed, Z.; Angelis, A. L. S.; Antonenko, V.; Arefiev, V.; Astakhov, V.; Avdeitchikov, V.; Awes, T. C.; Baba, P. V. K. S.; Badyal, S. K.; Bathe, S.; Batiounia, B.; Baumann, C.; Bernier, T.; Bhalla, K. B.; Bhatia, V. S.; Blume, C.; Bucher, D.; Busching, H.; Carlen, L.; Chattopadhyay, S.; Decowski, M. P.; Delagrange, H.; Donni, P.; Majumdar, M. R. D.; El Chenawi, K.; Dubey, A. K.; Enosawa, K.; Fokin, S.; Frolov, V.; Ganti, M. S.; Garpman, S.; Gavrishchuk, O.; Geurts, F. J. M.; Ghosh, T. K.; Glasow, R.; Guskov, B.; Gustafsson, H. A.; Gutbrod, H. H.*; Hrivnacova, I.; Ippolitov, M.; Kalechofsky, H.; Kamermans, R.; Karadjev, K.; Karpio, K.; Kolb, B. W.*; Kosarev, I.; Koutcheryaev, I.; Kugler, A.; Kulinich, P.; Kurata, M.; Lebedev, A.; Lohner, H.; Luquin, L.; Mahapatra, D. P.; Manko, V.; Martin, M.; Martinez, G.; Maximov, A.; Miake, Y.; Mishra, G. C.; Mohanty, B.; Mora, M. J.; Morrison, D.; Mukhanova, T.; Mukhopadhyay, D. S.; Naef, H.; Nandi, B. K.; Nayak, S. K.; Nayak, T. K.; Nianine, A.; Nikitine, V.; Nikolaev, S.; Nilsson, P.; Nishimura, S.; Nomokonov, P.; Nystrand, J.; Oskarsson, A.; Otterlund, I.; Pavliouk, S.; Peitzmann, T.; Peressounko, D.; Petracek, V.; Phatak, S. C.; Pinganaud, W.; Plasil, F.; Purschke, M. L.; Rak, J.; Rammler, M.; Raniwala, R.; Raniwala, S.; Rao, N. K.; Retiere, F.; Reygers, K.; Roland, G.; Rosselet, L.; Roufanov, I.; Roy, C.; Rubio, J. M.; Sambyal, S. S.; Santo, R.; Sato, S.; Schlagheck, H.; Schmidt, H.-R.*; Schutz, Y.; Shabratova, G.; Shah, T. H.; Sibiriak, I.; Siemiarczuk, T.; Silvermyr, D.; Sinha, B. C.; Slavine, N.; Söderström, K.; Sood, G.; Sörensen, S. P.; Stankus, P.; Stefanek, G.; Steinberg, P.; Stenlund, E.; Sumbera, M.; Svensson, T.; Tsvetkov, A.; Tykarski, L.; Von der Pijll, E. C.; Eijndhoven, N. V.; Nieuwenhuizen, G. J. V.; Vinogradov, A.; Viyogi, Y. P.; Vodopianov, A.; Vörös, S.; Wyslouch, B.; Young, G. R.: **Suppression of high-p(T) neutral pion production in central Pb+Pb collisions at $\sqrt{s(NN)}$=17.3 GeV relative to p+C and p+Pb collisions.** *Physical review letters* **100**(24): 242301. DOI:10.1103/physrevlett.100.242301

013 Aksyutina, Y.*; Johansson, H. T.; Adrich, P.*; Aksouh, F.*; Aumann, T.*; Boretzky, K.*; Borge, M. J. G.; Chatillon, A.; Chulkov, L. V.*; Cortina-Gil, D.*; Datta Pramanik, U.*; Emling, H.*; Forssen, C.; Fynbo, H. O. U.; Geissel, H.*; Hellström, M.; Ickert, G.*; Jones, K. L.*; Jonson, B.; Kliemkiewicz, A.*; Kratz, J. V.; Kulessa, R.; Lantz, M.; LeBleis, T.*; Lindahl, A. O.; Mahata, K.*; Matos, M.*; Meister, M.*; Münzenberg, G.*; Nilsson, T.; Nyman, G.; Palit, R.; Pantea, M.*; Paschalis, S.; Prokopowicz, W.*; Reifarth, R.*; Richter, A.; Riisager, K.; Schrieder, G.; Simon, H.*; Sümmerer, K.*; Tengblad, O.; Walus, W.; Weick, H.*; Zhukov, M. V.: **Lithium isotopes beyond the drip line.** *Physics letters B* **666**(5):

430–434. DOI:10.1016/j.physletb.2008.07.093 Also part of: 'Large-scale facilities for research with photons, neutrons and ions'.

014 Alkofer, R.; Fischer, C. S.*; Williams, R.: **U_A(1) anomaly and eta-mass from an infrared singular quark-gluon vertex.** *The European physical journal A, Hadrons and nuclei* **38**(1): 53–60. DOI:10.1140/epja/i2008-10646-x

015 Alt, C.; Anticic, T.; Baatar, B.; Barna, D.; Bartke, J.; Betev, L.; Bialkowska, H.; Blume, C.*; Boimska, B.; Botje, M.; Bracinik, J.; Bramm, R.*; Buncic, P.; Cerny, V.; Christakoglou, P.; Chung, P.; Chvala, O.; Cramer, J. G.; Csato, P.; Dinkelaker, P.; Eckardt, V.; Flierl, D.; Fodor, Z.; Foka, P.*; Friese, V.*; Gal, J.; Gazdzicki, M. G.; Genchev, V.; Gladysz, E.; Grebieszkow, K.; Hegyi, S.; Hoehne, C.; Kadija, K.; Karev, A.; Kikola, D.; Kliemant, M.; Kniege, S.; Kolesnikov, V. I.; Kollegger, T.; Kornas, E.; Kowalski, M.; Kraus, I.*; Kreps, M.; Laszlo, A.; Lacey, R.; van Leeuwen, M.; Levai, P.; Litov, L.; Lungwitz, B.; Makariev, M.; Malakhov, A. I.; Mateev, M.; Melkumov, G. L.; Mischke, A.; Mitrovski, M.; Molnar, J.; Mrowczynski, S.; Nicolic, V.; Palla, G.; Panagiotou, A. D.; Panayotov, D.; Petridis, A.; Peryt, W.; Pikna, M.; Pluta, J.; Prindle, D.; Uhlhofer, F. P.; Renfordt, R.; Roland, C.; Roland, G.; Rybczynski, M.; Rybicki, A.; Sandoval, A.*; Schmitz, N.; Schuster, T.; Seyboth, P.; Sikler, F.; Sitar, B.; Skrzypczak, E.; Slodkowski, M.; Stefanek, G.; Stock, R.; Strabel, C.; Ströbele, H. S.; Susa, T.; Szentpetery, I.; Sziklai, J.; Szuba, M.; Szymanski, P.; Trubnikov, V.; Varga, D.; Vassiliou, M.; Veres, G. I.; Vesztergombi, G.; Vranic, D.*; Wetzler, A.; Wlodarczyk, Z.; Yoo, I. K.; Zimanyi, J.; NA49 Collaboration*: **Pion and kaon production in central Pb plus Pb collisions at 20A and 30A GeV: Evidence for the onset of deconfinement.** *Physical review C, Nuclear physics* **77**(2): 024903. DOI:10.1103/physrevc.77.024903

016 Alt, C.; Anticic, T.; Baatar, B.; Barna, D.; Bartke, J.; Betev, L.; Bialkowska, H.; Blume, C.; Boimska, B.; Botje, M.; Bracinik, J.; Bramm, R.; Buncic, P.; Cerny, V.; Christakoglou, P.; Chung, P.; Chvala, O.; Cramer, J. G.; Csato, P.; Dinkelaker, P.; Eckardt, V.; Flierl, D.; Fodor, Z.; Foka, P.*; Friese, V.*; Gal, J.; Gazdzicki, M.; Genchev, V.; Georgopoulos, G.; Gladysz, E.; Grebieszkow, K.; Hegyi, S.; Höhne, C.*; Kadija, K.; Karev, A.; Kikola, D.; Kliemant, M.; Kniege, S.; Kolesnikov, V. I.; Kollegger, T.; Kornas, E.; Korus, R.; Kowalski, M.; Kraus, I.*; Kreps, M.; Kresan, D.; Laszlo, A.; Lacey, R.; van Leeuwen, M.; Levai, P.; Litov, L.; Lungwitz, B.; Makariev, M.; Malakhov, A. I.; Mateev, M.; Melkumov, G. L.; Mischke, A.; Mitrovski, M.; Molnar, J.; Mrowczynski, S.; Nicolic, V.; Palla, G.; Panagiotou, A. D.; Panayotov, D.; Petridis, A.; Peryt, W.; Pikna, M.; Pluta, J.; Prindle, D.; Pühlhofer, F.; Renfordt, R.; Roland, C.; Roland, G.; Rybczynski, M.; Rybicki, A.; Sandoval, A.*; Schmitz, N.; Schuster, T.; Seyboth, P.; Sikler, K.; Sitar, B.; Skrzypczak, E.; Slodkowski, M.; Stefanek, G.; Stock, R.; Strabel, C.; Ströbele, H.; Susa, T.; Szentpetery, I.; Sziklai, J.; Szuba, M.; Szymanski, P.; Trubnikov, V.; Varga, D.; Vassiliou, M.; Veres, G. I.; Vesztergombi, G.; Vranic, D.*; Wetzler, A.; Wlodarczyk, Z.; Yoo, I. K.; Zimanyi, J.; NA49 Collaboration*: **Energy dependence of phi meson production in central Pb+Pb collisions at $\sqrt{SNN}$ = 6 to 17 GeV.** *Physical review C, Nuclear physics* **78**(4): 044907. DOI:10.1103/physrevc.78.044907

017 Alt, C.; Anticic, T.; Baatar, B.; Barna, D.; Bartke, J.; Betev, L.; Bialkowska, H.; Blume, C.; Boimska, B.; Botje, M.; Bracinik, J.; Bramm, R.; Buncic, P.; Cerny, V.; Christakoglou, P.; Chung, P.; Chvala, O.; Cramer, J. G.; Csato, P.; Dinkelaker, P.; Eckardt, V.; Flierl, D.; Fodor, Z.; Foka, P.*; Friese, V.*; Gal, J.; Gazdzicki, M.; Genchev, V.; Georgopoulos, G.; Gladysz, E.; Grebieszkow, K.; Hegyi, S.; Höhne, C.*; Kadija, K.; Karev, A.; Kikola, D.; Kliemant, M.; Kniege, S.; Kolesnikov, V. I.; Kornas, E.; Korus, R.; Kowalski, M.; Kraus, I.*; Kreps, M.; Laszlo, A.; Lacey, R.; van Leeuwen, M.; Levai, P.; Litov, L.; Lungwitz, B.; Makariev, M.; Malakhov, A. I.; Mateev, M.; Melkumov, G. L.; Mischke, A.; Mitrovski, M.; Molnar, J.; Mrowczynski, S.; Nicolic, V.; Palla, G.; Panagiotou, A. D.; Panayotov, D.; Petridis, A.; Peryt, W.; Pikna, M.; Pluta, J.; Prindle, D.; Puhlhofer, F.; Renfordt, R.; Roland, C.; Roland, G.; Rybczynski, M.; Rybicki, A.; Sandoval, A.*; Schmitz, N.; Schuster, T.; Seyboth, P.; Sikler, F.; Sitar, B.; Skrzypczak, E.; Slodkowski, M.; Stefanek, G.; Stock, R.; Strabel, C.; Stroble, H.; Susa, T.; Szentpetery, I.; Sziklai, J.; Szuba, M.; Szymanski, P.; Trubnikov, V.; Varga, D.; Vassiliou, M.; Veres, G. I.; Vesztergombi, G.; Vranic, D.*; Wetzler, A.; Wlodarczyk, Z.; Wojtaszek, A.; Yoo, I. K.; Zimanyi, J.; NA49 Collaboration*: **High transverse momentum hadron spectra at $\sqrt{sNN}$=17.3 GeV in Pb+Pb and p+p collisions.** *Physical review C, Nuclear physics* **77**(3): 034906. DOI:10.1103/physrevc.77.034906

018 Alt, C.; Anticic, T.; Baatar, B.; Barna, D.; Bartke, J.; Betev, L.; Bialkowska, H.; Blume, C.; Boimska, B.; Botje, M.; Bracinik, J.; Bramm, R.; Buncic, P.; Cerny, V.; Christakoglou, P.; Chung, P.; Chvala, O.; Cramer, J. G.; Csato, P.; Dinkelaker, P.; Eckardt, V.; Flierl, D.; Fodor, Z.; Foka, P.*; Friese, V.*; Gal, J.; Gazdzicki, M.; Genchev, V.; Georgopoulos, G.; Gladysz, E.; Grebieszkow, K.; Hegyi, S.; Höhne, C.*; Kadija, K.; Karev, A.; Kikola, D.; Kliemant, M.; Kniege, S.; Kolesnikov, V. I.; Kornas, E.; Korus, R.; Kowalski, M.; Kraus, I.*; Kreps, M.; Laszlo, A.; Lacey, R.; van Leeuwen, M.; Levai, P.; Litov, L.; Lungwitz, B.; Makariev, M.; Malakhov, A. I.; Mateev, M.; Melkumov, G. L.; Mischke, A.; Mitrovski, M.; Molnar, J.; Mrowczynski, S.; Nicolic, V.; Palla, G.; Panagiotou, A. D.; Panayotov, D.; Petridis, A.; Peryt, W.; Pikna, M.; Pluta, J.; Prindle, D.; Pühlhofer, F.; Renfordt, R.; Roland, C.; Roland, G.; Rybczynski, M.; Rybicki, A.; Sandoval, A.*; Schmitz, N.; Schuster, T.; Seyboth, P.; Sikler, F.; Sitar, B.; Skrzypczak, E.; Slodkowski, M.; Stefanek, G.; Stock, R.; Strabel, C.; Ströbele, H.; Susa, T.; Szentpetery, I.; Sziklai, J.; Szuba, M.; Szymanski, P.; Trubnikov, V.; Utvic, M.;

Varga, D.; Vassiliou, M.; Veres, G. I.; Vesztergombi, G.; Vranic, D.*; Wetzler, A.; Wlodarczyk, Z.; Wojtaszek, A.; Yoo, I. K.; Zimanyi, J.: **Energy dependence of multiplicity fluctuations in heavy ion collisions at 20A to 158A GeV.** *Physical review C, Nuclear physics* **78**(3): 034914. DOI:10.1103/physrevc.78.034914

019 Alt, C.; Anticic, T.; Baatar, B.; Barna, D.; Bartke, J.; Betev, L.; Bialkowska, H.; Blume, C.; Boimska, B.; Botje, M.; Bracinik, J.; Bramm, R.; Buncic, P.; Cerny, V.; Christakoglou, P.; Chung, P.; Chvala, O.; Cramer, J. G.; Csato, P.; Dinkelaker, P.; Eckardt, V.; Flierl, D.; Fodor, Z.; Foka, P.*; Friese, V.*; Gal, J.; Gazdzicki, M.; Genchev, V.; Georgopoulos, G.; Gladysz, E.; Grebieszkow, K.; Hegyi, S.; Höhne, C.*; Kadija, K.; Karev, A.; Kikola, D.; Kliemant, M.; Kniege, S.; Kolesnikov, V. I.; Kornas, E.; Korus, R.; Kowalski, M.; Kraus, I.*; Kreps, M.; Laszlo, A.; Lacey, R.; van Leeuwen, M.; Levai, P.; Litov, L.; Lungwitz, B.; Makariev, M.; Malakhov, A. I.; Mateev, M.; Melkumov, G. L.; Mischke, A.; Mitrovski, M.; Molnar, J.; Mrowczynski, S.; Nicolic, V.; Palla, G.; Panagiotou, A. D.; Panayotov, D.; Petridis, A.; Peryt, W.; Pikna, M.; Pluta, J.; Prindle, D.; Pühlhofer, F.; Renfordt, R.; Roland, C.; Roland, G.; Rybczynski, M.; Rybicki, A.; Sandoval, A.*; Schmitz, N.; Schuster, T.; Seyboth, P.; Sikler, F.; Sitar, B.; Skrzypczak, E.; Slodkowski, M.; Stefanek, G.; Stock, R.; Strabel, C.; Ströbele, H.; Susa, T.; Szentpetery, I.; Sziklai, J.; Szuba, M.; Szymanski, P.; Trubnikov, V.; Varga, D.; Vassiliou, M.; Veres, G. I.; Vesztergombi, G.; Vranic, D.*; Wetzler, A.; Wlodarczyk, Z.; Wojtaszek, A.; Yoo, I. K.; Zimanyi, J.: **Bose-Einstein correlations of $\pi^-\pi^-$ pairs in central Pb+Pb collisions at 20A, 30A, 40A, 80A, and 158A GeV.** *Physical review C, Nuclear physics* **77**(6): 064908. DOI:10.1103/physrevc.77.064908

020 Alt, C.; Anticic, T.; Baatar, B.; Barna, D.; Bartke, J.; Betev, L.; Bialkowska, H.; Blume, C.; Boimska, B.; Botje, M.; Bracinik, J.; Bramm, R.; Buncic, P.; Cerny, V.; Christakoglou, P.; Chung, P.; Chvala, O.; Cramer, J. G.; Csato, P.; Dinkelaker, P.; Eckardt, V.; Flierl, D.; Fodor, Z.; Foka, P.*; Friese, V.*; Gal, J.; Gazdzicki, M.; Genchev, V.; Gladysz, E.; Grebieszkow, K.; Hegyi, S.; Höhne, C.*; Kadija, K.; Karev, A.; Kikola, D.; Kliemant, M.; Kniege, S.; Kolesnikov, V. I.; Kornas, E.; Kowalski, M.; Kraus, I.*; Kreps, M.; Laszlo, A.; Lacey, R.; van Leeuwen, M.; Levai, P.; Litov, L.; Lungwitz, B.; Makariev, M.; Malakhov, A. I.; Mateev, M.; Melkumov, G. L.; Meurer, C.; Mischke, A.; Mitrovski, M.; Molnar, J.; Mrowczynski, S.; Nicolic, V.; Palla, G.; Panagiotou, A. D.; Panayotov, D.; Petridis, A.; Peryt, W.; Pikna, M.; Pluta, J.; Prindle, D.; Pühlhofer, F.; Renfordt, R.; Richard, A.; Roland, C.; Roland, G.; Rybczynski, M.; Rybicki, A.; Sandoval, A.*; Schmitz, N.; Schuster, T.; Seyboth, P.; Sikler, F.; Sitar, B.; Skrzypczak, E.; Slodkowski, M.; Stefanek, G.; Stock, R.; Strabel, C.; Ströbele, H.; Susa, T.; Szentpetery, I.; Sziklai, J.; Szuba, M.; Szymanski, P.; Trubnikov, V.; Utvic, M.; Varga, D.; Vassiliou, M.; Veres, G. I.; Vesztergombi, G.; Vranic, D.*; Wetzler, A.; Wlodarczyk, Z.; Wojtaszek, A.; Yoo, I. K.; Zimanyi, J.; NA49 Collaboration*: **Energy dependence of Λ and Ξ production in central Pb plus Pb collisions at 20A, 30A, 40A, 80A, and 158A GeV measured at the CERN Super Proton Synchrotron.** *Physical review C, Nuclear physics* **78**(3): 034918. DOI:10.1103/physrevc.78.034918

021 Andrianov, V.*; Beckert, K.*; Beller, P.*; Bleile, A.*; Egelhof, P.*; Gumberidze, A.*; Ilieva, S.; Kiselev, O.*; Kilbourne, C.; Kluge, H.-J.*; Kraft-Bermuth, S.*; McCammon, D.; Meier, J. P.*; Reuschl, R.; Stöhlker, T.*; Trassinelli, M.*: **First experiments aiming for precise Lamb shift measurements on hydrogen-like heavy ions with low temperature calorimeters.** *Journal of Low Temperature Phyiscs* **151**(3): 1049–1054. DOI:10.1007/s10909-008-9792-8 Also part of: 'Large-scale facilities for research with photons, neutrons and ions'.

022 Andronic, A.*; Braun-Munzinger, P.*; Redlich, K.; Stachel, J.: **Charmonium and open charm production in nuclear collisions at SPS/FAIR energies and the possible influence of a hot hadronic medium.** *Physics letters B* **659**(1): 149–155. DOI:10.1016/j.physletb.2007.10.064

023 Andronic, A.*; Braun-Munzinger, P.; Redlich, K.; Stachel, J.: **Statistical hadronization of charm: from FAIR to the LHC.** *Journal of physics G, Nuclear and particle physics* **35**(10): 104155. DOI:10.1088/0954-3899/35/10/104155

024 Antalic, S.; Heßberger, F. P.*; Hofmann, S.*; Ackermann, D.*; Heinz, S.*; Kindler, B.*; Kojouharov, I.*; Kuusiniemi, P.; Leino, M.; Lommel, B.*; Mann, R.*; Nishio, K.; Saro, S.; Streicher, B.; Sulignano, B.*; Venhart, M.: **Decay studies of neutron-deficient lawrencium isotopes.** *The European physical journal A, Hadrons and nuclei* **38**(2): 219–226. DOI:10.1140/epja/i2008-10665-7

025 Arcones, A.; Martinez-Pinedo, G.*; O'Connor, E.; Schwenk, A.; Janka, H. T.; Horowitz, C. J.; Langanke, K.*: **Influence of light nuclei on neutrino-driven supernova outflows.** *Physical review C, Nuclear physics* **78**(1): 015806. DOI:10.1103/physrevc.78.015806

026 Armbruster, P.*: **Shifting the closed proton shell to Z=122 - A possible scenario to understand the production of superheavy elements Z=112-118.** *The European physical journal A, Hadrons and nuclei* **37**(2): 159–167. DOI:10.1140/epja/i2008-10607-5

027 Armesto, N.; Borghini, N.; Jeon, S.; Wiedemann, U. A.; Abreu, S.; Akkelin, S. V.; Alam, J.; Albacete, J. L.; Andronic, A.*; Antonov, D.; Arleo, F.; Armesto, N.; Arsene, I. C.; Barnaföldi, G. G.; Barrette, J.; Bäuchle, B.; Becattini, F.; Betz, B.; Bleicher, M.; Bluhm, M.; Boer, D.; Bopp, F. W.; Braun-Munzinger, P.*; Bravina, L.; Busza, W.; Cacciari, M.; Capella, A.; Casalderrey-Solana, J.; Chatterjee,

R.; Chen, L.-W.; Cleymans, J.; Cole, B. A.; Del Valle, Z. C.; Csernai, L. P.; Cunqueiro, L.; Dainese, A.; de Deus, J. D.; Ding, H. T.; Djordjevic, M.; Drescher, H.; Dremin, I. M.; Dumitru, A.; Engel, R.; d'Enterria, D.; Eskola, K. J.; Fai, G.; Ferreiro, E. G.; Fries, R. J.; Frodermann, E.; Fujii, H.; Gale, C.; Gelis, F.; Goncalves, V. P.; Greco, V.; Greiner, C.; Gyulassy, M.; van Hees, H.; Heinz, U.; Honkanen, H.; Horowitz, W. A.; Iancu, E.; Ingelman, G.; Jalilian-Marian, J.; Jeon, S.; Kaidalov, A. B.; Kämpfer, B.; Kang, Z. B.; Karpenko, I. A.; Kestin, G.; Kharzeev, D.; Ko, C. M.; Koch, B.; Kopeliovich, B.; Kozlov, M.; Kraus, I.; Kuznetsova, I.; Lee, S. H.; Lednicky, R.; Letessier, J.; Levin, E.; Li, B. A.; Lin, Z. W.; Liu, H.; Liu, W.; Loizides, C.; Lokhtin, I. P.; Machado, M. V. T.; Malinina, L. V.; Managadze, A. M.; Mangano, M. L.; Mannarelli, M.; Manuel, C.; Martinez, G.; Milhano, J. G.; Mocsy, A.; Molnar, D.; Nardi, M.; Nayak, J. K.; Niemi, H.; Oeschler, H.; Ollitrault, J. Y.; Paic, G.; Pajares, C.; Pantuev, V. S.; Papp, G.; Peressounko, D.; Petreczky, P.; Petrushanko, S. V.; Piccinini, F.; Pierog, T.; Pirner, H. J.; Porteboeuf, S.; Potashnikova, I.; Qin, G. Y.; Qiu, J. W.; Rafelski, J.; Rajagopal, K.; Ranft, J.; Rapp, R.; Räsänen, S. S.; Rathsman, J.; Rau, P.; Redlich, K.; Renk, T.; Rezaeian, A. H.; Rischke, D.; Roesler, S.; Ruppert, J.; Ruuskanen, P. V.; Salgado, C. A.; Sapeta, S.; Sarcevic, I.; Sarkar, S.; Sarycheva, L. I.; Schmidt, I.; Shoshi, A. I.; Sinha, B.; Sinyukov, Y. M.; Snigirev, A. M.; Srivastava, D. K.; Stachel, J.; Stasto, A.; Stöcker, H.*; Teplov, C. Y.; Thews, R. L.; Torrieri, G.; Pop, V. T.; Triantafyllopoulos, D. N.; Tuchin, K. L.; Turbide, S.; Tywoniuk, K.; Utermann, A.; Venugopalan, R.; Vitev, I.; Vogt, R.; Wang, E.; Wang, X. N.; Werner, K.; Wessels, E.; Wheaton, S.; Wicks, S.; Wiedemann, U. A.; Wolschin, G.; Xiao, B. W.; Xu, Z.; Yasui, S.; Zabrodin, E.; Zapp, K.; Zhang, B.; Zhang, B.-W.; Zhang, H.; Zhou, D.: **Heavy-ion collisions at the LHC-Last call for predictions.** *Journal of physics G, Nuclear and particle physics* **35**(5): 054001. DOI:10.1088/0954-3899/35/5/054001

028 Aumann, T.*: **Giant resonances in exotic nuclei experimental status and perspectives.** *Nuclear physics A, Nuclear and hadronic physics* **805**: 198C–209C. DOI:10.1016/j.nuclphysa.2008.02.248

029 Bacca, S.*; Barnea, N.; Leidemann, W.; Orlandini, G.: **Longitudinal response function of He-4 with a realistic force.** *Few-Body Systems* **44**(1): 321–324. DOI:10.1007/s00601-008-0318-3

030 Bacca, S.*; Feldmeier, H.*; Neff, T.*: **Long range tensor correlations in charge and parity projected fermionic molecular dynamics.** *Physical review C, Nuclear physics* **78**(4): 044306. DOI:10.1103/physrevc.78.044306

031 Barbieri, C.*; Caurier, E.; Langanke, K.*; Martinez-Pinedo, G.*: **Pygmy dipole response of proton-rich argon nuclei in random-phase approximation and no-core shell model.** *Physical review C, Nuclear physics* **77**(2): 424
024304. DOI:10.1103/physrevc.77.024304

032 Barbieri, C.*; Caurier, E.; Langanke, K.*; Martinez-Pinedo, G.*: **Reply to "Comment on 'Pygmy dipole response of proton-rich argon nuclei in random-phase approximation and no-core shell model' ".** *Physical review C, Nuclear physics* **78**(3): 039802. DOI:10.1103/physrevc.78.039802

033 Behr, K.-H.*; Achenbach, B.*; Brünle, A.*; Geissel, H.*; Gleim, M.*; Müller, W.*; Karagiannis, C.*; Münzenberg, G.*; Scheidenberger, C.*; Sümmerer, K.*; Weick, H.*; Winkler, M.*: **Remote-handling systems at the high-radiation areas of the GSI fragment separator FRS.** *Nuclear instruments & methods in physics research, Section B, Beam interactions with materials and atoms* **266**(19): 4280–4283. DOI:10.1016/j.nimb.2008.05.062

034 Benlliure, J.; Fernandez-Ordonez, M.; Audouin, L.; Boudard, A.; Casarejos, E.; Ducret, J. E.; Enqvist, T.; Heinz, A.*; Henzlova, D.*; Henzl, V.*; Kelic, A.*; Leray, S.; Napolitani, P.*; Pereira, J.; Rejmund, F.; Ricciardi, M. V.*; Schmidt, K. H.*; Schmitt, C.*; Stephan, C.; Tassan-Got, L.; Volant, C.; Villagrasa, C.; Yordanov, O.*: **Production of medium-mass neutron-rich nuclei in reactions induced by ^{136}Xe projectiles at 1 A GeV on a beryllium target.** *Physical review C, Nuclear physics* **78**(5): 054605. DOI:10.1103/physrevc.78.054605

035 Berdermann, E.*; Caragheorgheopol, A.; Ciobanu, M.*; Pomorski, M.*; Pullia, A.; Riboldi, S.; Traeger, M.*; Weick, H.*: **Ion spectroscopy - A diamond characterization tool.** *Diamond and related materials* **17**(7): 1159–1163. DOI:10.1016/j.diamond.2008.03.036

036 Betz, B.*; Gyulassy, M.; Rischke, D. H.; Stöcker, H.*; Torrieri, G.: **Jet propagation and Mach cones in (3+1)d ideal hydrodynamics.** *Journal of physics G, Nuclear and particle physics* **35**(10): 104106. DOI:10.1088/0954-3899/35/10/104106

037 Block, M.; Bachelet, C.; Bollen, G.; Facina, M.; Folden, C. M.; Guenaut, C.; Kwiatkowski, A. A.; Morrissey, D. J.; Pang, G. K.; Prinke, A.; Ringle, R.; Savory, J.; Schury, P.; Schwarz, S.: **Mass measurements of rare isotopes with the LEBIT facility at the NSCL.** *Nuclear instruments & methods in physics research, Section B, Beam interactions with materials and atoms* **266**(19): 4521–4526. DOI:10.1016/j.nimb.2008.05.098 Also part of: 'Large-scale facilities for research with photons, neutrons and ions'.

038 Bockstiegel, C.; Steinhauser, S.; Schmidt, K.-H.*; Clerc, H. G.; Grewe, A.; Heinz, A.; de Jong, M.; Junghans, A. R.*; Muller, J.; Voss, B.*: **Nuclear-fission studies with relativistic secondary beams: Analysis of fission channels.** *Nuclear physics A, Nuclear and hadronic physics* **802**: 12–25. DOI:10.1016/j.nuclphysa.2008.01.012

039 Borzov, I. N.*; Cuenca-Garcia, J. J.*; Langanke, K.*; Martinez-Pinedo, G.*; Montes, F.: **Beta-decay of Z $<$ 50 nuclei near the N=82 closed neutron shell.** *Nuclear physics A, Nuclear and hadronic physics* **814**: 159–173. DOI:10.1016/j.nuclphysa.2008.09.010

040 Boutin, D.; Geissel, H.*; Plaß, W.; Weick, H.*; Winkler, M.*; Yavor, M.: **Ion-optical layout of the focusing system in front of the Super-FRS target.** *Nuclear instruments & methods in physics research, Section B, Beam interactions with materials and atoms* **266**(19): 4192–4195. DOI:10.1016/j.nimb.2008.05.028

041 Bravina, L. V.; Arsene, I.; Nilsson, M. S.; Tywoniuk, K.; Zabrodin, E. E.; Bleibel, J.; Faessler, A.; Fuchs, C.; Bleicher, M.; Burau, G.; Stöcker, H.*: **Microscopic models and effective equation of state in nuclear collisions in the vicinity of E_{lab}=30A GeV at the GSI Facility for Antiproton and Ion Research (FAIR) and beyond.** *Physical review C, Nuclear physics* **78**(1): 014907. DOI:10.1103/physrevc.78.014907

042 Chulkov, L. V.*: **Halo-nucleus structure obtained from quasi-free scattering.** *Few-Body Systems* **44**(1): 263–267. DOI:10.1007/s00601-008-0305-8

043 Clement, E.; Görgen, A.; Korten, W.; Bürger, A.; Chatillon, A.; Le Coz, Y.; Theisen, C.; Zielinska, M.; Blank, B.; Davies, P. J.; Fox, S. P.; Gerl, J.*; Georgiev, G.; Grevy, S.; Iwanicki, J.; Jenkins, D. G.; Johnston-Theasby, F.; Joshi, P.; Matea, I.; Napiorkowski, P. J.; Santos, F. D.; Pellegriti, M. G.; Wadsworth, R.: **A new device for combined Coulomb excitation and isomeric conversion electron spectroscopy with fast fragmentation beams.** *Nuclear instruments & methods in physics research, Section A, Accelerators, spectrometers, detectors and associated equipment* **587**(2): 292–299. DOI:10.1016/j.nima.2008.01.059

044 Dapo, H.; Schäfer, B.-J.; Wambach, J.*: **Hyperon-nucleon single-particle potentials with low-momentum interactions.** *The European physical journal A, Hadrons and nuclei* **36**(1): 101–110. DOI:10.1140/epja/i2008-10542-5

045 Dietz, B.; Friedrich, T.*; Harney, H. L.; Miski-Oglu, M.; Richter, A.; Schäfer, F.; Weidenmüller, H. A.: **Chaotic scattering in the regime of weakly overlapping resonances.** *Physical Review E, statistical, nonlinear, and soft matter physics* **78**(5): 055204. DOI:10.1103/physreve.78.055204

046 Dillmann, I.; Rauscher, T.; Heil, M.*; Käppeler, F.; Rapp, W.; Thielemann, F. K.: **p-Process simulations with a modified reaction library.** *Journal of physics G, Nuclear and particle physics* **35**(1): 014029. DOI:10.1088/0954-3899/35/1/014029

047 Dohmann, H.; Bäumer, C.; Frekers, D.; Grewe, E. W.; Harakeh, M. N.; Hollstein, S.; Johansson, H.*; Popescu, L.; Rakers, S.; Savran, D.; Simon, H.*; Thies, J. H.; den Berg, A. M.; Wörtche, H. J.; Zilges, A.: **The (d,^{2}He) reaction on ^{96}Mo and the double-β decay matrix elements for ^{96}Zr.** *Physical review C, Nuclear physics* **78**(4): 041602. DOI:10.1103/physrevc.78.041602

048 Domingo-Pardo, C.; Abbondanno, U.; Aerts, G.; Alvarez, H.; Alvarez-Velarde, F.; Andriamonje, S.; Andrzejewski, J.; Assimakopoulos, P.; Audouin, L.; Badurek, G.; Baumann, P.; Becvar, F.; Berthoumieux, E.; Bisterzo, S.; Calvino, F.; Calviani, M.; Cano-Ott, D.; Capote, R.; Carrapico, C.; Cennini, P.; Chepel, V.; Colonna, N.; Cortes, G.; Couture, A.; Cox, J.; Dahlfors, M.; David, S.; Dillmann, I.; Dridi, W.; Duran, I.; Eleftheriadis, C.; Embid-Segura, M.; Ferrant, L.; Ferrari, A.; Ferreira-Marques, R.; Fujii, K.; Furman, W.; Gallino, R.; Goncalves, I.; Gonzalez-Romero, E.; Gramegna, F.; Guerrero, C.; Gunsing, F.; Haas, B.; Haight, R.; Heil, M.*; Herrera-Martinez, A.; Igashira, M.; Jericha, E.; Kadi, Y.; Käppeler, F.; Karadimos, D.; Karamanis, D.; Kerveno, M.; Koehler, P.; Kossionides, E.; Krticka, M.; Lamboudis, C.; Leeb, H.; Lindote, A.; Lopes, I.; Lozano, M.; Lukic, S.; Marganiec, J.; Marrone, S.; Massimi, C.; Mastinu, P.; Mengoni, A.; Milazzo, P. M.; Mosconi, M.; Neves, F.; Oberhummer, H.; O'Brien, S.; Pancin, J.; Papachristodoulou, C.; Papadopoulos, C.; Paradela, C.; Patronis, N.; Pavlik, A.; Pavlopoulos, P.; Perrot, L.; Pigni, M. T.; Plag, R.; Plompen, A.; Plukis, A.; Poch, A.; Pretel, C.; Quesada, J.; Rauscher, T.; Reifarth, R.; Rubbia, C.; Rudolf, G.; Rullhusen, P.; Salgado, J.; Santos, C.; Sarchiapone, L.; Savvidis, I.; Stephan, C.; Tagliente, G.; Tain, J. L.; Tassan-Got, L.; Tavora, L.; Terlizzi, R.; Vannini, G.; Vaz, P.; Ventura, A.; Villamarin, D.; Vincente, M. C.; Vlachoudis, V.; Vlastou, R.; Voss, F.; Walter, S.; Wiescher, M.; Wisshak, K.: **The measurement of the ^{206}Pb(n,γ) cross section and stellar implications.** *Journal of physics G, Nuclear and particle physics* **35**(1): 014020. DOI:10.1088/0954-3899/35/1/014020

049 Doornenbal, P.*; Reiter, P.; Grawe, H.*; Wollersheim, H. J.*; Bednarczyk, P.*; Caceres, L.; Cederkall, J.; Ekström, A.; Gerl, J.*; Gorska, M.*; Jhingan, A.; Kojouharov, I.*; Kumar, R.; Prokopowicz, W.*; Schaffner, H.*; Singh, R. P.: **Enhanced strength of the $2_1^+ -> 0_{g.s.}^+$ transition in ^{114}Sn studied via Coulomb excitation in inverse kinematics.** *Physical review C, Nuclear physics* **78**(3): 031303. DOI:10.1103/physrevc.78.031303

050 Dragojevic, I.; Gregorich, K. E.; Düllmann, C. E.*; Garcia, M. A.; Gates, M.; Nelson, S. L.; Stavsetra, L.; Sudowe, R.; Nitsche, H.: **Influence of projectile neutron number in the ^{208}Pb(^{48}Ti,n)^{255}Rf and ^{208}Pb(^{50}Ti,n)^{257}Rf reactions.** *Physical review C, Nuclear physics* **78**(2): 024605. DOI:10.1103/physrevc.78.024605

051 Düllmann, C. E.*: **Physical separators for the heaviest elements.** *Nuclear instruments & methods in physics research, Section B, Beam interac-*

tions with materials and atoms **266**(19): 4123–4130. DOI:10.1016/j.nimb.2008.05.022

052 Düllmann, C. E.*; Türler, A.: **^{248}Cm (^{22}Ne,xn)$^{270-x}$Sg reaction and the decay properties of ^{265}Sg reexamined.** *Physical review C, Nuclear physics* **77**(6): 064320. DOI:10.1103/physrevc.77.064320

053 Dürr, M.; Dimopoulou, C.*; Najjari, B.; Dorn, A.; Bartschat, K.; Bray, I.; Fursa, D. V.; Chen, Z. J.; Madison, D. H.; Ullrich, J.: **Higher-order contributions observed in three-dimensional (e, 2e) cross-section measurements at 1-keV impact energy.** *Physical review A, Atomic, molecular, and optical physics* **77**(3): 032717. DOI:10.1103/physreva.77.032717

054 Dvorak, J.; Brüchle, W.*; Chelnokov, M.; Düllmann, C. E.*; Dvorakova, Z.; Eberhardt, K.; Jäger, E.*; Krücken, R.; Kuznetsov, A.; Nagame, Y.; Nebel, F.; Nishio, K.; Perego, R.; Qin, Z.*; Schädel, M.*; Schausten, B.*; Schimpf, E.*; Schuber, R.; Semchenkov, A.*; Thörle, P.; Türler, A.; Wegrzecki, M.; Wierczinski, B.; Yakushev, A.; Yeremin, A.: **Observation of the 3n evaporation channel in the complete hot-fusion reaction ^{26}Mg+^{248}Cm leading to the new superheavy nuclide ^{271}Hs.** *Physical review letters* **100**(13): 132503. DOI:10.1103/physrevlett.100.132503

055 Eberhardt, K.; Brüchle, W.*; Düllmann, C. E.*; Gregorich, K. E.; Hartmann, W.*; Hübner, A.*; Jäger, E.*; Kindler, B.*; Kratz, J. V.; Liebe, D.; Lommel, B.*; Maier, H. J.; Schädel, M.*; Schausten, B.*; Schimpf, E.*; Semchenkov, A.*; Steiner, J.*; Szerypo, J.; Thörle, P.; Türler, A.; Yakushev, A.: **Preparation of targets for the gas-filled recoil separator TASCA by electrochemical deposition and design of the TASCA target wheel assembly.** *Nuclear instruments & methods in physics research, Section A, Accelerators, spectrometers, detectors and associated equipment* **590**(1): 134–140. DOI:10.1016/j.nima.2008.02.069

056 Efremov, A. A.; Koshurnikova, E. K.; Lobanov, Y. Y.; Makarov, A. F.; Orth, H.*; Sissakian, A. N.; Vodoplanov, A. S.: **2T superconducting detector solenoid for the PANDA target spectrometer.** *Nuclear instruments & methods in physics research, Section A, Accelerators, spectrometers, detectors and associated equipment* **585**(3): 182–200. DOI:10.1016/j.nima.2007.11.021

057 Eliseev, S.*; Block, M.*; Dworschak, M.*; Herfurth, F.*; Kluge, H.-J.*; Martin, A.*; Rauth, C.*; Vorobjev, G.*: **A new cryogenic gas-filled stopping chamber for SHIPTRAP.** *Nuclear instruments & methods in physics research, Section B, Beam interactions with materials and atoms* **266**(19): 4475–4477. DOI:10.1016/j.nimb.2008.05.055 Also part of: 'Large-scale facilities for research with photons, neutrons and ions'.

058 Feng, Z. Q.*; Jin, G. M.; Zhang, F. S.: **Dynamical analysis on heavy-ion fusion reactions near Coulomb barrier.** *Nuclear physics A, Nuclear and hadronic physics* **802**: 91–106. DOI:10.1016/j.nuclphysa.2008.01.022

059 Fernandez-Ramirez, C.; Martinez, M. C.; Vignote, J. R.*; Udias, J. M.: **Spin asymmetry for the $^{16}(\vec{\gamma},\pi^-$ p reaction in the $\Delta(1232)$ region within an effective Lagrangian approach.** *Physics letters B* **664**(1): 57–63. DOI:10.1016/j.physletb.2008.05.003

060 Fischer, C. S.*; Williams, R.: **Beyond the rainbow: Effects from pion back-coupling.** *Physical Review D, particles, fields, gravitation, and cosmology* **78**(7): 074006. DOI:10.1103/physrevd.78.074006

061 Fohl, K.; Bettoni, D.; Branford, D.; Britting, A.; Carassiti, V.; Cecchi, A.; Dodokhof, V. K.; Düren, M.; Ehrenfried, M.; Eyrich, W.; Glazier, D. I.; Hoek, M.; Hohler, R.; Kaiser, R.; Lehmann, A.; Lehmann, D.; Lu, S.; Marton, J.; Merle, O.; Peters, K.*; Pizzolotto, C.; Rosner, G.; Schepers, G.*; Schmidt, R.; Schmitt, L.*; Schonmeier, P.; Schwarz, C.*; Seitz, B.; Sfienti, C.*; Suzuki, K.; Teufel, A.; Vodopianov, A. S.; Watts, D. P.: **The DIRC detectors of the PANDA experiment at FAIR.** *Nuclear instruments & methods in physics research, Section A, Accelerators, spectrometers, detectors and associated equipment* **595**(1): 88–91. DOI:10.1016/j.nima.2008.07.094

062 Frohlich, I.; Kajetanowicz, M.*; Korcy, K.; Krzemien, W.; Palka, M.; Salabura, P.*; Schrader, C.; Skott, P.*; Strobele, H.*; Stroth, J.*; Tarantola, A.; Traxler, M.*; Trebacz, R.; Yurevich, S.: **A general purpose trigger and readout board for HADES and FAIR-experiments.** *IEEE transactions on nuclear science* **55**(1): 59–66. DOI:10.1109/tns.2007.913487

063 Garnsworthy, A. B.; Regan, P. H.; Caceres, L.*; Pietri, S.; Sun, Y.; Rudolph, D.; Gorska, M.*; Podolyak, Z.; Steer, S.; Hoischen, R.*; Heinz, A.*; Becker, F.*; Bednarczyk, P.*; Doornenbal, P.*; Geissel, H.*; Gerl, J.*; Grawe, H.*; Grebosz, J.*; Kelic, A.*; Kojouharov, I.*; Kurz, N.*; Montes, F.; Prokopowicz, W.*; Saito, T.*; Schaffner, H.*; Tachenov, S.*; Werner-Malento, E.; Wollersheim, H. J.*; Benzoni, G.; Blank, B. B.; Brandau, C.*; Bruce, A. M.; Camera, F.; Catford, W. N.; Cullen, I. J.; Dombradi, Z.; Estevez, E.; Gelletly, W.; Ilie, G.; Jolie, J.; Jones, G. A.; Jungclaus, A.; Kmiecik, M.; Kondev, F. G.; Kurtukian-Nieto, T.; Lalkovski, S.; Liu, Z.; Maj, A.; Myalski, S.; Pfutzner, M.; Schwertel, S.; Shizuma, T.; Simons, A. J.; Walker, P. M.; Wielandi, O.; Xu, F. R.: **Neutron-proton pairing competition in N = Z nuclei: Metastable state decays in the proton dripline nuclei $^{82}_{41}$Nb and $^{86}_{43}$Tc.** *Physics letters B* **660**(4): 326–330. DOI:10.1016/j.physletb.2008.01.017

064 Gates, J. M.; Garcia, M. A.; Gregorich, K. E.; Düllmann, C. E.*; Dragojevic, I.; Dvorak, J.; Eichler, R.; Folden, C. M.; Loveland, W.; Nelson, S. L.; Pang, G. K.; Stavsetra, L.; Sudowe, R.; Türler, A.; Nitsche, H.:

Synthesis of rutherfordium isotopes in the ^{238}U(^{26}Mg, xn)$^{264-x}$Rf reaction and study of their decay properties. *Physical review C, Nuclear physics* **77**(3): 034603. DOI:10.1103/physrevc.77.034603

065 Geissel, H.*; Lavinov, Y. A.*: **Experiments with the FRS facility at GSI.** *Nuclear instruments & methods in physics research, Section B, Beam interactions with materials and atoms* **266**(19): 4176–4182. DOI:10.1016/j.nimb.2008.05.093

066 Gerl, J.*; Sai, K. V.; Sainath, M.; Gowrishankar, R.; Venkataramaniah, K.: **Internal conversion coefficients of high multipole transitions: Experiment and theories.** *Atomic Data and Nuclear Data Tables* **94**(5): 701–738. DOI:10.1016/j.adt.2008.04.001

067 Golabek, C.; Villari, A. C. C.; Heinz, S.*; Mittig, W.; Bhattacharyya, S.; Boilley, D.; De France, G.; Drouart, A.; Gaudefroy, L.; Giot, L.; Marchix, A.; Maslov, V.; Morjean, M.; Mukherjee, G.; Navin, A.; Penionzkevich, Y.; Rejmund, F.; Rejmund, M.; Roussel-Chomaz, P.; Stodel, C.: **Search for a long living giant system in ^{238}U+^{238}U collisions near the Coulomb barrier.** *International journal of modern physics E, Nuclear physics* **17**(10): 2235–2239. DOI:10.1142/S0218301308011409

068 Gorbunov, S.*; Kebschull, U.; Kisel, I.; Lindenstruth, V.; Müller, W. F. J.*: **Fast SIMDized Kalman filter based track fit.** *Computer Physics Communications* **178**(5): 374–383. DOI:10.1016/j.cpc.2007.10.001

069 Grewe, E. W.; Bäumer, C.; Dohmann, H.; Frekers, D.; Harakeh, M. N.; Hollstein, S.; Johansson, H.*; Langanke, K.*; Martinez-Pinedo, G.*; Nowacki, F.; Petermann, I.*; Popescu, L.; Rakers, S.; Savran, D.; Sieja, K.; Simon, H.*; Thies, J. H.; van den Berg, A. M.; Wortche, H. J.; Zilges, A.: **Studies on the double-β decay nucleus ^{64}Zn using the (d,^{2}He) reaction.** *Physical review C, Nuclear physics* **77**(6): 064303. DOI:10.1103/physrevc.77.064303

070 Grewe, E. W.; Bäumer, C.; Dohmann, H.; Frekers, D.; Harakeh, M. N.; Hollstein, S.; Johansson, H.*; Popescu, L.; Rakers, S.; Savran, D.; Simon, H.*; Thies, J. H.; van den Berg, A. M.; Wörtche, H. J.; Zilges, A.: **The (d,^{2}He) reaction on ^{76}Se and the double-β-decay matrix elements for A=76.** *Physical review C, Nuclear physics* **78**(4): 044301. DOI:10.1103/physrevc.78.044301

071 Grigorenko, L. V.*; Zhukov, M. V.: **Problems with the interpretation of the ^{10}He ground state.** *Physical review C, Nuclear physics* **77**(3): 034611. DOI:10.1103/physrevc.77.034611

072 Höhne, C.*; CBM Collaboration: **Di-lepton spectroscopy in CBM.** *Journal of physics G, Nuclear and particle physics* **35**(10): 104160. DOI:10.1088/0954-3899/35/10/104160

073 Höhne, C.*; Das, S.*; Dürr, M.; Galatyuk, T.*; Koczon, P.*; Lebedev, S.*; Maevskaya, A.; Ososkov, G.: **Development of a RICH detector for electron identification in CBM.** *Nuclear instruments & methods in physics research, Section A, Accelerators, spectrometers, detectors and associated equipment* **595**(1): 187–189. DOI:10.1016/j.nima.2008.07.029

074 Heinz, S.*: **Cluster effects in ^{25}Mg +^{206}Pb reactions studied with the velocity filter SHIP.** *International journal of modern physics E, Nuclear physics* **17**(10): 2231–2234. DOI:10.1142/S0218301308011392

075 Heinz, S.*; Comas, V.; Heßberger, F. P.*; Hofmann, S.*; Ackermann, D.*; Burkhard, H.*; Gan, Z.; Heredia, J.; Khuyagbaatar, J.; Kindler, B.*; Lommel, B.*; Mann, R.*; Maurer, J.*; Nishio, K.; Sulignano, B.: **Di-nuclear systems studied with the velocity filter SHIP.** *The European physical journal A, Hadrons and nuclei* **38**(2): 227–232. DOI:10.1140/epja/i2008-10671-9 Also part of: 'Large-scale facilities for research with photons, neutrons and ions'.

076 Henning, W. F.*: **FAIR - recent developments and status.** *Nuclear physics A, Nuclear and hadronic physics* **805**: 502C–510C. DOI:10.1016/j.nuclphysa.2008.02.288

077 Henzlova, D.*; Schmidt, K.-H.*; Ricciardi, M. V.*; Kelic, A.*; Henzl, V.*; Napolitani, P.*; Audouin, L.; Benlliure, J.; Boudard, A.; Casarejos, E.; Ducret, J. E.; Enqvist, T.; Heinz, A.; Junghans, A.; Jurado, B.; Krasa, A.; Kurtukian, T.; Leray, S.; Ordonez, M. F.; Pereira, J.; Pleskac, R.; Rejmund, F.; Schmitt, C.*; Stephan, C.; Tassan-Got, L.; Villagrasa, C.; Volant, C.; Wagner, A.; Yordanov, O.*: **Experimental investigation of the residues produced in the ^{136}Xe+Pb and ^{124}Xe+Pb fragmentation reactions at 1A GeV.** *Physical review C, Nuclear physics* **78**(4): 044616. DOI:10.1103/physrevc.78.044616

078 Heuser, J. M.*; CBM Collaboration: **The Compressed Baryonic Matter experiment at FAIR: physics of strangeness and charm, status of preparations.** *Journal of physics G, Nuclear and particle physics* **35**(4): 044049. DOI:10.1088/0954-3899/35/4/044049

079 Hoek, M.; Bennet, E. D.; Branford, D.; Cowie, E. N.; Düren, M.; Fohl, K.; Glazier, D.; Kaiser, R.*; Lehmann, A.; Lu, S.; Marton, J.; Ostendorf, R.; Schepers, G.*; Schwarz, C.*; Seitz, B.; Teufel, A.; Watts, D.: **Radiation hardness study on fused silica.** *Nuclear instruments & methods in physics research, Section A, Accelerators, spectrometers, detectors and associated equipment* **595**(1): 190–193. DOI:10.1016/j.nima.2008.07.098

080 Hurnmrich, H.; Banik, N. L.; Breckheimer, M.; Brüchle, W.*; Buda, R.; Feist, F.; Jäger/, E.* Kratz, J. V.; Kuczewski, B.; Liebe, D.; Niewisch, L.; Schädel, M.*; Schausten, B.*; Schimpf, E.*; Wiehl, N.: **Electrodeposition methods in superheavy ele-**

ment chemistry. *Radiochimica acta* **96**(2): 73–83. DOI:10.1524/ract.2008.1473 OPEN ACCESS.

081 Ishii, Y.; Toyoshima, A.; Tsukada, K.; Asai, M.; Toume, H.; Nishinaka, I.; Nagame, Y.; Miyashita, S.; Mori, T.; Suganuma, H.; Haba, H.; Sakamaki, M.; Goto, S.; Kudo, H.; Akiyama, K.; Oura, Y.; Nakahara, H.; Tashiro, Y.; Shmohara, A.; Schädel, M.*; Brüchle, W.*; Pershina, V.*; Kratz, J. V.: **Fluoride complexation of element 104, rutherfordium (Rf), investigated by cation-exchange chromatography.** *Chemistry Letters* **37**(3): 288–289. DOI:10.1246/cl.2008.288

082 Ivanov, Y. B.*; Russkikh, V. N.*: **Transverse-mass effective temperature in heavy-ion collisions from AGS to SPS.** *The European physical journal A, Hadrons and nuclei* **37**(2): 139–142. DOI:10.1140/epja/i2008-10634-2

083 Ivanov, Y. B.*; Russkikh, V. N.*: **Transverse-mass spectra in heavy-ion collisions at energies E_{lab}=2-160 GeV/nucleon.** *Physical review C, Nuclear physics* **78**(6): 064902. DOI:10.1103/physrevc.78.064902

084 Jido, D.; Kolomeitsev, E. E.*; Nagahiro, H.; Hirenzaki, S.: **Level crossing of particle-hole and mesonic modes in eta-mesonic nuclei.** *Nuclear physics A, Nuclear and hadronic physics* **811**(1): 158–178. DOI:10.1016/j.nuclphysa.2008.07.012

085 Juodagalvis, A.*; Sampaio, J. M.; Langanke, K.*; Hix, W. R.: **Extended pool of electron-capture rates for core-collapse supernovae simulations.** *Journal of physics G, Nuclear and particle physics* **35**(1): 014031. DOI:10.1088/0954-3899/35/1/014031

086 Jurkiewicz, J.; Lukaszewski, G.; Nowak, M. A.*: **Diagrammatic approach to fluctuations in the Wishart ensemble.** *Acta physica Polonica B, Particle physics and field theory, nuclear physics, theory of relativity* **39**(4): 799–809. URL OPEN ACCESS.

087 Köster, U.; Arndt, O.; Bouquerel, E.; Fedoseyev, V. N.; Franberg, H.; Joinet, A.; Jost, C.; Kerkines, I. S. K.; Kirchner, R.*; TARGISOL Collaboration: **Progress in ISOL target-ion source systems.** *Nuclear instruments & methods in physics research, Section B, Beam interactions with materials and atoms* **266**(19): 4229–4239. DOI:10.1016/j.nimb.2008.05.152

088 Karpov, A. V.; Kelic, A.*; Schmidt, K.-H.*: **On the topographical properties of fission barriers.** *Journal of physics G, Nuclear and particle physics* **35**(3): 035104. DOI:10.1088/0954-3899/35/3/035104

089 Kellermann, C.; Fischer, C. S.*: **Running coupling from the four-gluon vertex in Landau gauge Yang-Mills theory.** *Physical Review D, particles, fields, gravitation, and cosmology* **78**(2): 025015. DOI:10.1103/physrevd.78.025015

090 Khuyagbaatar, J.*; Hofmann, S.*; Heßberger, F. P.*; Ackermann, D.*; Burkhard, H. G.*; Heinz, S.*; Kindler, B.*; Kojouharov, I.*; Lommel, B.*; Mann, R.*; Maurer, J.*; Nishio, K.; Novikov, Y.: **Spontaneous fission of neutron-deficient fermium isotopes and the new nucleus Fm-241.** *The European physical journal A, Hadrons and nuclei* **37**(2): 177–183. DOI:10.1140/epja/i2008-10608-4 Also part of: 'Large-scale facilities for research with photons, neutrons and ions'.

091 Khvorostukhin, A. S.; Toneev, V. D.*; Voskresensky, D. N.*: **Relativistic mean-field model with scaled hadron masses and couplings.** *Nuclear physics A, Nuclear and hadronic physics* **813**(3): 313–346. DOI:10.1016/j.nuclphysa.2008.09.013

092 Kindler, B.*; Ackermann, D.*; Hartmann, W.*; Heßberger, F. P.*; Hofmann, S.*; Hübner, A.*; Lommel, B.*; Mann, R.*; Steiner, J.*: **Uranium fluoride and metallic uranium as target materials for heavy-element experiments at SHIP.** *Nuclear instruments & methods in physics research, Section A, Accelerators, spectrometers, detectors and associated equipment* **590**(1): 126–130. DOI:10.1016/j.nima.2008.02.031

093 Klein-Boesing, M.; Andronic, A.*; Bartos, D.; Berceanu, I.; Catanescu, V.; Garabatos, C.*; Heine, N.; Herghelegiu, A.; Magureanu, C.; Moisa, D.; Petris, M.; Petrovici, M.; Radu, A.; Simion, V.; Uhlig, F.; Wessels, J. P.; Wilk, A.: **Position resolution of a high efficiency transition radiation detector for high counting rate environments.** *Nuclear instruments & methods in physics research, Section A, Accelerators, spectrometers, detectors and associated equipment* **585**(1): 83–87. DOI:10.1016/j.nima.2007.11.008

094 Klosowski, M.; Czopyk, L.; Olko, P.; Rebisz, M.*; Voss, B.*; Waligorski, M. P. R.: **TL efficiency of LiF : Mg,Cu,P (MCP-N) 2-D thermoluminescence detectors to raster-scanned carbon ion beams.** *Radiation Measurements* **43**(2): 994–997. DOI:10.1016/j.radmeas.2007.12.019

095 Kolomeitsev, E. E.; Voskresensky, D. N.+: **Neutrino emission due to Cooper-pair recombination in neutron stars reexamined.** *Physical review C, Nuclear physics* **77**(6): 065808. DOI:10.1103/physrevc.77.065808

096 Korcyl, K.; Kuehn, W.; Otwinowski, J.*; Salabura, P.*; Schmitt, L.* KV: **Modeling of the architectural studies for the PANDA DAT system.** *IEEE transactions on nuclear science* **55**(1): 429–434. DOI:10.1109/tns.2007.912070

097 Kozlova, E.*; Weick, H.*; Achenbach, B.*; Behr, K. H.*; Fehrenbacher, G.*; Geissel, H.*; Gleim, M.*; Karagiannis, C.*; Kelic, A.*; Kratz, A.*; Radon, T.*; Sümmerer, K.*; Winkler, M.*: **Layout of the Super-FRS target hall.** *Nuclear instruments & meth-*

ods in physics research, Section B, Beam interactions with materials and atoms **266**(19): 4275–4279. DOI:10.1016/j.nimb.2008.05.141

098 Kurcewicz, J.*; Litvinov, Y. A.*; Bosch, F.*; Geissel, H.*; Patyk, Z.; Winckler, N.*; Batist, L.; Beckert, K.*; Beller, P.*; Boutin, D.; Brandau, C.*; Chen, L.; Dimopoulou, C.*; Faestermann, T.; Grigorenko, L.; Kienle, P.; Knöbel, R.*; Kozhuharov, C.*; Litvinov, S. A.*; Maier, L.; Mazzocco, M.*; Montes, F.*; Münzenberg, G.*; Musumarra, A.; Nociforo, C.*; Nolden, F.*; Pfützner, M.; Plass, W.; Scheidenberger, C.*; Steck, M.*; Sun, B.*; Weick, H.*; Winkler, M.*: **Orbital electron capture and β^+ decay of H-like ^{140}Pr ions.** *Acta physica Polonica B, Particle physics and field theory, nuclear physics, theory of relativity* **39**(2): 501–506. URL OPEN ACCESS. Also part of: 'Large-scale facilities for research with photons, neutrons and ions'.

099 Kurtukian-Nieto, T.; Benlliure, J.; Schmidt, K.-H.*: **A new analysis method to determine beta-decay half-lives in experiments with complex background.** *Nuclear instruments & methods in physics research, Section A, Accelerators, spectrometers, detectors and associated equipment* **589**(3): 472–483. DOI:10.1016/j.nima.2008.02.098

100 Langanke, K.*: **Weak interaction, nuclear physics and supernovae.** *Acta physica Polonica B, Particle physics and field theory, nuclear physics, theory of relativity* **39**(2): 265–281. URL OPEN ACCESS.

101 Langanke, K.*; Martinez-Pinedo, G.*; Müller, B.; Janka, H. T.; Marek, A.; Hix, W. R.; Juodagalvis, A.*; Sampaio, J. M.: **Effects of inelastic neutrino-nucleus scattering on supernova dynamics and radiated neutrino spectra.** *Physical review letters* **100**(1): 011101. DOI:10.1103/physrevlett.100.011101

102 Le Fèvre, A.*; Aichelin, J.: **Bimodality: A sign of critical behavior in nuclear reactions.** *Physical review letters* **100**(4): 042701. DOI:10.1103/physrevlett.100.042701

103 Le Fèvre, A.*; Schwarz, C.*; Auger, G.; Begemann-Blaich, M. L.*; Bellaize, N.; Bittiger, R.*; Bocage, F.; Borderie, B.; Bougault, R.; Bouriquet, B.; Charvet, U.; Chbihi, A.; Dayras, R.; Durand, D.; Frankland, J. D.; Galichet, E.; Gourio, D.; Guinet, D.; Hudan, S.; Lautesse, P.; Lavaud, F.; Legrain, R.; Lopez, O.; Lukasik, J.*; Lynen, U.*; Müllerr, W. F. J.*; Nalpas, L.; Orth, H.*; Plagnol, E.; Rosato, E.; Saija, A.; Sfienti, C.*; Tarnain, B.; Trautmann, W.*; Trzcinski, A.; Turzo, K.*; Vient, E.; Vigilante, M.; Volant, C.; Zwieglinski, B.: **Source shape determination with directional fragment-fragment velocity correlations.** *Physics letters B* **659**(4): 807–812. DOI:10.1016/j.physletb.2007.11.081

104 Le Gentil, E.; Aumann, T.*; Bacri, C. O.; Benlliure, J.; Bianchin, S.*; Bohmer, M.; Boudard, A.; Brzychczyk, J.; Casarejos, E.; Combet, M.; Donadille, L.; Ducret, J. E.; Fernandez-Ordonez, M.; Gernhäuser, R.; Johansson, H.*; Kezzar, K.*; Kurtukian-Nieto, T.; Lafriakh, A.; Lavaud, F.; Le Fèvre, A.*; Leray, S.; Lühning, J.*; Lukasik, J.*; Lynen, U.*; Müller, W. F. J.*; Pawlowski, P.; Pietri, S.; Rejmund, F.; Schwarz, C.*; Sfienti, C.*; Simon, H.*; Trautmann, W.*; Volant, C.; Yordanov, O.*: **Coincidence measurement of residues and light particles in the reaction ^{56}Fe+p at 1 GeV per nucleon with the spallation reactions setup SPALADIN.** *Physical review letters* **100**(2): 022701. DOI:10.1103/physrevlett.100.022701

105 Lehmann, A.; Britting, A.; Eyrich, W.; Pizzolotto, C.; Teufel, A.; Düren, M.; Fohl, K.; Hoek, M.; Lu, S.; Schepers, G.*; Seitz, B.; Sfienti, C.*: **Performance studies of microchannel plate PMTs in high magnetic fields.** *Nuclear instruments & methods in physics research, Section A, Accelerators, spectrometers, detectors and associated equipment* **595**(1): 173–176. DOI:10.1016/j.nima.2008.07.083

106 Lewandowski, B.; Nowak, H.; Peters, K.*; Pitz, N.; Wilms, A. KV: **Large area APDs for the PANDA EMC.** *IEEE transactions on nuclear science* **55**(3): 1304–1307. DOI:10.1109/tns.2008.924076

107 Liebe, D.; Eberhardt, K.; Hartmann, W.*; Hager, T.; Hübner, A.*; Kratz, J. V.; Kindler, B.*; Lommel, B.*; Thörle, P.; Schädel, M.*; Steiner, J.*: **The application of neutron activation analysis, scanning electron microscope, and radiographic imaging for the characterization of electrochemically deposited layers of lanthanide and actinide elements.** *Nuclear instruments & methods in physics research, Section A, Accelerators, spectrometers, detectors and associated equipment* **590**(1): 145–150. DOI:10.1016/j.nima.2008.02.075

108 Liebendorfer, M.; Fischer, T.; Fröhlich, C.; Hix, W. R.; Langanke, K.*; Martinez-Pinedo, G.*; Mezzacappa, A.; Scheidegger, S.; Thielemann, F.-K.; Whitehouse, S. C.: **Nuclear physics in core-collapse supernovae.** *New Astronomy Reviews* **52**(7): 373–376. DOI:10.1016/j.newar.2008.05.006

109 Li, Q.; Bleicher, M.; Stöcker, H.*: **The effect of "preformed" hadron potentials on the dynamics of heavy ion collisions and the HBT puzzle.** *Physics letters B* **659**(3): 525–530. DOI:10.1016/j.physletb.2007.11.080

110 Li, Q. F.; Bleicher, M.; Stöcker, H.*: **Transport model study of the m_T-scaling for Λ, K, and π HBT-correlations.** *Physics letters B* **663**(5): 395–399. DOI:10.1016/j.physletb.2008.04.024

111 Litvinova, E.*; Ring, P.; Tselyaev, V.: **Relativistic quasiparticle time blocking approximation: Dipole response of open-shell nuclei.** *Physical review C, Nuclear physics* **78**(1): 014312. DOI:10.1103/physrevc.78.014312

112 Litvinov, Y. A.*: **Mass and half-life measurements of stored exotic nuclei at the FRS-ESR facility.** *Nuclear physics A, Nuclear and hadronic physics* **805**: 260C–269C. DOI:10.1016/j.nuclphysa.2008.02.254

113 Litvinov, Y. A.*; Bosch, F.*; Winckler, N.*; Boutin, D.; Essel, H. G.*; Faestermann, T.; Geissel, H.*; Hess, S.*; Kienle, P.; Knöbel, R.; Kozhuharov, C.*; Kurcewicz, J.*; Maier, L.; Becker, K.*; Beller, P.*; Brandau, C.*; Chen, L.* Dimopoulou, C.*; Fabian, B.; Fragner, A.; Haettner, E.; Hausmann, M.; Litvinov, S. A.*; Mazzocco, M.*; Montes, F.; Musumarra, A.; Nociforo, C.*; Nolden, F.*; Plaß, W.; Prochazka, A.*; Reda, R.*; Reuschl, R.*; Scheidenberger, C.*; Steck, M.*; Stöhlker, T.*; Torilov, S.; Trassinelli, M.*; Sun, B.*; Weick, H.*; Winkler, M.*: **Observation of non-exponential orbital electron capture decays of hydrogen-like ^{140}Pr and ^{142}Pm ions.** *Physics letters B* **664**(3): 162–168. DOI:10.1016/j.physletb.2008.04.062 Also part of: PhotonsNeutronsandNuclei.

114 Loens, H. P.*; Langanke, K.*; Martinez-Pinedo, G.*; Rauscher, T.; Thielemann, F. K.: **Complete inclusion of parity-dependent level densities in the statistical description of astrophysical reaction rates.** *Physics letters B* **666**(4): 395–399. DOI:10.1016/j.physletb.2008.07.073

115 Lommel, B.*; Brüchle, W.*; Eberhardt, K.*; Hartmann, W.*; Hübner, A.*; Kindler, B.*; Kratz, J. V.; Liebe, D.; Schädel, M.*; Steiner, J.*: **Backings and targets for chemical and nuclear studies of transactinides with TASCA.** *Nuclear instruments & methods in physics research, Section A, Accelerators, spectrometers, detectors and associated equipment* **590**(1): 141–144. DOI:10.1016/j.nima.2008.02.045

116 Lopez, X.*; FOPI Collaboration*: **Strange resonances measured in Al+Al collisions at root $\sqrt{s(NN)}$ =2.65 GeV with the FOPI detector.** *Journal of physics G, Nuclear and particle physics* **35**(4): 044020. DOI:10.1088/0954-3899/35/4/044020

117 Lozeva, R. L.; Simpson, G. S.; Grawe, H.*; Neyens, G.; Atanasova, L. A.; Balabanski, D. L.; Bazzacco, D.; Becker, F.*; Bednarczyk, P.*; Benzoni, G.; Blasi, N.; Blazhev, A.; Bracco, A.; Brandau, C.; Caceres, L.; Camera, F.; Chamoli, S. K.; Crespi, F. C. L.; Daugas, J. M.; Detistov, P.; De Rydt, M.; Doornenbal, P.*; Fahlander, C.; Farnea, E.; Georgiev, G.; Gerl, J.*; Gladnishki, K. A.*; Gorska, M.*; Grebosz, J.*; Hass, M.; Hoischen, R.; Ilie, G.; Ionescu-Bujor, M.; Iordachescu, A.; Jolie, J.; Jungclaus, A.; Kmiecik, M.; Kojouharov, I.*; Kurz, N.*; Lakshmi, S. P.; Lo Bianco, G.; Mallion, S.; Maj, A.; Montanari, D.; Perru, O.; Pfützner, M.; Pietri, S.; Pinston, J. A.; Podolyak, Z.; Prokopowicz, W.*; Rudolph, D.; Rusev, G.; Saitoh, T. R.*; Saltarelli, A.; Schaffner, H.*; Schwengner, R.; Tashenov, S.*; Turzo, K.; Valiente-Dobon, J. J.; Vermeulen, N.; Walker, J.*; Werner-Malento, E.; Wieland, O.; Wollersheim, H.-J.*: **New sub-μs isomers in $125, 127, 129$Sn and isomer systematics of $^{124-130}$Sn.** *Physical review C, Nuclear physics* **77**(6): 064313. DOI:10.1103/physrevc.77.064313 Also part of: 'Large-scale facilities for research with photons, neutrons and ions'.

118 Lukasik, J.*; Adrich, P.*; Aumann, T.*; Bacri, C. O.; Barczyk, T.; Bassini, R.; Bianchin, S.*; Boiano, C.; Botvina, A. S.*; Boudard, A.; Brzychczyk, J.; Chbihi, A.; Cibor, J.; Czech, B.; Ducret, J. E.; Emling, H.*; Frankland, J.; Hellström, M.*; Henzlova, D.*; Imme, G.; Iori, I.; Johansson, H.*; Kezzar, K.*; Lafriakh, A.; Le Fèvre, A.*; Le Gentil, E.; Leifels, Y.*; Lühning, J.*; Lynchi, W. G.; Lynen, U.*; Majka, Z.; Mocko, M.; Müller, W. F. J.*; Mykulyak, A.; De Napoli, M.; Orth, H.*; Otte, A. N.*; Palit, R.*; Pawlowski, P.; Pullia, A.; Raciti, G.; Rapisarda, E.; Sann, H.*; Schwarz, C.*; Sfienti, C.*; Simon, H.*; Sümmerer, K.*; Trautmann, W.*; Tsang, M. B.; Verde, G.; Volant, C.; Wallace, M.; Weick, H.*; Wiechula, J.*; Wieloch, A.; Zwieglinski, B.: **Discriminant analysis and secondary-beam charge recognition.** *Nuclear instruments & methods in physics research, Section A, Accelerators, spectrometers, detectors and associated equipment* **587**(2): 413–419. DOI:10.1016/j.nima.2008.01.071

119 Lutz, M. F. M.*; Korpa, C. L.; Möller, M.*: **Antikaons and hyperons in nuclear matter with saturation.** *Nuclear physics A, Nuclear and hadronic physics* **808**: 124–159. DOI:10.1016/j.nuclphysa.2008.05.008

120 Lutz, M. F. M.*; Leupold, S.*: **On the radiative decays of light vector and axial-vector mesons.** *Nuclear physics A, Nuclear and hadronic physics* **813**(1): 96–170. DOI:10.1016/j.nuclphysa.2008.09.005

121 Lutz, M. F. M.*; Soyeur, M.: **Open-charm meson systems in the hadrogenesis conjecture.** *Progress in particle and nuclear physics* **61**(1): 155–161. DOI:10.1016/j.ppnp.2007.12.038

122 Lutz, M. F. M.*; Soyeur, M.: **Radiative and isospin-violating decays of D_s-mesons in the hadrogenesis conjecture.** *Nuclear physics A, Nuclear and hadronic physics* **813**(1): 14–95. DOI:10.1016/j.nuclphysa.2008.09.003

123 Martinez-Pinedo, G.*: **Nuclear physics aspects of supernovae evolution and nucleosynthesis.** *Journal of physics G, Nuclear and particle physics* **35**(1): 014057. DOI:10.1088/0954-3899/35/1/014057

124 Martinez-Pinedo, G.*: **Selected topics in nuclear astrophysics.** *European Physical Journal - Special Topics* **156**: 123–149. DOI:10.1140/epjst/e2008-00611-5

125 Martinez-Pinedo, G.*: **Weak interaction processes in core-collapse supernova.** *Nuclear physics A, Nuclear and hadronic physics* **805**: 478C–485C. DOI:10.1016/j.nuclphysa.2008.02.269

126 Mazzocco, A.; Ackermann, D.*; Block, A.; Geissel, H.*; Herfurth, F.*; Heßberger, F. P.*; Hofmann, S.*; Iwasa, N.*; Nishio, K.*; Plaß, W. R.; Scheidenberger, C.*; Weick, H.*; Winkler, A.*; SHIPTRAP Collaborat: **MOCADI_FUSION: Extension of the monte-carlo code MOCADI to heavy-ion fusion-evaporation reactions.** *Nuclear instruments & methods in physics research, Section B, Beam interactions with materials and atoms* **266**(15): 3467–3480. DOI:10.1016/j.nimb.2008.04.017 Also part of: 'Large-scale facilities for research with photons, neutrons and ions'.

127 Mazzocco, M.*; Farinon, F.*; Glodariu, T.; Geissel, H.*; Guglielmetti, A.; Iwasa, N.; La Commara, N.; Martin, B.; Mazzocchi, C.; Pierroutsakou, D.; Romoli, M.; Sandoli, M.; Signorini, C.; Soramel, F.; Stroe, L.; Vardaci, E.; Weick, H.*; Winkler, M.*: **Production and separation of light low-energy radioactive ion beams with the EXOTIC beam-line at LNL.** *Nuclear instruments & methods in physics research, Section B, Beam interactions with materials and atoms* **266**(19): 4665–4669. DOI:10.1016/j.nimb.2008.05.112

128 Mertens, R.; Bock, W.; Lommel, B.*; Kolbesen, B. O.: **Annealing of thin B/Nb_2N bilayers, B/Nb bilayers and Nb/B/Nb trilayers via rapid thermal processing (RTP).** *Analytical and Bioanalytical Chemistry* **390**(6): 1517–1525. DOI:10.1007/s00216-007-1672-6

129 Miskowiec, D.*; Braun-Munzinger, P.*: **Laser calibration system for the CERES Time Projection Chamber.** *Nuclear instruments & methods in physics research, Section A, Accelerators, spectrometers, detectors and associated equipment* **593**(3): 188–202. DOI:10.1016/j.nima.2008.02.034

130 Mosconi, M.; Heil, M.*; Käppeler, F.; Plag, R.; Mengoni, A.; Fujii, K.; Domingo-Pardo, C.; Aerts, G.; Terlizzi, R.; Gallino, R.; Abbondanno, U.; Alvarez, H.; Alvarez-Velarde, F.; Andriamonje, S.; Andrzejewski, J.; Assimakopoulos, P.; Audouin, L.; Badurek, G.; Baumann, P.; Becvar, F.; Berthoumieux, E.; Calvino, F.; Calviani, M.; Cano-Ott, D.; Capote, R.; Carrapico, C.; Cennini, P.; Chepel, V.; Colonna, N.; Cortes, G.; Couture, A.; Cox, J.; Dahlfors, M.; David, S.; Dillmann, I.; Dridi, W.; Duran, I.; Eleftheriadis, C.; Embid-Segura, M.; Ferrant, L.; Ferrari, A.; Ferreira-Marques, R.; Furman, W.; Goncalves, I.; Gonzalez-Romero, E.; Gramegna, F.; Guerrero, C.; Gunsing, F.; Haas, B.; Haight, R.; Herrera-Martinez, A.; Igashira, M.; Jericha, E.; Kadi, Y.; Karadimos, D.; Karamanis, D.; Kerveno, M.; Koehler, P.; Kossionides, E.; Krticka, M.; Lamboudis, C.; Leeb, H.; Lindote, A.; Lopes, I.; Lozano, M.; Lukic, S.; Marganiec, J.; Marrone, S.; Massimi, C.; Mastinu, P.; Milazzo, P. M.; Neves, F.; Oberhummer, H.; O'Brien, S.; Pancin, J.; Papachristodoulou, C.; Papadopoulos, C.; Paradela, C.; Patronis, N.; Pavlik, A.; Pavlopoulos, P.; Perrot, L.; Pigni, M. T.; Plompen, A.; Plukis, A.; Poch, A.; Pretel, C.; Quesada, J.; Rauscher, T.; Reifarth, R.; Rubbia, C.; Rudolf, G.; Rullhusen, P.; Salgado, J.; Santos, C.; Sarchiapone, L.; Savvidis, I.; Stephan, C.; Tagliente, G.; Tain, J. L.; Tassan-Got, L.; Tavora, L.; Vannini, G.; Vaz, P.; Ventura, A.; Villamarin, D.; Vincente, M. C.; Vlachoudis, V.; Vlastou, R.; Voss, F.; Walter, S.; Wiescher, M.; Wisshak, K.; n TOF Collaboration: **Nuclear physics for the Re/Os clock.** *Journal of physics G, Nuclear and particle physics* **35**(1): 014015. DOI:10.1088/0954-3899/35/1/014015

131 Mukha, I.; Grawe, H.; Roeckl, E.*; Tabor, S.: **Comment on "Level structure of ^{92}Rh: Implications for the two-proton decay of ^{94}Ag^m".** *Physical review C, Nuclear physics* **78**(3): 039803. DOI:10.1103/physrevc.78.039803

132 Mukha, I.; Grigorenko, L.*; Sümmerer, K.*; Acosta, L.; Alvarez, M. A. G.; Casarejos, E.; Chatillon, A.; Cortina-Gil, D.; Espino, J. M.; Fomichev, A.; Garcia-Ramos, J. E.; Geissel, H.*; Gomez-Camacho, J.; Hofmann, J.*; Kiselev, O.*; Korsheninnikov, A.; Kurz, N.*; Litvinov, Y.*; Martel, I.; Nociforo, C.*; Ott, W.*; Pfützner, M.; Rodriguez-Tajes, C.; Roeckl, E.*; Stanoiu, M.; Weick, H.*; Woods, P. J.: **Proton-proton correlations observed in two-proton decay of ^{19}Mg and ^{16}Ne.** *Physical review C, Nuclear physics* **77**(6): 061303. DOI:10.1103/physrevc.77.061303

133 Nakano, E.*; Nitta, M.; Matsuura, T.: **Non-Abelian Strings in Hot or Dense QCD.** *Progress of theoretical physics Supplement* (174): 254–257. DOI:10.1143/PTPS.174.254

134 Nakano, E.*; Wen, W. Y.: **Critical magnetic field in a holographic superconductor.** *Physical Review D, particles, fields, gravitation, and cosmology* **78**(4): 046004. DOI:10.1103/physrevd.78.046004

135 Neff, T.*; Feldmeier, H.*: **Cluster and shell structures in the fermionic molecular dynamics approach.** *International journal of modern physics E, Nuclear physics* **17**(10): 2005–2013. DOI:10.1142/S0218301308010994

136 Neff, T.*; Feldmeier, H.*: **Clustering and other exotic phenomena in nuclei.** *European Physical Journal - Special Topics* **156**(1): 69–92. DOI:10.1140/epjst/e2008-00609-y

137 Nelson, S. L.; Folden, C. M.; Gregorich, K. E.; Dragojevic, I.; Düllmann, C. E.*; Eichler, R.; Garcia, M. A.; Gates, J. M.; Sudowe, R.; Nitsche, H.: **Comparison of complementary reactions for the production of ^{261,262}Bh.** *Physical review C, Nuclear physics* **78**(2): 024606. DOI:10.1103/physrevc.78.024606

138 Nickel, D.; Alkofer, R.; Wambach, J.*: **Neutrality of the color-flavor-locked phase in a Dyson-Schwinger approach.** *Physical Review D, particles, fields, gravitation, and cosmology* **77**(11): 114010. DOI:10.1103/physrevd.77.114010

139 Nishio, K.; Ikezoe, H.; Mitsuoka, S.; Nishinaka, I.; Nagame, Y.; Watanabe, Y.; Ohtsuki, T.; Hirose, K.; Hofmann, S.*: **Effects of nuclear orientation on the mass distribution of fission fragments in the reaction of ^{36}S+^{238}U.** *Physical review C, Nuclear physics* **77**(6): 064607. DOI:10.1103/physrevc.77.064607

140 Ohnishi, T.; Kubo, T.; Kusaka, K.; Yoshida, A.; Yoshida, K.; Fukuda, N.; Ohtake, M.; Yanagisawa, Y.; Takeda, H.; Kameda, D.; Yamaguchi, Y.; Aoi, N.; Yoneda, K. I.; Otsu, H.; Takeuchi, S.; Sugimoto, T.; Kondo, Y.; Scheit, H.; Gono, Y.; Sakurai, H.; Motobayasi, T.; Suzuki, H.; Nakao, T.; Kimura, H.; Mizo, Y.; Matsushita, M.; Ieki, K.; Kuboki, T.; Yamaguchi, T.; Suzuki, T.; Ozawa, A.; Moriguchi, T.; Yasuda, Y.; Nakamura, T.; Nannichi, T.; Shimamura, T.; Nakayama, Y.; Geissel, H.*; Weick, H.*; Nolen, J. A.; Tarasov, O. B.; Nettleton, A. S.; Bazin, D. P.; Sherrill, B. M.; Morrissey, D. J.; Mittig, W.: **Identification of new isotopes ^{125}Pd and ^{126}Pd produced by in-flight fission of 345MeV/nucleon ^{238}U: First results from the RIKEN RI beam factory.** *Journal of the Physical Society of Japan* **77**(8): 083201. DOI:10.1143/jpsj.77.083201

141 Patyk, Z.; Geissel, H.*; Litvinov, Y. A.*; Musumarra, A.; Nociforo, C.*: **α-decay half-lives for neutral atoms and bare nuclei.** *Physical review C, Nuclear physics* **78**(5): 054317. DOI:10.1103/physrevc.78.054317

142 Patyk, Z.; Kurcewicz, J.; Bosch, F.*; Geissel, H.*; Litvinov, Y. A.*; Pfützner, M.*: **Orbital electron capture decay of hydrogen- and helium-like ions.** *Physical review C, Nuclear physics* **77**(1): 014306. DOI:10.1103/physrevc.77.014306 Also part of: 'Large-scale facilities for research with photons, neutrons and ions'.

143 Pellegriti, M. G.; Hammache, F.; Roussel, P.; Audouin, L.; Beaumel, D.; Descouvemont, P.; Fortier, S.; Gaudefroy, L.; Kiener, J.; Lefebvre-Schuhl, A.; Stanoiu, M.*; Tatischeff, V.; Vilmay, M.: **Indirect study of the ^{13}C(α,n)^{16}O-16 reaction via the ^{13}C(^{7}Li,t)^{17}O transfer reaction.** *Physical review C, Nuclear physics* **77**(4): 042801. DOI:10.1103/physrevc.77.042801

144 Pershina, V.*; Anton, J.; Jacob, T.: **Fully relativistic density-functional-theory calculations of the electronic structures of MO_4 (M = Ru, Os, and element 108, Hs) and prediction of physisorption.** *Physical review A, Atomic, molecular, and optical physics* **78**(3): 032518. DOI:10.1103/physreva.78.032518

145 Pershina, V.*; Borschevsky, A.; Eliav, E.; Kaldor, U.: **Adsorption of inert gases including element 118 on noble metal and inert surfaces from ab initio Dirac-Coulomb atomic calculations.** *Journal of Chemical Physics* **129**(14): 144106. DOI:10.1063/1.2988318

146 Pershina, V.*; Borschevsky, A.; Eliav, E.; Kaldor, U.: **Atomic Properties of Element 113 and Its Adsorption on Inert Surfaces from ab Initio Dirac-Coulomb Calculations.** *Journal of Physical Chemistry A* **112**(51): 13712–13716. DOI:10.1021/jp8061306

147 Pershina, V.*; Borschevsky, A.; Eliav, E.; Kaldor, U.: **Prediction of the adsorption behavior of elements 112 and 114 on inert surfaces from ab initio Dirac-Coulomb atomic calculations.** *Journal of Chemical Physics* **128**(2): 024707. DOI:10.1063/1.2814242

148 Petersen, H.; Steinheimer, J.; Burau, G.; Bleicher, M.; Stöcker, H.*: **Fully integrated transport approach to heavy ion reactions with an intermediate hydrodynamic stage.** *Physical review C, Nuclear physics* **78**(4): 044901. DOI:10.1103/physrevc.78.044901

149 Petrich, D.; Heil, M.*; Käppeler, F.; Kaltenbaek, J.; Knaetsch, E. P.; Litfin, K.; Roller, D.; Seith, W.; Stieglitz, R.; Voss, F.; Walter, S.: **A neutron production target for FRANZ.** *Nuclear instruments & methods in physics research, Section A, Accelerators, spectrometers, detectors and associated equipment* **596**(3): 269–275. DOI:10.1016/j.nima.2008.08.131

150 Petrick, M.; Plaß, W. R.*; Behr, K.-H.*; Brünle, A.*; Caceres, L.*; Clark, J.; Di, Z.*; Elisseev, S.*; Facina, M.; Fettouhi, A.*; Geissel, H.*; Hüller, W.*; Huyse, M.; Karagiannis, C.*; Kindler, B.*; Knöbel, R.*; Kudryavtsev, Y.; Kurcewicz, J.*; Levant, T.; Litvinov, Y. A.*; Lommel, B.*; Maier, M.*; Morrissey, D. J.; Münzenberg, G.*; Portillo, M.; Savard, G.; Scheidenberger, C.*; Van Duppen, P.; Weick, H.*; Winkler, M.*; Zabransky, B.; FRS Ion Catcher Collaboration: **Online test of the FRS Ion Catcher at GSI.** *Nuclear instruments & methods in physics research, Section B, Beam interactions with materials and atoms* **266**(19): 4493–4497. DOI:10.1016/j.nimb.2008.07.007

151 Plaß, W. R.*; Dickel, T.; Czok, U.; Geissel, H.*; Petrick, M.; Reinheimer, K.; Scheidenberger, C.*; Yavor, M. I.: **Isobar separation by time-of-flight mass spectrometry for low-energy radioactive ion beam facilities.** *Nuclear instruments & methods in physics research, Section B, Beam interactions with materials and atoms* **266**(19): 4560–4564. DOI:10.1016/j.nimb.2008.05.079

152 Qin, Z.*; Brüchle, W.*; Ackermann, D.*; Eberhardt, K.; Heßberger, F. P.*; Jäger, E.*; Kratz, J. V.; Kuusiniemi, R.*; Liebe, D.; Münzenberg, G.*; Nayak, D.; Novikov, Y. N.*; Schädel, M.*; Schausten, B.*; Schimpf, E.*; Semchenkov, A.*; Sulignano, B.*; Thörle, P.; Wu, X. L.*: **Search for the "missing" α-decay branch in ^{239}Cm.** *Radiochimica acta* **96**(8): 455–460. DOI:10.1524/ract.2008.1517 OPEN ACCESS.

153 Raciti, G.; Rapisarda, E.; De Napoli, M.; Amorini, F.; Calabretta, L.; Cardella, G.; Cosentino, G.; Sfienti, C.*; Shchepunov, V.: **Intermediate energies tagged RIBS.** *Nuclear instruments & methods in physics research, Section B, Beam interactions with materials and atoms* **266**(19):

4632–4636. DOI:10.1016/j.nimb.2008.05.153

154 Radtke, T.; Surzhykov, A.; Fritzsche, S.*: **Polarization correlation in the two-photon decay of atomic hydrogen: nonlocality versus entanglement.** *The European physical journal: D, Atomic, molecular and optical physics* **49**(1): 7–12. DOI:10.1140/epjd/e2008-00132-1

155 Rauth, C.*; Ackermann, D.*; Blaum, K.; Block, M.*; Chaudhuri, A.; Di, Z.; Eliseev, S.*; Ferrer, R.; Habs, D.; Herfurth, F.*; Heßberger, F. P.*; Hofmann, S.*; Kluge, H.-J.*; Maero, G.*; Martin, A.*; Marx, G.; Mukherjee, M.*; Neumayr, J. B.; Plaß, W. R.; Rahaman, S.*; Rodriguez, D.; Scheidenberger, C.*; Schweikhard, L.; Thirolf, P. G.; Vorobjev, G.*; Weber, C.*: **First penning trap mass measurements beyond the proton drip line.** *Physical review letters* **100**(1): 012501. DOI:10.1103/physrevlett.100.012501 Also part of: 'Large-scale facilities for research with photons, neutrons and ions'.

156 Redlich, K.; Friman, B.*; Sasaki, C.: **Density fluctuations and chiral phase transition.** *Journal of physics G, Nuclear and particle physics* **35**(4): 044013. DOI:10.1088/0954-3899/35/4/044013

157 Romoli, M.; Vardaci, E.; Anastasio, A.; Boiano, C.; Bonetti, R.; Cassese, F.; Corti, D.; D'Aquino, B.; DeRosa, A.; Di Meo, P.; Energico, S.; Farinon, F.*; Glodariu, T.; Guglietmetti, A.; Inglima, G.; La Commara, M.; Manea, C.; Martina, B.; Masone, V.; Mazzocchi, C.; Mazzocco, M.; Mizoi, Y.; Nicoletto, M.; Parascandolo, L.; Parascandolo, P.; Pierroutsakou, D.; Pontoriere, G.; Randazzo, N.; Roscilli, L.; Sandoli, M.; Signorini, C.; Sipala, V.; Soramel, F.; Store, L.; Valentino, M.; Watanabe, Y.: **EXPADES: A new detection system for charged particles in experiments with RIBs.** *Nuclear instruments & methods in physics research, Section B, Beam interactions with materials and atoms* **266**(19): 4637–4642. DOI:10.1016/j.nimb.2008.05.121

158 Rudolph, D.; Hoischen, R.; Hellström, M.; Pietri, S.; Podolyak, Z.; Regan, P. H.; Garnsworthy, A. B.; Steer, S. J.; Becker, F.*; Bednarczyk, P.*; Caceres, L.*; Doornenbal, P.*; Gerl, J.*; Gorska, M.*; Grebosz, J.*; Kojouharov, I.*; Kurz, N.*; Prokopowicz, W.*; Schaffner, H.*; Wollersheim, H.-J.*; Andersson, L. L.; Atanasova, L.; Balabanski, D. L.; Bentley, M. A.; Blazhev, A.; Brandau, C.*; Brown, J. R.; Fahlander, C.; Johansson, E. K.; Jungclaus, A.; Lenzi, S. M.: **Isospin symmetry and proton decay: Identification of the 10^+ isomer in ^{54}Ni.** *Physical review C, Nuclear physics* **78**(2): 021301. DOI:10.1103/physrevc.78.021301 Also part of: 'Large-scale facilities for research with photons, neutrons and ions'.

159 Rudolph, D.; Hoischen, R.; Hellström, M.; Pietri, S.; Podolyak, Z.; Regan, P. H.; Garnsworthy, A. B.; Steer, S. J.; Becker, F.; Bednarczyk, P.* ; Caceres, L.*; Doornenbal, P.*; Gerl, J.*; Gorska, M.*; Grebosz, J.*; Kojouharov, I.*; Kurz, N.*; Prokopowicz, W.*; Schaffner, H.*; Wollersheim, H. J.*; Andersson, L. L.; Atanasova, L.; Balabanski, D. L.; Bentley, M. A.; Blazhev, A.; Brandau, C.; Brown, J. R.; Fahlander, C.; Johansson, E. K.; Jungclaus, A.: **Evidence for an isomeric 3/2(-) state in ^{53}Co.** *The European physical journal A, Hadrons and nuclei* **36**(2): 131–138. DOI:10.1140/epja/i2008-10587-4

160 Saito, T. R.*; Saito, N.*; Starosta, K.; Beller, J.; Pietralla, N.; Wollersheim, H. J.*; Balabanski, D. L.; Banu, A.*; Bark, R. A.; Beck, T.*; Becker, F.*; Bednarczyk, P.*; Behr, K. H.*; Benzoni, G.; Bizzeti, P. G.; Boiano, C.; Bracco, A.; Brambilla, S.; Brünle, A.*; Bürger, A.; Caceres, L.*; Camera, F.; Crespi, F. C. L.; Doornenbal, P.*; Garnsworthy, A. B.; Geissel, H.*; Gerl, J.*; Gorska, M.*; Grebosz, J.*; Hagemann, G.; Jolie, J.; Kavatsyuk, M.*; Kavatsyuk, O.*; Koike, T.; Kojouharov, I.*; Kurz, N.*; Leske, J.; Lo Bianco, G.; Maj, A.; Mallion, S.; Mandal, S.*; Maliage, M.; Otsuka, T.; Petrache, C. M.; Podolyak, Z.; Prokopowicz, W.*; Rainovski, G.; Reiter, P.; Richard, A.; Schaffner, H.; Schielke, S.; Sletten, G.; Thompson, N. J.; Tonev, D.; Walker, J.*; Warr, N.; Wieland, O.; Zhong, Q.: **Yrast and non-yrast 2^+ states of ^{134}Ce and ^{136}Nd populated in relativistic Coulomb excitation.** *Physics letters B* **669**(1): 19–23. DOI:10.1016/j.physletb.2008.09.027

161 Sasaki, C.; Friman, B.*; Redlich, K.: **Chiral phase transition in the presence of spinodal decomposition.** *Physical Review D, particles, fields, gravitation, and cosmology* **77**(3): 034024. DOI:10.1103/physrevd.77.034024

162 Sasaki, C.; Friman, B.*; Redlich, K.: **Density fluctuations and a first-order chiral phase transition in non-equilibrium.** *Modern Physics Letters A* **23**(27): 2469–2472. DOI:10.1142/S0217732308029605

163 Sasaki, C.; Friman, B.*; Redlich, K.: **Density fluctuations as signature of a non-equilibrium first-order phase transition.** *Journal of physics G, Nuclear and particle physics* **35**(10): 104095. DOI:10.1088/0954-3899/35/10/104095

164 Schönmeier, P.; Branford, D.; Düren, M.; Ehrenfried, M.; Eyrich, W.; Fohl, K.; Hoek, M.; Kaiser, R.; Lehmann, A.; Lu, S. J.; Merle, O.; Seitz, B.; Schepers, G.*; Schmidt, R.; Schwarz, C.*: **Disc DIRC endcap detector for PANDA(at)FAIR.** *Nuclear instruments & methods in physics research, Section A, Accelerators, spectrometers, detectors and associated equipment* **595**(1): 108–111. DOI:10.1016/j.nima.2008.07.096

165 Schmidt, K. H.*; Kelic, A.*; Ricciardi, M. V.*: **Experimental evidence for the separability of compound-nucleus and fragment properties in fission.** *Europhysics letters* **83**(3): 32001. DOI:10.1209/0295-5075/83/32001

166 Schwarz, C.*; Bettoni, D.; Branford, D.; Carassiti, V.;

Cecchi, A.; Dodokhof, V. K.; Düren, M.; Fohl, K.; Hohler, R.; Kaiser, R.; Lehmann, A.; Lehmann, D.; Marton, H.; Peters, K.*; Schepers, G.*; Schmitt, L.*; Schonmeier, P.; Seitz, B.; Sfienti, C.*; Teufel, A.; Vodopianov, A. S.: **The barrel DIRC of the PANDA experiment.** *Nuclear instruments & methods in physics research, Section A, Accelerators, spectrometers, detectors and associated equipment* **595**(1): 112–115. DOI:10.1016/j.nima.2008.07.053

167 Senger, P.*: **Probing dense matter with strangeness production in nuclear collisions.** *Nuclear physics A, Nuclear and hadronic physics* **804**: 274–285. DOI:10.1016/j.nuclphysa.2008.01.014

168 Senger, P.*: **What do we learn about dense nuclear matter from heavy-ion collision experiments?.** *Acta physica Polonica B, Particle physics and field theory, nuclear physics, theory of relativity* **39**(2): 321–331. URL OPEN ACCESS.

169 Senger, P.*: **What do we learn about dense nuclear matter from heavy-ion collision experiments?.** *Journal of physics G, Nuclear and particle physics* **35**(1): 014050. DOI:10.1088/0954-3899/35/1/014050

170 Seravalli, E.; de Boer, M.; Geurink, F.; Huizenga, J.; Kreuger, R.; Schippers, J. M.; van Eijk, C. W. E.; Voss, B.*: **A scintillating gas detector for 2D dose measurements in clinical carbon beams.** *Physics in medicine and biology* **53**(17): 4651–4665. DOI:10.1088/0031-9155/53/17/013

171 Simon, H.*: **Correlation studies in break-up experiments.** *Few-Body Systems* **43**(1): 199–205. DOI:10.1007/s00601-008-0232-8

172 Soyeur, M.; Lutz, M. F. M.*: **Radiative and strong decays of D_s-mesons in the hadrogensis conjecture.** *Modern Physics Letters A* **23**(27): 2242–2245. DOI:10.1142/S0217732308029113

173 Spataro, S.; Agakishiev, G.; Agodi, C.; Balanda, A.; Bellia, G.; Belver, D.; Belyaev, A.; Blanco, A.; Bohmer, M.; Boyard, J. L.; Braun-Munzinger, P.*; Cabanelas, P.; Castro, E.; Chernenko, S.; Christ, T.; Destefanis, M.; Diaz, J.; Dohrmann, F.; Dybczak, A.; Eberl, T.; Fabbietti, L.; Fateev, O.; Finocchiaro, P.; Fonte, P.; Friese, J.; Fröhlich, I.; Galatyuk, T.*; Garzon, J. A.; Gernhauser, R.; Gil, A.; Gilardi, C.; Golubeva, M.; Gonzalez-Diaz, D.*; Grosse, E.; Guber, F.; Heilmann, M.; Hennino, T.; Holzmann, R.*; Ierusalimov, A.; Iori, I.; Ivashkin, A.*GAST; Jurkovic, M.; Kampfer, B.; Kanaki, K.; Karavicheva, T.*GAST; Kirschner, D.; Koenig, I.*; Koenig, W.*; Kolb, B. W.*; Kotte, R.; Kozuch, A.; Krasa, A.*; Krizek, F.; Krücken, R.; Kuhn, W.; Kugler, A.; Kurepin, A.; Lamas-Valverde, J.; Lang, S.*; Lange, J. S.; Lapidus, K.; Lopes, L.; Lorenz, M.; Maier, L.; Mangiarotti, A.; Marin, J.; Markert, J.; Metag, V.; Micel, J.; Michalska, B.; Mishra, D.; Moriniere, E.; Mousa, J.; Müntz, C.; Naumann, L.; Novotny, R.; Otwinowski, J.; Pachmayer, Y. C.; Palka, M.; Parpotas, Y.; Pechenov, V.; Pechenova, O.; Cavalcanti, T. P.; Pietraszko, J.*; Przygoda, W.; Ramstein, B.; Reshetin, A.; Roy-Stephan, M.; Rustamov, A.*; Sadovsky, A.; Sailer, B.; Salabura, P.; Schmah, A.*; Simon, R.*; Sobolev, Y. G.; Spruck, B.; Ströbele, H.; Stroth, J.*; Sturm, C.; Sudol, M.; Tarantola, A.; Teilab, K.; Tlusty, P.; Traxler, M.*; Trebacz, R.; Tsertos, H.; Veretenkin, I.; Wagner, V.; Wen, H.; Wisniowski, M.; Wojcik, T.; Wüstenfeld, J.; Yurevich, S.*; Zanevsky, Y.; Zhou, P.; Zumbruch, P.*; HADES Collaboration*: **Dielectron spectroscopy at 1-2 AGeV with HADES.** *The European physical journal A, Hadrons and nuclei* **38**(2): 163–166. DOI:10.1140/epja/i2008-10618-2

174 Stanoiu, M.*; Sümmerer, K.*; Mukha, I.; Chatillon, A.*; Gil, E. C.; Heil, M.*; Hoffman, J.*; Kiselev, O. A.*; Kurz, N.*; Ott, W.*; Collaboration S271: **A novel Si strip array to investigate reaction and decay mechanisms.** *Nuclear instruments & methods in physics research, Section B, Beam interactions with materials and atoms* **266**(19): 4625–4627. DOI:10.1016/j.nimb.2008.05.116

175 Steer, S. J.; Podolyak, Z.; Pietri, S.; Gorska, M.*; Regan, P. H.; Rudolph, D.; Werner-Malento, E.*; Garnsworthy, A. B.; Hoischen, R.; Gerl, J.*; Wollersheim, H. J.*; Maier, K. H.; Grawe, H.*; Becker, F.*; Bednarczyk, P.*; Caceres, L.*; Doornenbal, P.*; Geissel, H.*; Greabosz, J.*; Kelic, A.*; Kojouharov, I.*; Kurz, N.*; Montes, F.*; Prokopowicz, W.*; Saito, T.*; Schaffner, H.*; Tashenov, S.*; Heinz, A.; Pfützner, M.; Kurtukian-Nieto, T.; Benzoni, G.; Jungclaus, A.; Balabanski, D. L.; Brandau, C.*; Brown, B. A.; Bruce, A. M.; Catford, W. N.; Cullen, I. J.; Dombradi, Z.; Estevez, M. E.; Gelletly, W.; Ilie, G.; Jolie, J.; Jones, G. A.; Kmiecik, M.; Kondev, F. G.; Krücken, R.; Lalkovski, S.; Liu, Z.; Maj, A.; Myalski, S.; Schwertel, S.; Shizuma, T.; Walker, P. M.; Wieland, O.: **Single-particle behavior at N=126: Isomeric decays in neutron-rich ^{204}Pt.** *Physical review C, Nuclear physics* **78**(6): 061302. DOI:10.1103/physrevc.78.061302

176 Steinheimer, J.; Bleicher, M.; Petersen, H.; Schramm, S.; Stöcker, H.*; Zschiesche, D.: **(3+1)-dimensional hydrodynamic expansion with a critical point from realistic initial conditions.** *Physical review C, Nuclear physics* **77**(3): 034901. DOI:10.1103/physrevc.77.034901

177 Strasik, I.*; Mustafin, E.*; Fertman, A.*; Hinca, R.; Pavlovic, M.; Schardt, D.*; Sobolevskiy, N.*; Golubev, A.*; Sharkov, B.*; Fehrenbacher, G.*; Hofmann, I.*; Iwase, H.*; Kozlova, E.*; Mustafina, G.*: **Experimental study of the residual activity induced by 950 MeV/u uranium ions in stainless steel and copper.** *Nuclear instruments & methods in physics research, Section B, Beam interactions with materials and atoms* **266**(15): 3443–3452. DOI:10.1016/j.nimb.2008.05.013 Also part of: 'Health: Cancer research'.

178 Strohschein, D.; Röhrbein, D.; Kirchner, T.; Fritzsche, S.*; Baran, J.; Tanis, J. A.: **Nonstatistical enhancement**

of the 1s2s2p ^{4}P state in electron transfer in 0.5-1.0-MeV/u $^{4,5+}$CHe and Ne collisions. *Physical review A, Atomic, molecular, and optical physics* **77**(2): 022706. DOI:10.1103/physreva.77.022706

179 Sun, B.*; Knöbel, R.*; Litvinov, Y. A.*; Geissel, H.*; Meng, J.; Beckert, K.*; Bosch, F.*; Boutin, D.; Brandau, C.*; Chen, L.; Cullen, I. J.; Dimopoulou, C.*; Fabian, B.; Hausmann, M.; Kozhuharov, C.*; Litvinov, S. A.*; Mazzocco, M.; Montes, F.; Münzenberg, G.*; Musumarra, A.; Nakajima, S.; Nociforo, C.*; Nolden, F.*; Ohtsubo, T.; Ozawa, A.; Patyk, Z.; Plaß, W. R.; Scheidenberger, C.*; Steck, M.*; Suzuki, T.; Walker, P. M.; Weick, H.*; Winckler, N.*; Winkler, M.*; Yamaguchi, T.: **Nuclear structure studies of short-lived neutron-rich nuclei with the novel large-scale isochronous mass spectrometry at the FRS-ESR facility.** *Nuclear physics A, Nuclear and hadronic physics* **812**: 1–12. DOI:10.1016/j.nuclphysa.2008.08.013 Also part of: 'Large-scale facilities for research with photons, neutrons and ions'.

180 Sun, B.*; Montes, F.*; Geng, L. S.; Geissel, H.*; Litvinov, Y. A.*; Meng, J.: **Application of the relativistic mean-field mass model to the r-process and the influence of mass uncertainties.** *Physical review C, Nuclear physics* **78**(2): 025806. DOI:10.1103/physrevc.78.025806

181 Szymanska, K.; Achenbach, P.; Agnello, M.; Botta, E.; Bracco, A.; Bressani, T.; Camera, F.; Cederwall, B.; Feliciello, A.; Ferro, F.; Gerl, J.*; Iazzi, F.; Kavatsyuk, M.*; Kojouharov, I.*; Pochodzalla, J.; Raciti, G.; Saito, T. R.*; Lorente, A. S.; Tegner, P.-E.; Wieland, O.: **Resolution, efficiency and stability of HPGe detector operating in a magnetic field at various gamma-ray energies.** *Nuclear instruments & methods in physics research, Section A, Accelerators, spectrometers, detectors and associated equipment* **592**(3): 486–492. DOI:10.1016/j.nima.2008.04.017

182 Tashenov, S.*; Gerl, J.*: **Imaging algorithm for background suppression in the planned gamma tracking array of DESPEC.** *Nuclear instruments & methods in physics research, Section A, Accelerators, spectrometers, detectors and associated equipment* **586**(2): 224–228. DOI:10.1016/j.nima.2007.11.057

183 Tauschwitz, A.; Maruhn, J. A.; Efremov, V.; Geissel, H.*; Kelic, A.*; Sümmerer, K.*; Weick, H.*; Winkler, M.*: **Dynamics of tensile pressure in ion beam heated matter applied to a liquid lithium production target for the Super-FRS at FAIR.** *Nuclear instruments & methods in physics research, Section A, Accelerators, spectrometers, detectors and associated equipment* **591**(3): 447–452. DOI:10.1016/j.nima.2008.03.102

184 Thierfelder, C.; Schwerdtfeger, P.; Heßberger, F. P.*; Hofmann, S.*: **Dirac-Hartree-Fock studies of X-ray transitions in meitnerium.** *The European physical journal A, Hadrons and nuclei* **36**(2): 227–231. DOI:10.1140/epja/i2008-10584-7

185 Tolos, L.; Friman, B.*; Schwenk, A.: **Neutron matter at finite temperature.** *Nuclear physics A, Nuclear and hadronic physics* **806**: 105–116. DOI:10.1016/j.nuclphysa.2008.02.309

186 Toyoshima, A.; Haba, H.; Tsukada, K.; Asai, M.; Akiyama, K.; Goto, S.; Ishii, Y.; Nishinaka, I.; Sato, T. K.; Nagame, Y.; Sato, W.; Tani, Y.; Hasegawa, H.; Matsuo, K.; Saika, D.; Kitamoto, Y.; Shinohara, A.; Ito, M.; Saito, J.; Kudo, H.; Yokoyama, A.; Sakama, M.; Sueki, K.; Oura, Y.; Nakahara, H.; Schädel, M.*; Brüchle, W.*; Kratz, J. V.: **Hexafluoro complex of rutherfordium in mixed HF/HNO_3 solutions.** *Radiochimica acta* **96**(3): 125–134. DOI:10.1524/ract.2008.1474 OPEN ACCESS.

187 Trautmann, W.*; Adrich, P.*; Aumann, T.*; Bacri, C. O.; Barczyk, T.; Bassini, R.; Bianchin, S.*; Boiano, C.; Botvina, A. S.*; Boudard, A.; Brzychczyk, J.; Chbihi, A.; Cibor, J.; Czech, B.; De Napoli, M.; Ducret, J. E.; Emling, H.*; Frankland, J. D.; Hellström, M.*; Henzlova, D.*; Imme, G.; Iori, I.; Johansson, H.*; Kezzar, K.*; Lafriakh, A.; Le Fèvre, A.*; Le Gentil, E.; Leifels, Y.*; Lühning, J.*; Lukasik, J.*; Lynch, W. G.; Lynen, U.*; Majka, Z.; Mocko, M.*; Müller, W. F. J.*; Mykulyak, A.; Orth, H.*; Otte, A. N.*; Palit, R.*; Pawlowski, P.; Pullia, A.; Raciti, G.; Rapisarda, E.; Sann, H.*; Schwarz, C.*; Sfienti, C.*; Simon, H.*; Sümmerer, K.*; Tsang, M. B.; Verde, G.; Volant, C.; Wallace, M.; Weick, H.*; Wiechula, J.*; Wieloch, A.; Zwieglinski, B.: **N/Z dependence of projectile fragementation.** *International journal of modern physics E, Nuclear physics* **17**(9): 1838–1849. DOI:10.1142/S0218301308010829

188 Typel, S.*; Baur, G.: **Scaling laws and higher-order effects in Coulomb excitation of neutron halo nuclei.** *The European physical journal A, Hadrons and nuclei* **38**(3): 355–361. DOI:10.1140/epja/i2008-10684-4

189 Ukai, M.; Ajimura, S.; Akikawa, H.; Alburger, D. E.; Banu, A.*; Chrien, R. E.; Franklin, G. B.; Franz, J.; Hashimoto, O.; Hayakawa, T.; Hotchi, H.; Imai, K.; Kishimoto, T.; May, M.; Millener, D. J.; Minami, S.; Miura, Y.; Miyoshi, T.; Mizunuma, K.; Nagae, T.; Nakamura, S. N.; Nakazawa, K.; Okayasu, Y.; Pile, P.; Quinn, B. P.; Rusek, A.; Sato, Y.; Sutter, R.; Takahashi, H.; Tang, L.; Tamura, H.; Tanida, K.; Zhou, S. H.; E903 01 Collaboration: **γ-ray spectroscopy of $^{16}_{\Lambda}$O and $^{15}_{\Lambda}$N hypernuclei via the ^{16}O(K^-, $\pi^-\gamma$) reaction.** *Physical review C, Nuclear physics* **77**(5): 054315. DOI:10.1103/physrevc.77.054315

190 Voskresensky, D. N.*: **Thermodynamics of resonances and blurred particles.** *Nuclear physics A, Nuclear and hadronic physics* **812**: 158–185. DOI:10.1016/j.nuclphysa.2008.08.016

191 Wagner, M.*; Leupold, S.*: **τ decay and the structure of the a_1.** *Physics letters B* **670**(1): 22–26.

DOI:10.1016/j.physletb.2008.10.025

192 Wagner, M.; Leupold, S.*: **Information on the structure of the a(1) from tau decay.** *Physical Review D, particles, fields, gravitation, and cosmology* **78**(5): 053001. DOI:10.1103/physrevd.78.053001

193 Wallner, A.; Coquard, L.; Dillmann, I.; Forstner, O.; Golser, R.; Heil, M.*; Käppeler, F.; Kutschera, W.; Mengoni, A.; Michlmayr, L.; Priller, A.; Steier, P.; Wiescher, M.: **Measurement of the stellar cross sections for the reactions ^{9}Be-(n,γ)^{10}Be and ^{13}C(n,γ)^{14}C via AMS.** *Journal of physics G, Nuclear and particle physics* **35**(1): 014018. DOI:10.1088/0954-3899/35/1/014018

194 Weber, C.; Elomaa, V. V.; Ferrer, R.; Fröhlich, C.; Ackermann, D.*; Äystö, J.; Audi, G.; Batist, L.; Blaum, K.*; Block, M.*; Chaudhuri, A.*; Dworschak, M.; Eliseev, S.*; Eronen, T.; Hager, U.; Hakala, J.; Herfurth, F.*; Heßberger, F. P.*; Hofmann, S.*; Jokinen, A.; Kankainen, A.; Kluge, H.-J.*; Langanke, K.*; Martin, A.*; Martinez-Pinedo, G.*; Mazzocco, M.*; Moore, I. D.; Neumayr, J. B.; Novikov, Y. N.*; Penttilae, H.; Plaß, W. R.*; Popov, A. V.; Rahaman, S.; Rauscher, T.; Rauth, C.*; Rissanen, J.; Rodriguez, D.; Saastamoinen, A.; Scheidenberger, C.*; Schweikhard, L.; Seliverstov, D. M.; Sonoda, T.; Thielemann, F. K.; Thirolf, P. G.; Vorobjev, G. K.*: **Mass measurements in the vicinity of the r p-process and the ν p-process paths with the Penning trap facilities JYFLTRAP and SHIPTRAP.** *Physical review C, Nuclear physics* **78**(5): 054310. DOI:10.1103/physrevc.78.054310 Also part of: 'Large-scale facilities for research with photons, neutrons and ions'.

195 Xu, Z.; Greiner, C.*; Stöcker, H.*: **Perturbative QCD calculations of elliptic flow and shear viscosity in Au plus Au collisions at $\sqrt{s(NN)}$=200 GeV.** *Physical review letters* **101**(8): 082302. DOI:10.1103/physrevlett.101.082302

196 Xu, Z.; Greiner, C.; Stöcker, H.*: **QCD plasma thermalization, collective flow and extraction of shear viscosity.** *Journal of physics G, Nuclear and particle physics* **35**(10): 104016. DOI:10.1088/0954-3899/35/10/104016

197 Yamaguchi, T.; Suzuki, T.; Ohnishi, T.; Becker, F.*; Fukuda, M.; Geissel, H.*; Hosoi, M.; Janik, R.; Kimura, K.; Kuboki, T.; Mandel, S.*; Matsuo, M.; Münzenberg, G.*; Nakajima, S.; Ohtsubo, T.; Ozawa, A.; Prochazka, A.; Shindo, M.; Sitar, B.; Strmen, P.; Suda, T.; Sümmerer, K.*; Sugawara, K.; Szarka, I.; Takechi, M.; Takisawa, A.; Tanaka, K.; Yamagami, M.: **Nuclear matter radii of neutron-deficient Kr isotopes.** *Physical review C, Nuclear physics* **77**(3): 034315. DOI:10.1103/physrevc.77.034315

2. Further publications [1]

001 Afanasiev, S.: **Source breakup dynamics in Au+Au Collisions at s(NN)**(1/2) = 200-GeV via three-dimensional two-pion source imaging.** In: *Physical Review Letters* **100***(23)*, 232301 p. HANU

002 Alekseev, M. et al.: **The Polarised Valence Quark Distribution from semi-inclusive DIS.** In: *Phys. Lett. B* **660**, 458p. HANU

003 Altinpinar, S.: **Reise nach 13.700.000.000 v. Chr.** In: *Monatliche Zeitschrift Zukunft*, HANU

004 Antipin, Konstantin: **Systematic Study of the Optimization Potential for Di-Electron Measurements in the CBM Experiment.** In: *Proceedings of Quark Matter 2008, February 4-10, 2008, Jaipur, India*, HANU

005 Bertini, Denis; Al-Turany, Mohammad; Malzacher, Peter; Koenig, Ilse; Uhlig, Florian: **The FAIR simulation and analysis framework.** In: *J. Phys.: Conf. Ser.* **119**, 032011p. HANU

006 Brancus, I.M.: **WILLI: A scintillator detector setup for studies of the zenith and azimuth variation of charge ratio and flux of atmospheric muons.** In: *Nucl. Phys. Proc. Suppl. 175-176*, 370p. HANU

007 Braun-Munzinger, P.: **Das Publikationsverhalten in Gross-Kollaborationen.** In: *Diskussionspapiere der Alexander von Humboldt-Stiftung / Nr. 12*, 51p. HANU

008 Erni, W. et al.: **Panda Electromagnetic Calorimeter (EMC).** In: Novotny, R: *Technical Design Report*, 1p. HANU

009 Friese, Volker: **The CBM Experiment at FAIR.** In: *Proceedings - published in PoS(CPOD07)056*, HANU

010 Galatyuk, Tetyana: **Di-lepton spectroscopy in CBM.** In: *Proceedings of the XLVI International Winter Meeting on Nuclear Physics, Bormio (Italy), 2008*, HANU

011 Galatyuk, Tetyana; Das, Supriya: **Di-electron Spectroskopy in CBM.** In: *Proceedings of Quark Matter 2008, February 4-10, 2008, Jaipur, India*, HANU

012 Goeringer, H.*; Feyerabend, M.*; Sedykh, S.*: **Experince with gStore, a scalable Mass Storage Syste with Tape Backend.** In: *Journal of Physics/Conference Series* **199**, DOI:10.1088/1742-65961/119/052018 OPEN ACCESS HANU

013 Goetzen, K.: **Fast simulations for the PANDA experiment at FAIR.** In: *J. Phys. Conf. Ser.* **119**, 032020p. HANU

[1] Unproved announcements of the scientific and technical divisions.

014 Haungs, A.: **Investigations of muons in EAS with KASCADE-Grande.** In: *Nucl. Phys. Proc. Suppl. 175-176*, 354p. HANU

015 Hofmann, S.: **Study of superheavy elements at GSI - recent results and perspectives.** In: Hamilton, J. H.; Ramayya, A. V.; Carter, H. K: *Proc. Fourth. Int. Conf. on Fission and Properties of Neutron-Rich Nuclei (Sanibel Island, Florida, USA, 11-17 November 2007)*, 283p. HANU

016 Hofmann, S.: **Superheavy Elements.** In: Roeckl, E.; Al-Khalili. J: *Lecture Notes in Physics 764*, 203p. HANU

017 Hohler, R.;Lehmann, D.; Peters, K.; Schepers, G.; Schwarz, C.; Sfienti, C.; Koenig, W.; Palka, M.; Traxler, M.: **Protype of a DIRC-barrel for the PANDA Experiment.** In: *IEEE Nuclear Science Symposium Conference Record*, HANU

018 Kiseleva, Anna; Bhaduri, Partha; Chattopadhyay, S.; Dubey, A.K.; Ganti, M.S.; Ghosh, P.; Senger, P.; Vassiliev, I.; Khanzadeev, A.; Kryshen, E.; Nikolin, V.; Samsonov, V.; Rzyhinskiy, M.;: **Di-muon measurements with the CBM experiment at FAIR.** In: *Proceedings of Quark Matter 2008, February 4-10, 2008, Jaipur, India*, HANU

019 Kühn, W. et al.: **Fpga Based Compute Nodes For High Level Triggering In Panda.** In: *J. Phys. Conf. Ser.* **119** , 022027p. HANU

020 Kuhn, W.: **FPGA based compute nodes for high level triggering in PANDA.** In: *J. Phys. Conf. Ser. 119*, 022027p. HANU

021 Malzacher, P.: **RGLite, an interface between ROOT and gLite: PROOF on the grid.** In: *J.Phys.Conf.Ser. 119*, 072022p. HANU

022 Morse, J.; Salome, M.; Berdermann, E.; Pomorski, M.; Grant, J.; O'Shea, V.; Ilinski, P.: **Single Crystal CVD Diamand Detectors: Position and Temporal Response Measurements using a Synchrotron Microprobe Beam.** In: *Proceedings Materials Research Society Symposium 1039*, HANU

023 Schmitt, L.; Kühn, W.; Korcyl, K.; Salabura, P.; Otwinowski, J.: **Modelling of the architectural studies for the PANDA DAT system.** In: *IEEE Trans. Nucl. Sci.* **55**, 429p. HANU

024 Senger, Peter: **Exploring dense nuclear matter.** In: *Proceedings of the '24th Winter Workshop in Nuclear Dynamics', South Padre Island, USA, April 5-12, 2008*, HANU

025 Tahir, N. A.; Schmidt, R.; Brugger, M.; Assmann, R.; Shutov, A. V.; Lomonosov, I. V.; Piriz, A. R..; Hoffmann, D. H. H..; Deutsch, C.; Fortov, V. E.: **The CERN Super Proton Synchrotron as a Tool to Study High Energy Density Physics.** In: *Bull. Am. Phys. Soc 53* , 149p. HANU:Accelerator

026 Ulrich, H.: **Status of the KASCADE-Grande experiment.** In: *Nucl. Phys. Proc. Suppl. 175-176*, 273p. HANU

GSI publications to the programme 'Large-scale facilities for research with photons, neutrons and ions' published in 2008

1. Reviewed publications

001 Aksyutina, Y.*; Johansson, H. T.; Adrich, P.*; Aksouh, F.*; Aumann, T.*; Boretzky, K.*; Borge, M. J. G.; Chatillon, A.; Chulkov, L. V.*; Cortina-Gil, D.*; Datta Pramanik, U.*; Emling, H.*; Forssen, C.; Fynbo, H. O. U.; Geissel, H.*; Hellström, M.; Ickert, G.*; Jones, K. L.*; Jonson, B.; Kliemkiewicz, A.*; Kratz, J. V.; Kulessa, R.; Lantz, M.; LeBleis, T.*; Lindahl, A. O.; Mahata, K.*; Matos, M.*; Meister, M.*; Münzenberg, G.*; Nilsson, T.; Nyman, G.; Palit, R.; Pantea, M.*; Paschalis, S.; Prokopowicz, W.*; Reifarth, R.*; Richter, A.; Riisager, K.; Schrieder, G.; Simon, H.*; Sümmerer, K.*; Tengblad, O.; Walus, W.; Weick, H.*; Zhukov, M. V.: **Lithium isotopes beyond the drip line.** *Physics letters B* **666**(5): 430–434. DOI:10.1016/j.physletb.2008.07.093 HANU.PNI.

002 Ali, M.; Bayer, V.*; Schiedt, B.; Neumann, R.*; Ensinger, W.: **Fabrication and functionalization of single asymmetric nanochannels for electrostatic/hydrophobic association of protein molecules.** *Nanotechnology* **19**(48): 485711. DOI:10.1088/0957-4484/19/48/485711 PNI.

003 Ali, M.; Schiedt, B.*; Healy, K.; Neumann, R.*; Ensinger, A.: **Modifying the surface charge of single track-etched conical nanopores in polyimide.** *Nanotechnology* **19**(8): 085713. DOI:10.1088/0957-4484/19/8/085713 PNI.

004 Ali, M.; Yameen, B.; Neumann, R.*; Ensinger, W.; Knoll, W.; Azzaroni, O.: **Biosensing and Supramolecular Bioconjugation in Single Conical Polymer Nanochannels. Facile Incorporation of Biorecognition Elements into Nanoconfined Geometries.** *Journal of the American Chemical Society* **130**(48): 16351–16357. DOI:10.1021/ja8071258 PNI.

005 Allen, F. I.; Biedermann, C.; Radtke, R.; Fussmann, G.; Fritzsche, S.*: **Energy dependence of angular momentum capture states in charge exchange collisions between slow highly charged argon ions and argon neutrals.** *Physical review A, Atomic, molecular, and optical physics* **78**(3): 032705. DOI:10.1103/physreva.78.032705 PNI.

006 Andersen, H. H.; Breese, M.; Rehn, L.; Trautmann, C.*; Vickridge, I.: **NIMB Editorial for 2008.** *Nuclear instruments & methods in physics research, Section B, Beam interactions with materials and atoms* **266**(1): 1–1. DOI:10.1016/j.nimb.2007.11.032 PNI.

007 Andrianov, V.*; Beckert, K.*; Beller, P.*; Bleile, A.*; Egelhof, P.*; Gumberidze, A.*; Ilieva, S.; Kiselev, O.*; Kilbourne, C.; Kluge, H.-J.*; Kraft-Bermuth, S.*; McCammon, D.; Meier, J. P.*; Reuschl, R.; Stöhlker, T.*; Trassinelli, M.*: **First experiments aiming for precise Lamb shift measurements on hydrogen-like heavy ions with low temperature calorimeters.** *Journal of Low Temperature Phyiscs* **151**(3): 1049–1054. DOI:10.1007/s10909-008-9792-8 HANU.PNI.

008 Anton, J.; Fricke, B.; Mukherjee, P. K.; Fritzsche, S.*: **Ab-initio relativistic density functional calculations for spectral line shifts of Rb atoms in liquid helium.** *Physics Letters A* **372**(24): 4462–4464. DOI:10.1016/j.physleta.2008.04.022 PNI.

009 Bachelet, C.; Audi, G.; Gaulard, C.; Guenaut, C.; Herfurth, F.*; Lunney, D.; Simon, M. D.; Thibault, C.: **New binding energy for the two-neutron halo of ^{11}Li.** *Physical review letters* **100**(18): 182501. DOI:10.1103/physrevlett.100.182501 PNI.

010 Barton, C.; Cederkall, J.; Delahaye, P.; Kester, O.*; Lamy, T.; Marie-Jeanne, M.: **Status of the PHOENIX electron cyclotron resonance charge breeder at ISOLDE, CERN.** *Review of scientific instruments* **79**(2): 02A905. DOI:10.1063/1.2819746 PNI.

011 Basu, E.; Dey, S.; Fischer, B.*; Maulik, A.; Mazumdar, A.; Raha, S.; Saha, S.; Saha, S. K.; Syam, D.: **Charge response of polyethylene terephthalate polymers (PET) to light and heavy nuclei.** *Radiation Measurements* **43**: S95–S97. DOI:10.1016/j.radmeas.2008.04.089 PNI.

012 Becker, R.; Currell, F. J.; Donets, E. D.; Donets, E. E.; Kester, O.*; Quint, W.*; Ptitsin, V. E.: **Investigation of an electron string ion source with field emission cathode.** *Review of scientific instruments* **79**(2): 02A701. DOI:10.1063/1.2812796 PNI.

013 Becker, R.; Kester, O.*: **In-line ion detector.** *Review of scientific instruments* **79**(2): 02B721. DOI:10.1063/1.2822112 PNI.

014 Block, M.; Bachelet, C.; Bollen, G.; Facina, M.; Folden, C. M.; Guenaut, C.; Kwiatkowski, A. A.; Morrissey, D. J.; Pang, G. K.; Prinke, A.; Ringle, R.; Savory, J.; Schury, P.; Schwarz, S.: **Mass measurements of rare isotopes with the LEBIT facility at the NSCL.** *Nuclear instruments & methods in physics research, Section B, Beam interactions with materials and atoms* **266**(19): 4521–4526. DOI:10.1016/j.nimb.2008.05.098 HANU.PNI.

015 Brandau, C.*; Kozhuharov, C.*; Harman, Z.; Müller, A.; Schippers, S.; Kozhedub, Y. S.; Bernhardt, D.; Boehm, S.; Jacobi, J.; Schmidt, E. W.; Mokler, P. H.*; Bosch, F.*; Kluge, H.-J.*; Stöhlker, T.*; Beckert, K.*; Beller, P.*; Nolden, F.*; Steck, M.*; Gumberidze, A.*; Reuschl, R.*; Spillmann, U.*G; Currell, F. J.; Tupitsyn, I. I.; Shabaev, V. M.; Jentschura, U. D.; Keitel, C. H.; Wolf, A.; Stachura, Z.: **Isotope shift in the dielectronic recombination of three-electron ^{A}Nd^{57+}.** *Physical review letters* **100**(7): 073201. DOI:10.1103/physrevlett.100.073201 PNI.HANU:Accelerator.

016 Breitenfeldt, M.; Baruah, S.; Blaum, K.*; Herlert, A.; Kretzschmar, M.; Martinez, F.; Marx, G.; Schweikhard, L.; Walsh, N.: **The elliptical Penning trap: Experimental investigations and simulations.** *International Journal of Mass Spectrometry and Ion Physics* **275**(1): 34–44. DOI:10.1016/j.ijms.2008.05.008 PNI.

017 Caricato, A. P.; Lamperti, A.; Ossi, P. M.; Trautmann, C.*; Vanzetti, L.: **Modifications of yttria fully stabilized zirconia thin films by ion irradiation in the inelastic collision regime.** *Journal of Applied Physics* **104**(9): 093534. DOI:10.1063/1.3010302 PNI.

018 Chiper, A. S.; Cazan, R.; Popa, G. KV: **On the Secondary Discharge of an Atmospheric-Pressure Pulsed DBD in He with Impurities.** *IEEE transactions on plasma science* **36**(5): 2824–2830. DOI:10.1109/tps.2008.2001425 PNI.

019 Cornelius, T. W.*; Picht, O.*; Müller, S.*; Neumann, R.*; Völklein, F.; Karim, S.*; Duan, J. L.: **Burnout current density of bismuth nanowires.** *Journal of Applied Physics* **103**(10): 103713. DOI:10.1063/1.2927443 PNI.

020 Cornelius, T. W.*; Toimil-Molares, M. E.*; Karim, S.; Neumann, R.*: **Oscillations of electrical conductivity in single bismuth nanowires.** *Physical review: B, Condensed matter and materials physics* **77**(12): 125425. DOI:10.1103/physrevb.77.125425 PNI.

021 Costantini, J. M.; Guillet, F.; Lambert, S.; Grebille, D.; Beuneu, F.; Trautmann, C.*: **X-ray diffraction study of the damage induced in yttria-stabilized zirconia by swift heavy ion irradiations.** *Journal of Applied Physics* **104**(7): 073504. DOI:10.1063/1.2986280 PNI.

022 Dallanora, A.; Marcondes, T. L.; Bermudez, G. G.; Fichtner, P. F. P.; Trautmann, C.*; Toulemonde, M.; Papaleo, R. M.: **Nanoporous SiO2/Si thin layers produced by ion track etching: Dependence on the ion energy and criterion for etchability.** *Journal of Applied Physics* **104**(2): 024307. DOI:10.1063/1.2957052 PNI.

023 Dangwal, A.; Pandey, C. S.; Muller, G.; Karim, S.; Cornelius, T. W.*; Trautmann, C.*: **Field emission properties of electrochemically deposited gold nanowires.** *Applied physics letters* **92**(6): 063115. DOI:10.1063/1.2844853 PNI.

024 Du, G.*; Fischer, B. E.*; Voss, K. O.*; Becker, G.*; Taucher-Scholz, G.*; Kraft, G.*; Thiel, G.: **The absence of an early calcium response to heavy-ion radiation in mammalian cells.** *Radiation research* **170**(3): 316–326. DOI:10.1667/RR1270.1 Cancer.PNI.

025 Dworschak, M.*; Audi, G.; Blaum, K.*; Delahaye, P.; George, S.; Hager, U.; Herfurth, F.*; Herlert, A.; Kellerbauer, A.; Kluge, H.-J.*; Lunney, D.; Schweikhard, L.; Yazidjian, C.*: **Restoration of the N=82 shell gap from direct mass measurements of ^{132,134}Sn.** *Physical review letters* **100**(7): 072501. DOI:10.1103/physrevlett.100.072501 PNI.

026 Ekström, A.; Cederkäl, J.; Fahlander, C.; Hjorth-Jensen, M.; Ames, F.; Butler, P. A.; Davinson, T.; Eberth, J.; Fincke, F.; Gögen, A.; Gorska, M.*; Habs, D.; Hurst, A. M.; Huyse, M.; Ivanov, O.; Iwanicki, J.; Kester, O.*; Koster, U.; Marsh, B. A.; Mierzejewski, J.; Reiter, P.; Scheit, H.; Schwalm, D.; Siem, S.; Sletten, G.; Stefanescu, I.; Tveten, G. M.; de Walle, J. V.; Van Duppen, P.; Voulot, D.; Warr, N.; Weisshaar, D.; Wenander, F.; Zielinska, M.: **$0^{+}_{gs} \rightarrow 2^{+}_{1}$ transition strengths in ^{106}Sn and ^{108}Sn.** *Physical review letters* **101**(1): 012502. DOI:10.1103/physrevlett.101.012502 PNI.

027 Eliseev, S.*; Block, M.*; Dworschak, M.*; Herfurth, F.*; Kluge, H.-J.*; Martin, A.*; Rauth, C.*; Vorobjev, G.*: **A new cryogenic gas-filled stopping chamber for SHIPTRAP.** *Nuclear instruments & methods in physics research, Section B, Beam interactions with materials and atoms* **266**(19): 4475–4477. DOI:10.1016/j.nimb.2008.05.055 HANU.PNI.

028 Enculescu, I.; Sima, M.; Enculescu, M.; Matei, E.; Toimil Molares, M. E.*; Cornelius, T.*: **Nickel nanotubes prepared by electroless deposition in ion track templates.** *Optoelectronics and Advanced Materials - Rapid Communications* **2**(3): 133–136.PNI.

029 Fritzsche, S.*; Grum-Grzhimailo, A. N.; Gryzlova, E. V.; Kabachnik, N. M.*: **Angular distributions and angular correlations in sequential two-photon double ionization of atoms.** *Journal of physics B, Atomic, molecular and optical physics* **41**(16): 165601. DOI:10.1088/0953-4075/41/16/165601 PNI.

030 Fritzsche, S.*; Jänkälä, K.; Huttula, M.; Urpelainen,

S.; Aksela, H.: **Photoelectron satellite structure from the 3d and 4d inner-shell ionization of rubidium and cesium: Role of atomic relaxation.** *Physical review A, Atomic, molecular, and optical physics* **78**(3): 032514. DOI:10.1103/physreva.78.032514 PNI.

031 Fritzsche, S.*; Kabachnik, N. M.; Surzhykov, A.: **Angular distribution of the dielectronic satellite lines from relativistic high-Z ions: Multipole-mixing effects.** *Physical review A, Atomic, molecular, and optical physics* **78**(3): 032703. DOI:10.1103/physreva.78.032703 PNI.

032 Geithner, W.; Neff, T.*; Audi, G.; Blaum, K.*; Delahaye, P.; Feldmeier, H.*; George, S.; Guenaut, C.; Herfurth, F.*; Herlert, A.; Kappertz, S.; Keim, M.; Kellerbauer, A.; Kluge, H.-J.*; Kowalska, M.; Lievens, P.; Lunney, D.; Marinova, K.; Neugart, R.; Schweikhard, L.; Wilbert, S.; Yazidjian, C.*: **Masses and Charge Radii of $^{17-22}$Ne and the Two-Proton-Halo Candidate ^{17}Ne.** *Physical review letters* **101**(25): 252502. DOI:10.1103/physrevlett.101.252502 PNI.

033 George, S.*; Audi, G.; Blank, B.; Blaum, K.*; Breitenfeldt, M.; Hager, U.; Herfurth, F.*; Herlert, A.; Kellerbauer, A.; Kluge, H. J.*; Kretzschmar, M.; Lunney, D.; Savreux, R.*; Schwarz, S.; Schweikhard, L.; Yazidjian, C.*: **Time-separated oscillatory fields for high-precision mass measurements on short-lived Al and Ca nuclides.** *Europhysics letters* **82**(5): 50005. DOI:10.1209/0295-5075/82/50005 PNI.

034 Geppert, C.: **Laser systems for on-line laser ion sources.** *Nuclear instruments & methods in physics research, Section B, Beam interactions with materials and atoms* **266**(19): 4354–4361. DOI:10.1016/j.nimb.2008.05.036 PNI.

035 Ghenescu, M.; Ion, L.; Enculescu, L.; Tazlaoanu, C.; Antohe, V. A.; Sima, M.; Enculescu, M.; Matei, E.; Neumann, R.*; Ghenescu, O.; Covlea, V.; Antohe, S.: **Electrical properties of electrodeposited CdS nanowires.** *Physica E - Low-dimensional Systems and Nanostructures* **40**(7): 2485–2488. DOI:10.1016/j.physe.2007.09.188 PNI.

036 Gonta, D.; Fritzsche, S.*; Radtke, T.: **Generation of four-partite Greenberger-Horne-Zeilinger and W states by using a high-finesse bimodal cavity.** *Physical review A, Atomic, molecular, and optical physics* **77**(6): 062312. DOI:10.1103/physreva.77.062312 PNI.

037 Harres, K.; Schollmeier, M.; Brambrink, E.; Audebert, P.; Blazevic, A.*; Flippo, K.; Gautier, D. C.; Geissel, M.; Hegelich, B. M.; Nürnberg, F.; Schreiber, J.; Wahl, H.; Roth, M.: **Development and calibration of a Thomson parabola with microchannel plate for the detection of laser-accelerated MeV ions.** *Review of scientific instruments* **79**(9): 093306. DOI:10.1063/1.2987687 PNI.

038 Heinz, S.*; Comas, V.; Heßberger, F. P.*; Hofmann, S.*; Ackermann, D.*; Burkhard, H.*; Gan, Z.; Heredia, J.; Khuyagbaatar, J.; Kindler, B.*; Lommel, B.*; Mann, R.*; Maurer, J.*; Nishio, K.; Sulignano, B.: **Di-nuclear systems studied with the velocity filter SHIP.** *The European physical journal A, Hadrons and nuclei* **38**(2): 227–232. DOI:10.1140/epja/i2008-10671-9 HANU.PNI.

039 Ishikawa, N.; Chimi, Y.; Michikami, O.; Ohta, Y.; Ohhara, K.; Lang, M.*; Neumann, R.*: **Study of structural change in CeO2 irradiated with high-energy ions by means of X-ray diffraction measurement.** *Nuclear instruments & methods in physics research, Section B, Beam interactions with materials and atoms* **266**(12): 3033–3036. DOI:10.1016/j.nimb.2008.03.159 PNI.

040 Jänkälä, K.; Urpelainen, S.; Huttula, M.; Fritzsche, S.*; Heinäsmäki, S.; Aksela, S.; Aksela, H.: **Inner-shell 2p photoionization and Auger decay of atomic silicon.** *Physical review A, Atomic, molecular, and optical physics* **77**(6): 062504. DOI:10.1103/physreva.77.062504 PNI.

041 Kaluza, M. C.; Santala, M. I. K.; Schreiber, J.; Tsakiris, G. D.; Witte, K.* J.: **Time-sequence imaging of relativistic laser-plasma interactions using a novel two-color probe pulse.** *Applied physics B, Lasers and optics* **92**(4): 475–479. DOI:10.1007/s00340-008-3150-z PNI.

042 Kankainen, A.; Elomaa, V. V.; Batist, L.; Eliseev, S.*; Eronen, T.; Hager, U.; Hakala, J.; Jokinen, A.; Moore, I. D.; Novikov, Y. N.*; Penttilä, H.; Popov, A.; Rahaman, S.*; Rinta-Antila, S.; Rissanen, J.; Saastamoinen, A.; Seliverstov, D. M.; Sonoda, T.; Vorobjev, G.*; Weber, C.; Äystö, J.: **Mass measurements and implications for the energy of the high-spin isomer in ^{94}Ag.** *Physical review letters* **101**(14): 142503. DOI:10.1103/physrevlett.101.142503 PNI.

043 Karim, S.*; Ensinger, W.; Cornelius, T. W.*; Khan, E. U.; Neumann, R.*: **Tuning the Characteristics of Electrochemically Fabricated Gold Nanowires.** *Journal of Nanoscience and Nanotechnology* **8**(11): 5659–5666. DOI:10.1166/jnn.2008.258 PNI.

044 Karim, S.; Ensinger, W.; Cornelius, T. W.*; Neumann, R.*: **Investigation of size effects in the electrical resistivity of single electrochemically fabricated gold nanowires.** *Physica E - Low-dimensional Systems and Nanostructures* **40**(10): 3173–3178. DOI:10.1016/j.physe.2008.05.011 PNI.

045 Kaye, R. A.; Myers, C. S.; Doring, J.*; Tabor, S. L.; Gerbick, S. M.; Baldwin, T. D.; Campbell, D. B.; Chandler, C.; Cooper, M. W.; Hallstrom, M. A.; Hoffman, C. R.; Pavan, J.; Riley, L. A.; Wiedeking, M.: **Linear polarization measurements and negative-parity states in ^{80}Sr.** *Physical review C, Nuclear physics* **78**(3): 037303. DOI:10.1103/physrevc.78.037303 PNI.

046 Kazamias, S.; Cassou, K.; Ros, D.; Ple, F.; Jamelot, G.; Klisnick, A.; Lundh, O.; Lindau, F.; Persson, A.; Wahlstrom, C. G.; de Rossi, S.; Joyeux, D.; Zielbauer, B.*; Ursescu, D.*; Kühl, T.*: **Characterization of a transient collisional Ni-like molybdenum soft-x-ray laser pumped in grazing incidence.** *Physical review A, Atomic, molecular, and optical physics* **77**(3): 033812. DOI:10.1103/physreva.77.033812 PNI.

047 Ketelaer, J.; Krämer, J.; Beck, D.; Blaum, K.*; Block, M.*; Eberhardt, K.; Eitel, G.; Ferrer, R.; Geppert, C.*; George, S.*; Herfurth, F.*; Ketter, J.; Nagy, S.; Neidherr, D.; Neugart, R.; Nörtershäuser, W.; Repp, J.; Smorra, C.; Trautmann, N.; Weber, C.: **TRIGA-SPEC: A setup for mass spectrometry and laser spectroscopy at the research reactor TRIGA Mainz.** *Nuclear instruments & methods in physics research, Section A, Accelerators, spectrometers, detectors and associated equipment* **594**(2): 162–177. DOI:10.1016/j.nima.2008.06.023 PNI.

048 Khuyagbaatar, J.*; Hofmann, S.*; Heßberger, F. P.*; Ackermann, D.*; Burkhard, H. G.*; Heinz, S.*; Kindler, B.*; Kojouharov, I.*; Lommel, B.*; Mann, R.*; Maurer, J.*; Nishio, K.; Novikov, Y.: **Spontaneous fission of neutron-deficient fermium isotopes and the new nucleus Fm-241.** *The European physical journal A, Hadrons and nuclei* **37**(2): 177–183. DOI:10.1140/epja/i2008-10608-4 HANU.PNI.

049 Kluge, H. J.*; Beier, T.*; Blaum, K.*; Dahl, L.*; Eliseev, S.*; Herfurth, F.*; Hofmann, B.*; Kester, O.*; Koszudowski, S.*; Kozhuharov, C.*; Maero, G.*; Nörtershäuser, W.*; Pfister, J.*; Quint, W.*; Ratzinger, U.; Schempp, A.; Schuch, R.; Stöhlker, T.*; Thompson, R. C.; Vogel, M.*; Vorobjev, G.*; Winters, D. F. A.*; Werth, G.: **HITRAP: A facility at GSI for highly charged ions.** *Advances in Quantum Chemistry* **53**: 83–98. DOI:10.1016/s0065-3276(07)53007-8 PNI.

050 Kluge, H.-J.*; Herfurth, F.*; Kester, O.*; Nörtershäuser, W.*; Quint, W.*: **How to measure nuclear ground-state properties in simple systems such as ^{11}Li or U^{91+}?.** *Nuclear instruments & methods in physics research, Section B, Beam interactions with materials and atoms* **266**(19): 4542–4546. DOI:10.1016/j.nimb.2008.05.099 PNI.

051 Kluth, P.; Schnohr, C. S.; Pakarinen, O. H.; Djurabekova, F.; Sprouster, D. J.; Giulian, R.; Ridgway, M. C.; Byrne, A. P.; Trautmann, C.*; Cookson, D. J.; Nordlund, K.; Toulemonde, M.: **Fine Structure in Swift Heavy Ion Tracks in Amorphous SiO_2.** *Physical review letters* **101**(17): 175503. DOI:10.1103/physrevlett.101.175503 PNI.

052 Koukharenko, E.; Li, X.; Nandhakumar, I.; Frety, N.; Beeby, S. P.; Cox, D.; Tudor, M. J.; Schiedt, B.*; Trautmann, C.*; Bertsch, A.; White, N. M.: **Towards a nanostructured thermoelectric generator using ion-track lithography.** *Journal of micromechanics and microengineering* **18**(10): 104015. DOI:10.1088/0960-1317/18/10/104015 PNI.

053 Koukharenko, E.; Li, X.; Nandhakumar, I.; Schiedt, B.*; Trautmann, C.*; Speed, J.; Tudor, M. J.; Beeby, S. P.; White, N. M.: **Development of nanostructures for thermoelectric microgenerators using ion-track lithography.** *Electronic Letters* **44**(7): 500–U12. DOI:10.1049/el:20080111 PNI.

054 Kowalska, M.; Yordanov, D. T.; Blaum, K.*; Himpe, P.; Lievens, P.; Mallion, S.; Neugart, R.; Neyens, G.; Vermeulen, N.: **Nuclear ground-state spins and magnetic moments of ^{27}Mg, ^{29}Mg, and ^{31}Mg.** *Physical review C, Nuclear physics* **77**(3): 034307. DOI:10.1103/physrevc.77.034307 PNI.

055 Kozhedub, Y. S.; Andreev, O. V.; Shabaev, V. M.; Tupitsyn, I. I.; Brandau, C.*; Kozhuharov, C.*; Plunien, G.; Stöhlker, T.*: **Nuclear deformation effect on the binding energies in heavy ions.** *Physical review A, Atomic, molecular, and optical physics* **77**(3): 032501. DOI:10.1103/physreva.77.032501 PNI.

056 Krauser, J.; Nix, A.-K.; Gehrke, H. G.; Hofsäss, H.; Trautmann, C.*; Weidinger, A.; Wunsch, F.; Bruns, J.: **Ion track lithography and graphitic nanowires in diamond-like carbon.** *Journal of Vacuum Science and Technology B* **26**(6): 2468–2472. DOI:10.1116/1.3010738 PNI.

057 Kreidi, H. K.; Akoury, D.; Jahnke, T.; Weber, T.; Staudte, A.; Schöffler, M.; Neumann, N.; Titze, J.; Schmidt, L. P. H.; Czasch, A.; Jagutzki, O.; Fraga, R. A. C.; Grisenti, R. E.*; Smolarski, M.; Ranitovic, P.; Cocke, C. L.; Osipov, T.; Adaniya, H.; Thompson, J. C.; Prior, M. H.; Belkacem, A.; Landers, A. L.; Schmidt-Böcking, H.*; Dörner, R.: **Interference in the collective electron momentum in double photoionization of H_2.** *Physical review letters* **100**(13): 133005. DOI:10.1103/physrevlett.100.133005 PNI.

058 Kurcewicz, J.*; Litvinov, Y. A.*; Bosch, F.*; Geissel, H.*; Patyk, Z.; Winckler, N.*; Batist, L.; Beckert, K.*; Beller, P.*; Boutin, D.; Brandau, C.*; Chen, L.; Dimopoulou, C.*; Faestermann, T.; Grigorenko, L.; Kienle, P.; Knöbel, R.*; Kozhuharov, C.*; Litvinov, S. A.*; Maier, L.; Mazzocco, M.*; Montes, F.*; Münzenberg, G.*; Musumarra, A.; Nociforo, C.*; Nolden, F.*; Pfützner, M.; Plass, W.; Scheidenberger, C.*; Steck, M.*; Sun, B.*; Weick, H.*; Winkler, M.*: **Orbital electron capture and β^+ decay of H-like ^{140}Pr ions.** *Acta physica Polonica B, Particle physics and field theory, nuclear physics, theory of relativity* **39**(2): 501–506. URL OPEN ACCESS. HANU.PNI.

059 Lang, M.; Lian, J.; Zhang, F. X.; Hendriks, B. W. H.; Trautmann, C.*; Neumann, R.*; Ewing, R. C.: **Fission tracks simulated by swift heavy ions at crustal pressures**

and temperatures. *Earth and Planetary Science Letters* **274**(3): 355–358. DOI:10.1016/j.epsl.2008.07.039 PNI.

060 Lang, M.; Zhang, F. X.; Lian, J.; Trautmann, C.*; Neumann, R.*; Ewing, R. C.: **Irradiation-induced stabilization of zircon ($ZrSiO_4$) at high pressure.** *Earth and Planetary Science Letters* **269**(1): 291–295. DOI:10.1016/j.epsl.2008.02.027 PNI.

061 Lestinsky, M.; Lindroth, E.; Orlov, D. A.; Schmidt, E. W.; Schippers, S.; Böhm, S.; Brandau, C.*; Sprenger, F.; Terekhov, A. S.; Müller, A.; Wolf, A.*: **Screened radiative corrections from hyperfine-split dielectronic resonances in lithiumlike scandium.** *Physical review letters* **100**(3): 033001. DOI:10.1103/physrevlett.100.033001 PNI.

062 Liu, J.; Glasmacher, U. A.; Lang, M.*; Trautmann, C.*; Voss, K. O.*; Neumann, R.*; Wagner, G. A.; Miletich, R.: **Raman spectroscopy of apatite irradiated with swift heavy ions with and without simultaneous exertion of high pressure.** *Applied Physics A, Materials Science and Processing* **91**(1): 17–22. DOI:10.1007/s00339-008-4402-9 PNI.

063 Lomonosov, I. V.; Tahir, N. A.*: **Theoretical investigation of shock wave stability in metals.** *Applied physics letters* **92**(10): 101905. DOI:10.1063/1.2894197 PNI.

064 Lozeva, R. L.; Simpson, G. S.; Grawe, H.*; Neyens, G.; Atanasova, L. A.; Balabanski, D. L.; Bazzacco, D.; Becker, F.*; Bednarczyk, P.*; Benzoni, G.; Blasi, N.; Blazhev, A.; Bracco, A.; Brandau, C.; Caceres, L.; Camera, F.; Chamoli, S. K.; Crespi, F. C. L.; Daugas, J. M.; Detistov, P.; De Rydt, M.; Doornenbal, P.*; Fahlander, C.; Farnea, E.; Georgiev, G.; Gerl, J.*; Gladnishki, K. A.*; Gorska, M.*; Grebosz, J.*; Hass, M.; Hoischen, R.; Ilie, G.; Ionescu-Bujor, M.; Iordachescu, A.; Jolie, J.; Jungclaus, A.; Kmiecik, M.; Kojouharov, I.*; Kurz, N.*; Lakshmi, S. P.; Lo Bianco, G.; Mallion, S.; Maj, A.; Montanari, D.; Perru, O.; Pfützner, M.; Pietri, S.; Pinston, J. A.; Podolyak, Z.; Prokopowicz, W.*; Rudolph, D.; Rusev, G.; Saitoh, T. R.*; Saltarelli, A.; Schaffner, H.*; Schwengner, R.; Tashenov, S.*; Turzo, K.; Valiente-Dobon, J. J.; Vermeulen, N.; Walker, J.*; Werner-Malento, E.; Wieland, O.; Wollersheim, H.-J.*: **New sub-μs isomers in $125,127,129$Sn and isomer systematics of $^{124-130}$Sn.** *Physical review C, Nuclear physics* **77**(6): 064313. DOI:10.1103/physrevc.77.064313 HANU.PNI.

065 Lushchik, A.; Kudryavtseva, I.; Liblik, P.; Lushchik, C.; Nepomnyashchikh, A. I.; Schwartz, K.*; Vasil'chenko, E.: **Electronic and ionic processes in LiF : Mg,Ti and LiF single crystals.** *Radiation Measurements* **43**(2): 157–161. DOI:10.1016/j.radmeas.2007.10.001 PNI.

066 Lushchik, A.; Lushchik, C.; Schwartz, K.*; Vasil'chenko, E.; Kärner, T.; Kudryavtseva, I.; Isakhanyan, V.; Shugai, A.: **Stabilization and annealing of interstitials formed by radiation in binary metal oxides and fluorides.** *Nuclear instruments & methods in physics research, Section B, Beam interactions with materials and atoms* **266**(12): 2868–2871. DOI:10.1016/j.nimb.2008.03.132 PNI.

067 Maiorova, A. V.; Telnov, D. A.; Shabaev, V. M.; Plunien, G.; Stöhlker, T.*: **Coulomb glory in low-energy antiproton scattering by a heavy nucleus: screening effect of vacuum polarization.** *Journal of physics B, Atomic, molecular and optical physics* **41**(24): 245203. DOI:10.1088/0953-4075/41/24/245203 PNI.

068 Manika, I.; Maniks, J.; Schwartz, K.*: **Investigation of heavy ion tracks in LiF crystals by dislocation mobility method.** *Nuclear instruments & methods in physics research, Section B, Beam interactions with materials and atoms* **266**(12): 2741–2744. DOI:10.1016/j.nimb.2008.03.108 PNI.

069 Manika, I.; Maniks, J.; Schwartz, K.*: **Swift-ion-induced hardening and reduction of dislocation mobility in LiF crystals.** *Journal of Physics D - Applied Physics* **41**(7): 074008. DOI:10.1088/0022-3727/41/7/074008 PNI.

070 Marie-Jeanne, M.; Alonso, J.; Blaum, K.*; Djekic, S.; Dworschak, M.;* Hager, U.; Herlert, A.; Nagy, S.; Savreux, R.; Schweikhard, L.; Stahl, S.*; Yazidjian, C.*: **Towards a magnetic field stabilization at ISOLTRAP for high-accuracy mass measurements on exotic nuclides.** *Nuclear instruments & methods in physics research, Section A, Accelerators, spectrometers, detectors and associated equipment* **587**(2): 464–473. DOI:10.1016/j.nima.2008.01.061 PNI.

071 Matei, E.; Enculescu, I.; Enculescu, M.; Neumann, R.*: **Effect of additives on nickel nanowires electrochemical deposition.** *Journal of optoelectronics and advanced materials* **10**(3): 508–511. URL PNI.

072 Mazzocco, A.; Ackermann, D.*; Block, A.; Geissel, H.*; Herfurth, F.*; Heßberger, F. P.*; Hofmann, S.*; Iwasa, N.*; Nishio, K.*; Plaß, W. R.; Scheidenberger, C.*; Weick, H.*; Winkler, A.*; SHIPTRAP Collaborat: **MOCADI_FUSION: Extension of the monte-carlo code MOCADI to heavy-ion fusion-evaporation reactions.** *Nuclear instruments & methods in physics research, Section B, Beam interactions with materials and atoms* **266**(15): 3467–3480. DOI:10.1016/j.nimb.2008.04.017 HANU.PNI.

073 Moskovkin, D. L.; Shabaev, V. M.; Quint, W.*: **Zeeman effect of the hyperfine-structure levels in lithiumlike ions.** *Physical review A, Atomic, molecular, and optical physics* **77**(6): 063421. DOI:10.1103/physreva.77.063421 PNI.

074 Moskovkin, D. L.; Shabaev, V. M.; Quint, W.*:

g factor of Li-like ions with a nonzero nuclear spin. *Optics and Spectroscopy* **104**(5): 637–649. DOI:10.1134/s0030400x08050019 PNI.

075 Mukherjee, M.*; Beck, D.*; Blaum, K.*; Bollen, G.; Delahaye, P.; Dilling, J.; George, S.*; Guenaut, C.; Herfurth, F.*; Herlert, A.; Kellerbauer, A.; Kluge, H.-J.*; Koster, U.; Lunney, D.; Schwarz, S.; Schweikhard, L.; Yazidjian, C.*: **Mass measurements and evaluation around A=22.** *The European physical journal A, Hadrons and nuclei* **35**(1): 31–37. DOI:10.1140/epja/i2007-10523-2 PNI.

076 Mukherjee, M.*; Beck, D.*; Blaum, K.*; Bollen, G.; Dilling, J.; George, S.*; Herfurth, F.*; Herlert, A.; Kellerbauer, A.; Kluge, H.-J.*; Schwarz, S.; Schweikhard, L.; Yazidjian, C.*: **ISOLTRAP: An on-line Penning trap for mass spectrometry on short-lived nuclides.** *The European physical journal A, Hadrons and nuclei* **35**(1): 1–29. DOI:10.1140/epja/i2007-10528-9 PNI.

077 Neidherr, D.; Blaum, K.*; Block, M.*; Ferrer, R.; Herfurth, F.*; Ketelaer, J.; Nagy, S.; Weber, C.*: **Measurement and simulation of the pressure ratio between the two traps of double Penning trap mass spectrometers.** *Nuclear instruments & methods in physics research, Section B, Beam interactions with materials and atoms* **266**(19): 4556–4559. DOI:10.1016/j.nimb.2008.05.102 PNI.

078 Neubrech, F.; Pucci, A.; Cornelius, T. W.*; Karim, S.*; Garcia-Etxarri, A.; Aizpurua, J.: **Resonant Plasmonic and Vibrational Coupling in a Tailored Nanoantenna for Infrared Detection.** *Physical review letters* **101**(15): 157403. DOI:10.1103/physrevlett.101.157403 PNI.

079 Newirkowez, A.; Fuess, H.; Neumann, R.*; Trautmann, C.*; Voss, K. O.*: **Material modifications induced by swift heavy ions in NbTi superconducting wires.** *Phase Transition* **81**(4): 285–292. DOI:10.1080/01411590701695695 PNI.

080 Nicolai, P.; Stenz, C.; Kasperczuk, A.; Pisarczyk, T.; Klir, D.; Juha, L.; Krousky, E.; Masek, K.; Pfeifer, M.; Rohlena, K.; Skala, J.; Tikhonchuk, V.; Ribeyre, X.; Galera, S.; Schurtz, G.; Ullschmied, J.; Kalal, M.; Kravarik, J.; Kubes, P.; Pisarczyk, P.; Schlegel, T.*: **Studies of supersonic, radiative plasma jet interaction with gases at the Prague Asterix Laser System facility.** *Physics of plasmas* **15**(8): 082701. DOI:10.1063/1.2963083 PNI.

081 Ni, P. A.; Kulish, M. I.; Mintsev, V.; Nikolaev, D. N.; Ternovoi, V. Y.; Hoffmann, D. H. H.; Udrea, S.; Hug, A.; Tahir, N. A.*; Varentsov, D.*: **Temperature measurement of warm-dense-matter generated by intense heavy-ion beams.** *Laser and particle beams* **26**(4): 583–589. DOI:10.1017/s0263034608000645 PNI.

082 Ohgai, T.*; Hjort, K.; Spohr, R.*; Neumann, R.*: **Electrodeposition of cobalt based ferro-magnetic metal nanowires in polycarbonate films with cylindrical nanochannels fabricated by heavy-ion-track etching.** *Journal of Applied Electrochemistry* **38**(5): 713–719. DOI:10.1007/s10800-008-9499-1 PNI.

083 Palffy, A.; Harman, Z.; Kozhuharov, C.*; Brandau, C.*; Keitel, C. H.; Scheid, W.; Stöhlker, T.*: **Nuclear excitation by electron capture followed by fast x-ray emission.** *Physics letters B* **661**(4): 330–334. DOI:10.1016/j.physletb.2008.02.027 PNI.

084 Patyk, Z.; Kurcewicz, J.; Bosch, F.*; Geissel, H.*; Litvinov, Y. A.*; Pfützner, M.*: **Orbital electron capture decay of hydrogen- and helium-like ions.** *Physical review C, Nuclear physics* **77**(1): 014306. DOI:10.1103/physrevc.77.014306 HANU.PNI.

085 Piriz, A. R.; Cela, J. J. L.; Tahir, N. A.*; Hoffmann, D. H. H.: **Richtmyer-Meshkov instability in elastic-plastic media.** *Physical Review E, statistical, nonlinear, and soft matter physics* **78**(5): 056401. DOI:10.1103/physreve.78.056401 PNI.

086 Quint, W.*; Moskovkhin, D. L.; Shabaev, V. M.; Vogel, M.: **Laser-microwave double-resonance technique for g-factor measurements in highly charged ions.** *Physical review A, Atomic, molecular, and optical physics* **78**(3): 032517. DOI:10.1103/physreva.78.032517 PNI.

087 Quint, W.*; Nikoobakht, B.; Jentschura, U. D.: **Double-resonance g-factor measurements by quantum jump spectroscopy.** *JETP Letters* **87**(1): 30–34. DOI:10.1007/s11448-008-1008-6 PNI.

088 Radtke, T.; Fritzsche, S.*: **Simulation of n-qubit quantum systems. IV. Parametrizations of quantum states, matrices and probability distributions.** *Computer Physics Communications* **179**(9): 647–664. DOI:10.1016/j.cpc.2008.06.007 PNI.

089 Radtke, T.; Surzhykov, A.; Fritzsche, S.*: **Photon pairs with tailor-made entanglement obtained from the two-photon decay of atomic hydrogen.** *Physical review A, Atomic, molecular, and optical physics* **77**(2): 022507. DOI:10.1103/physreva.77.022507 PNI.

090 Rauth, C.*; Ackermann, D.*; Blaum, K.; Block, M.*; Chaudhuri, A.; Di, Z.; Eliseev, S.*; Ferrer, R.; Habs, D.; Herfurth, F.*; Heßberger, F. P.*; Hofmann, S.*; Kluge, H.-J.*; Maero, G.*; Martin, A.*; Marx, G.; Mukherjee, M.*; Neumayr, J. B.; Plaß, W. R.; Rahaman, S.*; Rodriguez, D.; Scheidenberger, C.*; Schweikhard, L.; Thirolf, P. G.; Vorobjev, G.*; Weber, C.*: **First penning trap mass measurements beyond the proton drip line.** *Physical review letters* **100**(1): 012501. DOI:10.1103/physrevlett.100.012501 HANU.PNI.

091 Reuschl, R.*; Gumberidze, A.*; Kozhuharov, C.*; Spillmann, U.*; Tashenov, S.*; Stöhlker, T.*; Eichler, J.: **State-selective x-ray studies of radiative recombination into bare and H-like uranium at threshold energies.** *Physical review A, Atomic, molecular, and optical physics* **77**(3): 032701. DOI:10.1103/physreva.77.032701 PNI.

092 Rudolph, D.; Hoischen, R.; Hellström, M.; Pietri, S.; Podolyak, Z.; Regan, P. H.; Garnsworthy, A. B.; Steer, S. J.; Becker, F.*; Bednarczyk, P.*; Caceres, L.*; Doornenbal, P.*; Gerl, J.*; Gorska, M.*; Grebosz, J.*; Kojouharov, I.*; Kurz, N.*; Prokopowicz, W.*; Schaffner, H.*; Wollersheim, H.-J.*; Andersson, L. L.; Atanasova, L.; Balabanski, D. L.; Bentley, M. A.; Blazhev, A.; Brandau, C.*; Brown, J. R.; Fahlander, C.; Johansson, E. K.; Jungclaus, A.; Lenzi, S. M.: **Isospin symmetry and proton decay: Identification of the 10^+ isomer in ^{54}Ni.** *Physical review C, Nuclear physics* **78**(2): 021301. DOI:10.1103/physrevc.78.021301 HANU.PNI.

093 Sattonnay, G.; Moll, S.; Thome, L.; Legros, C.; Herbst-Ghysel, M.; Garrido, F.; Costantini, J. M.; Trautmann, C.*: **Heavy-ion irradiation of pyrochlore oxides: Comparison between low and high energy regimes.** *Nuclear instruments & methods in physics research, Section B, Beam interactions with materials and atoms* **266**(12): 3043–3047. DOI:10.1016/j.nimb.2008.03.161 PNI.

094 Schollmeier, M.; Becker, S.; Geissel, M.; Flippo, K. A.; Blazevic, A.*; Gaillard, S. A.; Gautier, D. C.; Grüner, F.; Harres, K.; Kimmel, M.; Nürnberg, F.; Rambo, P.; Schramm, U.; Schreiber, J.; Schütrumpf, J.; Schwarz, J.; Tahir, N. A.*; Atherton, B.; Habs, D.; Hegelich, B. M.; Roth, M.: **Controlled transport and focusing of laser-accelerated protons with miniature magnetic devices.** *Physical review letters* **101**(5): 055004. DOI:10.1103/physrevlett.101.055004 PNI.

095 Schollmeier, M.*; Harres, K.*; Nürnberg, F.; Blazevic, A.*; Audebert, P.; Brambrink, E.; Fernandez, J. C.; Flippo, K. A.; Gautier, D. C.; Geissel, M.; Hegelich, B. M.; Schreiber, J.; Roth, M.*: **Laser beam-profile impression and target thickness impact on laser-accelerated protons.** *Physics of plasmas* **15**(5): 053101. DOI:10.1063/1.2912451 PNI.

096 Schwartz, K.*; Sorokin, M. V.*; Lushchik, A.; Lushchik, C.; Vasilchenko, E.; Papaleo, R. M.; de Souza, D.; Volkov, A. E.; Voss, K. O.*; Neumann, R.*; Trautmann, C.*: **Color center creation in LiF crystals irradiated with 5-and 10-MeV Au ions.** *Nuclear instruments & methods in physics research, Section B, Beam interactions with materials and atoms* **266**(12): 2736–2740. DOI:10.1016/j.nimb.2008.03.107 PNI.

097 Schwartz, K.*; Volkov, A. E.; Sorokin, M. V.*; Trautmann, C.*; Voss, K. O.*; Neumann, R.*; Lang, M.: **Effect of electronic energy loss and irradiation temperature on color-center creation in LiF and NaCl crystals irradiated with swift heavy ions.** *Physical review: B, Condensed matter and materials physics* **78**(2): 024120. DOI:10.1103/physrevb.78.024120 PNI.

098 Schwarz, S.; Bollen, G.; Lopez-Urrutia, J. R. C.; Dilling, J.; Johnson, M.; Kester, O.*; Kostin, M.; Marti, F.; Wilson, C.; Zavodszky, P.: **An electron beam ion trap for the NSCL reaccelerator.** *Nuclear instruments & methods in physics research, Section B, Beam interactions with materials and atoms* **266**(19): 4466–4470. DOI:10.1016/j.nimb.2008.05.056 PNI.

099 Schwellnus, F.; Blaum, K.; Geppert, C.; Gottwald, T.; Kluge, H.-J.*; Mattolat, C.; Nörtershäuser, W.*; Wies, K.; Wendt, K.: **The laser ion source and trap (LIST) - A highly selective ion source.** *Nuclear instruments & methods in physics research, Section B, Beam interactions with materials and atoms* **266**(19): 4383–4386. DOI:10.1016/j.nimb.2008.05.065 PNI.

100 Spillmann, U.*; Bräuning, H.*; Heß, S.*; Beyer, H.*; Stöhlker, T.*; Dousse, J.-C.; Protic, D.; Krings, T.: **Performance of a Ge-microstrip imaging detector and polarimeter.** *Review of scientific instruments* **79**(8): 083101. DOI:10.1063/1.2963046 PNI.

101 Spohr, R.*: **Real-time control of track etching and recent experiments relevant to micro and nano fabrication.** *Radiation Measurements* **43**: S560–S570. DOI:10.1016/j.radmeas.2008.03.078 PNI.

102 Stöhlker, T.*; Gumberidze, A.*; Kumar, A.*; Reuschl, R.*; Trassinelli, M.*: **Quantum electrodynamics in one- and two-electron high-Z ions.** *Advances in Quantum Chemistry* **53**: 57–65. DOI:10.1016/s0065-3276(07)53005-4 PNI.

103 Stork, H.; Dinse, K. P.; Fujara, F.; Hamburger, A.; Jakes, P.; Neumann, R.*; Schuster, B.*; Schwartz, K.*; Trautmann, C.*: **Spatially resolved characterization of Xe ion irradiated LiF crystals using static field gradient NMR.** *Journal of physics Condensed matter* **20**(46): 465215. DOI:10.1088/0953-8984/20/46/465215 PNI.

104 Stork, H.; Hamburger, A.; Gädke, A.; Fujara, F.; Schwartz, K.*: **Spatially resolved characterization of heavy ion irradiated crystals using static field gradient nuclear magnetic resonance.** *Journal of physics Condensed matter* **20**(27): 275236. DOI:10.1088/0953-8984/20/27/275236 PNI.

105 Sun, B.*; Knöbel, R.*; Litvinov, Y. A.*; Geissel, H.*; Meng, J.; Beckert, K.*; Bosch, F.*; Boutin, D.; Brandau, C.*; Chen, L.; Cullen, I. J.; Dimopoulou, C.*; Fabian, B.; Hausmann, M.; Kozhuharov, C.*; Litvinov, S. A.*; Mazzocco, M.; Montes, F.; Münzenberg, G.*; Musumarra, A.; Nakajima, S.; Nociforo, C.*; Nolden, F.*; Ohtsubo, T.; Ozawa, A.; Patyk, Z.; Plaß, W. R.; Scheidenberger, C.*; Steck, M.*; Suzuki, T.; Walker, P. M.; Weick, H.*; Winck-

ler, N.*; Winkler, M.*; Yamaguchi, T.: **Nuclear structure studies of short-lived neutron-rich nuclei with the novel large-scale isochronous mass spectrometry at the FRS-ESR facility.** *Nuclear physics A, Nuclear and hadronic physics* **812**: 1–12. DOI:10.1016/j.nuclphysa.2008.08.013 HANU.PNI.

106 Surzhykov, A.; Jentschura, U. D.; Stöhlker, T.*; Fritzsche, S.*: **Electron capture into few-electron heavy ions: Independent particle model.** *The European physical journal: D, Atomic, molecular and optical physics* **46**(1): 27–36. DOI:10.1140/epjd/e2007-00269-3 PNI.

107 Surzhykov, A.; Jentschura, U. D.; Stöhlker, T.*; Gumberidze, A.*; Fritzsche, S.*: **Alignment of heavy few-electron ions following excitation by relativistic Coulomb collisions.** *Physical review A, Atomic, molecular, and optical physics* **77**(4): 042722. DOI:10.1103/physreva.77.042722 PNI.

108 Tahir, N. A.*; Kim, V. V.; Matvechev, A. V.; Ostrik, A. V.; Shutov, A. V.; Lomonosov, I. V.; Piriz, A. R.; Cela Lopez, J. J.; Hoffmann, D. H. H.: **High energy density and beam induced stress related issues in solid graphite Super-FRS fast extraction targets.** *Laser and particle beams* **26**(2): 273–286. DOI:10.1017/s0263034608000347 PNI.

109 Tahir, N. A.*; Schmidt, R.; Brugger, M.; Assmann, R.; Shutov, A. V.*GAST; Lomonosov, I. V.; Piriz, A. R.; Hoffmann, D. H. H.; Deutsch, C.; Fortov, V. E.: **The CERN Super Proton Synchrotron as a tool to study high energy density physics.** *New Journal of Physics* **10**: 073028. DOI:10.1088/1367-2630/10/7/073028 OPEN ACCESS. PNI.

110 Tahir, N. A.*; Spiller, P.*; Piriz, A. R.; Shutov, A.; Lomonosov, I. V.; Schollmeier, M.; Pelka, A.; Hoffmann, D. H. H.; Deutsch, C.: **Studies of high-energy density states using isochoric heating of matter by intense heavy ion beams: the HEDgeHOB Collaboration.** *Physica scripta* **T132**: 014023. DOI:10.1088/0031-8949/2008/t132/014023 PNI.HANU:Accelerator.

111 Tahir, N. A.*; Weick, H.*; Shutov, A.; Kim, V.; Matveichev, A.; Ostrik, A.; Sultanov, V.; Lomonosov, I. V.; Piriz, A. R.; Cela Lopez, J. J.; Hoffmann, D. H. H.: **Simulations of a solid graphite target for high intensity fast extracted uranium beams for the Super-FRS.** *Laser and particle beams* **26**(3): 411–423. DOI:10.1017/s0263034608000426 PNI.

112 Tazlaoanu, C.; Ion, L.; Enculescu, I.*GAST; Sima, M.; Enculescu, M.; Matei, E.; Neumann, R.*; Bazavan, R.; Bazavan, D.; Antohe, S.: **Transport properties of electrodeposited ZnO nanowires.** *Physica E - Low-dimensional Systems and Nanostructures* **40**(7): 2504–2507. DOI:10.1016/j.physe.2007.07.013 PNI.

113 Truckenmuller, R.; Giselbrecht, S.; van Blitterswijk, C.; Dambrowsky, N.; Gottwald, E.; Mappes, T.; Rolletschek, A.; Saile, V.; Trautmann, C.*; Weibezahn, K.-F.; Welle, A.: **Flexible fluidic microchips based on thermoformed and locally modified thin polymer films.** *Lab on a Chip* **8**(9): 1570–1579. DOI:10.1039/b803619e PNI.

114 Varentsov, D.*; Fertman, A. D.; Turtikov, V. I.; Ulrich, A.; Wieser, J.; Fortov, V. E.; Golubev, A. A.; Hoffmann, D. H. H.; Hug, A.*; Kulish, M.; Mintsev, V.; Ni, P. A.; Nikolaev, D.; Sharkov, B. Y.; Shilkin, N.; Ternovoi, V. Y.; Udrea, S.: **Transverse Optical Diagnostics for Intense Focused Heavy Ion Beams.** *Contributions to Plasma Physics* **48**(8): 586–594. DOI:10.1002/ctpp.200810092 PNI.

115 Verdu, J.; Kreim, S.; Blaum, K.*; Kracke, H.; Quint, W.*; Ulmer, S.; Walz, J.: **Calculation of electrostatic fields using quasi-Green's functions: application to the hybrid Penning trap.** *New Journal of Physics* **10**: 103009. DOI:10.1088/1367-2630/10/10/103009 OPEN ACCESS. PNI.

116 Vogel, M.*; Alonso, J.; Blaum, K.*; Quint, W.*; Schabinger, B.; Sturm, S.; Verdu, J.; Wagner, A.; Werth, G.: **The anomalous magnetic moment of the electron in hydrogenlike ions.** *European Physical Journal - Special Topics* **163**: 113–126. DOI:10.1140/epjst/e2008-00814-8 PNI.

117 Weber, C.*; Audi, G.; Beck, D.*; Blaum, K.*; Bollen, G.; Herfurth, F.*; Kellerbauer, A.*; Kluge, H.-J.*; Lunney, D.; Schwarz, S.: **Atomic mass measurements of short-lived nuclides around the doubly-magic ^{208}Pb.** *Nuclear physics A, Nuclear and hadronic physics* **803**(1): 1–29. DOI:10.1016/j.nuclphysa.2007.12.014 PNI.

118 Weber, C.; Elomaa, V. V.; Ferrer, R.; Fröhlich, C.; Ackermann, D.*; Äystö, J.; Audi, G.; Batist, L.; Blaum, K.*; Block, M.*; Chaudhuri, A.*; Dworschak, M.; Eliseev, S.*; Eronen, T.; Hager, U.; Hakala, J.; Herfurth, F.*; Heßberger, F. P.*; Hofmann, S.*; Jokinen, A.; Kankainen, A.; Kluge, H.-J.*; Langanke, K.*; Martin, A.*; Martinez-Pinedo, G.*; Mazzocco, M.*; Moore, I. D.; Neumayr, J. B.; Novikov, Y. N.*; Penttilae, H.; Plaß, W. R.*; Popov, A. V.; Rahaman, S.; Rauscher, T.; Rauth, C.*; Rissanen, J.; Rodriguez, D.; Saastamoinen, A.; Scheidenberger, C.*; Schweikhard, L.; Seliverstov, D. M.; Sonoda, T.; Thielemann, F. K.; Thirolf, P. G.; Vorobjev, G. K.*: **Mass measurements in the vicinity of the r p-process and the ν p-process paths with the Penning trap facilities JYFLTRAP and SHIPTRAP.** *Physical review C, Nuclear physics* **78**(5): 054310. DOI:10.1103/physrevc.78.054310 HANU.PNI.

119 Weikusat, C.; Glasmacher, U. A.; Miletich, R.; Neumann, R.*; Trautmann, C.*: **Raman spectroscopy of heavy ion induced damage in cordierite.** *Nuclear instruments & methods in physics research, Section B, Beam interactions with materials and atoms* **266**(12): 2990–2993.

DOI:10.1016/j.nimb.2008.03.152 PNI.

120 Yamaki, T.; Rohani, R.; Koshikawa, H.; Takahashi, S.; Hasegawa, S.; Asano, M.; Voss, K. O.*; Neumann, R.*; Maekawa, Y.: **Etching Behavior of Poly(vinylidene fluoride) Thin Films Irradiated with Ion Beams - Effect of Irradiated Ions and Pretreatment.** *Kobunshi Ronbunshu* **65**(3): 273–276.PNI.

121 Yan, Z.-C.; Nörtershäuser, W.*; Drake, G. W. F.: **High precision atomic theory for Li and Be^+: QED shifts and isotope shifts.** *Physical review letters* **100**(24): 243002. DOI:10.1103/physrevlett.100.243002 PNI.

122 Yao, J. M.; Sun, B.*; Woods, P. J.; Meng, J.: **Effects of triaxial deformation and pairing correlation on the proton emitter ^{145}Tm.** *Physical review C, Nuclear physics* **77**(2): 024315. DOI:10.1103/physrevc.77.024315 PNI.

123 Zimmer, D.; Zielbauer, B.*; Bagnoud, V.*; Eisenbarth, U.*; Javorkova, D.*; Kuehl, T.*: **An improved double-pulse non-normal incidence pumping geometry for transient collisionally excited soft X-ray lasers.** *Optics Express* **16**(14): 10398–10403. URL OPEN ACCESS. PNI.

124 Zou, J. P.; Sautivet, A. M.; Fils, J.; Martin, L.; Abdeli, K.; Sauteret, C.; Wattellier, B.: **Optimization of the dynamic wavefront control of a pulsed kilojoule/nanosecond-petawatt laser facility.** *Applied Optics* **47**(5): 704–710.PNI.

2. Further publications [1]

001 Blaum, K.; Eberhardt, K.; Hampel, G.; Heil, W.; Kratz, J.-V.; Nörtershäuser, W.: **Forschung mit Neutronen in Chemie und Physik am TRIGA Mainz.** In: *Natur und Geist, Forschungsmagazin der Universität Mainz. 24*, 65p. PNI

002 Blaum, K.; Herfurth, F.Edd: **Trapped Charged Particles and Fundamental Interactions.** In: : *Lect. Notes Phys*, PNI

003 Blaum, K.*; Litvinov, Y. A.*; Schweikhard, L.*: **Masses of Short-Lived Nuclides: Precision Measurement Techniques and Applications.** In: *Nuclear Physics News* **18***(3)*, 29p. DOI:10.1080/10506890802336281 PNI

004 Drake, G. W. F., Lu, Z.-T.; Nörtershäuser, W.; Yan, Z.-C.: **Halo Nuclei in Laser Light.** In: *Precision Physics of Simple Atoms and Molecules*, 131p. PNI

005 Giselbrecht, S.; Gottwald, E.; Welle, A.; Gietzelt, T.; Weibezahn, K. F.; Truckenmller, R.; Trautmann, C.; Heckele, M.; Saile, V.: **Microstructured, thermoformed polymer films for 3D cell culture in bioreactors.** In: *Galvanotechnik* **99**, 456p. PNI

006 Herfuth, F.; Ackermann, D.; Blaum, K.; Blick, M.; Chaudhuri, A.; Dworschak, M.; Eliseev, S.; Ferrer, R.; Heßberger, F.; Hofmann, S.; Kluge, H. J.; Maero, G.; Martin, A.; Marx, G.; Mazzocco, M.; Neidherr, D.; Neumayr, J. B.; Plaß, W.; Rahaman, S.; Rauth, C. Rodriguez, D.; Schweikhard, L.; Thirolf, P.; Vorobjev, G. Weber, C.: **Precise Mass Measurements of Exotic Nuclei - the SHIPTRAP Penning Trap Mass Spectrometer.** In: *AIP Conference Proceedings* , 319p. PNI

007 Lange, M.; Blaum, K.; Frosse, M.; Grieser,, M.; Kaiser, D.; Menk, S.; Orlov, D. A.; Sieber, T.; Varju, J.; von Hahn, R.; Wolf, A.; Heber, O.; Papport, M.; Toker, J.: **Commissioning of the Heidelberg cryogenic trap for fast ion beams (CTF).** In: *MOPC 110*, PNI

008 Liu, J. Glasmacher,U. A.; Lang, M.; Trautmann, C.; Voss, K.-O.; Neumann, R.; Wagner, G. A.; Miletich, R.: **Raman spectroscopy of apatite irradiated with swift heavy ions with and without simultaneous exertion of high pressure.** In: *Appl. Phys. A* **91**, 17p. PNI

009 Nagy, S.; Blaum, K., Schuch, B.: **Highly-Charged ions and high-resolution mass spectrometry in a Penning trap.** In: Blaum, K.; Herfurth, F:: *Trapped Charged Particles and Fundamental Interactions 749*, 119p. PNI

010 Quint, W.; Nikoobakht, B.; Jentschura, U. D.: **Double-Resonance g-Factor Measurements by Quantum Jump Spectroscopy.** In: *Pis'ma v ZhETF 87* , 36p. PNI

011 Schollmeier, M.; Roth, M.; Schaumann, G.; Blazevic, A.; Flippo, K.; Frank, A.; Fernandez, J. C.; Gautier, D. C.; Harres, K.; Hessling, T.; Hegelich, B. M.; Nuernberg, F.; Pelka, A.; Ruhl, H.; Schreiber, J.; Schumacher, D.; Witte, K.; Zielbauer, B. ;Hoffman, D. H. H.: **Plasma physics experiments at GSI.** In: *J. Phys.: Conf. Ser. 112*, 042068p. PNI

012 Stöhlker, T.; Gumberidze, A.; Trassinelli, M.; Andrianov, V.; Beyer, H.; Kraft-Bermith, S.; Beile, A.; Egelhof, P.: **Quantum Electrodynamics in Extreme Fields: Precision Spectroscopy of High-Z H-like Systems.** In: *Precision Physics of Simple Atoms and Molecules 745*, 157p. PNI

013 Sun, B.; Geissel, H.; Hausmann, M.; Kozhuharov, C.; Knöbel, R.; Litvinov, Y. A.; Meng, J.; Patyk, Z.; Radon, T.: **Identification of Time-of-Flight Spectra for Isochronous Mass Measurements.** In: *Chinese Physics C 32* , 1p. PNI

014 Tahir, N. A.: **Studies of High Energy Density Matter Using Intense Ion Beams: The HEDgeHOB Collaboration.** In: *Bulletin Am. Physical Soc. 53 (5)*, 193p. PNI

[1] Unproved announcements of the scientific and technical divisions.

015 Tahir, N. A.; Lomonosov, I. V.; Shutov, A.; Kim, V.; Fortov, V. E.; Piriz, A. R.; Wouchuk, G.; Serna Moreno, M. C.; Lopez Cela, J. J.; Hoffmann, D. H. H..; Deutsch, C.: **High Energy Density Matter Research Using Intense Heavy Ion Beams at the Future FAIR Facility at Darmstadt: The HEDgeHOB Collaboration.** In: *J. Phys.: Conf. Series*, PNI

016 Tahir, N. A.; Shutov, A.; Lomonosov, I. V.; Piriz, A. R.; Hoffmann, D. H. H..; Deutsch, C.: **High Energy Density Physics Research Using Intense Ion Beams: The HEDgeHOB Collaboration.** In: *Bull. Am. Phys. Soc 53 (14)*, 288p. PNI

GSI Publications to the programme 'Health' in the field 'Cancer research' published in 2008

1. Reviewed publications

001 Achenbach, P.; Gayoso, C. A.; Bernauer, J. C.; Böhm, R.; Distler, M. O.; Doria, L.; de la Paz, M. G. R.; Merkel, H.; Müller, U.; Nungesser, L.; Pochodzalla, J.; Majos, S. S.; Schlimme, B. S.; Walcher, T.; Weinriefer, M.; Debenjak, L.; Potokar, M.; Sirca, S.; Kavatsyuk, M.*; Lepyoshkina, O.*; Minami, S.*; Nakajima, D.*; Rappold, C.*; Saito, T. R.*; Schardt, D.*; Träger, M.*; Iwase, H.; Ajimura, S.; Sakaguchi, A.; Mizoi, Y.: **In-beam tests of scintillating fibre detectors at MAMI and at GSI.** *Nuclear instruments & methods in physics research, Section A, Accelerators, spectrometers, detectors and associated equipment* **593**(3): 353–360. DOI:10.1016/j.nima.2008.05.017 Cancer.HANU

002 Bert, C.*; Grözinger, S. O.*; Rietzel, E.*: **Quantification of interplay effects of scanned particle beams and moving targets.** *Physics in medicine and biology* **53**(9): 2253–2265. DOI:10.1088/0031-9155/53/9/003 Cancer

003 Bert, C.*; Saito, N.*; Schmidt, A.; Chaudhri, N.; Schardt, D.*; Rietzel, E.*: **Techniques for the radiation of respiratory movement target volumes with scanned partial radiation.** *Strahlentherapie und Onkologie* **184**: 17–17. Cancer

004 Chapman, K. L.; Kelly, J. W.; Lee, R.*; Goodwin, E. H.; Kadhim, M. A.: **Tracking genomic instability within irradiated and bystander populations.** *Journal of Pharmacy and Pharmacology* **60**(8): 959–968. URL Cancer

005 Du, G.*; Fischer, B. E.*; Voss, K. O.*; Becker, G.*; Taucher-Scholz, G.*; Kraft, G.*; Thiel, G.: **The absence of an early calcium response to heavy-ion radiation in mammalian cells.** *Radiation research* **170**(3): 316–326. DOI:10.1667/RR1270.1 Cancer.PNI

006 Durante, M.*: **Physical and biomedical countermeasures for space radiation risk.** *Zeitschrift für medizinische Physik* **18**(4): 244–252. DOI:10.1016/j.zemedi.2008.06.010 Cancer

007 Durante, M.*; Cucinotta, F. A.: **Heavy ion carcinogenesis and human space exploration.** *Nature Reviews Cancer* **8**(6): 465–472. DOI:10.1038/nrc2391 Cancer

008 Ellerbrock, M.; Jäkel, O.; Krämer, M.*; Nikogbosyan, A.; Schulz-Ertner, D.; Karger, C. P.; Ackennann, B.; Hee, P.; Debus, J.: **Clinical implementation of intensity modulated radiotherapy using carbon ions.** *International journal of radiation oncology, biology, physics* **72**(1): S592–S592. DOI:10.1016/j.ijrobp.2008.06.199 Cancer

009 Elsässer, T.*; Cunrath, R.*; Krämer, M.*; Scholz, M.*: **Impact of track structure calculations on biological treatment planning in ion radiotherapy.** *New Journal of Physics* **10**: 075005. DOI:10.1088/1367-2630/10/7/075005 OPEN ACCESS. Cancer

010 Elsässer, T.*; Krämer, M.*; Scholz, M.*: **Accuracy of the local effect model for the prediction of biologic effects of carbon ion beams in vitro and in vivo.** *International journal of radiation oncology, biology, physics* **71**(3): 866–872. DOI:10.1016/j.ijrobp.2008.02.037 Cancer

011 Gemmel, A.* Hasch, B.; Ellerbrock, M.; Weyrather, W. K.*; Kräer, M.*: **Biological dose optimization with multiple ion fields.** *Physics in medicine and biology* **53**(23): 6991–7012. DOI:10.1088/0031-9155/53/23/022 Cancer

012 Grözinger, S. O.*; Bert, C.*; Haberer, T.*; Kraft, G.*; Rietzel, E.*: **Motion compensation with a scanned ion beam: a technical feasibility study.** *Radiation Oncology* **3**: 34. DOI:10.1186/1748-717x-3-34 Cancer

013 Grossi, G.; Bettega, D.; Calzolari, P.; Durante, M.*; Elsässer/Elsasser, T.*; Gialanella, G.; Hessel, P.*; Manti, L.; Pugliese, M.; Ritter, S.* EMAIL; Santini, M. T.; Scampoli, P.; Weyrather, W. K.*: **Late cellular effects of ^{12}C ions.** *Nuovo Cimento C - Colloquia on Physics* **31**(1): 39–47. DOI:10.1393/ncc/i2008-10278-4 Cancer

014 Gunzert-Marx, K.*; Iwase, H.*; Schardt, D.*; Simon, R. S.*: **Secondary beam fragments produced by 200 MeVu^{-1} ^{12}C ions in water and their dose contributions in carbon ion radiotherapy.** *New Journal of Physics* **10**: 075003. DOI:10.1088/1367-2630/10/7/075003 OPEN ACCESS. Cancer

015 Herskind, C.; Milanovic, D.; Wang, M.; Ritter, S.*; Wenz, F.: **Induction of telomerase activity in peripheral blood lymphocytes with dense ionised radiother-**

apy. *Strahlentherapie und Onkologie* **184**: 113–113. Cancer

016 Jakel, O.; Ellerbrock, M.; Heeg, P.*; Ackermann, B.; Winter, M.*; Brons, S.*; Parodi, K.; Haberer, T.; Karger, C. P.; Bert, C.*; Krämer, M.*; Debus, J.: **Medical physics research at the Heidelberg ion beam therapy center.** *Strahlentherapie und Onkologie* **184**: 21–22. Cancer

017 Karger, C. P.; Jäkel, O.; Scholz, M.*; Peschke, P.; Debus, J.: **What is the clinically relevant relative biologic effectiveness? A warning for fractionated treatments with high linear energy transfer radiation: In regard to Dasu and Toma-Dasu. (Int J Radiat Oncol Biol Phys 2008;70 : 867-874).** *International journal of radiation oncology, biology, physics* **70**(5): 1614–1614. DOI:10.1016/j.ijrobp.2007.12.032 Cancer

018 Kase, Y.; Kanai, T.; Matsufuji, N.; Furusawa, Y.; Elsässer, T.*; Scholz, M.*: **Biophysical calculation of cell survival probabilities using amorphous track structure models for heavy-ion irradiation.** *Physics in medicine and biology* **53**(1): 37–59. DOI:10.1088/0031-9155/53/1/003 Cancer

019 Kraft-Weyrather, W.*; Bohl, J.*; Elsaesser, T.*; Schulz-Ertner, D.; Debus, J.; Combs, S. E.: **Radiobiological evaluation and correlation with the Local effect Model (LEM) of carbon ion radiation therapy and temozolomide in glioblastoma cell lines.** *International journal of radiation oncology, biology, physics* **72**(1): S705–S705. DOI:10.1016/j.ijrobp.2008.06.530 Cancer

020 Longo, R.; Durante, M.*; Bottigli, U.: **Papers presented at the workshop "La Radiobiologia all INFN" Trieste, 7 February 2008, - Preface.** *Nuovo Cimento C - Colloquia on Physics* **31**(1): 1–2. DOI:10.1393/ncc/i2008-10285-5 Cancer

021 Maalouf, M.*; Alphonse, G.*; Battiston-Montagne, P.*; Beuve, M.; Coltiaux, A.*; Fournier, C.*; Taucher-Scholz, G.*; Rodriguez-Lafrasse, C.*: **Differential cell death process activated in two HNSCC cell models in response to radiation (carbon and photon).** *Bulletin du Cancer* **95**: S71–S71. Cancer

022 Peschke, P.; Karger, C.; Scholz, M.*; Debus, J.; Huber, P.: **Relative biological effectiveness (RBE) of carbon ions in the normal central nervous system (CNS)..** *Strahlentherapie und Onkologie* **184**: 79–80. Cancer

023 Pignalosa, D.*; Bertucci, A.; Gialariella, G.; Grossi, G.; Manti, L.; Pugliese, M.; Scampoli, P.; Durante, M.*: **Chromosome inter- and intrachanges detected by arm-specific DNA probes in the progeny of human lymphocytes exposed to energetic heavy ions.** *Radiation research* **170**(4): 458–466. DOI:10.1667/RR1326.1 Cancer

024 Rietzel, E.*; Liu, A. K.; Chen, G. T. Y.; Choi, N. C.: **Maximum-intensity volumes for fast contouring of lung tumors including respiratory motion in 4DCT planning.** *International journal of radiation oncology, biology, physics* **71**(4): 1245–1252. DOI:10.1016/j.ijrobp.2008.03.030 Cancer

025 Schlampp, I.; Karger, C. P.; Jäkel, O.; Scholz, M.*; Didinger, B.; Nikoghosyan, A.; Hoess, A.; Krämer, M.*; Debus, J.; Schulz-Ertner, D.: **Clinical validation of the local effect model (LEM) in the treatment planning of carbon ion RT in patients with skull base tumors.** *International journal of radiation oncology, biology, physics* **72**(1): S229–S229. DOI:10.1016/j.ijrobp.2008.06.699 Cancer

026 Schmidt, A.*; Bert, C.*; Saito, N.*; Iancu, G.*; von Neubeck, C.*; Chaudhri, N.*; Schardt, D.*; Rietzel, E.*: **Experimental validation of a beam tracking system for the treatment of moving targets with scanned ion beams.** *International journal of radiation oncology, biology, physics* **72**(1): S27–S27. DOI:10.1016/j.ijrobp.2008.06.827 Cancer

027 Scholz, M.*; Elsässer, T.*: **Radiobiologic parameters and local effect model predictions for head-and-neck squamous cell carcinomas exposed to high linear energy transfer ions: In regard to Beuve et al..** *International journal of radiation oncology, biology, physics* **72**(1): 302–303. DOI:10.1016/j.ijrobp.2008.05.032 Cancer

028 Strasik, I.*; Mustafin, E.*; Fertman, A.*; Hinca, R.; Pavlovic, M.; Schardt, D.*; Sobolevskiy, N.*; Golubev, A.*; Sharkov, B.*; Fehrenbacher, G.*; Hofmann, I.*; Iwase, H.*; Kozlova, E.*; Mustafina, G.*: **Experimental study of the residual activity induced by 950 MeV/u uranium ions in stainless steel and copper.** *Nuclear instruments & methods in physics research, Section B, Beam interactions with materials and atoms* **266**(15): 3443–3452. DOI:10.1016/j.nimb.2008.05.013 Cancer.HANU

029 Voss, K. O.*; Fournier, C.*; Taucher-Scholz, G.*: **Heavy ion microprobes: a unique tool for bystander research and other radiobiological applications.** *New Journal of Physics* **10**: 075011. DOI:10.1088/1367-2630/10/7/075011 OPEN ACCESS. Cancer

030 Wang, J. F.; Li, R. M.; Guo, C. L.; Fournier, C.*; Kraft-Weyrather, W.*: **The influence of fractionation on cell survival and premature differentiation after carbon ion irradiation.** *Journal of Radiation Research* **49**(4): 391–398. DOI:10.1269/jrr.08012 OPEN ACCESS. Cancer

031 Zaconte, V.; Belli, F.; Bidoli, V.; Casolino, M.; Di Fino, L.; Narici, L.; Picozza, P.; Rinaldi, A.; Sannita, W. G.; Finetti, N.; Nurzia, G.; Rantucci, E.; Scrimaglio, R.; Segreto, E.; Schardt, D.*: **ALTEA: The instrument calibration.** *Nuclear instruments &*

methods in physics research, Section B, Beam interactions with materials and atoms **266**(9): 2070–2078. DOI:10.1016/j.nimb.2008.02.072 Cancer

2. Further publications [1]

001 Amaldi, U., Kraft, G.: **Particle Accelerators Take up the Fight against Cancer.** In: *Association of Asia Pacific Physical Societies 18(1)*, 19p. Cancer

002 Averbeck, N., Gao, X.-D., Nishimura, S.-I., Dean, N.: **The second step of N-linked protein glycosylation in Saccharomyces cerevisiae is regulated by the proteasome.** In: *Molecular Biology of the Cell 19(5)*, 2169p. Cancer

003 Belli, M., Bettega, D., Calzolari, P., Cherubini, R., Cuttone, G., Durante, M., Esposito, G., Furusawa, Y., Gerardi, S., Gialanella, G., Grossi, G., Manti, L., Marchesini, R., Pugliese, M., Scampoli, P., Simone, G., Sorrentino, E., Tabocchini, M.A., Tallone, L.: **Effectiveness of monoenergetic and spread-out Bragg peak carbon ions for inactivation of various normal and tumour human cell lines.** In: 597p. Cancer

004 Bert, C.*; Saito, N.*; Schmidt, A.*; Chaudhri, N.*; Schardt, D.*; Rietzel, E.*: **TH-C-350-05: Performance of a Beam Tracking System for Treatment of Moving Targets with Scanned Ion Beams.** In: *Medical Physics* **35***(6)*, 2967p. DOI:10.1118/1.2962830 Cancer

005 Durante, M.: **[Editorial] Focus on Heavy Ions in Biophysics and Medical Physics.** In: *New Journal of Physics* **10** , 075002p. DOI:10.1088/1367-2630/10/7/075002 OPEN ACCESS Cancer

006 Durante, M.; Manti, L.: **Human response to high-background radiation environments on Earth and in space.** In: *Advances in Space Research* **42***(6)*, 999p. DOI:10.1016/j.asr.2007.02.014 Cancer

007 Elsässer, T., Psonka, K., Scholz, M., Brons, S., Gudowska-Nowak, E., Taucher-Scholz, G.: **Biophysical Modelling of Fragment Distributions of DNA Plasmids after Heavy Ion Irradiation.** In: Connerade, J., Solov'yov, A: *Latest Advances in Atomic Cluster Collisions: Structure and Dynamics from the Nuclear to the Biological Scale*, 389p. Cancer

008 Elssäser, T.*; Scholz, M.*: **TU-EE-A2-02: Impact of Track Structure Calculations On Biological Treatment Planning in Carbon Ion Radiotherapy.** In: *Medical Physics* **35***(6)*, 2911p. DOI:10.1118/1.2962612 Cancer

009 Grossi, G.; Bettega, D.; Calzolari, P.; Durante, M.*; Elsässer, T.; Gialanella, G.; Hessel, P.; Manti, L.; Pugliese, M.; Ritter, S.*; Santini, M. T.; Scampoli, P.; Weyrather, W.*: **Late cellular effects of C-12 ions.** In: *Nuovo Cimento Soc. Ital. Fis. C-Geophys. Space Phys.* **31***(1)*, 39p. DOI:10.1393/ncc/i2008-10278-4 Cancer

010 Lobascio, C., Briccarello, M., Destefanis, R., Faraud, M., Gialanella, G., Grossi, G., Guarnieri, V., Manti, L., Pugliese, M., Rusek, A., Scampoli, P., Durante, M.: **Accelerator-based tests of radiation shielding properties of materials used in human space infrastructures.** In: *Health Physics. The Radiation Safety Journal 94 (3)*, 242p. Cancer

011 Longo, R.; Durante, M.*; Bottigli, U.: **Papers presented at the workshop 'La Radiobiologia all INFN' Trieste, 7 February 2008, - Preface.** In: *Nuovo Cimento Soc. Ital. Fis. C-Geophys. Space Phys.* **31***(1)*, 1p. DOI:10.1393/ncc/i2008-10285-5 Cancer

012 Peschke, P., Karger, C.P., Scholz, M., Debus, J., Huber, P.: **DEGRO-GRO 2008: Relative biological effectiveness (RBE) of carbon ions in the normal central nervous system (CNS).** In: *Strahlentherapie und Onkologie 184 (Suppl.1)* , 79p. Cancer

013 Pignalosa, D.; Bertucci, A.; Gialariella, G.; Grossi, G.; Manti, L.; Pugliese, M.; Scampoli, P.; Durante, M.*: **Chromosome inter- and intrachanges detected by arm-specific DNA probes in the progeny of human lymphocytes exposed to energetic heavy ions.** In: *Radiation Research* **170***(4)*, 458p. Cancer

014 Pugliese, M., Casolino, M., Cerciello, V., Durante, M., Grossi, G., Gialanella, G., Manti, L., Morgia, A., Roca, V., Scampoli, P., Zaconte, V.: **SPADA: a project to study the effectiveness of shielding materials in space.** In: *Il Nuovo Cimento C 31(1)*, 91p. Cancer

015 Scampoli, P., Bisogni, M.G., Carpentieri, G., Di Martino, F., Durante, M., Gialanella, G., Giannelli, M., Grossi, G., Magaddino, V., Manti, L., Moriello, C., Pugliese, M., Righi, S.: **BIORT: an experiment for the assessment of the biological effects of very high dose rate and dose per pulse electron irradiations.** In: *Il Nuovo Cimento C 31(1)*, 3p. Cancer

016 Schmidt, A.; Bert, C.; Saito, N.; Chaudhri, N.; Iancu, G.*; von Neubeck, C.*; Rietzel, E.*: **TU-EE-A2-03: Target Motion Tracking with a Scanned Particle Beam: Calculation and Experimental Validation of Biologically Effective Doses in the Presence of Motion.** In: *Medical Physics* **35***(6)*, 2911p. DOI:10.1118/1.2962613 Cancer

[1] Unproved announcements of the scientific and technical divisions.

GSI as pulisher and academic works

Compiled by K. Große

Special conference

International Symposium on Heavy Ion Physics 2008: November 17-20, 2008 at GSI, Darmstadt The contributions can be found at http://wwww.gsi.de/iship2008 under program.

Accelerator notes

ACC-note-2008-008 Paret, S.; Kornilov, V.; Sorge, S.; Boine-Frankenheim, O.: Chromaticity Measurement with Electron Cooling and Schottky Noise

ACC-note-2008-007 Golubev, A.; Smolyakov, A.; Kantsyrev, A.; Markov, N.; Stolbunov, V.; Mustafin, E.: Radiation Hardiness Experiment: Insulator Materials Irradiation at the Proton Linac I-2 at ITEP

ACC-note-2008-006 Kornilov, V.; Boine-Frankenheim, O.; Hofmann, I.: Transverse Collective Instabilities in SIS 100

ACC-note-2008-005 Mustafin, E.; Plotnikov, A.; Latycheva, L.; Sobolevsky, N.; Smolyakov, A.: Radiation Damage to Some Accelerator Elements in FAIR

ACC-note-2008-004 Golubev, A.; Smolyakov, A.; Kantsyrev, A.; Markov, N.; Titarenko, Yu.; Batyaev, V.; Smirnov, G., Mustafin, E.; Plotnikov, A.; Seidl, T.: Radiation Hardiness Experiment: Insulator and Magnetic Alloy Materials, Irradiation at the U-10 Synchrotron at ITEP

ACC-note-2008-003 Golubev, A.; Kantsyrev, A.; Smolyakov, A.; Markov, N.; Stolbunov, V.; Mustafin, E.; Plotnikov, A.: Radiation Hardiness Experiment: Insulator and Magnetic Alloy Materials, Irradiation at the Proton Linac I-2 at ITEP

ACC-note-2008-002 Parfenova, A.; Franchetti, G.; Bayer, W.: Resonance Induced Beam Loss in SIS18 affected by CO distortion and chromatic sextupoles

ACC-note-2008-001 Fabio, P.; Franchetti, G.: Elliptic and circular representation of the magnetic field in SIS 100

GSI Reports

GSI Report 2008-05 P. Mulser (Ed.): ILIAS Ion and Laser Beam Interaction and Application Studies

GSI Report 2008-04 P. Senger (Ed): CBM Progress Report 2007

GSI Report 2008-03 Prozorov, A.; Labzowsky, L.; Plunien, G.; Liesen, D.; Bosch, F.; Fritzsche, S.; Surzhykov, A.: Ion Beam Polarization in Storage Rings: Production, controlling and Preservation

GSI Report 2008-2 K. Weyrich (Ed.): High Energy Density Physics with Intense Ion and Laser Beams: Annual Report 2007

GSI Report 2008-1 K. Große (Ed.): GSI Scientific Report 2007

Academic works

GSI Diss 2009-06 C. Novotny: Laser spectroscopy on lithium ions stored at a velocity of 33.8% of the speed of light (2008)

GSI Diss 2009-05 M. Bussmann: Laser-cooled ion beams and strongly coupled plasmas for precision experiments (2008)

GSI Diss 2009-01 C. Oment: Kollimatorsystem zur Stabilisierung des dynamischen Restgasdruckes im Schwerionensynchrotron SIS18 (2008)

GSI Diss 2008-19 D. Severin:Study of the degradation process of polyimide induced by high energetic ion irradiation (2008)

GSI Diss 2008-18 S. A. Litvinov: Investigation of the Isochronous Mode of the Experimental Storage Ring (ESR) and the Collector Ring (CR). Decay Spectroscopy of Highly Charged Stored ^{140}Pr Ions at the FRS-ESR Facility (2008)

GSI Diss 2008-17 R. Cussons: A unified and microscopic approach to astrophysical nuclear reactions using fermionic molecular dynamics (2008)

GSI Diss 2008-16 Y. C. Pachmayer: Dielektronenpro-

duktion in $^{1}2C + {}^{1}2C$ Kollisionen bei 1 GeV pro Nukleon

GSI Diss 2008-15 G. Maero: Cooling of highly charged ions in a Penning trap for HITRAP (2008)

GSI Diss 2008-14 B. Zielbauer: Characterization and optimization of an X-Ray Laser for the spectroscopy of Li-like Heavy-Ions (2007)

GSI Diss 2008-13 K. Kezzar: Etude des effets de la masse et de l'isospin dans le processus de la multifragmentation (2008)

GSI Diss 2008-12 O. Chorniy: Measurement and interpretation of the bunched beam transfer function in SIS-18 with space charge (2008)

GSI Diss 2008-11 N. Lineva: Emission niederenergetischer Elektronen in Stößen von schweren Ionen mit Festkörpertargets (2008)

GSI Diss 2008-10 A. Parfenova: Linear and nonlinear Response Matrix and its application to the SIS18 synchrotron (2008)

GSI Diss 2008-09 S. M. Lang: Analyse der Elektronpaarproduktion im Stoystem Ar + KCI bei 1,76 AGeV (2008)

GSI Diss 2008-08 M. Sudol: Measurement of low-mass e^+e^- pair production in 2 AGeV C-C collisions with HADES (2007)

GSI Diss 2008-07 V. Gostishchev: Internal Target Effects in Ion Storage Rings with Beam Cooling (2008)

GSI Diss 2008-06 M. Deveaux: Development of fast and radiation hard Monolithic Active Pixel Sensors (MAPS) optimized for open charm messon detection with the CBM-vertex detector (2008)

GSI Diss 2008-05 A. M. Schmah: Produktion von Seltsamkeit in Ar+KCI Reaktionen bei 1.756 AGeV mit HADES (2008)

GSI Diss 2008-04 M. Rebisz: Alternative methods for heavy-ion therapy dosimetry (2008)

GSI Diss 2008-03 G. Du: A Calcium imaging setup at the single ion hit facility at GSI and its application to the investigation of Calcium response ti ion irradiation in mammalian cells (2008)

GSI Diss 2008-02 M. Bender: Untersuchung der Mechanismen Schwerioneninduizierter Desorption an Beschleunigerrelevanten Materialien (2008)

GSI Diss 2008-01 F. Riek: Mesonic and Isobar modes in matter (2007)

GSI Dipl 2008-14 M. Horcicka: Mehrfelderoptimierung für die biologisch effective Dosis in der Schwerionentherapie: nichtlineare Methoden und numerische Analyse (2008)

GSI Dipl 2008-13 M. Lorenz: Geladene Kaonen Produktion in Ar+KCI Reaktionen bei 1.756 AGeV (2008)

GSI Dipl 2008-12 P. Steidl: A new control system for the high-energy rasterscan facility at GSI and precision measurements of Bragg ionisation functions (2008)

GSI Dipl 2008-11 T. Mack: Der Maulwurf: Entwicklung und Fertigung eines komplexen Magnetmesssystems

GSI Dipl 2008-10 -

GSI Dipl 2008-09 E. Gütlich: Untersuchungen zu Leuchtschirmen für die Hochstrom-Strahlprofilmessung am UNILAC der GSI (2008)

GSI Dipl 2008-08 C. Smorra: Setup of a carbon-cluster laser ion source for high-pecision mass spectrometry

GSI Dipl 2008-07 S. Müller: Thermoelectric Properties of Bismuth Nanowires (2008)

GSI Dipl 2008-06 T. Fleckenstein: Unfluence of Mass Uncertainties of Exotic Nuclei on the rp- and vp- Process Model

GSI Dipl 2008-05 K. Reinheimer: Aufbau und Charakterisierung einer Ionenfalle fr ein Multireflexions-Flugzeitsprektrometer (2008)

GSI Dipl 2008-04 M. Nothhelfer: Aufbau und Test eines Frequenzkammerstabilisierten Lasersystems für die Spektroskopie an Berylliumionen in einer Paulfalle (2007)

GSI Dipl 2008-03 C. Halfpap: Aufbau und Inbetriebnahme eines heizbaren Targethalters zur Messung der NEG-Aktivierung mittels ERDA und von Diffusionssperren mittels RBS (2008)

GSI Dipl 2008-02 M. Wengenroth: Charakterisierung von kryogenen Sorptionsflächen im variablen Temperaturbereich zwischen 10-50 K für das SIS 100/300 (2008)

GSI Dipl 2008-01 G. Eitel: Aufbau eines ortsauflösenden Ionennachweisdetektors für die Penningfallen-Massenspektrometrie (2007)

GSI Master 2008-01 M. Fasel: Hadron Production in Proton-Proton Collisions (2008)

The ExtreMe Matter Institute EMMI at GSI

P. Braun-Munzinger[1,2,3] and C. Ewerz[1]

[1]ExtreMe Matter Institute EMMI, GSI, Darmstadt, Germany; [2]GSI, Darmstadt, Germany; [3]Technical University Darmstadt, Germany

The Helmholtz Alliance Program

In the framework of the Helmholtz Alliance program the Helmholtz Association offers financial and material resources to give their participating scientists and researchers opportunities to investigate new topics and to innovatively advance research topics of current interest. The alliances aim to strategically enhance the profiles of the participating Helmholtz Centres and to transfer successful developments into one of the Helmholtz Association's research programs.

The research performed within the Helmholtz Alliances is collaborative and brings universities, Helmholtz Centres and other non-university research institutions together. Foreign research partners and companies can also be integrated into these alliances. Each Helmholtz Alliance has its own management structure and specifically develops measures to promote young researchers and to implement equal opportunity. The alliance's budget is jointly financed by the Helmholtz President's Initiative and Networking Fund and the participating Helmholtz Centres and their partners.

The Helmholtz Alliance 'Cosmic Matter in the Laboratory'

In November 2007 the senate of the Helmholtz foundation decided to fund the Helmholtz Alliance 'Extremes of Density and Temperature: Cosmic Matter in the Laboratory'. The funding contribution from the Helmholtz Association amounts to 18.745 Mio. Euro for a funding period of 5 years.

The scientific aim of the Alliance is to perform forefront research in the area of matter under extreme conditions. This comprises in particular four key areas of the research field 'Structure of Matter' of the Helmholtz Association:

- quark-gluon matter
- neutron matter
- plasmas of high energy density
- extreme states in atomic physics.

The relevant science themes range from the quark-gluon plasma as it existed shortly after the Big Bang, to hot and highly compressed classical bulk plasmas, and to the astrophysically relevant dense medium of nucleons and neutrons that governs the properties of the evolution of supernovae and neutron stars. The key idea is to conduct this research in a really interdisciplinary framework, based upon common underlying concepts for the theoretical and phenomenological understanding of the physical phenomena in the four areas.

Under the lead management of the GSI Helmholtz Centre for Heavy Ion Research the Alliance links the following German and international research centers and universities as partner institutions:

- GSI Helmholtzzentrum für Schwerionenphysik, Darmstadt, Germany
- Forschungszentrum Jülich, Germany
- Ruprecht-Karls-Universität Heidelberg, Germany
- Johann Wolfgang Goethe Universität Frankfurt, Germany
- FIAS Frankfurt Institute for Advanced Studies, Germany
- Technische Universität Darmstadt, Germany
- Universität Münster, Germany
- Université VI, Paris, France
- Max-Planck-Institut für Kernphysik, Heidelberg, Germany
- Lawrence Berkeley National Laboratory, Berkeley, USA
- Joint Institute for Nuclear Astrophysics (JINA), USA
- RIKEN, Saitama, Japan
- University of Tokyo, Japan.

In addition, the Alliance benefits from the expertise of internationally renowned scientist who are closely linked to it as Associated Partners for the four research fields. Currently, the Alliance has 29 Associated Partners, among them two Nobel laureates.

The ExtreMe Matter Institute EMMI

An important part of the strategic positioning of the Helmholtz Alliance 'Cosmic matter in the Laboratory' is to establish a new, world-leading institute for research on matter at the extremes of density and temperature: the ExtreMe Matter Institute EMMI hosted by GSI.

The ExtreMe Matter Institute EMMI was founded on April 1st, 2008, when also the Helmholtz Alliance 'Cosmic Matter in the Laboratory' started. EMMI coordinates the Alliance and conducts research in all important areas of the Alliance. Contracts about the collaboration have been signed with all partner institutions which constitute the basis for the financial resources of EMMI and of the Alliance.

The partner institutions have committed themselves to creating 18 new professorships (tenure-track and tenure) in the framework of the Alliance, and the recruiting process for these positions has already started. Further, four expert groups will be established at GSI with tenure-track positions for the group leaders (EMMI Fellows) and further non-tenured positions. All four groups are expected to take up their research activities in 2009.

The central steering body of EMMI and of the Alliance is the Scientific Council, consisting of the EMMI Director, of

one representative from each partner institution, and of two representatives of the Associated Partners. The Scientific Council was constituted already in November 2007, and it elected P. Braun-Munzinger as the first Director of EMMI for a term of five years. The EMMI management consists, besides the Director, of an Administrative Director and a Scientific Coordinator.

A kick-off meeting with more than 150 participants from science, science administration and politics took place in July 2008 and found a good resonance in the media. The main focus of this meeting was on the new themes at the heart of the interdisciplinary approach to the investigation of matter under extreme conditions.

An important activity of the ExtreMe Matter Institute EMMI is to organize and to host workshops and research programs on topical and interdisciplinary subjects in the area of matter under extreme conditions. In 2008 several workshops took already place, most of them lasting for a few days. The EMMI research programs, on the other hand, aim at bringing together experts from at least two of the EMMI research areas for several weeks in order to create an environment for cross-disciplinary discussions and collaboration. It is intended to invite applications for support of EMMI workshops on a regular basis. A program advisory committee of external experts will support EMMI in the selections of workshop proposals.

Further, EMMI is strongly committed to fostering the education and training of young researchers through a postdoctoral research program and structured training of graduate students. This educational aspect will be realized in close collaboration with the university partner institutions and other graduate training programs, like for the example the Helmholtz Graduate School for Heavy-Ion Research (HGS-HIRe).

As a result of the discussions at the EMMI workshops in 2008 new ideas and research directions have already been developed. Some examples are

- the physics of strongly correlated quantum systems with emphasis on universal behavior in ultra-cold quantum gases, in the quark-gluon plasma, as well as in strongly coupled neutron matter as it occurs at the surface of neutron stars,
- the physics of phase transitions in electromagnetic plasmas and in the quark-gluon plasma, and their study using lattice gauge theory,
- a new approach to understanding atoms in supercritical electromagnetic fields.

Further exciting developments in the EMMI research areas will certainly be triggered by the advent of new experimental tools in the near future. Especially important will be for example the Large Hadron Collider (LHC) at CERN – here in particular the ALICE heavy-ion experiment – for the study of the quark-gluon plasma; intense rare isotope beams at GSI and the EMMI partner institutions in Japan and the United States which will allow one to investigate nuclear properties essential for the structure and dynamics of astrophysical objects and for the synthesis of the elements in the universe; the world-wide unique combination of highly compressed energetic bunches of heavy-ion beams as well as intense laser pulses from the petawatt laser PHELIX at GSI which can be used to drive and diagnose strongly coupled plasmas; ion traps and storage ring facilities at GSI and EMMI partner institutions at which one can study atomic interactions important for plasma ignition and processes in the interior of stars; and steadily improved experiments at the EMMI partner institutions for the study of ultra-cold quantum gases at which especially cross-disciplinary aspects of strongly coupled systems can be studied.

The new structures developed within EMMI provide a new and within Europe unique research infrastructure. It is therefore the explicit plan of GSI together with its partner institutions to establish EMMI as a permanent institute to foster interdisciplinary research on matter under extreme conditions.

Helmholtz Graduate School for Hadron and Ion Research "HGS-HIRe for FAIR"

H. Appelshäuser[1] and H. Büsching[1,2]

[1]Institut für Kernphysik, Goethe Universität, Frankfurt, Germany; [2]FIAS, Frankfurt, Germany

The new Helmholtz Graduate School for Hadron and Ion Research "HGS-HIRe for FAIR" officially started its activities in October 2008. HGS-HIRe is a joint endeavor of GSI, the universities of Darmstadt, Frankfurt, Giessen, Heidelberg and Mainz together with FIAS, Frankfurt, to promote and support structured PhD education for research associated with GSI and FAIR. The school is funded by the Initiative and Networking Fund of the Helmholtz Association (HGF).

New facilities and engagements as the major participation of GSI in the LHC heavy-ion program at CERN and the start of FAIR will give direction to the research in Hadron and Ion physics for the next decades. The operation of these large international facilities demands trained young researchers on a large scale. It was therefore seen mandatory to implement a dedicated structure for the recruitment and training of excellent young scientists in this research field to exploit the discovery potential of the upcoming facilities.

The investments are further augmented by a variety of recent projects to provide further intellectual and technical infrastructure for optimal use of the new facilities: In April 2008 the Helmholtz Alliance on the Physics of Cosmic Matter in the Laboratory and its "ExtreMe Matter Institute" (EMMI) started operation with twelve international institutions and many experts as associated partners. The newly founded Helmholtz International Center for FAIR (HIC for FAIR), aims to provide a platform to bundle activities in advanced simulations, experimental design and detector developments. Both initiatives will enhance the traditionally close ties with the surrounding universities which have pledged to make Hadron and Ion research a top priority in their research programs.

In a joint effort GSI together with its partner universities and institutions initiated a coherent framework for a structured education of PhD students working in the field of hadron and ion research relevant for GSI and FAIR: HGS-HIRe for FAIR. The Graduate School will bundle the existing structured programs of HIC for FAIR, EMMI, the Helmholtz Research School H-QM and structured PhD programs at the universities Giessen and Mainz. Coordination and integration of these activities into a network of competence will establish a sound basis for centre-wide structured PhD education, resting upon the principles of excellence and equal opportunities. Currently about 300 PhD students have been identified as potential participants, with a ratio of foreign PhD students of about 30%.

HGS-HIRe is one of six Graduate Schools in Germany funded by the HGF. Each Graduate School is supported for an initial period of six years with 3.6 million Euro by the Initiative and Networking Fund of the the President of the HGF. The partner schools are at MDC (Berlin), UFZ (Leipzig), AWI (Bremerhaven), DKFZ (Heidelberg) and HZI Braunschweig. HGS-HIRe is embedded in this network of Helmholtz Graduate Schools, allowing e.g. for the organization of common activities to promote interdisciplinary aspects of PhD education.

In difference to a Research School ('Graduiertenkolleg') HGS-HIRe is covering a broader area of scientific topics and is predominant responsible to create the necessary structures and procedures to allow the scientific partner institutions and scientists to realize new educational approaches.

The School aims at the preparation of young scientists for a future career in basic or applied research, in research management or industry. It will develop the synergies resulting from the different experiences and knowledge of the participating scientists to create new concepts for graduate education. These imply modular elements of specialized lectures and workshops as well as cross-disciplinary courses and soft-skill education. PhD students in the school shall participate in these activities on a regular basis.

Specific measures are foreseen to guide the students to an efficient time management and a solid scientific achievement of their thesis work. PhD committees will accompany the students during the project and external mentors will provide guidance if deemed necessary.

The School aims to increase the educational level of the students, establish common standards, facilitate organization processes, unify recruitment procedures, and enhance social integration. The educational measures at HGS-HIRe will be complementary to the teaching programs offered at the participating universities, often with focus on interdisciplinary aspects.

The school is run by a Spokesperson, Prof. Dr. Harald Appelshäuser, a Managing Director, Dr. Henner Büsching, and a Scientific Coordinator, Dr. Gerhard Burau. In October 2008 the recruiting of participants of the school was started and groundwork was laid to integrate activities at the partner universities, institutions and programs. The start of the academic training is planed for January 2009. Further information about the school can be found at www.hgs-hire.de.

EU projects at GSI in 2008

Compiled by R. Simon, I. Reinhard, K. Große

FAIR Design Study 'DIRACsecondary-Beams'/FP6 (515873)
<http://www.gsi.de/fair/EU-Design-Study/index.html>
Coordinator: GSI, Darmstadt (Germany)
Project coordinator: J. Eschke
Steering committee: J. Eschke (GSI, chair), H. H. Gutbrod (GSI), W. F. Henning/H. Stöcker (GSI), P. Gianotti (Frascati), R. Krücken (München), R. Maier (FZJ), B. Franzke (GSI), D. Krämer (GSI)
Contact at GSI: J. Eschke, K. Berghöfer, F. Weißbach

Contributions in this report:
FAIR-ACCELERATORS-01
FAIR-ACCELERATORS-02
FAIR-ACCELERATORS-04
FAIR-ACCELERATORS-10
FAIR-ACCELERATORS-11
FAIR-ACCELERATORS-13
FAIR-ACCELERATORS-16
FAIR-EXPERIMENTS-28
FAIR-EXPERIMENTS-35
FAIR-EXPERIMENTS-37
GSI-ACCELERATORS-12
INSTRUMENTS-METHODS-43

FAIR Construction 'DIRAC-PHASE 1'/FP6 (515876)
<http://www.gsi.de/fair/EU-Construction/index.html>
Coordinator: GSI, Darmstadt (Germany)
Project coordinator: J. Eschke
Steering committee: J. Eschke (GSI, chair), H. H. Gutbrod (GSI), W. F. Henning/H. Stöcker (GSI), H. Eickhoff (GSI), J.-E. Ducret (CEA), H. Ströbele (U-Frankfurt/M.)
Contact at GSI: J. Eschke, K. Berghöfer, F. Weißbach

Contribution in this report:
FAIR-ACCELERATORS-18
GSI-ACCELERATORS-13
GSI-ACCELERATORS-14
GSI-ACCELERATORS-15
GSI-ACCELERATORS-16
INSTRUMENTS-METHODS-30
NQMA-EXPERIMENTS-07

HADRONPHYSICS/FP6 (RII3-CT-2004-506078)
<http://hadronphysics.infn.it/>
Coordinator: INFN Frascati (Italy)
Project coordinator: C. Guaraldo (LNF-INFN)
Management board: M. Anselmino (INFN), B. Erazmus (CNRS/IN2P3), M. Garcon (CEA), T. Johansson (Univ. Uppsala), H. Koch (Univ. Bochum), L. Riccati (INFN), G. Rosner (Univ. Glasgow), P. Senger (GSI)
Project coordinator at GSI: R. Simon
Finished in December 2008.

Contributions in this report:
FAIR-EXPERIMENTS-03
FAIR-EXPERIMENTS-04
FAIR-EXPERIMENTS-05
FAIR-EXPERIMENTS-06
FAIR-EXPERIMENTS-07
FAIR-EXPERIMENTS-08
FAIR-EXPERIMENTS-09
FAIR-EXPERIMENTS-10
FAIR-EXPERIMENTS-11
FAIR-EXPERIMENTS-12
FAIR-EXPERIMENTS-14
FAIR-EXPERIMENTS-15
FAIR-EXPERIMENTS-17
FAIR-EXPERIMENTS-18
NQMA-THEORY-01
INSTRUMENTS-METHODS-02
INSTRUMENTS-METHODS-17
INSTRUMENTS-METHODS-22
INSTRUMENTS-METHODS-23
INSTRUMENTS-METHODS-24
INSTRUMENTS-METHODS-26
INSTRUMENTS-METHODS-37
INSTRUMENTS-METHODS-40
INSTRUMENTS-METHODS-41

EURONS/FP6 (RII3-CT-2004-506065)
<http://www.gsi.de/informationen/jofu/EURONS/>
Coordinator: GSI, Darmstadt (Germany)
Project coordinator: A. C. Müller (IN2P3-IPNO), C. Scheidenberger (GSI, deputy coordinator)
Executive board: P. Butler (CERN), P. Van Duppen (U- Leuven), K.-D. Groß (GSI), S. Harissopoulos (NCSR Demokritos), R. Julin (Univ. Jyväskylä), S. Lenzi (INFN Padova)
Contact at GSI: I. Reinhard; M. Pantea

Contributions in this report:
FAIR-ACCELERATORS-30
FAIR-EXPERIMENTS-19
FAIR-EXPERIMENTS-20
FAIR-EXPERIMENTS-21
FAIR-EXPERIMENTS-22
FAIR-EXPERIMENTS-27
FAIR-EXPERIMENTS-30
GSI-ACCELERATORS-08
NUSTAR-EXPERIMENTS-06
NUSTAR-EXPERIMENTS-07
NUSTAR-EXPERIMENTS-08
NUSTAR-EXPERIMENTS-09
NUSTAR-EXPERIMENTS-11
NUSTAR-EXPERIMENTS-12
NUSTAR-EXPERIMENTS-13
NUSTAR-EXPERIMENTS-14

NUSTAR-EXPERIMENTS-16
NUSTAR-EXPERIMENTS-19
ATOMIC-PHYSICS-01
ATOMIC-PHYSICS-03
ATOMIC-PHYSICS-05
ATOMIC-PHYSICS-12
ATOMIC-PHYSICS-13
ATOMIC-PHYSICS-14
ATOMIC-PHYSICS-20
ATOMIC-PHYSICS-23
RADIATION-BIOPHYSICS-18
RADIATION-BIOPHYSICS-19

CARE/FP6 (RII3-CT-2003-506395)
<http://esgard.lal.in2p3.fr/Project/Activities/Current/>
Coordinator: CEA Saclay (France)
Project coordinator: R. Aleksan (CEA)
Project coordinator at GSI: H. Eickhoff
Contact at GSI: L. Groening

Contributions in this report:
FAIR-ACCELERATORS-05
FAIR-ACCELERATORS-24
GSI-ACCELERATORS-11

EGEE/FP6 (INFSO-RI-508833)
<http://public.eu-egee.org/>
Coordinator: CERN (Switzerland)
Project coordinator: B. Jones (CERN), D. Kranzlmüller (CERN)
Project coordinator at GSI: P. Malzacher
Contact at GSI: P. Malzacher

Contributions in this report:
INSTRUMENTS-METHODS-14

Laserlab/FP6 (RII3-CT-2003-506350)
<http://www.laserlab-europe.net>
Coordinator: Forschungsverbund Berlin (Germany)
Project coordinator: W. Sandner (Berlin)
Project coordinator at GSI: T. Kühl
Contact at GSI: T. Kühl

Contributions in this report:
PLPY-PHELIX-19
PLPY-PHELIX-20
PLPY-PHELIX-21
PLPY-PHELIX-22

EUROTeV/FP6 (011899 RIDS)
<http://www.eurotev.org>
Coordinator: DESY, Hamburg (Germany)
Project coordinator: E. Elsen (DESY)
Project coordinator at GSI: H. Eickhoff
Contact at GSI: P. Schütt

Cellion/FP6 (MRTN-CT-2003-503923)
Network of Excellence
<http://cellion.ifj.edu.pl>
Project coordinator: Z. Stachura (PAN)
Contact at GSI: B. Fischer
Contribution in this report:
RADIATION-BIOPHYSICS-03

EURISOL-Design Study/FP6 (515768 RIDS)
<http://www.eurisol.org>
Coordinator: INFN-LNL (Italy)
Project coordinator: Y. Blumenfeld (IPN-Orsay)
Project coordinator at GSI: K.-H. Schmidt
Contact at GSI: A. Kelic

Contributions in this report:
GSI-ACCELERATORS-17
ATOMIC-PHYSICS-17

EUROTRANS/FP6 (516520 F16W)
<http://nuclear-server.fzk.de/eurotrans/>
Coordinator: FZK, Karlsruhe (Germany)
Project coordinator: J. U. Knebel (NUCLEAR)
Project coordinator at GSI: K.-H. Schmidt
Contact at GSI: A. Kelic

FAIR-PP/FP7 (211382)
Coordinator: GSI, Darmstadt (Germany)
Project Coordinator: J. Eschke
Contact at GSI: J. Eschke

Spiral2-PP/FP7 (212692)
Coordinator: GANIL, Cean (France)
Project Coordinator: Lewitowicz
Project Coordinator at GSI: J. Gerl
Contact at GSI: J. Gerl

HiPER/FP7 (211737)
Coordinator: STFC (UK)
Project Coordinator: M. Dunne
Project Coordinator at GSI: K. Witte
Contact at GSI: K. Witte

SLHC-PP/FP7 (212114)
Coordinator: CERN, Geneva (Switzerland)
Project Coordinator: L. Evans
Project Coordinator at GSI: G. Fehrenbacher
Contact at GSI: G. Fehrenbacher

EGEE III/FP7 (222667)
Coordinator: CERN, Geneva (Switzerland)
Project Coordinator: B. Jones
Project Coordinator at GSI: P. Malzacher
Contact at GSI: P. Malzacher

NuPNET/FP7 (202914)
Coordinator: CNRS (France)
Project Coordinator: S. Gales
Project Coordinator at GSI: I. Reinhard
Contact at GSI: I. Reinhard

MC-PAD/FP7 (214560)
Coordinator: CERN, Geneva (Switzerland)

Project Coordinator: C. Joram
Project Coordinator at GSI: C. Schmidt
Contact at GSI: C. Schmidt

(MC-)DITANET/FP7 (215080)
Coordinator: KPI Heidelberg (Germany)
Project Coordinator: C. Welsch
Project Coordinator at GSI: P. Forck
Contact at GSI: P. Forck

Contributions to other EU projects:
FAIR-ACCELERATORS-29
FAIR-EXPERIMENTS-23
FAIR-EXPERIMENTS-24
NUSTAR-EXPERIMENTS-17
NQMA-THEORY-10
NQMA-THEORY-17
INSTRUMENTS-METHODS-39
RADIATION-BIOPHYSICS-33

GSI Projektträger / KKS

D. Müller / I. Reinhard

Projektträger des Bundesministeriums für Bildung und Forschung (BMBF)

GSI is the managing institution for the BMBF project funding (so called "Verbundforschung") in the field of "Hadron- and Nuclear Physics". These public funds are foreseen to support research groups at universities in Germany to strengthen their ability to participate in experiments and projects performed at scientific institutions like GSI and CERN which are funded to a significant level from federal resources.

BMBF project funding: 111 running projects with a total budget of 48,6 Mio. € (18,0 Mio. € in 2008).

GSI F&E contracts ("Forschungs- und Entwicklungsvereinbarungen")

Since 1969 GSI has special research and development contracts with German universities to strengthen the collaboration between these universities and GSI. Mainly resources for personnel are provided to enhance the participation of PhD students and young Post-Docs within GSI projects.

GSI F&E Contracts: 100 running projects with a total budget of 12,9 Mio. € (4,4 Mio. € in 2008).

Helmholtz Association "Initiative and Networking Fund (IVF)"

This fund is one of the Helmholtz Association's key instruments in achieving its strategic goals in Research and Innovation. It consists mainly of "Helmholtz Virtual Institutes" (Networks between GSI and University groups) and a programm to promote Young Researchers.

GSI-HGF-IVF: 7 running projects with a total budget of 5,9 Mio. € (1,2 Mio. € in 2008).

EU Framework Programm 6, EURONS

GSI is the managing institution for the European Integrated Infrastructure Initiative (I3) in nuclear structure physics (EURONS). It consists of 45 institutions in 21 countries.

EURONS: 27 projects with a total budget of 14,0 Mio. € (3,6 Mio. € in 2008).

International and national collaborations *

Compiled by K. Große

The FAIR Collaborations

FAIR: The BIOMAT Collaboration

The High-Energy Irradiation Facility for Biophysics and Materials Research
Spokespersons: M. Durante, Naples (Italy)/Darmstadt (Germany); S. Klaumünzer, Berlin (Germany)

Contributions in this report:
FAIR-EXPERIMENTS-34

FAIR: The CBM Collaboration

The Condensed Baryonic Matter experiment
<http://www.gsi.de/zukunftsprojekt/experimente/CBM/index_e.html>
Spokesperson: P. Senger Darmstadt (Germany)

Contributions in this report:
FAIR-EXPERIMENTS-06
FAIR-EXPERIMENTS-07
FAIR-EXPERIMENTS-08
FAIR-EXPERIMENTS-09
FAIR-EXPERIMENTS-10
FAIR-EXPERIMENTS-11
FAIR-EXPERIMENTS-12
FAIR-EXPERIMENTS-13
FAIR-EXPERIMENTS-14
FAIR-EXPERIMENTS-15
FAIR-EXPERIMENTS-16
FAIR-EXPERIMENTS-17
FAIR-EXPERIMENTS-18
INSTRUMENTS-METHODS-16
INSTRUMENTS-METHODS-26
INSTRUMENTS-METHODS-40
INSTRUMENTS-METHODS-41

FAIR: The FLAIR Collaboration

A Facility for Low-energy Antiproton and Ion Research
< http://www-linux.gsi.de/∼flair/>
Spokesperson: E. Widmann (Austria)

Contributions in this report:
FAIR-EXPERIMENTS-32

FAIR: The HEDgeHOB Collaboration

High Energy Density Matter generated by Heavy iOn Beams
<http://hedgehob.physik.tu-darmstadt.de>
Spokesperson: Hoffmann, D. H. H., Darmstadt (Germany)

Contributions in this report:
PLPY-PHELIX-09
PLPY-PHELIX-11
PLPY-PHELIX-12
PLPY-PHELIX-14

The PANDA Collaboration

<http://www.ep1.rub.de/∼panda/auto/_home.htm>
Spokesperson: U. Wiedner, Uppsala (Sweden)
Contributions in this report:

FAIR-EXPERIMENTS-02
FAIR-EXPERIMENTS-03
FAIR-EXPERIMENTS-04
FAIR-EXPERIMENTS-05
INSTRUMENTS-METHODS-23
INSTRUMENTS-METHODS-42
INSTRUMENTS-METHODS-43

FAIR: The NUSTAR Collaboration

International Nuclear Structure and Astrophysics Community GSI
<http://www.gsi.de/forschung/kp/kp2/nustar.html>

As part of FAIR-NUSTAR: The DESPEC Collaboration

Decay Spectroscopy
Spokesperson: B. Rubio, Valencia (Spain)
Contributions in this report:
FAIR-EXPERIMENTS-26
FAIR-EXPERIMENTS-27
FAIR-EXPERIMENTS-29

As part of FAIR-NUSTAR: The HISPEC Collaboration

High resolution Spectroscopy
Spokesperson: Z. Podolyak, Surrey (United Kingdom)
Contributions in this report:
FAIR-EXPERIMENTS-25
FAIR-EXPERIMENTS-28

* Only listed are colloborations contributed to this report.

As part of FAIR-NUSTAR: The R^{3}B Collaboration

Reactions with Relativistic Radioactive Beams
<http://www-land.gsi.de/r3b/>
Spokesperson: T. Aumann Darmstadt (Germany)
Contributions in this report:
FAIR-EXPERIMENTS-19
FAIR-EXPERIMENTS-20
FAIR-EXPERIMENTS-21
FAIR-EXPERIMENTS-22

As part of FAIR-NUSTAR: The ELISe Collaboration

ELectron-Ion Scattering in a Storage Ring (eA collider)
<http://www.gsi.de/zukunftsprojekt/experimente/elise/>
Spokesperson: H. Simon, Darmstadt (Germany)
Contribution in this report:
FAIR-EXPERIMENTS-23
FAIR-EXPERIMENTS-24

As part of FAIR-NUSTAR: The EXL Collaboration

Exotic nuclei studied in light-ion induced reactions at the NESR storage ring
<http://ns.ph.liv.ac.uk/∼mc/EXL/collaboration/EXL-collaboration.html>
Spokesperson: M. Chartier, Liverpool (United Kingdom)
Contributions in this report:
FAIR-EXPERIMENTS-30
FAIR-EXPERIMENTS-31

As part of FAIR-NUSTAR: The LEB Collaboration

Low Energy Branch
Spokesperson: C. Scheidenberger, Darmstadt (Germany)
Contributions in this report:
FAIR-ACCELERATORS-11
FAIR-EXPERIMENTS-35
FAIR-EXPERIMENTS-36

FAIR: The SPARC Collaboration

Stored Particles Atomic Physics Collaboration
<http://www.gsi.de/zukunftsprojekt/experimente/sparc/index_e.html>
Spokesperson: R. Schuch, Stockholm (Sweden)

Contributions in this report:
ATOMIC-PHYSICS-19
ATOMIC-PHYSICS-26

FAIR: The WDM Collaboration

Radiative Properties of Warm Dense Matter Produced by Intense Heavy Ion Beams
<http://www.gsi.de/phelix/Experiments/FAIR/WDM/index.html>
Spokesperson: F. B. Rosmej

Contributions in this report:
FAIR-EXPERIMENTS-33

FAIR: The Super-FRS Collaboration

Contributions in this report:

FAIR-ACCELERATORS-10
INSTRUMENTS-METHODS-06
INSTRUMENTS-METHODS-07
INSTRUMENTS-METHODS-08
INSTRUMENTS-METHODS-09

FAIR: The HypHI Collaboration

<http://www.gsi.de/forschung/helmholtz-group/HYPERNuclei>
Spokesperson: T. R. Saito, GSI

Contributions in this report:
FAIR-EXPERIMENTS-49
FAIR-EXPERIMENTS-50
FAIR-EXPERIMENTS-51

The SIS/ESR/UNILAC Collaborations

FAIR: The CHARMS Collaboration

Collaboration for High-Accuracy Experiments on Nuclear Reaction Mechanisms with magnetic Spectrometers
<http://www.gsi.de/charms/>
Spokesperson: Karl-Heinz Schmidt, GSI

Contributions in this report:
NUSTAR-EXPERIMENTS-17
NUSTAR-EXPERIMENTS-18
NUSTAR-EXPERIMENTS-20
NUSTAR-THEORY-11

The FOPI Collaboration

4π Detector System for Charged Particles
<http://www-fopi.gsi.de/>
Spokesperson: N. Herrmann, Heidelberg (Germany)

Contributions in this report:
INSTRUMENTS-METHODS-24
INSTRUMENTS-METHODS-25
NQMA-EXPERIMENTS-05
NQMA-EXPERIMENTS-06

The HADES Collaboration

<http://www-hades.gsi.de>
Spokesperson: P. Salabura

Contributions in this report:
INSTRUMENTS-METHODS-30
NQMA-EXPERIMENTS-07

The HITRAP Collaboration

HITRAP - A Facility for Experiments with Heavy Highly Charged Ions and Antiprotons
< http://www.gsi.de/forschung/ap/projects/hitrap/index.html>
Technical Coordinator: O. Kester (GSI), Scientific Coordinator: W. Quint (GSI)

Contributions in this report:
ATOMIC-PHYSICS-15
ATOMIC-PHYSICS-16
ATOMIC-PHYSICS-18
ATOMIC-PHYSICS-24
ATOMIC-PHYSICS-25
ATOMIC-PHYSICS-30
GSI-ACCELERATORS-10

The PHELIX Collaboration

Petawatt High-Energy Laser for Heavy Ion Experiments
<http://www.gsi.de/forschung/phelix>
Spokesperson: K. Witte (GSI)

Contributions in this report:
ATOMIC-PHYSICS-28
PLPY-PHELIX-15
PLPY-PHELIX-16
PLPY-PHELIX-17
PLPY-PHELIX-19
PLPY-PHELIX-21
PLPY-PHELIX-27

The NoRDia Collaboration

Novel Radiation Hard CVD Diamond Detectors for Hadron Physics
<http://www-norhdia.gsi.de>
Cordinator at GSI: E. Berdermann.

Contributions in this report:
INSTRUMENTS-METHODS-02
INSTRUMENTS-METHODS-03

The RISING Collaboration

<http://www-linux.gsi.de/EB_at_GSI/index.html>
Spokesperson: H.-J. Wollersheim, GSI, Darmstadt (Germany)
Contributions in this report:
NUSTAR-EXPERIMENTS-06
NUSTAR-EXPERIMENTS-07
NUSTAR-EXPERIMENTS-08
NUSTAR-EXPERIMENTS-10
NUSTAR-EXPERIMENTS-11
NUSTAR-EXPERIMENTS-12
NUSTAR-EXPERIMENTS-13
NUSTAR-EXPERIMENTS-14

The SHIP Collaboration

Separator for Heavy Ion reaction Products
<http:/www.gsi.de/forschung/kp/kp2/ship/>
Spokesperson: S. Hofmann, GSI Contributions in this report:
NUSTAR-SHE-01
NUSTAR-SHE-02
NUSTAR-SHE-03
NUSTAR-SHE-04
NUSTAR-SHE-05

The SHIPTRAP Collaboration

<http://www.gsi.de/forschung/ap/projects/shiptrap/>
Spokesperson: F. Herfurth, Darmstadt (Germany)
Contributions in this report:
ATOMIC-PHYSICS-12
ATOMIC-PHYSICS-23

The TASCA Collaboration

Transactinide Separator and Chemistry Apparatus
<http://www.gsi.de/tasca/>
Spokesperson: M. Schädel, GSI

Contributions in this report:
NUSTAR-SHE-09
NUSTAR-SHE-10
NUSTAR-SHE-11
NUSTAR-SHE-12
INSTRUMENTS-METHODS-05

Other collaborations e. g. at external institutions

The ALICE Collaboration

A Large Ion Collider Experiment at CERN LHC
<http://alice.web.cern.ch/Alice/AliceNew/collaboration/>
Leader at the GSI: P. Braun-Munzinger

Contributions in this report:
NQMA-EXPERIMENTS-14
NQMA-EXPERIMENTS-15
INSTRUMENTS-METHODS-31
INSTRUMENTS-METHODS-32
INSTRUMENTS-METHODS-33

The ALICE TRD Collaboration

The Transition Radiation Detector of the ALICE experiment at LHC
<http://www-alice.gsi.de/trd>
Project leader: J. Stachel, Heidelberg (Germany)
Contributions in this report:
INSTRUMENTS-METHODS-34
INSTRUMENTS-METHODS-35
INSTRUMENTS-METHODS-36
INSTRUMENTS-METHODS-38
INSTRUMENTS-METHODS-39

The CERES Collaboration

Cherenkov Ring Electron Pair Spectrometer at the CERN SPS
<http://www.physi.uni-heidelberg.de/physi/ceres/>
Spokesperson: J. Stachel, Heidelberg (Germany)

Contributions in this report:
NQMA-EXPERIMENTS-08
NQMA-EXPERIMENTS-09
NQMA-EXPERIMENTS-10

The NA49 Collaboration

Large Acceptance Hadron Detector for an Investigation of Pb-induced Reactions at the CERN SPS
<http://na49info.cern.ch/>
Spokesperson: P. Seyboth

Contributions in this report:
NQMA-EXPERIMENTS-11
NQMA-EXPERIMENTS-12
NQMA-EXPERIMENTS-13
NQMA-EXPERIMENTS-16

The ISOLTRAP Collaboration

<http://isoltrap.web.cern.ch/isoltrap>

Contributions in this report:
ATOMIC-PHYSICS-13
ATOMIC-PHYSICS-14

Other collaborations:

FAIR-ACCELERATORS-29
NUSTAR-EXPERIMENTS-09
NUSTAR-EXPERIMENTS-19
INSTRUMENTS-METHODS-22
INSTRUMENTS-METHODS-27
INSTRUMENTS-METHODS-29
MATERIALS-14
MATERIALS-23
RADIATION-BIOPHYSICS-02
RADIATION-BIOPHYSICS-23

Connections between contributions to this report and experiment numbers at the GSI accelerators

Bio07 RADIATION-BIOPHYSICS-04
Bio13 RADIATION-BIOPHYSICS-15
Bio14 RADIATION-BIOPHYSICS-12
Bio14 RADIATION-BIOPHYSICS-14
Bio14 RADIATION-BIOPHYSICS-17
Bio14 RADIATION-BIOPHYSICS-20
Bio16 RADIATION-BIOPHYSICS-03
E039 ATOMIC-PHYSICS-03
E045 ATOMIC-PHYSICS-06
E065 ATOMIC-PHYSICS-07
E067 ATOMIC-PHYSICS-02
E069 ATOMIC-PHYSICS-09
E069 ATOMIC-PHYSICS-10
E070 ATOMIC-PHYSICS-01
E070 ATOMIC-PHYSICS-08
E075 ATOMIC-PHYSICS-15
P008 PLPY-PHELIX-22
R240 NUSTAR-SHE-05
S139 INSTRUMENTS-METHODS-28
S184 NUSTAR-EXPERIMENTS-17
S185 NQMA-EXPERIMENTS-02
S227 NUSTAR-EXPERIMENTS-03
S244 NUSTAR-EXPERIMENTS-06
S244 NUSTAR-EXPERIMENTS-07
S244 NUSTAR-EXPERIMENTS-10
S244a NUSTAR-EXPERIMENTS-08
S248 NUSTAR-EXPERIMENTS-19
S254 NQMA-EXPERIMENTS-01
S254 NQMA-EXPERIMENTS-03
S258 FAIR-EXPERIMENTS-36
S261 NQMA-EXPERIMENTS-05
S271 NUSTAR-EXPERIMENTS-16
S280 INSTRUMENTS-METHODS-02
S286 INSTRUMENTS-METHODS-37
S291 FAIR-ACCELERATORS-29
S299 NUSTAR-EXPERIMENTS-12
S305 NUSTAR-EXPERIMENTS-09
S310 NUSTAR-EXPERIMENTS-13
S311 NUSTAR-EXPERIMENTS-11
S311 NUSTAR-EXPERIMENTS-14
S319 INSTRUMENTS-METHODS-27
S319 INSTRUMENTS-METHODS-29
S319 NUSTAR-EXPERIMENTS-21
S319 NUSTAR-EXPERIMENTS-22
S328 FAIR-EXPERIMENTS-20
SBio01 RADIATION-BIOPHYSICS-21
SBio08 RADIATION-BIOPHYSICS-26
SBio09 RADIATION-BIOPHYSICS-19
SITH EXTERNAL-HIT-08
SITH RADIATION-BIOPHYSICS-28
STHE RADIATION-BIOPHYSICS-30
STHE RADIATION-BIOPHYSICS-35
U165 ATOMIC-PHYSICS-11
U197 NUSTAR-EXPERIMENTS-05
U205 NUSTAR-SHE-06
U205 NUSTAR-SHE-07
U210 NUSTAR-SHE-08
U215 NUSTAR-SHE-04
U217 ATOMIC-PHYSICS-12
U219 NUSTAR-SHE-09
U219 NUSTAR-SHE-10
U219 NUSTAR-SHE-11
U219 NUSTAR-SHE-12
U224 PLPY-PHELIX-07
U224 PLPY-PHELIX-08
U225 NUSTAR-SHE-03
U226 PLPY-PHELIX-03
UMAT MATERIALS-24
OTHERS ATOMIC-PHYSICS-17
OTHERS RADIATION-BIOPHYSICS-10
OTHERS NQMA-EXPERIMENTS-07

Workshops, meetings, seminars and talks at the GSI in 2008

Compiled by K. Große

Andreas Schäfer/Universität Regensburg: **The Structure of Hadrons.** GSI Kolloquium, 15.01.2008.

D. Schardt, GSI Darmstadt: **Applications of High-energy Ion Beams in Space Research.** Atomphysik-Seminar, 16.01.2008.

P. Schnizer, GSI, B. Schnizer, TU Graz: **Magnetic Field Characterization in Elliptic Apertures and Application to SIS100 Magnets.** Beschleuniger-Palaver, 17.01.2008.

C. Schacht, Fa Swipe, Nürnberg: **E-Mail-Archivierung mit Exchange(et)PAM.** IT/EE-Palaver, 22.01.2008.

Roland Sauerbrey/Forschungszentrum Rossendorf: **Laser-Particle-Acceleration.** GSI Kolloquium, 22.01.2008.

C. Novotny, Universität Mainz: **Doppler-free spectroscopy of Lithium ions with 34% of the speed of light.** Atomphysik-Seminar, 23.01.2008.

Yuri Litvinov, GSI: **Recent decay studies in the ESR.** NuSTAR Seminar, 23.01.2008.

Volker Metag/Universität Gießen: **Testing our understanding of hadron masses.** GSI Kolloquium, 29.01.2008.

C. Hanhart, Jülich: **A method to identify hadronic molecules and its application to X(3872).** Theorie-Seminar, 30.01.2008.

Horst Stöcker: **Das kleine schwarze Loch - Abfalleimer und Energielieferant.** Wissenschaft für Alle, 30.01.2008.

U. Schramm, FZ Dresden-Rossendorf: **Momentum Control of Charged Particles with Light.** Atomphysik-Seminar, 30.01.2008.

NUSTAR Annual Meeting. 30.01-01.02.2008.

Rajendran Raja, Fermilab: **The MIPP Experiment - Status and Upgrade plans.** Sonderseminar, 02.02.2008.

CS Framework HandsOn-Training. 04.02-20.00.2008.

P. Thirolf, LMU München: **Particle acceleration by high power lasers: A novel tool for fundamental physics studies in the ultrahigh-field regime.** Atomphysik-Seminar, 06.02.2008.

CS Framework Workshop 2008. 07.-08.02.2008.

N. A. Tahir, GSI: **Summary and Highlights of the 28th HIRSCHEGG Workshop on High Energy Density Physics.** Physik dichter Plasmen mit Schwerionen- und Laserstrahlen, 12.02.2008.

R. O. Erhardt, Firma Diginet: **Appliance-Lösungen zur E-Mail-Archivierung mit den Produkten BytStorMail und E-Mail Archive Appliance, EMA.** IT/EE-Palaver, 12.02.2008.

Y. Litvinov and F. Bosch, GSI Darmstadt: **Observation of non-exponential orbital electron capture of hydrogen-like ^{140}Pr and ^{142}Pm ions.** Atomphysik-Seminar, 13.02.2008.

Alexander Volkov, Russian Research Centre 'Kurchatov Institute', Moscow: **Thermal spike models of material excitation in swift heavy ion tracks. Effect of experiments made in GSI.** Seminar der Materialforschung, 18.02.2008.

W. Schön: **Das Lustre Filesystem bei GSI.** IT/EE-Palaver, 19.02.2008.

Andrea Accomazzo, ESOC: **Rosetta: trip to a comet.** NuSTAR Seminar, 20.02.2008.

Christoph Bert: **Bestrahlung von bewegten Tumoren - Weiterentwicklung der Schwerionentherapie.** Wissenschaft für Alle, 20.02.2008.

XI CBM Collaboration Meeting. 26.-29.02.2008.

XI Collaboration Meeting of CBM Experiment at FAIR. 26.-29.02.2008.

Leonid Grigorenko, JINR-Dubna: **New vision of ^{8,9,10}He spectra - theory and experiment.** NuSTAR Seminar, 27.02.2008.

Petra Schütt: **Remote Trouble Shooting with GANMVL.** Beschleuniger-Palaver, 28.02.2008.

H. Pant, Bhabha Atomic Research Centre Bombay: **Laser-induced Shock Pressure Multiplication in Multi-Layer Thin-Foil Targets.** Physik dichter Plasmen mit Schwerionen- und Laserstrahlen, 9.02.2008.

Jens Schwarz, Matthias Geissel: **Sandia's Z-Backlighter Facility update and recent experiments with the 100TW laser system.** Physik dichter Plasmen mit Schwerionen- und Laserstrahlen, 03.03.2008.

XXIV. PANDA Collaboration Meeting. 03.-07.03.2008.

Dietrich Beck, GSI: **Neues vom CS-Framework.** IT/EE-Palaver, 11.03.2008.

Leonid Dubrovinsky, Bayerisches Geoinstitut, Universität Bayreuth: **Chemistry at extreme conditions: from geosciences to synthesis of new materials.** Seminar der Materialforschung, 11.03.2008.

Sebastian Hess: **Beschleuniger im Himmel und auf Er-**

den - oder: Verbotene Farben - wie das Nebulium zu seinem Namen kam. Wissenschaft für Alle, 16.03.2008.

Workshop on Strangeness at SIS Energies. 17.03.2008.

Ralf Rosenberger, Fa. Additive: **Mathematica 6: Mathematica Reinvented.** IT/EE-Palaver, 18.03.2008.

Charles Rhodes, University of Illinois, Chicago: **Power scaling optimization of 2.9 angstrom Xe (L) x-ray amplifier to the multi-petawatt level.** Physik dichter Plasmen mit Schwerionen- und Laserstrahlen, 28.03.2008.

Hideyuki Sakai, University of Tokyo: **Study of the intermediate states of double-beta decay via (p,n) and (n,p) reactions.** Sonderseminar, 31.03.2008.

Michael Schreckenberg/Universität Duisburg-Essen: **Phenomena and Theory of Traffic Dynamics.** GSI Kolloquium, 01.04.2008.

Stefan Typel, GSI a. TU München: **Pseudospin, supersymmetry and the shell structure of atomic nuclei.** NuSTAR Seminar, 02.04.2008.

Gerhard Materlik/Diamond House, UK: **Diamond Light Source: a Next Generation Synchrotron User Facility.** GSI Kolloquium, 04.04.2008.

V. T. Tikhonchuk, Centre Lasers Intenses et Applications, Universit Bordeaux 1, CEA, CNRS, Talence, France: **Smoothing of laser beam intensity fluctuations in a low density foam plasma.** Physik dichter Plasmen mit Schwerionen- und Laserstrahlen, 08.04.2008.

Saidur Rahaman, University of Jyväskylä: **The JYFLTRAP facility for accurate mass and Q-value determinations.** NuSTAR Seminar, 10.04.2008.

Ionenstrahlphysik und Nanotechnologie GSI-Workshop. 11.-12.04.2008.

Dimitri Batani, Universita di Milano Bicocca, Milano, Italy: **Smoothing of laser energy deposition for Inertial Confinement Fusion.** Physik dichter Plasmen mit Schwerionen- und Laserstrahlen, 15.04.2008.

Dominique Vernhet/Universite Pierre et Marie Curie, Paris: **Converting laser light to x-rays using clusters.** GSI Kolloquium, 15.04.2008.

Ralf Rosenberger, Fa. Additive: **Origin 8: Der Datenanalyse- und Graphik-Workspace.** IT/EE-Palaver, 15.04.2008.

Jens Stadlmann: **Das Heer der Ringe - die FAIR-Beschleunigeranlage.** Wissenschaft für Alle, 16.04.2008.

Julia H. Jungmann, RuG / KVI: **Simplified Optimal Digital Trigger - with guidelines for experimental controls interaction.** NuSTAR Seminar, 16.04.2008.

L.-W. Chen, Shanghai: **Probing the nuclear symmetry energy with heavy-ion reactions induced by neutron rich nuclei.** Theorie-Seminar, 16.04.2008.

J. Adamczewski, H. Essel, S. Linev: **Data Acquisition Backbone Core DABC: Design, Performance, MBS-Demo.** IT/EE-Palaver, 22.04.2008.

Peter Spiller, GSI Darmstadt: **Perspectives for Plasma Physics Experiments by the SIS18 upgrade Program.** Physik dichter Plasmen mit Schwerionen- und Laserstrahlen, 22.04.2008.

Ulrich Heinz, The Ohio State University/CERN: **Quark soup - the perfect liquid.** GSI Kolloquium, 22.04.2008.

C. Eichhorn, Univ. Stuttgart: **Laser-induced fluorescence on xenon for application on ion thruster plasma parameter investigations: First steps towards two-photon spectroscopy.** Atomphysik-Seminar, 23.04.2008.

G. Thiamova, Waterloo: **Coupled SU(3) models of rotational states in nuclei and quasi-dynamical symmetry.** Theorie-Seminar, 23.04.2008.

Brigitte Cros, Universite Paris Sud, Orsay: **Controlled electron acceleration in plasmas: Overview of the EuroLEAP project.** Physik dichter Plasmen mit Schwerionen- und Laserstrahlen, 29.04.2008.

Ulf-G. Meissner, Univ. Bonn and FZ Jülich: **Nuclear physics from simulations.** GSI Kolloquium, 29.04.2008.

B. O'Rourke, Queens University Belfast and GSI Darmstadt: **Collisions of Highly Charged Ions with Electrons and Surfaces.** Atomphysik-Seminar, 30.04.2008.

Birgit Kindler, GSI: **Solid targets at GSI.** NuSTAR Seminar, 30.04.2008.

Federico Carminati/CERN: **Software Development in HEP: a critical look.** GSI Kolloquium, 30.04.2008.

Jürgen Meyer-ter Vehn, Max-Planck-Institut für Quantum Optik, Garching: **Neue Ideen zur Erzeugung von intensiven Ionen-, Elektronen- und Photonen-Pulsen durch Laserbestrahlung von Nanometer-dicken Folien.** Physik dichter Plasmen mit Schwerionen- und Laserstrahlen, 06.05.2008.

D. B. Thorn, Univ. of California, Davis, and Lawrence Livermore Nat. Lab. Livermore, USA: **Spectroscopic Investigations of Highly Charged Xenon with a Quantum Microcalorimeter.** Atomphysik-Seminar, 07.05.2008.

Concettina Sfienti, GSI: **Exploring the symmetry energy with heavy ion reactions.** NuSTAR Seminar, 11.05.2008.

Jens Stadlmann, GSI: **From source to target.** NuSTAR Seminar, 14.05.2008.

M. Bussmann, FZ Dresden: **Laser-Cooling of Ion Beams at Relativistic Energies.** Atomphysik-Seminar, 14.05.2008.

Dao Tien Khoa, INST Hanoi: **From suppression of nu-**

clear rainbow to a flaw in DWBA analysis of quasi-elastic nucleus-nucleus scattering. NuSTAR Seminar, 19.05.2008.

Björn Manuel Hegelich, Los Alamos National Laboratory, USA: **Relativistic Particle Acceleration and High-field physics with Ultrahigh Power Lasers.** Physik dichter Plasmen mit Schwerionen- und Laserstrahlen, 20.05.2008.

Marco Durante/GSI: **Mission impossible? Protection from cosmic radiation for Mars exploration.** GSI Kolloquium, 20.05.2008.

T. Lange, Uni Köln: **Vollautomatische Installationen mit FAI.** IT/EE-Palaver, 20.05.2008.

N. Tsirova, Samara: **Electromagnetic structure of composite systems in Poincare-invariant quantum mechanics.** Theorie-Seminar, 21.05.2008.

Paulo Fonte, LIPC: **Timing Resistive Plate Chamber applications in HADES and in Medical Imaging.** NuSTAR Seminar, 21.05.2008.

S. Toleikis, DESY Hamburg: **Exploring Warm Dense Matter FLASH.** Atomphysik-Seminar, 21.05.2008.

P. McKenna, University of Strathclyde, Glasgow: **Manipulating MeV proton acceleration and electron transport in solid targets irradiated by ultraintense laser pulses.** Physik dichter Plasmen mit Schwerionen- und Laserstrahlen, 27.05.2008.

Paul Hoyer/University of Helsinki: **Hadron scattering and QCD.** GSI Kolloquium, 27.05.2008.

A. Tawfik, Cairo: **The early universe, phase transitions and cosmological consequences.** Theorie-Seminar, 28.05.2008.

Pierre Capel, ULB: **Analysis of 8B Coulomb breakup within a Dynamical Eikonal Approximation.** NuSTAR Seminar, 28.05.2008.

V. Shevelko, Lebedev Physical Institute, Moscow: **Multi-Electron Ionization Cross Sections for Fast Heavy Ions Colliding with Neutral Atoms in the Energy-Deposition Model.** Atomphysik-Seminar, 28.05.2008.

A. P. L. Robinson, STFC Rutherford-Appleton Lab.: **Laser-Acceleration of Ions by the Radiation Pressure Acceleration Mechanism.** Physik dichter Plasmen mit Schwerionen- und Laserstrahlen, 03.06.2008.

Gerald Gabrielse/Harvard: **One-Electron Quantum Cyclotron: A New Value for the Electron Magnetic Moment and the Fine Structure Constant.** GSI Kolloquium, 03.06.2008.

G. Brenner, MPI-K Heidelberg: **QED contributions to lifetime of metastable states.** Atomphysik-Seminar, 04.06.2008.

Christian Stöckl: **Short - Pulse Experiments at LLE.** Physik dichter Plasmen mit Schwerionen- und Laserstrahlen, 05.06.2008.

Patrick Kluth: **Material Modification using Swift Heavy Ion Irradiation: from Nanoparticles to Ion Tracks.** Seminar der Materialforschung, 06.06.2008.

4th NoRHDia WorkshopGSI: Novel Radiation Hard Diamond Detectors for Hadron Physics. 08.-10.06.2008.

Frank Maas/GSI: **The structure of the nucleon, from parity violation to antiproton annihilation.** GSI Kolloquium, 10.06.2008.

H. Brand: **Object oriented programming with LabVIEW.** IT/EE-Palaver, 10.06.2008.

Ingo Hofmann, GSI Darmstadt: **Energy equipartition in intense beams.** Physik dichter Plasmen mit Schwerionen- und Laserstrahlen, 10.06.2008.

Gaitanos Theodoros, Univ. Giessen: **Theoretical description of fragment formation in reactions at SIS/GSI energies within a combined BUU+SMM approach.** NuSTAR Seminar, 11.06.2008.

Martin Veselsky, Bratislava: **Possibilities for investigations of hot exotic nuclei at FAIR.** NuSTAR Seminar, 11.06.2008.

V. Shevelko, Lebedev Physical Institute, Moscow: **Single-Electron Capture of Fast Heavy Ions Colliding with Residual-Gas Atoms and Molecules.** Atomphysik-Seminar, 11.06.2008.

Thomas Walther, TU Darmstadt: **Was ist Licht?** Wissenschaft für Alle, 14.06.2008.

A. Siemko, CERN: **Performance Evaluation and Quality Assurance Management during the Cold Series Power Tests of the LHC Main Lattice Magnets.** Beschleuniger-Palaver, 17.06.2008.

Naeem A. Tahir, GSI Darmstadt, and Alexander Shutov, IPCP Chernogolovka: **Development of Simulation Models and Their Applications to High Energy.** Physik dichter Plasmen mit Schwerionen- und Laserstrahlen, 17.06.2008.

Wolfram Fischer/Brookhaven: **RHIC status and upgrade plans.** GSI Kolloquium, 17.06.2008.

A. Blazevic, GSI Darmstadt: **Interaction Studies of Swift Heavy Ions Penetrating Laser (PHELIX/nhelix) Generated Plasma.** Atomphysik-Seminar, 18.06.2008.

Q. Wang, Hefei: **BCS-BEC crossover in relativistic systems.** Theorie-Seminar, 18.06.2008.

Roman Gernhaeuser, TU-Muenchen: **Probing the single particle structure around ^{54}Ca with one-neutron knockout.** NuSTAR Seminar, 18.06.2008.

Carsten Fortmann, Universität Rostock: **Diagnostics of dense plasmas using Thomson scattering.** Physik dichter Plasmen mit Schwerionen- und Laserstrahlen, 24.06.2008.

Karl-Heinz Kampert/Universität Wuppertal: **The most energetic particles in the Universe - Results from the Pierre Auger Observatory.** GSI Kolloquium, 24.06.2008.

L. Bureyeva, Institute of Spectroscopy of the RAS: **Universal representation of Hydrogen-like spectral line shapes in astrophysical and laboratory plasmas.** Atomphysik-Seminar, 25.06.2008.

Leonid Batist, PNPI-Gatchina: **Gamow-Teller strength systematics from beta+ decay near ^{100}Sn.** NuSTAR Seminar, 25.06.2008.

M. Russina, HMI: **Research capabilities at Berlin Neutron Scattering Center.** Theorie-Seminar, 25.06.2008.

S. Kalcher, Uni Heidelberg: **General Purpose Computation on NVIDIA Graphical Processing Units.** IT/EE-Palaver, 27.06.2008.

Jose Alonso: **Festkollouium- 60. Geburtstag von Hartmut Eickhoff . Medical accelerators - history and visions.** GSI Kolloquium, 01.07.2008.

Vladimir Y. Ternovoi, Institute of Problems of Chemical Physics, Cernogolovka, Russia: **Experimental Study of Metal Liquid-Gas Transition under Intense Shock Wave Loading.** Physik dichter Plasmen mit Schwerionen- und Laserstrahlen, 01.07.2008.

P. Müller, Argonne National Laboratory: **Laser Trapping and Probing of Exotic Helium Isotopes.** Atomphysik-Seminar, 02.07.2008.

Stoyanka Ilieva, GSI: **Study of the nuclear density distribution of exotic Be and B nuclei with proton elastic scattering.** NuSTAR Seminar, 02.07.2008.

Vladimir Novikov, Keldysh Institute of Applied Mathematics, Moscow, Russia: **Quantum-Statistical Models of Hot Dense Matter.** Physik dichter Plasmen mit Schwerionen- und Laserstrahlen, 03.07.2008.

Robert E. Grisenti, J. W. Goethe-Universität and GSI-Darmstadt: **Cryogenic liquid microjet sources and their application for laser-driven microscopic plasma generation.** Physik dichter Plasmen mit Schwerionen- und Laserstrahlen, 08.07.2008.

D. Fischer, MPI-K Heidelberg: **An ultra-cold target for precision studies of heavy-ion atom collisions.** Atomphysik-Seminar, 09.07.2008.

David Miller, MSU: **Investigating 'island of inversion' nuclei 31,33Mg with gamma-ray angular distribution and linear polarization with fast in-flight beams.** NuSTAR Seminar, 09.07.2008.

PANDA Mechanical Design Workshop. 09.-10.07.2008.

Kornelius Nielsch, Institut für Angewandte Physik, Universität Hamburg: **Thermoelektrische Nanostäbe aus Verbindungshalbleitern.** Seminar der Materialforschung, 20.07.2008.

V. Shevelko, P. N. Lebedev Physical Institute, Moscow: **Multiple Ionization of Fast Heavy Ions by Neutral Atoms in the Energy-Deposition Model.** Beschleuniger-Palaver, 08.08.2008.

Sylvain Costes, Lawrence Berkeley Laboratory, USA: **Modeling the cellular response to heavy ions exposure: from y-H2AX foci formation to population behavior.** Biophysik-Seminar, 11.08.2008.

Jörn Splinter, GSI: **Rendezvous mit Folgen - Wenn ein Schwerion die DNA trifft.** Wissenschaft für Alle, 13.08.2008.

N. Pyka, FAIR Synchrotrons: **Planungsstand der Strahlextraktion aus den FAIR Synchrotrons und Verbesserungen für die SIS18 Extraktion.** Beschleuniger-Palaver, 14.08.2008.

V. Rozanov, P. N. Lebedev Physical Institute Moscow: **Analysis of the energy transfer in low-density foam-like targets in the experiments carried out at the laser facilities PALS and LIL.** Physik dichter Plasmen mit Schwerionen- und Laserstrahlen, 28.08.2008.

Adriana de O. Delgado, Universidade de So Paulo, So Paulo, Brazil: **Study of ion beam irradiated polymers.** Seminar der Materialforschung, 29.08.2008.

XXX ECLIM European Conference on Laser Interaction with Matter. 02.09.2008.

K. Seth, Evanston: **Recent developments in quarkonium physics.** Theorie-Seminar, 03.09.2008.

Klaus Unser: **A Review on Beam Diagnostics and Accelerator Instrumentation and New Proposals for LHC and FAIR.** Beschleuniger-Palaver, 11.09.2008.

Yefim Aglitskiy, Science Applications International Corporation, McLean, and Naval Research Laboratory, Washington: **Classical and Ablative Richtmyer-Meshkov and Rayleigh-Taylor Instabilities and Other ICF-Relevant Plasma Flows Diagnosed with Monochromatic X-Ray Imaging.** Physik dichter Plasmen mit Schwerionen- und Laserstrahlen, 12.09.2008.

Thomas Schönitz, National Instruments, München: **Schneller von Messdaten zum Ergebnisbericht mit NI DIAdem 11.** IT/EE-Palaver, 16.09.2008.

Thomas Schönitz, National Instruments: **Schneller von Messdaten zum Ergebnisbericht mit NI DIAdem 11.** Sonderseminar, 16.09.2008.

Peter Malzacher, GSI: **Datenauswertung im Wunderland: Vom ALICE Detektor zum besseren Verständnis der Kernmaterie.** Wissenschaft für Alle, 17.09.2008.

Beatriz Jurado, CENBG: **The surrogate reaction method: a technique to determine cross sections of short-lived nuclei.** NuSTAR Seminar, 01.10.2008.

Elena A. Stefanova, Texas Southern University: **Staggered M1 transitions in a four-quasiparticle structure in 66Ge. Near spherical shell-model structure of the 2+ state in ^{40}Ar**

from g-factor measurements. NuSTAR Seminar, 06.10.2008.

Frank Merrill, LANL: **High Energy Proton Radiography.** Sonderseminar, 06.10.2008.

T. Debelle, National Instruments: **Leveraging off-the-shelf technologies for large physics experiments.** IT/EE-Palaver, 07.10.2008.

A. Kumar, GSI Darmstadt: **Two-photon Decay of the 1s2s 1S0 State in Helium-like Heavy Ions.** Atomphysik-Seminar, 15.10.2008.

Norbert Pietralla, TU Darmstadt: **Kugeln, Zigarren und Birnen: Wie sehen Atomkerne aus?** Wissenschaft für Alle, 15.10.2008.

ExtreMe Matter Institute EMMI - Kick-Off Meeting & Symposium. 16.-17.10.2008.

Marian Cholewa, Monash Centre for Synchroton Science MCSS, Monash Univeristy, Australia: **New materials for highly efficient and high speed detectors.** Seminar der Materialforschung, 20.10.2008.

Fritz Riehle/Physikal.-Techn. Bundesanstalt: **Optical Atomic Clocks.** GSI Kolloquium, 21.10.2008.

J. Macek, Univ. of Tennessee and Oak Ridge Nat. Lab.: **Imaging of Atomic Wave Functions.** Atomphysik-Seminar, 21.10.2008.

M. Fraiß: **Lizenzmanagement für Windows und Applikationen.** IT/EE-Palaver, 21.10.2008.

W. Nörtershäuser, Univ. Mainz: **On-line and off-line applications of a frequency comb at GSI.** Atomphysik-Seminar, 21.10.2008.

Carsten Welsch, MPI-K Heidelberg: **Atomic Physics and Accelerator Sciences in the QUASAR Group.** Atomphysik-Seminar, 22.10.2008.

David Neely, Rutherford Appleton Laboratory: **The potential for Laser driven ion acceleration in the UK.** Physik dichter Plasmen mit Schwerionen- und Laserstrahlen, 28.10.2008.

H. Kreiser: **Rechenzentrum für Alice-Tier-2 ein neuer Raum und neue Infrastruktur.** IT/EE-Palaver, 28.10.2008.

Josef Jochum/Universität Tübingen: **Direct Dark Matter Search.** GSI Kolloquium, 28.10.2008.

Shadi Salem, GSI Darmstadt: **Simultaneous excitation and ionization of He-like Uranium ions in relativistic collisions and the angular distribution of photons after REC.** Atomphysik-Seminar, 29.10.2008.

NuPNET OPEN DAYS 2. 30.-31.10.2008.

E. Plagnol, APC Paris: **From the complexity of heavy ions to the simplicity of black holes ... or is it vice versa?** Symposium on the occasion of Wolfgang Trautmann's 65th Birthday, 03.11.2008.

H. Wolter, LMU München: **ALADIN"s magic lantern: light into the mechanism of heavy ion collisions.** Symposium on the occasion of Wolfgang Trautmann's 65th Birthday, 03.11.2008.

Regina Reuschl, GSI Darmstadt und Univ. Münster: **Quantum electrodynamic effects in heavy H- and He-like systems.** Atomphysik-Seminar, 05.11.2008.

Margit Zacharias/Universität Freiburg: **Nanostructures-la carte: From size controlled Si nanocrystals to ordered arranged ZnO Nanowires.** GSI Kolloquium, 11.11.2008.

O. Wirth: **Ausbau der GSI WAN Anbindung für Alice Tier 2.** IT/EE-Palaver, 11.11.2008.

Alexander Dorn, MPI-K, Heidelberg: **Studies of Electron- and Photon-Induced Atomic Few-Body Reactions Using Multi-Particle Imaging Techniques.** Atomphysik-Seminar, 12.11.2008.

Markus Roth, GSI: **Die Physik von Star Trek.** Wissenschaft für Alle, 12.11.2008.

Thomas Neff, GSI: **Exotic nuclei studied in Fermionic Molecular Dynamics.** NuSTAR Seminar, 12.11.2008.

W. G. Holzmann, Columbia: **Probing bulk partonic matter with jets from RHIC to LHC.** Theorie-Seminar, 12.11.2008.

Alexander Molodozhentsev, KEK: **Beam Dynamics in Main Ring of the Japanese Particle Accelerator Complex, JPARC.** Beschleuniger-Palaver, 13.11.2008.

Shawn McCaslin, National Instruments: **Algorithm Engineering for Multicore-Systems.** Sonderseminar, 13.11.2008.

International Symposium on Heavy Ion Physics, ISHIP 2008. 17.-20.11.2008.

Theodor W. Hänsch/MPI f. Quantenoptik Garching & LMU: **A Passion for Precision.** GSI Kolloquium, 18.11.2008.

Matthias Kühnel, Univ. Frankfurt: **Cryogenically cooled droplet beam internal target at the ESR.** Atomphysik-Seminar, 19.11.2008.

Eike Hohmann, PSI Villigen: **Neutronenspektrometrie an Hochenergiebeschleunigern in gepulsten Feldern hinter Abschirmungen.** Sonderseminar, 21.11.2008.

EMMI 2008 Workshop on Plasma Physics with Intense Ion and Laser Beams. 21.-22.11.2008.

Dennis Klein: **Verteilte Versionskontrolle mit Git.** IT/EE-Palaver, 25.11.2008.

Daniel Rodrguez, Universidad de Huelva, Spain: **Measurement of the β-ν correlation in the decay of ^{6}He using a**

transparent Paul trap. Atomphysik-Seminar, 26.11.2008.

Marco Meoni, CERN: **Current status of CAF and ongoing PROOF developments.** Sonderseminar, 26.11.2008.

Olga Ershova, GSI: **Acoustic effects produced by particles interacting with matter and their application for high energy neutrino astrophysics.** NuSTAR Seminar, 26.11.2008.

Oleksandr Chorniy, GSI: **RF capture in single and dual harmonic rf buckets at high intensities in SIS-18.** Beschleuniger-Palaver, 27.11.2008.

Fritz Caspers, CERN-AB-RF: **Electron cloud diagnostics with the microwave transmission method.** Beschleuniger-Palaver, 01.12.2008.

Dino Jaroszynski, University of Strathclyde: **The ALPHA-X project: Advanced Laser Plasma High-energy Accelerators towards X-rays.** Physik dichter Plasmen mit Schwerionen- und Laserstrahlen, 02.12.2008.

Mike Dunne/Rutherford Appleton Laboratory - UK: **HiPER: The European path to laser fusion and related plasma science.** GSI Kolloquium, 02.12.2008.

Lucia Caceres Monllor, GSI: **Nuclear structure studies in the vicinity of the doubly-magic ^{132}Sn nucleus.** NuSTAR Seminar, 03.12.2008.

TASCA 08 - 7th Workshop on Recoil Separator for Superheavy Element Chemistry. 08.-12.12.2008.

XXVII. PANDA Collaboration Meeting. 08.-12.12.2008.

Klaus Eidmann, MPQ Garching: **Erzeugung und Anwendung lasergeheizter Hohlräume.** Physik dichter Plasmen mit Schwerionen- und Laserstrahlen, 09.12.2008.

Norbert Holtkamp/ITER Organization: **Overview and challenges of the ITER Project.** GSI Kolloquium, 09.12.2008.

Holger Gies, Univ. Jena: **Quantum vacuum phenomena in strong fields.** Atomphysik-Seminar, 10.12.2008.

Klaus Sümmerer, GSI: **High-energy reactions to study low-energy phenomena - Nuclear Astrophysics at GSI.** NuSTAR Seminar, 10.12.2008.

Daniel Severin, TU Darmstadt: **Radiation hardness of FAIR relevant insulators A challenge for materials analysis.** Beschleuniger-Palaver, 11.12.2008.

Adriana Gagyi-Palffy, Max-Planck-Institut für Kernphysik, Heidelberg: **Coupling Nuclei to Intense Photon Fields.** Physik dichter Plasmen mit Schwerionen- und Laserstrahlen, 16.12.2008.

Gabriel Martinez Pinedo, GSI: **A primer in weak interaction processes in supernova evolution.** NuSTAR Seminar, 16.12.2008.

Giacomo Cuttone/INFN Catania, Italien: **Light Ion Fragmentation Measurements for Medical and Space Applications.** GSI Kolloquium, 16.12.2008.

S. Guskov, P. N. Lebedev Physical Institute Moscow: **Non-Equilibrium Laser-Produced Plasma of volume-structured media.** Physik dichter Plasmen mit Schwerionen- und Laserstrahlen, 16.12.2008.

Yuri A. Litvinov, GSI: **Nuclear Physics in Storage Rings.** Physik dichter Plasmen mit Schwerionen- und Laserstrahlen, 16.12.2008.

Verleihung des Christoph-Schmelzer-Preises 2008. 16.12.2008.

Fritz Bosch, GSI: **Am farbigen Abglanz haben wir die Welt - Zur Physik des Lichts.** Wissenschaft für Alle, 17.12.2008.

Michael Dworschak, GSI: **The storage ring project at IMP in Lanzhou recent developments in the field of isochronous mass measurements.** Atomphysik-Seminar, 17.12.2008.

Experiments performed at the GSI accelerators in 2008

Compiled by Andreas Tauschwitz, beam time coordinator 2007/2008

In all tables 1 shift represents 8 hours of beam delivered to an experiment including necessary accelerator tuning time.

Exp	Short title	Spokesperson	Area	Ion	Shifts main	Shifts parasitic
U182	Hs chemistry and development of SHE chemistry	Kratz	X1	^{22}Ne	5	
U211	Study of the even-even nucleus 260-Sg	Sulignano	Y7	^{36}S		24
U217	Mass measurements at SHIPTRAP	Block	Y7	^{12}C	9	
U219	TASCA commissioning	Schädel	X8	^{22}Ne, ^{48}Ca, ^{64}Ni	60	33
U221	Test of a CVD diamond detector	Bräuning-Demian	HTA	^{124}Xe	5	
U222	Mass of rp-nuclei at SHIPTRAP	Plaß	Y7	^{36}Ar	15	
U226	Energy loss in laser generated plasmas	Roth	Z6	^{36}S, ^{36}Ar		29
U229	Island of strong deformationabove Z = 82	Andreyev	Y7	^{40}Ca	21	
U231	Q-value effects on the production of superheavy elements	Türler	X1	^{36}S	39	
U233	Study of fusion of the reaction 64Ni + 238U => 302/120	Hofmann	Y7	^{22}Ne, ^{64}Ni	295	34
U235	Neutron-deficient isotopes of uranium and plutonium	Heredia	Y7	^{40}Ca	3	
U238	Mass Measurements of nobelium isotopes with SHIPTRAP	Block	Y7	^{12}C, ^{48}Ca	24	4
UBIO	Biology Experiments at UNILAC	Scholz	X6	^{12}C, ^{64}Ni, ^{208}Pb, ^{124}Xe	13	33
UMAT	Material science at UNILAC	Trautmann,Voss	X0	^{12}C, ^{64}Ni, ^{181}Ta, ^{197}Au, ^{208}Pb	90	11

Exp	Short title	Spokesperson	Area	Ion	Shifts main	Shifts parasitic
S245	Bound and unbound nuclei near and at the driplines	Jonson	HTC	^{12}C	8	
S293	Proton-induced fission in the GeV domain with SPALADIN	Boudard	FRS	^{181}Ta	12	
S310	g-factors of isomeric states	Balabanski	FRS	^{64}Ni		27
S317	High-intensity effects and beam induced losses	Hofmann	SIS	^{40}Ar	6	
S319	HypHI	Saito	HTA	^{6}Li	3	
S325	Charged Kaon Measurements with FOPI	Herrmann	HTB	^{58}Ni, ^{64}Ni	20	5
S327	Dipole response of proton-rich nuclei - pygmy and giant resonances in 32Ar and 34Ar	Boretzky	HTC	^{36}Ar, ^{40}Ar	26	1
S330	Investigation of 100Sn	Faestermann	FRS	^{124}Xe	58	3
S331	High-Energy-Density Matter Generated by Intense Heavy Ion Beams	Mintsev	HHT	^{124}Xe, ^{238}U		30
S333	Vector meson production in proton nucleus and pion nucleus collisions	Salabura	HAD	p, ^{12}C	92	
S341	Neutron knockout reactions from proton-rich carbon isotopes	Enders	FRS	^{12}C	6	1
S347	Along the N=126 closed shell	Podolyak	FRS	^{238}U		20
S349	Search for the kaonic nuclear cluster K^-pp with FOPI	Fabbietti	HTB	p		24
S352	Study of N>>=Z proton dripline nuclei 96, 97, 98Cd	Blezhev	FRS	^{124}Xe	15	
S357	Detector tests of a multi-track detector for spallation studies	Ducret	HTC	^{12}C, ^{64}Ni		11
S366	Detektor test for CBM	Niebur	HTD	p		9
SBIO	Biology experiments at SIS	Schardt, Scholz	HTM, HTA	^{12}C, ^{132}Xe	22	
SiSt	Radiation safety	Fehrenbacher	HTA	^{12}C	6	
SMAT	Materials research at SIS	Trautmann	HTA	^{124}Xe, ^{132}Xe, ^{238}U	17	
STHE	Therapy studies	Schardt	HTA	^{12}C	4	

E000	ESR development	Steck	ESR	^{64}Ni, ^{124}Xe, ^{132}Xe	21	
E056	Storage lifetimes and cross sections	Dubois	ESR	^{124}Xe, ^{238}U	12	
E069	Bremsstrahlung during electron transfer to continuum	Hagmann	ESR	^{238}U	18	
E073	Electron Screening and alpha-decay	Musumarra	FRS	^{238}U	10	
E074	Radiative Double Electron Capture	Warczak	ESR	^{124}Xe	8	
E075	HITRAP commissioning	Kester	HI-TRAP	^{64}Ni, ^{197}Au	35	
E077	Spectroscopy of two-body beta-decays	Litvinov	ESR	^{132}Xe	10	
E079	Isotope shift in the dielectronic recombination of L-shell ions	Kozhuharov	ESR	^{238}U	5	
E080	Study of a novel low-Z internal-target cluster beam	Grisenti	ESR	^{124}Xe	14	
E082	Single-Ion spectroscopy of two-body beta-decays	Litvinov	ESR	^{132}Xe	38	

Facts and Figures

Compiled by J. Heilmann, C. Kausch

Gesellschafter/Shareholders since 1969, December 17th

Federal Republic of Germany	90% of budget (and of share capital)
State of Hesse/Land Hessen	10% of budget (and of share capital)

Accelerators

FAIR	Facility for Antiprotons and Ion Research		pre- construction R&D
UNILAC	UNIversal Linear ACcelerator	13 MeV/u for U	in operation since 1976
SIS	Schwer-Ionen-Synchrotron	50–1000 MeV/u for U	in operation since 1989
ESR	Experimental Storage Ring	3–400 MeV/u for U	in operation since 1990

Users of the accelerator complex

In 2008, GSI provided access to 25 experimental areas to more than 1550 scientific users.

GSI Funding in Mio. Euro

research area Structure of Matter	78.3	
research area Health	3.5	
special tasks and Helmholtz-ctivities	2.8	
third party funding	5.4	
total budget		**90 Mio. Euro**

Personnel 2008 in person years

research area Structure of Matter	374	
FAIR-activities (Structure of Matter)	137	
research area Health	33	
management and management support	66	
scientific and technical infrastructure	226	
personnel involved in projects funded by nat./internat. funding agencies	124	
total personnel		**960 person years**

Statutory organs and scientific advisory committees of GSI (2008)

Compiled by K.-D. Groß

Supervisory Board/Aufsichtsrat:

Dr. B. Vierkorn-Rudolph [chair],
Bundesministerium für Bildung und Forschung, Bonn/Berlin (Germany),
as representative of the Federal Republic of Germany

Ministerialrat Dr. R. Koepke,
Bundesministerium für Bildung und Forschung, Bonn/Berlin (Germany),
as representative of the Federal Republic of Germany

Ministerialdirigent Dr. R. Bernhardt,
Hessisches Ministerium für Wissenschaft und Kunst, Wiesbaden (Germany),
as representative of the State Hessen in Germany

Prof. Dr. R. Klanner,
Universität Hamburg/DESY (Germay),
as representatives of the Scientific Council of the GSI

Scientific Directorate/Wissenschaftliches Direktorium WD:

Prof. Dr. H. Stöcker, C. Neumann,
Dr. H. Eickhoff, Prof. Dr. K.-H. Langanke, B. Schönfelder,

Divisions/Direktionsbereiche:

Accelerator: H. Eickhoff
Administration: C. Neumann
FAIR TD: D. Krämer
Research: K. Langanke
Scientific and Technical Infrastructure: B. Schönfelder

Research Departments/Forschungsabteilungen:

ALICE: P. Braun-Munzinger
Atomic Physics: T. Stöhlker
Biophysics: M. Durante/G. Kraft
CBM: P. Senger
FOPI: Y. Leifels
HADES: J. Stroth
Hadron Physics I: K. Peters
Hadron Physics II: F. Maas
Materials Research: R. Neumann
Nuclear Reactions and Astrophysics: T. Aumann
Nuclear Structure Physics: C. Scheidenberger
Plasma Physics and PHELIX: T. Stöhlker/K. Witte
Superheavy Element/Nuclear Chemitry: S. Hofmann/M. Schädel
Theory: Lattice QCD: F. Karsch
Theory: Nuclear Structure and Astrophysics: K. Langanke
Theory: Transport and Simulation: H. Stöcker
Theory: QCD and Hadron Physics: J. Wambach

Scientific Council/Wissenschaftlicher Rat WR:
<http://www.gsi.de/informationen/users/EAC/wr/>

R. Klanner [chair], Universität Hamburg (Germany); D. von Harrach [vice chair], Johannes-Gutenberg-Universität Mainz (Germany); C. Leemann, Thomas Jefferson National Accelerator Facility, Newport News (USA); B. Mueller, Duke University, Durham, North Carolina (USA); S. Myers, CERN AB, Geneva (Switzerland); T. Roser, BNL, Upton (USA); A. Shotter, TRIUMF, Vancouver (Canada); M. Soyeur, DSM/DAPNIA/SPhN, Gif-sur-Yvette (France); R. Sauerbrey, Forschungszentrum Rossendorf, Dresden (Germany); D. Vernhet, Université Paris (France); M. C. Wiescher, University of Notre Dame, Notre Dame, Indiana (USA).
Secretary: K.-D. Groß

Scientific Committee/Wissenschaftlicher Ausschuss WA:
<http://www-w2k.gsi.de/wa/scientific_committee.htm>

S. Richter [chair]; H. Simon [vice chair]; A. Bräuning-Demian; T. Cornelius; B. Friman; Y. Leifels; B. Lommel; P. Malzacher; H. Reich-Sprenger; [C. Scheidenberger]; L. Schmitt; M. Scholz; P. Senger; J. Stadlmann; A. Tauschwitz; M. Traxler; D. Varentsov; G. Walter; H. Weick; M. Kreiser (for the Betriebsrat).

Scientific Advisory Committees to GSI

GSI General Programme Advisory Committee G-PAC:
<http://www.gsi.de/informationen/users/EAC/ea/>

J. Aichelin, SUBATECH, Nantes (France); W. Catford, University of Surrey, Guildford (UK); P. Giubellino, INFN Turin, Torino (Italy); R. Hoekstra, KVI Groningen, Groningen (The Netherlands); R. Krücken, Technische Universität München, Physik-Department (Germany); M. Lewitowicz, GANIL, Caen (France); T. Peitzmann, Utrecht University (The Netherlands); N. Pietralla, Technische Universität Darmstadt, Darmstadt (Germany); H. Schatz, Michigan State University, East Lansing (USA); M. Wada, RIKEN, Saitama (Japan); M. Weidemüller, Universität Freiburg (Germany); E. Widmann, Stefan-Meyer-Institut für subatomare Physik, Österreichische Akademie der Wissenschaften, Vienna (Austria).
Secretary: A. Tauschwitz

GSI Phelix and Plasmaphysics Program Advisory Committee (PPAC):
<http://www.gsi.de/informationen/users/EAC/ppac/>

M. H. R. Hutchinson [Chair], Rutherford Appleton Lab (United Kingdom); S. Jacquemot, LULI, Ecole Polytechnique, Palaiseau (France); G. Logan, LBL Berkeley (USA); T. A. Mehlhorn, Sandia National Laboratories, Albuquerque (USA); R. Sauerbrey, Forschungszentrum Rossendorf, Dresden (Germany); B. Sharkov, Inst. of Theoretical and Experimental Physics Moscow (Russia).
Secretary: K. Füssel

GSI Biophysics & Radio-Biology Program Advisory Committee (Bio-PAC):
<http://www.gsi.de/informationen/users/EAC/bio-pac/>

G. Iliakis [Chair], Institut für Medizinische Strahlenbiologie Universitätsklinikum Essen (Germany); F. A. Cucinotto, NASA Johson Space Center, Houston TX (USA); R. Engenhardt-Cabillic, Klinik für Strahlentherapie Philipps-Universität Marburg Klinikum (Germany); B. Michael, Gray Lab (Cancer Research Trust), Mount-Vernon-Hospital, Northwood (United Kingdom); R. Okayasu, National Institute of Radiological Sciences, Chiba-shi (Japan); E. Pedroni, Paul Scherrer Institut, Villigen (Switzerland).
Secretary: K. Füssel

GSI Materials Research Program Advisory Committee (Mat-PAC):
<http://www.gsi.de/informationen/users/EAC/mat-pac/>

P. Apel, JINR Dubna (Russia); S. Bouffard, CEA-CNRS-ENSICAEN Caen (France); K. Hjort, University of Uppsala (Sweden); W. Wesch, Friedrich Schiller Universittät Jena (Germany).
Secretary: A. Tauschwitz

GSI Users' Group Executive Committee (UEC):

<http://www.gsi.de/forschung/usersgroup/index.html>

P. Regan (UK) [Chair-elected]; W. Cassing (Germany); D. Cortina (Spain); D. Dauvergne (France); T. Faestermann (Germany); J. Friese (Germany); U. Glasmacher (Germany), J. Jacoby (Germany); A. Jungclaus (Spain); R. Klein (Germany); J. Kratz (Germany); T. Kühl (Germany); R. Kulessa (Poland); S. Lang (Germany); L. Narici (Italy); M. Petrovici (Romania); P. Salabura (Poland); A. Warczak (Poland).

Scientific Coordination:

Dr. K. D. Groß

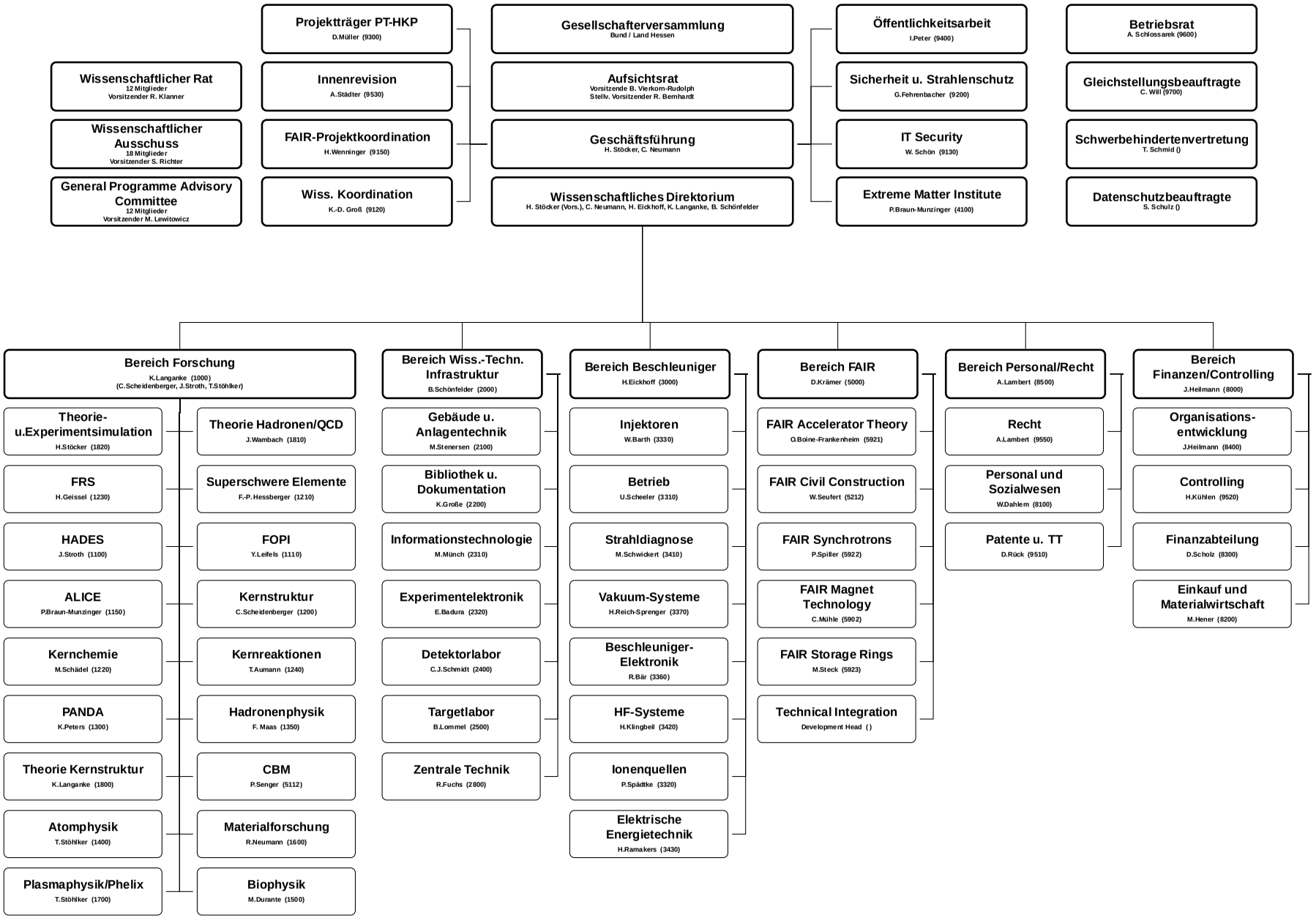

Stand April 24, 2009

List of Authors